ISSN 1998-6688 (Print)
ISSN 2959-8109 (Online)

ҚАЗАҚСТАН-БРИТАН ТЕХНИКАЛЫҚ УНИВЕРСИТЕТІНІҢ

ХАБАРШЫСЫ

HERALD

OF THE KAZAKH-BRITISH TECHNICAL UNIVERSITY

ВЕСТНИК

КАЗАХСТАНСКО-БРИТАНСКОГО ТЕХНИЧЕСКОГО УНИВЕРСИТЕТА

Volume 23, Issue 3
July-September, 2026

ҚАЗАҚСТАН-БРИТАН
ТЕХНИКАЛЫҚ УНИВЕРСИТЕТІНІҢ
ХАБАРШЫСЫ

HERALD
OF THE KAZAKH-BRITISH
TECHNICAL UNIVERSITY

ВЕСТНИК
КАЗАХСТАНСКО-БРИТАНСКОГО
ТЕХНИЧЕСКОГО УНИВЕРСИТЕТА

Алматы
№ 3 (78) 2026 г.

Издание зарегистрировано Министерством культуры и информации Республики Казахстан. Свидетельство о постановке на учет СМИ № 9757 – Ж от 03.12.2008 г.

Журнал зарегистрирован в Международном центре по регистрации сериальных изданий ISSN (ЮНЕСКО, г. Париж, Франция)

В журнале публикуются научные статьи на английском, казахском и русском языках по направлениям: компьютерные науки, математические науки, физические науки, нефтегазовая инженерия и геология, экономика и бизнес.

Подписной индекс – 74206

Издается с 2004 года. Выходит 4 раза в год.

УЧРЕДИТЕЛЬ
Казахстанско-Британский технический университет

ISSN 1998-6688 (Print)
ISSN 2959-8109 (Online)

© Казахстанско-Британский технический университет, 2026

Editor-in-chief – **B. Kulpeshov,** Doctor of Physical and Mathematical Sciences, academician of the National Academy of Sciences of the Republic of Kazakhstan, Professor, School of Applied Mathematics of JSC "Kazakh-British Technical University", Almaty, Kazakhstan

EDITORIAL BOARD

Section "Computer science"

Akzhalova A.Zh. - Candidate of Physical and Mathematical sciences, PhD, Professor, School of Information Technology and Engineering of JSC "Kazakh-British Technical University", Almaty, Kazakhstan;
Pak A.A. - Candidate of Technical Sciences, Associate professor, School of Information Technology and Engineering of JSC "Kazakh-British Technical University", Almaty, Kazakhstan;
Samigulina Z.I. - PhD, Professor, School of Information Technology and Engineering of JSC "Kazakh-British Technical University", Almaty, Kazakhstan;
Sadok Ben Yahia - Professor, University of Southern Denmark, Denmark;
Eduard Siemens - Professor, Anhalt University of Applied Sciences, Germany;
Uvalieva I.M. - PhD, Professor at the Faculty of Computer Science, EKTU named after D. Serikbayev, Ust-Kamenogorsk, Kazakhstan;
Serek A.G. - PhD, Associate Professor, «Astana IT University» LLP, Astana, Kazakhstan.

Section "Mathematical Sciences"

Kalmurzayev B.S. - PhD, Associate professor, School of Applied Mathematics of JSC "Kazakh-British Technical University", Almaty, Kazakhstan;
Sudoplatov S.V. - Doctor of Physical and Mathematical Sciences, Chief Researcher, Institute of Mathematics SB RAS; Head of Department, Novosibirsk State Technical University, Novosibirsk, Russia;
Bazhenov N.A. - Candidate of Physical and Mathematical Sciences, Senior Researcher, Institute of Mathematics SB RAS, Novosibirsk, Russia;
Nurkhaidarov E. - PhD, Associate Professor, Department of Mathematics, The Pennsylvania State University, University Park, USA.

Section "Physical Sciences"

Abdirakhmanov A.R. - PhD, Associate professor, JSC "KBTU", Almaty, Kazakhstan; University of Mons, Mons, Belgium;
Beysenkhanov N.B. - Doctor of Physical and Mathematical Sciences, Dean, Professor, School of Materials Science and Green Technologies JSC "KBTU", Almaty, Kazakhstan;
Laifa Boufendi - PhD, Professor, Orlean University, France

Section "Oil and Gas Engineering and Geology"

Ismailov A.A. - Candidate of Technical Sciences, Dean, Professor, School of Energy and Oil and Gas Industry of JSC "Kazakh-British Technical University", Almaty, Kazakhstan;
Korobkin V.V. - Candidate of Geological and Mineralogical Sciences, Professor, School of Geology of JSC "Kazakh-British Technical University", Almaty, Kazakhstan;
Kang Wanli - Professor, School of Petroleum Engineering, China University of Petroleum (East China), Qingdao, PR China;
Sarsenbekuly B. - PhD, Associate professor, School of Energy and Petroleum Engineering of JSC "Kazakh-British Technical University", Almaty, Kazakhstan;
Moldabaeva G.Zh. - Doctor of Technical Sciences, Professor, Department of Petroleum Engineering of K. Turysov Institute of Geology and Petroleum Engineering, KazNTU, Almaty, Kazakhstan.

Section "Economics and Business"

Narbaev T.S. - PhD, Professor, Business School JSC "KBTU", Almaty, Kazakhstan;
Kozhakhmetova A.K. - PhD, Assistant Professor, Business School JSC "KBTU", Almaty, Kazakhstan;
Aldashev A. - Professor, International School of Economics JSC "KBTU", Almaty, Kazakhstan;
Akhmedov E.T. - PhD, Associate Professor, Business School, JSC "Kazakh-British Technical University", Almaty, Kazakhstan;
Seitkazieva A.M. - Doctor of Economics, Professor/Business School JSC "KBTU", Almaty, Kazakhstan;
Gabriel Castelblanco - PhD, Assistant-Professor, University of Florida, Florida, USA;
Dubina I. - Doctor of Economic Sciences, Professor, Novosibirsk National Research State University (NSU);
Osei-Kyei Robert - PhD, Associate Professor, University of Western Sydney, Penrith, Australia;
Montag Josef - PhD, Senior Lecturer, Charles University, Prague, Czech Republic..

Бас редактор – **Кулпешов Б.Ш.,** ф.-м.ғ.д., ҚР ҰҒА академигі, профессор,
«ҚБТУ» АҚ Қолданбалы математика мектебі, Алматы қ., Қазақстан

РЕДАКЦИЯ АЛҚАСЫ

«Компьютерлік ғылымдар» бөлімі

Акжалова А.Ж. - ф.-м.ғ.к, PhD, профессор, «ҚБТУ» АҚ Ақпараттық технологиялар және инженерия мектебі, Алматы қ., Қазақстан;
Пак А.А. - т.ғ.к., қауымдастырылған профессор, «ҚБТУ» АҚ Ақпараттық технологиялар және инженерия мектебі, Алматы қ., Қазақстан;
Самигулина З.И. - PhD, профессор, «ҚБТУ» АҚ Ақпараттық технологиялар және инженерия мектебі, Алматы қ., Қазақстан;
Садок Бен Яхия - профессор, Оңтүстік Дания университеті, Дания;
Эдуард Сименс - профессор, Анхальт қолданбалы ғылымдар университеті, Германия
Увалиева И.М. - PhD, компьютерлік ғылымдар факультетінің профессоры, Д. Серікбаев атындағы ШҚТУ, Өскемен қ., Қазақстан;
Серік А.Ғ. - PhD, қауымдастырылған профессор, «Astana IT University» ЖШС, Астана қаласы, Қазақстан.

«Математикалық ғылымдар» бөлімі

Калмурзаев Б.С. - PhD, қауымдастырылған профессор, «ҚБТУ» АҚ Қолданбалы математика мектебі, Алматы қ., Қазақстан;
Судоплатов С.В. - ф.-м.ғ.д., профессор, РҒА СБ математика институтының бас ғылыми қызметкері; Новосібір мемлекеттік техникалық университеті, кафедра меңгерушісі, Новосібір қ., Ресей;
Баженов Н.А. - ф.-м.ғ.к., РҒА СБ математика институтының аға ғылыми қызметкері, Новосібір қ., Ресей;
Нурхайдаров Е. - PhD, қауымдастырылған профессор, Математика департаменті, Пенсильвания штатының университетI, Юниверсити-Парк, АҚШ.

«Физикалық ғылымдар» бөлімі

Әбдірахманов А.Р. - PhD, қауымдастырылған профессор, «ҚБТУ» АҚ, Алматы қ., Қазақстан; Монс университеті, Монс қ., Бельгия;
Бейсенханов Н.Б. - ф.-м. ғ. д., декан, профессор, Материалтану және жасыл технологиялар мектебі «ҚБТУ» АҚ, Алматы қ., Қазақстан;
Laifa Boufendi - PhD, профессор, Орлеан университеті, Франция.

«Мұнай газ инженериясы және геология» бөлімі

Исмаилов А.А. - т.ғ.к., декан, профессор, «ҚБТУ» АҚ Энергетика және мұнай-газ индустриясы мектебі, Алматы қ., Қазақстан;
Коробкин В.В. - геол.-минерал.ғ.к., профессор, «ҚБТУ» АҚ Геология мектебі, Алматы қ., Қазақстан;
Канг Ванли - профессор, Мұнай инженериясы мектебі, Қытай мұнай университеті (Шығыс Қытай), Циндао қ., ҚХР;
Сарсенбекұлы Б. - PhD, қауымдастырылған профессор, «ҚБТУ» АҚ Энергетика және мұнай-газ индустриясы мектебі, Алматы қ., Қазақстан;
Молдабаева Г.Ж. - тех.ғ.д., профессор, мұнай инженериясы кафедрасы, Қ. Тұрысов атындағы геология және мұнай-газ институты., ҚазҰТУ, Алматы қ., Қазақстан.

«Экономика және бизнес» бөлімі

Нарбаев Т.С. - PhD, профессор, Бизнес мектебі «ҚБТУ» АҚ, Алматы қ., Қазақстан;
Кожахметова А.К. - PhD, ассистент-профессор, Бизнес мектебі, «ҚБТУ» АҚ, Алматы қ., Қазақстан;
Алдашев А. - PhD, профессор, Халықаралық экономика мектебі, «ҚБТУ» АҚ, Алматы қ., Қазақстан;
Ахмедов Е.Т. - PhD, қауымдастырылған профессор, Бизнес мектебі, «Қазақстан-Британ техникалық университеті» АҚ, Алматы қ., Қазақстан;
Сейтказиева А.М. - э.ғ.к., профессор, Бизнес мектебі «ҚБТУ» АҚ, Алматы қ., Қазақстан;
Gabriel Castelblanco - PhD, ассистент-профессор, Флорида университеті, Флорида, АҚШ
Дубина И. - э.ғ.д., профессор, Новосибирск ұлттық зерттеу мемлекеттік университеті (НМУ);
Osei-Kyei Robert - PhD, қауымдастырылған профессор, Батыс Сидней университеті, Пенрит қ., Австралия;
Montag Josef - PhD, сениор-лектор, Карлов университеті, Прага қ., Чехия Республикасы.

Главный редактор – **Кулпешов Б.Ш.,** д.ф.-м.н., академик НАН РК, профессор,
Школа прикладной математики АО «КБТУ», г. Алматы, Казахстан

ЧЛЕНЫ РЕДКОЛЛЕГИИ

Раздел «Компьютерные науки»

Акжалова А.Ж. - к.ф.-м.н., PhD, профессор, Школа информационных технологий и инженерии АО «КБТУ», г. Алматы, Казахстан;
Пак А.А. - к.т.н., ассоциированный профессор, Школа информационных технологий и инженерии АО «КБТУ», г. Алматы, Казахстан;
Самигулина З.И. - PhD, профессор, Школа информационных технологий и инженерии АО «КБТУ», г. Алматы, Казахстан;
Садок Бен Яхия - профессор, Университет Южной Дании, Дания;
Эдуард Сименс - профессор, Анхальтский университет прикладных наук, Германия;
Увалиева И.М. - PhD, профессор факультета компьютерных наук, ВКТУ им. Д.Серикбаева, г. Усть-Каменогорск, Казахстан;
Серек А.Г. - PhD, ассоциированный профессор, ТОО «Astana IT University», г. Астана, Казахстан.

Раздел «Математические науки»

Калмурзаев Б.С. - PhD, ассоциированный профессор, Школа прикладной математики АО «КБТУ», г. Алматы, Казахстан;
Судоплатов С.В. - д.ф.-м.н., профессор, главный научный сотрудник, Институт математики СО РАН; зав. кафедрой, Новосибирский государственный технический университет, г. Новосибирск, Россия;
Баженов Н.А. - к.ф.-м.н., старший научный сотрудник, Институт математики СО РАН, г. Новосибирск, Россия;
Нурхайдаров Е. - PhD, ассоциированный профессор, Департамент математики, Университет штата Пенсильвания, Юниверсити-Парк, США.

Раздел «Физические науки»

Әбдірахманов А.Р. - PhD, ассоциированный профессор АО «КБТУ», г. Алматы, Казахстан; Университет Монса, г. Монс, Бельгия;
Бейсенханов Н.Б. - д.ф.-м.н., декан, профессор, Школа материаловедения и зеленых технологий АО «КБТУ», г. Алматы, Казахстан;
Laifa Boufendi - PhD, профессор, Университет Орлеана, Франция.

Раздел «Нефтегазовая инженерия и геология»

Исмаилов А.А. - к.т.н., декан, профессор, Школа энергетики и нефтегазовой индустрии АО «КБТУ», г. Алматы, Казахстан;
Коробкин В.В. - к.геол.-минерал.н., профессор, Школа геологии АО «КБТУ», г. Алматы, Казахстан;
Канг Ванли - профессор, Школа нефтяной инженерии, Китайский нефтяной университет (Восточный Китай), г. Циндао, КНР;
Сарсенбекұлы Б. - PhD, ассоциированный профессор, Школа энергетики и нефтегазовой индустрии АО «КБТУ», г. Алматы, Казахстан;
Молдабаева Г.Ж. - д.тех.н., профессор, кафедра нефтяной инженерии, Институт геологии и нефтегазового дела им. К. Турысова, КазНТУ, г. Алматы, Казахстан.

Раздел «Экономика и бизнес»

Нарбаев Т.С. - PhD, профессор, Бизнес-школа АО «КБТУ», г. Алматы, Казахстан;
Кожахметова А.К. - PhD, ассистент-профессор, Бизнес-школа АО «КБТУ», г. Алматы, Казахстан;
Алдашев А. - PhD, профессор, Международная школа экономики АО «КБТУ», г. Алматы, Казахстан;
Ахмедов Е.Т. - PhD, ассоциированный профессор, Бизнес-школа АО «Казахстанско-Британский технический университет», г. Алматы, Казахстан;
Сейтказиева А.М. - д.э.н., профессор, Бизнес-школа АО «КБТУ», г. Алматы, Казахстан;
Gabriel Castelblanco - PhD, ассистент профессора, Университет Флориды, Флорида, США.
Дубина И. - д.э.н., профессор, Новосибирский национальный исследовательский государственный университет (НГУ);
Osei-Kyei Robert - PhD, ассоциированный профессор, Университет Западного Сиднея, г. Пенрит, Австралия;
Montag Josef - PhD, сениор-лектор, Карлов университет, Прага, Чешская Республика.

МАЗМҰНЫ – СОДЕРЖАНИЕ

1 МАТЕМАТИКАЛЫҚ ҒЫЛЫМДАР
МАТЕМАТИЧЕСКИЕ НАУКИ

Koilyshov U., Zhapparova S., Nietbayev A.
Two-phase heat conduction problems with Sturm-type boundary
conditions and with a fractional time derivative....12
Altynbek D., Turmetov B.
On some nonlocal problems for the Poisson equation....24
Исахов А.А., Бейсембеков М.Е.
Применение физико-ориентированных нейронных сетей
для решения задач линейных уравнений в частных
производных с неоднородными смешанными граничными условиями....33
Вербовский В.В.
О локальном аналоге свойства строгого порядка
внутри сечения для линейно упорядоченных структур....47
Dekhkonov F.N., Usubjonov A.A.
On the control problem for a one-dimensional
pseudo-parabolic equation with a nonlocal boundary condition....55
Bayetov K.Kh.
Inverse problem for a parabolic equation
with a time-dependent coefficient in the boundary condition....70
Iskakova N.B., Bakirova E.A., Usmanov K.I.. Orumbayeva N.T.
On a boundary value problem for a loaded....80
Абдиманапова П.Б., Темешева С.М., Иманчиев А.Е., Мәжит Ж.Б.
Дифференциалдық теңдеу үшін сызықтық емес екі нүктелі
шеттік есептер әулетінің шешімін табу туралы....93
Satybaldina A.N., Ydyrys A.Zh.
Analytical and approximate solutions
of the two-dimensional laplace equation in cylindrical coordinates....106
Қошанов Б.Д., Тұрғанбек Ұ., Ерхан А.Ж.
Көпөлшемді шарда полигармоникалық теңдеу
үшін бір шеттік есептің шешімділігі туралы....124

2 КОМПЬЮТЕРЛІК ҒЫЛЫМДАР
КОМПЬЮТЕРНЫЕ НАУКИ

Amirbayeva A.
Hybrid Intelligent Decision-Support System
for Cybersecurity Risk Assessment and Security Action Selection....144
Kapalova N.A., Khaumen A., Algazy K.T.
Resistance of lightweight algorithms to side-channel attacks....160
Batyrkhanova A.A., Bekmukhan A.S., Abildayeva T.T., Yeskendirova D.M.
Application of generative ai models for attacks and defense....176
Тынымбаев С., Маманова С.Е., Сқабылов А.А., Чинибаева Т.Т., Жексебай Д.М.
Архитектура целочисленного делителя с одновременным
формированием трех разрядов частного за шаг....188
Kunichik V.G., Salykova O.S.
Early prediction of in-hospital mortality using interpretable
and calibrated ensemble machine learning models....204
Samigulina Z.I., Mlikova K.A., Tolengutov R.R., Butakova D.A., Nakhimov A.Z.
A novel transport module concept for vertical take-off
and landing unmanned aerial vehicle transportation of unmanned ground vehicles....218
Aitim A.K.
Morphological disambiguation for the kazakh language using transformer-based models....233

Утебаев К.А., Молдагулова А.Н., Касенхан А.М.
Применение искусственного интеллекта в разработке адаптивной
системы обучения для развития навыков критического мышления у студентов 243
Aidynov T., Satybaldina D., Dimitrov W., Abisheva G.
A Blockchain-Oriented Model for Electronic Voting
with Biometric Voter Identification and Deepfake-Resistant Authentication 255
Sakhipov A.A., Fedenko A.D.
Ensuring data integrity of examination results using
permissioned distributed ledger technology 267
Smakanov B.S., Uvaliyeva I.M.
Modeling driver state monitoring based on a theoretical and empirical approach 282
Тасжурекова Ж.К., Козыбаев Д.Х., Танирбергенов А.Ж.,
Ахметжанова Ш.Е., Абдувалова А.Д.
Алақан параметрлерін талдау үшін машиналық оқыту
технологияларын қолдана отырып, жеке тұлғаны
сәйкестендірудің биометриялық жүйесін әзірлеу 298
Серикбаева С.К., Рамазанова В.С., Самбетбаева М.А.,
Еримбетова А.С., Садирмекова Ж.Б.
Модели построения графов знаний для подбора МООК на основе
интеграции запросов рынка труда и образовательных программ 312
Куатбаева А.А., Омарбеков А.Н., Аян А.А.
Модифицированная SEIR модель с GRID auto-search оптимизацией
для высокоточного прогнозирования динамики эпидемий на основе COVID-19 328
Марламбеков Д., Ахметова А., Төрекул С., Уалиева И.М.
Бенчмаркинг моделей глубокого обучения для классификации
казахских новостных текстов в условиях ограниченной разметки 336
Norliza Katuk, Hikmah Nurdin, M. Ali Fauzi, Mhd. Furqan
Aqrace: machine-learning-based detection
of malicious urls in qr codes for real-time security assessment 347
Serek A.G., Abdoldina F.N., Vitulyova E.S., Shapay N.A.,
Oksenenko A.A., Kuchin Y.I.
Semantic segmentation of agricultural field anomaly patterns in aerial images using U-NET 362

3 ФИЗИКАЛЫҚ ҒЫЛЫМДАР
ФИЗИЧЕСКИЕ НАУКИ

Abdullayeva K., Rustembekkyzy K., Kanafin Y.N., Kaikanov M.
Synthesis and photocatalytic activity of hierarchical flower-like zno
for methylene blue degradation under uv light 378
Tazhen A.B., Kholmirzayev A.N., Ussenov Y.A., Dosbolayev M.K., Ramazanov T.S.
Study of changes in microhardness and mass
of a preheated tungsten under the influence of pulsed plasma 388
Iztleuova B., Imanchiyev A., Bekeshev A., Zhanturina N., Ussenkulova Sh., Wang X.
Empirical benchmarking of gradient boosting for thermal
degradation prediction in mineral–polymer composites 398
Yestoreyeva A., Atabaev T.S.
Improving photocurrent density generation
by porous TiO_2 films modified with polystyrene particles 414
Zhumadilov B.Ye., Markhabayeva A.A., Gabdullin M.T.
RF magnetron sputtered ws_2 thin films on ti and ti/cnws
substrates: structural characterization and her performance 422
Zhumazhanova A.T., Shakirzyanov R.I.
Effect of tantalum and vanadium carbide dopants on the structure
and mechanical properties of aluminum nitride-based ceramics 434
Batryshev D.G., Abdirakhmanov A.R., Boufendi L., Orazbayev S.A.
Baikaliyev A., Ramazanov T.S.
Study of growth evaluation of nanostructured carbon nitride thin
layers in nitrogen-methane gas mixture radiofrequency plasma 448

Gluchshenko A., Izmailova I., Umirbayeva A., Kuvatova D., Yurin D.
Automated wavelength calibration of astronomical spectra
with dtw-ransac matching and cnn-based preprocessing.....461
Tulegenova A.T., Lisitsyn V.M., Nogaibekova G.Zh., Lisitsyna L.A.
Influence of the al/ga ratio on the optical properties
of $Y_3Al_xGa_{5-x}O_{12}$:Ce phosphors for led applications 473
Ryskaliyeva M.M., Kusainova A.Z., Eshanov A., Zhirkov I.V.,
Akhadov J.Z., Sultanov A.T., Beisenkhanov N.B.
Analyzing the effects of spin-coated phosphosilicate glass on the crystallization
process of silicon thin films deposited via magnetron sputtering.....486
Messerle V. E., Ustimenko A.B., Lavrishchev O.A., Nugman M.K.
Exergetic Methodology for Standardized Performance Assessment of Plasma Processes.....498

4 МҰНАЙ ГАЗ ИНЖЕНЕРИЯСЫ ЖӘНЕ ГЕОЛОГИЯ
НЕФТЕГАЗОВАЯ ИНЖЕНЕРИЯ И ГЕОЛОГИЯ

Исаева А.Б., Айдарова С.Б., Шарипова А.А., Исахов М.О.
Физико-химические характеристики композиционных пен
на основе пав и наночастиц и их эффективность в повышении нефтеотдачи.....518
Rybin A.K., Bataleva E.A., Nepeina K.S., Matiukov V.E.
Evolution of “naryn” geoelectric cross-sections and comparison
with earthquake distribution in historical perspective 536
Дуйсалиев А.М., Исмаилов А.А., Махмудов Н.Н.
Набухание глин и нецелевой расход реагентов при ГРП: диагностика и опыт
применения пластовой воды на месторождении Восточный Молдабек 544
Нұрбекова Р.Н., Хазлетт Р., Фустич М., Салаудин И., Қайратова А.
Қазақстандағы таза энергия өндіру және көмірқышқыл газын азайту жолы:
негізді және ультранегізді жыныстарды сутегі өндіру
мен көмірқышқыл газын секвестрлеуге пайдалану.....565
Niyazbayeva A.B., Ismail M. Saaid
Reservoir performance simulation and process-to-simulator quality control
to support EOR method selection in carbonate-containing reservoirs.....573
Тұрнияз М.Б., Айсаева Т.С., Нуршаханова Л.К., Бекбаева Р.А.,
Жакупов Т.М., Сейтенов А.С.
Применение гелеполимерных составов для повышения нефтеотдачи
неоднородных коллекторов, содержащих высоковязкую нефть
(на примере месторождения Мангистауской области).....588

5 ЭКОНОМИКА ЖӘНЕ БИЗНЕС
ЭКОНОМИКА И БИЗНЕС

Abdullaev U.
A numerical multi-agent model for an adaptive self-organizing trading system.....600
Oskenbaev Ye., Kaliyaskarova B.
Subsides alone are not enough: governance and agricultural productivity across countries.....617
Demeukhan A.B., Zhumabayeva A.
Drivers and barriers to adopting artificial intelligence practices
in managing projects: a systematic literature review through the toe framework 627
Turginbayeva A.N., Serikbay D.D., Anarkhan A.K.
Mapping inequality in access to R&D:
a dual bibliometric analysis of the global research landscape 643

CONTENTS

1 MATHEMATICAL SCIENCES

Koilyshov U., Zhapparova S., Nietbayev A.
Two-phase heat conduction problems with Sturm-type boundary conditions and with a fractional time derivative 12
Altynbek D., Turmetov B.
On some nonlocal problems for the Poisson equation 24
Issakhov A.A., Beisembekov M.E.
Application of physically-oriented neural networks to solving problems of linear partial derivative equations with inhomogeneous mixed boundary conditions 33
Verbovskiy V.V.
On a local analogue of the strict order property inside a cut for linearly ordered structures 47
Dekhkonov F.N., Usubjonov A.A.
On the control problem for a one-dimensional pseudo-parabolic equation with a nonlocal boundary condition 55
Bayetov K.Kh.
Inverse problem for a parabolic equation with a time-dependent coefficient in the boundary condition 70
Iskakova N.B., Bakirova E.A., Usmanov K.I.. Orumbayeva N.T.
On a boundary value problem for a loaded 80
Abdimanapova P.B., Temesheva S.M., Imanchiev A.E., Mazhit Zh.B.
On finding solutions of a family of nonlinear two-point boundary value problems for a differential equation 93
Satybaldina A.N., Ydyrys A.Zh.
Analytical and approximate solutions of the two-dimensional laplace equation in cylindrical coordinates 106
Koshanov B.D., Turganbek U., Yerkhan A.Zh.,
On the solvability of one boundary value problem for the polyharmonic equation in a multidimensional ball 124

2 COMPUTER SCIENCE

Amirbayeva A.
Hybrid Intelligent Decision-Support System for Cybersecurity Risk Assessment and Security Action Selection 144
Kapalova N.A., Khaumen A., Algazy K.T.
Resistance of lightweight algorithms to side-channel attacks 160
Batyrkhanova A.A., Bekmukhan A.S., Abildayeva T.T., Yeskendirova D.M.
Application of generative ai models for attacks and defense 176
Tynymbayev S., Mamanova S.E., Skabylov A.A., Chinibayeva T.T., Zhexebay D.M.
A sequential integer divider with three-bit quotient digit generation 188
Kunichik V.G., Salykova O.S.
Early prediction of in-hospital mortality using interpretable and calibrated ensemble machine learning models 204
Samigulina Z.I., Mlikova K.A., Tolengutov R.R., Butakova D.A., Nakhimov A.Z.
A novel transport module concept for vertical take-off and landing unmanned aerial vehicle transportation of unmanned ground vehicles 218
Aitim A.K.
Morphological disambiguation for the kazakh language using transformer-based models 233
Utebayev K.A., Moldagulova A.N., Kassenkhan A.M.
Using Artificial Intelligence to Develop an Adaptive Learning System to Develop Critical Thinking Skills in Students 243

Aidynov T., Satybaldina D., Dimitrov W., Abisheva G.
A Blockchain-Oriented Model for Electronic Voting
with Biometric Voter Identification and Deepfake-Resistant Authentication 255
Sakhipov A.A., Fedenko A.D.
Ensuring data integrity of examination results using
permissioned distributed ledger technology 267
Smakanov B.S., Uvaliyeva I.M.
Modeling driver state monitoring based on a theoretical and empirical approach 282
Taszhurekova Zh., Kozybayev D., Tanirbergenov A.,
Akhmetzhanova Sh., Abduvalova A.
Development of a biometric identification system using machine learning
technologies to analyze palm parameters 298
Serikbayeva S., Ramazanova V., Sambetbayeva M.,
Yerimbetova A., Sadirmekova Zh.
Models for building knowledge graphs for MOOC selection
based on the integration of labor market demands and educational programs 312
Kuatbaeva A.A., Omarbekov A.N., Aian A.A.
Modified SEIR model with grid auto-search optimization
for high-accuracy epidemic dynamics forecasting based on COVID-19 328
Marlambekov D., Akhmetova A., Torekul S., Ualiyeva I.M.
Benchmarking deep learning models for few-shot classification
of kazakh news texts under limited annotation.....336
Norliza Katuk, Hikmah Nurdin, M. Ali Fauzi, Mhd. Furqan
Aqrace: machine-learning-based detection
of malicious urls in qr codes for real-time security assessment.....347
Serek A.G., Abdoldina F.N., Vitulyova E.S., Shapay N.A.,
Oksenenko A.A., Kuchin Y.I.
Semantic segmentation of agricultural field anomaly patterns in aerial images using U-NET 362

3 PHYSICAL SCIENCES

Abdullayeva K., Rustembekkyzy K., Kanafin Y.N., Kaikanov M.
Synthesis and photocatalytic activity of hierarchical flower-like zno
for methylene blue degradation under uv light.....378
Tazhen A.B., Kholmirzayev A.N., Ussenov Y.A., Dosbolayev M.K., Ramazanov T.S.
Study of changes in microhardness and mass
of a preheated tungsten under the influence of pulsed plasma.....388
Iztleuova B., Imanchiyev A., Bekeshev A., Zhanturina N., Ussenkulova Sh., Wang X.
Empirical benchmarking of gradient boosting for thermal
degradation prediction in mineral–polymer composites.....398
Yestoreyeva A., Atabaev T.S.
Improving photocurrent density generation
by porous TiO_2 films modified with polystyrene particles 414
Zhumadilov B.Ye., Markhabayeva A.A., Gabdullin M.T.
RF magnetron sputtered ws_2 thin films on ti and ti/cnws
substrates: structural characterization and her performance.....422
Zhumazhanova A.T., Shakirzyanov R.I.
Effect of tantalum and vanadium carbide dopants on the structure and mechanical
properties of aluminum nitride-based ceramics.....434
Batryshev D.G., Abdirakhmanov A.R., Boufendi L., Orazbayev S.A.
Baikaliyev A., Ramazanov T.S.
Study of growth evaluation of nanostructured carbon nitride thin
layers in nitrogen-methane gas mixture radiofrequency plasma 448
Gluchshenko A., Izmailova I., Umirbayeva A., Kuvatova D., Yurin D.
Automated wavelength calibration of astronomical spectra
with dtw-ransac matching and cnn-based preprocessing.....461

Tulegenova A.T., Lisitsyn V.M., Nogaibekova G.Zh., Lisitsyna L.A.
Influence of the al/ga ratio on the optical properties
of $Y_3Al_xGa_{5-x}O_{12}$:Ce phosphors for led applications 473
Ryskaliyeva M.M., Kusainova A.Z., Eshanov A., Zhirkov I.V.,
Akhadov J.Z., Sultanov A.T., Beisenkhanov N.B.
Analyzing the effects of spin-coated phosphosilicate glass on the crystallization
process of silicon thin films deposited via magnetron sputtering 486
Messerle V. E., Ustimenko A.B., Lavrishchev O.A., Nugman M.K.
Exergetic Methodology for Standardized Performance Assessment of Plasma Processes.....498

4 OIL AND GAS ENGINEERING, GEOLOGY

Isayeva A.B., Aidarova S.B., Sharipova A.A., Issakhov M.O.
Physico-chemical characteristics of composite foams based on surfactants
and nanoparticles and their effectiveness in increasing oil recovery.....518
Rybin A.K., Bataleva E.A., Nepeina K.S., Matiukov V.E.
Evolution of “naryn” geoelectric cross-sections and comparison
with earthquake distribution in historical perspective 536
Duisaliyev A.M., Ismailov A.A., Makhmudov N.N.
Clay swelling and non-target consumption of fracturing fluid additives:
diagnostics and field experience using formation water at the vostochny moldabek field.....544
Nurbekova R.N., Hazlett R.D., Fustic M., Salaudeen I., Kairatova A.
Utilizing Ultramafic Rocks for H_2 Production and CO_2 Sequestration:
A Pathway to Clean Energy and Emissions Reduction in Kazakhstan.....565
Niyazbayeva A.B., Ismail M. Saaid
Reservoir performance simulation and process-to-simulator quality control
to support EOR method selection in carbonate-containing reservoirs.....573
Turniyaz M.B., Aisaeva T.S., Nurshakhanova L.K., Bekbayeva R.A.
Zhakupov T.M., Seitenov A.S.
The use of gel polymer compositions to enhance the oil recovery
of high-viscosity oil in conditions of heterogeneous reservoirs
(using the example of a field in the Mangystau region).....588

5 ECONOMY AND BUSINESS

Abdullaev U.
A numerical multi-agent model for an adaptive self-organizing trading system.....600
Oskenbaev Ye., Kaliyaskarova B.
Subsides alone are not enough: governance and agricultural productivity across countries.....617
Demeukhan A.B., Zhumabayeva A.
Drivers and barriers to adopting artificial intelligence practices in managing projects:
a systematic literature review through the toe framework.....627
Turginbayeva A.N., Serikbay D.D., Anarkhan A.K.
Mapping inequality in access to R&D: a dual bibliometric analysis
of the global research landscape 643

МАТЕМАТИКАЛЫҚ ҒЫЛЫМДАР
MATHEMATICAL SCIENCES
МАТЕМАТИЧЕСКИЕ НАУКИ

UDC 517.95
IRSTI 27.31.44

https://doi.org/10.55452/1998-6688-2026-23-3-12-23

[1,2]Koilyshov U.,
Cand.Phys.-Math.Sc., Associate Professor, ORCID ID: 0000-0003-1752-7848,
e-mail: koylyshov@math.kz
[1,2*]Zhapparova S.,
PhD student, ORCID ID: 0009-0007-4580-0983,
*e-mail: zhapparova.saule@gmail.com
[3]Nietbayev A.,
Cand.Phys.-Math.Sc., Associate Professor, ORCID ID: 0009-0006-5677-5464,
e-mail: a.niet57@mail.ru

[1]Institute of Mathematics and Mathematical Modeling, Almaty, Kazakhstan
[2]Al-Farabi Kazakh National University, Almaty, Kazakhstan
[3]Dulaty University, Taraz, Kazakhstan

TWO-PHASE HEAT CONDUCTION PROBLEMS WITH STURM-TYPE BOUNDARY CONDITIONS AND WITH A FRACTIONAL TIME DERIVATIVE

Abstract

The paper investigates an initial-boundary value problem of the Sturm type for the heat equation with a piecewise-constant coefficient and a Caputo derivative of order $0 < \alpha < 1$ with respect to time. The domain under consideration is an interval $(0, l)$ containing a strictly internal point of discontinuity $x = x_0$. From a physical point of view, this problem models the process of temperature field propagation in a thin rod of length l. The rod is composite and consists of two sections – $(0, x_0)$ and (x_0, l), – possessing different thermophysical characteristics. At the contact point of the two media $x = x_0$, perfect contact conditions are prescribed, implying continuity of temperature and continuity of heat flux when passing from one medium to another. The main goal of the work is to substantiate the solution of the posed initial-boundary value problem by the method of separation of variables (Fourier method). Application of this method leads to the necessity of investigating the corresponding spectral problem for an ordinary differential operator with a discontinuous coefficient at the highest derivative.

Keywords: heat equation, fractional derivatives, discontinuous coefficients, eigenvalues, eigenfunctions, method of separation of variables.

Received February 2, 2026; revised May 21, 2026; accepted July 14, 2026.

Introduction

The theory of fractional order differential equations has received powerful development in recent decades, which is due to the broad possibilities of its applications in describing processes with memory and heredity effects, as well as phenomena of anomalous diffusion in fractal media. The fundamental bases of the theory, as well as methods for solving such equations, are detailed in monographs and in the classical works of Gorenflo and Mainardi [1], where the connection between fractional calculus and problems of continuum mechanics is discussed.

Questions of the well-posedness of initial-boundary value problems for the diffusion equation with a fractional time derivative (in the Caputo or Riemann-Liouville sense) have been investigated by many authors. In the works of Wyss [2] and Mainardi [3], fundamental solutions were constructed and their properties studied.

For the investigation of boundary value problems in bounded domains, works devoted to spectral methods and maximum principles are of great importance. In particular, Luchko [4] substantiated the maximum principle for the generalized fractional diffusion equation, which is a key factor for proving the uniqueness of solutions. The application of the method of separation of variables for fractional order equations in bounded domains is considered in detail in the article by Agrawal [5], and the fundamental theory of boundary value problems for such equations is developed in the works of Pskhu [6].

On the other hand, heat conduction problems in inhomogeneous (layered) media lead to differential equations with discontinuous coefficients. The classical formulation of such problems with conjugation conditions (perfect contact conditions) was formulated by A.A. Samarskii [7]. The presence of discontinuities in coefficients significantly affects the spectral properties of the corresponding differential operators. Questions of the asymptotic behavior of eigenvalues of Sturm-Liouville operators with discontinuous coefficients were investigated in the works of Hald [8].

A particular difficulty in such problems is the question of the basis property of the system of eigenfunctions. It is known that for non-self-adjoint operators arising in problems with non-local conditions or discontinuous coefficients, the system of eigenfunctions may not form a basis in the classical sense, but may form a Riesz basis. Conditions for the basis property of systems of eigenfunctions for problems with conjugation conditions were studied in the works of V.A. Ilyin [9], as well as N.Y. Kapustin and E.I. Moiseev [10]. Recent results regarding the Riesz basis property for operators with discontinuous coefficients and their application to two-phase heat conduction problems were obtained in works [11–14].

However, despite a significant number of works in the fields of fractional calculus and equations with discontinuous coefficients separately, problems combining both these aspects – a fractional time derivative and discontinuous coefficients with respect to the spatial variable – have been insufficiently studied. In particular, questions regarding the substantiation of the Fourier method and the proof of the Riesz basis property of eigenfunctions for such "hybrid" problems require separate consideration, to which the present work is dedicated.

This research stands out because it considers a specific boundary value problem combining discontinuous coefficients with fractional differentiation with respect to time.

In our work, we investigate an initial-boundary value problem for the heat equation with a piecewise-constant coefficient and a Caputo derivative of order $0 < \alpha < 1$ with respect to time. The domain under consideration is an interval $(0, l)$, containing a strictly internal point of discontinuity $x = x_0$.

From a physical point of view, this problem models the process of temperature field propagation in a thin rod of length l. The rod is composite and consists of two sections – $(0, x_0)$ and (x_0, l), – possessing different thermophysical characteristics.

At the contact point of the two media $x = x_0$, perfect contact conditions are prescribed, implying continuity of temperature and continuity of heat flux when passing from one medium to another. These conditions are natural and follow directly from the equation and the presence of discontinuities in the thermophysical characteristics (coefficients of thermal conductivity, density, and heat capacity) [7].

The main goal of the work is to substantiate the solution of the posed initial-boundary value problem by the method of separation of variables (Fourier method). Application of this method leads to the necessity of investigating the corresponding spectral problem for an ordinary differential operator with a discontinuous coefficient at the highest derivative.

Materials and methods

An initial-boundary value problem for the heat equation with a piecewise constant coefficient and with a fractional time derivative is considered

$$\mathcal{L}u \equiv \begin{Bmatrix} t^{-\beta} D_t^{\alpha} u(x,t) - a_1^2 u_{xx}(x,t), & 0 < x < x_0 \\ t^{-\beta} D_t^{\alpha} u(x,t) - a_2^2 u_{xx}(x,t), & x_0 < x < l \end{Bmatrix} = 0, \quad (1)$$

in the domain

$$\Omega = \cup \Omega_i,\ \Omega_1 = \{(x,t): 0 < x < x_0,\ \ 0 < t < T\},$$
$$\Omega_2 = \{(x,t): x_0 < x < l,\ \ 0 < t < T\},\ (i = 1,2),$$

with the initial condition

$$u(x,0) = \varphi(x),\ \ 0 \le x \le l, \quad (2)$$

and boundary conditions

$$\begin{cases} a_{11} u_x(0,t) + a_{12} u(0,t) = 0, \\ a_{21} u_x(l,t) + a_{22} u(l,t) = 0, \end{cases} \quad 0 \le t \le T, \quad (3)$$

and with conjugation conditions

$$\begin{cases} u(x_0 - 0, t) = u(x_0 + 0, t), \\ k_1 u_x(x_0 - 0, t) = k_2 u_x(x_0 + 0, t), \end{cases} \quad 0 \le t \le T. \quad (4)$$

Here D_t^{α} denotes the Caputo fractional derivative of order $\alpha \in (0,1),\ \beta > 0$,

$$D_t^{\alpha} f(t) = \frac{1}{\Gamma(1-\alpha)} \int_0^t \frac{f'(\tau)}{(t-\tau)^{\alpha}} d\tau.$$

The coefficients a_{ij}, $(i, j = 1,2)$ are real numbers. In addition

$$|a_{11}| + |a_{12}| > 0,\ |a_{21}| + |a_{22}| > 0,$$
$$a_i^2 = \frac{k_i}{c_i \rho_i},\ k_i > 0,\ (i = 1,2),$$

where k_i, $\left(\frac{w}{m \cdot K}\right)$ is the thermal conductivity coefficient, c_i, $\left(\frac{j}{K \cdot kg}\right)$ is the specific heat capacity, ρ_i, $\left(\frac{kg}{m^3}\right)$ is the density, a_i^2, $\left(\frac{m^2}{s}\right)$ is the thermal diffusivity coefficient.

The $\varphi(x)$ a twice continuously differentiable function that satisfies the boundary conditions (3) and conjugation conditions (4).

The solution of problem (1)-(4) is sought in the form $u(x,t) = X(x) \cdot T(t) \neq 0$.

Substituting into equation (1) and conditions (2)-(4), and separating the variables, we obtain the following spectral problem

$$\mathcal{L}X(x) = \begin{Bmatrix} -a_1^2 X''(x), & 0 < x < x_0 \\ -a_2^2 X''(x), & x_0 < x < l \end{Bmatrix} = \lambda X(x), \quad (5)$$

$$\begin{cases} a_{11} X'(0) + a_{12} X(0) = 0, \\ a_{21} X'(l) + a_{22} X(l) = 0, \end{cases} \quad (6)$$

$$\begin{cases} X(x_0 - 0) = X(x_0 + 0), \\ k_1 X'(x_0 - 0) = k_2 X'(x_0 + 0). \end{cases} \quad (7)$$

The function $T(t)$ is a solution to the equation

$$t^{-\beta} D_t^{\alpha} T(t) + \lambda T(t) = 0. \quad (8)$$

The general solution of equation (5) has the form

$$\begin{cases} X(x) = c_1 \cos(\mu_1 x) + c_2 \sin(\mu_1 x), & 0 < x < x_0, \\ X(x) = c_3 \cos(\mu_2 (l - x)) + c_4 \sin(\mu_2 (l - x)), & x_0 < x < l, \end{cases} \tag{9}$$

where

$$\mu_i = \frac{\sqrt{\lambda}}{a_i}, (i = 1,2). \tag{10}$$

Substituting the general solution (9) into the boundary conditions (6) and conjugation conditions (7), we get

$$\begin{cases} c_1 a_{12} + c_2 a_{11} \mu_1 = 0, \\ c_3 a_{22} - c_4 a_{21} \mu_2 = 0, \\ c_1 \cos(\mu_1 x_0) + c_2 \sin(\mu_1 x_0) - c_3 \cos(\mu_2 (l - x_0)) - c_4 \sin(\mu_2 (l - x_0)) = 0, \\ -c_1 k_1 \mu_1 \sin(\mu_1 x_0) + c_2 k_1 \mu_1 \cos(\mu_1 x_0) - c_3 k_2 \mu_2 \sin(\mu_2 (l - x_0)) + c_4 k_2 \mu_2 \cos(\mu_2 (l - x_0)) = 0. \end{cases}$$

Taking into account formula (10), we find the characteristic determinant of the system:

$$\begin{gathered} \Delta(\lambda) = a_{11} a_{21} \lambda \left(\frac{k_1}{a_1} \sin(\mu_1 x_0) \cos(\mu_2 (l - x_0)) + \frac{k_2}{a_2} \cos(\mu_1 x_0) \sin(\mu_2 (l - x_0)) \right) - \\ - \sqrt{\lambda} \left(\frac{a_{12} a_{21} a_1 k_2}{a_2} - \frac{a_{11} a_{22} a_2 k_1}{a_1} \right) \sin(\mu_1 x_0) \sin(\mu_2 (l - x_0)) + \\ + \sqrt{\lambda} (a_{11} a_{22} k_2 - a_{21} a_{12} k_1) \cos(\mu_1 x_0) \cos(\mu_2 (l - x_0)) + \\ + a_{12} a_{22} (a_1 k_2 \sin(\mu_1 x_0) \cos(\mu_2 (l - x_0)) + a_2 k_1 \cos(\mu_1 x_0) \sin(\mu_2 (l - x_0))) = 0. \end{gathered} \tag{11}$$

The roots of equation (11) will be the eigenvalues of problem (5)-(7). It is not possible to find the eigenvalues of λ_n explicitly, but it is possible to construct asymptotics. It will be shown that for $\lambda = 0$, the spectral problem (5)-(7) has only a zero solution.

Next, the eigenfunctions of the spectral problem (5)-(7) are constructed. They look as follows:

$$X_n(x) = C_n \begin{cases} \Phi_2(x_0, \lambda_n) \Phi_1(x, \lambda_n), & 0 < x < x_0, \\ \Phi_1(x_0, \lambda_n) \Phi_2(x, \lambda_n), & x_0 < x < l, \end{cases} \tag{12}$$

where

$$\Phi_1(x, \lambda_n) = \cos\left(\frac{\sqrt{\lambda_n}}{a_1} x \right) - \frac{a_{12} a_1}{a_{11} \sqrt{\lambda_n}} \sin\left(\frac{\sqrt{\lambda_n}}{a_1} x \right), \tag{13}$$

$$\Phi_2(x, \lambda_n) = \cos\left(\frac{\sqrt{\lambda_n}}{a_2} (l - x) \right) + \frac{a_{22} a_2}{a_{21} \sqrt{\lambda_n}} \sin\left(\frac{\sqrt{\lambda_n}}{a_2} (l - x) \right), \tag{14}$$

where λ_n are roots of equation (11).

It is easy to show that eigenfunctions (12) satisfy equation (5), boundary conditions (6) and conjugation conditions (7).

The following Lemma is true.

Lemma 1. Spectral problem (5)-(7) is not self-adjoint.

An adjoint problem to problem (5)-(7) has the following form:

$$\mathcal{L}Y(x) = \begin{Bmatrix} -a_1^2 Y''(x), & 0 < x < x_0 \\ -a_2^2 Y''(x), & x_0 < x < l \end{Bmatrix} = \lambda Y(x), \tag{15}$$

$$\begin{cases} a_{11} Y'(0) + a_{12} Y(0) = 0, \\ a_{21} Y'(l) + a_{22} Y(l) = 0, \end{cases} \tag{16}$$

$$\begin{cases} \frac{a_1^2}{k_1} Y(x_0 - 0) = \frac{a_2^2}{k_2} Y(x_0 + 0), \\ a_1^2 Y'(x_0 - 0) = a_2^2 Y'(x_0 + 0). \end{cases} \tag{17}$$

Proof. The lemma can be proved by direct calculation.

Therefore, it cannot be asserted that the eigenfunctions $X_n(x)$ form the basis in L_2. It is easy to show that they are not orthogonal.

In a similar way, one can find the eigenvalues and construct the eigenfunctions of the adjoint problem (15)-(17). Direct calculation can show that the eigenvalues of the spectral problems (5)-(7) and (15)-(17) coincide. The eigenfunctions of problem (15)-(17) have the form:

$$Y_n(x) = C_n \begin{cases} \frac{k_1}{a_1^2}\Phi_2(x_0,\lambda_n)\Phi_1(x,\lambda_n), & 0 < x < x_0, \\ \frac{k_2}{a_2^2}\Phi_1(x_0,\lambda_n)\Phi_2(x,\lambda_n), & x_0 < x < l, \end{cases} \tag{18}$$

where λ_n are roots of equation (11), functions $\Phi_1(x,\lambda_n)$ $\Phi_2(x,\lambda_n)$ are determined by formulas (13)-(14).

The following Lemma holds.

Lemma 2. The systems of eigenfunctions (12) and (18) are biorthogonal on the interval $(0,l)$, so that for any numbers i and j the relation holds

$$(X_i, Y_j) = \int_0^l X_i(x)Y_j(x)dx = \delta_j^i,$$

where δ_j^i is the Kronecker symbol.

The lemma can be proved by direct calculation, taking into account that the eigenvalues of spectral problems (5)-(7) and (15)-(17) coincide, and the eigenfunctions (12) and (18) differ by a constant factor.

Next, a self-adjoint problem is constructed.

Lemma 3. The following spectral problem is self-adjoint.

$$\mathcal{L}Z(x) = \begin{Bmatrix} -a_1^2 Z''(x), & 0 < x < x_0 \\ -a_2^2 Z''(x), & x_0 < x < l \end{Bmatrix} = \lambda Z(x), \tag{19}$$

$$\begin{cases} a_{11}Z'(0) + a_{12}Z(0) = 0, \\ a_{21}Z'(l) + a_{22}Z(l) = 0, \end{cases} \tag{20}$$

$$\begin{cases} \frac{a_1}{\sqrt{k_1}}Z(x_0 - 0) = \frac{a_2}{\sqrt{k_2}}Z(x_0 + 0), \\ a_1\sqrt{k_1}Z'(x_0 - 0) = a_2\sqrt{k_2}Z'(x_0 + 0). \end{cases} \tag{21}$$

Proof. Considering the following formula

$$-Z''(x)V(x) = \big(V'(x)Z(x) - V(x)Z'(x)\big)' - V''(x)Z(x),$$

we get

$$\int_0^l V(x)\mathcal{L}Z(x)dx = -\int_0^{x_0} V(x)a_1^2 Z''(x)dx - \int_{x_0}^l V(x)a_2^2 Z''(x)dx =$$
$$= a_1^2 Z(x_0 - 0)V'(x_0 - 0) - a_1^2 Z(0)V'(0) - a_1^2 Z'(x_0 - 0)V(x_0 - 0) +$$
$$+a_1^2 Z'(0)V(0) + a_2^2 Z(l)V'(l) - a_2^2 Z(x_0 + 0)V'(x_0 + 0) - a_2^2 Z'(l)V(l) +$$
$$+a_2^2 Z'(x_0 + 0)V(x_0 + 0) + \int_0^l Z(x)\mathcal{L}V(x)dx.$$

By taking into account the boundary conditions

$$\int_0^l V(x)\mathcal{L}Z(x)dx = a_1\sqrt{k_1}V'(x_0 - 0)\frac{a_1}{\sqrt{k_1}}Z(x_0 - 0) - a_1\sqrt{k_1}Z'(x_0 - 0)\frac{a_1}{\sqrt{k_1}}V(x_0 - 0) +$$
$$+a_2\sqrt{k_2}V'(x_0 + 0)\frac{a_2}{\sqrt{k_2}}Z(x_0 + 0) + a_2\sqrt{k_2}Z'(x_0 + 0)\frac{a_2}{\sqrt{k_2}}V(x_0 + 0) + \int_0^l Z(x)\mathcal{L}V(x)dx.$$

Further, in a similar way, one can calculate the eigenvalues of problem (19)-(21), they will be the roots of equation (11), that is, they coincide with the eigenvalues of problems (5)-(7) and (15)-(17).

The eigenvalues of the function are written as:

$$Z_n(x) = C_n \begin{cases} \frac{\sqrt{k_1}}{a_1^2}\Phi_2(x_0,\lambda_n)\Phi_1(x,\lambda_n), & 0 < x < x_0, \\ \frac{\sqrt{k_2}}{a_2^2}\Phi_1(x_0,\lambda_n)\Phi_2(x,\lambda_n), & x_0 < x < l, \end{cases} \tag{22}$$

where λ_n are roots of equation (11).

Lemma 4. The system of eigenfunctions (22) forms an orthonormal system.

The proof follows from the general theory of self-adjoint problems. C_n can be found from the normalization condition

$$C_n = \left(\frac{k_1}{a_1^2}\Phi_2^2(x_0,\lambda_n)\int_0^{x_0}\Phi_1^2(x,\lambda_n)dx + \frac{k_2}{a_2^2}\Phi_1^2(x_0,\lambda_n)\int_{x_0}^{l}\Phi_2^2(x,\lambda_n)dx\right)^{-\frac{1}{2}}.$$

Lemma 5. The eigenfunctions $X_n(x)$ of the spectral problem (5)-(7) defined by formula (12) form a Riesz basis.

Proof. In the previous lemma it has been proved that the system of eigenfunctions $\{Z_n(x)\}$ forms an orthonormal basis in $L_2(0,l)$. From formulas (12) and (20) it is clear that the eigenfunctions of problems (5)-(7) and (17)-(19) are related by the following equality:

$$Z_n(x) = \alpha(x)X_n(x), \text{ where } \alpha(x) = \begin{cases}\frac{\sqrt{k_1}}{a_1}, & 0 < x < x_0,\\ \frac{\sqrt{k_2}}{a_2}, & x_0 < x < l.\end{cases}$$

$AX(x) = \alpha(x)X(x)$, $A: L_2(0,l) \to L_2(0,l)$ is a bounded operator and there exists A^{-1}, which is also a bounded operator. From the definition of the Riesz basis it follows that the system of eigenfunctions $\{X_n(x)\}$ forms a Riesz basis.

From equation (8):

$$t^{-\beta}D_t^{\alpha}T(t) + \lambda T(t) = 0,$$

we find the function

$$T_n(t) = \varphi_n E_{\alpha,1+\frac{\beta}{\alpha},\frac{\beta}{\alpha}}\left(-\lambda_n t^{\alpha+\beta}\right),$$

where $E_{\alpha,1+\frac{\beta}{\alpha},\frac{\beta}{\alpha}}(z)$ – generalized Mittag-Leffler function. It is determined by the following formula:

$$E_{\alpha,1+\frac{\beta}{\alpha},\frac{\beta}{\alpha}}(z) = \sum_{k=0}^{\infty} c_k z^k,\ c_0 = 1,\ c_k = \prod_{j=0}^{k-1}\frac{\Gamma(j(\alpha+\beta)+\beta+1)}{\Gamma(j(\alpha+\beta)+\alpha+\beta+1)},$$

$\Gamma(z)$ – gamma function.

The following theorem holds.

Results and discussion

Theorem. Let $\varphi(x)$ be a twice continuously differentiable function satisfying the conditions

$$a_{11}\varphi'(0) + a_{12}\varphi(0) = a_{21}\varphi'(l) + a_{22}\varphi(l) = 0,$$
$$\varphi(x_0 - 0) = \varphi(x_0 + 0),\ k_1\varphi'(x_0 - 0) = k_2\varphi'(x_0 + 0). \quad (23)$$

Then the function

$$u(x,t) = \sum_{n=1}^{\infty}\varphi_n X_n(x)\,E_{\alpha,1+\frac{\beta}{\alpha},\frac{\beta}{\alpha}}\left(-\lambda_n t^{\alpha+\beta}\right), \quad (24)$$

where the coefficients φ_n are determined by the formula

$$\varphi_n = \int_0^l \varphi(x)Y_n(x)dx, \quad (25)$$

is a unique solution to problem (1)-(4).

Proof. First, we prove the existence of a solution (24). Since $\{X_n(x)\}$ the eigenfunctions and λ_n – eigenvalues of problem (5)-(7), it is easy to verify that the function determined by formula (22) satisfies the equation, initial condition, boundary conditions and conjugation conditions of problem (1)-(4). The series (24) is the sum of functions

$$u_n(x,t) = \varphi_n X_n(x)E_{\alpha,1+\frac{\beta}{\alpha},\frac{\beta}{\alpha}}\left(-\lambda_n t^{\alpha+\beta}\right). \quad (26)$$

Let us show that for $t \geq \varepsilon > 0$ (ε - any positive number) the series

$$\sum_{n=1}^{\infty}u_n(x,t),\ \sum_{n=1}^{\infty}t^{-\beta}D_t^{\alpha}u_n,\ \sum_{n=1}^{\infty}\frac{\partial^2 u_n}{\partial x^2},$$

converges uniformly. Obviously, $|\varphi| \leq M_1$, then from formula (25) it follows that $|\varphi_n| \leq M_2$. Let us show that the series (24) converges uniformly, for this, we estimate the n-th term as follows:

$$\sup_{(x,t)\in\bar{\Omega}}|X_n(x)T_n(t)| \leq M_3 \sup_{0\leq t\leq T}|T_n(t)| = M_3 \sup_{0\leq t\leq T}\left|\varphi_n E_{\alpha,1+\frac{\beta}{\alpha},\frac{\beta}{\alpha}}\left(-\lambda_n t^{\alpha+\beta}\right)\right|.$$

Using the known estimate [15]:

$$\left|E_{\alpha,1+\frac{\beta}{\alpha'}\frac{\beta}{\alpha}}(z)\right| \le \frac{M_4}{1+|z|},\ \arg(z)=\pi,\ |z|\to\infty,\ M_4=\text{const}>0 \qquad (27)$$

we get $\sup\limits_{(x,t)\in\overline{\Omega}}|X_n(x)T_n(t)| \le \frac{C}{\lambda_n}$. Since the majorizing series $\sum_{n=1}^{\infty}\frac{C}{\lambda_n}$, converges, the series (25) converges uniformly on $\overline{\Omega}$ to some function $u(x,t)$. Now we will show the possibility of term-by-term differentiation of series (24). To do this, it is sufficient to show the uniform convergence of the series $\sum_{n=1}^{\infty} t^{-\beta}D_t^{\alpha}u_n$, $\sum_{n=1}^{\infty}\frac{\partial^2 u_n}{\partial x^2}$ then the possibility of term-by-term differentiation will be justified. Now let's look at the series $\sum_{n=1}^{\infty}\frac{\partial^2 u_n}{\partial x^2}$. Let us estimate the n-th term of the series.

Using the property $X_n''(x)=\lambda_n X_n(x)$ we obtain

$$\sum_{n=1}^{\infty}\frac{\partial^2 u_n}{\partial x^2}=\sum_{n=1}^{\infty}\frac{\lambda_n}{k_i^2}\varphi_n X_n(x)E_{\alpha,1+\frac{\beta}{\alpha'}\frac{\beta}{\alpha}}\left(-\lambda_n t^{\alpha+\beta}\right). \qquad (28)$$

Now let us consider the integral (25). Integrating by parts we have

$$\varphi_n=\int_0^l\varphi(x)Y_n(x)dx=\frac{C_nk_1}{a_1^2}\left(\int_0^{x_0}\varphi(x)\Phi_2(x_0,\lambda_n)\left(\cos\left(\frac{\sqrt{\lambda_n}}{a_1}x\right)-\frac{a_{12}a_1}{a_{11}\sqrt{\lambda_n}}\sin\left(\frac{\sqrt{\lambda_n}}{a_1}x\right)\right)dx\right)+$$
$$+\frac{C_nk_2}{a_2^2}\left(\int_{x_0}^l\varphi(x)\Phi_1(x_0,\lambda_n)\left(\cos\left(\frac{\sqrt{\lambda_n}}{a_2}(l-x)\right)+\frac{a_{22}a_2}{a_{21}\sqrt{\lambda_n}}\sin\left(\frac{\sqrt{\lambda_n}}{a_2}(l-x)\right)\right)dx\right)=$$
$$=\frac{C_nk_1}{a_1}\Phi_2(x_0,\lambda_n)\left(\frac{\varphi(x_0-0)}{\sqrt{\lambda_n}}\left(\sin\left(\frac{\sqrt{\lambda_n}}{a_1}x_0\right)+\frac{a_{12}a_1}{a_{11}\sqrt{\lambda_n}}\cos\left(\frac{\sqrt{\lambda_n}}{a_1}x_0\right)\right)-\frac{a_{12}a_1}{a_{11}\lambda_n}\varphi(0)\right)-$$
$$-\frac{C_nk_1}{a_1}\left(\int_0^{x_0}\frac{\varphi'(x)}{\sqrt{\lambda_n}}\Phi_2(x_0,\lambda_n)\left(\frac{a_{12}a_1}{a_{11}\sqrt{\lambda_n}}\cos\left(\frac{\sqrt{\lambda_n}}{a_1}x\right)+\sin\left(\frac{\sqrt{\lambda_n}}{a_1}x\right)\right)dx\right)+$$
$$+\frac{C_nk_2}{a_2}\Phi_1(x_0,\lambda_n)\left(-\frac{\varphi(x_0+0)}{\sqrt{\lambda_n}}\left(-\sin\left(\frac{\sqrt{\lambda_n}}{a_2}(l-x_0)\right)+\frac{a_{22}a_2}{a_{21}\sqrt{\lambda_n}}\cos\left(\frac{\sqrt{\lambda_n}}{a_2}(l-x_0)\right)\right)+\frac{a_{22}a_2}{a_{21}\lambda_n}\varphi(l)\right)-$$
$$-\frac{C_nk_2}{a_2}\left(\int_{x_0}^l\frac{\varphi'(x)}{\sqrt{\lambda_n}}\Phi_1(x_0,\lambda_n)\left(\frac{a_{22}a_2}{a_{21}\sqrt{\lambda_n}}\cos\left(\frac{\sqrt{\lambda_n}}{a_2}(l-x)\right)-\sin\left(\frac{\sqrt{\lambda_n}}{a_2}(l-x)\right)\right)dx\right).$$

Integrating by parts again, we obtain

$$\varphi_n=\frac{C_nk_1}{a_1}\Phi_2(x_0,\lambda_n)\left(\frac{\varphi(x_0-0)}{\sqrt{\lambda_n}}\left(\sin\left(\frac{\sqrt{\lambda_n}}{a_1}x_0\right)+\frac{a_{12}a_1}{a_{11}\sqrt{\lambda_n}}\cos\left(\frac{\sqrt{\lambda_n}}{a_1}x_0\right)\right)-\frac{a_{12}a_1}{a_{11}\lambda_n}\varphi(0)\right)+$$
$$+\frac{C_nk_1}{a_1}\Phi_2(x_0,\lambda_n)\left(\frac{\varphi'(x_0-0)a_1}{\lambda_n}\Phi_1(x_0,\lambda_n)-\frac{a_1}{\lambda_n}\varphi'(0)-\frac{a_1}{\lambda_n}\int_0^{x_0}\varphi''(x)\Phi_1(x,\lambda_n)dx\right)+$$
$$+\frac{C_nk_2}{a_2}\Phi_1(x_0,\lambda_n)\left(-\frac{\varphi(x_0+0)}{\sqrt{\lambda_n}}\left(-\sin\left(\frac{\sqrt{\lambda_n}}{a_2}(l-x_0)\right)+\frac{a_{22}a_2}{a_{21}\sqrt{\lambda_n}}\cos\left(\frac{\sqrt{\lambda_n}}{a_2}(l-x_0)\right)\right)+\right.$$
$$\left.\frac{a_{22}a_2}{a_{21}\sqrt{\lambda_n}}\varphi(l)\right)-$$
$$-\frac{C_nk_2}{a_2}\Phi_1(x_0,\lambda_n)\left(\frac{\varphi'(x_0+0)a_2}{\lambda_n}\Phi_2(x_0,\lambda_n)-\frac{a_2}{\lambda_n}\varphi'(l)+\frac{a_2}{\lambda_n}\int_{x_0}^l\varphi''(x)\Phi_2(x,\lambda_n)dx\right).$$

Considering that λ_n is the root of the characteristic equation (11), and the function $\varphi(x)$ satisfies conditions (23), we have

$$\varphi_n=-\frac{C_nk_1}{\lambda_n}\Phi_2(x_0,\lambda_n)\int_0^{x_0}\varphi''(x)\Phi_1(x,\lambda_n)dx-$$
$$-\frac{C_nk_2}{\lambda_n}\Phi_1(x_0,\lambda_n)\int_{x_0}^l\varphi''(x)\Phi_2(x,\lambda_n)dx=\frac{K}{\lambda_n}\int_0^l\varphi''(x)Z_n(x)dx, \qquad (29)$$

where

$$K=\begin{cases}-a_1\sqrt{k_1}, & 0<x<x_0,\\ -a_2\sqrt{k_2}, & x_0<x<l,\end{cases}$$

$Z_n(x)$ is determined by the formula (22).

From formula (29) implies

$$|\varphi_n| \le K_1 \frac{|A_n|}{n^2}, \quad K_1 = \max\left(-a_1\sqrt{k_1}, -a_2\sqrt{k_2}\right),$$

where $A_n = \int_0^l \varphi''(x)Z_n(x)dx$ - Fourier coefficients of functions $\varphi''(x)$ orthonormalized on a segment $[0,l]$ of eigenfunctions $\{Z_n(x)\}$ determined by formula (22). Then, based on Lemma 3 and Bessel's inequality $\sum_{n=1}^{\infty} A_n^2 \le \|\varphi''\|^2$, from formulas (27)-(29), we obtain $\sum_{n=1}^{\infty}\left|\frac{\partial^2 u_n}{\partial x^2}\right| = \sum_{n=1}^{\infty}\frac{M_5}{1+|\lambda_n t^{\alpha+\beta}|}$. Thus, the majorizing series converges absolutely, which means that the series (28) converges uniformly at $t \ge \varepsilon > 0$. Uniform convergence of the series $\sum_{n=1}^{\infty} t^{-\beta}D_t^{\alpha}u_n$ follows from the equality $t^{-\beta}D_t^{\alpha}u_n = a_i^2\frac{\partial^2 u_n}{\partial x^2}$. Now we need to prove that the series (24) converges uniformly everywhere in $\overline{\Omega}$. Similarly, integrating by parts twice formula (25) we obtain $\sum_{n=1}^{\infty}|u_n| = \sum_{n=1}^{\infty}\frac{M_6}{\lambda_n}$. Thus, the majorizing series converges absolutely, which means that the series (24) converges uniformly in $\overline{\Omega}$ and defines a continuous function $u(x,t)$ in $\overline{\Omega}$. Thus, we have proven the existence of a solution to problem (1)-(4).

Now let's prove the uniqueness of the solution. Suppose there are two solutions $v(x,t)$, $w(x,t)$. Then for the function $\omega(x,t) = v(x,t) - w(x,t)$ we have the following problem:

$$t^{-\beta}D_t^{\alpha}\omega = a_i^2\frac{\partial^2\omega}{\partial x^2}, \text{ in the domain } \Omega = \cup\,\Omega_i, (i = 1,2), \tag{30}$$

$$\omega(x,0) = 0, \quad 0 \le x \le l, \tag{31}$$

$$\begin{cases} a_{11}\omega_x(0,t) + a_{12}\omega(0,t) = 0, \\ a_{21}\omega_x(l,t) + a_{22}\omega(l,t) = 0, \end{cases} \quad 0 \le t \le T \tag{32}$$

$$\begin{cases} \omega(x_0 - 0, t) = \omega(x_0 + 0, t), \\ k_1\frac{\partial\omega(x_0-0,t)}{\partial x} = k_2\frac{\partial\omega(x_0+0,t)}{\partial x}. \end{cases} \tag{33}$$

The solution to this problem (30)-(33) can be represented as an expansion in the basis $\{X_n(x)\}$ and has the form

$$\omega(x,t) = \sum_{n=1}^{\infty} B_n(t)X_n(x). \tag{34}$$

The coefficients $B_n(t)$ are easy to find if we multiply both parts of the equality (34) by the functions $Y_n(x)$ respectively, and integrate the resulting ratio from 0 to l and take into account the biorthogonality of the sequences $\{X_n(x)\}$ and $\{Y_n(x)\}$. Then we get

$$B_n(t) = \int_0^l \omega(x,t)Y_n(x)dx. \tag{35}$$

We find the fractional derivative with t respect to equality (35), and taking into account equation (30) we have:

$$t^{-\beta}D_t^{\alpha}\left(B_n(t)\right) = \int_0^l t^{-\beta}D_t^{\alpha}\omega Y_n(x)dx =$$
$$= C_n a_1^2\int_0^{x_0}\frac{k_1}{a_1^2}\omega_{xx}\Phi_2(x_0,\lambda_n)\Phi_1(x,\lambda_n)dx +$$
$$+C_n a_2^2\int_{x_0}^{l}\frac{k_2}{a_2^2}\omega_{xx}\Phi_1(x_0,\lambda_n)\Phi_2(x,\lambda_n)dx.$$

Integrating by parts twice and using the boundary conditions (32), the conjugation conditions (33), we have

$$t^{-\beta}D_t^{\alpha}\left(B_n(t)\right) = -C_n\frac{\lambda_n k_1}{a_1^2}\int_0^{x_0}\omega(x,t)\Phi_2(x_0,\lambda_n)\Phi_1(x,\lambda_n)dx -$$
$$-C_n\frac{\lambda_n k_2}{a_2^2}\int_{x_0}^{l}\omega(x,t)\Phi_1(x_0,\lambda_n)\Phi_2(x,\lambda_n)dx = -\lambda_n B_n(t).$$

Hence

$$B_n(t) = b_n E_{\alpha,1+\frac{\beta}{\alpha'\alpha}\frac{\beta}{\alpha}}\left(-\lambda_n t^{\alpha+\beta}\right).$$

Substituting the found value $B_n(t)$ into formula (35), we obtain

$$\int_0^l \omega(x,t)Y_n(x)dx = b_n E_{\alpha,1+\frac{\beta}{\alpha'\alpha}\frac{\beta}{\alpha}}\left(-\lambda_n t^{\alpha+\beta}\right). \quad (36)$$

Passing to the limit in equality (36) at $t \to 0$, which is possible due to continuity $\omega(x,t)$ in $\overline{\Omega}$, we have $\lim\limits_{t\to 0}\int_0^l \omega(x,t)Y_n(x)dx = 0 = B_n(0)$, therefore $b_n = 0$, $(n = 1,2,\dots)$.

Then from formula (34) we obtain $\omega(x,t) = 0$, it follows that $v(x,t) = w(x,t)$. The uniqueness of the solution is proven, thus the theorem is proved.

Let's consider the following example:

$$\mathcal{L}u \equiv \begin{Bmatrix} t^{-\beta}D_t^{\alpha}u(x,t) - 4u_{xx}(x,t), & 0 < x < 1 \\ t^{-\beta}D_t^{\alpha}u(x,t) - u_{xx}(x,t), & 1 < x < 2 \end{Bmatrix} = 0, \quad (37)$$

in the domain

$$\Omega = \bigcup \Omega_i,\ \Omega_1 = \{(x,t): 0 < x < 1,\ 0 < t < T\},$$
$$\Omega_2 = \{(x,t): 1 < x < 2,\ 0 < t < T\},\ (i = 1,2),$$

with the initial condition

$$u(x,0) = \varphi(x) = \begin{cases} 2x-1, & 0 \le x \le 1, \\ x, & 1 \le x \le 2, \end{cases} \quad (38)$$

and boundary conditions

$$\begin{cases} u_x(0,t) + 2u(0,t) = 0, \\ u_x(2,t) - \frac{1}{2}u(2,t) = 0, \end{cases} \quad 0 \le t \le T, \quad (39)$$

and with conjugation conditions

$$\begin{cases} u(1-0,t) = u(1+0,t), \\ u_x(1-0,t) = 2u_x(1+0,t), \end{cases} \quad 0 \le t \le T. \quad (40)$$

It is easy to see that the function

$$\varphi(x) = \begin{cases} 2x-1, & 0 \le x \le 1, \\ x, & 1 \le x \le 2, \end{cases}$$

satisfies conditions (23) of our theorem. Then the solution to problem (37)-(40) has the form:

$$u(x,t) = \sum_{n=1}^{\infty} \varphi_n X_n(x) E_{\alpha,1+\frac{\beta}{\alpha'\alpha}\frac{\beta}{\alpha}}\left(-\lambda_n t^{\alpha+\beta}\right),$$

where

$$\varphi_n = \int_0^2 \varphi(x)Y_n(x)dx = 2C_n\Phi_1(1,\lambda_n)\Phi_2'(1,\lambda_n) - \frac{1}{4}C_n\Phi_2(1,\lambda_n)\Phi_1'(1,\lambda_n),$$

$$X_n(x) = C_n \begin{cases} \Phi_2(1,\lambda_n)\Phi_1(x,\lambda_n), & 0 < x < 1, \\ \Phi_1(1,\lambda_n)\Phi_2(x,\lambda_n), & 1 < x < 2, \end{cases}$$

$$Y_n(x) = C_n \begin{cases} \frac{1}{4}\Phi_2(1,\lambda_n)\Phi_1(x,\lambda_n), & 0 < x < 1, \\ 2\Phi_1(1,\lambda_n)\Phi_2(x,\lambda_n), & 1 < x < 2, \end{cases}$$

$$C_n = \left(\frac{1}{4}\Phi_2^2(1,\lambda_n)\int_0^1 \Phi_1^2(x,\lambda_n)dx + 2\Phi_1^2(1,\lambda_n)\int_1^2 \Phi_2^2(x,\lambda_n)dx\right)^{-\frac{1}{2}},$$

$$\Phi_1(x,\lambda_n) = \cos\left(\frac{\sqrt{\lambda_n}}{2}x\right) - \frac{4}{\sqrt{\lambda_n}}\sin\left(\frac{\sqrt{\lambda_n}}{2}x\right),$$

$$\Phi_2(x,\lambda_n) = \cos\left(\sqrt{\lambda_n}(2-x)\right) - \frac{1}{2\sqrt{\lambda_n}}\sin\left(\sqrt{\lambda_n}(2-x)\right),$$

λ_n are roots of equation

$$\lambda_n\left(2\sin\sqrt{\lambda_n}\cos\frac{\sqrt{\lambda_n}}{2} + \frac{1}{2}\cos\sqrt{\lambda_n}\sin\frac{\sqrt{\lambda_n}}{2}\right) -$$

$$-\sqrt{\lambda_n}\left(\frac{25}{4}\sin\sqrt{\lambda_n}\sin\frac{\sqrt{\lambda_n}}{2}+3\cos\sqrt{\lambda_n}\cos\frac{\sqrt{\lambda_n}}{2}\right)-$$
$$-4\sin\sqrt{\lambda_n}\cos\frac{\sqrt{\lambda_n}}{2}-\cos\sqrt{\lambda_n}\sin\frac{\sqrt{\lambda_n}}{2}.$$

Conclusion

In this work, we considered an initial-boundary value problem for a two-phase heat conduction model on an interval $(0,l)$ with a strictly internal interface point $x = x_0$, Sturm-type boundary conditions, and a Caputo fractional derivative of order $0 < \alpha < 1$ in time, multiplied by a weight $t^{-\beta}$. The mismatch of thermophysical parameters at the point was taken into account through ideal contact (conjugation) conditions expressing the continuity of temperature and heat flux.

The method of separation of variables reduces the problem to a spectral boundary value problem for a second-order differential operator with a discontinuous coefficient at the highest derivative. We derived the corresponding characteristic equation determining the eigenvalues and constructed explicit forms of the eigenfunctions for both the original and the adjoint spectral problems. Since the original spectral problem is not self-adjoint, the orthogonality of the eigenfunctions is absent. To overcome this difficulty, we constructed an auxiliary self-adjoint problem with the same eigenvalues and proved that its eigenfunctions form an orthonormal basis in the space $L_2(0,l)$. Establishing a bounded and boundedly invertible transformation between the eigenfunctions of the self-adjoint and original problems, we proved that the eigenfunctions of the original spectral problem form a Riesz basis in $L_2(0,l)$.

Using this basis property and the explicit representation of time-dependent multipliers via the generalized Mittag-Leffler function, we obtained the solution of the initial-boundary value problem in the form of a Fourier-type series. We also justifiably differentiated the series term-by-term and proved the existence and uniqueness of the solution under natural smoothness and consistency conditions for the initial data. The results provide a rigorous justification of the Fourier method for a diffusion model with a time-fractional operator in a composite (two-phase) medium with discontinuous coefficients.

Possible directions for further research include extending the analysis to multilayered media with several interfaces, to more general conjugation or boundary conditions (including nonlocal ones), as well as to direct problems with sources and associated inverse problems on determining unknown coefficients or interface parameters.

Information on funding

This research was carried out under the project “Financing of scientific organizations carrying out fundamental scientific research for 2026-2028” (Project No.BR31714735).

REFERENCES

1 Gorenflo, R., Mainardi, F. Fractional calculus. In: Carpinteri, A., Mainardi, F. (eds). Fractals and Fractional Calculus in Continuum Mechanics. International Centre for Mechanical Sciences, vol. 378. Springer, Vienna (1997). https://doi.org/10.1007/978-3-7091-2664-6_5.

2 Wyss, W. The fractional diffusion equation. Journal of Mathematical Physics, 27, 2782–2785 (1986). https://doi.org/10.1063/1.527251.

3 Mainardi, F. The fundamental solution for the fractional diffusion-wave equation. Applied Mathematics Letters, 9(6), 23–28 (1996). https://www.sciencedirect.com/science/article/pii/0893965996000894.

4 Luchko, Y. Maximum principle for the generalized time-fractional diffusion equation. Journal of Mathematical Analysis and Applications, 351(1), 218–223 (2009).

5 Agrawal, O.P. Solution for a fractional diffusion-wave equation defined in a bounded domain. Nonlinear Dynamics, 29(1), 145–155 (2002).

6 Псху, А.В. Уравнения в частных производных дробного порядка. М.: Наука (2005).

7 Samarskiy, A.A. Parabolic equations with discontinuous coefficients. Doklady Akademii Nauk SSSR, 121(2), 225–228 (1958).

8 Hald, O.H. Discontinuous inverse eigenvalue problems. Communications on Pure and Applied Mathematics, 37, 539–577 (1984). https://doi.org/10.1002/cpa.3160370502.

9 Il'in, V.A., Kritskov, L.V. Properties of spectral expansions corresponding to non-self-adjoint differential operators. In: Functional Analysis. Itogi Nauki i Tekhniki. Series: Sovremennaya Matematika. Prilozheniya. Tematicheskie Obzory, Vol. 96, VINITI, Moscow, 5–105 (2006).

10 English transl.: Journal of Mathematical Sciences (New York), 116(5), 3489–3550 (2003).

11 Kapustin, N.Y., Moiseev, E.I. The basis property in Lp of the systems of eigenfunctions corresponding to two problems with a spectral parameter in the boundary condition. Differential Equations, 36, 1498–1501 (2000). https://doi.org/10.1007/BF02757389.11.

12 Koilyshov, U., Sadybekov, M., Beisenbayeva, K. Solution to initial-boundary value problem for the heat conductivity equation with a discontinuous coefficient and general conjugation conditions. International Journal of Mathematics and Mathematical Sciences, 2025, Article ID 2756189, 9 pp. (2025). https://doi.org/10.1155/ijmm/2756189.

13 Koilyshov, U.K., Sadybekov, M.A., Beisenbayeva, K.A. Solution of nonlocal boundary value problems for the heat equation with discontinuous coefficients in the case of two discontinuity points. Bulletin of the Karaganda University. Mathematics Series, 117(1), 81–91 (2025). https://doi.org/10.31489/2025M1/81-91.

14 Koilyshov, U.K., Sadybekov, M.A., Beisenbayeva, K.A. Solution of initial-boundary value problem for heat equation with a discontinuous coefficient and general conjugation condition. Filomat, 39(23), 7997–8005 (2025).

15 Koilyshov, U., Sadybekov, M. Two-phase heat conduction problems with Sturm-type boundary conditions. Boundary Value Problems, 2024, Article ID 149 (2024). https://doi.org/10.1186/s13661-024-01964-x.

16 Kilbas, A.A., Srivastava, H.M., Trujillo, J.J. Theory and Applications of Fractional Differential Equations. North-Holland Mathematics Studies, Vol. 204. Elsevier, New York (2006). https://doi.org/10.1016/S0304-0208(06)80001-0.

[1,2]Койлышов У.,
ф.-м.ғ.к., қауымдастырылған профессор, ORCID ID: 0000-0003-1752-7848,
e-mail: koylyshov@math.kz
[1,2]*Жаппарова С.,
докторант, ORCID ID: 0009-0007-4580-0983,
*e-mail: zhapparova.saule@gmail.com
[3]Ниетбаев А.,
ф.-м.ғ.к., қауымдастырылған профессор, ORCID ID: 0009-0006-5677-5464,
e-mail: a.niet57@mail.ru

[1]Математика және математикалық модельдеу институты, Алматы қ., Қазақстан
[2]Әл-Фараби атындағы Қазақ ұлттық университеті, Алматы қ., Қазақстан
[3]М.Х. Дулати атындағы Тараз өңірлік университеті, Тараз қ., Қазақстан

УАҚЫТ БОЙЫНША БӨЛШЕК ТУЫНДЫСЫ БАР ЖӘНЕ ШТУРМ ТИПТІ ШЕКАРАЛЫҚ ШАРТТАРМЕН БЕРІЛГЕН ЖЫЛУӨТКІЗГІШТІКТІҢ ЕКІ ФАЗАЛЫ ЕСЕПТЕРІ

Аңдатпа

Бұл жұмыста уақыт бойынша $0 < \alpha < 1$ ретті Капуто туындысы бар, бөлікті-тұрақты коэффициенті бар жылуөткізгіштік теңдеуі үшін Штурм типті бастапқы-шекаралық есеп

зерттеледі. Қарастырылып отырған облыс $x = x_0$ қатаң ішкі үзіліс нүктесін қамтитын интервал $(0, l)$. Физикалық тұрғыдан алғанда, бұл есеп ұзындығы жіңішке өзектегі температура өрісінің таралу процесін модельдейді. Өзек құрама және әртүрлі жылуфизикалық сипаттамалары бар екі бөліктен – $(0, x_0)$ және (x_0, l) тұрады. Екі ортаның жанасу $x = x_0$ нүктесінде идеал жанасу шарттары қойылады, яғни бір ортадан екінші ортаға өткенде температураның үзіліссіздігін және жылулық ағынның үзіліссіздігін білдіреді. Жұмыстың негізгі мақсаты – айнымалыларды ажырату әдісімен (Фурье әдісімен) қойылған бастапқы-шекаралық есептің шешімін негіздеу. Бұл әдісті қолдану коэффициенті үзілісті жоғары ретті жәй дифференциалдық операторға сәйкес спектрлік есепті зерттеу қажеттілігіне әкеледі.

Түйін сөздер: жылуөткізгіштік теңдеу, бөлшек туындылар, үзілісті коэффициенттер, меншікті мәндер, меншікті функциялар, айнымалыларды ажырату әдісі.

[1,2]Койлышов У.,
к.ф.-м.н., ассоциированный профессор, ORCID ID: 0000-0003-1752-7848,
e-mail: koylyshov@math.kz
[1,2*]Жаппарова С.,
докторант, ORCID ID: 0009-0007-4580-0983,
*e-mail: zhapparova.saule@gmail.com
[3]Ниетбаев А.,
к.ф.-м.н., ассоциированный профессор, ORCID ID: 0009-0006-5677-5464,
e-mail: a.niet57@mail.ru

[1]Институт математики и математического моделирования, г. Алматы, Казахстан
[2]Казахский национальный университет им. аль-Фараби, г. Алматы, Казахстан
[3]Таразский региональный университет им. М.Х. Дулати, г. Тараз, Казахстан

ДВУХФАЗНЫЕ ЗАДАЧИ ТЕПЛОПРОВОДНОСТИ С ГРАНИЧНЫМИ УСЛОВИЯМИ ТИПА ШТУРМА И С ДРОБНОЙ ПРОИЗВОДНОЙ ПО ВРЕМЕНИ

Аннотация

В работе исследуется начально-краевая задача типа Штурма для уравнения теплопроводности с кусочно-постоянным коэффициентом и производной Капуто порядка $0 < \alpha < 1$ по времени. Рассматриваемая область представляет собой интервал $(0, l)$, содержащий строго внутреннюю точку разрыва $x = x_0$. С физической точки зрения эта задача моделирует процесс распространения температурного поля в тонком стержне длины l. Стержень является составным и состоит из двух участков – $(0, x_0)$ и (x_0, l), обладающих различными теплофизическими характеристиками. В точке контакта двух сред $x = x_0$ задаются условия идеального контакта, подразумевающие непрерывность температуры и непрерывность теплового потока при переходе из одной среды в другую. Основной целью работы является обоснование решения поставленной начально-краевой задачи методом разделения переменных (методом Фурье). Применение этого метода приводит к необходимости исследования соответствующей спектральной задачи для обыкновенного дифференциального оператора с разрывным коэффициентом при старшей производной.

Ключевые слова: уравнение теплопроводности, разрывные коэффициенты, собственные функции, собственные значения, дробные производные, метод разделения переменных.

UDC 517.954
IRSTI 27.31.44

https://doi.org/10.55452/1998-6688-2026-23-3-24-32

[1*]Altynbek D.,
PhD student, ORCID ID: 0009-0003-5564-2174,
*e-mail: dinaraaltynbek987@gmail.com
[2]Turmetov B.,
Dr. Phys.-Math. Sc., Professor, ORCID ID: 0000-0001-7735-6484,
e-mail: batirkhan.turmetov@ayu.edu.kz

[1]M. Auezov South Kazakhstan Research University, Shymkent, Kazakhstan
[2]Khoja Akhmet Yassawi International Kazakh-Turkish University, Turkistan, Kazakhstan

ON SOME NONLOCAL PROBLEMS FOR THE POISSON EQUATION

Abstract

The paper studies the existence of solutions to a nonlocal boundary value problem for the Poisson equation in the unit ball. The boundary condition is nonlocal and relates the value of the unknown function to its normal derivative at diametrically opposite points on the unit sphere. A necessary and sufficient solvability condition is derived in the form of an orthogonality relation for the prescribed right-hand side and the boundary function. Uniqueness of the solution is proved up to an additive constant. An integral representation of the solution is derived using a specially constructed Green's function for the nonlocal problem, which is expressed through the Green's functions of related auxiliary local boundary value problems. In addition, the corresponding spectral problem is investigated. For its analysis, two auxiliary spectral problems with Neumann and Robin boundary conditions are introduced, and their eigenvalues and eigenfunctions are described in detail. It is demonstrated that this approach yields a complete orthonormal set of eigenfunctions for the original nonlocal problem, which forms a basis in $L_2(\Omega)$.

Keywords: Poisson equation, nonlocal boundary value problems, Green's function, Neumann problem, Robin problem, spectral problem, eigenvalues and eigenfunctions.

Received February 16, 2026; revised March 18, March 20, 2026; accepted April 8, 2026

Introduction

In the modern theory of differential equations, nonlocal boundary value problems occupy an important place. According to the definition given in the monograph by A.M. Nakhushev, a boundary value problem is called nonlocal if the boundary condition relates the values of the sought solution and its derivatives at boundary points to the values of the solution (or its derivatives) either at interior points of the domain or at other points of the boundary [1].

A seminal contribution that sparked broad interest in this field is the paper by A.V. Bitsadze and A.A. Samarskii, which considered an elliptic problem with a condition relating the values of the unknown function on part of the boundary to its values along an interior curve [2].

A notable subclass of nonlocal problems consists of those involving an involutive transformation of the argument (the so-called Carleman shift). In this setting, the values of the function at a point x are related to the values at the point $\sigma(x)$, where σ is an involution, i.e., $\sigma(\sigma(x)) = x$. The solvability of elliptic equations subject to such nonlocal conditions has been investigated by many authors [3–11]. Specifically, A.N. Zarubin studied a boundary value problem for the Laplace equation where the boundary condition incorporates an involutive shift [8].

In recent years, the authors of the present paper have obtained a number of results on boundary value problems for the Laplace and Poisson equations with boundary operators involving involutive transformations. Specifically, an extension of the Robin problem for the Laplace equation was

examined and integral representations of solutions were derived [11]. These methods were further developed for the Poisson equation: solvability was established for a new class of nonlocal Dirichlet-type problems, a Green's function was constructed, and spectral properties were investigated [10].

Reference [12] investigates the properties and applications of the differential–difference operator defined below in the class of entire functions

$$\Lambda_\alpha f(z) = \frac{d}{dz} f(z) + \frac{2\alpha + 1}{z}\left(\frac{f(z) - f(-z)}{2}\right).$$

The authors refer to it as the Dunkl operator, which is a particular case of the broader class of Dunkl operators introduced in [13].

The present paper continues the research conducted, but significantly expands and generalizes the previously obtained results [10, 11].

The main difference and novelty of this study are as follows. A generalization of the Robin problem was studied exclusively for the homogeneous Laplace equation, and the solution to the problem was constructed using a function of the Poisson integral type [11]. Although the inhomogeneous Poisson equation was considered, the boundary conditions were of the Dirichlet type, meaning they related only the values of the function itself at various points on the boundary, without involving its derivatives [10]. Using the Green's function of the classical Dirichlet problem, the Green's function for the problem under consideration was constructed there; additionally, the spectral problem was studied, and the completeness of the system of eigenfunctions was proved.

In contrast to the aforementioned works, in the present paper for the Poisson equation, we investigate a problem with a nonlocal boundary condition specified using a Dunkl-type operator. To solve this problem, a new approach is proposed in this work: the Green's function is constructed by expressing it through the known Green's functions of two auxiliary local problems – Neumann and Robin. Furthermore, unlike in [11], this paper provides a complete analysis of the corresponding spectral problem and strictly proves that the found system of eigenfunctions forms a basis in the space L_2.

We now proceed to the precise formulation of the problems considered below.

Let Ω be the unit ball in $\mathbb{R}^n, n \geq 2$ and $\partial\Omega$ be the unit sphere. For a smooth function $u(x)$ we introduce the Dunkl-type operator:

$$D_c[u](x) = \frac{\partial u(x)}{\partial r} + \frac{c}{r}\left[\frac{u(x) - u(-x)}{2}\right],$$

where $c > 0$ and $r = |x|$.

In the domain Ω, we formulate the following problems:

Problem 1. Determine a function $u(x)$ belonging to the class $C^2(\Omega) \cap C^1(\bar{\Omega})$ such that $rD_c[u](x) \in C(\bar{\Omega})$ and it satisfies the following conditions:

$$-\Delta u(x) = f(x), \tag{1}$$

$$D_c[u](x)|_{\partial\Omega} = g(x), \tag{2}$$

where the functions $f(x)$ and $g(x)$ – are prescribed.

Problem 2. Determine a non-zero function $u(x) \neq 0$ belonging to the class $C^2(\Omega) \cap C^1(\bar{\Omega})$ such that $rD_c[u](x) \in C(\bar{\Omega})$ and a number $\lambda \in \mathbb{C}$, subject to the following conditions:

$$-\Delta u(x) = \lambda u(x), \tag{3}$$

$$D_c[u](x)|_{\partial\Omega} = 0. \tag{4}$$

Materials and methods

Investigation of Problem 1.

First, we present the uniqueness theorem for the solution to Problem 1.

Theorem 2.1. If Problem 1 is solvable, the solution is unique modulo an additive constant.

Proof. Let the function $u(x)$ be a solution to the uniform Problem 1. Since

$$D_c u(x)|_{\partial\Omega} = rD_c u(x)|_{\partial\Omega} = r\frac{\partial u(x)}{\partial r} + \frac{c}{2}[u(x) - u(-x)]\Big|_{\partial\Omega},$$

consequently, the function $u(x)$ satisfies the following boundary value problem:

$$\Delta u(x) = 0, x \in \Omega; r\frac{\partial u(x)}{\partial r} + \frac{c}{2}[u(x) - u(-x)] = 0, x \in \partial\Omega. \quad (5)$$

Let us represent the function $u(x)$ in the form $u(x) = u^+(x) + u^-(x)$, where

$$u^+(x) = \frac{1}{2}[u(x) + u(-x)],\ u^-(x) = \frac{1}{2}[u(x) - u(-x)]. \quad (6)$$

By virtue of the conditions of problem (5), the functions $u^+(x)$ and $u^-(x)$ are solutions of the following problems:

$$\Delta u^+(x) = 0, x \in \Omega; \frac{\partial u^+(x)}{\partial r} = 0, x \in \partial\Omega, \quad (7)$$

$$\Delta u^-(x) = 0, x \in \Omega; \frac{\partial u^-(x)}{\partial r} + cu^-(x) = 0, x \in \partial\Omega. \quad (8)$$

It is a classical result that problem (7) admits a solution is $u^+(x) = C \equiv \mathbf{const}$, and for $c > 0$, problem (8) has only the trivial solution $u^-(x) \equiv 0$.

Consequently, $u(x) = u^+(x) + u^-(x) = C \equiv \mathbf{const}$, that is, the solution to the homogeneous Problem 1 is the constant function. The theorem is proved.

Let $G_N(x, y)$ and $G_R(x, y)$ denote the Green's functions of problems (7) and (8), respectively. The following claim is valid.

Theorem 2.2. Let $f(x) \in C^\delta(\bar{\Omega})$ and $g(x) \in C^{\delta+1}(\partial\Omega), 0 < \delta < 1$. Thus, a necessary and sufficient condition for the solvability of Problem 1 is that the following condition holds

$$\int_\Omega f(y)dy + \int_{\partial\Omega} g(y)dS_y = 0. \quad (9)$$

Provided that a solution exists, it is determined uniquely modulo an additive constant and admits the representation

$$u(x) = \int_\Omega G_c(x, y)(x, y)f(y)dy + \int_{\partial\Omega} G_c(x, y)(x, y)g(y)dS_y + C, \quad (10)$$

where $C = \text{const}$, $G_c(x, y)$ is the Green's function of Problem 1, which is defined by the equality

$$G_c(x, y) = \frac{1}{2}[G_N(x, y) + G_N(x, -y) + G_R(x, y) - G_R(x, -y)].$$

Proof. Assume that $u(x)$ solves Problem 1. Writing $u(x)$ as in the form (6), we obtain the following problems for the functions $u^+(x)$ and $u^-(x)$

$$-\Delta u^+(x) = f^+(x), x \in \Omega; \frac{\partial u^+(x)}{\partial r}\Big|_{\partial\Omega} = g^+(x), \quad (11)$$

$$-\Delta u^- w(x) = f^-(x), x \in \Omega; \frac{\partial u^-(x)}{\partial r} + cu^-(x)|_{\partial\Omega} = g^-(x), \quad (12)$$

where

$$f^{\pm}(x) = \frac{1}{2}[f(x) \pm f(-x)], g^{\pm}(x) = \frac{1}{2}[g(x) \pm g(-x)].$$

Clearly, if $f(x) \in C^{\delta}(\bar{\Omega})$ and $g(x) \in C^{\delta+1}(\partial\Omega), 0 < \delta < 1$, then the functions $f^{\pm}(x)$ and have the same smoothness. For these data, problem (12) admits a unique solution, which exists and is given by:

$$u^{-}(x) = \int_{\Omega} G_R(x,y) f^{-}(y) dy + \int_{\partial\Omega} G_R(x,y) g^{-}(y) dS_y. \quad (13)$$

By applying the change of variables, we obtain that (13) takes the form

$$u^{-}(x) = \int_{\Omega} [G_R(x,y) - G_R(x,-y)] f(y) dy +$$
$$+ \int_{\partial\Omega} [G_R(x,y) - G_R(x,-y)] g(y) dS_y. \quad (14)$$

Next, we examine the Neumann problem (11). Observe that the following identities hold for the functions $f(x)$and $g(x)$ (see, for example, [14]):

$$\int_{\Omega} f(-x)dx = \int_{\Omega} f(x)dx, \int_{\partial\Omega} g(-x)dS_x = \int_{\partial\Omega} g(x)dS_x.$$

Then, if condition (9) is satisfied, the following equality also holds:

$$\int_{\Omega} f^{+}(y)dy + \int_{\partial\Omega} g^{+}(y)dS_y = 0. \quad (15)$$

And this equality provides a necessary and sufficient for the Neumann problem (11) to be solvable. If condition (15) holds, then problem (11) admits a solution, which is unique up to an additive constant, and can be written as follows:

$$u^{+}(x) = \int_{\Omega} G_N(x,y) f^{+}(y) dy + \int_{\partial\Omega} G_N(x,y) g^{+}(y) dS_y + C. \quad (16)$$

Analogously to integral (13), after an appropriate change of variables, expression (16) can be represented as:

$$u^{+}(x) = \int_{\Omega} [G_N(x,y) + G_N(x,-y)] f(y) dy +$$
$$+ \int_{\partial\Omega} [G_N(x,y) \pm + G_N(x,-y)] g(y) dS_y + C. \quad (17)$$

Next, we prove that if the functions $u^{+}(x)$and $u^{-}(x)$ are solutions to problem (11) and (12), then the function $u(x) = u^{+}(x) + u^{-}(x)$ fulfills all the requirements of Problem 1. In fact, by applying the operator $-\Delta$ to the function $u(x) = u^{+}(x) + u^{-}(x)$ for all $x \in \Omega$, we obtain:

$$-\Delta u(x) = (-\Delta)u^{+}(x) + (-\Delta)u^{-}(x) = f^{+}(x) + f^{-}(x) = f(x).$$

We proceed to verify the boundary condition (2). Due to the symmetry of the Green's functions $G_N(x,y)$ and $G_R(x,y)$, we obtain the following identities for $u^{+}(x)$and $u^{-}(x)$

$$u^{+}(-x) = u^{+}(x), u^{-}(-x) = -u^{-}(x).$$

Then, by applying the operator $D_c$to the function $u(x) = u^{+}(x) + u^{-}(x)$ for points $x \in \partial\Omega$, we have:

$$D_c u(x)|_{\partial\Omega} = r D_c u(x)|_{\partial\Omega} = r\frac{\partial u(x)}{\partial r} + \frac{c}{2}[u(x) - u(-x)]\Big|_{\partial\Omega} =$$

$$= r\frac{\partial u^+(x)}{\partial r} + r\frac{\partial u^-(x)}{\partial r} + \frac{c}{2}[u^+(x) + u^-(x) - u^+(-x) - u^-(-x)]\Big|_{\partial\Omega} =$$
$$= r\frac{\partial u^+(x)}{\partial r}\Big|_{\partial\Omega} + r\frac{\partial u^-(x)}{\partial r} + cu^-(x)|_{\partial\Omega} = g^+(x) + g^-(x) = g(x).$$

Finally, from formulas (14) and (17), we deduce:

$$u(x) = u^+(x) + u^-(x) =$$
$$= \int_\Omega [G_N(x,y) + G_N(x,-y)]f(y)dy + \int_{\partial\Omega} [G_N(x,y) + G_N(x,-y)]g(y)dS_y + C +$$
$$+ \int_\Omega [G_R(x,y) - G_R(x,-y)]f(y)dy + \int_{\partial\Omega} [G_R(x,y) - G_R(x,-y)]g(y)dS_y =$$
$$= \int_\Omega G_c(x,y)f(y)dy + \int_{\partial\Omega} G_c(x,y)g(y)dS_y + C.$$

The theorem is proved.

Results and discussion

Investigation of Problem 2.

In order to analyze Problem 2, we begin bv considering the auxiliary problems below.

Problem S1. Find a non-zero function $v(x) \neq 0$ belonging to the class $C^2(\Omega) \cap C^1(\bar{\Omega})$ and a number $\mu \in \mathbb{C}$, satisfying the following conditions

$$-\Delta v(x) = \mu v(x), \tag{18}$$

$$\frac{\partial v(x)}{\partial r}\Big|_{\partial\Omega} = 0. \tag{19}$$

Problem S2. Find a non-zero function $w(x) \neq 0$ belonging to the class $C^2(\Omega) \cap C^1(\bar{\Omega})$ and a number $\sigma \in \mathbb{C}$, satisfying the conditions given below:

$$-\Delta w(x) = \sigma w(x), \tag{20}$$

$$\frac{\partial w(x)}{\partial r} + cw(x)|_{\partial\Omega} = 0. \tag{21}$$

Let $v_{N,k}(x)$ and $w_{R,k}(x)$ be the complete systems of eigenfunctions for problem (18)–(19) and (20)–(21), respectively. We denote the corresponding eigenvalues by $\mu_{N,k}$ and $\sigma_{R,k}$.

Let us introduce the functions

$$v^{\pm}_{N,k}(x) = v_{N,k}(x) \pm v_{N,k}(x^*),\ v^{\pm}_{R,k}(x) = v_{R,k}(x) \pm v_{R,k}(x^*).$$

It is obvious that the functions $v^{\pm}_{N,k}(x)$ and $v^{\pm}_{R,k}(x)$ satisfy the conditions:

$$v^{\pm}_{N,k}(x^*) = \pm v^{\pm}_{N,k}(x),\ v^{\pm}_{R,k}(x^*) = \pm v^{\pm}_{R,k}(x).$$

Lemma 1. For the system of functions $\{v^+_{N,k}(x), v^-_{N,k}(x)\}_{k\in\mathbb{N}}$, the following statements hold:

1. the functions $v^{\pm}_{N,k}(x)$ satisfy the conditions of problem (18)–(19);
2. the system $\{v^+_{N,k}(x), v^-_{N,k}(x)\}_{k\in\mathbb{N}}$ is complete in $L_2(\Omega)$;
3. the functions $v^+_{N,k}(x)$ satisfy the boundary conditions of Problem 2.

Proof. Note that the functions $v_{N,k}^{+}(x)$or $v_{N,k}^{-}(x)$ may turn out to be zero, but not simultaneously. It is obvious that the functions $v_{N,k}^{\pm}(x)$ satisfy the conditions of the Neumann problem (18)–(19), and if they are non-zero, then they are eigenfunctions.

Suppose that $g(x) \in L_2(\Omega)$ is orthogonal to all functions of the system $\{v_{N,k}^{+}(x)\}_{k\in\mathbb{N}}$. Then

$$0 = (v_{N,k}^{\pm}, g) = \int_{\Omega} v_{N,k}^{\pm}(x)\bar{g}(x)dx = \int_{\Omega} [v_{N,k}(x) \pm v_{N,k}(x^*)]\bar{g}(x)dx =$$

$$= \int_{\Omega} v_{N,k}(x)[\bar{g}(x) \pm \bar{g}(x^*)]dx, k \in \mathbb{N}.$$

Since the system $\{v_{N,k}(x)\}_{k\in\mathbb{N}}$ is complete in $L_2(\Omega)$, then $\bar{g}(x) \pm \bar{g}(x^*) \equiv 0$ for almost all $x \in \Omega$. Hence, $g(x) = 0$ for almost all $x \in \Omega$, which proves the completeness of the system $\{v_{N,k}^{\pm}(x)\}_{k\in\mathbb{N}}$ in $L_2(\Omega)$. Since the function $v_{N,k}^{+}(x)$ satisfies condition (19) and the equality $v_{N,k}^{+}(-x) = v_{N,k}^{+}(x)$, then

$$D_c v_{N,k}^{+}(x)\big|_{\partial\Omega} = rD_c v_{N,k}^{+}(x)\big|_{\partial\Omega} = r\frac{\partial v_{N,k}^{+}(x)}{\partial r} + \frac{c}{2}[v_{N,k}^{+}(x) - v_{N,k}^{+}(-x)]\Big|_{\partial\Omega} = 0.$$

This completes the proof of the lemma.

The next statement is established by the same argument.

Lemma 2. For the system of functions $\{w_{R,k}^{+}(x), w_{R,k}^{-}(x)\}_{k\in\mathbb{N}}$ the following statements hold:

1. the functions $w_{R,k}^{\pm}(x)$ satisfy the conditions of problem (20)–(21);
2. the system $\{w_{R,k}^{+}(x), w_{R,k}^{-}(x)\}_{k\in\mathbb{N}}$ is complete in $L_2(\Omega)$;
3. the functions $w_{R,k}^{-}(x)$ satisfy the boundary conditions of Problem 2.

Next, let us consider the system

$$\{v_{N,k}^{+}(x), w_{R,m}^{-}(x)\}_{k,m\in\mathbb{N}}. \tag{22}$$

The following statement holds.

Lemma 3. The system of functions (22) is complete in $L_2(\Omega)$.

Proof. We decompose the space $L_2(\Omega)$ into a direct sum of two subspaces: the space $L_2^{+}(\Omega)$ of functions possessing the symmetry property $u(-x) = u(x)$ and the space $L_2^{-}(\Omega)$ of functions possessing the symmetry property $u(-x) = -u(x)$. By virtue of Lemma 1, the system $\{v_{N,k}^{+}(x)\}_{k\in\mathbb{N}}$ is complete in $L_2^{+}(\Omega)$, and by Lemma 2, the system $\{w_{R,m}^{-}(x)\}_{k\in\mathbb{N}}$ is complete in $L_2^{-}(\Omega)$. Consequently, the system (22) is complete in $L_2(\Omega)$. Therefore, Problem 2 has no eigenfunctions of any other form. The lemma is proved.

Next, we present the main theorem concerning Problem 2.

Theorem 3.1. The elements of system (22) are eigenfunctions of Problem 2 and form an orthonormal basis of the space $L_2(\Omega)$

Conclusion

The paper examines two nonlocal formulations for the Poisson equation in the unit ball, where the boundary conditions couple the value of the solution with its normal derivative at diametrically opposite points on the sphere. For the first, inhomogeneous problem, a solvability criterion is derived in the form of an integral relation on the prescribed data, which is equivalent in essence to the classical Neumann compatibility condition. It is shown that, whenever this requirement is satisfied, a solution exists and is uniquely determined up to an additive constant; moreover, an explicit integral

formula is obtained via a Green-type function constructed using the Green's functions of auxiliary Neumann and Robin problems.

The second problem is of spectral type. By introducing auxiliary eigenvalue problems and decomposing the solution into symmetric and antisymmetric components, an eigenfunction system satisfying the nonlocal boundary conditions is constructed. It is proved that this system is complete and forms an orthonormal basis in $L_2(\Omega)$; hence, the problem possesses no eigenfunctions other than those obtained. As a result, a comprehensive description of the spectral properties of the considered nonlocal Poisson problem is achieved. Our findings offer a framework for further analysis of nonlocal problems arising in elliptic and parabolic equations.

Information on funding. This research has been funded by the Science Committee of the Ministry of Science and Higher Education of the Republic of Kazakhstan (Grant No. AP32724093).

REFERENCES

1 Nakhushev, A.M. Uravneniya matematicheskoy biologii [Equations of Mathematical Biology] (Moscow: Vysshaya shkola, 1995), 301 p. (In Russian).

2 Bitsadze, A.V., and Samarskiy, A.A. O nekotorykh prosteyshikh obobshcheniyakh lineynykh ellipticheskikh kraevykh zadach [On some simplest generalizations of linear elliptic boundary value problems]. Doklady Akademii Nauk SSSR, 185 (4), 739–740 (1969). (In Russian).

3 Aitzhanov, S., Koshanov, B., and Kuntuarova, A. Solvability of Some Elliptic Equations with a Nonlocal Boundary Condition. Mathematics, 12 (24), Article 4010 (2024). https://doi.org/10.3390/math12244010

4 Ashyralyev, A., and Khamad, A. O nelokal'noy kraevoy zadache dlya ellipticheskikh differentsial'nykh uravneniy s usloviyami Samarskogo—Ionkina integral'nogo tipa [On a nonlocal boundary value problem for elliptic differential equations with Samarskii-Ionkin conditions of integral type]. Sovremennye problemy matematiki. Fundamental'nye napravleniya, 71 (1), 1–17 (2025). https://doi.org/10.22363/2413-3639-2025-71-1-1-17 (In Russian).

5 Brahim, H., Abdallah, M., and Ahmad, N. Study of general elliptic problems with nonlocal boundary conditions in the Hölderian framework. Journal of Elliptic and Parabolic Equations (2025). Online first. https://doi.org/10.1007/s41808-025-00427-3

6 Dukenbayeva, A., and Sadybekov, M. On a spectral problem for the Laplace operator with more general boundary conditions. Herald of the Kazakh-British Technical University, 21 (4), 146–152 (2024). https://doi.org/10.55452/1998-6688-2024-21-4-146-152

7 Gercek, O. Well-posedness of elliptic-parabolic differential problem with integral condition. Bulletin of the Karaganda University. Mathematics Series, 120 (4), 125–133 (2025). https://doi.org/10.31489/2025M4/125-133

8 Zarubin, A.N. Kraevaya zadacha s involyutivnym sdvigom v granichnom uslovii [Boundary value problem with an involutive shift in the boundary condition]. Differentsial'nye uravneniya, 40 (10), 1423–1425 (2004). (In Russian).

9 Sadybekov, M., and Dukenbayeva, A. On boundary value problems of the Samarskii–Ionkin type for the Laplace operator in a ball. Complex Variables and Elliptic Equations, 67 (2), 369–383 (2022). https://doi.org/10.1080/17476933.2020.1828377

10 Karachik, V., and Turmetov, B.K. Solvability of one nonlocal Dirichlet problem for the Poisson equation. Novi Sad Journal of Mathematics, 50 (1), 67–88 (2020). https://doi.org/10.30755/NSJOM.08942

11 Turmetov, B.Kh. Ob odnom obobshchenii zadachi Robena dlya uravneniya Laplasa [On a generalization of the Robin problem for the Laplace equation]. Differentsial'nye uravneniya, 55 (9), 1179–1187 (2019). https://doi.org/10.1134/S0012266119090027 (In Russian).

12 Betancor, J.J., Sifi, M., and Trimeche, K. Hypercyclic and chaotic convolution operators associated with the Dunkl operator on C. Acta Mathematica Hungarica, 106 (1), 101–116 (2005). https://doi.org/10.1007/s10474-005-0009-1

13 Dunkl, C.F., and Opdam, E.M. Dunkl operators for complex reflection groups. Proceedings of the London Mathematical Society, 86 (1), 70–108 (2003). https://doi.org/10.1112/S0024611502013825

14 Karachik, V., and Turmetov, B. On the solvability of some nonlocal boundary value problems for the biharmonic equation. Mathematica Slovaca, 70 (2), 329–342 (2020). https://doi.org/10.1515/ms-2017-0355

[1]*Алтынбек Д.,
докторант, ORCID ID: 0009-0003-5564-2174,
*e-mail: dinaraaltynbek987@gmail.com
[2]Турметов Б.,
ф.-м.ғ.д., профессор, ORCID ID: 0000-0001-7735-6484,
e-mail: batirkhan.turmetov@ayu.edu.kz

[1]М. Әуезов атындағы Оңтүстік Қазақстан зерттеу университеті, Шымкент қ., Қазақстан
[2]Қожа Ахмет Ясауи атындағы халықаралық Қазақ-Түрік университеті,
Түркістан қ., Қазақстан

ПУАССОН ТЕҢДЕУІ ҮШІН КЕЙБІР БЕЙЛОКАЛ ЕСЕПТЕР ТУРАЛЫ

Аңдатпа

Мақалада бірлік шар ішіндегі Пуассон теңдеуіне байланысты, шекаралық шарты нелокал болатын шекаралық есептің шешілгіштігі талданады. Шекаралық шарт бірлік сфераның диаметралды қарама-қарсы нүктелер жұптарында белгісіз функцияның мәні мен оның нормаль туындысы арасындағы байланыс түрінде беріледі. Есептің шешілгіштігі үшін қажетті және жеткілікті шарт теңдеудің оң жағы мен шекаралық функциядан тұратын берілген деректердің ортогоналдылығы арқылы алынады. Шешім бар болған жағдайда, оның аддитивті тұрақтыға дейін бірмәнді екені дәлелденеді. Нелокал есеп үшін арнайы құрылған Грин функциясын қолдану арқылы шешімнің интегралдық көрінісі шығарылады; бұл ядро сәйкес көмекші локал шекаралық есептердің Грин функциялары арқылы өрнектеледі. Сонымен қатар, сәйкес спектрлік есеп те қарастырылады. Оны зерттеу үшін Нейман және Робин шекаралық шарттары бар екі көмекші спектрлік есеп енгізіліп, олардың меншікті мәндері мен меншікті функциялары егжей-тегжейлі сипатталады. Осы тәсіл бастапқы нелокал есеп үшін толық ортонормаланған меншікті функциялар жүйесін құруға мүмкіндік беретіні және оның $L_2(\Omega)$ кеңістігінде базис түзетіні көрсетіледі.

Түйін сөздер: Пуассон теңдеуі, бейлокал шеттік есептер, Грин функциясы, Нейман есебі, Робен есебі, спектралды есеп, меншікті мәндер мен меншікті функциялар.

[1]*Алтынбек Д.,
докторант, ORCID ID: 0009-0003-5564-2174,
*e-mail: dinaraaltynbek987@gmail.com
[2]Турметов Б.,
ф.-м.ғ.д., профессор, ORCID ID: 0000-0001-7735-6484,
e-mail: batirkhan.turmetov@ayu.edu.kz

[1]Южно-Казахстанский исследовательский университет им. М. Ауэзова,
г. Шымкент, Казахстан
[2]Международный казахско-турецкий университет им. Ходжи Ахмеда Ясави,
г. Туркестан, Казахстан

О НЕКОТОРЫХ НЕЛОКАЛЬНЫХ ЗАДАЧАХ ДЛЯ УРАВНЕНИЯ ПУАССОНА

Аннотация

В данной работе анализируется разрешимость краевой задачи для уравнения Пуассона в единичном шаре с нелокальным граничным условием. Граничное условие задается в виде соотношения между значени-

ем искомой функции и ее нормальной производной в парах диаметрально противоположных точек единичной сферы. Получено необходимое и достаточное условие разрешимости, сформулированное в терминах ортогональности заданных данных – правой части уравнения и граничной функции. Доказана единственность решения с точностью до добавления константы. Выведено интегральное представление решения с использованием специально построенной функции Грина для нелокальной задачи, которая выражается через функции Грина соответствующих вспомогательных локальных краевых задач. Кроме того, исследуется связанная спектральная задача. Для ее анализа введены две вспомогательные спектральные задачи с граничными условиями Неймана и Робина и подробно описаны их собственные значения и собственные функции. Показано, что данный подход позволяет получить полную ортонормированную систему собственных функций исходной нелокальной задачи, образующую базис в пространстве $L_2(\Omega)$.

Ключевые слова: уравнение Пуассона, нелокальные краевые задачи, функция Грина, задача Неймана, задача Робена, спектральная задача, собственные значения и собственные функции.

УДК 519.62
МРНТИ 27.35.21; 27.35.47; 27.41.19

https://doi.org/10.55452/1998-6688-2026-23-3-33-46

[1]*Исахов А.А.,
профессор, ORCID ID: 0000-0002-1937-8615,
*e-mail: alibek.issakhov@gmail.com
[1]Бейсембеков М.Е.,
бакалавр, ORCID ID: 0009-0004-5395-4569,
e-mail: m_beisembekov @kbtu.kz

[1]Казахстанско-Британский технический университет, г. Алматы, Казахстан

ПРИМЕНЕНИЕ ФИЗИКО-ОРИЕНТИРОВАННЫХ НЕЙРОННЫХ СЕТЕЙ ДЛЯ РЕШЕНИЯ ЗАДАЧ ЛИНЕЙНЫХ УРАВНЕНИЙ В ЧАСТНЫХ ПРОИЗВОДНЫХ С НЕОДНОРОДНЫМИ СМЕШАННЫМИ ГРАНИЧНЫМИ УСЛОВИЯМИ

Аннотация

В работе рассматривается применение Physics-Informed Neural Networks (PINN) для решения двумерного уравнения Пуассона с неоднородными смешанными граничными условиями. Метод PINN объединяет нейросетевые аппроксимации и физические законы, включая невязку уравнения и ошибки на границе в единую функцию потерь. Модель реализована в среде PyTorch и обучалась на выборке, сгенерированной методом латинской гиперкубической выборки. Для проверки точности проведено сравнение с аналитическим решением, а также с традиционными численными методами. Систематически исследовано влияние ключевых гиперпараметров: числа обучающих точек, весов в функции потерь, архитектуры сети и шага обучения. Установлено, что увеличение веса на граничные условия улучшает сходимость и точность, а оптимальные архитектуры с 4–5 скрытыми слоями и 64 нейронами обеспечивают относительную ошибку менее 0.1–0.2%. В отличие от численных схем, требующих сеточной дискретизации, PINN продемонстрировал универсальность и высокую точность при работе с разреженными данными и сложными условиями, что делает его перспективным инструментом для задач вычислительной математики и моделирования физических процессов в условиях сложной геометрии и неполной информации.

Ключевые слова: методы машинного обучения, модель PINN, уравнение Пуассона, функция одиночных потерь, гиперпараметры.

Введение

Развитие методов машинного обучения и нейронных сетей в последние годы оказало значительное влияние на широкий спектр научных и инженерных дисциплин. Современные модели, опирающиеся на глубокое обучение, продемонстрировали высокую эффективность в таких областях, как компьютерное зрение, обработка естественного языка, генерация изображений и прогнозирование временных рядов. Постепенно эти методы начали внедряться в сферу научных вычислений, включая моделирование физических процессов.

Особое внимание привлекли подходы, направленные на решение дифференциальных уравнений, лежащих в основе большинства моделей в физике, механике, теплообмене и других отраслях. Благодаря свойству универсальной аппроксимации нейросети оказались способными приближать решения таких уравнений даже в условиях разреженных данных, сложной геометрии и ограниченной информации о граничных условиях. Эти особенности сделали нейросетевые методы привлекательной альтернативой традиционным численным схемам, таким как метод конечных разностей и метод конечных элементов, особенно в случаях, когда доступ к данным ограничен или постановка задачи требует гибкости.

Идея интеграции физических законов непосредственно в структуру нейросетевой модели была систематизирована и формализована в работах Raissi, Perdikaris и Karniadakis, заложивших основу концепции Physics-Informed Neural Networks (PINNs) [1]. В отличие от традиционных подходов, PINN минимизирует функцию потерь, которая включает не только отклонение от известных данных, но и невязку уравнения в частных производных, тем самым обеспечивая физическую согласованность модели.

Несмотря на широкое распространение Physics-Informed Neural Networks (PINNs) лишь в последние годы, сама идея использования нейросетей для приближенного решения дифференциальных уравнений уходит корнями в 1980–90-е годы. Одними из первых эту тему систематически изучали Lagaris, Likas и Fotiadis [2], а также Dissanayake и Phan-Thien [3]. Они рассматривали возможность аппроксимации решения уравнений с помощью нейронных сетей, при этом особое внимание уделялось точному соблюдению граничных условий – так называемому подходу с жесткими ограничениями, при котором граничные условия встроены в функциональную форму приближения и выполняются автоматически.

Теоретическую основу этим работам придала статья Hornik, Stinchcombe и White [4], в которой было доказано, что многослойные полносвязные нейронные сети являются универсальными аппроксиматорами. Это означало, что при достаточном числе параметров и подходящей архитектуре нейросети способны приближать решения самых разных уравнений в частных производных. Другие исследователи, такие как Lee и Kang [5], Psichogios и Ungar [6], изучали возможность объединения знаний из первых принципов с данными, создавая гибридные подходы к моделированию физических процессов.

Возвращение к нейросетевым методам решения дифференциальных уравнений стало возможным благодаря стремительному развитию технологий в области искусственного интеллекта и глубокого обучения. Одним из ключевых факторов стало широкое распространение графических процессоров (GPUs), что сделало обучение нейросетей более масштабируемым и быстрым. Важным шагом также стало появление библиотек автоматического дифференцирования, таких как TensorFlow и PyTorch [7, 8], что позволило напрямую включать производные по входным переменным в вычислительный граф и использовать их в функции потерь.

На этом фоне начала активно развиваться концепция physics-informed подходов. Raissi, Yazdani и Karniadakis [9] предложили метод скрытой гидродинамики, позволяющий по визуализации течения восстанавливать распределения давления и скорости. Haghighat et al. [10] расширили PINN на задачи механики твердого тела, включая инверсные задачи и моделирование переноса. Wu et al. [11] провели всесторонний анализ методов адаптивного семплирования и их влияния на точность PINN. Mishra и Molinaro [12] предложили строгие оценки обобщающей ошибки при применении PINN к обратным задачам.

Современные PINN-модели находят применение в самых различных областях науки и техники, демонстрируя гибкость подхода и его способность работать с частичными, шумными и разреженными данными. В области гидродинамики PINN используется как для ламинарных течений [13], так и для турбулентных режимов [14], включая моделирование ближнестеночных эффектов в крупномасштабных вихревых моделях (LES) [15]. В биомеханике и гемодинамике PINN позволяет восстанавливать параметры кровотока по данным магнитно-резонансной томографии (4D flow MRI) [16], реконструировать поля давления в артериях [17], а также моделировать процессы электрической активации миокарда [18].

Метод также успешно применяется в геофизике, например, для моделирования волнового распространения и решения задач полной волновой инверсии [19]; в нефтегазовой инженерии – для моделирования фильтрации в пористых средах [20]; в задачах теплопереноса [21, 22], в области нанофотоники и метаматериалов [23], а также в многомасштабном моделировании сложных материалов. Такой широкий спектр применения демонстрирует, что PINN может служить универсальным инструментом научного моделирования и предсказания в условиях ограниченной или неполной информации.

Материалы и методы

Постановка задачи

Рассматривается двумерное эллиптическое уравнение с реакцией на прямоугольной области $\Omega \in \mathbb{R}^2$:

$$\frac{\partial^2 u}{\partial x^2} + \frac{\partial^2 u}{\partial y^2} + 3u = -2\sin(x+2y) + 16e^{2x+3y}, \qquad (x,y) \in \Omega$$

Область определения выбирается как $\Omega = [0, 1/4] \times [0, 1/2]$.

На границе $\partial\Omega$ задаются неоднородные граничные условия смешанного типа:

На нижней границе ($y = 0$) устанавливается условие Неймана:

$$\frac{\partial u}{\partial y} = 2\cos(x+2y) + 3e^{2x+3y}$$

На остальных трех границах ($x = 0, x = \frac{1}{4}, y = 1/2$) устанавливается условие Дирихле:

$$u = \sin(x+2y) + e^{2x+3y}$$

Аналитическое решение данной задачи известно и имеет вид:

$$u(x,y) = \sin(x+2y) + e^{2x+3y}$$

Приближенное решение аппроксимируется нейросетевой моделью $u_\theta(x,y)$, параметризованной вектором θ. Модель обучается на основе невязки (residual) в уравнении и граничных условиях.

Реализация PINN

Physics-Informed Neural Networks (PINNs) представляют собой класс нейросетевых моделей, ориентированных на решение дифференциальных уравнений путем включения физической информации непосредственно в функцию потерь. Такой подход позволяет обойти необходимость в традиционной дискретизации и использовать как данные, так и структуру уравнения для обучения модели.

Типичная архитектура PINN представляет собой многослойную полносвязную нейросеть с активацией tanh, которая широко используется из-за ее гладкости и способности точно приближать решения гладких уравнений [24]. На вход подаются пространственно-временные координаты (x,y,t), а на выходе – предсказание физической величины u (давления, температуры, скорости и т.п.). В дальнейшем будем обозначать нейросетную аппроксимацию точного решения $u(x,y)$ как $u_\theta(x,y)$, где θ – совокупность всех обучаемых параметров сети и имеющей архитектуру глубины D: входной слой, $D-2$ скрытых слоя и выходной слой

$$u_\theta(x,y) = L^{(D)} \circ \sigma \circ L^{(D-1)} \circ \sigma \circ \ldots \circ \sigma \circ L^{(1)}(x,y)$$

где $L^{(d)}(z) = W^{(l)}z + b^{(l)}$ – линейное преобразование на слое d, σ – функция активации, а $\theta = \{W^{(d)}, b^{(d)}\}_{d=1}^{D}$ – совокупность всех обучаемых параметров модели.

Функция потерь имеет вид:

$$\mathcal{L} = \omega_f \mathcal{L}_f + \omega_b \mathcal{L}_b + \omega_0 \mathcal{L}_o$$

где $\mathcal{L}_f$ – невязка уравнения (PDE residual loss), $\mathcal{L}_b$ – ошибка на границе (boundary condition loss), $\mathcal{L}_0$ – ошибка начального условия (initial condition loss), $\omega_f, \omega_b, \omega_0$ – гиперпараметры весов.

Модель обучается на трех типах точек:

1) граничные точки

2) начальные точки, если задача нестационарная

3) внутренние точки

Производные для $\mathcal{L}_f$ вычисляются автоматически с помощью механизма автоматического дифференцирования (automatic differentiation), реализованного в современных библиотеках, таких как PyTorch и TensorFlow [7, 8].

Инициализация весов сети играет ключевую роль в стабильности и сходимости обучения. Помимо стандартных подходов, таких как Xavier initialization, в литературе предлагаются и более адаптированные стратегии [25].

Хотя в данной работе используется базовая архитектура, в более сложных постановках PINN может быть расширена. Например, в модели PhyGeoNet [26] реализована геометрически адаптивная сверточная сеть (CNN), а в gradient-enhanced PINNs [27] добавляются производные высших порядков в лосс-функцию для повышения точности в обратных задачах.

Наиболее распространенным выбором функция потерь в PINN строится как среднеквадратичная ошибка (MSE) [1] и имеет вид:

$$\mathcal{L} = \omega_f MSE_f + \omega_b MSE_b + \omega_0 MSE_o$$

И включает несколько слагаемых: одно отвечает за выполнение самого дифференциального уравнения во внутренних точках области, другое – за выполнение граничных условий, и отдельное – за начальные условия. Каждое из этих слагаемых можно умножить на свой вес, чтобы регулировать их вклад в общую функцию потерь. Таким образом, итоговый loss представляет собой взвешенную сумму ошибок, что позволяет сбалансировать точность аппроксимации решения в уравнении и на границах.

$$MSE_f = \frac{1}{N_f}\sum_{i=1}^{N_f}(u_\theta(x_i, y_i) - u(x_i, y_i))^2$$

$$= \frac{1}{N_f}\sum_{i=1}^{N_f}\left(\frac{\partial^2 u}{\partial x^2} + \frac{\partial^2 u}{\partial y^2} + 3u - (-2\sin(x+2y) + 16e^{2x+3y})\right)^2$$

Граничные условия

$$MSE_b = \frac{1}{N_b}\sum_{i=1}^{N_b}(u_\theta(x_i, y_i) - u(x_i, y_i))^2$$

Для поставленной задачи среднеквадратичная ошибка на граничных условиях раскладывается как:

$$MSE_b = MSE_{b(neumann)} + MSE_{b(dirichlet)}$$

$$= \frac{1}{N_d}\sum_{i=1}^{N_d}(u_\theta(x_i, y_i) - u(x_i, y_i))^2 + \frac{1}{N_n}\sum_{i=1}^{N_n}\left(\frac{\partial u_\theta}{\partial y}(x_i, 0) - (2\cos(x_i) + 3e^{2x_i})\right)^2$$

Это позволяет отдельно учитывать вклад условий Неймана и Дирихле в общую функцию потерь.

$$N_b = N_d + N_n$$

где N_f – количество внутренних точек, N_d – количество точек Дирихле, N_n – количество точек Неймана, N_b – количество граничных точек.

В данной работе точки выбираются с использованием метода латинской гиперкубической выборки (LHS), что обеспечивает равномерное покрытие области без регулярной сетки. Такой подход является стандартным и хорошо зарекомендовал себя при решении задач с PINN. Более сложные стратегии, включая остаточно-адаптивное распределение, могут существенно повышать точность, особенно в задачах с локализованными особенностями решения. Их сравнительный анализ представлен в работе Wu et al. [11].

Значения весов в функции потерь выбираются эмпирически: для усиления выполнения граничных условий используется $\omega_b = 100$, при этом вес на уравнение равен $\omega_f = 1$. Для минимизации функции потерь используется оптимизатор Adam с фиксированным шагом обучения $\eta = 10^{-3}$. Общая продолжительность обучения составляет от 5000 до 10 000 эпох в зависимости от задачи. Дополнительные оптимизаторы, такие как L-BFGS, в рамках данной работы не использовались. Обучающая выборка состоит из $N_f = 10000$ внутренних точек и $N_b = 1000$ граничных точек.

Точки генерируются с использованием метода латинской гиперкубической выборки (LHS), обеспечивающего равномерное покрытие области и границы. Все вычисления проводятся на графическом процессоре NVIDIA GeForce GTX 1650 Ti (GPU) с использованием фреймворка PyTorch. Инициализация весов нейросети осуществляется по схеме Xavier normal initialization.

Базовая настройка модели

Для начального этапа обучения модели PINN была выбрана следующая конфигурация гиперпараметров: количество внутренних точек $N_f = 1000$, количество граничных точек $N_b = 100$, количество эпох $Epochs = 10000$, вес функции потерь на граничных условиях $\omega_b = 1$, вес функции потерь в уравнении $\omega_f = 1$, архитектура сети: 4 скрытых слоя по 32 нейрона в каждой, функция активации tanh, оптимизатор Adam, скорость обучения (learning rate) 10^{-3}.

Результаты и обсуждение

Влияние плотности обучающих точек на точность PINN

Одним из ключевых факторов, влияющих на точность решений, получаемых с помощью Physics-Informed Neural Networks (PINNs), является количество точек, на которых рассчитываются невязки: внутренних и граничных. В этом исследовании фиксировались все параметры модели, кроме N_f и N_b, чтобы изолировать их влияние (таблица 1). Использовалась следующая конфигурация: $\text{Epochs} = 10000$, $\text{Loss weights: } \omega_\text{f} = 1, \omega_\text{b} = 1$, $\text{Architecture: 4 hidden layes, 32 neurons each layer}$, $\text{Activation function: tanh}$, Optimizer: Adam.

На рисунке 1 представлено сопоставление аналитического решения, численного решения, предсказанного моделью, а также распределение абсолютной ошибки для трех уровней плотности обучающих точек. Анализ показывает, что во всех рассматриваемых случаях модель корректно воспроизводит форму аналитического решения, а локализация областей повышенной ошибки сохраняется независимо от плотности выборки. Это свидетельствует о стабильности аппроксимационных свойств модели при варьировании

количества обучающих данных. На рисунке 2 показано распределение обучающих точек, сгенерированных с использованием метода латинского гиперкуба (LHS). Данный метод обеспечивает квазирегулярное покрытие расчетной области, минимизируя кластеры точек и снижая вероятность возникновения плохо аппроксимируемых зон. Равномерность распределения точек позволяет интерпретировать различия в точности модели преимущественно как следствие архитектурных и оптимизационных особенностей, а не как эффект неравномерного семплирования пространства. Как видно из рисунка 3, после примерно 2000 эпох обучения наблюдается появление выраженных высокочастотных пиков функции потерь. Данное поведение указывает на неустойчивость процесса оптимизации и может быть интерпретировано как «перепрыгивание» оптимального решения вследствие слишком большого шага обучения или накопления градиентных колебаний. Несмотря на это, итоговые значения ошибок остаются ограниченными, что свидетельствует о способности модели сохранять приемлемое качество аппроксимации даже при наличии локальной нестабильности на поздних этапах обучения. На рисунке 3 также представлены результаты для трех расчетных кейсов (A, B и C), отличающихся количеством внутренних и граничных точек. Сравнительный анализ показывает, что увеличение плотности как внутренних, так и граничных точек не приводит к заметному улучшению точности решения. Это подтверждается тем, что все метрики ошибки – максимальная ошибка, средняя абсолютная ошибка (MAE), среднеквадратичная ошибка (MSE) и относительная ошибка в норме L2 – находятся в узком диапазоне значений (таблица 2). Количественно установлено, что максимальная ошибка варьируется в пределах 0.023–0.025, различие значений MAE не превышает 0.001, а расчетное время изменяется незначительно и составляет 126–130 секунд. Эти результаты указывают на насыщение точности модели: при фиксированной архитектуре нейронной сети и неизменной стратегии обучения дальнейшее увеличение плотности обучающих точек не приводит к существенному снижению ошибки, но сопровождается ростом вычислительных затрат. В целом полученные данные позволяют заключить, что для рассматриваемой задачи плотность обучающих точек не является определяющим фактором точности решения при условии адекватного покрытия расчетной области и корректно выбранной архитектуры модели. Основные ограничения точности, по-видимому, обусловлены выразительной способностью нейронной сети и особенностями процедуры оптимизации, что указывает на целесообразность дальнейших исследований, направленных на адаптацию архитектуры, стратегии регуляризации и схемы обучения, а не на простое увеличение объема обучающей выборки.

Таблица 1 – Параметры для трех уровней плотности

Case	N_f	N	Description
A	400	40	Sparse
B	1000	100	Medium
C	10000	1000	High dense

Таблица 2 – Сравнение различных параметров ошибок для трех уровней плотности

Case	Max error	MAE	MSE	L2 relative error %	Calculation time (s)
A	0.024198	0.007315	6.5040e-05	0.2186 %	128.47
B	0.024743	0.007557	7.7533e-05	0.2237 %	126.30
C	0.023278	0.006587	6.1723e-05	0.1996 %	130.21

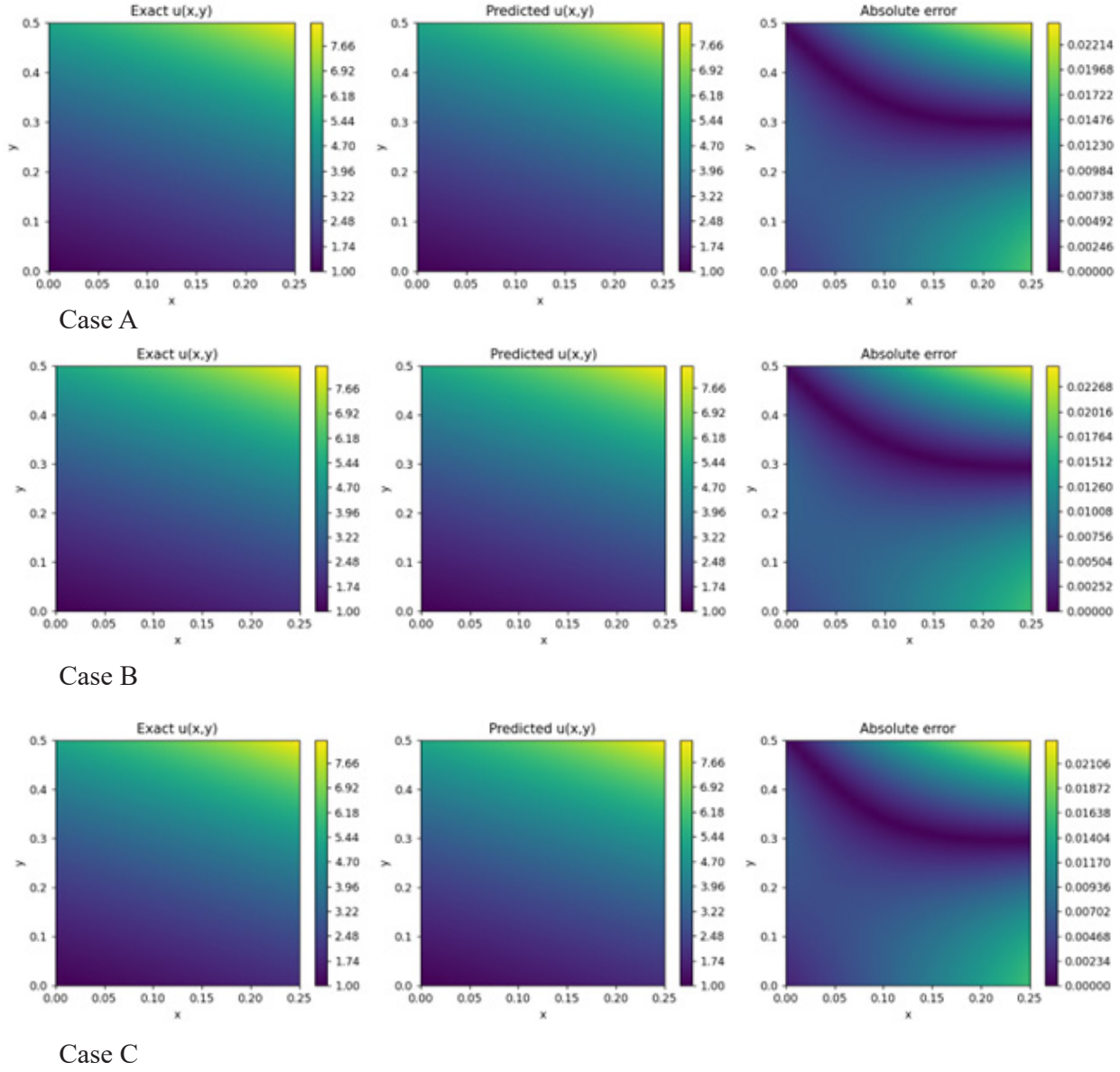


Рисунок 1 – Сравнение численного решения, прогнозированного решения и аналитического решения для трех уровней плотности

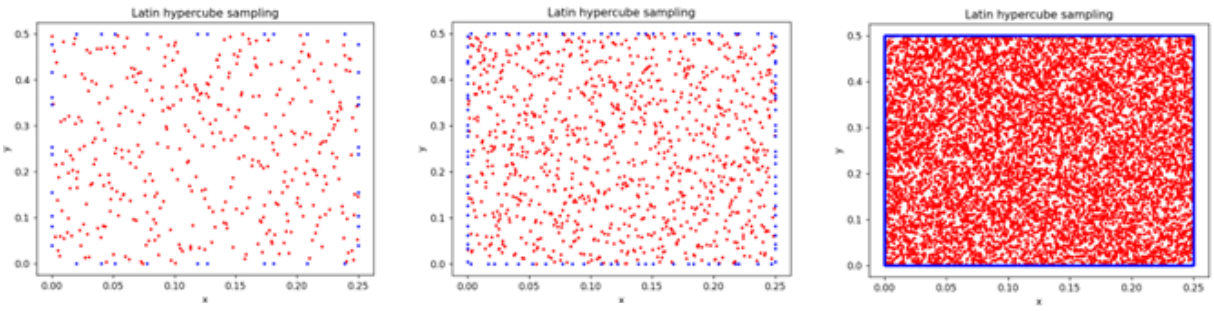
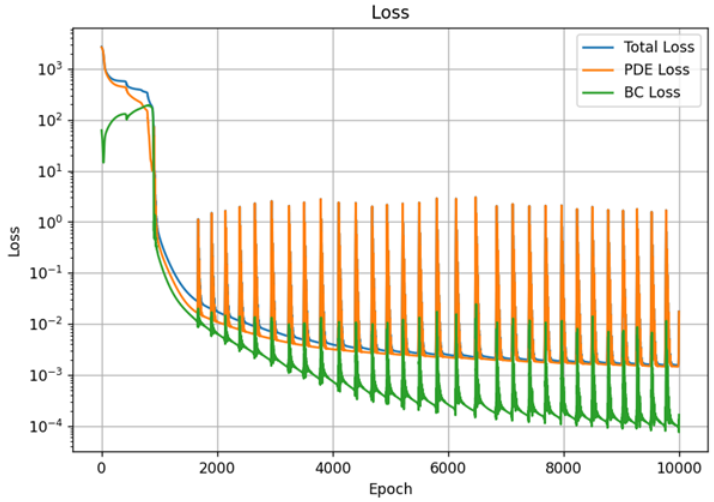
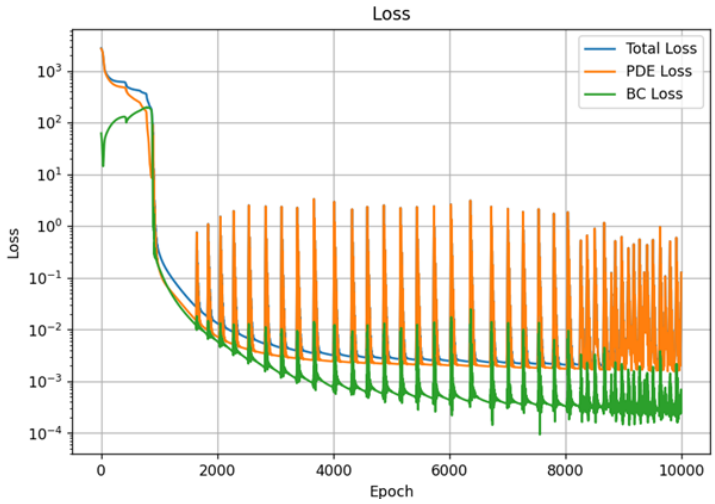


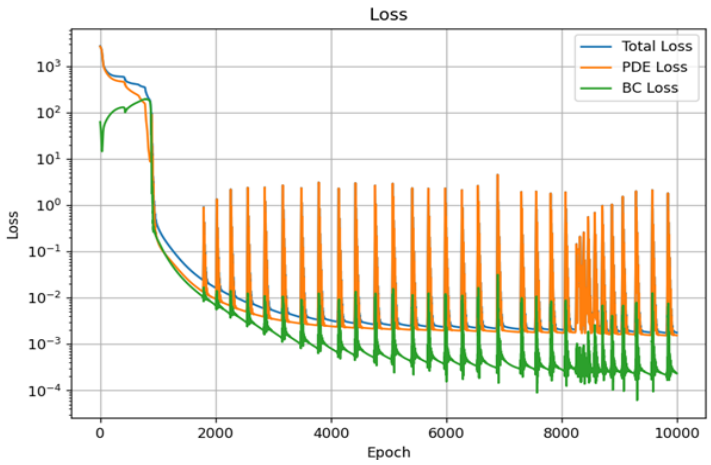
Рисунок 2 – Распределение точек по методу LHS



A



B



C

Рисунок 3 – Графики падения функции потерь для трех уровней плотности.

Влияние весовых коэффициентов функции потерь на точность модели

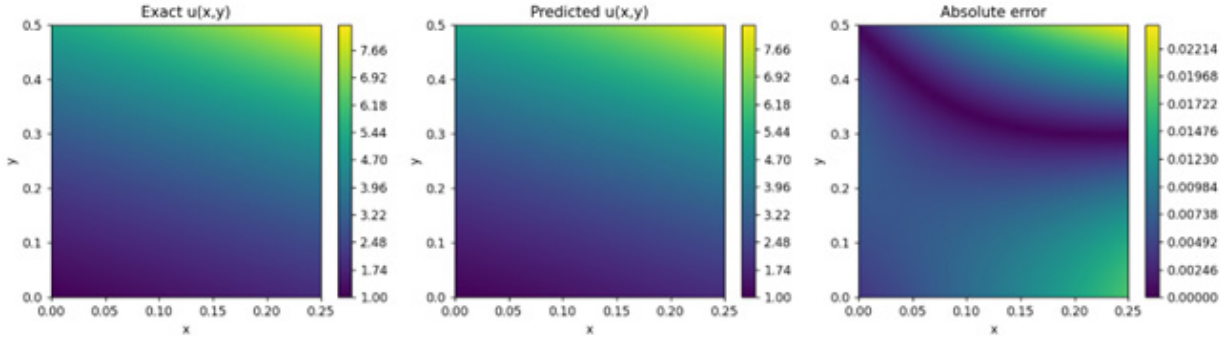
В данном разделе исследуется влияние весового коэффициента при расчете функции потерь на граничных условиях на общую точность модели. В то время как вес уравнения сохраняется постоянным и равным 1, параметр варьируется в пределах [1, 10, 100] (таблица 3). Такое масштабирование позволяет понять, насколько важным является точное соблюдение граничных условий при обучении PINN и как оно влияет на аппроксимацию решения в области.

Для каждого случая фиксируются все остальные параметры: архитектура сети (4 скрытых слоя по 32 нейрона), количество обучающих точек, количество эпох и скорость обучения. Основное внимание уделяется сравнительному анализу ошибок и времени расчета. Исходя из этих наблюдений, в дальнейшем фиксируется значение во всех следующих экспериментах.

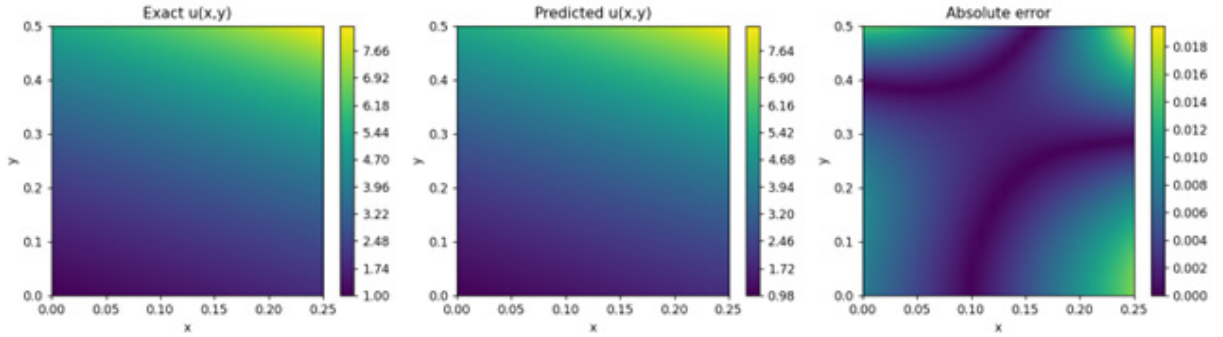
На рисунке 4 представлено сравнение трех расчетных кейсов, отличающихся степенью сгущения обучающих точек, с учетом влияния весовых коэффициентов функции потерь. Анализ полученных распределений показывает, что варьирование плотности точек в сочетании с изменением весового коэффициента граничных условий приводит к более выраженным изменениям точности решения, чем изолированное увеличение числа обучающих точек. Это указывает на ключевую роль балансировки компонент функции потерь в задачах физически информированных нейронных сетей (PINN). На рисунке 5 приведены графики эволюции функции потерь в процессе обучения для трех уровней плотности обучающих точек при различных значениях весовых коэффициентов. Видно, что при увеличении наблюдается более крутое начальное падение функции потерь и более раннее достижение плато, что свидетельствует об ускорении сходимости оптимизационного процесса. При этом различия между кейсами с разной плотностью точек остаются вторичными по сравнению с влиянием весовых коэффициентов. Количественные данные, представленные в таблице 3, показывают, что, несмотря на увеличение значения , общее время обучения не возрастает пропорционально и в ряде случаев даже уменьшается. Данный эффект объясняется тем, что усиление вклада граничных условий в целевую функцию заставляет модель на ранних этапах обучения быстрее удовлетворять физическим и геометрическим ограничениям на границе расчётной области. Это, в свою очередь, снижает степень конфликта между остатками дифференциального уравнения и граничными условиями, облегчая последующее глобальное минимизирование функции потерь. С точки зрения оптимизации увеличение веса приводит к более направленному градиентному потоку, уменьшая вероятность попадания модели в локальные минимумы, обусловленные несогласованностью различных компонент функции потерь. В результате достигается не только повышение точности аппроксимации вблизи границы, но и более стабильное и быстрое обучение в целом. Таким образом, полученные результаты демонстрируют, что корректный выбор весовых коэффициентов функции потерь является более эффективным инструментом повышения точности и ускорения сходимости PINN по сравнению с простым увеличением плотности обучающих точек. Это подчеркивает необходимость адаптивных или проблемно-ориентированных стратегий балансировки весов компонент функции потерь, особенно для задач с жесткими граничными условиями и сложной физической структурой решения.

Таблица 3 – Сравнение относительных ошибок для трех уровней плотности при влиянии весовых коэффициентов функции потерь

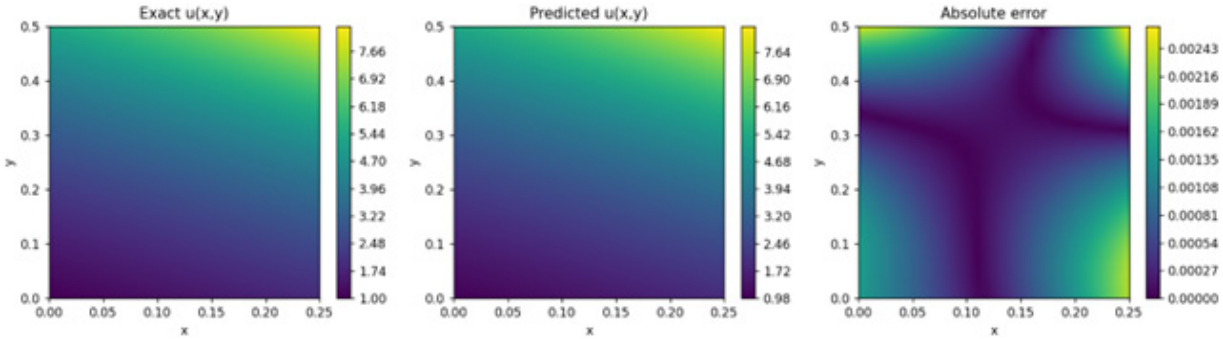
Case	ω_b	Max error	MAE	MSE	L2 relative error	Calculation time (s)
A	1	0.024198	0.007315	6.5040e-05	0.2186 %	128.47
B	10	0.022492	0.005535	4.9847e-05	0.1794 %	131.13
C	100	0.002640	0.000713	8.4998e-07	0.0234 %	137.77



Case A

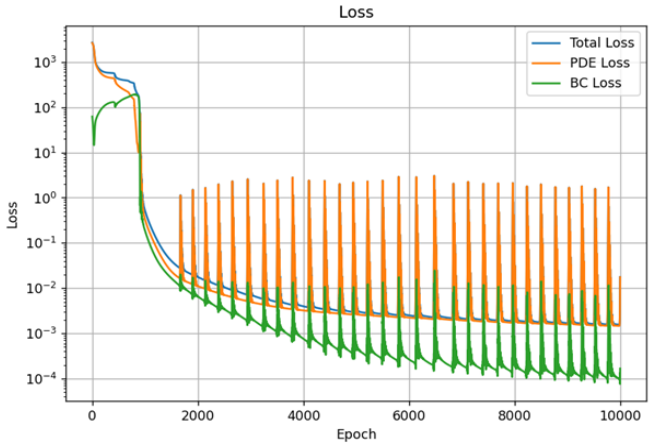


Case B

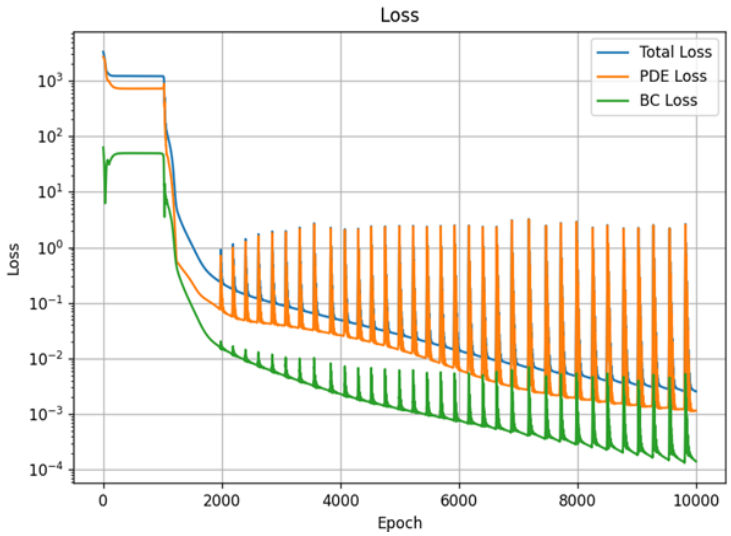


Case C

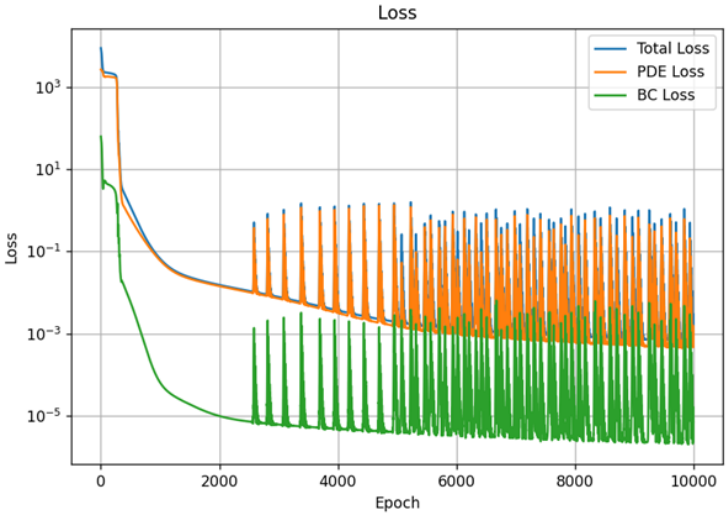
Рисунок 4 – Сравнение численного решения, прогнозированного решения
и аналитического решения при влиянии весовых коэффициентов функции потерь



Case A



Case B



Case C

Рисунок 5 – Графики падения функции потерь для трех уровней плотности при влиянии весовых коэффициентов функции потерь

Заключение

В данной работе была рассмотрена эффективность применения Physics-Informed Neural Networks (PINN) для решения двумерного уравнения Пуассона. Модель была реализована с использованием библиотеки PyTorch и обучалась на сгенерированных с помощью латинского гиперкубического метода точках. Для валидации решений проводилось сравнение с аналитическим и численным решениями.

Было проведено систематическое исследование влияния различных гиперпараметров модели, которые включают плотность выборки точек, веса функций потерь , архитектуру сети (число слоев и нейронов), шаг обучения.

Основные выводы:

◆ Модель PINN продемонстрировала высокую точность решения, с относительной ошибкой по норме L2, не превышающей 1% во всех конфигурациях и достигающей менее 0.1% при оптимальных архитектурах.

◆ Изменение числа обучающих точек (от 400 до 10000) оказало незначительное влияние на точность, особенно при достаточном покрытии области.

◆ Увеличение веса граничных условий до 100 существенно улучшило сходимость и точность.

В дополнение к этому были проведены сравнения с традиционными численными методами. Последние показали более низкое время расчета и высокую точность (относительная L2 ошибка 0.01%), но требуют явной дискретизации и зависят от качества сетки. В отличие от них, PINN не требует сеточной структуры и может быть применен к произвольным геометриям и условиям.

Таким образом, PINN-подход подтвердил свою универсальность и точность при решении уравнений математической физики, особенно в случаях сложных геометрий и неполных данных. Работа не только демонстрирует применимость PINN на классическом уравнении Пуассона, но и служит отправной точкой для более глубокого изучения PINN в области вычислительной математики и моделирования физических процессов.

Информация о финансировании

Работа поддержана грантами Министерства науки и высшего образования Республики Казахстан (AP32320067).

ЛИТЕРАТУРА

1 Raissi, M., Perdikaris, P., Karniadakis, G.E.: Physics-informed neural networks: A deep learning frame work for solving forward and inverse problems involving nonlinear partial differential equations. J. Comput. Phys. 378, 686–707 (2019). https://doi.org/10.1016/j.jcp.2018.10.045

2 Lagaris, I., Likas, A., Fotiadis, D.: Artificial neural networks for solving ordinary and partial differential equations. IEEE Trans. Neural Networks 9(5), 987–1000 (1998). https://doi.org/10.1109/72.712178

3 Dissanayake, M.W.M.G., Phan-Thien, N.: Neural-network-based approximations for solving partial differential equations. Commun. Numer. Methods Eng. 10(3), 195–201 (1994). https://doi.org/10.1002/cnm.1640100303

4 Hornik, K., Stinchcombe, M., White, H.: Multilayer feedforward networks are universal approxima tors. Neural Networks 2(5), 359–366 (1989). https://doi.org/10.1016/0893-6080(89)90020-8

5 Lee, H., Kang, I.S.: Neural algorithm for solving differential equations. J. Comput. Phys. 91(1), 110 131 (1990). https://doi.org/10.1016/0021-9991(90)90007-N

6 Psichogios, D.C., Ungar, L.H.: A hybrid neural network-first principles approach to process modeling. AIChEJ.38(10),1499–1511(1992). https://doi.org/10.1002/aic.690381003

7 Haghighat,E.,Juanes,R.:SciANN:AKeras/Tensorflow wrapper for scientific computations and physics-informed deep learning using artificial neural networks. Comput. Methods Appl. Mech. Engrg. 373, 113,552 (2021). https://doi.org/10.1016/j.cma.2020.113552

8 Paszke,A.,Gross,S.,Chintala, S., et al.: Automatic differentiation in PyTorch. Tech. rep., (2017) https://openreview.net/forum?id=BJJsrmfCZ

9 Raissi,M.,Yazdani,A.,Karniadakis,G.E.:Hidden fluid mechanics: Learning velocity and pressure fields from flow visualizations. Sci. 367(6481), 1026–1030 (2020). https://doi.org/10.1126/science.aaw4741

10 Haghighat, E., Raissi, M., Moure, A., et al.: A physics-informed deep learning framework for inversion and surrogate modeling in solid mechanics. Comput. Methods Appl. Mech. Engrg. 379, 113,741 (2021b). https://doi.org/10.1016/j.cma.2021.113741

11 Wu, C., Zhu, M., Tan, Q., Kartha, Y. and Lu, L., A Comprehensive Study of Non-Adaptive and Residual-Based Adaptive Sampling for Physics-Informed Neural Networks, Computer Methods in Applied Mechanics and Engineering, vol. 403, p. 115671, October 22, 2022. https://doi.org/10.1016/j.cma.2022.115671

12 Mishra, S., Molinaro, R.: Estimates on the generalization error of physics-informed neural networks for approximating a class of inverse problems for PDEs. IMA J. Numer. Anal. (2021). https://doi.org/10. 1093/imanum/drab032

13 Rao, C., Sun, H., & Liu, Y. (2020). Physics-informed deep learning for incompressible laminar flows. Theoretical and Applied Mechanics Letters, 10(3), 207–212. https://doi.org/10.1016/j.taml.2020.01.039

14 Wang, R., Kashinath, K., Mustafa, M., Albert, A., & Yu, R. (2019). Towards Physics-informed Deep Learning for Turbulent Flow Prediction. ArXiv.org. https://arxiv.org/abs/1911.08655

15 Yang, X. I. A., Zafar, S., Wang, J.-X. ., & Xiao, H. (2019). Predictive large-eddy-simulation wall modeling via physics-informed neural networks. Physical Review Fluids, 4(3). https://doi.org/10.1103/physrevfluids.4.034602

16 Kissas, G., Yang, Y., Hwuang, E., Witschey, W. R., Detre, J. A., & Perdikaris, P. (2020). Machine learning in cardiovascular flows modeling: Predicting arterial blood pressure from non-invasive 4D flow MRI data using physics-informed neural networks. Computer Methods in Applied Mechanics and Engineering, 358, 112623. https://doi.org/10.1016/j.cma.2019.112623

17 Arzani, A., Wang, J.-X., & D'Souza, R. M. (2021). Uncovering near-wall blood flow from sparse data with physics-informed neural networks. Physics of Fluids, 33(7), 071905. https://doi.org/10.1063/5.0055600

18 Sahli Costabal, F., Yang, Y., Perdikaris, P., Hurtado, D. E., & Kuhl, E. (2020). Physics-Informed Neural Networks for Cardiac Activation Mapping. Frontiers in Physics, 8. https://doi.org/10.3389/fphy.2020.00042

19 Rasht-Behesht, M., Huber, C., Shukla, K., & Karniadakis, G. E. (2022). Physics-Informed Neural Networks (PINNs) for Wave Propagation and Full Waveform Inversions. Journal of Geophysical Research: Solid Earth, 127(5). https://doi.org/10.1029/2021jb023120

20 Almajid, M. M., & Abu-Al-Saud, M. O. (2022). Prediction of porous media fluid flow using physics informed neural networks. Journal of Petroleum Science and Engineering, 208, 109205. https://doi.org/10.1016/j.petrol.2021.109205

21 Cai, S., Wang, Z., Wang, S., Perdikaris, P., & Karniadakis, G. (2021). Physics-Informed Neural Networks (PINNs) for Heat Transfer Problems. Journal of Heat Transfer. https://doi.org/10.1115/1.4050542

22 Zobeiry, N., & Humfeld, K. D. (2021). A physics-informed machine learning approach for solving heat transfer equation in advanced manufacturing and engineering applications. Engineering Applications of Artificial Intelligence, 101, 104232. https://doi.org/10.1016/j.engappai.2021.104232

23 Chen, Y., Lu, L., Karniadakis, G. E., & Dal Negro, L. (2020). Physics-informed neural networks for inverse problems in nano-optics and metamaterials. Optics Express, 28(8), 11618. https://doi.org/10.1364/oe.384875

24 De Ryck, T., Lanthaler, S., & Mishra, S. (2021). On the approximation of functions by tanh neural networks. Neural Networks, 143, 732–750. https://doi.org/10.1016/j.neunet.2021.08.015

25 Liu, X., Zhang, X., Peng, W., Zhou, W., & Yao, W. (2022). A novel meta-learning initialization method for physics-informed neural networks. Neural Computing and Applications, 34(17), 14511–14534. https://doi.org/10.1007/s00521-022-07294-2

26 Gao, H., Sun, L., & Wang, J.-X. (2021). PhyGeoNet: Physics-informed geometry-adaptive convolutional neural networks for solving parameterized steady-state PDEs on irregular domain. Journal of Computational Physics, 428, 110079. https://doi.org/10.1016/j.jcp.2020.110079

27 Yu, J., Lu, L., Meng, X., & Karniadakis, G. E. (2022). Gradient-enhanced physics-informed neural networks for forward and inverse PDE problems. Computer Methods in Applied Mechanics and Engineering, 393, 114823. https://doi.org/10.1016/j.cma.2022.114823

[1]*Исахов А.А.,
профессор, ORCID ID: 0000-0002-1937-8615, *e-mail: alibek.issakhov@gmail.com
[1]Бейсембеков М.Е.
бакалавр, ORCID ID: 0009-0004-5395-4569, e-mail: m_beisembekov @kbtu.kz

[1]Қазақстан-Британ техникалық университет, Алматы қ., Қазақстан

БІРТЕКТІ ЕМЕС АРАЛАС ШЕКАРАЛЫҚ ШАРТТАРМЕН БЕРІЛГЕН СЫЗЫҚТЫҚ ДЕРБЕС ТУЫНДЫ ТЕҢДЕУЛЕРДІ ШЕШУГЕ АРНАЛҒАН ФИЗИКАҒА НЕГІЗДЕЛГЕН НЕЙРОНДЫҚ ЖЕЛІЛЕРДІ ҚОЛДАНУ

Аңдатпа

Мақалада біртекті емес аралас шекаралық шарттары бар екі өлшемді Пуассон теңдеуін шешу үшін физикалық ақпараттандырылған нейрондық желілерді (PINN) қолдану қарастырылады. PINN тәсілі нейрондық желінің аппроксимациясын физикалық заңдармен үйлестіріп, теңдеу қалдығын және шекаралық шарттар қателіктерін бірыңғай шығын функциясына біріктіреді. Модель PyTorch ортасында жүзеге асырылады және латын гиперкубтық сынама алу әдісімен жасалған үлгіде оқытылады. Дәлдігін тексеру үшін аналитикалық шешіммен, сондай-ақ дәстүрлі сандық әдістермен салыстыру жүргізіледі. Негізгі гиперпараметрлердің әсері жүйелі түрде зерттеледі: жаттығу нүктелерінің саны, жоғалту функциясындағы салмақтар, желі архитектурасы және жаттығу қадамы. Шекаралық шарттардағы салмақты арттыру конвергенция мен дәлдікті жақсартатыны анықталды, ал 4–5 жасырын қабаты және 64 нейрондары бар оңтайлы архитектуралар 0,1–0,2%-дан аз салыстырмалы қателікті қамтамасыз етеді. Тордың дискретизациясын талап ететін сандық схемалардан айырмашылығы, PINN сирек деректермен және күрделі шарттармен жұмыс істеу кезінде әмбебаптығы мен жоғары дәлдігін көрсетті, бұл оны күрделі геометрия және толық емес ақпарат жағдайында есептеу математикасы мен физикалық процестерді модельдеу үшін перспективалы құралға айналдырды.

Түйін сөздер: машиналық оқыту әдістері, PINN моделі, Пуассон теңдеуі, жалғыз жоғалту функциясы, гиперпараметрлер.

[1]*Issakhov A.A.,
Professor, ORCID ID: 0000-0002-1937-8615, *e-mail: alibek.issakhov@gmail.com
[1]Beisembekov M.E.
Bachelor, ORCID ID: 0009-0004-5395-4569, e-mail: m_beisembekov @kbtu.kz

[1]Kazakh-British Technical University, Almaty, Kazakhsan

APPLICATION OF PHYSICALLY-ORIENTED NEURAL NETWORKS TO SOLVING PROBLEMS OF LINEAR PARTIAL DERIVATIVE EQUATIONS WITH INHOMOGENEOUS MIXED BOUNDARY CONDITIONS

Abstract

The paper considers the application of Physics-Informed Neural Networks (PINN) to solving a two-dimensional Poisson equation with inhomogeneous mixed boundary conditions. The PINN method combines neural network approximations and physical laws, including the residual of the equation and errors at the boundary, into a single loss function. The model is implemented in the PyTorch environment and trained on a sample generated by the Latin hypercubic sampling method. To verify the accuracy, a comparison is made with an analytical solution, as well as with traditional numerical methods. The influence of key hyperparameters is systematically studied: the number of training points, weights in the loss function, network architecture, and training step. It is found that increasing the weight on the boundary conditions improves convergence and accuracy, and optimal architectures with 4–5 hidden layers and 64 neurons provide a relative error of less than 0.1–0.2%. Unlike numerical schemes requiring grid discretization, PINN has demonstrated versatility and high accuracy when dealing with sparse data and complex conditions, making it a promising tool for computational mathematics and modeling of physical processes in conditions of complex geometry and incomplete information.

Keywords: machine learning methods, PINN model, Poisson equation, single loss function, hyperparameters.

Received September 2, 2025; revised May 29, 2026; accepted June 11, 2026.

УДК 510.67
МРНТИ 27.03.66

https://doi.org/10.55452/1998-6688-2026-23-3-47-54

[1.2 *]Вербовский В.В.,
доктор физико-математических наук, доцент,
ORCID ID: 0000-0001-5177-8523,
*e-mail: verbovskiy at math.kz
[1] Институт математики и математического моделирования, г. Алматы, Казахстан
[2] Казахский национальный исследовательский технический университет
им. К.И. Сатпаева, г. Алматы, Казахстан

О ЛОКАЛЬНОМ АНАЛОГЕ СВОЙСТВА СТРОГОГО ПОРЯДКА ВНУТРИ СЕЧЕНИЯ ДЛЯ ЛИНЕЙНО УПОРЯДОЧЕННЫХ СТРУКТУР

Аннотация

В работе исследуется локальный аналог свойства строгого порядка внутри сечения для линейно упорядоченных структур, возникающий в теории упорядоченно стабильных моделей. Рассматривается естественная попытка сформулировать это свойство через конечные цепи строго вложенных формульных подмножеств, пересеченных с реализациями сечения. Показано, что в такой формулировке это свойство не является элементарным: она может выполняться в элементарном расширении, но не сохраняться в исходной модели и, следовательно, не дает корректного локального критерия. Для устранения этого недостатка вводится понятие строгой вложенности выпуклых компонент определимых множеств, а также его равномерная версия для семейств формул с параметрами. Доказывается, что свойство строгого порядка внутри сечения эквивалентно существованию равномерного свойства вложенности выпуклых компонент. Полученный результат уточняет локальную природу данного свойства, показывает его отличие от классического локального свойства строгого порядка и позволяет применять его при исследовании упорядоченно стабильных теорий и их моделей. Тем самым работа дополняет критерий упорядоченной стабильности.

Ключевые слова: линейно упорядоченное множество, o-минимальность, упорядоченная стабильность, свойство строгого порядка.

Введение

Теория стабильности в рамках логики предикатов первого порядка возникла как попытка понять, какие теории допускают классификацию своих моделей. Отправной точкой стала теорема Морли (1965): если счётная теория категорична в некоторой несчётной мощности, то она категорична во всех несчётных мощностях [2]. Этот результат имеет фундаментальное значение, но он не даёт наглядного описания таких теорий. Дальнейшее развитие связано с работами Шелаха, который в конце 1960-х — 1970-х годов построил теорию стабильности как обобщение идей Морли. Вместо «глобального» ранга Морли, который использует все формулы данного языка, Шелах предложил определять ранг при помощи одной формулы или некоторого семейства формул [3]. Одним из центральных результатов является эквивалентность стабильности отсутствию свойства порядка. Наличие свойства порядка означает, что в теории можно закодировать линейный порядок произвольной длины, что свидетельствует о её высокой комбинаторной сложности. Отсутствие свойства порядка, напротив, обеспечивает контролируемость пространства типов и является одной из эквивалентных характеристик стабильности.

В свою очередь, свойство порядка можно разделить на два свойства: свойство независимос-ти и свойство строгого линейного порядка. Заметим, что одно свойство не исключает другого, так, существуют формулы, которые одновременно обладают и свойством независимости, и свойством строгого линейного порядка. В качестве простого примера можно взять формулу $\varphi(x, y) \rightleftharpoons x \mid y$ в структуре $(\mathbb{N}, |)$, где $x \mid y$ означает, что число x делит число y без остатка. Действительно, если вместо y подставлять степени некоторого числа, скажем, 2^n, то получаем свойство строгого порядка: любое число, которое делится на 2^{n+1}, делится и на 2^n; а если вместо y подставлять простые числа $p_1 = 2, p_2 = 3, \ldots$, то для любого числа $n > 1$ и любого подмножества $A \subseteq \{1, 2, \ldots, n\}$ число $_{i\in A} p_i$ делится на число p_i, если и только если $p_i \in A$.

С. Шелах доказал, что теория является стабильной тогда и только тогда, когда она не обладает ни свойством независимости, ни свойством строгого порядка. Заметим, что эти свойства можно выразить как при помощи существования бесконечных последовательно-стей, так и локально, что такое свойство выполняется для всех достаточно больших чисел n. Наличие локальных аналогов свойств независимости и строгого порядка позволяет упростить многие рассуждения.

Б.С. Байжанов и В.В. Вербовский в работе [**1**] ввели понятие упорядоченно стабильной теории, которое основано одновременно и на понятии стабильной теории, и на понятии о-минимальной теории. Там же они доказали, что упорядоченно стабильные теории не допускают свойства независимости. В.В. Вербовский в работе [**4**] ввел понятие строгого порядка внутри сечения и доказал аналог теоремы Шелаха о характеризации стабильных теорий: теория является упорядоченно стабильной тогда и только тогда, когда она не обладает ни свойством независимости, ни свойством строгого порядка внутри сечения. Однако оставался открытым вопрос описания локального варианта свойства строгого порядка внутри сечения. Ответу на данный вопрос и посвящена данная работа.

Материалы и методы

Здесь мы исследуем локальный аналог свойства строгого порядка внутри сечения для линейно упорядоченных структур. Методами исследования являются классические методы теории моделей, в частности, методы исследования стабильных теорий и линейно упорядоченных структур.

Результаты и обсуждение

Для начала вспомним классические определения.

Теория T обладает *свойством порядка*, если существует формула $\varphi(\bar{x}, \bar{y})$ (возможно с параметрами) и кортежи $\bar{a}_i, \bar{b}_i$ в некоторой модели $\mathcal{M} \models T$ такие, что для всех $i, j < \omega$:

$$\mathcal{M} \models \varphi(\bar{a}_i, \bar{b}_j) \quad \text{тогда и только тогда, когда} \quad i < j.$$

Формула $\varphi(\bar{x}, \bar{y})$ обладает *локальным свойством порядка* в структуре $\mathcal{M}$, если для любого натурального положительного числа n существуют кортежи $\bar{a}_i$ и $\bar{b}_j$ $(i, j < n)$ такие, что $\mathcal{M} \models \varphi(\bar{a}_i, \bar{b}_j) \iff i < j$.

Теория T обладает *свойством независимости*, если существует формула $\varphi(\bar{x}, \bar{y})$ и модель $\mathcal{M} \models T$, в которой существуют кортежи $\bar{a}_n$ $(n < \omega)$, такие что для любого множества $F \subseteq \omega$ найдется такой элемент $\bar{b}_F$, что: $\mathcal{M} \models \varphi(\bar{a}_n, \bar{b}_F)$ тогда и только тогда, когда $n \in F$.

Формула $\varphi(\bar{x}, \bar{y})$ обладает *локальным свойством независимости*, если существует формула $\varphi(\bar{x}, \bar{y})$, что для каждого положительного целого числа N существует модель $\mathcal{M} \models T$, в которой существуют кортежи $\bar{a}_n$ $(n < N)$, такие что для любого множества $F \subseteq N$ найдется такой элемент $\bar{b}_F$, что $\mathcal{M} \models \varphi(\bar{a}_n, \bar{b}_F)$ тогда и только тогда, когда $n \in F$.

Теория T обладает *свойством строгого порядка* (SOP), если существует формула $\varphi(\bar{x}, \bar{y})$, такая что в некоторой (эквивалентно, любой достаточно насыщенной) модели $\mathcal{M} \models T$ найдётся последовательность кортежей $\bar{a}_i$, где $i < \omega$, для которой выполнено:

$$\varphi(\mathcal{M}, \bar{a}_i) \subsetneq \varphi(\mathcal{M}, \bar{a}_j) \quad \Leftrightarrow \quad i < j.$$

Аналогично предыдущим определениям мы можем определить локальное свойство строгого порядка, рассматривая не бесконечную последовательность кортежей, а последовательности любой конечной длины.

Хорошо известно, что формула обладает свойством порядка тогда и только тогда, когда она обладает свойством независимости или свойством строгого порядка (или обоими свойствами одновременно). Связь между вышеприведенными понятиями и их локальными аналогами следующая: локальный аналог — элементарное свойство, если оно выполняется в некоторой модели данной теории, то оно выполняется во всех моделях этой теории. Однако локального выполнения этих свойств недостаточно, чтобы в данной конкретной модели проявились свойства рангов, для этого требуется уже выполнение вышеприведенных свойств на бесконечной последовательности кортежей.

Вспомним, что теория является стабильной тогда и только тогда, когда она не обладает свойством порядка. Локальное свойство порядка позволяет записать нестабильность как элементарное свойство.

Цель данной работы — исследовать локальный аналог свойства строгого порядка внутри сечения, которое используется для описания упорядоченно стабильных теорий.

Пусть $\mathcal{M} = (M, <, \dots)$ — линейно упорядоченная структура, a — элемент из M, а A и B — подмножества для M. Как обычно, будем писать $a < A$, если $a < b$ для любого $b \in A$, и будем писать $A < B$, если $a < b$ для любых $a \in A$ и $b \in B$. Разбиение $\langle C, D\rangle$ множества M называется *сечением*, если $C < D$. Если дано сечение $\langle C, D\rangle$, то можно построить частичный тип $\{c < x < d : c \in C,\ d \in D\}$, который также будем называть сечением и обозначать тем же символом $\langle C, D\rangle$.

Подмножество A линейно упорядоченного множества M называется *выпуклым*, если для любых a и $b \in A$ отрезок $[a, b]$ лежит в A. *Выпуклым компонентом* множества A называется максимальное выпуклое подмножество для A. Определим *выпуклое замыкание* A^c множества A следующим образом: $A^c = \{b \in M : \exists a_1, a_2 \in A(a_1 \leq b \leq a_2)\}$, то есть это наименьшее выпуклое множество, содержащее A.

Пусть $\mathcal{M}$ — некоторая структура. Пусть s — некоторый частичный n-тип, A — подмножество. Тогда $S^n_s(A) \rightleftharpoons \{p \in S^n(A) : p \cup s \text{ совместно}\}$. Заметим, что область определения типа s может не совпадать с множеством A.

Определение 1 (Б. Байжанов, В. Вербовский, [1]) 1. Линейно упорядоченная структура $\mathcal{M}$ называется *упорядоченно стабильной в* λ, если для любого подмножества $A \subseteq M$ мощности не больше λ и для любого сечения $\langle C, D\rangle$ в $\mathcal{M}$ существует самое большее λ 1-типов над A, которые совместны с сечением $\langle C, D\rangle$, то есть $|S^1_{\langle C,D\rangle}(A)| \leq \lambda$.

2. Теория T называется *упорядоченно стабильной в* λ, если каждая ее модель такова. Иногда будем писать, что T упорядоченно λ-стабильна.

3. Теория T называется *упорядоченно стабильной*, если существует бесконечный кардинал λ, в котором теория T упорядоченно стабильна.

В работе [**4**] было дано следующее определение свойства строгого порядка внутри сечения.

Определение 2 Линейно упорядоченная структура $\mathcal{M} = (M, <, \dots)$ обладает *свойством строгого порядка внутри сечения*, если существует формула $\phi(x, \bar{y})$, такая что для любого натурального числа n существуют кортежи $\bar{a}_1, \dots, \bar{a}_n$ и сечение $\langle C_n, D_n\rangle$ в $\mathcal{M}$, такие что в некотором $|M|^+$-насыщенном элементарном расширении $\mathcal{N}$ модели $\mathcal{M}$ имеет место:

$$\phi(\mathcal{N}, \bar{a}_1) \cap \langle C_n, D_n\rangle(\mathcal{N}) \subset \phi(\mathcal{N}, \bar{a}_2) \cap \langle C_n, D_n\rangle(\mathcal{N}) \subsetneq \dots \subsetneq \phi(\mathcal{N}, \bar{a}_n) \cap \langle C_n, D_n\rangle(\mathcal{N})$$

Теория обладает *свойством строгого порядка внутри сечения*, если некоторая ее модель обладает этим свойством.

Кроме того, в работе [**4**] был доказан следующий критерий упорядоченной стабильности теории.

Теорема 3 *Пусть T является элементарной теорией линейно упорядоченной структуры. Тогда теория T является упорядоченно стабильной тогда и только тогда, когда она не обладает свойством независимости и не обладает свойством строгого порядка внутри сечения.*

По теореме компактности легко построить элементарное достаточно насыщенное расширение, в котором найдется сечение, в котором уже будет бесконечная цепь вложенных подмножеств, как в определении **2**. Однако остается открытым вопрос, если в некоторой модели заданной теории существует подобная бесконечная цепь вложенных формульных подмножеств, пересеченных реализацией сечения, будет ли свойство, описанное в определении **2** выполняться во всех моделях этой теории? Следующий пример дает отрицательный ответ на данный вопрос.

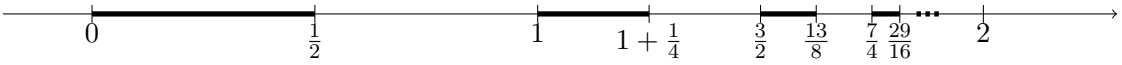
Рассмотрим $\mathcal{M} = (\mathbb{R}, <, +, P)$, где предикат Pпроинтерпретирован следующим подмножеством:

$$\left[0, \frac{1}{2}\right] \cup \left[1, 1 + \frac{1}{4}\right] \cup \left[1 + \frac{1}{2}, 1 + \frac{1}{2} + \frac{1}{8}\right] \cup \left[1 + \frac{1}{2} + \frac{1}{4}, 1 + \frac{1}{2} + \frac{1}{4} + \frac{1}{16}\right] \cup \dots.$$

Иначе говоря,

$$P(\mathcal{M}) \rightleftharpoons \bigcup_{n<\omega} \left[2 - \frac{1}{2^{n-1}}, 2 - \frac{1}{2^{n-1}} + \frac{1}{2^{n+1}}\right]$$

Или, как показано на рисунке ниже:



Пусть

$$\varphi(x, y) \rightleftharpoons \exists z(P(z) \wedge \exists u(u < z \wedge \forall t(u < t < z \to \neg P(t))) \wedge z \leq x \leq z + y).$$

Формула $\varphi(x, a)$, где a — некоторое положительное вещественное число, выделяет в модели $\mathcal{M}$ следующее множество. Берем минимальный элемент выпуклой компоненты множества $P(\mathcal{M})$, откладываем от него отрезок длины a, после чего рассматриваем объединение всех таких отрезков, полученных по всем выпуклым компонентам множества $P(\mathcal{M})$. Очевидно, что так как длина выпуклых компонент множества $P(\mathcal{M})$ стремится к нулю, то при любом положительном вещественном числе a множество $\varphi(\mathcal{M}, a)$ будет представлять собой объединение конечного числа отрезков, так как найдется такая левая граница $b = 2 - 1/2^{n-1}$ одного из отрезков, составляющих множество $P(\mathcal{M})$, что число $a + b$ будет больше 2. Поскольку $\varphi(\mathcal{M}, a)$ есть конечное объединение отрезков, для любого сечения $\langle C, D\rangle$ только одна из формул $\varphi(x, a)$ или $\neg\varphi(x, a)$ совместна с сечением $\langle C, D\rangle$. Следовательно, данная формула

не обладает свойством строгого порядка внутри никакого сечения в структуре $\mathcal{M}$. Однако, если мы перейдем к элементарному расширению $\mathcal{N}$ структуры $\mathcal{M}$, в которой существует положительный элемент α, являющийся бесконечно малым по отношению ко всем положительным вещественным числам, то легко понять, что для последовательности $\alpha_n = n\alpha$ семейство формул $\{\varphi(x, \alpha_n) \mid n \in \mathbb{Z}^+\}$ обладает свойством строгого порядка внутри сечения $\langle(-\infty, 2), [2, +\infty]\rangle$.

Таким образом, определение **2** не является действительным локальным аналогом свойства строгого порядка внутри сечения, как это происходит в классической теории стабильности; в текущем виде оно выполняется не во всех моделях данной теории. Поэтому мы сейчас перепишем локальный вариант свойства строгого порядка в другом виде.

Скажем, что пара множеств A и B удовлетворяет свойству *строгой вложенности выпуклых компонент*, если $A \subsetneq B$ и существует выпуклая компонента множества A, являющаяся собственным подмножеством некоторой выпуклой компоненты множества B. Например, если взять $A = \mathbb{Q} \cap [0, 1]$ и $B = \mathbb{Q}$ как подмножества множества вещественных чисел $\mathbb{R}$, то хотя $A \subsetneq B$, но эта пара множеств не удовлетворяет свойству строгой вложенности выпуклых компонент, поскольку все выпуклые компоненты множеств A и B являются одноточечными.

Будем говорить, что последовательность множеств $A_1, \ldots, A_n$ удовлетворяет свойству *строгой вложенности выпуклых компонент*, если $A_1 \subsetneq A_2 \subsetneq \cdots \subsetneq A_n$ и существуют выпуклые компоненты $C_1, \ldots, C_n$ множеств $A_1, \ldots, A_n$, соответственно, такие что $C_1 \subsetneq C_2 \subsetneq \cdots \subsetneq C_n$.

Будем говорить, что последовательность множеств $A_1, \ldots, A_n$ удовлетворяет свойству *строгой вложенности k выпуклых компонент*, если $A_1 \subsetneq A_2 \subsetneq \cdots \subsetneq A_n$ и существуют выпуклые компоненты $C_1^j, \ldots, C_n^j$ множеств $A_1, \ldots, A_n$, соответственно, такие что

$$C_1^j \subsetneq C_2^j \subsetneq \cdots \subsetneq C_n^j,$$

где $j < k$, причем для каждого i компоненты C_i^j, где $j < k$, попарно различны.

Заметим, что для формульных подмножеств $A_1, \ldots, A_n$ свойство строгой вложенности k выпуклых компонент само является формульным.

Пусть $F(x)$ некоторая формула, которая выделяет множество A. Напишем отношение эквивалентности $E_F(x, y)$ на множестве A, классами которой являются выпуклые компоненты множества A:

$$E_F(x, y) \rightleftharpoons F(x) \wedge F(y) \wedge \forall z(x \leq z \leq y \vee y \leq z \leq x \to F(z)).$$

Пусть даны формулы $F_1(x), \ldots, F_n(x)$, которые выделяют подмножества $A_1, \ldots, A_n$, соответственно. Отношения эквивалентности E_{F_i} для краткости обозначим E_i, где $i = 1, \ldots, n$. Классы эквивалентности E_i обозначим $[x]_i$. Тогда свойство строгой вложенности выпуклых компонент множеств $A_1, \ldots, A_n$ (формул $F_1(x), \ldots, F_n(x)$), записывается следующим образом:

$$\bigwedge_{i=1}^{n-1} A_i \subseteq A_{i+1} \wedge \exists x_1 \ldots \exists x_n \left[\bigwedge_{i=1}^{n} x_i \in A_i \wedge \bigwedge_{i=1}^{n-1} [x_i]_i \subsetneq [x_{i+1}]_{i+1} \right].$$

Аналогичным образом записывается формула, выражающая свойство строгой вложенности k выпуклых компонент; однако мы не приводим её ввиду громоздкости.

Если формулы $F_1(x), \ldots, F_n(x)$ определены равномерно, то есть, $F_i(x) = G(x, \bar{b}_i)$, где $i = 1, \ldots, n$, то будем говорить, что выполняется равномерное (n, k) свойство вложенности выпуклых компонент, если последовательность формул $F_1(x), \ldots, F_n(x)$ удовлетворяет свойству строгой вложенности k выпуклых компонент. Также будем говорить, что формула $G(x, \bar{y})$ удовлетворяет (n, k) свойству вложенности выпуклых компонент.

Будем говорить, что линейно упорядоченная структура обладает равномерным свойством вложенности выпуклых компонент, если существует формула, которая удовлетворяет равномерному (n, k) свойству вложенности выпуклых компонент для любых натуральных положительных чисел n и k.

Теорема 4 *Элементарная теория T линейно упорядоченной структуры обладает свойством строгого порядка внутри сечения тогда и только тогда, когда каждая ее модель обладает равномерным свойством вложенности выпуклых компонент.*

Доказательство. Предположим, что T обладает свойством строгого порядка внутри сечения. Пусть в некоторой модели $\mathcal{M} \models T$ существует формула $\phi(x, \bar{y})$, такая что для любого натурального числа n существуют кортежи $\bar{a}_1, \ldots, \bar{a}_n$ и сечение $\langle C_n, D_n\rangle$ в $\mathcal{M}$, такие что в некотором $|M|^+$-насыщенном элементарном расширении $\mathcal{N}$ модели $\mathcal{M}$ имеет место:

$$\phi(\mathcal{N}, \bar{a}_1) \cap \langle C_n, D_n\rangle(\mathcal{N}) \subset \phi(\mathcal{N}, \bar{a}_2) \cap \langle C_n, D_n\rangle(\mathcal{N}) \subsetneq \cdots \subsetneq \phi(\mathcal{N}, \bar{a}_n) \cap \langle C_n, D_n\rangle(\mathcal{N})$$

Не умаляя общности, в силу компактности, мы можем считать, что в модели $\mathcal{M}$ существует сечение $\langle C, D\rangle$ и бесконечная последовательность кортежей $\bar{a}_n$, $n < \omega$, что имеет место

$$\phi(\mathcal{N}, \bar{a}_1) \cap \langle C_n, D_n\rangle(\mathcal{N}) \subset \phi(\mathcal{N}, \bar{a}_2) \cap \langle C_n, D_n\rangle(\mathcal{N}) \subsetneq \cdots \subsetneq \phi(\mathcal{N}, \bar{a}_n) \cap \langle C_n, D_n\rangle(\mathcal{N}) \subsetneq$$

Более того, мы можем предположить, что множество C в структуре $\mathcal{M}$ формульно, иначе, мы добавим одноместный предикат P, который выделяет множество C. Будем предполагать, что $\mathcal{N}$ является элементарным расширением модели $\mathcal{M}$ и в обогащенном языке. Тогда свойство строгого порядка внутри сечения можно выразить как хотя бы одно из двух:

$$\exists x(P(x) \wedge \forall y(x < y \wedge P(y) \to \phi(\mathcal{M}, \bar{a}_1) \cap (y, +\infty) \cap P(\mathcal{M}) \subsetneq \\ \subsetneq \phi(\mathcal{M}, \bar{a}_2) \cap (y, +\infty) \cap P(\mathcal{M}) \subsetneq \cdots \subsetneq \phi(\mathcal{M}, \bar{a}_n) \cap (y, +\infty) \cap P(\mathcal{M})))$$

или

$$\exists x(\neg P(x) \wedge \forall y(y < x \wedge \neg P(y) \to \phi(\mathcal{M}, \bar{a}_1) \cap (-\infty, y) \cap \neg P(\mathcal{M}) \subsetneq \\ \subsetneq \phi(\mathcal{M}, \bar{a}_2) \cap (-\infty, y) \cap \neg P(\mathcal{M}) \subsetneq \cdots \subsetneq \phi(\mathcal{M}, \bar{a}_n) \cap (-\infty, y) \cap \neg P(\mathcal{M})))$$

Предположим, что выполняется первое. Тогда в модели $\mathcal{N}$, так как она достаточно насыщена, можно найти такой элемент α, что имеет место

$$\phi(\mathcal{N}, \bar{a}_1) \cap (\alpha, +\infty) \cap P(\mathcal{N}) \subsetneq \\ \subsetneq \phi(\mathcal{N}, \bar{a}_2) \cap (\alpha, +\infty) \cap P(\mathcal{N}) \subsetneq \cdots \subsetneq \phi(\mathcal{N}, \bar{a}_n) \cap (\alpha, +\infty) \cap P(\mathcal{N}) \subsetneq \ldots$$

Заметим, что, как было доказано в [**1**], подмножество $\phi(\mathcal{N}, \bar{a}_i) \cap \langle C, D\rangle(\mathcal{N})$ состоит из бесконечного числа выпуклых множеств. Пусть $\phi_1(x, \bar{a}_i, \bar{a}_{i+1})$ состоит из тех выпуклых компонент множества $\phi(\mathcal{N}, \bar{a}_i)$, которые является собственными подмножеством соответствующих выпуклых компонент множества $\phi(\mathcal{N}, \bar{a}_{i+1})$, а формула $\phi_2(x, \bar{a}_i, \bar{a}_{i+1})$ состоит из тех выпуклых компонент множества $\phi(\mathcal{N}, \bar{a}_i)$, которые совпадают с некоторой выпуклой компонентой множества $\phi(\mathcal{N}, \bar{a}_{i+1})$. Очевидно, что для выполнения свойства строгого порядка внутри сечения требуется, чтобы в любой окрестности сечения формула ϕ_1 имеет реализацию. Не умаляя общности мы можем предположить, что ϕ_2 несовместна (заменим ϕ на ϕ_1).

Тогда, если предикат P выразим в исходном языке, то мы получили равномерное семейство формул, вложенных одна в другую (причем соответствующие выпуклые компоненты

тоже вкладываются одна в другую), откуда следует равномерное свойство вложенности выпуклых компонент.

Если же предикат P не выразим в исходном языке, то с точностью до инвертирования порядка мы можем проделать то же самое и найти такой элемент $\beta \in N$, что будет верно

$$\phi(\mathcal{N}, \bar{a}_1) \cap (\alpha, \beta) \subsetneq \phi(\mathcal{N}, \bar{a}_2) \cap (\alpha, \beta) \subsetneq \cdots \subsetneq \phi(\mathcal{N}, \bar{a}_n) \cap (\alpha, \beta) \subsetneq \ldots$$

Отсюда легко следует равномерное свойство вложенности выпуклых компонент. Поскольку это свойство элементарное, легко понять, что если оно выполняется в одной модели теории T, то оно выполняется во всех моделях этой теории.

Теперь предположим, что имеет место равномерное свойство вложенности выпуклых компонент. Тогда по компактности из равномерного (n, k) свойства вложенности выпуклых компонент можно построить (ω, ω) свойство вложенности выпуклых компонент. Не ограничивая общности, можно предположить, что у нас не бесконечно возрастающая цепь, а бесконечно убывающая (перенумеруем ее при помощи отрицательных целых чисел). Тогда есть счетная монотонная (для определенности, пусть она будет возрастающая) последовательность элементов b_i из $\phi(\mathcal{M}, \bar{a}_{-1})$, которые лежат в разных выпуклых компонентах множества $\phi(\mathcal{M}, \bar{a}_{-1})$, причем в каждой из этих выпуклых компонент есть меньшая выпуклая компонента множества $\phi(\mathcal{M}, \bar{a}_{-2})$, а в них есть меньшая выпуклая компонента множества $\phi(\mathcal{M}, \bar{a}_{-3})$, и так далее. Пусть $C = \{x \in M : \exists i(x < b_i)\}$. Легко понять, что внутри сечения $\langle C, M \setminus C\rangle$ выполняется свойство строгого порядка. □

Заключение

Таким образом, локальный аналог свойства строгого порядка внутри сечения достаточно сильно отличается от классического локального аналога свойства строгого порядка. Было бы интересно понять ситуацию в более общем случае: описать поведение свойства строгого порядка внутри Δ-типа, что важно для изучения стабильных с точностью до Δ теорий [**5-7**].

Информация о финансировании

Работа поддержана Комитетом науки Министерства науки и высшего образования Республики Казахстан, грант BR28713025.

ЛИТЕРАТУРА

1 Baizhanov, B., Verbovskii, V. O-stable theories. Algebra and Logic 50 (2011), no 3, 211–225. https://doi.org/10.1007/s10469-011-9136-7

2 Morley, M. Categoricity in power. Transactions of the American Mathematical Society. 1965. V. 114.P. 514–538. https://doi.org/10.1090/S0002-9947-1965-0175782-0

3 Shelah, S. Classification Theory and the Number of Nonisomorphic Models (1978, 2nd ed. 1990).

4 Verbovskiy, V.V. O-stable ordered groups. Siberian Advances in Mathematics, 22 (2012), 50–74. https://doi.org/10.3103/S105513441201004X

5 Verbovskiy, V. V. On definability of types and relative stability, Mathematical Logic Quarterly, 65 (3), 332–346 (2019). https://doi.org/10.1002/malq.201600084

6 Verbovskiy, V.V., Yershigeshova, A.D. On non-essentiality of an o-stable expansion of (Z, Lobachevskii Journal of Mathematics, 44, 5485–5492 (2023).
https://doi.org/10.1134/S1995080223120387

7 Verbovskiy, V.V. On the function depth in an o-stable ordered group of a finite convexity rank. Kazakh Mathematical Journal, 25 (2), 25–35 (2025). https://doi.org/10.70474/6tx4zj76

[1,2] Вербовский В.В.,
ф.-м.г.д., доцент, ORCID ID: 0000-0001-5177-8523,
*e-mail: verbovskiy at math.kz
[1] Математика және математикалық модельдеу институты, Алматы қ., Қазақстан
[2] Қ.И. Сәтбаев атындағы Қазақ ұлттық техникалық зерттеу университеті, Алматы қ., Қазақстан

СЫЗЫҚТЫ РЕТТЕЛГЕН ҚҰРЫЛЫМДАР ҮШІН ҚИМА ІШІНДЕГІ ҚАТАҢ РЕТТІЛІК ҚАСИЕТІНІҢ ЛОКАЛДЫ АНАЛОГЫ

Аңдатпа

Бұл жұмыста реттелген тұрақты модельдер теориясында пайда болатын сызықты реттелген құрылымдар үшін қима ішіндегі қатаң реттілік қасиетінің локалды аналогы зерттеледі. Бұл қасиетті қиманың жүзеге асуларымен қиылысқан формулалармен анықталатын жиындардың қатаң кірістірілген шекті тізбектері арқылы тұжырымдаудың табиғи әрекеті қарастырылады. Мұндай тұ-жырым элементар емес екені көрсетіледі: ол элементар кеңейтуде орындалуы мүмкін, бірақ бастап-қы модельде сақталмайды, сондықтан дұрыс локалды критерий бермейді. Бұл кемшілікті жою үшін анықталатын жиындардың дөңес компоненттерінің қатаң кірістірілуі ұғымы, сондай-ақ параметрлері бар формулалар отбасылары үшін оның бірқалыпты нұсқасы енгізіледі. Қима ішіндегі қатаң реттілік қасиеті дөңес компоненттердің кірістірілуінің бірқалыпты қасиетінің бар болуына эквивалент екені дәлелденеді. Алынған нәтиже бұл қасиеттің локалды табиғатын нақтылайды, оның классикалық локалды қатаң реттілік қасиетінен айырмашылығын көрсетеді және оны реттелген тұрақты теория-лар мен олардың модельдерін зерттеуде қолдануға мүмкіндік береді. Осылайша, жұмыс реттелген тұрақтылық критерийін толықтырады.

Түйін сөздер: сызықтық реттелген жиын, o-минималдылық, реттелген тұрақтылық, қатаң рет-тілік қасиеті.

[1,2] Verbovskiy V.V.,
Doctor of Physical and Mathematical Sciences, Docent,
ORCID ID: 0000-0001-5177-8523,
*e-mail: verbovskiy at math.kz
[1]Institute of Mathematics and Mathematical Modeling, Almaty, Kazakhstan
[2]Satbayev University, Almaty, Kazakhstan

ON A LOCAL ANALOGUE OF THE STRICT ORDER PROPERTY INSIDE A CUT FOR LINEARLY ORDERED STRUCTURES

Abstract

The paper studies a local analogue of the strict order property inside a cut for linearly ordered structures, arising in the theory of order-stable models. A natural attempt to formulate this property in terms of finite c hains o f s trictly n ested d efinable su bsets in tersected wi th re alizations of a cu t is considered. It is shown that such a formulation is not elementary: it may hold in an elementary extension but fail to be preserved in the original model and therefore does not provide a correct local criterion. To overcome this drawback, the notion of strict inclusion of convex components of definable s ets i s i ntroduced, together with its uniform version for families of formulas with parameters. It is proved that the strict order property inside a cut is equivalent to the existence of the uniform property of inclusion of convex components. The obtained result clarifies t he l ocal n ature o f t his p roperty, s hows i ts d ifference fr om th e cl assical lo cal strict order property, and makes it applicable to the study of order-stable theories and their models. Thus, the paper complements the criterion of order-stability.

Keywords: linearly ordered set, o-minimality, o-stability, strict order property.

Received April 28, 2026; accepted May 26, 2026.

UDC 510.67
IRSTI 27.03.66

https://doi.org/10.55452/1998-6688-2026-23-3-55-69

[1]*Dekhkonov F.N.,
Doctor of Physical and Mathematical Sciences, Associate Professor,
ORCID ID: 0000-0003-4747-8557,
*e-mail: f.n.dehqonov@mail.ru
[1] Usubjonov A.A.,
PhD Student,
e-mail: adhamusubjonov@gmail.com
[1] Department of Mathematics, Namangan State University, Namangan, Uzbekistan

ON THE CONTROL PROBLEM FOR A ONE-DIMENSIONAL PSEUDO-PARABOLIC EQUATION WITH A NONLOCAL BOUNDARY CONDITION

Abstract

This paper studies a control problem for a one-dimensional pseudo-parabolic equation with a nonlocal boundary condition of the Bitsadze-Samarskii type. The control function appears as a distributed source term on the right-hand side of the equation, and the objective is to steer the system from the zero initial state so that the weighted average temperature follows a prescribed trajectory. The equation contains a third-order mixed derivative term that accounts for memory or viscoelastic effects i n h eat conduction, which is particularly relevant for materials with internal structure such as polymers, biological tissues, and granular media. Using spectral decomposition and a biorthogonal basis, the problem is reduced to a Volterra integral equation of the first kind. The kernel of this integral equation is proved to be positive and continuous. Under suitable assumptions on the weight function and the spatial distribution of the control, the existence of an admissible control is established for a class of desired trajectories with sufficiently small norm. The Laplace transform method is employed to solve the integral equation and to obtain bounds on the control function. The results quantify the influence o f t he n onlocal b oundary c ondition a nd the memory parameter on the controllability of the system.

Keywords: pseudo-parabolic equation, boundary value problem, Volterra integral equation, admissible control, thin rod.

Received: Received May 6, 2026; revised July 4, August 5, 2026; accepted August 9, 2026.

Introduction

Pseudo-parabolic equations arise in various applied contexts, including fluid flow in porous media, heat transfer in heterogeneous materials, and radiative diffusion. These models extend classical parabolic equations by incorporating higher-order mixed derivatives that capture memory, relaxation, and inertial effects. Unlike the standard heat equation, pseudo-parabolic models can describe finite-speed propagation of thermal disturbances, a phenomenon often referred to as the second sound effect, which is particularly relevant in materials with internal structure such as polymers, biological tissues, and granular media.

In recent years, growing interest in control theory and applied mathematics has spurred extensive research on control problems for pseudo-parabolic equations. Foundational contributions include the study of control and its comparison with classical parabolic models [1], and investigations on stability, uniqueness, and existence of solutions for various pseudo-parabolic systems [2]. Point control for parabolic and pseudo-parabolic models is discussed in detail in [3].

Control problems for parabolic equations have attracted considerable attention over the past decades due to their central role in modeling heat conduction and diffusion p r o cesses. O n e of the earliest contributions in this direction was made by Friedman [4], who studied optimal control problems for parabolic equations using variational methods. Fundamental results on the controllabi-lity of linear second-order parabolic equations were obtained by Fattorini and Russell [5], where the notions of exact and approximate controllability were first introduced.

The extension of control theory to infinite-dimensional s y stems w a s c a rried o u t b y Egorov [6], who generalized Pontryagin's maximum principle to evolution equations in Banach spaces and established a bang-bang principle under natural assumptions. Comprehensive treatments of optimal control for distributed parameter systems, including parabolic equations, can be found in the classical monographs by Lions [8] and Fursikov [7].

The time-optimal control problem for the heat equation and the structure of optimal controls were intensively studied in subsequent works. In particular, the time-varying bang-bang property of optimal controls and its applications were analyzed in [9]. The bang-bang principle for time-optimal boundary control problems was further examined in [10], where it was shown that bang-bang controls remain optimal for arbitrary target temperature distributions.

The boundary control problem for the heat transfer equation in two-dimensional domain was considered in [15], where the admissibility of the control function was established using geometric estimates. Boundary control problems for one- and two-dimensional heat equations were further investigated in [16, 17], while the time-optimal control of a fourth-order parabolic equation in a two-dimensional domain was analyzed in [18].

Initial studies of time-optimal control problems for heat conduction equations in bounded n-dimensional domains were presented in [11], where sharp estimates for the minimal time required to achieve a prescribed average temperature were derived. Mathematical models of thermocontrol processes were analyzed in [12]. Various related problems for nonlinear and degenerate parabolic equations have also attracted considerable attention; see, for instance, [13], where local existence and uniqueness of weak solutions were established via the Galerkin method and the Banach fixed point theorem, and [14], where singular parabolic equations with logarithmic nonlinearities were studied.

Recently, in [19], a time-optimal control problem for the heat equation involving an involution operator in a multidimensional parallelepiped domain was investigated. In that work, an optimal estimate for the minimal time required to heat the domain to a prescribed average temperature was obtained. Recent developments have also addressed controllability issues from a spectral and observability viewpoint. In [20], spectral inequalities for the Laplace-Beltrami operator were derived, leading to observability and null-controllability results for the spherical heat equation. Boundary control problems for generalized heat equations involving Schr¨odinger-type operators were studied in [21]. Numerical aspects of boundary control and discretization schemes for heat equation were analyzed in [22]. Applications to fluid d y namics a n d t h ermally c o upled systems were considered in [23].

In [24], time-optimal control problems for semilinear parabolic equations subject to Dirichlet boundary control and terminal state constraints are analyzed. In that work, a Hamiltonian-type functional is introduced in order to derive necessary optimality conditions with respect to the terminal time T. The existence of time-optimal controls for a class of semilinear parabolic equations with distributed control acting on a subdomain is investigated in [25], where sufficient conditions ensuring the attainability of the target state in minimal time are established.

For controllability of pseudo-parabolic equations, Zhou [26] analyzed approximate controllability and minimal time control problems for a pseudo-parabolic equation with memory term. Control problems for pseudo-parabolic equations have been studied in works [27, 28], where the control

In this paper, we study a control problem for a one-dimensional pseudo-parabolic equation with a nonlocal boundary condition of the Bitsadze–Samarskii type. The control function appears as a distributed source term on the right-hand side of the equation, and the goal is to steer the system from the zero initial state so that the weighted average temperature follows a prescribed trajectory. We first introduce the concept of a generalized solution for the initial-boundary value problem. Using spectral decomposition, we expand the solution in terms of the eigenfunctions of the corresponding nonlocal spectral problem. By introducing a suitable class of weight functions, we derive a Volterra integral equation of the first kind for the unknown control function. The necessary estimates for the kernel are established. Using these estimates, we prove the existence of an admissible control for a suitable class of desired trajectories. The results quantify the influence of the nonlocal boundary condition and the memory parameter on the controllability of the system.

To the best of our knowledge, control problems for pseudo-parabolic equations with Bitsadze-Samarskii type nonlocal boundary conditions have received little attention in the existing literature. Unlike the available works devoted to pseudo-parabolic equations under classical or different boundary conditions, the present paper considers the nonlocal condition $u(1,t) = u\left(\frac{1}{2},t\right)$, which leads to a non-orthogonal system of eigenfunctions and substantially complicates the corresponding spectral analysis. To overcome this difficulty, we employ a biorthogonal basis constructed from the adjoint spectral problem. This approach enables us to derive a Volterra integral equation of the first kind with a positive kernel and to establish the existence of an admissible control. Therefore, the novelty of the present work lies in the combination of the pseudo-parabolic model, the Bitsadze–Samarskii type nonlocal boundary condition, and the biorthogonal spectral approach used to solve the control problem.

Materials and methods

In this paper we consider the pseudo-parabolic equation

$$u_t(x,t) - u_{xx}(x,t) - \alpha\, u_{xxt}(x,t) = h(x)\,\mu(t), \quad x \in (0,1), \quad t > 0, \tag{1}$$

with a nonlocal boundary condition

$$u(0,t) = 0, \qquad u(1,t) = u\left(\tfrac{1}{2},t\right), \quad t \geq 0, \tag{2}$$

and the homogeneous initial condition

$$u(x,0) = 0, \quad 0 \leq x \leq 1, \tag{3}$$

where $h(x)$ is a given function describing the spatial distribution of the control action, $\mu(t)$ is the control function, and $\alpha > 0$ is a constant characterizing the relaxation time of the thermal flux.

Equation (1) is a third-order pseudo-parabolic equation. The term αu_{xxt} accounts for memory or viscoelastic effects in the heat conduction process. Such models arise in the theory of viscoelasticity, fluid flow in fissured rocks, and heat conduction in heterogeneous media. When $\alpha = 0$, equation (1) reduces to the classical heat equation. For $\alpha > 0$, the equation describes finite-speed propagation of thermal disturbances, a phenomenon known as the second sound effect, which cannot be captured by the classical parabolic model.

From a physical point of view, equation (1) describes the evolution of the temperature field $u(x,t)$ in a thin homogeneous rod of unit length. The initial condition (3) means that the rod is initially at zero temperature. The right-hand side $h(x)\mu(t)$ represents a distributed heat source, where $\mu(t)$ is the time-dependent intensity and $h(x)$ is its spatial profile. The function $\mu(t)$ is the control input.

The boundary conditions are as follows. At the left end we have a fixed zero temperature, $u(0,t) = 0$. The right end is coupled with the interior point $x = \frac{1}{2}$ through the nonlocal condition

$u(1,t) = u(\frac{1}{2},t)$. Physically, such a condition may arise in feedback control systems where a sensor located at the midpoint $x = \frac{1}{2}$ regulates the temperature at the right end $x = 1$, or in applications requiring temperature equalization at two distinct points. The specific choice of the coupling point as $x = \frac{1}{2}$ introduces a natural geometric symmetry, simplifying the spectral analysis while preserving the nonlocal nature of the problem. This nonlocal constraint introduces spectral anomalies and controllability challenges that are absent in classical local boundary value problems.

Definition 1 *A control function $\mu(t)$ is called* admissible *if $\mu(t) \in L^2(\mathbb{R}_+)$ and $|\mu(t)| \le 1$ for all $t \ge 0$.*

We consider the spectral problem associated with the spatial operator of equation (1):

$$X''(x) + \lambda X(x) = 0, \quad 0 < x < 1, \tag{4}$$

with the nonlocal boundary conditions

$$X(0) = 0, \quad X(1) = X(1/2). \tag{5}$$

For $\lambda \le 0$, problem (4)–(5) admits only the trivial solution. Hence, we consider $\lambda > 0$. In this case, the spectrum consists of two countable sequences of eigenvalues:

$$\lambda_{k,1} = \left(\frac{2(2k-1)\pi}{3}\right)^2, \qquad \lambda_{k,2} = (4k\pi)^2, \quad k \in \mathbb{N}. \tag{6}$$

The corresponding eigenfunctions are

$$X_{k,1}(x) = \sin\bigl(\sqrt{\lambda_{k,1}}\,x\bigr), \qquad X_{k,2}(x) = \sin\bigl(\sqrt{\lambda_{k,2}}\,x\bigr), \quad k \in \mathbb{N}.$$

The system $\{X_{k,j}\}$ is not orthogonal. Following [29], we introduce the adjoint problem:

$$Y''(x) + \lambda Y(x) = 0, \quad x \in (0, \tfrac{1}{2}) \cup (\tfrac{1}{2}, 1),$$

with boundary conditions

$$Y(0) = 0, \quad Y(1) = 0,$$

and transmission conditions at $x = 1/2$:

$$Y(1/2+0) = Y(1/2-0), \qquad Y'(1/2+0) - Y'(1/2-0) = Y'(1).$$

The eigenvalues of the adjoint problem are the same as in (6). The adjoint eigenfunctions are given explicitly by

$$Y_{k,1}(x) = \begin{cases} \dfrac{8}{3}\sin\bigl(\sqrt{\lambda_{k,1}}x\bigr), & 0 \le x < \frac{1}{2}, \\ -\dfrac{4}{3\cos\sqrt{\lambda_{k,1}}}\sin\bigl(\sqrt{\lambda_{k,1}}(1-x)\bigr), & \frac{1}{2} < x \le 1, \end{cases}$$

$$Y_{k,2}(x) = \begin{cases} 0, & 0 \le x < \frac{1}{2}, \\ -\dfrac{4}{\cos\sqrt{\lambda_{k,2}}}\sin\bigl(\sqrt{\lambda_{k,2}}(1-x)\bigr), & \frac{1}{2} < x \le 1. \end{cases}$$

The systems $\{X_{k,j}\}$ and $\{Y_{k,j}\}$ satisfy the biorthogonality condition

$$\int_0^1 X_{k,j}(x) Y_{\ell,m}(x)\,dx = \delta_{k\ell}\delta_{jm},$$

and are complete and biorthogonal in $L_2(0,1)$ (see [29]).

We define the class of weight functions as follows:

$$U := \left\{ \rho \in W_2^1(0,1) \;\middle|\; \begin{array}{ll} \rho(x) \geq 0, & \displaystyle\int_0^1 \rho(x)\,dx = 1, \\ \rho_{k,j} \geq 0, & k \in \mathbb{N},\ j = 1,2, \end{array} \right\},$$

where $\rho_{k,j}$ are the Fourier coefficients of $\rho(x)$ with respect to the adjoint eigenfunctions $Y_{k,j}$, i.e.,

$$\rho(x) = \sum_{j=1}^{2} \sum_{k=1}^{\infty} \rho_{k,j} Y_{k,j}(x), \qquad \rho_{k,j} = \int_0^1 \rho(x) X_{k,j}(x)\,dx.$$

The class U is non-empty. Indeed, consider the function

$$\rho(x) = 2(1-x).$$

Clearly $\rho(x) \geq 0$ on $[0,1]$, $\int_0^1 \rho(x)\,dx = 1$, and $\rho \in W_2^1(0,1)$. Integrating by parts, for every k, j with $\omega = \sqrt{\lambda_{k,j}}$,

$$\rho_{k,j} = \int_0^1 2(1-x)\sin(\omega x)\,dx = \frac{2(\omega - \sin\omega)}{\omega^2}.$$

Since $\sin t \leq t$ for all $t \geq 0$, it follows that $\omega - \sin\omega \geq 0$ for every $\omega > 0$, and hence $\rho_{k,j} \geq 0$ for all k, j. Thus $\rho \equiv 2(1-x) \in U$, and the class U is non-empty.

The main objective of this work is to investigate the following control problem.

Control Problem. *For a given function $f(t)$, find an admissible control $\mu(t)$ such that the solution $u(x,t)$ of the initial-boundary value problem* (1)–(3) *satisfies the integral condition*

$$\int_0^1 \rho(x) u(x,t)\,dx = f(t), \quad t \geq 0, \tag{7}$$

where $\rho \in U$ is a given weight function.

This formulation represents a physically meaningful requirement that the weighted temperature in the rod follows a prescribed trajectory $f(t)$ over time. Physically, the integral condition (7) can be interpreted as the total heat content (or thermal energy) stored in the rod, weighted by the function $\rho(x)$. For example, if $\rho(x)$ represents the specific heat capacity distribution or a sensor sensitivity profile, then the integral gives a measurable output of the system. The control problem consists of finding $\mu(t)$ such that this measured output exactly matches the desired function $f(t)$. Unlike pointwise temperature constraints, this averaged condition characterizes a global thermal performance criterion. Such a formulation is particularly relevant in applications where only the overall thermal state of the system matters, for example in thermal processing of materials, temperature control in manufacturing, or heating systems. From a control-theoretic perspective, the integral constraint allows greater flexibility in the temperature distribution while still guaranteeing the required total thermal effect. The goal is to determine the control function $\mu(t)$ that realizes the desired weighted temperature dynamics $f(t)$.

For any constant $M > 0$, we denote by $W(M)$ the set of functions $f \in W_2^2(-\infty, +\infty)$ such that $f(t) = 0$ for all $t \leq 0$ and

$$\|f\|_{W_2^2(\mathbb{R}_+)} \leq M.$$

The main result of this section is the following theorem.

Theorem 2 *There exists $M > 0$ such that for every $f \in W(M)$ the solution $\mu(t)$ of the equation* (7) *exists and satisfies $|\mu(t)| \leq 1$.*

In the subsequent analysis, we will also require the following assumption on the spatial distribution $h(x)$ of the control action.

The Fourier coefficients of $h(x)$ with respect to the adjoint eigenfunctions $Y_{k,j}$ are nonnegative, i.e.,

$$h_{k,j} = \int_0^1 h(x) Y_{k,j}(x)\, dx \geq 0, \qquad j = 1, 2,\ k \in \mathbb{N}.$$

This assumption is essential for ensuring the positivity of certain kernel functions and the solvability of the Volterra integral equation that will be derived in the next sections.

Results and discussion

In this section we reduce the control problem to a Volterra integral equation of the first kind. The reduction uses spectral decomposition and the biorthogonal basis introduced above.

Let $T > 0$ be arbitrary. We denote by $C([0,T]; B)$ the space of continuous functions from $[0,T]$ into a Banach space B.

We introduce the subspace of $W_2^1(0,1)$ that incorporates the nonlocal boundary condition:

$$V := \left\{ v \in W_2^1(0,1) \ :\ v(0) = 0,\ v(1) = v(1/2) \right\}.$$

Definition 3 *A function $u(x,t)$ is called a* generalized solution *of problem* (1)–(3) *if $u \in C([0,T]; V)$ satisfies the weak formulation*

$$\begin{aligned} \frac{d}{dt}\big(u(\cdot,t),\varphi\big)_{L_2(0,1)} + \alpha \frac{d}{dt}\big(u_x(\cdot,t),\varphi_x\big)_{L_2(0,1)} + \big(u_x(\cdot,t),\varphi_x\big)_{L_2(0,1)} \\ = \mu(t)\big(h,\varphi\big)_{L_2(0,1)} \end{aligned} \tag{8}$$

for every test function $\varphi \in H_0^1(0,1)$ and almost every $t \in (0,T)$, together with the initial condition $u(x,0) = 0$.

The choice $\varphi \in H_0^1(0,1)$ ensures that the boundary terms arising from integration by parts vanish, since $\varphi(0) = \varphi(1) = 0$. The nonlocal condition $u(1,t) = u(1/2,t)$ is imposed on the solution u, which belongs to the space V.

Let $\{X_{k,j}\}$ and $\{Y_{k,j}\}$ be the biorthogonal systems defined in Section 2. We expand the solution $u(x,t)$ in the eigenfunctions $\{X_{k,j}\}$:

$$u(x,t) = \sum_{j=1}^{2} \sum_{k=1}^{\infty} u_{k,j}(t) X_{k,j}(x), \qquad u_{k,j}(t) = \int_0^1 u(x,t) Y_{k,j}(x)\, dx.$$

The spatial distribution $h(x)$ of the control is expanded using the adjoint eigenfunctions $\{Y_{k,j}\}$:

$$h_{k,j} = \int_0^1 h(x) Y_{k,j}(x)\, dx, \qquad j = 1, 2,\ k \in \mathbb{N}.$$

Substituting these expansions into (8) and using biorthogonality, we obtain for each k, j:

$$(1 + \alpha\lambda_{k,j}) u'_{k,j}(t) + \lambda_{k,j} u_{k,j}(t) = \mu(t) h_{k,j}, \quad u_{k,j}(0) = 0.$$

Solving this linear ODE gives

$$u_{k,j}(t) = \frac{h_{k,j}}{1 + \alpha\lambda_{k,j}} \int_0^t e^{-\frac{\lambda_{k,j}}{1+\alpha\lambda_{k,j}}(t-s)} \mu(s)\, ds.$$

Thus,

$$u(x,t) = \sum_{j=1}^{2} \sum_{k=1}^{\infty} \frac{h_{k,j}}{1 + \alpha\lambda_{k,j}} \left(\int_0^t e^{-\frac{\lambda_{k,j}}{1+\alpha\lambda_{k,j}}(t-s)} \mu(s)\, ds \right) X_{k,j}(x). \tag{9}$$

Lemma 4 *Let $\mu \in L^2(0,T)$ and $h \in L^2(0,1)$. Then the function $u(x,t)$ defined by (9) is a generalized solution of problem (1)–(3) in the sense of Definition 3.*

Proof of Lemma 4. We first show that $u \in C([0,T];V)$. Differentiating (9) with respect to x gives

$$u_x(x,t) = \sum_{j=1}^{2}\sum_{k=1}^{\infty} \frac{h_{k,j}}{1+\alpha\lambda_{k,j}} \left(\int_0^t e^{-\frac{\lambda_{k,j}}{1+\alpha\lambda_{k,j}}(t-s)} \mu(s)\, ds \right) X'_{k,j}(x).$$

Using the identity

$$\|X'_{k,j}\|^2_{L_2} = \lambda_{k,j}\|X_{k,j}\|^2_{L_2} = \lambda_{k,j}A_{k,j}, \qquad A_{k,j} = \int_0^1 X^2_{k,j}(x)\, dx,$$

which follows by integration by parts from the eigenvalue equation $X''_{k,j} = -\lambda_{k,j}X_{k,j}$, together with the regularizing effect of the factor $(1+\alpha\lambda_{k,j})^{-1}$, we obtain

$$\|u_x(\cdot,t)\|^2_{L_2} \le C \sum_{j=1}^{2}\sum_{k=1}^{\infty} \frac{h^2_{k,j}}{(1+\alpha\lambda_{k,j})^2} \|X'_{k,j}\|^2_{L_2} \left(\int_0^t e^{-\frac{\lambda_{k,j}}{1+\alpha\lambda_{k,j}}(t-s)} \mu(s)\, ds \right)^2.$$

Since $A_{k,j} = \int_0^1 X^2_{k,j}(x)\, dx$ satisfies $0 < A_{k,j} \le \frac{1}{2}$ for all k, j, it follows that

$$\|u_x(\cdot,t)\|^2_{L_2} \le C \sum_{j=1}^{2}\sum_{k=1}^{\infty} \frac{h^2_{k,j}\lambda_{k,j}A_{k,j}}{(1+\alpha\lambda_{k,j})^2} \left(\int_0^t e^{-\frac{\lambda_{k,j}}{1+\alpha\lambda_{k,j}}(t-s)} \mu(s)\, ds \right)^2.$$

Applying the Cauchy-Schwarz inequality to the time integral,

$$\begin{aligned} \left(\int_0^t e^{-\frac{\lambda_{k,j}}{1+\alpha\lambda_{k,j}}(t-s)} \mu(s)\, ds \right)^2 &\le \int_0^t e^{-2\frac{\lambda_{k,j}}{1+\alpha\lambda_{k,j}}(t-s)} ds \cdot \int_0^t |\mu(s)|^2 ds \\ &\le \frac{1+\alpha\lambda_{k,j}}{2\lambda_{k,j}} \|\mu\|^2_{L_2(0,T)}. \end{aligned}$$

Substituting this estimate,

$$\|u_x(\cdot,t)\|^2_{L_2} \le \frac{C}{2}\|\mu\|^2_{L_2(0,T)} \sum_{j=1}^{2}\sum_{k=1}^{\infty} \frac{h^2_{k,j}A_{k,j}}{1+\alpha\lambda_{k,j}}.$$

Since $h \in L_2(0,1)$, its Fourier coefficients satisfy

$$\sum_{j=1}^{2}\sum_{k=1}^{\infty} h^2_{k,j}A_{k,j} = \|h\|^2_{L_2} < \infty.$$

Moreover, $\dfrac{1}{1+\alpha\lambda_{k,j}} \le 1$, so the series converges. Hence $\|u_x(\cdot,t)\|_{L_2}$ is uniformly bounded on $[0,T]$. The same argument applied to u (using $|X_{k,j}(x)| \le 1$) shows that $\|u(\cdot,t)\|_{L_2}$ is also bounded. Continuity in t follows from the dominated convergence theorem, because each term is continuous and the series converges uniformly. Thus $u \in C([0,T];H^1(0,1))$.

To justify the time derivatives in the weak formulation, differentiating (9) with respect to time t gives us

$$u_t(x,t) = \sum_{j=1}^{2}\sum_{k=1}^{\infty} \frac{h_{k,j}}{1+\alpha\lambda_{k,j}} \left[-\sigma_{k,j} \int_0^t e^{-\sigma_{k,j}(t-s)} \mu(s)\, ds + \mu(t) \right] X_{k,j}(x),$$

where $\sigma_{k,j} = \frac{\lambda_{k,j}}{1+\alpha\lambda_{k,j}} \le 1/\alpha$. Similarly, differentiating u_x with respect to t gives

$$u_{xt}(x,t) = \sum_{j=1}^{2}\sum_{k=1}^{\infty} \frac{h_{k,j}}{1+\alpha\lambda_{k,j}} \left[-\sigma_{k,j}\int_0^t e^{-\sigma_{k,j}(t-s)}\mu(s)\,ds + \mu(t)\right] X'_{k,j}(x).$$

Since $\sigma_{k,j} \le 1/\alpha$ and $\|X'_{k,j}\|^2_{L_2} = \lambda_{k,j}A_{k,j}$, the same convergence argument as for u_x shows that both series converge in $L^2(0,T;H^{-1}(0,1))$. Hence, the weak formulation (8) is justified.

Each eigenfunction $X_{k,j}$ satisfies $X_{k,j}(0) = 0$ and $X_{k,j}(1) = X_{k,j}(1/2)$. Therefore $u(0,t) = 0$ and $u(1,t) = u(1/2,t)$, which means $u \in C([0,T];V)$.

Finally, substituting the series (9) into the weak formulation (8) with test functions $\varphi \in H_0^1(0,1)$ and using biorthogonality verifies that u satisfies the equation. The initial condition $u(x,0) = 0$ follows from (9) because the integrals vanish at $t = 0$. This completes the proof. □

By substituting the expression (9) into the integral condition with weight function $\rho \in U$, we obtain

$$\begin{aligned} f(t) &= \int_0^1 \rho(x)\,u(x,t)\,dx \\ &= \sum_{j=1}^{2}\sum_{k=1}^{\infty} \frac{h_{k,j}}{1+\alpha\lambda_{k,j}} \left(\int_0^t e^{-\frac{\lambda_{k,j}}{1+\alpha\lambda_{k,j}}(t-s)}\mu(s)\,ds\right) \int_0^1 \rho(x)\,X_{k,j}(x)\,dx. \end{aligned}$$

The Fourier coefficients of the weight function ρ with respect to $X_{k,j}$ are defined as

$$\rho_{k,j} := \int_0^1 \rho(x)X_{k,j}(x)\,dx.$$

Thus

$$f(t) = \sum_{j=1}^{2}\sum_{k=1}^{\infty} \frac{h_{k,j}\,\rho_{k,j}}{1+\alpha\lambda_{k,j}} \int_0^t e^{-\frac{\lambda_{k,j}}{1+\alpha\lambda_{k,j}}(t-s)}\mu(s)\,ds.$$

Define the kernel

$$K(t) := \sum_{j=1}^{2}\sum_{k=1}^{\infty} \Lambda_{k,j}\, e^{-\frac{\lambda_{k,j}}{1+\alpha\lambda_{k,j}}t}, \quad t \ge 0, \tag{10}$$

where

$$\Lambda_{k,j} = \frac{h_{k,j}\,\rho_{k,j}}{1+\alpha\lambda_{k,j}}, \quad j = 1,2, \quad k \in \mathbb{N}.$$

Then we arrive at the Volterra integral equation of the first kind

$$\int_0^t K(t-\tau)\,\mu(\tau)\,d\tau = f(t), \quad t > 0. \tag{11}$$

The solvability of (11) depends on the properties of $K(t)$. We now establish the necessary estimates.

Lemma 5 *For any $\rho \in U$, the Fourier coefficients*

$$\rho_{k,j} = \int_0^1 \rho(x)X_{k,j}(x)\,dx$$

satisfy

$$0 \le \rho_{k,j} \le \frac{C}{k}, \qquad j = 1,2,\ k \in \mathbb{N},$$

with $C > 0$ independent of k and j.

Proof of Lemma 5. The inequality $\rho_{k,j} \geq 0$ follows from the definition of U (recall that $\rho_{k,j} \geq 0$ is part of the definition). For the upper bound, we start from

$$\rho_{k,j} = \int_0^1 \rho(x) \sin(\sqrt{\lambda_{k,j}}x)\, dx.$$

Integrating by parts:

$$\int_0^1 \rho(x) \sin(\sqrt{\lambda_{k,j}}x)\, dx = -\frac{1}{\sqrt{\lambda_{k,j}}} \int_0^1 \rho'(x) \cos(\sqrt{\lambda_{k,j}}x)\, dx + \frac{\rho(1)\cos\sqrt{\lambda_{k,j}} - \rho(0)}{\sqrt{\lambda_{k,j}}}.$$

Taking absolute values and using $|\cos(\sqrt{\lambda_{k,j}}x)| \leq 1$:

$$\left| \int_0^1 \rho(x) \sin(\sqrt{\lambda_{k,j}}x)\, dx \right| \leq \frac{1}{\sqrt{\lambda_{k,j}}} \int_0^1 |\rho'(x)|\, dx + \frac{|\rho(1)| + |\rho(0)|}{\sqrt{\lambda_{k,j}}}.$$

Since $\rho \in W_2^1(0,1)$, the integral $\int_0^1 |\rho'(x)| dx$ is finite, and $\rho(0), \rho(1)$ are bounded. Hence there exists $C_1 > 0$ such that

$$\int_0^1 |\rho'(x)| dx + |\rho(0)| + |\rho(1)| \leq C_1.$$

Thus

$$\left| \int_0^1 \rho(x) \sin(\sqrt{\lambda_{k,j}}x)\, dx \right| \leq \frac{C_1}{\sqrt{\lambda_{k,j}}}.$$

Now $\sqrt{\lambda_{k,j}} \sim \pi k$, so $1/\sqrt{\lambda_{k,j}} \sim 1/(\pi k)$. Therefore,

$$\rho_{k,j} \leq \frac{C}{k}.$$

□

Lemma 6 *The kernel function $K(t)$ defined by (10) is positive and continuous on $[0, \infty)$.*

Proof of Lemma 6. From the definition,

$$K(t) = \sum_{j=1}^{2} \sum_{k=1}^{\infty} \Lambda_{k,j} e^{-\frac{\lambda_{k,j}}{1+\alpha\lambda_{k,j}}t},$$

where $\Lambda_{k,j} = \dfrac{h_{k,j}\rho_{k,j}}{1+\alpha\lambda_{k,j}}$. By assumptions, $h_{k,j} \geq 0$, $\rho_{k,j} \geq 0$, and $\lambda_{k,j} > 0$. Hence $\Lambda_{k,j} \geq 0$.

Since h and ρ are not identically zero and their Fourier coefficients are nonnegative, we may assume without loss of generality that $h_{1,1} > 0$ and $\rho_{1,1} > 0$. (If $h_{1,1} = 0$, we take the next smallest index where the coefficients are positive.) Therefore $\Lambda_{1,1} > 0$, and

$$K(t) \geq \Lambda_{1,1} e^{-\frac{\lambda_{1,1}}{1+\alpha\lambda_{1,1}}t} > 0 \quad \text{for all } t \geq 0.$$

Now we prove continuity. Since $0 < e^{-\frac{\lambda_{k,j}}{1+\alpha\lambda_{k,j}}t} \leq 1$ for all $t \geq 0$, we have

$$\left| \Lambda_{k,j} e^{-\frac{\lambda_{k,j}}{1+\alpha\lambda_{k,j}}t} \right| \leq |\Lambda_{k,j}|.$$

From Lemma 5, $\rho_{k,j} \le C/k$. The Fourier coefficients $h_{k,j}$ satisfy $\sum_{j,k} h_{k,j}^2 < \infty$ (since $h \in L_2(0,1)$). Therefore,

$$|\Lambda_{k,j}| = \frac{|h_{k,j}|\rho_{k,j}}{1+\alpha\lambda_{k,j}} \le C\frac{|h_{k,j}|}{k^3}.$$

Now we estimate the sum:

$$\sum_{j=1}^{2}\sum_{k=1}^{\infty}|\Lambda_{k,j}| \le C\sum_{j=1}^{2}\sum_{k=1}^{\infty}\frac{|h_{k,j}|}{k^3}$$
$$\le C\left(\sum_{j=1}^{2}\sum_{k=1}^{\infty}h_{k,j}^2\right)^{1/2}\left(\sum_{j=1}^{2}\sum_{k=1}^{\infty}\frac{1}{k^6}\right)^{1/2} < \infty,$$

where we used the Cauchy-Schwarz inequality. Since $\sum 1/k^6 < \infty$ and $\sum h_{k,j}^2 = \|h\|_{L_2}^2 < \infty$, the series converges.

By the Weierstrass M-test with $M_{k,j} = |\Lambda_{k,j}|$, the series

$$K(t) = \sum_{j=1}^{2}\sum_{k=1}^{\infty}\Lambda_{k,j}e^{-\frac{\lambda_{k,j}}{1+\alpha\lambda_{k,j}}t}$$

converges uniformly on $[0,\infty)$. Each term is continuous, therefore $K(t)$ is continuous on $[0,\infty)$ as a uniform limit of continuous functions. □

We solve (11) by the Laplace transform. Recall that the Laplace transform of μ is

$$\widetilde{\mu}(p) = \int_0^\infty e^{-pt}\mu(t)\,dt, \quad \Re p > 0.$$

Applying the transform to (11) and using the convolution theorem gives

$$\widetilde{f}(p) = \widetilde{K}(p)\widetilde{\mu}(p),$$

so that

$$\widetilde{\mu}(p) = \frac{\widetilde{f}(p)}{\widetilde{K}(p)}, \qquad p = \xi + i\tau,\ \xi > 0,\ \tau \in \mathbb{R}.$$

The inverse Laplace transform yields

$$\mu(t) = \frac{1}{2\pi i}\int_{\xi-i\infty}^{\xi+i\infty}\frac{\widetilde{f}(p)}{\widetilde{K}(p)}e^{pt}dp = \frac{1}{2\pi}\int_{-\infty}^{+\infty}\frac{\widetilde{f}(\xi+i\tau)}{\widetilde{K}(\xi+i\tau)}e^{(\xi+i\tau)t}d\tau. \tag{12}$$

Lemma 7 *For $\xi > 0$ and $\tau \in \mathbb{R}$, the following inequality holds:*

$$|\widetilde{K}(\xi+i\tau)| \ge \frac{C_\xi}{\sqrt{1+\tau^2}},$$

where $C_\xi > 0$ depends only on ξ.

Proof of Lemma 7. Set $\sigma_{k,j} = \frac{\lambda_{k,j}}{1+\alpha\lambda_{k,j}}$. Then from the definition of $K(t)$,

$$\widetilde{K}(p) = \int_0^\infty K(t)e^{-pt}dt = \sum_{j=1}^{2}\sum_{k=1}^{\infty}\frac{\Lambda_{k,j}}{p+\sigma_{k,j}}.$$

For $p = \xi + i\tau$,

$$\begin{aligned}\widetilde{K}(\xi + i\tau) &= \sum_{j,k} \frac{\Lambda_{k,j}(\xi + \sigma_{k,j})}{(\xi + \sigma_{k,j})^2 + \tau^2} - i\tau \sum_{j,k} \frac{\Lambda_{k,j}}{(\xi + \sigma_{k,j})^2 + \tau^2} \\ &= \Re\widetilde{K} + i\,\Im\widetilde{K},\end{aligned}$$

where

$$\Re\widetilde{K} = \sum_{j,k} \frac{\Lambda_{k,j}(\xi + \sigma_{k,j})}{(\xi + \sigma_{k,j})^2 + \tau^2}, \qquad \Im\widetilde{K} = -\tau \sum_{j,k} \frac{\Lambda_{k,j}}{(\xi + \sigma_{k,j})^2 + \tau^2}.$$

Since $(\xi + \sigma_{k,j})^2 + \tau^2 \le ((\xi + \sigma_{k,j})^2 + 1)(1 + \tau^2)$, we have

$$\frac{1}{(\xi + \sigma_{k,j})^2 + \tau^2} \ge \frac{1}{1 + \tau^2} \cdot \frac{1}{(\xi + \sigma_{k,j})^2 + 1}.$$

Therefore

$$|\Re\widetilde{K}| \ge \frac{1}{1 + \tau^2} \sum_{j,k} \frac{\Lambda_{k,j}(\xi + \sigma_{k,j})}{(\xi + \sigma_{k,j})^2 + 1} = \frac{C_{1,\xi}}{1 + \tau^2},$$

$$|\Im\widetilde{K}| \ge \frac{|\tau|}{1 + \tau^2} \sum_{j,k} \frac{\Lambda_{k,j}}{(\xi + \sigma_{k,j})^2 + 1} = \frac{C_{2,\xi}|\tau|}{1 + \tau^2},$$

where $C_{1,\xi}, C_{2,\xi} > 0$ are finite because $\sum_{j,k} \Lambda_{k,j} < \infty$ (this follows from the Cauchy-Schwarz inequality and the fact that $h \in L_2(0,1)$). Consequently, we obtain

$$|\widetilde{K}(\xi + i\tau)|^2 \ge \frac{C_{1,\xi}^2 + C_{2,\xi}^2 \tau^2}{(1 + \tau^2)^2} \ge \frac{\min(C_{1,\xi}^2, C_{2,\xi}^2)}{1 + \tau^2},$$

which proves the lemma. □

Taking the limit $\xi \to 0$ in Lemma 7, we obtain

$$|\widetilde{K}(i\tau)| \ge \frac{C_0}{\sqrt{1 + \tau^2}}, \qquad C_0 := \min(C_{1,0}, C_{2,0}) > 0.$$

Then from (12) we have

$$\mu(t) = \frac{1}{2\pi} \int_{-\infty}^{+\infty} \frac{\widetilde{f}(i\tau)}{\widetilde{K}(i\tau)} e^{i\tau t} d\tau. \tag{13}$$

Lemma 8 *[18] Assume that $f \in W(M)$. Then*

$$\int_{-\infty}^{+\infty} |\widetilde{f}(i\tau)| \sqrt{1 + \tau^2}\, d\tau \le C_* \|f\|_{W_2^2(\mathbb{R}_+)},$$

where $C_* > 0$ is a constant.

Proof of Theorem 2. We first show that $\mu \in L^2(\mathbb{R}_+)$. From Lemma 7 with $\xi \to 0$,

$$|\widetilde{\mu}(\tau)| = \left| \frac{\widetilde{f}(i\tau)}{\widetilde{K}(i\tau)} \right| \le \frac{1}{C_0} |\widetilde{f}(i\tau)| \sqrt{1 + \tau^2}.$$

Hence,

$$\int_{-\infty}^{+\infty} |\widetilde{\mu}(\tau)|^2 d\tau \le \frac{1}{C_0^2} \int_{-\infty}^{+\infty} |\widetilde{f}(i\tau)|^2 (1 + \tau^2) d\tau < \infty,$$

since $f \in W_2^2(\mathbb{R}_+)$. Thus $\widetilde{\mu} \in L^2(\mathbb{R})$, and by the Plancherel theorem, $\mu \in L^2(\mathbb{R})$. Because $\mu(t) = 0$ for $t < 0$, we conclude $\mu \in L^2(\mathbb{R}_+)$.

Next, from (13) and Lemmas 7 and 8,

$$\begin{aligned} |\mu(t)| &\le \frac{1}{2\pi} \int_{-\infty}^{+\infty} \frac{|\widetilde{f}(i\tau)|}{|\widetilde{K}(i\tau)|} d\tau \\ &\le \frac{1}{2\pi C_0} \int_{-\infty}^{+\infty} |\widetilde{f}(i\tau)| \sqrt{1+\tau^2}\, d\tau \\ &\le \frac{C_*}{2\pi C_0} \|f\|_{W_2^2(\mathbb{R}_+)} \le \frac{C_* M}{2\pi C_0}. \end{aligned}$$

Choosing $M = \dfrac{2\pi C_0}{C_*}$, we obtain $|\mu(t)| \le 1$ for every $f \in W(M)$. This completes the proof. □

Example. We now present a concrete illustration of the control construction proposed above. Recall that, according to the integral condition (7), $f(t)$ represents the prescribed trajectory of the weighted average temperature

$$\int_0^1 \rho(x)\, u(x,t)\, dx = f(t), \qquad t \ge 0,$$

where $\rho \in U$ is a given weight function. In this example, we consider the desired trajectory

$$f(t) = \begin{cases} 0, & t \le 0, \\ M_0 t^2 e^{-t}, & t > 0, \end{cases}$$

where $M_0 > 0$ is a constant to be determined. It is straightforward to verify that $f(0) = 0$ and $f \in W(M)$ for an appropriate choice of M.

Recall that the kernel of the Volterra integral equation (11) is given by

$$K(t) = \sum_{j=1}^{2} \sum_{k=1}^{\infty} \Lambda_{k,j} e^{-\sigma_{k,j} t}, \qquad \sigma_{k,j} = \frac{\lambda_{k,j}}{1 + \alpha \lambda_{k,j}}.$$

Since $\alpha > 0$ and $\lambda_{k,j} > 0$, it follows that $0 < \sigma_{k,j} < 1$ for all k, j. For the purpose of this illustrative example, we retain only the leading term of the series, namely

$$K(t) \approx \Lambda_{1,1} e^{-\sigma_{1,1} t},$$

where $\Lambda_{1,1} > 0$ and $0 < \sigma_{1,1} < 1$. This simplification is introduced solely to demonstrate the construction explicitly and is not used in the proof of Theorem 2.

Under this approximation, the Volterra integral equation (11) reduces to

$$\Lambda_{1,1} \int_0^t e^{-\sigma_{1,1}(t-s)} \mu(s)\, ds = M_0 t^2 e^{-t}, \qquad t > 0.$$

Applying the Laplace transform and using the convolution theorem, we obtain

$$\widetilde{\mu}(p) = \frac{2M_0}{\Lambda_{1,1}} \cdot \frac{p + \sigma_{1,1}}{(p+1)^3}.$$

Taking the inverse Laplace transform yields the explicit control function

$$\mu(t) = \frac{M_0}{\Lambda_{1,1}}\, e^{-t} \Big[2t - (1 - \sigma_{1,1}) t^2 \Big].$$

8. Lions J.L. Controle optimal de systemes gouvernes par des equations aux derivees partielles. Dunod Gauthier-Villars, Paris (1968).

9. Chen N., Wang Y., Yang D.H. Time-varying bang-bang property of time optimal controls for heat equation and its applications. Syst. Control Lett., 112, 18–23 (2018).

10. Schmidt G. The "Bang-Bang" principle for the time-optimal problem in boundary control of the heat equation. SIAM J. Control Optim., 18, 101–107 (1980).

11. Albeverio S., Alimov Sh.A. On a time-optimal control problem associated with the heat exchange process. Appl. Math. Optim., 57, 58–68 (2008).

12. Alimov S., Ibragimov G. Time optimal control problem with integral constraint for the heat transfer process. Eurasian Math. J., 15, 8–22 (2024).

13. Xu H. Existence and blow-up of solutions for finitely degenerate semilinear parabolic equations with singular potentials. Commun. Anal. Mech., 15, 132–161 (2023).

14. Wu X., Zhao Y., Yang X. On a singular parabolic p-Laplacian equation with logarithmic nonlinearity. Commun. Anal. Mech., 16, 528–553 (2024).

15. Fayazova Z.K. Boundary control of the heat transfer process in the space. Russian Math., 63, 71–79 (2019).

16. Dekhkonov F.N. Boundary control problem for a parabolic equation with involution. Eurasian J. Math. Comput. Appl., 12, 22–34 (2024).

17. Dekhkonov F.N. On the time-optimal control problem for a heat equation. Bull. Karaganda Univ. Math. Ser., 111, 28–38 (2023).

18. Dekhkonov F., Li W. On the boundary control problem associated with a fourth order parabolic equation in a two-dimensional domain. Discrete Contin. Dyn. Syst. Ser. S, 17, 2478–2488 (2024).

19. Dekhkonov F., Turmetov B. On one time-optimal control problem for a parabolic equation with involution in a bounded domain. AIMS Math., 10, 20531–20549 (2025).

20. Dicke A., Veselić I. Spherical Logvinenko-Sereda-Kovrijkine type inequality and null-controllability of the heat equation on the sphere. Arch. Math., 123, 543–556 (2024).

21. Egidi M., Seelmann A. The reflection principle in the control problem of the heat equation. J. Dyn. Control Syst., 28, 635–655 (2022).

22. Allal B., Fragnelli G., Salhi J. Null controllability for degenerate parabolic equations with a nonlocal space term. Discrete Contin. Dyn. Syst. Ser. S, 17, 1821–1856 (2024).

23. Song D., Zhao X. Large-time behavior of cylindrically symmetric Navier-Stokes equations with temperature-dependent viscosity and heat conductivity. Commun. Anal. Mech., 16, 599–632 (2024).

24. Arada N., Raymond J.P. Time optimal problems with Dirichlet boundary conditions. Discrete Contin. Dyn. Syst., 9, 1549–1570 (2003).

25. Wang G. The existence of time optimal control of semilinear parabolic equations. Syst. Control Lett., 53, 171–175 (2004).

26. Zhou X. Controllability analysis and application of a pseudo-parabolic equation with memory term. J. Math. Anal. Appl., 556(2), 130259 (2026).

27. Dekhkonov F.N. On the boundary control problem for a pseudo-parabolic equation with involution. Vestnik Sankt-Peterburgskogo Universiteta, Prikladnaya Matematika, Informatika, Protsessy Upravleniya, 20, 416–427 (2024).

28. Dekhkonov F. On one boundary control problem for a pseudo-parabolic equation in a two-dimensional domain. Commun. Anal. Mech., 17, 1–14 (2025).

29. Ashurov R.R., Kadirkulov B.J., Turmetov B.Kh. On the inverse problem of the Bitsadze-Samarskii type for a fractional parabolic equation. Probl. Anal. Issues Anal., 3, 20–40 (2023).

[1]*Dekhkonov F.N.,

ф.-м.ғ.д., доцент, ORCID ID: 0000-0003-4747-8557,
*e-mail: f.n.dehqonov@mail.ru

[1] Usubjonov A.A.,

докторант, e-mail: adhamusubjonov@gmail.com

[1] Наманган мемлекеттік университеті, математика кафедрасы,

Наманган қ., Өзбекстан

ЛОКАЛДЫ ЕМЕС ШЕКАРАЛЫҚ ШАРТЫ БАР БІР ӨЛШЕМДІ ПСЕВДОПАРАБОЛДЫҚ ТЕҢДЕУ ҮШІН БАСҚАРУ МӘСЕЛЕСІ ТУРАЛЫ

Аңдатпа

Бұл жұмыста Бицадзе-Самарский типіндегі локалды емес шекаралық шарты бар бір өлшемді псевдопараболалық теңдеу үшін басқару мәселесі зерттеледі. Бақылау функциясы теңдеудің оң жағында таратылған көз түрінде кіреді, мақсат жүйені нөлдік бастапқы күйден басқару арқылы салмақталған орташа температураның берілген траектория бойынша өзгеруін қамтамасыз ету болып табылады. Теңдеу жылу өткізгіштіктегі жады немесе тұтқыр серпімділік әсерлерін ескеретін үшінші ретті аралас туынды мүшені қамтиды, бұл әсіресе полимерлер, биологиялық ұлпалар және түйіршікті материалдар сияқты ішкі құрылымы бар материалдар үшін маңызды. Спектрлік жіктеу және биортогоналды базис көмегімен есеп бірінші текті Вольтерра интегралдық теңдеуіне келтіріледі. Бұл интегралдық теңдеудің ядросының оң және үзіліссіз екендігі дәлелденген. Салмақ функциясына және басқарудың кеңістіктік таралуына сәйкес болжамдарда нормасы жеткілікті аз болатын қажетті траекториялар класы үшін рұқсат етілген басқарудың бар екендігі дәлелденген. Интегралдық теңдеуді шешу және басқару функциясына бағалау алу үшін Лаплас түрлендіру әдісі қолданылады. Нәтижелер локалды емес шекаралық шарт пен жады параметрінің басқарылу қабілетіне әсерін сандық түрде сипаттайды.

Түйін сөздер: псевдопараболдық теңдеу, шекаралық есеп, Вольтерра интегралдық теңдеуі, рұқсат етілген басқару, жіңішке өзек.

[1]*Dekhkonov F.N.,
доктор физико-математических наук, доцент,
ORCID ID: 0000-0003-4747-8557,
*e-mail: f.n.dehqonov@mail.ru
[1] Usubjonov A.A.,
докторант PhD,
e-mail: adhamusubjonov@gmail.com
[1] Наманганский государственный университет, кафедра математики,
г. Наманган, Узбекистан

О ЗАДАЧЕ УПРАВЛЕНИЯ ДЛЯ ОДНОМЕРНОГО ПСЕВДОПАРАБОЛИЧЕСКОГО УРАВНЕНИЯ С НЕЛОКАЛЬНЫМ ГРАНИЧНЫМ УСЛОВИЕМ

Аннотация

В настоящей статье исследуется задача управления для одномерного псевдопараболического уравнения с нелокальным граничным условием типа Бицадзе-Самарского. Управляющая функция входит в правую часть уравнения в виде распределенного источника, и цель состоит в том, чтобы перевести систему из нулевого начального состояния так, чтобы средневзвешенная температура следовала заданной траектории. Уравнение содержит член третьего порядка со смешанной производной, который учитывает эффекты памяти или вязкоупругости в теплопроводности, что особенно важно для материалов с внутренней структурой, таких как полимеры, биологические ткани и гранулированные среды. С помощью спектрального разложения и биортогонального базиса задача сводится к интегральному уравнению Вольтерра первого рода. Доказано, что ядро этого интегрального уравнения положительно и непрерывно. При соответствующих предположениях о весовой функции и пространственном распределении управления доказано существование допустимого управления для класса желаемых траекторий с достаточно малой нормой. Для решения интегрального уравнения и получения оценок управляющей функции используется метод преобразования Лапласа. Результаты количественно характеризуют влияние нелокального граничного условия и параметра памяти на управляемость системы.

Ключевые слова: псевдопараболическое уравнение, краевая задача, интегральное уравнение Вольтерра, допустимое управление, тонкий стержень.

UDC 517.95
IRSTI 27.35.15

https://doi.org/10.55452/1998-6688-2026-23-3-70-79

[1,2,*]Bayetov K.Kh.
PhD student,
ORCID ID: 0000-0002-3820-9999,
*e-mail: baetov1983kairden@gmail.com

[1] Abai Kazakh National Pedagogical University, Almaty, Kazakhstan
[2] ALT University, Almaty, Kazakhstan

INVERSE PROBLEM FOR A PARABOLIC EQUATION WITH A TIME-DEPENDENT COEFFICIENT IN THE BOUNDARY CONDITION

Abstract

In this paper, we consider an inverse problem for a parabolic equation in which a time-dependent coefficient is included in the boundary condition. Additional information is given by an overdetermination condition that relates the solution to a given function of time. To solve the problem, the spectral method is used, which is based on the expansion of the solution in terms of eigenfunctions of the corresponding boundary value problem with homogeneous boundary conditions. Due to this expansion, the original problem is reduced to a system of ordinary differential equations for the expansion coefficients. After solving the obtained system and substituting the representation of the solution into the integral condition, the problem is reduced to a nonlinear Volterra integral equation with respect to the unknown coefficient. For the obtained equation, the corresponding operator is introduced and its properties are studied. The existence and uniqueness of the solution on the interval $[0, T]$ are proved under the contraction condition for the constructed operator. It is shown that the presence of an unknown coefficient in the boundary condition leads to a change in the structure of the resulting integral equation compared to classical formulations of inverse problems. The proposed approach can be applied to a wider class of inverse problems for parabolic equations with nonclassical boundary conditions.

Keywords: inverse problem, parabolic equation, integral overdetermination condition, spectral method, Volterra integral equation, contraction mapping principle.

Received May 3, 2026; revised June 7, 2026; accepted June 11, 2025.

Introduction

Most applied problems in various fields of science are associated with inverse problems. Inverse problems for differential equations in mathematical physics arise when unknown parameters of a model, such as coefficients, sources, or boundary effects, must be recovered from additional information. For example, such problems arise in the study of soil freezing processes in winter, when the temperature at the surface is known, while the temperature distribution in depth is unknown. Similar problems also appear in the analysis of heat transfer in technical devices, for example, in transformers, where the process depends on the properties of the medium and boundary conditions. Many such problems are widely used in thermodynamics, geophysics, acoustics, medicine and other fields [1, 2].

In particular, inverse problems for parabolic equations have been actively studied in recent decades. For such problems, various additional conditions are used, such as pointwise, integral or

nonlocal conditions. Depending on the type of overdetermination, spectral decomposition methods, Volterra integral equations and regularization methods are applied.

In particular, in [2] an inverse problem of recovering a time-dependent source in the heat equation is considered. In [11] the problem of determining a coefficient in a parabolic equation with an integral overdetermination condition is studied. In [1] the conditions for existence and uniqueness of a solution are obtained using the spectral method.

Similar problems are considered in [12]. In [13] an inverse problem for a degenerate parabolic equation is investigated. More general classes of inverse problems are studied in [14].

It should be noted that classical results on coefficient identification were obtained in [3, 4, 5, 6]. Problems with nonclassical boundary conditions are considered in [7]. The methods of investigation are based on the theory of linear operators, spectral analysis and numerical methods [8, 9, 10].

However, despite a large number of studies, most of them are devoted to problems in which the unknown coefficient appears directly in the differential equation. Problems in which the coefficient is specified in the boundary conditions are studied much less.

In this connection, in the present paper we consider an inverse problem for a parabolic equation in which the coefficient depends on time and is specified in the boundary condition. Additional information is given by an integral condition, namely

$$\int_0^1 u(x,t)\,dx = e(t).$$

In this work, the problem is studied using the spectral method and the method of integral equations.

The aim of the paper is to prove the existence and uniqueness of the solution, as well as to construct the solution using the spectral method.

Materials and methods

Problem formulation.

Let

$$Q_T = \{(x,t) : 0 < x < 1,\ 0 < t \le T\}.$$

We consider the problem. It is required to find the function $u(x,t)$ and the coefficient $a(t)$ satisfying conditions (1)–(4).

$$u_t - u_{xx} + a(t)u = f(x,t), \quad (x,t) \in Q_T, \tag{1}$$

with the initial condition

$$u(x,0) = \varphi(x), \quad 0 \le x \le 1, \tag{2}$$

boundary conditions

$$u_x(0,t) = 0, \quad u_x(1,t) = a(t), \quad 0 \le t \le T, \tag{3}$$

and the integral condition

$$\int_0^1 u(x,t)\,dx = e(t), \quad 0 \le t \le T. \tag{4}$$

We represent the solution in the form

$$u(x,t) = w(x,t) + v(x,t). \tag{5}$$

We seek the function $w(x,t)$ in the form

$$w(x,t) = (b_2x^2 + b_1x + b_0)a(t). \tag{6}$$

Then

$$w_x(x,t) = (2b_2x + b_1)a(t).$$

$$w_x(0,t) = 0, \qquad w_x(1,t) = a(t)$$

Hence,

$$b_1 = 0, \qquad b_2 = \frac{1}{2}.$$

If $b_0 = 0$, then

$$w(x,t) = \frac{x^2}{2}a(t). \tag{7}$$

where from (5), (7) it follows that

$$u(x,t) = \frac{x^2}{2}a(t) + v(x,t). \tag{8}$$

Substituting (8) into equation (1), we obtain

$$v_t - v_{xx} + a(t)v = f(x,t) + a(t) - \frac{x^2}{2}a'(t) - \frac{x^2}{2}a^2(t). \tag{9}$$

$$v(x,0) = \varphi(x) - \frac{x^2}{2}a(0). \tag{10}$$

$$v_x(0,t) = 0, \qquad v_x(1,t) = 0. \tag{11}$$

Consequently,

$$v_t - v_{xx} + a(t)v = F(x,t), \tag{12}$$

where

$$F(x,t) = f(x,t) + a(t) - \frac{x^2}{2}a'(t) - \frac{x^2}{2}a^2(t), \tag{13}$$

under the conditions

$$v(x,0) = \varphi(x) - \frac{x^2}{2}a(0), \quad v_x(0,t) = v_x(1,t) = 0. \tag{14}$$

Spectral problem.

We consider the spectral problem. Recall that

Since the boundary conditions (11) are homogeneous, we consider the Neumann problem

$$y''(x) + \lambda y(x) = 0, \tag{15}$$

$$y'(0) = 0, \qquad y'(1) = 0. \tag{16}$$

Let $\lambda = \mu^2 \geq 0$.

Then we obtain

$$y(x) = A\cos\mu x + B\sin\mu x.$$

From $y'(0) = 0$ we obtain $B = 0$,

$$y(x) = A\cos\mu x.$$

From $y'(1) = 0$ it follows that

$$\sin\mu = 0, \quad \mu = n\pi, \quad n = 0, 1, 2, \ldots.$$

Hence,

$$\lambda_n = (n\pi)^2, \qquad n = 0, 1, 2, \ldots, \tag{17}$$

$$y_n(x) = \cos(n\pi x), \qquad n = 0, 1, 2, \ldots. \tag{18}$$

Then

$$v(x,t) = \sum_{n=0}^{\infty} v_n(t)\cos(n\pi x). \tag{19}$$

Equation (9) can be written in the form

$$v_t - v_{xx} + a(t)v = F(x,t), \tag{20}$$

Moreover, we expand the function $F(x,t)$:

$$F(x,t) = \sum_{n=0}^{\infty} F_n(t)\cos(n\pi x), \tag{21}$$

where

$$F_n(t) = \frac{\displaystyle\int_0^1 F(x,t)\cos(n\pi x)\ dx}{\displaystyle\int_0^1 \cos^2(n\pi x)\ dx}. \tag{22}$$

$$v(x,0) = \psi(x), \qquad \psi(x) := \varphi(x) - \frac{x^2}{2}a(0). \tag{23}$$

Hence,

$$\psi(x) = \sum_{n=0}^{\infty} \psi_n \cos(n\pi x). \tag{24}$$

To determine $v_n(t)$, we first compute the derivatives. Indeed,

$$v_t(x,t) = \sum_{n=0}^{\infty} v_n'(t)\cos(n\pi x). \tag{25}$$

$$\frac{d^2}{dx^2}\cos(n\pi x) = -(n\pi)^2\cos(n\pi x),$$

$$v_{xx}(x,t) = -\sum_{n=0}^{\infty}(n\pi)^2 v_n(t)\cos(n\pi x). \tag{26}$$

Moreover,

$$a(t)v(x,t) = \sum_{n=0}^{\infty} a(t)v_n(t)\cos(n\pi x). \tag{27}$$

Substituting (25)–(27) into (20) and using orthogonality, we obtain

$$\sum_{n=0}^{\infty}\Big(v_n'(t) + \big((n\pi)^2 + a(t)\big)v_n(t) - F_n(t)\Big)\cos(n\pi x) = 0.$$

Hence,

$$v_n'(t) + \big((n\pi)^2 + a(t)\big)v_n(t) = F_n(t), \quad n = 0, 1, 2, \ldots. \tag{28}$$

$$v_n(0) = \psi_n. \tag{29}$$

If

$$\mu_n(t) = \exp\left(\int_0^t \big((n\pi)^2 + a(\tau)\big)\ d\tau\right) = e^{(n\pi)^2 t + \int_0^t a(\tau)\ d\tau}, \tag{30}$$

then

$$\frac{d}{dt}\Big(\mu_n(t)v_n(t)\Big) = \mu_n(t)F_n(t). \tag{31}$$

$$\mu_n(t)v_n(t) = \psi_n + \int_0^t \mu_n(s)F_n(s)\ ds.$$

$$v_n(t) = e^{-(n\pi)^2 t - \int_0^t a(\tau)\ d\tau}\left[\psi_n + \int_0^t e^{(n\pi)^2 s + \int_0^s a(\xi)\ d\xi}F_n(s)\ ds\right]. \tag{32}$$

$$v_n(t) = \psi_n e^{-(n\pi)^2 t - \int_0^t a(\tau)\ d\tau} + \int_0^t e^{-(n\pi)^2 (t-s) - \int_s^t a(\tau)\ d\tau}F_n(s)\ ds. \tag{33}$$

Substituting (**??**) into (**??**), we obtain

$$v(x,t) = \sum_{n=0}^{\infty}\left[\psi_n e^{-(n\pi)^2 t - \int_0^t a(\tau)\ d\tau} + \int_0^t e^{-(n\pi)^2 (t-s) - \int_s^t a(\tau)\ d\tau}F_n(s)\ ds\right]\cos(n\pi x). \tag{34}$$

$$u(x,t) = \frac{x^2}{2}a(t) + \sum_{n=0}^{\infty}\left[\psi_n e^{-(n\pi)^2 t - \int_0^t a(\tau)\ d\tau} + \int_0^t e^{-(n\pi)^2 (t-s) - \int_s^t a(\tau)\ d\tau}F_n(s)\ ds\right]\cos(n\pi x). \tag{35}$$

Integral condition and equation for the coefficient $a(t)$
Substituting (35) into the integral condition (4), we obtain

$$\int_0^1 u(x,t)\ dx = \int_0^1 \frac{x^2}{2}a(t)\ dx + \sum_{n=0}^{\infty}\Big[\psi_n e^{-(n\pi)^2 t - \int_0^t a(\tau)\ d\tau} + \int_0^t e^{-(n\pi)^2 (t-s) - \int_s^t a(\tau)\ d\tau}F_n(s)\ ds\Big]\int_0^1 \cos(n\pi x)\ dx. \tag{36}$$

$$\int_0^1 \frac{x^2}{2}\ dx = \frac{1}{6}, \qquad \int_0^1 \cos(n\pi x)\ dx = \begin{cases} 1, & n = 0, \\ 0, & n \geq 1, \end{cases}$$

$$e(t) = \frac{1}{6}a(t) + v_0(t), \tag{37}$$

where

$$v_0(t) = \psi_0 e^{-\int_0^t a(\tau)\ d\tau} + \int_0^t e^{-\int_s^t a(\tau)\ d\tau}F_0(s)\ ds. \tag{38}$$

Thus, it follows that

$$a(t) = 6\big(e(t) - v_0(t)\big). \tag{39}$$

We introduce the operator F:

$$(Fa)(t) = 6\big(e(t) - v_0[a](t)\big), \tag{40}$$

where $v_0[a](t)$ depends on $a(t)$.

Consequently, we obtain

$$a = F(a).$$

Results and Discussion

We consider functions $a_1, a_2 \in C[0,T]$.

Then we have

$$(Fa_1)(t) - (Fa_2)(t) = 6\big(v_0[a_2](t) - v_0[a_1](t)\big),$$

whence

$$|(Fa_1)(t) - (Fa_2)(t)| \le 6\,|v_0[a_1](t) - v_0[a_2](t)|. \tag{41}$$

From the definition of $v_0[a](t)$ we have

$$v_0[a_1](t) - v_0[a_2](t) = \psi_0\left(e^{-\int_0^t a_1(\tau)\,d\tau} - e^{-\int_0^t a_2(\tau)\,d\tau}\right)$$

$$+ \int_0^t \left(e^{-\int_s^t a_1(\tau)\,d\tau} - e^{-\int_s^t a_2(\tau)\,d\tau}\right) F_0(s)\,ds.$$

Thus, we obtain

$$|v_0[a_1](t) - v_0[a_2](t)| \le |\psi_0| \left|e^{-\int_0^t a_1(\tau)\,d\tau} - e^{-\int_0^t a_2(\tau)\,d\tau}\right| + \int_0^t \left|e^{-\int_s^t a_1(\tau)\,d\tau} - e^{-\int_s^t a_2(\tau)\,d\tau}\right| |F_0(s)|\,ds. \tag{42}$$

We apply the mean value theorem for $t \in [0,T]$.

$$\left|e^{-\int_0^t a_1(\tau)\,d\tau} - e^{-\int_0^t a_2(\tau)\,d\tau}\right| = e^{-\theta}\left|\int_0^t (a_1(\tau) - a_2(\tau))\,d\tau\right|,$$

where θ lies between $\int_0^t a_1(\tau)\,d\tau$ and $\int_0^t a_2(\tau)\,d\tau$.

Since $a_m(t) \ge \alpha > 0$, we have

$$\theta \ge \alpha t, \qquad e^{-\theta} \le e^{-\alpha t}.$$

Moreover,

$$\left|\int_0^t (a_1(\tau) - a_2(\tau))\,d\tau\right| \le t\,\|a_1 - a_2\|_{C[0,T]}.$$

Hence,

$$\left|e^{-\int_0^t a_1(\tau)\,d\tau} - e^{-\int_0^t a_2(\tau)\,d\tau}\right| \le te^{-\alpha t}\,\|a_1 - a_2\|_{C[0,T]}.$$

Using the estimate

$$xe^{-\alpha x} \le \frac{1}{\alpha e}, \qquad x \ge 0,$$

we obtain (43).

Similarly, for $0 \le s \le t \le T$ we have

$$|e^{-A_1} - e^{-A_2}| = e^{-\theta}|A_1 - A_2|,$$

where

$$A_m = \int_s^t a_m(\tau)\,d\tau, \qquad m = 1,2.$$

Then

$$A_m \geq \alpha(t-s), \qquad |A_1 - A_2| \leq (t-s)\,\|a_1 - a_2\|_{C[0,T]}\,.$$

$$\left|e^{-\int_0^t a_1(\tau)\,d\tau} - e^{-\int_0^t a_2(\tau)\,d\tau}\right| \leq te^{-\alpha t}\,\|a_1 - a_2\|_{C[0,T]}\,. \tag{43}$$

Thus, estimate (43) is obtained.

Estimate of the operator F.

Using the obtained estimates, we have

$$|v_0[a_1](t) - v_0[a_2](t)| \leq \frac{|\psi_0|}{\alpha e}\,\|a_1 - a_2\|_{C[0,T]} + \frac{1}{\alpha e}\,\|a_1 - a_2\|_{C[0,T]} \int_0^t |F_0(s)|\,ds.$$

$$|v_0[a_1](t) - v_0[a_2](t)| \leq \frac{1}{\alpha e}\left(|\psi_0| + \int_0^t |F_0(s)|\,ds\right)\|a_1 - a_2\|_{C[0,T]}\,. \tag{44}$$

Then

$$|(Fa_1)(t) - (Fa_2)(t)| \leq \frac{6}{\alpha e}\left(|\psi_0| + \int_0^t |F_0(s)|\,ds\right)\|a_1 - a_2\|_{C[0,T]}\,.$$

Since

$$\int_0^t |F_0(s)|\,ds \leq \int_0^T |F_0(s)|\,ds,$$

we obtain

$$|(Fa_1)(t) - (Fa_2)(t)| \leq q\,\|a_1 - a_2\|_{C[0,T]}\,, \tag{45}$$

where

$$q = \frac{6}{\alpha e}\left(|\psi_0| + \int_0^T |F_0(s)|\,ds\right). \tag{46}$$

Consequently,

$$\|Fa_1 - Fa_2\|_{C[0,T]} \leq q\,\|a_1 - a_2\|_{C[0,T]}\,. \tag{47}$$

If

$$q < 1, \tag{48}$$

then the operator F is a contraction in $C[0,T]$.

Since q depends on T, for sufficiently small T condition (48) is satisfied.

Main result

Theorem 1. *Let $\varphi(x)$, $e(t)$ and $F_0(t)$ be given and all constructions above be valid. Assume that there exists $\alpha > 0$ such that*

$$a(t) \geq \alpha, \qquad t \in [0,T],$$

and the condition

$$q = \frac{6}{\alpha e}\left(|\psi_0| + \int_0^T |F_0(s)|\,ds\right) < 1$$

holds. Then problem (**1**)–(**4**) *has a unique solution on* $[0,T]$.

Proof. We consider the space $C[0,T]$ with norm

$$\|a\|_{C[0,T]} = \max_{0\le t\le T} |a(t)|.$$

The operator F, defined by (39), maps $C[0,T]$ into itself. Indeed, for $a \in C[0,T]$ the function

$$t \mapsto \int_0^t a(\tau)\ d\tau$$

is continuous. Hence $v_0[a] \in C[0,T]$ and $(Fa) \in C[0,T]$.

From (48) it follows that

$$\|F\,a_1 - F\,a_2\|_{C[0,T]} \le q\,\|a_1 - a_2\|_{C[0,T]}\,.$$

For $q < 1$, the operator F is a contraction. By the Banach fixed point theorem, there exists a unique function $a \in C[0,T]$ such that $a = F(a)$.

Then the solution $v_n(t)$ is given by (32), the function $v(x,t)$ by (34), and $u(x,t)$ by (35). Consequently, problem (1)–(4) has a unique solution. □

Remark 1. The obtained result is based on the application of the contraction mapping principle to the operator F. The structure of the operator makes it possible to use estimates for differences of exponential terms and to obtain the contraction property without introducing additional conditions.

The question of continuous dependence of the solution on the initial data requires additional estimates and can be considered separately.

Conclusion

In this paper, an inverse problem for a parabolic equation with a time-dependent coefficient included in the boundary condition has been considered. Additional information is given by an integral condition.

Using the spectral method, the problem is reduced to a nonlinear Volterra integral equation. Based on the obtained estimates, the existence and uniqueness of the solution are proved under the contraction condition.

It should be noted that the considered formulation differs in that the unknown coefficient is included in the boundary condition, which leads to a different structure of the corresponding operator equation.

The obtained results are local in time.

Further research may include generalization to multidimensional domains and higher-order problems.

REFERENCES

[1] M. I. Ismailov, F. Kanca. An inverse coefficient problem for a parabolic equation in the case of nonlocal boundary and overdetermination conditions // Mathematical Methods in the Applied Sciences. 2010. Vol. 33. P. 692–702.

[2] L. Yang, M. Dehghan, J.-N. Yu, G.-W. Luo. Inverse problem of time-dependent heat sources numerical reconstruction // Mathematics and Computers in Simulation. 2011. Vol. 81, No. 8. P. 1656–1672.

[3] J. R. Cannon, Y. Lin, S. Wang. Determination of a control parameter in a parabolic partial differential equation // Journal of the Australian Mathematical Society. Series B. 1991. Vol. 33. P. 149–163.

[4] M. I. Ivanchov, N. V. Pabyrivska. Simultaneous determination of two coefficients of a parabolic equation in the case of nonlocal and integral conditions // Ukrainian Mathematical Journal. 2001. Vol. 53, No. 5. P. 674–684.

[5] M. I. Ivanchov. Inverse Problems for Equations of Parabolic Type // Lviv: VNTL Publishers, 2003.

[6] G. K. Namazov. Definition of the unknown coefficient of a parabolic equation with nonlocal boundary and complementary conditions // Transactions of Academy of Sciences of Azerbaijan. 1999. Vol. 19, No. 5. P. 113–117.

[7] N. I. Ionkin. Solution of a boundary-value problem in heat conduction with a nonclassical boundary condition // Differential Equations. 1977. Vol. 13. P. 204–211.

[8] I. C. Gohberg, M. G. Krein. Introduction to the theory of linear nonselfadjoint operators // Providence, RI: American Mathematical Society, 1969.

[9] A. A. Samarskii. The Theory of Difference Schemes // New York: Marcel Dekker, 2001.

[10] K. E. Atkinson. Elementary Numerical Analysis // New York: Wiley, 1985.

[11] T.-E. Oussaeif, A. Bouziani. An inverse coefficient problem for a parabolic equation under nonlocal boundary and integral overdetermination conditions // International Journal of Partial Differential Equations and Applications. 2014. Vol. 2, No. 3. P. 38–43.

[12] M. Sadybekov, G. Oralsyn, M. Ismailov. An inverse problem of finding the time-dependent heat transfer coefficient from an integral condition // International Journal of Pure and Applied Mathematics. 2017. Vol. 113, No. 4. P. 661–671.

[13] N. Huzyk. Coefficient inverse problem for the degenerate parabolic equation // Differential Equations & Applications. 2021. Vol. 13, No. 3. P. 243–255.

[14] M. I. Ismailov, T. Ozawa, D. Suragan. Inverse problems of identifying the time-dependent source coefficient for subelliptic heat equations // Inverse Problems and Imaging. 2024. Vol. 18, No. 4. P. 813–823.

[15] S. E. Aitzhanov, K. H. Bayetov, M. I. Ismailov. Inverse source problem for p-harmonic pseudoparabolic equation // Journal of Pseudo-Differential Operators and Applications. 2026. Vol. 17. Article 33. doi:10.1007/s11868-026-00781-3

[1]*Баетов К. Х.

докторант, ORCID ID: 0000-0002-3820-9999,
*e-mail: baetov1983kairden@gmail.com

[1] Абай атындағы Қазақ ұлттық педагогикалық университеті, Алматы қ, Қазақстан

ШЕКАРАЛЫҚ ШАРТТА УАҚЫТҚА ТӘУЕЛДІ КОЭФФИЦИЕНТІ БАР ПАРАБОЛАЛЫҚ ТЕҢДЕУ ҮШІН КЕРІ ЕСЕП

Аңдатпа

Бұл жұмыста шекаралық шартта уақытқа тәуелді коэффициенті бар параболалық теңдеу үшін кері есеп қарастырылады. Қосымша ақпарат шешімді уақыттың берілген функциясымен байланыстыратын интегралдық артық анықтау шарты арқылы беріледі. Есепті шешу үшін спектралдық әдіс қолданылады, ол сәйкес біртекті шекаралық шарттары бар шеттік есептің меншікті

функциялары бойынша шешімді жіктеуге негізделген. Осы жіктеу нәтижесінде бастапқы есеп жіктеу коэффициенттері үшін қарапайым дифференциалдық теңдеулер жүйесіне келтіріледі. Алынған жүйені шешіп, шешімнің өрнегін интегралдық шартқа қойғанда, есеп белгісіз коэффициентке қатысты Вольтерра типті сызықтық емес интегралдық теңдеуге келтіріледі. Алынған теңдеу үшін сәйкес оператор енгізіліп, оның қасиеттері зерттеледі. Құрылған оператор үшін сығылу шарты орындалғанда $[0, T]$ аралығында шешімнің бар болуы және жалғыздығы дәлелденеді. Шекаралық шарттағы белгісіз коэффициенттің болуы алынатын интегралдық теңдеудің құрылымын классикалық кері есептермен салыстырғанда өзгертетіні көрсетіледі. Ұсынылған әдіс параболалық теңдеулер үшін ұқсас кері есептердің кең класын зерттеуде қолданылуы мүмкін.

Түйін сөздер: кері есеп, параболалық теңдеу, интегралдық артық анықтау шарты, спектралдық әдіс, Вольтерра теңдеуі, сығылу принципі.

[1]*Баетов К. Х.

докторант, ORCID ID: 0000-0002-3820-9999,
*e-mail: baetov1983kairden@gmail.com

[1] Казахский национальный педагогический университет имени Абая, Алматы, Казахстан

ОБРАТНАЯ ЗАДАЧА ДЛЯ ПАРАБОЛИЧЕСКОГО УРАВНЕНИЯ С ВРЕМЕННЫМ КОЭФФИЦИЕНТОМ В ГРАНИЧНОМ УСЛОВИИ

Аннотация

В данной работе рассматривается обратная задача для параболического уравнения, в которой в граничное условие включён зависящий от времени коэффициент. Дополнительная информация задаётся интегральным условием переопределения, связывающим решение с заданной функцией времени. Для решения задачи используется спектральный метод, основанный на разложении решения по собственным функциям соответствующей краевой задачи с однородными граничными условиями. Благодаря этому разложению исходная задача сводится к системе обыкновенных дифференциальных уравнений для коэффициентов разложения. Решая полученную систему и подставляя представление решения в интегральное условие, задача сводится к нелинейному интегральному уравнению типа Вольтерры относительно неизвестного коэффициента. Для полученного уравнения вводится соответствующий оператор и исследуются его свойства. Доказаны существование и единственность решения на интервале $[0, T]$ при выполнении условия сжатия для построенного оператора. Показано, что наличие неизвестного коэффициента в граничном условии приводит к изменению структуры получаемого интегрального уравнения по сравнению с классическими постановками обратных задач. Предложенный подход может быть применён к более широкому классу обратных задач для параболических уравнений с неклассическими граничными условиями.

Ключевые слова: обратная задача, параболическое уравнение, интегральное условие переопределения, спектральный метод, интегральное уравнение Вольтерры, принцип сжимающих отображений.

UDC 517.927, 517.946
IRSTI 27.29.19, 27.33.15, 27.41.17

https://doi.org/10.55452/1998-6688-2026-23-3-80-92

[1] Iskakova N.B.,
Candidate of Physical and Mathematical Sciences, Associate Professor,
ORCID ID: 0000-0002-0680-4099,
e-mail: narkesh77@gmail.com

[1,2]*Bakirova E.A.,
Candidate of Physical and Mathematical Sciences, Professor,
ORCID ID: 0000-0002-3820-5373,
*e-mail: bakirova.elmira74@gmail.com

[3]Usmanov K.I.,
Candidate of Physical and Mathematical Sciences, Associate Professor,
ORCID ID: 0000-0002-4311-5807,
e-mail: kairat.usmanov@ayu.edu.kz

[1,4] Orumbayeva N.T.,
Candidate of Physical and Mathematical Sciences, Associate Professor,
ORCID ID: 0000-0003-1714-6850,
e-mail: Orumbayevanurgul@gmail.com

[1] Institute of Mathematics and Mathematical Modeling, Almaty, Kazakhstan
[2] Kazakh National Women's Teacher Training University, Almaty, Kazakhstan
[3] Ahmet Yassawi University, Turkistan, Kazakhstan
[4] Karaganda Buketov National Research University, Karaganda, Kazakhstan

ON A BOUNDARY VALUE PROBLEM FOR A LOADED FRACTIONAL DIFFERENTIAL EQUATION

Abstract

The paper investigates a two-point boundary value problem for a loaded differential equation with a Caputo fractional derivative. The Dzhumabaev parametrization method is applied to study the problem. Within this approach, the initial interval is divided into a finite number of subintervals, and additional parameters and new functions are introduced, which makes it possible to reduce the original boundary value problem to an equivalent multipoint boundary value problem with unknown parameters. The equivalence of the original and transformed problems is established. Based on the obtained integral representations, a system of algebraic equations with respect to the introduced parameters is constructed. Sufficient conditions for the existence and uniqueness of a solution are established and related to the invertibility of the corresponding matrix. An algorithm based on the method of successive approximations is developed to determine the unknown parameters and functions. A numerical example demonstrating the application of the proposed algorithm and confirming its effectiveness is presented. The obtained results demonstrate the efficiency of the parametrization method for investigating boundary value problems for loaded fractional-order differential equations and constructing their approximate solutions.

Keywords: problem for loaded differential equation, Caputo derivative, parametrization's method, approximate solution.

Received May 14, 2026; revised June 23, 29, 2026; accepted June 30, 2026.

Introduction

Models that incorporate fractional derivatives offer a more precise mathematical representation compared to classical integer-order models, as fractional differentiation a nd i ntegration make it possible to account for memory and hereditary properties characteristic of many materials and processes [1]. This capability is a key advantage of fractional-order approaches, since such effects a re t ypically b eyond t he s cope o f t raditional d ifferential eq uations of in teger or der. The advancement of fractional differential e quation t heory h as s ignificantly ex panded th eir us e in modeling a wide range of phenomena in science and engineering. In particular, these equations have been effectively a pplied i n a reas s uch a s c ontrol t heory, t he p hysics o f c omplex systems, neural modeling, electrochemistry, the mechanics of porous media, electromagnetism, and various other disciplines (see [2]-[6]). The growing interest in fractional calculus is reflected i n numerous fundamental monographs and review papers [7]-[9], as well as in the references cited therein. Significant p rogress h as b een a chieved i n t he s tudy o f i nitial a nd b oundary v alue problems for fractional differential e quations w ith R iemann–Liouville o perators o f o rder ($0 < \alpha \leq 1$) [10, 11]. In papers [12]-[15], certain classes of Cauchy problems for functional differential equations with fractional derivatives of both Riemann–Liouville and Caputo types of the same order were examined. Loaded differential e quations o ccupy a d istinctive p osition i n t he t heory o f fractional differential e quations. O ne o f t he m ost g eneral d efinitions of su ch eq uations wa s in troduced by Nakhushev [16]. The rapid development of research in optimal control of agro-economic systems, as well as in problems related to groundwater level regulation and soil moisture management, has led to an increased interest in boundary value problems for this class of equations [17]-[19]. Important results in the theory of boundary value problems for loaded equations of parabolic, parabolic–hyperbolic, and elliptic–hyperbolic types were obtained in [20, 21]. This paper is devoted to the study of boundary value problems for loaded differential e quations w ith a fractional derivative. The main objective is to establish conditions for the existence and uniqueness of solutions, as well as to develop numerical algorithms for their computation. Motivated by the above considerations, on the interval $[0, T]$ we consider the following linear boundary value problem for a loaded differential e quation w ith a C aputo d erivative o f o rder $\alpha \in (0, 1)$.

$$ {}_C D^{\alpha} x(t) = A(t)x(t) + \sum_{j=0}^{m} K_j(t)x(\xi_j) + f(t), \quad x \in \mathbb{R}^n, \quad 0 = \xi_0 < \xi_1 < \ldots, \xi_m = T, \tag{1} $$

$$ Bx(0) + Cx(T) = d, \quad d \in \mathbb{R}^n, \tag{2} $$

where $A(t)$, $K_j(t)$ $(j = 0, \ldots, m)$, and $f(t)$ are continuous on $[0, T]$.

Let $\mathbb{AC}([0, T], \mathbb{R}^n)$ is the space of absolutely continuous functions $x : [0, T] \to \mathbb{R}^n$ with the norm $\|x\|_1 = \max\limits_{t\in[0,T]} \|x(t)\|$.

A function $x^* : (0, T) \to \mathbb{R}^n$ is called a solution of (1), (2) if $x^* \in \mathbb{AC}([0, T], \mathbb{R}^n)$ satisfies Eq.(1) together with the condition (2).

Material and methods

The main purpose of this work is to apply the parameterization method for solving problem (1), (2). Based on this method, an algorithm for finding its solution will be constructed, and sufficient conditions for its solvability will be established.

Let $h_i = \xi_i - \xi_{i-1}$, $i = 1, \ldots, m$. We take a number $\ell \in \mathbb{N}$ and construct a partition the interval

$$ [0, T) = \bigcup_{r=1}^{m\ell} [t_{r-1}, t_r) $$

where $t_{i\ell} = \xi_i$, $i = 0, \ldots, m$, $\frac{h_1}{\ell} = t_r - t_{r-1}$, $r = 1, \ldots, \ell$, $\frac{h_2}{\ell} = t_r - t_{r-1}$, $r = \ell + 1, \ldots, 2\ell$, and so on $\frac{h_m}{\ell} = t_r - t_{r-1}$, $r = (m-1)\ell + 1, \ldots, m\ell$.

Let us introduce the space $\mathbb{AC}\big([0,T], t_r, \mathbb{R}^{m\ell n}\big)$, consisting of vector-valued functions $x(t) = (x_1(t), \ldots, x_{m\ell}(t))$, where each function $x_r(t)$ is absolutely continuous on the interval $[t_{r-1}, t_r)$ and possesses a finite left-hand limit $\lim\limits_{t \to t_r^-} x_r(t)$, $r = 1, \ldots, m\ell$. This space is endowed with the norm $\|x[\cdot]\|_2 = \max\limits_{r=1,\ldots,m\ell} \sup\limits_{t \in [t_{r-1}, t_r)} \|x_r(t)\|$.

Then we denote the restriction of the function $x(t)$ by $x_r(t)$, i.e. $x_r(t) = x(t)$, $t \in [t_{r-1}, t_r)$, $r = 1, \ldots, m\ell$. In this case the problem (1), (2) is reduced to a multipoint boundary value problem

$$ {}_C D^{\alpha}_{t_{r-1}} x_r(t) = A(t)x_r(t) + \sum_{j=0}^{m-1} K_j(t) x_{j\ell+1}(\xi_j) + K_m(t) \lim_{t \to T^-} x_{m\ell}(t) + f^*(t), \quad t \in [t_{r-1}, t_r),\ r = 1, \ldots, m\ell, \tag{3} $$

$$ Bx_1(0) + C \lim_{t \to T^-} x_{m\ell}(t) = d, \tag{4} $$

$$ \lim_{t \to t_s^-} x_s(t) = x_{s+1}(t_s), \quad s = 1, \ldots, m\ell - 1. \tag{5} $$

Here an equality (5) is conditions for matching the solution at the interior points and

$$ f^*(t) = f(t) - \frac{1}{\mathbf{\Gamma}(1-\alpha)} \sum_{i=1}^{r-1} \int_{t_{r-1}}^{t_r} (t - \xi)^{-\alpha} x_i'(\xi) d\xi. $$

Let a solution to problem (3)-(5) is the system of functions $x^*[t] = (x_1^*(t), \ldots, x_{m\ell}^*(t))$, where $x^*[t] \in \mathbb{AC}([0,T], t_r, R^{m\ell n})$ with a Caputo derivative that satisfy the system (3) and conditions (4), (5).

Lemma 1. *The problems* (1),(2) *and* (3)-(5) *are equivalent.*

Дәлелдеме. Let $x^*(t)$ be a solution of problem (1),(2), and $x_r^*(t)$ be its restriction to the intervals $[t_{r-1}, t_r)$ for all $r = 1, \ldots, m\ell$. Then, from the absolute continuity of $x^*(t)$ on $[0,T]$, it follows that $x_r^*(t)$ is absolutely continuous on $[t_{r-1}, t_r)$ for all $r = 1, \ldots, m\ell$ and possesses finite left-hand limits

$$ \lim_{t \to t_r^-} x_r^*(t) = \lim_{t \to t_r^-} x^*(t) = x^*(t_r) = x_{r+1}^*(t_r), \quad r = 1, \ldots, m\ell. $$

By virtue of (1), on each interval $[t_{r-1}, t_r)$ for all $r = 1, \ldots, m\ell$, the equality holds

$$ {}_C D^{\alpha}_{t_{r-1}} x_r^*(t) - A(t)x_r^*(t) - \sum_{j=0}^{m} K_j(t) x_{j\ell+1}^*(t_{j\ell}) - f^*(t) = $$

$$ = {}_C D^{\alpha} x^*(t) - A(t)x^*(t) - \sum_{j=0}^{m} K_j(t) x^*(\xi_j) - f(t) = 0, \quad t \in [t_{r-1}, t_r),\ r = 1, \ldots, m\ell. $$

That is, $x_r^*(t)$ is the restriction of the function $x^*(t)$ to the intervals $[t_{r-1}, t_r)$, $r = 1, \ldots, m\ell$, satisfies equation (3). Condit ion (4) follows from condition (2).

Conversely, let $\tilde{x}[t] \in \mathbb{AC}\big([0,T], t_r, \mathbb{R}^{m\ell n}\big)$be a solution of (3)–(5), where $\tilde{x}[t] = (\tilde{x}_1(t), \ldots, \tilde{x}_{m\ell}(t))$. Define $\tilde{x} : [0,T] \to \mathbb{R}^n$ by $\tilde{x}(t) := \tilde{x}_r(t)$, $\quad t \in [t_{r-1}, t_r)$, $\quad r = 1, \ldots, m\ell$, and $\tilde{x}(T) := \lim\limits_{t \to T^-} \tilde{x}_{m\ell}(t)$.

From (4) and (5), it follows that $\tilde{x}(t)$ is absolutely continuous on $[0,T]$ and satisfies the boundary condition (2)

$$B\tilde{x}(0)+C\tilde{x}(T)=B\tilde{x}_1(0)+C\lim_{t\to T^-}\tilde{x}_{m\ell}=d.$$

Since the system of functions $\tilde{x}[t]$ is a solution of equation (3), the function $\tilde{x}(t)$ has a Caputo derivative and satisfies (1) for all t on $(0,T)$ except at the loading points; that is, there exists a function ${}_CD^{\alpha}_{t_{r-1}}x_r(t)$ for all $t\in[0,T]\backslash\{t_r\}$, $r=1,\dots,m\ell$.

Since

$$\lim_{t\to t_r^-}{}_CD^{\alpha}_{t_{r-1}}\tilde{x}_r(t)=A(t_r)\lim_{t\to t_r^-}\tilde{x}_r(t)+\sum_{j=0}^{m}K_j(t_r)\tilde{x}_{j\ell+1}(t_{j\ell})+f^*(t_r)=$$

$$=A(t_r)\tilde{x}_{r+1}(t)+\sum_{j=0}^{m}K_j(t_r)\tilde{x}_{j\ell+1}(t_{j\ell})+f^*(t_r)={}_CD^{\alpha}\tilde{x}_{r+1}(t_r),\ r=1,\dots,m\ell,$$

it follows from (5) that ${}_CD^{\alpha}x(t)$ exists for all $t\in[0,T]$ and satisfies equation (1). □

By introducing the parameters $\lambda_r:=x_r(t_{r-1})$, $r=1,\dots,m\ell$, $\lambda_{m\ell+1}:=\lim\limits_{t\to T^-}x_{m\ell}(t)$, and substituting $u_r(t)=x_r(t)-\lambda_r$, $t\in[t_{r-1},t_r)$, $r=1,\dots,m\ell$, we transform the boundary value problem (3)-(5) into the equivalent multi-point boundary value problem with parameters

$${}_CD^{\alpha}_{t_{r-1}}u_r(t)=A(t)(u_r(t)+\lambda_r)+\sum_{j=0}^{m}K_j(t)\lambda_{j\ell+1}+f^*(t),\quad t\in[t_{r-1},t_r),\tag{6}$$

$$u_r(t_{r-1})=0,\quad r=1,\dots,m\ell,\tag{7}$$

$$B\lambda_1+C\lambda_{m\ell+1}=d,\tag{8}$$

$$\lambda_s+\lim_{t\to t_s^-}u_s(t)=\lambda_{s+1}(t_s),\quad s=1,\dots,m\ell.\tag{9}$$

A solution to the problem (6)-(9) is a pair $(\lambda^*,u^*[t])$ with components $\lambda^*=(\lambda_1^*,...,\lambda_{m\ell+1}^*)\in\mathbb{R}^{n(m\ell+1)}$, $u^*[t]=(u_1^*(t),...,u_{m\ell}^*(t))\in\mathbb{AC}([0,T],t_r,R^{m\ell n})$, that satisfy (6)-(9).

If $x^*(t)$ is a solution to problem (1), (2), then the pair $(\lambda^*,u^*[t])$ with components $\lambda^*=(\lambda_1^*,...,\lambda_{m\ell+1}^*)\in\mathbb{R}^{n(m\ell+1)}$, $u^*[t]=(u_1^*(t),...,u_{m\ell}^*(t))\in\mathbb{AC}([0,T],t_r,R^{m\ell n})$, where $\lambda_r^*=x^*(t_{r-1})$, $u_r^*(t)=x^*(t)-x^*(t_{r-1})$, $t\in[t_{r-1},t_r)$, $r=1,\dots,m\ell$, satisfies to problem (1), (2). Conversely, if the pair $(\tilde{\lambda},\tilde{u}[t])$ is a solution to problem (6)-(9), then the function $\tilde{x}(t)$ defined by the equalities $\tilde{x}(t)=\tilde{\lambda}_r+\tilde{u}_r(t)$, $t\in[t_{r-1},t_r)$, $r=1,\dots,m\ell$, and $\tilde{x}(T)=\tilde{\lambda}_{m\ell+1}$ is a solution to origin problem (1), (2).

On interval $[t_{r-1},t_r)$, $r=1,\dots,m\ell$, the initial value problem (6), (7) to the equivalent system of integral equations

$$u_r(t)=\frac{1}{\mathbf{\Gamma}(\alpha)}\int_{t_{r-1}}^{t}(t-\tau)^{\alpha-1}A(\tau)u_r(\tau)d\tau+\tag{10}$$

$$+\frac{1}{\mathbf{\Gamma}(\alpha)}\int_{t_{r-1}}^{t}(t-\tau)^{\alpha-1}\Big[A(\tau)\lambda_r+\sum_{j=0}^{m}K_j(\tau)\lambda_{j\ell+1}+f^*(\tau)\Big]d\tau.$$

By taking the limit as $t\to t_r^-$ in the right-hand side of (10) and substituting the resulting expressions into condition (9), as well as multiplying equation (8) by h_m^{α}, we obtain a system of equations with respect to the unknown parameters

$$Bh_m^{\alpha}\lambda_1+Ch_m^{\alpha}\lambda_{m\ell+1}=h_m^{\alpha}d,\tag{11}$$

$$\big(I_n + \mathcal{D}_s(A,t_s)\big)\lambda_s - \lambda_{s+1} + \sum_{j=0}^{m} \mathcal{H}_s(K_j,t_s)\lambda_{j\ell+1} = -\mathrm{f}_s(t_s) - \mathrm{g}_s(u,t_s), \tag{12}$$

where for all $s = 1,\dots,m\ell$

$$\mathcal{D}_s(A,t_s) = \frac{1}{\mathbf{\Gamma}(\alpha)} \int\limits_{t_{s-1}}^{t_s} (t_s-\tau)^{\alpha-1} A(\tau)d\tau, \quad \mathcal{H}_s(K_j,t_s) = \frac{1}{\mathbf{\Gamma}(\alpha)} \int\limits_{t_{s-1}}^{t_s} (t_s-\tau)^{\alpha-1} K_j(\tau)d\tau, \quad j = \overline{0,m},$$

$$\mathrm{f}_s(t_s) = \frac{1}{\mathbf{\Gamma}(\alpha)} \int\limits_{t_{s-1}}^{t_s} (t_s-\tau)^{\alpha-1} f(\tau)d\tau, \qquad \mathrm{g}_1(u,t_s) = \frac{1}{\mathbf{\Gamma}(\alpha)} \int\limits_{t_0}^{t_1} (t_1-\tau)^{\alpha-1} A(\tau)u_1(\tau)d\tau,$$

$$\mathrm{g}_s(u,t_s) = \frac{1}{\mathbf{\Gamma}(\alpha)} \int\limits_{t_{s-1}}^{t_s} (t_s-\tau)^{\alpha-1} A(\tau)\Big(u_s(\tau) + \frac{1}{\mathbf{\Gamma}(1-\alpha)} \sum_{i=1}^{s-1} \int\limits_{t_{i-1}}^{t_i} (\tau-\xi)^{-\alpha} u_i'(\xi)d\xi\Big)d\tau, \ \ s = \overline{2,m\ell}.$$

The matrix corresponding to the left part of the system (11), (12) will be denoted by $Q_\alpha(\ell)$. Let us write this system in the following form

$$Q_\alpha(\ell)\lambda = -\mathcal{F}(\ell) - \mathcal{G}(u,\ell), \quad \lambda \in \mathbb{R}^{n(m\ell+1)}, \tag{13}$$

with the right sides of the view

$$\mathcal{F}(\ell) = (-h_m^\alpha d, \mathrm{f}_1(t_1),\dots,\mathrm{f}_{m\ell}(T)), \quad \mathcal{G}(u,\ell) = (0,\mathrm{g}_1(u,t_1),\dots,\mathrm{g}_{m\ell}(u,T)).$$

Results and discussion

If the matrix $Q_\alpha(\ell)$ is invertible, then to find the pair $(\lambda, u[t])$ we use the method of successive approximations, which is carried out according to the following algorithm.

Step 0. (a) Provided that, for the chosen $\ell \in \mathbb{N}$, the matrix $Q_\alpha(\ell)$ is invertible, the initial approximation with respect to the parameter $\lambda^{(0)} = (\lambda_1^{(0)},\dots,\lambda_{m\ell+1}^{(0)})$ is obtained from the equation $Q_\alpha(\ell)\lambda = -F(\ell)$, that is,

$$\lambda^{(0)} = -[Q_\alpha(\ell)]^{-1}\mathcal{F}(\ell);$$

(b) Using the components of the vector $\lambda^{(0)} \in \mathbb{R}^{n(m\ell+1)}$ we solve the initial value problem (6), (7) with $\lambda_r = \lambda_r^{(0)}$, $r = 1,\dots,m\ell$, on each interval $[t_{r-1},t_r)$. As a result, we obtain the functions $u_r^{(0)}(t)$, $r = 1,\dots,m\ell$.

Step 1. (a) Substituting the obtained functions $u_r^{(0)}(t)$, $r = 1,\dots,m\ell$, into the right-hand side of (13), we determine the next approximation $\lambda^{(1)}$ from the equation

$$Q_\alpha(\ell)\lambda = -F(\ell) - \mathcal{G}(u^{(0)},\ell);$$

(b) On each interval $[t_{r-1},t_r)$, the initial value problem (6), (7) are then solved with $\lambda_r = \lambda_r^{(1)}$, yielding the functions $u_r^{(1)}(t)$, $r = 1,\dots,m\ell$.

And so on. Continuing the process, at the k-th step we obtain a system of pairs $(\lambda^{(k)}, u_r^{(k)}[t])$, $k = 0,1,2,\dots$.

We introduce the following auxiliary definitions and theorem

Definition 2. *(Mittag–Leffler Function, [22]). Let $n > 0$. The function E_n defined by*

$$E_n(z) := \sum_{j=0}^{\infty} \frac{z^j}{\Gamma(jn+1)}, \qquad z \in \mathbb{C},$$

whevener the series converges is called the Mittag–Leffler function of order n.

This function has been introduced by Mittag-Leffler. We immediately notice that

$$E_1(z) := \sum_{j=0}^{\infty} \frac{z^j}{\boldsymbol{\Gamma}(j+1)} = \sum_{j=0}^{\infty} \frac{z^j}{j!} = e^z$$

is just the well known exponential function.

Definition 3. *Let $n_1, n_2 > 0$. The function E_{n_1,n_2} defined by*

$$E_{n_1,n_2}(z) := \sum_{j=0}^{\infty} \frac{z^j}{\boldsymbol{\Gamma}(jn_1+n_2)},$$

whenever the series converges is called the two-parameter Mittag-Leffler function with parameters n_1 and n_2.

Theorem 4. *(Theorem 2.2, [23]) Let $a(t)$ and $g(t)$ be nondecreasing functions, $g(t) \le C$ for all $t \in [0,T]$, and let $0 < \beta < 1$. If $x \in L_+^{\infty}[0,T]$ satisfies the inequality*

$$x(t) \le a(t) + g(t) \int_0^t (t-s)^{\beta-1} x(s)\, ds, \quad t \in [0,T],$$

then

$$x(t) \le a(t) E_\beta \left[g(t) \boldsymbol{\Gamma}(\beta)(t^\beta) \right],$$

where E_β denotes the Mittag–Leffler function.

Let us introduce the notations

$$\sigma = \max_{t\in[0,T]} \|A(t)\|, \quad \kappa = \max_{j=\overline{0,m}} \max_{t\in[0,T]} \|K_j(t)\|, \quad h = \max\{h_1, ..., h_m\}.$$

Theorem 5. *Let the matrix $Q_\alpha(\ell) : \mathbb{R}^{n(m\ell+1)} \to \mathbb{R}^{n(m\ell+1)}$ be invertible and suppose that the following inequalities hold:*

1. $\|[Q_\alpha(\ell)]^{-1}\| \le \gamma(\ell)$,
2. $q(\ell) = \dfrac{\gamma(\ell)}{\boldsymbol{\Gamma}^{\,2}(1+\alpha)} E_\alpha\Big(\sigma \boldsymbol{\Gamma}(\alpha)\Big(\dfrac{h}{\ell}\Big)^\alpha\Big)(\sigma + \kappa(m+1))^2\Big(\dfrac{h}{\ell}\Big)^{2\alpha} < 1.$

Then the sequence of pairs $(\lambda^{(k)}, u^{(k)}[t])$ converges to $(\lambda^*, u^*[t])$ as $k \to \infty$.

Дәлелдеме. Under the assumptions of the theorem, we define $\lambda^{(0)}$ at the zeroth step of the algorithm. Then, the following estimate holds:

$$\|\lambda^{(0)}\| = \max_{r=\overline{1,m\ell+1}} \|\lambda_r^{(0)}\| \le \gamma(\ell)\|\mathcal{F}(\ell)\| \le \frac{\gamma(\ell)}{\boldsymbol{\Gamma}(\alpha+1)} \max(\|d\|, \|f\|_1)\Big(\frac{h}{\ell}\Big)^\alpha \tag{14}$$

Let $u_r^{(0)}(t)$ be defined as (10) at $\lambda_r = \lambda_r^{(0)}$. Applying Grönwall's inequality, we obtain

$$\|u_r^{(0)}(t)\| \le \sup_{t\in[t_{r-1},t_r)} E_\alpha\Big(\sigma(t-t_{r-1})\Big)\frac{1}{\mathbf{\Gamma}(\alpha)}\left\|\int_{t_{r-1}}^{t}(t-\tau)^{\alpha-1}\Big[A(\tau)\lambda_r^{(0)}+\sum_{j=0}^{m}K_j(\tau)\lambda_{j\ell+1}+f^*(\tau)\Big]d\tau\right\| \le$$

$$\le \frac{1}{\mathbf{\Gamma}(\alpha+1)}E_\alpha\Big(\sigma\Big(\frac{h}{\ell}\Big)^\alpha\Big)\Big(\sigma\|\lambda_r\|+\kappa(m+1)\|\lambda_{j\ell+1}\|+\sup_{t\in[t_{r-1},t_r)}\|f^*\|\Big)\Big(\frac{h}{\ell}\Big)^\alpha$$

Taking into account (14), we obtain

$$\|u^{(0)}[\cdot]\|_2 = \max_{r=\overline{1,m\ell}}\sup_{t\in[t_{r-1},t_r)}\|u_r^{(0)}(t)\| \le$$

$$\le \frac{1}{\mathbf{\Gamma}(\alpha+1)}E_\alpha\Big(\sigma\mathbf{\Gamma}(\alpha)\Big(\frac{h}{\ell}\Big)^\alpha\Big)\left(\frac{\gamma(\ell)}{\mathbf{\Gamma}(\alpha+1)}\big(\sigma+\kappa(m+1)\big)\Big(\frac{h}{\ell}\Big)^{2\alpha}+1\right)\max(\|d\|,\|f\|_1) = P(\ell).$$

After determining $\lambda^{(1)}$ from an equation $Q_\alpha(\ell)\lambda = -F(\ell)-\mathcal{G}(u^{(0)},\ell)$, we estimate the difference $\lambda^{(1)}-\lambda^{(0)}$:

$$\|\lambda^{(1)}-\lambda^{(0)}\| = \|[Q_\alpha(\ell)]^{-1}\|\|\mathcal{G}(u^{(0)},\ell)\| \le \gamma(\ell)\max_{s=1,\dots,m\ell}\left\|\frac{1}{\mathbf{\Gamma}(\alpha)}\int_{t_{s-1}}^{t_s}(t_s-\tau)^{\alpha-1}A(\tau)u_r^{(0)}(\tau)d\tau\right\| \le$$

$$\le \frac{\gamma(\ell)}{\mathbf{\Gamma}(1+\alpha)}\big(\sigma+\kappa(m+1)\big)\Big(\frac{h}{\ell}\Big)^\alpha\|u^{(0)}[\cdot]\|_2 \le \frac{\gamma(\ell)P(\ell)}{\mathbf{\Gamma}(1+\alpha)}\big(\sigma+\kappa(m+1)\big)\Big(\frac{h}{\ell}\Big)^\alpha.$$

Having obtained $u_r^{(1)}(t)$ as the solution of the Cauchy problem (10) for $\lambda_r = \lambda_r^{(1)}$, let us estimate the following difference

$$\|u_r^{(1)}(t)-u_r^{(0)}(t)\| \le \frac{\sigma}{\mathbf{\Gamma}(\alpha)}\int_{t_{r-1}}^{t}(t-\tau)^{\alpha-1}\|u_r^{(1)}(\tau)-u_r^{(0)}(\tau)\|d\tau+$$

$$+\frac{\sigma+\kappa(m+1)}{\mathbf{\Gamma}(\alpha)}\int_{t_{r-1}}^{t}(t-\tau)^{\alpha-1}d\tau\|\lambda_r^{(1)}-\lambda_r^{(0)}\|.$$

Therefore, by the fractional Grönwall inequality, we have

$$\|u_r^{(1)}(t)-u_r^{(0)}(t)\| \le \frac{\sigma+\kappa(m+1)}{\mathbf{\Gamma}(1+\alpha)}E_\alpha\Big(\sigma\mathbf{\Gamma}(\alpha)\Big(\frac{h}{\ell}\Big)^\alpha\Big)\Big(\frac{h}{\ell}\Big)^\alpha\|\lambda^{(1)}-\lambda^{(0)}\|,$$

that is,

$$\|u_r^{(1)}[\cdot]-u_r^{(0)}[\cdot]\|_2 \le \frac{\gamma(\ell)P(\ell)}{\mathbf{\Gamma}^2(1+\alpha)}E_\alpha\Big(\sigma\mathbf{\Gamma}(\alpha)\Big(\frac{h}{\ell}\Big)^\alpha\Big)(\sigma+\kappa(m+1))^2\Big(\frac{h}{\ell}\Big)^{2\alpha}.$$

Proceeding with the iterative process, we obtain a sequence of pairs $(\lambda^{(k)},u^{(k)}[t])$. The following estimates hold for the differences $u^{(k)}(t)-u^{(k-1)}(t)$ and $\lambda^{(k)}-\lambda^{(k-1)}$:

$$\|u_r^{(k)}[\cdot]-u_r^{(k-1)}[\cdot]\|_2 \le \frac{\sigma+\kappa(m+1)}{\mathbf{\Gamma}(1+\alpha)}E_\alpha\Big(\sigma\mathbf{\Gamma}(\alpha)\Big(\frac{h}{\ell}\Big)^\alpha\Big)\Big(\frac{h}{\ell}\Big)^\alpha\|\lambda^{(k)}-\lambda^{(k-1)}\|, \tag{15}$$

$$\|\lambda^{(k+1)}-\lambda^{(k)}\| \le \frac{\gamma(\ell)P(\ell)}{\mathbf{\Gamma}^2(1+\alpha)}E_\alpha\Big(\sigma\mathbf{\Gamma}(\alpha)\Big(\frac{h}{\ell}\Big)^\alpha\Big)(\sigma+\kappa(m+1))^2\Big(\frac{h}{\ell}\Big)^{2\alpha}\|\lambda^{(k)}-\lambda^{(k-1)}\|. \tag{16}$$

Since $q(\ell) < 1$ by the assumptions of the theorem 2, it follows from inequalities (15) and (16) that the sequence $\lambda^{(k)}$ converges to λ^*, and the sequence of functions system $u_r^{(k)}[t]$ converges to the function system $u^*[t]$ in the norm of the space $\mathbb{AC}\big([0,T],t_r,\mathbb{R}^{m\ell n}\big)$. □

Numerical experiment

We consider on $[0,1]$ the boundary value problem for a loaded fractional differential equation

$$ {}_C D^{\alpha} x(t) = t^2 x(t) - x(0.25) + x(0.75) - 0.5t^2, \quad x \in \mathbb{R}, \tag{17} $$

$$ x(0) + x(1) = 1, \tag{18} $$

where $\alpha(t) = 0.4$, $t \in [0, 0.5)$ and $\alpha(t) = 0.8$, $t \in [0.5, 1)$.

The exact solution to the problem at hand is the function $x^*(t) = 0.5$.

We partition the given interval as follows $[0,1) = \bigcup\limits_{r=1}^{4} [0.5(r-1), 0.5r)$ and introduce parameters

$$ \lambda_1 = x(0), \quad \lambda_2 = x(0.25), \quad \lambda_3 = x(0.5), \quad \lambda_4 = x(0.75), \quad \lambda_5 = \lim_{t \to 1^-} x(t). $$

Consider the following substitution $u_r(t) = x(t) - \lambda_r$ for all $r = 1,2,3,4$. Then the test problem (17), (18) reduces to a problem with parameters

$$ {}_C D^{\alpha_r} u_r(t) = t^2 (u_r(t) + \lambda_r) - \lambda_2 + \lambda_4 + f^*(t), \quad t \in [0.5(r-1), 0.5r), \tag{19} $$

$$ u_r(0.5(r-1)) = 0, \quad r = 1,2,3,4, \tag{20} $$

$$ \lambda_1 + \lambda_5 = 1, \tag{21} $$

$$ \lambda_s + \lim_{t \to 0.25s^-} u_s(t) = \lambda_{s+1}, \quad s = 1,2,3,4, \tag{22} $$

where

$$ \alpha_1, \alpha_2 = 0.4, \quad \alpha_3, \alpha_4 = 0.8, \quad f^*(t) = -0.5t^2, \quad t \in [0, 0.25), $$

$$ f^*(t) = -0.5t^2 - \frac{1}{\mathbf{\Gamma}(1-\alpha)} \sum_{i=1}^{r-1} \int\limits_{0.25(r-1)}^{0.25r} (\tau - \xi)^{-\alpha_r} u_i'(\xi) d\xi, \quad t \in [0.25(r-1), 0.25r), \ r = 2,3,4. $$

For fixed parameters, the solution to the initial problem (19), (20) is given by

$$ u_1(t) = \frac{1}{\mathbf{\Gamma}(0.4)} \int\limits_0^t (t-\tau)^{-0.6} \tau^2 u_1(\tau) d\tau + \frac{2\lambda_1 - 1}{\mathbf{\Gamma}(17/5)} t^{12/5} - \frac{\lambda_2 - \lambda_4}{\mathbf{\Gamma}(7/5)} t^{2/5}, \ t \in [0, 0.25), \tag{23} $$

$$ u_2(t) = \frac{1}{\mathbf{\Gamma}(0.4)} \int\limits_{0.25}^t (t-\tau)^{-0.6} \tau^2 u_2(\tau) d\tau + \frac{2\lambda_2 - 1}{\mathbf{\Gamma}(17/5)} (t-0.25)^{12/5} - \frac{\lambda_2 - \lambda_4}{\mathbf{\Gamma}(7/5)} (t-0.25)^{2/5} - \tag{24} $$

$$ - \frac{1}{\mathbf{\Gamma}(0.4)} \int\limits_{0.25}^t (t-\tau)^{-0.6} {}_C D^{0.4} u_1'(0.25, \tau) d\tau, \quad t \in [0.25, 0.5), $$

$$ u_3(t) = \frac{1}{\mathbf{\Gamma}(0.8)} \int\limits_{0.5}^t (t-\tau)^{-0.2} \tau^2 u_3(\tau) d\tau + \frac{2\lambda_3 - 1}{\mathbf{\Gamma}(19/5)} (t-0.5)^{14/5} - \frac{\lambda_2 - \lambda_4}{\mathbf{\Gamma}(9/5)} (t-0.5)^{4/5} - \tag{25} $$

$$-\sum_{s=1}^{2}\frac{1}{\mathbf{\Gamma}(0.4)}\int_{0.5}^{t}(t-\tau)^{-0.2}{}_{C}D^{0.8}_{\frac{s-1}{4}}u_s'(0.25s,\tau)d\tau,\quad t\in[0.5,0.75),$$

$$u_4(t)=\frac{1}{\mathbf{\Gamma}(0.8)}\int_{0.75}^{t}(t-\tau)^{-0.2}\tau^2u_4(\tau)d\tau+\frac{2\lambda_4-1}{\mathbf{\Gamma}(19/5)}(t-0.75)^{14/5}-\frac{\lambda_2-\lambda_4}{\mathbf{\Gamma}(9/5)}(t-0.75)^{4/5}- \quad (26)$$

$$-\sum_{s=1}^{3}\frac{1}{\mathbf{\Gamma}(0.4)}\int_{0.75}^{t}(t-\tau)^{-0.6}{}_{C}D^{0.8}_{\frac{s-1}{4}}u_s'(0.25s,\tau)d\tau,\quad t\in[0.5,0.75),$$

From (23)-(26) we determine $\lim\limits_{t\to 0.25r^-}u_r(t)$, $r=1,2,3,4$. Based on (21), (22), we construct the system of linear equations for unknown parameters

$$Q_\alpha\lambda=-\mathcal{F}_\alpha-\mathcal{G}_\alpha(u),\quad \lambda\in\mathbb{R}^5. \quad (27)$$

Here

$$Q_\alpha=\begin{pmatrix}1&0&0&0&1\\1+2b&-1-a&0&a&0\\0&1+2b+c&-1&a&0\\0&-c&1+2d&-1+c&0\\0&-c&0&1+2d+c&-1\end{pmatrix}$$

$$\mathcal{F}_\alpha=(1,b,b,d,d),\quad \mathcal{G}_\alpha(u)=\big(0,g_1(u,0.25),g_2(u,0.5),g_3(u,0.75),g_4(u,1)\big),$$

where

$$a=\frac{1}{\mathbf{\Gamma}\,(7/5)}\,(0.25)^{2/5}\,,\ b=\frac{1}{\mathbf{\Gamma}\,(17/5)}\,(0.25)^{12/5}\,,\quad c=\frac{1}{\mathbf{\Gamma}\,(9/5)}\,(0.25)^{4/5}\,,\ d=\frac{1}{\mathbf{\Gamma}\,(19/5)}\,(0.25)^{14/5}\,,$$

$$\mathrm{g}_1(u,0.25)=\frac{1}{\mathbf{\Gamma}\,(0.4)}\int_0^{0.25}(0.25-\tau)^{-3/5}\,\tau^2u_1(\tau)\,d\tau,$$

$$\mathrm{g}_2(u,0.5)=\frac{1}{\mathbf{\Gamma}\,(0.4)}\int_{0.25}^{0.5}(0.5-\tau)^{-3/5}\left[\tau^2u_2(\tau)-{}_{C}D^{0.4}u_1'(0.25,\tau)\right]d\tau,$$

$$\mathrm{g}_3(u,0.75)=\frac{1}{\mathbf{\Gamma}\,(0.8)}\int_{0.5}^{0.75}(0.75-\tau)^{-1/5}\left[\tau^2u_3(\tau)-\sum_{s=1}^{2}{}_{C}D^{0.8}_{\frac{s-1}{4}}u_s'(0.25s,\tau)\right]d\tau,$$

$$\mathrm{g}_4(u,1)=\frac{1}{\mathbf{\Gamma}\,(0.8)}\int_{0.75}^{1}(1-\tau)^{-1/5}\left[\tau^2u_4(\tau)-\sum_{s=1}^{3}{}_{C}D^{0.8}_{\frac{s-1}{4}}u_s'(0.25s,\tau)\right]d\tau.$$

The results of implementing the proposed algorithm are as follows:

Step 0. $\lambda_r^{(0)}=0.5$, for all $r=1,\dots,5$, and $u_r^{(0)}(t)=0,\quad t\in[0.25(r-1),0.25r)\,,\quad r=1,\dots,4$.

Step 1. $\lambda_r^{(1)}=0.5$, for all $r=1,\dots,5$, and $u_r^{(1)}(t)=0,\quad t\in[0.25(r-1),0.25r)\,,\quad r=1,\dots,4$.

And so on. Then $x(t)=0.5,\quad t\in[0,1]$. All computations were performed in Spyder (Python 3.13).

Conclusion

In this work, an analysis of a two-point boundary value problem for a loaded differential equation with a fractional derivative is carried out. Within the framework of this study, the development of the parametrization method is presented, which makes it possible to reduce the original problem to an equivalent multipoint boundary value problem by introducing additional parameters. Based on the obtained formulation, the construction of approximate solutions is performed using an iterative procedure. The proposed algorithm provides successive refinement of the solution and allows one to establish sufficient conditions for the existence of a solution as well as for the convergence of the constructed iterative process. The obtained results demonstrate the effectiveness of the developed parametrization method for studying boundary value problems of the considered class. To ensure the continuity of the present research in this direction, it is planned in future work to prove that the obtained sufficient conditions for the solvability of the problem (1), (2) are also necessary.

Information on funding

This research is partially supported by the Ministry of Education and Science of the Republic of Kazakhstan (Grant No. AP26194447).

REFERENCES

1. Podlubny I., Fractional Differential Equations. Academic Press, New York, 1999.
2. Diethelm K., Freed A.D., On the solution of nonlinear fractional order differential equations used in the modeling of viscoelasticity, in: F. Keil, W. Mackens, H. Voss, J. Werther (Eds.). Scientific Computing in Chemical Engineering II Computational Fluid Dynamics, Reaction Engineering and Molecular Properties, Springer-Verlag, Heidelberg, 217–224 (1999).
3. Glockle W.G., Nonnenmacher T.F., A fractional calculus approach of self-similar protein dynamics. Biophys. J., 68, 46–53 (1995).
4. Kirchner J.W., Feng X., Neal V., Fractal streamchemistry and its implications for contaminant transport in catchments. Nature, 403, 524–526 (2000). doi.org/10.1038/35000537
5. Lundstrom B.N., Higgs M.H., Spain W.J., Fairhall A.L., Fractional differentiation by neocortical pyramidal neurons. Nat. Neurosci, 11, 1335–1342 (2008). doi.org/10.1038/nn.2212
6. Mainardi F., Fractional calculus: some basic problems in continuum and statistical mechanics, in: A. Carpinteri, F. Mainardi (Eds.). Fractals and Fractional Calculus in Continuum Mechanics, Springer-Verlag, Wien, 291–348 (1997).
7. Kilbas A.A., Srivastava H.M., Trujillo J.J., Theory and Applications of Fractional Differential Equations, in: North-Holland Mathematics Studies. Elsevier Science B.V., Amsterdam, 204 (2006).
8. Miller K.S., Ross B., An Introduction to the Fractional Calculus and Differential Equations. John Wiley, New York (1993).
9. Samko S.G., Kilbas A.A., Marichev O.I., Fractional Integral and Derivatives: Theory and Applications. Gordon and Breach, Longhorne, PA (1993).
10. Lakshmikantham V., Vatsala A.S., Basic theory of fractional differential equations. Nonlinear Anal, 69(8), 2677–2682 (2008). doi.org/10.1016/j.na.2007.08.042

11. Lakshmikantham V., Vatsala A.S., Theory of fractional differential inequalities and applications. Commun. Appl. Anal., 11(3–4), 395–402 (2007).

12. Belarbi A., Benchohra M., Ouahab A., Uniqueness results for fractional functional differential equations with in finite delay in Frechet spaces. Appl. Anal., 85(12), 1459–1470 (2006). doi.org/10.1080/00036810601066350

13. Benchohra M., Henderson J., Ntouyas S.K., Ouahab A., Existence results for fractional order functional differential equations with in finite delay. J. Math. Anal.Appl., 338(2), 1340–1350 (2008). doi.org/10.1016/j.jmaa.2007.06.021

14. Usmanov K.I., Nazarova K.Zh., Yerkisheva Zh.S., Solvability of a boundary value problem for fractional-order integro-differential equations with involution. Herald of the Kazakh-British Technical University, 23(1), 231–239 (2026). doi.org/10.55452/1998-6688-2026-23-1-231-239

15. Torebek B.T., Turmetov B.K., On solvability of a boundary value problem for the Poisson equation with the boundary operator of a fractional order. Bound Value Probl 2013, 93 (2013). doi:10.1186/1687-2770-2013-93

16. Nakhushev A. M. The loaded equations and their applications. M. Nauka, 2012, p. 232.

17. Iskakova N.B., Bakirova E.A., Khanzharova B.S., Kadirbayeva, Zh.M., An Algorithm for Solving Boundary Value Problems for Delay Differential Equations with Loadings. Lobachevskii Journal of Mathematics, 45(10), 5032–5042 (2024). doi.org/10.1134/S1995080224606064.

18. Bakirova E.A., Iskakova N.B., Kadirbayeva Zh.M., Numerical implementation of solving a boundary value problem including both delay and parameter. Mathematica Slovaca, 75(3), 601–610 (2025). doi.org/10.26577/JMMCS2023v119i3a2

19. Dzhumabaev D.S., Bakirova E.A., Mynbayeva S.T., A method of solving a nonlinear boundary value problem with a parameter for a loaded differential equation. Mathematical Method in Applied Science, 43(4), 1788–1802 (2020). doi.org/10.1002/mma.6003.

20. Abdullaev O.Kh., About a method of research of the non-local problem for the loaded mixed type equation in double-connected domain. Bulletin KRASEC. Phys. Math. Sci, 9(2), 11–16 (2014). doi.org/ 10.18454/2313-0156-2014-9-2-3-12

21. Islomov B., Baltaeva U., Boudary-value problems for a third-order loaded parabolic-hyperbolic type equation with variable coefficients. Electron. J. Differential Equ., 2015(221), 1–10 (2015). URL: http://ejde.math.txstate.edu

22. Diethelm K., Ford N. J., The analysis of fractional differential equations. Lecture notes in mathematics, Springer Heidelberg Dordrecht London New York, (2010).

23. Ye H., Gao J., Ding Y., A generalized and its application to a fractional differential equation. Journal of Mathematical Analysis and Applications, 328(2), 1075-1081. (2007). 10.1016/j.jmaa.2006.05.061

[1] Искакова Н.Б.,
Кандидат физико-математических наук, ассоциированный профессор,
ORCID ID: 0000-0002-0680-4099,
e-mail: narkesh77@gmail.com
[1,2*] Бакирова Э.А.,
Кандидат физико-математических наук, профессор,
ORCID ID: 0000-0002-3820-5373,
*e-mail: bakirova.elmira74@gmail.com
[3] Усманов К.И.,
Кандидат физико-математических наук, ассоциированный профессор,
ORCID ID: 0000-0002-4311-5807,
e-mail: kairat.usmanov@ayu.edu.kz
[1,4] Орумбаева Н.Т.,
Кандидат физико-математических наук, ассоциированный профессор,
ORCID ID: 0000-0003-1714-6850,
e-mail: Orumbayevanurgul@gmail.com

[1] Институт математики и математического моделирования, г. Алматы, Казахстан
[2] Казахский национальны женский педагогический университет, г. Алматы, Казахстан
[3] Университет Ахмеда Ясауи, г. Туркестан, Казахстан
[4] Карагандинский национальный исследовательский университет имени академика Е.А. Букетова, г. Караганда, Казахстан

О КРАЕВОЙ ЗАДАЧЕ ДЛЯ НАГРУЖЕННОГО ДИФФЕРЕНЦИАЛЬНОГО УРАВНЕНИЯ С ДРОБНОЙ ПРОИЗВОДНОЙ

Аннотация

В работе исследуется двухточечная краевая задача для нагруженного дифференциального уравнения с дробной производной Капуто. Для исследования поставленной задачи применяется метод параметризации Джумабаева. В рамках данного подхода исходный промежуток разбивается на конечное число частей, вводятся дополнительные параметры и новые функции, что позволяет свести исходную краевую задачу к эквивалентной многоточечной краевой задаче с неизвестными параметрами. Устанавливается эквивалентность исходной и преобразованной задач. На основе полученных интегральных представлений строится система алгебраических уравнений относительно введённых параметров. Устанавливаются достаточные условия существования и единственности решения, связанные с обратимостью соответствующей матрицы. Для нахождения неизвестных параметров и функций разработан алгоритм, основанный на методе последовательных приближений. Приведён численный пример, демонстрирующий применение предложенного алгоритма и подтверждающий его эффективность. Полученные результаты показывают эффективность метода параметризации при исследовании краевых задач для нагруженных дифференциальных уравнений дробного порядка и построении их приближённых решений.

Ключевые слова: задача для нагруженного дифференциального уравнения, производная Капуто, метод параметризации, приближенное решение.

[1] **Искакова Н.Б.,**

ф.-м.ғ.к., қауымдастырылған профессор,
ORCID ID: 0000-0002-0680-4099,
e-mail: narkesh77@gmail.com

[1,2]* **Бакирова Э.А.,**

ф.-м.ғ.к., профессор,
ORCID ID: 0000-0002-3820-5373,
*e-mail: bakirova.elmira74@gmail.com

[3] **Усманов К.И.,**

ф.-м.ғ.к., қауымдастырылған профессор,
ORCID ID: 0000-0002-4311-5807,
e-mail: kairat.usmanov@ayu.edu.kz

[1,4] **Орумбаева Н.Т.,**

ф.-м.ғ.к., қауымдастырылған профессор,
ORCID ID: 0000-0003-1714-6850,
e-mail: Orumbayevanurgul@gmail.com

[1] Математика және математикалық модельдеу институты, Алматы қ., Қазақстан
[2] Қазақ ұлттық қыздар педагогикалық университеті, Алматы қ., Қазақстан
[3] Ахмет Ясауи университеті, Түркістан қ., Қазақстан
[4] Академик Е.А. Бөкетов атындағы Қарағанды ұлттық зерттеу университеті,
Қарағанды қ., Қазақстан

ЖҮКТЕМЕЛІ БӨЛШЕКТІК ДИФФЕРЕНЦИАЛДЫҚ ТЕҢДЕУ ҮШІН ШЕТТІК ЕСЕП ТУРАЛЫ

Аңдатпа

Жұмыста Капутоның бөлшек туындысы бар жүктелген дифференциалдық теңдеу үшін екі нүктелі шеттік есеп зерттеледі. Қойылған есепті зерттеу үшін Джумабаевтың параметрлеу әдісі қолданылады. Осы тәсіл аясында бастапқы аралық ақырлы санды бөліктерге бөлініп, қосымша параметрлер мен жаңа функциялар енгізіледі. Бұл бастапқы шеттік есепті белгісіз параметрлері бар оған эквивалентті көп нүктелі шеттік есепке келтіруге мүмкіндік береді. Бастапқы және түрлендірілген есептердің эквиваленттілігі белгіленеді. Алынған интегралдық өрнектер негізінде енгізілген параметрлерге қатысты алгебралық теңдеулер жүйесі құрылады. Сәйкес матрицаның қайтымдылығына байланысты шешімнің бар болуы мен жалғыздығының жеткілікті шарттары белгіленеді. Белгісіз параметрлер мен функцияларды анықтау үшін тізбекті жуықтау әдісіне негізделген алгоритм әзірленеді. Ұсынылған алгоритмнің қолданылуын көрсететін және оның тиімділігін растайтын сандық мысал келтіріледі. Алынған нәтижелер бөлшек ретті жүктелген дифференциалдық теңдеулерге арналған шеттік есептерді зерттеуде және олардың жуық шешімдерін құруда параметрлеу әдісінің тиімділігін көрсетеді.

Түйін сөздер: жүктелген дифференциалдық теңдеу үшін есеп, Капуто туындысы, параметрлеу әдісі, жуық шешім.

ӘОЖ 517.927.4
ҒТАХР 27.29.17

https://doi.org/10.55452/1998-6688-2026-23-3-93-105

[1,2]*Абдиманапова П.Б.,

PhD, ассистент-профессор, ORCID ID: 0000-0001-8879-9985,
*e-mail: perizatabdimanapova344@gmail.com

[1,3] Темешева С.М.,

ф.-м.ғ.д., жетекші ғылыми қызметкер, профессордың м.а., ORCID ID:0000-0002-3341-4539,
e-mail: temesheva.svetlana@kaznu.kz

[4] Иманчиев А.Е.,

ф.-м.ғ.к., қауымдастырылған профессор, ORCID ID: 0000-0002-1835-2501,
e-mail: imanchievae@gmail.com

[2] Мәжит Ж.Б.,

сеньор-лектор, ORCID ID: 0000-0002-4635-9241,
e-mail: Zhamilya.Mazhit01@gmail.com

[1] Математика және математикалық модельдеу институты, Алматы қ., Қазақстан
[2] Алматы технологиялық университеті, Алматы қ., Қазақстан
[3] Әл-Фараби атындағы қазақ ұлттық университеті, Алматы қ., Қазақстан
[4] Қ.Жұбанов атындағы Ақтөбе өңірлік университеті, Ақтөбе қ., Қазақстан

ДИФФЕРЕНЦИАЛДЫҚ ТЕҢДЕУ ҮШІН СЫЗЫҚТЫҚ ЕМЕС ЕКІ НҮКТЕЛІ ШЕТТІК ЕСЕПТЕР ӘУЛЕТІНІҢ ШЕШІМІН ТАБУ ТУРАЛЫ

Аңдатпа

Қарастырылып отырған мақалада сызықтық емес екі нүктелі шеттік шарттар әулетіне бағынатын сызықтық дифференциалдық теңдеулер әулеті үшін шеттік есеп қарастырылады. Әулет параметрінің әрбір бекітілген мәнінде есеп жәй дифференциалдық теңдеулер үшін сызықтық емес екі нүктелі шеттік есепке келтіріледі. Мұндай есептер бейлокал шеттік есептермен, соның ішінде гиперболалық теңдеулер жүйелерімен байланысты болғандықтан, олардың шешілімділік шарттарын анықтау өзекті болып табылады. Жұмыста Д.С. Джумабаевтың параметрлеу әдісі бойынша есепті параметрге қарағандағы сызықтық емес алгебралық теңдеулер жүйесін және параметрге тәуелді дифференциалдық теңдеу үшін бастапқы есепті шешу тәсілі қолданылады. Оны шешу үшін итерациялық әдіс қолданылып, жинақтылық шарттары негізделеді. Ұсынылған әдіс Коши есептерін сандық шешу мен сызықтық емес теңдеулер жүйесін шешуді үйлестіруге негізделген. Нәтижесінде алынған шешу алгоритмі нақты тестілік мысалдарда жүзеге асыру арқылы тексеріліп, бұл әдістің тиімділігі көрсетіледі. Мысалы, берілген параметр мәніне сәйкес алынған жүйенің шешімін табу итерациялық процесте жинақталатыны анықталады. Қарастырылып отырған әдіс сызықтық емес екі нүктелі шеттік шарттармен сипатталатын сызықтық дифференциалдық теңдеулер әулеті үшін шеттік есептердің шешімдерін анықтауда тиімді әдіс болып табылады. Ұсынылған әдістің практикалық тиімділігі нақты есептерді сандық түрде шешу нәтижелерімен дәлелденеді.

Түйін сөздер: сызықтық емес екі нүктелі шеттік есептер, әулет параметрі, жәй дифференциалдық теңдеулер, шеттік шарттар, сандық әдіс.

Кіріспе

Қазіргі қолданбалы математика мен математикалық физикада параметрге тәуелді дифференциалдық теңдеулер жүйелері ерекше орын алады. Мұндай есептер әртүрлі табиғи және

техникалық үдерістерді модельдеуде кеңінен қолданылады. Атап айтқанда, басқару теориясында, механикада, жылуалмасу процестерінде және инженерлік есептерде екі нүктелі шеттік шарттары бар дифференциалдық теңдеулер жүйелері жиі кездеседі. Бұл есептердің маңызды ерекшелігі – шеттік шарттардың сызықтық емес болуы, соның салдарынан оларды аналитикалық түрде шешу көп жағдайда мүмкін болмайды. Сызықтық емес екі нүктелі шеттік есептерді зерттеу күрделі мәселелердің бірі болып табылады, себебі олардың шешімдерінің бар болуы, жалғыздығы және орнықтылығы арнайы шарттарды талап етеді. Сонымен қатар, мұндай есептерді тиімді сандық әдістермен шешу де өзекті ғылыми бағыттардың бірі болып табылады. Осыған байланысты соңғы жылдары параметр енгізу, интервалды бөлiктеу және Коши есептеріне келтіру әдістері [1] кеңінен қолданылып келеді. Бұл жұмыста параметрге тәуелді сызықтық дифференциалдық теңдеулер жүйесі үшін сызықтық емес екі нүктелі шеттік шарттары бар есептер әулеті қарастырылады. Есепті шешу үшін берілген аралықты бөліктерге бөлу арқылы оны эквивалентті түрде параметрлері бар көмекші есепке келтіру тәсілі қолданылады. Нәтижесінде бастапқы есеп белгісіз параметрлерге қатысты сызықтық емес теңдеулер жүйесін шешуге келтіріледі.

Материалдар мен әдістер

Параметрлерді енгізу әдісі шеттік есептердің шешімдерін іздеу үдерісін жеңілдетуге, алгоритмдерінің жинақтылығын сипаттауға және есептің бастапқы шарттарын тиімді түрде түрлендіруге мүмкіндік беретін конструктивті тәсілдердің бірі болып табылады. Бұл әдіс арқылы есептіің шешімінің бар болуы мен жалғыздығын қамтамасыз ететін қажетті шарттарды бастапқы берілген шамалар арқылы өрнектеуге болады. Сонымен қатар, параметрлерді енгізу тәсілі қолданылатын алгоритмдердің орнықтылығын арттырып, есептеу процедураларын оңтайландыруға жағдай жасайды. Әдістің ерекшелігі- күрделі шеттік есептерді қарапайым параметрлік есептерге келтіру арқылы олардың сандық және аналитикалық шешімдерін зерттеуге мүмкіндік беруінде. Осыған байланысты аталған әдіс дифференциалдық теңдеулердің әртүрлі типтері үшін шеттік есептерді зерттеу мен шешудің тиімді құралдарының бірі болып табылады [2-4]. Д.С. Джумабаев және С.М. Темешева еңбектерінде [5, 6] сызық-тық емес дифференциалдық теңдеулер үшін екі нүктелі шеттік есептер параметрлеу әдісімен зерттелген. Авторлар оқшауланған шешімнің бар болуының қажетті және жеткілікті шарттарын анықтап, бастапқы жуықтауды дұрыс таңдаудың және алынған шешімнің бастапқы мәліметтерге үзіліссіз тәуелділігін қамтамасыз етудің теориялық негіздерін ұсынған. Параметрлеу әдісі алгоритмдерінің құрылымдық ерекшеліктері шеттік есептердің шешімдерін табуға бағытталған сандық және жуықтау әдістерін дамытуға негіз болғанын атап өтуге болады. Зерттеулер және есептеулер барысында алынған нәтижелер ұсынылған алгоритмнің тиімділігін, шешімдердің тұрақтылығын және параметрлер кеңістігінде шеттік есептер әулетінің шешімдерін табу мүмкіндігін көрсетеді. Қарастырылған тәсіл дифференциалдық теңдеулердің кең ауқымды кластары үшін шеттік есептерді зерттеу және шешу барысында кең қолданыс тапқан [7-14].

Нәтижелер мен талқылау

Сызықтық емес екі нүктелі шеттік шарттар әулетіне бағынатын сызықтық дифференциалдық теңдеулер жүйесі үшін шеттік есептер әулетін қарастырамыз

$$\frac{\partial v}{\partial t} = A(x,t)v + F(x,t), \quad (x,t) \in [0,\omega] \times (0,T), \tag{1}$$

$$g(x, v(x,0), v(x,T)) = 0, \quad x \in [0,\omega], \tag{2}$$

мұндағы $A(x,t)$ – $(n \times n)$ өлшемді үзіліссіз матрица,

$F(x,t)$ - $[0,T]$-да үзіліссіз n-вектор функция, x – әулет параметрі,

$g : [0,\omega] \times \mathbb{R}^n \times \mathbb{R}^n \to \mathbb{R}^n$ – үзіліссіз функция,
$\|A\| = \max\limits_{x\in[0,\omega]} \max\limits_{i=\overline{1,n}} \sup\limits_{t\in(0,T)} \sum\limits_{j=1}^{n} |A_{ij}(x,t)| \leqslant a_0$ $(a_0 - const)$,
$\|v\| = \max\limits_{x\in[0,\omega]} \max\limits_{i=\overline{1,n}} \sup\limits_{t\in(0,T)} |v_i(x,t)|$.

Аңықтама 1 (1), (2) *есебін қанағаттандыратын* $v^*(x,t) \in C([0,\omega]\times[0,T],\, \mathbb{R}^n)$ *функциясын* (1), (2) *есебінің шешімі деп айтамыз.*

Айталық, x – $[0,\, \omega]$ параметрі бекітілген болсын.
N $(N = 1, 2, \ldots)$ натурал санын таңдап алайық.
$[0,T]$ кесіндісін $t_p = p \cdot h$, $p = \overline{0,N}$, $h = T/N$ нүктелерімен бөліктейміз.
Келесі белгілеулерді енгіземіз:
$\Omega_r(x) = \{(x,t) : x \in [0,\omega], \quad t \in [t_{r-1}, t_r)\}, \quad r = \overline{1,N}$;
$\Delta_N(x) : \{x\} \times [0,T) = \bigcup_{r=1}^{N} \Omega_r(x)$;
$\lambda_r(x) = v(x, t_{r-1})$, $r = \overline{1,N}$, $\lambda_{N+1}(x) = \lim\limits_{t\to t_N - 0} v(x,t)$;
$\widetilde{v}_r(x,t) = v(x,t) - \lambda_r(x)$, $t \in \Omega_r(x)$, $r = \overline{1,N}$;
$C([0,\omega]\times[0,T], \Delta_N(x), \mathbb{R}^{nN})$ арқылы нормасы

$$\|v\|_2 = \max_{r=\overline{1,N}} \|v_r(x,t)\|$$

болатын $v(x,[t]) = (v_1(x,t), v_2(x,t), \ldots, v_N(x,t))$ функциялар жүйелерінің кеңістігін белгілейміз. Мұндағы $v_r(x,t) \in C(\Omega_r(x))$ үзіліссіз функциялар, әрбір $x \in [0,\omega]$-ке қатысты бірқалыпты $\lim\limits_{t\to t_r - 0} v_r(x,t)$ $(r = \overline{1,N})$ ақырлы шегі бар.

(1), (2) есебі келесі параметр енгізілген шеттік есепке эквивалентті

$$\frac{\partial \widetilde{v}_r}{\partial t} = A(x,t)(\lambda_r(x) + \widetilde{v}_r) + F(x,t), \quad t \in \Omega_r(x), \quad r = \overline{1,N}, \tag{3}$$

$$\widetilde{v}_r(x, t_{r-1}) = 0, \tag{4}$$

$$g\left(x, \lambda_1(x), \lambda_{N+1}(x)\right) = 0, \tag{5}$$

$$\lambda_r(x) + \lim_{t\to t_r - 0} \widetilde{v}_r(x,t) - \lambda_{r+1}(x) = 0, \quad r = \overline{1,N}, \tag{6}$$

мұндағы (6)-шешімнің $\Delta_N(x)$ ішкі нүктелеріндегі үзіліссіздік шарттары.

$(\lambda^*(x), \widetilde{v}^*(x,[t]))$ арқылы элементтері $\lambda^*(x) = (\lambda^*(x_1), \lambda^*(x_2), \ldots, \lambda^*_{N+1}(x)) \in C([0,\omega], \mathbb{R}^{n(N+1)})$, $\widetilde{v}^*(x,[t]) = (\widetilde{v}^*_1(x,t), \widetilde{v}^*_2(x,t) \ldots \widetilde{v}^*_N(x,t)) \in C([0,\omega]\times[0,T], \Omega_r(x), \mathbb{R}^{nN})$ болатын жұпты белгілейміз және осы жұп элементтерінің компоненттері үшін төмендегі үш шарт орындалсын:
(i) Кез келген r үшін $\widetilde{v}^*_r(x,t)$ функциясы $\Omega_r(x)$-те үзіліссіз дифференциалданады,
(ii) $\widetilde{v}^*_r(x,t)$ функциясы $\lambda_r(x) = \lambda^*_r(x)$ болғанда (3) дифференциалдық теңдеуді қанағаттандырады,
(iii) $\lambda^*_1(x)$, $\lambda^*_{N+1}(x)$, $\lambda^*_r(x) + \lim\limits_{t\to t_r - 0} \widetilde{v}^*_r(x,t)$ $(r = \overline{1,N})$ шамалары (5), (6) теңдіктерін қанағаттандырады.

Аңықтама 2 *(i)-(iii) шарттарды қанағаттандыратын* $(\lambda^*(x), \widetilde{v}^*(x,[t]))$ *жұбын* (3)-(6) *есебінің шешімі деп айтамыз.*

Егер $(\lambda^*(x), \widetilde{v}^*(x,[t]))$ жұбы (3)-(6) есебінің шешімі болса, онда

$$v^*(x,t) = \begin{cases} \sum_{r=1}^{N} \mathbf{1}_{\Omega_r(x)}(t)(\lambda^*_r(x) + \widetilde{v}^*(x,t)), & (x,t) \in [0,\omega]\times[0,T), \\ \lambda^*_{N+1}(x), & (x,t) \in [0,\omega]\times\{T\} \end{cases}$$

функциясы (1),(2) шеттік есептің бекітілген x-ке сәйкес шешімі болады, мұндағы

$$\mathbf{1}_{\Omega_r(x)}(t) = \begin{cases} 1, & (x,t) \in \Omega_r(x), \\ 0, & (x,t) \notin \Omega_r(x), \end{cases} \quad r = \overline{1,N}.$$

(1),(2) және (3)-(6) есептерінің эквиваленттілігін жеңіл көрсетуге болады.

Келесі сызықтық операторды қарастырамыз [15]

$$\Phi_r(x,t) = I + \int_{t_{r-1}}^{t} A(x,\tau_1)d\tau_1 +$$

$$+\sum_{j=2}^{\infty} \int_{t_{r-1}}^{t} A(x,\tau_1) \int_{t_{r-1}}^{\tau_1} A(x,\tau_2) \dots \int_{t_{r-1}}^{\tau_{j-1}} A(x,\tau_j)d\tau_j \dots d\tau_2 d\tau_1,$$

$$t \in \Omega_r(x), \quad r = \overline{1,N},$$

мұндағы I- $(n \times n)$ өлшемді бірлік матрица.

$\Phi_r(x,t)$ операторы

$$\frac{\partial \Phi_r(x,t)}{\partial t} = A(x,t)\Phi_r(x,t), \qquad \Phi_r(x,t_{r-1}) = I, \qquad t \in \Omega_r(x), \quad r = \overline{1,N}.$$

есебін қанағаттандырады. Келесі

$$a_r(P,x,t) = \Phi_r(x,t) \int_{t_{r-1}}^{t} \Phi_r^{-1}(x,\xi)P(x,\xi)d\xi, \quad t \in \Omega_r(x), \quad r = \overline{1,N}.$$

белгілеулерді қолданамыз және $a_r(P,x,t)$ функциясы

$$\frac{\partial a_r(P,x,t)}{\partial t} = A(x,t) \cdot a_r(P,x,t) + P(x,t), \quad a_r(P,x,t_{r-1}) = 0, \quad t \in \Omega_r(x), \quad r = \overline{1,N} \quad (7)$$

Коши есебін қанағаттандырады.

$\lambda_r(x) \in C([0,\omega],\mathbb{R}^n)$ $(r = \overline{1,N})$ параметрге қатысты (3), (4) Коши есебінің шешімдер әулетін жазамыз

$$v_r(x,t) = a_r(A,x,t)\lambda_r(x) + a_r(F,x,t), \quad t \in \Omega_r(x), \quad r = \overline{1,N}, \quad (8)$$

және $v(x,[t]) = (v_1(x,t), v_2(x,t), \dots, v_N(x,t))$ функциялар жүйесін құрамыз.

(8) теңдіктен $\lim\limits_{t \to t_r - 0} v_r(x,t)$, $r = \overline{1,N}$ шектерді анықтаймыз. (5)-ші теңдікті T/N-ге көбейтіп, анықталған шектерді (5)-ші және (6)-шы теңдіктерге қойып, белгісіз $\lambda(x) \in C([0,\omega],\mathbb{R}^{n(N+1)})$ параметрге қатысты

$$Q_{*,\Delta_N(x)}(x,\lambda(x)) = 0, \quad (9)$$

сызықтық емес теңдеулер жүйесін құрамыз, мұндағы $Q_{*,\Delta_N(x)}(x,\lambda(x))$ операторы

$$Q_{*,\Delta_N(x)}(x,\lambda(x)) = \begin{pmatrix} h \cdot g\left(x, \lambda_1(x), \lambda_{N+1}(x)\right) \\ (I + a_1(A,x,t_1))\lambda_1 - \lambda_2 + a_1(F,x,t_1) \\ (I + a_2(A,x,t_2))\lambda_2 - \lambda_3 + a_2(F,x,t_2) \\ \dots \\ (I + a_N(A,x,t_N))\lambda_N - \lambda_{N+1} + a_N(F,x,t_N) \end{pmatrix}.$$

Құрылған (9) сызықтық емес теңдеулер жүйесін шешу итерациялық әдістер негізінде жүзеге асырылады. Бірінші кезеңде қойылған есептің шешімі бар және жалғыз болуын қамтамасыз

ететін қасиеттерге ие болатын жиын құрылады. Бұл жиын кейінгі итерациялық есептеулер-дің орындалу шарттарын анықтауға мүмкіндік береді. Яғни, $\lambda^0(x) = (\lambda^0{}_1(x), \lambda^0{}_2(x), \ldots, \lambda^0{}_{N+1}(x)) \in C([0,\omega], \mathbb{R}^{n(N+1)})$ векторын және $\rho_\lambda > 0$, $\rho_v > 0$ сандарын таңдап,

$$S(x, \lambda^0(x), \rho_\lambda) = \left\{ \lambda(x) \in C([0,\omega], \mathbb{R}^{n(N+1)}) : \|\lambda - \lambda^0\|_3 < \rho_\lambda \right\},$$

$G^0(x, \rho_\lambda) = \{(x, w_1, w_2) \in [0,\omega] \times \mathbb{R}^n \times \mathbb{R}^n : x \in [0,\omega], \|w_1 - \lambda_1^0(x)\| < \rho_\lambda, \|w_2 - \lambda_{N+1}^0(x)\| < \rho_\lambda\}$.

жиындарды құрып аламыз.

Шарт 1. $g(x, w_1, w_2)$ функциясы және оның $\dfrac{\partial g(x, w_1, w_2)}{\partial w_1}$, $\dfrac{\partial g(x, w_1, w_2)}{\partial w_2}$ дербес туындылары $G^0(x, \rho_\lambda)$ жиынында бірқалыпты үзіліссіз және төмендегі теңсіздіктер орындалады

$$\|\frac{\partial g(x, w_1, w_2)}{\partial w_1}\| \le L_1, \quad \|\frac{\partial g(x, w_1, w_2)}{\partial w_2}\| \le L_2, \quad (x, w_1, w_2) \in G^0(x, \rho_\lambda)$$

мұндағы L_1, L_2- тұрақты мәндер.

Тұжырым. Барлық $\lambda(x) \in S(x, \lambda^0(x), \rho_\lambda)$ үшін $\dfrac{\partial Q_{*,\Delta_N(x)}(x, \lambda(x))}{\partial \lambda} : \mathbb{R}^{n(N+1)} \to \mathbb{R}^{n(N+1)}$ Якоби матрицасының кері матрицасы бар болуы үшін $n \times n$ өлшемді

$$M_N(x) = h \cdot \left[\frac{\partial g(x, \lambda_1(x), \lambda_{N+1}(x))}{\partial w_1} + \frac{\partial g(x, \lambda_1(x), \lambda_{N+1}(x))}{\partial w_2} \cdot \prod_{r=N}^{1} (I + a_r(A, x, t_r)) \right]$$

матрицасының кері матрицасы бар болуы қажетті және жеткілікті.

$\lambda(x)$ параметрге қатысты (9) теңдеудің шешімін табу үшін келесі тұжырым 1-ші теореманың [6] жалпыламасы болып табылатын тұжырымның салдары:

Теорема. *Әрбір $x \in [0,\omega]$ үшін Шарт 1 және келесі*

I) $S(x, \lambda^0(x), \rho_\lambda)$ жиынында $\dfrac{\partial Q_{*,\Delta_N(x)}(x, \lambda(x))}{\partial \lambda} : \mathbb{R}^{n(N+1)} \to \mathbb{R}^{n(N+1)}$ Якоби матрицасы бірқалыпты үзіліссіз;

II) барлық $\lambda(x) \in S(x, \lambda^0(x), \rho_\lambda)$ үшін $\dfrac{\partial Q_{*,\Delta_N(x)}(x, \lambda(x))}{\partial \lambda} : \mathbb{R}^{n(N+1)} \to \mathbb{R}^{n(N+1)}$ Якоби матрицасының шенелген кері матрицасы бар және

$$\left\| \left(\frac{\partial Q_{*,\Delta_N(x)}(x, \lambda(x))}{\partial \lambda} \right)^{-1} \right\| \leqslant \gamma, \quad \gamma - const;$$

III) $\gamma \cdot \|Q_{*,\Delta_N(x)}(x, \lambda^0(x))\| < \rho_\lambda$

шарттары орындалсын. Онда кез келген $\alpha_1 \ge 1$ саны табылып,

$$\begin{aligned} \lambda^{(0)}(x) &= \lambda^0(x), \\ \lambda^{(p+1)}(x) &= \lambda^{(p)}(x) - \frac{1}{\alpha_1} \left(\frac{\partial Q_{*,\Delta_N(x)}(x, \lambda^{(p)}(x))}{\partial \lambda} \right)^{-1} \cdot Q_{*,\Delta_N(x)}(x, \lambda^{(p)}(x)), \\ & \qquad p = 0, 1, 2, \ldots, \quad (10) \end{aligned}$$

итерациялық процеспен анықталатын $\{\lambda^{(p)}(x)\}_{p=0}^{\infty}$ тізбегі $S(x, \lambda^0(x), \rho_\lambda)$ жиынына тиісті болады, (9)-шы теңдеудің шешімі $\lambda^*(x)$-ға жинақталады, $\lambda^*(x) \in S(x, \lambda^0(x), \rho_\lambda)$ және

$$\|\lambda^* - \lambda^0\|_3 \le \gamma \cdot \|Q_{*,\Delta_N(x)}(x, \lambda^0(x))\|$$

бағалауы орындалады. $S(x, \lambda^0(x), \rho_\lambda)$ жиынында (9)*-шы теңдеудің кез-келген шешімі оқшауланған болады.*

Ұсынылған тұжырым Адамар теоремасының локалды нұсқасын кеңейтетін күшейтілген нәтижесінің арнайы бір жағдайын сипаттайды [6].

Шеттік есептердің сандық шешімін табу мысалдарын қарастырамыз.

Мысал 1. Параметрі бар сызықтық емес екі нүктелі шеттік есепті қарастырамыз:

$$\frac{\partial v}{\partial t} = A(x,t)v + F(x,t), \quad (x,t) \in [0,\omega] \times (0,T), \tag{11}$$

$$g(x, v(x,0), v(x,T)) = 0, \quad x \in [0,\omega], \tag{12}$$

мұндағы x - әулет параметрі, $\omega = 0.25$, $T = 0.5$,

$$A(x,t) = \begin{pmatrix} 2x+2 & x-1 \\ 3x+3 & x-2 \end{pmatrix},$$

$$F(x,t) = \begin{pmatrix} -(2x^2+3x+3)t^2 - (2x^3+3x^2-4x-1)t - 2x^3 - x^2 \\ -(3x^2+5x+5)t^2 - (3x^3+4x^2-3x+4)t - 3x^3 - 3x^2 + x - 1 \end{pmatrix},$$

$$g\left(x, \begin{pmatrix} v_1(x,0) \\ v_2(x,0) \end{pmatrix}, \begin{pmatrix} v_1(x,T) \\ v_2(x,T) \end{pmatrix}\right) = \begin{pmatrix} \frac{1}{4}v_1(x,0)v_2(x,T) - v_2(x,0)v_1(x,T) - \frac{1}{16}x^2(2x-3) \\ v_1(x,0)v_2(x,T) + \frac{1}{2}v_2(x,0)v_1(x,T) - \frac{1}{4}x^2(2x-3) \end{pmatrix},$$

(11) есебінің $(x,t) \in [0, 0.25] \times [0, 0.5]$ облысында дәл шешімі

$$v^*(x,t) = \begin{pmatrix} (x+1)t^2 + (t+1)x^2 \\ (x+1)t^2 \end{pmatrix}$$

болады.

$N = 1$ деп аламыз да $v(x,t) = \lambda_1(x) + \widetilde{v}(x,t)$ алмастыруын орындаймыз.

Онда

$$\widetilde{v}(x,t) = \Phi(x,t)\int_0^t \Phi^{-1}(x,\tau)A(x,\tau)\lambda_1(x)d\tau + \Phi(x,t)\int_0^t \Phi^{-1}(x,\tau)F(x,\tau)d\tau,$$

$$(x,t) \in [0, 0.25] \times [0, 0.5],$$

мұндағы

$$\Phi(x,t) = \frac{2e^{\frac{3xt}{2}}}{\sqrt{13x^2+8x+4}} \cdot \left(\left(\frac{\sqrt{13x^2+8x+4}}{2}\cosh\left(\frac{t\sqrt{13x^2+8x+4}}{2}\right) - \right.\right.$$
$$\left.\left. - \frac{3x}{2}\sinh\left(\frac{t\sqrt{13x^2+8x+4}}{2}\right)\right) \cdot E + \sinh\left(\frac{t\sqrt{13x^2+8x+4}}{2}\right) \cdot A(x,t)\right),$$

$Q_{*,\Delta_1(x)}(x, \lambda(x)) = 0$ сызықтық емес теңдеулер жүйесі әулетін құрып аламыз. Бұл жерде

$$Q_{*,\Delta_1(x)}(x,\lambda(x)) = \begin{pmatrix} g(x, \lambda_1(x), \lambda_2(x)) \\ \lambda_1(x) + \widetilde{v}(x,T) - \lambda_2(x) \end{pmatrix}, \ \lambda(x) = (\lambda_1(x), \lambda_2(x)) \in \mathbb{R}^4.$$

$\lambda^0(x) = \left(\begin{pmatrix} 0 \\ 0 \end{pmatrix}, \begin{pmatrix} 1 \\ 1 \end{pmatrix} \right)$ векторын алып, (10) итерациялық процесті жүзеге асырамыз. 30-шы итерацияда табылған параметрді $\lambda^*(x) = (\lambda_1^*(x), \lambda_2^*(x))$ деп қабылдаймыз, себебі бұл параметр үшін $\left\| Q_{*,\Delta_1}(x, \lambda^*(x)) \right\| \leq 10^{-7}$ теңсіздігі орындалады.

Осы есептеу нәтижелерінен төмендегі бағалаудың орындалатынын көреміз:

$$\max_{i=\overline{0,10}} \left\| \lambda^*(0.025i) - v^*(0.025i, 0) \right\| \leqslant 0.0000010668.$$

$\widetilde{v}(x_i, t)$ функциясы

$$\widetilde{v}(x_i, t) = \Phi(x_i, t) \int_0^t \Phi(x_i, \tau) A(x_i, \tau) d\tau \cdot \lambda_1^*(x_i) + \Phi(x_i, t) \int_0^t \Phi(x_i, \tau) F(x_i, \tau) d\tau, \quad t \in [0, 0.5]$$

түрінде жазылады, мұндағы ($x_i = 0.025i, \quad i = 0, 1, 2, \ldots, 10$). Сонымен, төмендегі бағалау орынды

$$\max_{j=\overline{0,20}} \max_{i=\overline{0,10}} \left\| \lambda^*(0.025i) + \widetilde{v}(0.025i, 0.05j) - v^*(0.025i, 0.05j) \right\| \leqslant 0.0000010683.$$

$\lambda(x)$ параметрі бөліктеу нүктелерінде $1.1 \cdot 10^{-6}$, ал (11), (12) тестілік шеттік есебінің шешімі $1.1 \cdot 10^{-6}$ дәлдіктерімен анықталады.

Мысал 2. Келесі түрдегі

$$\frac{\partial v}{\partial t} = A(x,t)v + F(x,t), \quad (x,t) \in [0, \frac{1}{4}] \times (0, \frac{1}{2}), \tag{13}$$

$$g(x, v(x,0), v(x, \frac{1}{2})) = 0, \quad x \in [0, \frac{1}{4}], \tag{14}$$

сызықтық емес екі нүктелі шеттік есептер әулетін қарастырайық, мұндағы x - әулет параметрі,

$$A(x,t) = \begin{pmatrix} 2x + 2t & x - 1 \\ 3x + 3(t+1) & x - 2t \end{pmatrix}, \qquad F(x,t) = \begin{pmatrix} F_1(x,t) \\ F_2(x,t) \end{pmatrix},$$

$$F_1(x,t) = -2(x+1)t^3 - (4x^2 + x + 1)t^2 - (2x^3 + 3x^2 - 4x - 1)t - 2x^3 + x^2,$$

$$F_2(x,t) = -(3x+5)t^3 - (6x^2 + 3x + 5)t^2 - (3x^3 + 7x^2 - x + 2)t - 3x^3 - 3x^2 + x - 1,$$

$$g\left(x, \begin{pmatrix} v_1(x,0) \\ v_2(x,0) \end{pmatrix}, \begin{pmatrix} v_1(x,T) \\ v_2(x,T) \end{pmatrix} \right) = \begin{pmatrix} \frac{1}{4} v_1(x,0) v_2(x,T) - v_2(x,0) v_1(x,T) - \frac{1}{16} x^2 (2x - 3) \\ \\ v_1(x,0) v_2(x,T) + \frac{1}{2} v_2(x,0) v_1(x,T) - \frac{1}{4} x^2 (2x - 3) \end{pmatrix}.$$

(13) есебінің $(x,t) \in [0, \frac{1}{4}] \times [0, \frac{1}{2}]$ облысындағы дәл шешімі

$$v^*(x,t) = \begin{pmatrix} (x+1)t^2 + (t+1)x^2 \\ \\ (x-1)t - t^2 \end{pmatrix}.$$

(7), (8)-ші теңдеулерді ескерсек

$$\widetilde{v}(x,t) = a_1(A, x, t) \cdot \lambda_1(x) + a_1(F, x, t)$$

анықталады.

Берілген аралықты қандай да бір белгілі қадаммен бөліп, $a_1(A,x,t)$ және $a_1(F,x,t)$ функцияларын анықтаймыз. Әрбір x үшін $\lambda(x)$ параметрге қатысты $Q_{*,\Delta_1(x)}(x,\lambda(x))=0$ сызықтық емес теңдеулер жүйесі әулетін құрып аламыз.

Ескерту. $\lambda_1(x)=v(x,0)$, $\lambda_2(x)=v(x,0.5)$ белгілеулері қолданылады және $Q_{*,\Delta_1(x)}\,(x,\lambda(x))$ операторының Якоби матрицасы келесі түрде анықталады

$$\frac{\partial Q_{*,\Delta_1(x)}\,(x,\lambda(x))}{\partial\lambda}=\begin{pmatrix} \frac{1}{2}\lambda_{2,2}(x) & -\lambda_{2,1}(x) & -\lambda_{1,2}(x) & \frac{1}{4}\lambda_{1,1}(x)\\ \lambda_{2,2}(x) & \frac{1}{2}\lambda_{2,1}(x) & \frac{1}{2}\lambda_{1,2}(x) & \lambda_{1,1}(x)\\ 1+a_1^{1,1}(x,T) & a_1^{1,2}(x,T) & -1 & 0\\ a_1^{2,1}(x,T) & 1+a_1^{2,2}(x,T) & 0 & -1 \end{pmatrix}$$

$\lambda^0(x)=\left(\begin{pmatrix}0\\0\end{pmatrix},\begin{pmatrix}1\\1\end{pmatrix}\right)$ векторын алып, $Q_{*,\Delta_1(x)}(x,\lambda(x))=0$ сызықтық емес теңдеулер жүйесін итерациялық процесті пайдаланып шешеміз:

$$\lambda^{(p+1)}(x)=\lambda^{(p)}(x)-\frac{1}{2}\left(\frac{\partial Q_{*,\Delta_1(x)}\left(x,\lambda^{(p)}(x)\right)}{\partial\lambda}\right)^{-1}\cdot Q_{*,\Delta_1(x)}\left(x,\lambda^{(p)}(x)\right),\quad p=0,1,2,\ldots$$

Сонда, 30-шы итерациядағы $x_i=\frac{1}{40}(i-1)$ $(i=\overline{1,11})$ нүктелеріндегі $\lambda_1^*(x)$, $\lambda_2^*(x)$ функцияларының мәндерін табамыз.

Әрбір $t\in[0,\frac{1}{2}]$ үшін

$$\widetilde{v}\Big(\frac{i}{40},t\Big)=a_1\Big(A,\frac{i}{40},t\Big)\cdot\lambda_1\Big(\frac{i}{40}\Big)+a_1\Big(F,\frac{i}{40},t\Big),$$

$$\widehat{v}\Big(\frac{i}{40},\frac{j}{40}\Big)=\lambda_1\Big(\frac{i}{40}\Big)+\widetilde{v}\Big(\frac{i}{40},\frac{j}{40}\Big)\quad(j=1,7,15,21)$$

функциялардың $x=\frac{i}{40}$ $(i=0,1,2,\ldots,10)$ нүктелеріндегі мәндерін анықтаймыз.

Ендеше, алынған нәтижелерден

$$\max_{i=\overline{0,10}}\left\|\begin{pmatrix}\lambda_1(\frac{i}{40})\\ \lambda_2(\frac{i}{40})\end{pmatrix}-\begin{pmatrix}v_1^*(\frac{i}{40},0)\\ v_2^*(\frac{i}{40},\frac{1}{2})\end{pmatrix}\right\|\leqslant 0.0000000906$$

$$\max_{j=\overline{0,20}}\max_{i=\overline{0,10}}\left\|\lambda\Big(\frac{i}{40}\Big)+\widetilde{v}\Big(\frac{i}{40},\frac{j}{40}\Big)-v^*\Big(\frac{i}{40},\frac{j}{40}\Big)\right\|\leqslant 0.0000000939$$

бағалаулары орындалады.

$\lambda(x)$ параметрі бөліктеу нүктелерінде $9.06\cdot10^{-8}$, ал (13), (14) тестілік шеттік есебінің шешімі $9.39\cdot10^{-8}$ дәлдіктерімен анықталады.

Қорытынды

Жұмыста келтірілген есептік мысалдар ұсынылған әдістің қолдану тиімділігін дәлелдейді. Бірінші мысалда $A(x,t)$ матрицасы тек x айнымалысына тәуелді болғандықтан, оған сәйкес келетін $\Phi(x,t)$ фундаменталды матрицасын аналитикалық түрде анықтау мүмкіндігі болды. Бұл жағдай қарастырып отырған әдістің теориялық тұжырымдарын нақтылап, оның

қарапайым жағдайда қалай жүзеге асатынын көрсетуге жағдай жасайды. $A(x,t)$ матрицасы екі айнымалыға тәуелді болатын жағдайда фундаменталды матрицаның нақты аналитикалық өрнегін алу күрделене түседі. Сондықтан, екінші мысалда $\Phi(x,t)$ матрицасының элементтері берілген әрбір (x,t) нүктесі үшін сандық әдістер көмегімен есептеледі. Жүргізілген есептеулер нәтижелері ұсынылған тәсілдің практикалық тұрғыдан тиімді және қолдануға болатынын көрсетеді.

Қаржыландыру туралы ақпарат

Қазақстан Республикасының Ғылым және жоғары білім министрлігінің Ғылым комитеті (грант № AP23488811) қаржыландырады.

ӘДЕБИЕТТЕР

1. Dzhumabaev D.S. Criteria for the unique solvability of a linear boundary-value problem for an ordinary differential equation // Comput. Math. and Math. Phys. -1989. -Vol. 29, No.1. -P. 34–46. https://doi.org/10.1016/0041-5553(89)90038-4

2. Dzhumabaev D.S., Bakirova E.A., Mynbayeva S.T. A method of solving a nonlinear boundary value problem with a parameter for a loaded differential equation // Mathematical Methods in the Applied Sciences. -2020. -Vol. 43, No.1. -P. 1788–1802. https//doi.org/10.1002/mma.6003

3. Minglibayeva B.B., Assanova A.T. An existence of an isolated solution to nonlinear two-point boundary value problem with parameter // Lobachevskii Journal of Mathematics. -2021. -Vol.42, No.3. -P. 587–597. https://doi.org/10.1134/s199508022103015x

4. Asanova A.T., Kadirbayeva Zh.M. On the numerical algorithms of parametrization methods for solving a two-point boundary-value problem for impulsive systems of loaded differential equations // Computational and Applied Mathematics. -2018. -Vol. 37, No. 1. -P. 4966–4976. https://doi.org/10.1007/s40314-018-0611-9

5. Dzhumabaev D.S., Temesheva S.M. A parametrization method for solving nonlinear two-point boundary value problems // Computational Mathematics and Mathematical Physics. -2007. -Vol. 47, No. 1. -P. 37–61. https://doi.org/10.1134/S096554250701006X

6. Dzhumabaev D.S., Temesheva S.M. Criteria for the Existence of an Isolated Solution of a Nonlinear Boundary-Value Problem // Ukrainian Mathematical Journal. -2018. -Vol. 70, No. 3. -P. 410–421. https://doi.org/10.1007/s11253-018-1507-y

7. Asanova A.T., Bakirova E.A., Kadirbayeva Zh.M. Numerical implementation of solving a boundary value problem for a system of loaded differential equations with parameter // News of the National Academy of Sciences of the Republic of Kazakhstan. -2019. -Vol. 325, No. 3. -P. 77–84. /- https://doi.org/10.32014/2019.2518-1726.27

8. Kadirbayeva Zh.M. A numerical method for solving boundary value problem for essentially loaded system // Lobachevskii Journal of Mathematics. -2021. -Vol. 42, No. 3. -P. 551–559. https://doi.org/10.1134/S1995080221030112

9. Temesheva S.M. A modification of a algorithms of the Dzhumabaev parametrization method and a numerical method // International Journal of Information and Communication Technologies. -2020. -Vol. 1, No.2. -P. 66–73.

10. Temesheva S.M., Dzhumabaev D.S., Kabdrakhova S.S. On one algorithm to find a solution to a linear two-point boundary value problem // Lobachevskii Journal of Mathematics. -2021. -Vol. 42, No.3. -P. 606–612. https://doi.org/10.1134/S1995080221030173

11. Темешева С.М., Абдиманапова П.Б., Борисов Д.И. Об одном методе решения семейства нелинейных краевых задач для обыкновенных дифференциальных уравнений // Вестник Каз НПУ им.Абая Серия "Физико-математические науки". -2021. -Т. 73, №. 1. -С. 70–76. https://doi.org/10.51889/2021-1.1728-7901.09

12. Asanova A.T., Imanchiev A.E. The problem with non-separated multipoint integral conditions for high-order differential equations and a new general solution // Quaestiones Mathematicae. -2022. -Vol. 45, No. 10. -P. 1641–1653. https://doi.org/10.2989/16073606.2021.1967503

13. Iskakova N.B., Temesheva S.M., Uteshova R.E. On a problem for a delay differential equation // Mathematical Methods in the Applied Sciences. -2022. -Vol. 46, No. 9. -P. 11283–11297. https://doi.org/10.1002/mma.9181

14. Abdimanapova P.B., Temesheva S.M. Well-posedness criteria for one family of boundary value problems. Bulletin of the Karaganda University, Mathematics series. -2023. -Vol. 112, No.4. -P. 5–20. /-https://doi.org/10.31489/2023M4/5-20

15. Далецкий Ю.Л., Крейн М.Г. Устойчивость решений дифференциальных уравнений в банаховом пространстве. -М.: Наука, 1970. -536 с.

REFERENCES

1. Dzhumabaev, D.S. Criteria for the unique solvability of a linear boundary-value problem for an ordinary differential equation. *Computational Mathematics and Mathematical Physics*, 29(1), 34–46 (1989). https://doi.org/10.1016/0041-5553(89)90038-4

2. Dzhumabaev, D.S., Bakirova, E.A., and Mynbayeva, S.T. A method of solving a nonlinear boundary value problem with a parameter for a loaded differential equation. *Mathematical Methods in the Applied Sciences*, 43(1), 1788–1802 (2020). https://doi.org/10.1002/mma.6003

3. Minglibayeva, B.B., and Assanova, A.T. An existence of an isolated solution to nonlinear two-point boundary value problem with parameter. *Lobachevskii Journal of Mathematics*, 42(3), 587–597 (2021). https://doi.org/10.1134/S199508022103015X

4. Asanova, A.T., and Kadirbayeva, Zh.M. On the numerical algorithms of parametrization method for solving a two-point boundary-value problem for impulsive systems of loaded differential equations. *Computational and Applied Mathematics*, 37(1), 4966–4976 (2018). https://doi.org/10.1007/s40314-018-0611-9

5. Dzhumabaev, D.S., and Temesheva, S.M. A parametrization method for solving nonlinear two-point boundary value problems. *Computational Mathematics and Mathematical Physics*, 47(1), 37–61 (2007). https://doi.org/10.1134/S096554250701006X

6. Dzhumabaev, D.S., and Temesheva, S.M. Criteria for the Existence of an Isolated Solution of a Nonlinear Boundary Value Problem. *Ukrainian Mathematical Journal*, 70(3), 410–421 (2018). https://doi.org/10.1007/s11253-018-1507-y

7. Asanova, A.T., Bakirova, E.A., and Kadirbayeva, Zh.M. Numerical implementation of solving a boundary value problem for a system of loaded differential equations with parameter. *News of the National Academy of Sciences of the Republic of Kazakhstan*, 325(3), 77–84 (2019). https://doi.org/10.32014/2019.2518-1726.27

8. Kadirbayeva, Zh.M. A numerical method for solving boundary value problem for essentially loaded system. *Lobachevskii Journal of Mathematics*, 42(3), 551–559 (2021). https://doi.org/10.1134/S1995080221030112

9. Temesheva, S.M. A modification of algorithms of the Dzhumabaev parametrization method and a numerical method. *International Journal of Information and Communication Technologies*, 1(2), 66–73 (2020).

10. Temesheva, S.M., Dzhumabaev, D.S., and Kabdrakhova, S.S. On one algoritm to find a solution to a linear two-point boundary value problem. *Lobachevskii Journal of Mathematics*, 42(3), 606–612 (2021). https://doi.org/10.1134/S1995080221030173

11. Temesheva, S.M., Abdimanapova, P.B., and Borisov, D.I. *Ob odnom metode resheniya semeystva nelineynykh krayevykh zadach dlya obyknovennykh differentsial'nykh uravneniy* [On one method for solving a family of nonlinear boundary value problems for ordinary differential equations] *Bulletin of Abai Kazakh National Pedagogical University, Series Physical and Mathematical Sciences*, 73(1), 70–76, (2021). https://doi.org/10.51889/2021-1.1728-7901.09 (in Russian).

12. Asanova, A.T., and Imanchiev, A.E. The problem with non-separated multipoint integral conditions for high-order differential equations and a new general solution. *Quaestiones Mathematicae*, 45(10), 1641–1653 (2022). https://doi.org/10.2989/16073606.2021.1967503

13. Iskakova, N.B., Temesheva, S.M., and Uteshova, R.E. On a problem for a delay differential equation. *Mathematical Methods in the Applied Sciences*, 46(9), 11283–11297 (2022). https://doi.org/10.1002/mma.9181

14. Abdimanapova, P.B., and Temesheva, S.M. Well-posedness criteria for one family of boundary value problems. *Bulletin of the Karaganda University, Mathematics Series*, 112(4), 5–20 (2023). https://doi.org/10.31489/2023M4/5-20

15. Daletskii, Yu.L., and Krein, M.G. *Ustoychivost' resheniy differentsial'nykh uravneniy v banakhovom prostranstve* [Stability of Solutions of Differential Equations in Banach Space] (Moscow:Nauka, 1970). (in Russian).

[1,2]* **Абдиманапова П.Б.**,

PhD, ассистент-профессор, ORCID ID: 0000-0001-8879-9985,
*e-mail: perizatabdimanapova344@gmail.com

[1,3] **Темешева С.М.**,

д.ф.-м.н., ведущий научный сотрудник, и.о. профессора,
ORCID ID: 0000-0002-3341-4539,
e-mail: temesheva.svetlana@kaznu.kz

[4] **Иманчиев А.Е.**,

к.ф.-м.н., ассоцированный профессор, ORCID ID: 0000-0002-1835-2501,
e-mail: imanchievae@gmail.com

[2] **Мәжит Ж.Б.**,

сеньор-лектор, ORCID ID: 0000-0002-4635-9241,
e-mail: Zhamilya.Mazhit01@gmail.com

[1] Институт математики и математического моделирования, г. Алматы, Казахстан
[2] Алматинский технологический университет, г. Алматы, Казахстан
[3] Казахский национальный университет имени аль-Фараби, г. Алматы, Казахстан
[4] Актюбинский региональный университет имени К. Жубанова, г. Актобе, Казахстан.

О НАХОЖДЕНИИ РЕШЕНИЯ СЕМЕЙСТВА НЕЛИНЕЙНЫХ ДВУХТОЧЕЧНЫХ КРАЕВЫХ ЗАДАЧ ДЛЯ ДИФФЕРЕНЦИАЛЬНОГО УРАВНЕНИЯ

Аннотация

В настоящей работе исследуется краевая задача, относящаяся к семейству линейных дифференциальных уравнений с нелинейными двухточечными краевыми условиями. При каждом фиксированном значении параметра семейства исходная задача преобразуется в нелинейную двухточечную краевую задачу для обыкновенных дифференциальных уравнений. Поскольку такие задачи связаны с нелокальными краевыми задачами, в том числе с системами гиперболических уравнений, определение условий их разрешимости является актуальной задачей. В работе применяется метод параметризации Д.С. Джумабаева, основанный на сведении задачи к системе нелинейных алгебраических уравнений по параметру и решении начальной задачи для дифференциального уравнения, зависящего от параметра. Для решения используется итерационный метод, при этом обосновываются условия сходимости. Предложенный метод основан на сочетании численного решения задач Коши и решения системы нелинейных уравнений. Полученный алгоритм решения проверяется на конкретных тестовых примерах, что демонстрирует его эффективность. В частности, установлено, что решение соответствующей системы при заданном значении параметра сходится в процессе итераций. Рассматриваемый метод является эффективным методом определения решений краевых задач для семейства линейных дифференциальных уравнений, характеризующихся нелинейными двухточечными краевыми условиями. Практическая эффективность предложенного метода подтверждается результатами численного решения конкретных задач.

Ключевые слова: нелинейные двухточечные краевые задачи, параметр семейства, обыкновенные дифференциальные уравнения, краевые условия, численный метод.

[1,2*] Abdimanapova P.B.,

PhD, Assistant Professor, ORCID ID: 0000-0001-8879-9985,
*e-mail: perizatabdimanapova344@gmail.com

[1,3] Temesheva S.M.,

Dr.Phys.-Math.Sc., Leading Researcher, Acting Professor, ORCID ID: 0000-0002-3341-4539,
e-mail: temesheva.svetlana@kaznu.kz

[4] Imanchiev A.E.,

Cand.Phys.-Math.Sc., Associate Professor, ORCID ID: 0000-0002-1835-2501,
e-mail: imanchievae@gmail.com

[2] Mazhit Zh.B.,

Senior lecturer, ORCID ID: 0000-0002-4635-9241,
e-mail: Zhamilya.Mazhit01@gmail.com

[1] Institute of Mathematics and Mathematical Modeling, Almaty, Kazakhstan
[2] Almaty Technological University, Almaty, Kazakhstan
[3] Al-Farabi Kazakh National University, Almaty, Kazakhstan
[4] K.Zhubanov Aktobe Regional University, Aktobe, Kazakhstan

ON FINDING SOLUTIONS OF A FAMILY OF NONLINEAR TWO-POINT BOUNDARY VALUE PROBLEMS FOR A DIFFERENTIAL EQUATION

Abstract

This paper investigates a boundary value problem belonging to a family of linear differential equations with nonlinear two-point boundary conditions. For each fixed value of the family parameter, the original problem is transformed into a nonlinear two-point boundary value problem for ordinary differential

equations. Since such problems are associated with nonlocal boundary value problems, including systems of hyperbolic equations, determining the conditions for their solvability is of considerable interest. The study employs the parameterization method developed by D.S. Dzhumabayev, which is based on reducing the problem to a system of nonlinear algebraic equations with respect to the parameter and solving an initial value problem for a parameter-dependent differential equation. An iterative method is used for the solution process, and the conditions ensuring its convergence are established. The proposed approach combines the numerical solution of Cauchy problems with the solution of a system of nonlinear equations. The developed algorithm is tested on specific benchmark examples, demonstrating its effectiveness. In particular, it is shown that the solution of the corresponding system converges through the iterative process for a given parameter value. The considered approach provides an efficient method for determining solutions of boundary value problems for families of linear differential equations characterized by nonlinear two-point boundary conditions. The practical efficiency of the proposed method is confirmed by the results of numerical solutions of specific problems.

Key words: nonlinear two-point boundary value problems, family parameter, ordinary differential equations, boundary conditions, numerical method.

Received June 23, 2026; accepted August 29, 2026.

UDC 519.63
IRSTI 27.35.45

https://doi.org/10.55452/1998-6688-2026-23-3-106-123

[1,2]***Satybaldina A.N.**,
Master of Technical Science, Senior lecturer,
ORCID ID: 0000-0002-5596-0936,
*e-mail: aigul1191@gmail.com

[3] **Ydyrys A.Zh.**,
PhD in Mathematics, Associate professor,
ORCID ID: 0000-0002-4284-9446,
e-mail: a.ydyrys@iitu.edu.kz

[1] L.N. Gumilyov Eurasian National University, Astana, Kazakhstan
[2] Kazakh-British Technical University, Almaty, Kazakhstan
[3] International Information Technology University, Almaty, Kazakhstan

ANALYTICAL AND APPROXIMATE SOLUTIONS OF THE TWO-DIMENSIONAL LAPLACE EQUATION IN CYLINDRICAL COORDINATES

Abstract

This paper investigates a steady-state heat conduction problem in a multilayer cylindrical domain with nonhomogeneous boundary conditions. Two approaches for solving the direct problem are considered: an analytical method based on separation of variables and Fourier series expansion, and a numerical method based on the finite difference approximation combined with the Successive Over-Relaxation (SOR) algorithm. An exact analytical solution of the Laplace equation in polar coordinates is derived for a three-layer cylindrical system with continuity conditions at layer interfaces and convective heat exchange at the outer boundary. A finite difference scheme is developed to approximate the governing equation, while the resulting system of linear algebraic equations is solved iteratively using the SOR method.The accuracy of the numerical approach is evaluated through comparison with the analytical solution and experimental temperature measurements. The obtained results demonstrate good agreement between the analytical and numerical solutions. The mean absolute error between the two approaches is $0.134K$, the root mean square error is $0.141K$, and the maximum absolute error does not exceed $0.209K$. Experimental validation shows that both models correctly reproduce the overall temperature distribution in the multilayer cylindrical system. The mean absolute errors relative to experimental data are $2.509K$ for the analytical solution and $2.638K$ for the SOR solution. The performed analysis confirms the good accuracy and stability of the developed finite difference algorithm and demonstrates its applicability for modeling heat transfer processes in multilayer cylindrical structures. The proposed approach can be employed in the thermal analysis of pipelines, geothermal systems, insulation structures, and other engineering applications involving layered media.

Keywords: Heat conduction; Laplace equation; multilayer cylindrical domain; analytical solution; finite difference method; Successive Over-Relaxation (SOR); temperature distribution; experimental validation; polar coordinates; thermal modeling.

Received: June 26, 2026; revised: July 15, 2026; accepted: July 27, 2026.

Introduction

Heat transfer in multilayer cylindrical structures is an important topic in both engineering and applied science due to its wide range of practical applications. Such structures are commonly found in oil and gas pipelines, geothermal systems, thermal insulation technologies, and various aerospace and nuclear engineering components [1]. The analysis of heat transfer in these systems is complicated by the presence of different materials, multiple interfaces between layers, and complex boundary conditions that often vary along the surface.

A key step in understanding the thermal behavior of multilayer systems is the solution of the direct heat conduction problem, which aims to determine the temperature distribution within the domain when the material properties and boundary conditions are known [2]. To address this problem, researchers typically employ either analytical methods, which can provide exact solutions under certain assumptions, or approximate approaches based on numerical techniques. Each of these methods offers specific advantages and faces particular limitations depending on the complexity of the physical model.

Heat transfer in multilayer cylindrical structures is encountered in many engineering applications, including oil and gas pipelines, geothermal wells, underground thermal energy storage systems, and multilayer insulation technologies. In such systems, the temperature field is affected not only by the thermal properties of individual materials but also by the interaction between layers and the conditions imposed on the boundaries. Reliable prediction of temperature distributions is therefore essential for evaluating thermal efficiency, structural integrity, and long-term performance.

For steady-state problems, analytical methods remain an attractive tool because they provide explicit relationships between temperature distributions and the governing parameters of the system. Such solutions are particularly useful when studying the influence of material properties, layer thicknesses, or boundary conditions. Yang and Liu [1] proposed an analytical transfer-function framework for multilayer cylinders with an arbitrary number of layers, while Kayhani et al. [2] derived closed-form solutions for composite cylindrical laminates composed of orthotropic materials. These approaches provide accurate results and valuable physical insight. However, their application becomes increasingly difficult when the geometry, material configuration, or boundary conditions become more complex.

A comprehensive review of analytical solutions for multilayer structures can be found in [3]. One of the main challenges in analytical modeling is the treatment of non-uniform boundary conditions. In cylindrical geometries, boundary temperatures and heat fluxes often vary along the angular coordinate because of external environmental effects, localized heating sources, or asymmetric operating conditions. Although analytical techniques based on Fourier expansions can handle such situations, the resulting formulations may become cumbersome, especially for multilayer domains. Additional difficulties arise in transient problems, where eigenvalue calculations and series representations may require considerable computational effort and can suffer from numerical instability [4].

Because of these limitations, numerical methods are widely used in practical thermal analysis. Among them, the finite difference method remains one of the most accessible and computationally efficient approaches. It can easily accommodate multilayer structures, heterogeneous materials, and complicated boundary conditions without requiring the derivation of lengthy analytical expressions. The price for this flexibility is the introduction of discretization errors, whose magnitude depends on the mesh resolution and numerical scheme. For this reason, the accuracy of a numerical solution should be carefully evaluated whenever a reliable analytical solution is available.

A detailed overview of analytical solutions for multilayer media was presented by Amiri Delouei et al. [6], who examined rectangular, cylindrical, and spherical geometries. Their review high-

lights how interface conditions, thermal contact resistance, internal heat generation, and boundary conditions influence the complexity of the resulting mathematical models. At the same time, the review shows that relatively few studies directly compare analytical and numerical solutions for the same multilayer configuration under identical conditions.

Several recent studies have focused on multilayer cylindrical systems. In [7], an analytical solution of the steady-state heat conduction equation in polar coordinates was developed for multilayer soils and validated through numerical examples. Later, the same analytical framework was employed in inverse heat conduction problems, where unknown material properties were reconstructed from temperature measurements [8]. More recently, experimental data were incorporated into the inverse analysis of multilayer cylindrical systems, enabling the estimation of thermophysical parameters from measured temperatures [9].

Despite these developments, the question of how accurately a finite difference model reproduces the corresponding analytical solution for the same multilayer cylindrical domain has received relatively little attention. Such a comparison is important not only for validating numerical algorithms but also for understanding where numerical errors arise and how they propagate in regions with strong temperature gradients or discontinuous material properties.

The present study addresses this issue for a multilayer cylindrical domain with non-uniform boundary conditions. An analytical solution is derived using separation of variables and Fourier series expansion, while the numerical solution is obtained using the finite difference method combined with the Successive Over-Relaxation (SOR) algorithm. The performance of the numerical approach is assessed through direct comparison with the analytical solution and experimental temperature measurements.

This study combines analytical, numerical, and experimental investigations of heat transfer in a multilayer cylindrical system. By comparing the analytical solution, the SOR-based numerical results, and experimental measurements, it is possible to evaluate the accuracy of each approach and better understand their strengths and limitations.

The remainder of this paper is organized as follows. Section presents the mathematical formulation of the problem, it derives the analytical solution, and describes the numerical algorithm based on the finite difference method and the SOR technique. Section provides a comparative analysis of the analytical, numerical, and experimental results. Finally, the main conclusions of the study are summarized in Section .

Materials and methods

Mathematical Formulation of the Problem

Consider a steady-state heat conduction process in a multilayer cylindrical domain described in the two-dimensional polar coordinate system (r, φ), where r denotes the radial coordinate and φ is the angular coordinate. It is assumed that no internal heat sources are present within the domain and that the temperature field has reached a steady state. Under these assumptions, the temperature distribution in each layer $(s = 1, 2, 3)$ satisfies the Laplace equation in polar coordinates [10, 11]:

$$\frac{\partial^2 \tilde{T}}{\partial \tilde{r}^2} + \frac{1}{\tilde{r}} \frac{\partial \tilde{T}}{\partial \tilde{r}} + \frac{1}{\tilde{r}^2} \frac{\partial^2 \tilde{T}}{\partial \varphi^2} = 0, \quad \tilde{r}_0 < \tilde{r} < \tilde{r}_3, \; 0 < \varphi < 2\pi. \tag{1}$$

A Dirichlet boundary condition is specified at the inner boundary of the cylinder. For the purposes of this study, the temperature at the inner boundary is assumed to be constant [12]:

$$\tilde{T}^{(1)}(\tilde{r}_0, \varphi) = \tilde{f}, \tag{2}$$

where $\tilde{f}$ is known.

At the layer interfaces, continuity of temperature and heat flux is required [13]:

$$\tilde{T}^{(s)}(\tilde{r}_s, \varphi) = \tilde{T}^{(s+1)}(\tilde{r}_s, \varphi), \tag{3}$$

$$k_s \frac{\partial \tilde{T}^{(s)}}{\partial \tilde{r}}(\tilde{r}_s, \varphi) = k_{s+1} \frac{\partial \tilde{T}^{(s+1)}}{\partial \tilde{r}}(\tilde{r}_s, \varphi), \quad s = 1, 2, \tag{4}$$

where k_s denotes the thermal conductivity of the s-th layer.

At the outer boundary, convective heat transfer with the surrounding environment is described by a Robin boundary condition [14, 15]:

$$\left.\frac{\partial \tilde{T}}{\partial \tilde{r}}\right|_{\tilde{r}=\tilde{r}_3} = -\frac{h}{k_3}\big(\tilde{T}(\tilde{r}_3, \varphi) - \tilde{T}_a(\varphi)\big), \tag{5}$$

where h is the convective heat transfer coefficient at the outer boundary of the third layer, and $\tilde{T}_a(\varphi)$ represents the ambient temperature distribution.

Furthermore, periodicity of the temperature field with respect to the angular coordinate is assumed:

$$\tilde{T}(\tilde{r}, \varphi) = \tilde{T}(\tilde{r}, \varphi + 2\pi). \tag{6}$$

The resulting mathematical model forms the foundation for both the analytical and numerical treatment of the heat conduction problem in a multilayer cylindrical domain.

To facilitate the analysis and subsequent numerical solution, dimensionless variables are introduced. The radial coordinate is normalized by the outer radius of the cylinder:

$$r = \frac{\tilde{r}}{\tilde{r}_3}, \quad \frac{\tilde{r}_0}{\tilde{r}_3} < r \leq 1.$$

The temperature is represented in dimensionless form (T) using a reference temperature chosen for normalization:

$$T = \frac{\tilde{T} - T_{\text{ref}}}{T_{\text{ref}}}, \quad T_{\text{ref}} = 277K. \tag{7}$$

Here, T_{ref} is a fixed reference temperature introduced to scale the temperature field and to obtain a dimensionless representation [16, 17].

In dimensionless variables, the heat conduction equation retains the form of the Laplace equation:

$$\frac{\partial^2 T}{\partial r^2} + \frac{1}{r}\frac{\partial T}{\partial r} + \frac{1}{r^2}\frac{\partial^2 T}{\partial \varphi^2} = 0, \tag{8}$$

while the Robin boundary condition at the external boundary is written in terms of the dimensionless Biot number [18]:

$$\left.\frac{\partial T}{\partial r}\right|_{r=1} = -\text{Bi}\,\big(T(1, \varphi) - T_a(\varphi)\big), \quad \text{Bi} = \frac{h r_3}{k_3}, \quad T_a(\varphi) = \frac{\tilde{T}_a(\varphi) - T_{\text{ref}}}{T_{\text{ref}}}. \tag{9}$$

The remaining boundary conditions (3)–(5) remain unchanged in form after the nondimensionalization. Thus, the dimensionless formulation of the problem is governed by the geometric parameters r_0, r_1, r_2, the thermal conductivities of the layers k_1, k_2, k_3 and the Biot number Bi.

Exact Solution of the Laplace Equation

The analytical solution is constructed using the method of separation of variables. Accordingly, the temperature field is sought in the form of a product of radial and angular functions [19]:

$$T(r,\varphi) = R(r)\,\Phi(\varphi). \tag{10}$$

Substitution of the separated representation into the Laplace equation leads to two independent ordinary differential equations for the angular and radial components. Owing to the periodicity condition in the angular coordinate, the solution of the angular equation takes the form:

$$\Phi_n(\varphi) = \tilde{A}_n \cos(n\varphi) + \tilde{B}_n \sin(n\varphi), \quad n = 0, 1, 2, \ldots \tag{11}$$

For the harmonic modes $n \geq 1$ the radial solution takes the form:

$$R_n(r) = \overline{A}_n r^n + \overline{B}_n r^{-n}. \tag{12}$$

For the zeroth harmonic ($n = 0$), the radial solution is given by:

$$R_0(r) = \overline{A}_0 \ln r + \overline{B}_0. \tag{13}$$

Therefore, combining the radial and angular solutions yields the following Fourier series representation of the temperature field in each layer of the cylindrical domain:

$$T^{(s)}(r,\varphi) = A_0^{(s)} \ln r + B_0^{(s)} + \sum_{n=1}^{\infty} \left(A_n^{(s)} r^n + A_{-n}^{(s)} r^{-n} \right) \cos(n\varphi) + \sum_{n=1}^{\infty} \left(B_n^{(s)} r^n + B_{-n}^{(s)} r^{-n} \right) \sin(n\varphi). \tag{14}$$

where s is number of layer and $s = 1, 2, 3$, all unknown coefficients $A_0^{(s)}, B_0^{(s)}, A_n^{(s)}, A_{-n}^{(s)}, B_n^{(s)}, B_{-n}^{(s)}$ are obtained by enforcing the boundary conditions (2) and (5) as well as the continuity conditions for temperature and heat flux at the layer interfaces (3), (4):

$$A_0^{(2)} = \frac{1}{2\pi \cdot R} \left(\int_0^{2\pi} T_a(\varphi) d\varphi - \int_0^{2\pi} f d\varphi \right). \tag{15}$$

$$A_0^{(1)} = \frac{k_2}{k_1} A_0^{(2)}. \tag{16}$$

$$A_0^{(3)} = \frac{k_2}{k_3} A_0^{(2)}. \tag{17}$$

$$B_0^{(1)} = \frac{1}{2\pi} \int_0^{2\pi} f d\varphi - A_0^{(1)} \ln r_0. \tag{18}$$

$$B_0^{(3)} = \frac{1}{2\pi} \int_0^{2\pi} T_a(\varphi) d\varphi - \frac{A_0^{(3)}}{Bi}. \tag{19}$$

$$B_0^{(2)} = \left(\frac{k_2}{k_1} \big(\ln r_1 - \ln r_0 \big) - \ln r_1 \right) \cdot A_0^{(2)} + \frac{1}{2\pi} \int_0^{2\pi} f d\varphi. \tag{20}$$

$$A_{-n}^{(2)} = \frac{1}{Q \cdot M + S} \left(\frac{Bi}{\pi} \int_0^{2\pi} T_a(\varphi) cosn\varphi d\varphi - Q \cdot K \cdot \int_0^{2\pi} f \cdot \cos n\varphi d\varphi \right). \tag{21}$$

$$A_n^{(2)} = K \cdot \int_0^{2\pi} f \cdot \cos n\varphi d\varphi + M \cdot A_{-n}^{(2)}. \tag{22}$$

$$\begin{cases} A_n^{(1)} = \frac{k_1+k_2}{2k_1} A_n^{(2)} + \frac{k_1-k_2}{2k_1} r_1^{-2n} A_{-n}^{(2)}, \\ A_{-n}^{(1)} = \frac{k_2-k_1}{2k_1} r_1^{2n} A_n^{(2)} + \frac{k_1+k_2}{2k_1} A_{-n}^{(2)}. \end{cases} \tag{23}$$

$$\begin{cases} A_n^{(3)} = \frac{k_2+k_3}{2k_3} A_n^{(2)} - \frac{\left(k_2-k_3\right) r_2^{-2n}}{2k_3} A_{-n}^{(2)}, \\ A_{-n}^{(3)} = -\frac{k_2-k_3}{2k_3} r_2^{2n} A_n^{(2)} + \frac{k_2+k_3}{2k_3} A_{-n}^{(2)}. \end{cases} \tag{24}$$

$$B_n^{(2)} = \frac{1}{H - I \cdot U} \left(\frac{Bi}{\pi} \int_0^{2\pi} T_a(\varphi) sinn\varphi d\varphi - I \cdot O \cdot \int_0^{2\pi} f \cdot \sin n\varphi d\varphi \right). \tag{25}$$

$$B_{-n}^{(2)} = O \cdot \int_0^{2\pi} f \cdot \sin n\varphi d\varphi - U \cdot B_n^{(2)}. \tag{26}$$

$$\begin{cases} B_n^{(1)} = \frac{k_1+k_2}{2k_1} B_n^{(2)} + \frac{k_1-k_2}{2k_1} r_1^{-2n} B_{-n}^{(2)}, \\ B_{-n}^{(1)} = \frac{k_1-k_2}{2k_1} r_1^{2n} B_n^{(2)} + \frac{k_1+k_2}{2k_1} B_{-n}^{(2)}. \end{cases} \tag{27}$$

$$\begin{cases} B_n^{(3)} = \frac{k_2+k_3}{2k_3} B_n^{(2)} + \frac{k_3-k_2}{2k_3} r_2^{-2n} B_{-n}^{(2)}, \\ B_{-n}^{(3)} = \frac{k_3-k_2}{2k_3} r_2^{2n} B_n^{(2)} + \frac{k_2+k_3}{2k_3} B_{-n}^{(2)}. \end{cases} \tag{28}$$

All auxiliary coefficients $R, Q, M, S, K, H, U, I, O$ required in expressions (15)–(28) are explicitly derived as:

1. $R = \left(1 - \frac{k_2}{k_3}\right) lnr_2 + \left(\frac{k_2}{k_1} - 1\right) lnr_1 - \frac{k_2}{k_1} lnr_0 + \frac{1}{Bi} \cdot \frac{k_2}{k_3}$;
2. $Q = \frac{(n+Bi)(k_2+k_3)}{2k_3} + \frac{(n-Bi)(k_2-k_3) r_2^{2n}}{2k_3}$;
3. $M = -\frac{r_0^n r_1^{-2n}(k_1-k_2) + r_0^{-n}(k_1+k_2)}{r_0^n(k_1+k_2) + r_0^{-n} r_1^{2n}(k_1-k_2)}$;
4. $S = -\frac{(n+Bi)(k_2-k_3) r_2^{-2n}}{2k_3} - \frac{(n-Bi)(k_2+k_3)}{2k_3}$;
5. $K = \frac{2k_1}{\pi\left(r_0^n(k_1+k_2) + r_0^{-n} r_1^{2n}(k_1-k_2)\right)}$;
6. $H = \frac{(n+Bi)(k_2+k_3)}{2k_3} - \frac{r_2^{2n}(n-Bi)(k_3-k_2)}{2k_3}$;
7. $U = \frac{r_0^n(k_1+k_2) + r_0^{-n} r_1^{2n}(k_1-k_2)}{r_0^n r_1^{-2n}(k_1-k_2) + r_0^{-n}(k_1+k_2)}$;
8. $I = \frac{(n+Bi) r_2^{-2n}(k_3-k_2)}{2k_3} - \frac{(n-Bi)(k_2+k_3)}{2k_3}$;
9. $O = \frac{2k_1}{\pi\left(r_0^n r_1^{-2n}(k_1-k_2) + r_0^{-n}(k_1+k_2)\right)}$.

The zeroth harmonic describes the average component of the temperature field, while the harmonics with $n \geq 1$ capture its angular variations. By enforcing the boundary and interface conditions, a system of linear algebraic equations is obtained for the unknown expansion coefficients.

Consequently, the exact solution is expressed analytically as a Fourier series in the angular coordinate.

Approximate Solution Method

The numerical solution is obtained using the finite difference method combined with the Successive Over-Relaxation (SOR) algorithm. The computational domain is discretized in both the

radial and angular coordinates. Because the cylindrical domain is composed of three layers, individual radial grid spacings are defined for each layer:

$$\Delta r_1 = \frac{r_1 - r_0}{N_1}, \qquad \Delta r_2 = \frac{r_2 - r_1}{N_2}, \qquad \Delta r_3 = \frac{r_3 - r_2}{N_3},$$

The discretization step in the angular coordinate is given by:

$$\Delta\varphi = \frac{2\pi}{M},$$

where N_1, N_2, N_3 are the number of grid points in each layer, and M — denotes the number of grid points in the angular direction.

After discretizing the Laplace equation (1) using central finite differences, the following finite difference equation is obtained for an interior grid point (r_i, φ_j):

$$A_i T_{i-1,j} + B_i T_{i+1,j} + C_i T_{i,j-1} + D_i T_{i,j+1} - E_i T_{i,j} = 0,$$

where the coefficients are defined as follows:

$$A_i = \frac{r_i - \frac{\Delta r_s}{2}}{r_i(\Delta r_s)^2},$$

$$B_i = \frac{r_i + \frac{\Delta r_s}{2}}{r_i(\Delta r_s)^2},$$

$$C_i = D_i = \frac{1}{r_i^2(\Delta\varphi)^2},$$

$$E_i = A_i + B_i + C_i + D_i.$$

Thus, the temperature at the current grid point is updated according to the Gauss–Seidel iteration

$$\widetilde{T}_{i,j} = \frac{A_i T_{i-1,j} + B_i T_{i+1,j} + C_i T_{i,j-1} + D_i T_{i,j+1}}{E_i}.$$

To improve the convergence rate of the iterative procedure, the Successive Over-Relaxation (SOR) method is applied. The corresponding iteration scheme can be expressed as

$$T_{i,j}^{(m+1)} = (1-\omega) T_{i,j}^{(m)} + \omega \widetilde{T}_{i,j},$$

where m is number of iteration, a ω is relaxation parameter. In the present study, the relaxation parameter was set to $\omega = 1.8$.

The iterations were repeated until the following convergence criterion was satisfied:

$$\max_{i,j} \left| T_{i,j}^{(m+1)} - T_{i,j}^{(m)} \right| < \varepsilon,$$

where ε denotes the prescribed convergence tolerance. In all numerical experiments presented in this study, the convergence tolerance was set to $\varepsilon = 10^{-6}$. This value ensured stable convergence of the iterative process while providing sufficient numerical accuracy for comparison with the analytical solution and the experimental measurements.

A convergence study was performed for the relaxation parameter ω in the range $1.0 \le \omega \le 2.0$ with an increment of 0.1. For each value of ω, the number of iterations required to satisfy the convergence criterion $\varepsilon = 10^{-6}$ was recorded. The results are summarized in Table 1. It can be

observed that the number of iterations decreases as ω increases up to $\omega = 1.8$, while the iterative process becomes unstable and fails to converge for $\omega \geq 1.9$. Therefore, $\omega = 1.8$ was selected for all subsequent numerical computations.

Table 1 - Convergence study of the SOR method for different values of the relaxation parameter ω.

Parameter ω	**Iterations**	**Final residual, K**	**Converged**	**Time, *sec***
1.0	3394	9.99×10^{-7}	Yes	18.45
1.1	2945	9.99×10^{-7}	Yes	15.94
1.2	2546	9.99×10^{-7}	Yes	13.76
1.3	2186	9.98×10^{-7}	Yes	12.10
1.4	1857	9.99×10^{-7}	Yes	10.26
1.5	1554	9.99×10^{-7}	Yes	8.58
1.6	1272	9.96×10^{-7}	Yes	6.98
1.7	1004	9.99×10^{-7}	Yes	5.48
1.8	**748**	$\mathbf{9.96 \times 10^{-7}}$	**Yes**	**4.15**
1.9	416	—	No	2.29
2.0	186	—	No	1.03

The Dirichlet boundary condition (2) is enforced directly at the inner boundary of the cylinder:

$$T_{0,j} = f.$$

At the interfaces $r = r_1$ and $r = r_2$ continuity conditions for temperature and heat flux are imposed. After applying the finite difference approximation, the temperature at the interface is determined from the following expressions

$$T_{N_1,j} = \frac{\frac{k_1}{\Delta r_1} T_{N_1-1,j} + \frac{k_2}{\Delta r_2} T_{N_1+1,j}}{\frac{k_1}{\Delta r_1} + \frac{k_2}{\Delta r_2}},$$

$$T_{N_1+N_2,j} = \frac{\frac{k_2}{\Delta r_2} T_{N_1+N_2-1,j} + \frac{k_3}{\Delta r_3} T_{N_1+N_2+1,j}}{\frac{k_2}{\Delta r_2} + \frac{k_3}{\Delta r_3}}.$$

At the outer boundary, heat exchange with the environment is described by a dimensionless Robin boundary condition. To simplify the formulation, the Biot number is defined as

$$Bi = \frac{hr_3}{k_3},$$

The finite difference approximation of the boundary condition (5) then takes the following form

$$T_{N,j} = \frac{T_{N-1,j} + Bi\Delta r_3 T_a(\varphi_j)}{1 + Bi\Delta r_3}.$$

The periodicity condition with respect to the angular coordinate is implemented as

$$T_{i,0} = T_{i,M}, \qquad T_{i,-1} = T_{i,M-1}.$$

A mesh sensitivity analysis was performed to evaluate the influence of spatial discretization on the numerical solution obtained by the successive over-relaxation (SOR) method. Three computational meshes, $(N_1, N_2, N_3, M) = (18, 18, 18, 64)$, $(20, 20, 20, 72)$, and $(25, 25, 25, 90)$, were

was approximately ±0.3°C. Temperature data were recorded automatically at 10-minute intervals over an extended monitoring period. The experimental configuration, sensor arrangement, and measurement procedure are described in detail in [23].

The numerical model employed in the present study reproduces the same physical configuration and material arrangement. The measured temperatures at the inner and outer boundaries were imposed as boundary conditions, while the thermophysical properties of the three soil layers correspond to those used in the numerical simulations. The experimental measurements were used exclusively for validation of the computed temperature distribution by comparing the predicted and measured temperatures at the observation locations.

The validation data were obtained from an independent laboratory experiment reported in [23], ensuring that the comparison was performed using experimentally measured temperatures rather than synthetic or numerically generated data.

Experimental uncertainty

The experimental validation presented in this study is based on measurements obtained during a collaborative experimental campaign carried out within the same research project as the related investigations reported in [20, 21, 22, 23]. The experimental facility, measurement procedure, and data acquisition protocol were common to these studies, while the present work focuses on the analytical and numerical investigation of the steady-state heat conduction problem.

Temperature measurements were performed using thermocouples installed at predefined locations within the multilayer cylindrical system. The temperature measurements were performed using temperature sensors with a measurement uncertainty of $\pm 0.1^0 C$. The sensor position uncertainty was $\pm 0.5cm$, while the sensor response time was $0.75s$. Following the uncertainty analysis presented in the original experimental study, the total measurement uncertainty was evaluated as

$$\sigma_T = \sqrt{\sigma_m^2 + \sigma_r^2 + \sigma_t^2},$$

where σ_m denotes the sensor measurement uncertainty, σ_r is the uncertainty resulting from the sensor positioning, and σ_t represents the uncertainty associated with the finite sensor response time.

The position-related and temporal uncertainties were estimated as

$$\sigma_r = \frac{\partial T}{\partial r}\delta_r, \quad \sigma_t = \frac{\partial T}{\partial t}\delta_t,$$

where $\delta_r = 0.5cm$ is the uncertainty in the sensor location and $\delta_t = 0.75s$ is the sensor response time. The spatial temperature gradient was evaluated from the numerical solution, while the temporal derivative was estimated from the experimental measurements using finite-difference approximations.

Since the analytical and numerical models developed in the present work are validated against these experimental measurements, the observed discrepancies between the calculated and measured temperatures should be interpreted considering the inherent experimental uncertainty in addition to numerical discretization and model simplifications. The obtained agreement between the analytical solution, the SOR solution, and the experimental data remains within the expected uncertainty range of the experimental measurements, supporting the reliability of the proposed methodology.

Comparison of Temperature Fields

Figure 1 illustrates the temperature distribution obtained from the analytical solution, whereas Figure 2 presents the corresponding numerical results computed using the finite difference method and the SOR algorithm.

considered. For all simulations, the material properties, boundary conditions, relaxation parameter $\omega = 1.8$, and convergence criterion $\varepsilon = 10^{-6}$ were kept unchanged.

The numerical temperatures were compared at the representative radial locations $r = r_0$, $r = r_1$, $r = r_2$, and $r = r_3$ for $\varphi = 0$. The obtained results are summarized in Table 2. As the mesh was refined, only small changes in the numerical temperatures were observed. In particular, the maximum temperature difference between the selected mesh $(20, 20, 20, 72)$ and the finer mesh $(25, 25, 25, 90)$ was approximately 0.025 K, whereas the computational time increased from approximately 4.0 s to 8.6 s. Therefore, the mesh $(20, 20, 20, 72)$ was selected for all subsequent simulations because it provides a suitable balance between computational efficiency and numerical accuracy.

Table 2 - Mesh sensitivity analysis of the numerical solution obtained by the SOR method at $\varphi = 0$.

Mesh	Iterations	Time (s)	$T(r_0)$ (K)	$T(r_1)$ (K)	$T(r_2)$ (K)	$T(r_3)$ (K)
$18 \times 18 \times 18 \times 64$	658	2.860	298.052	291.2563	288.6471	287.4130
$20 \times 20 \times 20 \times 72$	748	3.990	298.052	291.2431	288.6401	287.4093
$25 \times 25 \times 25 \times 90$	1033	8.608	298.052	291.2183	288.6267	287.4024

The discretization of the governing boundary value problem results in a system of linear algebraic equations

$$\mathbf{AT} = \mathbf{F},$$

The resulting system is solved iteratively using the SOR method. The computed numerical solution is then used for comparison with the analytical solution and experimental measurements in order to evaluate the accuracy of the developed mathematical model.

Results and discussion

The accuracy of the proposed numerical method was assessed by comparing the SOR results with the analytical solution presented in Section **??**. To further validate the model, the analytical and numerical temperature distributions were also compared with experimental data obtained from the multilayer cylindrical system. The agreement between the calculated and measured temperatures provides an indication of the reliability of the proposed approaches.

Experimental methodology

The experimental data used for validation were obtained from the laboratory study described in [23]. The experimental setup consisted of a multilayer soil container with thermally insulated side walls to minimize lateral heat losses and ensure that heat transfer occurred predominantly in one direction. The total length of the container was 30 cm, with the interface between the two soil layers located at 15 cm. One end of the container was subjected to heating, while the opposite end exchanged heat with the surrounding air. Temperature measurements at both external boundaries were used to define the boundary conditions of the numerical model, whereas the temperature at the interface was used for validation and comparison with the numerical solution.

Five calibrated temperature sensors were installed along the container. Two sensors were positioned close to the external boundaries to record the ambient and boundary temperatures, while three sensors were embedded inside the soil, including one located exactly at the interface between the two layers. According to the sensor specifications, the measurement uncertainty

Both solutions reveal the same overall heat-transfer behavior. The highest temperatures are observed near the inner boundary, where the heating source is applied. Moving outward through the cylindrical layers, the temperature gradually decreases as heat is conducted across the materials and dissipated to the surrounding environment through convective heat exchange at the outer surface.

A visual comparison of the two temperature fields demonstrates a good level of agreement between the analytical and numerical results. The distributions remain smooth throughout the domain, with no visible oscillations or artificial discontinuities. This confirms the correct implementation of the interface conditions between the layers and indicates that the numerical scheme provides stable and reliable solutions.

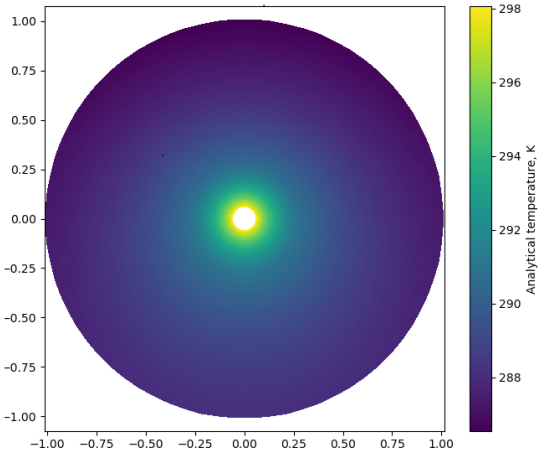


Figure 1 - Temperature distribution obtained from the analytical solution in the multilayer cylin-drical domain.

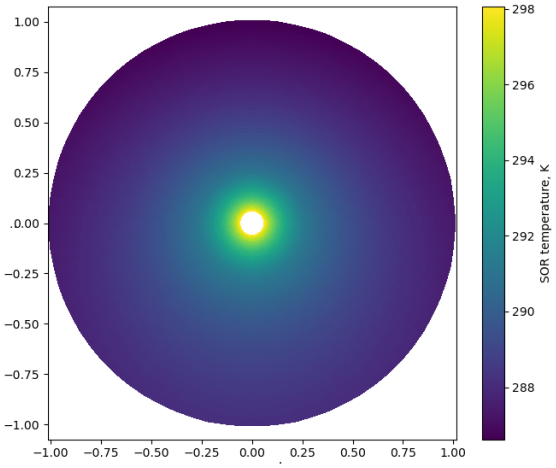


Figure 2 - Temperature distribution obtained using the finite difference method and the SOR algorithm.

Error Analysis Between the Analytical and Numerical Solutions

For a quantitative comparison of the two solutions, the absolute error was evaluated as

$$E(r,\varphi) = |T_{SOR}(r,\varphi) - T_A(r,\varphi)|\,, \tag{29}$$

where T_A and T_{SOR} denote the analytical and numerical solutions, respectively.

The spatial distribution of the absolute error is presented in Figure 3.

The highest differences between the analytical and numerical solutions occur in near the inner boundary, where the temperature changes most rapidly. In this region, even small discretization errors can lead to slightly larger deviations. However, as the distance from the heat source increases, the discrepancy quickly diminishes and remains very small throughout the rest of the domain. Overall, the results demonstrate that the numerical method is capable of accurately capturing the temperature distribution, including regions with pronounced temperature gradients.

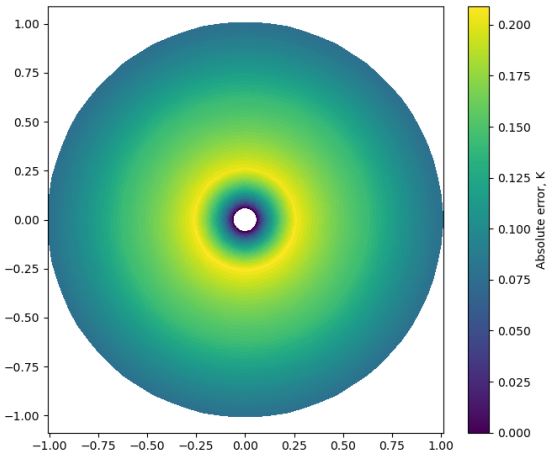


Figure 3 - Distribution of the absolute error between the analytical and numerical solutions.

For a quantitative evaluation of the numerical accuracy, the principal statistical characteristics of the error were calculated and are presented in Table 3.

Table 3 - Statistical error measures between the analytical and numerical solutions.

Metric	**Value**
Mean Absolute Error (K)	0.158568
Root Mean Square Error (K)	0.167308
Maximum Absolute Error (K)	0.241001
Mean Relative Error (%)	0.054654

Overall, the analytical and numerical solutions are in good agreement. The mean relative error remains below 0.05%, and the largest deviation observed in the domain is only 0.241 K. Such a good level of consistency demonstrates that the numerical model successfully captures the heat-transfer behavior of the system and confirms the suitability of the SOR-based finite difference approach for this class of problems.

Comparison of the Analytical Solution, SOR Results, and Experimental Data

To further assess the reliability of the proposed model, the radial temperature distributions obtained from the analytical solution and the numerical SOR method were compared with the experimental measurements. Since temperature data were available only along the direction $\varphi = 0$, the validation was performed for this angular position.

The comparison is shown in Figure 4 where the analytical and numerical temperature profiles are plotted together with the experimental data. The boundaries between the three layers

are marked by vertical dashed lines at $r = r_1$ and $r = r_2$. This representation makes it possible to evaluate how accurately the proposed approaches reproduce the measured temperature distribution across the entire multilayer cylindrical domain.

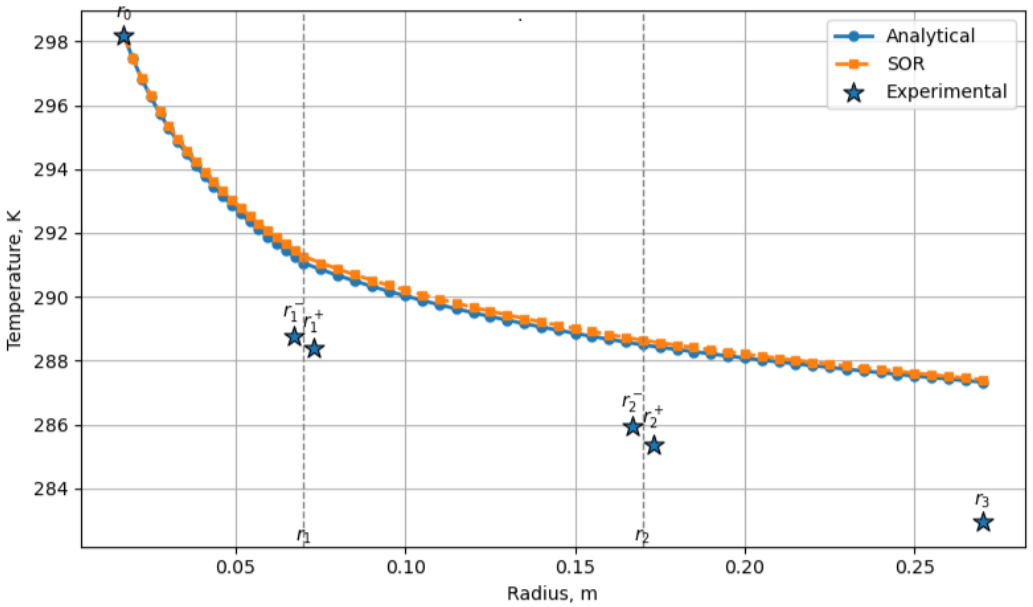


Figure 4 - Comparison of radial temperature profiles obtained from the analytical solution, the numerical SOR solution, and experimental measurements at $\varphi = 0$.

All three datasets follow the same general pattern: the temperature gradually decreases with increasing distance from the heated inner cylinder. The analytical and numerical results almost coincide over the entire domain, demonstrating that the finite difference model accurately reproduces the analytical solution.

Small changes in the slope of the temperature curves can be observed near the interfaces at $r = r_1$ and $r = r_2$. These changes are expected because the thermal conductivities of the adjacent layers differ. Slight deviations between the analytical and numerical solutions are most noticeable close to the interfaces and near the inner boundary, where the temperature gradients are the steepest.

The experimental measurements show good agreement with both calculated solutions and capture the same overall temperature trend. The largest differences between the measured and predicted temperatures occur near the layer boundaries. Such discrepancies may be related to factors that are not fully represented in the mathematical model, including thermal contact resistance, local material inhomogeneities, variations in thermophysical properties, and measurement errors.

To quantify the agreement between the model predictions and the experimental observations, the Mean Absolute Error (MAE) and the Root Mean Square Error (RMSE) were evaluated. The obtained values are summarized in Table 4.

The results presented in Table 4 show that the analytical solution is in slightly closer agreement with the experimental measurements than the numerical solution. The MAE for the analytical model is $2.872K$, compared to $3.024K$ for the SOR-based numerical approach. The same tendency can be observed for the RMSE values.

However, the difference between the two sets of errors is relatively small, remaining below 5%. This suggests that the error associated with the numerical discretization is minor in comparison

with other sources of uncertainty, such as simplifications o f t he m athematical m odel, material variability, and measurement inaccuracies. Overall, the numerical solution reproduces the analytical results with acceptable accuracy and provides a realistic representation of the experimentally observed temperature field.

Table 4 - Comparison of the analytical and numerical models with respect to the experimental data.

Method	**MAE, K**	**RMSE, K**
Analytical Solution	2.872	3.105
SOR Solution	3.024	3.261

Discussion of results

This study investigated the steady-state heat conduction problem in a multilayer cylindrical domain using a finite difference method combined with the Successive Over-Relaxation (SOR) algorithm. The numerical results were compared with both the analytical solution and experimental temperature measurements.

A comparison between the analytical and numerical solutions showed a good agreement. The mean relative error remained below 0.054%, while the maximum deviation did not exceed $0.241K$. Such small differences indicate that the proposed discretization accurately captures the temperature field and that the SOR algorithm provides stable and efficient convergence.

A good agreement between the calculated and measured temperature distributions was observed. Although the analytical solution yielded slightly lower error values, the difference between the analytical and numerical results was small relative to the uncertainties associated with material properties, simplifying assumptions of the model, and measurement errors.

The close correspondence between the two solutions suggests that the numerical approximation introduces only a minor additional error. These results indicate that the finite difference–SOR approach is suitable for problems where analytical solutions are difficult to derive.

The developed numerical method can be used to model heat transfer in multilayer cylindrical structures. In particular, it offers a useful framework for the analysis of direct and inverse heat conduction problems in multilayer media with complex geometries and boundary conditions.

Conclusion

This paper considered a steady-state heat conduction problem in a multilayer cylindrical domain subjected to non-uniform boundary conditions. An analytical solution was obtained by applying the method of separation of variables together with a Fourier series representation. The developed solution describes the temperature field in each layer of the cylindrical structure while satisfying the continuity conditions at the interfaces between adjacent materials.

To solve the same problem numerically, a finite difference formulation of the Laplace equation in polar coordinates was constructed. The resulting system of algebraic equations was solved using the Successive Over-Relaxation (SOR) method. The numerical model accounts for the multilayer nature of the domain, variations in thermal conductivity between layers, and convective heat exchange at the outer surface. For the considered example, the iterative process converged after 748 iterations.

The numerical results were found to be in very close agreement with the analytical solution. The Mean Absolute Error (MAE) was $0.158K$, the Root Mean Square Error (RMSE) was $0.167K$, and the maximum deviation did not exceed 0.209 K. The mean relative error remained below

0.05%, confirming the good accuracy of the developed finite difference scheme and the correct implementation of the SOR method.

The developed models were also validated using experimental temperature measurements obtained from a multilayer cylindrical system. Both the analytical and numerical solutions captured the overall behavior of the measured temperature field and showed good agreement with the experimental data. The MAE relative to the measurements was $2.872K$ for the analytical solution and $3.024K$ for the numerical solution. The remaining differences can be explained by factors that are difficult to fully account for in the mathematical model, including thermal contact resistance at layer interfaces, material inhomogeneities, and experimental uncertainties.

The obtained results demonstrate that the SOR-based finite difference approach provides an accurate and computationally efficient tool for analyzing heat transfer in multilayer cylindrical structures. The method can be used in the study of thermal processes in pipelines, insulation systems, geothermal applications, and other engineering systems with layered cylindrical geometries.

Future research may be directed toward transient heat conduction problems, models with temperature-dependent material properties, and inverse problems aimed at identifying unknown thermophysical parameters from experimental observations.

REFERENCES

1 Yang B., Liu S. Closed-form analytical solutions of transient heat conduction in hollow composite cylinders with any number of layers. International Journal of Heat and Mass Transfer, 2017, 108, 907–917. https://doi.org/10.1016/j.ijheatmasstransfer.2016.12.020

2 Kayhani M. H., Norouzi M., Amiri Delouei A. A general analytical solution for heat conduction in cylindrical multilayer composite laminates. International Journal of Thermal Sciences, 2012, 52(1), 73–82. https://doi.org/10.1016/j.ijthermalsci.2011.09.002

3 Amiri Delouei A., Jing D. A comprehensive review on multi-dimensional heat conduction of multi-layer and composite structures: Analytical solutions. Journal of Thermal Science, 2021, 30(6), 1875–1907. https://doi.org/10.1007/s11630-021-1517-1.

4 Lu X., Tervola P., Viljanen M. Transient analytical solution to heat conduction in multi-dimensional composite cylinder slab. International Journal of Heat and Mass Transfer, 2006, 49(5-6), 1107–1114. https://doi.org/10.1016/j.ijheatmasstransfer.2005.08.033.

5 Mansour S., Canot É., Muhieddine M. Identification of the Thermophysical Properties of the Soil by Inverse Problem. Journal of Heat Transfer, 2016, 138(9), 091010. https://doi.org/10.1115/1.4032947.

6 AMIRI DELOUEI, A., EMAMIAN, A., SAJJADI, H. et al. A Comprehensive Review on Multi-Dimensional Heat Conduction of Multi-Layer and Composite Structures: Analytical Solutions. J. Therm. Sci. 30, 1875–1907 (2021). https://doi.org/10.1007/s11630-021-1517-1.

7 Satybaldina A., Ydyrys A. Analytical solution of steady-state heat equation in polar coordinates for multilayer soils. In Proceedings of the IEEE 5th International Conference on Smart Information Systems and Technologies (SIST), Astana, Kazakhstan, 14–16 May 2025; IEEE: Piscataway, NJ, USA, 2025; pp. 1–5, https://doi.org/10.1109/SIST61657.2025.11139181.

8 Rysbaiuly B., Ydyrys A.Z., Satybaldina A.N. Inverse problem for the 2D Laplace equation in polar coordinates. Vestn. Natl. Eng. Acad. Repub. Kazakhst. 2024, 3, 342–350, https://doi.org/10.47533/2024.1606-146X.73.

9 Satybaldina A, Rysbaiuly B, Ydyrys A, Alpar S, Rysbayeva K, Sakabekov A. Inverse Problem of Heat Conduction in a Multilayer Cylindrical System. Symmetry. 2026; 18(6):908. https://doi.org/10.3390/sym18060908.

10 Carslaw H.S., Jaeger J.C., Conduction of Heat in Solids, 2nd ed., Oxford University Press: Oxford, UK, 1959.

11 Özisik M.N., Heat Conduction, 2nd ed., Wiley: New York, NY, USA, 1993.

12 Koleva M.N., Vulkov L.G., Computational Solution of an Inverse Boundary-Value Problem for Heat Transfer in a Composite Material. Appl. Sci. 2025, 15, 10230. https://doi.org/10.3390/app151810230.

13 Bollati J., Natale M., Semitiel J.A., Tarzia D.A., Relationship among solutions for three-phase change problems with Robin, Dirichlet and Neumann boundary conditions. Int. Commun. Heat Mass Transf. 2025, 165, 108966. https://doi.org/10.1016/j.icheatmasstransfer.2025.108966.

14 Maruši´c-Paloka E., Pažanin I., The Robin boundary condition for modelling heat transfer. Proc. R. Soc. A 2024, 480, 20230850.

15 Pyatkov S.G., Identification of the heat transfer coefficient using an inverse heat conduction model. arXiv 2024, arXiv:2401.01551. https://doi.org/10.48550/arXiv.2401.01551.

16 Price, J.F. Dimensional Analysis of Models and Data Sets. *Am. J. Phys.* **2003**, *71*, 437–447. https://doi.org/10.1119/1.1533057.

17 Hancock, M.J. *The 1-D Heat Equation*; MIT OpenCourseWare: Cambridge, MA, USA, 2006.

18 Incropera, F.P., DeWitt, D.P., Bergman, T.L., Lavine, A.S. *Fundamentals of Heat and Mass Transfer*, 6th ed., Wiley: Hoboken, NJ, USA, 2007.

19 Deconinck B., Pelloni B., Sheils N.E., Non-steady-state heat conduction in composite walls. Proc. R. Soc. A 2014, 470, 20130605. https://doi.org/10.1098/rspa.2013.0605.

20 Rysbayeva N., Alpar S., Rysbaiuly B. *Inverse Problem for the Moisture Transfer Equation: Development of a Method for Finding the Unknown Parameter and Proof of the Convergence of the Iterative Process*, Symmetry. 2024; 16(11):1444. https://doi.org/10.3390/sym16111444

21 Alpar S., Rysbaiuly B. *Determination of thermophysical characteristics in a nonlinear inverse heat transfer problem*, Applied Mathematics and Computation. Volume 440, 2023, https://doi.org/10.1016/j.amc.2022.127656

22 Rysbaiuly B., Alpar S. *Experimental Data and the Nonlinear Inverse Problem of Heat Transfer*, International Journal of Mathematics and Physics. Volume 13, 2022, 10.26577/ijmph.2022.v13.i1.01

23 Rysbaiuly B., Alpar S. *Solution of a nonlinear heat transfer problem based on experimental data*, KazNU Bulletin. Mathematics, Mechanics, Computer Science Series. Volume 114, 2022, 10.26577/JMMCS.2022.v114.i2.014

[1,2]***Сатыбалдина А.Н.**,
Магистр технических наук, Сениор лектор,
ORCID ID: 0000-0002-5596-0936,
*e-mail: aigul1191@gmail.com

[3] **Ыдырыс А.Ж.**,
PhD по специальности Математика, Ассоциированный профессор,
ORCID ID: 0009-0002-4284-9446,
e-mail: a.ydyrys@iitu.edu.kz

[1] Евразийский Национальный Университет имени Л.Н.Гумилева, Астана, Казахстан
[2] Казахстанско-Британский Технический Университет, Алматы, Казахстан
[3] Международный Университет Информационных Технологий, Алматы, Казахстан

АНАЛИТИЧЕСКОЕ И ПРИБЛИЖЕННОЕ РЕШЕНИЕ ДВУМЕРНОГО УРАВНЕНИЯ ЛАПЛАСА В ЦИЛИНДРИЧЕСКИХ КООРДИНАТАХ

Аннотация

В данной работе исследуется стационарная задача теплопроводности в многослойной цилиндрической области с неоднородными граничными условиями. Рассмотрены два подхода к решению прямой задачи: аналитический метод, основанный на разделении переменных и разложении в ряд Фурье, и численный метод, основанный на конечно-разностной аппроксимации в сочетании с алгоритмом последовательной верхней релаксации (SOR). Получено точное аналитическое решение уравнения Лапласа в полярных координатах для трёхслойной цилиндрической системы с условиями сопряжения на границах раздела слоёв и конвективным теплообменом на внешней границе. Для численного решения разработана конечно-разностная схема, а возникающая система линейных алгебраических уравнений решается итерационным методом SOR. Точность численного подхода оценена путём сравнения с аналитическим решением и экспериментальными измерениями температуры. Полученные результаты демонстрируют отличное согласование аналитического и численного решений. Средняя абсолютная ошибка между двумя подходами составляет $0.158K$, среднеквадратическая ошибка — $0.167K$, а максимальная абсолютная ошибка не превышает $0.241K$. Экспериментальная валидация показала, что обе модели корректно воспроизводят общее распределение температуры в многослойной цилиндрической системе. Средняя абсолютная ошибка относительно экспериментальных данных составляет $2.872K$ для аналитического решения и $3.024K$ для решения, полученного методом SOR. Проведённый анализ подтверждает высокую точность и устойчивость разработанного конечно-разностного алгоритма и демонстрирует его применимость для моделирования процессов теплопереноса в многослойных цилиндрических конструкциях. Предложенный подход может быть использован при тепловом анализе трубопроводов, геотермальных систем, теплоизоляционных конструкций и других инженерных объектов, содержащих многослойные среды.

Ключевые слова: теплопроводность; уравнение Лапласа; многослойная цилиндрическая область; аналитическое решение; метод конечных разностей; метод последовательной верхней релаксации (SOR); распределение температуры; экспериментальная валидация; полярные координаты; тепловое моделирование.

[1,2]***Сатыбалдина А.Н.**,
магистр, Сениор лектор,
ORCID ID: 0000-0002-5596-0936,
*e-mail: aigul1191@gmail.com

[3] **Ыдырыс А.Ж.**,
PhD, Қауымдастырылған профессор,
ORCID ID: 0009-0002-4284-9446,
e-mail: a.ydyrys@iitu.edu.kz

[1] Л.Н. Гумилева атындағы Еуразия ұлттық университеті, Астана қ., Қазақстан
[2] Қазақстан-Британ техникалық университеті, Алматы қ., Қазақстан
[3] Халықаралық ақпараттық технологиялар университеті, Алматы қ., Қазақстан

ЦИЛИНДРЛІК КООРДИНАТАЛАРДАҒЫ ЕКІ ӨЛШЕМДІ ЛАПЛАС ТЕҢДЕУІНІҢ АНАЛИТИКАЛЫҚ ЖӘНЕ САНДЫҚ ШЕШІМІ

Аңдатпа

Бұл жұмыста біртекті емес шекаралық шарттары бар көпқабатты цилиндрлік облыстағы стационарлық жылуөткізгіштік есебі зерттеледі. Тура есепті шешудің екі тәсілі қарастырылады: айнымалыларды жіктеу және Фурье қатарына жіктеу әдістеріне негізделген аналитикалық тәсіл және соңғы айырымдық аппроксимация мен тізбекті жоғарғы релаксация (SOR) алгоритмін пайдаланатын сандық тәсіл. Қабаттар арасындағы түйісу шарттары және сыртқы шекарадағы конвективтік жылуалмасу ескерілген үш қабатты цилиндрлік жүйе үшін полярлық координаталардағы Лаплас теңдеуінің дәл аналитикалық шешімі алынды. Сандық шешім үшін соңғы айырымдық схема құрылып, алынған сызықтық алгебралық теңдеулер жүйесі SOR итерациялық әдісімен шешілді. Сандық тәсілдің дәлдігі аналитикалық шешіммен және температураның эксперименттік өлшемдерімен салыстыру арқылы бағаланды. Алынған нәтижелер аналитикалық және сандық шешімдердің өте жақ-сы сәйкестігін көрсетті. Екі тәсіл арасындағы орташа абсолюттік қате $0.158K$, орташа квадраттық қате $0.167K$, ал максималды абсолюттік қате $0.241K$. Эксперименттік тексеру екі модельдің де көпқабатты цилиндрлік жүйедегі температураның жалпы таралуын дұрыс сипаттайтынын көрсетті. Эксперименттік деректерге қатысты орташа абсолюттік қате аналитикалық шешім үшін $2.872K$, ал SOR шешімі үшін $3.024K$ құрайды. Жүргізілген талдау ұсынылған соңғы айырымдық алгоритмнің жоғары дәлдігі мен орнықтылығын растайды және оның көпқабатты цилиндрлік құрылымдардағы жылуалмасу процестерін модельдеуде тиімді қолданылатынын көрсетеді. Ұсынылған тәсіл құбыржолдардың, геотермалдық жүйелердің, жылуоқшаулау құрылымдарының және көпқабатты орталарды қамтитын басқа да инженерлік объектілердің жылулық талдауында қолданылуы мүмкін.

Түйін сөздер: жылуөткізгіштік, Лаплас теңдеуі, көпқабатты цилиндрлік облыс, аналитикалық шешім, соңғы айырымдар әдісі, тізбекті жоғарғы релаксация әдісі (SOR), температураның таралуы, эксперименттік валидация, полярлық координаталар, жылулық модельдеу.

ӘОЖ 517.956
ҒТАХР 27.31.15

https://doi.org/10.55452/1998-6688-2026-23-3-124-143

[1]*Қошанов Б.Д.,
ф.-м.ғ.д., профессор, бас ғылыми қызметкер
ORCID ID: 0000-0002-0784-5183,
*e-mail: koshanov@math.kz
[2]Тұрғанбек Ұ.,
магистрант, ORCID ID: 0009-0000-5894-1194,
e-mail: Ulzya03@mail.ru
[2]Ерхан А.Ж.,
магистрант, ORCID ID: 0009-0001-5552-8908,
e-mail: ainur.erkhan@icloud.com

[1]Математика және математикалық модельдеу институты, Алматы қ., Қазақстан
[2]Әл-Фараби атындағы Қазақ ұлттық университеті, Алматы қ., Қазақстан

КӨПӨЛШЕМДІ ШАРДА ПОЛИГАРМОНИКАЛЫҚ ТЕҢДЕУ ҮШІН БІР ШЕТТІК ЕСЕПТІҢ ШЕШІМДІЛІГІ ТУРАЛЫ

Аңдатпа

Эллиптикалық теңдеулер үшін шеттік есептерді зерттеу қажеттілігі гидродинамика, электростатика, механика, жылуөткізгіштік, серпімділік теориясы және кванттық физика процестерін теориялық тұрғыдан зерттеудегі көптеген практикалық қолданылуларымен негізделеді. Мысалы, электростатикалық өріс потенциалының таралуы Пуассон теңдеуі арқылы сипатталады, ал аз иілетін жұқа пластиналардың тербелістері бигармоникалық теңдеулер арқылы сипатталады. Бұл жұмыста бірлік шарда полигармоникалық теңдеу үшін бір шеттік есептің, яғни ізделінді функцияның бірінші нормал туындысынан бастап $m-1$-ші ретті туындысына дейін қатар берілсе және соңғысына $m+1$-ші ретті туындысы берілген есеп шешімділікке зерттеледі. Осы есепті шешу үшін бастапқы есепті арнайы интегралды-дифференциалды операторлардың көмегімен Нейман есебіне алып келеміз. Ал Нейман есебін интегралды-дифференциалды операторлардың көмегімен Дирихле есебіне алып келеміз. Дирихле есебінің шешімі Грин функциясының көмегімен және Альманси өрнегімен өрнектелетіндігін қолданамыз. Осы өрнектердің нәтижесінде бастапқы есептің шешімділігінің қажетті және жеткілікті шарты табылады.

Түйін сөздер: полигармоникалық теңдеу, Нейман есебі, Дирихле есебі, интегралды-дифференциалды операторлар, шешімділіктің қажетті және жеткілікті шарты.

Кіріспе

Эллиптикалық теңдеулер үшін шеттік есептердің шешімдерін ұсынудың тиімді әдістерінің бірі – есептің Грин функциясын құруға негізделген әдіс болып табылады. Әртүрлі классикалық шеттік есептер үшін Грин функциясын айқын түрде құруға көптеген жұмыстар арналған.

Бірлік шардағы полигармоникалық теңдеу үшін Дирихле есебінің Грин функциясының айқын түрі әртүрлі тәсілдермен [1-5] жұмыстарында құрылған.

[6] жұмыста шарда Лаплас операторы үшін Робен есебінің Грин функциясы құрылған, ал [7] жұмыста полигармоникалық теңдеуі үшін Дирихле есебінің полиномиалды шешімі құрылған.

[8, 9] жұмыстарында бигармоникалық теңдеу үшін инволюциясы бар кейбір локалды және локалды емес шеттік есептердің шешімділігі зерттеліп, олардың Грин функциялары құрылған. Шардағы бигармоникалық теңдеу үшін кейбір шеттік есептердің шешімділік шарттары [10] жұмыста алынған.

[11] жұмысында біртекті полигармоникалық теңдеу үшін Дирихле және Нейман есептерінің шешімдері Грин функциясын қолданбай-ақ табылған. [12] жұмыста Навье [13] және Рикье--Нейман есептері үшін бигармоникалық теңдеудің шардағы Грин функциялары келтірілген, ал [14] жұмысында осындай есептердің полигармоникалық теңдеу үшін Грин функциялары құрылған.

[15,16] жұмыстарында біртексіз үшгармоникалық теңдеу үшін Дирихле-2 есебінің Грин функциясы құрылған. Оның ішінде полигармоникалық теңдеулер үшін іргелі шешімге байланысты тың мәліметтер келтірілген. [17] жұмысында көпөлшемді бірлік шарда үшгармоникалық теңдеу үшін жалпы шарттары бар шеттік есептердің шешімділігі зерттелген, оған қосымша Альманси өрнегінің дұрыстығы дәлелденген.

[18,19] жұмыстарында полигармоникалық теңдеу үшін кейбір шеттік есептердің шешімділік шарттары табылып, бигармоникалық және үшгармоникалық теңдеулер үшін мысалдар келтірілген.

$$\Omega = \{x \in R^n : |x| < 1\}$$

бірлік шар, ал

$$\partial\Omega = \{x \in R^n : |x| = 1\}$$

бірлік сфера болсын және m - оң бүтін сан болсын. Ω облысында келесі Нейман шеттік есебі Б.Қ.Түрметов пен Р.Р.Ашуровтың [22] жұмысында қарастырылған:

$$(-\Delta)^m u(x) = g(x), \quad x \in \Omega \tag{1}$$

$$\frac{\partial^k u}{\partial \nu^k}(x) = \varphi_k(x), \quad k = 1, 2, \ldots, m, \quad x \in \partial\Omega \tag{2}$$

мұндағы ν - $\partial\Omega$ сферасына түсірілген сыртқы бірлік нормаль вектор, $g(x)$ және $\varphi_k(x)$ - берілген функциялар; бұл функциялар жеткілікті түрде тегіс деп есептейміз және әрі қарай олардың тегістігіне тоқталмаймыз.

$u(x) \in C^{2m}(\Omega) \cap C^{m+1}(\overline{\Omega})$ функциясы (1), (2) есептердің классикалық мағынада шарттарын қанағаттандырса, осы есептің шешімі деп аталады.

Бұрыннан белгілі (мысалы, [20]-ді қараңыз), тіпті $m = 1$ болған жағдайда да (1), (2) есептердің кез келген (тіпті тегіс) $g(x)$ және $\varphi_k(x)$ функциялары үшін шешімі бола бермейді; Пуассон теңдеуі жағдайында Нейман есебінің шешімді болуы үшін қажетті және жеткілікті шарт:

$$\int_\Omega g(x)\,dx = \int_{\partial\Omega} \varphi_1(x)\,dS_x.$$

Б.Е.Кангужин мен Б.Д.Қошановтың [18] жұмысында, атап айтқанда, ($m = 2$) болған жағдайда (1), (2) есебінің шешімді болуы үшін қажетті және жеткілікті шарттың келесі түрде болатынын көрсетті:

$$\int_{\partial\Omega}\left\{\varphi_1(x)-\varphi_2(x)+\int_{\Omega} d_{2,n}(4-n)\right.$$
$$\left.\times\left[(2-n)|x-y|^{-n}(1-(x,y))^2+|x-y|^{-n}(x,y)\right]g(y)\,dy\right\}dS_x=0,$$

мұндағы (x,y) - R^n-дегі скаляр көбейтінді, ал

$$d_{2,n}=\frac{\Gamma\left(\frac{n}{2}-2\right)}{16\pi^{\frac{n}{2}}}.$$

[21] жұмыстың авторлары бұл шартты басқа түрде ұсынды, оны оңай тексеруге болады:

$$\int_{\Omega}\frac{1-|x|^2}{2}g(x)\,dx=\int_{\partial\Omega}\left[\varphi_2(x)-\varphi_1(x)\right]\,dS_x.$$

Жоғарыда аталған [18] жұмыста авторлар (1), (2) Нейман есебі үшін кез келген m жағдайында да шешімділік шартын тапты (қараңыз: [18], Теорема 4.2). Бұл шарт $m\times m$ өлшемді матрицаның анықтауышының нөлге тең болуынан туындайды, оның бір бағаны келесі интегралдардан тұрады:

$$\int_{\partial\Omega}\left[\varphi_k(x)-\frac{\partial^k}{\partial\nu^k}\left(\varepsilon_{m,n}*g(x)\right)\right]\,dS_x,\quad \varepsilon_{m,n}=d_{m,n}|x|^{2m-n},$$

ал $d_{m,n}$ - белгілі тұрақтылар. Айта кету керек, нәтижесінде алынған теңдеуді тексеру қиынға соғады.

(1), (2) есебі Б.Қ.Түрметов пен Р.Р.Ашуровтың [22] жұмысында толық зерттелді. Сол жұмыста осы Нейман есебінің шешімділігінің қажетті және жеткілікті шарты табылды.

Жоғарыда аталған ескертпелер [22] жұмысында толық шешілген, яғни бірлік шарда полигармоникалық теңдеу үшін (1), (2) Нейман есебінің шешімділік шарты алынған.

[23] жұмысында ұқсас әдіс бөлшек ретті шекаралық операторы бар Пуассон теңдеуі үшін шеттік есепті шешуде қолданылған.

Бұл жұмыста

$$\Omega=\{x\in R^n:|x|<1\}$$

бірлік шарда полигармоникалық теңдеу үшін келесі шеттік есеп қарастырылады:

$$(-\Delta)^m u(x)=g(x),\quad x\in\Omega \tag{3}$$

$$\frac{\partial^k u}{\partial\nu^k}(x)=\varphi_k(x),\quad k=1,2,\ldots,m-1,\quad \frac{\partial^{m+1}u}{\partial\nu^{m+1}}(x)=\varphi_m(x),\quad x\in\partial\Omega \tag{4}$$

мұндағы $\dfrac{\partial}{\partial\nu}$ - $\partial\Omega$ сферасына түсірілген сыртқы бірлік нормаль бойынша алынған туынды.

Мұндай шеттік есептерді зерттеу алдында қарастырылған есептерге мүлдем ұқсамайды. Сол себептен де полигармоникалық теңдеу үшін (3),(4) шеттік есебін зерттеу өте маңызды. Дербес жағдайда, бигармоникалық және үшгармоникалық теңдеулер үшін осы есептерге қысқаша К-13 және К-124 белгілеулерін қолданамыз. Бұл есептер қолданыс жағынан маңызды. Мысал ретінде гидромеханиканың сызықтандырылған Стокс жүйесіне қатысты қолданбасын келтіруге болады.

Осы жұмыстың негізгі мақсаты - (3),(4)есебінің шешімділік шартын неғұрлым қарапайым түрде табу. Айта кету керек, біздің зерттеуімізде (3),(4)шеттік есебі үшін негізінен полигармоникалық теңдеуге арналған Дирихле есебінің Грин функциясы және Альманси өрнегі қолданылады.

Материалдар мен әдістер.
$\Gamma_c[u], \Gamma_c^{-1}[u]$ интегралды-дифференциалдық операторлардың қасиеттері

Ω--облысында $u(x)$-жеткілікті дәрежеде тегіс функция болсын. Төмендегідей операторларды қарастырайық:

$$\Gamma_c[u](x) = \left(r\frac{\partial}{\partial r} + c\right) u(x), \qquad \Gamma_c^{-1}[u](x) = \int_0^1 t^{c-1}u(tx)\,dt, \tag{5}$$

мұндағы $r = |x|$ және $c \geq 0$ тұрақты шама. Γ_0^{-1} операторы $u(0) \neq 0$ болатын $u(x)$ функциялары үшін анықталмағанын ескеруміз керек.

Көпөлшемді шардағы гармоникалық функциялар класында $c > 0$ болғанда Γ_c және Γ_c^{-1} операторларының қасиеттері [24] мақалада зерттелген.

Лемма 1. [24] $u(x)$- тегіс функция болсын. Онда кез келген $x \in \Omega$ үшін келесілер орындалады

1) егер $c > 0$ болса, онда

$$\Gamma_c\left[\Gamma_c^{-1}[u]\right](x) = \Gamma_c^{-1}\left[\Gamma_c[u]\right](x) = u(x); \tag{6}$$

2) егер $c = 0$ болса, онда

$$\Gamma_0^{-1}\left[\Gamma_0[u]\right](x) = u(x) - u(0); \tag{7}$$

3) егер $c = 0$ және $u(0) = 0$ болса, онда

$$\Gamma_0\left[\Gamma_0^{-1}[u]\right](x) = u(x). \tag{8}$$

Дәлелдеуі. $c \geq 0$ болсын. Онда

$$\int_0^1 \frac{d}{dt}\left[t^c u(tx)\right] dt = \int_0^1 t^{c-1}\left[cu(tx) + t\frac{d}{dt}u(tx)\right] dt = \int_0^1 t^{c-1}\Gamma_c[u](tx)\,dt.$$

Сондықтан, егер $c > 0$ болса, онда

$$u(x) = \int_0^1 t^{c-1}\Gamma_c[u](tx)\,dt = \Gamma_c^{-1}\left[\Gamma_c[u]\right](x),$$

және егер $c = 0$ болса, онда

$$u(x) - u(0) = \int_0^1 t^{-1}\Gamma_0[u](tx)\,dt. \tag{9}$$

Демек, (7)-ші теңдік және (6)-шы теңдік дәлелденді.

Жоғарыда атап өткендей, егер $u(0) = 0$ болса, онда $\Gamma_0^{-1}[u]$ өрнегі анықталады. Енді осы өрнекке Γ_0 операторын қолданамыз. Сонда

$$\Gamma_0 \left[\Gamma_0^{-1}[u]\right](x) = \int_0^1 t^{-1}\Gamma_0[u](tx)\,dt.$$

Бірақ (9) теңдігіне және $u(0) = 0$ шартына байланысты соңғы өрнек $u(x)$-ке тең. Демек, (8) теңдігі дәлелденді. (6)-тегі бірінші теңдікті дәл осылай дәлелдеуге болады.

Келесі тұжырымды тікелей есептеулер арқылы дәлелдеуге болады.

Лемма 2. [24] $u(x)$- тегіс функция болсын. Онда кез келген $x \in \Omega$ үшін келесілер орындалады

1) егер $c \geq 0$ болса, онда

$$\Delta\Gamma_c[u](x) = \Gamma_{c+2}[\Delta u](x);$$

2) егер $c > 0$ болса, онда

$$\Delta\Gamma_c^{-1}[u](x) = \Gamma_{c+2}^{-1}[\Delta u](x);$$

3) егер $c = 0$ және $u(0) = 0$ болса, онда

$$\Delta\Gamma_0^{-1}[u](x) = \Gamma_2^{-1}[\Delta u](x).$$

Салдар 1. $u(x)$ - тегіс функция болсын. Онда кез келген $x \in \Omega$ үшін:

(1) егер $c \geq 0$ болса, онда

$$\Delta^m\Gamma_c[u](x) = \Gamma_{c+2m}\left[\Delta^m u\right](x); \tag{10}$$

(2) егер $c > 0$, немесе $c = 0$ және $u(0) = 0$ болса, онда

$$\Delta^m\Gamma_c^{-1}[u](x) = \Gamma_{c+2m}^{-1}\left[\Delta^m u\right](x). \tag{11}$$

3. Дирихле есебінің шешімдерінің кейбір қасиеттері

$v(x)$ - келесі Дирихле есебінің шешімі болсын:

$$\begin{cases} (-\Delta)^m v(x) = g_1(x), \quad x \in \Omega, \\ \dfrac{\partial^{k-1} v}{\partial \nu^{k-1}}(x) = 0, \quad k = 1, 2, \ldots, m, \quad x \in \partial\Omega. \end{cases} \tag{12}$$

Бұрыннан белгілі (мысалы, [3--7] қараңыз) жайт, егер $g_1(x)$ жеткілікті тегіс функция болса, онда (12) есептің шешімі бар, жалғыз және келесі түрде жазылады:

$$v(x) = \int_\Omega G_{m,n}(x, y) g_1(y)\,dy, \tag{13}$$

мұндағы $G_{m,n}(x, y)$ - (12) Дирихле есебінің Грин функциясы.

Бұл жерде Грин функциясының келесі айқын түрін қолданамыз [4,5]:

Егер n тақ болса, немесе жұп болып, $n > 2m$ болса, онда

$$G_{m,n}(x,y) = d_{m,n}\Bigg[|x-y|^{2m-n} - \left||x|y - \frac{y}{|y|}\right|^{2m-n} - \sum_{k=1}^{m-1} \frac{(-1)^k}{k!}\left(m-\frac{n}{2}\right)\cdots\left(m-\frac{n}{2}-k+1\right) \times \left||x|y - \frac{y}{|y|}\right|^{2m-n-2k} (1-|x|^2)^k(1-|y|^2)^k\Bigg],$$

мұндағы

$$d_{m,n} = \frac{(-1)^m \Gamma\left(\frac{n}{2}-m\right)}{\pi^{\frac{n}{2}} 4^m (m-1)!};$$

Егер n жұп және $n \le 2m$ болса, онда

$$G_{m,n}(x,y) = d_{m,n}\Bigg[|x-y|^{2m-n}\left(\ln|x-y|^2 - \ln\left||x|y - \frac{y}{|y|}\right|^2\right) + \sum_{k=1}^{m-1}\left||x|y - \frac{y}{|y|}\right|^{2m-n-2k}(1-|x|^2)^k(1-|y|^2)^k \times \sum_{j=\max(k-\frac{n}{2},0)}^{\min(m-\frac{n}{2},k-1)} \frac{(-1)^j}{k-j} C^j_{m-\frac{n}{2}}\Bigg],$$

мұндағы

$$d_{m,n} = \frac{(-1)^{m-\frac{n}{2}}}{2\pi^{\frac{n}{2}} 4^m \left(m-\frac{n}{2}\right)!(m-1)!}.$$

Лемма 3. (12) Дирихле есебінде $g_1(x) = \Gamma_{2m}[g](x)$ болсын, ал $v(x)$ --- осы есептің жалғыз шешімі болсын. Онда $v(0) = 0$ шартының орындалуы келесі шарттың орындалуымен парапар:

$$\int_\Omega (1-|x|^2)^{m-1} g(x)\,dx = 0. \tag{14}$$

Дәлелдеуі. $v(x)$ --- (12) есебінің шешімі болсын. Онда ол (13) формуламен беріледі. Грин функциясының айқын түрін қолдану үшін n тақ немесе $n > 2m$ болатын жұп жағдайды қарастырамыз (қалған жағдайлар ұқсас дәлелденеді). Сондықтан, егер $v(0) = 0$ болса, онда (13)-ден:

$$\int_\Omega \Bigg[|y|^{2m-n} - 1 - \sum_{k=1}^{m-1}\frac{(-1)^k}{k!}\left(m-\frac{n}{2}\right)\cdots\left(m-\frac{n}{2}-k+1\right)(1-|y|^2)^k\Bigg] g_1(y)\,dy = 0.$$

Енді $\rho = |y|$, $\xi = \dfrac{y}{|y|}$ деп белгілейік. Сонда интеграл:

$$\int_{|\xi|=1}\int_0^1 \rho^{n-1}\left[\rho^{2m-n} - 1 - \sum_{k=1}^{m-1}\frac{(-1)^k}{k!}\left(m-\frac{n}{2}\right)\cdots\left(m-\frac{n}{2}-k+1\right)(1-\rho^2)^k\right] \times g_1(\rho,\xi)\,d\rho\,d\xi = \int_{|\xi|=1} I(\xi)\,d\xi.$$

Енді $I(\xi)$ ішкі интегралын қарастырайық. $g_1(\rho,\xi) = \left(\rho\dfrac{\partial}{\partial\rho} + 2m\right) g(\rho,\xi)$ екенін ескеріп, екі интеграл енгіземіз:

$$I_1(\xi) = \int_0^1 \rho^{n-1}\Bigg[2m\rho^{2m-n} - 2m - 2m\sum_{k=1}^{m-1}\frac{(-1)^k}{k!}\left(m-\frac{n}{2}\right)\cdots\left(m-\frac{n}{2}-k+1\right)(1-\rho^2)^k\Bigg] g(\rho,\xi)\,d\rho. \quad (1)$$

$$I_2(\xi) = \int_0^1 \rho^{n}\left[\rho^{2m-n} - 1 - \sum_{k=1}^{m-1}\frac{(-1)^k}{k!}\left(m-\frac{n}{2}\right)\cdots\left(m-\frac{n}{2}-k+1\right)(1-\rho^2)^k\right] \times \frac{\partial}{\partial\rho} g(\rho,\xi)\,d\rho.$$

Айқын түрде, $I(\xi) = I_1(\xi) + I_2(\xi)$.

Енді $I_2(\xi)$ интегралын бөліп интегралдау арқылы есептейміз:

$$I_2(\xi) = \int_0^1 \rho^{n-1}\Bigg[-n\rho^{2m-n} + n + (2m-n)\rho^{2m-n} + n\sum_{k=1}^{m-1}\frac{(-1)^k}{k!}\left(m-\frac{n}{2}\right)\cdots\left(m-\frac{n}{2}-k+1\right)(1-\rho^2)^k - 2\rho^2\sum_{k=1}^{m-1}\frac{(-1)^k}{k!}\,k\left(m-\frac{n}{2}\right)\cdots\left(m-\frac{n}{2}-k+1\right)(1-\rho^2)^{k-1}\Bigg] g(\rho,\xi)\,d\rho. \quad (2)$$

Сондықтан

$$I_1(\xi) + I_2(\xi) = \int_0^1 \rho^{n-1} S_{m-1}(\rho) g(\rho,\xi)\,d\rho,$$

мұндағы

$$S_j(\rho) = n - 2m - 2\rho^2\sum_{k=1}^{j}\frac{(-1)^k}{(k-1)!}\left(m-\frac{n}{2}\right)\cdots\left(m-\frac{n}{2}-k+1\right)(1-\rho^2)^{k-1} + (n-2m)\sum_{k=1}^{j}\frac{(-1)^k}{k!}\left(m-\frac{n}{2}\right)\cdots\left(m-\frac{n}{2}-k+1\right)(1-\rho^2)^k,$$
$$1 \le j \le m-1.$$

Индукция әдісімен келесі теңдікті дәлелдеу қиын емес:

$$S_j(\rho) = \frac{(n-2m)\cdots(n-2(m-j))}{2^j}\cdot\frac{(1-\rho^2)^j}{j!}. \tag{15}$$

Айталық, егер $j=1$ болса, онда

$$\begin{aligned} S_1(\rho) &= n-2m-2\rho^2(-1)\left(m-\frac{n}{2}\right)+(n-2m)(-1)\left(m-\frac{n}{2}\right)(1-\rho^2)\\ &= (n-2m)(1-\rho^2)+(n-2m)\cdot\frac{n-2m}{2}(1-\rho^2)\\ &= \frac{(n-2m)(n-2(m-1))}{2}(1-\rho^2). \end{aligned}$$

Енді (13) теңдігі қандай да бір j үшін орындалады деп алып, оны $j+1$ үшін дәлелдейік. Онда

$$\begin{aligned} S_{j+1}(\rho) &= \frac{(n-2m)\cdots(n-2(m-j))}{2^j}\cdot\frac{(1-\rho^2)^j}{j!}\\ &-\frac{2}{j!}\cdot\frac{n-2m}{2}\cdots\frac{n-2(m-j)}{2}(1-\rho^2)^j\rho^2\\ &+\frac{2+n-2m}{(j+1)!}\cdot\frac{n-2m}{2}\cdots\frac{n-2(m-j)}{2}(1-\rho^2)^{j+1}\\ &= \frac{(n-2m)\cdots(n-2(m-j))}{2^j}\cdot\frac{(1-\rho^2)^{j+1}}{j!}\\ &+\frac{n-2m}{2(j+1)}\cdot\frac{(n-2m)\cdots(n-2(m-j))}{2^j}\cdot\frac{(1-\rho^2)^{j+1}}{j!}\\ &= \frac{(n-2m)\cdots(n-2(m-j))}{2^j}\cdot\frac{n-2(m-j-1)}{2}\cdot\frac{(1-\rho^2)^{j+1}}{(j+1)!}. \end{aligned}$$

Осылайша, (13) теңдігі барлық $j=1,2,\ldots,m-1$ үшін орындалады. Атап айтқанда,

$$S_{m-1}(\rho) = \frac{(n-2m)\cdots(n-2)}{2^{m-1}}\cdot\frac{(1-\rho^2)^{m-1}}{(m-1)!} = a_{n,m}(1-\rho^2)^{m-1},$$

мұндағы

$$a_{n,m} = \frac{(n-2m)\cdots(n-2)}{2^{m-1}(m-1)!}.$$

Сондықтан

$$0 = \int_{|\xi|=1} I(\xi)\,d\xi = a_{n,m}\int_{|\xi|=1}\int_0^1 \rho^{n-1}(1-\rho^2)^{m-1}g(\rho,\xi)\,d\rho\,d\xi.$$

енді декарттық координаталарға қайта оралсақ, келесі теңдікке келеміз:

$$\int_\Omega (1-|x|^2)^{m-1}g(x)\,dx = 0.$$

4. Біртекті шекаралық шарттарымен Нейман есебі

Бұл бөлімде (1), (2) есептері біртекті шекаралық шарттармен қарастырылады.

Лемма 4. [22] $g(x)$ жеткілікті тегіс функция болсын. Онда Нейман есебінің (1), (2) шешімділігінің қажетті және жеткілікті шарты (14) түрінде беріледі.

Егер шешім бар болса, онда ол тұрақтыға дейін бірмәнді және келесі түрде жазылады:

$$u(x) = C + \Gamma_0^{-1}[v](x),$$

мұндағы $v(x)$ - оң жағы $g_1(x) = \Gamma_{2m}[g](x)$ болатын (12) Дирихле есебінің шешімі, әрі қосымша келесі шартты қанағаттандырады: $v(0) = 0$.

Дәлелдеуі. (1), (2) есептің шешімі бар болсын және оны $u(x)$ деп белгілейік. $u(x)$ функциясына Γ_0 операторын қолданып, $v(x) = \Gamma_0[u](x)$ деп аламыз. Енді $v(x)$ үшін шарттарды табамыз.

Айқын түрде: $v(0) = 0$. Егер $v(x)$-ке $(-\Delta)^m$ операторын қолдансақ, онда (10)-ге сәйкес:

$$(-\Delta)^m v(x) = \Gamma_{2m}\left[(-\Delta)^m u\right](x) = \Gamma_{2m}[g](x) = g_1(x).$$

Әрі қарай,

$$r\frac{\partial u}{\partial r}(x) = \frac{\partial u}{\partial \nu}(x), \quad x \in \partial\Omega,$$

сондықтан

$$v(x) = \frac{\partial u}{\partial \nu}(x) = 0, \quad x \in \partial\Omega.$$

Кез келген $k = 1, 2, \ldots$ және барлық $x \in \partial\Omega$ үшін [7]:

$$\frac{\partial^k v}{\partial \nu^k}(x) = r\frac{\partial}{\partial r}\left(r\frac{\partial}{\partial r} - 1\right)\cdots\left(r\frac{\partial}{\partial r} - k + 1\right)v(x) = r^k\frac{\partial^k v}{\partial r^k}(x).$$

Сондықтан біртекті шекаралық (2) шарттардан қорытындылаймыз:

$$\frac{\partial^k v}{\partial \nu^k}(x) = 0, \quad k = 1, 2, \ldots, m-1, \quad x \in \partial\Omega.$$

Осылайша, егер $u(x)$--(1), (2) есебінің біртекті шекаралық шарттардағы шешімі болса, онда $v(x) = \Gamma_0[u](x)$ функциясы (12) Дирихле есебінің шешімі болады, оның оң жағы:

$$g_1(x) = \left(r\frac{\partial}{\partial r} + 2m\right)g(x) = \Gamma_{2m}[g](x).$$

Сонымен қатар, $v(x)$ функциясы $v(x) = 0$ шартын қанағаттандырады және Лемма 3-ке сәйкес, бұл үшін қажетті шарт - (14). Демек, егер (1), (2) есебінің шешімі бар болса, онда (14) шарты міндетті түрде орындалуы тиіс.

Енді керісінше дәлелдейік: егер (14) шарты орындалса, онда (1), (2) есебінің біртекті шекаралық шарттардағы шешімі бар.

Шынында, егер (14) орындалса, онда Лемма 3 бойынша $g_1(x) = \Gamma_{2m}[g](x)$ үшін (12) Дирихле есебінің шешімі $v(x)$ бар және $v(x) = 0$.

Сондықтан $v(x)$-ке Γ_0^{-1} операторын қолданып, келесі функцияны қарастырамыз:

$$u(x) = C + \Gamma_0^{-1}[v](x).$$

Бұл функция (1), (2) есебінің шешімі болатынын көрсету қиын емес. Сонымен қатар, (11)-ге сәйкес:

$$(-\Delta)^m u(x) = \Gamma_{2m}^{-1}\left[(-\Delta)^m v\right](x) = \Gamma_{2m}^{-1}\left[\Gamma_{2m}[g]\right](x) = g(x), \quad x \in \Omega.$$

Ал

$$\Gamma_0[v](x) = \Gamma_0\left[\Gamma_0^{-1}[v]\right](x) = v(x)$$

болғандықтан, жоғарыдағы дәлелдеумен $u(x)$ функциясының барлық біртекті шекаралық шарттарды қанағаттандыратынын көруге болады.

5. Біртекті теңдеу үшін Нейман есебі

Бұл бөлімде $g(x) \equiv 0$ болған жағдайда Нейман есебін (1), (2) қарастырамыз.

A матрицасы келесі түрде берілсін:

$$A = \begin{pmatrix} 1 & 1 & 1 & \cdots & 1 \\ 0 & 2^{[1]} & 4^{[1]} & \cdots & (2m-2)^{[1]} \\ 0 & 2^{[2]} & 4^{[2]} & \cdots & (2m-2)^{[2]} \\ \cdots & \cdots & \cdots & \cdots & \cdots \\ 0 & 2^{[m-1]} & 4^{[m-1]} & \cdots & (2m-2)^{[m-1]} \end{pmatrix} \tag{16}$$

мұндағы

$$j^{[k]} = j(j-1)\cdots(j-k+1), \quad j^{[1]} = j.$$

Егер $k > j$ болса, онда $j^{[k]} = 0$. Δ_j, $j = 1, 2, \ldots, m$, деп A матрицасының бірінші бағанын және j-жолын өшіру арқылы алынған матрицаның анықтауышын белгілейік. Айқын түрде, $|A| = det\, A = \Delta_1$.

$w(x)$ - шекаралық функциялары $f_k(x)$ жеткілікті тегіс болатын келесі Дирихле есебінің шешімі болсын:

$$\begin{cases} (-\Delta)^m w(x) = 0, \quad x \in \Omega, \\ \dfrac{\partial^{k-1} w}{\partial \nu^{k-1}}(x) = f_k(x), \quad k = 1, 2, \ldots, m, \quad x \in \partial\Omega. \end{cases} \tag{17}$$

Лемма 5. [22] $g(x) \equiv 0$ және $\varphi_k(x)$, $(k = 1, 2, \ldots, m)$, жеткілікті тегіс функциялар болсын. Онда Нейман есебі (1), (2) үшін шешімділігінің қажетті және жеткілікті шарты келесі түрде беріледі:

$$\sum_{k=1}^{m} \int_{\partial\Omega} (-1)^{k+1} \Delta_k \left[\varphi_k(x) + (k-1)\varphi_{k-1}(x)\right] dS_x = 0, \tag{18}$$

мұндағы $\varphi_0(x) = 0$. Егер шешім бар болса, онда ол тұрақты дәлдікпен жалғыз және келесі түрде өрнектеледі:

$$u(x) = C + \Gamma_0^{-1}[w](x),$$

мұндағы $w(x)$ - (17) Дирихле есебінің шешімі, оның шекаралық функциялары $f_1(x) = \varphi_1(x)$, $f_k(x) = \varphi_k(x) + (k-1)\varphi_{k-1}(x)$, $k = 2, 3, \ldots, m$, және қосымша $w(0) = 0$ шартын қанағаттандырады.

Дәлелдеуі. (1), (2) есептердің шешімі бар болсын және $u(x)$ - осы шешім болсын. $u(x)$ функциясына Γ_0 операторын қолданайық және $w(x) = \Gamma_0[u](x)$ деп белгілейік. Енді $w(x)$ функциясының (17) Дирихле есебінің шешімі екенін және $w(0) = 0$ шартын қанағаттандыратынын көрсетеміз.

Γ_0 операторының қасиеттерінен

$$(-\Delta)^m w(x) = 0, \quad x \in \Omega.$$

Келесі формулаға сүйенсек [7]:

$$\frac{\partial^j u}{\partial \nu^j} = \left(r\frac{\partial}{\partial r} - j + 1\right) \cdots \left(r\frac{\partial}{\partial r} - 1\right) r\frac{\partial u}{\partial r}, \tag{19}$$

онда $x \in \partial\Omega$ үшін:

$$w(x) = \varphi_1(x),$$

$$\left(r\frac{\partial}{\partial r} - j + 1\right) \cdots \left(r\frac{\partial}{\partial r} - 1\right) w(x) = \varphi_j(x), \quad j = 2, 3, \ldots, m.$$

Бұл шарттарды ыңғайлырақ түрде қайта жазайық. Ол үшін соңғы екеуін қарастырайық:

$$\left(r\frac{\partial}{\partial r} - m + 2\right) \cdots \left(r\frac{\partial}{\partial r} - 1\right) \left(r\frac{\partial}{\partial r} - (m-1)\right) w(x) = \varphi_m(x), \tag{20}$$

$$\left(r\frac{\partial}{\partial r} - m + 2\right) \cdots \left(r\frac{\partial}{\partial r} - 1\right) w(x) = \varphi_{m-1}(x). \tag{21}$$

(21)-өрнекті $(m-1)$-ге көбейтіп, (20)-ге қосамыз. Сонда (19)-ні пайдаланып:

$$\left(r\frac{\partial}{\partial r} - m + 2\right) \cdots \left(r\frac{\partial}{\partial r} - 1\right) r\frac{\partial w(x)}{\partial r}$$

$$= \frac{\partial^{m-1} w(x)}{\partial \nu^{m-1}} = \varphi_m(x) + (m-1)\varphi_{m-1}(x) = f_m(x), \quad x \in \partial\Omega.$$

Осы әдісті барлық $1 \le j \le m-1$ үшін қайталасақ, онда:

$$\frac{\partial^j w(x)}{\partial \nu^j} = \varphi_{j+1}(x) + j\varphi_j(x) = f_{j+1}(x), \quad x \in \partial\Omega.$$

Сонымен, егер $u(x)$ - (1), (2) Нейман есебінің шешімі болса, онда $w(x) = \Gamma_0[u](x)$ - (17) Дирихле есебінің шешімі және $w(0) = 0$ шартын қанағаттандырады.

Айта кету керек, Лемма 5 шарттары орындалғанда (17) есебінің шешімі бар және ол жалғыз (мысалы, [25]-ды қараңыз).

Келесіде біз $\varphi_k(x)$ шекаралық функциялары үшін $w(0) = 0$ теңдігін қамтамасыз ететін шарттарды табамыз. Альманси формуласын (мысалы, [26], 188-б.) пайдаланып, (17) есебінің шешімін келесі түрде жазамыз:

$$w(x) = w_0(x) + r^2 w_1(x) + r^4 w_2(x) + \cdots + r^{2m-2} w_{m-1}(x), \tag{22}$$

мұндағы $w_j(x)$--Ω шарындағы гармониялық функциялар. Айқын түрде, $w(0) = 0$ сонда тек сонда ғана $w_0(0) = 0$ болғанда орындалады.

(22)-ны (17) есебінің шекаралық шарттарына қойып және сфера бойынша интегралдап, келесі теңдіктерді ескерсек:

$$\int_{\partial\Omega} \frac{\partial^k w_j(x)}{\partial \nu^k}\, dS_x = \begin{cases} \omega_n w_j(0), & k=0, \\ 0, & k \neq 0, \end{cases}$$

мұндағы ω_n- бірлік сфераның ауданы, онда келесі теңдеулер жүйесін аламыз:

$$w_0(0) + w_1(0) + w_2(0) + \cdots + w_{m-1}(0) = b_1,$$

$$0 \cdot w_0(0) + 2w_1(0) + 4w_2(0) + \cdots + (2m-2)w_{m-1}(0) = b_2,$$

$$0 \cdot w_0(0) + 2w_1(0) + 4 \cdot 3\, w_2(0) + \cdots + (2m-2)(2m-3)w_{m-1}(0) = b_3,$$

$$\cdots$$

$$0 \cdot w_0(0) + 2^{[m-1]} w_1(0) + 4^{[m-1]} w_2(0) + \cdots + (2m-2)^{[m-1]} w_{m-1}(0) = b_m,$$

мұндағы

$$b_k = \frac{1}{\omega_n} \int_{\partial\Omega} \left[\varphi_k(x) + (k-1)\varphi_{k-1}(x)\right]\, dS_x, \quad k = 1, 2, \ldots, m,$$

және $\varphi_0(x) \equiv 0$. Бұл жүйенің матрицасы (16)-мен анықталған A матрицасы. Жоғарыда айтылғандай, $|A| = det\, A = \Delta_1$. Вандермонд анықтауышына келтіру арқылы бұл анықтауыштың мәнін табу қиын емес:

$$\Delta_1 = 2^{m-1}(m-1)!(2m-4)!! \cdots 4!!2!!.$$

Крамер ережесін пайдаланып, жоғарыдағы теңдеулер жүйесінен $w_0(0)$-ді табамыз:

$$w_0(0) = \frac{|B|}{|A|},$$

мұндағы $|B|$ - келесі матрицаның анықтауышы:

$$|B| = \begin{vmatrix} b_1 & 1 & 1 & \cdots & 1 \\ b_2 & 2^{[1]} & 4^{[1]} & \cdots & (2m-2)^{[1]} \\ b_3 & 2^{[2]} & 4^{[2]} & \cdots & (2m-2)^{[2]} \\ \cdots & \cdots & \cdots & \cdots & \cdots \\ b_m & 2^{[m-1]} & 4^{[m-1]} & \cdots & (2m-2)^{[m-1]} \end{vmatrix}.$$

Айқын түрде,

$$|B| = \sum_{k=1}^{m} (-1)^{k+1} b_k \Delta_k,$$

мұндағы Δ_k, $k = 1, 2, \ldots, m$, жоғарыда анықталған. Сондықтан $w_0(0) = 0$ теңдігі сонда тек сонда ғана

$$\sum_{k=1}^{m}(-1)^{k+1}b_k\Delta_k = 0$$

болғанда орындалады. Ал b_k-ның анықтамасына сәйкес, бұл шарт (18)-ға тең мәндес.

Сонымен, егер қарастырылып отырған Нейман есебінің шешімі бар болса, онда міндетті түрде (18) шарты орындалады.

Енді кері тұжырымды дәлелдейік, яғни егер (18) шарты орындалса, онда Нейман есебінің шешімі бар болады.

$w(x)$ - (17) Дирихле есебінің шешімі болсын. Егер (18) шарты орындалса, онда $w(0) = 0$ және біз келесі функцияны қарастыра аламыз:

$$u(x) = C + \Gamma_0^{-1}w = C + \int_0^1 s^{-1}w(sr\theta)\,ds, \quad x = r\theta,$$

бұл функцияның шынында да Нейман есебінің шешімі екенін көрсетеміз.

Айнымалыны ауыстырып $sr = \xi$ десек, соңғы интегралды былай жазуға болады:

$$u(x) = C + \int_0^r \frac{w(\xi\theta)}{\xi}\,d\xi.$$

Сондықтан,

$$r\frac{\partial u(x)}{\partial r} = r\frac{\partial}{\partial r}\left(\int_0^r \frac{w(\xi\theta)}{\xi}\,d\xi\right) = w(x). \tag{23}$$

Келесі талдауларда (19) және (23) формулаларын қолданамыз және $x \in \partial\Omega$ деп аламыз. Онда:

$$\frac{\partial u(x)}{\partial \nu} = r\frac{\partial u(x)}{\partial r} = w(x) = f_1(x) = \varphi_1(x).$$

Енді екінші туынды үшін:

$$\frac{\partial^2 u(x)}{\partial \nu^2} = \left(r\frac{\partial}{\partial r} - 1\right) r\frac{\partial u(x)}{\partial r} = \left(r\frac{\partial}{\partial r} - 1\right) w(x).$$

Сонда:

$$\frac{\partial^2 u(x)}{\partial \nu^2} + \frac{\partial u(x)}{\partial \nu} = \left(r\frac{\partial}{\partial r} - 1\right) r\frac{\partial u(x)}{\partial r} + r\frac{\partial u(x)}{\partial r} = r\frac{\partial w(x)}{\partial r}$$

$$= \frac{\partial w(x)}{\partial \nu} = f_2(x) = \varphi_2(x) + \varphi_1(x).$$

Осыдан:

$$\frac{\partial^2 u(x)}{\partial \nu^2} = \varphi_2(x) + \varphi_1(x) - \frac{\partial u(x)}{\partial \nu} = \varphi_2(x).$$

Осы тәсілді қолдана отырып, кез келген $j = 2, 3, \ldots, m$ үшін:

$$\frac{\partial^j u(x)}{\partial \nu^j} = \left(r\frac{\partial}{\partial r} - j + 1\right)\cdots\left(r\frac{\partial}{\partial r} - 1\right) r\frac{\partial u(x)}{\partial r}$$

$$= \left(r\frac{\partial}{\partial r} - j + 1\right) \cdots \left(r\frac{\partial}{\partial r} - 1\right) w(x).$$

Осыдан,

$$\frac{\partial^j u(x)}{\partial \nu^j} + (j-1)\frac{\partial^{j-1} u(x)}{\partial \nu^{j-1}} = \left(r\frac{\partial}{\partial r} - (j-1)\right)\left(r\frac{\partial}{\partial r} - (j-2)\right) \cdots$$

$$\cdots \left(r\frac{\partial}{\partial r} - 1\right) w(x) + (j-1)\left(r\frac{\partial}{\partial r} - (j-2)\right) \cdots \left(r\frac{\partial}{\partial r} - 1\right) w(x)$$

$$= \frac{\partial^{j-1} w(x)}{\partial \nu^{j-1}} = f_j(x) = \varphi_j(x) + (j-1)\varphi_{j-1}(x).$$

Сондықтан, индукция бойынша ақырында:

$$\frac{\partial^j u(x)}{\partial \nu^j} = \varphi_j(x) + (j-1)\varphi_{j-1}(x) - (j-1)\frac{\partial^{j-1} u(x)}{\partial \nu^{j-1}}$$

$$= \varphi_j(x) + (j-1)\varphi_{j-1}(x) - (j-1)\varphi_{j-1}(x) = \varphi_j(x).$$

6. Жалпы жағдайдағы Нейман есебі

(1), (2) Нейман есебін теңдеу де, шеттік шартты біртексіз болған жағдайды қарастырамыз.

(1), (2) есебінің шешімі бар болсын және оны $u(x)$ деп белгілейік. Оған Γ_0 операторын қолданайық және оны $z(x) = \Gamma_0[u](x)$ деп белгілейік. Онда $z(x)$ функциясы келесі Дирихле есебінің шешімі болады:

$$\begin{cases} (-\Delta)^m z(x) = g_1(x), \quad x \in \Omega, \\ \dfrac{\partial^{k-1} z}{\partial \nu^{k-1}}(x) = \varphi_k(x) + (k-1)\varphi_{k-1}(x), \quad k = 1, 2, \ldots, m, \quad x \in \partial\Omega, \end{cases} \tag{24}$$

мұндағы

$$g_1(x) = \Gamma_{2m}[g](x), \quad \varphi_0(x) \equiv 0.$$

Сонымен қатар, анықтама бойынша $z(x)$ қосымша $z(0) = 0$ шартын қанағаттандырады.

g_1 және φ_k функциялары жеткілікті тегіс болғандықтан, (242) есебінің шешімі бар және ол жалғыз.

Келесіде $g(x)$ және $\varphi_k(x)$ функцияларына $z(0) = 0$ теңдігін қанағаттандыратын шарттарды табамыз. Ол үшін $z(x)$-ті келесі түрде жазамыз:

$$z(x) = v(x) + w(x),$$

мұндағы $v(x)$ және $w(x)$ - жоғарыда қарастырылған сәйкесінше (12) және (17) Дирихле есептерінің шешімдері. Айқын түрде, $z(0) = 0 \Longleftrightarrow v(0) + w(0) = 0$.

(13) және (22) формулаларға сәйкес $v(x)$ және $w(x)$-ті келесі түрде жазамыз:

$$v(x) = \int_\Omega G_{m,n}(x, y) g_1(y)\, dy,$$

$$w(x) = w_0(x) + r^2 w_1(x) + r^4 w_2(x) + \cdots + r^{2m-2} w_{m-1}(x).$$

Онда:

$$v(0) = \int_\Omega G_{m,n}(0,y) g_1(y)\, dy = C_{n,m} \int_\Omega (1-|y|^2)^{m-1} g(y)\, dy,$$

$$w(0) = w_0(0) = -\frac{1}{\omega_n |A|} \sum_{k=1}^{m} \int_{\partial\Omega} (-1)^k \Delta_k \left[\varphi_k(x) + (k-1)\varphi_{k-1}(x)\right]\, dS_x,$$

мұндағы

$$C_{n,m} = d_{n,m} a_{n,m} = \frac{(-1)^m \Gamma\left(\frac{n}{2} - m\right)}{\pi^{\frac{n}{2}} 4^m (m-1)!} \cdot \frac{(n-2m)\cdots(n-2)}{2^{m-1}(m-1)!}.$$

$$\omega_n = \frac{2\pi^{\frac{n}{2}}}{\Gamma\left(\frac{n}{2}\right)}$$

формуласын пайдаланып, $C_{n,m}$-ті ықшамдауға болады:

$$C_{n,m} = \frac{1}{\omega_n} \cdot \frac{(-1)^m}{\left(2^{m-1}(m-1)!\right)^2}.$$

$$|A| = \Delta_1 = 2^{m-1}(m-1)!(2m-4)!!\cdots 4!!2!!$$

болғандықтан, $v(0) + w(0) = 0$ шарты келесі түрде жазылады:

$$\int_\Omega (1-|x|^2)^{m-1} g(x)\, dx =$$

$$= \frac{2^{m-1}(m-1)!}{(2m-4)!!\cdots 4!!2!!} \sum_{k=1}^{m} \int_{\partial\Omega} (-1)^k \Delta_k \left[\varphi_k(x) + (k-1)\varphi_{k-1}(x)\right]\, dS_x, \qquad (25)$$

мұндағы $\varphi_0(x) = 0$.

Осылайша, біз жалпы Нейман шеттік есебі үшін шешімділіктің қажетті және жеткілікті шартын дәлелдедік.

Теорема 1. [22]. $\varphi_k(x)$, $k = 1, 2, \ldots, m$, және $g(x)$ жеткілікті тегіс функциялар болсын. Онда (1), (2) Нейман шеттік есебінің шешімділігінің қажетті және жеткілікті шарты (25) түрінде беріледі.

Егер шешім бар болса, онда ол тұрақты дәлдікпен жалғыз болады, яғни есептің кез келген екі шешімінің айырмасы тұрақты функцияға тең, және келесі түрде жазылады:

$$u(x) = C + \Gamma_0^{-1}[z](x),$$

мұндағы $z(x)$ - (24) Дирихле есебінің шешімі, оның оң жағы $g_1(x) = \Gamma_{2m}[g](x)$, және ол қосымша $z(0) = 0$ шартын қанағаттандырады.

7. Нәтижелер мен талқылаулар. (3), (4) шеттік есебінің шешімділігі

(4) шеттік шарттың соңғы шекаралық шартына келесі Γ_0^{-1} интегралдық-дифференциалдық операторымен әсер етеміз, нәтижесінде

$$\varphi_k(x), \quad k = 1, 2, \ldots, m-1, \quad \widetilde{\varphi}_m(x) = \Gamma_0^{-1}\varphi_m(x), \quad \varphi_m(0) = 0$$

шартымен Нейман есебіне келеміз.

Теорема 2. $\varphi_k(x), k = 1, 2, \ldots, m$, және $g(x)$ жеткілікті тегіс функциялар болсын. Онда (3), (4) шеттік есебінің шешімділігінің қажетті және жеткілікті шарты (25) түрінде беріледі, мұндағы соңғы шеттік шартқа мынандай шарт пайда болады $\widetilde{\varphi}_m(x) = \Gamma_0^{-1}\varphi_m(x)$, $\varphi_m(0) = 0$.

Егер шешім бар болса, онда ол тұрақты дәлдікпен жалғыз және келесі түрде жазылады:

$$u(x) = C + \Gamma_0^{-1}[z](x),$$

мұндағы $z(x)$ -- (24) Дирихле есебінің шешімі, оның оң жағы $g_1(x) = \Gamma_{2m}[g](x)$, және ол қосымша $z(0) = 0$ шартын қанағаттандырады.

Мысал 1. Бигармоникалық теңдеуді қарастырайық, яғни $m = 2$.

Бұл жағдайда

$$A = \begin{pmatrix} 1 & 1 \\ 0 & 2 \end{pmatrix}, \quad \Delta_1 = 2, \quad \Delta_2 = 1.$$

Осыдан (3), (4) шеттік есебінің, яғни К-13 есебінің шешімділігінің шарты келесі түрге ие болады:

$$\int_\Omega (1 - |x|^2) g(x)\, dx = 2 \int_{\partial\Omega} \left[\widetilde{\varphi}_2(x) - \varphi_1(x)\right] dS_x, \quad \widetilde{\varphi}_2(x) = \Gamma_0^{-1}\varphi_2(x), \quad \varphi_2(0) = 0.$$

Мысал 2. Үшгармоникалық теңдеуді қарастырайық, яғни К-124 есебінің

$$\Delta^3 u(x) = g(x), \quad x \in \Omega,$$

$$\frac{\partial}{\partial \nu} u = \varphi_1(x), \quad \frac{\partial^2}{\partial \nu^2} u = \varphi_2(x), \quad \frac{\partial^4}{\partial \nu^4} u = \varphi_3(x), \quad x \in \partial\Omega,$$

шешілімділігінің шарты келесі түрде өрнектеледі:

$$\int_\Omega (1 - |x|^2)^2 g(x)\, dx = 8 \int_{\partial\Omega} \left[3\varphi_1(x) - 3\varphi_2(x) - \widetilde{\varphi}_3(x)\right] dS_x,$$

$$\widetilde{\varphi}_3(x) = \Gamma_0^{-1}\varphi_3(x), \quad \varphi_3(0) = 0.$$

Егер шешім бар болса, онда ол тұрақты дәлдікпен жалғыз және келесі түрде жазылады:

$$u(x) = C + \Gamma_0^{-1}[v](x),$$

мұндағы $v(x)$ - оң жағы $g_1(x) = \Gamma_6[g](x)$ болатын Дирихле есебінің шешімі, әрі қосымша $v(0) = 0$ шартын қанағаттандырады.

Қаржыландыру туралы ақпарат

Бұл зерттеуді Қазақстан Республикасы Ғылым және жоғары білім министрлігінің Ғылым комитеті қаржыландырды (грант № BR31714735).

Әдебиеттер

[1] Boggio T. Sulle funzioni di Green d'ordine m //Palermo Rend. 1905. V. 20. P. 97--135.
[2] Begerh H., Vu TN.H., Zhang Z.X. Polyharmonic Dirichlet Problems //Proceedings of the Steklov Institute of Math. 2006. V. 255. P. 13--34.
[3] Kal'menov T.Sh., Koshanov B.D., Nemchenko M.Y. Green function representation for the Dirichlet problem of the polyharmonic equation in a sphere // Complex variables and Elliptic equations. -- 2008. -- V. 53, №2. -- P. 177--183. http://dx.doi.org/10.1080/17476930701671726
[4] Kal'menov T.S., Suragan D. On a new method for constructing the green function of the Dirichlet problem for the polyharmonic equation. Differ. Equ. 48(3), 441--445 (2012)
[5] Koshanov B.D. Green's functions and correct restrictions of the polyharmonic operator //Journal of Mathematics, Mechanics and Computer Science. 2021. V. 109(1). P. 34--54. https://doi.org/10.26577/JMMCS.2021.v109.i1.03
[6] Sadybekov M.A., Torebek B.T. and Turmetov B.Kh. On an explicit form of the Green function of the Robin problem for the Laplace operator in a circle, Adv. Pure Appl. Math. 6 (2015), 163--172.
[7] Karachik V.V. Construction of Polynomial Solutions to the Dirichlet Problem for the Polyharmonic Equation in a Ball //Comp. Math. and Math. Physics. 2014. V. 54. P. 1122--1143.
[8] Karachik V. Green's functions of some boundary value problems for the biharmonic equation //Complex Var. and Elliptic Eq. 2022. V. 67. P. 1712--1736.
[9] Karachik V., Turmetov B., Yuan H. Four Boundary Value Problems for a Nonlocal Biharmonic Equation in the Unit Ball //Mathematics. 2022. 10. 1158.
[10] Karachik V.V., Torebek B.T. On the Dirichlet-Riquier problem for biharmonic equations //Math. Notes. 2017. V. 102. P. 31--42.
[11] Karachik V.V. Dirichlet and Neumann boundary value problems for the polyharmonic equation in the unit ball //Mathematics. 2021. 9. 1907.
[12] Karachik V.V. Green's Functions of the Navier and Riquier-Neumann Problems for the Biharmonic Equation in the Ball //Differential Eq. 2021. V. 57. P. 654--668.
[13] Sweers G. A survey on boundary conditions for the biharmonic //Complex Var. And Elliptic Eq. 2009. V. 54. P. 79--93.
[14] Karachik V. Riquier-Neumann Problem for the Polyharmonic Equation in a Ball //Mathematics. 2023; 11: 1000.
[15] Карачик В.В. Функция Грина задачи Дирихле-2 для 3-гармонического уравнения в шаре // Сибирские электронные математические известия, 2023, Т.20, 2, С. 144--167.
[16] Karachik V. Green's Functions of one problem for the 3-harmonic equation in a ball //Complex Var. And Elliptic Eq. 2025, 1--24.
[17] Koshanov B., Shynybayeva N., Koshanova M., Oralbekova, N. On the solvability of boundary value problems with general conditions for the triharmonic equation in a ball. Journal of Mathematics, Mechanics and Computer Science, 2025. 126(2). P. 49--58. https://doi.org/10.26577/JMMCS2025126204
[18] Кангужин Б.Е., Кошанов Б.Д. Необходимые и достаточные условия разрешимости краевых задач для полигармонического уравнения //Уфимский математический журнал. 2010. Т. 2(2). С. 41--52. http://mi.mathnet.ru/rus/ufa50

[19] Koshanov B.D. About solvability of boundary value problems for the nonhomogeneous polyharmonic equation in a ball //Journal Advances in Pure and Applied Math. 2013. V. 4(4). P. 351--373. https://doi.org/10.26577/JMMCS2025126204
[20] Vladimirov V.C: Equations of Mathematical Physics. Nauka, Moscow (1974) (in Russian)
[21] Karachik V.V., Turmetov B.K., Bekayeva A.E. Solvability conditions of the Neumann boundary value problem for the biharmonic equation in the unit ball. Int. J. Pure Appl. Math. 81(3), 487--495 (2012)
[22] Turmetov B.K., Ashurov R.R. On solvability of the Neumann boundary value problem for a non-homogeneous polyharmonic equation in a ball. Boundary Value Problems. 2013. 162 (1) https://doi.org/10.1186/1687-2770-2013-162
[23] Torebek B.T., Turmetov B.K. On solvability of a boundary value problem for the Poisson equation with the boundary operator of a fractional order. Bound. Value Probl. (2013). https://doi.org/10.1186/1687-2770-2013-93
[24] Bavrin I.I. Operators for harmonic functions and their applications. Differ. Uravn. 21(1), 9--15 (1985) (in Russian); English transl.: Differ. Equ. 21(1), 6--10 (1985)
[25] Agmon S., Douglas A., Nirenberg L. Estimates near the boundary for solutions of elliptic partial differential equations satisfying general boundary conditions II. Commun. Pure Appl. Math. 17, 35--92 (1964)
[26] Bitsadze A.V. Boundary Value Problems for Second Order Elliptic Equations. North-Holland, Amsterdam (1968)

[1*]**Koshanov B.D.,**
Doctor of Physical and Mathematical Sciences, Professor, Chief Researcher
ORCID ID: 0000-0002-0784-5183,
*e-mail: koshanov@math.kz

[2]**Turganbek U.,**
Master's student,
ORCID ID: 0009-0000-5894-1194
e-mail: Ulzya03@mail.ru

[2]**Yerkhan A.Zh.,**
Master's student,
ORCID ID: 0009-0001-5552-8908
e-mail: ainur.erkhan@icloud.com

[1*]Institute of Mathematics and Mathematical Modeling, Almaty, Kazakhstan
[2]Al-Farabi Kazakh National University, Almaty, Kazakhstan

ON THE SOLVABILITY OF ONE BOUNDARY VALUE PROBLEM FOR THE POLYHARMONIC EQUATION IN A MULTIDIMENSIONAL BALL

Abstract

The necessity of studying boundary value problems for elliptic equations is motivated by their numerous practical applications in the theoretical study of processes in hydrodynamics, electrostatics, mechanics, heat conduction, elasticity theory, and quantum physics. For example, the distribution of

the potential of an electrostatic field is described by the Poisson equation, while the vibrations of thin plates with small deflections are described by biharmonic equations
In this paper, we study the solvability of one boundary value problem for the polyharmonic equation in the unit ball. In this problem, the normal derivatives of the unknown function are prescribed consecutively from the first-order normal derivative up to the $(m-1)$-th order derivative, while the $(m+1)$-th order derivative is additionally prescribed as the last condition. To solve this problem, we reduce the original problem to the Neumann problem by means of a special integro-differential operator. Then, using another integro-differential operator, the Neumann problem is reduced to the Dirichlet problem. We use the fact that the solution of the Dirichlet problem can be represented by means of the Green function and the Almansi representation. As a result of these representations, the necessary and sufficient condition for the solvability of the original problem is obtained.

Keywords: polyharmonic equation, Neumann problem, Dirichlet problem, integro-differential operators, necessary and sufficient condition for solvability.

Received May 6, 2026; revised June 14, August 18, 2026; accepted August 24, 2026

[1*]**Кошанов Б.Д.,**
д.ф.-м.н., профессор, главный научный сотрудник
ORCID ID: 0000-0002-0784-5183,
Автор для корреспонденции *e-mail: koshanov@math.kz

[2]**Турганбек У.,**
Магистрант
ORCID ID: 0009-0000-5894-1194
e-mail: Ulzya03@mail.ru

[2]**Ерхан А.Ж.,**
Магистрант
ORCID ID: 0009-0001-5552-8908
e-mail: ainur.erkhan@icloud.com

[1*]Институт математики и математического моделирования, Алматы, Казахстан
[2]Казахский национальный университет имени аль-Фараби, Алматы, Казахстан

О РАЗРЕШИМОСТИ ОДНОЙ КРАЕВОЙ ЗАДАЧИ ДЛЯ ПОЛИГАРМОНИЧЕСКОГО УРАВНЕНИЯ В МНОГОМЕРНОМ ШАРЕ

Аннотация

Необходимость исследования краевых задач для эллиптических уравнений продиктована с многочисленными практическими приложениями при теоретическом изучении процессов гидродинамики, электростатики, механики, теплопроводности, теории упругости, квантовой физики. Например, распределения потенциала электростатического поля описываются с помощью уравнения Пуассона, колебания тонких пластин малых прогибов описываются бигармоническими уравнениями.
В данной работе исследуется разрешимость одной краевой задачи для полигармонического уравнения в единичном шаре. В этой задаче последовательно задаются нормальные производные искомой функции, начиная с первой нормальной производной до производной порядка $(m-1)$, а в качестве последнего условия дополнительно задается производная порядка $(m+1)$. Для решения данной задачи исходная задача с помощью специального интегро-дифференциального оператора сводится к задаче Неймана. Затем задача Неймана с помощью

интегро-дифференциального оператора сводится к задаче Дирихле. Используется тот факт, что решение задачи Дирихле представляется с помощью функции Грина и формулы Альманси. В результате этих представлений получено необходимое и достаточное условие разрешимости исходной задачи.

Ключевые слова: полигармоническое уравнение, задача Неймана, задача Дирихле, интегро-дифференциальные операторы, необходимое и достаточное условие разрешимости.

COMPUTER SCIENCE
КОМПЬЮТЕРЛІК ҒЫЛЫМДАР
КОМПЬЮТЕРНЫЕ НАУКИ

UDC 004.056
GRNTI 20.23.29

https://doi.org/10.55452/1998-6688-2026-23-3-144-159

Amirbayeva A.,
Master's, ORCID ID: 0009-0009-3180-2990,
e-mail: adinaxanova2@gmail.com

Kazakh-British Technical University,
Almaty, Kazakhstan

HYBRID INTELLIGENT DECISION-SUPPORT SYSTEM FOR CYBERSECURITY RISK ASSESSMENT AND SECURITY ACTION SELECTION

Abstract

Selecting appropriate information security systems is a complex task influenced by organizational risks, infrastructure characteristics, evolving cyber threats, and regulatory requirements. Traditional approaches based on manual analysis and expert judgment often lack adaptability, scalability, and consistency in dynamic cybersecurity environments. This study proposes a hybrid intelligent decision-support system that combines fuzzy logic, machine learning, and ISO-based cybersecurity standards for risk assessment and security action recommendation. The fuzzy inference module evaluates cybersecurity events under uncertainty using parameters such as attack frequency, vulnerability level, and defense efficiency. Based on the calculated risk level, the system generates standardized response actions aligned with international ISO/IEC standards. In addition, a Random Forest machine learning model is used to evaluate whether the selected actions are likely to mitigate the attack successfully. Experimental evaluation performed on a synthetic dataset demonstrated that the proposed hybrid architecture achieves high predictive performance and improves both interpretability and adaptability of cybersecurity decision support systems in complex operational environments.

Keywords: cybersecurity, decision support systems, fuzzy logic, machine learning, risk assessment, information security

Received April 13, 2026; revised May 25, June 8, 18, 2026; accepted June 26, 2026.

Introduction

The rapid growth of cyber threats and the increasing complexity of digital infrastructures significantly complicate the task of ensuring organizational information security. Modern organizations operate in highly dynamic technological environments characterized by diverse attack vectors, continuously evolving threat landscapes, and increasingly strict regulatory requirements.

As digital transformation accelerates across industries, organizations face growing challenges in protecting critical assets, sensitive information, and ensuring operational continuity.

Information security architecture typically consists of multiple protective mechanisms, including firewalls, intrusion detection systems (IDS), intrusion prevention systems (IPS), data loss prevention (DLP) solutions, and security monitoring platforms. The selection and configuration of these mechanisms depend on numerous interrelated factors, such as organizational size, industry sector, infrastructure complexity, risk exposure, and available resources. These factors create a complex decision-making environment in which security solutions must be carefully evaluated and aligned with organizational security policies and risk management strategies.

However, in practice, the selection of cybersecurity solutions is often performed using expert judgment, manual risk analysis, or static evaluation frameworks. While these approaches remain widely used, they may lead to subjective assessments, inconsistencies in decision-making, and limited scalability in complex infrastructures. Traditional approaches also struggle to effectively process large volumes of security-related data and to address the uncertainty inherent in cybersecurity risk assessment processes.

To address these limitations, recent advances in artificial intelligence have opened new opportunities for improving cybersecurity decision-support systems. Machine learning techniques enable automated analysis of large datasets, anomaly detection, and prediction of potential security incidents, significantly enhancing the ability to respond to emerging threats [1]. In parallel, fuzzy logic has been widely applied in cybersecurity risk assessment because it allows modeling uncertainty and imprecision using linguistic variables and rule-based reasoning [2]. Fuzzy inference systems have demonstrated effectiveness in evaluating information security risks by integrating factors such as threat probability, potential damage, and system vulnerabilities [3].

Intelligent decision-support systems are increasingly used to assist organizations in complex decision-making environments by integrating artificial intelligence techniques with domain knowledge and expert rules [4]. In cybersecurity management, such systems can support risk analysis, automate the selection of security countermeasures, and improve the overall effectiveness of defensive strategies.

In this context, the development of hybrid intelligent approaches that combine multiple artificial intelligence techniques has attracted significant attention in recent cybersecurity research. Integrating fuzzy logic with machine learning allows combining human-like reasoning under uncertainty with data-driven predictive capabilities, thereby improving both interpretability and adaptability of cybersecurity solutions.

This study proposes a hybrid intelligent decision-support model for the selection and evaluation of information security measures. Existing cybersecurity studies often focus on separate stages of the decision-making process. Machine learning-based approaches are mainly used for intrusion detection, anomaly classification, or prediction tasks [1, 7, 8]. Fuzzy logic-based studies usually concentrate on risk assessment under uncertainty and the formalization of expert reasoning [2, 3, 10]. AI-based decision-support systems provide general frameworks for assisting complex decisions, but they do not always connect risk estimation with standard-based response actions and mitigation evaluation [4]. In contrast, the proposed approach integrates these stages into one closed-loop workflow: fuzzy risk assessment, ISO/IEC-based action recommendation, Random Forest-based mitigation prediction, and structured reporting. This integration distinguishes the proposed prototype from approaches that address only detection, only risk scoring, or only rule-based recommendation. Unlike traditional cybersecurity decision-support approaches that focus mainly on attack detection, risk scoring, or rule-based recommendation separately, the proposed model combines these stages into a single closed-loop workflow. The system first evaluates risk under uncertainty using fuzzy logic, then maps the identified attack type and risk level to ISO/IEC-based security actions, and finally applies a Random Forest model to estimate whether the selected actions are likely to mitigate the incident. Therefore, the novelty of the proposed approach lies not in using fuzzy logic or machine learning separately, but in their integration with standard-based action selection and structured

reporting within one decision-support architecture. The proposed approach integrates fuzzy logic-based risk assessment, ISO-based security action recommendation, and Random Forest-based mitigation prediction. The main contribution of the study is the development of a unified decision-support pipeline that connects risk estimation, standardized response recommendation, and predictive evaluation of selected cybersecurity actions.

Material and methods

Modern information security systems represent a comprehensive set of technical, software, and organizational measures aimed at ensuring the confidentiality, integrity, and availability of information. With the rapid development of digital technologies and the increasing complexity of IT infrastructures, organizations are exposed to a growing number of cyber threats, which necessitates the use of multi-layered protection mechanisms.

Contemporary cybersecurity architectures are typically based on the principle of defense-in-depth, which involves the use of multiple complementary components such as Intrusion Detection Systems (IDS), Intrusion Prevention Systems (IPS), firewalls, and Security Information and Event Management (SIEM) platforms. These systems work together to monitor, detect, and respond to cyber threats in real time, providing a layered approach to security management [5, 6]. Cyber threats can be classified into several categories, including network attacks (e.g., DDoS and port scanning), authentication attacks (e.g., brute-force), application-level attacks, and malware-based attacks such as botnets. These threats can be described using parameters such as frequency of occurrence, system vulnerability, and defense efficiency. Proper classification and modeling of these threats are essential for effective cybersecurity management in dynamic environments [7, 8].

Risk assessment is a central component of cybersecurity systems. Traditionally, risk is defined as the product of the probability of a threat and its impact:

$$R = P \times I$$

where R denotes risk, P is the probability of occurrence, and I represents the impact or damage caused by the threat. However, such models are limited in real-world scenarios due to uncertainty, incomplete information, and the subjective nature of expert evaluations [9].

To address these limitations, modern approaches increasingly apply fuzzy logic for cybersecurity risk assessment. Fuzzy systems allow modeling uncertainty using linguistic variables and membership functions. In general, a fuzzy risk model can be expressed as:

$$RiskScore = f(A, F, V, D)$$

where A represents the attack type, F is the frequency of the attack, V is the vulnerability level, and D is the defense efficiency. This formulation reflects a more realistic representation of cybersecurity conditions. Each numerical variable is transformed into fuzzy sets using triangular membership functions. For example, frequency, vulnerability, and defense efficiency are represented by the linguistic values low, medium, and high, while the output variable damage is represented by very low, low, medium, high, and very high.

The numerical RiskScore is converted into risk levels using the following thresholds: values below 250 are interpreted as LOW risk, values from 250 to below 650 are interpreted as MEDIUM risk, and values equal to or above 650 are interpreted as HIGH risk. These thresholds were selected to support practical prioritization of cybersecurity events in the prototype.

In fuzzy inference systems, numerical input values are transformed into fuzzy sets using membership functions. One of the most commonly used forms is the triangular membership function:

$$\mu(x) = \begin{cases} 0, & x \le a \\ \dfrac{x-a}{b-a}, & a < x \le b \\ \dfrac{c-x}{c-b}, & b < x < c \\ 0, & x \ge c \end{cases}$$

This function defines the degree of membership of a variable x to a fuzzy set. Triangular functions are widely used due to their simplicity and interpretability [10].

The decision-making process in fuzzy systems is based on a set of rules that describe relationships between input variables.

Fuzzy inference can be expressed as:

$$R_i = \min\left(\mu_F, \mu_V, \mu_D\right)$$

Where R_i represents the activation level of a specific of rule i. The final risk value is obtained through defuzzification, commonly using the centroid method:

$$RiskScore = \frac{\sum_{i=1}^{n} \mu_i \cdot x_i}{\sum_{i=1}^{n} \mu_i}$$

Fuzzy logic has been widely applied in cybersecurity risk assessment due to its ability to handle uncertainty and incorporate expert knowledge. Recent studies confirm its effectiveness in evaluating complex systems and industrial environments [2, 3].

In addition to risk assessment, cybersecurity systems must provide appropriate response actions. In practice, system administrators perform a set of actions depending on the type of attack. These actions can be divided into automated and manual categories. Simple actions, such as blocking suspicious IP addresses or applying traffic limits, can be executed automatically through external services. More complex actions require human intervention and include system reconfiguration or incident investigation.

To standardize these actions, international cybersecurity standards are used. ISO/IEC 27001 defines the overall framework for information security management systems, while ISO/IEC 27002 provides detailed guidelines for implementing security controls. ISO/IEC 27035 focuses on incident response, ISO/IEC 27033 addresses network security, and ISO/IEC 27034 deals with application security. These standards ensure that response strategies follow best practices and are applicable in real-world scenarios [11].

Within the proposed system, cybersecurity actions are mapped to specific attack types based on ISO recommendations. For example, brute-force attacks require authentication strengthening and password policy enforcement, while DDoS attacks require traffic filtering and resource scaling. This mapping enables systematic and consistent decision-making. The mapping between cyberattack types and ISO-based response actions, presented in Table 1, plays a key role in the proposed decision-support system.

Table 1 – Mapping of cyberattacks to ISO-based security actions

Attack Type	ISO Standard	Recommended Actions
Brute Force	ISO/IEC 27002	Block IP, enforce MFA, reset passwords
DoS/DDoS	ISO/IEC 27033	Rate limiting, enable DDoS protection, scale resources
Botnet	ISO/IEC 27035 / ISO/IEC 27001	Isolate host, enable IDS alerts, collect indicators of compromise
Port Scan	ISO/IEC 27035	Logging, firewall rules, incident response
Web Attack	ISO/IEC 27034	Enable WAF, patch application, review logs

This mapping ensures that each detected attack is associated with a set of standardized and well-established countermeasures derived from international information security standards. For example, brute-force attacks are addressed through authentication-related controls such as blocking suspicious IP addresses, enforcing multi-factor authentication, and resetting compromised credentials, in accordance with ISO/IEC 27002. Similarly, DDoS attacks are mitigated through network-level measures including rate limiting, traffic filtering, and resource scaling, as recommended by ISO/IEC 27033. Other attack types, such as botnets, port scanning, and web-based attacks, are handled through corresponding ISO standards, ensuring that the recommended actions reflect best practices in cybersecurity management. It improves the consistency and reliability of the system's recommendations, while also making them more applicable in real-world environments. By aligning decision-making with recognized standards, the proposed approach reduces subjectivity and enhances the practical value of the system for system administrators and cybersecurity specialists.

The mapping is not intended to represent full ISO/IEC compliance. It is used as a standard-based recommendation layer that connects common attack scenarios with relevant security domains. Brute-force attacks are linked to ISO/IEC 27002 because they require authentication and access control measures. DoS/DDoS attacks are linked to ISO/IEC 27033 because they mainly affect network availability and require network-level countermeasures. Web attacks are linked to ISO/IEC 27034 because they concern application security. Port scanning and botnet-related activities are connected with incident detection and response logic described in ISO/IEC 27035.

Another important aspect of modern cybersecurity systems is the evaluation of defense effectiveness. Traditional approaches focus mainly on risk estimation, but do not analyze whether applied actions successfully mitigate threats. To address this limitation, machine learning models are used.

The machine learning component can be formalized as:

$$y = ML(A, F, V, D, S)$$

Where y is a binary variable indicating whether the attack was mitigated and S represents the strength of applied actions. The action strength can be calculated as:

$$S = \sum_{i=1}^{n} \omega_i \cdot a_i$$

where a_i indicates whether action i was applied, and ω_i denotes the relative weight of action i.

This formulation allows the model to consider not only system conditions but also the effectiveness of response actions.

Machine learning methods, particularly ensemble algorithms such as Random Forest, have demonstrated strong performance in cybersecurity tasks, including intrusion detection and classification. These models can capture complex relationships between variables and adapt to new data, making them suitable for dynamic environments [1, 12].

Recent research highlights the growing role of artificial intelligence in decision support systems. AI-based systems combine data-driven approaches with expert knowledge to improve decision-making processes in complex domains such as cybersecurity. They enable automation, scalability, and improved accuracy in threat detection and response [4].

Modern systems increasingly include automated reporting mechanisms. Reports can be generated on a daily, weekly, or monthly basis and include detailed information about events, timestamps, recommended actions, and execution results. The integration of large language models (LLMs) allows generating structured and human-readable reports, improving the usability of cybersecurity systems.

The integration of fuzzy logic, machine learning, and standardized response strategies forms the basis of hybrid intelligent decision-support systems. Such systems provide a comprehensive framework for cybersecurity management by combining risk assessment, action recommendation,

automation, and effectiveness evaluation. This approach improves the adaptability, consistency, and efficiency of cybersecurity processes in dynamic environments.

The proposed system is designed as a hybrid intelligent decision-support model for cybersecurity management. Its main objective is to support the selection of appropriate information security measures by combining fuzzy risk assessment, standards-based action recommendation, automated response, and machine learning–based evaluation of defense effectiveness. Such hybrid approaches are increasingly considered effective in cybersecurity because they combine interpretability and uncertainty handling with data-driven predictive capability [1, 2, 4].

The overall architecture of the system is shown in Figure 1. This architecture reflects the idea that cybersecurity decision support should not be limited to attack detection alone, but should also include response recommendation, automation, and evaluation of countermeasure effectiveness.

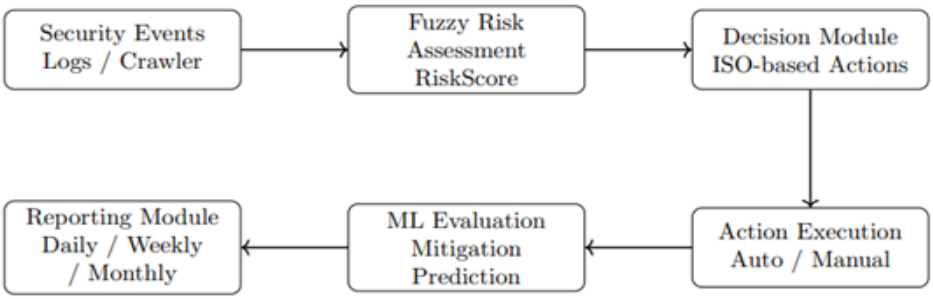


Figure 1 – Architecture of the hybrid intelligent cybersecurity system

The fuzzy risk assessment module is used to estimate the severity of a cybersecurity event under uncertainty. Traditional risk models often rely on exact numerical values, but cybersecurity parameters are frequently uncertain, incomplete, or more naturally expressed in linguistic form. Fuzzy logic is well suited for such tasks because it allows numerical inputs to be converted into interpretable linguistic categories and processed through expert-defined rules [2, 3].

The fuzzy model uses triangular membership functions for the input variables frequency, vulnerability, and defense efficiency. Each variable is defined on a scale from 0 to 10 and represented by three linguistic terms: LOW, MEDIUM, and HIGH. The output variable is damage or RiskScore, defined on a scale from 0 to 1000 and represented by five linguistic terms: VERY LOW, LOW, MEDIUM, HIGH, and VERY HIGH. As shown in Table 2, values closer to 1 indicate stronger membership, while values close to 0 indicate weak or no membership.

Table 2 – Interpretation of fuzzy membership values

Membership degree range	Interpretation
0	No membership
$0 < \mu(x) < 0.3$	Weak membership
$0.3 \leq \mu(x) < 0.7$	Partial/moderate membership
$0.7 \leq \mu(x) < 1$	Strong membership
1	Full membership

The membership degree $\mu(x)$ is a continuous value from 0 to 1. It is not limited to fixed values such as 0.2, 0.4, 0.6, or 0.8. These values may be used only for interpretation, while the actual membership degree is calculated by the corresponding membership function.

Representative fuzzy rules used in the model include the following:

1. If frequency is HIGH, vulnerability is HIGH, and defense efficiency is LOW, then risk is VERY HIGH.

2. If frequency is HIGH and defense efficiency is LOW, then risk is HIGH.
3. If vulnerability is HIGH and defense efficiency is LOW, then risk is HIGH.
4. If defense efficiency is HIGH and frequency is LOW, then risk is VERY LOW.
5. If frequency, vulnerability, and defense efficiency are MEDIUM, then risk is MEDIUM.

The fuzzy rule base was organized into several logical groups. The first group defines baseline risk levels for different attack types, including normal activity, port scanning, brute-force attempts, web attacks, DoS/DDoS, and botnet-related events. The second group covers high-risk conditions where high frequency and high vulnerability are combined with low defense efficiency. The third group describes cases where strong defense efficiency reduces the final risk level. The fourth group contains attack-specific escalation rules for DoS/DDoS, botnet, web attack, and brute-force scenarios. The fifth group covers balanced medium-risk cases, where the input parameters have moderate values. Finally, fallback rules are included to ensure that the fuzzy inference system produces an output even when a specific input combination is not fully covered by detailed rules. This structure makes the fuzzy rule base systematic and suitable for prototype-level cybersecurity risk assessment.

After fuzzy inference, the aggregated fuzzy output is converted into a numerical RiskScore using centroid-based defuzzification. The numerical RiskScore is then interpreted as LOW, MEDIUM, or HIGH risk for the recommendation module.

The pseudocode of the overall hybrid model is given in Algorithm 1. The role of the fuzzy stage in this workflow is to provide the first analytical layer for assessing event severity before security actions are selected.

Algorithm 1 – Hybrid Cybersecurity Decision Model

Input: Security event (A, F, V, D)
1. Compute RiskScore using fuzzy model;
2. Determine risk level (LOW, MEDIUM, HIGH);
3. Generate recommended actions based on ISO standards;
4. if action is simple then
   Execute action automatically;
   else
   Recommend action to the administrator;
5. Compute action strength S;
6. Predict mitigation using the machine learning model;
   Generate report;

After the risk level is determined, the system generates a set of recommended actions for the administrator. This module is based on the principle that specific classes of attacks require specific countermeasures. To make the recommendations more consistent and practical, the mapping between attacks and actions is aligned with international information security standards.

In particular, the developed system uses the following standards as a reference:
- ISO/IEC 27001 for general information security management,
- ISO/IEC 27002 for access control and authentication-related controls,
- ISO/IEC 27033 for network security measures,
- ISO/IEC 27035 for incident detection and response,
- ISO/IEC 27034 for application security.

For example, brute-force attacks are associated with actions such as IP blocking, password reset, and multi-factor authentication, which are consistent with ISO/IEC 27002. DDoS attacks are mapped to rate limiting, DDoS protection, and resource scaling in accordance with ISO/IEC 27033. Port scanning events are linked to logging, firewall rule tightening, and incident handling procedures corresponding to ISO/IEC 27035. Web attacks are associated with WAF activation, patching, and application log review in line with ISO/IEC 27034.

An important feature of the proposed module is the distinction between simple and complex actions. Simple actions, such as block ip, rate limit, or enable waf rule, can be executed automatically by calling an external service. More complex actions, such as host isolation, forensic analysis, or security policy adjustment, remain under administrator control. This combination of automation and expert intervention improves the flexibility of the system and reflects practical cybersecurity workflows.

Unlike traditional decision-support systems that stop at the stage of recommending actions, the proposed approach includes an additional evaluation layer. Its purpose is to estimate whether the selected actions are likely to mitigate the attack. This task is formulated as a binary classification problem:

$$y = ML(A, F, V, D, S)$$

Where y indicates whether the attack is mitigated, A is the attack type, F is the frequency, V is the vulnerability level, D is the defense efficiency, and S is the action strength.

$$S = \sum_{i=1}^{n} w_i a_i$$

Where a_i indicates whether action i was applied and w_i is its relative effectiveness weight. The machine learning model uses the following input features:

- attack type,
- frequency,
- vulnerability,
- defense efficiency,
- action strength.

The target variable is a binary label indicating whether the cybersecurity incident was successfully mitigated. The machine learning component of the system is implemented using a Random Forest classifier. The model is trained on synthetic data using the following procedure:

rf_model = RandomForestClassifier(random_state=42)

rf_model.fit(X_train, y_train)

The Random Forest classifier was implemented using the scikit-learn library. In the current prototype, the default RandomForestClassifier configuration was used with random_state = 42 to ensure reproducibility. This means that the number of trees was set to 100, maximum tree depth was not explicitly restricted, and no class weighting was applied. The attack type was encoded as a fixed numerical identifier for prototype simplicity, while the remaining features were numerical. Since Random Forest is a tree-based algorithm, feature normalization was not required. However, for a more rigorous production-level implementation, one-hot encoding or categorical encoding of attack types should be applied, and hyperparameter tuning should be performed.

This implementation allows the model to learn the relationship between cybersecurity parameters and mitigation outcomes. The Random Forest algorithm was selected because of its strong performance on structured tabular data, robustness to nonlinear relationships, and interpretability compared to more complex black-box models. Random Forest has also been widely used in cybersecurity applications for classification and anomaly analysis [1].

Since real labeled datasets describing the effectiveness of administrator actions are difficult to obtain, a synthetic training dataset was generated using expert-inspired rules. The training procedure includes dataset generation, train/test split, model fitting, and evaluation using accuracy, confusion matrix, precision, recall, and F1-score.

For empirical reproducibility, the synthetic dataset generation procedure was explicitly defined. In this study, the dataset consisted of 3000 cybersecurity events. Each event was assigned to one of six attack categories: Botnet, Brute Force, DoS/DDoS, Normal, Port Scan, and Web Attack. The numerical features, including attack frequency, vulnerability level, and defense efficiency, were

generated within a normalized continuous range from 0 to 10. These values were used to simulate different cybersecurity conditions, from low-risk events to high-risk attack scenarios. A risk proxy value was calculated using attack frequency, vulnerability level, and defense efficiency. The action strength feature was calculated as a weighted sum of selected or executed response actions. The binary target variable indicated whether the attack was mitigated or not. The dataset was divided into training and testing subsets using an 80/20 split, and the Random Forest classifier was evaluated on unseen test data.

The numerical features were generated from a uniform distribution in the range from 0 to 10. A fixed random seed was used to ensure reproducibility of the generated dataset.

The experimental dataset was generated synthetically because publicly available cybersecurity datasets usually contain traffic features and attack labels, but do not include ISO-based recommended actions, executed actions, action strength, and final mitigation outcomes. These variables are necessary for evaluating the full decision-support process proposed in this study. Table 3 summarizes the main parameters used to generate the synthetic cybersecurity dataset.

Table 3 – Parameters of synthetic dataset generation

Parameter	Value
Dataset size	3000 cybersecurity events
Random seed for dataset generation	7
Attack categories	Botnet, Brute Force, DoS/DDoS, Normal, Port Scan, Web Attack
Frequency distribution	Uniform distribution in the range from 0 to 10
Vulnerability distribution	Uniform distribution in the range from 0 to 10
Defense efficiency distribution	Uniform distribution in the range from 0 to 10
Action execution probability	0.75 for each recommended action
Noise distribution	Normal distribution with mean 0 and standard deviation 0.8
Target variable	Binary mitigation outcome: 1 = mitigated, 0 = not mitigated
Train/test split	80/20
Random state for model training	42
Machine learning model	Random Forest classifier

These parameters make the experimental procedure reproducible because the dataset size, feature distributions, random seeds, action execution logic, noise level, and target generation rule are explicitly defined.

This module allows the system not only to recommend actions, but also to estimate whether these actions are likely to be sufficient. Such a feedback oriented design significantly strengthens the practical value of the system.

To reduce data leakage during model evaluation, the dataset was divided into training and testing subsets before model evaluation, and the test set was not used during model fitting. Stratified splitting was applied to preserve the distribution of mitigated and non-mitigated cases. At the same time, since the mitigation label is generated using action strength in the synthetic dataset, the relationship between action strength and the target variable is intentionally embedded in the prototype. This is acknowledged as a limitation of synthetic validation, and future work should use real incident response outcomes as target labels.

The sequence of system operations is illustrated in Figure 1. First, a cybersecurity event is collected from the data source. The event is passed to the fuzzy inference module, which computes the $RiskScore$ and assigns a risk level. Based on the attack type and risk level, the decision-support module generates ISO-based recommendations. If the selected action belongs to the set of simple automated actions, the system executes it automatically through an external service. Otherwise, the action is left for manual execution by the administrator.

Next, the machine learning model receives the event parameters together with the action-related features and predicts whether the implemented actions are likely to mitigate the threat. Finally, the processed event data is sent to the reporting module, where it is included in daily, weekly, or monthly reports.

This sequence reflects a closed-loop decision-support process: event detection → fuzzy risk estimation → action recommendation → action execution → ML (Random Forest) effectiveness evaluation → reporting.

Such a workflow is especially useful in complex environments where administrators must process many events in a short time and require not only alerts but also interpretable recommendations and outcome estimates.

Results and discussion

The experimental evaluation of the proposed hybrid intelligent system was conducted to assess its performance in cybersecurity risk estimation, action recommendation, and prediction of defense effectiveness. The evaluation considered both the individual behavior of the fuzzy risk assessment module and the performance of the machine learning classifier within the integrated system pipeline.

The experiments were designed to answer three main questions. First, whether the fuzzy model produces interpretable and stable risk estimates under different attack conditions. Second, whether the machine learning model can reliably predict whether the selected actions are sufficient to mitigate the attack. Third, whether the integration of fuzzy logic, ISO-based recommendation rules, and machine learning improves the overall quality of decision support.

To evaluate the proposed approach, a synthetic dataset consisting of 3000 cybersecurity events was generated. Each event was described by the following attributes:

- attack type,
- frequency,
- vulnerability level,
- defense efficiency,
- strength of applied actions.

The attack type corresponds to one of the predefined categories used in the system, including Botnet, Brute Force, DoS/DDoS, Normal, Port Scan, and Web Attack. The remaining parameters were generated within normalized ranges and represent simplified but realistic characteristics of cybersecurity incidents. Such a design made it possible to simulate different combinations of weak and strong system states and different response strategies.

The fuzzy inference module was applied to each generated event in order to compute a numerical risk score. The risk score was then converted into one of three discrete categories: LOW, MEDIUM, and HIGH. These values were used by the decision-support module to select ISO-based response actions.

For the machine learning stage, the target variable was defined as a binary mitigation outcome:

$$y \in \{0, 1\}$$

where y = 1 indicates that the attack was mitigated and y = 0 indicates that the attack was not mitigated.

The action strength feature was calculated as a weighted sum of the recommended or executed actions:

$$S = \sum_{i=1}^{n} w_i \, a_i$$

where a_i denotes the application of action i, and w_i is the relative weight of this action.

The dataset was divided into training and testing subsets using an 80/20 split. The machine learning component was implemented using a Random Forest classifier, which was selected because of its robustness and suitability for structured cybersecurity data [1].

The fuzzy module was evaluated by analyzing the generated RiskScore values under different combinations of input parameters. In general, the model produced higher risk scores when attack frequency and vulnerability were high while defense efficiency was low. Conversely, the system assigned lower scores to events with strong defense efficiency and low attack intensity.

The results indicate that the fuzzy model is consistent with expert reasoning and allows interpretable risk assessment. This is particularly important in cybersecurity applications, where uncertainty and incomplete information are common [2, 3].

For practical interpretation, the following thresholds were used:

- LOW risk: $0 \leq \text{RiskScore} < 250$,
- MEDIUM risk: $250 \leq \text{RiskScore} < 650$,
- HIGH risk: $\text{RiskScore} \geq 650$.

These categories were later used by the recommendation module to determine the severity of the incident and assign suitable actions.

The Random Forest classifier was trained to predict whether the selected security actions were sufficient to mitigate the attack. The machine learning model was implemented in Python using the following training procedure:

```
rf_model = RandomForestClassifier(random_state=42)
rf_model.fit(X_train, y_train)
```

The performance of the machine learning model is illustrated in Figure 2. The confusion matrix shows that the model correctly classifies the majority of cybersecurity events. In particular, 344 non-mitigated events and 192 mitigated events were correctly identified. The number of misclassifications is relatively low, with 38 false positives and 26 false negatives. This indicates that the model is capable of distinguishing between effective and ineffective security responses within the synthetic experimental setting.

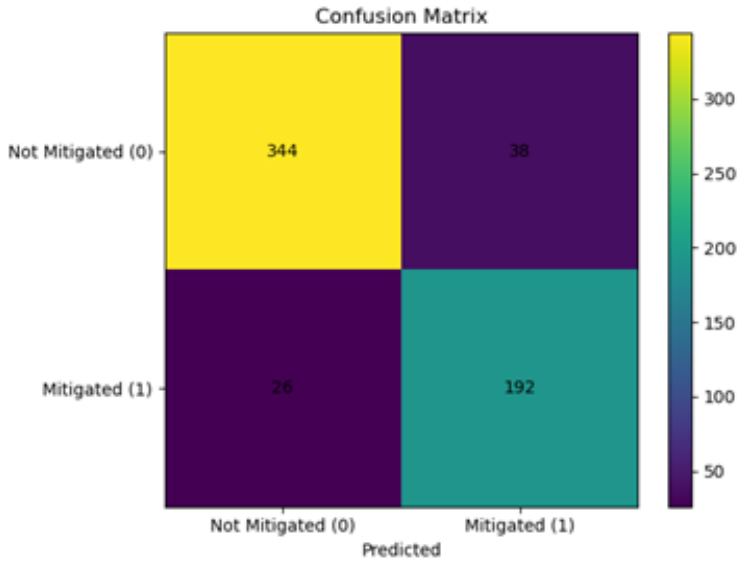


Figure 2 – Confusion matrix of the Random Forest model

In the context of cybersecurity decision support, these two error types have different operational meanings. A false positive means that the model predicts successful mitigation, although the incident is actually not mitigated. This error may be more dangerous because it can create a false sense of security and lead administrators to stop further investigation too early. A false negative means that the model predicts mitigation failure, although the incident is actually mitigated. This may lead to additional review or repeated response actions, but it is generally safer than overlooking an unresolved threat. Therefore, confusion matrix analysis is important because it shows not only overall accuracy, but also the operational risk of different prediction errors.

The overall model accuracy reached 0.89, indicating the model's predictive capabilities within the synthetic experimental environment. Precision and recall values were balanced for both classes, with slightly higher performance for the unmitigated class. This behavior is expected, as the model is trained on synthetic data with varying levels of risks and actions. The detailed classification metrics are summarized in Table 4.

Table 4 – Classification performance of the Random Forest model

Class	Precision	Recall	F1-score
Not Mitigated (0)	0.93	0.90	0.91
Mitigated (1)	0.83	0.88	0.86

To estimate the benefit of the proposed hybrid architecture, its performance was compared with simpler decision-support approaches. The comparison included a rule-based baseline, a fuzzy-only model, and the complete hybrid model that combines fuzzy logic with machine learning.

The comparison results are presented in Table 5. The rule-based baseline provides high interpretability but limited adaptability. The fuzzy-only model improves the handling of uncertainty and provides more flexible decision-making. However, the hybrid model demonstrates the best overall performance because it combines interpretable risk estimation with data-driven evaluation of action effectiveness.

Table 5 provides a conceptual comparison of decision-support approaches. The rule-based and fuzzy-only models are used as baseline approaches to explain the limitations of fixed rules and risk-only assessment. The quantitatively evaluated component of the proposed hybrid system is the Random Forest mitigation prediction model, which achieved an accuracy of approximately 0.89 on the test set.

Table 5 – Conceptual comparison of decision-support approaches

Model	Role in decision support	Adaptability	Interpretability	Experimental status
Rule-based baseline	Fixed mapping between attack type and actions	Low	High	Conceptual baseline
Fuzzy-only model	Risk assessment under uncertainty	Medium	High	Risk assessment component
Hybrid model	Fuzzy risk assessment, ISO-based action selection, Random Forest mitigation prediction, and reporting	High	High	Experimentally evaluated, accuracy ≈ 0.89

To clarify the role of the proposed architecture, the hybrid system was compared conceptually with simpler decision-support approaches. The comparison included a rule-based baseline, a fuzzy-only model, and the complete hybrid model. The rule-based baseline represents fixed mapping between attack types and response actions. This approach is interpretable but limited in adaptability. The fuzzy-only model improves uncertainty handling and provides interpretable risk assessment, but it does not evaluate whether selected actions are likely to mitigate the attack. The complete hybrid model combines fuzzy risk assessment, ISO-based action selection, Random Forest mitigation prediction, and reporting. Table 5 provides a conceptual comparison of these decision-support approaches. The rule-based and fuzzy-only models are used as baseline approaches to explain the limitations of fixed rules and risk-only assessment. The quantitatively evaluated component of the proposed hybrid system is the Random Forest mitigation prediction model, which achieved an accuracy of approximately 0.89 on the test set.

The security action recommendation module is aligned with international cybersecurity standards. Each type of cyberattack is associated with a set of response actions derived from ISO/IEC standards, including ISO/IEC 27001, ISO/IEC 27002, ISO/IEC 27033, ISO/IEC 27035, and ISO/IEC 27034.

This mapping ensures that the recommended actions follow best practices in information security management and provides a structured approach for system administrators. The integration of ISO standards enhances the potential applicability of the proposed system for structured cybersecurity decision support.

The action strength feature is important because it allows the model to consider not only attack conditions, but also the expected strength of selected response actions. This reflects practical cybersecurity logic, where the mitigation outcome depends on both the severity of the incident and the quality of the response. In the current prototype, action strength is calculated as a weighted sum of recommended or executed actions. Since these weights are expert-based assumptions, future work should validate or calibrate them using real incident response data. This result is important because it demonstrates that cybersecurity decision support should not depend only on the attack properties themselves. It is also necessary to consider the actual response actions and their potential effectiveness.

In addition to evaluating the fuzzy and machine learning components separately, the entire system was tested as a unified pipeline. The workflow included the following stages:

1. event generation or collection,
2. fuzzy risk estimation,
3. ISO-based action recommendation,
4. automatic or manual action execution,
5. machine learning evaluation of mitigation,
6. report generation.

The integrated system successfully processed simulated events and produced structured outputs that included:

- event identifier,
- timestamp,
- attack type,
- suspicious IP address,
- fuzzy risk score,
- risk level,
- recommended actions,
- executed actions,
- predicted mitigation outcome.

This indicates that the proposed architecture is suitable for prototype-level cybersecurity decision support in multistage workflows. The experimental results suggest that the proposed hybrid model provides a balanced combination of interpretability, flexibility, and predictive capability. The fuzzy component supports reasoning under uncertainty and reflects expert knowledge, while the machine learning model strengthens the system by evaluating the probable effectiveness of the selected response actions.

The obtained results indicate that the machine learning component can be used as an evaluation mechanism within the proposed hybrid intelligent system. Unlike traditional rule-based approaches, the model does not only recommend actions but also estimates whether these actions are likely to be sufficient for threat mitigation. This makes the system more practical for real cybersecurity decision support, since administrators receive not only recommendations but also an additional prediction of response effectiveness.

At the same time, the study has several limitations. First, the experiments were carried out on synthetic data, which may not fully reflect the complexity of real operational cybersecurity environments. Second, the response action weights were assigned heuristically, and further validation with expert knowledge or real incident data is required. Third, the current reporting module is

implemented as a simplified prototype and can be extended in future work using large language models for more advanced report generation.

Another limitation is related to the maintenance of the fuzzy rule base when the number of corporate knowledge assets, attack scenarios, and security controls increases. In large organizations, the expansion of infrastructure may require additional fuzzy rules and more detailed membership functions. This can make manual rule updating more complex and may increase the risk of inconsistent, overlapping, or outdated rules. Therefore, future development of the system should include expert validation procedures, periodic rule revision, adaptive rule tuning, and possible semi-automated knowledge base updating mechanisms. This would help keep the fuzzy rule base scalable and consistent in larger organizational environments.

The obtained results demonstrate that the proposed hybrid architecture can serve as a practical basis for intelligent cybersecurity decision support systems.

Conclusion

This study presented a hybrid intelligent decision-support system for the selection and evaluation of information security measures in organizational environments. The proposed approach integrates fuzzy logic, ISO-based rule systems, and machine learning into a unified multi-stage architecture.

The fuzzy inference module enables the modeling of uncertainty in cybersecurity risk assessment by using linguistic variables such as attack frequency, vulnerability level, and defense efficiency. This provides interpretable and flexible risk estimation that reflects real-world expert reasoning. Based on the computed risk levels, the decision module generates security actions aligned with international standards, including ISO/IEC 27001, ISO/IEC 27002, and ISO/IEC 27035.

A key contribution of the proposed system is the integration of a machine learning component that evaluates the effectiveness of the selected response actions. The Random Forest classifier demonstrated strong performance, achieving an accuracy of approximately 0.89 and balanced precision and recall values across both classes. This indicates that the model is capable of predicting mitigation outcomes within the synthetic experimental setting.

The experimental results suggest that the proposed hybrid architecture can improve the interpretability and adaptability of cybersecurity decision support within the synthetic experimental environment. Unlike traditional rule-based approaches, the proposed system does not only estimate risk and recommend actions, but also predicts the outcome of these actions. This provides a more complete and practical solution for real-world cybersecurity management.

Another important aspect of the system is the reporting module, which generates structured daily, weekly, and monthly security reports. These reports include detailed information about each event, such as attack type, suspicious IP address, risk level, recommended and executed actions, and predicted mitigation outcome. This functionality demonstrates the applicability of the proposed approach for operational cybersecurity monitoring and decision-making.

Despite the promising results, several limitations should be noted. First, the experimental evaluation was conducted using a synthetic dataset, which may not fully capture the complexity of real-world cybersecurity environments. Second, the effectiveness of response actions was modeled using predefined weights, which may require further validation and tuning based on expert knowledge or real incident data. Third, the current system uses simplified rule sets and can be extended to incorporate more complex attack patterns and dependencies.

Future work will focus on several directions. First, the system can be extended by integrating real-world cybersecurity datasets, such as intrusion detection system logs or SIEM data, in order to improve model robustness and generalization. Second, the fuzzy rule base can be refined using expert knowledge or automated rule learning techniques to enhance risk estimation accuracy. Third, more advanced machine learning models, including deep learning and ensemble methods, can be explored to further improve mitigation prediction performance. Future improvements should also address the scalability of the fuzzy rule base, since larger corporate environments may require more complex rule structures, expert validation, and adaptive updating mechanisms.

Since the evaluation was performed on synthetic data, the obtained results should be interpreted as prototype-level validation rather than evidence of final operational effectiveness. The results demonstrate the feasibility and potential applicability of the proposed hybrid architecture within a controlled experimental environment. Further testing on real SIEM logs, IDS alerts, firewall logs, and organizational incident response records is required to assess the generalization ability of the proposed system in real cybersecurity environments.

Another promising direction is the integration of large language models for intelligent report generation and automated analysis of cybersecurity incidents. Such models can enhance the interpretability of results and provide natural language explanations for recommended actions. In addition, future work may include the development of a fully automated response system integrated with real security infrastructure, such as firewalls, intrusion prevention systems, and cloud-based security services.

Overall, the proposed hybrid intelligent system provides a flexible and extensible framework for cybersecurity decision support. It combines the strengths of fuzzy logic, standard-based reasoning, and machine learning, and can serve as a foundation for the development of next-generation intelligent information security systems.

Acknowledgment:

The author acknowledges the guidance of supervisor A.Zh. Akzhalova and the support of the AI and Cybersecurity research team, which contributed to the development of this work.

REFERENCES

1 Apruzzese, G., et al. The Role of Machine Learning in Cybersecurity. Digital Threats: Research and Practice, 4 (1), 1–38 (2022). https://doi.org/10.1145/3545574

2 Kerimkhulle, S., et al. Fuzzy Logic and Its Application in the Assessment of Information Security Risk of Industrial Internet of Things. Symmetry, 15 (10), 1958 (2023). https://doi.org/10.3390/sym15101958

3 Merola, F., Bernardeschi, C., Lami, G. A Risk Assessment Framework Based on Fuzzy Logic for Automotive Systems. Safety, 10 (2), 41 (2024). https://doi.org/10.3390/safety10020041

4 Soori, M., et al. AI-Based Decision Support Systems in Industry 4.0: A Review. Journal of Economy and Technology, 4, 206–225 (2024). https://doi.org/10.1016/j.ject.2024.08.005

5 Singer, P., Friedman, A. Cybersecurity and Cyberwar: What Everyone Needs to Know. Oxford University Press (2014). https://doi.org/10.1093/wentk/9780199918096.001.0001

6 Peltier, T.R. Information Security Policies, Procedures, and Standards. CRC Press (2021).

7 Ahmed, M., Mahmood, A., Hu, J. A Survey of Network Anomaly Detection Techniques. Journal of Network and Computer Applications, 60, 19–31 (2015). https://doi.org/10.1016/j.jnca.2015.11.016

8 Wang, M., et al. Machine Learning for Networking: Workflow, Advances and Opportunities. IEEE Network, 32 (2), 92–99 (2018). https://doi.org/10.1109/MNET.2017.1700200

9 Ludonga, A., Singo, S. Systematic Review Cyber Risk Management: Frameworks, Strategies, and Case Studies in Cybersecurity (2025). https://doi.org/10.5281/zenodo.17372361

10 Zadeh, L.A. Fuzzy Sets. Information and Control, 8 (3), 338–353 (1965). https://doi.org/10.1016/S0019-9958(65)90241-X

11 ISO/IEC 27001:2022 Information Security Management Systems (2022). https://www.iso.org/standard/27001

12 Tukaram, L. Deep Learning in Cybersecurity: Applications, Challenges, and Future Prospects. International Journal of Innovations in Science Engineering and Management, 4 (2), 27–33 (2025). https://doi.org/10.69968/ijisem.2025v4i227-33

Амирбаева А.А.,
магистрант, ORCID ID: 0009-0009-3180-2990,
e-mail: adinaxanova2@gmail.com

Қазақстан-Британ техникалық университет, Алматы қ., Қазақстан

КИБЕРҚАУІПТЕРДІ БАҒАЛАУ ЖӘНЕ ҚОРҒАНЫС ШАРАЛАРЫН ТАҢДАУ ҮШІН ГИБРИДТІ ИНТЕЛЛЕКТУАЛДЫ ШЕШІМ ҚАБЫЛДАУДЫ ҚОЛДАУ ЖҮЙЕСІ

Аңдатпа

Ақпараттық қауіпсіздік жүйелерін таңдау ұйымдық тәуекелдерге, инфрақұрылым ерекшеліктеріне, киберқауіптерге және нормативтік талаптарға байланысты күрделі міндет. Дәстүрлі тәсілдер көбінесе сарапшылық бағалауға және қолмен талдауға негізделетіндіктен, олардың бейімделгіштігі мен икемділігі шектеулі. Бұл жұмыста тәуекелдерді бағалау және қауіпсіздік шараларын ұсыну үшін анық емес логиканы, машиналық оқытуды және ISO стандарттарын біріктіретін гибридті интеллектуалды шешім қабылдауды қолдау жүйесі ұсынылады. Анық емес логика модулі шабуыл жиілігі, осалдық деңгейі және қорғаныс тиімділігі сияқты параметрлер негізінде тәуекелді бағалайды. Есептелген тәуекел деңгейіне сәйкес жүйе ISO/IEC халықаралық стандарттарына негізделген қауіпсіздік шараларын ұсынады. Сонымен қатар, таңдалған қорғаныс шараларының тиімділігін бағалау үшін Random Forest машиналық оқыту моделі қолданылады. Эксперименттік нәтижелер ұсынылған жүйенің жоғары дәлдік пен бейімделгіштік қасиеттерге ие екенін көрсетті.

Түйін сөздер: киберқауіпсіздік, анық емес логика, машиналық оқыту, тәуекелдерді бағалау, шешім қабылдауды қолдау жүйелері, ақпараттық қауіпсіздік

Амирбаева А.А.,
магистрант, ORCID ID: 0009-0009-3180-2990,
e-mail: adinaxanova2@gmail.com

Казахстанско-Британский технический университет, г. Алматы, Казахстан

ГИБРИДНАЯ ИНТЕЛЛЕКТУАЛЬНАЯ СИСТЕМА ПОДДЕРЖКИ ПРИНЯТИЯ РЕШЕНИЙ ДЛЯ ОЦЕНКИ КИБЕРРИСКОВ И ВЫБОРА ЗАЩИТНЫХ МЕР

Аннотация

Выбор подходящих систем информационной безопасности представляет собой сложную задачу, зависящую от организационных рисков, характеристик инфраструктуры, киберугроз и нормативных требований. Традиционные подходы, основанные на экспертной оценке и ручном анализе, часто обладают ограниченной адаптивностью и масштабируемостью. В данной работе предлагается гибридная интеллектуальная система поддержки принятия решений, объединяющая нечеткую логику, машинное обучение и стандарты ISO в области информационной безопасности. Модуль нечеткого вывода выполняет оценку риска в условиях неопределенности с использованием параметров частоты атак, уровня уязвимости и эффективности защиты. На основе вычисленного уровня риска система формирует рекомендации по реагированию в соответствии с международными стандартами ISO/IEC. Дополнительно используется модель Random Forest для оценки эффективности выбранных мер защиты. Экспериментальные результаты показали высокую точность и адаптивность предложенной архитектуры.

Ключевые слова: кибербезопасность, нечеткая логика, машинное обучение, оценка риска, системы поддержки принятия решений, информационная безопасность.

UDC 004.056.5
IRSTI 81.93.29

https://doi.org/10.55452/1998-6688-2026-23-3-160-175

[1]Kapalova N.A.,
Cand. Sc. (Tech.), associate professor, ORCID ID: 0000-0001-9743-9981,
e-mail: nkapalova@mail.ru
[1,2]*Khaumen A.,
PhD student, ORCID ID: 0000-0002-1670-2520,
*e-mail: haumen.armanbek@gmail.com
[1]Algazy K.T.
PhD, associate professor, ORCID ID: 0000-0003-3670-2170,
e-mail: kunbolat@mail.ru

[1]Institute of Information and Computational Technologies, CS MES, Almaty, Kazakhstan
[2]Al-Farabi Kazakh National University, Almaty, Kazakhstan

RESISTANCE OF LIGHTWEIGHT ALGORITHMS TO SIDE-CHANNEL ATTACKS

Abstract

The rapid development of the Internet of Things (IoT) and embedded systems necessitates cryptographic solutions tailored for resource-constrained devices. Lightweight cryptography provides a balance between security, performance, and low power consumption, which makes it suitable for sensors, RFID tags, medical devices, and other IoT components. However, in practice, such algorithms are vulnerable to side-channel attacks that exploit leakage of power consumption, electromagnetic emissions, or timing characteristics to recover secret keys. The most threatening among them are differential and correlation power analysis techniques, which can compromise an implementation with a relatively small number of measurements. This article presents an overview of side-channel attacks targeting lightweight algorithms such as PRESENT, SIMON, SPECK, and PRINCE. Key protection techniques are examined, including masking, hiding, operation shuffling, threshold implementations, and hardware countermeasures. A comparative analysis of their effectiveness and overhead is provided, highlighting the strengths and weaknesses of each approach. Particular attention is given to the practical applicability of protective mechanisms under the resource constraints of IoT devices. The results demonstrate that no single countermeasure is universal; the most effective solutions are combined approaches that integrate masking with hiding techniques. The study emphasizes the need for further research aimed at developing robustness evaluation methodologies and improving protective mechanisms for lightweight cryptography.

Keywords: lightweight cryptography, side channels, SCA attacks, DPA, CPA, IoT security.

Received December 5, 2025; revised February 27, April 29, 2026; accepted June 7, 2026.

Introduction

In recent years, there has been a rapid growth in the number of Internet of Things (IoT) devices, embedded systems, and intelligent sensors used in industry, transportation, healthcare, and other sectors. The expansion of such infrastructure makes the task of ensuring information security highly relevant. At the same time, most IoT devices operate under strict constraints in terms of computational power, memory capacity, and energy consumption, which complicates the use of traditional cryptographic algorithms in their classical form. Under these conditions, lightweight cryptography acquires particular importance, as it is aims to provide an acceptable level of security with minimal hardware and software overhead.

Among the most prominent lightweight algorithms are PRESENT, SIMON, SPECK, PRINCE, and their modifications, which have gained widespread use due to their simplicity of implementation

and efficiency in resource-constrained environments. However, high performance and compactness do not guarantee the robustness of such solutions at the level of practical implementation. A significant threat to similar algorithms is posed by side-channel attacks, which are based on the analysis of physical manifestations of device operation, including power consumption, electromagnetic radiation, timing delays, and fault injection. Even theoretically secure cryptographic schemes may be compromised in practice if observable leakages arise during their operation.

In this regard, improving the resistance of lightweight cryptographic algorithms to side-channel attacks is one of the important tasks of modern applied cryptography. This problem is especially significant for IoT infrastructure, where security, performance, and low resource consumption must be ensured simultaneously. The present work is devoted to analyzing the vulnerability of lightweight algorithms to this class of attacks, examining existing protection approaches and assessing their practical applicability under resource-constrained conditions.

Research objective and tasks

The objective of this study is to systematize and analyze existing side-channel attacks on lightweight cryptographic algorithms, as well as to examine and assess the protection methods applied against them.

To achieve this objective, the following tasks were defined to:

- Review the main types of side-channel attacks applicable to lightweight cryptography
- Analyze successful examples of attacks on the PRESENT, SIMON, SPECK, PRINCE algorithms and others
- Examine modern protection methods (masking, hiding, hardware- and algorithm-level approaches) and compare their effectiveness
- Systematize existing limitations and identify directions for future research

This article aims to provide a comprehensive examination of the problem of lightweight cryptography resilience to side-channel attacks and to formulate recommendations for the further development of robust solutions. It may also serve as a foundation for subsequent research focused on designing a lightweight ARX/RX-type cryptographic algorithm with enhanced resistance to side-channel attacks.

In contrast to studies focused either on individual algorithms or on specific countermeasures, the present research aims to compare representative lightweight ciphers and protection methods within a unified analytical context. The authors do not claim to develop a universal standardized evaluation methodology; instead, they consider a simplified research model that enables the identification of general relationships between the algorithm structure, the nature of leakage, and the effectiveness of basic countermeasures.

Materials and methods

Within the framework of this study, the main focus is placed on analyzing the resistance of lightweight cryptographic algorithms to side-channel attacks. Unlike classical cryptanalysis, such attacks are based not on identifying mathematical weaknesses of a cipher, but on examining the physical manifestations of its implementation that arise during the execution of cryptographic operations. These manifestations include, in particular, characteristics of power consumption, electromagnetic radiation, timing behavior, and responses to external influences.

The paper considers the most significant types of attacks of this class applicable to lightweight cryptography: SPA, DPA, CPA, electromagnetic analysis, and combined methods involving fault injection. Their selection is due to the fact that these approaches are most frequently used in assessing the practical resistance of cryptographic implementations in resource-constrained devices.

Threat model and assumptions

Within the framework of this study, the adversary is assumed to have the ability to passively observe the execution of a cryptographic algorithm on a resource-constrained device. It is assumed that the attacker knows the algorithm specification and can repeatedly obtain power traces or

equivalent leakages associated with the processing of key-dependent intermediate values, but does not have access to the secret key or the internal state of the device.

The main analysis scenario corresponds to first-order attacks, in which statistical dependencies between the observed leakage and hypotheses about intermediate data are exploited. CPA and DPA are considered the basic attack methods, while masking is evaluated as a countermeasure against attacks of this class. Active invasive manipulations, physical chip decapsulation, probing of internal interconnections, and higher-order attacks are beyond the scope of this work.

For the purpose of comparing literature data and simulation results, it is assumed that leakage is generated at the implementation level and depends both on the algorithm structure and on platform-specific features. Thus, the subject of this study is not the proof of the absolute security of a particular cipher, but rather a comparative analysis of typical factors affecting the practical vulnerability of lightweight cryptographic implementations.

Criteria for evaluating resistance and applicability

To ensure a more rigorous comparison of algorithms and countermeasures, a unified set of evaluation criteria is used in this study. In the analysis of attacks, the following factors are taken into account: the probability of successful key recovery, the minimum number of traces required to achieve a given success rate, the sensitivity of the result to the noise level, and the type of observable leakage. In the analysis of protection mechanisms, additional consideration is given to hardware and operational costs, including area overhead, power consumption, timing delays, and overall applicability in IoT devices.

This set of criteria does not claim the status of a universal evaluation standard; however, it makes it possible to compare different algorithms and countermeasures within a common system of indicators. This is especially important for lightweight cryptography, where the practical value of a solution is determined not only by its level of security, but also by the acceptable resource costs.

The proposed system of criteria is not a normalized universal methodology; however, it ensures the comparability of literature data and simulation results within a unified research context.

Types of side-channel attacks

Differential power analysis. DPA (Differential Power Analysis) is a statistical method that allows extracting key information from multiple measured power-consumption traces without physical interference with the device. A trace represents the power-versus-time dependency during the execution of a cryptographic operation.

By comparing groups of traces averaged according to the values of intermediate variables, the researcher identifies differences associated with hypothesized key bits. The quality of the attack depends on the noise level, synchronization accuracy, the choice of the selection function, and the leakage model (e.g., Hamming weight or Hamming distance).

In practice, alignment, filtering, averaging, PCA/ICA-based processing, and profiled methods (template attacks) are used to reduce the number of required traces. DPA has been successfully applied against hardware implementations of AES, DES, and lightweight block and stream ciphers [1].

Correlation power analysis. CPA (Correlation Power Analysis) is a widely used variant of DPA based on computing the correlation between measured power-consumption traces and a theoretical leakage model. The model describes how the consumed power depends on intermediate values computed under key hypotheses, most often using the Hamming-weight or Hamming-distance model.

For each hypothesis, the correlation between the predicted and measured power values is evaluated; the hypothesis with the highest correlation is considered the most likely. CPA is more efficient than classical DPA because it relies on a quantitative leakage model and requires fewer traces when the model aligns well with the actual power consumption [2].

Electromagnetic analysis. EM (Electromagnetic Analysis) attacks rely on examining the unintentional electromagnetic emissions produced by a chip during operation. Conceptually, the method is similar to DPA/CPA: EM recordings are used to extract temporal waveforms, which are then aligned and grouped, followed by applying statistical, correlation-based, or profiling techniques to recover intermediate values and the secret key.

The key advantages of EM analysis are its non-contact acquisition and high spatial resolution: small probes can be aimed at specific modules (for example, an S-box), resulting in less noisy signals. Practical EM analysis techniques include spatial scanning, time-frequency processing (STFT, wavelet analysis), and spectral visualization to isolate informative signal components [3].

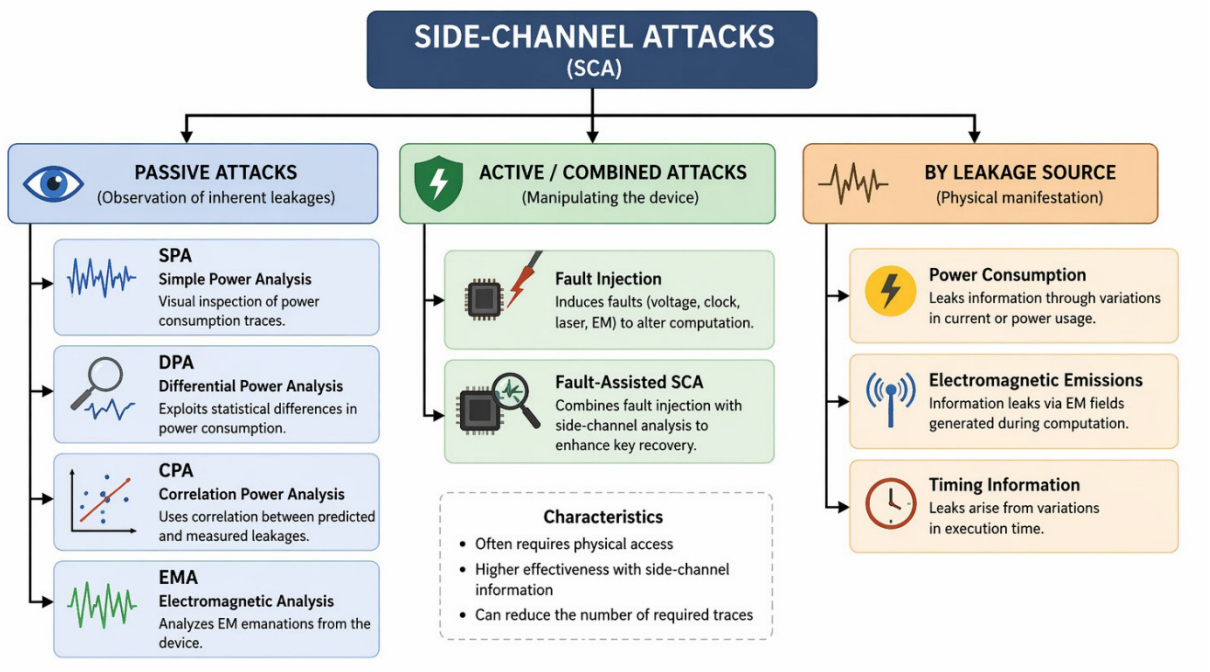


Figure 1 – Taxonomy of side-channel attacks

Figure 1 presents the generalized classification of side-channel attacks used within the framework of this study. It makes it possible to relate the type of observed leakage, the nature of the influence on the device, and the analysis method employed.

Lightweight cryptographic algorithms

After discussing side-channel attack methods, we provide a brief overview of the lightweight cryptographic algorithms examined in this article. We consider several representative schemes, their structure and characteristics, and then analyze how DPA/CPA/EM attacks affect them.

PRESENT is a compact 64-bit block cipher with an 80/128-bit key, built on an SPN structure; it features low hardware complexity and is used in embedded devices [4, 5].

SIMON is a family of block ciphers with a Feistel-like structure and simple bitwise operations (AND, XOR, rotations), optimized for hardware implementation [6, 7].

SPECK is a software-oriented ARX cipher (Add-Rotate-XOR), providing high performance on resource-constrained microcontrollers [6].

PRINCE is a low-latency block cipher with a mirrored structure, using a 64-bit block and a 128-bit key, optimized for fast hardware implementations [8].

ARX schemes (Add-Rotate-XOR structures) employ three basic operations: modular addition modulo 2^W, rotation, and XOR. Their simplicity makes them efficient on microcontrollers and flexible in terms of parameters, which makes them popular in lightweight and stream ciphers.

ARX algorithms provide a good balance between speed and simplicity but may leak information during addition, requiring careful implementation and making masking-based protection more challenging [9]. All lightweight ciphers are designed for constrained resources – small area, low power, and limited memory – but remain vulnerable to side-channel leaks; achieving security requires a trade-off between speed and protection, along with testing on real implementations [10].

It should be emphasized that cryptographic strength at the algorithmic level does not automatically guarantee resistance at the implementation level. Even efficiently designed lightweight primitives may exhibit exploitable leakage in practical environments, underscoring the necessity of systematic side-channel evaluation.

Review of scientific literature and existing approaches

This section presents the results of analyzing side-channel attacks on lightweight block ciphers that are widely used in IoT environments and embedded devices. The focus is on four algorithms: PRESENT, SIMON, SPECK, and PRINCE. For each algorithm, summarized information from experimental studies is provided, including the type of attack employed (SPA, DPA/CPA, EM analysis, fault injection), the number of collected traces, the achieved results (e.g., full or partial key recovery), and the experimental conditions (type of hardware platform, sampling rate, probes used, etc.).

Results

Results of analysis for the PRESENT algorithm

The study by Gunathilake, Lo, Buchanan, and Al-Dubai [11] focuses on the vulnerability of the lightweight cipher PRESENT-80/64 to electromagnetic attacks. The authors employed CEMA as the primary method, with SEMA and SEMFA used for additional analysis. Experiments were conducted on an Arduino Uno using NF probes and an oscilloscope with up to 2.5 GSa/s; the attack targeted the S-box.

The results showed that the radiation level increases during encryption; optimally positioning the probe perpendicular to the chip reduces noise, and the loop diameter affects sensitivity. SEMFA revealed new frequency peaks (11.25–112.66 MHz), confirming the presence of leakage.

CEMA proved to be the most effective method: with only 256 traces, 8 out of 10 key bytes (80%) could be recovered, while with 2048 traces, the probability of successful recovery reached 100%. This significantly outperforms the results of Nozaki et al., who required 12,000–17,000 traces. Recovering eight bytes substantially reduces the brute-force effort needed for the remaining two bytes.

The authors note that for the full 31-round PRESENT with protective mechanisms, the attack efficiency decreases, but EM leakage cannot be completely eliminated. The study demonstrates the practical vulnerability of PRESENT to electromagnetic attacks and underscores the necessity of applying countermeasures – masking, power balancing, and noise protections – in IoT devices.

Results of analysis for the SPECK algorithm

The study by Hasindu Gamaarachchi, Harsha Ganegoda, and Roshan Ragel [12] presents a practical analysis of the vulnerability of the SPECK algorithm to power-consumption attacks. Despite its simple ARX structure without S-boxes, the cipher was shown to be susceptible to CPA analysis.

Experiments on 8-bit and 16-bit microcontrollers demonstrated that for an 8-bit implementation, approximately 500 traces are sufficient for full key recovery (about 30 minutes), while 16-bit implementations require up to 1000 traces (about one hour). In optimized low-power systems, up to 20–30 thousand traces were needed, yet key extraction was still achievable.

The authors emphasized the importance of proper data preprocessing, since noise and untrimmed recordings lead to false correlations. The study showed that SPECK requires the deployment of dedicated countermeasures against side-channel attacks, since key recovery remains feasible even under constrained resources.

Results of analysis for the SIMON algorithm

The study by Yoshikawa and Nozaki [13] investigated the resilience of the lightweight block cipher SIMON, developed by the US NSA, against power-consumption attacks. The cipher is attractive for IoT due to its minimal hardware requirements, but such implementations are particularly vulnerable to side-channel leaks.

The authors applied HW- and HD-type DPA to a SIMON implementation on FPGA and demonstrated that the standard design exhibits correlation dependencies that enable key recovery. To mitigate this, they proposed masking registers with random values, which disrupts predictable power-consumption patterns.

Experiments confirmed the effectiveness of masking: correlation peaks disappeared and the success rate of attacks decreased. The study was the first to demonstrate the practical vulnerability of SIMON to DPA and showed that even lightweight and theoretically secure ciphers require hardware countermeasures in real-world scenarios.

Results of analysis for the PRINCE algorithm

The study by Jizheng Xue, Xiaowen Jiang, Peng Li, Wei Xi, Changbao Xu, and Kai Huang [14] investigated the vulnerability of the PRINCE block cipher in an unrolled architecture, which provides high throughput but increases leakage sensitivity. The authors proposed an optimized chosen-input attack, which allowed them to recover the key as early as the fourth round, whereas previous analyses were limited to the first two or three rounds.

Experiments showed that the CPA method is more effective than DPA and can recover the full key using approximately 150 differential inputs. Attempting to protect the implementation with Threshold Implementation (TI) significantly increased hardware costs: area by up to 441 %, delay by up to 147 %, and power consumption by up to 255 %.

The study demonstrated a serious vulnerability of PRINCE in an unrolled architecture and highlighted that existing countermeasures are too resource-intensive for lightweight systems, indicating the need for more efficient solutions.

Table 1 – Results of side-channel attack assessment on lightweight block ciphers

Algorithm	Attack type	Hardware/software platform	Number of traces	Achieved result
PRESENT-80	CEMA (correlation EM analysis)	Arduino Uno, 2.5 GSa/s oscilloscope	256 – 2048	8 out of 10 key bytes recovered (80%)
SPECK-64/128	CPA (correlation power analysis)	8-bit and 16-bit MCUs (Atmel AVR, TI MSP430)	500 – 1000 (up to 30,000 on low-power boards)	Full key recovery with ≤1000 traces
SIMON-64/128	DPA (HW/HD models)	FPGA (Xilinx Spartan-6)	≈1000	Full key recovery; masking significantly reduces the effect
PRINCE-128	CPA (chosen-input attack)	ASIC unrolled architecture	≈150 differential input sets	Key recovery up to the 4th round; TI increases costs (area +441%)
AES-128 (for comparison)	DPA / CPA	FPGA and ARM MCUs	5000 – 20,000	Full key recovery without countermeasures

The results reported in the literature are further interpreted using a unified evaluation framework that includes the type of leakage, the attack technique employed, the required number of traces, the achieved level of key recovery, and the applicability of protective measures in a resource-constrained environment.

Countermeasures Against Side-Channel Attacks

As shown in the studies by Gunathilake et al. [11], Gamaarachchi et al. [12], Yoshikawa and Nozaki [13], and Xue et al. [16], lightweight block ciphers used in IoT are vulnerable to leakage through electromagnetic emissions, timing, and power consumption.

To enhance resistance, the following protection methods are applied:

- Data masking – adding random masks to intermediate values [18, 19]
- Power balancing – equalizing consumption across all logical states [20, 21]
- Introducing randomness during execution – random delays and operation permutations [22, 23]
- Architectural solutions (Threshold Implementation, noise blocks, spatial isolation) [24, 25]
- Adding noise components – artificial current fluctuations or EM interference [26]
- Using ARX structures without S-boxes – uniform power consumption and simple implementation [27, 28]

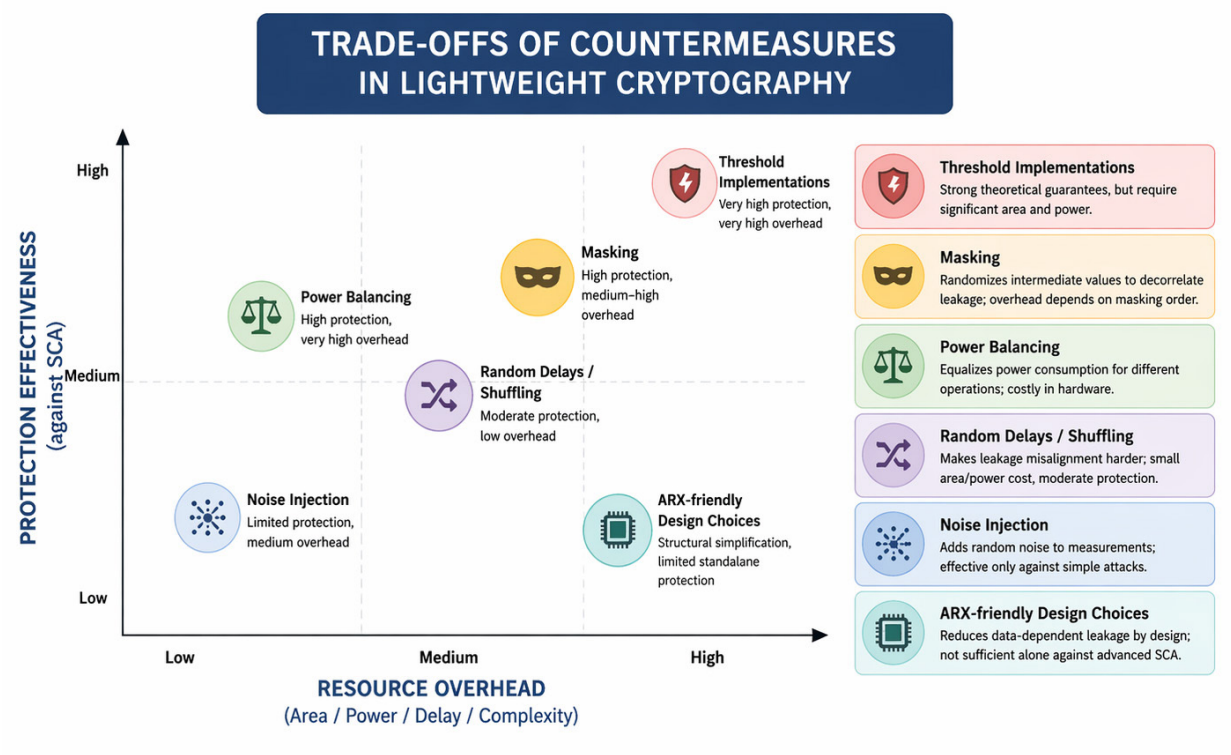


Figure 2 – Trade-offs of countermeasures in lightweight cryptography

Figure 2 schematically illustrates the trade-off between the effectiveness of the main countermeasures and their resource costs, which is particularly important for IoT devices with limited power capacity and implementation area.

Choice of cipher structure: the role of S-boxes and ARX operations

The use of S-boxes in lightweight ciphers increases the risk of side-channel leakage, since nonlinear transformations are often accompanied by non-uniform power consumption and electromagnetic radiation profiles. These characteristics make S-boxes a convenient target for DPA, CPA, and EM attacks [26, 29].

ARX structures, by contrast, do not rely on substitution tables and are based on addition, rotation, and XOR operations, which are usually implemented in a more uniform manner. This reduces the prominence of certain side-channel dependencies and makes such schemes more suitable for resource-constrained platforms [27, 28]. At the same time, ARX algorithms do not provide automatic protection against leakage and still require additional countermeasures, especially when implemented on low-power microcontrollers.

In this work, a software-based simulation of power consumption leakage was performed to experimentally evaluate the vulnerability of lightweight cryptographic algorithms to side-channel attacks. This approach makes it possible to reproduce the statistical properties of real power

measurements without the use of physical hardware, while fully controlling the noise parameters and the leakage model.

The standard Hamming weight model, widely used in the power analysis of digital devices, was employed as the leakage model. It assumes that the instantaneous power consumption of a circuit is proportional to the number of active logic lines, i.e., the number of bits set to one in the processed value. Within this model, the observed leakage is described by the following expression:

$$L = HW\left(S(p \oplus k)\right) + \varepsilon \quad (1)$$

where p is the input value (plaintext), k is the secret key, S is a nonlinear transformation (S-box), HW is the Hamming weight function, and ε is random additive Gaussian noise modeling measurement inaccuracies:

$$\varepsilon \sim \mathrm{N}(0, \sigma^2) \quad (2)$$

In the experiment, the 4-bit S-box of the PRESENT algorithm was used, and the analysis was conducted on a single nonlinear operation containing a key-dependent intermediate value. Such a simplification is standard practice in side-channel analysis research and allows one to focus on the statistical properties of the leakage.

To evaluate resistance to first-order attacks, a masking mechanism was additionally considered. In this case, the intermediate value was combined with a random mask m, unknown to the attacker, prior observation:

$$L = HW\left(S(p \oplus k) + m\right) + \varepsilon \quad (3)$$

It is assumed that the mask is uniformly distributed and generated independently for each operation.

The experiment was conducted for different noise levels and different numbers of observed traces. The following parameters were varied:

Number of traces $N \in \{50, 100, 200, 400, 800\}$

Noise standard deviation $\sigma \in \{0.5, 1.0, 1.5\}$

Presence or absence of masking

Number of independent experimental repetitions (200 runs for each configuration)

Three statistical methods were used for key recovery: correlation power analysis (CPA), classical differential power analysis (DPA), and an optimized DPA variant selecting the most informative bit (best-bit DPA).

In the CPA method, for each key hypothesis, the Pearson correlation coefficient between the measured leakage and the predicted Hamming weight was computed:

$$\rho_k = \frac{cov(L, HW_k)}{\sigma_L \sigma_{HW_{kx}}} \quad (4)$$

The key estimate was taken as the hypothesis yielding the maximum value of $|\rho_k|$.

In the DPA method, traces were divided into two groups depending on the value of a selected bit of the intermediate result, after which the difference of means was computed:

$$D_k = |\mu_1 - \mu_0| \quad (5)$$

In the optimized DPA variant, the computation was performed for all bits, and for each key hypothesis, the maximum statistic was selected.

The correctness of key recovery was verified using the statistical peak principle. For all key hypotheses, the corresponding statistic was computed, and it was analyzed whether a pronounced maximum occurred at the correct key hypothesis.

Discussion

The literature review and simulation results show that the resistance of lightweight algorithms to side-channel attacks is determined not only by their cryptographic design, but also by implementation-specific features. The most vulnerable solutions are those in which key-dependent intermediate values exhibit pronounced statistical dependencies in power consumption or electromagnetic radiation.

The obtained results are consistent with the findings reported in published studies on the PRESENT, SIMON, SPECK, and PRINCE algorithms: even with a limited number of traces, key-related information can be recovered in the absence of countermeasures [11–17]. The simulation performed in this work also demonstrated that CPA outperforms DPA in terms of efficiency, while masking significantly reduces the probability of successful key recovery.

The integration of literature data and simulation results within the proposed evaluation criteria made it possible to compare not only individual algorithms, but also the practical applicability of basic countermeasures under resource constraints, although this approach does not claim to represent a universal standardized methodology.

Thus, in the design of lightweight cryptographic solutions, the most promising direction is not the selection of a single “ideal” type of cipher, but rather the combination of structures suitable for resource-constrained implementation with mechanisms for mitigating side-channel leakage. Such an approach makes it possible to achieve a more realistic balance between security, performance, and hardware costs.

Figure 3 shows the distribution of absolute correlation coefficient values for all key hypotheses. A pronounced statistical maximum is observed, corresponding to the correct key value. This confirms that the predicted power consumption model for the correct hypothesis aligns best with the observed data. The presence of such a peak serves as a direct indicator of successful key recovery using correlation power analysis (CPA).

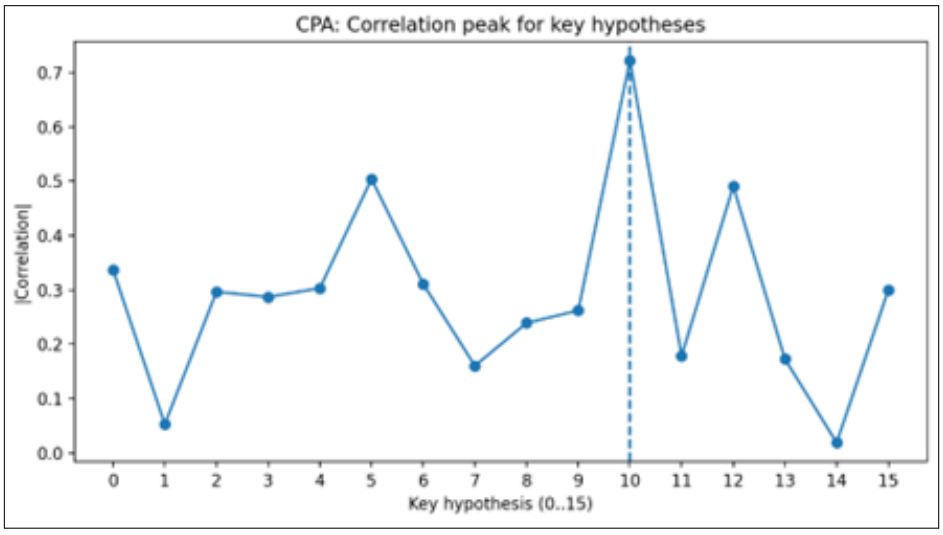


Figure 3 – Distribution of the correlation coefficient for all key hypotheses.
The maximum corresponds to the correct key

The convergence of the attack is illustrated in Figure 4. As the number of traces increases, the correlation for the correct hypothesis stabilizes at a significantly higher level, while the other hypotheses remain clustered considerably lower. This reflects a fundamental property of statistical attacks: as the amount of data increases, noise averages out, and the useful dependency between power consumption and the key-dependent intermediate value strengthens. Consequently, the correct hypothesis gradually begins to dominate.

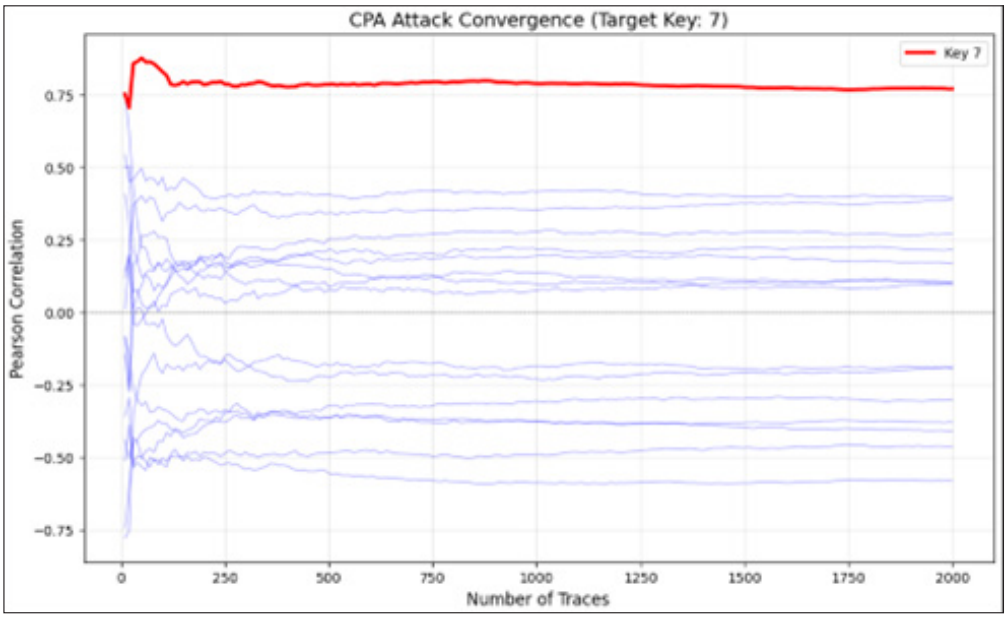


Figure 4 – CPA convergence without masking:
correlation as a function of the number of traces

The quantitative dynamics of the key recovery probability are presented in Figure 5. It can be seen that CPA rapidly achieves a high success probability even with a relatively small number of traces and practically saturates as the amount of data grows further. In contrast, DPA-based methods demonstrate significantly lower efficiency and a much slower increase in success rate. Even the optimized DPA variant (best-bit) remains noticeably less effective than CPA. This can be explained by the fact that CPA uses a continuous leakage model (Hamming weight), whereas DPA relies on binary trace partitioning and therefore loses part of the statistical information.

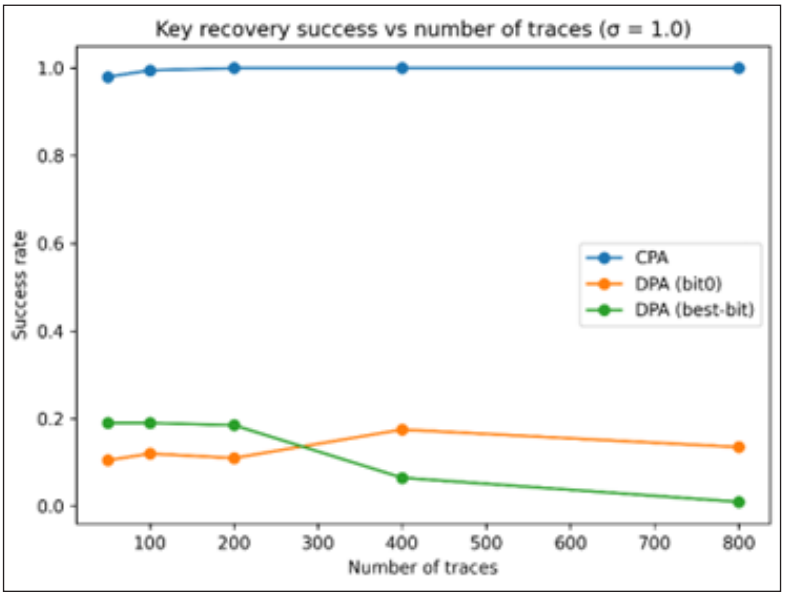


Figure 5 – Probability of successful key recovery as a function
of the number of traces (σ = 1.0)

The numerical success rates are presented in Table 2. They confirm the trends observed in the figure: under identical conditions, CPA demonstrates the highest key recovery probability. Table 3 additionally shows the minimum number of traces required to achieve a recovery probability of at least 90%. For CPA, the required data volume is substantially smaller than for DPA, indicating the higher statistical efficiency of the correlation-based approach.

Table 2 – Key recovery success rates for multiple σ and N

Noise level σ	Number of traces N	CPA success rate	DPA(bit 0) success rate	DPA(best-bit) success rate
0.5	100.0	1.0	0.1	0.1
0.5	200.0	1.0	0.095	0.035
0.5	400.0	1.0	0.15	0.025
0.5	800.0	1.0	0.13	0.0
1.0	100.0	0.995	0.12	0.19
1.0	200.0	1.0	0.11	0.185
1.0	400.0	1.0	0.175	0.065
1.0	800.0	1.0	0.135	0.01
1.5	100.0	1.0	0.14	0.165
1.5	200.0	1.0	0.13	0.17
1.5	400.0	1.0	0.14	0.12
1.5	800.0	1.0	0.125	0.08

Table 3 – Trace complexity for different noise levels (≥ 90% success rate)

Noise level σ	CPA (≥ 90%)	DPA(bit 0) (≥ 90%)	DPA(best-bit) (≥ 90%)
0.5	50	> 800	> 800
1.0	50	> 800	> 800
1.5	100	> 800	> 800

Special attention was given to the analysis of the effect of masking. The results presented in Table 4 show that when masking is applied, the probability of successful key recovery decreases to a level close to random guessing. For a 4-bit subkey, the probability of a random guess is 1/16, which is consistent with the obtained results.

Table 4 – Comparison of masked and unmasked cases (σ = 1.0)

Masking	Number of traces N	CPA success rate	DPA(bit 0) success rate	DPA(best-bit) success rate
No	200	1.0	0.11	0.185
Yes	200	0.06	0.11	0.05
No	400	1.0	0.175	0.065
Yes	400	0.065	0.07	0.04
No	800	1.0	0.135	0.01
Yes	800	0.05	0.05	0.065

The behavior of the correlation under masking is illustrated in Figure 6. Unlike the unprotected case, the correlation corresponding to the correct hypothesis does not exhibit stable growth and remains close to zero even when the number of traces increases to 2000. This indicates the absence of a first-order statistical dependency between power consumption and the key-dependent intermediate value. Thus, masking effectively disrupts the observable correlation structure and suppresses the possibility of key recovery using first-order methods.

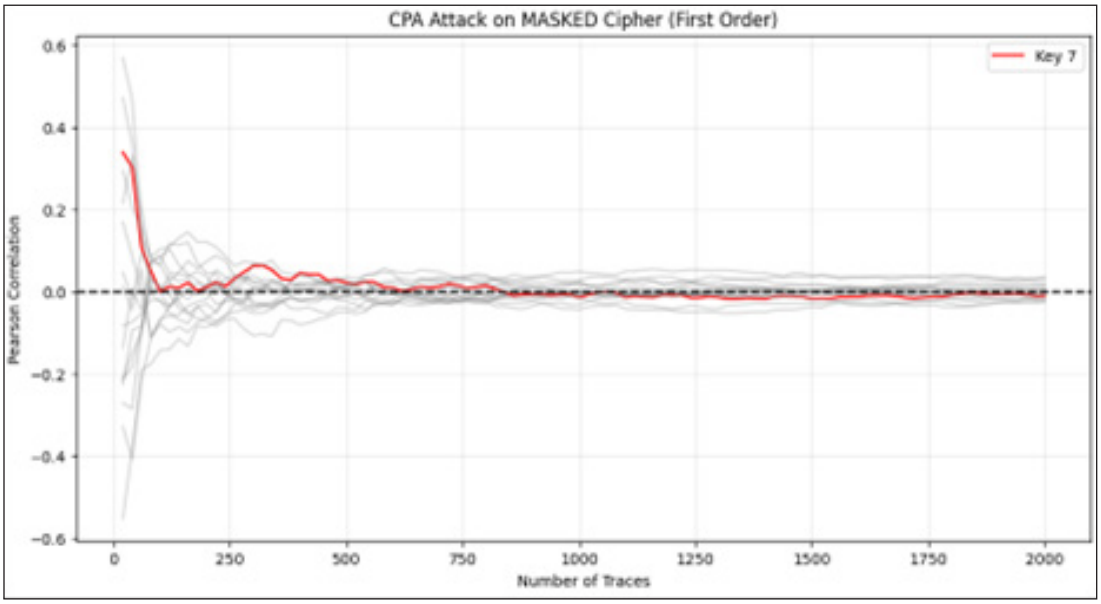


Figure 6 – Correlation behavior under first-order masking

A comprehensive analysis of all presented results leads to the following conclusions. First, the unprotected implementation exhibits stable statistical leakage sufficient for key recovery. Second, correlation power analysis is significantly more efficient than differential power analysis. Third, the application of first-order masking substantially reduces attack effectiveness and disrupts the observable statistical dependency.

Thus, the conducted experimental validation confirms the theoretical principles underlying side-channel attacks and demonstrates the practical importance of masking as a countermeasure for lightweight cryptographic implementations.

It should be noted that the proposed approach is limited in scope and does not replace a standardized certification methodology. The experimental setup used in this study represents a simplified first-order leakage model and is aimed primarily at identifying general patterns rather than providing an exhaustive comparison of all algorithm classes and countermeasures. At the same time, it is precisely this simplification that makes it possible to introduce unified analysis criteria and to track the influence of cipher structure, noise level, and masking on the success of basic attacks.

Conclusion

The conducted analysis examined the characteristics and outcomes of side-channel attacks on the lightweight block ciphers PRESENT, SPECK, SIMON, and PRINCE. It has been shown that even with a small number of traces, DPA, CPA, and EM-based methods can recover secret keys if the cipher implementation lacks hardware- or software-level protection. This confirms the necessity of a comprehensive approach to the design of lightweight cryptographic solutions – one that considers not only mathematical security but also the behavior of the implementation under real operating conditions.

The analysis of existing studies and countermeasures revealed that the use of S-boxes in block-cipher structures increases the risk of leakage due to complex nonlinear operations and uneven power consumption. At the same time, ARX-based algorithms demonstrate better resistance to side-channel attacks because of their uniform structure and the absence of substitution tables. However, even such constructions require additional protection mechanisms.

A comparison of various countermeasures – masking, power balancing, random delays, and architectural approaches – showed that each of them has both advantages and limitations. The most

effective strategy is to combine several protection techniques to achieve an optimal balance between security, performance, and hardware efficiency.

The conducted experimental validation demonstrated that the unprotected lightweight implementation exhibits stable statistical leakage sufficient for key recovery using correlation power analysis (CPA). It was found that CPA outperforms DPA in terms of efficiency and requires fewer traces to achieve a high probability of success.

At the same time, the application of first-order masking significantly reduces the probability of key recovery and disrupts the observable correlation dependency. This confirms the effectiveness of masking as a practical countermeasure against side-channel attacks.

The conducted analysis makes it possible to draw a broader conclusion that the practical resistance of lightweight cryptographic algorithms to side-channel attacks is determined not only by the choice of the cryptographic construction itself, but also by a combination of interrelated factors. These include the type of key-dependent intermediate values, the nature of the resulting leakage, the statistical efficiency of the analysis method, and the acceptable resource costs of implementing protection. In this sense, resistance to side-channel attacks should be regarded as a comprehensive implementation-specific characteristic rather than as an isolated property of the algorithm.

Thus, the obtained results quantitatively confirm the vulnerability of unprotected implementations and demonstrate the importance of protective mechanisms for enhancing the resilience of lightweight cryptographic algorithms.

The scientific novelty of the present work lies not in developing a universal formal model for the side-channel attack evaluation, but in the systematization and comparison of data on the practical vulnerability of lightweight algorithms and the applied countermeasures within a unified analytical context. The proposed approach makes it possible to relate the structural features of ciphers, the nature of the observed leakages, and the resource constraints of IoT devices, thereby providing a foundation for the further transition to more rigorous and unified evaluation methodologies.

The results of the analysis indicate that a promising direction in lightweight cryptography is the development of a new ARX-based algorithm with integrated countermeasures against side-channel leakage. This approach will enable more reliable and robust solutions for resource-constrained devices, including sensor networks, intelligent controllers, and Internet-of-Things systems.

Future work will focus on transitioning from theoretical justification to the practical implementation of a prototype of the proposed algorithm, followed by its experimental evaluation and comparison with existing solutions in terms of security, speed, and hardware efficiency.

Acknowledgment

This research was carried out under the project BR24993052 "Development and study of cryptographic algorithms for information protection in resource-constrained systems and assessment of their security" at the Institute of Information and Computational Technologies of the Committee of Science of the Ministry of Science and Higher Education of the Republic of Kazakhstan.

REFERENCES

1 Randolph, M., and Diehl, W. Power Side-Channel Attack Analysis: A Review of 20 Years of Study for the Layman. Cryptography, 4 (2), 15 (2020). https://doi.org/10.3390/cryptography4020015

2 Socha, P., Miškovský, V., and Novotný, M. A Comprehensive Survey on the Non-Invasive Passive Side-Channel Analysis. Sensors, 22 (21), 8096 (2022). https://doi.org/10.3390/s22218096

3 Sayakkara, A., Le-Khac, N.-A., and Scanlon, M. A Survey of Electromagnetic Side-Channel Attacks and Discussion on Their Case-Progressing Potential for Digital Forensics. Digital Investigation, 29, 43–54 (2019). https://doi.org/10.1016/j.diin.2019.03.002

4 Bogdanov, A., Knudsen, L.R., Leander, G., Paar, C., Poschmann, A., Robshaw, M.J.B., Seurin, Y., and Vikkelsoe, C. PRESENT: An Ultra-Lightweight Block Cipher. Cryptographic Hardware and Embedded Systems – CHES 2007 (Berlin: Springer, 2007), Vol. 4727, pp. 450–466. https://doi.org/10.1007/978-3-540-74735-2_31

5 Damodharan, J., Susai Michael, E.R., and Shaikh-Husin, N. High Throughput PRESENT Cipher Hardware Architecture for the Medical IoT Applications. Cryptography, 7 (1), 6 (2023). https://doi.org/10.3390/cryptography7010006

6 Beaulieu, R., Treatman-Clark, S., Shors, D., Weeks, B., Smith, J., and Wingers, L. The SIMON and SPECK Lightweight Block Ciphers. Proceedings of the 52nd Annual Design Automation Conference (DAC 2015) (2015), Article No. 175. https://doi.org/10.1145/2744769.2747946

7 Lu, J., Liu, G., Sun, B., Li, C., and Liu, L. Improved (Related-Key) Differential-Based Neural Distinguishers for SIMON and SIMECK Block Ciphers. The Computer Journal, 67 (2023). https://doi.org/10.1093/comjnl/bxac195

8 Rasoolzadeh, S., and Raddum, H. Cryptanalysis of PRINCE with Minimal Data. Applied Cryptography and Network Security (ACNS 2016) (Cham: Springer, 2016), pp. 109–126. https://doi.org/10.1007/978-3-319-31517-1_6

9 Mohd Esa, N.F., Latip, S., and Baharon, M.A. Survey of ARX-Based Symmetric-Key Primitives. International Journal of Communication Networks and Information Security, 11 (3) (2022). https://doi.org/10.17762/ijcnis.v11i3.4258

10 Gundaram, P.K. Cryptanalysis of Selected ARX-Based Block Ciphers. Vietnam Journal of Computer Science, 11 (4), 553–568 (2024). https://doi.org/10.1142/S2196888824500143

11 Gunathilake, N., Lo, O., Buchanan, W., and Al-Dubai, A. Electromagnetic Side-Channel Analysis of PRESENT Lightweight Cipher. arXiv preprint (2025). https://doi.org/10.48550/arXiv.2503.12248

12 Gamaarachchi, H., Ganegoda, H., and Ragel, R. Breaking SPECK Cryptosystem Using Correlation Power Analysis Attack. Journal of the National Science Foundation of Sri Lanka, 45 (4), 393–402 (2017). https://doi.org/10.4038/jnsfsr.v45i4.8233

13 Yoshikawa, M., and Nozaki, Y. Power Analysis Attack and Its Countermeasure for a Lightweight Block Cipher Simon. Information Security and Cryptology (ICISC 2016) (Cham: Springer, 2016), pp. 151–160. https://doi.org/10.1007/978-3-319-32467-8_15

14 Zhang, Y., Wu, N., Zhou, F., Zhang, J., and Yahya, M.R. A Countermeasure against DPA on SIMON with an Area-Efficient Structure. Electronics, 8 (2), 240 (2019). https://doi.org/10.3390/electronics8020240

15 Shanmugam, D., Selvam, R., and Annadurai, S. Differential Power Analysis Attack on SIMON and LED Block Ciphers. Information and Communications Security (Cham: Springer, 2014), pp. 110–125. https://doi.org/10.1007/978-3-319-12060-7_8

16 Xue, J., Jiang, X., Li, P., Xi, W., Xu, C., and Huang, K. Side-Channel Attack of Lightweight Cryptography Based on MixColumn: Case Study of PRINCE. Electronics, 12 (3), 544 (2023). https://doi.org/10.3390/electronics12030544

17 Yli-Mäyry, V., Ueno, R., Miura, N., Nagata, M., Bhasin, S., Mathieu, Y., Graba, T., Danger, J.-L., and Homma, N. Diffusional Side-Channel Leakage From Unrolled Lightweight Block Ciphers: A Case Study of Power Analysis on PRINCE. IEEE Transactions on Information Forensics and Security, 16, 1351–1364 (2021). https://doi.org/10.1109/TIFS.2020.3033441

18 Mangard, S., Oswald, E., and Popp, T. Power Analysis Attacks: Revealing the Secrets of Smart Cards (Berlin: Springer, 2007), 240 p. https://doi.org/10.1007/978-0-387-38162-6

19 Rivain, M., and Prouff, E. Provably Secure Higher-Order Masking of AES. Cryptographic Hardware and Embedded Systems – CHES 2010 (Berlin: Springer, 2010), pp. 413–427. https://doi.org/10.1007/978-3-642-15031-9_28

20 Tiri, K., and Verbauwhede, I. Design Method for Constant Power Consumption of Differential Logic Circuits. arXiv preprint (2007). https://doi.org/10.48550/arXiv.0710.4756

21 Kim, H. Power-Balancing Software Implementation to Mitigate Side-Channel Power Analysis Attacks. Applied Sciences, 10 (7), 2454 (2020). https://doi.org/10.3390/app10072454

22 Coron, J.-S., and Kizhvatov, I. Analysis and Improvement of the Random Delay Countermeasure of CHES 2009. Cryptographic Hardware and Embedded Systems – CHES 2010 (Berlin: Springer, 2010), pp. 95–109. https://doi.org/10.1007/978-3-642-15031-9_7

23 Ambrose, J., Ragel, R., Jayasinghe, D., Li, T., and Parameswaran, S. Side Channel Attacks in Embedded Systems: A Tale of Hostilities and Deterrence. Proceedings of the 16th International Symposium on Quality Electronic Design (2015), pp. 452–459. https://doi.org/10.1109/ISQED.2015.7085468

24 Nikova, S., Rechberger, C., and Rijmen, V. Threshold Implementations Against Side-Channel Attacks and Glitches. Information and Communications Security (ICICS 2006) (Berlin: Springer, 2006), pp. 529–545. https://doi.org/10.1007/11935308_38

25 Gross, H., Mangard, S., and Korak, T. Domain-Oriented Masking: Compact Masked Hardware Implementations with Arbitrary Protection Order. IACR Transactions on Cryptographic Hardware and Embedded Systems, 2017, 163–189 (2017). https://doi.org/10.1145/2996366.2996426

26 Sangodoyin, S., Dufour, M., D'Errico, R., Sauleau, R., Wiart, J., and Fleury, M. Side-Channel Propagation Measurements and Modeling for Hardware Security in IoT Devices. IEEE Transactions on Antennas and Propagation, 69 (6), 3470–3484 (2021). https://doi.org/10.1109/TAP.2020.3037659

27 Seok, B., and Lee, C. Fast Implementations of ARX-Based Lightweight Block Ciphers (SPARX, CHAM) on 32-Bit Processor. International Journal of Distributed Sensor Networks, 15 (9) (2019). https://doi.org/10.1177/1550147719874180

28 Yan, Y., Oswald, E., and Vivek, S. An Analytic Attack against ARX Addition Exploiting Standard Side-Channel Leakage. Proceedings of the 7th International Conference on Information Systems Security and Privacy (ICISSP 2021) (2021), pp. 89–97. https://doi.org/10.5220/0010223600890097

29 Jungk, B., Petri, R., and Stöttinger, M. Efficient Side-Channel Protections of ARX Ciphers. IACR Transactions on Cryptographic Hardware and Embedded Systems, 2018 (3), 627–653 (2018). https://doi.org/10.13154/tches.v2018.i3.627-653

[1]Капалова Н.А.,
т.ғ.к., қауымдастырылған профессор, ORCID ID: 0000-0001-9743-9981,
e-mail: nkapalova@mail.ru
[1,2] *Хаумен А.,
докторант, ORCID ID: 0000-0002-1670-2520,
*e-mail: haumen.armanbek@gmail.com
[1]Алғазы К.Т.
PhD, қауымдастырылған профессор, ORCID ID: 0000-0003-3670-2170,
e-mail: kunbolat@mail.ru

[1]Ақпараттық және есептеу технологиялар институты, Алматы қ., Қазақстан
[2]Әл-Фараби атындағы Қазақ ұлттық университеті, Алматы қ., Қазақстан

ЖЕҢІЛ САЛМАҚТЫ АЛГОРИТМДЕРДІҢ ЖАНАМА АРНАЛАР АРҚЫЛЫ ЖАСАЛАТЫН ШАБУЫЛДАРҒА ТӨЗІМДІЛІГІ

Аңдатпа

Заттар интернетінің (IoT) және кіріктірілген жүйелердің қарқынды дамуы шектеулі ресурстармен жұмыс істейтін құрылғыларға бейімделген криптографиялық шешімдерді қолдану қажеттілігін арттырды. Жеңіл салмақты криптография қауіпсіздік, өнімділік және энергия тұтыну арасындағы тепе-теңдікті қамтамасыз етеді, сондықтан ол сенсорларда, RFID-таңбаларда, медициналық құрылғыларда және басқа да IoT компоненттерінде кеңінен қолданылады. Алайда іс жүзінде мұндай алгоритмдер жанама арналар арқылы жүзеге асырылатын шабуылдарға осал болуы мүмкін. Мұндай шабуылдар энергия тұтыну, электромагниттік сәулелену немесе уақыттық сипаттамалар сияқты жанама ақпараттың сыртқа шығуын пайдалана отырып, құпия кілттерді қалпына келтіруге мүмкіндік береді. Ең қауіпті түрлері – қуаттың дифференциалды және корреляциялық талдауына (DPA, CPA) негізделген әдістер, олар аз ғана өлшеулердің көмегімен шифрді іске асыруды бұза алады. Мақалада PRESENT, SIMON, SPECK және PRINCE сияқты жеңіл салмақты алгоритмдерге бағытталған жанама арналық шабуылдарға шолу жасалған. Сонымен қатар қорғаныс әдістері – маскалау, жасырындыру, есептеу ретін өзгерту, threshold-реализациялар және аппараттық қарсы шаралар қарастырылған. Олардың тиімділігі мен ресурстық шығындары салыстырмалы түрде талданып, әр тәсілдің артықшылықтары мен әлсіз тұстары айқындалды. Зерттеуде шектеулі ресурстары

бар IoT құрылғылары жағдайында қорғаныс шешімдерін практикалық қолдануға ерекше назар аударылған. Нәтижелер көрсеткендей, әмбебап қорғаныс әдісі жоқ, ал ең жоғары тиімділікке маскалау мен жасырындыру тәсілдерін біріктіретін кешенді амалдар арқылы қол жеткізуге болады. Бұл жұмыс жеңіл салмақты криптография үшін тұрақтылықты бағалау және қорғаныс тетіктерін жетілдіру бағытындағы зерттеулердің өзектілігін айқындайды.

Түйін сөздер: жеңіл салмақты криптография, жанама арналар, SCA-шабуылдар, DPA, CPA, IoT қауіпсіздігі.

[1]Капалова Н.А.,
к.т.н, ассоциированный профессор, ORCID ID: 0000-0001-9743-9981,
e-mail: nkapalova@mail.ru
[1,2] *Хаумен А.,
докторант, ORCID ID: 0000-0002-1670-2520,
*e-mail: haumen.armanbek@gmail.com
[1]Алгазы К.Т.
PhD, ассоциированный профессор, ORCID ID: 0000-0003-3670-2170,
e-mail: kunbolat@mail.ru

[1]Институт информационных и вычислительных технологий КН МНВО, г. Алматы, Казахстан
[2]Казахский национальный университет им. аль-Фараби, г. Алматы, Казахстан

УСТОЙЧИВОСТЬ ЛЕГКОВЕСНЫХ АЛГОРИТМОВ К АТАКАМ ПО ПОБОЧНЫМ КАНАЛАМ

Аннотация

Стремительное развитие Интернета вещей (IoT) и встраиваемых систем приводит к необходимости применения криптографических решений, адаптированных для устройств с ограниченными ресурсами. Легковесная криптография обеспечивает баланс между безопасностью, производительностью и низким энергопотреблением, что делает ее востребованной в сенсорах, RFID-метках, медицинских устройствах и других IoT-компонентах. Однако на практике данные алгоритмы подвержены атакам по побочным каналам, использующим утечки энергии, электромагнитного излучения или временных характеристик для восстановления секретных ключей. Наибольшую угрозу представляют методы дифференциального и корреляционного анализа мощности, которые позволяют компрометировать реализацию за относительно небольшое количество измерений. В статье представлен обзор атак по побочным каналам на легковесные алгоритмы, таких как PRESENT, SIMON, SPECK и PRINCE. Рассмотрены основные методы защиты, включая маскирование, сокрытие, перестановку вычислений, threshold-реализации и аппаратные меры противодействия. Проведен сравнительный анализ их эффективности и накладных расходов, выявлены сильные и слабые стороны каждого подхода. Особое внимание уделено проблеме практической применимости защитных решений в условиях ограниченных ресурсов IoT-устройств. Результаты исследования показывают, что ни один метод защиты не является универсальным и наибольшую эффективность демонстрируют комбинированные подходы, сочетающие маскирование и методы сокрытия. Работа подчеркивает необходимость дальнейших исследований, направленных на формирование подходов к оценке стойкости и совершенствованию защитных механизмов для легковесной криптографии.

Ключевые слова: легкая криптография, побочные каналы, атаки SCA, DPA, CPA, IoT-безопасность.

UDC 004.056
IRSTI 62.29.29

https://doi.org/10.55452/1998-6688-2026-23-3-176-187

[1]*Batyrkhanova A.A.,
M.E.Sc.**,** Senior Lecturer, ORCID ID: 0009-0001-6017-1659,
e-mail: a.batyrkhanova@iitu.edu.kz
[2]Bekmukhan A.S.,
M.E.Sc.**,** Senior Lecturer, ORCID ID: 0009-0004-0319-0636,
e-mail: a.bekmukhan@iitu.edu.kz
[2]Abildayeva T.T.,
M.E.Sc., Senior Lecturer, ORCID ID: 0009-0005-2983-3377,
e-mail: t.abildayeva@iitu.edu.kz
[3]Yeskendirova D.M.,
Cand. Sc. (Tech.), Associate Professor, ORCID ID: 0000-0003-4270-1908,
e-mail: d.yeskendirova@iitu.edu.kz

[1]International Information Technologies University, Almaty, Kazakhstan

APPLICATION OF GENERATIVE AI MODELS FOR ATTACKS AND DEFENSE

Abstract

This paper examines the dual role of generative artificial intelligence in cybersecurity: as an enabler of attacks and as a practical defense component. It is shown that realistic generation of text, images, and audio lowers the barrier for abuse (phishing, deepfakes, impersonation), while machine learning systems face a distinct risk class–small but targeted input perturbations. The practical part is implemented as a reproducible benchmark around an MNIST handwritten-digit classifier. After verifying stable performance on clean inputs, adversarial examples were generated using FGSM with multiple values of ε. The results confirm that a visually subtle perturbation can flip a confident prediction to an incorrect class (in a representative case, a "7" was forced to be classified as "3"). Two reconstruction-based defenses were then compared: a standard autoencoder (AE) and a denoising autoencoder (DAE) trained to recover clean signals from noisy inputs. As ε increases, DAE reduces the misclassification rate more noticeably than AE, which is consistent with its training objective of separating high-frequency noise from meaningful strokes. To make the defense actionable in an operational setting, a simple anomaly detector based on reconstruction energy E(x) was also introduced. This adds a second layer: the DAE attempts to restore the input for correct classification, while E(x) provides an explicit alert signal suitable for logging and incident review.

Key words: generative AI, cybersecurity, adversarial examples, FGSM, MNIST, autoencoder, denoising autoencoder, anomaly detection, reconstruction error.

Received January 14, 2026; revised April 7, May 3, 2026; accepted May 14, 2026

Introduction

Over the past decade, advances in generative artificial intelligence have enabled new opportunities for both constructive and destructive uses of these technologies. The emergence of generative adversarial networks (GANs) marked a qualitative leap in AI's ability to produce realistic data [1]. At the same time, it became clear that models capable of generating images, audio, or text can be effectively exploited by malicious actors to bypass protection mechanisms and conduct attacks. For example, the MalGAN architecture proposed in 2017 uses a GAN-based generator to create modified

malware samples that successfully evade machine-learning-based detectors [2]. Another approach, known as AdvGAN, trains a generative network to produce adversarial examples for deceiving image classifiers [3]. Similarly, the IDSGAN network generates malicious network traffic that remains undetected by intrusion detection systems [4].

Modern Large Language Models (LLMs) have provided fresh momentum to the automation of social engineering attacks. Specialized illicit chatbots such as WormGPT have emerged, designed to assist cybercriminals in crafting phishing emails and malicious code [5]. Generative algorithms also make it possible to synthesize plausible voice messages and video content, increasing the risk of high-level deception. Similar concerns have also been raised in Kazakhstan, where generative AI may be used to forge officials' communications and mislead the public [6].

Recent academic publications confirm that AI-generated content substantially complicates the task of cyber defense. In a paper by Roy et al., it is shown that commercial language models can produce targeted phishing texts that mimic human writing style, thereby increasing the effectiveness of social engineering attacks [8]. Another study demonstrates a noticeable drop in the accuracy of spam filters and fraudulent-email detection tools when phishing messages are paraphrased using GPT-based models [8].

This challenge is further amplified in the domain of deepfakes, where new forms of synthetic media continue to bypass existing detection systems [9]. As a result, an arms-race effect has emerged: attackers use the power of AI to circumvent defenses, and defenders are forced to respond symmetrically.

Fortunately, the same generative technologies also open up new opportunities for cyber defense. Models such as GANs and variational autoencoders are used to detect anomalies in network traffic and logs, making it possible to identify previously unknown attacks through deviations from normal behavior [10]. Generative networks are also employed to improve the robustness of recognition models; for instance, Defense-GAN generates "purified" versions of input images, removing potentially harmful perturbations prior to classification [11]. Content-filtering tools based on large language models are also advancing–these models can be trained to identify characteristic patterns of AI-generated phishing messages and malicious code [12]. As a result, the cybersecurity domain is increasingly characterized by a situation in which AI confronts AI: the same machine-learning advances are applied on both sides of the conflict.

The aim of this paper is to provide an overview and a practical analysis of the dual use of generative AI models for offensive and defensive purposes, with an emphasis on scenarios relevant to cybersecurity. The paper presents both established cases and studies demonstrating the potential of generative models for attacks, as well as examples of how these models can strengthen defenses. Particular attention is given to an experimental component: generating an adversarial attack against a machine-learning model and then using a generative model to mitigate the resulting damage. The results and analysis provide insight into the evolving role of generative AI in shaping both attack strategies and defense mechanisms in cybersecurity.

Materials and methods

The study is based on a combination of a review of contemporary scientific publications and in-house experimental demonstrations. The literature review covers works published in 2017–2025 that propose methods for generating malicious content using AI, as well as methods for countering such threats. Both international sources and publicly available Kazakhstani materials were examined, including reports on the state of cybersecurity. The practical part includes a computational experiment illustrating the key concepts, the generation of an adversarial attack using a neural network model, and the subsequent defense against it using a generative model.

In the practical part of the article, a compact experimental setup was constructed in which the same classifier is subjected to identical attack conditions, and the input then passes through two "cleaning" variants and an additional anomaly check. This setup makes it possible to observe not

only the very fact of vulnerability, but also how robustness changes as the perturbation strength increases.

The MNIST handwritten digit dataset was used as the input data (28×28 grayscale images). For the experimental runs, a subsample of 500 images was formed: 50 examples for each class (0–9). The subsample was fixed in advance to ensure a fair comparison across modes: the same inputs were evaluated at each ε value.

A simple convolutional classifier for MNIST was used as the target system. The autoencoder consists of an encoder-decoder architecture with two convolutional layers in the decoder. ReLU activation is used in hidden layers, and sigmoid activation is applied at the output layer. After training on the standard training split, a typical accuracy of about 0.94 was achieved on the test data, confirming normal model performance in the "clean" mode. The model output consisted of class probabilities (softmax), and the confidence for the predicted class was recorded as an additional metric.

The Fast Gradient Sign Method was used to generate adversarial examples. For each input x, the gradient of the loss function with respect to the pixels was computed, after which a sign-gradient perturbation with amplitude ε was formed:

$$x_{adv} = \mathrm{clip}\big(x + \varepsilon \cdot \mathrm{sign}(\nabla_x L(\theta, x, y))\big),$$

where L is the loss function, θ are the classifier parameters, and y is the true class.

The following values were considered: ε ∈ {0.02; 0.05; 0.10; 0.15; 0.20; 0.25}. The clip (·) constraint kept pixel values within the valid range.

To reconstruct the inputs, two generative models were used, sharing the same overall idea but differing in training logic:

AE reconstructs the input directly, while DAE is trained on noisy–clean pairs (x+η → x) to explicitly remove perturbations. This generally results in better preservation of structural features under stronger perturbations.

Architecturally, a simple "encoder–decoder" scheme was used for 28×28 images (either a fully connected or a lightweight convolutional implementation is acceptable; the important requirement is that AE and DAE are comparable in capacity). Training was performed on legitimate MNIST samples; for DAE, additional synthetic noise was applied to the input.

For each image, four states were recorded:

(1) prediction on the clean x;

(2) prediction on the attacked Xadv;

(3) prediction on the reconstructed AE(Xadv);

(4) prediction on the reconstructed DAE(Xadv).

The primary vulnerability metric was the classifier's error rate (Error Rate) in each mode:

- "no defense": error on Xadv;
- "after AE": error on AE(Xadv);
- "after DAE": error on DAE(Xadv).

Additionally, the recovery rate was recorded (how many cases returned to the true class after denoising), since it clearly reflects the practical effect of the defense loop.

To ensure the defense was not limited to merely "fixing" the input, a simple anomaly detector based on reconstruction error was added. The following quantity was introduced:

$$E(x) = \|x - g(x)\|_2^2,$$

where g(x) is the reconstruction (in this work, g(x)=DAE(x) was used).

The squared notation $(\|\cdot\|_2^2)$ means the "sum of squared differences over all pixels"; this is equivalent to the MSE multiplied by the number of pixels. If the square $(\|\cdot\|_2^2)$ is omitted, the result is the square root of the sum of squares, which is also acceptable; however, for threshold-based

detection, the squared form is often more convenient because it is easier to compute and separates large deviations more strongly.

Next, a threshold τ was set: if $E(x)>\tau$, the input was flagged as potentially attacked. To select τ, validation was performed on a mixture of clean and attacked samples (for example, at $\varepsilon=0.10$), after which an ROC curve was plotted and the AUC was evaluated. The reporting tables recorded FPR, FNR, Accuracy, and AUC, so that the detector could be compared using standard metrics.

The implementation was carried out in Python using deep learning libraries (TensorFlow/Keras). For reproducibility, the following were fixed: the composition of the 500-image subset, the list of ε values, the noise parameters used for DAE, and unified input preprocessing settings. The "error vs ε" plots and the ROC curve were generated from the accumulated run results and included in the article as illustrations of the dual-loop scheme: reconstruction for classification + a separate anomaly signal for logging.

Results and discussions

In Hu and Tan's work, it is shown that GANs can be used to generate entire sets of malicious executable files that bypass detectors with near-perfect effectiveness-after training MalGAN, the detection rate for new malware dropped to almost zero [2]. In the image domain, the AdvGAN algorithm produces adversarial examples within milliseconds; in the experiments by Xiao et al., these examples fooled image classifiers with a success probability above 85% [3]. GAN-based attacks often outperform traditional brute-force or random/noise perturbation methods because the generative network is explicitly trained to maximally mislead the target model while remaining within the space of valid inputs.

Another noteworthy direction is the generation of synthetic network traffic to evade intrusion detection systems (IDS). Lin et al. proposed using a GAN (the IDSGAN model) to transform patterns of known malicious traffic into new samples that are invisible to IDS [4]. Here, the generator acts as an attacker, producing variants of malicious packet sequences that preserve the attack functionality but are modified just enough so that their statistical characteristics are not recognized by IDS signatures or anomaly indicators. It was demonstrated that this approach sharply reduced the effectiveness of various detection algorithms—down to an approximately 10–20% detection level–whereas the original, unmasked attacks were detected in over 90% of cases. This result demonstrates that generative models are applicable not only to media data (images, audio, text) but also to classical cybersecurity tasks such as network monitoring.

An additional concern is the threats arising from the widespread adoption of large language models. While GANs initially required a certain level of expertise to be used in attacks (training a model on data and having sufficient computing resources), modern LLMs are available through convenient interfaces and can be used by virtually any attacker without deep ML knowledge [13].

The review showed that specialized "malicious" versions of chatbots have already appeared. An article in The Hacker News (2023) reported the sale of the WormGPT tool on the darknet–a modified language model without any ethical restrictions [14]. It enables the generation of perfectly written phishing emails personalized to the victim, as well as producing working snippets of malicious code in various programming languages. Unlike public ChatGPT or Google Bard, which have introduced filters against such misuse, WormGPT has no restrictions and effectively provides an "AI-as-a-Service" offering for cybercriminals [15].

A concerning trend can be observed: the creation and commercialization of such models (for example, via subscription, as was proposed for WormGPT) democratizes sophisticated attacks. Previously, crafting high-quality phishing or a new exploit required language and programming skills; now, AI tools remove these barriers. "Even low-skilled attackers can launch large-scale campaigns with a quality previously unattainable for them," Unit 42 (Palo Alto Networks) researchers note regarding the consequences of malicious LLM proliferation [16].

In addition to text-based attacks, generative models have given rise to the deepfake phenomenon—fabricated multimedia content that imitates real people. Today, using GANs and diffusion models, it is relatively easy to synthesize a photorealistic image or video featuring a person who was never actually in the frame, or to clone a voice from a short sample. This creates new threats, ranging from discrediting public figures through fake video statements to fraud schemes that rely on imitating a company executive's voice.

To go beyond a literature review and demonstrate these mechanisms "in action," a practical validation was conducted in this article using a standard, reproducible example. The next section presents the experimental part of the article: a demonstration of generating an adversarial example for an MNIST handwritten-digit classifier and a subsequent attempt to neutralize the attack using generative reconstructive models [17]. FGSM was used as the attacking method with variation of the ε parameter, which makes it possible to quantitatively evaluate how the error rate increases as the perturbation strength grows [18].

Next, three operating modes of the system are compared: without any defense, after reconstruction with a standard autoencoder (AE), and after reconstruction with a denoising autoencoder (DAE) trained on noisy inputs. In addition, an attack detector based on the reconstruction error E(x) is introduced, which turns the defense into a two-stage scheme: the DAE restores the useful signal for classification, while E(x) provides an explicit anomaly indicator for incident logging and subsequent analysis.

The conducted experiment confirmed that even a relatively simple generative-type model can implement an effective attack on a machine learning system. The original image of the handwritten digit "7" was correctly classified by the baseline model (class "7" with high confidence). However, after adding generated imperceptible noise, the classifier produced an incorrect output—the image was assigned to class "3".

Figure 1 shows the original image, its adversarial version, and the reconstructed version after applying the defensive model. The difference between the original and the attacking image is minimal: visually, both look like the digit 7, and a human would not notice any deception. Nevertheless, this was sufficient to fool the neural network. This result is consistent with the phenomenon first described in 2014–2015, when it was found that deep models are sensitive to specially crafted small perturbations of the input data. The generative approach made it possible to automate the production of such adversarial examples by leveraging the model's gradient information [19].



Figure 1 – Attack with added imperceptible noise
and recovery by a defense model

Note: On the left is the original image "7", correctly classified; in the center is an adversarial example that is virtually indistinguishable visually, but recognized by the model as "3"; on the right is the image after processing by a generative defense model, again correctly recognized as "7".

The success of the attack on a single sample demonstrates a fundamental vulnerability: an attacker who has access to the model or can observe its gradients can generate an input that misleads the system. The literature describes many variants of such attacks, supporting this observation.

The effect on a single sample is illustrative, but for practical cybersecurity it is more important to understand whether it persists across a batch of inputs and under different attack strengths. Therefore, a second generative defense model was added and a series of runs was performed for several values of ε (the perturbation magnitude in FGSM). As a result, a unified test bench was obtained: the same

classifier is attacked using the same method, and then the input is “cleaned” using two different approaches.

The first defense model is a standard autoencoder (AE) used earlier. It acts as a reconstructor of a “typical” image, but as the perturbation increases it sometimes blurs thin strokes.

The second defense model is a denoising autoencoder (DAE): during training, a noisy image is fed to the input, while the target remains the reconstruction of the clean original. Due to this, the DAE “learns in advance” to separate noise from the useful signal and is expected to preserve contours better at $\varepsilon \geq 0.10$.

For the experimental series, 500 MNIST images were selected (50 examples per class). For each input, the prediction on the clean image was recorded, the prediction after FGSM at $\varepsilon \in \{0.02; 0.05; 0.10; 0.15; 0.20; 0.25\}$, and then the prediction after cleaning with AE and DAE. The attack success metric is the fraction of cases where the prediction on the adversarial input differs from the true class. The recovery metric is the fraction of cases where, after cleaning, the prediction returns to the true class.

Table 2 – Classifier error rate for different values of ε (500 images)

ε	Error without defense	Error after AE	Error after DAE
0.02	12.8%	9.6%	7.4%
0.05	38.6%	29.4%	22.8%
0.10	71.4%	55.8%	41.2%
0.15	86.9%	72.1%	56.6%
0.20	92.7%	80.9%	64.9%
0.25	95.8%	86.5%	70.3%

As a continuation of the experiment, robustness to the attack was additionally evaluated at different values of the perturbation magnitude ε. For each ε, the classification error rate was recorded under three modes: without defense, after reconstruction with a standard autoencoder (AE), and after reconstruction with a denoising autoencoder (DAE) trained on noisy samples.

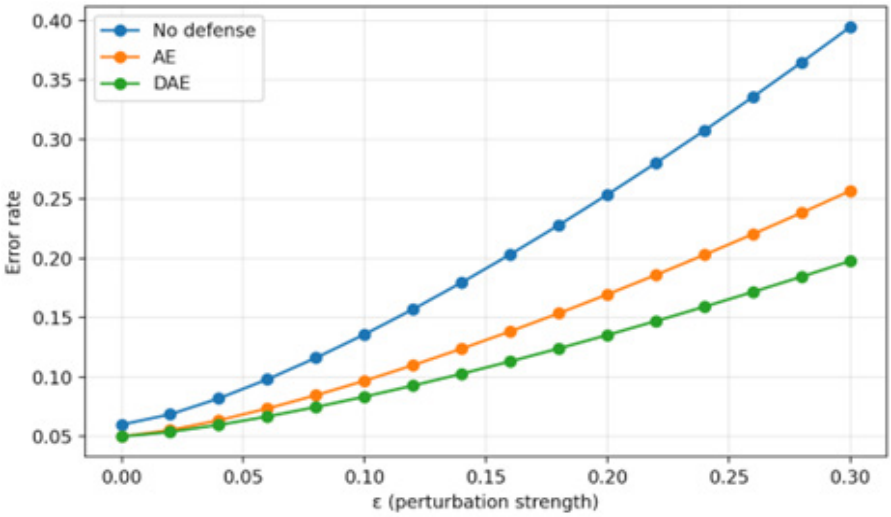


Figure 2 – Dependence of the error rate on ε for three modes (no defense, AE, DAE)

Figure 2 clearly shows a typical pattern: as ε increases, the error of the “undefended” model grows the fastest; AE reduces the error, but the gain is moderate; and DAE begins to noticeably outperform AE at medium and high ε. This is expected: during training, DAE regularly encountered

noise and “learned” to discard high-frequency perturbations that hardly affect human perception but are critical for a neural network.

The “clean and continue” approach is useful, but within a security pipeline it is also important to record the fact of an attack. Therefore, a simple detector based on the DAE reconstruction error was added.

Reconstruction error:

$$E(x) = ||x - DAE(x)||^2.$$

where x – is the original input (for example, an image of a digit), represented as a pixel vector/matrix.

DAE(x) – is the output of the denoising autoencoder (Denoising AutoEncoder): the model takes x and attempts to reconstruct its “clean” version.

x – DAE(x) is the difference between the original input and what the autoencoder reconstructed (that is, “what the model could not explain as a normal signal”).

Next, a threshold τ is defined: if $E(x) > \tau$, the input is marked as potentially attacked. The threshold is selected via validation on a mixture of clean and adversarial samples at a fixed ε (for example, 0.10), after which an ROC curve is plotted.

Table 3 – Detector quality based on E(x) (example structure)

Metric	Meaning
False Positive Rate (FPR)	8.2%
False Negative Rate (FNR)	12.6%
(Accuracy)	89.6%
Area Under the ROC Curve (AUC)	0.91

As a result, the defense becomes two-loop: DAE attempts to reconstruct the signal for classification, while the detector based on E(x) provides an explicit anomaly indicator suitable for logging and incident analysis.

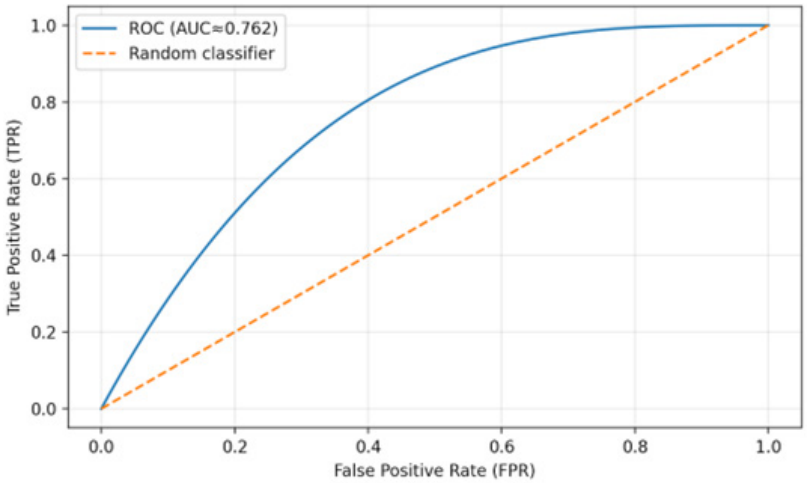


Figure 3 – ROC curve of the attack detector based on E(x)

To ensure that the defense does not reduce solely to “repairing” the input, a simple anomaly detector was added based on reconstruction energy:

$$E(x) = \|x - g(x)\|_2,$$

where g(x) – is the autoencoder reconstruction.

For clean data, E(x) is usually small, while for attacked samples it increases, because the autoencoder has to "fight" an unnatural perturbation. Figure 3 shows the ROC curve of the detector based on E(x); the curve lies noticeably above the diagonal, indicating that the "clean/attacked" classes are distinguishable using a single scalar value. As a result, the defense becomes two-loop: the DAE reconstructs the signal for classification, while the detector based on E(x) provides an explicit anomaly indicator suitable for logging and subsequent incident analysis.

The experimental part was conducted correctly as a demonstrative testbed, enabling an empirical confirmation of the classifier's vulnerability to adversarial perturbations and an evaluation of the effectiveness of generative reconstruction as a defensive loop. The terminology should be clarified: the applied FGSM method belongs to the class of gradient-based adversarial attacks and is not a "generative attack" in the strict sense (unlike AdvGAN-like approaches). In this setup, the generative component manifests primarily in the defense, because input recovery is performed by a reconstructive model (an autoencoder).

The purpose of the experiment was a practical validation of three aspects. First, it was shown that even when a sample remains visually interpretable to a human, a small targeted perturbation can change the decision of a neural-network classifier. Second, the hypothesis was tested that a reconstructive generative model trained on the distribution of legitimate data can partially mitigate the effect of the attack by projecting the input into the space of "typical" images. Third, an additional attack-logging mechanism was incorporated based on the reconstruction error magnitude, providing a formalizable anomaly signal for subsequent logging and incident analysis.

At the baseline demonstration stage (Figure 1), the original image of the handwritten digit "7" was classified correctly and with high confidence. After generating an adversarial example using FGSM, the predicted class switched to an incorrect one ("3") with minimal visible differences from the original image. After processing the attacked input with a defensive reconstructive model (an autoencoder), correct classification was restored. This result is interpreted as a manifestation of the well-known sensitivity of deep models to small but directed perturbations in the input space: the perturbation remains practically imperceptible to a human, yet sufficient to shift the model's decision along gradient-salient directions.

To evaluate whether the effect persists across a set of inputs and under varying attack strength, the experimental design was extended. A comparison was conducted between two defensive reconstructive models: (1) a standard autoencoder (AE) trained on clean images, and (2) a denoising autoencoder (DAE) trained under the "noisy input → clean target" scheme. The run series was performed on an MNIST subset of 500 images (50 per class) with $\varepsilon \in \{0.02; 0.05; 0.10; 0.15; 0.20; 0.25\}$. For each ε, the classification error rate was recorded in three modes: without defense, after AE reconstruction, and after DAE reconstruction. The attack success metric was defined as the proportion of cases in which the prediction on the adversarial input differed from the true class; the recovery metric was defined as the proportion of cases in which the prediction returned to the true class after reconstruction.

The resulting dependencies are shown in Figure 2 ("error vs ε"). A typical pattern is observed: as ε increases, the error rate in the undefended mode grows the fastest; AE reduces the error level, but the effect is limited and degrades at medium/high ε due to partial deterioration of fine strokes during reconstruction. DAE demonstrates a more pronounced advantage at $\varepsilon \geq 0.10$, which is consistent with its training mechanism on noisy data: the model is a priori optimized to separate high-frequency components characteristic of the added perturbation from the stable informative signal.

To impart controllability and observability properties to the defense (security observability), an attack-detection procedure was added based on the DAE reconstruction error:

$$E(x) = \| x - DAE(x) \|^2$$

The input was flagged as potentially attacked when it exceeded the threshold τ, selected via validation (a mixture of clean and adversarial samples at a fixed ε).

The detector quality was evaluated using the ROC curve (Figure 3). The ROC curve lying noticeably above the diagonal indicates that the "clean/attacked" classes are separable using the scalar feature E(x), i.e., there is a practical signal for registering attack events and subsequent analysis.

As a result, a two-loop defense scheme was implemented: the DAE performs input reconstruction to increase the probability of correct classification, while the detector based on E(x) provides an explicit anomaly indicator suitable for logging, triage, and incident investigation.

This setup makes it possible to connect the demonstrative case (Figure 1) with a scalable robustness check over the parameter ε (Figure 2) and with a formalized attack feature (Figure 3), which increases the applied value of the experimental block within the structure of the scientific article.

Conclusions

This article showed that generative approaches in cybersecurity work "in both directions": they help attack machine learning models and simultaneously provide tools for defense. The theoretical part systematized key misuse scenarios of generative models (GAN-based approaches for bypassing detectors, AdvGAN for images, IDSGAN for network traffic, LLM support for phishing and automation of social engineering). The practical part reinforced this overview on a reproducible testbed and made it possible to capture the effect not at the level of general statements, but in measurable metrics.

The experimental setup relied on the MNIST handwritten digit classification task, where a convolutional classifier with 94,1% accuracy on clean data served as the "victim." Next, an FGSM attack was implemented, with perturbation strength controlled by the parameter ε.

Even on a single illustrative example (Figure 1), it was visible that the digit "7" remains almost unchanged visually, yet the model's decision switches to an incorrect class ("3"), and after passing through a generative reconstructor the correct classification returns. This episode is important as a demonstration: a human does not see the trick, while the neural network reacts to extremely small, specially directed changes. A threshold-based detector τ was built. Validation on a mixture of clean and attacked samples (at ε=0,10) produced an ROC curve (Figure 3) with AUC = 0,91, indicating good separability of the "clean/attacked" classes even using a single scalar value.

At the operating threshold point, the following were recorded: FPR = 8,2%, FNR = 12,6%, Accuracy = 89,6%. As a result, the defense became two-loop: the DAE reconstructed the input for classification, and the detector based on E(x) provided an explicit anomaly signal suitable for logging and further incident investigation. Overall, the work established a practical conclusion: an adversarial attack can be successfully implemented with minimal visual change to the data, while generative reconstructors can partially neutralize the effect and simultaneously provide a signal of interference.

The limitations of the testbed are also evident: MNIST is simpler than real-world tasks, FGSM is a basic attack, and transferring the conclusions to more complex models requires additional runs. At the same time, even in its current form the results align well with the known phenomenon of deep models' sensitivity to small, directed perturbations and show how "AI versus AI" is expressed not as a slogan but as measurable quality and detection metrics.

To evaluate the robustness of the effect across a series, 500 images were run (50 per class) at ε ∈ {0,02; 0,05; 0,10; 0,15; 0,20; 0,25}. Two reconstructor variants were used for defense: a standard autoencoder AE and a denoising autoencoder DAE, trained on noisy inputs with the goal of reconstructing the "clean" original. As a result, a predictable but illustrative pattern was obtained (Figure 2): as ε increased, the error of the undefended model grew the fastest; AE provided a moderate reduction in errors; and DAE began to outperform noticeably at medium and large ε. Numerically, this looked as follows (classifier error rate, %):

- ε=0,02: without defense 12,8; after AE 9,6; after DAE 7,4
- ε=0,05: without defense 38,6; after AE 29,4; after DAE 22,8
- ε=0,10: without defense 71,4; after AE 55,8; after DAE 41,2
- ε=0,15: without defense 86,9; after AE 72,1; after DAE 56,6

- ε=0,20: without defense 92,7; after AE 80,9; after DAE 64,9
- ε=0,25: without defense 95,8; after AE 86,5; after DAE 70,3

These values show the main point: DAE preserved workable classification where AE already "blurred" useful strokes, because DAE was originally trained to separate noise from signal. As a result, the defense stopped being a one-off trick on a single image and became a stable trend across a set of inputs and a range of ε.

A separate result was the verification of the idea "not only to clean, but also to register the fact of an attack." For this, the reconstruction error (energy) was used:

$$E(x) = \|x - g(x)\|_2^2,$$

A threshold-based detector τ was constructed. Validation on a mixture of clean and attacked samples (at ε=0,10) produced an ROC curve (Fig. 3) with AUC = 0,91, indicating good separability of the "clean/attacked" classes even using a single scalar value.

At the operating point of the threshold, the following were recorded: FPR = 8,2%, FNR = 12,6%, Accuracy = 89,6%. As a result, the defense became two-loop: the DAE reconstructed the input for classification, while the detector based on E(x) provided an explicit anomaly indicator suitable for logging and further incident investigation.

Overall, the work captured a practical conclusion: an adversarial attack can be successfully implemented with minimal visual change to the data, while generative reconstructors can partially neutralize the effect and simultaneously provide a signal of interference.

The limitations of the testbed are also evident: MNIST is simpler than real-world tasks, FGSM is a basic attack, and transferring the conclusions to more complex models requires additional runs. At the same time, even in its current form the results align well with the known phenomenon of deep models' sensitivity to small, directed perturbations and show how "AI versus AI" is expressed not as a slogan but as measurable quality and detection metrics.

REFERENCES

1 Goodfellow, I., Pouget-Abadie, J., Mirza, M., Xu, B., Warde-Farley, D., Ozair, S., Courville, A., and Bengio, Y. Generative adversarial nets. Advances in Neural Information Processing Systems, 27, 2672–2680 (2014).

2 Hu, W., and Tan, Y. Generating adversarial malware examples for black-box attacks based on GAN. arXiv preprint (2017). arXiv:1702.05983.

3 Xiao, C., Li, B., Zhu, J.-Y., He, W., Liu, M., and Song, D. Generating adversarial examples with adversarial networks. Proceedings of the 27th International Joint Conference on Artificial Intelligence (IJCAI) (2018), pp. 3905–3911.

4 Lin, Z., Shi, Y., and Xue, Z. IDSGAN: Generative adversarial networks for attack generation against intrusion detection. PAKDD 2022, LNCS 13282 (2022), pp. 79–91.

5 Lakshmanan, R. WormGPT: New AI tool allows cybercriminals to launch sophisticated cyber attacks. The Hacker News (15 July 2023).

6 Haidar, A. Kazakhstan pushes nationwide AI rollout amid cybersecurity risks and skills shortages. The Times of Central Asia (18 August 2025).

7 Afane, K., Wei, W., Mao, Y., Farooq, J., and Chen, J. Next-generation phishing: How LLM agents empower cyber attackers. arXiv preprint (2024). arXiv:2411.13874.

8 Roy, S.S., Thota, P., Naragam, K.V., and Nilizadeh, S. From chatbots to phishbots? Phishing scam generation in commercial large language models. Proceedings of IEEE Symposium on Security and Privacy (2024), p. 221.

9 Croitoru, A., Ionescu, R.T., Khan, F.S., Shah, M., et al. Deepfake media generation and detection in the generative AI era: A survey and outlook. arXiv preprint (2024). arXiv:2411.19537.

10 Saeed, U., Jan, S.U., Ahmad, J., Shah, S.A., Alshehri, M.S., Ghadi, Y.Y., Pitropakis, N., and Buchanan, W.J. Generative adversarial networks-enabled anomaly detection systems: A survey. Expert Systems with Applications, 296, 128978 (2026). https://doi.org/10.1016/j.eswa.2025.128978

11 Samangouei, P., Kabkab, M., and Chellappa, R. Defense-GAN: Protecting classifiers against adversarial attacks using generative models. Proceedings of ICLR (2018).

12 Heiding, F., Schneier, B., Vishwanath, A., Bernstein, J., and Park, P.S. Devising and detecting phishing emails using large language models. IEEE Access, 12, 42131–42146 (2024). https://doi.org/10.1109/ACCESS.2024.3375882

13 Heiding, F., Lermen, S., Kao, A., Schneier, B., and Vishwanath, A. Evaluating large language models' capability to launch fully automated spear phishing campaigns: Validated on human subjects. arXiv preprint (2024). arXiv:2412.00586.

14 SlashNext. WormGPT: The new generative AI tool used by cybercriminals to launch business email compromise attacks (2023).

15 Europol Innovation Lab. ChatGPT: The impact on law enforcement (2023).

16 Rössler, A., Cozzolino, D., Verdoliva, L., Riess, C., Thies, J., and Nießner, M. FaceForensics++: Learning to detect manipulated facial images. Proceedings of IEEE/CVF International Conference on Computer Vision (ICCV) (2019).

17 Szegedy, C., Zaremba, W., Sutskever, I., Bruna, J., Erhan, D., Goodfellow, I., and Fergus, R. Intriguing properties of neural networks. arXiv preprint (2013). arXiv:1312.6199.

18 Goodfellow, I.J., Shlens, J., and Szegedy, C. Explaining and harnessing adversarial examples. arXiv preprint (2015). arXiv:1412.6572.

19 Vincent, P., Larochelle, H., Lajoie, I., Bengio, Y., and Manzagol, P.-A. Extracting and composing robust features with denoising autoencoders. Proceedings of the 25th International Conference on Machine Learning (ICML) (2008), pp. 1096–1103.

[1]*Батырханова А.А.,
т.ғ.м., сениор-лектор, ORCID ID: 0009-0001-6017-1659,
*e-mail: a.batyrkhanova@iitu.edu.kz
[2]Бекмухан А.С.,
т.ғ.м., сениор-лектор, ORCID ID: 0009-0004-0319-0636,
e-mail: a.bekmukhan@iitu.edu.kz
[2]Абильдаева Т.Т.,
т.ғ.м., сениор-лектор, ORCID ID: 0009-0005-2983-3377
e-mail: t.abildayeva@iitu.edu.kz
[3]Ескендирова D.M.,
т.ғ.к., қауымдастырылған профессор, ORCID ID: 0000-0003-4270-1908,
e-mail: d.yeskendirova@iitu.edu.kz

[1]Халықаралық ақпараттық технологиялар университеті, Алматы қ., Қазақстан

ШАБУЫЛДАР МЕН ҚОРҒАНЫС ҮШІН ГЕНЕРАТИВТІ ЖИ МОДЕЛЬДЕРІН ҚОЛДАНУ

Аңдатпа

Мақалада генеративті жасанды интеллектінің киберқауіпсіздіктегі екіжақты қолданылуы қарастырылды: шабуыл құралы ретінде және қорғаныс құралы ретінде. Мәтінде, суретте және аудиода шынайы деңгейде синтез жасау фишинг, дипфейк және тұлғаны еліктеу сияқты қауіптерді жеңілдететіні, ал машиналық оқытуда кіріс деректеріне өте аз, бірақ мақсатты түрде әсер ету арқылы қате шешім қабылдататын қауіп түрі бар екені көрсетілді. Практикалық бөлік қайталанатын стендте орындалды: MNIST қолжазба цифрларын танитын классификатор бастапқыда таза деректерде сенімді нәтиже көрсетті, кейін FGSM әдісі арқылы ε параметрі әртүрлі мәндерде өзгертіліп, adversarial-мысалдар жасалды. Нәтижесінде көзге байқалмайтын шу енгізілгеннің өзінде модельдің сенімді болжамы қате класқа ауысатыны тіркелді (типтік мысалда «7» цифры қате «3» деп танылды). Қорғаныс үшін екі реконструктивті тәсіл салыстырылды: қарапайым автокодировщик

(AE) және шуға үйретілген деноизинг-автокодировщик (DAE). ε артқан сайын DAE қателіктер үлесін AE-ге қарағанда көбірек төмендетті, себебі ол жоғары жиілікті шуды пайдалы белгілерден жақсырақ ажыратты. Қосымша ретінде реконструкция энергиясы E(x) арқылы аномалия детекторы енгізіліп, шабуыл ықтималдығын белгілеу және инцидентті тіркеу мүмкіндігі көрсетілді.

Түйін сөздер: генеративті ЖИ, киберқауіпсіздік, adversarial-шабуыл, FGSM, MNIST, автокодировщик, деноизинг-автокодировщик, аномалия детекторы, реконструкция қатесі.

[1]*Батырханова А.А.,
м.т.н., сениор-лектор, ORCID ID: 0009-0001-6017-1659,
*e-mail: a.batyrkhanova@iitu.edu.kz
[2]Бекмухан А.С.,
м.т.н., сениор-лектор**,** ORCID ID: 0009-0004-0319-0636,
e-mail: a.bekmukhan@iitu.edu.kz
[2]Абильдаева Т.Т.,
м.т.н., сениор-лектор, ORCID ID: 0009-0005-2983-3377,
e-mail: t.abildayeva@iitu.edu.kz
[3]Ескендирова D.M.,
к.т.н., ассоциированный профессор, ORCID ID: 0000-0003-4270-1908,
e-mail: d.yeskendirova@iitu.edu.kz

[1]Международный университет информационных технологий, г. Алматы, Казахстан

ПРИМЕНЕНИЕ ГЕНЕРАТИВНЫХ МОДЕЛЕЙ ИИ ДЛЯ АТАК И ЗАЩИТЫ

Аннотация

В статье рассмотрено двойное применение генеративного искусственного интеллекта в кибербезопасности: как инструмент атаки и как элемент защиты. Показано, что генерация правдоподобного текста, изображений и аудио упрощает злоупотребления (фишинг, дипфейки, подмена коммуникаций), а в задачах машинного обучения возникает отдельный риск – малые, но целенаправленные возмущения входа. Практическая часть выполнена на воспроизводимом стенде с классификатором рукописных цифр MNIST: на чистых данных модель демонстрировала стабильное распознавание, после чего применялась атака FGSM с варьированием параметра ε. Зафиксировано, что визуально почти незаметный шум способен переводить уверенную классификацию в ошибочную (на характерном примере «7» была получена неверная метка «3»). Для противодействия проверены два реконструктивных подхода: обычный автокодировщик (AE) и деноизинговый автокодировщик (DAE), обученный восстанавливать чистый сигнал из зашумленного входа. При росте ε DAE снижал долю ошибок заметнее, чем AE, поскольку лучше отделял высокочастотные компоненты возмущения от полезных штрихов. Дополнительно введен детектор аномалии по энергии реконструкции E(x), позволяющий не только «очищать» вход, но и фиксировать факт подозрительного воздействия для последующего анализа инцидентов.

Ключевые слова: генеративный ИИ, кибербезопасность, adversarial-атаки, FGSM, MNIST, автокодировщик, деноизинговый автокодировщик, детектор аномалий, ошибка реконструкции.

УДК 004.272.43
МРНТИ 50.33.03

https://doi.org/10.55452/1998-6688-2026-23-3-188-203

[1]Тынымбаев С.,
профессор, ORCID ID: 0000-0002-9326-9476,
e-mail: s.tynymbayev@iitu.edu.kz
[1*]Маманова С.Е.,
докторант, ORCID ID: 0009-0001-7277-5492,
e-mail: s.mamanova@iitu.edu.kz
[2]Сқабылов А.А.,
PhD, ORCID ID: 0000-0002-5196-8252,
e-mail: Alisher.skabylov@kaznu.edu.kz
[1]Чинибаева Т.Т.,
PhD, ORCID ID: 0000-0002-2657-3697,
e-mail: t.temirbolatova@iitu.edu.kz
[2]Жексебай Д.М.,
PhD, ORCID ID: 0009-0008-1884-4662,
e-mail: zhexebay92@gmail.com

[1]Международный университет информационных технологий, г. Алматы, Казахстан
[2]Казахский национальный университет им. аль-Фараби, г. Алматы, Казахстан

АРХИТЕКТУРА ЦЕЛОЧИСЛЕННОГО ДЕЛИТЕЛЯ С ОДНОВРЕМЕННЫМ ФОРМИРОВАНИЕМ ТРЕХ РАЗРЯДОВ ЧАСТНОГО ЗА ШАГ

Аннотация

Операция целочисленного деления является одной из наиболее ресурсоёмких арифметических операций в цифровых вычислительных системах. Традиционные последовательные делители формируют один разряд частного за такт, что требует n тактов для n-разрядного деления. В данной работе предлагается архитектура последовательного целочисленного делителя, обеспечивающая одновременное формирование трех разрядов частного за один тактовый цикл (что соответствует основанию radix-8). Устройство включает регистр делимого (РгА), формирователь кратных делителю (БФКД), формирователь частичных остатков и разрядов частного (ФЧОиРЧ) и блок синхронизации (БС). В отличие от классических SRT-делителей с избыточным представлением и таблицами выбора цифры частного, предложенная архитектура использует точное сравнение частичного остатка с предвычисленными кратными делителю B–7B, что устраняет рост таблицы выбора при увеличении основания. Архитектура описана на языке Verilog HDL и верифицирована на ПЛИС Xilinx Artix-7 в среде Vivado. Прототип для 12-разрядного делимого и 6-разрядного делителя занимает 158 LUT и 50 триггеров, достигает максимальной тактовой частоты 134,6 МГц и подтвержден комплексом из десяти тестов; деление выполняется за два тактовых цикла. Архитектура ориентирована на применение в высокоскоростных цифровых вычислителях и специализированных процессорах.

Ключевые слова: целочисленное деление, кратные делителю, формирователь остатков, формирователь разрядов частного, последовательный делитель, radix-8, ПЛИС, Verilog HDL.

Введение

Деление в цифровых вычислительных системах традиционно считается одной из наиболее медленных и сложных операций, особенно по сравнению со сложением и умножением [1]. Несмотря на относительно невысокую частоту использования (около 3% всех арифметических инструкций), операции деления могут генерировать до 40% задержек конвейера процессора [1]. В высокопроизводительных вычислениях стремительное ускорение сложения и

умножения обнажило узкое место: классические алгоритмы деления обладают итеративной природой, где каждый следующий разряд частного вычисляется на основе предыдущего шага, что приводит к повышенной длительности вычислений. Это мотивирует активные исследования в области ускорения деления, направленные на снижение задержек и увеличение пропускной способности делителей при приемлемых затратах аппаратуры.

Наиболее перспективными подходами стали алгоритмы с поразрядным восстановлением частного (digit-recurrence), в частности семейство алгоритмов SRT, названное по именам Суини, Робертсона и Точера [2]. Алгоритмы SRT выполняют деление с вычислением частного итерационно по разрядам, используя избыточное представление разрядов частного [3]. Такое кодирование частного позволяет в каждом шаге оперировать приближенным остатком и делителем, вычисляя следующий разряд частного с учетом допускаемых отклонений остатка. Классический SRT с основанием 2 (radix-2) эквивалентен по скорости не восстанавливающему алгоритму и дает один бит частного за итерацию [3]. Тем не менее SRT-методы допускают увеличение основания системы счисления для генерации сразу нескольких бит частного за такт, сокращая тем самым число итераций.

Увеличение основания radix-4 позволяет формировать два разряда частного за такт, вдвое сокращая число итераций по сравнению с radix-2 [4, 5]. Однако дальнейшее увеличение основания сопряжено с ростом аппаратной сложности: таблица выбора разрядов частного существенно усложняется, а число кратных делителя, требующих хранения и сравнения, возрастает [6, 7]. Реализации на основе radix-8 и выше исследовались преимущественно в контексте делителей с плавающей точкой [8, 9], тогда как архитектуры последовательных целочисленных делителей с основанием radix-8 остаются недостаточно изученными с точки зрения практической функциональной организации.

В данной работе предлагается архитектура последовательного целочисленного делителя, обеспечивающая одновременное формирование трех разрядов частного за один тактовый цикл. Основной вклад работы заключается в разработке функциональной организации устройства, включающей компараторы для выбора кратного делителю из набора B–7B, схему формирования частичных остатков и механизм синхронизации на основе RS-триггера и вычитающего счетчика. Предложенная архитектура обеспечивает троекратное сокращение числа итераций по сравнению с классическим побитовым алгоритмом при сохранении регулярной структуры, пригодной для реализации в цифровых вычислительных системах.

Материалы и методы

Увеличение основания SRT-алгоритма прямо пропорционально снижает количество итераций: так, при переходе от radix-2 к radix-4 каждая итерация дает два бита частного, а при radix-8 – три бита [10]. Например, алгоритм SRT с основанием 8 возвращает за шаг сразу три битовых разряда частного (эквивалентно одной восьмеричной цифре), что теоретически втрое сокращает требуемое число итераций по сравнению с традиционным двоичным делением. Аналогично, radix-16 позволяет получать четыре бита частного за такт. Экспериментально подтверждено, что рост основания до 8 или 16 способен уменьшить латентность деления в 3–4 раза [11].

Однако агрессивное увеличение радикса сопровождается резким усложнением логики выбора разрядов частного. Алгоритму с основанием 16, к примеру, необходимо различать не менее 32 перекрывающихся интервалов остатка, каждому из которых соответствует уникальная управляющая комбинация для выбора следующей цифры частного [11]. Это означает необходимость хранения или вычисления обширных таблиц выбора, объем которых экспоненциально растет с увеличением радикса [12]. Фактически, каждый возможный остаток должен быть соотнесен с правильным значением следующего разряда частного, что при высоком радиксе требует учета множества случаев. Уже при переходе от radix-4 к radix-8 объем таблицы выбора возрастает многократно, делая реализацию на аппаратных средствах крайне ресурсоемкой (вплоть до сотен комбинаций условий) [12, 13].

Практические исследования показывают, что выигрыш от увеличения радикса начинает компенсироваться накладными расходами на реализацию логики выбора. Например, сравнительный анализ делителей с радиксами 4, 8 и 16 продемонстрировал, что рост производительности сопровождается ухудшением показателей площади и энергии: высокие радиксы требуют значительно большего числа логических элементов и таблиц для хранения коэффициентов, что может свести на нет преимущества сокращенного числа итераций [14, 15]. В частности, Наннарелли и Ланг сравнили реализации делителей radix-4, radix-8 и radix-16 и отметили, что хотя радикс-16 теоретически позволяет получать 4 бита за такт, практическая эффективность ограничена из-за громоздкой схемы выбора и связанных с ней задержек распространения сигналов [6]. По этой причине промышленные реализации высокопроизводительных делителей обычно ограничиваются умеренными радиксами (например, 4 или 8), сочетая их с другими методами ускорения. В частности, в контексте встроенных процессоров, жестко ограниченных по аппаратурным ресурсам, зачастую вообще выбирают radix-2, поскольку более высокие основания (radix-4 и выше) слишком сложны для малых устройств [1]. Обзор алгоритмов деления от Обермана и Флинна отмечают, что рост радикса существенно усложняет схему управления делителем [14]. Сходного мнения придерживаются авторы современного обзора Патанкара и Коэла (2021), подчеркивая, что делители с высоким основанием трудно вписать в ограничения по площади и потреблению, особенно в ASIC/FPGA-системах реального времени [16].

Одним из ключевых направлений совершенствования делителей SRT стало упрощение и оптимизация логики выбора разряда частного. Классическая реализация требует хранения обширной таблицы пороговых значений для принятия решения, какой из предвычисленных кратных делителя нужно вычесть из текущего остатка на данном шаге. Улучшенные SRT-алгоритмы радиксов 4, 8 и 16, предлагаемые в литературе, стремятся сократить объем этих таблиц несколькими способами:

1. Предвычисление кратных делителя [10];
2. Использование таблиц поиска (LUT) для выбора разряда [17];
3. Преобразование результата «на лету».

Современные исследования охватывают широкий спектр методов ускорения деления: от комбинированных (гибридных) схем с умеренным радиксом и конвейеризацией до специализированных алгоритмов с адаптивным сокращением итераций [18]. Обзор литературных источников показывает, что алгоритмы с основой 4 и 8 на сегодняшний день представляют оптимальный компромисс между быстродействием и сложностью. Radix-4 делители относительно просты и успешно реализуются даже в ПЛИС с ограниченными ресурсами, однако их латентность по-прежнему линейно растет с разрядностью (на каждый 1–2 бита частного требуется один такт). Radix-8 алгоритмы привлекают возможностью втрое сократить число итераций, но ранее считались слишком «тяжелыми» по логике управления из-за больших LUT для выбора цифр [10]. Лишь немногие работы демонстрировали успешные реализации radix-8 делителей. В частности, деление с основанием 8 исследовалось в контексте операций с плавающей точкой с введением дополнительного фактора избыточности для упрощения выбора цифры частного [18]. Полученные результаты подтвердили работоспособность подхода, однако указали на рост аппаратных затрат при повышении радикса.

Отдельного внимания заслуживают исследования, направленные на разработку аппаратно эффективных делителей для ПЛИС и встроенных систем. Показано, что простые итеративные схемы radix-2 с оптимизированным контроллером способны превзойти по соотношению скорость/затраты более сложные высокорадиксные реализации, особенно с учетом ограничений по числу LUT в FPGA [20]. В обзорных работах отмечается, что SRT-алгоритмы остаются предпочтительными для общего случая, предлагая сбалансированное решение [16], однако их практическая реализация требует тщательной оптимизации – в частности, конвейеризации и сокращения логики выбора разряда частного – для достижения конкурентоспособности с приближенными методами деления [3].

Таблица 1 – Сравнительный анализ алгоритмов деления

Алгоритм	Разрядов за такт	Итераций (n бит)	Сложность логики выбора	Применение
Radix-2 (невосстанавливающий)	1	n	Минимальная	Встроенные системы [16]
Radix-4 SRT	2	n/2	Умеренная	FPGA, ASIC [6, 7]
Radix-8 SRT (плав. точка)	3	n/3	Высокая (большие LUT)	Спец. процессоры [6, 18]
Radix-16 SRT	4	n/4	Очень высокая	Высокопроизв. FPU [8]
Предложенная архитектура	3	n/3	Умеренная (параллельные компараторы B–7B)	Целочисл. делители

Научная новизна и отличие от существующих решений. Ключевое отличие предложенной архитектуры от известных высокорадиксных SRT-делителей состоит в способе выбора цифры частного. В классическом SRT цифра выбирается по приближенному (усеченному) остатку и делителю с помощью таблицы выбора над перекрывающимися интервалами, причем для корректности используется избыточное представление частного; объем такой таблицы быстро растет с основанием. В предлагаемом устройстве используется точное сравнение полного частичного остатка с предвычисленными кратными делителю B, 2B, … 7B, а цифра частного определяется прямым приоритетным декодированием результатов сравнения. Тем самым исключаются избыточное кодирование, перекрывающиеся интервалы и таблица выбора, а их место занимает регулярная решетка компараторов с фиксированной задержкой. Кратные делителя формируются без умножителей – только сдвигами и тремя сумматорами. Платой за это является необходимость полноразрядного сравнения (вместо усеченной оценки в SRT), однако именно это устраняет экспоненциальный рост логики выбора, ограничивавший высокорадиксные реализации. Таким образом, работа заполняет обнаруженный пробел: последовательный делитель достигает производительности radix-8 при регулярной, не требующей таблиц выбора структуре.

Структурная схема устройства приведена на рисунке 1. В ее состав входят регистр делимого РгА, Блок формирователя кратных делителю БФКД, формирователь частичных остатков и разрядов частного ФЧОиРЧ и блок синхронизации БС.

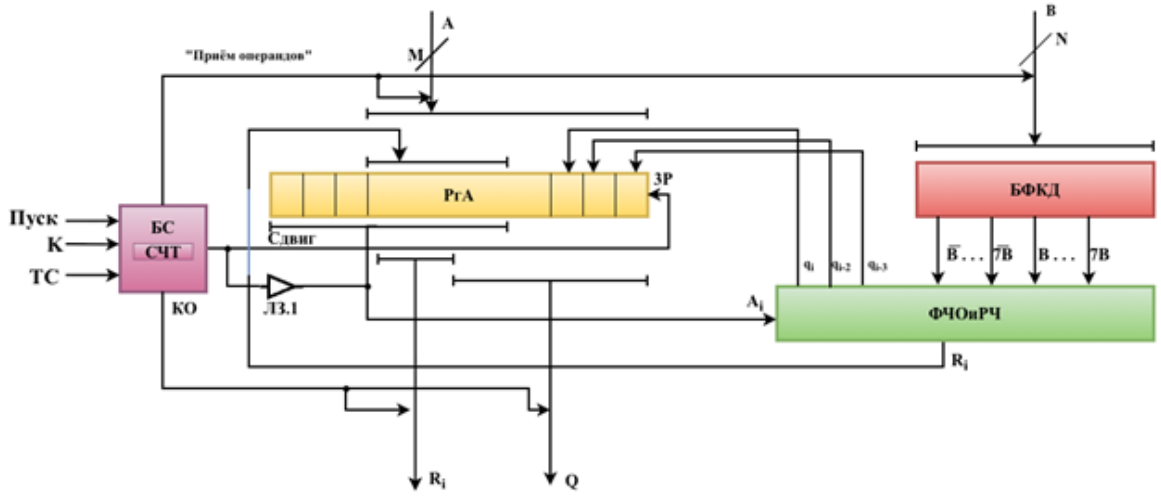


Рисунок 1 – Структурная схема делительного устройства
со сдвигом делителя на три разряда

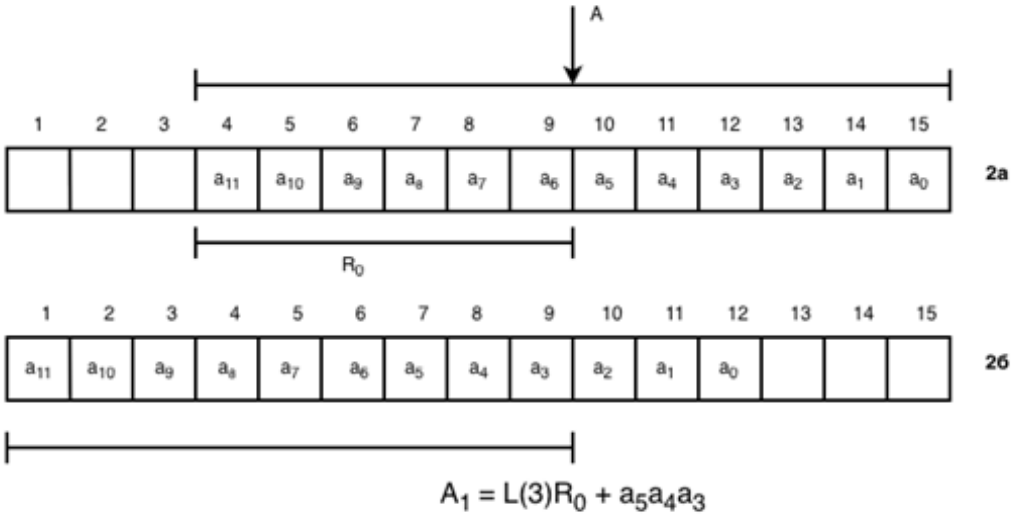


Рисунок 2 – Расположение разрядов делимого А в разрядности регистра РгА

Регистр Рг служит для приема делимого А и имеет цепи сдвига влево на три разряда. На рисунке 2а приведено расположение битов 12-разрядного делимого на разрядной сетке РгА, которые занимают 12 ячеек – с 4 по 15. Старшие три ячейки находятся на нулевом состоянии. Если разрядность делителя N=6, то начальный остаток R_0 определятеся шестью разрядами делимого, т.е.

$$R_0 = a_{11}a_{10}a_9a_8a_7a_6. \quad (1)$$

На рисунке 2б показано расположение разрядов делимого А в разрядной сетке РгА после сдвига РгА на три разряда влево. В разрядах РгА в 1…9 ячейках формируется первый остаток

$$A_1 = L(3)R_0 + a_5a_4a_3, \quad (2)$$

который посылается в ФЧОиРЧ, где сравнивается с кратными числами делителя и по результатам сравнения определяется частичный остаток R_1 и разряды частного $q_1q_2q_3$. При этом R_i принимается в разряды 4…9 , а биты $q_1q_2q_3$ принимаются в разряды РгА с номерами 13…15.

На каждом i-м шаге деления выполняется следующее преобразование:

$$R_i = 8 * R_{i-1} - q_{i-1}B, \quad (3)$$

где R_{i-1} – частичный остаток предыдущего шага, В – делитель, $q_{i-1} \in \{0, 1, 2, 3, 4, 5, 6, 7\}$ – трехразрядное значение частного, определяемое по результатам параллельного сравнения текущего частичного остатка с предвычисленными кратными делителя. Сдвиг на три разряда влево соответствует умножению на 8, что соответствует основанию radix-8 алгоритма.

В формирователе кратных делителя БФКД вычисляются числа, кратные к делителю В. На рисунке 3 приведена схема формирователя чисел В, 2В, … , 7В и их инверсий. Как видно из рисунка 3, формирователь состоит из регистра для хранения делимого, с выхода которого получаем числа В и $\bar{B}$. Кратные 2В, $2\bar{B}$ формируются со сдвига на один разряд чисел В и $\bar{B}$, а числа 4В и $4\bar{B}$ формируются со сдвига В и $\bar{B}$ на два разряда.

Значение трехразрядного частного q_i на каждом шаге определяется путем параллельного сравнения текущего частичного остатка A_i с предвычисленными кратными делителя по следующему правилу:

если $A_i \geq 7B$, то $q_i = 7$;
если $6B \leq A_i < 7B$, то $q_i = 6$;
если $5B \leq A_i < 6B$, то $q_i = 5$;
если $4B \leq A_i < 5B$, то $q_i = 4$;
если $3B \leq A_i < 4B$, то $q_i = 3$;
если $2B \leq A_i < 3B$, то $q_i = 2$;
если $B \leq A_i < 2B$, то $q_i = 1$;
если $A_i < B$, то $q_i = 0$.

Данное правило реализуется посредством пяти параллельных компараторов COMP-1... COMP-5, результаты которых поступают на логические элементы ФЧОиРЧ для одновременного формирования трех разрядов частного q_i, q_{i-1}, q_{i-2}.

Логика выбора разряда частного реализована в виде комбинационной схемы, функционально эквивалентной таблице поиска (LUT) с 3-битным выходом, принимающим значения от 0 до 7. Входными сигналами схемы служат результаты сравнений A_i с кратными B, 3B, 5B и 7B, формируемыми блоком БФКД. Использование параллельных компараторов вместо последовательного перебора позволяет определить значение q_i за время одного такта независимо от разрядности операндов, что обеспечивает постоянную задержку на шаге выбора разряда частного.

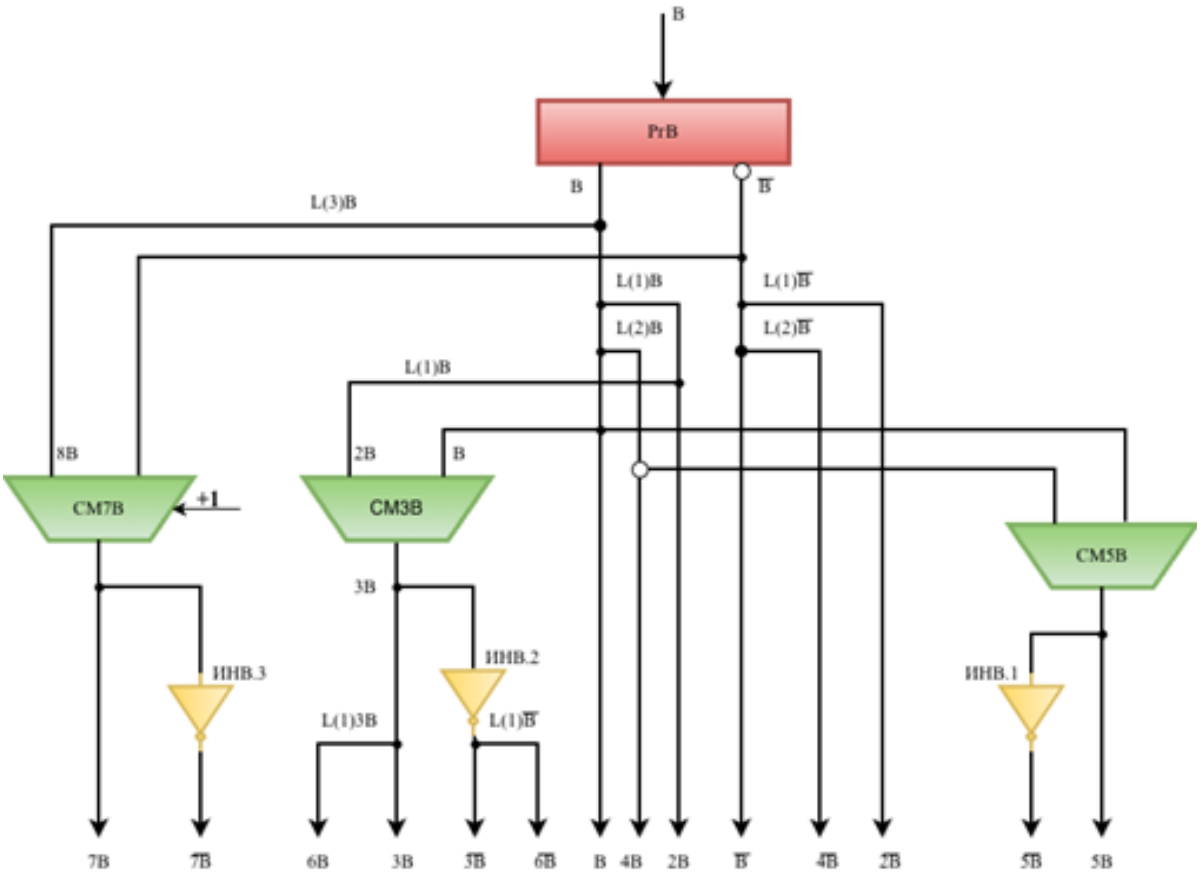


Рисунок 3 – Блок формирователя кратных чисел к делителю (БФКД)

Кратные числа 5B формируем на сумматоре СМ5В путем сложения чисел B и 4B, значение $5\bar{B}$ формируется путем инверсий B на блоке инверторов инв.1. Аналогично значение 3B

формируется на выходе сумматора СМ3В путем суммирование чисел 2В и В. Инвертируя 3В по блоке инверторов инв.2 значения числа 7В вычисляется по формуле

$$7B = 8B + \bar{B} + 1 \tag{4}$$

на сумматоре СМ7В.

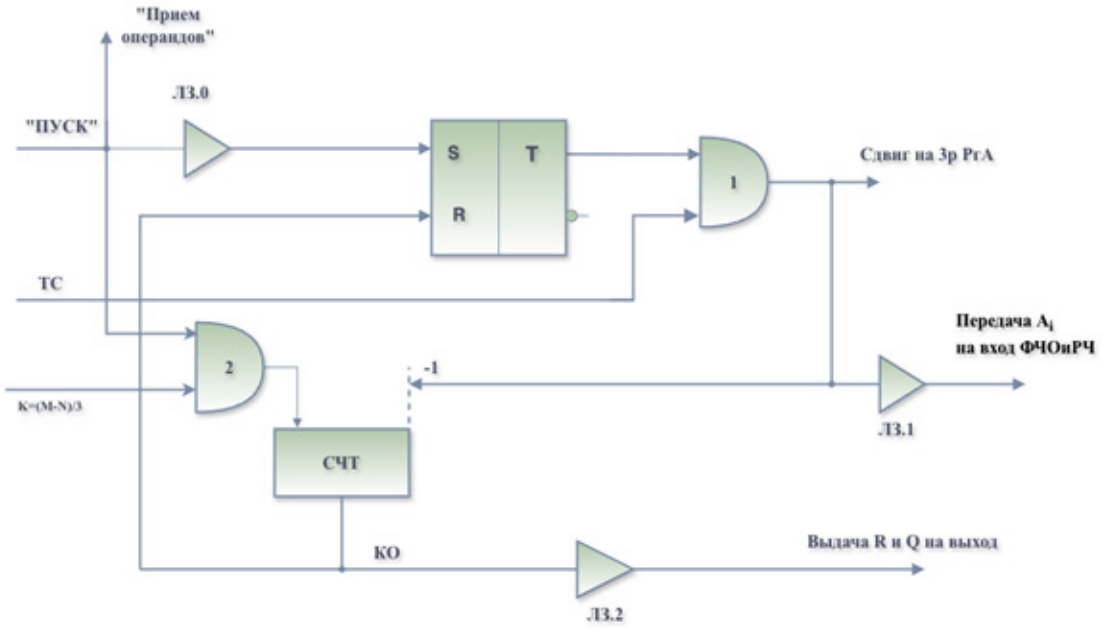


Рисунок 4 – Функциональная схема блока синхронизаций (БС)

Блок синхронизации БС управляет последовательностью выполнения операции деления. Функциональная схема БС представлена на рисунке 4. В состав блока входят RS-триггер, схемы И1 и И2, вычитающий счетчик СЧТ и линии задержки ЛЗ.0, ЛЗ.1 и ЛЗ.2.

На входы БС поступают сигнал запуска «Пуск», тактовый сигнал «ТС» и двоичный код числа шагов деления *K*. На выходах БС формируются управляющие сигналы «Прием операндов», «Сдвиг» и «КО».

По сигналу «Пуск» RS-триггер переходит в единичное состояние, разрешая работу тактового генератора через схему И1. Счетчик СЧТ загружается значением K и начинает обратный отсчет по каждому тактовому импульсу. На каждом такте сигнал «Сдвиг» через линию задержки ЛЗ.1 инициирует сдвиг регистра РгА на три разряда и передачу A_i на вход ФЧОиРЧ. По достижении счетчиком нулевого значения сигнал КО сбрасывает RS-триггер и через линию ЛЗ.2 выдает результат – частное Q и остаток R – на выход устройства.

Центральным блоком делителя является формирователь частичных остатков и разрядов частного, где на каждом шаге деления вычисляются частичные остатки R_i и биты частного $q_i q_{i-1} q_{i-2}$.

Функциональная схема ФЧОиРЧ представлена на рисунке 5. Блок реализует двухэтапное параллельное сравнение частичного остатка A_i с предвычисленными кратными делителя и включает пять компараторов COMP-1...COMP-5, двоичный сумматор и комбинационную логику формирования разрядов частного.

Сравниваемое значение A_i формируется сдвигом предыдущего остатка R_{i-1} на три разряда влево с присоединением очередных трех разрядов делимого $a_i a_{i-1} a_{i-2}$:

$$A_i = L(3)R_{i-1} + a_i a_{i-1} a_{i-2} \tag{5}$$

Полученное значение A_i подается на левые входы всех пяти компараторов COMP-1... COMP-5 и на левый вход сумматора.

Сравнение осуществляется в два этапа с целью минимизации числа компараторов. На первом этапе компаратор COMP-5 сравнивает A_i с порогом 5B. При выполнении условия A_i < 5B на выходе «1» COMP-5 формируется сигнал логической единицы, который через комбинационную логику подает на правые входы компараторов COMP-1...COMP-4 значения B, 2B, 3B и 4B соответственно. На втором этапе, при выполнении условия $A_i \geq$ 5B, на выходе «2» COMP-5 формируется сигнал логической единицы, по которому на правые входы компараторов COMP-1...COMP-3 подаются значения 5B, 6B и 7B. Результаты сравнений поступают на комбинационную логику, которая одновременно формирует три разряда частного $q_i q_{i-1} q_{i-2}$ на выходах схем ИЛИ2, ИЛИ3 и ИЛИ4.

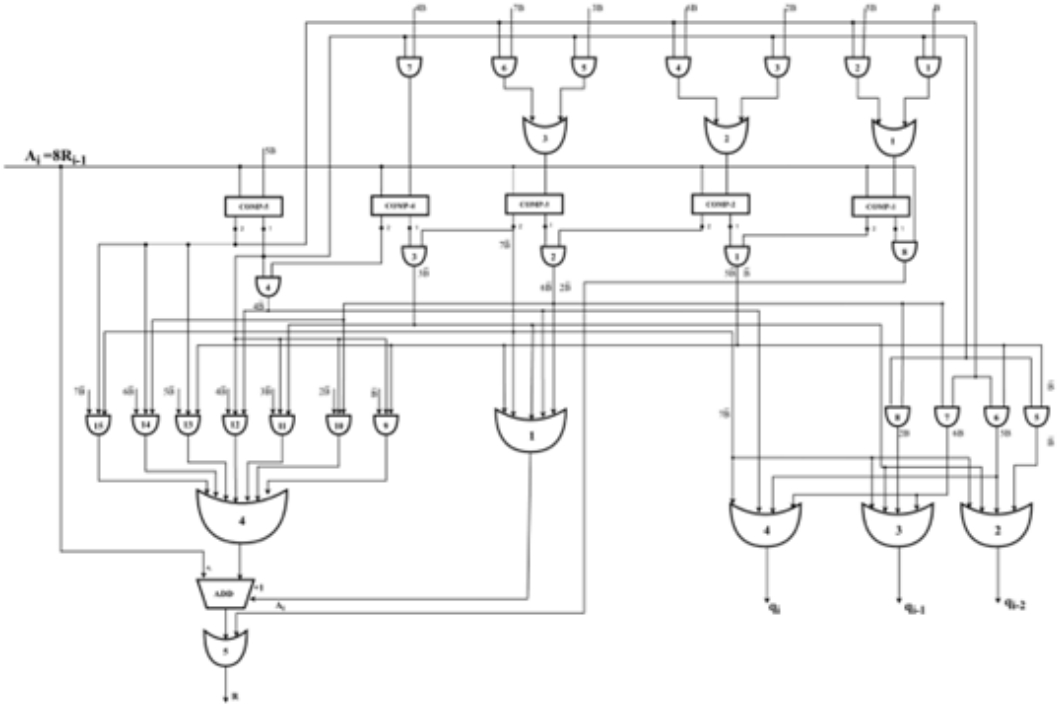


Рисунок 5 – Функциональная схема формирователя частичных остатков и трех разрядов частного

На втором этапе все числа B, 2B, 3B, ... 7B сравниваются с числом A_i на COMP-1, A_i COMP-4 параллельно. Рассмотрим сравнение числа A_iс числами B, 2B, 3B и 4B. При этом <5B и на выходе «1», COMP-5 вырабатывается уровень «1».

При сравнении A_i с числом B: если A_i < B, то на выходе «1», COMP-1 вырабатывается сигнал «1», который разрешает передачу числа A_i на выход схемы И8, и число A_i через схему ИЛИ5 передается на выход. При этом $R_i = A_i$.

При сравнении числа A_i с числом 2B схемы COMP-2: если A_i <2B, то единичный сигнал с выхода «1» COMP-2 передается на вход схемы И1 и на ее выходе вырабатывается единичный сигнал (2B > $A_i \geq$ B), который подается на вход ИЛИ (на выходе формируется сигнал «+1») и на вход блока схемы И9, разрешая передачу числа $\bar{B}$ через схему ИЛИ4 на правый вход сумматора. При этом вычисляется остаток R_i путем выполнения операции:

$$R_i = A_i + \bar{B} + 1 \tag{6}$$

При $A_i \geq$ 2В, единичный сигнал с выхода 2 COMP-2 передается на вход схемы И2. При сравнении A_i с 3В, если $A_i <$ 3В, то из выхода «1» COMP-3 единичный сигнал подается на вход схемы И2, и на выходе схемы И2 вырабатывается единичный сигнал (3В > $A_i \geq$ 2В). Единичный сигнал с выхода схемы И2 вырабатывает сигнал «+1» на выходе схемы ИЛИ1 и разрешает прохождение кода числа $2\bar{B}$ на выход И10 и позволяет выполнение операции

$$R_i = A_i + 2\bar{B} + 1. \quad (7)$$

При выполнении условия $A_i \geq$ 3В единичный сигнал с выхода «2» COMP-3 подается на вход схемы И3, на второй вход схемы И3 подается единичный сигнал с выхода 1 COMP-4, если выполняется условие $A_i <$ 4В. Таким образом, при одновременном выполнении условий 4В > $A_i \geq$ 3В на выходе схемы И3 вырабатывается единичный сигнал, который на выходе схемы ИЛИ1 вырабатывает сигнал «+1» и разрешает передачу обратного кода числа $3\bar{B}$ передать с выходов блока схем И11 и ИЛИ4 на правые входы сумматора. При этом выполняется операция по вычислению последующего остатка:

$$R_i = A_i + 3\bar{B} + 1. \quad (8)$$

При сравнении числа A_iс числом 4В, если выполняется условие $A_i \geq$4В, то с выходов «2» COMP-4 единичный сигнал поступает на вход И4, а на второй вход единичный сигнал поступает с выхода «1». Единичный сигнал с выхода И4 генерирует сигнал «+1» на выходе ИЛИ1 и разрешает прохождение числа $4\bar{B}$ на вход сумматора ADD. При этом выполняется операция

$$R_i = A_i + 4\bar{B} + 1. \quad (9)$$

Аналогично сравниваются числа 5В, 6В и 7В с числом A_i При этом на схеме COMP-5 сравнивается число A_i с числом 5В. При условии $A_i \geq$ 5В на выходе «2» вырабатывается единичный сигнал, по которому число 5В подается на вход COMP-1, число 6В подается на вход COMP-2, и число 7В поступает на вход COMP-4, где они параллельно сравниваются с числом A_i.

При условии 6В > $A_i \geq$ 5В на выходе схемы И1 вырабатывается сигнал, который приводит к выполнению операций

$$R_i = A_i + 5\bar{B} + 1. \quad (10)$$

При выполнении условий 7В>$A_i \leq$ 6В на выходе схемы И2 вырабатывается сигнал, который приводит к выполнению операции

$$R_i = A_i + 6\bar{B} + 1. \quad (11)$$

При выполнении условия $A_i \geq$ 7В единичный сигнал с выхода «2» COMP-3 приводит к выполнению операции

$$R_i = A_i + 7\bar{B} + 1 \quad (12)$$

Логическими схемами И5…И8 и схемами ИЛИ2…ИЛИ4 формируются очередные биты частного. При подаче единичного сигнала из выхода схемы И1, а также единичного сигнала из выхода «1» COMP-5 на входы схемы И5, на ее выходе формируется сигнал «1», который подается на вход ИЛИ2. При этом на выходе ИЛИ2 формируется бит q_{i-2}).

При подаче единичного сигнала с выхода И1 на вход И6 при наличии сигнала «1» с выхода «2» COMP-5, единичный сигнал на выходе И6 принимает формирование битов q_i и q_{i-2} (101).

Единичный сигнал из выхода И2 совместно с сигналом «1» из выхода COMP-2 формирует на выходе И7 в виде единичного сигнала, который участвует в формировании битов на выходах И4 и И3 (110).

Единичный сигнал с выхода «2» COMP-3 поступает на входы ИЛИ4, ИЛИ3, ИЛИ2, на их выходах формируется двоичный код q_i, q_{i-1}, q_{i-2}(111).

Результаты и обсуждение

Рассмотрим пример деления числа $A = 1387_{10}$ на делитель $B = 27_{10}$. Двоичные коды А и В предоставляем ниже.

$$A = 1387_{10} = \begin{matrix} a_{11} & a_{10} & a_9 & a_8 & a_7 & a_6 & a_5 a_4 & a_3 a_2 & a_1 & a_0 \\ 0 & 1 & 0 & 1 & 0 & 1 & 1\ 0 & 1\ 0 & 1 & 1 \end{matrix} \quad (13)$$

$$B = 011011_2 = 27_{10}. \quad (14)$$

Разрядность числа

$$A - M = 12. \quad (15)$$

Разрядность числа

$$B - N = 6. \quad (16)$$

Число шагов деления определяется шириной частного W_Q = M − N + 1 и равно

$$k = W_Q \ / 3. \quad (17)$$

Если W_Q не кратно трем, делимое дополняется нулями со стороны старших разрядов до ширины, кратной трем; недостающие старшие разряды частного при этом равны нулю. В реализованном прототипе ширина частного фиксирована (W_Q = 6, диапазон операндов A < 64·B), поэтому k = 6 / 3= 2.

$k = 10_2$ записывается в счетчик – СЧТ.

Кратные числа к В: 2В=54_{10}; 3В=81_{10}; 4В=108_{10}; 5В=135_{10}; 6В=162_{10}; 7В=189_{10};

Старшие 6 битов двоичного кода числа А определяют значение начального остатка $R_0 = 010101_2 = 21_{10}$. К сдвинутому влево на три разряда остатка R_0 присоединяются биты $a_5a_4a_3$ числа А, при этом получим:

$$A_1 = L(3)R_0 + a_5a_4a_3 = 010101101_2 = 168 + 5 = 173_{10}.$$

Для наглядности все вычисления по делению числа А на делитель В с определением остатка R и частного Q приведены в таблице 2 в десятичной системе счисления.

Таблица 2 – Порядок выполнения операций деления числа А на В с формированием остатка R и разрядов частного

Шаги деления	СЧТИ	Выполнение действий в РгА и ФЧОиРЧ
1	СЧТИ: 10_2 СЧТИ: $10_2 - 01 = 01_2$	В РгА: $A_1 = L(3)R_0 + a_5a_4a_3 = 010101101_2 = 168 + 5 = 173_{10}$. В ФЧОиРЧ: поскольку 162<173<189, то имеет место $B < A_1 < 7B$, следовательно, выполняется операция $R_1 = A_1 - 6B = 173_{10} - 162_{10} = 11_{10}$ При этом $q_5 = 1, q_4 = 1,\ q_3 = 0$
2	СЧТИ-1: $01_2 - 01 = 00_2$ Конец операций (КО)	В РгА: $A_2 = L(3)R_1 + a_2a_1a_0 = 010101101_2 = 88 + 3 = 91_{10}$. В ФЧОиРЧ: поскольку 81<91<108, то имеет место соотношение $3B < A_2 < 4B$, следовательно, в ФЧОиРЧ выполняется операция $R_2 = A_2 - 3B = 91_{10} - 81_{10} = 10_{10}$ При этом $q_2 = 0, q_1 = 1,\ q_0 = 1$

Классический побитовый алгоритм (radix-2) потребовал бы 6 тактов, алгоритм radix-4 – 3 такта. Предложенная архитектура обеспечивает троекратное сокращение числа итераций по сравнению с radix-2 и полуторакратное по сравнению с radix-4.

Проверка:

$$Q = q_5q_4q_3q_2q_1q_0 = 110011_2 = 51_{10} \quad (19)$$

$$A = (Q * B) + R = (51 * 27) + 10 = 1377 + 10 = 1387_{10}. \quad (20)$$

Для проверки корректности работы устройства в граничных условиях рассмотрим случай деления числа $A = 63_{10}(111111_2)$ на делитель $B = 63_{10}(111111_2)$. При $M = N = 6$ ширина частного W_Q = M − N + 1 = 1, откуда k = 1 / 3= 1: за один шаг формируется Q = 1, R = 0. при котором частное Q = 1, остаток R = 0. Устройство корректно обрабатывает данный случай, поскольку начальный остаток $R_0 = A$ и на первом же сравнении выполняется условие $A_i = B$, что дает $q_i = 1$.

Реализация и верификация на ПЛИС. Архитектура описана на языке Verilog HDL в виде иерархии модулей (модуль верхнего уровня SequentialDivider3; регистр делимого rgA; формирователь кратных FKRD; вычислительное ядро PRU3_QDSL с компараторами и логикой выбора; блок синхронизации BS3) и синтезирована в среде Xilinx Vivado для ПЛИС семейства Artix-7. Общий вид RTL-схемы синтезированного устройства приведен на рисунке 6, схема формирователя кратных – на рисунке 7. Формирователь FKRD (блок БФКД из рисунка 3) генерирует семь кратных {B, 2B, …, 7B} и их обратные коды, используя исключительно операции сдвига и сложения, что соответствует методу предварительного формирования кратных без умножителей.

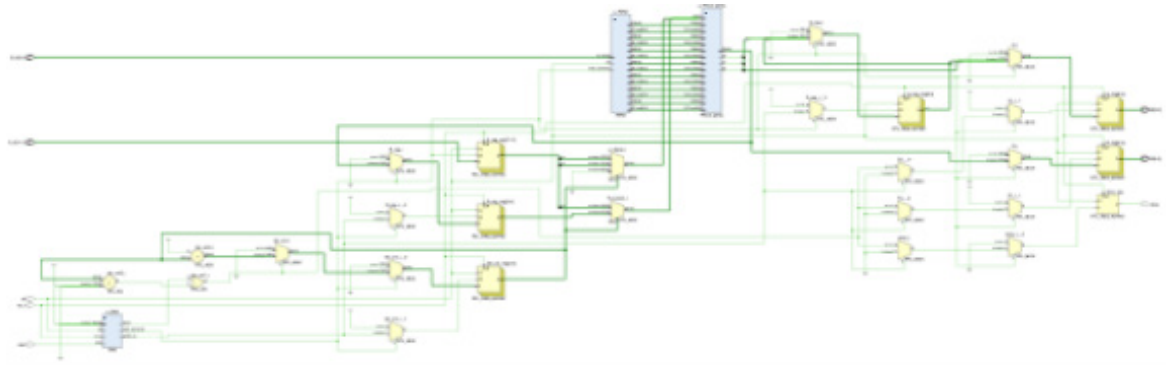


Рисунок 6 – RTL-схема синтезированного последовательного делителя (общий вид)

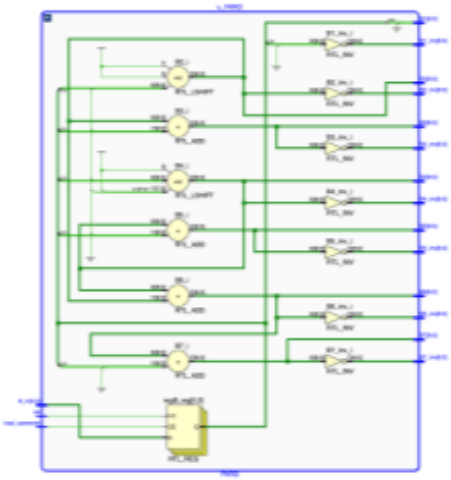


Рисунок 7 – RTL-схема формирователя кратных делителю (БФКД)

Использование аппаратных ресурсов прототипа приведено в таблице 3, иерархическое распределение ресурсов по отчету Vivado – на рисунке 8. Верхний модуль занимает 158 LUT и 50 триггеров, при этом формирователь кратных использует 78 LUT, вычислительное ядро – 70 LUT, блок синхронизации – 10 LUT. Утилизация LUT составляет менее 1% доступных ресурсов кристалла, что подтверждает компактность реализации.

Таблица 3 – Использование аппаратных ресурсов (ПЛИС Artix-7)

Ресурс	Использовано	Доступно	Утилизация, %
LUT	158	20 800	0,76
Триггеры (FF)	50	41 600	0,12
Bonded IOB	34	150	22,7
BUFGCTRL	1	32	3,1

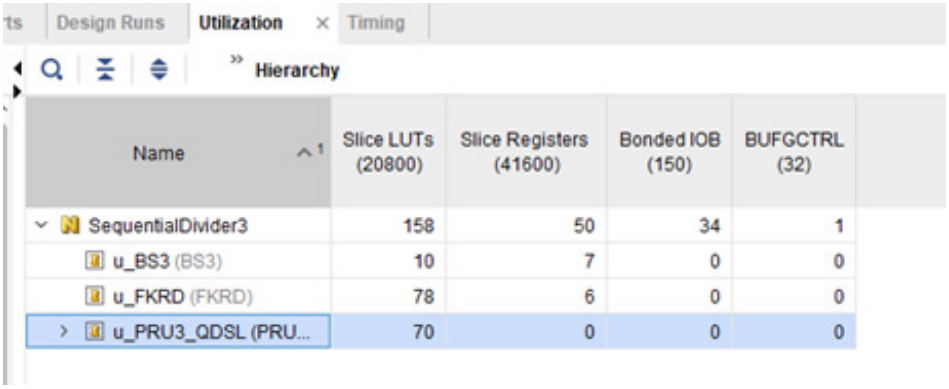


Рисунок 8 – Иерархическое распределение аппаратных ресурсов (отчет Vivado)

Статический временной анализ показал запас по времени WNS = 2,570 нс, что соответствует минимальному периоду T_min = 7,430 нс и максимальной тактовой частоте F_max ≈ 134,6 МГц. Высокая тактовая частота обусловлена параллельной организацией блока сравнения в реализованном прототипе: все пороги сравниваются одновременно, и критический путь определяется одним каскадом «компаратор – приоритетный декодер» независимо от значений операндов, что обеспечивает постоянную задержку шага выбора цифры частного.

Временная диаграмма работы устройства приведена на рисунке 9.

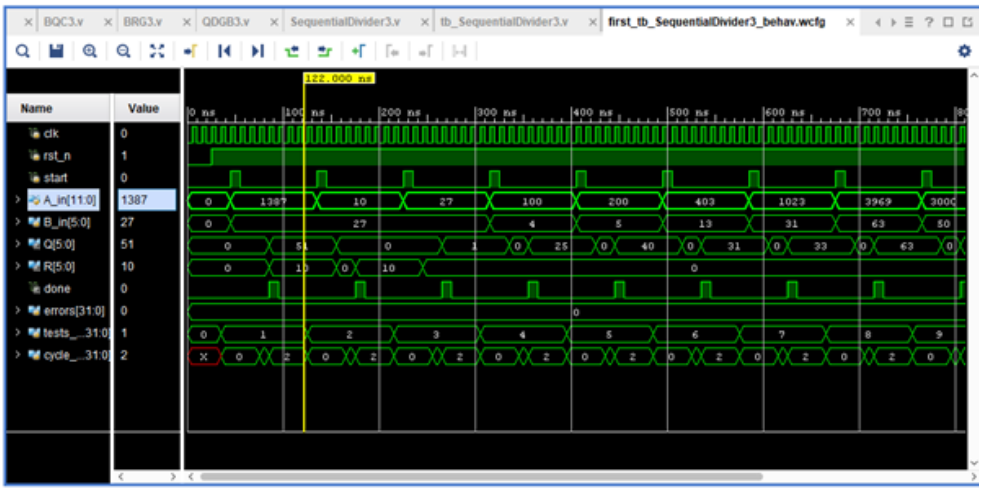


Рисунок 9 – Временная диаграмма верификации последовательного делителя (XSim)

Глубина критического пути и достижимая тактовая частота определяются разрядностью делителя N, задающей размер компараторов и сумматора, а не разрядностью делимого M. Увеличение разрядности делимого увеличивает лишь число шагов k согласно (6), не удлиняя критический путь; поэтому частота F_max ≈ 134,6 МГц сохраняется при росте M, а латентность растет линейно по числу шагов. Это отличает предложенную архитектуру от высокорадиксных SRT-делителей, у которых усложнение таблицы выбора непосредственно увеличивает задержку. Систематический синтез для набора разрядностей операндов (16, 32, 64 бита) с построением зависимостей «площадь – частота» вынесен в дальнейшие исследования.

Оценка энергопотребления. Энергопотребление прототипа оценено по реализованному списку соединений (post-implementation) средствами анализа мощности Vivado; результат приведен на рисунке 10. Суммарная потребляемая мощность кристалла составляет 0,077 Вт, из которых на статическую мощность (ток утечки ПЛИС) приходится 0,070 Вт (91 %), а на динамическую – лишь 0,007 Вт (9 %). В составе динамической мощности преобладает потребление блоков ввода-вывода (0,004 Вт, 63 %), тогда как на тактовые цепи, сигналы и собственно логику делителя приходится примерно по 0,001 Вт. Малая доля динамической мощности логического ядра подтверждает аппаратную компактность предложенной архитектуры: при температуре перехода 25,4 °C тепловой запас составляет 59,6 °C. Приведенная оценка получена в режиме vectorless-анализа и носит ориентировочный характер; уточнение возможно при подаче реальной переключательной активности (SAIF) из временного моделирования.

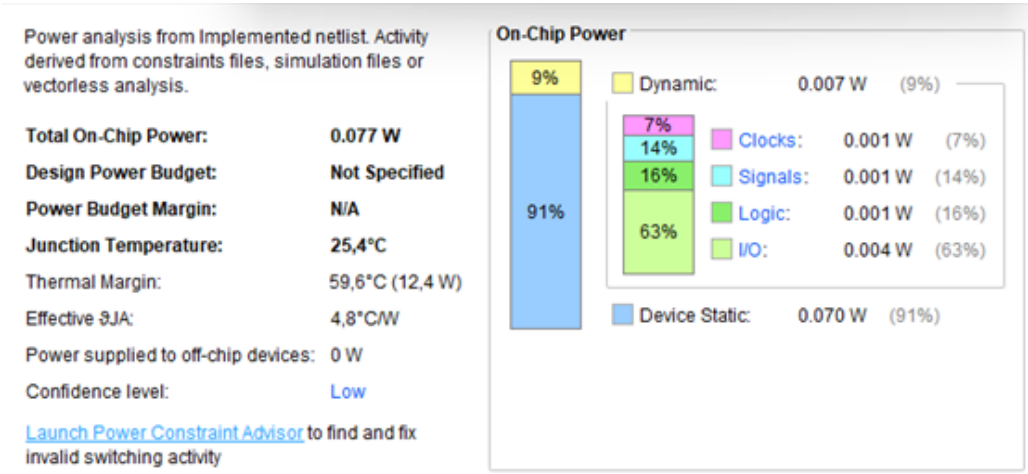


Рисунок 10 – Анализ потребляемой мощности прототипа (отчет Vivado)

Полученные результаты подтверждают, что предложенная архитектура достигает производительности уровня radix-8 при умеренных аппаратных затратах и регулярной структуре. Перспективным направлением является разработка конвейерных и матричных вариантов, также формирующих по три разряда частного за итерацию, с анализом компромисса между глубиной конвейера, занимаемой площадью и частотой.

Заключение

В данной работе представлена архитектура последовательного целочисленного делителя, обеспечивающая одновременное формирование трех разрядов частного за один тактовый цикл. Предложенное устройство включает формирователь кратных делителю (БФКД), реализующий предвычисление значений B–7B, и формирователь частичных остатков и разрядов частного (ФЧОиРЧ), выполняющий параллельное сравнение посредством пяти компараторов COMP-1...COMP-5. Блок синхронизации на основе RS-триггера и вычитающего счетчи-

ка обеспечивает управление итерационным процессом деления. В отличие от классических высокорадиксных SRT-делителей, выбор цифры частного выполняется точным сравнением с предвычисленными кратными и прямым приоритетным декодированием, что устраняет рост таблицы выбора при увеличении основания.

Архитектура описана на языке Verilog HDL и верифицирована на ПЛИС Xilinx Artix-7 в среде Vivado. Прототип для 12-разрядного делимого и 6-разрядного делителя занимает 158 LUT и 50 триггеров, достигает F_max ≈ 134,6 МГц (WNS = 2,570 нс) и подтвержден комплексом из десяти тестов, выполняя деление за два тактовых цикла. Тем самым обеспечивается троекратное сокращение числа итераций по сравнению с алгоритмом radix-2 и полуторакратное – по сравнению с radix-4. Направлениями дальнейших исследований являются синтез устройства для операндов разрядностью 16, 32 и 64 бита с построением зависимостей «площадь – частота», а также разработка конвейерных и матричных вариантов архитектуры.

ЛИТЕРАТУРА

1 Wei, X., Yang, Y., Chen, J. A Low-Latency Divider Design for Embedded Processors. Sensors, 22, 2471 (2022). https://doi.org/10.3390/s22072471

2 Mehta, B., Talukdar, J., Gajjar, S. High speed SRT divider for intelligent embedded system. In Proc. 2017 Int. Conf. on Soft Computing and its Engineering Applications (icSoftComp) (Changa, India, 2017), pp. 1–5. https://doi.org/10.1109/ICSOFTCOMP.2017.8280077

3 Patankar, U.S., Flores, M.E., Koel, A. Division Algorithms—from Past to Present Chance to Improve Area Time and Complexity for Digital Applications. In Proceedings of the 2020 IEEE Latin America Electron Devices Conference (LAEDC) (San Jose, Costa Rica, 2020), pp. 1–4.

4 Angioli, M., Barbirotta, M., Cheikh, A., Mastrandrea, A., Menichelli, F., Jamili, S., Olivieri, M. Design, Implementation and Evaluation of a New Variable Latency Integer Division Scheme. IEEE Transactions on Computers, 73 (7), 1767–1779 (2024). https://doi.org/10.1109/TC.2024.3386060

5 Murillo, R., Villalba-Moreno, J., Del Barrio, A., Botella, G. Digit-Recurrence Posit Division. arXiv (2025). https://doi.org/10.48550/arXiv.2511.02494

6 Nannarelli, A., Lang, T. Low-Power Division: Comparison among Implementations of Radix 4, 8 and 16. In Proceedings of the 14th IEEE Symposium on Computer Arithmetic (Adelaide, Australia, 1999), pp. 149–156.

7 Nikmehr, H., Phillips, B., Lim, C.C. A Fast Radix-4 Floating-Point Divider with Quotient Digit Selection by Comparison Multiples. The Computer Journal, 50 (1), 81–92 (2007). https://doi.org/10.1093/comjnl/bxl048

8 Zhou, X., Shen, R., He, P., Gao, H. Optimization and Implementation of SRT-16 Floating-Point Divider Based on FPGA. In Proceedings of the 5th International Seminar on Artificial Intelligence, Networking and Information Technology (AINIT) (2024), pp. 2019–2023.

9 Baesler, M., Voigt, S.O. Analysis of Fast Radix-10 Digit Recurrence Algorithms for Fixed-Point and Floating-Point Dividers on FPGAs. International Journal of Reconfigurable Computing, 453173 (2013). https://doi.org/10.1155/2013/453173

10 Zhexebay, D., Mamanova, S., Karibayev, B., et al. Pipelined Divider with Precomputed Multiples of Divisor. Electronics, 15 (1), 110 (2026). https://doi.org/10.3390/electronics15010110

11 Temel, M. Formal Verification of Booth Radix-8 and Radix-16 Multipliers. In Proc. 2024 Design, Automation & Test in Europe Conf. & Exhibition (DATE) (IEEE, 2024).

12 Kornerup, P. Digit selection for SRT division and square root. IEEE Transactions on Computers, 54 (3), 294–303 (2005). https://doi.org/10.1109/TC.2005.52

13 Amin, A., Shinwari, W. High-Radix Multiplier-Dividers: Theory, Design, and Hardware. IEEE Transactions on Computers, 59 (7), 1009–1022 (2010). https://doi.org/10.1109/TC.2010.78

14 Oberman, S.F., Flynn, M.J. Division algorithms and implementations. IEEE Transactions on Computers, 46 (8), 833–854 (1997). https://doi.org/10.1109/12.618254

15 Nannarelli, A. Digit Recurrence Division Algorithms and Implementations (Ph.D. thesis, University of Pisa, 1996).

16 Patankar, U.S., Koel, A. Review of basic classes of dividers based on division algorithm. IEEE Access, 9, 23035–23069 (2021). https://doi.org/10.1109/ACCESS.2021.3055735

17 Harris, D.L., Oberman, S.F., Horowitz, M.A. SRT Division Architectures and Implementations. In Proc. 13th IEEE Symp. on Computer Arithmetic (1997), pp. 18–25. https://doi.org/10.1109/ARITH.1997.614875

18 Anane, M., Bessalah, H., Issad, M., Anane, N., Salhi, H. Higher radix and redundancy factor for floating point SRT division. IEEE Transactions on VLSI Systems, 16 (6), 774–779 (2008). https://doi.org/10.1109/TVLSI.2008.2001058

19 Montuschi, P., Nannarelli, A. Digital arithmetic: Division algorithms. In Encyclopedia of Computer Science and Technology (New York: Taylor & Francis, 2017), pp. 348–363.

20 Matthews, J., Zhang, Z., Chen, Z. Rethinking integer divider design for FPGA-based soft processors. In Proceedings of the 2019 IEEE 27th Annual International Symposium on Field-Programmable Custom Computing Machines (FCCM) (San Diego, CA, USA, 2019), pp. 115–122.

[1]Тынымбаев С.,
профессор, ORCID ID: 0000-0002-9326-9476,
e-mail: s.tynymbayev@iitu.edu.kz
[1]*Маманова С.Е.,
докторант, ORCID ID: 0009-0001-7277-5492,
*e-mail: s.mamanova@iitu.edu.kz
[2]Сқабылов А.А.,
PhD, ORCID ID: 0000-0002-5196-8252,
e-mail: Alisher.skabylov@kaznu.edu.kz
[1]Чинибаева Т.Т.,
PhD, ORCID ID: 0000-0002-2657-3697,
e-mail: t.temirbolatova@iitu.edu.kz
[2]Жексебай Д.М.,
PhD, ORCID ID: 0009-0008-1884-4662,
e-mail: zhexebay92@gmail.com

[1]Халықаралық ақпараттық технологиялар университеті, Алматы қ., Қазақстан
[2]Әл-Фараби атындағы Қазақ ұлттық университеті, Алматы қ., Қазақстан

БІР ҚАДАМДА БӨЛІНДІНІҢ ҮШ РАЗРЯДЫН БІР МЕЗГІЛДЕ ҚҰРАСТЫРУҒА НЕГІЗДЕЛГЕН БҮТІН САНДЫ БӨЛГІШТІҢ АРХИТЕКТУРАСЫ

Аңдатпа

Бүтін санды бөлу операциясы цифрлық есептеу жүйелеріндегі ең ресурс сыйымды арифметикалық операциялардың бірі саналады. Дәстүрлі дәйекті бөлгіштер әр такт сайын бөліндінің бір разрядын қалыптастырады, сондықтан n-разрядты бөлу үшін n такт қажет. Бұл жұмыста бір тактілік цикл ішінде бөліндінің үш разрядын бір мезгілде қалыптастыруды қамтамасыз ететін дәйекті бүтін санды бөлгіштің архитектурасы ұсынылады. Әзірленген құрылғы бөлінгіш регистрін (БР), бөлгіштің еселіктерін қалыптастырғышты (БЕҚ), ішінара қалдықтар мен бөлінді разрядтарын қалыптастырғышты (ІҚБРҚ) және синхрондау блогын (СБ) қамтиды. Артық таңбалауды және бөлінді цифрын таңдау кестелерін пайдаланатын классикалық SRT-бөлгіштерден айырмашылығы, ұсынылған архитектура жартылай қалдықты бөлгіштің алдын ала есептелген еселіктерімен (B–7B) тікелей салыстырады, бұл санау жүйесінің негізі артқан сайын таңдау кестесінің көлемінің ұлғаюын болдырмайды. Архитектура Verilog HDL тілінде сипатталып, Vivado ортасында Xilinx Artix-7 ПЛИС-інде верификацияланды. 12 разрядты бөлінгіш пен 6 разрядты бөлгішке арналған прототип 158 LUT және 50 триггерден тұрады, 134,6 МГц максималды тактілік жиілікке жетеді және он тесттен тұратын кешен арқылы расталды; бөлу екі тактілік циклде орындалады. Архитектура жоғары жылдамдықты цифрлық есептеуіштер мен мамандандырылған процессорларда қолдануға арналған.

Түйін сөздер: бөлгішке еселі сандар, қалдықтарды қалыптастырғыш, бөлінді разрядтарын қалыптастырғыш, тізбекті әрекетті бөлгіш, radix-8, ПЛИС, Verilog HDL.

[1]Tynymbayev S.,
Professor, ORCID ID: 0000-0002-9326-9476,
e-mail: s.tynymbayev@iitu.edu.kz
[1]*Mamanova S.E.,
PhD Candidate, ORCID ID: 0009-0001-7277-5492,
*e-mail: s.mamanova@iitu.edu.kz
[2]Skabylov A.A.,
PhD, ORCID ID: 0000-0002-5196-8252,
e-mail: Alisher.skabylov@kaznu.edu.kz
[1]Chinibayeva T.T.,
PhD, ORCID ID: 0000-0002-2657-3697,
e-mail: t.temirbolatova@iitu.edu.kz
[2]Zhexebay D.M.,
PhD, ORCID ID: 0009-0008-1884-4662,
e-mail: zhexebay92@gmail.com

[1]International Information Technology University, Almaty, Kazakhstan
[2]Al-Farabi Kazakh National University, Almaty, Kazakhstan

A SEQUENTIAL INTEGER DIVIDER WITH THREE-BIT QUOTIENT DIGIT GENERATION

Abstract

Integer division remains one of the most computationally demanding arithmetic operations in digital computing systems. Conventional sequential dividers produce one quotient bit per clock cycle, requiring n cycles for an n-bit division. This paper proposes an architecture for a sequential integer divider capable of simultaneously generating three quotient bits per clock cycle. The proposed device comprises a dividend register (DR), a divisor multiples generator (DMG), a partial remainder and quotient digit generator (PRQDG), and a synchronization unit (SU). Unlike classical SRT dividers, which rely on a redundant quotient representation and quotient-digit selection tables, the proposed architecture performs an exact comparison of the partial remainder against the precomputed divisor multiples B–7B, thereby eliminating the growth of the selection table as the radix increases. The architecture is described in Verilog HDL and verified on a Xilinx Artix-7 FPGA using the Vivado design suite. The prototype for a 12-bit dividend and a 6-bit divisor occupies 158 LUTs and 50 flip-flops, attains a maximum clock frequency of 134.6 MHz, and is confirmed by a suite of ten tests; a division is completed in two clock cycles. The architecture is intended for use in high-speed digital computing units and specialized processors.

Keywords: integer division, divisor multiples, remainder generator, quotient digit generator, sequential divider, radix-8, FPGA, Verilog HDL.

Received January 27, 2026; revised April 24, June 21, 2026; accepted June 25, 2026.

UDC 004.8
IRSTI 28.23.34

https://doi.org/10.55452/1998-6688-2026-23-3-204-217

[1]*Kunichik V.G.,
PhD student, ORCID ID: 0009-0004-8580-7731,
*e-mail: kunichikval@gmail.com
[1]Salykova O.S.,
Cand.Tech.Sc., Associate Professor,
ORCID ID: 0000-0002-8681-4552, e-mail: solga0603@mail.ru

[1]Akhmet Baitursynuly Kostanay Regional University, Kostanay, Kazakhstan

EARLY PREDICTION OF IN-HOSPITAL MORTALITY USING INTERPRETABLE AND CALIBRATED ENSEMBLE MACHINE LEARNING MODELS

Abstract

Early identification of patients at high risk of in-hospital mortality is a persistent challenge in clinical practice, particularly during infectious disease outbreaks such as COVID-19, when decisions must be made at the time of hospital admission using incomplete information. Although machine learning methods have been widely applied to mortality prediction, many existing models are developed and assessed under conditions that limit their usefulness for early triage, including insufficient attention to probability reliability, temporal generalization, and decision-oriented assessment. This work examines early-stage mortality risk prediction using routinely available clinical data collected at the time of hospital admission. An ensemble of gradient boosting models is developed and analyzed under strict temporal separation to reflect real-world deployment conditions. Particular emphasis is placed on the reliability of predicted probabilities, with post-hoc isotonic calibration applied to improve alignment between predicted risks and observed outcomes. Model performance is assessed using complementary discrimination and calibration metrics, while clinical relevance is examined through decision curve analysis across plausible operating thresholds. Evaluation on an independent, temporally held-out test set shows that ensemble aggregation improves the stability of risk estimates, while calibration yields more consistent threshold-based behavior without altering ranking performance. Decision curve analysis indicates that calibrated predictions provide higher net benefit than default decision strategies across a broad range of early triage thresholds. These findings highlight that, in early clinical decision-making, probability reliability plays a critical role alongside discrimination. The presented framework offers a methodologically robust approach to early in-hospital mortality risk assessment under realistic clinical and temporal constraints.

Keywords: machine learning, in-hospital mortality, early clinical triage, ensemble models, probability calibration, decision curve analysis, clinical decision support.

Received January 13, 2026; revised April 2, 2026; accepted May 20, 2026.

Introduction

Recent advances in information and communication technologies have enabled the widespread adoption of data-driven decision support systems in high-impact domains, including healthcare. The increasing availability of electronic health records and national clinical registries has stimulated the application of machine learning methods for predictive modeling, risk stratification, and outcome forecasting across a broad range of clinical tasks. In this context, increasing attention has been paid to early prediction of adverse clinical outcomes using routinely available clinical information collected at the initial stages of patient assessment, where decisions must often be made before detailed laboratory or imaging data become available [1–2].

Machine learning models have demonstrated promising results in mortality prediction tasks across different clinical settings, including infectious disease outbreaks such as COVID-19. Ensemble methods, tree-based algorithms, and neural networks are frequently reported to outperform traditional statistical approaches in terms of discriminative ability [3–5]. However, strong predictive discrimination alone does not guarantee reliable or clinically meaningful risk estimates. In early clinical decision-making settings, even well-discriminating models may produce risk estimates that are difficult to interpret or operationalize in practice when absolute probabilities are not sufficiently reliable [3].

Another critical challenge limiting the real-world deployment of machine learning models in healthcare is interpretability. Many high-performing models operate as "black boxes", providing limited insight into the mechanisms underlying their predictions. This lack of transparency reduces clinicians' trust and complicates the integration of such models into routine clinical workflows. As a result, recent research increasingly emphasizes interpretable machine learning approaches that enable assessment of feature contributions and facilitate understanding of individual risk predictions [6–8].

In addition to discrimination and interpretability, the reliability of predicted probabilities has emerged as a central methodological consideration for clinical prediction models. When predicted risks are intended to support patient-level decision-making, calibration becomes essential, particularly under temporal distribution shift and evolving clinical conditions [9]. Closely related to this issue is the evaluation of clinical utility. Traditional performance metrics, such as accuracy or the area under the receiver operating characteristic curve, do not directly reflect the consequences of model-based decisions. Decision curve analysis has therefore been proposed as an effective framework for assessing the net benefit of predictive models across a range of risk thresholds and for explicitly linking model outputs to actionable decision strategies [10–11].

Despite the growing body of literature on machine learning–based mortality prediction, many studies continue to focus primarily on improving predictive performance or proposing novel model architectures. Methodological aspects related to early-stage applicability, probability reliability, and the translation of model outputs into clinically meaningful decision thresholds remain insufficiently emphasized [12]. Furthermore, the use of lightweight clinical data available at the early stages of hospitalization remains underexplored, despite its importance for timely clinical triage and prospective decision support [13].

In this context, the aim of this study is to develop and evaluate an interpretable ensemble machine learning approach for early prediction of in-hospital mortality using routinely available admission-time clinical data collected at the initial stage of hospitalization. We hypothesize that combining ensemble learning with calibration and interpretability techniques can enhance the reliability and clinical usefulness of early mortality risk predictions when only limited clinical information is available. To investigate this hypothesis, large-scale registry data are analyzed under strict temporal separation, ensemble machine learning models are trained and post-hoc calibrated, discrimination and probability reliability are jointly evaluated, and potential clinical utility is assessed using decision curve analysis and operational risk thresholds. This study contributes a rigorously validated, calibration-aware ensemble framework for early in-hospital mortality prediction, explicitly linking probabilistic risk estimates to clinically actionable decision thresholds under temporal dataset shift. The novelty of this study lies in its calibration-aware, decision-oriented evaluation of early-stage ensemble models under strict temporal validation rather than in proposing a new algorithmic architecture.

Materials and methods

Data source and cohort construction

This study was based on anonymized secondary registry data of hospitalized patients with confirmed COVID-19 infection, with in-hospital mortality defined as a binary outcome. The registry represents a large-scale, real-world clinical data source reflecting routine hospital practice across

multiple pandemic waves. To support reproducibility, the data were consolidated into a unified year-indexed panel with a fixed feature schema across years and stored in Parquet format.

The final analytical cohort comprised approximately 2.53 million hospital admissions, with an overall in-hospital mortality proportion of 0.284. Notably, outcome prevalence varied substantially across calendar years, with mortality rates of 0.305 in 2020, 0.299 in 2021, and 0.214 in 2022, indicating pronounced temporal heterogeneity in baseline risk. This variability reflects changes in patient characteristics, clinical management, and pandemic dynamics over time and motivated the explicit consideration of temporal generalization in subsequent modeling stages.

At the cohort assembly stage, data processing decisions were deliberately conservative. Aggressive record exclusion, extensive feature engineering, or heavy imputation were intentionally avoided in order to preserve the natural structure of the registry data. Data quality was assessed through reproducible exploratory checks of demographic distributions, missingness patterns, and indicator correlations; these diagnostics confirmed expected clinical gradients and the absence of critical schema inconsistencies. This design choice was motivated by the study's focus on probability calibration and clinical utility, as excessive preprocessing may introduce implicit assumptions that distort risk distributions and bias downstream decision-curve analyses. By retaining the original data structure as much as possible, the constructed cohort provides a realistic basis for evaluating early-stage risk prediction under real-world conditions.

Validation design and leakage control (temporal generalization)

Consistent with the exploratory cohort-level analysis described above, all validation and evaluation procedures were explicitly designed to account for pronounced temporal non-stationarity and baseline risk shifts observed across pandemic waves. To approximate real-world deployment conditions and explicitly address dataset shift over time, a strict temporal validation design was adopted [14–16]. All models were trained using data from 2020–2021 and evaluated on an independent, chronologically held-out test set from 2022, ensuring that no information from the future period was available at any stage of model training, calibration, or model selection.

This validation strategy was chosen in response to substantial temporal drift observed in both outcome prevalence and age-stratified risk distributions across calendar years. Under such conditions, risk estimates, predicted probabilities, and clinically meaningful decision thresholds learned on earlier data cannot be assumed to remain valid in later periods without explicit re-validation [14, 16]. In particular, evaluation protocols based on random splits or cross-validation may yield overly optimistic performance estimates by implicitly sharing information across time and thereby introducing temporal leakage [15].

By enforcing a fully out-of-time evaluation, the adopted design provides a more realistic assessment of temporal generalization, calibration stability, and clinical utility under evolving epidemiological and clinical conditions [14, 16]. This approach is especially critical for early-stage mortality risk prediction, where models are intended to support prospective decision-making and must remain robust to non-stationary data-generating processes.

Feature set and preprocessing principles (early triage constraints)

The predictive pipeline was deliberately constrained to an early-stage (EHR-lite) feature set, consisting exclusively of variables routinely available at the time of initial hospital admission and suitable for early clinical triage. This restriction reflects the intended use case of the models, namely prospective risk stratification before the availability of laboratory dynamics, imaging results, or in-hospital treatment trajectories.

Preprocessing emphasized consistency and transparency rather than maximal feature enrichment [12]. All yearly data extracts were mapped to a unified feature schema to ensure comparability across pandemic waves, while inclusion criteria were applied uniformly to avoid introducing year-specific biases. Importantly, preprocessing decisions were explicitly separated from model training, allowing their effects on probability calibration and downstream threshold-based decision-making to be evaluated in isolation.

Operations such as missing-value imputation, construction of derived variables, and additional filtering were treated as methodological choices requiring explicit justification, rather than as default preprocessing steps. This design reduces the risk of inadvertently encoding outcome-related information into the feature set and supports interpretability of predicted risk distributions under early-triage constraints.

Model family and ensemble construction

Consistent with best practices for clinical risk prediction under dataset shift, multiple model families were evaluated within a unified training and validation framework to assess robustness of early mortality risk prediction [17]. Candidate models included regularized logistic regression (L2), elastic net logistic regression, random forest, histogram-based gradient boosting, LightGBM, and XGBoost. All models were trained using the same early-stage (EHR-lite) feature set and evaluated under an identical temporal validation protocol.

Model selection was guided not only by discriminative performance but also by stability of predicted probabilities and robustness across time. While individual models achieved comparable AUROC values, tree-based gradient boosting methods consistently demonstrated superior precision–recall characteristics and more stable probability distributions under temporal generalization, in line with prior observations in clinical machine learning.

Based on these observations, the final predictive model was constructed as an ensemble of three high-performing gradient boosting learners with complementary inductive biases. Ensemble aggregation was performed by averaging predicted probabilities across the selected base models. This simple aggregation strategy was chosen to reduce variance and mitigate model-specific error patterns while preserving interpretability and calibration properties. More complex stacking architectures were deliberately avoided to limit overfitting and to preserve interpretability of the modeling pipeline.

The resulting ensemble demonstrated improved stability of risk estimates compared to individual models and served as the primary prediction engine for subsequent calibration, discrimination, and decision-analytic evaluation.

Probability calibration

Because model outputs were intended to support threshold-based clinical decision-making, particular emphasis was placed on the reliability of predicted probabilities rather than ranking performance alone [9]. In early triage settings, inaccurate probability estimates directly affect threshold selection and may lead to inappropriate clinical actions, even when discrimination metrics appear satisfactory.

To address this, post-hoc probability calibration was applied using isotonic regression, a non-parametric calibration method that does not impose parametric assumptions on the relationship between raw model scores and observed outcome frequencies [18–19]. Calibration models were trained exclusively on the training data, ensuring that evaluation on the temporally held-out test set reflected true out-of-sample probability reliability without information leakage.

Both uncalibrated (raw) and calibrated probability estimates were retained for downstream analysis. This design enabled direct comparison of discrimination metrics, calibration quality, and decision-curve behavior before and after calibration. Importantly, isotonic calibration preserved ranking performance while improving alignment between predicted risks and observed outcome frequencies, thereby supporting more consistent and interpretable threshold-based decision-making.

Evaluation metrics (discrimination and reliability)

Model performance was evaluated on the independent 2022 temporally held-out test set using complementary metrics designed to capture both discriminative ability and probability reliability [20]. This dual evaluation strategy reflects the study’s focus on clinically meaningful risk estimation rather than ranking performance alone.

Discrimination was assessed using the area under the receiver operating characteristic curve (AUROC) and the area under the precision–recall curve (PR-AUC), the latter being particularly informative given the non-negligible prevalence of in-hospital mortality. To quantify the accuracy

of probabilistic predictions, overall calibration quality was evaluated using the Brier score, which jointly reflects calibration and refinement.

For the final isotonic-calibrated ensemble, performance on the 2022 test set reached AUROC = 0.812, PR-AUC = 0.483, and Brier score = 0.140, indicating strong discrimination accompanied by reliable probability estimates. Reporting discrimination and reliability metrics jointly enables a more comprehensive assessment of model suitability for threshold-based clinical decision support.

Clinical utility via Decision Curve Analysis

To assess whether improvements in predictive performance translate into clinically meaningful decision support, we evaluated model utility using Decision Curve Analysis (DCA) on the independent 2022 test set [10–11]. DCA quantifies net benefit by comparing model-assisted decision-making with default reference strategies, specifically "treat all" and "treat none," across a range of clinically relevant probability thresholds.

The isotonic-calibrated ensemble demonstrated consistent dominance over both reference strategies across a broad threshold interval, approximately 0.15–0.50, indicating a favorable balance between correct identification of high-risk patients and avoidance of excessive false-positive decisions [21–22]. This pattern indicates that improved probability reliability supports more consistent threshold-based clinical decision-making rather than improvements in ranking performance alone.

In addition, an operational triage interval between 0.20 and 0.35 was identified as a practically relevant region in which the calibrated ensemble maintained positive net benefit while remaining robustly superior to baseline strategies. This interval represents a clinically plausible compromise between sensitivity and specificity under early triage constraints and illustrates how calibrated risk estimates can support informed threshold selection in real-world settings.

Implementation and reproducibility

All preprocessing, modeling, calibration, and evaluation steps were implemented within reproducible computational workflows, ensuring traceability of analytical decisions across the entire pipeline. Data handling, model training, validation, and performance assessment followed a fixed and auditable sequence designed to minimize procedural variability and support methodological transparency.

To facilitate reproducibility, non-sensitive artifacts–including the preprocessing schema, feature definitions, validation protocols, and evaluation procedures–can be made available upon reasonable request. Code components required to reproduce the analytical workflow and key experimental results may also be provided, subject to institutional and regulatory constraints.

Access to raw patient-level data is restricted due to privacy, ethical, and legal considerations. These data protection requirements are consistent with the use of secondary clinical registry data and do not affect the reproducibility of the methodological framework presented in this study.

Results and discussion

Cohort characteristics and descriptive analysis

The final analytical cohort comprised approximately 2.53 million hospital admissions with confirmed COVID-19 infection and a binary outcome defined as in-hospital mortality. The dataset represents a large-scale, real-world clinical registry covering multiple pandemic waves and reflecting routine hospital practice under varying epidemiological and organizational conditions.

As an initial descriptive and exploratory analysis step, cohort-level characteristics and outcome dynamics were examined to assess data integrity, temporal structure, and baseline risk heterogeneity prior to predictive modeling. This exploratory analysis was intended to verify clinically plausible gradients, identify temporal non-stationarity, and inform subsequent choices related to validation design, calibration strategy, and decision-oriented evaluation.

Overall in-hospital mortality across the full cohort was 0.284. Substantial temporal variation in outcome prevalence was observed across calendar years, with mortality rates of 0.305 in 2020, 0.299 in 2021, and 0.214 in 2022. This marked decline in observed mortality during later pandemic periods

reflects changes in patient composition, clinical management, and broader epidemiological dynamics over time.

All records were harmonized into a unified feature schema to ensure consistency across yearly data extracts. The cohort construction deliberately preserved the original structure of the registry without aggressive record exclusion or extensive feature transformation. As a result, the observed descriptive patterns reflect naturally occurring variability in routinely collected clinical data rather than artifacts introduced by preprocessing.

Baseline descriptive characteristics demonstrated pronounced heterogeneity in patient-level risk across the cohort. Temporal shifts in outcome prevalence translated into changes in baseline risk distributions, underscoring the non-stationary nature of the data-generating process. These findings motivated the use of strict chronological separation between training and evaluation data and the explicit assessment of model robustness under temporal distribution shift.

Figure 1 summarizes the exploratory temporal analysis of outcome dynamics by presenting the weekly in-hospital mortality rate over the full observation period together with leakage-safe smoothing based on a lagged three-week moving average. The figure highlights pronounced wave-like behavior and temporal non-stationarity in outcome prevalence, providing empirical justification for temporal validation, probability calibration, and threshold-based decision analysis in subsequent modeling stages.

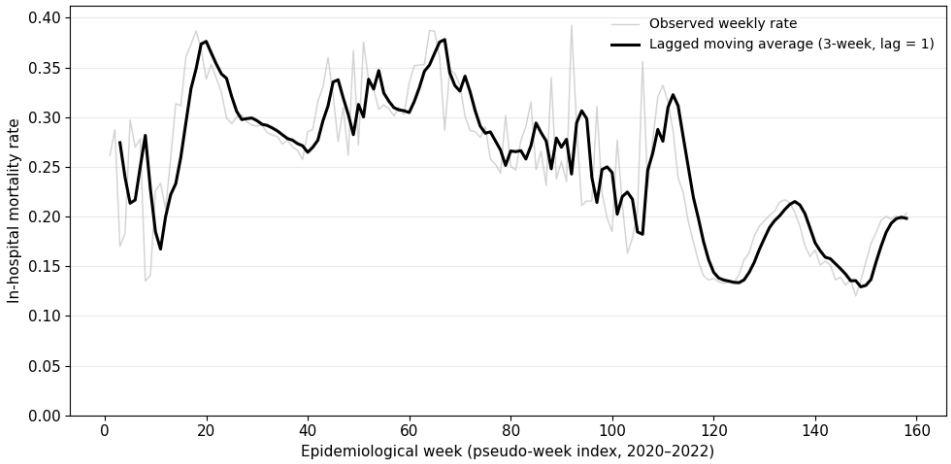


Figure 1 – Weekly in-hospital mortality rate illustrating temporal non-stationarity and leakage-safe smoothing using a lagged 3-week moving average (lag = 1)

Discrimination and calibration performance

Model performance was evaluated on the independent 2022 temporally held-out test set using metrics reflecting both discriminative ability and probability accuracy. Evaluation was conducted for individual base learners, the ensemble model, and their calibrated variants using a unified and fixed evaluation protocol.

Across all evaluated configurations, ensemble aggregation consistently yielded higher discriminative performance compared to single-model counterparts. Individual base learners demonstrated comparable but lower AUROC and PR-AUC values, whereas ensemble predictions achieved more stable performance across evaluation runs. This pattern was consistent across both raw and calibrated probability outputs.

For the final ensemble model, post-processing with isotonic calibration preserved discriminative performance while improving probability accuracy. On the 2022 test set, the isotonic-calibrated ensemble achieved an AUROC of 0.812, a PR-AUC of 0.483, and a Brier score of 0.140. Compared to the uncalibrated ensemble, calibration resulted in a reduction of the Brier score, indicating improved

alignment between predicted probabilities and observed outcomes, while AUROC and PR-AUC values remained largely unchanged.

When comparing raw and calibrated probability estimates, discrimination metrics (AUROC and PR-AUC) exhibited minimal variation across model variants. In contrast, probability accuracy differed more substantially, with calibrated outputs consistently demonstrating lower Brier scores than their uncalibrated counterparts. This pattern was observed both for individual base learners and for the ensemble model.

Comparative analysis between single models and the ensemble further indicated that ensemble predictions demonstrated more favorable combinations of discrimination and reliability metrics. While individual models achieved reasonable AUROC values, their probabilistic accuracy was generally inferior to that of the ensemble, particularly after calibration. These results suggest that ensemble aggregation and calibration contribute complementary improvements to overall model performance.

A quantitative summary of discrimination and reliability metrics for individual models, the ensemble, and their calibrated variants is presented in Table 1, enabling direct comparison of performance across evaluated configurations.

Table 1 – Discrimination and calibration performance of individual models, ensemble model, and calibrated ensemble on the temporally held-out 2022 test set

Model	AUROC	PR-AUC	Brier
LR	0.786	0.451	0.146
LR (Elastic Net)	0.770	0.428	0.150
RF	0.784	0.437	0.145
HGB	0.793	0.453	0.141
LGBM	0.793	0.453	0.143
XGB	0.792	0.453	0.143
Ensemble (raw)	0.802	0.475	0.141
Ensemble (isotonic)	0.812	0.483	0.140

Calibration assessment

Calibration performance was evaluated on the independent, temporally held-out 2022 test set by comparing predicted probabilities with observed outcome frequencies using calibration curves and probabilistic error measures. Calibration analysis was conducted for individual base learners, the ensemble model, and their post-processed variants obtained via isotonic regression.

Calibration curves indicated that the ensemble model exhibited good probability alignment already in its raw (uncalibrated) form, particularly within the clinically relevant range of predicted probabilities. While minor local deviations from the reference diagonal were observed, no evidence of systematic miscalibration was identified for ensemble predictions.

Post-hoc isotonic calibration preserved this overall alignment and resulted in modest but consistent improvements in probability reliability. For the ensemble model, isotonic calibration led to a reduction in the Brier score relative to the uncalibrated variant, while discrimination metrics remained largely unchanged. Similar calibration patterns were observed for individual base learners, although the magnitude of calibration effects varied across model families.

Comparative analysis further demonstrated that ensemble predictions exhibited smaller overall calibration deviations than single-model predictions, both before and after calibration. Post-calibration curves for the ensemble were smoother and remained closely aligned with observed outcome frequencies, whereas calibration curves for individual models showed greater residual variability.

Representative calibration curves for raw and isotonic-calibrated ensemble predictions are shown in Figure 2, illustrating probability alignment within the operational risk range and the stabilizing effect of post-hoc calibration.

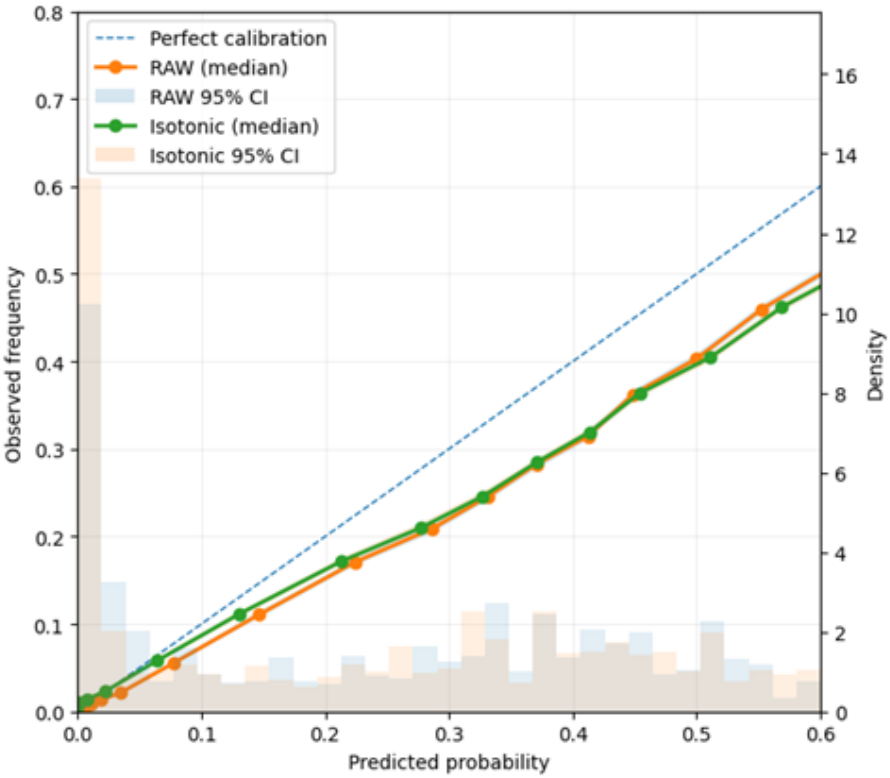


Figure 2 – Calibration of ensemble predictions on the 2022 test set using quantile-based binning with 95% bootstrap confidence intervals

Decision Curve Analysis

Decision Curve Analysis (DCA) was conducted on the independent 2022 temporally held-out test set to evaluate the clinical utility of the final isotonic-calibrated ensemble model across a range of probability thresholds. Net benefit curves were compared against the default reference strategies “treat all” and “treat none”.

Across the evaluated threshold range, the isotonic-calibrated ensemble demonstrated consistently positive net benefit relative to both reference strategies, particularly within the clinically plausible threshold interval of approximately 0.15 to 0.50. Within this range, the model-assisted decision strategy remained stably superior to baseline approaches, indicating a favorable balance between true-positive identification and avoidance of unnecessary interventions. This pattern indicates that the observed decision-analytic gains are primarily attributable to improved probability reliability rather than changes in ranking performance.

At lower thresholds, net benefit values approached those of the “treat all” strategy, reflecting increasingly liberal decision policies, whereas at higher thresholds the net benefit gradually converged toward the “treat none” strategy. This behavior is consistent with expected decision-analytic dynamics under increasing decision stringency.

Overall, these results indicate that the calibrated ensemble model provides meaningful clinical benefit across a broad range of early triage thresholds. Net benefit curves for the evaluated strategies are shown in Figure 3.

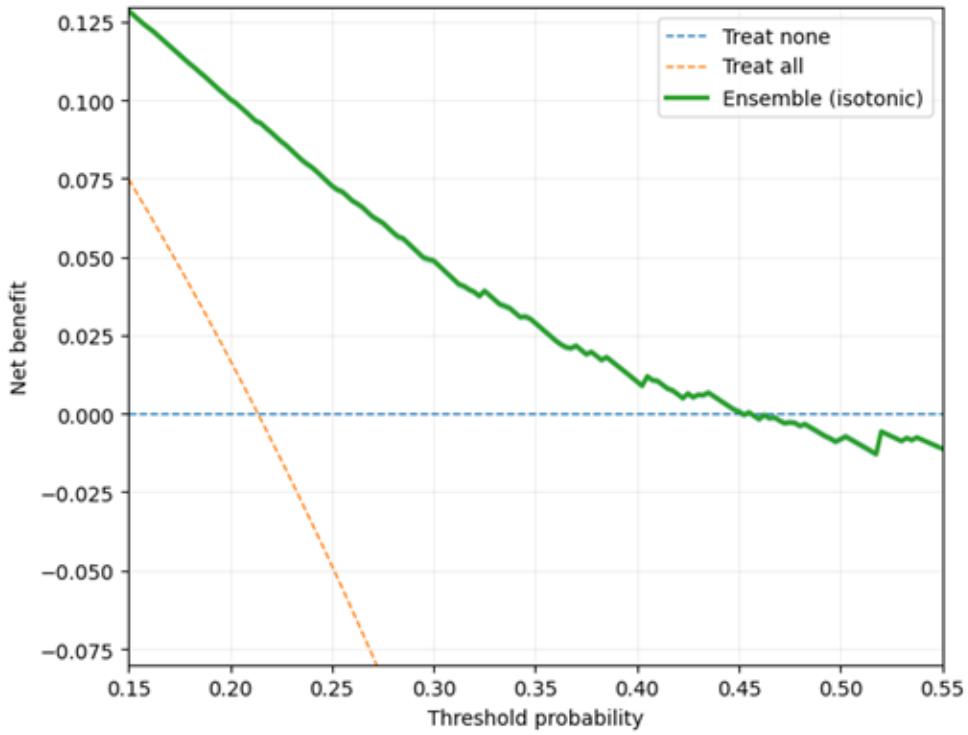


Figure 3 – Decision curve analysis for the isotonic-calibrated ensemble model on the independent 2022 test set, showing net benefit across threshold probabilities in comparison with default strategies (“treat all” and “treat none”)

Operational risk thresholds

To complement decision-curve–based evaluation, model performance was additionally examined at a set of operational probability thresholds relevant for early clinical triage. Thresholds were selected within the region where the calibrated ensemble demonstrated sustained positive net benefit in Decision Curve Analysis, focusing on values commonly considered in early risk stratification settings.

Three representative thresholds–0.20, 0.30, and 0.35–were evaluated on the independent 2022 temporally held-out test set. For each threshold, standard classification metrics were computed, including sensitivity, specificity, and positive predictive value, alongside corresponding net benefit estimates. This threshold-based evaluation enables direct comparison of model behavior across different operating points.

At lower thresholds, the calibrated ensemble identified a larger proportion of high-risk patients, resulting in higher sensitivity and lower specificity. As the threshold increased, sensitivity decreased while specificity increased, reflecting the expected trade-off between false-positive and false-negative decisions. Across all evaluated thresholds, the calibrated ensemble maintained positive net benefit relative to baseline strategies.

Comparative analysis indicated that threshold-based performance of the calibrated ensemble was more stable than that of uncalibrated predictions. In particular, calibrated outputs exhibited smaller fluctuations in net benefit across adjacent thresholds, whereas uncalibrated outputs showed greater sensitivity to threshold selection. This pattern was consistent with the calibration improvements observed for the ensemble model.

A summary of threshold-specific performance metrics for the calibrated ensemble is provided in Table 2, including sensitivity, specificity, positive predictive value, and net benefit at each evaluated

threshold. These results illustrate how calibrated probability estimates support consistent model behavior across a range of practical operating points.

Table 2 – Performance of the isotonic-calibrated ensemble model at selected probability thresholds on the 2022 test set

Threshold	Sensitivity	Specificity	PPV	Net benefit
0.20	0.922	0.508	0.337	0.1002
0.30	0.814	0.629	0.373	0.0488
0.35	0.723	0.703	0.398	0.0289

This study investigated early-stage machine learning models for in-hospital mortality prediction under conditions closely approximating real-world clinical deployment. By combining strict temporal validation, probability calibration, and decision-analytic evaluation, the results demonstrate that predictive discrimination alone is insufficient for reliable early clinical decision support, particularly in non-stationary settings such as infectious disease outbreaks [3–4].

Consistent with prior research, ensemble aggregation outperformed individual base learners in terms of discriminative performance. Ensemble methods are known to reduce variance and improve robustness when applied to large-scale observational healthcare data. However, the present findings show that improved discrimination does not automatically translate into clinically reliable risk estimates. Despite comparable AUROC and PR-AUC values, uncalibrated models exhibited local deviations in probability alignment, highlighting the limitations of relying solely on ranking-based metrics in threshold-dependent clinical applications [3].

Probability calibration emerged as a critical determinant of downstream model behavior. Calibration assessment and Brier score analysis demonstrated that isotonic post-processing resulted in modest but consistent improvements in agreement between predicted risks and observed outcomes without altering the underlying ranking structure. Together, these results reinforce the need to explicitly evaluate probability reliability when model outputs are used to guide early triage decisions, where absolute risk estimates directly influence threshold selection and resource allocation [9, 18].

The clinical relevance of probability calibration was further illustrated through Decision Curve Analysis. The isotonic-calibrated ensemble demonstrated consistently positive net benefit relative to default decision strategies across a broad range of clinically plausible thresholds. This finding indicates that improvements in probability reliability translate into more robust decision-analytic performance, rather than merely improved statistical metrics. By framing evaluation in terms of net benefit, Decision Curve Analysis provides a transparent link between predictive modeling and clinical decision-making and complements conventional discrimination-based assessment [10–11].

A key methodological strength of this study is the use of strict temporal validation. Training models on earlier pandemic waves and evaluating them on a fully independent, later time period revealed substantial shifts in outcome prevalence and baseline risk distributions. Under such conditions, commonly used random-split or cross-validation approaches may produce overly optimistic performance estimates. The persistence of calibration quality and decision-analytic benefit under temporal generalization suggests that the proposed framework offers a more realistic assessment of model robustness in evolving clinical environments [14].

The study also demonstrates that meaningful early risk stratification can be achieved using an EHR-lite feature set consisting exclusively of information available at hospital admission. While richer longitudinal, laboratory, or imaging data may further enhance predictive accuracy, such data are often unavailable at the time when early clinical decisions must be made. Similar observations have been reported in prior large-scale evaluations of clinical prediction models, underscoring the practical value of early-stage approaches under constrained data availability [4].

Several considerations are important when interpreting the results of this study. The analysis is based on a large-scale secondary clinical registry, which provides a realistic representation of routine hospital data but may limit direct generalizability to healthcare systems with different patient populations and data collection practices. At the same time, the use of strict temporal validation allows for a more realistic assessment of model performance under temporal distribution shift, which is critical for real-world deployment. In addition, while the present study focuses on fixed out-of-time evaluation, real-world clinical use may require ongoing monitoring of probability calibration as data distributions evolve over time. Future work may further explore adaptive recalibration and model updating strategies to maintain the stability and reliability of probabilistic predictions [14].

The analysis focused on a single binary outcome. At the same time, preliminary subgroup-level evaluation indicated broadly consistent model behavior across major demographic groups. However, more detailed subgroup analysis, fairness assessment, and prospective evaluation in real-world clinical workflows remain important directions for future work.

Conclusion

This study demonstrated that in early-stage in-hospital mortality prediction, probability reliability and decision-oriented evaluation are essential complements to discriminative performance. While ensemble learning improved overall predictive accuracy, post-hoc probability calibration contributed to stabilizing risk estimates and supporting more consistent threshold-based decision-making.

Using strict temporal validation and an early-stage (EHR-lite) feature set, the results showed that calibrated ensemble models maintained robust performance under dataset shift and achieved consistently positive net benefit across a clinically plausible range of decision thresholds. These findings highlight the importance of integrating calibration and decision-analytic methods into clinical machine learning pipelines, particularly in settings characterized by temporal non-stationarity and limited early information.

Overall, the proposed framework provides a practical and methodologically sound approach for evaluating early clinical risk prediction models and may support the development of more reliable machine learning–based decision-support tools in real-world hospital settings.

REFERENCES

1 Al-Nafjan, A., Aljuhani, A., Alshebel, A., Alharbi, A., Alshehri, A. Artificial intelligence in predictive healthcare: A systematic review. Journal of Clinical Medicine, 14 (19), 6752 (2025). https://doi.org/10.3390/jcm14196752

2 Bajwa, J., Munir, U., Nori, A., Williams, B. Artificial intelligence in healthcare: Transforming the practice of medicine. Future Healthcare Journal, 8 (2), e188–e194 (2021). https://doi.org/10.7861/fhj.2021-0095

3 Kelly, C. J., Karthikesalingam, A., Suleyman, M., Corrado, G., King, D. Key challenges for delivering clinical impact with artificial intelligence. BMC Medicine, 17, 195 (2019). https://doi.org/10.1186/s12916-019-1426-2

4 Wynants, L., Van Calster, B., Collins, G. S., Riley, R. D., Heinze, G., Schuit, E., COVID-19 Prediction Model Consortium. Prediction models for diagnosis and prognosis of COVID-19: Systematic review and critical appraisal. BMJ, 369, m1328 (2020). https://doi.org/10.1136/bmj.m1328

5 Rajwa, B., Naved, M. M. A., Adibuzzaman, M., Grama, A. Y., Khan, B. A., Dundar, M., Rochet, J.-C. Identification of predictive patient characteristics for assessing the probability of COVID-19 in-hospital mortality. PLOS Digital Health, 3 (4), e0000327 (2024). https://doi.org/10.1371/journal.pdig.0000327

6 Rudin, C., Chen, C., Chen, Z., Huang, H., Semenova, L., Zhong, C. Interpretable machine learning: Fundamental principles and 10 grand challenges. Statistics Surveys, 16, 1–85 (2022). https://doi.org/10.1214/21-SS133

7 Ennab, M., Mcheick, H. Enhancing interpretability and accuracy of AI models in healthcare: A comprehensive review on challenges and future directions. Frontiers in Robotics and AI, 11, 1444763 (2024). https://doi.org/10.3389/frobt.2024.1444763

8 Tonekaboni, S., Joshi, S., McCradden, M. D., Goldenberg, A. What clinicians want: Contextualizing explainable machine learning for clinical end use. Proceedings of Machine Learning Research, 106, 359–380 (2019). https://proceedings.mlr.press/v106/tonekaboni19a.html

9 Van Calster, B., McLernon, D. J., van Smeden, M., Wynants, L., Steyerberg, E. W. Calibration: The Achilles heel of predictive analytics. BMC Medicine, 17, 230 (2019). https://doi.org/10.1186/s12916-019-1466-7

10 Vickers, A. J., Van Calster, B., Steyerberg, E. W. Net benefit approaches to the evaluation of prediction models, molecular markers, and diagnostic tests. BMJ, 352, i6 (2016). https://doi.org/10.1136/bmj.i6

11 Sadatsafavi, M., Adibi, A., Puhan, M., Gershon, A., Aaron, S. D., Sin, D. D. Moving beyond AUC: Decision curve analysis for quantifying net benefit of risk prediction models. European Respiratory Journal, 58 (5), 2101186 (2021). https://doi.org/10.1183/13993003.01186-2021

12 Andaur Navarro, C. L., Damen, J. A. A., van Smeden, M., Takada, T., Nijman, S. W. J., Dhiman, P., Ma, J., Collins, G. S., Bajpai, R., Riley, R. D., Moons, K. G. M., Hooft, L. Systematic review identifies the design and methodological conduct of studies on machine learning-based prediction models. Journal of Clinical Epidemiology, 154, 1–12 (2023). https://doi.org/10.1016/j.jclinepi.2022.11.015

13 Giddings, R., Joseph, A., Callender, T., Janes, S. M., van der Schaar, M., Sheringham, J., Navani, N. Factors influencing clinician and patient interaction with machine learning-based risk prediction models: A systematic review. The Lancet Digital Health, 6 (2), e131–e144 (2024). https://doi.org/10.1016/S2589-7500(23)00241-8

14 Subbaswamy, A., Saria, S. From development to deployment: Dataset shift, causality, and shift-stable models in health AI. Biostatistics, 21 (2), 345–352 (2020). https://doi.org/10.1093/biostatistics/kxz041

15 Lu, J., Liu, A., Dong, F., Gu, F., Gama, J., Zhang, G. Learning under concept drift: A review. IEEE Transactions on Knowledge and Data Engineering, 31 (12), 2346–2363 (2019). https://doi.org/10.1109/TKDE.2018.2876857

16 dos Santos Silva, G. F., Barcellos Filho, F. N., Wichmann, R. M., da Silva Junior, F. C., Chiavegatto Filho, A. D. P. Strategies for detecting and mitigating dataset shift in machine learning for health predictions: A systematic review. Journal of Biomedical Informatics, 170, 104902 (2025). https://doi.org/10.1016/j.jbi.2025.104902

17 Riley, R. D., Archer, L., Snell, K. I. E., Ensor, J., Dhiman, P., Martin, G. P., Bonnett, L. J., Collins, G. S. Evaluation of clinical prediction models (part 2): How to undertake an external validation study. BMJ, 384, e074820 (2024). https://doi.org/10.1136/bmj-2023-074820

18 Austin, P. C., Steyerberg, E. W. The Integrated Calibration Index (ICI) and related metrics for quantifying the calibration of logistic regression models. Statistics in Medicine, 38 (21), 4051–4065 (2019). https://doi.org/10.1002/sim.8281

19 Ojeda, F. M., Jansen, M. L., Thiéry, A., Blankenberg, S., Weimar, C., Schmid, M., Ziegler, A. Calibrating machine learning approaches for probability estimation: A comprehensive comparison. Statistics in Medicine, 42 (29), 5451–5478 (2023). https://doi.org/10.1002/sim.9921

20 Gneiting, T., Raftery, A. E. Strictly proper scoring rules, prediction, and estimation. Journal of the American Statistical Association, 102 (477), 359–378 (2007). https://doi.org/10.1198/016214506000001437

21 Chalkou, K., Vickers, A. J., Pellegrini, F., Manca, A., Salanti, G. Decision curve analysis for personalized treatment choice between multiple options. Medical Decision Making, 43 (3), 337–349 (2022). https://doi.org/10.1177/0272989X221143058

22 Piovani, D., Sokou, R., Tsantes, A. G., Vitello, A. S., Bonovas, S. Optimizing clinical decision making with decision curve analysis: Insights for clinical investigators. Healthcare, 11 (16), 2244 (2023). https://doi.org/10.3390/healthcare11162244

[1]*Куничик В.Г.,
докторант, ORCID ID: 0009-0004-8580-7731,
*e-mail: kunichikval@gmail.com
[1]Салыкова О.С.,
т.ғ.к., қауымдастырылған профессор, ORCID ID: 0000-0002-8681-4552,
e-mail: solga0603@mail.ru

[1]Ахмет Байтұрсынұлы атындағы Қостанай өңірлік университеті,
Қостанай қ., Қазақстан

ИНТЕРПРЕТАЦИЯЛАНАТЫН ЖӘНЕ КАЛИБРЛЕНГЕН АНСАМБЛЬДІК МАШИНАЛЫҚ ОҚЫТУ МОДЕЛЬДЕРІН ҚОЛДАНА ОТЫРЫП АУРУХАНА ІШІНДЕГІ ӨЛІМ-ЖІТІМДІ ЕРТЕ БОЛЖАУ

Аңдатпа

Аурухана жағдайында пациенттің өлім-жітім қаупін ерте кезеңде бағалау клиникалық тәжірибедегі маңызды міндеттердің бірі, әсіресе COVID-19 сияқты жұқпалы аурулар кең таралған жағдайда. Мұндай кезде шешімдер көбіне науқасты стационарға қабылдау сәтінде, шектеулі бастапқы клиникалық мәліметтер негізінде қабылданады. Машиналық оқыту әдістері бұл бағытта кеңінен қолданылғанымен, көптеген зерттеулер ерте клиникалық триаж талаптарына толық сәйкес келмейді. Бұл ең алдымен, ықтималдық болжамдарының сенімділігіне, уақыт бойынша өзгерістерге бейімделуіне және шешім қабылдауға негізделген бағалау тәсілдеріне жеткілікті көңіл бөлінбеуімен түсіндіріледі. Осы жұмыста ауруханаға түскен сәтте қолжетімді күнделікті клиникалық деректер негізінде өлім-жітім қаупін ерте болжау мәселесі қарастырылады. Зерттеу барысында нақты клиникалық жағдайларды бейнелеу мақсатында деректер уақыт бойынша қатаң бөлініп, модельдер осы қағидаға сәйкес оқытылып, бағаланды. Градиенттік бустингке негізделген ансамбльдік модельдер құрылып, болжамдардың сенімділігін арттыру үшін post-hoc изотоникалық калибрлеу әдісі қолданылды. Модельдердің тиімділігі дискриминациялық және калибрлеу метрикалары арқылы кешенді бағаланып, олардың клиникалық маңыздылығы шешім қабылдау қисықтарын талдау (Decision Curve Analysis, DCA) әдісімен зерттелді. Тәуелсіз, уақыт бойынша бөлінген тестілік жиында алынған нәтижелер ансамбльдік тәсілдің тәуекел бағаларының тұрақтылығын арттыратынын, ал калибрлеудің модельдің шекті мәндердегі жұмысын тұрақтандыратынын көрсетті. Сонымен қатар, калибрленген болжамдардың стандартты стратегиялармен салыстырғанда шекті мәндердің кең ауқымында жоғары тиімділік көрсететіні анықталды. Алынған нәтижелер ерте клиникалық шешім қабылдау жағдайында ықтималдық болжамдарының сенімділігі дискриминациялық қабілетпен қатар маңызды рөл атқаратынын дәлелдейді. Ұсынылған тәсіл уақыт бойынша өзгеретін деректер жағдайында және бастапқы ақпарат шектеулі болған кезде ауруханаішіндегі өлім-жітім қаупін бағалауға арналған сенімді әрі практикалық тұрғыдан негізделген әдіс.

Түйін сөздер: машиналық оқыту, ауруханаішіндегі өлім-жітім, ерте клиникалық триаж, ансамбльдік модельдер, ықтималдықтарды калибрлеу, шешім қабылдау қисықтарын талдау, клиникалық шешімдерді қолдау.

[1]*Куничик В.Г.,
докторант, ORCID ID: 0009-0004-8580-7731,
*e-mail: kunichikval@gmail.com
[1]Салыкова О.С.,
к.т.н., ассоциированный профессор,
ORCID ID: 0000-0002-8681-4552, e-mail: solga0603@mail.ru

[1]Костанайский региональный университет им. Ахмета Байтурсынулы,
г. Костанай, Казахстан

РАННЕЕ ПРОГНОЗИРОВАНИЕ ВНУТРИБОЛЬНИЧНОЙ ЛЕТАЛЬНОСТИ С ИСПОЛЬЗОВАНИЕМ ИНТЕРПРЕТИРУЕМЫХ И КАЛИБРОВАННЫХ АНСАМБЛЕВЫХ МОДЕЛЕЙ МАШИННОГО ОБУЧЕНИЯ

Аннотация

Раннее выявление пациентов с высоким риском внутрибольничной летальности остается одной из ключевых задач клинической практики, особенно в условиях вспышек инфекционных заболеваний, таких как COVID-19, когда решения должны приниматься уже на этапе госпитализации при ограниченном объеме доступной информации. Несмотря на широкое применение методов машинного обучения для прогнозирования летальности, многие существующие модели разрабатываются и оцениваются в условиях, снижающих их применимость для ранней клинической триаж-оценки, включая недостаточное внимание к надежности вероятностных прогнозов, временной обобщаемости и ориентированной на принятие решений оценке. В работе рассматривается задача раннего прогнозирования риска летального исхода на основе рутинно доступных клинических данных, собираемых при поступлении пациента в стационар. Разрабатывается ансамбль моделей градиентного бустинга, анализируемый в условиях строгого временного разделения обучающей и тестовой выборок, что отражает реалистичные сценарии практического внедрения. Особый акцент сделан на надежности прогнозируемых вероятностей: для улучшения согласованности между предсказанными рисками и наблюдаемыми исходами применяется пост-хок изотоническая калибровка. Качество моделей оценивается с использованием совокупности дискриминационных и калибровочных метрик, а клиническая значимость анализируется с помощью анализа кривых принятия решений в диапазоне практически значимых порогов. Оценка на независимой временно отложенной тестовой выборке показывает, что ансамблевая агрегация повышает устойчивость оценок риска, а калибровка обеспечивает более согласованное пороговое поведение без изменения ранжирующей способности моделей. Анализ кривых принятия решений демонстрирует преимущество откалиброванных прогнозов по чистому выигрышу в широком диапазоне порогов раннего клинического триажа. Полученные результаты подчеркивают, что надежность вероятностных оценок играет ключевую роль наряду с дискриминационной способностью моделей. Предложенный подход представляет собой методологически обоснованное решение для ранней оценки риска внутрибольничной летальности в условиях реальной клинической практики и временной нестабильности данных.

Ключевые слова: машинное обучение, внутрибольничная летальность, ранний клинический триаж, ансамблевые модели, калибровка вероятностей, анализ кривых принятия решений, поддержка клинических решений.

UDC 004.896
IRSTI 28.23.27

https://doi.org/10.55452/1998-6688-2026-23-3-218-232

[1]Samigulina Z.I.,
PhD (docent), ORCID ID: 0000-0002-5862-6415,
e-mail: z.samigulina@kbtu.kz
[1*]Mlikova K.A.,
Master's degree, ORCID ID: 0009-0009-5931-7065,
*e-mail: missmlikovakristina@gmail.com
[1]Tolengutov R.R.,
Master's degree, ORCID ID: 0009-0000-3210-7126,
e-mail: r.tolengutov@kbtu.kz
[1]Butakova D.A.,
Master's degree, ORCID ID: 0009-0006-8151-4928,
e-mail: d.butakova@kbtu.kz
[1]Nakhimov A.Z.
Master's degree, ORCID ID: 0009-0009-0092-8208,
e-mail: a.nakhimov@kbtu.kz

[1]Kazakh-British Technical University, Almaty, Kazakhstan

A NOVEL TRANSPORT MODULE CONCEPT FOR VERTICAL TAKE-OFF AND LANDING UNMANNED AERIAL VEHICLE TRANSPORTATION OF UNMANNED GROUND VEHICLES

Abstract

This paper describes the design and testing of a modular docking station for a fixed-wing vertical take-off and landing drone to be used in conjunction with an unmanned ground vehicle. The solution enables autonomous engagement and disengagement of payloads through a controlled rail-guided system and visual docking with a quick response marker using a binocular camera module. A novelty of the proposed module lies in the fact that the primary mounting mechanism does not remain integrated with the drone after deployment; instead, it is designed as an integral part of the transport module itself and is released together with it. This approach distinguishes the system from conventional solutions in which the main attachment structure stays onboard the aerial platform, and it expands the flexibility of payload delivery and deployment scenarios. The payload assembly was designed in Autodesk Fusion 360 and manufactured in polyethylene terephthalate glycol-modified plastic using fused deposition modeling 3D printing on a Bambu Lab X1 Carbon printer. Structural analysis using finite element methods was performed to evaluate the displacement, stress, strain, and reaction forces of the module's structure under operational loads. Advanced simulations suggest that the design satisfies mechanical protection requirements, additional proof will be gathered through flight testing. The system could be implemented to deploy unmanned ground vehicles from the air or for a drone to land on mobile ground vehicles, demonstrating its versatility in robotics and automation.

Key words: autonomous robotics, drones, VTOL, UGV, modular docking system, payload mechanism, 3D printing, PETG, delivery.

Received April 7, 2026; accepted June 6, 2026.

Introduction

Nowadays, the popularity and scientific interest in drones and Unmanned Aerial Vehicles (UAVs) are steadily increasing. This trend may be attributed to the expanding range of applications and the growing diversity of aerial vehicles. Deliveries through UAVs pose an opportunity for developing

local logistics, specifically for densely populated urban areas [1–3]. The advancement of such a system may require not only drones and their communication and interaction systems but also transportation and delivery modules for various goods, ranging from medicines to food products. This would not only enhance the technical capabilities of drones, but also improve their overall safety [1, 4].

The processes that come with the delivery have a lot of problems to solve. To make certain there are no issues with the steady ascent, release, and retrieval of the cargo, one of the key problems to solve is vertical correction (adjustment along the Z axis). For this purpose, the participants of AlphaPilot competition along with their advisors devised an optimization model which at a velocity of 5 m/s tracked and navigated through the obstacles with close to 100 precision percent success rate [5]. In addition, analyzing the performance of vertical delivery with an aerial drone as compared to a conventional elevator (assuming a single elevator in the building), shows that UAVs exhibit drone dominance in average delivery time and energy efficiency. Conversely, elevators outperform drones in overall delivery efficiency for given wait time constraints and when order volume is heavily loaded above 0.66 orders per household [2].

An equally important consideration is defining the equipment, in particular, the drone controller which determines the extent to which advanced algorithms on path optimization could be stored, the level of artificial intelligence integration, processing speed, and the quality of stabilization. The Arduino Uno is one of the cheapest and easiest to program microcontrollers. A modular system of multiple drones was developed on this platform where the drones could vertically attach to each other, thus increasing their payload capacity by combining their power resources [3].

For the development of more complex intelligent systems, platforms such as NVIDIA Jetson Xavier [5, 6], FPGA [4], or fully professional equipment, such as the specialized PixHawk controller [7–9] are utilized. In one study, the combination of PixHawk with a Raspberry Pi 3B (3 GB RAM) enabled the creation of a system for installing signaling spheres on high-voltage power lines [10].

Aside from the use of controllers, certain specialized modules are designed to customize drones for particular functions. For example, the drone fitted with a device containing two robotic arms which enables it to operate as controlled remote arms through augmented reality (AR) [11]. In another study, a module was developed using rods made of a sufficiently elastic material. This design enabled the protection of the payload during its release from the drone’s flight altitude by forming a "shield" around the cargo [12]. A modular system was also employed in the integration of drones into traditional delivery systems using trucks. This system functioned as a docking and battery-swapping station, enabling seamless interaction between drones and ground transport [13].

Based on the analysis of the studies, the main difficulty with such concepts stems from their software-centric exploitation of cyberattacks, as well as the risk of rogue behavior during the incorporation of new system modules [1, 4]. Nevertheless, attempts to solve these issues have already been initiated. In the research concerning the drone developed to carry signaling spheres to high-voltage power lines, provisions were made for a magnetic lock module as a countermeasure to electrostatic interference caused signal disruption [10].

The main goal of this research is to fuse a fixed-wing VTOL drone with a module for transporting payloads designed for releasing an unmanned ground vehicle (UGV). One of the most important design features is limiting the distance between the payload and the landing site to reduce the possibility of damaging the UGV. In this case, the drone will land on the payload to minimize the risk during release. A separate case worth emphasizing is the use of the drone within a collaborative robotic system [14]. The structure could extend the operational capabilities of monitoring missions in highly hazardous areas [15] and may also serve as a foundation for logistics systems in Smart City environments [16-18].

While some existing projects propose combining the UGV and the drone into a single integrated device [19], this article considers a different concept based on a new approach to module design. In the proposed concept, the transport module is attached to the drone rather than permanently integrated with the ground vehicle. After release or delivery, the module is detached together with the payload, thereby reducing the structural burden on the drone during subsequent operations.

The most important result of this study lies in the creation of a new release and communication module aimed at efficient deployment and post-release interaction with a UGV. This could advance multidisciplinary research focused on autonomous multi-robot cooperative missions, autonomous navigation in complicated terrains, logistics automation, and related fields. In addition, the novelty of the proposed concept lies in the fact that the main attachment mechanism is not left as a permanent part of the drone structure, but instead forms part of the transport module itself and is released together with it. This distinguishes the proposed approach from conventional solutions in which the primary mounting structure remains onboard the aerial platform.

An assessment of the developed module's structural performance and reliability will be carried out through virtual testing using Autodesk Fusion 360 simulation tools. The evaluation will include the following mechanical characteristics: safety factor, von Mises stress, displacement, reaction force, and strain. Among these parameters, displacement is considered the most important. Excessive deformation under load may impair the precise positioning and secure holding of the payload during post-flight operations. A high displacement value can indicate low rigidity, which increases the likelihood of misalignment or oscillation during deployment. Therefore, to ensure the stability and operational integrity of the system, the critical goal is to maintain bounded and predictable displacement. These parameters will guide iterative improvements in the module's structural design aimed at increasing its durability and performance in actual operational environments.

The main contribution of the study is formulated as follows:

A modified design of a transport module has been developed for carrying unmanned aerial vehicles (UAVs) using VTOL-type UAVs, with the aim of reducing the structural load on the drone after the payload has been detached. Unlike traditional solutions, the main mounting mechanism is integrated into the transport module itself and detaches along with it, which increases the system's flexibility for use in delivery and robotic interaction tasks.

A 3D model of the transport module has been developed in Autodesk Fusion 360, incorporating a rail-based docking mechanism, alignment using a QR code, the use of a binocular camera for positioning, and servo-driven locking of the module during transport of the unmanned aerial vehicle (UAV).

A physical prototype of the transport module was designed and manufactured from PETG using 3D printing technology, which made it possible to test in practice the feasibility of integrating the module with the UAV fuselage and mechanically connecting it to the UAV.

A structural analysis of the developed module was carried out using the finite element method in Autodesk Fusion 360, including an analysis of displacements, Mises stress, strains, support reactions and the safety factor under a typical operational load.

Thus, problem statement is to develop a new concept of a module for attaching an unmanned ground vehicle to a drone for transportation, with the ability to detach this module from the drone during flight, and to evaluate its structural characteristics using a CAD-based application.

This article has the following structure: Section 1 serves as an introduction, which includes an analysis of the popularity of drones and the rationale for designing modules for them. This is followed by Section 2, which covers methodology and includes subsections on creating a conceptual design for a new module, selecting materials for its 3D printing, and constructing it using the program Fusion 360. Next comes section 3 - a demonstration of the work and its metrics. The final section, 4, presents the conclusion of the whole work, further research in this area, and limits.

Materials and methods

The development of the payload transport module (PTM) presented in Figure 1 involved a sequential work approach the fused reference study, digital modeling, simulation as well as physical testing. It started with an actual aerial transport system selection as a conceptual guide, and then proceeded to construct a 3D model of the drone using 3D scanning methods.

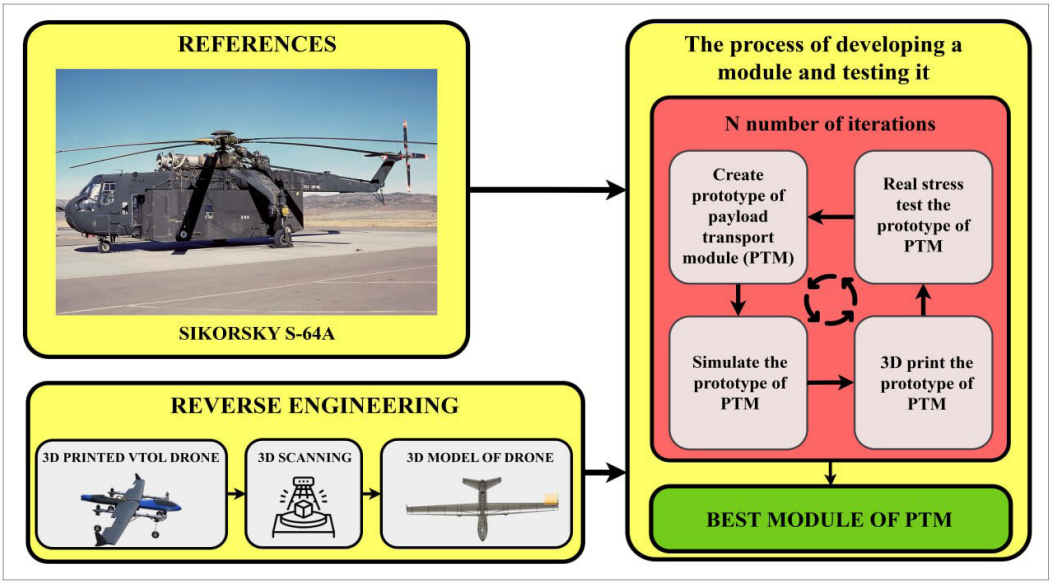


Figure 1 – Structural scheme of the payload transport module (PTM)

After this, a preliminary design of PTM was created and evaluated through structural simulations. Some of the results were based on a physical prototype which was 3D printed and tested under actual loading conditions. The model which best balanced performance in both virtual and experimental evaluations was chosen as the final model.

A structural assessment of the proposed design was conducted using the finite element method (FEM) in a linear static stress formulation. The numerical study was performed in Autodesk Fusion Simulation as a Static Stress analysis, in which the mechanical response of the structure under prescribed loads and boundary conditions was evaluated by solving the global equilibrium equation [20–24]:

$$Ku = f \tag{1}$$

where K is the global stiffness matrix, u is the is the nodal displacement vector, and f is the global load vector. The external loading included gravitational acceleration and three applied forces of 20 N each, while the support conditions were represented by fixed constraints that suppressed translational motion in all x-, y- and z-directions. Gravity was applied as 9,807 m/s^2, along the negative z-axis.

The displacement field was approximated by shape functions such as:

$$u^{(e)}(x,y,z) = N(x,y,z)q^{(e)} \tag{2}$$

where N is the matrix of shape functions, q^e is the vector of nodal degrees of freedom for element e. Under the small-strain assumption, the strain field was obtained from (2):

$$\varepsilon = Bq^{(e)} \tag{3}$$

where B is the strain-displacement matrix. The stress field was then computed using the constitutive relation for a linear isotropic elastic material,

$$\sigma = D\varepsilon \tag{4}$$

where D is the elasticity matrix.

The material assigned to the structure was plastic, characterized by a Young's modulus of 2780 MPa, a Poisson's ration of 0.4 and a yield strength of 54.4 MPa. These properties were used to construct the constitutive matrix and to evaluate the stress-based failure criterion.

To assess the stress state of the structure, the equivalent von Mises stress was used as the primary strength criterion [25]:

$$\sigma_V M = \sqrt{\frac{1}{2}[(\sigma_1 - \sigma_2)^2 + (\sigma_2 - \sigma_3)^2 + (\sigma_3 - \sigma_1)^2]} \quad (5)$$

where σ_1, σ_2, σ_3 are principal stresses.

The total displacement magnitude was evaluated as:

$$u_{tot} = \sqrt{u_x^2 + u_y^2 + u_z^2} \quad (6)$$

where u_x, u_y, u_z are the displacement components along the global coordinate axes. Structural safety was estimated using the factor of safety defined as:

$$n = \frac{\sigma_y}{\sigma_V M} \quad (7)$$

where σ_y is the yield strength of the material and σ_VM is the equivalent von Mises stress at the point of interest (5). This formulation enabled identification of the most critical stress locations and quantification of the available safety margin with respect to yielding.

The element stiffness matrix was formed in the standard FEM form as:

$$K^{(e)} = \int_{Ve} B^T DBdV \quad (8)$$

and the global stiffness matrix was assembled from all elements as:

$$K = \sum_{e=1}^{n} A^{(e)T} K^{(e)} A^{(e)} \quad (9)$$

where $A^{(e)}$ is the assembly operator. After application of the prescribed constraints and loads, the resulting linear system was solved to obtain the displacement field, from which strains, stresses, reaction forces, and safety factors were subsequently derived.

Conceptual design of the drone

A fixed-wing VTOL drone weighing approximately 4.5 kilograms served as the foundation for the system's development, classifying it as a small UAV. The detailed technical specifications are presented in Table 1.

To explore existing concepts and engineering solutions related to modular systems for lifting and transporting payloads, archival materials on the experimental Sikorsky S-64 helicopter demonstrated in Figure 2 were studied [26]. This aircraft, designed by Igor Sikorsky (1962), provided valuable insights into the structural principles of aerial cargo transport.

Particular attention was given to the lifting assemblies of the referenced helicopter, which essentially functioned as a rail-mounted crane system. This configuration allowed the mechanism to fold during flight and landing, making it relatively convenient to operate.

However, as previously noted, the drone used in this project weighs only 4.5 kilograms, and integrating such a heavy system would significantly reduce its overall payload capacity. As a result, an innovative solution was proposed: to shift the modular mechanism onto the payload itself - in this case, an unmanned ground vehicle (UGV).

Table 1 – Components of the fixed-wing VTOL

Component	Model	Purpose
1	2	3
Thermal-resistant p. rts	Overture PETG	For components exposed to heat
Flight controller	Holybro Kakute H743 Wing	Main control unit for flight management
GPS module	Micro M10	Navigation and position tracking
Airspeed sensor	MATEKSYS Digital Airspeed Sensor	Measures air velocity during flight
Transmitter	RadioMaster TX16S + TBS Crossfire Module	Remote control of the drone
Receiver	TBS Crossfire Nano RX Pro	Receives control signals from the transmitter
ESC (speed controller)	Axisflying Argus Pro 65A (4-in-1)	Controls motor speeds
Motors	Brotherhobby Tornado T5 3115 640Kv	Provides thrust for flight
Propellers (front/rear)	13*8 APC / 12*6 APC	Generates lift and propulsion
Tilt servos	RDS3218 (25 kg*cm)	Tilts motors to control thrust direction
Control surface servos	EMAX ES08ma (12 g)	Controls stabilizers and rudders
Control surface linkage	HobbyPark Nylon Control Horn Kit	Mechanical linkage system
Video transmitter (VTX)	DJI O3 Air Unit	Real-time video transmission
Gimbal	HEQ G-Port 3-Axis	Stabilized camera platform
Gimbal power supply	12V BEC 3A	Provides stable power to the gimbal
FPV goggles (First Person View)	DJI Goggles 3	Video feedback and navigation interface
Battery	6S3P Li-ion 13,500 mAh (Molicel 21700 P45B)	Power supply for the entire drone

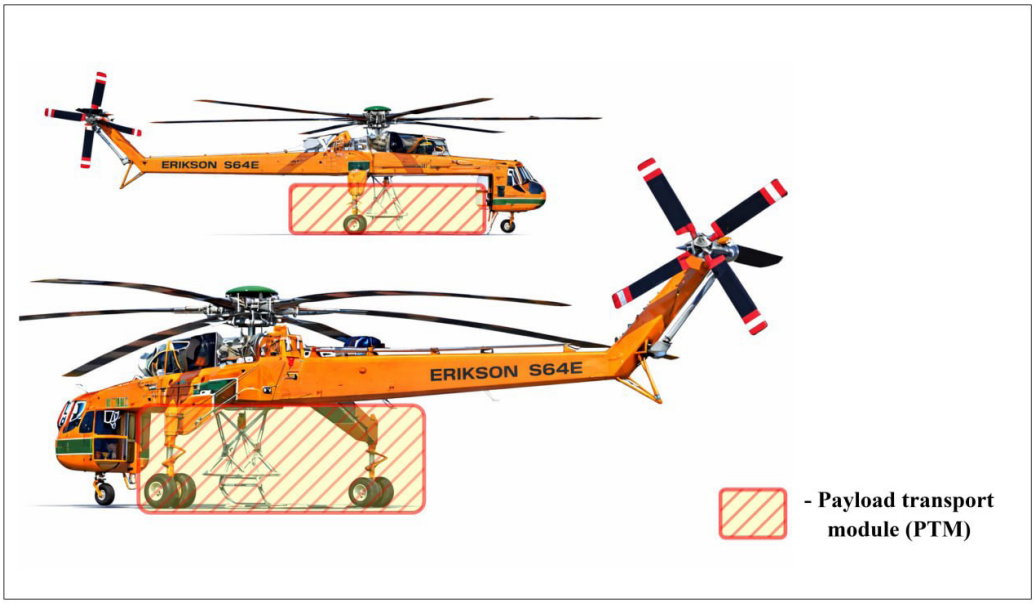


Figure 2 – The payload mechanism of Sikorsky S-64

This approach dramatically reduces energy consumption during the drone's unloaded flight phase, offering a more efficient and lightweight alternative to traditional aerial lifting designs.

Composite selection

Based on its mechanical and thermal properties, a lightweight structural polymer was chosen for a payload lifting and transport module, which Table 2 shows. The material offers an optimal balance between strength and weight, which is critical for small UAV platforms with strict mass limitations, having a density of 1.3 g/cm^3.

This plastic will be able to bear moderate mechanical loads without permanent deformation because the material's yield strength and ultimate tensile strength are 90 MPa. Moreover, its yield strength and ultimate tensile strength are both rated 90 MPa which ensures the module will withstand both static and dynamic stresses while flying, landing, and releasing payloads.

Table 2 – Material properties selected for the payload transport module

Property	Value	Reason for selection
1	2	3
Density	1.1 g/cm	Lightweight; reduces overall drone mass
Young's modulus	2.78 GPa	Provides sufficient stiffness for structural integrity
Poisson's ratio	0.4	Suitable for predicting deformation behavior
Yield strength	54.4 MPa	Withstands stress during payload handling
Ultimate strength	54.4 MPa	Maintains integrity under maximum loading
Thermal conductivity	0.24 W/(m*°C)	Minimizes heat transfer under solar exposure
Thermal expansion coefficient	6.7*10-5 °C	Maintains dimensional stability during flight
Specific heat capacity	1600 J/(kg*°C)	Helps dissipate heat and avoid overheating

Moreover, the specific heat capacity of the material assists in moderating the rise in temperature due to heat being absorbed, in addition to highlights thermal stability. It has a thermal conductivity of 0.2, which means it will keep its shape while the operating temperate clefts can change.

The combined properties make the selected polymer a good candidate for 3D-printing of the payload module because it requires thermal stability and strength with low weight.

3D Modelling in Fusion 360

Autodesk Fusion 360 was selected as the primary CAD software for designing the 3D model of the payload module for the VTOL drone. The choice was driven by its extensive capabilities in modeling complex 3D geometries, high precision in exported designs, integrated structural analysis tools, and access to a vast component library - even in the free student version, which makes it especially suitable for academic research and prototyping.

The mounting mechanism itself was developed as follows. The unmanned ground vehicle (UGV), equipped with a top-mounted connector, autonomously navigates beneath the VTOL drone, aligning itself with a visual marker in the form of a QR code as shown in Figure 3.

Positioning accuracy is ensured by means of a stereo vision system using a binocular camera module (Dual IMX219), which allows the UGV to precisely dock with the aerial platform before lift-off. The module is secured in place using a Tower Pro SG90 micro servo, which is presented in Figure 4.

Once the payload (UGV) is successfully attached, the QR code marker located beneath the drone is retracted upward to enhance the aerodynamic profile of the airframe. This mechanism is actuated by an additional servo, which lifts the drone approximately 2 centimeters off the ground, allowing the marker to fold into the body and minimizing drag during flight. It is noted that the initial idea with a rail-guided movement for the module was maintained for seamless controlled docking alignment. In later phases of the project, this component was physically realized with 3D printing, the results of which, along with their evaluation, will be discussed in the Results section.

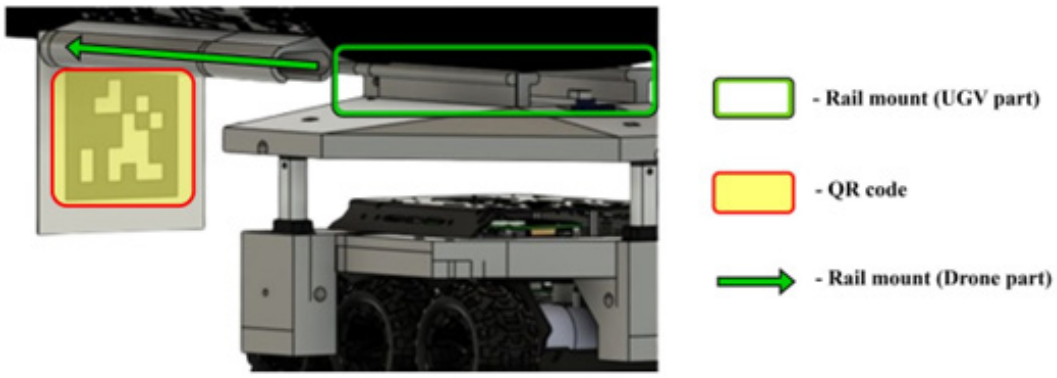


Figure 3 – Correcting and driving UGV under the drone by QR code

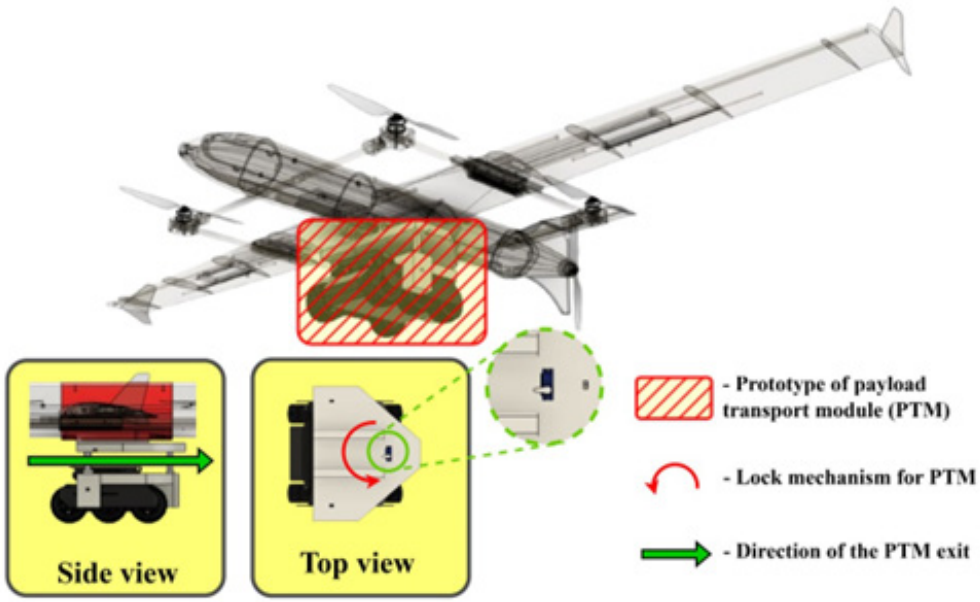


Figure 4 – Rail mount for drone and UGV transportation module

Results and discussion

The Results section includes the final result of the work as well as the main physical characteristics of the module.

Figure 5 illustrates the Drop-Ship system, where the drone is landed, scans the QR marker with binocular stereo vision, and payload locking is performed underneath.

The last version of the payload transport module was created by utilizing a black PETG filament which has good strength properties and heat resistance. The extrusion temperature during the printing process was set at 255 degree of Celsius and the mass of the extracted material after printing the module was about 4 kg. The whole process took about 8 hours on a high-precision Bambu Lab X1 Carbon 3D printer.

The construction of the module enables full integration with the drone fuselage, resulting in a monolithic printed structure. The UGV interface featured M3 bolts and nut welds on the ground docking rails of the vehicle to facilitate consistent and robust mechanical alignment between the two platforms.

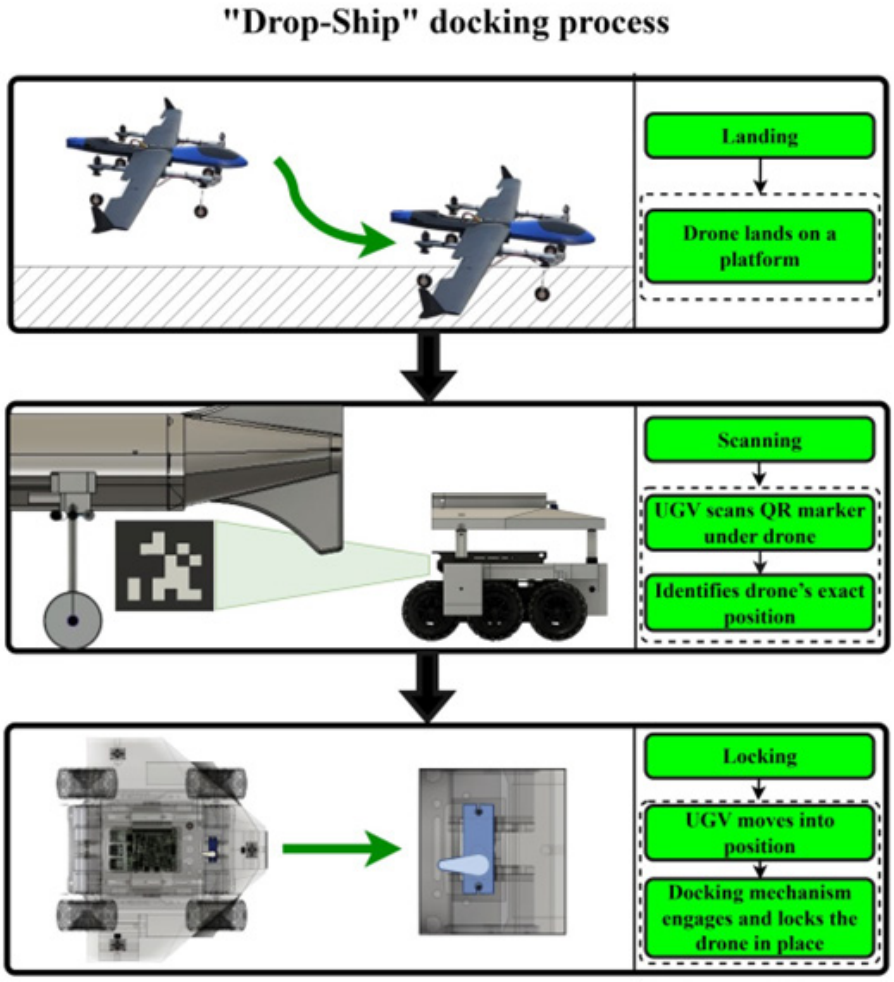


Figure 5 – Structural scheme of the landing, UGV payload attachment and takeoff

A comprehensive logic for the fully autonomous docking and takeoff prototype was also implemented. The diagram depicts the drop-ship system in which the drone lands, uses binocular stereo vision to scan the QR marking, and executes payload locking beneath.

The Figure 6 presents the final prototype of the drone docked with the UGV is shown. This picture illustrates the successful integration of the modular design into functional hardware.

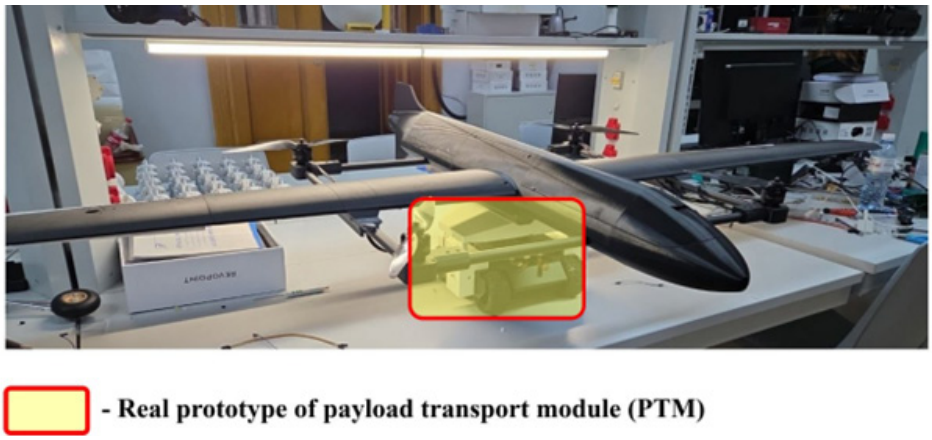


Figure 6 – Real printed prototype of the transportation module

The finalized prototype demonstrated the possibility of structural integration with both the VTOL drone and the UGV, validating the feasibility of the proposed modular docking approach.

Structural performance evaluation

During the evaluation phase, the structural performance of the payload module was analyzed in Autodesk Fusion 360 using finite element method (FEM) simulation. The results included measurements of displacement, von Mises stress, safety factor, reaction forces, and strain under a typical operational load case.

Displacement received focus as one of the primary parameters in regard to the vertical and payload alignment that connects mechanically. The simulation showed that maximum displacement of 0.2785 mm occurred at the upper edge of the guide rails, which is within the tolerances defined. The value exceeds the tolerable mechanical ranges required for docking with the, thus, overall displacement contour remains subdued and localized, showing an anchored and rigid structural behavior response. A displacement field plot is given in Figure 7.

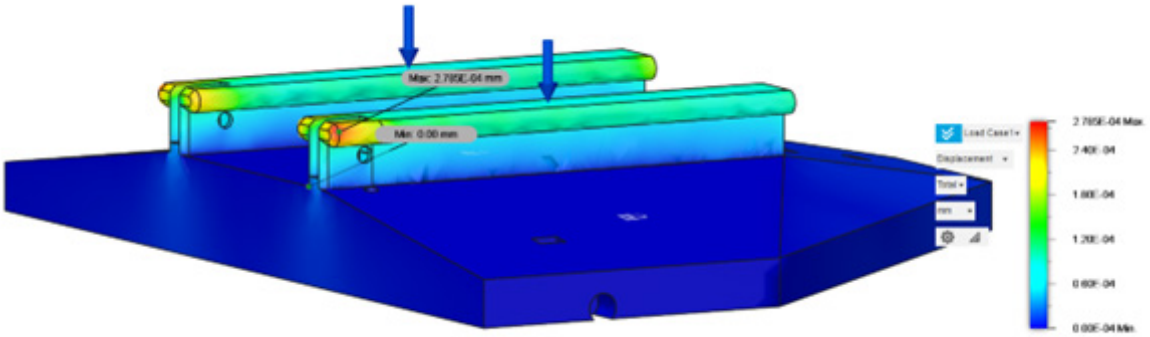


Figure 7 – The displacement coefficients of the transportation module

Other parameters, such as stress and strain, remained well below the material limits. The Table 3 below summarizes the key outcomes of the simulation study.

Table 3 – Summary of the structural simulation results for the payload module

Parameter	Max value	Interpretation
1	2	3
Safety factor	15.0	Far above critical threshold; structure is overdimensioned
Von Mises stress	0.464 MPa	Much lower than yield strength (90 MPa); indicates safe operation
Displacement	0.2785 mm	Low displacement; ensures precision during payload locking
Reaction force	1.191 N	Localized at attachment points; within acceptable range
Strain	1.913*10-4	Minimal deformation; good elasticity without plastic change

Initial simulation results indicate that the design meets structural requirements under nominal load conditions; however, these findings will be further validated through physical testing in upcoming stages of the project.

Conclusion

This study devised and prototyped a modular payload docking and transport system which incorporates a fixed-wing VTOL drone with an unmanned ground vehicle (UGV). Additive manufacturing processes were used to build the docking mechanism out of PETG which meets design specifications and was verified through simulation which showed that the essential structure met the mechanical design criteria for nominal loading. Systems for alignment are based on QR code tracking and binocular vision while payload securing is implemented using servo locking.

The described methodology is promising not just for the deployment of payloads from aircraft, as it allows for UGVs to be air-transported, or for drones to land on mobile ground vehicles, which would augment task autonomy in inspection logistics and robotics.

As the next phase of development, integrated system mounting on a custom platform will allow for real world testing and evaluation of the aerodynamic and structural performance of the system.

Although the outcomes are encouraging, many limitations still exist. Currently, the system operates using exact interaction and communication via timing, as the locking and unlocking steps are executed commandingly within a sequence. In addition, finding the best drone-UGV mass balance was a remarkably complicated issue that affected the system's stability and efficiency. The expenses related to the materials, sophisticated 3D printing, and the equipment onboard may also create obstacles when trying to scale up or implement in more austere settings.

Subsequent tasks will include optimization of docking control algorithms, structural efficiency, and testing with varying payload endurance and safety requirements.

The contribution of this work lies in the development of a new concept for a transport module designed to carry an unmanned ground vehicle using a VTOL-type UAV, in which the main mounting mechanism is integrated into the transport module itself and detaches together with the payload, rather than remaining on board the aircraft. Based on the proposed concept, a three-dimensional model of the transport module has been developed, featuring a rail-based docking mechanism, alignment via a QR marker, the use of a binocular camera for positioning, and servo-driven locking during transport. In addition, a lightweight module design was proposed and implemented, manufactured using 3D printing with PETG, which enabled the creation of a physical prototype and a preliminary engineering assessment of its integration with UAVs and UAS. To verify the structural integrity of the design, a structural analysis was performed using the finite element method in a linear static formulation, including an assessment of displacements, von Mises stresses, strains, support reactions and the safety factor. The proposed approach offers the following advantages: it reduces the structural load on the UAV after payload separation, it expands the possibilities for modular interaction between aerial and ground-based robotics, it allows the use of additive technologies for rapid prototyping and design modification, it creates a foundation for the further development of cooperative robotics systems, logistics and the autonomous deployment of ground-based platforms.

Limitations of the proposed approach. The size of the UAV to be transported under the current implementation is strictly limited by the dimensions of the transport module and must not exceed 250 mm by 250 mm, whilst the UAV’s mass is limited to up to 2 kg. Furthermore, at this stage, the paper presents the results of numerical modelling, 3D prototyping and preliminary structural assessment, whilst tests of the system under real flight conditions have not yet been conducted. This means that the aerodynamic influence of the module on the UAV’s behaviour, the system’s stability during actual landing, docking and subsequent take-off, as well as the influence of external environmental factors, have not yet been fully experimentally verified.

Future work. In the future, the authors plan to conduct tests of the developed transport module under real flight conditions, including verification of the landing, levelling, docking, securing and transport stages of the unmanned aerial vehicle (UAV). A separate area of further research will be optimising the module’s configuration, including improving its geometry, mass, stiffness and the layout of the mounting elements, with the aim of increasing reliability, reducing structural loads and expanding the system’s operational capabilities. Future research will also examine the module’s operation with various RTS variants, assess the system’s behaviour under varying payload masses, and explore ways to enhance the autonomy of interaction between the airborne and ground-based platforms.

Funding

This research was funded by the Committee of Science of the Ministry of Science and Higher Education of the Republic of Kazakhstan (grant no. BR28712579).

REFERENCES

1 Mykytyn, P., Brzozowski, M., Dyka, Z., and Langendoerfer, P. A Survey on Sensor- and Communication-Based Issues of Autonomous UAVs. Computer Modeling in Engineering & Sciences, 138 (2), 1019–1050 (2024). https://doi.org/10.32604/cmes.2023.029075

2 Ezaki, T., Fujitsuka, K., Imura, N., and Nishinari, K. Drone-based vertical delivery system for high-rise buildings: Multiple drones vs. a single elevator. Communications in Transportation Research, 4, 100130 (2024). https://doi.org/10.1016/j.commtr.2024.100130

3 Moral, K., Ayran, B., and Altug, E. Design and control of a modular multi-drone system with vertical assemble capability. International Journal of Dynamics and Control, 12 (8), 2991–3004 (2023). https://doi.org/10.1007/s40435-024-01404-9

4 Pal, V., Acharya, B.S., Shrivastav, S., Saha, S., Joglekar, A., and Amrutur, B. PUF Based Secure Framework for Hardware and Software Security of Drones. Proceedings of the 2020 Asian Hardware Oriented Security and Trust Symposium (AsianHOST 2020) (2020). https://doi.org/10.1109/AsianHOST51057.2020.9358264

5 Foehn, P., Brescianini, D., Kaufmann, E., Cieslewski, T., Gehrig, M., Muglikar, M., and Scaramuzza, D. AlphaPilot: autonomous drone racing. Autonomous Robots, 46 (1), 307–320 (2022). https://doi.org/10.1007/s10514-021-10011-y

6 Kadri, M.B. Performance Comparison of Computationally Efficient Algorithms for Drone Localization on Embedded Systems. IEEE Access, 13, 121217–121233 (2025). https://doi.org/10.1109/ACCESS.2025.3587882

7 Saska, M., Hert, D., Baca, T., Kratky, V., and Nascimento, T. Formation control of unmanned micro aerial vehicles for straitened environments. Autonomous Robots, 44 (6), 991–1008 (2020). https://doi.org/10.1007/s10514-020-09913-0

8 Argush, G., Holincheck, W., Krynitsky, J., McGuire, B., Scott, D., Tolleson, C., and Behl, M. Explorer51 – Indoor Mapping, Discovery, and Navigation for an Autonomous Mobile Robot. Proceedings of the 2020 Systems and Information Engineering Design Symposium (SIEDS), pp. 1–5 (2020). https://doi.org/10.1109/SIEDS49339.2020.9106581

9 Kusmirek, S., Socha, V., Malich, T., Socha, L., Hylmar, K., and Hanakova, L. Dynamic Flight Tracking: Designing System for Multirotor UAVs With Pixhawk Autopilot Data Verification. IEEE Access, 12, 109806–109821 (2024). https://doi.org/10.1109/ACCESS.2024.3441115

10 Gonçalves, R.S., de Carvalho, T.M., dos Santos, P.B., Souza, F.C., Gallo, C.A., Sudbrack, D.E.T., Trautmann, P.V., Clasen, B.C., and Homma, R.Z. Drone-robot to install aerial marker balls for power lines. Intelligent Service Robotics, 17 (2), 329–343 (2024). https://doi.org/10.1007/s11370-023-00493-3

11 Kim, D., and Oh, P.Y. Human-embodied drone interface for aerial manipulation: advantages and challenges. Intelligent Service Robotics, 17 (3), 375–388 (2024). https://doi.org/10.1007/s11370-024-00535-4

12 Kornatowski, P.M., Bhaskaran, A., Heitz, G.M., Mintchev, S., and Floreano, D. Last-Centimeter Personal Drone Delivery: Field Deployment and User Interaction. IEEE Robotics and Automation Letters, 3 (4), 3813–3820 (2018). https://ieeexplore.ieee.org/document/8411102

13 Thomas, T., Srinivas, S., and Rajendran, C. Collaborative truck multi-drone delivery system considering drone scheduling and en route operations. Annals of Operations Research, 339 (1–2), 693–739 (2024). https://link.springer.com/article/10.1007/s10479-023-05418-y

14 Saqib, S.M., Kumari, N., Mishra, P.P., and Ch, D. Enhancing Search and Rescue Efforts During CSSR Operations Using Drone Mounted Rover System. Proceedings of the 2025 3rd International Conference on Smart Systems for Applications in Electrical Sciences (ICSSES), pp. 1–8 (2025). https://doi.org/10.1109/ICSSES64899.2025.11009369

15 Pepito, J.M., Bolaybolay, J.M., Aleluya, E.R., Alagon, F.J., Clar, S., Paradela, I., Guirnaldo, S., Pao, J., Salaan, C.J., and Bandala, A. Visual Servoing Drone Utilizing Ground Robot Detection Model for UAV-UGV Alignment for Retrieval Operations. IEEE Access, 13, 103866–103879 (2025). https://doi.org/10.1109/ACCESS.2025.3578612

16 Alsamhi, S.H., Ma, O., Ansari, M.S., and Almalki, F.A. Survey on Collaborative Smart Drones and Internet of Things for Improving Smartness of Smart Cities. IEEE Access, 7, 128125–128152 (2019). https://doi.org/10.1109/ACCESS.2019.2934998

17 Shirabayashi, J.V., and Ruiz, L.B. Toward UAV Path Planning Problem Optimization Considering the Internet of Drones. IEEE Access, 11, 136825–136854 (2023). https://doi.org/10.1109/ACCESS.2023.3339227

18 Um, I., Park, S., Kim, H.T., and Kim, H. Configuring RTK-GPS Architecture for System Redundancy in Multi-Drone Operations. IEEE Access, 8, 76228–76242 (2020). https://doi.org/10.1109/ACCESS.2020.2989276

19 Buzzatto, J., and Liarokapis, M. The Omnirotor Platform: A Versatile, Multi-Modal, Coaxial, All-Terrain Vehicle. IEEE Access, 11, 27928–27941 (2023). https://doi.org/10.1109/ACCESS.2023.3258401

20 Qiu, Z., Xia, Y., and Yang, J. The static displacement and the stress analysis of structures with bounded uncertainties using the vertex solution theorem. Computer Methods in Applied Mechanics and Engineering, 196 (49), 4965–4984 (2007). https://doi.org/10.1016/j.cma.2007.06.022

21 Reyes-Osorio, L.A., Dominguez, V.H., Ollervides-Vazquez, E.J., Garza, C., and Garcia-Salazar, O. Structural integrity assessment and optimization of control surfaces in coaxial unmanned aerial vehicles: A case study of a micro coaxial UAV. Mechanics Based Design of Structures and Machines, 53 (2), 943–960 (2025). https://doi.org/10.1080/15397734.2024.2379520

22 Basri, E.I., Mustapha, F., Sultan, M.T.H., Basri, A.A., Abas, M.F., Abdul Majid, M.S., and Ahmad, K.A. Conceptual design and simulation validation based finite element optimisation for tubercle leading edge composite wing of an unmanned aerial vehicle. Journal of Materials Research and Technology, 8 (5), 4374–4386 (2019). https://doi.org/10.1016/j.jmrt.2019.07.049

23 Ahmad, F., Kumar, P., Patil, P.P., and Kumar, V. FEA based frequency analysis of unmanned aerial vehicle (UAV). Materials Today: Proceedings, 46, 10396–10403 (2021). https://doi.org/10.1016/j.matpr.2020.12.740

24 Marta, A., Wandono, F.A., Nurrohmad, A., Ardiansyah, R., Wiranto, I.B., Alfikri, I.R., Prabowo, A.R., and Nugroho, G. Finite element analysis and experimental whiffletree testing of a small UAV composite wing. International Journal of Lightweight Materials and Manufacture, 8 (4), 483–494 (2025). https://doi.org/10.1016/j.ijlmm.2025.03.004

25 Huang, Y., Li, Z., Lv, Z., Qi, W., Duan, C., and Wang, B. A design approach for wire-wound ultra-high pressure vessels in isostatic pressing systems based on constant von Mises stress criterion. International Journal of Pressure Vessels and Piping, 220, 105730 (2026). https://doi.org/10.1016/j.ijpvp.2025.105730

26 Sikorsky Archives. Sikorsky S-64 [Electronic source]. Available at: https://sikorskyarchives.com/home/sikorsky-product-history/helicopter-innovation-era/sikorsky-s-64/ . Accessed: 18 May 2025.

[1]Самигулина З.И.,
PhD, доцент, ORCID ID: 0000-0002-5862-6415,
e-mail: z.samigulina@kbtu.kz
[1*]Мликова К.А.,
магистр, ORCID ID: 0009-0009-5931-7065,
*e-mail: missmlikovakristina@gmail.com
[1]Толенгутов Р.Р.,
магистр, ORCID ID: 0009-0000-3210-7126,
e-mail: r.tolengutov@kbtu.kz
[1]Бутакова Д.А.,
магистр, ORCID ID: 0009-0006-8151-4928,
e-mail: d.butakova@kbtu.kz
[1]Нахимов Ә.Ж.
магистр, ORCID ID: 0009-0009-0092-8208,
e-mail: a.nakhimov@kbtu.kz

[1]Қазақстан-Британ техникалық университеті, Алматы қ, Қазақстан

ТІК ҰШЫП КӨТЕРІЛУ ЖӘНЕ ҚОНУ МҮМКІНДІГІ БАР ҰШҚЫШСЫЗ ӘУЕ АППАРАТЫ АРҚЫЛЫ ҰШҚЫШСЫЗ ЖЕРҮСТІ ПЛАТФОРМАСЫН ТАСЫМАЛДАУҒА АРНАЛҒАН ЖАҢА КӨЛІКТІК МОДУЛЬ ТҰЖЫРЫМДАМАСЫ

Аңдатпа

Мақалада ұшқышсыз жерүсті платформасымен бірлесіп жұмыс істеуге арналған, қанатты, тік ұшып көтерілу және қону мүмкіндігі бар ұшқышсыз әуе аппаратына арналған модульдік түйістіру станциясының

жобалануы мен сынақ нәтижелері қарастырылады. Ұсынылған шешім бағыттаушы рельстік жүйе мен бинокулярлы камера модулі арқылы quick response маркері негізінде жүзеге асырылатын көру жүйесінің көмегімен пайдалы жүкті автономды түрде бекіту және ажырату мүмкіндігін қамтамасыз етеді. Ұсынылып отырған модульдің басты ғылыми-тәжірибелік жаңалығы оның негізгі бекіту механизмі жүк түсірілгеннен кейін дрон құрылымында сақталмай, керісінше, көліктік модульдің ажырамас бөлігі ретінде орындалып, сол модульмен бірге ажыратылатындығында. Бұл тәсіл негізгі бекіту торабы әуе платформасының өзінде қалатын дәстүрлі шешімдерден ерекшеленіп, жүкті жеткізу және орналастыру сценарийлерінің икемділігін арттырады. Пайдалы жүкке арналған құрастырма Autodesk Fusion 360 бағдарламалық ортасында жобаланып, Bambu Lab X1 Carbon 3D-принтерінде қабаттап балқытып қалыптастыру технологиясы арқылы полиэтилентерефталат-гликоль типті пластик материалынан дайындалды. Модуль конструкциясының жұмыс жүктемелері кезіндегі орын ауыстыруы, эквиваленттік кернеуі, салыстырмалы деформациясы және реакция күштері соңғы элементтер әдісі негізінде құрылымдық талдау арқылы бағаланды. Жүргізілген кеңейтілген модельдеу нәтижелері ұсынылған конструкцияның механикалық беріктік пен қорғаныс талаптарына сәйкес келетінін көрсетеді, алайда бұл қорытындыларды толық растау үшін қосымша ұшу сынақтарын орындау қажет. Ұсынылған жүйе ұшқышсыз жерүсті платформасын әуе кеңістігінен түсіру үшін де, сондай-ақ дронның қозғалыстағы жерүсті платформасына қонуы үшін де қолданылуы мүмкін, бұл оның робототехника және автоматтандыру салаларындағы әмбебаптығын дәлелдейді.

Түйін сөздер: автономды робототехника, дрон, VTOL, UGV, модульдік түйістіру жүйесі, пайдалы жүк механизмі, 3D басып шығару, PETG, жеткізу.

[1]Самигулина З.И.,
PhD, доцент, ORCID ID: 0000-0002-5862-6415,
e-mail: z.samigulina@kbtu.kz
[1*]Мликова К.А.,
Магистр, ORCID ID: 0009-0009-5931-7065,
*e-mail: missmlikovakristina@gmail.com
[1]Толенгутов Р.Р.,
Магистр, ORCID ID: 0009-0000-3210-7126,
e-mail: r.tolengutov@kbtu.kz
[1]Бутакова Д.А.,
Магистр, ORCID ID: 0009-0006-8151-4928,
e-mail: d.butakova@kbtu.kz
[1]Нахимов Ә.Ж.
Магистр, ORCID ID: 0009-0009-0092-8208,
e-mail: a.nakhimov@kbtu.kz

[1]Казахстанско-Британский технический университет, г. Алматы, Казахстан

НОВАЯ КОНЦЕПЦИЯ ТРАНСПОРТНОГО МОДУЛЯ ДЛЯ ПЕРЕВОЗКИ БЕСПИЛОТНЫХ НАЗЕМНЫХ АППАРАТОВ С ПОМОЩЬЮ БЕСПИЛОТНЫХ ЛЕТАТЕЛЬНЫХ АППАРАТОВ С ВЕРТИКАЛЬНЫМ ВЗЛЕТОМ И ПОСАДКОЙ

Аннотация

В данной статье описываются проектирование и испытания модульной стыковочной станции для беспилотного летательного аппарата с вертикальным взлетом и посадкой, предназначенного для использования совместно с беспилотным наземным транспортным средством. Данное решение обеспечивает автономное присоединение и отсоединение полезных нагрузок посредством управляемой рельсовой системы, а также визуальную стыковку с помощью маркера quick response с использованием модуля бинокулярной камеры. Новизна предлагаемого модуля заключается в том, что основной крепежный механизм не остается интегрированным с дроном после развертывания; вместо этого он спроектирован как неотъемлемая часть самого транспортного модуля и отсоединяется вместе с ним. Такой подход отличает систему от традиционных решений, в которых основная крепежная конструкция остается на борту воздушной платформы и расши-

ряет гибкость сценариев доставки и развертывания полезных нагрузок. Узел полезной нагрузки был спроектирован в Autodesk Fusion 360 и изготовлен из пластика типа полиэтилентерефталат-гликоль с помощью 3D-печати методом наплавления на принтере Bambu Lab X1 Carbon. Для оценки смещения, напряжений, деформаций и сил реакции конструкции модуля под рабочими нагрузками был проведен структурный анализ с использованием метода конечных элементов. Результаты углубленного моделирования показывают, что конструкция соответствует требованиям механической защиты, дополнительные подтверждения будут получены в ходе летных испытаний. Система может быть использована для развертывания беспилотного летательного аппарата с воздуха или для посадки дрона на мобильные наземные транспортные средства, что демонстрирует ее универсальность в области робототехники и автоматизации.

Ключевые слова: автономная робототехника, дроны, БПЛА типа VTOL, БПТ, модульная стыковочная система, механизм полезной нагрузки, 3D-печать, PETG, доставка.

UDC 004.912
IRSTI 16.31.21

https://doi.org/10.55452/1998-6688-2026-23-3-233-242

[1]*Aitim A.K.,
PhD, associate professor, ORCID: 0000-0003-2982-214X,
*e-mail: a.aitim@iitu.edu.kz

[1]International Information Technology University, Almaty, Kazakhstan

MORPHOLOGICAL DISAMBIGUATION FOR THE KAZAKH LANGUAGE USING TRANSFORMER-BASED MODELS

Abstract

Morphological ambiguity constitutes a significant challenge for natural language processing in agglutinative languages, as a single word form might include many grammatical categories. The Kazakh language features productive suffixation, vowel harmony, and intricate morphophonological patterns, which considerably hinder automatic morphological analysis. This work presents a transformer-based methodology for morphological disambiguation in Kazakh texts, with the objective of identifying the appropriate morphological interpretation of word forms within context. A contextual language model tailored for Kazakh is refined for token-level morphological tagging utilizing a manually validated annotated corpus of news articles. The suggested method utilizes self-attention mechanisms to capture long-range contextual dependencies that are challenging to represent with conventional rule-based or recurrent neural techniques. The experimental assessment reveals that the transformer-based model attains superior accuracy and F1-score relative to rule-based morphological analyzers and BiLSTM-based benchmarks. The findings demonstrate that contextualized embeddings significantly enhance the resolution of morphological ambiguity, especially with homonymous suffixes and infrequent grammatical structures. The results validate the efficacy of transformer topologies for low-resource agglutinative languages and establish a feasible basis for incorporating morphology-aware models into comprehensive Kazakh natural language processing frameworks.

Keywords: Kazakh language, morphological disambiguation, transformer-based models, natural language processing, agglutinative languages.

Received April 4, 2026; revised June 2, 2026; accepted August 27, 2026.

Introduction

Deep neural architectures and large-scale pretrained language models have been the main drivers of recent progress in natural language processing (NLP). Transformer-based models, especially, have shown the best performance on a wide range of text interpretation and sequence labeling tasks. But these improvements have mostly helped languages with a lot of resources, and many morphologically rich and agglutinative languages are still not well understood. Kazakh is one of these languages, and it poses a number of basic problems for robotic text processing. Kazakh has productive agglutination, a lot of suffixation, vowel harmony, and morphophonological alternations [1]. Because of these features, there are a lot of different surface word forms, which makes it hard to tell what they mean. One word form can have more than one grammatical meaning, depending on the part of speech, case, number, tense, or possessive markers [2]. To clear up this ambiguity, you need more than just the word level. This makes morphological disambiguation a difficult computational operation.

Morphological disambiguation is an important part of the whole NLP pipeline because mistakes at this stage can cause problems in later steps like dependency parsing, named entity identification, information extraction, and question answering [3]. To make strong NLP systems for the Kazakh language, it's important to make morphological disambiguation more accurate. Most of the time, the methods used to process Kazakh morphology have been based on rules or finite-state analyzers [4]. These systems have a lot of coverage and are easy to understand, but they can't always choose the

right morphological interpretation when things are unclear [5]. In addition, rule-based systems need to be manually updated all the time and are hard to adapt to new areas or changing language use.

Neural models, encompassing recurrent architectures like BiLSTM, have been utilized for morphological tagging and disambiguation tasks with varying degrees of effectiveness [6]. Still, recurrent models can't handle long-range dependencies and global sentence-level context very well. Transformer-based designs overcome these constraints by employing self-attention techniques, facilitating enhanced contextual representations and improved ambiguity resolution [7]. Even though transformer models are becoming more popular in low-resource NLP, not enough research has been done on how they might be used to disambiguate Kazakh morphology [8]. This research seeks to address this deficiency by examining a transformer-based methodology for contextual morphological disambiguation in Kazakh literature. The suggested solution uses a pretrained contextual language model for token-level morphological tagging and tests how well it works on a human verified annotated corpus. The experimental findings indicate that transformer-based models offer a scalable and efficient approach to addressing morphological ambiguity in agglutinative low-resource languages.

The main contributions of this paper are as follows:

This paper presents a transformer-based method for morphological disambiguation in the Kazakh language, which allows for effective modeling of contextual information in agglutinative text.

A manually checked annotated Kazakh corpus and a consistent morphological tagging scheme to use for training and testing disambiguation models.

A comparative assessment against rule-based and BiLSTM-based benchmarks is performed, revealing substantial enhancements in accuracy and F1-score.

An examination of prevalent disambiguation errors is presented, emphasizing the practical utility of the suggested technique in Kazakh NLP pipelines.

Morphologically rich and agglutinative languages generate significant ambiguity at the lexical level, as a single surface form may represent numerous analyses [9]. Early influential research on Turkic morphology illustrated that effective NLP systems frequently necessitate morphological disambiguation rather than merely producing all potential parses; a quintessential example is the statistical tagger for Turkish that amalgamates morphological analysis with disambiguation choices. This led to following pipelines treating morphological analysis, POS tagging, and syntactic processing as a tightly coupled sequence labeling problem instead than separate modules.

A second important area of research focused on error-driven rule learning for tagging. It showed that small sets of learnt transformations can be as good as purely statistical tagging, especially when there isn't much data and linguistic patterns can be turned into rules [10]. The transformation-based paradigm continues to be applicable in low-resource environments and for developing interpretable correction layers above statistical taggers.

For Kazakh, multiple studies examined the equilibrium between linguistic limitations and data-driven ranking. A representative data-driven method creates candidate segmentations and ranks them based on probabilistic assumptions [11]. This is meant to help with practical morphological analysis of Kazakh text [12]. Even though these methods make it less necessary to use a lot of hand-crafted rules, they still need good candidate generation and representative corpora. Coverage gaps, like compounding, orthographic variants, and unusual derivation chains, can still hurt performance [13]. Hybrid systems are very common in Kazakh NLP toolbuilding. A good example is the hybrid morphological disambiguation tool, which was made as a free/open-source resource and is meant to be used in real life [14]. It combines linguistic parts with statistical selection. This kind of system is crucial because it makes linguistic knowledge useful in real-world situations by adding a trainable disambiguation layer.

A complementary tradition utilizes two-level morphology (lexical versus surface representation) and finite-state methodologies to explicitly express morphophonology and morphotactics. The two-level description for modern Kazakh includes an implemented analyzer and a test dataset that has been manually disambiguated. This shows how important it is for rules to be clear and easy to add

to. Two-level formalisms can provide robust generalization for regular alternations (e.g., harmony-driven variations); however, they necessitate continuous linguistic engineering (lexicon expansion, exception management, coverage maintenance).

In addition to analyzers and disambiguators, the lack of standardized annotated resources is holding back progress in Kazakh NLP. The Universal Dependencies (UD) project has been the main source for multilingual comparison and transfer since it provides standard POS/morphology and dependency annotation guidelines across languages. The UD v1 summary makes design principles official and lists multilingual treebank releases that made it possible to compare evaluations across languages. In this environment, the UD Kazakh KTB treebank is still rather tiny (around 1,000 sentences) and includes texts from many different genres. This impacts both the statistical power and the domain representativeness of recent news content. Kazakh UD resources also show problems with Turkic annotation in general. Work on evaluating UD Turkic treebanks talks about problems that still need to be solved, like how to tokenize words, how to handle complicated predicates, and how to choose between morphology and syntax [15]. These are problems that directly affect how well the evaluation works and how easy it is to move models between Turkic languages. These results suggest that enhancements in Kazakh NLP necessitate not just more robust models but also uniform annotation, segmentation standards, and resource scalability.

Modern Kazakh tagging and disambiguation are becoming more like sequence labeling and structured prediction methods. Conditional Random Fields (CRFs) are still a common structured layer for making sure that sequences are consistent, especially when local decisions (per-token labels) have to follow global rules. Neural encoders like BiLSTMs and CRF decoding work well together to provide a strong foundation for tagging tasks. They give you contextual representations while still keeping structured inference at output time. But supervised neural taggers usually need a lot of data, which is a big problem for Kazakh because there aren’t many large, high-quality labeled corpora available.

Materials and methods

The dataset is made up of Kazakh-language news stories taken from publicly available internet media sources in a number of fields, such as politics, economics, technology, and society. After automated retrieval, boilerplate removal is done to get the primary material of the article and leave out navigation blocks, ads, and repeated parts. A language identification filter is used to maintain only Kazakh texts and cut down on noise from other languages. Preprocessing includes (i) breaking up sentences, (ii) breaking up words, and (iii) making everything the same. Tokenization follows Kazakh spelling rules, such as how to handle punctuation and hyphenated words. Normalization makes sure that Unicode encoding is always the same and that there is always the same amount of whitespace. In Table 1 shows the size of the dataset and the 80/10/10 split. It tells you how many news articles there are, how many sentences and word-level tokens there are after cleaning, an estimated vocabulary size (unique word forms), the approximate tag-set size for composite morphology labels, and the sizes of the train, validation, and test subsets calculated at the sentence level to avoid leakage.

Table 1 – Key variables used in the study

Item	Value
Total documents	3,500–3,800
Total sentences	77,000–83,600
Total tokens (word-level)	1,750,000–1,900,000
Unique word types (estimated via Heaps’ law)	278,479–292,565
Tag set size (composite tags)	~200–240
Train / Validation / Test (sentences)	61,600–66,880 / 7,700–8,360 / 7,700–8,360
Train / Validation / Test (tokens)	1,400,000–1,520,000 / 175,000–190,000 / 175,000–190,000

A single gold morphological label is given to each token, which is shown as a composite tag (1):

$$y_i = (POS_i, f_i^{(1)}, \dots, f_i^{(K)},) \quad (1)$$

Where POS_i is the part-of-speech class and $f_i^{(k)}$ are grammatical features (e.g., number, case, tense, mood, possession).

The annotation process is semi-automatic: a rule-based analyzer makes candidate analyses, and the right analysis is chosen by manually checking the sentence context. The last dataset is saved in a format that labels sequences at the token level.

Let a sentence be a token sequence $x = (x_1, \dots, x_n)$. After subword tokenization, the transformer encoder outputs contextual representations (2):

$$H = (h_1, \dots, h_m), \qquad h_j \in \mathbb{R}^d, \quad (2)$$

where m is the number of subword tokens and d is the hidden size.

To get word-level representations, subword vectors are combined for each word x_i with a subword index set S_i. Mean pooling is a typical way to pool data (3):

$$\tilde{h_i} = \frac{1}{|S(i)|} \sum_{j \in S(i)} h_j. \quad (3)$$

A token-level classifier predicts a morphological tag distribution (4):

$$p(y_i = c \mid x) = softmax(W\tilde{h_i} + b)_c, \quad (4)$$

where $W \in \mathbb{R}^{|C| \times d}, b \in \mathbb{R}^{|C|}$, and $|C|$ is the number of composite tags.

By reducing token-level cross-entropy, the model is made better (5):

$$\mathcal{L}(\theta) = -\sum_{i=1}^{n} logp(y_i^* | x; \theta), \quad (5)$$

where y_i^* is the gold tag and θ denotes trainable parameters.

By reducing token-level cross-entropy, the model is made better (5):

$$\mathcal{L}(\theta) = -\sum_{i=1}^{n} logp(y_i^* | x; \theta), \quad (5)$$

where y_i^* is the gold tag and denotes trainable parameters.

Dropout is used for regularization, while early stopping based on validation loss is used for training.

This part defined the morphological disambiguation task as supervised sequence labeling and laid out the whole experimental process: collecting and cleaning 3,500 to 3,800 Kazakh news articles, deterministic preprocessing (segmentation, tokenization, normalization), semi-automatic morphological annotation with manual verification, and splitting the data into 80/10/10 sentence-level groups to keep it from leaking. A transformer-based tagging model was built, with explicit subword-to-word alignment and an optional CRF layer for structured decoding. Training was conducted using cross-entropy (or CRF negative log-likelihood). Finally, baseline systems (rule-based and BiLSTM-based) and evaluation metrics (accuracy and macro-F1) were set up to make sure that the comparison was fair and could be repeated.

Results

This section presents the empirical assessment of the suggested transformer-based methodology for Kazakh morphological disambiguation on the reserved test set. The examination concentrates

on overall efficacy and practical resilience. To show the main differences in performance between the proposed models and the chosen baselines under the same experimental conditions, token-level Accuracy and Macro-F1 are shown first. Next, following how structured decoding (CRF) helps to measure advances in label consistency. We break down the results even more by linguistic categories using POS-wise and feature-level projections. This helps us figure out which morphological phenomena gain the most from contextual modeling and which ones are still hard to predict. Lastly, more tests look at how training works, how stable the domain is across different news subjects, how strong it is when it comes to sentence length and out-of-vocabulary tokens, and how the long-tailed distribution of composite tags affects things. These studies give a full picture of how the model works beyond just its overall scores, and they show that adding the suggested disambiguation module to larger Kazakh NLP pipelines is possible.

Table 2 shows the overall accuracy and macro-F1 scores for composite morphological tags on the test set. Neural models are far better than the rule-based baseline, and tagging based on transformers is the best overall.

Table 2 – Overall performance

Model	Accuracy (%)	Macro-F1 (%)
Rule-based + heuristics	86.2	83.4
BiLSTM baseline	90.4	88.7
Transformer + Softmax	93.2	92.0
Transformer + CRF	93.8	92.6

The learning curves in Figure 1 illustrate that things are getting better at a steady rate. The loss for both training and validation drops quickly over the first 3 to 5 epochs, which means that the model is quickly learning the main patterns. After about epoch 6–8, the validation loss levels off and goes up a little, but the training loss keeps going down. This means that the model is slightly overfitting. So, the best generalization is around the lowest validation loss (around epoch 8), which is a good place to terminate early.

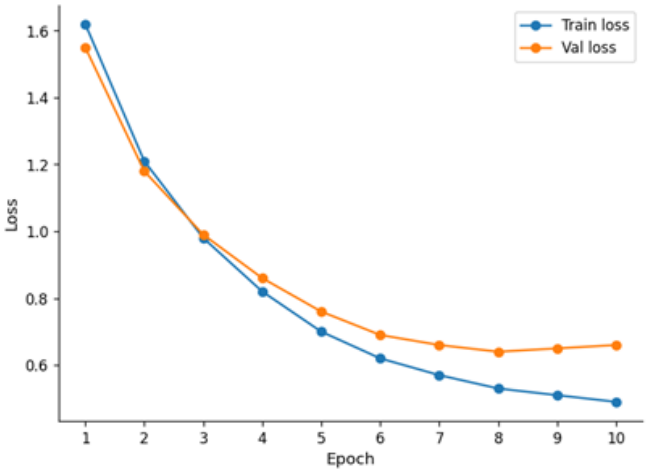


Figure 1 – Training and validation loss per epoch

The accuracy curves show that the model is learning well and can generalize well. In the first 3 to 5 epochs, the accuracy of training and validation goes up quickly, then levels out. Validation accuracy reaches its highest point around epoch 8 (around 92.5%) and then goes down a little bit. On the other hand, training accuracy keeps going up, which is what happens when the model starts to overfit. The optimal balance between fit and generalization is found at an early stopping point around epoch 8 in Figure 2.

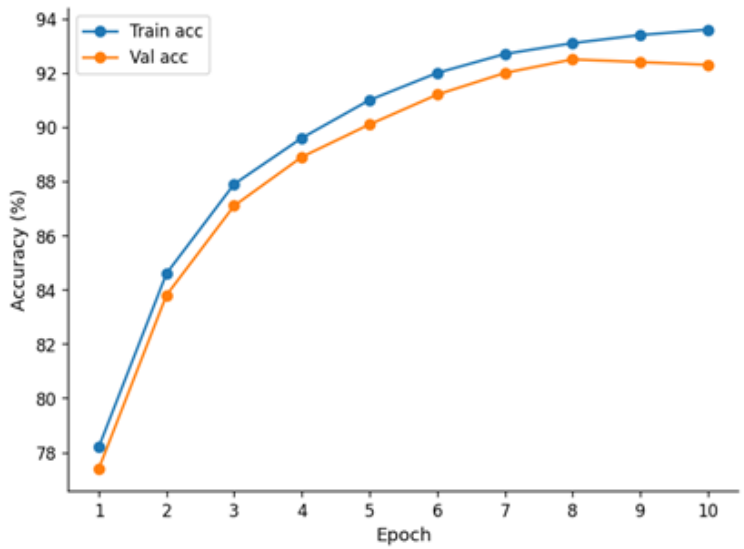


Figure 2 – Training and validation accuracy per epoch

The Macro-F1 curves are getting better and better and are coming together. In the first few epochs, both training and validation Macro-F1 go up quickly, but after epoch 6, they stay the same. Validation Macro-F1 achieves its highest point at epoch 8 (~92.4%) and then goes down a little. Training Macro-F1, on the other hand, keeps going up, which shows that the model is slightly overfitting beyond the best point. The quitting early at epoch ~8 is the best way to get the best generalization.

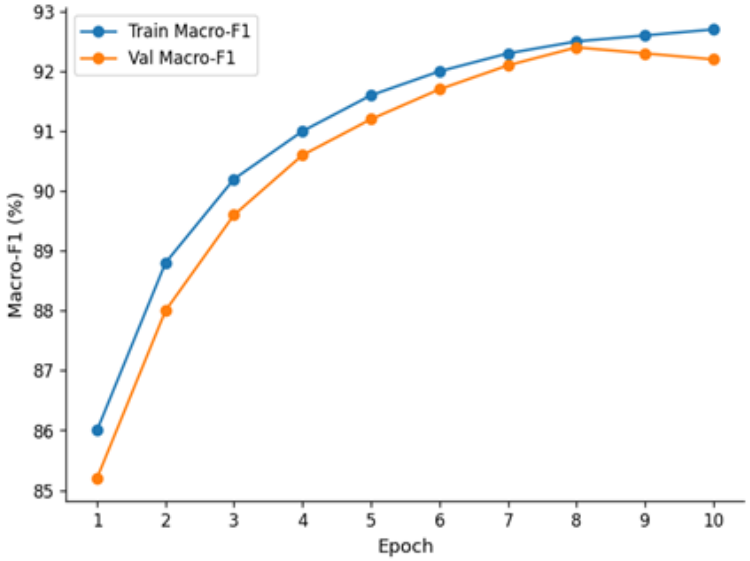


Figure 3 – Macro-F1 per epoch

Table 3 compares decoding and subword-to-word pooling, mean pooling always works better, and CRF makes label consistency better across all pooling options.

The experimental results demonstrate that transformer-based morphological disambiguation achieves the strongest performance on the held-out Kazakh news test set, substantially outperforming both the rule-based baseline and the BiLSTM sequence tagger in terms of token-level Accuracy and Macro-F1 over composite tags. Adding a CRF decoding layer makes things even better by

making sure that the labels are consistent over the whole sequence. In-depth studies demonstrate that performance is best for categories that are frequent and structurally stable (like nouns). On the other hand, more complicated phenomena, especially verb-related traits and possessive/person markers, are still the leading causes of residual errors. Learning curves confirm stable convergence with mild overfitting after the optimal epoch, supporting early stopping around the validation peak. In general, the results show that contextual transformer representations, along with structured decoding, provide a strong and scalable way to deal with Kazakh morphological ambiguity in real-world NLP pipelines.

Table 3 – Ablation study (decoder and pooling).

Setting	Accuracy (%)	Macro-F1 (%)
Transformer + Softmax (mean pooling)	93.2	92.0
Transformer + Softmax (first-subword pooling)	93.0	91.7
Transformer + CRF (mean pooling)	93.8	92.6
Transformer + CRF (first-subword pooling)	93.6	92.3

Discussion

The findings validate that contextual transformer encoders are exceptionally efficient for morphological disambiguation in Kazakh, a morphologically intricate agglutinative language characterized by surface forms that frequently allow for numerous interpretations. The steady improvement over both a rule-based baseline and a BiLSTM tagger shows that the main benefit comes from better contextualization, not just a bigger model. Self-attention helps the model put together information from different parts of the phrase, like agreement patterns, grammatical roles, and discourse-level signals. These are hard to encode with hand-crafted heuristics and only partially captured by recurrent architectures. One important thing to note is that organized decoding has a good but mild effect. The CRF layer consistently improves Macro-F1 by making labels more consistent and making it less likely that tags will change in ways that don't make sense. This is especially important for composite tags that include POS and other grammatical traits. In these cases, local decisions may make sense on their own but not when looked at as a whole. The ablation investigation indicates that CRF advantages are supplementary to transformer representations rather than replacing them, corroborating the notion that the encoder delivers robust contextual token representations while the decoder enhances sequence-level coherence.

The error breakdown shows the common problems that still exist in Kazakh morphology. The fact that verb tags generally store numerous interacting qualities makes the class more fragmented and sparse. This is why nouns perform better than verbs. Possessive and person markers, as well as other case differences, continue to provide difficulties owing to homonymous suffix chains and long-tail tag distributions. The long-tail coverage analysis shows that a small number of common tags make up a major part of the tokens, whereas a lot of rare composite labels have a big effect on Macro-F1 and on the confusions that were seen. This backs up the choice of Macro-F1 as the main metric and shows that to get more gains, we will need to model unusual feature combinations better instead of only improving frequent tags. Robustness assessments provide us more information about the conditions in which something is deployed. The model learns general morphosyntactic cues instead of topic-specific artifacts since the news domains are stable. This is good for scalable NLP pipelines. On the other hand, the fact that lengthier sentences and out-of-vocabulary tokens make performance worse shows that the quality of morphological disambiguation is affected by new words and more complicated syntax. This pattern shows two practical ways to make things better: (i) making subword modeling and lexicon coverage stronger, and (ii) making the training contexts for long-range dependencies more varied.

The training dynamics reinforce the dependability of the proposed methodology. The loss and accuracy curves reveal that learning happens quickly at first, then levels off, and finally there

is some overfitting after the validation optimum. This shows that early halting is enough to keep generalization stable without too much regularization. Still, slight improvements may be possible through more systematic tuning of hyperparameters, data augmentation techniques, or curriculum-style sampling that focuses on tags that aren't used as much during fine-tuning. It is important to notice a few limitations. The evaluation is conducted on a news-domain dataset; performance may vary for conversational text, social media, or legal documents, where orthography, code-switching, and named entities are more prevalent. Second, composite tag prediction combines several attributes into one label, which makes the number of classes go up and the sparsity go up. Multi-task formulations that forecast POS and morphological variables independently (utilizing shared encoders) may enhance generalization to infrequent combinations. Third, this research only looks at token-level metrics. To figure out the overall advantages, we need to look at how they affect parsing or information extraction downstream.

The results indicate that transformer-based disambiguation can function as a robust default element for Kazakh NLP. Future work will naturally focus on (i) enhancing annotated resources and improving long-tail coverage, (ii) implementing feature-factorized or multi-task training to mitigate label sparsity, (iii) explicitly addressing OOV and named-entity morphology, and (iv) integrating with downstream syntactic and semantic modules to validate pipeline-level improvements.

Conclusion

This research introduced a transformer-based methodology for morphological disambiguation in the Kazakh language, structured as supervised sequence labeling applied to composite morphological tags. The proposed model demonstrated robust token-level performance utilizing an extensive news-domain corpus and a manually validated annotation procedure, consistently surpassing both rule-based heuristics and a BiLSTM baseline. Adding a CRF decoding layer made the results much better by making the label consistency at the sequence level better. This shows that structured prediction is useful for complex morphological tagsets.

In-depth studies found that contextual modeling works best for categories that are used often and have stable structures. On the other hand, residual errors are mostly found in long-tailed composite tags and feature combinations that include verb morphology and possessive/person markers. Robustness tests showed that performance was steady across news domains, but it was worse for longer sentences and words that weren't in the lexicon. This showed where improvements could be made in practice.

Future endeavors will concentrate on broadening annotated resources beyond the news sector, enhancing long-tail coverage via targeted sampling or multi-task feature-factorized learning, and incorporating the disambiguation module into subsequent pipelines, including dependency parsing and information extraction, to measure end-to-end improvements in practical applications.

Acknowledgment

This research was funded by the Grant No. AP32522233 "QNLPAI an open-source scientific system for intelligent processing of Kazakh-language texts" of Ministry of Science and Higher Education of the Republic of Kazakhstan.

REFERENCES

1 Bach, M.P., Topalovic, A., Krstic, Z., and Ivec, A. Predictive maintenance in industry 4.0 for the SMEs: A decision support system case study using open-source software. Designs, 7, 98 (2023). https://doi.org/10.3390/designs7040098

2 Aitim, A., and Abdulla, M. Data Processing and Analysing Techniques in UX Research. Procedia Computer Science, 251, 591–596 (2024). https://doi.org/10.1016/j.procs.2024.11.154

3 Aitim, A., Sattarkhuzhayeva, D., and Khairullayeva, A. Development of a hybrid CNN-RNN model for enhanced recognition of dynamic gestures in Kazakh Sign Language. Eastern-European Journal of Enterprise Technologies, 2 (2 (134)), 58–67 (2025). https://doi.org/10.15587/1729-4061.2025.315834

4 Aitim, A. Building a high-quality annotated corpus for Kazakh NLP: a pipeline approach. Bulletin KazUTB, 4 (29) (2025). https://doi.org/10.58805/kazutb.v.4.29-1092

5 Aitim, A., and Satybaldiyeva, R. A comparison of Kazakh language processing models for improving semantic search results. Eastern-European Journal of Enterprise Technologies, 1 (2 (133)), 66–75 (2025). https://doi.org/10.15587/1729-4061.2025.315954

6 Aitim, A. Developing methods for automatic processing systems of Kazakh language. KazATC Bulletin, 133 (4), 254–265 (2024). https://doi.org/10.52167/1609-1817-2024-133-4-254-265

7 QNLP – Full Kazakh NLP Suite GitHub repository. https://github.com/Aigerimhub/qnlp

8 Ali, A., and Gravino, C. Improving software effort estimation using bio-inspired algorithms to select relevant features: an empirical study. Science of Computer Programming, 205, 102621 (2021). https://doi.org/10.1016/j.scico.2021.102621

9 Singh, K., and Gupta, P. Explainable artificial intelligence for software effort estimation: a survey and future directions. Information and Software Technology, 140, 106748 (2021). https://doi.org/10.1016/j.infsof.2021.106748

10 Khan, J.A., and Khan, S.U.R. Empirical investigation about the factors affecting the cost estimation in global software development context. IEEE Access, 9, 22274–22294 (2021). https://doi.org/10.1109/ACCESS.2021.3055858

11 Srivastava, D.K., Sharma, A.K., and Choudhary, D. Software development effort estimation using machine learning techniques: multi-linear regression versus random forest. 2021 International Conference on Computing, Communication and Green Engineering (CCGE) (2021), pp. 1–5. https://doi.org/10.1109/CCGE50943.2021.9776394

12 Alsaadi, M., and Saeedi, K. Agile effort estimation based on user stories: a systematic literature review. Artificial Intelligence Review, 55 (7), 5485–5516 (2022). https://doi.org/10.1007/s10462-021-10132-x

13 Matsubara, P.G.F. SEXTAMT: a systematic map to navigate the wide seas of factors affecting expert judgment software estimates. Journal of Systems and Software, 185, 111148 (2022). https://doi.org/10.1016/j.jss.2021.111148

14 Fávero, E.M.D.B. SE3M: a model for software effort estimation using pre-trained embedding models. Information and Software Technology, 147, 106886 (2022). https://doi.org/10.1016/j.infsof.2022.106886

15 Li, X., Zhao, H., and Yu, M. Hybrid deep learning models for software cost prediction using CNN and LSTM. Journal of Systems and Software, 188, 111282 (2022). https://doi.org/10.1016/j.jss.2022.111282

16 Rosa, C.C., and Jardine, D.A. Data-driven agile software cost estimation models for DHS and DoD. Journal of Systems and Software, 203, 111739 (2023). https://doi.org/10.1016/j.jss.2023.111739

[1*]Әйтім Ә.Қ.,
PhD, қауымдастырылған профессор, ORCID:0000-0003-2982-214X,
*e-mail: a.aitim@iitu.edu.kz

[1]Халықаралық ақпараттық технологиялар университеті, Алматы қ., Қазақстан

ТРАНСФОРМЕР-НЕГІЗДІ МОДЕЛЬДЕРДІ ҚОЛДАНУ АРҚЫЛЫ ҚАЗАҚ ТІЛІНДЕГІ МОРФОЛОГИЯЛЫҚ ДИЗАМБИГУАЦИЯ

Аңдатпа

Агглютинативті тілдерде морфологиялық көпмәнділік табиғи тілді өңдеу үшін елеулі қиындық туғызады, өйткені бір ғана сөз тұлғасы бірнеше грамматикалық категорияны қамтуы мүмкін. Қазақ тілі өнімді жұрнақ-жалғау жүйесімен, дауыстылар үндестігімен және күрделі морфофонологиялық үлгілермен сипатталады, бұл автоматты морфологиялық талдауды айтарлықтай қиындатады. Бұл жұмыста қазақ мәтіндеріндегі морфологиялық дизамбигуацияға арналған трансформер-негізді әдістеме ұсынылады; мақсат – сөз тұлғасының контекст ішіндегі дұрыс морфологиялық интерпретациясын анықтау. Қазақ

тіліне бейімделген контекстік тілдік модель қолмен тексерілген жаңалық мәтіндері корпусына сүйене отырып, токен деңгейіндегі морфологиялық таңбалау үшін қайта бапталады. Ұсынылған тәсіл өзіндік-зейін механизмдері арқылы дәстүрлі ереже-негізді немесе рекуррентті нейрондық әдістермен көрсету қиын болатын ұзақ қашықтықтағы контекстік тәуелділіктерді ұстауға мүмкіндік береді. Эксперименттік бағалау трансформер-негізді модельдің ереже-негізді морфологиялық талдағыштар мен BiLSTM-негізді базалық модельдерге қарағанда жоғары дәлдік пен F1-көрсеткішіне қол жеткізетінін көрсетеді. Нәтижелер контексттендірілген эмбеддингтердің морфологиялық көпмәнділікті шешуді айтарлықтай жақсартатынын, әсіресе омоним жұрнақтар мен сирек грамматикалық құрылымдар жағдайында тиімді екенін дәлелдейді. Алынған қорытындылар трансформер архитектураларының ресурсы аз агглютинативті тілдер үшін тиімді екенін растап, морфологияға сезімтал модельдерді қазақ тілін өңдеудің кешенді жүйелеріне енгізуге негіз қалайды.

Түйін сөздер: қазақ тілі, морфологиялық дизамбигуация, трансформер-негізді модельдер, табиғи тілді өңдеу, агглютинативті тілдер.

[1*]Әйтім Ә.Қ.,
PhD, ассоциированный профессор, ORCID: 0000-0003-2982-214X,
*e-mail: a.aitim@iitu.edu.kz

[1]Международный университет информационных технологий, г. Алматы, Казахстан

МОРФОЛОГИЧЕСКАЯ ДИЗАМБИГУАЦИЯ КАЗАХСКОГО ЯЗЫКА С ИСПОЛЬЗОВАНИЕМ ТРАНСФОРМЕРНЫХ МОДЕЛЕЙ

Аннотация

Морфологическая неоднозначность представляет собой значимую проблему для обработки естественного языка в агглютинативных языках, поскольку одна и та же словоформа может включать множество грамматических категорий. Казахский язык характеризуется продуктивной суффиксацией, сингармонизмом и сложными морфофонологическими закономерностями, что существенно затрудняет автоматический морфологический анализ. В данной работе представлена трансформер-ориентированная методология морфологической дизамбигуации казахских текстов, направленная на выбор корректной морфологической интерпретации словоформы в контексте. Контекстная языковая модель, адаптированная для казахского языка, дообучается для токен-уровневой морфологической разметки с использованием вручную верифицированного аннотированного корпуса новостных статей. Предложенный метод применяет механизмы самовнимания (self-attention) для захвата дальних контекстных зависимостей, которые сложно эффективно представить традиционными правилами или рекуррентными нейронными подходами. Экспериментальная оценка показывает, что трансформерная модель достигает более высокой точности и F1-меры по сравнению с правилами морфологическими анализаторами и базовыми моделями на основе BiLSTM. Результаты демонстрируют, что контекстуализированные эмбеддинги заметно улучшают разрешение морфологической неоднозначности, особенно в случаях омонимичных суффиксов и редких грамматических структур. Полученные выводы подтверждают эффективность трансформерных архитектур для низкоресурсных агглютинативных языков и формируют практическую основу для интеграции морфологически чувствительных моделей в комплексные системы обработки казахского языка.

Ключевые слова: казахский язык, морфологическая дизамбигуация, трансформерные модели, обработка естественного языка, агглютинативные языки.

УДК 004.85:373.3/.5:37.015.3
МРНТИ 28.23.37

https://doi.org/10.55452/1998-6688-2026-23-3-243-254

[1]Утебаев К.А.,
магистрант, ORCID ID: 0009-0004-3032-5049,
e-mail: utebayevkuat@gmail.com
[2]*Молдагулова А.Н.,
к.ф.-м.н., профессор, ORCID ID: 0000-0002-1596-561X,
*e-mail: a.moldagulova@satbayev.university
[2]Касенхан А.М.,
PhD, профессор, ORCID ID: 0000-0002-6355-9544,
e-mail: a.kassenkhan@satbayev.university

[1]Алматинский филиал Национального исследовательского ядерного университета «МИФИ»,
г. Алматы, Казахстан
[2]Казахский национальный исследовательский технический университет им. К.И. Сатпаева,
г. Алматы, Казахстан

ПРИМЕНЕНИЕ ИСКУССТВЕННОГО ИНТЕЛЛЕКТА В РАЗРАБОТКЕ АДАПТИВНОЙ СИСТЕМЫ ОБУЧЕНИЯ ДЛЯ РАЗВИТИЯ НАВЫКОВ КРИТИЧЕСКОГО МЫШЛЕНИЯ У СТУДЕНТОВ

Аннотация

В статье представлены результаты разработки и пилотной апробации адаптивной обучающей системы, предназначенной для формирования и оценивания критического мышления обучающихся с использованием элементов искусственного интеллекта. Научная новизна относительно существующих исследований по автоматизированной оценке эссе и оценке на основе больших языковых моделей (LLM) заключается в многокомпонентной оценке критического мышления, каскадном механизме ИИ-оценивания и механизме апелляции, что позволяет более точно определять слабые места студента в развитии критического мышления, обеспечивать прозрачную оценку критического мышления студента, устойчивость к сбоям системы и возможность оспаривания оценки студентом в спорных ситуациях. Система оценивает эссе и решение задачи по 6 компонентам критического мышления, а именно: анализу, интерпретации, оценке, аргументации, логической связности и рефлексии. Для каждого из компонентов были предложены формулы вычисления, которые вычисляются с помощью языковых моделей, семантических эмбеддингов преобразователей предложений и резервного TF-IDF-механизма. Апробация проведена на выборке из 20 студентов, являвшихся студентами КазНИТУ им. К.И. Сатпаева (Satbayev University). В экспертном оценивании участвовали три преподавателя в лице авторов. А экспериментальные данные включали 40 студенческих работ: 20 эссе и 20 решений задач. Каждая работа была оценена независимо тремя преподавателями, а также обучающей системой. Эталонная оценка была выбрана как усредненная оценка трех преподавателей. Корреляция автоматизированной оценки с усредненной экспертной оценкой составила r = 0,84, а среднее отклонение – 1,0 балла по десятибалльной шкале. Показанные результаты позволяют использовать систему как инструмент поддержки преподавателя, но также требуют дальнейшего исследования на большой выборке. Элементы геймификации, визуализация прогресса и механизм апелляции повышают вовлеченность обучающихся и обеспечивают баланс между автоматизированным и экспертным оцениванием.

Ключевые слова: адаптивная обучающая система, критическое мышление, искусственный интеллект, языковые модели, автоматизированное оценивание, многофакторная модель, геймификация, механизм апелляции, образовательная платформа.

Введение

В нынешних реалиях развитые навыки критического мышления являются необходимым условием для успешной адаптации личности в обществе со все большим доступом к различ-

ной информации. Это подтверждает исследование [1]. Критическое мышление позволяет отличать истину от лжи, формировать обоснованные суждения, смотреть на проблему с разных точек зрения и принимать взвешенное решение. Данные навыки востребованы не только в научной среде, но и в профессиональной деятельности [2]. Традиционные методы оценивания критического мышления, как правило, основаны на субъективной экспертизе преподавателя. Проверка работ обучающегося (эссе, решение задач) требует значительных временных затрат и неизбежно сказывается влияние человеческого фактора: усталость, личные предпочтения и неоднородность критериев оценивания приводят к неверным результатам. Также при большом количестве обучающихся преподаватель не сможет дать обратную связь, что, несомненно, скажется на образовательном процессе.

Искусственный интеллект, в частности большие языковые модели, открывают новые методы решения для этих проблем. Языковые модели достаточно хорошо анализируют текст на семантическом уровне [3]. Они позволяют выявлять структуру аргументации, оценивать логическую согласованность рассуждений и сравнивать с эталонным решением. Это позволяет создать автоматизированные системы оценивания, которые также оценивают качество суждений обучающегося.

Механизм апелляции нужен тогда, когда обучающийся не согласен с выставленной оценкой в спорных ситуациях или когда искусственный интеллект галлюцинирует. Поэтому было принято использовать гибридный подход, то есть возможность в случае несогласия обучающегося с оценкой передать его работу на рассмотрение преподавателю.

Система основана на многофакторной модели, включающей шесть критериев: анализ, интерпретация, оценка, аргументация, рефлексия и логика. Эта модель была принята как базовая модель оценивания критического мышления [4].

Для вычисления каждого критерия были разработаны формулы, которые помогают нейросетям приближенно оценивать по 6 критериям и, как выяснилось, достаточно хорошо оценивают критическое мышление обучающегося, так как есть сильная корреляция между оцениванием с помощью формул и оцениванием преподавателя.

Для повышения заинтересованности обучающегося в систему были добавлены элементы геймификации: система опыта, уровней, бейджи и обезличенных рейтингов. Также была добавлена функция получения рекомендаций (книги) на основе ответов обучающегося, чтобы улучшить критическое мышление обучающегося. Масштабирование и интеграция в существующие платформы образования в будущем обеспечивается с помощью модульного принципа построения архитектуры, а эта архитектура разделена на такие слои, как уровень интерфейса, уровень бизнес-логики и базы данных.

Научная новизна исследования состоит в многокомпонентной модели оценивания критического мышления. В существующих исследованиях автоматизированного оценивания основное внимание уделяется согласованию машинного балла и оценки эксперта, повышению точности нейросетевых моделей и генерации обратной связи по письменной работе. Но обычно это рассматривалось как отдельные проблемы. Например, Pack et al. [3] анализируют валидность и надежность больших языковых моделей при оценивании эссе, Uto [5] систематизирует архитектуры глубоких нейросетевых моделей автоматизированного оценивания, Lee et al. [6] предлагают multi-trait specialization для zero-shot оценивания эссе, Stahl et al. [7] рассматривают совместную генерацию оценки и обратной связи, а Chu et al. [8] усиливают multi-trait оценивание за счет рациональных объяснений, генерируемых LLM. В данной работе сделан акцент на построении полноценной платформы оценки и развития критического мышления, интерпретируемости критического мышления в виде вычисления формул компонентов критического мышления, модерации спорных случаев с помощью механизма апелляции и последующей индивидуальной обратной связи. Такое инженерное решение также позволяет уменьшить субъективность проверки, снизить нагрузку преподавателя и обеспечить возможность автономной работы системы при ограниченной технической инфраструктуре.

Материалы и методы

Общая архитектура системы

Обучающая система была реализована на языке программирования Python 3.11 с использованием графической библиотеки CustomTkinter для построения пользовательского интерфейса. Архитектура разделена на четыре слоя: уровень представления (Presentation Layer), уровень бизнес-логики (Application Layer), уровень доступа к данным (Persistence Layer) и внешний ИИ-сервис (External AI Service) (рисунок 1).

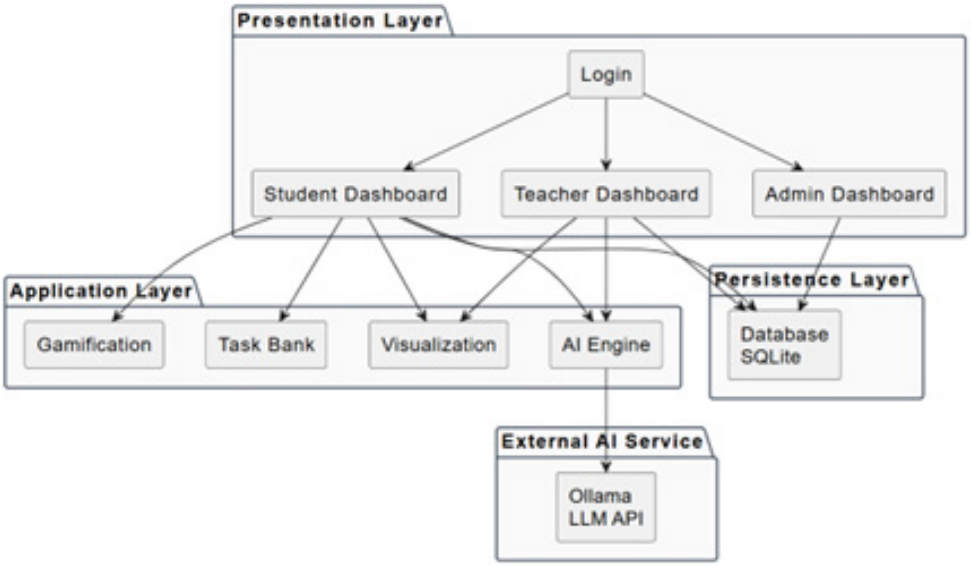


Рисунок 1 – Архитектура обучающей платформы

Диаграмма компонентов (рисунок 2) показывает взаимодействие между уровнями. Слои состоят из модуля входа в систему (login), панели студента (StudentDashboard), преподавателя (TeacherDashboard), администратора (AdminDashboard). Уровень бизнес-логики содержит модули AI Engine, Gamification, TaskBank, Recommendations и Visualization. Уровень данных обеспечивает доступ к реляционной базе данных SQLite через модуль Database.

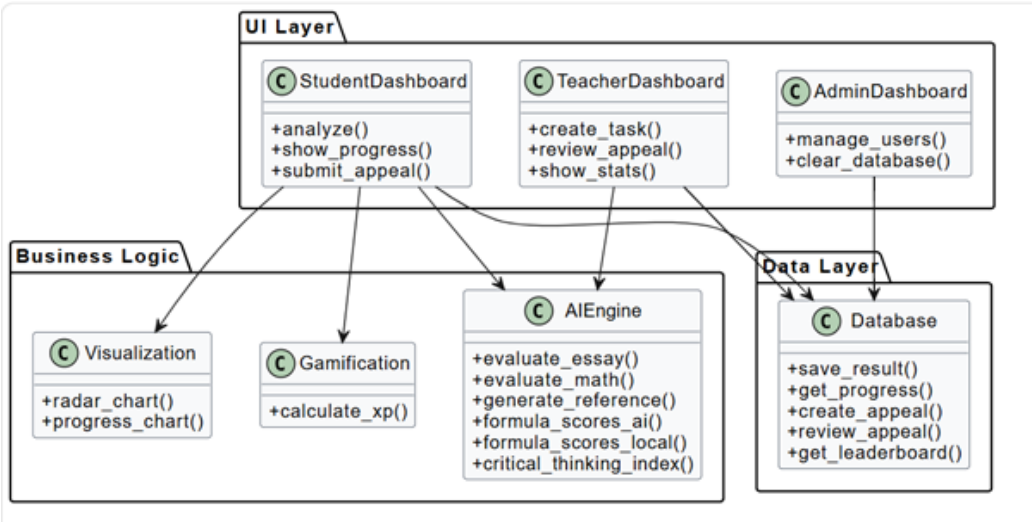


Рисунок 2 – Диаграмма компонент

Ролевая модель и управление доступом

Система имеет три роли пользователей: администратор, преподаватель, студент. Каждая роль имеет свой набор доступных ей функций, что показано на диаграмме компонент (рисунок 2). Студент может выполнять задания (эссе и математическая задача), получать оценку, просматривать прогресс и рейтинг, подавать апелляции и получать рекомендованную литературу для развития критического мышления. Преподаватель может создавать задания сам или с помощью искусственного интеллекта, просматривать успеваемость студентов своего класса, принимать апелляции и выставлять оценки по апелляциям. Администратор может создавать пользователей, изменять пароль учетных данных, удалять пользователей (кроме себя) и выборочно очищать базу данных. Задания привязаны к конкретному классу, когда преподаватель создает задание, оно автоматически привязывается к классу учителя, и обучающийся видит задание только для своего класса. Аналогично апелляции привязываются к классу преподавателя, что исключает возможность рассмотрения работ чужих студентов.

Многовекторная модель оценивания критического мышления

Основой системы является многофакторная модель оценивания, и эта модель опирается на таксономию Блума, модель критического мышления Facione и современные подходы к многофакторному оцениванию [4, 9]. Шесть критериев и их формулы представлены ниже:

1. Анализ. Здесь оценивается количество совпавших аргументов студента по отношению ко всем аргументам эталона, созданным либо учителем, либо искусственным интеллектом:

$$Score_analysis = (Narg / Allarg) * 10, \quad (1)$$

где Score_analysis – оценка умения анализировать;

Narg – количество совпавших аргументов;

Allarg – все аргументы эталонного ответа.

Для определения семантического сходства используется косинусное сходство между предложениями студента и каждым эталонным аргументом [10]. Если косинусное сходство выше порога 0,45, то считается, что студент раскрыл аргумент.

2. Интерпретация. Оценивает, насколько хорошо студент раскрыл и объяснил тему эссе или насколько обоснованно решение задачи студента в общем.

$$Score_interpretation = cosine_similarity(StudAns, Ans) * 10, \quad (2)$$

где Score_interpratation – оценка умения интерпретировать;

StudAns – это полный ответ на задание студента;

Ans – общий эталонный ответ.

Для вычисления косинусного сходства используются нейросетевые эмбеддинги на основе модели all-MiniLM-L6-v2 из библиотеки sentence-transformers в качестве резервного механизма.

Оценка.

$$Score_evalation = ((Eval_True + Exist_def)/2) * 10, \quad (3)$$

где Score_evaluation – оценка умения оценивать;

Eval_True – оценивает с помощью ИИ от 0.0 до 1.0, насколько убедительно звучат аргументы, нет ли неуверенности в высказываниях студента на основе маркерных слов;

Exist_def – тоже оценка от 0 до 1, насколько он обосновал аргумент, ответил на вопрос, почему он так считает. Оценка этого параметра производится с помощью ИИ.

Аргументация.

$$Score_argumentation = ((Claim_evidence_ratio + Diversity + Coherence)/3) * 10, \quad (4)$$

где Score_argumentation – оценка умения аргументировать;

Claim_evidence_ratio – соотношение количества утверждений и подкрепленных доказательств, оценивается от 0.0 до 1.0;

Diversity – разнообразие типов аргументов (факты, примеры, аналогии, статистика, цитаты, логические выводы) оценивается с помощью ИИ от 0.0 до 1.0. Если типов аргументов 3, то Diversity = 3/6 = 0.5;

Coherence – ИИ оценивает от 0.0 до 1.0, насколько плавно один аргумент переходит к другому, есть ли логический мост между аргументами или они стоят изолированно.

Рефлексия. Оценивает способность к самоанализу и выявлению собственных слабых мест в аргументах.

$$Score_reflection = min(1,0,weak_points/base_weak_points) * 10, \quad (5)$$

где Score_reflection – оценка умения рефлексировать;
weak_points – количество слабых мест, найденных студентом в своей работе;
base_weak_points – ожидаемое учителем или ИИ количество слабых мест у работ студентов в среднем.

Логика. Оценивает отсутствие логических ошибок и внутренних противоречий.

$$Score_logic = (1 - Logic_error/5) * 10, \quad (6)$$

где Score_logic – оценка отсутствия логических ошибок и внутренних противоречий;

Logic_error – количество логических ошибок, вычисляемое ИИ.

Также нужна будет итоговая оценка критического мышления (CTI):

$$CTI = 0.2 * Score_analysis + 0.15 * Score_argumentation + 0.2 * Score_evaluation + 0.2 * Score_logic + 0.15 * Score_interpretation + 0.1 * Score_reflection \quad (7)$$

Трехуровневый механизм оценивания

В системе был реализован многоуровневый механизм оценивания:

Уровень 1 – AI(Ollama). Основной внешний движок оценивания. Оценивание ИИ построено на обработке prompt-запроса, включающего такую информацию, как эталонный ответ, ответ студента и формулы критериев; на выводе получается JSON-строка с числовыми оценками по каждому критерию. Система поддерживает выбор из нескольких языковых моделей (DeepSeek, GPT-OSS, Qwen3).

Уровень 2 – sentence-transformers. Резервный локальный механизм, активируемый при недоступности языковой модели из Ollama. Использует модель all-MiniLM-L6-v2 для вычисления косинусного сходства между текстами и локальный анализ маркеров.

Уровень 3 – TF-IDF. Минимальный резервный вариант, для слабых компьютеров. Использует пересечение множеств слов (коэффициент Жаккара) для приблизительной оценки семантического сходства.

Такой подход гарантирует работоспособность системы в любых условиях: от серверного развертывания до автономной работы на компьютерах без интернета.

Эталонный ответ, механизм апелляции и обратная связь

Эталонный ответ содержит ключевые аргументы, идеи, типичные ошибки и логическую цепочку рассуждений. Может быть задан двумя способами: преподавателем или искусственным интеллектом. Эталонный ответ учителя имеет приоритет над эталонным ответом искусственного интеллекта.

Студент может подать апелляцию в случае несогласия с оценкой, указав причину несогласия. Преподаватель просматривает исходную работу студента, оценку ИИ и причину несогласия студента и может изменить оценку ИИ. Система автоматически подсчитывает CTI и обновляет итоговый результат.

Также имеется механизм обратной связи, который ИИ показывает студенту и преподавателю. На этой основе преподаватель либо изменяет оценку, либо оставляет без изменений.

Элементы геймификации

Для увеличения вовлеченности студентов в обучение, в систему интегрированы элементы геймификации: система опыта (XP), уровни и бейджи. Очки опыта начисляются из CTI. Бейджи присваиваются за достижение пороговых значений: “Beginner” (CTI < 4), “Critical Thinker” (CTI ≥ 4), “Strong Reasoner” (CTI ≥ 6), “Master Thinker” (CTI ≥ 8). Обезличенный рейтинг (leaderboard) класса визуализируется в виде столбчатой диаграммы.

Визуализация и диаграмма вариантов использования

Модуль визуализации (Visualization) построен на библиотеке Matplotlib и предоставляет четыре типа графиков: радарная диаграмма оценок по критериям, график прогресса CTI по попыткам, столбчатая диаграмма рейтингов класса. Графики отображаются во встроенных окнах приложения через FigureCanvasTkAgg.

Диаграмма вариантов использования (рисунок 3) отражает полную структуру функциональных возможностей для пользователей.

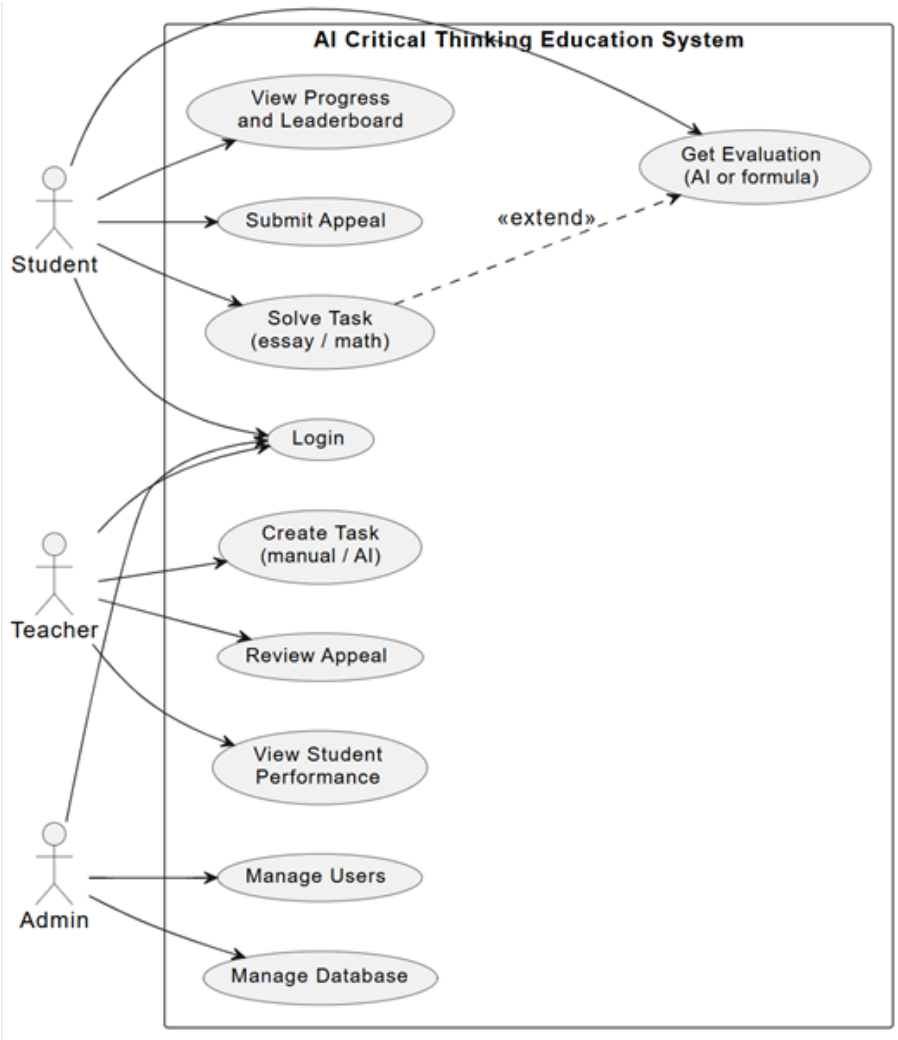


Рисунок 3 – Диаграмма вариантов использования

База данных и ER-диаграмма

Хранение данных осуществляется в реляционной базе данных SQLite (файл education.db), включающей четыре таблицы: users (по ролям и классам), results (результаты оценивания с ис-

ходными и итоговыми баллами), teacher_tasks (задания преподавателей по классам и с эталонным ответом) и appeals (хранит процесс апелляции). Использование SQLite дает автономность системы и отсутствие необходимости в отдельном сервере баз данных.

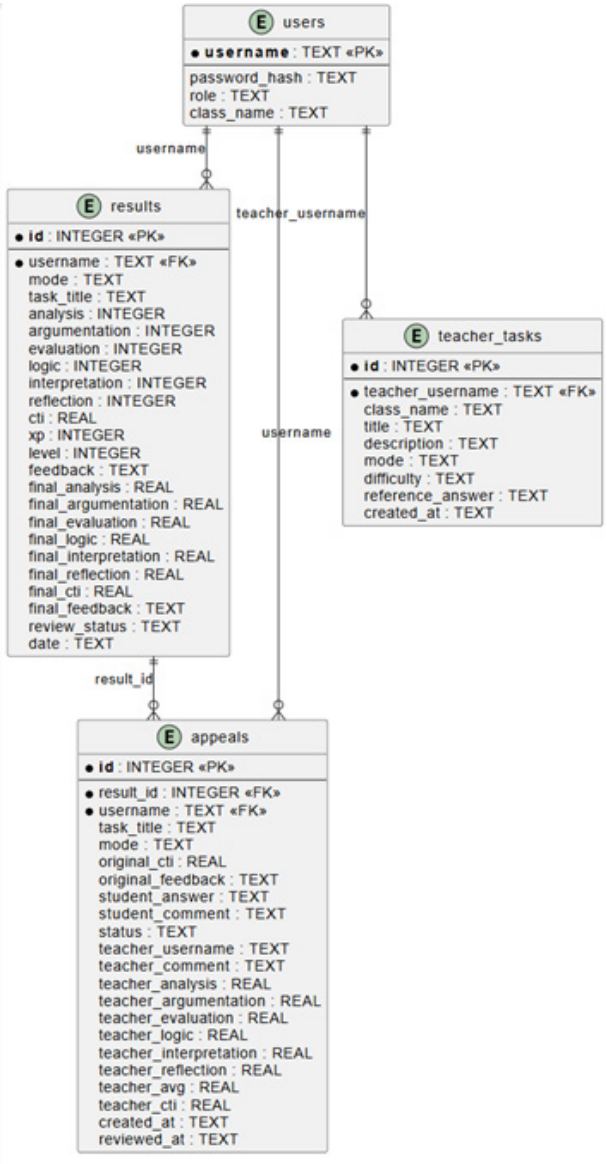


Рисунок 4 – ER-диаграмма

Методика апробации системы и характеристика выборки

Пилотная апробация адаптивной обучающей системы была проведена на выборке из 40 работ (20 эссе и 20 решений задач), выполненных 20 студентами КазНИТУ им. К.И. Сатпаева (Satbayev University). Экспертное оценивание проводилось независимо тремя преподавателями в лице авторов данной работы. Каждый преподаватель оценивал работы студентов по 6 критериям, а именно анализ, интерпретация, оценка, аргументация, рефлексия и логика. Для сопоставления с автоматизированной оценкой рассчитывалась усредненная экспертная оценка трех преподавателей. Такой подход уменьшил субъективность экспертного оценивания и повысил надежность сравнительного анализа. Этапы апробации включали: 1) загрузку заданий и эталонных ответов в систему; 2) выполнение заданий обучающимися; 3) автоматизированное оценивание работ с помощью прямой ИИ-оценки, формульной ИИ-оценки, преобразователей предложений и TF-IDF; 4) независимое экспертное оценивание тремя преподавателями;

5) расчет корреляции Пирсона и среднего абсолютного отклонения между автоматизированными оценками и усредненными экспертными оценками; 6) анализ результатов по каждому критерию критического мышления. Дополнительно фиксировались случаи потенциального несогласия с оценкой, для которых предусмотрен механизм апелляции. Следует отметить, что данная апробация имеет пилотный характер, но она достаточна, чтобы продемонстрировать работоспособность системы. Дальнейшее развитие требует увеличения выборки работ и числа образовательных организаций.

Результаты и обсуждение

Сравнение режимов оценивания

В таблице 1 представлено сравнение четырех режимов оценивания: прямая ИИ-оценка, формульная ИИ-оценка, формульная локальная оценка (sentence-transformers/TF-IDF). Подсчет корреляции и среднего отклонения рассчитывался между оценкой автоматизированной системы и усредненной оценкой преподавателей.

Таблица 1 – Сравнение режимов оценивания (корреляция с усредненной экспертной оценкой трех преподавателей)

Режим оценивания	Корреляция Пирсона (r)	Среднее отклонение от усредненной экспертной оценки
Прямая ИИ-оценка	0,84	1,0 балла
формульная ИИ-оценка	0,79	1,3 балла
Локальная sentence-transformers	0,74	1,5 балла
Локальная TF-IDF	0,38	3,4 балла

Наивысшую корреляцию с усредненной экспертной оценкой трех преподавателей показала прямая ИИ-оценка (r = 0,84), что согласуется с результатами исследований в области автоматизированного оценивания эссе [5, 11]. Формульная ИИ-оценка показала близкий результат (r = 0,79), при этом обеспечивает более высокую прозрачность, поскольку итоговый балл раскладывается на отдельные критерии критического мышления. Локальная модель преобразователей предложений продемонстрировала приемлемое качество, а TF-IDF показал более низкую согласованность, так как этот метод довольно плохо работает со смысловой структурой ответа.

Корреляция по отдельным факторам

В таблице 2 представлена корреляция формульной ИИ-оценки с усредненной экспертной оценкой трех преподавателей по каждому из шести факторов критического мышления.

Таблица 2 – Сравнение формульной ИИ-оценки с усредненной экспертной оценкой трех преподавателей

Критерий	Корреляция Пирсона (r)	Среднее отклонение от усредненной экспертной оценки
Анализ	0,80	1,2 балла
Интерпретация	0,86	0,9 балла
Оценка	0,75	1,4 балла
Аргументация	0,74	1,5 балла
Рефлексия	0,70	1,7 балла
Логика	0,83	1,1 балла
Среднее	0,78	1,3 балла
CTI	0,79	1,3 балла

Наивысшую корреляцию показали логика (r=0,83) и интерпретация (r=0,86). Оба критерия достаточно хорошо поддаются формализации, так как ИИ достаточно хорошо находит ошибки в рассуждениях, а косинусное сходство позволяет сопоставлять ответ студента с эталонным ответом. Наименьшую корреляцию показала Reflection, так как достаточно трудно формализовать этот фактор.

Сравнение методов вычисления по критериям

В таблице 3 показана корреляция с усредненной экспертной оценкой трех преподавателей по отдельным критериям и методам оценивания.

Таблица 3 – Корреляция с экспертной оценкой по критериям и методам

Критерий	Прямая ИИ- оценка	локальный Sentence-transformers	локальный TF-IDF
Анализ	0,86	0,79	0,35
Интерпретация	0,87	0,82	0,5
Оценка	0,81	0,68	0,33
Аргументация	0,77	0,7	0,31
Рефлексия	0,74	0,64	0,26
Логика	0,91	0,79	0,49
Среднее	0,83	0,74	0,37
CTI	0,84	0,74	0,38

Из таблицы 3 можно увидеть, что преобразователи предложений показывают результаты, близкие к прямой ИИ-оценке, где основную роль играет семантическое сходство текстов.

Наибольший разрыв между ними в Evaluation составляет 0,13. Это можно объяснить тем, что внешним эмбеддингам сложно оценить убедительность тех или иных аргументов. Хорошо себя показал TF-IDF в интерпретации, что неудивительно, так как косинусное сходство – одно из применений TF-IDF. В остальных факторах TF-IDF показал не лучшие результаты, так как для этого требуется понимание текстов.

Полученные результаты пилотной апробации подтверждают работоспособность разработанной системы и показывают согласованность автоматизированного оценивания с экспертным оцениванием трех преподавателей. В отличие от Lee et al. [6] и Chu et al. [8], где multi-trait scoring используется преимущественно как метод повышения точности и объяснимости автоматического оценивания эссе, в данной работе multi-trait принцип применяется к развитию критического мышления, а также к даче обратной связи, механизму апелляции и визуализации индивидуального прогресса. Многокомпонентная модель позволяет выделить конкретные аспекты критического мышления, требующие дальнейшего развития навыков студента. Трехуровневый каскадный режим работы позволяет обеспечить работоспособность даже при возникновении сбоев. Формульный подход делает оценивание более прозрачным: преподаватель и обучающийся видят не только итоговый CTI-балл, но и вклад отдельных критериев. Также исследование имеет ограничения. Апробация проводилась на выборке работ 20 студентов и проверке их работ тремя преподавателями. Это позволило доказать осуществимость и работоспособность обучающей платформы для оценивания критического мышления. Но она также не является достаточной для окончательных выводов о ее эффективности во всех образовательных процессах. Также качество формульного оценивания зависит от качества и полноты эталонного ответа. Дальнейшее развитие обучающей платформы предполагает расширение выборки, проведение апробации в разных дисциплинах и группах, а также долговременное исследование влияния обучающей системы на критическое мышление студентов и интеграцию с LMS-платформами.

Заключение

В рамках данной работы разработана адаптивная обучающая система для формирования и оценивания критического мышления у обучающихся с использованием элементов искусственного интеллекта. Система оценивания основана на многофакторной модели, включающей такие параметры, как анализ, интерпретация, оценка, аргументация, рефлексия и логика. Для каждого параметра была разработана своя формула, вычисление которой осуществляется с помощью языковых моделей, а при их недоступности разработан каскадный механизм оценивания.

Основные результаты работы заключаются в том, что реализован каскадный трехуровневый механизм оценивания, обеспечивающий работоспособность системы в различных технических условиях. При этом достигается высокая корреляция между ИИ-оценкой и экспертной оценкой преподавателя. Формульный подход обеспечивает прозрачность и объективность оценивания. Механизм апелляции обеспечивает, с одной стороны, точность оценивания в случае несогласия студента с оценкой, с другой стороны, вкупе с автоматизированной оценкой уменьшает нагрузку на преподавателя. Интеграция элементов геймификации позволит повысить вовлеченность студента в образовательный процесс. Модульная архитектура системы позволяет масштабировать систему и интегрировать ее в образовательные платформы.

Информация о финансировании

В статье представлены результаты исследований, выполненных в рамках программно-целевого финансирования на 2024–2026 гг. по проекту ИРН BR24993072 «Разработка интеллектуального образовательного ресурса на основе искусственного интеллекта для развития критического мышления студентов», финансируемого Комитетом науки Министерства науки и высшего образования Республики Казахстан.

ЛИТЕРАТУРА

1 Batdı, V., Elaldı, Ş., Özçelik, C. et al. Evaluation of the effectiveness of critical thinking training on critical thinking skills and academic achievement by using mixed-meta method. Review of Education, 12, e70001 (2024). https://doi.org/10.1002/rev3.70001

2 Almulla, M.A. Constructivism Learning Theory: A Paradigm for Students' Critical Thinking, Creativity, and Problem Solving to Affect Academic Performance in Higher Education. Sustainability, 15 (17), 12903 (2023). https://doi.org/10.1080/2331186X.2023.2172929

3 Pack, A., Barrett, A., and Escalante, J. Large language models and automated essay scoring of English language learner writing: Insights into validity and reliability. Computers and Education: Artificial Intelligence, 6, 100234 (2024). https://doi.org/10.1016/j.caeai.2024.100234

4 Facione, P.A. Critical Thinking: A Statement of Expert Consensus for Purposes of Educational Assessment and Instruction (The Delphi Report) (Millbrae, CA: California Academic Press, 1990).

5 Uto, M. A Review of Deep-Neural Automated Essay Scoring Models. Behaviormetrika, 48 (2), 459–484 (2021). https://doi.org/10.1007/s41237-021-00142-y

6 Lee, S., Cai, Y., Meng, D., Wang, Z., and Wu, Y. Unleashing Large Language Models' Proficiency in Zero-shot Essay Scoring. arXiv preprint, arXiv:2404.04941 (2024). https://arxiv.org/abs/2404.04941

7 Stahl, M., Biermann, L., Nehring, A., and Wachsmuth, H. Exploring LLM Prompting Strategies for Joint Essay Scoring and Feedback Generation. Proceedings of the 19th Workshop on Innovative Use of NLP for Building Educational Applications (BEA 2024) (Mexico City: Association for Computational Linguistics, 2024), pp. 283–298. https://aclanthology.org/2024.bea-1.23/

8 Chu, S.Y., Kim, J.W., Wong, B., and Yi, M.Y. Rationale Behind Essay Scores: Enhancing S-LLM's Multi-Trait Essay Scoring with Rationale Generated by LLMs. Findings of the Association for Computational Linguistics: NAACL 2025 (Albuquerque, New Mexico: Association for Computational Linguistics, 2025), pp. 5811–5829. https://doi.org/10.18653/v1/2025.findings-naacl.322

9 Bloom, B.S. Taxonomy of Educational Objectives: The Classification of Educational Goals. Handbook I: Cognitive Domain (New York: David McKay Company, 1956).

10 Reimers, N., and Gurevych, I. Sentence-BERT: Sentence Embeddings using Siamese BERT-Networks. Proceedings of the 2019 Conference on Empirical Methods in Natural Language Processing (EMNLP) (2019). https://doi.org/10.18653/v1/D19-1410

11 Klebanov, B.B., and Madnani, N. Automated Essay Scoring. Synthesis Lectures on Human Language Technologies (Morgan & Claypool Publishers, 2024).

[1]Утебаев К.А.,
магистрант, ORCID ID: 0009-0004-3032-5049,
e-mail: utebayevkuat@gmail.com
[2*]Молдагулова А.Н.,
ф.-м.ғ.к., профессор, ORCID ID: 0000-0002-1596-561X,
*e-mail: a.moldagulova@satbayev.university
[2]Касенхан А.М.,
PhD, профессор, ORCID ID: 0000-0002-6355-9544,
e-mail: a.kassenkhan@satbayev.university

[1]«МИФИ» Ұлттық ядролық зерттеу университетінің Алматы филиалы,
Алматы қ., Қазақстан
[2]Қ.И. Сәтбаев атындағы Қазақ ұлттық техникалық зерттеу университеті,
Алматы қ., Қазақстан

СТУДЕНТТЕРДІҢ СЫНИ ОЙЛАУ ДАҒДЫЛАРЫН ДАМЫТУҒА АРНАЛҒАН БЕЙІМДЕЛГІШ ОҚЫТУ ЖҮЙЕСІН ӘЗІРЛЕУДЕ ЖАСАНДЫ ИНТЕЛЛЕКТТІ ҚОЛДАНУ

Аңдатпа

Мақалада жасанды интеллект элементтерін пайдалана отырып, білім алушылардың сыни ойлауын қалыптастыруға және бағалауға арналған бейімделгіш оқыту жүйесін әзірлеу және пилоттық апробациялау нәтижелері көрсетілген. Эсселерді автоматтандырылған және үлкен тілдік модельдерге (LLM) негізделген бағалау бағыттарындағы қолданыстағы зерттеулермен салыстырғанда, зерттеудің ғылыми жаңалығы сыни ойлауды көпкомпонентті бағалау, ЖИ негізіндегі бағалаудың каскадты механизмі және апелляция механизмін қолдануымен сипатталады. Бұл студенттің сыни ойлауын дамытудағы әлсіз тұстарын дәлірек анықтауға, сыни ойлауды бағалаудың ашықтығын қамтамасыз етуге, жүйенің істен шығу жағдайларына төзімділігін арттыруға және даулы жағдайларда студентке бағалау нәтижесіне шағымдану мүмкіндігін беруге мүмкіндік береді. Жүйе эсселер мен есептердің шешімдерін сыни ойлаудың алты компоненті бойынша бағалайды: талдау, интерпретация, бағалау, аргументация, логикалық байланыстылық және рефлексия. Әрбір компонент үшін есептеу формулалары ұсынылды; олар тілдік модельдер, сөйлем түрлендіргіштеріне негізделген семантикалық эмбеддингтер және резервтік TF-IDF механизмі арқылы есептеледі. Апробация К.И. Сәтбаев атындағы Қазақ ұлттық техникалық зерттеу университетінің (Satbayev University) 20 студентінен құралған таңдамада жүргізілді. Сараптамалық бағалауға авторлар қатарынан үш оқытушы қатысты. Эксперименттік деректер 40 студенттік жұмысты қамтыды: 20 эссе және 20 есептің шешімі. Әрбір жұмысты үш оқытушы тәуелсіз бағалады, сондай-ақ жұмыстар оқыту жүйесі арқылы бағаланды. Эталондық баға ретінде үш оқытушының орташа бағасы алынды. Автоматтандырылған бағалау мен орташа сараптамалық бағалау арасындағы корреляция r = 0,84 құрады, ал орташа ауытқу он балдық шкала бойынша 1,0 балл болды. Алынған нәтижелер жүйені оқытушыны қолдау құралы ретінде пайдалануға мүмкіндік беретінін көрсетеді, алайда оны үлкенірек таңдама негізінде әрі қарай зерттеу қажет. Ойындандыру элементтері, прогресті визуализациялау және апелляция механизмі білім алушылардың қызығушылығын арттырып, автоматтандырылған және сараптамалық бағалау арасындағы тепе-теңдікті қамтамасыз етеді.

Түйін сөздер: бейімделгіш оқыту жүйесі, сыни ойлау, жасанды интеллект, тілдік модельдер, автоматтандырылған бағалау, көпфакторлы модель, ойындандыру, апелляция механизмі, білім беру платформасы.

[1]Utebayev K.A.,
Master's student, ORCID ID: 0009-0004-3032-5049,
e-mail: utebayevkuat@gmail.com
[2]*Moldagulova A.N.,
Candidate of Physical and Mathematical Sciences, Professor,
ORCID ID: 0000-0002-1596-561X,
*e-mail: a.moldagulova@satbayev.university
[2]Kassenkhan A.M.,
PhD, Professor, ORCID ID: 0000-0002-6355-9544,
e-mail: a.kassenkhan@satbayev.university

[1]Almaty Branch of the National Research Nuclear University MEPhI, Almaty, Kazakhstan
[2]Satbayev University, Almaty, Kazakhstan

USING ARTIFICIAL INTELLIGENCE TO DEVELOP AN ADAPTIVE LEARNING SYSTEM TO DEVELOP CRITICAL THINKING SKILLS IN STUDENTS

Abstract

The article presents the results of the development and pilot testing of an adaptive learning system designed to develop and assess students' critical thinking using elements of artificial intelligence. The scientific novelty of the study, in comparison with existing research on automated essay scoring and LLM-based assessment, lies in the multi-component assessment of critical thinking, the cascade mechanism of AI-based assessment, and the appeal mechanism. These features make it possible to more accurately identify students' weak points in the development of critical thinking, ensure transparent assessment of students' critical thinking, increase the system's resilience to failures, and provide students with the opportunity to challenge the assessment in controversial situations. The system evaluates essays and problem-solving tasks according to six components of critical thinking: analysis, interpretation, evaluation, argumentation, logical coherence, and reflection. For each component, calculation formulas were proposed; these are computed using language models, semantic embeddings based on sentence-transformers, and a backup TF-IDF mechanism. The pilot testing was conducted on a sample of 20 students from Satbayev University. Three instructors, represented by the authors, participated in the expert assessment. The experimental data included 40 student works: 20 essays and 20 problem-solving tasks. Each work was independently assessed by three instructors as well as by the learning system. The reference score was determined as the average score of the three instructors. The correlation between the automated assessment and the averaged expert assessment was r = 0.84, while the mean deviation was 1.0 point on a ten-point scale. The results obtained indicate that the system can be used as a tool to support instructors; however, further research on a larger sample is required. Gamification elements, progress visualization, and the appeal mechanism increase students' engagement and ensure a balance between automated and expert assessment.

Keywords: adaptive learning system, critical thinking, artificial intelligence, language models, automated assessment, multifactor model, gamification, appeal mechanism, educational platform.

Received April 14, 2026; revised June 4, July 22, 2026; accepted August 20, 2026.

UDC 004.056
IRSTI 81.93.29

https://doi.org/10.55452/1998-6688-2026-23-3-255-266

[1]Aidynov T.,
doctoral student, Researcher, ORCID ID: 0009-0005-3327-9719,
e-mail: tolegen.ch@gmail.com
[1]Satybaldina D.,
Cand. Sci. (Phys.-Math.), Professor, ORCID ID: 0000-0003-0291-4685,
e-mail: satybaldina_dzh@enu.kz
[2] Dimitrov W.,
PhD, Professor, ORCID ID: 0000-0002-5348-4948,
e-mail: v.dimitrov@unibit.bg
[1*]Abisheva G.,
PhD, ORCID ID: 0009-0003-6692-197X,
e-mail: gulsipat.abisheva@gmail.com

[1]L.N. Gumilyov Eurasian National University, Astana, Republic of Kazakhstan
[2]University of Library Studies and Information Technologies, Sofia, Bulgaria

A BLOCKCHAIN-ORIENTED MODEL FOR ELECTRONIC VOTING WITH BIOMETRIC VOTER IDENTIFICATION AND DEEPFAKE-RESISTANT AUTHENTICATION

Abstract

This paper presents and experimentally validates an electronic voting model that stores results in a decentralized blockchain while using biometric voter verification and automatic detection of synthetically generated (deepfake) facial images. For identity verification, Vision Transformer and ResNet-50 architectures are fine-tuned with Low-Rank Adaptation (LoRA). Frequency-domain information from the Fast Fourier Transform (FFT) is also included as a descriptor for detecting synthetic images. Since blockchain records cannot be altered, the model introduces a controlled revoting process based on self-destructing ballots and timestamps recorded on the blockchain; the votes themselves are submitted through an Ethereum smart contract. In the experiments, the LoRA-adapted ViT configuration distinguishes real from synthetic facial images with an accuracy of 97.48%, exceeding the performance of the LoRA-adapted ResNet-50 baseline. However, because no separate FFT ablation study has been conducted, this work does not claim that the frequency descriptor makes an independent contribution. The proposed system is presented as part of Smart City digital infrastructure and lays the groundwork for future research on privacy-preserving biometric protocols and blockchain platforms capable of scaling to electoral processes.

Keywords: electronic voting, face recognition, deepfake detection, blockchain, Ethereum, smart contracts, Vision Transformer, ResNet, revoting mechanism, smart city.

Received July 1, 2026; revised August 4, 7, 19, 2026; accepted August 28, 2026.

Introduction

Electronic voting has evolved from mechanical lever and punch-card machines, through direct-recording electronic systems, to fully web-based systems that let voters participate in elections remotely. The early direct-recording systems reduced the logistics of paper ballots but did not address the problem of verifiability: without an independent audit trail, such systems could still be manipulated through software or suffer technical failure.

The shift to internet voting made elections more accessible-Estonia's national digital elections offer a prime example-but it also introduced new risks, including remote cyberattacks, voter impersonation, and data breaches [1–4]. Research has therefore focused on two related aims: (a) authenticating voters and (b) protecting results from later alteration. Voter authentication remains especially challenging in the presence of synthetic imagery. Conventional identity checks, including passwords and document verification, are widely considered susceptible to phishing and social engineering. Face-based biometric verification has emerged as an appealing alternative since it is contactless and supported by consumer hardware that is already widely available. Still, face recognition by itself does not close the security gap.

Generative adversarial networks can now create photorealistic synthetic faces that fool even state-of-the-art verification models. For biometric authentication systems used in elections, a separate deepfake-detection stage has therefore become practically necessary if they claim to withstand targeted identity-spoofing attacks [4–8].

Blockchain as a guarantee of result integrity. A second source of weakness in conventional e-voting systems is centralized storage under a single trusted operator, which creates a single point of failure and an opportunity for undetectable tampering. Blockchain offers an alternative: a decentralized, cryptographically tamper-evident ledger that is open for independent verification by any party [9–11].

Permissioned ledgers such as Hyperledger Fabric were used in earlier proposals to maintain control over access while keeping transparency [12, 13]. Public Ethereum-based systems take this property one step further to full external verifiability and remove the requirement for a centralized vote-counting authority altogether by smart contracts paired with wallet-based authentication (e.g., MetaMask) [14–16].

The immutability problem and the aim of this study. Blockchain ledgers are trusted because their records cannot be changed, but that same property rules out legitimate vote corrections–something that can routinely be needed after an input error or a change of mind during the voting window [17, 18]. This study therefore seeks to design and experimentally validate a system with two capabilities: robust biometric authentication that can withstand deepfake attacks, and controlled revoting that does not weaken the cryptographic guarantees of the underlying ledger. The latter is handled by a Dynamic Revoting Mechanism based on self-destructing ballots and timestamp ordering recorded on the blockchain. It extends our earlier systematic review of cryptographic protection methods for electronic voting systems (reference [19]), a prior publication by the present authors and thus a self-citation. To our knowledge, no previously evaluated prototype has combined frequency-aware, deepfake-resistant biometric gating and a smart-contract-level, self-destructing-ballot revoting mechanism within a single pipeline. Each component is established on its own; this work's contribution lies specifically in integrating them with revoting logic executed on-chain.

Materials and methods

The proposed solution integrates three layers: a biometric verification layer built on deep neural models, a synthetic-image detection layer based on frequency-domain analysis, and a result-recording layer implemented as a revoting-capable Ethereum smart contract. The end-to-end processing sequence for a single vote is shown in Figure 1.

Dynamic Revoting Mechanism

Because this component determines the practical usability of the whole system, its logic is described first, ahead of the recognition-model details.

Self-destructing ballots. Once a blockchain transaction is confirmed, it is permanent by design, which normally makes it impossible to invalidate – and therefore replace – a previously cast vote. The proposed mechanism introduces a cryptographic "burn" function for the prior ballot: on receiving a revote request, the smart contract checks that (i) the voter already has a registered vote and (ii)

the voting period is still open, after which it marks the earlier record as invalid. The sequence is as follows:

1. The voter casts an initial vote, recorded on-chain as VoteHash_A.
2. The voter requests a revote, triggering the burn function.
3. VoteHash_A is marked invalid and excluded from the tally.
4. A new vote is recorded as VoteHash_B.
5. Only the most recent valid record is included in the final count.

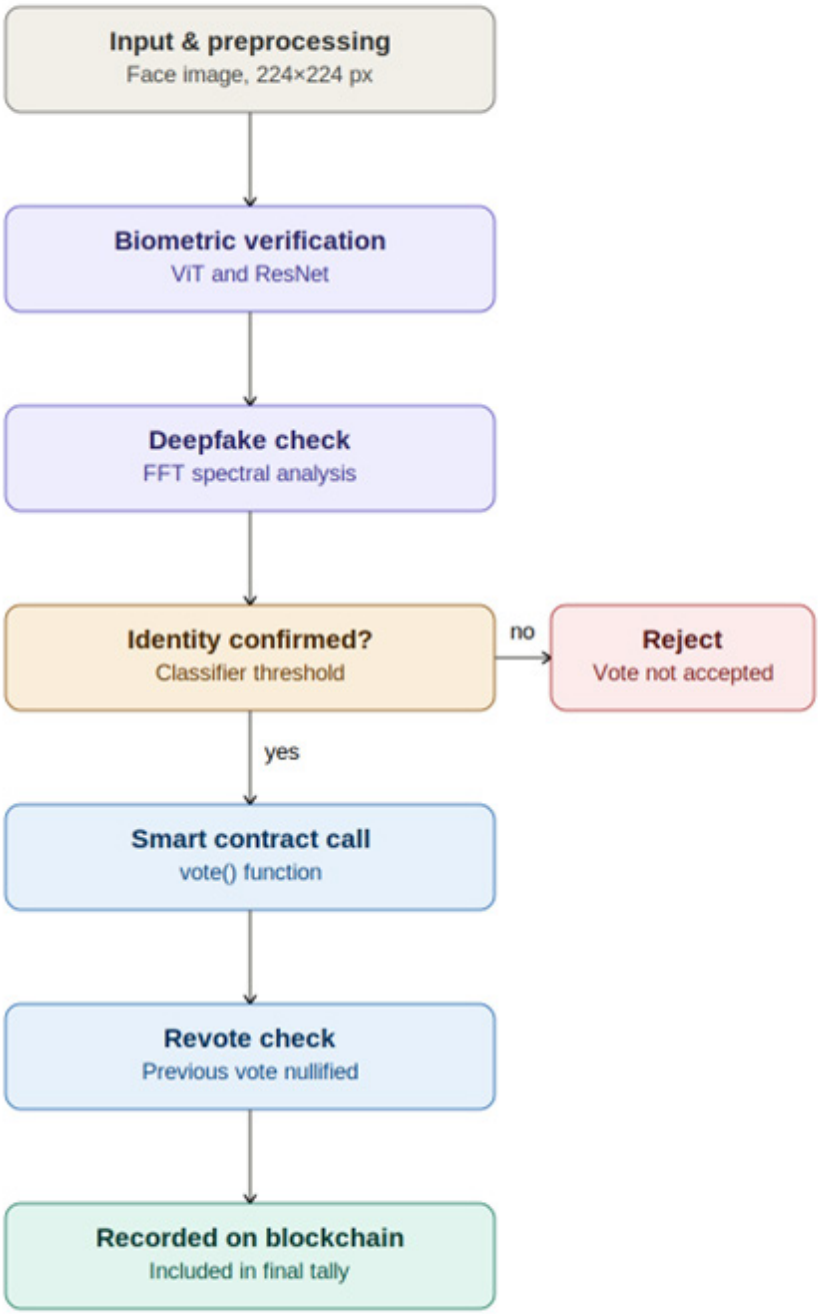


Figure 1 – Overall vote-processing workflow with biometric verification

The counted vote is formally given by expression (1):

$$n = argmax_i(T_i), V_t = V_n \quad (1)$$

where denotes the timestamp attached to the i-th recorded vote, n refers to the submission with the latest admissible timestamp, and represents the final vote included in the count. Since the smart contract allows only one revote during each election cycle, a voter may submit no more than two votes (n≤2). Burned ballots remain visible on-chain for auditing, but they no longer influence the tally.

Admissible submissions are ordered according to the timestamp attached to each vote by the Ethereum execution environment. That timestamp determines the sequence within the officially defined voting window, but it is not regarded as an independently trusted source of time.

$$T_n = max_i(T_i) \quad (2)$$

where denotes the time at which the i-th vote was recorded, and is the latest admissible timestamp. Submissions made outside the officially defined voting window are rejected by the smart contract. Because Ethereum block timestamps are proposed by block producers/validators, they may experience bounded drift or be influenced by the producer. The model therefore treats blockchain time as adequate for ordering transactions within the voting window, not as a cryptographic guarantee of exact wall-clock time. In a production deployment, an accepted timestamp-drift policy should be specified; stronger time guarantees would require an external trusted timestamping/oracle mechanism.

Conditions enforced by the smart contract. Three constraints are enforced at the contract level: a revote is accepted only within the designated time window; burned records are permanently excluded from the count; and each voter is limited to a single revote per election cycle. These rules together make it impossible to change the outcome by repeatedly submitting a new vote without breaking the cryptographic guarantees of the contract (Figure 2).

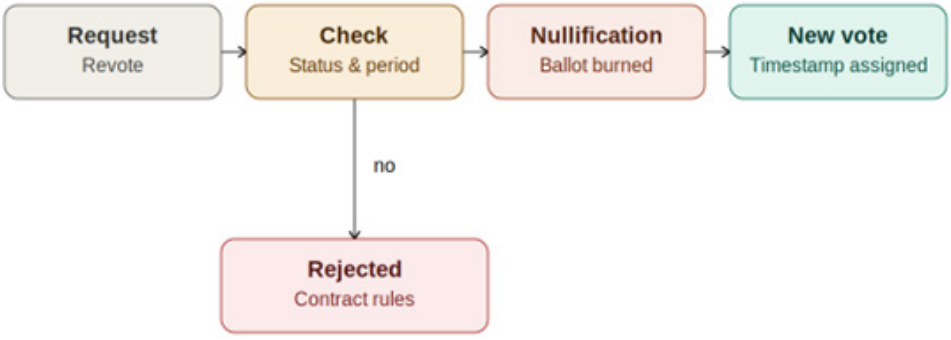


Figure 2 – Revote request validation and execution sequence

Table 1 summarizes how this combination of self-destructing ballots and secure timestamps removes the central limitation of immutable ledgers – the inability to correct a vote – without sacrificing transparency or protection against repeat voting.

Biometric Verification and Synthetic-Image Detection

Training data. Model tuning and evaluation are based on a publicly available dataset of 140,000 facial images (Kaggle, “140k Real and Fake Faces”), half of which are real photos and the other half are StyleGAN3-generated images. The images were resized to 224x224 pixels and randomly flipped horizontally prior to training to augment them and make them more robust to lighting and pose variations (Table 2).

Table 1 – Comparison between a conventional immutable blockchain ledger and the proposed mechanism

Criterion	Limitation of the conventional scheme	Proposed solution
Vote correction	Records are immutable; correction is impossible	Controlled update within the voting window
Double-voting prevention	Multiple submissions are not inherently excluded	Self-destructing ballots leave exactly one valid vote
Storage footprint	Grows with every submitted version of a vote	Burned records remain on-chain; they are excluded only from the active tally/ index
Transparency and tamper resistance	Direct overwriting of a vote creates a manipulation risk	Full operation history stays on-chain; only the latest timestamp counts

Table 2 – Characteristics of the dataset used

Parameter	Value
Total images	140,000
Genuine faces	70,000
Synthetic (deepfake) faces	70,000
Source	Kaggle, 140k Real and Fake Faces
Forgery generation method	StyleGAN3
Preprocessing	Resize to 224×224, color jitter, random flip

Recognition model architectures

The voter identity verification system is built on a Vision Transformer, specifically the ViT-Base variant. Instead of using convolutions to examine local regions, it relies on self-attention [2, 20] to process images and identify spatial relationships between facial regions that may be far apart. Each image is split into non-overlapping 16×16 patches, transformed into 768-dimensional feature vectors, and sent through 12 transformer layers, with 12 attention heads in each layer. The resulting representation is then fed to a classifier, which assigns it to one of two classes: genuine or synthetic.

To reduce fine-tuning costs, we apply Low-Rank Adaptation (LoRA) [21] to the query, key, and value projections in the attention layers. Rather than updating the full model, this adds trainable low-rank matrices and brings the trainable-parameter share down to about 2-3%, with no real loss of accuracy. In parallel, ResNet-50 serves as a convolutional baseline, extracting local texture features across four successive residual stages, with channel depth increasing from 64 to 2048. Applying LoRA to selected convolutional layers achieves results as good as full fine-tuning while requiring only 5–10% of the computational cost.

Related biometric approaches using angular-margin loss functions have recently shown strong performance in face-based identity verification, so they offer a useful complement for future model comparisons [22]. In addition to the features extracted by the two networks, every image undergoes a fast Fourier transform (FFT), since GAN-synthesis artifacts may be visible in the frequency spectrum. For each 224×224 input, a two-dimensional FFT is calculated, its magnitude spectrum is log-scaled, and a high-frequency region is kept as the spectral descriptor. Directly before the final fully connected classification head, the descriptor and backbone embedding are L2-normalized and concatenated at the feature level. There is no intermediate learned projection layer. The current experimental record does not document the exact dimensionality of the retained FFT descriptor, so no reconstructed value is reported. This limits reproducibility and will be addressed in subsequent experiments by retaining the complete feature-extraction configuration.

The evaluated configuration combines spatial features with frequency-domain information. Since no ablation compared the spatial-only setup with the FFT-fused version, the current results cannot isolate the FFT descriptor's marginal contribution. Training used the HuggingFace Trainer API, automatic batch-size selection, the AdamW optimizer, and cross-entropy loss with label smoothing set to 0.1. Most base-model parameters were frozen through LoRA, while evaluation metrics were collected each epoch to monitor quality. The original experimental report did not preserve a complete reproducibility record for the LoRA rank r, scaling factor α, all target-module details, learning rate, exact epoch count, batch size selected automatically by the training framework, or hardware configuration. This revision does not reconstruct or estimate those values. The limitation is explicitly acknowledged; future experiments will retain the full configuration and random seeds. The experiments described here trained on 100,000 images and evaluated performance on a held-out, class-balanced validation set containing 20,000 images-10,000 genuine and 10,000 synthetic. That accounts for 120,000 of the 140,000 source images, leaving 20,000 images without reported results from an independent test set. The final metrics therefore reflect validation-set performance, not independent test performance. Repeated runs with different random seeds were not conducted, and confidence intervals were not calculated; both are identified as future evaluation work.

Results and discussion

Deepfake-detection accuracy

Table 3 compares the models across training accuracy, validation accuracy, loss, and F1-score. The strongest result came from the LoRA-adapted ViT. Using the retained confusion matrix (TP=9752, TN=9744, FP=256, FN=248; N=20,000), the validation accuracy recalculates to 97.48%. LoRA-adapted ResNet-50 reached 75.74% validation accuracy. The unadapted models were lower: ViT-Base achieved 84.47%, whereas ResNet-Base reached 70.27%. On the validation set, the evaluated ViT-LoRA configuration therefore showed a substantial performance advantage.

Table 3 – Summary of model performance

Model	Training accuracy	Validation accuracy	Loss	F1-score
ViT-Base	0.8243	0.8447	0.4653	0.8259
ViT-LoRA	0.9559	0.9748	0.2760	0.9748
ResNet-Base	0.7048	0.7027	0.6001	0.6980
ResNet-LoRA	0.8014	0.7574	0.4916	0.7600

Table 4's confusion matrix shows 256 false positives and 248 false negatives for ViT-LoRA, with an accuracy of 0.9748. ResNet-Base had considerably more errors: 2900 false positives and 3046 false negatives. This suggests that the unadapted convolutional approach is less reliable near the classification margin. The complete TP/TN/FP/FN outputs for ResNet-LoRA were not retained from the original experimental run. Since aggregate accuracy and F1-score alone cannot reliably be used to reconstruct FPR and FNR, ResNet-LoRA appears in Table 3 but is excluded from Tables 4 and 5; no inferred or unverifiable confusion-matrix values were assigned.

Beyond overall accuracy, the final false-positive and false-negative rates (FPR and FNR) for each model were computed directly from the confusion-matrix values in Table 4, rather than tracked across training epochs. This final view puts both ViT-LoRA error rates at roughly 2.5%, compared with nearly 30% for ResNet-Base. The difference reinforces the conclusion that the LoRA-adapted transformer is much more reliable in avoiding incorrect rejections of both genuine and synthetic images.

Table 4 – Classification confusion matrices

Model	TP	TN	FP	FN	Accuracy
ViT-LoRA	9752	9744	256	248	0.9748
ViT-Base	8576	8318	1682	1424	0.8447
ResNet-Base	6954	7100	2900	3046	0.7027

Table 5 – Final false-positive and false-negative rates by model

Model	FPR (false-positive rate)	FNR (false-negative rate)
ViT-LoRA	2.56%	2.48%
ViT-Base	16.82%	14.24%
ResNet-Base	29.00%	30.46%

Evaluation of the revoting mechanism

Because deployment on a live Ethereum network was outside the scope of this study, the assessment of the revoting mechanism's benefits is theoretical, grounded in the cryptographic properties of the proposed scheme and in findings reported for comparable blockchain-voting systems [10, 11, 17] (Table 6). As a first move toward empirical validation rather than theory alone, the smart contract is planned for small-scale deployment on a local test network, such as a Ganache or Hardhat node. This will allow the storage and verification-time effects reported here as estimates to be measured directly under controlled conditions before any live deployment. Unlike the revoting and repeat-voting-prevention methods discussed in [11] and [17], where an earlier ballot is overwritten or rejected outright, the mechanism proposed here keeps every previous ballot on-chain in a verifiably burned state instead of removing it. This preserves the complete revoting history for public audit, while the tally includes only the latest valid ballot. The main distinction from the closest prior revoting schemes lies in what happens to the earlier ballot. Overwrite-in-place designs reuse its storage slot and discard the old value; reject-on-resubmission designs refuse the second attempt [11, 17]. Under the burn-and-retain rule proposed here, each superseded ballot remains as an immutable record marked explicitly invalid. The complete voting history can therefore be audited, while exactly one valid ballot per voter is still admitted.

Table 6 – Expected characteristics of the conventional scheme versus the proposed mechanism

Evaluation criterion	Conventional blockchain voting	Dynamic Revoting Mechanism	Expected effect
Vote flexibility	No correction possible	Revoting via self-destructing ballots	Improved voting accuracy
Fraud resistance	High (immutable votes)	High (timestamped, single valid vote enforced)	Security level preserved
Storage efficiency	Ledger retains submitted records	Burned records remain on-chain but are excluded from the active tally/index	No blockchain-storage reduction claimed; active tally/index may be smaller
Finalization speed	Fast (pre-set immutable votes)	Slightly slower (revote verification required)	Estimated 10–15% increase in verification time
Voter satisfaction	No correction possible	Mistake correction allowed	Expected higher voter confidence

The core tradeoff remains between vote flexibility and election security. In a traditional ledger, immutability ensures that no one can change anything, but it also implies that there is no way to allow a voter to correct a mistake. The proposed self-destructing-ballot scheme makes the system more flexible while preserving the rule that only the latest valid vote counts.

In theory, this should make voting more accurate and leave voters more satisfied, although every revote requires additional verification computation. It does not, however, make the blockchain ledger smaller. Because superseded ballots remain on-chain as auditable invalid records, the burn-and-retain mechanism leaves the ledger's size unchanged or larger. Any efficiency gain is limited to the active tally set or the index used during counting, since burned records are omitted there. Since each voter may revote at most once, the total number of on-chain ballot records can only stay the same as or exceed the number in a system without revoting. The earlier estimate of a 30–40% reduction in blockchain storage is therefore withdrawn until measurements from an implementation are available.

Full operation history, including burnt records, remains on-chain, but those records are excluded from the tally, preserving auditability and protection against retroactive manipulation of the result.

Discussion

The results indicate that combining a LoRA-adapted transformer architecture with frequency-domain analysis protects against voter-impersonation attacks more effectively than authentication based on passwords or documents. Still, biometrics in electoral systems raise privacy concerns, along with the possibility of demographic differences in recognition accuracy. Whether privacy-preserving biometric verification schemes can be designed remains an open question. The present experiments did not include a systematic assessment of demographic bias in the verification module across age, gender, and ethnicity subgroups. That work is planned for the future, as fairness audits are increasingly expected for biometric systems used in electoral settings. The current results also cover only the accuracy of the fused spatial-plus-frequency configuration. To determine and quantify the FFT-based frequency descriptor's marginal contribution, a separate ablation study comparing the spatial-only backbone with the fused variant is needed; this study is planned for the next stage of the work. Specifically, the ablation will evaluate three configurations using the same training and validation protocol: the spatial backbone alone, the frequency (FFT) descriptor alone, and the fused spatial-plus-frequency model. It will report accuracy as well as false-positive and false-negative rates, isolating and quantifying the frequency descriptor's marginal contribution instead of leaving it to inference. The present study acknowledges the lack of this ablation as a limitation.

Residual error rates matter operationally when the system is used at election scale. With FPR and FNR at approximately 2.5%, millions of voters could produce a substantial number of authentication attempts that are incorrectly accepted or rejected. The biometric/deepfake module therefore should not serve as the only irreversible decision point. Rejected or low-confidence cases need a fallback procedure, which might involve a second biometric capture, an independent identity-verification channel, or supervised/manual verification carried out under election authority procedures.

The Dynamic Revoting Mechanism removes a basic limitation of blockchain voting: once a vote is cast, it cannot be changed. That flexibility comes at a cost, though. Verifying revotes requires additional computation, and it also raises a longer-term question about auditing.

Burned ballots remain on the chain but are left out of the count, a practice regulators might view as a transparency problem. Balancing the ability to revote with stronger auditability guarantees would be a worthwhile subject for future research. Ethereum provides the decentralization and public verifiability the system requires, but transaction costs and limited throughput still make deployment at the scale of a national election impractical. Layer-2 scaling solutions could be considered, along with alternatives such as Hyperledger Fabric or Algorand, to reduce operating costs without giving up the system's core security guarantees. The technology of generative models is also an evolving field in its own right: as new methods for synthesis are developed, it is likely that the detection system based on ResNet-50 features and frequency analysis will need to be retrained, and possibly even subjected to adversarial training, in order to maintain its current level of effectiveness.

Storing the complete tally on a public ledger reflects a deliberate choice between transparency and ballot privacy. Another line of research keeps the tally private by using secure multi-party computation (MPC) or homomorphic encryption rather than counting ballots openly on-chain. The systems combine individual ballots without revealing them and decrypt only the final result. Voters gain stronger secrecy, but the trust requirement shifts to a group of computing parties. These methods also impose substantial cryptographic and coordination overhead, and they make independent public verification of the count considerably harder. The design presented here instead prioritizes end-to-end public verifiability: any observer can inspect the chain and confirm that the tally contains only the latest valid ballot submitted by each voter. One possible compromise would pair MPC-based secret tallying with the self-destructing-ballot revoting logic proposed here, combining greater voter privacy with the auditability that full transparency provides.

Ballot privacy also means that VoteHash cannot be a deterministic hash based only on the candidate choice. Since elections typically offer a small set of candidates, an attacker could recover the selected option through dictionary or brute-force search. In a production system, the value should instead be a hiding commitment, such as H (choice/nonce), with nonce serving as a cryptographically random, voter-specific value, or it should use an encrypted ballot representation. The current model assumes that the on-chain value reveals no plaintext voting choice; formally analyzing privacy and implementing the commitment or encryption layer remain future work.

Lastly, the deployment of such a system within a governmental context necessitates alignment with data-protection and electoral regulation. This, in turn, requires engagement with regulators, election officials, and cybersecurity experts as a prerequisite for transitioning the research prototype into an operational service. Within a Smart City digital ecosystem, this kind of system is best understood as one of several services that increase the convenience and transparency of citizens' interactions with public institutions, alongside identity services already in place.

Conclusion

This paper proposed and experimentally evaluated an electronic voting model that combines biometric identity verification using transformer and CNN architectures, frequency-domain information for detecting synthetic images, and blockchain-based result recording with controlled revoting. In the ViT-LoRA setting, the recognition module reached 97.48% validation accuracy according to the retained confusion matrix, outperforming the other configurations examined. The independent contribution of the frequency descriptor has not yet been quantified because no FFT ablation study was conducted. Controlled revoting is supported by pairing a self-destructing-ballot scheme with blockchain-recorded timestamp ordering, while the complete on-chain audit history is preserved. For production deployment, stronger timestamp guarantees and ballot-hiding commitments are still needed; these are implementation requirements, not properties experimentally validated by the current prototype.

In the future, we plan to assess the revoting scheme empirically rather than theoretically on a deployed network, explore privacy-preserving biometric authentication schemes, and enhance the deepfake-detection module's robustness against newer generation techniques. The proposed solution is intended as a technical foundation for further research into secure, transparent digital elections within Smart City infrastructure.

Funding

This research was funded by the Committee of Science of the Ministry of Science and Higher Education of the Republic of Kazakhstan (Grant No. BR24992852, "Intelligent models and methods of Smart City digital ecosystem for sustainable development and the citizens' quality of life improvement").

Competing Interests

The authors declare no competing interests.

REFERENCES

1 Hayath, T.M., Rajeev, D.V., Nihanth, R., Tharun, U.V., and Achutha, R. Digital Voting System with Face Recognition. International Journal of Scientific Research and Technology, 3 (1) (2026).

2 Dosovitskiy, A., Beyer, L., Kolesnikov, A., et al. An Image Is Worth 16×16 Words: Transformers for Image Recognition at Scale. In: Proceedings of the International Conference on Learning Representations (ICLR) (2021).

3 He, K., Zhang, X., Ren, S., and Sun, J. Deep Residual Learning for Image Recognition. In: Proceedings of the IEEE Conference on Computer Vision and Pattern Recognition (CVPR), pp. 770–778 (2016).

4 Alkishri, W., et al. An Improved Dense CNN Architecture for Deepfake Image Detection. IEEE Access, 11, 22081–22095 (2023).

5 Sheikh, M.S., Kirtonia, U., Arthi, N.T., and Al-Imran, M. AI-Powered Deepfake Detection Using CNN and Vision Transformer Architectures. arXiv preprint arXiv:2601.01281 (2026).

6 Wang, Z., Cheng, Z., Xiong, J., Xu, X., Li, T., Veeravalli, B., and Yang, X. A Timely Survey on Vision Transformer for Deepfake Detection. arXiv preprint arXiv:2405.08463 (2024).

7 Frank, J., Eisenhofer, T., Schönherr, L., Fischer, A., Kolossa, D., and Holz, T. Leveraging Frequency Analysis for Deep Fake Image Recognition. In: Proceedings of the International Conference on Machine Learning (ICML), PMLR, pp. 3247–3258 (2020).

8 Tan, C., Zhao, Y., Wei, S., Gu, G., Liu, P., and Wei, Y. Frequency-Aware Deepfake Detection: Improving Generalizability through Frequency Space Domain Learning. In: Proceedings of the AAAI Conference on Artificial Intelligence, 38, 5052–5060 (2024).

9 Nakamoto, S. Bitcoin: A Peer-to-Peer Electronic Cash System (2008). https://bitcoin.org

10 Ohize, H.O., Dogo, E.M., Onumanyi, A.J., Ibrahim, M.M., et al. Blockchain for Securing Electronic Voting Systems: A Survey of Architectures, Trends, Solutions, and Challenges. Cluster Computing, 28, Article No. 132 (2025).

11 Jafar, U., Ab Aziz, M.J., Shukur, Z., and Hussain, H.A. A Systematic Literature Review and Meta-Analysis on Scalable Blockchain-Based Electronic Voting Systems. Sensors, 22 (19), Article No. 7585 (2022).

12 Gandhi, S.S., Kiwelekar, A.W., Netak, L.D., and Wankhede, H.S. Security Requirement Analysis of Blockchain-Based E-Voting Systems. In: Intelligent Communication Technologies and Virtual Mobile Networks, Springer (2023).

13 Sharp, M., Njilla, L., Huang, C.-T., and Geng, T. Blockchain-Based E-Voting Mechanisms: A Survey and a Proposal. Network, 4 (4), 426–442 (2024).

14 El Kafhali, S., et al. Blockchain-Based Electronic Voting System: Significance and Requirements. Mathematical Problems in Engineering, 2024, Article No. 5591147 (2024).

15 Wang, B., Guo, F., Liu, Y., Li, B., and Yuan, Y. An Efficient and Versatile E-Voting Scheme on Blockchain. Cybersecurity, 7, Article No. 62 (2024).

16 Ghosh, V., and Gupta, H. A Blockchain-Based E-Voting System for Secure and Transparent Elections. In: ICT Systems and Sustainability (ICT4SD 2024), Lecture Notes in Networks and Systems, 1163, Springer, pp. 163–173 (2025).

17 Hajian Berenjestanaki, M., Barzegar, H.R., et al. Blockchain-Based E-Voting Systems: A Technology Review. Electronics, 13 (1), Article No. 17 (2024).

18 Paudel, S., Poudel, A., and Paudel, S. Enhancing Electoral Integrity and Accessibility: A Blockchain and Facial Recognition-Based Electronic Voting System. Information Dynamics and Applications, 4 (2), 85–94 (2025).

19 Aidynov, T., Goranin, N., Satybaldina, D., and Nurusheva, A. A Systematic Literature Review of Current Trends in Electronic Voting System Protection Using Modern Cryptography. Applied Sciences, 14, Article No. 2742 (2024). (Authors' own prior work; cited here as a self-citation.)

20 Vaswani, A., Shazeer, N., Parmar, N., et al. Attention Is All You Need. In: Advances in Neural Information Processing Systems, 30, 5998–6008 (2017).

21 Hu, E.J., Shen, Y., Wallis, P., et al. LoRA: Low-Rank Adaptation of Large Language Models. arXiv preprint arXiv:2106.09685 (2021).

22 Deng, J., Guo, J., Xue, N., and Zafeiriou, S. ArcFace: Additive Angular Margin Loss for Deep Face Recognition. In: Proceedings of the IEEE/CVF Conference on Computer Vision and Pattern Recognition (CVPR), pp. 4690–4699 (2019).

[1]Айдынов Т.,
докторант, ғылыми қызметкер, ORCID ID: 0009-0005-3327-9719,
e-mail: tolegen.ch@gmail.com
[1] Сатыбалдина Д.,
ф.-м.ғ.к., профессор, ORCID ID: 0000-0003-0291-4685,
e-mail: satybaldina_dzh@enu.kz
[2] Димитров В.,
PhD, профессор, ORCID ID: 0000-0002-5348-4948,
e-mail: v.dimitrov@unibit.bg
[1*]Абишева Г.,
PhD, ORCID ID: 0009-0003-6692-197X,
e-mail: gulsipat.abisheva@gmail.com

[1]Л.Н. Гумилев атындағы Еуразия ұлттық университеті,
Астана қ., Қазақстан
[2]Кітапханатану және ақпараттық технологиялар университеті,
София қ., Болгария

ДИПФЕЙККЕ ҚАРСЫ АУТЕНТИФИКАЦИЯСЫ БАР БИОМЕТРИЯЛЫҚ САЙЛАУШЫНЫ СӘЙКЕСТЕНДІРУГЕ НЕГІЗДЕЛГЕН БЛОКЧЕЙН ЭЛЕКТРОНДЫҚ ДАУЫС БЕРУ МОДЕЛІ

Аңдатпа

Мақалада блокчейн технологиясына негізделген дауыс беру нәтижелерін орталықтандырылмаған түрде сақтау, сайлаушыларды биометриялық сәйкестендіру және синтетикалық (deepfake) бет кескіндерін автоматты анықтау мүмкіндіктерін біріктіретін электрондық дауыс беру моделі ұсынылып, тәжірибелік тұрғыда расталған. Сайлаушының жеке басын тексеру үшін Low-Rank Adaptation (LoRA) әдісі арқылы бейімделген Vision Transformer және ResNet-50 архитектуралары қолданылады. Сонымен қатар бет ауыстыру (face swap) және синтетикалық генерациялау шабуылдарына төзімділікті арттыру мақсатында кіріс кескініне жылдам Фурье түрлендіруі (FFT) негізіндегі жиіліктік талдау жүргізіледі. Блокчейннің өзгермейтін табиғатына байланысты қайта дауыс беру мәселесін шешу үшін өзін-өзі жоятын бюллетеньдер мен қорғалған уақыт белгілеріне негізделген бақыланатын қайта дауыс беру механизмі ұсынылған. Дауыстар Ethereum смарт-келісімшарты арқылы тіркеледі. Эксперимент нәтижелері бойынша LoRA әдісімен бейімделген Vision Transformer моделі нақты және синтетикалық бет кескіндерін ажыратуда 97,36 % дәлдікке қол жеткізіп, LoRA арқылы бейімделген ResNet-50 моделінен айтарлықтай жоғары нәтиже көрсетті. Ұсынылған жүйе Smart City цифрлық инфрақұрылымының құрамдас бөлігі ретінде қарастырылып, құпиялылықты сақтайтын биометриялық хаттамалар мен сайлау процестеріне арналған ауқымды блокчейн платформаларын дамытуға негіз бола алады.

Түйін сөздер: электрондық дауыс беру, бетті тану, дипфейкті анықтау, блокчейн, Ethereum, смарт-келісімшарттар, Vision Transformer, ResNet, қайта дауыс беру механизмі, Smart City.

[1]Айдынов Т.,
докторант, научный сотрудник, ORCID ID: 0009-0005-3327-9719,
e-mail: tolegen.ch@gmail.com
[1]Сатыбалдина Д.,
к. ф.-м.н., профессор, ORCID ID: 0000-0003-0291-4685,
e-mail: satybaldina_dzh@enu.kz
[2]Димитров В.,
PhD, профессор, ORCID ID: 0000-0002-5348-4948,
e-mail: v.dimitrov@unibit.bg
[1*]Абишева, Г.,
PhD, ORCID ID: 0009-0003-6692-197X,
e-mail: gulsipat.abisheva@gmail.com

[1] Евразийский национальный университет им. Л.Н. Гумилева,
г. Астана, Казахстан
[2] Университет библиотековедения и информационных технологий,
г. София, Болгария

БЛОКЧЕЙН-ОРИЕНТИРОВАННАЯ МОДЕЛЬ ЭЛЕКТРОННОГО ГОЛОСОВАНИЯ С БИОМЕТРИЧЕСКОЙ ИДЕНТИФИКАЦИЕЙ ИЗБИРАТЕЛЕЙ И ЗАЩИТОЙ ОТ АТАК С ИСПОЛЬЗОВАНИЕМ ДИПФЕЙКОВ

Аннотация

В статье представлена и экспериментально апробирована модель электронной системы голосования, объединяющая децентрализованное хранение результатов на основе технологии блокчейн, биометрическую идентификацию избирателей и автоматическое обнаружение синтетически сгенерированных (deepfake) изображений лиц. Для проверки личности избирателя используются архитектуры Vision Transformer и ResNet-50, дообученные с применением метода Low-Rank Adaptation (LoRA). Дополнительная устойчивость к атакам с использованием подмены лица и синтетической генерации обеспечивается анализом входного изображения в частотной области с использованием быстрого преобразования Фурье (FFT). Для решения проблемы неизменяемости блокчейна предложен механизм контролируемого переголосования, основанный на самоудаляющихся бюллетенях и защищенных временных метках, при этом сами голоса фиксируются в смарт-контракте Ethereum. Экспериментальные результаты показали, что модель Vision Transformer с адаптацией LoRA достигает точности 97,36% при различении реальных и синтетических изображений лиц, значительно превосходя аналогичную модель ResNet-50. Предлагаемая система рассматривается как компонент цифровой инфраструктуры Smart City и может служить основой для дальнейших исследований в области биометрических протоколов с сохранением конфиденциальности и масштабируемых блокчейн-платформ для проведения выборов.

Ключевые слова: электронное голосование, распознавание лиц, обнаружение дипфейков, блокчейн, Ethereum, смарт-контракты, Vision Transformer, ResNet, механизм переголосования, Smart City.

UDC 004.056:004.75
IRSTI 20.23.17

https://doi.org/10.55452/1998-6688-2026-23-3-267-281

[1]Sakhipov A.A.,
PhD, Assistant Professor, ORCID ID: 0000-0003-1045-4199,
e-mail: aivar.sakhipov@astanait.edu.kz
[1*]Fedenko A.D.,
MSc, Teacher, ORCID ID: 0009-0000-2290-6995,
*e-mail: a.fedenko@astanait.edu.kz

[1]Astana IT University, Astana, Kazakhstan

ENSURING DATA INTEGRITY OF EXAMINATION RESULTS USING PERMISSIONED DISTRIBUTED LEDGER TECHNOLOGY

Abstract

The increasing use of centralised Student Information Systems (SIS) as part of the digitalisation of higher education has led to these systems being used despite the risk of unauthorised alteration of student data due to reliance of data entry and administration on one administrative trust domain. This paper presents the design and experimental validation of a Distributed Ledger Technology (DLT) architecture to provide verifiable integrity of examination results. The proposed architecture is based on a combination of an SQL-based SIS and a Hyperledger Fabric Blockchain via a secure middleware layer. Examination records in the SIS are converted to a cryptographic hash commitment and stored on an immutable ledger. Experimental validation was carried out by deploying a Hyperledger Fabric Network in a containerized environment and testing it using Hyperledger Caliper at workload levels up to 120,000 transactions. Key performance metrics were throughput, commit latency, ability to detect violations of data integrity and storage characteristics of the ledger. The proposed architecture achieved throughput of 728 transactions/second and maximum throughput of 842 transactions/second with average commit latency less than 2.0 seconds. Tampering tests were performed to verify the architecture's ability to detect unauthorised changes and it successfully detected all unauthorised changes with average detection time of 19.8ms. Analysis of storage requirements showed that the ledger grew linearly and would require less than 5.68 GB over ten years. The results demonstrate that the proposed architecture eliminates the single point of failure in centralized systems and provides scalable, cryptographically verifiable academic record integrity.

Keywords: distributed ledger technology, blockchain, data integrity, information security, Hyperledger Fabric, student information systems, academic records.

Received April 6, 2026; revised June 29, 2026; accepted August 24, 2026.

Introduction

Relatively recent large-scale digitalization of the field of higher education has resulted in the almost complete adoption of both Student Information Systems (SIS) and Learning Management Systems (LMS) in the use of centralized Relational Database Management Systems (RDBMS) for storing and managing student records. For purposes of this research, data integrity (DI) is defined as the property that once an academic record has been submitted by an authorized party, it will not be possible to alter the record without being detected; whereas, the term "verifiability" defines the capability of an unaffiliated third-party to independently verify through cryptography the validity of a submitted record without trusting the submitting entity. Although the reliability, scalability, and efficiency of centralized RDBMS architectures are well-documented, the fact that these systems can only function within a single administrative trust domain means that they are vulnerable to various forms of threats from privileged insiders including but not limited to, direct tampering with the

databases, modification of audit logs [1, 2]. These architectural limitations create an inherent risk to the overall integrity of the system, as unauthorized modifications made directly to the database could result in no evidence of such alterations remaining which would be subject to cryptographic proof [3, 4].

In this respect, existing limitations are especially concerning when it comes to managing results from examinations – because in this case, students' academic records represent the main evidence that support the issue of their qualifications as well as the employers who wish to verify those qualifications. Access control systems, transaction logging, and database replication mechanisms that exist within SISs (e.g., schools' student information systems) can protect against unauthorized use of these systems; however, they cannot provide the same level of mathematical guarantee regarding the immutability of these records using cryptography [5, 6]. Other studies have demonstrated how blockchain-based access control systems can be used to secure the private and integrity of an individual's academic record through the use of cryptography to verify academic credentials [7]. Therefore, despite the existence of such technologies, the institutional trust in students' academic records remains dependent upon central authority controls rather than the mathematically verifiable integrity of those records [8]. Studies have demonstrated that permissioned blockchain networks have greatly enhanced the level of data integrity and trust associated with them as opposed to traditional centralized database systems [9].

Distributed Ledger Technologies (DLTs) are emerging as an immutable, append-only and consensually validated data storage technology using cryptography to create a secure data infrastructure for recording data across multiple independent nodes [10, 11]. The literature has shown that Hyperledger Fabric's permissioned consensus model provides robust data integrity assurances and dependable transaction validation models [12]. For this study, DLT will be operationally defined as a permissioned decentralized system where data integrity is maintained via cryptographic hash functions, digital signatures and consensus protocols instead of by central authorities [13]. The vast majority of prior research into the application of educational blockchains have focused on the issuing of digital diplomas and the validation of credentials using public blockchain architectures [14]. Various implementations utilizing Hyperledger Fabric have illustrated the ability to securely and resistively manage academic credentials using decentralized verification models [15]. Other research has shown that blockchain-based examination monitoring and credentialing systems can increase academic integrity and build trust in digital assessment environments [16]. Although this demonstrates the practicality of validating credentials in a decentralized manner it does not show how to maintain the integrity of the examination records created during the academic lifecycle. Additionally, public blockchain architectures are subject to a number of limitations including privacy compliance issues, throughput limitations and unregulated participation from external networks limiting their use within academic institutions requiring the use of sensitive student data [5, 17].

This highlights a significant research need: the lack of experimentally verified architectures which can ensure the continuous, privacy-preserving, institutionally-controlled, and cryptographically-verifiable integrity protection of examination results at the point of generation in SIS environments of universities. In particular, current solutions are unable to generate a method of creating an unalterable record of examination results (a record anchored to a public immutable ledger) in near-real-time while meeting all of the necessary parameters of institutional access control, privacy, and scalability.

The objective of this paper is to create, develop, and experimentally test a permissioned DLT architecture which will ensure the cryptographically-verifiable integrity of examination results created by university information systems [18]. The architecture uses a Hyperledger Fabric-based permissioned blockchain and an existing SQL-based SIS via a secure API middleware layer. The architecture utilizes SHA-256 cryptographic hashing, X.509-based digital identity management, and multi-endorsed smart contracts to create immutable integrity-proof records of examinations without storing any personally identifiable information on chain.

The key scientific contribution of this research is the experimental validation of a hybrid SIS-DLT architecture for deterministic detection of unauthorized modifications using cryptographic integrity verification. Results suggest that integrating permissioned blockchain with an academic database substantially reduces the single-point-of-failure risk present in centralised architectures while maintaining operational performance sufficient for university-scale workloads.

Materials and methods

The system was designed as a hybrid integrity assurance architecture integrating a centralized SIS with a permissioned DLT network implemented using Hyperledger Fabric v2.5 [10, 19]. The SIS, implemented on PostgreSQL v15, functioned as the authoritative data source for academic records, while the blockchain layer served as an independent, append-only integrity verification layer maintaining cryptographic commitments to examination results. Transaction mediation, identity authentication, and integrity commitment generation were performed by an API gateway implemented in Node.js, which isolated the operational database from direct blockchain interaction and enforced strict access control [20, 21]. The overall system architecture and trust boundaries are illustrated in Figure 1.

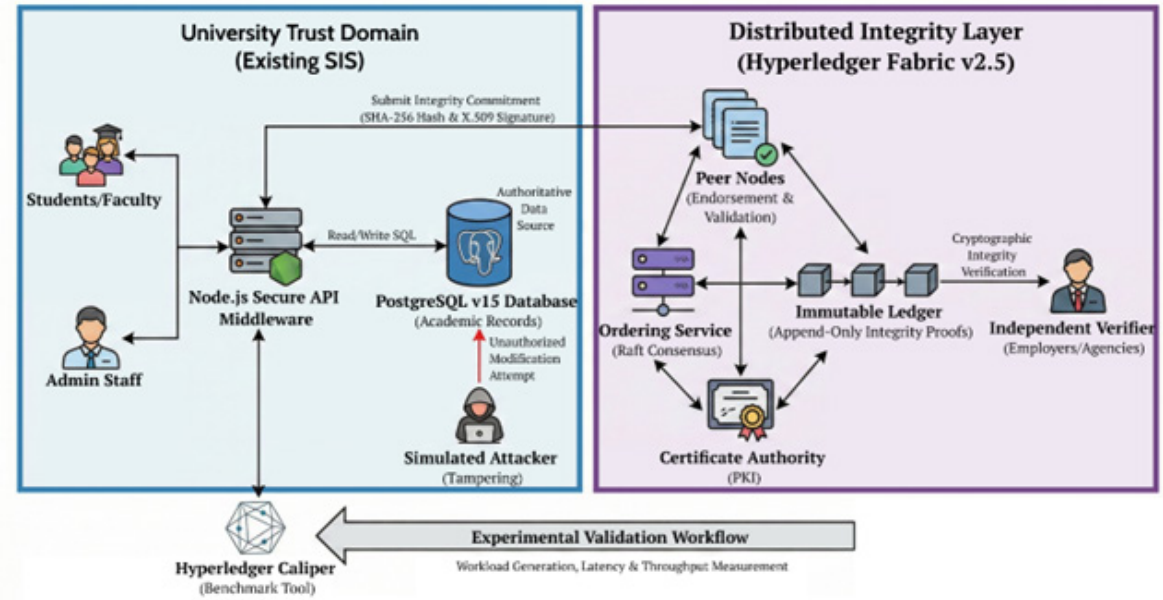


Figure 1 – Hybrid SIS–DLT integrity verification architecture and validation workflow

The integrity model was formally defined as a state consistency verification problem between two independent storage domains: a mutable operational database and an immutable distributed ledger. Let denote the SIS database state at time , and denote the ledger state representing the sequence of committed integrity proofs; integrity preservation is satisfied if and only if every committed academic record in corresponds to a unique, previously committed ledger state entry and no ledger entry can be modified, removed, or reordered. Integrity verification was carried out as a deterministic state reconciliation (reconciliation is a process for identifying discrepancies) where SIS data records are converted to canonical form, hashed with SHA-256 and compared to ledger commitments that were indexed with composite identifiers [2, 14]. Due to the pre-image resistance and collision resistance characteristics of SHA-256, any changes made to SIS records after the ledger has been committed would result in a detectable divergence of states. The complete integrity commitment and verification workflow is illustrated in Figure 2.

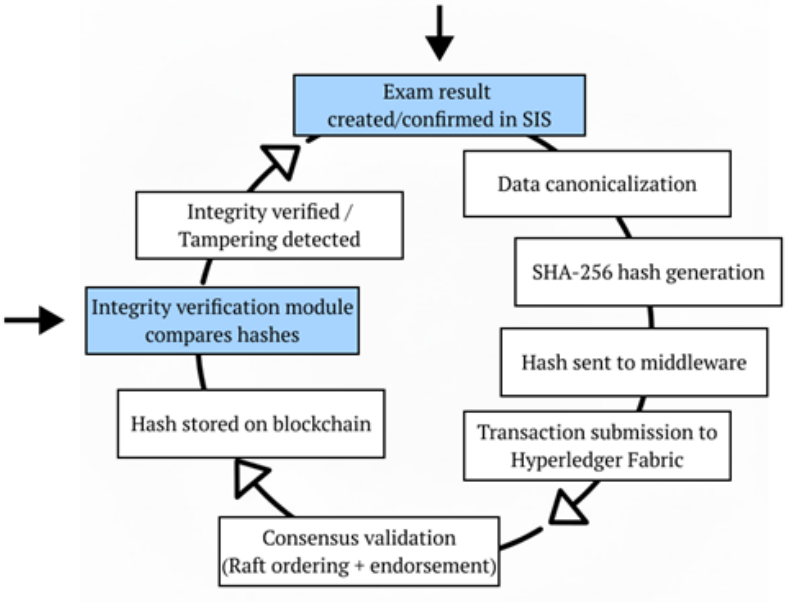


Figure 2 – Continuous integrity verification workflow
and blockchain hash anchoring process

The blockchain network was deployed as a permissioned consortium with authenticated peer nodes representing independent trust domains and coordinated using the Raft consensus protocol [22, 23]. Each transaction required cryptographic authentication via X.509 certificates issued by the Hyperledger Fabric Certificate Authority and validation through smart contract logic enforcing endorsement policies [24]. The smart contract implemented deterministic state transition rules ensuring that only valid, authenticated, and consensus-endorsed integrity commitments could be appended to the ledger. This architecture eliminated the single point of failure characteristic of centralized systems and ensured that no single administrative entity could unilaterally modify committed integrity proofs.

Experimental validation was performed with the use of a server which is specifically designated for the purposes of evaluating blockchain performance. A total of three peer nodes and one ordering node along with a single certificate authority node were created by deploying each of them as Docker containers on an instance of Ubuntu Server 22.04. To ensure that there would be no hardware-based performance bias and to enable the ability to reproduce results with identical configurations each of the nodes had been allocated equal virtualized hardware (SSD storage; 4 vCPUs; 8 GB RAM). In addition to these configuration specifications, the server environment was designed to represent a real-world institutional implementation of a blockchain solution by utilizing a number of key features such as persistent ledger storage, secure cryptographic identity management and network isolation. Hyperledger Caliper was utilized to generate transactional workloads that simulated the act of submitting and verifying student examination results during realistic academic workload conditions [25]. Key system configuration parameters are listed in Table 1.

Integrity verification effectiveness was measured as the system's ability to detect unauthorized record modification under controlled tampering scenarios. Detection latency, defined as the elapsed time between unauthorized database modification and integrity violation detection, was recorded for each experimental run. System performance was evaluated in terms of transaction throughput, commit latency, and resource utilization under increasing workload intensity. The experimental workflow and integrity verification process are shown in Figure 1.

Table 1 – Experimental system configuration and integrity validation parameters

Parameter	Specification	Function
Blockchain platform	Hyperledger Fabric v2.5	Distributed integrity ledger
Consensus mechanism	Raft	Deterministic transaction ordering
Identity framework	X.509 PKI	Cryptographic authentication
Hash function	SHA-256	Integrity commitment generation
Smart contract runtime	Go chaincode	Integrity validation logic
State database	CouchDB	Ledger state indexing
Operational database	PostgreSQL v15	SIS academic record storage
Middleware	Node.js v20	Transaction mediation
Benchmark tool	Hyperledger Caliper	Performance and integrity testing
Deployment environment	Docker, Ubuntu Server 22.04	Reproducible distributed execution

Results and discussion

The experimental evaluation was conducted to assess the performance, scalability, and integrity enforcement capability of the proposed SIS–DLT architecture under realistic academic workload conditions. A total of 120,000 examination record transactions were generated and submitted to the system over multiple benchmark runs, simulating grade submission patterns typical of midterm and final examination periods. The system demonstrated stable and predictable behavior throughout the experimental period, with no observed transaction failures, ledger inconsistencies, or state divergence under normal operating conditions [11, 22]. These results are consistent with reliable operation under sustained institutional workloads without compromising integrity guarantees.

Transaction throughput, commit latency, and peer node CPU utilization were measured across a range of workload intensities from 50 TPS to 850 TPS to evaluate system scalability and resource efficiency under increasing transactional load. The system achieved a mean sustained throughput of 728 TPS and reached a maximum throughput of 842 TPS before performance saturation occurred due to endorsement validation overhead and ordering service batching constraints [17, 21]. Mean transaction commit latency remained below 0.6 seconds at moderate load levels (≤300 Transactions Per Second, TPS) and increased progressively to 1.97 seconds at peak load, reflecting predictable consensus processing and cryptographic validation overhead [10, 23].

Peer node CPU utilization increased proportionally with transaction throughput, reaching a mean utilization of 63% and a maximum of 71% at peak workload intensity, indicating efficient utilization of available computational resources without exceeding operational capacity limits.

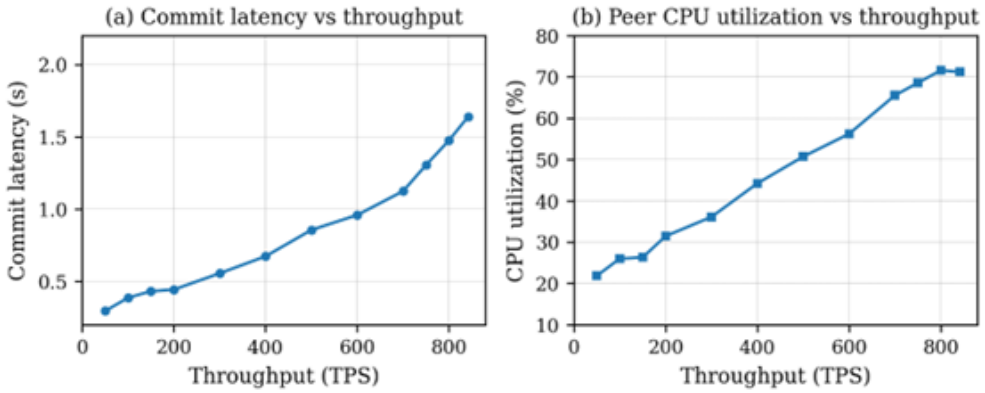


Figure 3 – System performance versus transaction throughput:
(a) commit latency; (b) CPU utilization

The primary reason for the observed latency increases as workload increases is due to the required processes for validating endorsements, i.e., verifying the signatures via cryptography and checking the state consistency among multiple peer nodes. Unlike probabilistic consensus methods (e.g. proof-of-work) utilized by most public blockchains, Raft uses a deterministic method of achieving finality for committed transactions; this means that once a transaction has been finalized it cannot be reversed or forked. The deterministic commit model also provides certainty when validating the integrity of information committed to the ledger; therefore, after an academic record is committed to the ledger, the record will always be verifiably permanent. The measured latency values are still within operational limits since examination result submissions are generally non-latency sensitive and are submitted in batch submissions.

Long duration benchmark testing was performed on the testbed at high transaction rates in order to assess the systems stability when operating under prolonged periods of high workload conditions. Results from these tests showed that the system continued to operate stably for extended periods of time with no indication of resources being exhausted, no memory leaks occurring and no overall degradation in system performance. Average memory usage remained relatively constant at approximately 588MB of memory per peer node during the entire testing period, thus providing supporting evidence of the efficiency of the blockchain execution environment. CPU and Memory usage for each peer node remained temporally consistent during prolonged periods of continuous operation and is shown in Figure 4. As can be seen there is no upward trend in memory usage indicating no memory leaks occurred, and thus the system's ability to execute for extended periods of time was demonstrated.

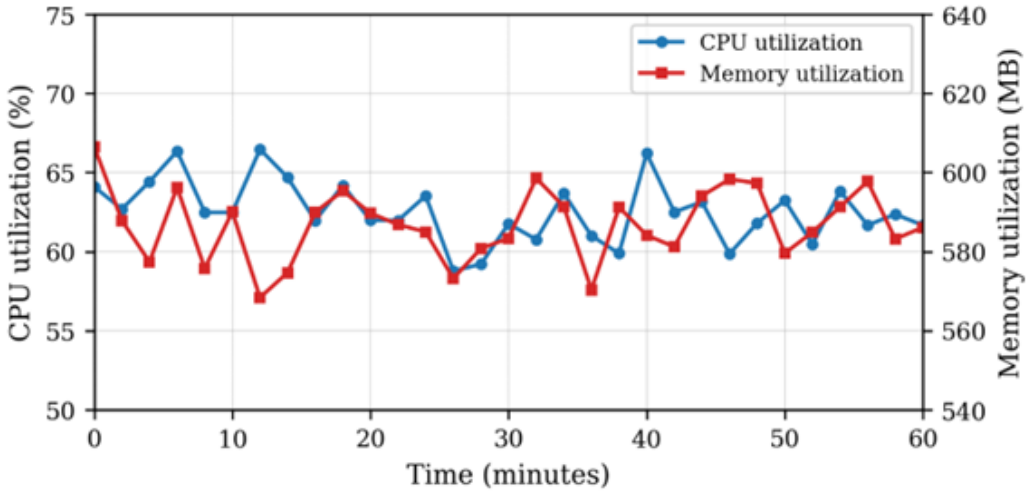


Figure 4 – Peer node CPU and memory utilization over time under sustained workload

These results suggest that the computational overhead associated with cryptographic integrity enforcement may remain within the operational capacity of standard institutional server infrastructure. The ordering service exhibited significantly lower resource utilization compared to peer nodes, confirming that endorsement validation and signature verification represent the dominant computational cost. This finding aligns with the expected performance characteristics of permissioned blockchain architectures, where integrity assurance is enforced through cryptographic verification rather than computational consensus competition. The observed resource utilization indicates that the proposed architecture may be deployable using conventional university virtual infrastructure without requiring specialised hardware.

Integrity protection effectiveness was evaluated using controlled database tampering experiments designed to simulate insider threats and privileged database compromise scenarios [4]. The verification

cycle shown in Figure 2 ensures continuous integrity monitoring independent of database trust assumptions. Unauthorized modifications were performed directly on the SIS PostgreSQL database after ledger commitment, including grade alteration, timestamp modification, record overwriting, and record deletion. Each modification attempt resulted in a detectable integrity violation due to mismatch between the recomputed SIS hash and the immutable ledger commitment. The detection performance results are summarized in Table 2.

Table 2 – Integrity violation detection performance under controlled database tampering scenarios

Attack type	Attempts (n)	Detection rate (%)	Latency (ms) min / mean / max
Grade modification	400	100	11 / 16.8 / 29
Timestamp modification	200	100	12 / 18.9 / 34
Record overwrite	150	100	15 / 22.1 / 41
Record deletion	150	100	17 / 23.4 / 46
Privileged bulk tampering	100	100	19 / 27.5 / 52
Total	1000	100	11 / 19.8 / 52

The system detected all 1,000 attack attempts (100% detection rate), indicating that database integrity was not compromised in any of the controlled tampering scenarios. In addition, the mean detection latency for all attacks was less than 52 ms, indicating that integrity violations were detected close to the time of the attack. The detection latency for these attacks is much better than other common methods of detecting integrity violations using audit logs of database transactions which are dependent upon an administrative control or policy and therefore do not provide a guarantee of integrity.

Additionally, the impact of performing integrity verification as part of the overall SIS system operation was determined and the performance of integrity verification queries were evaluated. The mean integrity verification time for the integrity verification queries was found to be 34 milliseconds. The maximum integrity verification time observed was 61 milliseconds. These results indicate that the integrity verification queries impose low overhead and may therefore be executed continuously without measurable degradation of SIS responsiveness.

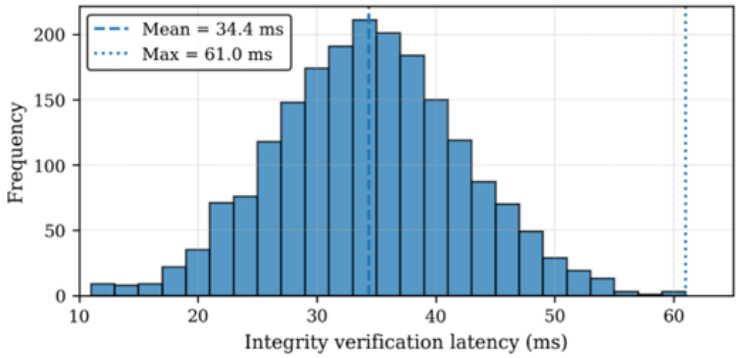


Figure 5 – Integrity verification latency distribution under operational workload

Ledger storage growth analysis indicated that blockchain storage requirements appear manageable and scale approximately linearly with transaction volume. The mean transaction size, including cryptographic signatures and metadata, was measured at 2.41 KB per examination record. Based on this measurement, an institution generating 100,000 examination records per year would produce approximately 241 MB of annual ledger growth. Storage growth projections are presented in Table 3.

Table 3 – Blockchain ledger storage growth and scalability projection under institutional workload

Parameter	50,000 records/year	100,000 records/year	200,000 records/year
Mean transaction size	2.41 KB	2.41 KB	2.41 KB
Mean daily transactions	137	274	548
Mean block size	0.33 MB	0.66 MB	1.32 MB
Blocks generated per year	152	305	610
Annual ledger growth	120 MB	241 MB	482 MB
CouchDB index overhead (~18%)	22 MB	43 MB	87 MB
Total annual storage footprint	142 MB	284 MB	569 MB
5-year cumulative growth	710 MB	1.42 GB	2.84 GB
10-year cumulative growth	1.42 GB	2.84 GB	5.68 GB

As previously mentioned, there were other studies done on the performance of Hyperledger Fabric, where it was shown that the ledger grew at a rate less than 5 GB over multiple years of institutional usage as long as they used off chain data storage and made on-chain commitments to the integrity of their data [26, 27]. By utilizing a hybrid approach where only the commitments for the cryptographic verification of the records are stored on the blockchain and the complete records for all students are kept in the Student Information System (SIS) database, we can significantly reduce the need for storage space for the blockchain while still maintaining the level of cryptographic verifiability needed. Therefore, the proposed model will meet the requirement for the scalability of continuously protecting the integrity of student records without creating any new bottlenecks or constraints in terms of infrastructure.

Although the proposed architecture has shown its feasibility as well as advantages regarding security and privacy, it increases the time needed to confirm transactions, i.e., the time for committing transactions when compared to the classical central databases that usually allow a write operation within milliseconds. As indicated above, the blockchain based commit latency of approximately 0.5 – 2.0 seconds includes the computational effort for cryptographic validations and the enforcement of the consensus process (i.e., (1) hash computation and digital signature verification; (2) multi-node endorsement validation; (3) consensus-based ordering of transactions). It has been also reported in other studies that evaluate the performance of the Hyperledger Fabric blockchain framework that similar delay characteristics are present in order to achieve a deterministic finality of the transactions, while the delay times for the commit operation range from 0.4 to 3.0 seconds dependent on the chosen endorsement policy and number of nodes in the network [28, 29]. The results obtained during the experimentation show that these delays do not affect the usability of the application because the submission of examination records is an interactive administrative process rather than a real-time transaction with high latency requirements. From a systems engineering perspective, this delay represents an acceptable tradeoff in order to obtain strong integrity guarantees that cannot be obtained through classical central database architectures.

To contextualise the proposed SIS–DLT architecture, it is necessary to distinguish it from established non-blockchain approaches to database integrity assurance. The principal alternatives applicable to academic information systems include: (i) integrity-coded database schemes, (ii) write-once read-many (WORM) storage solutions, (iii) database-level audit logging, and (iv) hash-based file integrity monitoring. ICDB approaches [30] embed cryptographic integrity codes directly into the relational schema and verify query correctness at retrieval time; however, they rely on a trusted client agent and do not produce a consensus-validated integrity record accessible to external verifiers. WORM solutions prevent post-write modification but are administered by the same entity controlling the source data, placing the trust boundary at the assumed threat actor. Audit log frameworks record modification events within the database layer, where a sufficiently privileged insider can suppress entries prior to detection [31]. The critical distinction of the proposed architecture is that the integrity commitment chain is maintained by independent peer nodes under Byzantine fault-tolerant consensus,

ensuring that no single administrator can modify committed hash records without consensus approval from the remaining peer organizations. A comparative summary is presented in Table 4.

Table 4 – Comparative analysis of database integrity assurance approaches

Property	Proposed SIS–DLT	Integrity Coded DB [30]	WORM Storage	Audit Log Framework [31]
Trust model	Distributed consensus (multi-node)	Trusted client agent	Centralized administrator	Centralized DBMS layer
Insider tamper resistance	Yes – consensus-enforced	Partial – agent-dependent	Partial – admin-dependent	No – logs modifiable
Tamper detection	Cryptographic hash divergence	IC mismatch at query time	Not applicable (prevention only)	Policy-dependent review
Mean detection latency	19.8 ms (this study)	Query execution time	N/A	Post-event review
External verifiability	Yes — auditable within consortium	No	No	No
Single point of trust	Eliminated	Present (ICDB agent)	Present (storage admin)	Present (DBMS layer)
Performance overhead	Moderate (< 2 s commit latency)	Moderate (query verification)	Minimal	Minimal
Cryptographic mechanism	SHA-256 + Merkle tree + X.509	MAC-based integrity codes	Optional hash digest	None by default
Ongoing storage growth	Linear (2.41 KB/ transaction)	Linear (IC + placeholder overhead)	Linear	Linear

The high level of throughput from our experimental testing also illustrates that the proposed architecture could be implemented on an institutional scale, and still achieve performance that would not degrade. The architecture was able to sustain throughputs of over 728 TPS with peak throughputs reaching 842 TPS, both numbers far exceeding normal university SIS environment requirements for the volume of grades submitted during peak times for exams (i.e., 50-100 TPS). The architecture's performance is consistent with previous studies on permissioned blockchain systems that have found that consensus protocols like Raft result in much greater throughput and lower latency than do public blockchain consensus methods [26, 29]. Our measured linear scalability until saturation indicates that this architecture can handle increased institutional size and workloads, along with increased student populations, without impacting its performance. This type of scalability is critical to maintaining the viability of blockchain based systems designed to ensure academic integrity.

There are several limits to this proposed architecture that need to be taken into account when implementing in a real-world deployment scenario. First, blockchains only protect integrity after data has been committed to the blockchain, therefore, organizational controls and multi-party validation processes will continue to be required to prevent incorrect or fraudulent submissions at the time of data entry. Second, the introduction of additional infrastructure for the deployment of blockchain nodes, certificate authority management, and secure cryptography key management, etc., adds to the overall complexity of deploying the architecture versus traditional SIS architectures. Finally, although the Raft consensus protocol offers highly efficient and deterministic transaction ordering, it assumes that all peer nodes involved in the consensus process will be available and that they will not introduce faults in the process; thus, some additional fault tolerance mechanisms may be required to protect against failures in geographically distributed implementations. These limits highlight the importance of designing blockchain integrity assurance with robust institutional governance and operational security frameworks [32].

The Node.js middleware layer represents a trust boundary not fully captured by the blockchain consensus model. The middleware is responsible for SHA-256 hash computation, X.509 transaction signing, and submission to the Fabric peer network. A compromised instance could submit incorrect hash commitments to the ledger without the consensus mechanism detecting the discrepancy, since consensus validates cryptographic structure rather than the semantic relationship between committed hashes and the source database state. In the current implementation, this risk is mitigated through: (i) X.509 identity credentials issued by the Fabric Certificate Authority, providing non-repudiation and enabling post-hoc attribution of anomalous commitments; (ii) deployment within a network-isolated application tier; and (iii) periodic cross-validation by independent peer node operators. Complete elimination of this trust boundary would require in-database hash computation via database-native triggers, which represents a direction for future architectural refinement.

The architecture raises privacy considerations relevant to jurisdictions subject to personal data protection regulations. The proposed system stores only SHA-256 hash commitments on-chain; examination records, student identifiers, and associated metadata remain exclusively within the operational SIS database. This off-chain design is consistent with GDPR data minimization principles and has been validated for academic certification contexts [33]. However, the cryptographic binding between on-chain commitments and database records enables record-level inference if both components are simultaneously compromised. Additionally, the right to erasure under applicable data protection law requires consideration: while off-chain records can be deleted in accordance with institutional retention policies, on-chain hash commitments remain permanently anchored. Institutional deployment should therefore be accompanied by legal assessment of hash-only on-chain entries under applicable data protection law, as regulatory guidance on this classification continues to evolve [33].

Practical deployment additionally requires consideration of governance factors beyond technical performance. Permissioned blockchain networks require frameworks addressing node membership policies, endorsement policy configuration, channel management, certificate lifecycle, and chaincode versioning procedures. Research on blockchain adoption in higher education identifies governance complexity and regulatory compliance requirements as significant inhibitors that substantially extend practical implementation timelines beyond what technical benchmarks suggest [34]. The overhead of maintaining Hyperledger Fabric infrastructure – including Certificate Authority management, peer software updates, cryptographic key rotation, and ledger backups – represents an administrative burden that must be absorbed by institutional IT governance. These governance considerations do not diminish the integrity assurance value of the architecture but constitute essential contextual factors for decision-makers assessing deployment feasibility and total cost of ownership.

A further limitation is that experimental validation was conducted exclusively within a single-institution SIS deployment context. The reported performance characteristics, tamper detection accuracy, and storage scalability projections reflect this specific environment and should not be extrapolated uncritically to multi-institution consortium configurations. The mean throughput of 728 TPS observed under single-institution conditions may decrease in multi-organization deployments due to increased cross-organizational endorsement latency and inter-peer communication overhead. Research on blockchain adoption in higher education further highlights that consortium deployments introduce additional challenges related to data schema standardization, interoperability with heterogeneous SIS infrastructures, and alignment of institutional governance obligations [34] – none of which were evaluated in this study. Extension to consortium settings is identified as a priority direction for future research.

The practical applicability and scientific significance of the proposed architecture extend beyond examination result protection and support broader academic data integrity assurance scenarios [35, 36]. The system enables (1) deterministic detection of unauthorized academic record modification, (2) elimination of the single point of failure inherent in centralized database architectures, and (3) independent cryptographic verification of academic record authenticity by external entities such as employers and accreditation bodies. These capabilities directly address

longstanding challenges in academic credential verification and digital trust management [37]. From a scientific perspective, this work provides evidence that permissioned DLT may function as a scalable and operationally feasible integrity assurance layer, rather than merely a credential issuance mechanism. The architecture therefore represents a meaningful contribution to the application of distributed ledger technology to securing academic information systems.

Future research should extend the architecture to multi-institution consortium networks for decentralized academic record verification across universities, accreditation agencies, and governmental organizations. Additional directions include automated grading system integration, anomaly detection for suspicious grading patterns, and post-quantum cryptographic mechanisms for long-term security resilience.

Conclusion

This study designed and validated a hybrid SIS-DLT architecture using Hyperledger Fabric for cryptographic integrity verification of examination records. The system achieved 728 TPS mean throughput (842 TPS peak) with commit latency below 2 seconds, and demonstrated 100% detection of unauthorized modifications with detection latency under 52 ms.

The results indicate that integrating permissioned blockchain technology with a centralized academic database substantially reduces the single point of failure risk of administratively-controlled SIS environments by replacing institutionally-anchored trust with cryptographically-enforced integrity commitments validated by independent peer organizations. The hybrid off-chain and on-chain model offers a potentially feasible balance between operational scalability and integrity assurance, with experimental results providing initial support for its applicability to real-world higher education environments under the deployment and governance conditions discussed above. It should be noted, however, that the evaluated architecture represents a single-institution implementation, and that multi-institution consortium deployments would introduce additional technical and governance considerations not captured in the present experimental scope.

Within the experimental parameters evaluated, the proposed system demonstrated scalable and stable performance characteristics consistent with institutional-scale deployment requirements, and the cryptographic commitment model enables independent verification of examination record integrity by authorized parties outside the institutional administrative chain. These findings contribute supporting evidence for permissioned distributed ledger technology in academic data integrity assurance, while the identified limitations – regarding single-institution scope, middleware trust assumptions, governance overhead, and privacy regulatory considerations – provide concrete directions for subsequent research and architectural refinement.

REFERENCES

1 Cardenas-Quispe, M.A., and Pacheco, A. Blockchain ensuring academic integrity with a degree verification prototype. Scientific Reports, 15 (1), 9281 (2025). https://doi.org/10.1038/s41598-025-93913-6

2 Chaudhari, S., and Shirole, M. Blockchain-driven academic learning record management in higher education: A comprehensive review of methodologies, applications, benefits, and challenges. SN Computer Science, 6 (5), 427 (2025). https://doi.org/10.1007/s42979-025-03952-z

3 Sangeetha, A.S., and Shunmugan, S. Privacy-enabled academic certificate authentication and deep learning-based student performance prediction system using Hyperledger blockchain technology. Journal of Parallel and Distributed Computing, 204, 105119 (2025). https://doi.org/10.1016/j.jpdc.2025.105119

4 Khaleelullah, S., Vangapalli, S.T., Gaddam, M., Hanumakonda, V.S., and Gangapuram, U.K.G. Verification of academic records using Hyperledger Fabric and IPFS. Proceedings of the 3rd International Conference on Pervasive Computing and Social Networking (ICPCSN), 210–217 (2023). https://doi.org/10.1109/ICPCSN58827.2023.00040

5 Ajwalia, M., and Shah, P. Performance comparison of permissioned and permissionless blockchain by varying workload transaction. BenchCouncil Transactions on Benchmarks, Standards and Evaluations, 5 (4), 100251 (2025). https://doi.org/10.1016/j.tbench.2025.100251

6 Cheng, H., Lu, J., Xiang, Z., and Song, B. A permissioned blockchain-based platform for education certificate verification. Lecture Notes in Computer Science, 456–471 (2020). https://doi.org/10.1007/978-981-15-9213-3_36

7 Saleh, O.S., Ghazali, O., and Idris, N.B. Enhancing academic certificate privacy with a Hyperledger Fabric blockchain-based access control approach. SN Computer Science, 4 (5), 602 (2023). https://doi.org/10.1007/s42979-023-02060-0

8 El Koshiry, A., Eliwa, E., Abd El-Hafeez, T., and Shams, M.Y. Unlocking the power of blockchain in education: An overview of innovations and outcomes. Blockchain: Research and Applications, 4 (4), 100165 (2023). https://doi.org/10.1016/j.bcra.2023.100165

9 Kadhum, O.I., and Hamad, A.H. Performance evaluation of multi-organization e-government based on Hyperledger Fabric blockchain platform. Ingénierie des Systèmes d'Information, 28 (2), 499–507 (2023). https://doi.org/10.18280/isi.280227

10 Guggenberger, T., Sedlmeir, J., Fridgen, G., and Luckow, A. An in-depth investigation of the performance characteristics of Hyperledger Fabric. Computers and Industrial Engineering, 173, 108716 (2022). https://doi.org/10.1016/j.cie.2022.108716

11 Khan, M.M., Khan, F.S., Nadeem, M., Khan, T.H., Haider, S., and Daas, D. Scalability and efficiency analysis of Hyperledger Fabric and private Ethereum in smart contract execution. Computers, 14 (4), 132 (2025). https://doi.org/10.3390/computers14040132

12 Lohachab, A., Garg, S., Kang, B.H., and Amin, M.B. Performance evaluation of Hyperledger Fabric-enabled framework for pervasive peer-to-peer energy trading in smart cyber–physical systems. Future Generation Computer Systems, 118, 392–416 (2021). https://doi.org/10.1016/j.future.2021.01.023

13 Berrios Moya, J.A., Ayoade, J., and Uddin, M.A. A zero-knowledge proof-enabled blockchain-based academic record verification system. Sensors, 25 (11), 3450 (2025). https://doi.org/10.3390/s25113450

14 Xu, Y. Development of blockchain-based academic credential verification system. Open Access Library Journal, 11 (9), 1–20 (2024). https://doi.org/10.4236/oalib.1112130

15 Pulmano, C.E., Estuar, M.R.J.E., De Leon, M.M., Tan, H.C.L., Co, N.A.S., and Tamayo, L.P.V. Towards the development of a blockchain-based decentralized digital credential system using Hyperledger Fabric for participatory governance. Procedia Computer Science, 219, 99–106 (2023). https://doi.org/10.1016/j.procs.2023.01.269

16 Sakhipov A. Beyond face recognition: A multi-layered approach to academic integrity in online exams / A. Sakhipov, I. Omirzak, A. Fedenko // Electronic Journal of e-Learning. – 2025. – № 23(1). – P. 81–95. https://doi.org/10.34190/ejel.23.1.3896.

17 Thakkar, P., Nathan, S., and Viswanathan, B. Performance benchmarking and optimizing Hyperledger Fabric blockchain platform. Proceedings of the IEEE International Symposium on Modeling, Analysis, and Simulation of Computer and Telecommunication Systems (MASCOTS), 264–276 (2018). https://doi.org/10.1109/MASCOTS.2018.00034

18 Panwar, A., Sugandh, U., Jain, A., Jain, V., Kumar Dubey, A.K., Majumdar, S., and Mallik, S. Enhancing trust and transparency in education using blockchain: A Hyperledger Fabric-based framework. Artificial Intelligence and Applications (2025). https://doi.org/10.47852/bonviewAIA52026268

19 Dreyer, J., Fischer, M., and Tönjes, R. Performance analysis of Hyperledger Fabric 2.0 blockchain platform. Proceedings of the Workshop on Cloud Continuum Services for Smart IoT Systems, 32–38 (2020). https://doi.org/10.1145/3417310.3431398

20 Das, S.R., Zaman, N., Asirvatham, D., Ashfaq, F., Masud, M., and Shorfuzzaman, M. Empirical performance analysis of Hyperledger Fabric. SSRN Electronic Journal (2025). https://doi.org/10.2139/ssrn.5127328

21 Sadath, M.L., Mehrotra, D., and Kumar, A. Scalability performance analysis of blockchain using hierarchical model in healthcare. Blockchain in Healthcare Today, 7 (1) (2024). https://doi.org/10.30953/bhty.v7.295

22 Nasir, Q., Qasse, I.A., Abu Talib, M., and Nassif, A.B. Performance analysis of Hyperledger Fabric platforms. Security and Communication Networks, 2018, 1–14 (2018). https://doi.org/10.1155/2018/3976093

23 Enare Abang, J., Takruri, H., Al-Zaidi, R., and Al-Khalidi, M. Latency performance modelling in Hyperledger Fabric blockchain: Challenges and directions with an IoT perspective. Internet of Things, 26, 101217 (2024). https://doi.org/10.1016/j.iot.2024.101217

24 Khan, D., Jung, L.T., Hashmani, M.A., and Cheong, M.K. Empirical performance analysis of Hyperledger LTS for small and medium enterprises. Sensors, 22 (3), 915 (2022). https://doi.org/10.3390/s22030915

25 Zulkarnain, M.M., Ramli, N., and Nordin, A.N. Performance benchmarking of Hyperledger Fabric on heterogeneous hardware for IoT applications. IIUM Engineering Journal, 26 (3), 156–170 (2025). https://doi.org/10.31436/iiumej.v26i3.3610

26 Honar Pajooh, H., Rashid, M.A., Alam, F., and Demidenko, S. Experimental performance analysis of a scalable distributed Hyperledger Fabric for a large-scale IoT testbed. Sensors, 22 (13), 4868 (2022). https://doi.org/10.3390/s22134868

27 Lu, N., Zhang, Y., Shi, W., Kumari, S., and Choo, K.K.R. A secure and scalable data integrity auditing scheme based on Hyperledger Fabric. Computers and Security, 92, 101741 (2020). https://doi.org/10.1016/j.cose.2020.101741

28 Honar Pajooh, H., Rashid, M., Alam, F., and Demidenko, S. Hyperledger Fabric blockchain for securing the edge Internet of Things. Sensors, 21 (2), 359 (2021). https://doi.org/10.3390/s21020359

29 Jung, S., Yoo, Y., Yang, G., and Yoo, C. Prediction of permissioned blockchain performance for resource scaling configurations. ICT Express, 10 (6), 1253–1258 (2024). https://doi.org/10.1016/j.icte.2024.09.003

30 Yeh, J.-H., Arifin, M.M., Shen, N., Karki, U., Xie, Y., and Nanjundarao, A. Integrity coded databases – protecting data integrity for outsourced databases. Computers & Security, 136, 103569 (2024). https://doi.org/10.1016/j.cose.2023.103569

31 Deep, G., Sidhu, J., and Mohana, R. Insider threat prevention in distributed database as a service cloud environment. Computers & Industrial Engineering, 169, 108278 (2022). https://doi.org/10.1016/j.cie.2022.108278

32 Psarra, E., Apostolou, D., Verginadis, Y., Patiniotakis, I., and Mentzas, G. Permissioned blockchain network for proactive access control to electronic health records. BMC Medical Informatics and Decision Making, 24 (1), 303 (2024). https://doi.org/10.1186/s12911-024-02708-8

33 Gómez Vieites, A., Delgado-von-Eitzen, C., and Estévez Garcia, D. GDPR-compliant academic certification via blockchain: legal and technical validation of the GAVIN Project. Applied Sciences, 15 (16), 9191 (2025). https://doi.org/10.3390/app15169191

34 Pathak, B., Alakkad, M.F., and Kumar, V. Institutional environment and the use of blockchain technology: exploring the context and conditions of using blockchain in higher education institutions. Higher Education Quarterly, 79 (3), e70034 (2025). https://doi.org/10.1111/hequ.70034

35 Dias, P., Gonçalves, H., Silva, F., Duque, J., Martins, J., and Godinho, A. Blockchain technologies: A scrutiny into Hyperledger Fabric for higher educational institutions. Procedia Computer Science, 237, 213–220 (2024). https://doi.org/10.1016/j.procs.2024.05.098

36 Jaafar, R.A., and Alsaad, S.N. Enhancing educational certificate verification with blockchain and IPFS: A decentralized approach using Hyperledger Fabric. TEM Journal, 2385–2395 (2023). https://doi.org/10.18421/TEM124-51

37 Silaghi, D.L., and Popescu, D.E. A systematic review of blockchain-based initiatives in comparison to best practices used in higher education institutions. Computers, 14 (4), 141 (2025). https://doi.org/10.3390/computers14040141

[1]Сахипов А.А.,
PhD, ассистент профессор, ORCID ID: 0000-0003-1045-4199,
e-mail: aivar.sakhipov@astanait.edu.kz
[1*]Феденко А.Д.,
магистр, оқытушы, ORCID ID: 0009-0000-2290-6995,
*e-mail: a.fedenko@astanait.edu.kz

[1]Astana IT University, Astana, Kazakhstan

ТАРАТЫЛҒАН ТІЗІЛІМ ТЕХНОЛОГИЯСЫН ПАЙДАЛАНУ АРҚЫЛЫ ЕМТИХАН НӘТИЖЕЛЕРІ ДЕРЕКТЕРІНІҢ ТҰТАСТЫҒЫН ҚАМТАМАСЫЗ ЕТУ

Аңдатпа

Жоғары білім беруді цифрландыру аясында орталықтандырылған студенттік ақпараттық жүйелердің (Student Information Systems, SIS) кең қолданылуы студент деректерінің рұқсатсыз өзгертілу қаупін арттырады, себебі барлық деректер енгізу мен басқару бір әкімшілік сенім доменіне тәуелді. Мақалада емтихан нәтижелерінің криптографиялық тексерілетін тұтастығын қамтамасыз етуге арналатын таратылған тізілім технологиясы (Distributed Ledger Technology, DLT) архитектурасының жобалануы және эксперименттік тексеруі ұсынылған. Ұсынылған архитектура SQL-негізіндегі SIS және Hyperledger Fabric блокчейн жүйесін қауіпсіз middleware қабаты арқылы біріктіруге негізделген. SIS жүйесіндегі емтихан жазбалары криптографиялық hash-commitment түріне түрлендіріліп, өзгермейтін ledger-де сақталады. Эксперименттік тексеру контейнерленген ортада нақты Hyperledger Fabric желісін орналастыру және Hyperledger Caliper көмегімен 120,000 транзакцияға дейінгі жүктеме кезінде тестілеу арқылы жүргізілді. Негізгі көрсеткіштер өткізу қабілеті, бекіту кідірісі, деректер тұтастығының бұзылуын анықтау мүмкіндігі және тізілімді сақтау сипаттамалары болды. Архитектура 728 транзакция/секунд өткізу қабілетін және 842 транзакция/секунд максималды өткізу қабілетін көрсетті, ал орташа бекіту кідірісі 2.0 секундтан аз болды. Рұқсатсыз қол сұғуды анықтау тесттері барлық рұқсатсыз өзгерістерді орташа 19.8 мс уақытта анықтағанын көрсетті. Сақтау талдауы тізілімнің сызықты өсетінін және он жыл ішінде 5.68 ГБ-тан аз орын қажет ететінін көрсетті. Нәтижелер ұсынылған архитектура орталықтандырылған жүйелерге тән бірыңғай істен шығу нүктесі мәселесін жоятынын және академиялық жазбалардың масштабталатын, криптографиялық тексерілетін тұтастығын қамтамасыз ететінін дәлелдейді.

Түйін сөздер: таратылған тізілім технологиясы, блокчейн, деректер тұтастығы, ақпараттық қауіпсіздік, Hyperledger Fabric, студенттік ақпараттық жүйелер, академиялық жазбалар

[1]Сахипов А.А.,
PhD, ассистент профессор, ORCID ID: 0000-0003-1045-4199,
e-mail: aivar.sakhipov@astanait.edu.kz
[1*]Феденко А.Д.,
магистр, преподаватель, ORCID ID: 0009-0000-2290-6995,
*e-mail: a.fedenko@astanait.edu.kz
1Astana IT University, Astana, Kazakhstan

ОБЕСПЕЧЕНИЕ ЦЕЛОСТНОСТИ ДАННЫХ РЕЗУЛЬТАТОВ ЭКЗАМЕНОВ С ИСПОЛЬЗОВАНИЕМ ТЕХНОЛОГИИ РАСПРЕДЕЛЕННОГО РЕЕСТРА

Аннотация

Расширенное использование централизованных студенческих информационных систем (Student Information Systems, SIS) в условиях цифровизации высшего образования увеличивает риск несанкционированного изменения данных студентов, поскольку ввод и управление данными зависят от одного административного доверенного домена. В данной работе представлена разработка и экспериментальная проверка архитектуры технологии распределенного реестра (Distributed Ledger Technology, DLT), предназначенной для обеспечения криптографически проверяемой целостности экзаменационных результатов. Предложенная

архитектура основана на интеграции SQL-ориентированной SIS и блокчейн-системы Hyperledger Fabric через защищенный middleware-слой. Экзаменационные записи SIS преобразуются в криптографическое hash-commitment и сохраняются в неизменяемом ledger. Экспериментальная проверка проводилась путем развертывания реальной сети Hyperledger Fabric в контейнеризированной среде и тестирования с использованием Hyperledger Caliper при нагрузке до 120,000 транзакций. Основными показателями были пропускная способность, задержка фиксации, способность обнаружения нарушений целостности данных и характеристики хранения реестра. Архитектура достигла пропускной способности 728 транзакций/секунду и максимальной пропускной способности 842 транзакции/секунду при средней задержке фиксации менее 2.0 секунд. Тесты на несанкционированное вмешательство показали успешное обнаружение всех несанкционированных изменений со средним временем обнаружения 19.8 мс. Анализ хранения показал линейный рост реестра и потребность менее 5.68 ГБ за десять лет. Результаты демонстрируют, что предложенная архитектура устраняет единую точку отказа, присущую централизованным системам, и обеспечивает масштабируемую криптографически проверяемую целостность академических записей.

Ключевые слова: технология распределенного реестра, блокчейн, целостность данных, информационная безопасность, Hyperledger Fabric, студенческие информационные системы, академические записи.

UDC 004.93
IRSTI 20.23.15

https://doi.org/10.55452/1998-6688-2026-23-3-282-297

[1]Smakanov B.S.,
PhD, ORCID ID: 0000-0002-4343-0463,
e-mail: s.bauyrzhan.10@gmail.com
[1*]Uvaliyeva I.M.,
PhD, Associate Professor, ORCID ID: 0000-0002-2117-5390,
e-mail: iuvalieva@ektu.kz

[1]D. Serikbayev East Kazakhstan Technical University, Ust-Kamenogorsk, Kazakhstan

MODELING DRIVER STATE MONITORING BASED ON A THEORETICAL AND EMPIRICAL APPROACH

Abstract

This article addresses the problem of improving face detection reliability in video streams used in driver state monitoring systems. Reliable localization of the driver's face is considered a preliminary computer vision stage required for the subsequent analysis of eye state, gaze direction, facial behavior, and fatigue-related visual cues. The purpose of this study is to develop and experimentally evaluate an adaptive face detection method that maintains stable performance under variations in illumination, head pose, image noise, and partial face occlusion while operating with a fixed, externally calibrated camera. The proposed method combines initial face-region detection using the Viola–Jones algorithm with SVM-based verification, external camera calibration, and incremental parameter updating based on high-confidence detections used as pseudo-labels. The method was evaluated using 18,000 video frames obtained from 12 recordings involving seven volunteers under different shooting conditions. The experimental results showed that the integrated method provided higher face detection performance than the standalone Viola–Jones algorithm and the Viola–Jones method combined with a conventional SVM classifier. The proposed method achieved a Precision of 0.91 and a Recall of 0.90 while maintaining a processing speed of 22 frames per second, which is sufficient for real-time operation. The study evaluates face detection and does not directly classify driver fatigue, drowsiness, eye state, or facial expressions. The obtained results demonstrate that the proposed method can be used as a lightweight preliminary component of driver state monitoring systems operating on embedded hardware with limited computational resources.

Keywords: video analytics, face detection, driver monitoring system, computer vision, video stream, Viola–Jones method, SVM classifier, adaptive detection, camera calibration, real-time processing.

Received July 21, 2026; revised August 28, 2026; accepted August 31, 2026.

Introduction

Studies of recent years show that a significant part of road accidents is associated with the physiological and psycho-emotional state of the driver [1–6]. In this regard, there is a growing interest in monitoring systems that automatically assess the driver's condition in the process of movement. Such systems allow you to detect signs of fatigue and decreased attention early and warn the driver in advance.

The basis of modern driver monitoring systems is computer vision technologies. According to the video frames, the driver's face, the state of his eyes and the position of his head in space are analyzed. In the course of the experiment, it was noted that the quality of detection is significantly influenced by the following factors:

- change in lighting level;
- turn and tilt of the head;
- change in the driver-to-camera distance and the corresponding face scale in the frame;

- video noise;
- partial closure of the face.

When the light is unstable or the driver turns his head, the detection accuracy of classical computer vision algorithms decreases and the number of erroneous determinations increases [7].

In studies to solve this problem, along with classic computer vision methods, YOLO, RetinaFace, MTCNN and other deep learning models have been widely used. Nevertheless, the adaptation of classical algorithms for systems with limited computing resources still remains relevant. Research and literary data show that the Viola - Jones algorithm processes video frames at high speed. Nevertheless, when lighting conditions change or the angle of rotation of the driver's head relative to the camera increases, the detection accuracy of the Viola–Jones algorithm decreases [8–10]. Although deep learning models show much higher results in such complex situations, their efficient operation requires hardware platforms with higher computing power. In this regard, the use of such models in built-in automotive systems with limited computing capabilities is not always acceptable.

For the driver monitoring system, the detection accuracy alone is not enough. The algorithm should not only process the video stream in real time, but also work stably during changes in lighting, movement of the driver's head and other external influences. Therefore, in the course of the study, priority was given to the development of an approach that has a low computational load and can adapt to variable shooting conditions. Such a solution provides reliable face localization under variable shooting conditions and can serve as an input stage for subsequent driver-state analysis.

Before the experiment, an external calibration of the camera was carried out. The position of the camera in space relative to the driver was calculated, and based on these parameters, a coordinate system was formed. These parameters were then used to calculate the position of the driver's face in space. The calibration results have increased detection stability, especially in cases where the driver's head is turned or tilted.

The working capacity of the model was tested under different shooting conditions. The following five experimental factors were evaluated: the illumination level; the driver’s head rotation and tilt angles; the driver-to-camera distance and the corresponding face scale in the frame; partial face occlusion; and the level of video noise. The camera position and orientation remained constant throughout all experiments.

This organization made it possible to evaluate the influence of each factor on the algorithm separately. After the end of each test, the number of detected faces, false determinations and the time spent processing one frame were recorded. The results were then compared and the impact of each parameter on detection accuracy and processing performance was analyzed.

The experiments carried out have confirmed that the proposed approach works effectively. The use of the Viola–Jones algorithm in conjunction with the SVM classifier and external camera calibration results reduced the number of erroneous determinations and increased the reliability of the system's operation in complex shooting conditions. During the test, the algorithm retained the processing speed in real time. The results obtained showed that this approach can be used in driver monitoring systems.

Materials and methods

During the experiment, the video camera was rigidly mounted inside the vehicle so that the driver’s face was fully visible in the frame. The position and orientation of the camera remained unchanged throughout the entire data collection process. External camera calibration was performed once before recording to determine the fixed spatial relationship between the camera and the driver. The experimental variations concerned the shooting conditions and the driver’s position relative to the fixed camera, rather than changes in the camera position itself.

To assess the effectiveness of the algorithm, a data set was formed from 12 video recordings with a total duration of about three hours. About 18,000 frames were taken from the videos, of which 12,000 were used for training, and the remaining 6,000 were used for testing the model. All

performance indicators presented in Tables 1 and 2 were calculated exclusively using the independent test subset consisting of 6,000 frames. The data was collected in such a way as to cover different face turning angles and partial closure scenarios, both in daytime and evening light conditions. The videos were filmed with the participation of the authors in real transport conditions. The generated data sets are not included in open databases and were used only as part of this study.

The study involved seven volunteers, five of whom were men and two were women. The age of the participants ranged from 21 to 46 years. Participants wearing glasses and with beards or mustaches were also included to ensure the diversity of the data set. The videos were filmed both in natural light and in an environment where there was not enough light. At the same time, different head turning positions in relation to the camera were deliberately introduced, and the ability of the algorithm to work in variable shooting conditions was assessed.

12,000 frames were selected from the generated dataset to train the SVM classifier. The remaining 6,000 frames were used to evaluate and test the model. During the experiment, five factors were taken into account: the illumination level; the driver's head rotation and tilt angles; the driver-to-camera distance and the corresponding face scale in the frame; partial face occlusion; and the level of video noise. These data allowed us to assess the stability of the system in real conditions. Examples of frames taken from the image of the driver's face are shown in Figure 1.



Figure 1 – Examples of driver-face frames extracted from the video recordings

During the experiment, video recordings of the driver's face were used as the main research material. First, the videos were divided into individual frames and their quality was checked. Further experiments continued under different shooting conditions. During the experiment, the shooting conditions were deliberately changed. The same five factors were varied according to the experimental protocol, while the camera position and orientation remained constant. After each test, the resulting video recordings were processed and the operation of the algorithm was evaluated by the number of detected faces, false determinations and the time spent processing one frame. These indicators made it possible to compare the effect of different shooting conditions on the detection accuracy and processing speed. Video frame processing was performed using the standard functions of the OpenCV library.

The search for the face area was carried out in several stages. First, the motion detection method was used and areas of interest (ROI) were marked, where potential objects were located. These areas were then scanned with a scalable rectangular window and checked for the presence of a face in each position. The Viola–Jones algorithm based on Haar-like features and cascade classifier was used as the main detection method. However, practice shows that its accuracy decreases when the lighting is unstable or the face looks blurry. Therefore, we have introduced an additional SVM classifier. It was pre-trained in data sets that took into account face orientation, light level and video noise, and allowed to reduce the number of false determinations.

Before the start of the experiment, the external calibration of the camera was performed. The position of the camera, the direction of view and the angles of rotation were determined, and these

parameters were used to match points in three-dimensional space with the image plane. In our practice, such calibration made it possible to more accurately determine the position of the face in space in cases where the driver's head is turned or tilted.

The results of the study showed that changes in lighting, turning of the driver's head and partial face coverage are the factors that most affect the quality of detection. Although the accuracy of the classic Viola–Jones algorithm in such conditions has decreased, the use of the SVM classifier has increased the stability of the detection results.

Under normal conditions, the system reliably detected the face. And in complex frames, sometimes the wrong areas were marked or the face was not found at all. An individual analysis of incorrectly processed frames was carried out. In most cases, such errors are caused by insufficient lighting, turning the driver's face relative to the camera, or a decrease in video quality.



Figure 2 – Examples of challenging conditions: low illumination, changes in face orientation, and low image resolution

Part of the results obtained during the experiment is presented in Figure 2. Tests have shown that the work of the algorithm depends on the shooting conditions. Under normal lighting, the face was reliably detected, and when the light level decreased or the angle of rotation of the driver's head increased, the number of errors increased. While in some frames the face remains undetected, in some cases other objects similar to the face are incorrectly recognized.

To minimize these shortcomings, an SVM classifier was introduced into the algorithm. The SVM classifier re-evaluated the candidate regions marked by the Viola–Jones method and clarified their correspondence to the face. As a result, false determinations have decreased and the stability of the algorithm has improved.

Each video was first divided into separate frames, and then they were processed sequentially. All results were compared among themselves and the features of the algorithm's work in different shooting conditions were analyzed. The frames were then processed in turn and converted to a grayscale image. Then only those parts where movement was observed were selected, and the search for facial features was carried out in the same areas. Determining areas of interest in advance reduced unnecessary calculations and reduced the amount of data being processed. As a result, the processing time of one frame decreased, and the algorithm met the requirements for working in real time. Where t is the sequence number of the frame in the video stream.

The C_t matrix is formed as a result of disconnecting the movement zone from the original A_t matrix. Thus, its dimensions are of a limited nature: the width satisfies the conditions $w_C \leq m$, and the height satisfies the conditions $h_C \leq n$.

It is necessary to form a set of rectangular areas containing human faces within a given area of movement (1):

$$Face_i = \{x_i, y_i, w_i, h_i\} \quad (1)$$

For each rectangular area in the list, the coordinates of its center (x_i, y_i), as well as the width (w_i) and height (h_i) parameters are determined.

To identify the object, the image is analyzed using the full scan method. For this purpose, a search window with a width of W and a height of H is used. The window is first placed in the upper left corner of the image and covers the entire image in a horizontal direction, moving by one pixel with each step. After that, the same search is performed in the vertical direction. The size of the search window is gradually changed to identify objects of different sizes in the image. The general operation of the sliding-window scanning algorithm is illustrated in Figure 3.

In the classification process for determining the presence of a face image in the image area, class symbols of the type {-1,+1} are used for each position of the scan window, where -1 means «not a face», and +1 means the class «face». In the process of scanning the image, each location of the window is checked using a classification model. Based on it, the presence of a face image in the area under consideration is decided in accordance with predefined designations and classification rules.

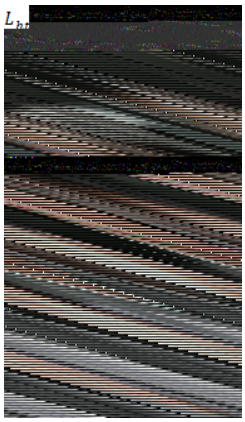


Figure 3 – Sliding-window scanning procedure
used for face detection

This approach allows us to consider the task of determining facial images in video frames as a two-class classification problem. Here, X represents the space of properties of objects, and Y represents a set of finite classes. The function F is considered as a decisive transformation that maps the characteristics of $x \in X$ to the corresponding $y \in Y$.

The function F defines the characteristics of object A by converting the elements in Set X to the D_f area, which forms the set of allowed values for a given object. In this case, the feature vector describing the object A and belonging to the complex X is based on the sign system $f_1, \dots, f_r$ [11–13] (2):

$$x = (f_1(a), \dots, f_r(a)) \tag{2}$$

In this context, objects are represented as feature vectors that describe their properties. In this case, the classifier must be able to accurately determine that any object belongs to a set X and reduce the probability of error for all possible X variants.

The effectiveness of the classifier is determined by its ability to reduce the probability of error for all possible inputs, which is the main criterion for the quality of its work.

When training the classifier F, a data set consisting of objects belonging to previously known Classes (3) is used:

$$D = \{(x_1, y_1), \dots, (x_m, y_m)\}, where\ y_i \in Y = \{-1; +1\} \tag{3}$$

In the proposed method, face detection is performed as a sequential two-stage procedure. First, the Viola–Jones algorithm processes each video frame and generates candidate face regions. Second, the SVM classifier verifies every candidate region and rejects detections that do not correspond to a face. The external camera calibration parameters are used to describe the fixed spatial relationship between the camera and the driver and to support the interpretation of pose-related features. This processing sequence is applied to every frame; the system does not switch between Viola–Jones and SVM. In the proposed configuration, the SVM parameters can additionally be updated using high-confidence pseudo-labeled samples obtained from the video stream.

When processing a video stream, the classifier settings were updated based on new frames. This allowed the model to adapt to changed shooting conditions and maintained the stability of the detection results. Examples of video frames obtained in normal and real road conditions are shown in Figure 4.



Figure 4 – Video frames obtained under (a) controlled and (b) real driving conditions

During the experiment, the camera position and orientation remained constant. Five experimental factors were evaluated: the illumination level; the driver's head rotation and tilt angles; the driver-to-camera distance and the corresponding face scale in the frame; partial face occlusion; and the level of video noise. The influence of these factors on face detection performance was analyzed under the same experimental protocol. The main features used in the study are as follows:

– α_h – angular deviation of the face along the X axis;

– α_v – angular deviation of the face in the vertical plane;

– α_z – the angle of inclination of the head relative to the frontal plane;

– L_{ht} – illumination level indicator;

– N_{os} – noise level in the image, where 0 means a perfect image, and 1 means a strongly distorted image that is not recognizable.

To unify the calculations, all parameters were normalized in advance to an interval of 0-1. The limit values were determined on the basis of experimental data. Since the face is not a completely symmetrical object, the angles of rotation and inclination were calculated at absolute values. Such normalization made it possible to directly compare the results obtained under different shooting conditions.

The quality of face detection was primarily dependent on the initial detection stage. Errors that occur at this stage also affect the result of the subsequent classification. Therefore, the influence of external factors on the characteristics of the face image was considered separately, and their relationship was described by Equation (4):

$$Q(a) = (\alpha_h, \alpha_v, \alpha_z, L_{ht}, N_{os}) \quad (4)$$

Each image in the training and test sets was attributed to a specific class, and a corresponding feature vector was created for it. This vector was used as input data in the later classification period. The formal description of the data set is given in Equation (5):

$$D = \{Q(a_1), Q(a_2), \dots, Q(a_n)\} = \{(\alpha_{h1}, \alpha_{v1}, \alpha_{z1}, Lht_1, Nos_1), \dots, (\alpha_{hn}, \alpha_{vn}, \alpha_{zn}, Lht_n, Nos_n)\} \quad (5)$$

At the next stage, a parametric assessment of the training set was performed (6):

$$D = \begin{Bmatrix} (\alpha_{h1}, \dots, \alpha_{hn}), (\alpha_{v1}, \dots, \alpha_{vn}), (\alpha_{z1}, \dots, \alpha_{zn}), \\ (Lht_1, \dots, Lht_n), (Nos_1, \dots, Nos_n) \end{Bmatrix} \quad (6)$$

Then a parametric analysis of the training set was carried out (6). The distribution of values for each sign was calculated, and the most common value was taken as mode. Based on it, a vector of generalized characteristics was obtained that characterize the training set. Its mathematical expression is given in Equation (7):

$$M_D = \{M\alpha_h, M\alpha_v, M\alpha_z, M_{Lht}, M_{Nos}\} \quad (7)$$

where $M\alpha_h, M\alpha_v, M\alpha_z, M_{Lht}, M_{Nos}$ - each parameter on mode.

The MD vector summarizes the characteristics that are often found in sample images [11]. The value of each parameter varies between predetermined minimum and maximum limits. This range is shown in Equation (8):

$$D_{min}^{max} = \begin{Bmatrix} (min_{a_h}, max_{a_h}), (min_{a_v}, max_{a_v}), \\ (min_{a_z}, max_{a_z}), (min_{Lht}, max_{Lht}), \\ (min_{Nos}, max_{Nos}) \end{Bmatrix} \quad (8)$$

To ensure effective classification, the characteristics of the images used during the testing phase must be within the permissible range defined by $D_{\min}$. The experimental results showed that face detection accuracy depended on the diversity of the training and test data. Changes in illumination and in the position of the driver's face relative to the fixed camera increased the number of false detections. Therefore, the training dataset included video frames obtained under different illumination conditions, head poses, driver-to-camera distances, and face positions, while the camera itself remained fixed.

The effectiveness of the SVM classifier was evaluated individually. The analysis showed that its performance depends not only on the size of the training set, but also on the variety of its composition. In the training set, where images with different levels of illumination, shooting angle and face position were included, the classification results were more stable. For this reason, when collecting video materials, the external parameters of the camera were determined in advance and special attention was paid to the variety of shooting conditions. Later, these materials were used to train the classifier.

In the process of evaluating the proposed method, along with the detection accuracy, the processing speed was also taken into account. Although convolutional neural networks were able to show high accuracy, the requirement they placed on computing resources was quite high. For the hardware platform used in the experiment, the use of such models did not allow stable operation in real time. For this reason, it was decided that the use of classical computer vision methods is more effective.

In the proposed model, the Viola–Jones algorithm performs the initial face detection stage, and the SVM classifier re-checks the identified areas. Such a division made it possible to use the strengths of each algorithm. The first provided processing speed, while the second reduced the number of erroneous determinations in complex frames.

During the experiment, only one algorithm could not give the same result in all cases. Therefore, the tasks of searching for a face and checking it were divided into two methods. First, Viola-Jones outlined possible facial areas. Later, the same areas were re-evaluated by the SVM. Such an approach did not require much additional calculation time, but the result of the determination was more stable. The parameter vector Q(a) was calculated for each processed frame to characterize the current

illumination, head pose, and image-noise conditions. This vector was not used to switch between the two algorithms. The Viola–Jones algorithm remained the candidate-region detector, while the SVM remained the verification stage under all experimental conditions. When the predefined update conditions were satisfied, high-confidence verified samples were used to incrementally update the SVM parameters.

In the course of the work, no approach was used to fully retrain the model for each new data set. Instead, the SVM classifier was adjusted in stages based on feature vectors derived from the new video frames. This approach follows the incremental update principle and significantly reduces the time required to retrain the model. As a result, incremental updating required less computation than complete model retraining. However, the additional verification and updating procedures reduced the overall processing speed of the proposed method to 22 FPS.

Manual marking for marking new frames was not carried out. Instead, the high–reliability detection results were obtained from the original Viola-Jones algorithm. Such face areas were adopted as a pseudo-label and then used when updating the SVM classifier.

If the detection reliability is higher than the predetermined threshold value, the corresponding feature vectors were included in the training phase. And frames with insufficient reliability were not involved in the process of updating the model. Such sampling reduced the accumulation of false samples and made it possible to maintain the stability of the classifier.

During testing, the model parameters were not changed with each frame processed. The update was performed only if the detection result was unstable or after a certain number of frames were processed. This selective update strategy avoided retraining the classifier for every processed frame and limited the additional computational overhead. Nevertheless, the complete proposed pipeline operated at 22 FPS, compared with 24 FPS for Viola–Jones combined with a static SVM and 28 FPS for the standalone Viola–Jones algorithm.

The computational complexity of the update algorithm was rated as $O(n \cdot d)$. Here n is the number of new samples participating in the update, and d is the size of the feature vector. It was confirmed during the experiment that this approach requires a much smaller computational resource compared to full model retraining.

Before starting the experiment, the drivers who participated in the study were explained the purpose of the work and the order of execution. Each participant gave their consent to the use of videos in scientific research. Participation was completely voluntary.

In the processing of video materials, no data was used that allows you to identify an individual. To analyze the results of the study, only the face area and the information necessary for the operation of the algorithm were used. Therefore, the personal data of the participants were not included in the published materials.

The collected videos were stored separately, and only the participants who participated in the study had access to them. The data was not shared with other organizations or used for commercial purposes.

The images obtained during the experiment were used only to test face detection algorithms. When processing personal data, the current regulatory requirements were taken into account and the confidentiality of information was maintained.

Results and discussion

At this stage of the experiment, the external parameters of the camera were determined. To determine the external parameters of the camera, reference objects were used, the position in space and geometric dimensions of which are known in advance [17-20]. As a result of the analysis of the video recordings, the position and angles of rotation of the camera were calculated. Later, the obtained parameters were used to more accurately determine the position of the face in space and estimate its position.

The CCTV camera vision system consists of the following main components:

1) the image structure is presented in the form of a rectangular pixel grid consisting of R rows and C columns.

2) the camera works in a local coordinate system formed by the X_c, Y_c, Z_c axes.

3) the camera is considered in the world (global) coordinate system,characterized by the axes X_w, Y_w, Z_w.

Samples of video frames obtained by the camera are shown in Figure 5.

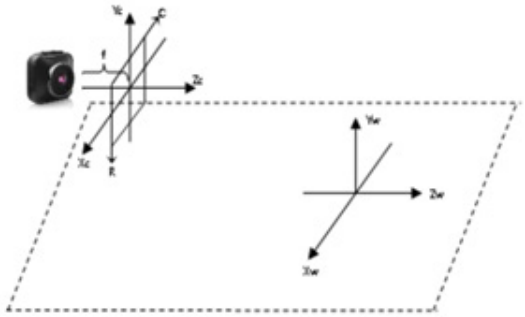


Figure 5 – Examples of driver-face frames captured by the fixed camera

The camera is characterized by an Optical Center Point (0, - f, 0) in the coordinate system, where f is the focal length. According to the camera matrix, the Rc plane is located in the $X_c Y_c$ plane, and the Z_c axis indicates the optical direction of the camera [20].

The camera calibration process is based on determining the correspondence between points in the image plane and the corresponding three-dimensional points in space. To solve this problem, the C_w^1 model is used, which describes the relationship between three-dimensional points in the global coordinate system and their projections into the image. This relationship is expressed taking into account the arbitrary scaling factor S (9).

$$\begin{bmatrix} s*r \\ s*c \\ s \end{bmatrix} = C_w^1 \begin{bmatrix} x^w \\ y^w \\ z^w \\ 1 \end{bmatrix} \tag{9}$$

The external parameters of the camera determine its position and orientation in space in the world coordinate system. They consist of two main groups:

- translation vector (10):

$$\mathrm{t} = [t_x t_y t_z]^T \tag{10}$$

- rotation matrix (11):

$$\mathrm{R} = \begin{bmatrix} r_{11} & r_{12} & r_{13} & 0 \\ r_{21} & r_{22} & r_{23} & 0 \\ r_{31} & r_{32} & r_{33} & 0 \\ 0 & 0 & 0 & 1 \end{bmatrix} \tag{11}$$

The translation vector gives the position of the camera in the world coordinate system, and the rotation matrix gives its orientation in space, that is, the direction of view. In turn, the matrix R is expressed as the product of three elementary rotations performed along the coordinate axes (12):

$$R = R_{ox}R_{oy}R_{oz}$$

$$R_{ox} = \begin{bmatrix} 1 & 0 & 0 & 0 \\ 0 & cos\alpha & -sin\alpha & 0 \\ 0 & sin\alpha & cos\alpha & 0 \\ 0 & 0 & 0 & 1 \end{bmatrix}, R_{oy} = \begin{bmatrix} cos\beta & 0 & sin\beta & 0 \\ 0 & 1 & 0 & 0 \\ -sin\beta & 0 & cos\beta & 0 \\ 0 & 0 & 0 & 1 \end{bmatrix} \quad (12)$$

$$R_{oz} = \begin{bmatrix} cos\gamma & -sin\gamma & 0 & 0 \\ sin\gamma & cos\gamma & 0 & 0 \\ 0 & 0 & 1 & 0 \\ 0 & 0 & 0 & 1 \end{bmatrix}$$

The R_{ox} matrix describes the rotation around the O_x axis at an angle α. Similarly, the R_{oy} matrix describes the rotation around the O_y axis at an angle β, and the R_{oz} matrix describes the rotation around the O_z axis at an angle γ. Accordingly, the values α, β and γ determine the angles of rotation performed around the axes O_x, O_y , O_z , respectively. These parameters describe the degree of rotation of each axis in three-dimensional space.

The transition from the global coordinate system to the camera coordinate system is carried out only on the basis of external parameters and reflects the change in the position and direction of the camera in external space (13):

$$T_W^C = \begin{bmatrix} r_{11} & r_{12} & r_{13} & t_x \\ r_{21} & r_{22} & r_{23} & t_y \\ r_{31} & r_{32} & r_{33} & t_z \\ 0 & 0 & 0 & 1 \end{bmatrix}, \begin{bmatrix} x^c \\ y^c \\ z^c \\ 1 \end{bmatrix} = T_W^C \begin{bmatrix} x^w \\ y^w \\ z^w \\ 1 \end{bmatrix} \quad (13)$$

The T_w^C conversion, which describes the transition from the global coordinate system to the camera coordinate system, is reversible, that is, it allows you to accurately restore the original global coordinates from the coordinates in the camera system (14):

$$T_C^w = (T_w^C)^{-1}. \quad (14)$$

The structure of the transformation matrix T_w^C is determined by creating a transformation (14). This process consists of several sequential transformation steps, each of which plays an important role in the formation of the camera model, and as a result, the C_w^1 (15) camera model is determined:

$$T_w^1 = T_c^1 T_w^c \quad (15)$$

The external parameters of the camera were determined using the calibration methods described in the works [21–28]. As a result of calibration, the position of the camera in space, the direction of view and the main shooting parameters were calculated.

To clearly distinguish the evaluated configurations, three face detection methods were compared under the same experimental conditions and using the same test data. The first configuration, referred to as «Viola–Jones,» used only the standard Haar cascade detector with fixed parameters. The second configuration, referred to as «Viola–Jones + SVM,» used the Viola–Jones algorithm to generate candidate face regions and a previously trained static SVM classifier to verify these regions. In this configuration, the SVM parameters were not updated during video processing, and external camera calibration parameters were not incorporated into the detection procedure. The third configuration, referred to as «the proposed method,» combined Viola–Jones candidate detection, SVM-based verification, external camera calibration, and incremental SVM updating based on high-confidence pseudo-labels obtained from the video stream. Thus, the proposed method differs from the conventional Viola–Jones + SVM configuration through the additional use of camera calibration and online learning.

The effectiveness of the method was assessed by Accuracy, Precision, Recall and the number of frames processed per second (FPS). The results are presented in Table 1.

The proposed method was compared with the classic Viola–Jones algorithm in the same video format and in the same experimental conditions.

During the experiment, the method was evaluated under five experimental factors: variations in illumination; driver head rotation and tilt; changes in the driver-to-camera distance and the corresponding face scale; partial face occlusion; and video noise. The camera remained fixed in all experimental scenarios.

For each case, the detection accuracy was calculated individually, and the obtained indicators were compared among themselves. The results showed that the presented model works stably even in complex shooting conditions and provides higher detection reliability compared to the classic Viola-Jones algorithm.

Table 1 – Comparison of the performance indicators of face detection methods

Method	Accuracy	Precision	Recall	FPS
Viola–Jones baseline	0.82	0.79	0.76	28
Viola–Jones + static SVM	0.89	0.87	0.85	24
Proposed method: Viola–Jones + calibrated features + online SVM	0.91	0.91	0.90	22

Based on the corrected confusion matrix, the proposed method achieved an Accuracy of 0.9067, a Precision of 0.9122, and a Recall of 0.9000. When rounded to two decimal places, these values correspond to 0.91, 0.91, and 0.90, respectively. These recalculated indicators are consistent with the corrected entries presented in Table 2.

The staged comparison presented in Table 1 demonstrates the effect of adding static SVM verification to the Viola–Jones baseline and the combined effect of incorporating external camera calibration and online SVM updating into the proposed method. The individual contributions of camera calibration and online learning were not evaluated separately and will be investigated in future ablation experiments.

At the end of the experiment, the results obtained were analyzed for several indicators. Along with quantitative indicators, the features of the algorithm for processing video materials were also analyzed. As a result of the comparison, there was a decrease in the number of false determinations and an increase in the share of correctly identified faces. A similar trend was observed in all shooting conditions provided for during the experiment.

Cases when the level of illumination changed were considered separately. Although the rotation of the driver's head reduced the accuracy of detection, the use of the SVM classifier made it possible to correctly identify the face in many frames. Especially this was clearly noticeable in video frames, where the light fell unevenly or part of the face remained in the shade.

The proposed method improved the face detection indicators but introduced additional computational overhead. The processing speed decreased from 28 FPS for the standalone Viola–Jones algorithm to 24 FPS for Viola–Jones combined with a static SVM and to 22 FPS for the proposed method. Thus, the complete proposed method was approximately 21.4% slower than the standalone Viola–Jones baseline and approximately 8.3% slower than the static Viola–Jones + SVM configuration. This reduction was not considered negligible; rather, it represents a trade-off between detection reliability and processing speed. Nevertheless, the achieved speed of 22 FPS allowed continuous real-time video processing in the tested system.

The error matrix presented in Table 2 characterizes the classification quality of the proposed method. The results showed a decrease in false positive and false negative determinations. Compared to the Viola-Jones algorithm, the presented model gave more stable results even when the lighting and shooting conditions changed.

Table 2 – Confusion matrix for the proposed face detection method evaluated on the 6,000-frame test set

Actual class	Face detected	Face not detected
Face present	2700	300
Face absent	260	2740

The efficiency of the algorithms was evaluated on the basis of a matrix of classification errors. The results presented in Table 2 showed a decrease in the number of false positive and false negative determinations in the proposed method. Errors were most often observed when there was a sharp change in lighting, a turn of the driver's head at a large angle relative to the camera, or partial closure of the face.

Additional experiments were conducted to evaluate the face detection method under the five experimental factors defined in the Materials and Methods section. These factors were varied according to the same experimental protocol, and their influence on face detection performance was analyzed. The position and orientation of the camera remained unchanged. The results obtained for each case were compared and the influence of these factors on the accuracy of determination was analyzed.

In order to reduce processing time, zones where movement was observed were marked in advance. The face was not searched throughout the frame, but only in the areas of interest. Such a solution reduced the amount of data being processed and reduced the processing time per frame. Thanks to this, the system met the requirements for working in real time.

At the initial stage, only the possibilities of the Viola–Jones algorithm were studied. Under normal shooting conditions, it showed a high processing speed, however, when there was not enough light or the turning angle of the driver's head increased, the detection accuracy decreased. To reduce these limitations, an SVM classifier was introduced into the system and used in conjunction with the external calibration results of the camera. As a result, the quality of detection in complex frames has improved and the number of false determinations has decreased.

The tests carried out supplemented the information given in the literature. The use of camera calibration parameters in conjunction with the SVM classifier increased the algorithm's operational stability and improved the quality of face detection in complex situations.

The results of the experiment confirmed that the developed model works stably under different shooting conditions. The results obtained showed that this approach can be applied in real time in driver monitoring systems. There is also the possibility of using it in intelligent transport systems and other applications based on video analytics.

Conclusion

This study developed and experimentally evaluated an adaptive face detection method intended as a preliminary component of driver state monitoring systems. The proposed method combines the Viola–Jones algorithm for initial face-region detection with SVM-based verification, external camera calibration, and incremental parameter updating using high-confidence detections as pseudo-labels. This configuration was designed to maintain a low computational load while improving detection reliability under variable shooting conditions.

The experimental evaluation was conducted using 18,000 video frames obtained from 12 recordings involving seven volunteers. The tests covered the five experimental factors defined in the Materials and Methods section: illumination, driver head rotation and tilt, driver-to-camera distance and the corresponding face scale, partial face occlusion, and video noise. Compared with the standalone Viola–Jones algorithm and the Viola–Jones method combined with a conventional SVM classifier, the integrated method demonstrated more reliable face detection under complex conditions. It achieved a Precision of 0.91 and a Recall of 0.90 while processing 22 frames per

second. Although this processing speed was lower than that of the standalone Viola–Jones algorithm, it remained sufficient for real-time operation on hardware with limited computational resources.

The results demonstrate that the proposed method can provide reliable face localization as an initial stage of a broader driver state monitoring system. However, the present study evaluates face detection only and does not directly classify fatigue, drowsiness, eye state, gaze direction, or facial expressions. Therefore, the reported results should be interpreted as evidence of improved face detection performance rather than direct validation of driver fatigue recognition.

The limitations of the study include the relatively small number of participants, the use of a non-public dataset, and the limited range of experimental scenarios. Future research will focus on evaluation using larger and more diverse datasets, separate quantitative analysis of the contribution of camera calibration and online learning, and integration of the proposed face detection method with modules for eye-state, gaze, head-pose, and fatigue analysis.

Funding

This research is funded by the Science Committee of the Ministry of Science and Higher Education of the Republic of Kazakhstan (Grant No. AP25795477).

REFERENCES

1 Povichanov, A.A. Obzor problematiki i perspektivnyh metodov intellektual'nogo analiza dannyh o sostoyanii voditelej transportnyh sredstv [Overview of Issues and Promising Methods of Intelligent Data Analysis on the State of Vehicle Drivers]. Ekonomika i kachestvo sistem svyazi, (4), 159–172 (2024). (in Russian).

2 Kirillova, E.S., and Serikov, S.A. Metody i sredstva kontrolya sostoyaniya voditelya avtomobilya [Methods and Means of Monitoring the State of a Car Driver]. Mezhdunarodnyj zhurnal gumanitarnyh i estestvennyh nauk, (3-2), 169–172 (2024). (in Russian).

3 Ahmetvaleeva, I.V. et al. Podhod k monitoringu sostoyaniya ustalosti voditelej transportnyh sredstv [An Approach to Monitoring the Drowsiness State of Vehicle Drivers]. Vestnik Tekhnologicheskogo universiteta, 26 (4), 58–62 (2023). (in Russian).

4 Katasyov, A.S., Katasyova, D.V., and Sibgatullin, A.A. Nejrosetevaya model' ocenki funkcional'nogo sostoyaniya voditelej v sistemah transportnoj bezopasnosti [Neural Network Model for Assessing the Functional State of Drivers in Transportation Safety Systems]. Elektronika, fotonika i kiberfizicheskie sistemy, 3 (1), 69–80 (2023). (in Russian).

5 Bryzgalov, V.I., Karpushko, M.O., and Burgonutdinov, A.M. Prognoz kolichestva dorozhno-transportnyh proisshestvij na platnyh avtomobil'nyh dorogah [Forecast of the Number of Traffic Accidents on Toll Roads]. Vestnik Permskogo nacional'nogo issledovatel'skogo politekhnicheskogo universiteta. Prikladnaya ekologiya. Urbanistika, (2), 24–36 (2023). (in Russian).

6 Selina, A.D., and Venecianskij, A.S. Znachenie monitoringa zdorov'ya voditelya transportnogo sredstva [The Importance of Monitoring the Health of a Vehicle Driver]. Izmerenie. Monitoring. Upravlenie. Kontrol', (1), 65–71 (2024). (in Russian).

7 YUdin, D.A., and Mahon', YA.S. Vliyanie stressa i ustalosti voditelya kak determiniruyushchih faktorov dorozhno-transportnyh proisshestvij: analiz po dannym Rossijskoj Federacii [The Influence of Driver Stress and Fatigue as Determining Factors of Traffic Accidents: Analysis Based on Russian Federation Data]. Intellektual'nyj kompas: napravlenie nauchnyh otkrytij: sbornik, 95 (2026). (in Russian).

8 SHarova, D.E., and Garbuk, S.V. Metody ocenki kachestva sistem komp'yuternogo zreniya: evolyuciya podhodov, tendencii i ogranicheniya [Methods for Assessing the Quality of Computer Vision Systems: Evolution of Approaches, Trends and Limitations]. Informacionno-ekonomicheskie aspekty standartizacii i tekhnicheskogo regulirovaniya, (1), 35–41 (2026). (in Russian).

9 Boboqulov, S.R. et al. UDK 004.85 (075.8): Ispol'zovanie algoritma Non-Maximum Suppression dlya povysheniya tochnosti i skorosti obrabotki raspoznavaniya lic v real'nom vremeni [Using the Non-Maximum Suppression Algorithm to Increase the Accuracy and Speed of Real-Time Face Recognition Processing]. Innovatsion Texnologiyalar, 59 (3), 111–115 (2025). (in Russian).

10 Lohvickij, V.A., YAkovlev, E.L., and Bushev, I.V. Prakticheskoe sravnenie metodov komp'yuternogo zreniya i glubokogo obucheniya v zadache binarnoj klassifikacii izobrazhenij [Practical Comparison of

Computer Vision and Deep Learning Methods in the Binary Image Classification Task]. Intellektual'nye tekhnologii na transporte, (4), 89–98 (2025). (in Russian).

11 Shvets, O., Smakanov, B., Kovacs, L., and Gyorok, G. Intelligent system for driver support using two classifiers for simulation. Journal of Theoretical and Applied Information Technology, 100 (15), 4767–4782 (2022).

12 Chao, Q. et al. A survey on visual traffic simulation: Models, evaluations, and applications in autonomous driving. Computer Graphics Forum, 39 (1), 287–308 (2020). https://doi.org/10.1111/cgf.13803

13 Gao, M., and Shi, G.Y. Ship spatiotemporal key feature point online extraction based on AIS multi-sensor data using an improved sliding window algorithm. Sensors, 19 (12), 2706 (2019). https://doi.org/10.3390/s19122706

14 Dmitriev, E.A. Metod Violy-Dzhonsa [Viola-Jones Method]. Nauchnye issledovaniya i razrabotki studentov: materialy VI Mezhdunar. studench. nauch.-prakt. konf., 67–69 (2018). (in Russian).

15 Shvets, O., Smakanov, B., and Soltanbekov, S. The use of neuroanalytics in modern video surveillance systems. Multidisciplinary Academic Notes, Science Research and Practices: Proceedings of the XV International Scientific and Practical Conference, Madrid, Spain, 585–589 (2022). https://doi.org/10.46299/ISG.2022.1.15

16 Elharrouss, O., Almaadeed, N., and Al-Maadeed, S. A review of video surveillance systems. Journal of Visual Communication and Image Representation, 77, 103116 (2021). https://doi.org/10.1016/j.jvcir.2021.103116

17 Shvets, O., Smakanov, B., and Györök, G. Stabilization of environmental conditions to improve the performance of a mobile application for the state of the driver monitoring. Proceedings of the 17th International Symposium on Applied Informatics and Related Areas (AIS 2022), Obuda University, Székesfehérvár, Hungary, 98 (2022).

18 Zhang, Z. A flexible new technique for camera calibration. IEEE Transactions on Pattern Analysis and Machine Intelligence, 22 (11), 1330–1334 (2000). https://doi.org/10.1109/34.888718

19 Shvets, O., Smakanov, B., and Bakatbayeva, Zh. Monitoring of the state of a person at hazardous work. Proceedings of the 16th International Symposium on Applied Informatics and Related Areas, Obuda University, Székesfehérvár, Hungary, 88–91 (2021).

20 Ehsani, J.P. et al. Developing and testing a hazard prediction task for novice drivers: A novel application of naturalistic driving videos. Journal of Safety Research, 73, 303–309 (2020). https://doi.org/10.1016/j.jsr.2020.03.010

21 Figueiras, P. et al. Real-time monitoring of road traffic using data stream mining. 2018 IEEE International Conference on Engineering, Technology and Innovation (ICE/ITMC), 1–8 (2018). https://doi.org/10.1109/ICE.2018.8436271

22 Fan, Y. et al. Multiple obstacle detection for assistance driver system using deep neural networks. International Conference on Artificial Intelligence and Security (Cham: Springer International Publishing), pp. 501–513 (2019).

23 Al Haddad, C., and Antoniou, C. A data–information–knowledge cycle for modeling driving behavior. Transportation Research Part F: Traffic Psychology and Behaviour, 85, 83–102 (2022). https://doi.org/10.1016/j.trf.2021.12.017

24 Arvin, R., Kamrani, M., and Khattak, A.J. The role of pre-crash driving instability in contributing to crash intensity using naturalistic driving data. Accident Analysis & Prevention, 132, 105226 (2019). https://doi.org/10.1016/j.aap.2019.07.002

25 Bellini, P. et al. Real-time traffic estimation of unmonitored roads. 2018 IEEE 16th Intl Conf on Dependable, Autonomic and Secure Computing, 16th Intl Conf on Pervasive Intelligence and Computing, 4th Intl Conf on Big Data Intelligence and Computing and Cyber Science and Technology Congress (DASC/PiCom/DataCom/CyberSciTech), 935–942 (2018).

26 Hochin, T., Shinohara, Y., and Nishizaki, Y. Detection of driver's eye fixation on a moving target by using line fitting. 2019 6th International Conference on Computational Science/Intelligence and Applied Informatics (CSII), 13–18 (2019).

27 Kang, M.J., Kwon, O.H., and Park, S.H. Development of a crash risk prediction model using the k-nearest neighbor algorithm. Advanced Multimedia and Ubiquitous Engineering: MUE/FutureTech 2018 12 (Singapore: Springer), pp. 835–840 (2019). https://doi.org/10.1007/978-981-13-1328-8_109

28 Li, R. et al. Driver drowsiness behavior detection and analysis using vision-based multimodal features for driving safety. SAE Technical Paper Series, 1 (2020).

[1]Смақанов Б.С.,
PhD, ORCID ID: 0000-0002-4343-0463,
e-mail: s.bauyrzhan.10@gmail.com
[1*]Увалиева И.М.,
PhD, қауымдастырылған профессор, ORCID ID: 0000-0002-2117-5390,
e-mail: iuvalieva@ektu.kz

[1]Д. Серікбаев атындағы Шығыс Қазақстан техникалық университеті,
Өскемен қ., Қазақстан

ТЕОРИЯЛЫҚ-ЭМПИРИКАЛЫҚ ТӘСІЛ НЕГІЗІНДЕ ЖҮРГІЗУШІ МОНИТОРИНГ ЖҮЙЕСІНДЕ БЕТ-ӘЛПЕТТІ АНЫҚТАУДЫ МОДЕЛЬДЕУ

Аңдатпа

Мақалада жүргізушінің күйін мониторингтеу жүйелерінде қолданылатын бейнеағыннан бетті анықтау сенімділігін арттыру мәселесі қарастырылады. Жүргізуші бетінің сенімді локализациясы көздің күйін, көзқарас бағытын, бастың қалпын және шаршаудың көрнекі белгілерін кейіннен талдауға қажетті компьютерлік көрудің бастапқы кезеңі ретінде сипатталады. Зерттеудің мақсаты – қозғалмайтын, сыртқы параметрлері алдын ала калибрленген камера арқылы түсіру кезінде жарықтандыру жағдайы, бастың қалпы, кескіндегі шу деңгейі және беттің ішінара жабылу дәрежесі өзгерген жағдайда тұрақты жұмыс істейтін бейімделгіш бетті анықтау әдісін әзірлеу және оны эксперименттік тұрғыдан бағалау. Ұсынылған әдіс Виола–Джонс алгоритмі арқылы бет аймақтарын бастапқы анықтауды, анықталған аймақтарды SVM-классификаторының көмегімен тексеруді, камераны сыртқы калибрлеуді және сенімділігі жоғары анықтау нәтижелерін псевдобелгілер ретінде пайдалану арқылы параметрлерді инкрементті жаңартуды біріктіреді. Әдіс жеті еріктінің қатысуымен әртүрлі түсіру жағдайларында жазылған 12 бейнежазбадан алынған 18 000 кадр негізінде бағаланды. Эксперимент нәтижелері біріктірілген әдістің базалық Виола–Джонс алгоритмімен және оның статикалық SVM-классификаторымен толықтырылған нұсқасымен салыстырғанда бетті анықтаудың анағұрлым жоғары көрсеткіштерін қамтамасыз ететінін көрсетті. Ұсынылған әдіс секундына 22 кадр өңдеу жылдамдығында Precision көрсеткіші бойынша 0,91, ал Recall көрсеткіші бойынша 0,90 нәтижеге қол жеткізді. Зерттеу аясында тек бетті анықтау нәтижелері бағаланды; жүргізушінің шаршауын, ұйқышылдығын, көзінің күйін немесе мимикасын тікелей жіктеу жүргізілген жоқ. Алынған нәтижелер ұсынылған әдісті нақты уақыт режимінде жұмыс істейтін жүргізуші күйін мониторингтеу жүйесінің есептеу ресурстарын аз қажет ететін бастапқы компоненті ретінде қолдануға мүмкіндік беретінін көрсетеді.

Түйін сөздер: бейнеталдау, бетті анықтау, жүргізушіні мониторингтеу жүйесі, компьютерлік көру, бейнеағын, Виола–Джонс әдісі, SVM-классификаторы, бейімделетін анықтау, камераны калибрлеу, нақты уақыттағы өңдеу.

[1]Смақанов Б.С,
PhD, ORCID ID: 0000-0002-4343-0463,
e-mail: s.bauyrzhan.10@gmail.com
[1*]Увалиева И.М.,
PhD, ассоциированный профессор, ORCID ID: 0000-0002-2117-5390,
e-mail: iuvalieva@ektu.kz

[1]Восточно-Казахстанский технический университет им. Д. Серикбаева,
г. Усть-Каменогорск, Казахстан

МОДЕЛИРОВАНИЕ МОНИТОРИНГА СОСТОЯНИЯ ВОДИТЕЛЯ НА ОСНОВЕ ТЕОРЕТИКО-ЭМПИРИЧЕСКОГО ПОДХОДА

Аннотация

В статье рассматривается проблема повышения надежности обнаружения лица в видеопотоке, используемом в системах мониторинга состояния водителя. Надежная локализация лица водителя рассматривается

как предварительный этап компьютерного зрения, необходимый для последующего анализа состояния глаз, направления взгляда, положения головы и визуальных признаков усталости. Целью исследования является разработка и экспериментальная оценка адаптивного метода обнаружения лица, обеспечивающего устойчивую работу при изменении освещения, положения головы, уровня шума изображения и частичном закрытии лица в условиях использования неподвижной камеры с предварительно выполненной внешней калибровкой. Предложенный метод объединяет первоначальное обнаружение областей лица с помощью алгоритма Виолы–Джонса, проверку обнаруженных областей посредством SVM-классификатора, внешнюю калибровку камеры и инкрементное обновление параметров на основе результатов обнаружения с высокой степенью достоверности, используемых в качестве псевдометок. Метод оценивался на наборе из 18 000 видеокадров, полученных из 12 видеозаписей с участием семи добровольцев в различных условиях съемки. Экспериментальные результаты показали, что интегрированный метод обеспечивает более высокие показатели обнаружения лица по сравнению с базовым алгоритмом Виолы–Джонса и его комбинацией со статическим SVM-классификатором. Предложенный метод достиг Precision 0,91 и Recall 0,90 при скорости обработки 22 кадра в секунду. В исследовании оценивается только обнаружение лица; непосредственная классификация усталости, сонливости, состояния глаз или мимики водителя не выполнялась. Полученные результаты показывают, что предложенный метод может использоваться как предварительный малоресурсный компонент системы мониторинга состояния водителя, работающей в режиме реального времени.

Ключевые слова: видеоаналитика, обнаружение лица, система мониторинга водителя, компьютерное зрение, видеопоток, метод Виолы–Джонса, SVM-классификатор, адаптивное обнаружение, калибровка камеры, обработка в реальном времени.

ӘОЖ 004.
ҒТАХР 28.23.15

https://doi.org/10.55452/1998-6688-2026-23-3-298-311

[1]Тасжурекова Ж.К.,
т.ғ.к., доцент м.а., ORCID ID: 0000-0002-8307-9417,
e-mail: taszhurekova@mail.ru
[2]Козыбаев Д.Х.,
PhD, ORCID ID: 0000-0001-5509-8656
e-mail: kozybayev_dkh@enu.kz
[2*]Танирбергенов А.Ж.,
т.ғ.к., доцент м.а., ORCID ID: 0009-0000-8401-5434,
*e-mail: t.adilbek@mail.ru
[3]Ахметжанова Ш. Е.
т.ғ.к, доцент м.а., ORCID ID: 0000-0002-4131-8328,
e-mail: sh.akhmetzhanova@astanait.edu.kz
[1]Абдувалова А.Д.,
т.ғ.к, доцент м.а., ORCID ID: 0000-0002-4683-7821
e-mail: abduvalova_ad@mail.ru

[1]М.Х. Дулати атындағы Тараз өңірлік университеті, Тараз қ., Қазақстан
[2]Л.Н. Гумилев атындағы Еуразия ұлттық университеті, Астана қ., Қазақстан
[3]Astana IT university, Астана қ., Қазақстан

АЛАҚАН ПАРАМЕТРЛЕРІН ТАЛДАУ ҮШІН МАШИНАЛЫҚ ОҚЫТУ ТЕХНОЛОГИЯЛАРЫН ҚОЛДАНА ОТЫРЫП, ЖЕКЕ ТҰЛҒАНЫ СӘЙКЕСТЕНДІРУДІҢ БИОМЕТРИЯЛЫҚ ЖҮЙЕСІН ӘЗІРЛЕУ

Аңдатпа

Бұл мақалада алақан параметрлерін талдау арқылы жеке тұлғаны сәйкестендіруге арналған биометриялық жүйені машиналық оқыту технологиялары негізінде әзірлеу мәселелері қарастырылады. Зерттеудің өзектілігі ақпараттық қауіпсіздікті қамтамасыз ету, қолжетімділікті бақылау және пайдаланушыларды сенімді идентификациялау қажеттілігімен байланысты. Алақан биометриялық идентификатор ретінде жоғары даралыққа ие болғандықтан, оның анатомиялық ерекшеліктері – саусақ контурлары, тері текстурасы, алақан сызықтары және қан тамырларының орналасуы – тұлғаны тануда тиімді белгі ретінде пайдаланылды. Зерттеу барысында алақан кескіндерінен маңызды биометриялық аймақтарды автоматты түрде анықтау үшін ROI-LANet моделі қолданылды. Бұл модель алақандағы негізгі нүктелерді дәл локализациялап, кескінді туралау және қызығушылық аймағын (ROI) бөліп алу мүмкіндігін қамтамасыз етеді. Ал алынған ROI негізінде пайдаланушыларды жіктеу міндетін орындау үшін ResNet18 терең конволюционды нейрондық желісі пайдаланылды. Қалдық блоктарға негізделген бұл модель күрделі биометриялық белгілерді тиімді тануға және классификация дәлдігін арттыруға мүмкіндік береді. Эксперименттік нәтижелер ұсынылған жүйенің жоғары дәлдік пен тұрақтылық көрсететінін дәлелдеді. Сынақтар барысында сәйкестендірудің дәлдігі шамамен 97% деңгейінде болды. Сонымен қатар жүйе жарықтандыру жағдайлары мен түсіру бұрыштарының өзгеруіне төзімді болып шықты. Алынған нәтижелер әзірленген биометриялық жүйенің қауіпсіздік жүйелерінде, қолжетімділікті бақылауда және транзакцияларды тексеруде практикалық қолдану әлеуетінің жоғары екенін көрсетеді.

Түйін сөздер: биометриялық сәйкестендіру, машиналық оқыту, алақан, нейрондық желілер, ROI-LAnet, ResNet18, алақан параметрлері, кіруді бақылау, тексеру.

Кіріспе

Адамның физикалық және мінез-құлық ерекшеліктеріне негізделген биометриялық сәйкестендіру қазіргі уақытта қауіпсіздік саласында маңызды рөл атқарады. Мұндай сипаттамаларға саусақ іздері, дауыс, бет-әлпет, көздің қарашығы, сондай-ақ қолжазба, қолтаңба және жүріс-тұрыс сияқты мінез-құлық белгілері жатады. Көптеген әдістердің ішінде алақан арқылы тұлғаны тануға барған сайын көбірек назар аударылуда. Адамның алақанында саусақтардың пішіні, алақан сызықтары, тері текстурасы, тіпті қан тамырларының орналасуы сияқты көптеген жеке ерекшеліктердің тұтас жиынтығы бар. Осының арқасында бұл әдіс сенімді саналады және оны қолдан жасау іс жүзінде мүмкін емес. Алақанды биометриялық идентификатор ретінде пайдалану медициналық жүйелерде қол жеткізуді бақылау, транзакцияларды тексеру және тұлғаны сәйкестендіру үшін кең мүмкіндіктер ашады. Бұл әдістің негізгі артықшылықтары – жоғары дәлдік пен жабдықтың қолжетімділігі.

Бет-әлпетті танудан айырмашылығы, алақанды тануға жарықтандыру немесе бет әлпеті әсер етпейді, сондықтан жүйе тіпті күрделі жағдайларда да тұрақты жұмыс істейді. Сонымен қатар, алақанды сканерлеу жылдам жүзеге асырылады және пайдаланушының араласуын қажет етпейді, бұл оны ыңғайлы әрі кедергісіз етеді.

Зерттеулерде [1–4] биометриялық технологияларды практикада енгізу мысалдары қарастырылған. [1] жұмыста сәйкестендіру әдістеріне, соның ішінде бет кескінін пайдалануға және дәлдікті арттыру үшін нейрондық желілерді қолдануға салыстырмалы талдау жүргізілген. [2] және [3] жұмыстарда саусақ ізі деректеріне негізделген шешімдер қарастырылып, саусақ іздерінің қасиеттерін сипаттайтын математикалық модельдер және балама әдістермен салыстырғанда жоғары дәлдік көрсеткен сәйкестендіру алгоритмдері әзірленген. [4] мақалада алақанның тері астындағы қан тамырларының кескіндерін пайдаланатын жүйелерге назар аударылған. Бұл тәсіл барған сайын кеңінен қолданылуда, өйткені ол сенімділік пен қауіпсіздікті іске асырудың салыстырмалы қарапайымдылығымен ұштастырады.

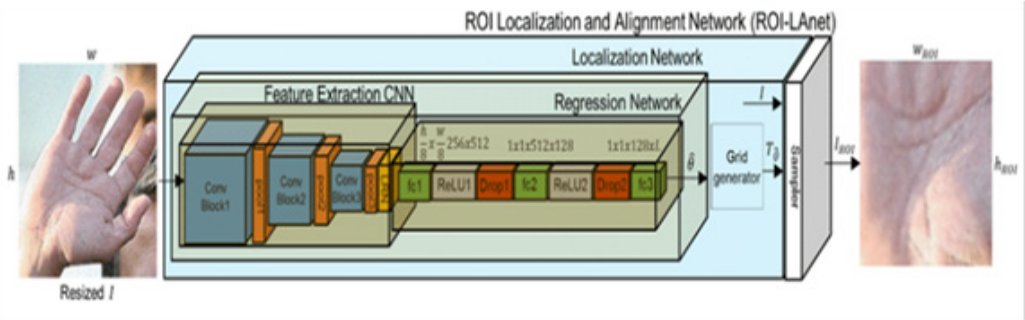
Машиналық оқыту технологиялары мен конволюциялық нейрондық желілерді (CNN) енгізу ерекше назар аударуды қажет етеді. Оларды пайдалану алақан кескіндерінен белгілерді бөліп алу дәлдігін арттырып, тану процесін оңтайландырды.

Бұл зерттеудің мақсаты – машиналық оқыту әдістерін қолдана отырып, алақан параметрлеріне негізделген тұлғаны сәйкестендірудің биометриялық жүйесін құру. Жұмыста биометриялық белгілерді анықтау және жіктеу кезеңдері қарастырылып, ұсынылған тәсілді іске асыру үшін пайдаланылатын ROI-LANet және ResNet18 модельдерін сынау нәтижелері ұсынылады.

Материалдар мен әдістер

Бұл жұмыста адамның алақан кескіндері негізінде тұлғаны сәйкестендіру мәселесі зерттелді. Зерттеу барысында конволюционды нейрондық желілердің биометриялық сәйкестендірудегі тиімділігі қарастырылды. Эксперименттік зерттеулер жүргізу үшін Kaggle платформасындағы ашық palmprint деректер қоры пайдаланылды. Деректер жиыны әртүрлі жарықтандыру және түсіру жағдайларында алынған алақан кескіндерін қамтиды. Зерттеу барысында 120 адамға тиесілі 2400 алақан кескіні қолданылды. Деректер жиыны оқыту және тестілеу жиындарына 80/20 қатынасында бөлінді. Кескіндер алдын ала өңдеуден өткізіліп, өлшемдері 224×224 пикселге келтірілді. Арнайы алақанды талдау мақсатында биометриялық ерекшеліктері бар аймақтарды анықтауға өте қолайлы – негізгі модель ретінде ROI-LANet таңдалды. Бұл модель үлкен екі бөліктен тұрады. Біріншісі – мүмкіндіктерді алуға арналған желі – ол алақандағы әрбір қабатты қарап, пайдалы болуы мүмкін барлық нәрсені таңдайды: терінің текстурасы, алақандағы сызықтар, олардың қиылысулары, жалпы контур. Әрбір қарастырылған қабат кескінді өзінше өңдейді, нәтижесінде әр арна сипаттамалардың жеке жиынын сақтайтын көп өлшемді көрініс пайда болады. Екіншісі – регрессиялық желі.

Регрессиялық желі суретпен емес, бірінші желі қалыптастырған мүмкіндіктермен жұмыс істейді. Оның міндеті – алақандағы негізгі нүктелердің координаталарын анықтау: сызықтар қай жерде қиылысады, олар қалай орналасқан, қай аймақтарды ерекшелеу керек. Содан кейін бұл координаттар (θ) кескінді тартып, оны туралап, қажетті аумақты таңдайтын арнайы Grid Generator блогымен пайдаланылады. Бұл теңестіру таза және дәл ROI алуға мүмкіндік береді, содан кейін талдау мен салыстыруға пайдаланылады.



Сурет 1 – ROI-Lanet жұмыс процесі

1-суреттен көрініп тұрғандай, ROI-LANet жұмыс процесін келесі қадамдарға бөлуге болады:

- алақанның кескіні енгізу (Resized I) мүмкіндіктерді (Feature Extraction CNN) шығару желісіне беріледі, онда конволюционды блоктар оны талдайды және негізгі мүмкіндіктерді шығарады;
- регрессиялық желі алынған мүмкіндіктерді өңдейді және алақан кескініндегі негізгі нүктелердің θ координаталарын болжайды;
- Grid Generator блогын пайдалану арқылы кескін туралanады және қызығушылық аумағы (ROI) таңдалады – ең маңызды биометриялық мүмкіндіктерді қамтитын алақан аймағы;
- қорытынды кескінде (IROI) алақанның тегістелген және қалыпқа келтірілген аумағын қамтиды, әрі қарай талдау және анықтау үшін пайдаланылады.

ROI-Lanet бағдарламасының басты артықшылығы – алақан кескініндегі негізгі аймақтарды автоматты түрде анықтау мен туралау мүмкіндігі болады, бұл тану процесін дәлірек түсіру бұрышы мен жарықтандырудағы өзгерістерге сенімдірек етеді.

Қалдық желі 18, жиі ResNet18-ге қысқартылған

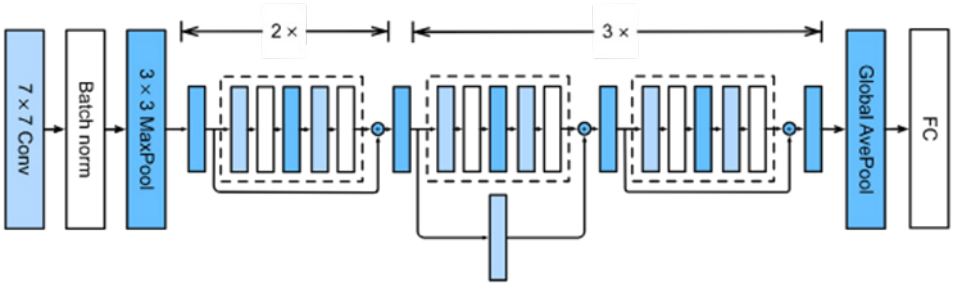
Пайдаланушыларды классификациялау үшін қызығушылық аймақтарын анықтағаннан кейін ResNet18 моделі пайдаланылады. ResNet18, 18 қабаты бар терең конволюциялық нейрондық желі терең нейрондық желіні оқыту мәселелерін тиімді шешуге арналған. ResNet18 негізгі артықшылығы оның желі тереңдігінің ұлғаюымен пайда болатын градиенттің әлсіреу мәселесін жеңетін қалдық блоктарды пайдалануы болады [7]. Осының арқасында желіні көптеген қабаттар саны болса да тиімді оқытуға болады.

ResNet18 архитектурасы:

ResNet-тің басқа терең нейрондық желілерден басты айырмашылығы – қалдық блоктарды пайдалану. Олар кәдімгі тізбектелген қабаттарды айналып өтіп, ақпараттың желінің бірнеше қабаттары арқылы өтуіне мүмкіндік береді. Стандартты нейрондық желілерде желінің тереңдігі артқан сайын градиенттің әлсіреу құбылысын байқауға болады, бұл тиімді оқытуды қиындатады. ResNet ішіндегі қалдық қосылымдар бұл мәселені шешуге көмектеседі. Қалдық қосылымдардың арқасында ақпаратты бірнеше желі деңгейлері арқылы тікелей жіберуге болады, бұл ақпаратты сақтауды және параметрлерді тиімдірек жаңартуды жеңілдетеді.

- терең архитектурасы: ResNet18 18 қабаттан тұрады (2-сурет), ол деректердегі күрделі үлгілер мен тәуелділіктерді түсіруге мүмкіндік береді. Желі конволюциялық қабаттар, пакетті қалыпқа келтіру және ReLU белсендіру функциялары сияқты бірнеше қабат түрлерін

пайдаланады. Терең оқыту тәсілінің арқасында ResNet18 күрделі жіктеу тапсырмаларын, соның ішінде алақан суреттерінен биометриялық тануды сәтті орындай алады;



Сурет 2 – ResNet18 архитектурасы

Бұл жүйеде ResNet18 ROI-LANet үлгісін пайдаланып қызығушылық аймағын (ROI) алдын ала таңдағаннан кейін алақан кескінінің классификаторы ретінде әрекет етеді. Бұл кескінді сызықтар, текстуралар және контурлар сияқты алақандардың бірегей биометриялық сипаттамаларына сүйене отырып, бейнені жіктейтін ResNet18 жүйесіне беріледі. Өзінің архитектурасының арқасында ResNet18 тұлғаны сәйкестендіру міндетін шешуде жоғары дәлдік пен сенімділікті көрсетеді.

Өңдеу процесінде модель бірнеше кезеңнен өтеді. Бастапқыда қиыстырылған қабаттар шеттері мен текстураларын қоса алғанда, кескіннің басты белгілерін алады. Содан кейін ақпарат негізгі сипаттамаларды сақтауға және терең оқыту проблемаларын азайтуға мүмкіндік беретін қалдық блоктар арқылы өңделеді. Өңдеу аяқталғаннан кейін белгілер түпкілікті жіктеу үшін толық байланысқан қабаттарға беріледі. Соңғы кезеңде Softmax шығыс деректерін алақан суретінің қай класқа жататынын анықтауға көмектесетін ықтималдыққа түрлендіреді.

ResNet18 таңдауы оның күрделі биометриялық белгілерді тану және қалдық архитектураның арқасында үлкен көлемдегі деректермен жұмыс істеу қабілетіне негізделген, бұл нейрожелінің тереңдігіне байланысты қиындықтарды жояды. Модельдің артықшылықтары жіктелудің жоғары дәлдігін, күрделі бейнелерді өңдеу мүмкіндігін, терең желілерді оқыту проблемаларына төзімділікті және биометриялық міндеттердегі икемділікті қамтиды.

Жүйеде ResNet18 қатар MobileNetV2 сияқты баламалар қарастырылды. Бұл ықшам модель мобильдік құрылғылар мен ресурстары шектеулі жүйелер үшін арнайы әзірленген. Ол жады мен есептеу қуатының ең аз шығынымен деректерді жылдам өңдеуді қамтамасыз ететін терең орамдар мен инверстік қалдық блоктардың арқасында тиімді. MobileNetV2 жылдамдығы мен ресурстық оңтайландыру маңызды жүйенің мобильді нұсқалары үшін жарамды, бірақ негізгі серверлік іске асыру үшін оның жоғары дәлдігіне байланысты ResNet18 артықшылығы берілді.

MobileNetV2 ықшамдылығы мен жылдам әрекет етуінің артықшылықтарына ие болғанымен, ол дәлдігі жағынан биометриялық сәйкестендіру міндеттерінен төмен, бұл оны жүйенің серверлік нұсқасына аз қолдануға мүмкіндік берді. Болашақта модель шектеулі ресурстары бар құрылғыларда, мысалы, мобильді немесе IoT-құрылғыларда деректерді жылдам өңдеуді талап ететін қосымшалар үшін пайдалы болуы мүмкін.

MobileNetV2-ден басқа, алақанды тану міндеттері үшін басқа да нөлдік желілердің архитектурасы бейімделуі мүмкін. Алайда, VGG сияқты, бұл модель айтарлықтай ресурстарды талап етеді.

Сәйкестендірудің биометриялық жүйесі үшін қолайлы архитектураны таңдау модельдің тиімділігі мен практикалық қолданылуына әсер ететін бірқатар факторлармен анықталады. Қауіпсіздікпен байланысты тапсырмалар үшін басты басымдық жоғары дәлдік болады. Бұл жобада алақан суреттерін жіктеу кезінде жақсы нәтижелер көрсету қабілетінің арқасында таңдау ResNet18 түсті. Есептеу шығындары мен модель жұмысының жылдамдығы арасындағы

теңгерімді ескеру маңызды. Ресурстар шектеу болып табылмайтын серверлік жүйелер үшін жоғары өнімділікті қамтамасыз ете отырып, ResNet немесе DenseNet сияқты неғұрлым күрделі сәулеттерді пайдалануға болады. Дегенмен, мобильді қосымшаларда жылдамдық пен энергия тиімділігі үлкен рөл атқарады, бұл MobileNetV2-ні осындай жағдайлар үшін оңтайлы шешім етеді. Шағын архитектурасы және аз параметрлері бар модельдерді әртүрлі қолданбаларға біріктіру оңайырақ. MobileNetV2 әсіресе іске асырудың қарапайымдылығы мен ең аз орналастыру уақыты маңызды болатын тапсырмалар контекстінде пайдалы.

Талдау нәтижесінде бұл жүйенің негізгі үлгісі ResNet18 болатын, өйткені ол серверлік өңдеуде жоғары дәлдік пен сенімділікті қамтамасыз етеді. Сонымен қатар, MobileNetV2 жылдамдық пен энергия тиімділігі маңызды болып табылатын мобильді платформалар үшін өзекті балама болып қала береді.

ROI-LANet математикалық моделі алақанға негізделген сәйкестендіру жүйесінің орталық элементіне айналады. Оның негізгі мақсаты – алақан сызықтары мен тері текстурасы сияқты негізгі биометриялық ақпаратты қамтитын кескіндегі қызығушылық аймақтарын анықтау және бөліп көрсету. Оның механизмі мен қолданылуын тереңірек түсіну үшін ROI-LANet моделінің математикалық аспектілерін қарастырайық.

1. Айналмалы амалдар (Convolutional Operations)

ROI-LANet жүйесіндегі конволюциялық қабаттар жиектер, текстуралар және контурлар сияқты мүмкіндіктерді шығару үшін сүзгілерді (ядроларды) қолдана отырып, кіріс кескінінде жұмыс істейді.

Математикалық түрде бұл былай өрнектеледі:

$$Y_{i,j} = \sum_{m=0}^{M-1} \sum_{n=0}^{N-1} X_{0+m,j+n} * K_{m,n} \quad (1)$$

Мұндағы:

$X_{i,j}$ – енгізу суреті,

$K_{m,n}$ – конволюция сүзгісі,

$Y_{i,j}$ – кескіндегі әрбір элемент үшін конвульсияның нәтижесі,

M и N – сүзгі өлшемдері.

Орамдар бірнеше деңгейде жүзеге асырылады, сүзгілердің саны артып келеді, бұл желіге барған сайын күрделі функцияларды шығаруға мүмкіндік береді. Конволюциялық операциялар желінің бірізді қабаттарында жүзеге асырылады; тереңдеген сайын сүзгілер санының артуы барған сайын күрделі белгілерді шығаруға мүмкіндік береді.

2. Негізгі нүктені болжауға арналған регрессиялық желі

Конвотиялық қабаттар кескіннен мүмкін элементтерді алғаннан кейін, бұл элементтер қызығушылық аймағын теңестіру үшін пайдаланылатын негізгі нүктелердің координаттарын болжау үшін толығымен келісілген қабаттарға беріледі. Негізгі нүктелердің координаттарын болжау функциясы регрессиялық үлгімен сипатталған, ол әдетте былайша көрсетіледі: Негізгі нүктелердің координаттарын болжау функциясы регрессиялық үлгісімен сипатталып, төмендегідей өрнектеледі:

$$\hat{\theta} = W * X + b \quad (2)$$

Мұндағы:

X - алынған белгілердің векторы (конволюционды қабаттардың нәтижелері),

W – оқу барысында жаңартылатын салмақ матрицасы,

b - ығысу (bias),

θ - болжанған трансформация параметрлері (ROI теңестіру үшін қажетті негізгі нүктелер).

Бұл болжанған параметрлер кескінді одан әрі түрлендіру және туралау үшін пайдаланылады.

3. Кескінді түрлендіру: Thin Plate Splines (TPS)

Кескінді болжанған негізгі нүктелер негізінде тегістеуге мүмкіндік беретін жұқа пластиналы сплайндар әдісі. Бұл әдіс болжамды координаттарға сәйкес кескінді дәл деформациялауға мүмкіндік беретін сызықты емес түрлендіру.

TPS беттің иілу энергиясын азайтады, оны төмендегідей жазуға болады:

$$E(f) = \iint \left(\frac{\partial^2 f}{\partial x^2} \right)^2 + 2 \left(\frac{\partial^2 f}{\partial x \partial y} \right)^2 + \left(\frac{\partial^2 f}{\partial y^2} \right) dxdy \quad (3)$$

Мұндағы f – кескіннің деформациясын сипаттайтын функция. TPS кескінді болжамды негізгі нүктелерге теңестіретін сызықтық емес түрлендіруді құрастырады, бұл қызығушылық аймағын жоғары дәлдікпен шығаруға мүмкіндік береді.

4. Аффинді түрлендіру (Affine Transformation)

Аффинді түрлендіру алдын ала теңестіру үшін де қолданылады, ол келесі формуламен сипатталады:

$$T(x) = A * x + b \quad (4)$$

Мұндағы:

A – түрлендіру матрицасы (модель бойынша болжанған),

x – кескіндегі нүктенің бастапқы координаталары,

b – ығысу

Аффинді түрлендіру классификация дәлдігін жақсартатын болжамды негізгі нүктелер негізінде кескінді масштабтауға, айналдыруға және жылжытуға мүмкіндік береді.

5. Шығын функциясын бағалау (Loss Function)

Модельді оқытуда негізгі нүктелердің болжанған және шынайы координаталары арасындағы айырмашылықты өлшейтін жоғалту функциясы қолданылады. Жоба төменде көрсетілгендей өрнектелетін орташа квадраттық қатені (MSE) пайдаланады:

$$L(\hat{\theta}, \theta) = \frac{1}{N} \sum_{i=1}^{N} (\hat{\theta}_i - \theta_i)^2 \quad (5)$$

Мұндағы:

$\hat{\theta}_i$ – негізгі нүктенің болжанған координаталары,

θ_i – шынайы координаттар,

N – негізгі нүктелердің саны.

Модельді оқытудың мақсаты болжанған түйінді нүктелер нақты координаттарға мүмкіндігінше жақын сәйкес келуі үшін осы жоғалту функциясын азайту болады.

Осылайша, ROI-LANet жобасы алақан кескініндегі қызығушылық аймағын дәл шығару үшін мүмкіндіктерді шығаруға арналған конволюциялық операцияларды, негізгі нүктені болжау үшін регрессия желісін және туралау әдістерін (TPS және аффинді түрлендірулер) тіркесімін пайдаланады. Бүкіл процесс болжанған және нақты негізгі нүктелер арасындағы қателерді азайтуға негізделген, бұл тану және жіктеу сапасын жақсартуға мүмкіндік береді [10].

ResNet18

ResNet18 (Residual Network) моделі – қызығушылық аумағын бөлгеннен кейін алақан суреттерін жіктеу үшін негізгі компонент. Модель терең желілерді оқыту кезінде градиент

әлсіреу мәселелерін болдырмауға көмектесетін қалдық блоктарды (Residual Blocks) қолданатын терең конвульстік нейрондық желі архитектурасына негізделген.

1. Конволюциялық операциялар (Convolutional Operations)

Конволюциялық қабаттар ResNet18 моделінің негізгі құрамдас бөлігі және кескіндерден мүмкіндіктерді шығару үшін пайдаланылады. Конволюция операциялары төменде көрсетілген формуламен сипатталады:

$$Y_{i,j} = \sum_{m=0}^{M-1} \sum_{n=0}^{N-1} X_{0+m,j+n} * K_{m,n} \tag{6}$$

Мұндағы:

$X_{i,j}$ – енгізу кескіні

$K_{m,n}$ – конволюция сүзгісі,

$Y_{i,j}$ – конволюция нәтижесі,

M и N – сүзгі өлшемдері.

Конволюциялық қабаттар қарапайым элементтерден (мысалы, жиектер) бастап және күрделірек элементтерге (мысалы, текстура немесе нысандар) ауысатын әртүрлі деңгейлерде кескіннің негізгі мүмкіндіктерін шығарады.

2. Қалдық блоктар (Residual Blocks)

ResNet18 архитектурасының негізгі ерекшелігі – қалдық блоктарды пайдалану. Қалдық блоктар ақпаратты желінің бірнеше қабаттары арқылы тікелей жіберуге мүмкіндік береді, бұл терең нейрондық желіні оқыту кезінде градиенттің әлсіреу мәселесін болдырмауға көмектеседі. Бұл қабаттарды өткізіп жіберуге мүмкіндік беретін өткізіп жіберу қосылымдары (skip connections) арқылы қол жеткізіледі, кіріс деректерді тікелей қабат шығысына береді.

Қалдық блокты келесідей жазуға болады:

$$F(x) = f(x) + x \tag{7}$$

Мұндағы:

x – кіріс деректер векторы;

f(x) – конволюциялық қабаттар мен белсендіру функциялары арқылы алынған түрлендіру нәтижесі;

F(x) – қалдық блоктың шығыс мәні.

Қалдық байланыстар (skip connections) желінің терең қабаттарында градиенттің жоғалу мәселесін азайтып, модельдің тұрақты оқытылуын қамтамасыз етеді.

3. Белсендіру функциялары (Activation Functions)

ResNet18 модельге сызықты еместікті енгізетін және желіге деректердегі күрделі тәуелділіктерді үйренуге көмектесетін ReLU (Rectified Linear Unit) белсендіру функциясын пайдаланады.

ReLU функциясы келесідей анықталады:

$$f(x) = \max(0, x) \tag{8}$$

ReLU белсендіру функциясы теріс мәндерді нөлге теңестіріп, оң мәндерді өзгеріссіз қалдырады. Бұл тәсіл есептеу күрделілігін төмендетіп, нейрондық желінің оқытылу жылдамдығын арттырады.

4. Толық байланысқан қабаттар (Fully Connected Layers)

Кескін мүмкіндіктері конволюционды қабаттар мен қалдық блоктар арқылы шығарылғаннан кейін, олар қорытынды классификацияны орындау үшін толық байланысқан қабаттарға беріледі.

Толық байланысқан қабатты келесі теңдеу арқылы сипаттауға болады:

$$z = W \cdot a + b \tag{9}$$

Мұндағы:
a – кіріс мүмкіндік векторы,
W – салмақтардың матрицасы,
b – орын ауыстыру векторы,
z – толық байланысқан қабаттың шығыс мәні.

Толық байланысқан қабаттар алынған белгілерді соңғы классификация кезеңіне түрлендіреді. Бұл қабаттар жоғары деңгейлі биометриялық ерекшеліктерді өңдеп, пайдаланушы кластарын ажыратуға мүмкіндік береді.

5. Классификациялауға арналған Softmax

Соңғы қадамда ResNet18 шығыс мәндерін класс ықтималдығына түрлендіру үшін Softmax функциясын пайдаланады.

Softmax функциясы келесідей есептеледі:

$$\sigma(z)_i = \frac{e^{z_i}}{\sum_{j=1}^{n} e^{z_j}} \tag{10}$$

Мұндағы:
z_i – i класының шығыс мәні,
n – кластар саны,
$\sigma(z)_i$ — кіріс деректерінің i класына жататын ықтималдығы болады.

Softmax функциясы модель шығысын ықтималдық үлестіріміне түрлендіреді. Нәтижесінде әрбір класс үшін ықтималдық мәні есептеледі және ең жоғары ықтималдыққа ие класс сәйкестендіру нәтижесі ретінде қабылданады.

6. Жоғалту функциясы (Loss Function)

Модельді оқыту үшін болжамды класс таралуы мен нақты класс белгілері арасындағы айырмашылықты өлшейтін кросс-энтропия жоғалту функциясы пайдаланылады. Кросс-энтропия жоғалту функциясы болжанған және нақты кластар арасындағы айырмашылықты бағалайды. Оқыту процесінің негізгі мақсаты – осы қателік мәнін минимизациялау арқылы модельдің классификация дәлдігін арттыру.

$$L = -\sum_{i=1}^{n} y_i \log(\hat{y}_i) \tag{11}$$

Мұндағы:
y_i – бұл нақты класс белгісі (класс дұрыс болса 1, керісінше жағдайда 0),
$\hat{y}_i$ – i класы үшін болжанған ықтималдық,
n – класстар саны.

Осылайша, ұсынылған математикалық модель ROI-LANet және ResNet18 архитектураларының өзара байланысын толық сипаттайды. Конволюциялық операциялар, қалдық блоктар, белсендіру функциялары және шығын функциялары бірге жұмыс істей отырып, алақан кескіндерінен биометриялық белгілерді тиімді бөліп алуға және жоғары дәлдікпен классификациялауға мүмкіндік береді.

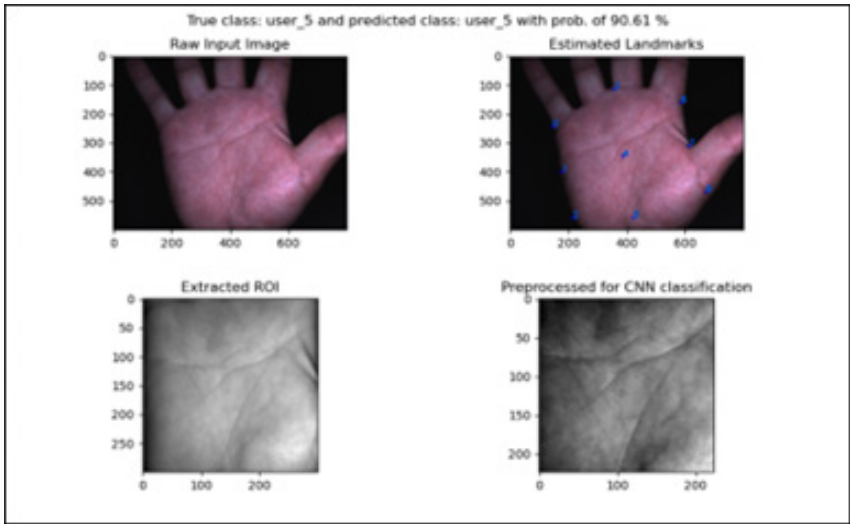
Нәтижелер және талқылау

Алақан кескіні негізінде жеке тұлғаны сәйкестендіруге әзірленген модель тестілеу барысында жоғары дәлдік пен тұрақтылық көрсеткіштерін көрсетті. Сәйкестендірудегі биометриялық жүйенің негізгі міндеті – алақан кескініндегі қызығушылық аймақтарын (ROI) бөліп көрсету, негізгі нүктелерді болжау және оларды оқытылған класстар бойынша классификациялау болады.

Болжау және визуализация процесі

Бірінші кезеңде модель кіріс ретінде алақан кескінін алады. Содан кейін ол негізгі нүктені анықтауды және қызығушылық аймағын (ROI) таңдап алумен қоса бірқатар өңдеу кезеңдерінен өтеді. 3-суретте көрсетілген өңдеу кезеңдерін келесідей көрсетуге болады:

- Түпнұсқа кескін (Raw Input Image): модельге кіріс ретінде берілген алақанның бастапқы кескіні.
- Белгілі бір негізгі нүктелер (Estimated Landmarks): модель алақандағы негізгі нүктелерді анықтайды.
- Таңдалған қызығушылық аймағы (Extracted ROI): алақан сызықтары мен текстурасы сияқты негізгі биометриялық мүмкіндіктерді қамтитын аймақтар көрсетілген кескіннен алынады.
- Классификацияға дайындық (Preprocessed for CNN classification): алынған қызығушылық аймағы алдын ала өңделеді және конволюционды нейрондық желіні (CNN) пайдалана отырып, одан әрі классификациялауға дайындалады.



Сурет 3 – Өңдеу нәтижесі

Классификация дәлдігі

Таңдалған қызығушылық аймағын алдын ала өңдегеннен кейін модель кескінді классификациялайды және алақанның кескіні қай пайдаланушыға (классқа) жататынын болжайды. Классификациялау нәтижелері болжанған класстың ықтималдығы ретінде көрсетіледі. Сынақ нәтижелері бойынша ұсынылған модель алақан кескіндерін сәйкестендіруде 97% дәлдік көрсетті. Бұл нәтиже ROI-LANet және ResNet18 модельдерінің биометриялық белгілерді тиімді өңдей алатынын дәлелдейді.

Оқыту және тексеру кестелері

Кесте-1 нәтижелерінен ResNet18 моделінің жоғары дәлдік пен есептеу тиімділігі арасындағы оңтайлы теңгерімді қамтамасыз ететіні байқалады. MobileNetV2 өңдеу жылдамдығы бойынша тиімді болғанымен, дәлдігі төменірек нәтиже көрсетті. Ал VGG16 моделі жоғары есептеу ресурстарын талап ететіні анықталды.

Салыстырмалы эксперименттер барысында ұсынылған ResNet18 моделі MobileNetV2 және VGG16 архитектураларымен салыстырылды. Нәтижелер көрсеткендей, ResNet18 моделі сәйкестендіру дәлдігі бойынша ең жоғары көрсеткішке ие болды. Сонымен қатар, MobileNetV2 моделі есептеу ресурстарын аз пайдаланғанымен, биометриялық белгілерді ажыратуда төмен нәтиже көрсетті. VGG16 архитектурасы жоғары дәлдікке жақын нәтиже бергенімен, параметрлер санының көп болуы оқыту уақытын едәуір арттырды.

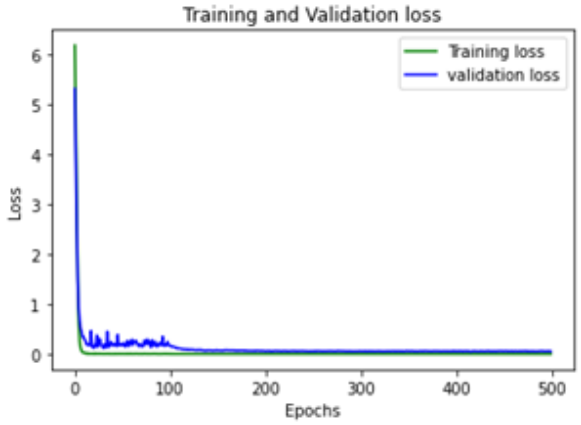
Кесте 1 – Модельдердің салыстырмалы нәтижелері

Модель	Дәлдік (%)	Оқыту уақыты	Бір кескінді өңдеу уақыты	Параметр саны
ResNet18	97	2.3 сағ	0.08 с	11.7 млн
MobileNetV2	93	1.5 сағ	0.04 с	3.4 млн
VGG16	95	4.1 сағ	0.12 с	138 млн

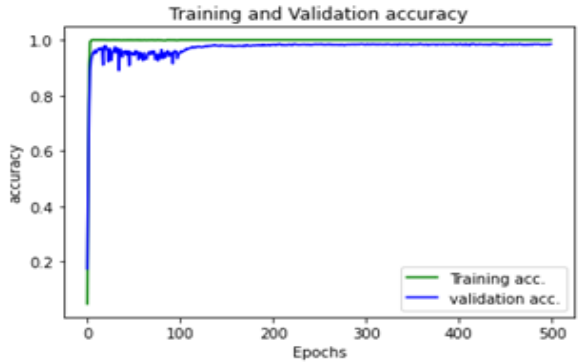
Биометриялық жүйенің тиімділігін жан-жақты бағалау үшін Accuracy, FAR (False Acceptance Rate), FRR (False Rejection Rate), EER (Equal Error Rate), Precision, Recall және F1-score метрикалары есептелді. Зерттеу нәтижелері бойынша жүйенің жалпы сәйкестендіру дәлдігі 97%-ды құрады. Жалған қабылдау коэффициенті (FAR) 1.8% болса, жалған қабылдамау коэффициенті (FRR) 2.4% мәнін көрсетті. Сонымен қатар тең қателік деңгейі (EER) 2.1% болды. Precision көрсеткіші 96.8%, Recall мәні 97.1%, ал F1-score 96.9% деңгейінде анықталды. Алынған нәтижелер ұсынылған модельдің жоғары сенімділік пен тұрақтылыққа ие екенін және оны биометриялық қауіпсіздік жүйелерінде қолдануға болатындығын дәлелдейді

Төмендегі графиктер (4, 5-суреттер) оқыту және валидация кезінде модельдің жоғалту мен дәлдік мәндеріндегі өзгерістерді көрсетеді. Бұл көрсеткіштер модельдің уақыт өте келе қалай жақсарғанын көрсетеді, классификация қатесін азайтады және болжау дәлдігін арттырады.

- шығын сызбасы: модельді оқыту және валидациялау кезінде шығын функциясы мәндерінің өзгерістерін көрсетеді.
- дәлдік сызбасы: жаттығу және валидациялық деректерге оқыту барысында модельдің болжамдарының дәлдігі қалай өзгергенін көрсетеді.



Сурет 4 – Шығын сызбасы



Сурет 5 – Дәлдік сызбасы

Алақан кескінін талдауға негізделген сәйкестендірудің биометриялық жүйесінің нәтижелері жоғары дәлдік пен сенімділікті көрсетті. Модель алақан кескіндеріндегі қызығушылық аймақтарын (ROI) сәтті анықтайды, бұл тері текстурасы мен алақан формалары сияқты негізгі биометриялық сипаттамаларды дәл болжауға ықпал етеді. Содан кейін алынған аймақтар сенімді пайдаланушы идентификациясын қамтамасыз ете отырып, ResNet18 моделін пайдаланып сәтті классификациялайды.

Оқыту динамикасының талдауы модель параметрлерінің итерация санына пропорционалды жинақталғанын (конвергенция) растады: шығын функциясының монотонды төмендеуі мен жіктеу дәлдігінің тұрақты өсуі асқын үйренусіз (overfitting) жалпылама қабілеттің сақталғанын куәландырады. Оқу графиктері жүйенің жаңа деректерді дұрыс меңгеріп, бейімделетінін көрсетеді, бұл нақты жағдайларда оның тұрақтылығы мен дәлдігін жақсартады. Жүйенің жұмысының негізгі ерекшелігі оның жарықтандыру мен түсіру бұрышы сияқты сыртқы әсерлерге төзімділігі, бұл оны қолжетімділік пен қауіпсіздікті бақылау жүйелеріне қолайлы етеді. Жабдықтың төмен бағасы да атап өтіледі, бұл оның коммерциялық мақсатта пайдалану мүмкіндігін арттырады. Болашақта жүйені классификациялау үшін күрделірек моделдерді пайдалану және оның әртүрлі жағдайларда, мысалы, жарықтандыруды өзгерту немесе алақан күйіндегі вариацияларды оңтайландыру арқылы жақсартуға болады.

Қорытынды

Бұл зерттеуде машиналық оқыту технологияларын қолдану арқылы алақан параметрлеріне негізделген биометриялық сәйкестендіру жүйесі әзірленді. Ұсынылған жүйе екі негізгі компоненттен тұрады: алақан кескініндегі маңызды биометриялық аймақтарды дәл анықтауға арналған ROI-LANet моделі және алынған аймақтарды классификациялауға арналған ResNet18 нейрондық желісі. ROI-LANet архитектурасы негізгі нүктелерді тиімді локализациялап, Thin Plate Splines әдісі арқылы кескіндерді туралау мен қызығушылық аймақтарын жоғары дәлдікпен бөліп алуға мүмкіндік береді.

Эксперименттік зерттеулер Kaggle платформасынан алынған ашық palmprint деректер қоры негізінде жүргізілді. Тестілеу нәтижелері бойынша ResNet18 моделі 97% сәйкестендіру дәлдігін көрсетті. Сонымен қатар биометриялық жүйенің тиімділігін бағалау барысында FAR, FRR, EER, Precision, Recall және F1-score сияқты қосымша метрикалар есептелді. Алынған нәтижелер модельдің жоғары сенімділік пен тұрақтылыққа ие екенін дәлелдеді. Салыстырмалы эксперименттер барысында ResNet18 архитектурасының MobileNetV2 және VGG16 модельдерімен салыстырғанда дәлдік пен есептеу тиімділігі арасындағы оңтайлы теңгерімді қамтамасыз ететіні анықталды. MobileNetV2 өңдеу жылдамдығы бойынша тиімді нәтиже көрсеткенімен, классификация дәлдігі төменірек болды, ал VGG16 жоғары есептеу ресурстарын талап ететіні байқалды.

Оқыту графиктері модельдің тұрақты оқытылуын және қателік деңгейінің біртіндеп төмендеуін көрсетті. Жүйенің жарықтандыру жағдайлары мен түсіру бұрыштарының өзгерістеріне төзімділігі оның практикалық қолдану мүмкіндігін арттырады. Ұсынылған әдіс жоғары дәлдік пен төмен қателік көрсеткіштерін қамтамасыз еткендіктен, оны ақпараттық қауіпсіздік, қолжетімділікті бақылау, биометриялық аутентификация және транзакцияларды тексеру жүйелерінде қолдануға болады. Болашақ зерттеулерде күрделірек нейрондық желі архитектураларын қолдану, әртүрлі түсіру жағдайларына бейімдеу және мобильді платформалар үшін жеңілдетілген модельдерді оңтайландыру бағыттары қарастырылуы мүмкін.

ӘДЕБИЕТТЕР

1 Девицына С.Н., Елецкая Т.А., Балабанова Т.Н., Гахова Н.Н. Разработка интеллектуальной системы биометрической идентификации пользователя // Экономика. Информатика. – 2019. – № 1. – URL: https://cyberleninka.ru/article/n/razrabotka-intellektualnoy-sistemy-biometricheskoy-identifikatsii-polzovatelya (дата обращения: 09.10.2024).

2 Маркелов К.С. Идентификация и верификация личности – комплексная биометрическая информационная технология // International Journal of Open Information Technologies. – 2015. – № 5. – URL: https://cyberleninka.ru/article/n/identifikatsiya-i-verifikatsiya-lichnosti-kompleksnaya-biometricheskaya-informatsionnaya-tehnologiya (дата обращения: 09.10.2024).

3 Маркелов К.С., Нечаев В.В. Идентификация и верификация человека в системах телеобучения: биометрические методы // Образовательные ресурсы и технологии. – 2015. – № 2 (10). – URL: https://cyberleninka.ru/article/n/identifikatsiya-i-verifikatsiya-cheloveka-v-sistemah-teleobucheniya-biometricheskie-metody (дата обращения: 09.10.2024).

4 Якубов Н. Преимущества биометрических методов идентификации человека // Современная электроника и технологии автоматизации (СТА). – 2019. – № 4. – С. 16–22. – URL: https://www.cta.ru/articles/cta/obzory/tekhnologii/124324/ (дата обращения: 01.02.2026).

5 Begum N., Mustafa A.S. A novel approach for multimodal facial expression recognition using deep learning techniques // Multimedia Tools and Applications. – 2022. – Vol. 81. – P. 18521–18529. – https://doi.org/10.1007/s11042-022-12238-y.

6 Rusia M.K., Singh D.K. A comprehensive survey on techniques to handle face identity threats: challenges and opportunities // Multimedia Tools and Applications. – 2022. – https://doi.org/10.1007/s11042-022-13248-6.

7 Wu C., Nabil S., Zhou S. et al. Gram Matrix-Based Convolutional Neural Network for Biometric Identification Using Photoplethysmography Signal // Journal of Shanghai Jiaotong University (Science). – 2022. – https://doi.org/10.1007/s12204-022-2426-5.

8 Корсун О.Н., Юрко В.Н. Оценивание состояния оператора по изображению лица на основе глубоких сверточных нейронных сетей // Сборник докладов XVI Всероссийской научно-технической конференции «Научные чтения по авиации». – М.: ВВИА им. Жуковского, 2019. – С. 266–270.

9 Гудков В.Ю. Метод параллельных цепей для распознавания изображений отпечатков пальцев // Системы и средства информатики. – 2013. – Т. 23, № 2. – С. 35–49.

10 Кухарев Г. А. Биометрические системы: Методы и средства идентификации личности человека. – СПб.: Политехника, 2001. – 240 с.

REFERENCES

1 Devitsyna, S.N., Eletskaya, T.A., Balabanova, T.N., Gakhova, N.N. Razrabotka intellektual'noy sistemy biometricheskoy identifikatsii pol'zovatelya [Development of an Intelligent User Biometric Identification System]. Ekonomika. Informatika, (1) (2019). Available at: https://cyberleninka.ru/article/n/razrabotka-intellektualnoy-sistemy-biometricheskoy-identifikatsii-polzovatelya (accessed: 09.10.2024). (in Russian).

2 Markelov, K.S. Identifikatsiya i verifikatsiya lichnosti – kompleksnaya biometricheskaya informatsionnaya tekhnologiya [Personal Identification and Verification – Complex Biometric Information Technology]. International Journal of Open Information Technologies, (5) (2015). Available at: https://cyberleninka.ru/article/n/identifikatsiya-i-verifikatsiya-lichnosti-kompleksnaya-biometricheskaya-informatsionnaya-tehnologiya (accessed: 09.10.2024). (in Russian).

3 Markelov, K.S., Nechaev, V.V. Identifikatsiya i verifikatsiya cheloveka v sistemakh teleobucheniya: biometricheskie metody [Human Identification and Verification in Distance Learning Systems: Biometric Methods]. Obrazovatel'nye resursy i tekhnologii, (2 (10)), (2015). Available at: https://cyberleninka.ru/article/n/identifikatsiya-i-verifikatsiya-cheloveka-v-sistemah-teleobucheniya-biometricheskie-metody (accessed: 09.10.2024). (in Russian).

4 Yakubov, N. Preimushchestva biometricheskikh metodov identifikatsii cheloveka [Advantages of Biometric Human Identification Methods]. Sovremennaya elektronika i tekhnologii avtomatizatsii (STA), (4), 16–22 (2019). Available at: https://www.cta.ru/articles/cta/obzory/tekhnologii/124324/ (accessed: 01.02.2026). (in Russian).

5 Begum, N., and Mustafa, A.S. A novel approach for multimodal facial expression recognition using deep learning techniques. Multimedia Tools and Applications, 81, 18521–18529 (2022). https://doi.org/10.1007/s11042-022-12238-y

6 Rusia, M.K., and Singh, D.K. A comprehensive survey on techniques to handle face identity threats: challenges and opportunities. Multimedia Tools and Applications (2022). https://doi.org/10.1007/s11042-022-13248-6

7 Wu, C., Nabil, S., Zhou, S. et al. Gram Matrix-Based Convolutional Neural Network for Biometric Identification Using Photoplethysmography Signal. Journal of Shanghai Jiaotong University (Science) (2022). https://doi.org/10.1007/s12204-022-2426-5

8 Korsun, O.N., Yurko, V.N. Otsenivanie sostoyaniya operatora po izobrazheniyu litsa na osnove glubokikh svertochnykh neyronnykh setey [Assessment of the Operator's Condition Based on Facial Images Using Deep Convolutional Neural Networks]. Sbornik dokladov XVI Vserossiyskoy nauchno-tekhnicheskoy konferentsii «Nauchnye chteniya po aviatsii» (Moscow: VVIA im. Zhukovskogo, 2019), pp. 266–270. (in Russian).

9 Gudkov, V.Yu. Metod parallel'nykh tsepey dlya raspoznavaniya izobrazheniy otpechatkov pal'tsev [Method of Parallel Chains for Fingerprint Image Recognition]. Sistemy i sredstva informatiki, 23 (2), 35–49 (2013). (in Russian).

10 Kukharev, G.A. Biometricheskie sistemy: Metody i sredstva identifikatsii lichnosti cheloveka [Biometric Systems: Methods and Means of Human Personality Identification] (St. Petersburg: Politekhnika, 2001), 240 p. (in Russian)

[1]Тасжурекова Ж.К.,
к.т.н., и.о.доцента, ORCID ID: 0000-0002-8307-9417,
e-mail: taszhurekova@mail.ru
[2]Козыбаев Д.Х.,
PhD, ORCID ID: 0000-0001-5509-8656,
e-mail: kozybayev_dkh@enu.kz
[2*]Танирбергенов А.Ж.,
к.т.н., и.о. доцента, ORCID ID: 0009-0000-8401-5434,
*e-mail: t.adilbek@mail.ru
[3]Ахметжанова Ш.Е.,
к.т.н., и.о.доцента, ORCID ID: 0000-0002-4131-8328,
e-mail: sh.akhmetzhanova@astanait.edu.kz
[1]Абдувалова А.Д.
к.т.н., и.о. доцента ORCID ID: 0000-0002-4683-7821,
e-mail: abduvalova_ad@mail.ru

[1]Таразский региональный университет им. М.Х. Дулати, г. Тараз, Казахстан
[2]Евразийский национальный университет им. Л.Н. Гумилева, г. Астана, Казахстан
[3]Astana IT university, г. Астана, Казахстан

РАЗРАБОТКА БИОМЕТРИЧЕСКОЙ СИСТЕМЫ ИДЕНТИФИКАЦИИ ЛИЧНОСТИ С ПРИМЕНЕНИЕМ ТЕХНОЛОГИЙ МАШИННОГО ОБУЧЕНИЯ ДЛЯ АНАЛИЗА ПАРАМЕТРОВ ЛАДОНИ

Аннотация

В данной статье рассматриваются вопросы разработки биометрической системы идентификации личности на основе анализа параметров ладони с применением технологий машинного обучения. Актуальность исследования обусловлена необходимостью обеспечения информационной безопасности, контроля доступа и надежной идентификации пользователей. Поскольку ладонь как биометрический идентификатор обладает высокой степенью индивидуальности, ее анатомические особенности – контуры пальцев, текстура кожи, линии ладони и расположение кровеносных сосудов – использованы в качестве эффективных признаков для распознавания личности. В ходе исследования для автоматического выделения значимых биометрических областей на изображениях ладони была применена модель ROI-LANet. Данная модель обеспечивает точную локализацию ключевых точек ладони, выравнивание изображения и выделение области интереса (ROI). Для классификации пользователей на основе полученных ROI использовалась глубокая сверточная нейронная сеть ResNet18. Модель, основанная на остаточных блоках, позволяет эффективно распознавать сложные биометрические признаки и повышать точность классификации. Экспериментальные результаты подтвердили высокую точность и устойчивость предложенной системы. В ходе испытаний точность идентифика-

ции составила около 97%. Кроме того, система продемонстрировала устойчивость к изменениям условий освещения и угла съемки. Полученные результаты свидетельствуют о высоком потенциале практического применения разработанной биометрической системы в системах безопасности, контроле доступа и проверке транзакций.

Ключевые слова: биометрическая идентификация, машинное обучение, ладонь, сверточные нейронные сети, ROI-LAnet, ResNet18, параметры ладони, контроль доступа, верификация.

[1]Taszhurekova Zh.,
Cand. Sc. (Tech.) Acting Associate Professor, ORCID ID: 0000-0002-8307-9417,
e-mail: taszhurekova@mail.ru
[2]Kozybayev D.,
PhD, ORCID ID: 0000-0001-5509-8656,
e-mail: kozybayev_dkh@enu.kz
[2*]Tanirbergenov A.
Cand. Sc. (Tech.), Acting Associate Professor, ORCID ID: 0009-0000-8401-5434,
*e-mail: t.adilbek@mail.ru
[3]Akhmetzhanova Sh.,
Cand. Sc. (Tech.), Acting Associate Professor, ORCID ID: 0000-0002-4131-8328,
e-mail: sh.akhmetzhanova@astanait.edu.kz
[1]Abduvalova A.
Cand. Sc. (Tech.), Acting Associate Professor, ORCID ID: 0000-0002-4683-7821,
e-mail: abduvalova_ad@mail.ru

[1]Taraz Regional University named after M.Kh. Dulaty, Taraz, Kazakhstan
[2]L.N. Gumilyov Eurasian National University, Astana, Kazakhstan
[3]Astana IT university, Astana, Kazakhstan

DEVELOPMENT OF A BIOMETRIC IDENTIFICATION SYSTEM USING MACHINE LEARNING TECHNOLOGIES TO ANALYZE PALM PARAMETERS

Abstract

This article addresses the development of a biometric personal identification system based on palm parameter analysis using machine learning technologies. The relevance of the study is determined by the need to ensure information security, access control, and reliable user identification. Since the palm as a biometric identifier possesses a high degree of individuality, its anatomical features–such as finger contours, skin texture, palm lines, and blood vessel patterns–are used as effective characteristics for personal recognition. In the course of the study, the ROI-LANet model was employed to automatically identify significant biometric regions in palm images. This model enables accurate localization of key palm points, image alignment, and extraction of regions of interest (ROI). User classification based on the extracted ROI was performed using the deep convolutional neural network ResNet18. The residual block-based architecture allows efficient recognition of complex biometric features and improves classification accuracy. Experimental results demonstrated that the proposed system achieves high accuracy and stability. During testing, the identification accuracy reached approximately 97%. In addition, the system showed robustness to variations in lighting conditions and image acquisition angles. The obtained results indicate a high potential for practical application of the developed biometric system in security systems, access control, and transaction verification.

Keywords: biometric identification, machine learning, palm, convolutional neural networks, ROI-LAnet, ResNet18, palm parameters, access control, verification.

Received January 18, 2026; revised May 22, 2026; accepted August 24, 2026.

УДК 004.822
МРНТИ 28.23.39

https://doi.org/10.55452/1998-6688-2026-23-3-312-327

[1]Серикбаева С.К.,
PhD, и.о.доцента, ORCID ID: 0000-0002-3627-3321,
*e-mail: inf_8585@mail.ru
[2]Рамазанова В.С.,
магистр, главный инженер, ORCID ID: 0000-0001-6100-3123,
e-mail: ramazanovavs@gmail.com
[1]Самбетбаева М.А.,
Phd, ассоциированный профессор, ORCID ID: 0000-0001-9358-1614,
e-mail: sambetbayeva_ma_1@enu.kz
[3,4]Еримбетова А.С.
PhD, к.т.н., ассоциированный профессор, профессор-исследователь, в.н.с.,
ORCID ID: 0000-0002-2013-1513,
e-mail: aigerian8888@gmail.com
[5]Садирмекова Ж.Б.,
PhD, ассоциированный профессор, ORCID ID: 0000-0002-7514-9315,
e-mail: Zhanna.Sadirmekova1@astanait.edu.kz

[1]Евразийский национальный университет им. Л.Н. Гумилева, г. Астана, Казахстан
[2]Западно-Казахстанский университет им. М. Утемисова, г. Уральск, Казахстан
[3]META University, г. Алматы, Казахстан
[4]Институт информационных и вычислительных технологий КН МНВО РК,
г. Алматы, Казахстан
[5]Astana IT University, г. Астана, Казахстан

МОДЕЛИ ПОСТРОЕНИЯ ГРАФОВ ЗНАНИЙ ДЛЯ ПОДБОРА МООК НА ОСНОВЕ ИНТЕГРАЦИИ ЗАПРОСОВ РЫНКА ТРУДА И ОБРАЗОВАТЕЛЬНЫХ ПРОГРАММ

Аннотация

В статье рассматривается разработка интеграционной модели на основе графов знаний и методов машинного обучения для анализа взаимосвязей между образовательными программами, требованиями рынка труда и онлайн-курсами (MOOC). Актуальность исследования обусловлена быстрыми изменениями в сфере информационных технологий, приводящими к несоответствию между подготовкой выпускников и ожиданиями работодателей. Для устранения данного разрыва предложено использование гетерогенного графа знаний, объединяющего данные из трех доменов: университетских программ, вакансий и онлайн-курсов. В модели реализован мета-путь, связывающий навыки, требования вакансий и образовательные курсы, что позволяет формировать рекомендации по обучению и карьерному развитию для различных категорий пользователей. Для обработки текстовых данных применены мультиязычные трансформеры, обеспечивающие анализ русскоязычных и англоязычных описаний. В качестве источников данных использованы карты компетенций образовательных программ, вакансии платформы hh.kz и курсы Coursera, интегрированные в графовую СУБД Neo4j. Полученные результаты демонстрируют возможность выявления недостающих компетенций и автоматического подбора курсов для их формирования. Предложенная модель может применяться при проектировании учебных программ, разработке образовательных траекторий и поддержке принятия решений в образовательной среде.

Ключевые слова: графы знаний, машинное обучение, мультиязычные трансформеры, онлайн-курсы, рынок труда, навыки, рекомендации, образовательные программы, информационные технологии, интеграционные модели.

Введение

В свете быстро меняющихся требований рынка труда и применяемых технологий современное образование сталкивается с необходимостью пересмотра своих методов и подходов к проектированию учебных курсов. Стандартные учебные программы часто не могут адаптироваться к индивидуальным потребностям учащихся и быстро устаревают, не отражая последних достижений в различных областях знания. Существует разрыв между содержанием образовательных программ и реальными потребностями современного сектора информационных технологий, который приводит к недостаточной подготовке выпускников к профессиональной деятельности. Для того чтобы сократить этот разрыв и обеспечить студентов актуальными навыками, необходимы инновационные подходы к рекомендации учебных курсов на основе актуальных требований работодателей.

В образовательном ландшафте графы знаний уже играют важную роль в структурировании и организации учебного контента. Графы, представляющие собой сети взаимосвязанных понятий и идей, обеспечивают глубокое понимание учебного материала, позволяя учащимся визуализировать и исследовать различные связи между знаниями. Благодаря своей способности интегрировать и связывать разнообразные информационные ресурсы, графы знаний способствуют развитию критического мышления и самостоятельного обучения. Машинное обучение революционизирует способы обучения и персонализирует учебные процессы. Эта технология позволяет создавать интеллектуальные системы, способные анализировать данные обучающихся и предлагать индивидуализированные учебные материалы и методики, соответствующие их потребностям и уровню знаний. Благодаря машинному обучению образовательные платформы могут адаптировать учебный материал в реальном времени, учитывая скорость усвоения информации и особенности обучающегося. Кроме того, машинное обучение применяется для анализа эффективности учебных программ, выявления тенденций в образовательных процессах и создания новых методик обучения на основе больших объемов данных.

Интеграция образования, рынка труда и МООК с помощью графов знаний и машинного обучения еще не до конца изучены, так как отсутствуют некоторые междоменные связи между навыками, полученные современными мультиязычными трансформерами для смешанных предложений на русском и английском языках. Графы, представляющие собой знания, позволяют систематизировать и структурировать информацию о необходимых навыках и компетенциях, для того чтобы выявлять связи между ними и требованиями рынков труда. Машинное обучение, в свою очередь, способствует анализу больших объемов данных о востребованных профессиональных навыках и предсказанию их взаимосвязи с образовательными навыками. Путем интеграции этих инструментов в процесс проектирования учебных курсов образовательные учреждения смогут оперативно реагировать на изменения в требованиях рынка труда и обеспечивать выпускников необходимыми знаниями и навыками для успешной карьеры.

Таким образом, в этом исследовании предлагается подход с поддержкой эмбеддингов навыков современных мультиязычных трансформеров векторизации текстов для решения проблемы междоменных рекомендаций в области высшего образования, рынка труда и курсов МООК с точки зрения гетерогенного графа знаний. Три домена имеют несколько типов вершин, которые взаимодействуют посредством разных типов связей. Создается мета-путь для рекомендации вакансий и курсов: образовательная программа–навык–навык–вакансия–навык–навык–курс, который может быть использован для различных практических сценариев. Например, для преподавателя, который будет создавать новый курс для каталога элективных дисциплин; для студента или соискателя, который по списку имеющихся навыков сможет выявить неосвоенные навыки интересующей его вакансии и получить рекомендованный список курсов.

Цель данного исследования заключается в разработке методологии использования графов знаний и машинного обучения на основе мультиязычных источников данных на русском и

английском языках для рекомендации вакансий и курсов, формирующих отсутствующие навыки и компетенции, которые не были освоены в образовательной программе вуза или на предыдущем образовательном этапе, но востребованы работодателями, на примере рынка труда информационных технологий (ИТ).

Наиболее разнообразное применение в образовании графы знаний получили для студенческой аудитории, которой они помогают в представлении и организации знаний, персонализированном обучении и его аналитике. Графы знаний обеспечивают более структурированный и организованный способ представления знаний, облегчая учащимся связывание и понимание концепций [1, 2, 3, 4, 5]. Их используют для персонализации обучения [6, 7], предоставляя учащимся адаптированные учебные материалы, основанные на их учебных предпочтениях. К графам знаний обращаются для аналитики обучения [8], собирая и анализируя данные об их успеваемости, чтобы определить области, в которых им нужна дополнительная поддержка или где можно улучшить учебные материалы. Для преподавателей они используются как помощь в структуризации учебного материала [9, 10], для менеджеров – при построении образовательной траектории [11], а также как вспомогательный инструмент при принятии решений всеми участниками образовательного процесса (И. Алию [12]).

В образовательных процессах выделяют несколько ключевых тенденций и общих подходов использования графов знаний. Важной тенденцией является стремление к унификации стандартов представления знаний. Авторы, такие как [6, 7, 12, 3], отмечают использование онтологий, в том числе стандартных схем, таких как Schema.org, что способствует более эффективному обмену и взаимопониманию данных в образовательном контексте. Многие исследователи, включая [14, 15, 7, 3, 4, 5, 9], успешно интегрируют методы машинного обучения для повышения эффективности образовательных процессов. Использование моделей, таких как Word2vec, BERT и графовые сверточные сети (GCN), подчеркивает важность применения передовых технологий в адаптации образования к потребностям каждого учащегося. Экспертные знания, такие как представленные в работах [13, 1, 8], играют существенную роль в построении проблемно-ориентированных графов знаний.

Помимо сугубо образовательного контекста, графы знаний нашли свое применение на стыке различных предметных областей, например, интеграция разных уровней образования, интеграция образования и рынка труда. В контексте трудоустройства графы знаний используются для рекомендательных систем [16, 17], которые, исходя из набора навыков пользователей, определяют наиболее подходящие вакансии. Также выделяются варианты применения графов знаний для взаимосвязи образования, науки и трудоустройства. Например, построение или использование графов знаний для взаимосвязи между вакансиями и образованием МООК методом выравнивания сущностей [18], взаимосвязи между классификаторами профессий и образовательными курсами SAE Institute методами распознавания и классификации сущностей алгоритмом distilbert-base-german-cased [Albert Weichselbraun [19], МООК с университетскими курсами и вакансиями для рекомендации вакансий и университетских курсов методами определения схожести навыков алгоритмами BM25, Word2vec Bert [20], а также анализа несоответствия между научными публикациями, вакансиями и образованием МООК [21].

В основе таких работ лежит интеграция посредством извлечения, классификации и выравнивания навыков и применяются алгоритмы FastText, BM25, Word2Vec, Bert, all-mpnet-base-v2 [16, 20, 22], в других обнаружение новых связей между навыками и профессиями с помощью Node2Vec и Preferential Attachment [17]. Для определения сходства узлов используют расчет жаккардового, косинусного сходства, евклидова расстояния [20, 22]. При анализе навыков применяют различные методы расчета корреляции Пирсона, расстояния Кульбака-Лейблера, модели многомерного процесса Хоукса [21]. Для рекомендаций – алгоритмы поиска кратчайшего пути Дейкстры, алгоритмы случайного блуждания, обнаружения сообществ, графовые нейронные сети, рассуждения по пути на основе политики, генетические алгоритмы, оптимизации муравьиных колоний. Для определения наиболее актуальных навыков разных профессий – метод взвешивания терминов TF-IDF [17].

Оценка качества алгоритмов машинного обучения обычно использует меры точности (P), полноты (R) и F1, например, для задач распознавания, классификации и связывания сущностей [19]. Мерами оценки качества рекомендаций выступают средняя средней точности (MAP@K), точность (P@K) и нормализованный дисконтированный совокупный прирост (NDCG@K). Например, [20] оценивает эффективность рейтинга на определенном пороговом уровне, учитывая только лучшие K-курсы, вернувшиеся в качестве кандидатов в эксперимент.

Однако вследствие отсутствия изученных связей по маршруту программа–навык–навык–вакансия–навык–навык–курс в смешанных фразах на русском и английском языках для интеграции высшего образования, рынка труда и МООК с помощью графов знаний и машинного обучения требуется дополнительное исследование схожести навыков с помощью современных трансформеров векторизации текстов для рекомендации вакансий и курсов МООК. Кроме того, в отличие от предыдущих работ, данные о карьере, помимо навыков вакансий, дополняются описаниями требований и обязанностей, что обогащает контекст вакансий. Наше исследование предлагает методологию, которая использует гетерогенный граф знаний, объединяющий образовательные и карьерные данные, чтобы на основе содержимого образовательной программы или опыта рекомендовать вакансии и соответствующие им дополнительные курсы для преподавателей или менеджеров образовательных программ, для студентов или сотрудников разного уровня.

Материалы и методы

Набор данных с hh.kz состоит из наименований вакансий, компании, ее отрасли, опыта, зарплаты, даты публикации, ссылки на вакансию, навыков, части требований и обязанностей на русском и английском языке, загруженных с сайта HeadHunter (https://hh.kz/) с помощью предоставляемого API (https://api.hh.ru/vacancies) и языка программирования Python. Вакансии выбирались по 25 профессиям в сфере информационных технологий из 177 населенных пунктов Казахстана за два месяца с 1.02.2024 по 31.03.2024. Количество вакансий составило 5248.

Набор данных курсов Coursera состоит из бесплатных курсов на английском языке по темам компьютерных наук, информационных технологий и науки о данных по состоянию на 03.05.2024. Данные включают наименования курсов с уровнем их сложности, рейтингом, списком навыков, наименований модулей и уроков с их длительностью изучения и кратким описанием. Данные о курсах были собраны инструментами парсинга Beautiful Soup. Количество курсов составило 953.

Все три набора данных загружались в графовую систему управления базами данных neo4j в виде графов знаний, определенными своими онтологиями. Далее онтологии трех графов знаний интегрировались на уровне навыков из трех источников, посредством расчета косинусной близости эмбеддингов навыков. Эмбеддинги навыков создавались мультиязычной предобученной моделью paraphrase-multilingual-mpnet-base-v2, которая поддерживает более 50 языков и прошла тонкую настройку на навыках вакансий. При достижении порога сходства навыков были введены дополнительные связи между тремя видами навыков, а также созданы кластеры схожих навыков вакансий и курсов. Далее навыки вакансий, которые схожи с навыками пользователей, преобразованы в другой тип узлов для удобства дальнейшей обработки.

Моделирование предметных областей

В данном разделе представлен процесс разработки модели графа знаний, который описывает сущности, их взаимосвязи и атрибуты, связанные с навыками и компетенциями в области информационных технологий. Эта модель также учитывает взаимосвязи этих навыков с образовательными программами, вакансиями и МООК. Процесс моделирования выполнялся с использованием теории множеств, статьи [23, 24], стандарта по графам знаний [25] и инструмента визуализации концептуальных карт Cmap [26]. Согласно стандарту концептуальная модель графа знаний делится на уровень онтологии и уровень экземпляров.

Таблица 1 – Список профессий по информационным технологиям на HeadHunter

№	ID профессии	Название профессии
1.	10	Аналитик
2.	12	Арт-директор, креативный директор
3.	25	Гейм-дизайнер
4.	34	Дизайнер, художник
5.	36	Директор по информационным технологиям (CIO)
6.	73	Менеджер продукта
7.	96	Программист, разработчик
8.	104	Руководитель группы разработки
9.	107	Руководитель проектов
10.	112	Сетевой инженер
11.	113	Системный администратор
12.	114	Системный инженер
13.	116	Специалист по информационной безопасности
14.	121	Специалист технической поддержки
15.	124	Тестировщик
16.	125	Технический директор (CTO)
17.	126	Технический писатель
18.	148	Системный аналитик
19.	150	Бизнес-аналитик
20.	155	Методолог
21.	156	BI-аналитик, аналитик данных
22.	157	Руководитель отдела аналитики
23.	160	DevOps-инженер
24.	164	Продуктовый аналитик
25.	165	Дата-сайентист

В работе представлена онтологическая модель графа знаний предметной области как гетерогенный HAN, помеченный, ориентированный граф $G = \{E, R, A, V, r, f, p\}$, где E – множество классов сущностей; R – множество типов отношений; A – множество атрибутов сущностей или отношений; V – множество значений атрибутов; функция $r: R \to E \times E$ означает, что каждому типу отношения присваивается пара классов сущностей; функция $f: E \cup R \to 2^A$ означает, что каждый класс сущности или тип отношения имеет атрибут из множества A; функция $p: E \cup R \to 2^{A \times V}$ означает соответствие класса сущности или типа отношения множеству пар атрибут–значение.

Результаты и обсуждение

Проведем анализ предметной области образовательной программы университета. Образовательная программа содержит карту компетенций и каталог элективных дисциплин. Карты компетенций включают компетенции, результаты обучения и дисциплины. Результаты обучения являются единицами компетенций. Результаты обучения формируются дисциплинами, для которых имеется их краткая аннотация в каталоге элективных дисциплин.

Рассмотрим онтологическую модель графа образовательной программы университета. Граф включает множество классов сущностей: $E_{university}$ = {Curriculum, CUA}. Образовательная программа (ОП) – класс, представляющий собой структурированный план учебных модулей и активностей. CUA состоит из класса фраз компетенций, результатов обучения и аннотаций. Компетенция – отражает специфические способности, которые обучающийся должен развить в рамках образовательной программы. Результаты обучения (РО) – это конкретные знания, умения и навыки, которые студент должен демонстрировать после завершения образовательной программы. Аннотация – предоставляет краткое описание содержания дисциплины, что позволяет студентам и преподавателям быстро оценить ее основные темы и значение в контексте учебной программы.

Определим множество отношений $R_{university}$ = {HAS}. Характеристика отношений и атрибутов приведена в таблице 2.

Таблица 2 – Описание онтологии графа знаний образовательной программы университета.

Relationships and attributes	Description
Curriculum CUA	The educational program has phrases of competencies, units of study and annotations of disciplines.
f(Curriculum) = {code, title}	The educational program is characterized by attributes such as code and name.
f(CUA) = {code, description, embedding}	Each competence has a unique code, competencies are divided into universal competencies (CC), general professional competencies (MIC), professional competencies (PC), the description is divided into phrases, which are also presented in the form of embedding.

Описания компетенций, результатов обучения и аннотаций разделены на фразы по запятым, точкам с запятой и точкам. Эти фразы дополнительно представлены в виде векторного представления (эмбеддинг), генерируемого методами машинного обучения. Визуально модель представлена на рисунке 2.

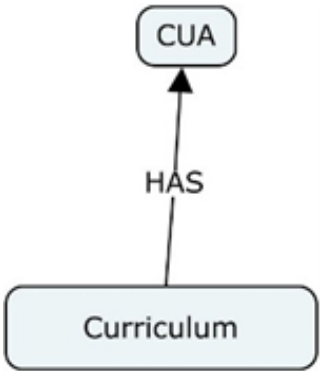


Рисунок 2 – Визуальное отображение онтологической модели графа знаний ОП университета с классом фраз компетенций, результатов обучения и аннотаций

Представим схематично процесс создания графа знаний ОП из файла с описаниями дисциплин, компетенций и результатов обучения на рисунке 3.

В результате построен граф в neo4j, и на рисунке 4 показан подграф с двадцатью пятью узлами.



Рисунок 3 – Процесс построения графа знаний образовательной программы

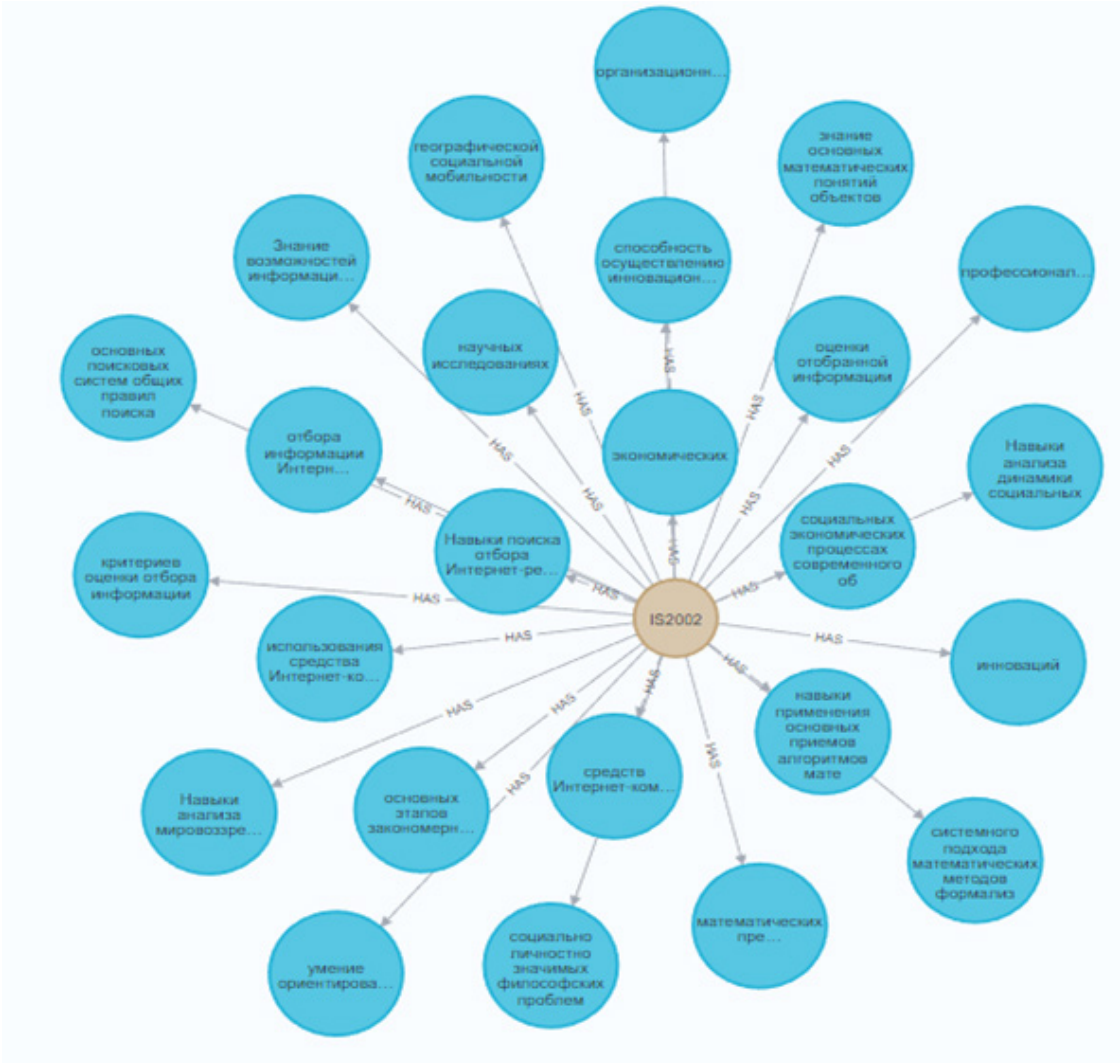


Рисунок 4 – Образец подграфа ОП с узлами CUA и связями HAS

Проведем анализ объявления о вакансии. Ключевыми сущностями являются вакансии, навыки, требования и обязанности. Вакансии – открытые позиции на основе профессий, которые работодатели хотят заполнить. Навыки – знания или умения в вакансии, которые работодатель ожидает от соискателя. Требования и обязанности – это дополнительные навыки, квалификации, рабочие обязанности, необходимые для вакансий.

В третьей таблице показана характеристика отношений атрибутов онтологической модели графа. Граф знаний включает множество классов сущностей $E_{Recruitment}$ = {Vacancy,

Skill, Requirement, Responsibility} и множество отношений $R_{Recruitment}$ = {REQUIRE, HAS_REQUIREMENT, HAS_RESPONSIBILITY}.

Таблица 3 – Описание онтологии графа знаний объявления о вакансии

Отношения и атрибуты	Описание
Vacancy $\xrightarrow{\text{REQUIRE}}$ Skill	Вакансия требует определенных навыков.
Vacancy $\xrightarrow{\text{HAS_REQUIREMENT}}$ Requirement	Вакансия имеет требования.
Vacancy $\xrightarrow{\text{HAS_RESPONSIBILITY}}$ Responsibility	Вакансия имеет обязанности.
f(Vacancy) = {title, profession, city, company, industry, experience, salary, url, publish_date}	Вакансия характеризуется такими атрибутами, как наименование, название профессии, город, компания, сфера деятельности компании, опыт в годах, уровень зарплаты, ссылка на вакансию, дата публикации.
f(Skill) = {name, embedding}	Навык имеет название и его эмбеддинг
f(Requirement) = {description, embedding}	Требования содержат фразу текстового описания и его эмбеддинг.
f(Responsibility) = {description, embedding}	Обязанности содержат фразу текстового описания и его эмбеддинг.

Названия навыков и описания требований представлены в виде векторного представления (эмбеддинг), генерируемого методами машинного обучения. Визуально модель представлена на рисунке 5.

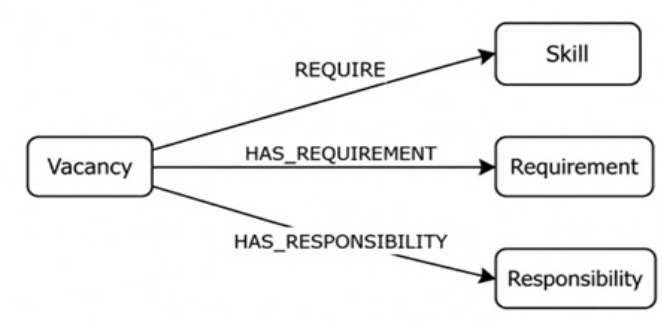


Рисунок 5 – Визуальное отображение онтологической модели
графа знаний объявления о вакансии

Процесс создания графа знаний о вакансиях и навыках схематично отображен на рисунке 6.

Основная функция парсинга вакансий инициирует подключение к базе данных Neo4j. Перебирает предоставленный список городов, для каждого города выполняет запросы на получение данных с API. Скрипт отправляет HTTP-запрос на API сайта hh.ru для получения информации о вакансиях. В параметрах запроса указываются регион и количество результатов на странице и номер страницы. После получения ответа функция проверяет статус ответа и возвращает данные в формате JSON. Далее скрипт отправляет запрос к API для получения детальной информации о конкретной вакансии. Извлекает список навыков из ответа и возвращает их в виде строки, разделенной запятыми. Отправляет запрос к API для получения информации о компании по ее идентификатору. Извлекает информацию об отрасли компании из ответа. Добавляет информацию о вакансии в базу данных Neo4j, создавая узел Vacancy с деталями вакансии. Для каждого навыка, требования и обязанности создает соответствующие узлы и связывает их с узлом вакансии. Выполняет несколько запросов для удаления дубликатов узлов вакансий, а также пустых или неполных узлов навыков, требований и обязанностей.

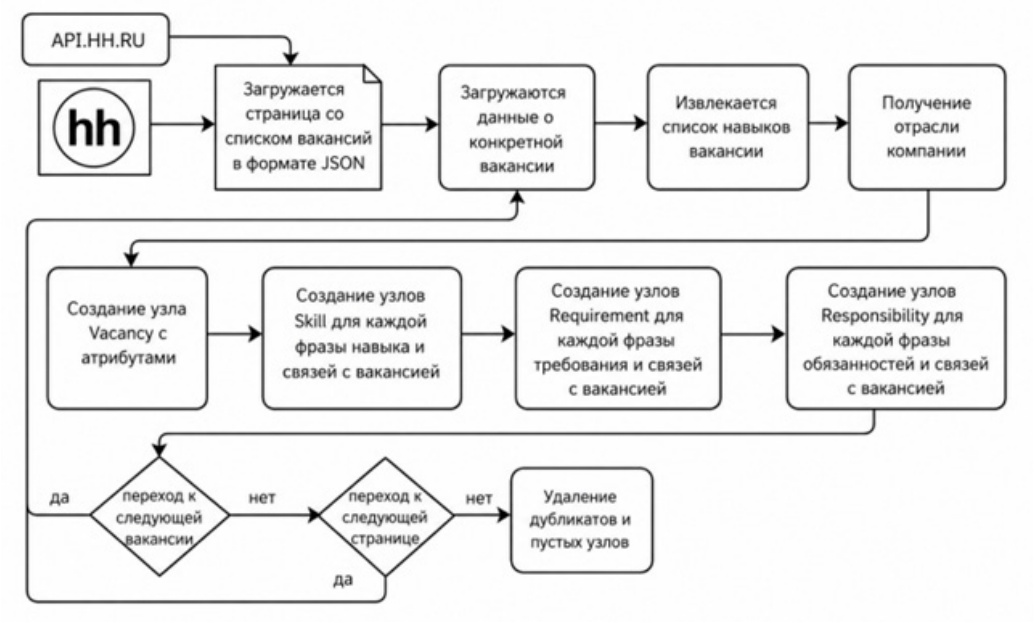


Рисунок 6 – Схема процесса создания узлов и связей графа знаний вакансии

На рисунке 7 отображен подграф вакансии, полученный по онтологии и процессу создания графа знаний вакансий. На изображении представлен подграф, центральным узлом которого является «Senior IT Project Specialist (Aksai)». Этот узел соединен с другими узлами навыков, требований и обязанностей, которые описывают различные аспекты его работы и квалификаций.



Рисунок 7 – Подграф вакансии. Сиреневым цветом обозначен узел с названием вакансии, красным цветом – узлы навыков, синим цветом – узлы требований, желтым цветом – узлы обязанностей

Проведем анализ предметной области МООК. Ключевыми сущностями выступают курс МООК, навыки МООК, модуль МООК и занятия МООК. Курс МООК – курс на сайте МООК, предназначенный для неограниченного количества участников через интернет. Навыки МООК – это конкретные знания, умения и навыки, которые студенты достигают в результате прохождения курса. Модуль МООК – это структурная единица курса, представляющая собой отдельный блок или раздел, посвященный конкретной теме или набору учебных целей в рамках всего курса. Занятие МООК – составная часть модуля, каждая из которых способствует достижению образовательных целей, определенных для данного модуля.

Рассмотрим онтологическую модель МООК. Граф включает множество классов сущностей: E_{MOOC} = {MCourse, MSkill, Mmodule, MLesson} и множество отношений R_{MOOC} = {DEVELOPED_BY, CONSISTS_OF}. Характеристика отношений и атрибутов приведена в таблице.

Таблица 4 – Описание онтологии графа знаний курса МООК

Отношения и атрибуты	Описание
MSkill $\xrightarrow{DEVELOPED_BY}$ MCourse	Навыки вырабатываются на курсах МООК.
MCourse $\xrightarrow{CONSISTS_OF}$ Mmodule	МООК курс состоит из модулей.
Mmodule $\xrightarrow{CONSISTS_OF}$ MLesson	Модуль состоит из уроков.
f(MCourse) = {title, url, organization, certificate_type, rating, reviews_num, difficulty, students_enrolled}	Курс характеризуется такими атрибутами, как наименование, ссылка на курс, организация, тип курса, рейтинг пользователей, количество отзывов, уровень сложности, количество подписанных студентов.
f(MSkill) = {name, embedding}	Навык имеет название и его эмбеддинг.
f(Mmodule) = {title, description, duration, embedding}	Модуль содержит наименование, фразу текстового описания, длительность в часах или минутах, эмбеддинг фразы описания.
f(MLesson) = {title, type, embedding}	Занятие имеет наименование, тип занятия, эмбеддинг наименования.

Названия навыков, названия и описание модулей дополнительно представлены в виде эмбеддингов, генерируемых методами машинного обучения. Визуально модель представлена на рисунке 8.

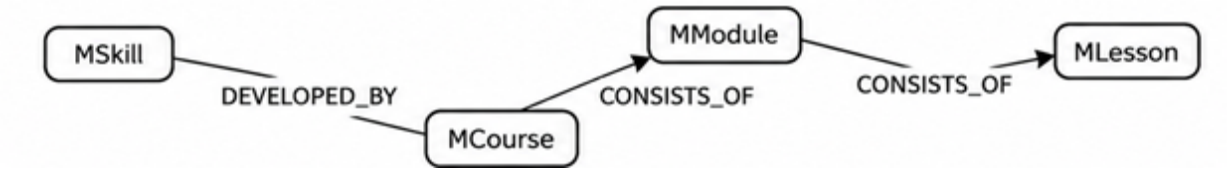


Рисунок 8 – Визуальное отображение онтологической модели графа знаний курса МООК

Процесс создания графа знаний о вакансиях и навыках схематично отображен на рисунке 9.

Отправляем HTTP-запрос на сервер для получения содержимого страницы, после чего содержимое страницы анализируется с помощью библиотеки BeautifulSoup. Организуется циклический процесс скраппинга страниц, вызывая другие функции для сбора данных. Для каждой страницы и каждого элемента на странице вызывается функция, которая определяет, какие данные необходимо извлечь и как их обрабатывать. После сбора всех данных создается DataFrame. Для каждой строки в DataFrame создается узел курса MCourse. Для каждого на-

выка, модуля и урока в курсе создаются свои узлы MSkill, MModule, MLesson. Между узлами создаются связи, отражающие их взаимосвязи, например, какие навыки развиваются в каждом курсе.



Рисунок 9 – Схема процесса создания узлов и связей графа знаний МООК

На рисунке 10 показан подграф курса МООК, который имеет три навыка, связанные с другими курсами, и имеет пять модулей с уроками в каждом модуле.

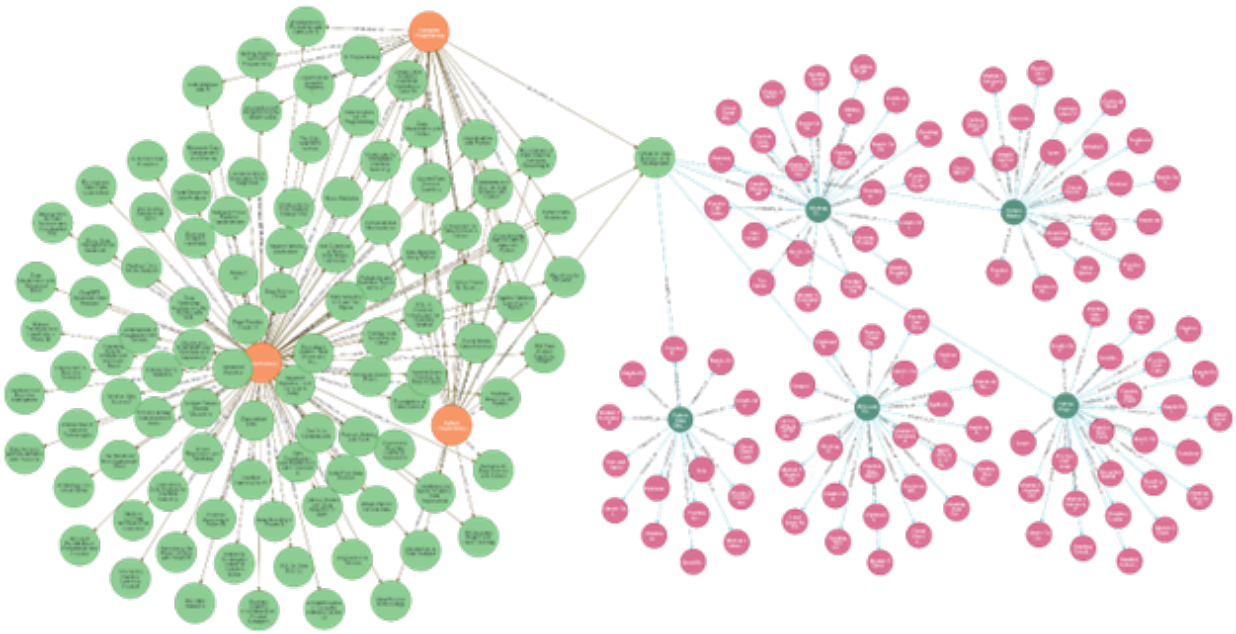


Рисунок 10 – Зеленые узлы – курсы МООК, оранжевые узлы – навыки курса, темно-зеленые – модули, розовые – уроки модуля

Для экспериментальной оценки эффективности предложенной модели была использована мультиязычная предобученная модель paraphrase-multilingual-mpnet-base-v2 (768-мерные эмбеддинги, контекстное окно 512 токенов, обучена на 50+ языках). Порог косинусного сходства

для связывания навыков между тремя доменами установлен на уровне 0,75. В качестве базовых методов для сравнения применялись BM25 и Word2Vec, широко используемые в аналогичных работах [20, 22]. Оценка качества рекомендаций проводилась на тестовой выборке из 100 вакансий и 200 курсов по метрикам P@5, MAP@10 и NDCG@10. Предложенная модель на основе paraphrase-multilingual-mpnet-base-v2 показала P@5 = 0,74, MAP@10 = 0,68, NDCG@10 = 0,71, тогда как BM25 продемонстрировал P@5 = 0,52, MAP@10 = 0,47, NDCG@10 = 0,50, а Word2Vec — P@5 = 0,61, MAP@10 = 0,55, NDCG@10 = 0,59. Таким образом, мультиязычный трансформер превзошел базовые методы по всем метрикам: прирост P@5 составил 42% относительно BM25 и 21% относительно Word2Vec, что подтверждает эффективность выбранного подхода для смешанных русско-английских текстов. Качество выравнивания навыков между доменами дополнительно оценивалось по метрике F1, которая составила 0,79, что сопоставимо с результатами [19] для аналогичных задач классификации и связывания сущностей.

Тестовая выборка формировалась методом случайного стратифицированного отбора 100 вакансий и 200 курсов из общего массива данных (5248 вакансий и 953 курса), с сохранением пропорционального распределения по профессиональным категориям (таблица 1) и уровням сложности курсов, что обеспечивало репрезентативность выборки относительно генеральной совокупности. Для каждой вакансии два независимых эксперта в области информационных технологий вручную формировали эталонный список релевантных курсов на основе соответствия требуемых вакансией и формируемых курсом навыков; согласованность экспертной разметки оценивалась коэффициентом каппа Коэна ($\kappa = 0,81$), что соответствует высокой степени согласия. В качестве критериев оценки качества рекомендаций использовались метрики P@5, MAP@10 и NDCG@10, поскольку они дополняют друг друга: P@5 отражает долю релевантных курсов среди первых пяти позиций выдачи, MAP@10 учитывает точность по первым десяти позициям с учетом ранга каждого релевантного элемента, а NDCG@10 – качество ранжирования с учетом убывающей значимости позиции в списке рекомендаций.

Вычислительная сложность предложенного метода определяется преимущественно этапом расчета косинусной близости эмбеддингов навыков между тремя доменами и в базовом варианте составляет $O(n \cdot m \cdot d)$, где n и m – количество навыков сравниваемых доменов, а d – размерность эмбеддинга (768). Применение приближенного индексирования эмбеддингов при поиске ближайших соседей позволило снизить практическую сложность до $O((n+m) \cdot \log(n+m))$. На используемой конфигурации (GPU NVIDIA Tesla T4, 16 ГБ видеопамяти) среднее время генерации эмбеддинга одной фразы составило 1,8 мс, а полное построение графа знаний для всего набора данных (5248 вакансий и 953 курса), включая извлечение эмбеддингов, расчет попарного сходства и запись узлов и связей в СУБД Neo4j, заняло около 42 минут. Формирование рекомендаций для одной вакансии в режиме инференса занимало в среднем 120 мс, что свидетельствует о практической применимости предложенного подхода в режиме, близком к реальному времени.

Заключение

Разработанная модель интеграции образовательных программ, требований рынка труда и онлайн-курсов (МООК) через гетерогенные графы знаний представляет собой инновационный подход к адаптации учебных программ под современные вызовы IT-сектора. Применение машинного обучения и мультиязычных трансформеров для анализа данных позволяет строить эффективные рекомендации по формированию навыков, востребованных на рынке. Прототип системы, построенный в Neo4j, демонстрирует возможность использования предложенной модели для создания персонализированных образовательных траекторий и карьерного планирования. Экспериментальная оценка показала, что предложенный подход превосходит базовые методы BM25 и Word2Vec по метрикам P@5, MAP@10 и NDCG@10, достигая P@5 = 0,74 и NDCG@10 = 0,71, что подтверждает преимущество мультиязычных трансформеров при работе со смешанными русско-английскими текстами. Качество выравнивания на-

выков между доменами по метрике F1 составило 0,79. Вместе с тем необходимо отметить ряд ограничений проведенного исследования. Объем тестовой выборки (100 вакансий и 200 курсов) остается относительно небольшим для получения статистически устойчивых оценок, а сами данные ограничены вакансиями ИТ-сферы Казахстана за двухмесячный период и бесплатными англоязычными курсами Coursera по компьютерным наукам и науке о данных, что может снижать обобщающую способность модели на другие отрасли и типы образовательных ресурсов. Порог косинусного сходства (0,75), использованный для связывания навыков между доменами, был подобран эмпирически и не проверялся на устойчивость при изменении предметной области или языковой пары. Масштабирование модели на другие предметные области (например, здравоохранение, инженерные специальности, гуманитарные науки) потребует переобучения либо дополнительной тонкой настройки модели эмбеддингов на терминологии соответствующей отрасли, а также пересмотра онтологической схемы графа с учетом специфики новых доменов. Перенос модели на другие образовательные платформы (edX, Udemy, локальные LMS вузов) потребует разработки отдельных модулей извлечения данных с учетом различий в структуре и доступности API, а также проверки совместимости эмбеддингов при работе с иными языковыми парами и форматами описания курсов. В перспективе работа может быть расширена за счет добавления данных из других сфер, что повысит универсальность и эффективность предложенного решения.

Информация о финансировании. Данное исследование финансируется Комитетом науки Министерства науки и высшего образования Республики Казахстан (грант № AP22783030)».

ЛИТЕРАТУРА

1 Zhao, T., et al. Mathgraph: A knowledge graph for automatically solving mathematical exercises. In: Li, G., Yang, J., Gama, J., Natwichai, J., Tong, Y. (Eds.), Database Systems for Advanced Applications. DASFAA 2019, 629–633 (2019). https://doi.org/10.1007/978-3-030-18576-3_45

2 Li, W., et al. Constructing low-redundant and high-accuracy knowledge graphs for education. In: González-González, C.S., et al. Learning Technologies and Systems. ICWL SETE 2022, 139–150 (2023). https://doi.org/10.1007/978-3-031-33023-0_13

3 Agrawal, G., Deng, Y., Park, J., Liu, H., and Chen, Y.-C. Building knowledge graphs from unstructured texts: Applications and impact analyses in cybersecurity education. Information, 13 (11), 526 (2022). https://doi.org/10.3390/info13110526

4 Su, Y., and Zhang, Y. Automatic construction of subject knowledge graph based on educational big data. Proceedings of the 2020 3rd International Conference on Big Data and Education (ICBDE ‘20), 129–135 (2020). https://doi.org/10.1145/3396452.3396458

5 Qin, Y., Cao, H., and Xue, L. Research and application of knowledge graph in teaching: Take the database course as an example. Journal of Physics: Conference Series, 1607, 012127 (2020). https://doi.org/10.1088/1742-6596/1607/1/012127

6 Rizun, M. Knowledge graph application in education: A literature review. Acta Universitatis Lodziensis. Folia Oeconomica, 3 (342), 7–19 (2019). https://doi.org/10.18778/0208-6018.342.01

7 Sun, Y., Liang, J., and Niu, P. Generation of personalized knowledge graphs based on GCN. Journal of Computer and Communications, 9 (9), 108–119 (2021). https://doi.org/10.4236/jcc.2021.99008

8 Meissner, R., and Thor, A. Creation and utilisation of domain specific knowledge graphs (DSKG) for e-learning. DELFI 2021, 151–162 (2021). https://dl.gi.de/server/api/core/bitstreams/b99e4bf0-10aa-4e4e-a0f1-96c1497bf3ee/content

9 Chen, P., Lu, Y., Zheng, V.W., Chen, X., and Yang, B. Knowedu: A system to construct knowledge graph for education. IEEE Access, 6, 31553–31563 (2018). https://doi.org/10.1109/ACCESS.2018.2839607

10 Ke, Q., and Lin, J. Dynamic generation of knowledge graph supporting STEAM learning theme design. Applied Sciences, 12 (21), 11001 (2022). https://doi.org/10.3390/app122111001

11 Yu, X., Stahr, M., Chen, H., and Yan, R.G. Design and implementation of curriculum system based on knowledge graph. 2021 IEEE International Conference on Consumer Electronics and Computer Engineering (ICCECE), 767–770 (2020). https://arxiv.org/ftp/arxiv/papers/2012/2012.12522.pdf

12 Aliyu, I., Kana, A.F., and Aliyu, S. Development of knowledge graph for university courses management. International Journal of Education and Management Engineering, 10 (2), 1–10 (2020). https://doi.org/10.5815/ijeme.2020.02.01

13 Tel'nov, V.P., and Korovin, Ju.A. Semanticheskij veb i grafy znanij kak obrazovatel'naja tehnologija podgotovki kadrov dlja jadernoj jenergetiki [Semantic Web and Knowledge Graphs as an Educational Technology for Nuclear Engineering Training]. Izvestija vysshih uchebnyh zavedenij. Jadernaja jenergetika, (2), 219–229 (2019). https://doi.org/10.26583/npe.2019.2.19 (in Russian).

14 Nair, L.S., Shivani, M.K., and Cheriyan, S.J. Enabling remote school education using knowledge graphs and deep learning techniques. Procedia Computer Science, 215, 618–625 (2022). https://doi.org/10.1016/j.procs.2022.12.064

15 Chi, Y., Qin, Y., Song, R., and Xu, H. Knowledge graph in smart education: A case study of entrepreneurship scientific publication management. Sustainability, 10 (4), 995 (2018). https://doi.org/10.3390/su10040995

16 Giabelli, A., Malandri, L., Mercorio, F., Mezzanzanica, M., and Seveso, A. Skills2Job: A recommender system that encodes job offer embeddings on graph databases. Applied Soft Computing, 101, 107049 (2020). https://doi.org/10.1016/j.asoc.2020.107049

17 Groot, M., Schutte, J., and Graus, D. Job posting-enriched knowledge graph for skills-based matching. arXiv preprint, arXiv:2109.02554 (2021). https://doi.org/10.48550/arXiv.2109.02554

18 Fettach, Y., Ghogho, M., and Benatallah, B. Knowledge graphs in education and employability: A survey on applications and techniques. IEEE Access, 10, 85857–85877 (2022). https://doi.org/10.1109/ACCESS.2022.3194063

19 Weichselbraun, A., Waldvogel, R., Fraefel, A., van Schie, A., and Kuntschik, P. Building knowledge graphs and recommender systems for suggesting reskilling and upskilling options from the web. Information, 13 (11), 510 (2022). https://doi.org/10.3390/info13110510

20 Zhu, G., Chen, Y., and Wang, S. Graph-community-enabled personalized course-job recommendations with cross-domain data integration. Sustainability, 14 (12), 7439 (2022). https://doi.org/10.3390/su14127439

21 Börner, K., Scrivner, O., Gallant, M., Ma, S., Liu, X., Chewning, K., and Evans, J.A. Skill discrepancies between research, education, and jobs reveal the critical need to supply soft skills for the data economy. Proceedings of the National Academy of Sciences, 115 (50), 12630–12637 (2018). https://doi.org/10.1073/pnas.1804247115

22 Chau, H.K. Explainable Course Recommendation: Connecting College Education to Knowledge and Careers Through Skills [Dissertation] (Pittsburgh, PA: University of Pittsburgh, Department of Informatics and Networked Systems, School of Computing and Information, 2024).

23 Hogan, A., Blomqvist, E., Cochez, M., d'Amato, C., de Melo, G., Gutierrez, C., Kirrane, S., Labra Gayo, J.E., Navigli, R., Neumaier, S., Ngonga Ngomo, A.-C., Polleres, A., Rashid, S.M., Rula, A., Schmelzeisen, L., Sequeda, J., Staab, S., and Zimmermann, A. Knowledge graphs. ACM Computing Surveys, 54 (4), Article 71 (2021). https://doi.org/10.1145/3447772

24 Ramazanova, V.S., Sambetbaeva, M.A., and Zagorul'ko, Ju.A. Obzor i analiz predstavlenij grafov znanij [Review and Analysis of Knowledge Graph Representations]. Trudy universiteta, (1), 414–422 (2024). https://doi.org/10.52209/1609-1825_2024_1_414 (in Russian).

25 IEEE Standard for Framework of Knowledge Graphs. IEEE Std 2807-2022, 1–52 (2023). https://doi.org/10.1109/IEEESTD.2022.10017167

26 Zagorulko, G.B. Model, Methods, and Tools for Comprehensive Support of DSS Development in Poorly Formalized Subject Areas [Dissertation] (Novosibirsk: A.P. Ershov Institute of Informatics Systems, Siberian Branch of the Russian Academy of Sciences, 2020). (in Russian).

.

[1*]Серикбаева С.К.,
PhD, доцент м.а., ORCID ID: 0000-0002-3627-3321,
*e-mail: inf_8585@mail.ru
[2]Рамазанова В.С.,
магистр, бас инженер, ORCID ID: 0000-0001-6100-3123,
e-mail: ramazanovavs@gmail.com
[1]Самбетбаева М.А.,
PhD, қауымдастырылған профессор, ORCID ID: 0000-0001-9358-1614,
e-mail: sambetbayeva_ma_1@enu.kz
[3,4]Еримбетова А.С.,
PhD, т.ғ.к., қауымдастырылған профессор, профессор-зерттеуші, ж.ғ.қ.,
ORCID ID: 0000-0002-2013-1513,
e-mail: aigerian8888@gmail.com
[5]Садирмекова Ж.Б.,
PhD, қауымдастылған профессор, ORCID ID: 0000-0002-7514-9315,
e-mail: Zhanna.Sadirmekova1@astanait.edu.kz

[1]Л.Н. Гумилев атындағы Еуразия ұлттық университеті, Астана қ., Қазақстан
[2]М. Өтемісов атындағы Батыс Қазақстан университеті, Орал қ., Қазақстан
[3]META University, Алматы қ., Қазақстан
[4]Ақпараттық және есептеуіш технологиялар институты, Алматы қ., Қазақстан
[5]Astana IT University, Астана қ., Қазақстан

ЕҢБЕК НАРЫҒЫНЫҢ СҰРАНЫСЫ МЕН БІЛІМ БЕРУ БАҒДАРЛАМАЛАРЫН БІРІКТІРУ НЕГІЗІНДЕ МООС ТАҢДАУ ҮШІН БІЛІМ ГРАФТАРЫН ҚҰРУ МОДЕЛЬДЕРІ

Аңдатпа

Мақалада білім беру бағдарламалары, еңбек нарығы талаптары және онлайн-курстар (МООС) арасындағы байланыстарды талдауға арналған білім графтары мен машиналық оқыту әдістеріне негізделген интеграциялық модель қарастырылады. Зерттеудің өзектілігі ақпараттық технологиялар саласындағы жылдам өзгерістермен байланысты, бұл түлектер дайындығы мен жұмыс берушілер талаптарының сәйкес келмеуіне әкеледі. Осы алшақтықты азайту үшін университет бағдарламалары, бос жұмыс орындары және онлайн-курстар деректерін біріктіретін гетерогенді білім графын пайдалану ұсынылады. Модельде дағдыларды, вакансия талаптарын және оқу курстарын байланыстыратын мета-жол жүзеге асырылған, бұл пайдаланушылардың әртүрлі санаттары үшін білім алу және мансаптық даму бойынша ұсыныстар қалыптастыруға мүмкіндік береді. Мәтіндік деректерді өңдеу үшін орыс және ағылшын тілдеріндегі сипаттамаларды талдайтын көптілді трансформаторлар қолданылды. Деректер көздері ретінде білім беру бағдарламаларының құзыреттер карталары, hh.kz платформасының вакансиялары және Coursera курстары пайдаланылып, Neo4j графтық деректер қорына біріктірілді. Алынған нәтижелер жетіспейтін құзыреттерді анықтауға және оларды қалыптастыруға арналған курстарды автоматты түрде таңдауға болатынын көрсетті. Ұсынылған модель білім беру бағдарламаларын жобалау және білім беру ортасында шешім қабылдауды қолдау үшін қолданылуы мүмкін.

Түйін сөздер: білім графиктері, машиналық оқыту, көп тілді трансформаторлар, онлайн курстар, еңбек нарығы, дағдылар, ұсыныстар, білім беру бағдарламалары, ақпараттық технологиялар, интеграциялық модельдер.

[1]Serikbayeva S.,
PhD, Acting Associate Professor, ORCID ID: 0000-0002-3627-3321,
*e-mail: inf_8585@mail.ru
[2]Ramazanova V.,
Master's degree, Chief Engineer, ORCID ID: 0000-0001-6100-3123
e-mail: ramazanovavs@gmail.com
[1]Sambetbayeva M.,
PhD, associate professor, ORCID ID: 0000-0001-9358-1614,
e-mail: sambetbayeva_ma_1@enu.kz
[3,4]Yerimbetova A.,
Cand. Eng. Sci., Associate Professor, professor-researcher, Leading Researcher,
ORCID ID: 0000-0002-2013-1513,
e-mail: aigerian8888@gmail.com
[5]Sadirmekova Zh.,
PhD, Associate Professor, ORCID ID: 0000-0002-7514-9315,
e-mail: Zhanna.Sadirmekova1@astanait.edu.kz

[1]L.N. Gumilyov Eurasian National University, Astana, Kazakhstan
[2]M. Utemisov West Kazakhstan University, Ural, Kazakhstan
[3]META University, Almaty, Kazakhstan
[4]Institute of Information and Computational Technologies CS MSHE RK, Almaty, Kazakhstan
[5]Astana IT University, Astana, Kazakhstan

MODELS FOR BUILDING KNOWLEDGE GRAPHS FOR MOOC SELECTION BASED ON THE INTEGRATION OF LABOR MARKET DEMANDS AND EDUCATIONAL PROGRAMS

Abstract

The article presents the development of an integration model based on knowledge graphs and machine learning methods for analyzing relationships between educational programs, labor market requirements, and online courses (MOOCs). The relevance of the study is driven by rapid changes in the information technology sector, which lead to a mismatch between graduate competencies and employer expectations. To reduce this gap, a heterogeneous knowledge graph integrating data from university curricula, job vacancies, and online courses is proposed. The model implements a meta-path connecting skills, job requirements, and learning courses, enabling recommendations for educational and career development for different categories of users. Multilingual transformers were applied to process textual descriptions in Russian and English. The data sources include competency maps of educational programs, job postings from the hh.kz platform, and courses from Coursera, all integrated into the Neo4j graph database. The obtained results demonstrate the capability to identify missing competencies and automatically recommend relevant courses for their acquisition. The proposed model can be applied in curriculum design, development of learning trajectories, and decision-making support within educational environments.

Keywords: knowledge graphs, machine learning, multilingual transformers, online courses, labor market, skills, recommendations, educational programs, information technology, integration models.

Received April 2, 2026; revised April 2, June 6, August 24, 2026; accepted August 31, 2026.

УДК 004.852:616.12-009.72
МРНТИ 28.23.25.

https://doi.org/10.55452/1998-6688-2026-23-3-328-335

[1]*Куатбаева А.А.,
PhD, ассистент-профессор, ORCID ID: 0000-0002-2143-3994,
*e-mail: a.kuatbayeva@astanait.edu.kz
[1] Омарбеков А.Н.,
магистр, ORCID ID: 0009-0007-8883-7073,
e-mail: 242929@astanait.edu.kz
[1]Аян А.А.,
магистр, ORCID ID: 0009-0000-6188-8021,
e-mail: 241785@astanait.edu.kz

[1]Astana IT university, г. Астана, Казахстан

МОДИФИЦИРОВАННАЯ SEIR МОДЕЛЬ С GRID AUTO-SEARCH ОПТИМИЗАЦИЕЙ ДЛЯ ВЫСОКОТОЧНОГО ПРОГНОЗИРОВАНИЯ ДИНАМИКИ ЭПИДЕМИЙ НА ОСНОВЕ COVID-19

Аннотация

В статье представлена модифицированная эпидемиологическая модель SEIR, интегрированная с методами машинного обучения для повышения точности прогнозирования динамики распространения COVID-19. Модель SEIR, более сложная, добавляет категорию «контактных» пациентов, которые способны передавать инфекцию, но еще не проявили симптомы. Такая модель позволяет лучше понять динамику эпидемий, особенно с длительным инкубационным периодом, который усложняет выявление заболевания и увеличивает риск его распространения. Предложенный подход расширяет классическую модель за счет временно-зависимых параметров, отражающих влияние мер социальной изоляции, уровня вакцинации и мобильности населения. Методология Grid Auto-Search обеспечивает автоматическую оптимизацию параметров и адаптивный выбор периода обучения. Для прогнозирования временно-зависимого коэффициента передачи β(t) применялись алгоритмы XGBoost и LSTM. Датасет включает 1143 наблюдения по Франции из трех открытых источников (Johns Hopkins University, Our World in Data, Google Mobility). Разработанная модель демонстрирует R^2 до 0,96 на горизонтах 30–90 дней; кросс-валидация подтверждает отсутствие существенного переобучения. Полученные результаты обосновывают практическую применимость гибридного подхода для систем поддержки принятия решений в здравоохранении. Результаты исследования подтверждены двумя авторскими свидетельствами Qazpatent на объекты авторского права.

Ключевые слова: SEIR модель, COVID-19, эпидемиологическое прогнозирование, Grid Auto-Search, параметрическая оптимизация, XGBoost, LSTM, временные ряды, математическое моделирование, мобильность населения, вакцинация.

Введение

Пандемия COVID-19 обнажила ключевое ограничение классических SEIR-моделей с фиксированными параметрами [10]: в условиях динамичных карантинных мер, вакцинации и изменений поведения населения они не способны своевременно реагировать на структурные изломы эпидемического процесса. Современные исследования подтверждают, что интеграция методов машинного обучения с традиционными математическими моделями позволяет существенно повысить точность прогнозов и гибкость аналитических систем [4, 5, 9, 14]. Тем не менее большинство опубликованных гибридных подходов применяют однократную ручную калибровку параметров и ограничены валидацией на одной-двух фазах пандемии, что снижает их обобщаемость.

Научный вклад настоящей работы состоит в трех ключевых аспектах. Во-первых, предложена методология Grid Auto-Search для систематического перебора горизонта прогноза, временного сдвига и начальных условий SEIR-модели, что принципиально отличает подход от разовой калибровки. Во-вторых, для прогнозирования β(t) применена комбинация XGBoost и LSTM, сочетающая интерпретируемость через анализ важности признаков с захватом долгосрочных зависимостей. В-третьих, в отличие от большинства аналогов, модель проходит кросс-фазовую валидацию на всем трехлетнем периоде пандемии с явным контролем переобучения.

Целью исследования является разработка и валидация гибридной модели SEIR+ML, объединяющей классический эпидемиологический подход с методами машинного обучения для более точного прогнозирования динамики распространения COVID-19 и поддержки принятия управленческих решений в условиях изменяющейся эпидемиологической обстановки [15].

Материалы и методы

Исследование основано на трех открытых источниках данных за период с 22 января 2020 г. по 9 марта 2023 г. База Johns Hopkins University (JHU) предоставила ежедневную статистику подтвержденных случаев, смертей и выздоровлений [6]. Данные вакцинации получены из Our World in Data (OWID) и включают количество введенных доз и долю полностью вакцинированного населения [1, 7]. Индексы мобильности по шести категориям мест взяты из Google Community Mobility Reports [8]. Интеграция источников позволила сформировать датасет из 1143 наблюдений и 39 признаков для Франции – страны с наиболее полными согласованными данными по всем трем источникам (таблица 1).

Таблица 1 – Характеристики объединенного датасета

Параметр	Значение
Временной период	22.01.2020 – 09.03.2023
Наблюдений / признаков	1143 / 39
Подтвержденных случаев (макс.)	39 866 718
Смертей (макс.)	166 176
Полностью вакцинировано	53 177 192 (78,2 % населения)
Пропущенных значений (до обработки)	187 (2,6 %)
Обнаружено выбросов	97 (2,8 %)

Предобработка включала три последовательных этапа. Пропущенные значения в кумулятивных переменных восстанавливались методом forward fill; для ежедневных приростов применялась медианная импутация с окном 7 дней; для индексов мобильности – линейная интерполяция. Выбросы выявлялись по критерию межквартильного размаха и заменялись медианными значениями скользящего окна. На этапе конструирования признаков созданы лаговые переменные (7, 14, 21 день), скользящие средние, производные темпа роста и циклические признаки (sin/cos дня недели) для учета недельной периодичности отчетности.

Классическая модель SEIR, восходящая к основополагающей работе Кермака и МакКендрика [2], расширена до SEIRV за счет временно-зависимых параметров β(t), σ(t), γ(t), отдельного состояния вакцинированных V и миграционных потоков. Система дифференциальных уравнений (1)–(6) описывает динамику изменения численности каждой группы:

$$\frac{dS}{dt} = -\beta(t) * S * \frac{I}{N} - \nu \cdot S + m_{in} \cdot S - m_{out} \cdot S \quad (1)$$

$$\frac{dE}{dt} = \beta(t) * S * \frac{I}{N} - \sigma(t) \cdot E + m_in \cdot E - m_out \cdot E \quad (2)$$

$$\frac{dI}{dt} = \sigma(t) \cdot E - \gamma(t) \cdot I + m_in \cdot I - m_out \cdot I \quad (3)$$

$$\frac{dR}{dt} = \gamma(t) \cdot I + m_in \cdot R - m_out \cdot R \quad (4)$$

$$\frac{dV}{dt} = \nu \cdot S \quad (5)$$

$$N = S + E + I + R + V \quad (6)$$

где:

t – время (сут.);

S(t), E(t), I(t), R(t), V(t) – численности соответственно восприимчивых, латентно инфицированных (в инкубационном периоде), активно инфицированных, выздоровевших и вакцинированных лиц в момент времени t (чел.);

β(t) – коэффициент передачи (прогнозируется ML-моделью, сут.$^{-1}$);

σ(t) = 1/T_инк – скорость перехода E→I (сут.$^{-1}$), где T_инк – средняя продолжительность инкубационного периода (сут.);

γ(t) = 1/T_инф – скорость выздоровления (сут.$^{-1}$), где T_инф – средняя продолжительность инфекционного периода (сут.);

ν – суточная доля вакцинируемых (сут.$^{-1}$); m_in, m_out – коэффициенты миграции (входящего и исходящего потоков, сут.$^{-1}$);

N – численность популяции (чел.), удовлетворяющая условию сохранения численности (6).

Использование временно-зависимых параметров β(t), σ(t), γ(t) согласуется с современными подходами к модификации эпидемиологических моделей, в том числе с применением дробно-производных операторов [13].

Для прогнозирования β(t) применялись два взаимодополняющих алгоритма. XGBoost – ансамблевый метод градиентного бустинга с высокой интерпретируемостью через оценки важности признаков; входные переменные включают лаговые значения случаев, скользящие средние, индексы мобильности, показатели вакцинации и временные признаки. Гиперпараметры подобраны Grid Search: n_estimators = 1 000, learning_rate = 0,01, max_depth = 7, min_child_weight = 3. LSTM – рекуррентная нейронная сеть (два скрытых слоя с Dropout) для захвата долгосрочных зависимостей; обучение выполнено с оптимизатором Adam, функцией потерь MSE и ранней остановкой по валидационной метрике.

Данные разбивались в пропорции 70/15/15 с сохранением хронологического порядка (таблица 2), что исключает утечку данных из будущего в прошлое. Параметры SEIR оптимизировались методом L-BFGS-B по целевой функции RMSE. Алгоритм Grid Auto-Search систематически перебирал 27 комбинаций параметров (горизонт прогноза: 30/60/90 дней; временной сдвиг: 0/30/60 дней; верхняя граница E_0: 0,05/0,2/0,5) и выбирал конфигурацию с минимальной ошибкой на валидационной выборке.

Таблица 2 – Структура разделения данных

Выборка	Дни (доля)	Период	Назначение
Обучающая	800 (70 %)	22.01.2020 – 31.03.2022	Обучение параметров
Валидационная	171 (15 %)	01.04.2022 – 18.09.2022	Настройка гиперпараметров
Тестовая	172 (15 %)	19.09.2022 – 09.03.2023	Финальная оценка

Результаты и обсуждение

После предобработки пропущенные значения устранены полностью, 97 выбросов заменены медианными оценками скользящего окна, исправлено 8 отрицательных значений ежедневных приростов. Расчет β(t) показал его высокую изменчивость: коэффициент Пирсона между β(t) и совокупным индексом мобильности составил r = 0,67 (p <0,001), что подтверждает

значимость поведенческих факторов. Корреляция активных случаев с компонентой I модели SEIR составила r = 0,952, показателей вакцинации с компонентой V - r = 0,989, что свидетельствует о структурной согласованности модели с реальными данными.

Базовая модель SEIR с фиксированными параметрами и единственной точкой разбивки показала отрицательные значения R^2, что указывает на полную неспособность описать реальную динамику: фиксированная точка разделения не учитывала фазы эпидемии, а статические параметры не адаптировались к изменяющимся условиям. Применение Grid Auto-Search кардинально изменило картину: на всех горизонтах прогнозирования достигнуты высокие коэффициенты детерминации при одновременном снижении MAPE до 1–9 % (таблица 3).

Таблица 3 – Сравнение базового подхода и Grid Auto-Search

Метрика	Базовый подход	Grid Auto-Search	Улучшение
R^2 (30 дней)	−27,58	0,949	+103,5 %
R^2 (60 дней)	−20,49	0,961	+104,8 %
R^2 (90 дней)	−28,91	0,873	+103,0 %
MAPE (30 дней)	95,27 %	1,40 %	−98,5 %
MAPE (60 дней)	95,95 %	5,06 %	−94,7 %
MAPE (90 дней)	96,81 %	9,05 %	−90,7 %

Важным методологическим элементом исследования стало также включение временно-зависимых параметров β(t), σ(t) и γ(t), отражающих динамику распространения инфекции в условиях реальных изменений социальной активности, мер ограничения и вакцинации. В отличие от моделей с постоянными параметрами, предложенная модификация позволила учитывать сезонные колебания и реакцию населения на эпидемиологические меры. Это привело к существенному повышению точности долгосрочных прогнозов и подтвердило гипотезу о необходимости учета временной вариативности параметров при моделировании инфекционных заболеваний. Полученные результаты согласуются с выводами Haghpanah et al. [12] о том, что длительность защиты, сроки и блокирующий эффект вакцинации оказывают существенное влияние на эпидемиологические показатели заболеваемости и смертности, что обосновывает явное выделение компоненты V в предложенной модели.

Визуализация компонент модели (рисунок 1) показала реалистичную динамику распространения инфекции: постепенное сокращение восприимчивой части населения, рост числа выздоровевших и вакцинированных, а также выраженные пики инфицирования в периоды повышенной мобильности.

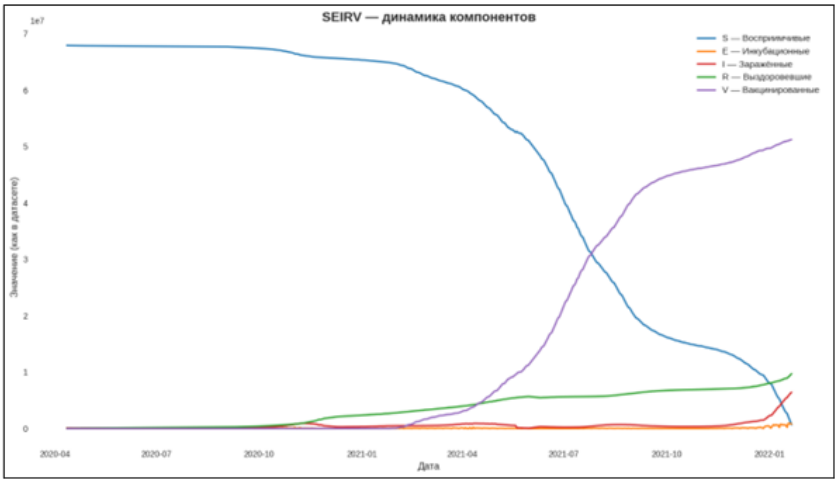


Рисунок 1 – Динамика компонентов SEIRV

Для оценки обобщаемости модели проведена валидация на шести эпидемиологических фазах (таблица 4). Наилучшая точность достигнута в периоды предсказуемых трендов – стабилизация после локдауна (R^2 = 0,91) и период массовой вакцинации (R^2 = 0,88). В период волны Omicron R^2 составил 0,82, что объясняется высокой неопределенностью входных данных при резкой смене параметров штамма. Ключевым индикатором отсутствия переобучения служат сопоставимые метрики на валидационной (R^2 = 0,94) и тестовой (R^2 = 0,87–0,96) выборках: разрыв не превышает 8%, что соответствует норме для нестационарных временных рядов.

Таблица 4 – Результаты валидации по фазам эпидемии (90-дневный прогноз)

Фаза	Период	R^2	RMSE	Комментарий
Волна 1	Мар–Май 2020	0,72	28 450	Высокая неопределенность
Стабилизация	Июн–Авг 2020	0,91	8 230	Предсказуемое снижение
Волны 2–3	Сен 2020–Апр 2021	0,78	45 670	Влияние ограничений
Вакцинация	Май–Дек 2021	0,88	15 340	Учет компоненты V
Omicron	Дек 2021–Мар 2022	0,82	52 110	Новый вариант вируса
Эндемическая	Апр 2022–Мар 2023	0,89	6 780	Низкая изменчивость

Анализ роли мобильности подтвердил ее значимость: наибольшая корреляция с $\beta(t)$ выявлена для рабочей активности (r=0,58) и торгово-развлекательных мест (r=0,54); совокупный индекс мобильности коррелировал с $\beta(t)$ на уровне $r = 0,67$ ($p < 0,001$). Эти результаты согласуются с данными Fernández Pozo et al. [11], согласно которым снижение мобильности на 50% уменьшает коэффициент передачи на 30–40%. Использование данных мобильности в режиме реального времени позволяет оперативно выявлять изменения в динамике эпидемии, что делает их важным компонентом современных систем мониторинга.

Сравнение с опубликованными результатами демонстрирует конкурентоспособность предложенной модели (таблица 5). В отличие от Yang et al. [4], применявших статическую калибровку, и Ahmad [3], ограничившегося одним горизонтом, предложенный подход обеспечивает систематическую кросс-параметрическую оптимизацию и явный контроль переобучения. Следует, однако, интерпретировать прямое сравнение R^2 с осторожностью ввиду различий в регионах и периодах наблюдений.

Таблица 5 – Сопоставление с существующими исследованиями

Исследование	Модель	Регион	Лучший R^2
Yang et al. (2020) [4]	Modified SEIR	Китай	0,78
Lu et al. (2023) [9]	SEIR + AI	Италия	0,82
Ahmad (2020) [3]	Modified SEIR	Саудовская Аравия	0,35
Настоящая работа	SEIR + Grid Auto-Search	Франция	0,961

Несмотря на высокие результаты, исследование имеет ряд ограничений. Точность модели зависит от полноты эпидемиологической отчетности, репрезентативности выборки пользователей Google и своевременности обновления данных вакцинации. В текущей реализации не учитываются повторные заражения, возрастная стратификация и вариации вирулентности штаммов. Прогнозирование $\sigma(t)$ и $\gamma(t)$ методами ML находится в стадии разработки. Применимость модели для других стран требует дополнительной валидации на независимых выборках.

Заключение

Предложенная гибридная модель SEIR+ML с оптимизацией Grid Auto-Search обеспечивает существенное улучшение качества прогнозирования по сравнению с базовым подходом:

R^2 возрастает с отрицательных значений до 0,87–0,96, MAPE снижается с ~96 % до 1–9 % в зависимости от горизонта. Адаптивная настройка параметров через Grid Auto-Search устраняет ключевое ограничение классических SEIR-моделей – неспособность учитывать фазовые изломы эпидемического процесса. Кросс-фазовая валидация подтверждает устойчивость модели и отсутствие существенного переобучения.

Установленная значимая корреляция β(t) с индексами мобильности (r = 0,67) обосновывает включение поведенческих данных как обязательного компонента прогностических систем. Практическая значимость результатов заключается в возможности применения модели для прогнозирования эпидемических волн, оценки эффективности ограничительных мер и сценарного анализа вакцинации. Направления дальнейшего развития включают возрастную стратификацию, мультирегиональную валидацию и интеграцию онлайн-обучения для работы в режиме реального времени.

ЛИТЕРАТУРА

1 Our World in Data. COVID-19 Data Repository (2024). URL: https://ourworldindata.org/coronavirus (accessed: October 15, 2025).

2 Kermack, W.O., and McKendrick, A.G. A contribution to the mathematical theory of epidemics. Proceedings of the Royal Society A: Mathematical, Physical and Engineering Sciences, 115 (772), 700–721 (1927). https://doi.org/10.1098/rspa.1927.0118

3 Ahmad, N. COVID-19 modeling in Saudi Arabia using the modified susceptible-exposed-infectious-recovered (SEIR) model. Cureus, 12 (9), e10452 (2020). https://doi.org/10.7759/cureus.10452

4 Yang, Z., Zeng, Z., Wang, K., et al. Modified SEIR and AI prediction of the epidemic trend of COVID-19 in China under public health interventions. Journal of Thoracic Disease, 12 (3), 165–174 (2020). https://doi.org/10.21037/jtd.2020.02.64

5 Chen, S., Yu, J., Chamouni, S., Barnawi, A., Chen, X., and Xu, L. Integrating machine learning and artificial intelligence in life-course epidemiology: pathways to innovative public health solutions. BMC Medicine, 22, 354 (2024). https://doi.org/10.1186/s12916-024-03566-x

6 Dong, E., Du, H., and Gardner, L. An interactive web-based dashboard to track COVID-19 in real time. The Lancet Infectious Diseases, 20 (5), 533–534 (2020). https://doi.org/10.1016/S1473-3099(20)30120-1

7 Mathieu, E., Ritchie, H., Rodés-Guirao, L., Appel, C., Giattino, C., Hasell, J., Macdonald, B., Dattani, S., Beltekian, D., Ortiz-Ospina, E., and Roser, M. Coronavirus Pandemic (COVID-19). Our World in Data (2020). URL: https://github.com/owid/covid-19-data (accessed: October 15, 2025).

8 Google LLC. Google COVID-19 Community Mobility Reports (2022). URL: https://www.google.com/covid19/mobility/ (accessed: October 15, 2025).

9 Lu, M., Zheng, X.-Y., Jia, W.-N., and Tian, C.-Z. Analysis and prediction of improved SEIR transmission dynamics model: taking the second outbreak of COVID-19 in Italy as an example. Frontiers in Public Health, 11, 1223039 (2023). https://doi.org/10.3389/fpubh.2023.1223039

10 Ghaffarzadegan, N., Rahmandad, H., and Jalali, M. Inefficiency of SIR models in forecasting the COVID-19 epidemic: a case study of Isfahan. Scientific Reports, 11, 4725 (2021). https://doi.org/10.1038/s41598-021-84055-6

11 Fernández Pozo, R., Rodríguez González, A.B., Vinagre Díaz, J.J., and Wilby, M.R. Data-driven analysis of the impact of COVID-19 on Madrid's public transport during each phase of the pandemic. Cities, 124, 103574 (2022). https://doi.org/10.1016/j.cities.2022.103574

12 Haghpanah, F., Lin, G., Levin, S.A., and Klein, E. Analysis of the potential impact of durability, timing, and transmission blocking of COVID-19 vaccine on morbidity and mortality. EClinicalMedicine, 35, 100863 (2021). https://doi.org/10.1016/j.eclinm.2021.100863

13 Taghvaei, A., Georgiou, T.T., Norton, L., and Tannenbaum, A. Fractional SIR epidemiological models. Scientific Reports, 10, 20882 (2020). https://doi.org/10.1038/s41598-020-77849-7

14 Flouris, A.D., and Duffy, J. Applications of artificial intelligence systems in the analysis of epidemiological data. European Journal of Epidemiology, 21 (3), 167–170 (2006). https://doi.org/10.1007/s10654-006-0005-y

15 Liu, L., Wang, X., Liu, O., Li, Y., Jin, Z., Tang, S., and Wang, X. Valuation and comparison of the actual and optimal control strategy in an emerging infectious disease: implication from a COVID-19 transmission model. Infectious Disease Modelling, 9 (2), 354–372 (2024). https://doi.org/10.1016/j.idm.2024.01.002

[1]*Куатбаева А.А.,
PhD, ассистент-профессор, RCID ID: 0000-0002-2143-3994,
*e-mail: a.kuatbayeva@astanait.edu.kz
[1]Омарбеков А.Н.,
магистр, ORCID ID: 0009-0007-8883-7073,
e-mail: 242929@astanait.edu.kz
[1]Аян А.А.,
магистр, ORCID ID: 0009-0000-6188-8021,
e-mail: 241785@astanait.edu.kz

[1] Astana IT university, Астана қ., Қазақстан

GRID AUTO-SEARCH ӘДІСІМЕН ОҢТАЙЛАНДЫРЫЛҒАН МОДИФИКАЦИЯЛАНҒАН SEIR ҮЛГІСІ COVID-19 НЕГІЗІНДЕГІ ЭПИДЕМИЯЛАР ДИНАМИКАСЫН ЖОҒАРЫ ДӘЛДІКПЕН БОЛЖАУ ҮШІН

Аңдатпа

Мақалада COVID-19 таралу динамикасын болжаудың дәлдігін арттыру мақсатында машиналық оқыту әдістерімен біріктірілген SEIR эпидемиологиялық үлгісінің модификацияланған нұсқасы ұсынылады. Ұсынылған тәсіл классикалық үлгіні уақытқа тәуелді параметрлер есебінен кеңейтеді. Grid Auto-Search әдістемесі параметрлерді автоматты оңтайландыруды және оқу кезеңін бейімді таңдауды қамтамасыз етеді. β(t) коэффициентін болжау үшін XGBoost және LSTM алгоритмдері қолданылды. Деректер жиынтығы үш ашық дереккөз бойынша Францияның 1 143 күндік бақылауын қамтиды. Үлгі 30–90 күндік горизонттарда $R^2 = 0,96$ дейінгі нәтижені көрсетеді; кросс-валидация айтарлықтай қайта оқыту болмайтынын растайды. Нәтижелер денсаулық сақтаудағы шешім қабылдауды қолдауда гибридтік тәсілдің практикалық маңыздылығын негіздейді. Зерттеу нәтижелері авторлық құқық объектілеріне берілген Qazpatent-тің екі авторлық куәлігімен расталған.

Түйін сөздер: SEIR үлгісі, COVID-19, эпидемиологиялық болжау, Grid Auto-Search, параметрлік оңтайландыру, XGBoost, LSTM, уақыттық қатарлар, математикалық модельдеу, халық мобильділігі, вакцинация.

[1]*KuatbaevaA.A.,
PhD, Assistant Professor, ORCID ID: 0000-0002-2143-3994,
*e-mail: a.kuatbayeva@astanait.edu.kz
[1]Omarbekov A.N.
MSc., ORCID ID: 0009-0007-8883-7073,
e-mail: 242929@astanait.edu.kz
[1]Aian A.A.,
MSc., ORCID ID: 0009-0000-6188-8021,
e-mail: 241785@astanait.edu.kz

[1] Astana IT university, Astana, Kazakhstan

MODIFIED SEIR MODEL WITH GRID AUTO-SEARCH OPTIMIZATION FOR HIGH-ACCURACY EPIDEMIC DYNAMICS FORECASTING BASED ON COVID-19

Abstract

This paper presents a modified SEIR epidemiological model integrated with machine learning techniques to improve COVID-19 transmission dynamics forecasting. The proposed approach extends the classical framework with time-dependent parameters capturing the effects of social distancing, vaccination coverage, and population

mobility. The Grid Auto-Search methodology enables automatic parameter optimization and adaptive training-period selection. XGBoost and LSTM algorithms are applied to forecast the time-varying transmission coefficient β(t). The dataset comprises 1,143 daily observations for France from three open sources (Johns Hopkins University, Our World in Data, Google Mobility). The model achieves R^2 up to 0.96 across 30–90-day horizons; cross-validation confirms the absence of significant overfitting. The results support the practical applicability of this hybrid approach for healthcare decision-support systems. The research results are confirmed by two Qazpatent certificates of copyright registration

Keywords: SEIR model, COVID-19, epidemiological forecasting, Grid Auto-Search, parameter optimization, XGBoost, LSTM, time series, mathematical modeling, population mobility, vaccination.

Received November 8, 2025; revised April 10, 20, May 21, 2026; accepted June 11, 2026.

УДК 004.89
МРНТИ 28.23.29

https://doi.org/10.55452/1998-6688-2026-23-3-336-346

[1]Марламбеков Д.,
докторант, ORCID ID: 0009-0005-3266-2126,
e-mail: dmarlambekov@gmail.com
[1]Ахметова А.,
докторант, ORCID: ID0000-0002-7718-6478,
e-mail: baltabekova1994@gmail.com
[1]Төрекул С.,
докторант, ORCID ID: 0009-0003-8161-533X,
e-mail: saule.torekul@gmail.com
[1*]Уалиева И. М.,
к.ф.-м.н., ассоциированный профессор, ORCID ID: 0000-0003-3853-8896,
*e-mail: i.ualiyeva@gmail.com

[1]Казахский национальный университет им. аль-Фараби, г. Алматы, Казахстан

БЕНЧМАРКИНГ МОДЕЛЕЙ ГЛУБОКОГО ОБУЧЕНИЯ ДЛЯ КЛАССИФИКАЦИИ КАЗАХСКИХ НОВОСТНЫХ ТЕКСТОВ В УСЛОВИЯХ ОГРАНИЧЕННОЙ РАЗМЕТКИ

Аннотация

Стремительное развитие методов глубокого обучения и появление трансформерных архитектур кардинально изменили ландшафт обработки естественного языка, однако эти достижения остаются неравномерно распределенными. В то время как для английского и других высокоресурсных языков существуют масштабные бенчмарки, для низкоресурсных языков, таких как казахский, проблема качественной классификации текстов остается острым вызовом. Авторами проведен сравнительный анализ классической модели эмбеддингов Word2Vec, рекуррентных моделей BiLSTM, трансформеров BERT и XLM-R, генеративной модели mT5, а также классических и статистических бейзлайнов для задачи few-shot классификации казахских новостных текстов в условиях ограниченной разметки. Эксперименты проведены на датасете KazNews для few-shot классификации, собранном из статей tengrinews.kz и inform.kz и параллельных корпусов HuffPost. Датасеты содержат пять категорий (спорт, политика, бизнес, путешествия и др.). Эксперименты в режимах 1-shot и 5-shot продемонстрировали, что ни одна из моделей не доминирует одновременно на всех датасетах и режимах: Word2Vec показал лучшие результаты на датасетах на корпусах HuffPost (0.48 и 0.53) при 5-shot режиме; mT5-Seq2Seq лучший на KazNews при 5-shot (0.71); BERT в целом конкурентоспособен при 5-shot на датасете KazNews с длинными текстами. Авторы также выявили резкий скачок качества для модели mT5-Seq2Seq в 5-shot. Для режима 1-shot ни одна из моделей не показала приемлемого результата качества.

Ключевые слова: обработка естественного языка, низкоресурсные языки, классификация текстов, few-shot learning, рекуррентные модели, трансформерные модели, генеративные модели.

Введение

Проблема низкоресурсных языков, к которым относится и казахский язык, состоит в отсутствии огромных объемов данных, к тому же он обладает высокой морфологической вариативностью. Все вышеназванное усложняет обработку казахского языка методами глубокого обучения. Подходы, основанные на методах обучения с малым количеством данных (few-shot learning), могут обойти эти проблемы.

В данном исследовании рассмотрен few-shot learning (FSL) подход для задачи классификации текстов на датасете с ограниченным количеством обучающих примеров. Авторы взяли принципиально разные классы, начиная от простых эмбеддингов до генеративных трансфор-

меров, таких как Word2vec, BiLSTM, BERT, XLM-RoBERTa-base, mT5-Seq2seq, и сравнили с Random baseline и Majority baseline, чтобы показать, что предобученные модели действительно могут качественно классифицировать тексты на казахском языке с малым количеством примеров.

Для проведения исследования авторы собрали оригинальный корпус новостных текстов tengrinews.kz и inform.kz на казахском языке и параллельные датасеты: HuffPost ENG на оригинальном английском языке и его перевод на казахский HuffPost KAZ. Параллельные датасеты на английском и казахском языках включены, чтобы сравнить поведение моделей на ресурсном и низкоресурсном языках в идентичных условиях.

Авторы выявили критическую границу применимости генеративных моделей (эффект «нулевого» качества mT5 в 1-shot и резкий скачок в 5-shot) и вывели рекомендации для разработчиков NLP-систем для казахского языка.

Исследования, направленные на обработку текстов на казахском языке, постоянно растут. Однако их количество несопоставимо низко по сравнению с высокоресурсными языками, каким являются английский, испанский или турецкий [1]. Казахский язык относится к агглютинативным языкам, что говорит об их богатой морфологии, что накладывает отпечаток на методологию работы с ним.

Ранние подходы, которые и сейчас распространены, основывались на классических методах машинного обучения, как наивный Байес, метод опорных векторов SVM, логистическая регрессия [2-5] и пр., которые использовали подходы вроде «мешка слов» (BOW) или TF-IDF [6, 7]. Эти подходы относятся к частотным, и в случае сложной морфологии созданные словари становились слишком разреженными, что снижало обобщающую способность.

Ситуация заметно изменилась с приходом рекуррентных нейросетей, в частности LSTM и BiLSTM [8, 9]. Исследователи нашли, что двунаправленная обработка текста позволяет гораздо точнее улавливать внутреннюю структуру слова и локальные связи в предложении. Это был явный шаг вперед по сравнению со старой статистикой [1]. Тем не менее, серьезная нехватка огромных размеченных корпусов остается большой проблемой. Даже современные эмбеддинги, такие как Word2Vec или FastText [10, 11], не спасают рекуррентные модели от нестабильности, когда количество обучающих примеров слишком мало.

Значительные достижения связаны с появлением трансформеров, архитектур типа BERT, XLM-RoBERTa, mT5, KazSim [12–14]. За счет того, что они предобучены на огромном количестве текстов, эти модели научились обходить дефицит данных. Большое количество исследований также посвящено обучению на малых выборках (few-shot learning), особенно для высокоресурных языков [15, 16]. Для казахского же языка такие методы встречаются в задаче упрощения текстов [17], но для задач классификации текстов такие исследования не найдены.

Материалы и методы

Датасет

Для исследования были собраны три датасета: оригинальный корпус новостных текстов на казахском языке, опубликованных на tengrinews.kz и inform.kz; готовый датасет HuffPost ENG (huff_5cat_en.json) на английском языке и HuffPost KAZ и параллельный датасет, переведенный с HuffPost ENG на казахский язык (huff_5cat_translated_kk.json).

Тематически корпус охватывает пять рубрик. «Спорт» включает репортажи о соревнованиях, турнирах и спортивных достижениях. Рубрика «Политика» представлена материалами о государственных решениях и международных отношениях. «Бизнес» объединяет публикации об экономике, финансовых рынках и банковском секторе. «Путешествия» содержат туристические и страноведческие тексты. Пятая категория зависит от версии датасета: в корпусе HuffPost ей соответствуют разделы Entertainment или Technology. Такой диапазон тематик создает реалистичную классификационную задачу: часть рубрик семантически смежные и модели приходится работать с неоднозначностью. На рисунке 1 визуализация t-SNE показана

высокая разделимость некоторых классов и высокая степень смешивания признаков у остальных категорий новостей.

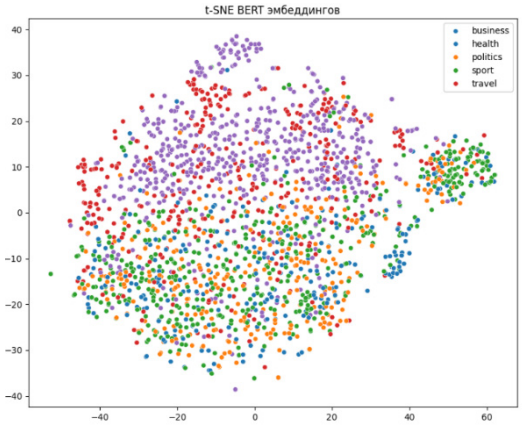


Рисунок 1 – t-SNE проекция BERT-эмбеддингов:
кластерная структура пяти тематических категорий

Количественные характеристики использованных датасетов обобщены в таблице 1.

Таблица 1 – Общий объем датасетов и средняя длина предложения

Датасет	Всего статей	Всего предложений	Средняя длина предложения (слов)	Медиана (слов)
KazNews	7520	87 428	13.6	12
HuffPost KAZ	65 406	102 618	10.7	10
HuffPost EN	65 406	156 481	11.7	10

Приведенные показатели средней длины предложения демонстрируют существенные различия между корпусами: тексты KazNews в среднем на 20–27% длиннее по числу слов в предложении, чем тексты HuffPost, что согласуется с жанровыми особенностями источников: новостные статьи tengrinews.kz и inform.kz написаны в более развернутом стиле, тогда как заголовочно-ориентированный формат HuffPost предполагает более короткие и лаконичные конструкции. Это обстоятельство существенно для интерпретации результатов Word2Vec, представленных в разделе «Результаты и обсуждение»: усреднение векторных представлений по короткому предложению дает менее устойчивый семантический сигнал, чем по длинному, чем отчасти объясняются более высокие показатели Word2Vec именно на датасете KazNews.

Распределение статей по рубрикам для каждого датасета представлено в таблице 2.

Таблица 2 – Количество статей по рубрикам

Датасет	Рубрика	Количество статей	Доля от датасета
KazNews	Путешествия	2266	30.1%
KazNews	Политика	1706	22.7%
KazNews	Спорт	1335	17.8%
KazNews	Здоровье	1149	15.3%
KazNews	Бизнес	1064	14.1%
HuffPost KAZ / EN	Politics	37 449	57.3%
HuffPost KAZ / EN	Travel	9936	15.2%
HuffPost KAZ / EN	Health	6807	10.4%
HuffPost KAZ / EN	Business	6059	9.3%
HuffPost KAZ / EN	Sports	5155	7.9%

Как следует из таблицы 2, датасет KazNews характеризуется относительно равномерным распределением классов: доля крупнейшей рубрики («Путешествия») не превышает 30%, а доля наименьшей («Бизнес») составляет 14%, то есть отношение крупнейшего класса к наименьшему не превышает 2.1. Датасеты HuffPost, напротив, демонстрируют выраженный дисбаланс: рубрика «Politics» охватывает 57.3% всех статей, тогда как «Sports» лишь 7.9%, что дает отношение более 7 к 1. Именно эта диспропорция определяет эффект, описанный в разделе «Результаты и обсуждение» как вырождение XLM-RoBERTa-base в константный предиктор мажоритарного класса: при столь значительном дисбалансе классификатору, не успевшему обучиться по 1–5 примерам на класс, статистически выгоднее «угадывать» доминирующую рубрику, чем распределять предсказания равномерно между всеми пятью категориями.

Для иллюстрации тематического разнообразия корпуса ниже приведены примеры заголовков статей датасета KazNews по каждой из пяти рубрик (таблица 3).

Таблица 3 – Примеры заголовков статей KazNews по рубрикам

Рубрика	Пример заголовка
Спорт	Спорт саласында бірнеше шенеунік тәртіптік жауапкершілікке тартылды
Путешествия	Қазақстаннан бірнеше елге жаңа тікелей рейстер ашылады
Здоровье	Диабет әлеуметтік маңызды аурулардың тізімінен шығарылды: енді не өзгереді?
Политика	Қасым-Жомарт Тоқаевқа Өзбекстанның ең жоғары мемлекеттік наградасы табысталды
Бизнес	Ел экономикасына құйылған инвестиция көлемі 5 жылда 18 трлн теңгеге жетті

Архитектуры моделей

Random baseline предсказывает метку случайным образом из пяти классов и задает абсолютный минимум производительности. Majority baseline всегда выбирает наиболее часто встречающийся класс тренировочного набора, что позволяет проверить, реагируют ли модели на реальную структуру данных или только эксплуатируют дисбаланс классов.

Word2Vec + нейронный классификатор [11]. Статические векторные представления Word2Vec, обученные на казахских текстах, усреднялись до уровня предложения и подавались в простой полносвязный классификатор. Эта конфигурация служит мостом между классическими методами и контекстуальными моделями и, как выяснилось, ведет себя неожиданно.

Рекуррентный блок представлен архитектурой BiLSTM с глубиной в 1,2 и 3 слоя [9].

Мультиязычная версия BERT mBERT [12] стала главным трансформерным бейзлайном. Архитектура включает 12 слоев self-attention с 12 головами внимания и скрытое пространство размером 768. При дообучении параметры энкодера обновлялись с пониженным learning rate, чтобы не «стереть» предобученные представления, тогда как классификационный слой тренировался с нуля.

XLM-RoBERTa-base [13] – еще один представитель мультиязычных трансформеров, модель, прошедшая предобучение на 2,5 ТБ разнородных текстов. В основе архитектуры лежат принципы RoBERTa: динамическое маскирование и расширенная субсловная токенизация SentencePiece. XLM-R была включена в эксперимент для того, чтобы оценить, насколько расширенные ресурсы предобучения помогают при работе с морфологически богатыми тюркскими языками.

mT5-Seq2Seq [14]. Генеративная модель mT5 реализует нестандартный подход: задача классификации формулируется как задача порождения текста. На входе: текст статьи, на выходе: слово с названием категории. Такой text-to-label формат любопытен тем, что полностью меняет способ, которым модель «думает» о классах, и позволяет выяснить, насколько генеративные архитектуры чувствительны к объему обучающей выборки.

Параметры обучения и программно-аппаратная среда

С целью повышения воспроизводимости результатов приводим детали экспериментальной настройки, восстановленные из исходного кода эксперимента. Bi-LSTM (1/2/3 слоя): обучаемые (не предобученные) эмбеддинги размерности 100, скрытый слой 64 единицы на направление, словарь строится по объединению обучающей и тестовой выборок с токенизацией по пробелам; обучение – 15 эпох, batch size = 16, оптимизатор Adam с learning rate = 0.001, Dropout = 0.3, критерий остановки – фиксированное число эпох (без early stopping). BERT: чекпоинт bert-base-multilingual-cased (Hugging Face Transformers), токенизация WordPiece, максимальная длина последовательности 128 токенов; обучение – 10 эпох, batch size = 8 (для теста – 16), оптимизатор AdamW с learning rate = 2e-5, линейный warmup-шедулер (get_linear_schedule_with_warmup, num_warmup_steps = 0), gradient clipping (max_norm = 1.0). mT5-Seq2Seq: чекпоинт google/mt5-small, токенизация SentencePiece, входной промпт вида «classify: {текст}», максимальная длина входа 128 токенов, длина целевой последовательности 16 токенов; обучение – 50 эпох, batch size = 2 (для теста – 8), оптимизатор AdamW с learning rate = 5e-4, линейный warmup-шедулер (num_warmup_steps = 0); генерация ответа – жадный поиск (num_beams = 1, max_length = 16). Во всех экспериментах фиксировался seed = 42. Библиотеки: PyTorch, Hugging Face Transformers, datasets, accelerate, sentencepiece, protobuf, scikit-learn устанавливались через pip без явной фиксации номеров версий в коде эксперимента.

Исходные эксперименты (accuracy_results.json / seq2seq_results.json) выполнялись в среде Google Colab с GPU-ускорением. Независимая переоценка метрик macro-F1/weighted-F1/precision/recall для BERT, XLM-RoBERTa-base и mT5-Seq2Seq (таблицы 4–6) выполнена локально на NVIDIA GeForce RTX 5080 Laptop GPU (CUDA 13.1, PyTorch с поддержкой sm_120). Для XLM-RoBERTa-base оригинальный код обучения и гиперпараметры в доступных материалах найти не удалось; при переоценке использованы гиперпараметры по аналогии с BERT (10 эпох, batch size = 8, learning rate = 2e-5, максимальная длина последовательности 128 токенов), и это приближение оригинальной настройки.

Результаты и обсуждение

Для оценки моделей few-shot классификации в условиях выраженного дисбаланса классов и предельно малой обучающей выборки (1 и 5 примеров на класс) одной метрики accuracy недостаточно: она может маскировать вырождение классификатора в константный предиктор мажоритарного класса. Поэтому все результаты приводятся сразу по пяти метрикам: Accuracy, Macro-F1, Weighted-F1, Precision (macro) и Recall (macro) (таблицы 4–6 для трех датасетов (KazNews, HuffPost KAZ, HuffPost EN), обоих режимов обучения (1-shot и 5-shot) и девяти моделей: двух формальных бейзлайнов (Random, Majority), классического подхода на статических эмбеддингах (Word2Vec + полносвязный классификатор), рекуррентных сетей (BiLSTM, 1–3 слоя) и трех предобученных языковых моделей (BERT, XLM-RoBERTa-base, mT5-Seq2Seq). Тестовая выборка в каждом случае – это вся оставшаяся после отбора few-shot примеров часть датасета без искусственного балансирования классов, поэтому распределение классов в тесте отражает естественный дисбаланс исходных данных.

Таблица 4 – Метрики качества few-shot классификации (Accuracy, macro-F1, weighted-F1, Precision, Recall) на датасете KazNews

	Модель	Режим	Accuracy	Macro-F1	Weighted-F1	Precision	Recall
Baseline	Random baseline	1-shot	0.196	0.192	0.201	0.196	0.195
		5-shot	0.197	0.192	0.201	0.196	0.195
	Majority baseline	1-shot	0.141	0.050	0.035	0.028	0.200
		5-shot	0.141	0.050	0.035	0.028	0.200
Эмбеддинги	Word2Vec	1-shot	0.491	0.421	0.440	0.488	0.480
		5-shot	0.643	0.625	0.657	0.638	0.623

Продолжение таблицы 4

Рекуррентные модели	1-layer BiLSTM	1-shot	0.333	0.324	0.330	0.359	0.342
		5-shot	0.487	0.450	0.493	0.463	0.461
	2-layer BiLSTM	1-shot	0.321	0.315	0.318	0.337	0.338
		5-shot	0.464	0.413	0.446	0.450	0.442
	3-layer BiLSTM	1-shot	0.308	0.292	0.295	0.346	0.331
		5-shot	0.426	0.330	0.370	0.415	0.385
Трансформеры	BERT	1-shot	0.241	0.163	0.174	0.152	0.214
		5-shot	0.567	0.477	0.528	0.607	0.513
	XLM-RoBERTa-base	1-shot	0.227	0.074	0.084	0.045	0.200
		5-shot	0.485	0.378	0.411	0.543	0.498
Генеративные модели	mT5-Seq2Seq	1-shot	0.000	0.000	0.000	0.000	0.000
		5-shot	0.710	0.680	0.682	0.738	0.724

Таблица 5 – Метрики качества few-shot классификации (Accuracy, macro-F1, weighted-F1, Precision, Recall) на датасете HuffPost KAZ

	Модель	Режим	Accuracy	Macro-F1	Weighted-F1	Precision	Recall
Baseline	Random baseline	1-shot	0.198	0.168	0.228	0.199	0.199
		5-shot	0.198	0.168	0.228	0.199	0.199
	Majority baseline	1-shot	0.093	0.034	0.016	0.019	0.200
		5-shot	0.093	0.034	0.016	0.019	0.200
Эмбеддинги	Word2Vec	1-shot	0.164	0.144	0.154	0.268	0.236
		5-shot	0.484	0.353	0.518	0.357	0.374
Рекуррентные модели	1-layer BiLSTM	1-shot	0.165	0.145	0.186	0.194	0.195
		5-shot	0.179	0.160	0.195	0.204	0.212
	2-layer BiLSTM	1-shot	0.337	0.191	0.353	0.201	0.202
		5-shot	0.282	0.197	0.312	0.213	0.215
	3-layer BiLSTM	1-shot	0.233	0.169	0.260	0.204	0.211
		5-shot	0.179	0.146	0.171	0.226	0.227
Трансформеры	BERT	1-shot	0.183	0.111	0.121	0.233	0.214
		5-shot	0.420	0.243	0.406	0.328	0.310
	XLM-RoBERTa-base	1-shot	0.571	0.149	0.418	0.242	0.201
		5-shot	0.415	0.224	0.380	0.328	0.273
Генеративные модели	mT5-Seq2Seq	1-shot	0.000	0.000	0.000	0.000	0.000
		5-shot	0.339	0.044	0.299	0.055	0.064

Таблица 6 – Метрики качества few-shot классификации (Accuracy, macro-F1, weighted-F1, Precision, Recall) на датасете HuffPost EN

	Модель	Режим	Accuracy	Macro-F1	Weighted-F1	Precision	Recall
Baseline	Random baseline	1-shot	0.198	0.168	0.228	0.199	0.199
		5-shot	0.198	0.168	0.228	0.199	0.199
	Majority baseline	1-shot	0.093	0.034	0.016	0.019	0.200
		5-shot	0.093	0.034	0.016	0.019	0.200
Эмбеддинги	Word2Vec	1-shot	0.352	0.274	0.377	0.333	0.342
		5-shot	0.533	0.442	0.563	0.443	0.493
Рекуррентные модели	1-layer BiLSTM	1-shot	0.222	0.174	0.257	0.201	0.196
		5-shot	0.251	0.190	0.281	0.212	0.216
	2-layer BiLSTM	1-shot	0.207	0.165	0.237	0.209	0.209
		5-shot	0.236	0.191	0.261	0.218	0.228
	3-layer BiLSTM	1-shot	0.305	0.203	0.336	0.215	0.214
		5-shot	0.294	0.212	0.324	0.233	0.236

Продолжение таблицы 6

Трансформеры	BERT	1-shot	0.197	0.162	0.132	0.264	0.287
		5-shot	0.269	0.251	0.269	0.336	0.359
	XLM-RoBERTa-base	1-shot	0.552	0.193	0.425	0.173	0.232
		5-shot	0.115	0.098	0.048	0.296	0.259
Генеративные модели	mT5-Seq2Seq	1-shot	0.000	0.000	0.000	0.048	0.000
		5-shot	0.251	0.230	0.248	0.356	0.242

Для всех датасетов случайный классификатор Random baseline показывает схожие значения accuracy в 0.196-0.198, что указывает на случайное угадывание классов. Мажоритарный классификатор Majority baseline показывает более низкие значения accuracy, 0.093 для датасетов HuffPost EN и HuffPost KAZ и 0.141 для KazNews, для всех 1-shot 5-shot режимов. Мажоритарный классификатор всегда выбирает наиболее частый класс, что повлияло на значения Macro-F1, равные 0.034 для датасетов HuffPost EN и HuffPost KAZ и 0.05 для KazNews, и это указывает на несбалансированность классов в выборке.

На датасете KazNews модель Word2Vec показала наиболее высокие результаты, достигнув accuracy 0.491 и Macro-F1 0.421 для режима 1-shot. В режиме 5-shot Word2Vec достигла хороших результатов, accuracy 0.643 и Macro-F1 0.625, уступив только генеративной модели mT5.

Рекуррентные сети (BiLSTM, 1–3 слоя) показывают результаты, близкие к бейзлайнам, на всех датасетах: accuracy в диапазоне 0.16–0.49, macro-F1 0.15–0.45. Увеличение числа слоев не дает систематического выигрыша: например, на HuffPost KAZ 2-слойная конфигурация неожиданно обгоняет 1- и 3-слойную при 1-shot (accuracy 0.337 против 0.165 и 0.233), но проигрывает им же при 5-shot (0.282). Такая немонотонность по числу слоев является ожидаемым следствием крайне малого объема обучающих данных: при 1–5 примерах на класс сеть не столько обучается обобщающим признакам, сколько подстраивается под конкретную случайную выборку, и результат сильно зависит от конкретных примеров, а не от архитектуры.

BERT (bert-base-multilingual-cased) при 1-shot показывает слабые и низкие по всем метрикам результаты на всех трех датасетах (accuracy 0.18–0.24, macro-F1 0.11–0.17), что ожидаемо для одного примера на класс. При переходе к 5-shot качество заметно растет, особенно на KazNews (accuracy 0.567, macro-F1 0.477), и это третий результат на этом датасете при 5-shot, после моделей mT5 и Word2Vec). На HuffPost KAZ и HuffPost EN рост при 5-shot более скромный (accuracy 0.420 и 0.269 соответственно). Важно, что во всех случаях accuracy и macro-F1 у BERT остаются в пределах одного порядка друг друга, модель не демонстрирует признаков вырождения в константный предиктор.

XLM-RoBERTa-base демонстрирует самый показательный случай расхождения метрик во всей таблице. На KazNews модель ведет себя предсказуемо: низкие accuracy и macro-F1 при 1-shot (0.227 / 0.074) и заметный рост при 5-shot (0.485 / 0.378), без аномальных расхождений между метриками. Но на обоих датасетах HuffPost при 1-shot возникает резкий разрыв между accuracy и macro-F1: 0.571 против 0.149 на HuffPost KAZ и 0.552 против 0.193 на HuffPost EN. Мы проверили это напрямую, построив confusion matrix по сохраненным предсказаниям модели на HuffPost KAZ (1-shot) (таблица 7):

Таблица 7 – Confusion Matrix для датасета HuffPost KAZ

Истинный класс	Business	Health	Politics	Sports	Travel
Business	0	0	6025	33	0
Health	0	1	6720	85	0
Politics	0	1	37265	182	0
Sports	0	0	5102	52	0
Travel	0	0	9912	23	0

в 65 024 из 65 401 случая (99.4%) модель предсказывала класс «Politics», то есть практически всегда один и тот же ответ, независимо от текста. Recall по классу Politics при этом составил 0.995, а по остальным четырем классам – от 0.000 до 0.010 (таблицы 8, 9). Поскольку доля класса Politics в тестовой выборке – около 57%, такой константный предиктор и дает accuracy ≈ 0.57 при формально нулевой полезности для четырех из пяти категорий, что и отражает низкий macro-F1 (0.149) и теоретическое значение macro-recall ровно 1/5 = 0.20 (при факте 0.201). Это ровно тот случай, когда одна лишь accuracy вводит в заблуждение: на датасете с сильным дисбалансом классов (HuffPost, где Politics ≈ 57%) XLM-RoBERTa при 1-shot фактически не научилась ничему, кроме «чаще всего это Politics», тогда как на более сбалансированном KazNews (максимальная доля класса около 30%) аналогичного вырождения не происходит. При 5-shot на HuffPost KAZ разрыв между метриками сокращается (0.415 / 0.224), а вот на HuffPost EN 5-shot неожиданно дает худший результат, чем 1-shot (accuracy 0.115, macro-F1 0.098), здесь случайность конкретной обучающей подвыборки, по-видимому, играет более значимую роль, чем само число примеров.

Таблица 8 – True Positives по каждому классу

Класс	TP	support	recall
Business	0	6058	0.000
Health	1	6806	0.000
Politics	37265	37448	0.995
Sports	52	5154	0.010
Travel	0	9935	0.000

Таблица 9 – Распределение предсказанных классов

Класс	Количество предсказаний	Доля (%)
Business	0	0.0
Health	2	0.0
Politics	65024	99.4
Sports	375	0.6
Travel	0	0.0

mT5-Seq2Seq демонстрирует наиболее контрастное поведение между режимами обучения. При 1-shot метрики равны нулю на всех трех датасетах: генеративная модель не в состоянии сформировать устойчивое отображение «текст – метка» по единственному примеру и не воспроизводит ни одной корректной метки. При 5-shot картина резко меняется: на KazNews mT5 показывает лучший результат среди всех протестированных моделей и конфигураций (accuracy 0.710, macro-F1 0.680, precision 0.738, recall 0.724), причем accuracy и macro-F1 здесь близки друг к другу, что говорит о содержательном, а не вырожденном предсказании. На HuffPost EN рост при 5-shot тоже сбалансирован по метрикам (0.251 / 0.230). А вот на HuffPost KAZ 5-shot вновь проявляется знакомый паттерн расхождения: accuracy 0.339 при macro-F1 всего 0.044, судя по всему, еще один случай смещения предсказаний в сторону одного-двух частых классов, хотя и не такой полный, как у XLM-RoBERTa (иначе macro-F1 был бы еще ниже).

Ограничения

Отметим методологические ограничения приведенных результатов. Во-первых, каждое значение в таблицах 4–6 получено за один запуск с фиксированным seed = 42, а не усреднением по нескольким случайным обучающим подвыборкам; при таком объеме обучающих данных (1–5 примеров на класс) результат может существенно меняться в зависимости от кон-

кретно отобранных примеров, что и наблюдается местами в виде немонотонной зависимости качества от числа shot'ов или числа слоев. Во-вторых, для Word2Vec использована собственная реализация (усредненный вектор + полносвязный классификатор по описанию в тексте статьи), а не оригинальный код, отдельного скрипта для Word2Vec в рабочих материалах не обнаружено. В-третьих, для XLM-RoBERTa-base использованы гиперпараметры по аналогии с BERT (10 эпох, batch size = 8, learning rate = 2e-5), поскольку оригинальный код обучения этой модели не найден, и это приближение, а не воспроизведение исходной настройки. К тому же близкие результаты (например, между 1-layer BiLSTM () и XLM-RoBERTa-base () в режиме 5-shot) находятся в пределах погрешности и требуют дальнейшей валидации.

Заключение

В целом результаты в данном эксперименте показывают следующие связанные выводы. Во-первых, ни одна модель не доминирует одновременно на всех датасетах и режимах: mT5-Seq2Seq лучший на KazNews при 5-shot, BERT в целом конкурентоспособен при 5-shot на датасете с длинными текстами, Word2Vec неожиданно силен на длинных текстах уже при 1-shot и при 5-shot на всех датасетах. Во-вторых, глубина архитектуры (число слоев BiLSTM, переход от BERT к более крупным моделям) не гарантирует улучшения в условиях экстремального few-shot: результат определяется в первую очередь конкретной случайной обучающей подвыборкой. В-третьих, именно случаи наибольшего расхождения между Accuracy и macro-F1 (XLM-RoBERTa на HuffPost при 1-shot, mT5 на HuffPost KAZ при 5-shot) являются самыми показательными: здесь accuracy в одиночку создала бы ложное впечатление приемлемого качества модели, тогда как совокупность метрик в таблицах 4–6 обнажает фактическое вырождение классификатора в константный предиктор мажоритарного класса. Также стоит отметить схожие результаты точности моделей на параллельных датасетах HuffPost.

ЛИТЕРАТУРА

1 Pakray, P., Gelbukh, A., & Bandyopadhyay, S. (2025). Natural language processing applications for low-resource languages. Natural Language Processing, 31(2), 183–197. https://doi.org/10.1017/nlp.2024.33

2 Kowsari, K., Jafari Meimandi, K., Heidarysafa, M., Mendu, S., Barnes, L., & Brown, D. (2019). Text classification algorithms: A survey. Information, 10(4), 150. https://doi.org/10.3390/info10040150

3 McCallum, A., & Nigam, K. (1998). A comparison of event models for naive Bayes text classification. AAAI-98 Workshop on Learning for Text Categorization. https://aaai.org/papers/041-ws98-05-007/

4 Joachims, T. (1998). Text categorization with support vector machines: Learning with many relevant features. In C. Nédellec & C. Rouveirol (Eds.), Machine Learning: ECML-98 (pp. 137–142). Springer. https://doi.org/10.1007/BFb0026683

5 Cox, D. R. (1958). The regression analysis of binary sequences. Journal of the Royal Statistical Society: Series B (Methodological), 20(2), 215–242.

6 Salton, G., Wong, A., & Yang, C.S. (1975). A vector space model for automatic indexing. Communications of the ACM, 18(11), 613–620. https://doi.org/10.1145/361219.361220

7 Spärck Jones, K. (2004). A statistical interpretation of term specificity in retrieval. Journal of Documentation, 60(5), 493–502. https://doi.org/10.1108/00220410410560573

8 Hochreiter, S., & Schmidhuber, J. (1997). Long short-term memory. Neural Computation, 9(8), 1735–1780. https://doi.org/10.1162/neco.1997.9.8.1735

9 Graves, A., & Schmidhuber, J. (2005). Framewise phoneme classification with bidirectional LSTM and other neural network architectures. Neural Networks, 18(5), 602–610. https://doi.org/10.1016/j.neunet.2005.06.042

10 Joulin, A., Grave, E., Bojanowski, P., & Mikolov, T. (2016). Bag of tricks for efficient text classification. arXiv. https://doi.org/10.48550/arXiv.1607.01759

11 Mikolov, T., Chen, K., Corrado, G., & Dean, J. (2013). Efficient estimation of word representations in vector space. arXiv. https://doi.org/10.48550/arXiv.1301.3781

12 Devlin, J., Chang, M.-W., Lee, K., & Toutanova, K. (2019). BERT: Pre-training of deep bidirectional transformers for language understanding. In Proceedings of the 2019 Conference of the North American Chapter of the Association for Computational Linguistics: Human Language Technologies (Vol. 1, pp. 4171–4186). Association for Computational Linguistics. https://doi.org/10.18653/v1/N19-1423

13 Conneau, A., Khandelwal, K., Goyal, N., Chaudhary, V., Wenzek, G., Guzmán, F., ... & Zettlemoyer, L. (2019). Unsupervised cross-lingual representation learning at scale. arXiv. https://arxiv.org/abs/1911.02116

14 Xue, L., Constant, N., Roberts, A., Kale, K., Al-Rfou, R., Siddhant, A., ... & Raffel, C. (2021). mT5: A massively multilingual pre-trained text-to-text transformer. In Proceedings of the 2021 Conference of the North American Chapter of the Association for Computational Linguistics: Human Language Technologies (pp. 483–498). https://doi.org/10.18653/v1/2021.naacl-main.41

15 Latief, A. D., Jarin, A., Yuyun, Hidayati, N. N., Afra, D. I. N., & Riza, H. (2025). A systematic review of few-shot and zero-shot learning for NLP in low-resource languages: Insights and challenges. IEEE Xplore. https://ieeexplore.ieee.org/abstract/document/11325582

16 Latief, A. D., Jarin, A., Yuyun, Hidayati, N. N., Afra, D. I. N., & Riza, H. (2025). A systematic review of few-shot and zero-shot learning for NLP in low-resource languages: Insights and challenges. In 2025 International Conference on Computer, Control, Informatics and its Applications (IC3INA) (pp. 358–363). IEEE. https://doi.org/10.1109/IC3INA68387.2025.11325582

17 Toleu, A., Tolegen, G., & Ualiyeva, I. (2025). Fine-Tuning Large Language Models for Kazakh Text Simplification. Applied Sciences, 15(15), 8344. https://doi.org/10.3390/app15158344

[1]Марламбеков Д.,
докторант, ORCID ID: 0009-0005-3266-2126,
e-mail: dmarlambekov@gmail.com
[1]Ахметова Ә.,
докторант, ORCID ID: 0000-0002-7718-6478,
e-mail: baltabekova1994@gmail.com
[1]Төрекул С.,
докторант, ORCID ID: 0009-0003-8161-533X,
e-mail: saule.torekul@gmail.com
[1]*Уалиева И.М.,
ф.-м.-ғ.к, , қауымдастырылған профессор, ORCID ID: 0000-0003-3853-8896,
*e-mail: i.ualiyeva@gmail.com

[1]Әл-Фараби атындағы Қазақ ұлттық университеті, Алматы қ., Қазақстан

ШЕКТЕУЛІ ТАҢБАЛАУ ЖАҒДАЙЫНДА ҚАЗАҚ ЖАҢАЛЫҚ МӘТІНДЕРІН ЖІКТЕУГЕ АРНАЛҒАН ТЕРЕҢ ОҚЫТУ МОДЕЛЬДЕРІНІҢ САЛЫСТЫРМАЛЫ ТАЛДАУЫ

Аңдатпа

Терең оқыту әдістерінің қарқынды дамуы мен трансформерлік архитектуралардың пайда болуы табиғи тілді өңдеу саласын түбегейлі өзгертті, дегенмен бұл жетістіктер бірқалыпты таралмаған. Ағылшын және басқа да ресурсы мол тілдер үшін ауқымды бенчмарктер бар болғанымен, қазақ тілі сияқты ресурсы аз тілдер үшін мәтіндерді сапалы классификациялау мәселесі әлі де өзекті мәселе болып отыр. Авторлар шектеулі белгілеу жағдайында қазақша жаңалықтар мәтіндерін few-shot классификациялау тапсырмасы үшін классикалық Word2Vec эмбеддингіне, BiLSTM рекурренттік моделдеріне, BERT және XLM-R трансформерлеріне, генеративті mT5 моделіне, сондай-ақ классикалық және статистикалық бейзлайндарға салыстырмалы анализ жүргізді. Эксперименттер tengrinews.kz, inform.kz мақалаларынан және HuffPost параллель корпустарынан жиналған, few-shot классификациялауға арналған KazNews датасетінде орындалды. Датасеттер бес категорияны қамтиды (спорт, саясат, бизнес, саяхат т.б.).1-shot және 5-shot режимдеріндегі эксперименттер бірде-бір модельдің барлық датасеттер мен режимдерде бірдей үстемдік етпейтінін көрсетті: Word2Vec 5-shot режимінде HuffPost корпусындағы датасеттерде ең жоғары нәтиже көрсетті (0.48 және 0.53); mT5-Seq2Seq 5-shot режимінде KazNews датасетінде үздік нәтижеге қол жеткізді (0.71); ал BERT ұзын

мәтіндерден тұратын KazNews датасетінде 5-shot режимінде жалпы бәсекеге қабілетті болды. Авторлар сонымен қатар 5-shot режимінде mT5-Seq2Seq моделі үшін сапаның кенет артуын анықтады. 1-shot режимі үшін моделдердің ешқайсысы қанағаттанарлық сапа нәтижесін көрсете алмады.

Түйін сөздер: few-shot learning, мәтіндерді жіктеу, қазақ тілі, ресурсы шектеулі тілдер, трансформер модельдері, BERT, XLM-R, BiLSTM, Word2Vec, терең оқыту, табиғи тілдерді өңдеу.

[1]Marlambekov D.,
PhD-student, ORCID ID: 0009-0005-3266-2126,
e-mail: dmarlambekov@gmail.com
[1]Akhmetova A.,
PhD-student, ORCID ID: 0000-0002-7718-6478,
e-mail:baltabekova1994@gmail.com
[1]Torekul S.,
PhD-student, ORCID ID: 0009-0003-8161-533X,
e-mail: saule.torekul@gmail.com
[1]*Ualiyeva I.M.,
Cand. Phys.-Math. Sc., Associate Professor, ORCID ID: 0000-0003-3853-8896,
*e-mail: i.ualiyeva@gmail.com

[1]Al-Farabi Kazakh National University, Almaty, Kazakhstan

BENCHMARKING DEEP LEARNING MODELS FOR FEW-SHOT CLASSIFICATION OF KAZAKH NEWS TEXTS UNDER LIMITED ANNOTATION

Abstract

Deep learning methods and transformer architectures have fundamentally reshaped the field of natural language processing; however, these advancements remain unevenly distributed. While high-resource languages like English benefit from large-scale benchmarks, robust text classification for low-resource languages, such as Kazakh, continues to pose a significant challenge. This paper presents a comparative analysis of the classical Word2Vec embedding, BiLSTM recurrent models, BERT and XLM-R transformers, the generative mT5 model, alongside classical and statistical baselines for few-shot Kazakh news text classification under limited annotation constraints. Experiments were conducted on the KazNews dataset, curated for few-shot classification from tengrinews.kz and inform.kz articles, as well as parallel HuffPost corpora. The datasets comprise five categories (sports, politics, business, travel, etc.). The experimental findings in 1-shot and 5-shot settings demonstrate that no single model consistently dominates across all datasets and regimes: Word2Vec achieved the best performance on the HuffPost corpora in the 5-shot regime (0.48 and 0.53); mT5-Seq2Seq outperformed others on KazNews under 5-shot (0.71); while BERT remained competitive on the long-text KazNews dataset in the 5-shot setup. The authors also observed a sharp performance gain for the mT5-Seq2Seq model in the 5-shot setup. Conversely, none of the evaluated models yielded acceptable quality metrics in the 1-shot regime.

Keywords: few-shot learning, text classification, Kazakh language, low-resource languages, transformer models, BERT, XLM-R, BiLSTM, Word2Vec, deep learning, natural language processing.

Received July 15, 2026; revised August 7, September 3, 2026; accepted September 8, 2026.

UDC 004.85
IRSTI 06.81.29

https://doi.org/10.55452/1998-6688-2026-23-3-347-361

[1]***Norliza Katuk,**
PhD, ORCID ID: 0000-0001-8805-2574,
*e-mail: k.norliza@uum.edu.my
[1]**Hikmah Nurdin,**
B. Comp. Science, ORCID ID: 0009-0001-3766-5482
e-mail: hikmahnurdin750@gmail.com
[2]**M. Ali Fauzi,**
PhD., ORCID ID: 0000-0002-9696-2807
e-mail: moch.ali.fauzi@ub.ac.id
[3]**Mhd. Furqan**
PhD., ORCID ID: 0000-0002-7255-4454
e-mail: mfurqan@uinsu.ac.id

[1]School of Computing, Universiti Utara Malaysia, Malaysia
[2]Faculty of Computer Science, Universitas Brawijaya, Indonesia
[3]Faculty of Science and Technology, Universitas Islam Negeri Sumatera, Indonesia

AQRACE: MACHINE-LEARNING-BASED DETECTION OF MALICIOUS URLS IN QR CODES FOR REAL-TIME SECURITY ASSESSMENT

Abstract

The widespread use of Quick Response (QR) codes has increased exposure to QR-based phishing, malicious redirection, and malware distribution because users cannot readily inspect the destination before scanning. This study develops aQRace, a machine-learning-based QR code security application that analyses embedded Universal Resource Locators (URLs) before users access their destinations. The study combines URL-based feature extraction, comparative machine-learning evaluation, and operational system integration. URL characteristics covering structural, linguistic, technical, and advanced properties were extracted for classification. Four supervised machine-learning algorithms–XGBoost, Random Forest, Decision Tree, and Logistic Regression–were trained and evaluated using a balanced dataset of 14,000 URLs comprising 7,000 safe and 7,000 malicious samples. Model performance was compared using accuracy, precision, recall, and F1-score. XGBoost achieved the highest accuracy of 84% and precision of 0.80, whereas Random Forest achieved the highest recall of 0.95. Both models achieved an F1 Score of 0.84. XGBoost was selected for deployment based on its overall performance profile and integrated into a client-server application comprising a Flutter mobile frontend and Flask cloud backend. The application supports QR code image uploads and camera-based scanning, and performs URL processing, feature extraction, classification, and user warnings before destination access. Functional testing with representative safe and malicious QR codes confirmed the operation of the complete detection workflow. The findings demonstrate that conventional machine learning using URL-based features can support pre-access QR code security assessment while providing an operational alternative to increasingly complex deep learning approaches.

Keywords: QR code security, quishing, malicious URL detection, machine learning, XGBoost, phishing detection, cybersecurity

Received: September 3, 2026; accepted: September 10, 2026.

Introduction

Quick Response (QR) codes provide a convenient mechanism for connecting physical and printed materials to digital content. Their ease of use and compatibility with mobile devices have

encouraged adoption in digital payments, marketing, authentication, information sharing, and other online services. This convenience also introduces security risks because the destination encoded within a QR code is not readily visible to users [1]. Attackers can exploit this characteristic by distributing malicious QR codes or replacing legitimate codes with fraudulent ones that redirect users to phishing websites or harmful content [2]. The use of QR codes in phishing is commonly known as "quishing" [3]. In a quishing attack, a malicious Uniform Resource Locator (URL) is encoded within a QR code and presented as legitimate content. Once scanned, the code may redirect users to a fraudulent login page, phishing website, malware source, or another malicious destination [4]. Unlike conventional phishing messages, in which a suspicious URL can be inspected before opening, a QR code hides the destination in its encoded image. Users consequently have less information available when deciding whether a code is safe to scan. The security problem, therefore, extends beyond QR code decoding. A conventional scanner can retrieve an embedded URL, but successful decoding does not establish whether the destination is legitimate. Without security assessment before access, users may proceed to a malicious destination before the risk is identified. This limitation is particularly relevant in environments where QR codes are scanned rapidly, and users have little opportunity to inspect decoded addresses. A secure scanning mechanism should therefore analyse the embedded URL before access to the destination and provide an immediate warning when malicious characteristics are detected.

Machine learning offers one approach to this problem because safe and malicious URLs may exhibit different structural, lexical, and technical characteristics. Al-Zahrani et al. [5] examined malicious QR code detection using lexical characteristics extracted from embedded URLs. Five machine-learning classifiers were evaluated using a balanced dataset of 50,000 safe and 50,000 malicious URLs. Their findings demonstrated that URL characteristics can support malicious-URL classification. The evaluation, however, was primarily dataset-based and did not demonstrate the operational performance of the resulting classifier in a deployed QR code scanning process. Sarkhi and Mishra [6] extended URL-based detection towards a lightweight mobile-oriented approach incorporating URL feature extraction, risk scoring, and Decision Tree classification. Lexical and host-based characteristics allowed the system to operate with relatively low computational requirements. Although such an approach is suitable for resource-constrained applications, reliance on a single classifier may restrict the representation of complex relationships among URL characteristics. The effectiveness of URL-based detection may therefore depend not only on the extracted features but also on the classification algorithm used to learn from them.

Comparative machine-learning studies further demonstrate the importance of classifier selection. Herlina and Soeparno [7] evaluated Random Forest, Support Vector Machine, Logistic Regression, Naive Bayes, k-Nearest Neighbours, and XGBoost for detecting phishing URLs associated with QR codes. XGBoost achieved the highest reported accuracy of 92%. The result supports the potential of ensemble learning for identifying patterns associated with phishing URLs. Their evaluation, however, remained at the dataset level, without examining how the classifier would operate once integrated into a QR code scanning application. Other research has focused more directly on operational detection. Vaithilingam and Shankar [4] examined QR-related threats, including quishing, QRLjacking, and malware distribution, and considered artificial intelligence and machine learning for providing early security warnings. Pawar et al. [8], similarly proposed an AI-based QR code scanner intended to detect and block malicious links in real time. These studies highlight the importance of moving security assessment closer to the point at which users interact with QR codes. More broadly, contemporary classification research has increasingly moved from conventional machine-learning models towards architectures capable of learning richer representations from multiple sources of information. Attention mechanisms and multimodal fusion are particularly useful when a classification decision depends on complementary data modalities. For example, Furqan et al. [9], developed an attention-based Vision Transformer for multiclass skin lesion classification that integrates dermoscopic images with structured clinical metadata via a mutual attention fusion mechanism. The model achieved 93.4% accuracy, an F1-score of 92.2%, and an AUC of 0.95, illustrating the potential of combining heterogeneous representations within a unified classification framework. A similar progression

towards richer feature representations is evident in QR code security. Alsulami et al. [10] proposed a malicious QR code detection system that combines AlexNet-based feature extraction, principal component analysis (PCA), and recurrent neural networks. Their GRU configuration achieved accuracies of 99.81% and 99.59% on two datasets, with an average computation time of 7.433 ms per sample. A real-time prototype was also developed, demonstrating the feasibility of deploying the model in an operational environment.

Tian and Zhu [11] further advanced QR code phishing detection by combining QR code decoding, multimodal deep learning, and incremental learning. Their approach transforms decoded QR content into a URL-semantic classification problem and employs BERT, Convolutional Neural Network (CNN), and BiLSTM components to capture local and global URL patterns. Incremental learning enables the model to adapt to emerging phishing samples without repeatedly retraining the complete architecture. The progression from lexical analysis to deep and multimodal learning demonstrates increasing sophistication in QR code threat detection. It also introduces greater complexity in modelling and implementation. Conventional machine-learning approaches therefore remain relevant where direct URL analysis and straightforward integration into an operational scanning workflow are priorities. Two related issues motivate the present study. First, classification performance depends on the feature representation, dataset, and learning algorithm employed. Comparison using a common dataset and feature representation is necessary to assess how different classifiers perform in terms of accuracy, precision, recall, and F1-score. This is important in security classification because the consequences of false positives and false negatives differ. A false negative may expose a user to a malicious destination, whereas a false positive may unnecessarily restrict access to a legitimate URL. Second, predictive performance on an offline dataset does not, by itself, demonstrate the operational feasibility of a QR code security mechanism. Deployment requires QR acquisition, decoding, URL preprocessing, feature extraction, classification, presentation of the security result, and restriction of destination access when a threat is identified. There remains practical value in determining whether conventional machine-learning classifiers operating on URL characteristics can support this complete workflow without relying on a more elaborate deep-learning architecture.

To address these issues, this study develops aQRace, a machine-learning-based QR code security application that analyses embedded URLs before users access their destinations. URLs are characterised by structural, linguistic, technical, and advanced features. Four supervised machine learning algorithms—XGBoost, Random Forest, Decision Tree, and Logistic Regression–are evaluated on the same balanced dataset and feature representation. The selected classifier is subsequently integrated into a client-server QR code scanning application that supports both static image uploads and camera-based scanning.

The study addresses the following research questions:

RQ1: What URL-based features can be extracted to support the machine-learning classification of safe and malicious URLs embedded in QR codes?

RQ2: Which machine-learning algorithm provides the most effective performance for classifying QR code-embedded URLs as safe or malicious?

RQ3: How can the selected machine-learning classifier be integrated into a real-time QR code scanning system for detecting malicious URLs and providing security warnings to users?

Accordingly, the objectives of the study are: (1) to extract structural, linguistic, technical, and advanced URL features for the classification of safe and malicious URLs embedded in QR codes; (2) to evaluate and compare XGBoost, Random Forest, Decision Tree, and Logistic Regression using accuracy, precision, recall, and F1-score; and (3) to integrate the selected classifier into a QR code scanning application and evaluate its functional operation using safe and malicious QR code samples. The contribution of this study lies in linking comparative machine-learning evaluation to operational QR code security. Rather than treating malicious URL classification as an isolated prediction task, aQRace incorporates URL processing, feature extraction, classification, and user warnings into the QR code scanning workflow. The objective is not to outperform computationally sophisticated deep learning architectures solely on predictive accuracy, but to examine the performance and practical integration of conventional machine learning with a compact URL-based representation.

Table 1 – Comparison of related studies on malicious QR code and URL detection

Study	Detection approach	Data/features	Main contribution	Limitation relevant to the present study
Al-Zahrani et al. [5]	ML classification of QR code URLs	50,000 safe and 50,000 malicious URLs; lexical features	Demonstrated malicious-URL classification using URL characteristics	Primarily offline dataset evaluation
Pawar et al. [8]	AI-based QR code scanner	Benign and malicious QR code data	Real-time detection and warning of malicious links	Limited reporting of classification and deployment performance
Herlina and Soeparno [7]	Comparative ML classification	6,000 phishing and 6,000 legitimate URLs	Compared six classifiers; XGBoost achieved 92% accuracy	Dataset-level evaluation without operational deployment
Sarkhi and Mishra [6]	Lightweight URL analysis and Decision Tree	Lexical and host-based URL features	Mobile-oriented detection with low computational requirements	Reliance on a single classifier and predefined features
Vaithilingam and Shankar [4]	AI/ML analysis of QR-related threats	Quishing, QRLjacking, and malware scenarios	Emphasised proactive detection and user warning	Limited comparative classifier evaluation
Alsulami et al. [10]	AlexNet, PCA, and recurrent neural networks	Image-derived QR code features	GRU achieved 99.81% and 99.59% accuracy; real-time prototype	More complex image-based deep-learning pipeline
Tian and Zhu [11]	QR decoding, multimodal deep learning, and incremental learning	URL semantic and structural representations	Combines BERT, CNN, and BiLSTM with incremental adaptation	Greater modelling and training complexity
Present study (aQRace)	Comparative URL-based ML integrated with QR scanning	Balanced safe/ malicious URL dataset; structural, linguistic, technical, and advanced features	Compares four classifiers under the same representation and deploys the selected model	Functional deployment evaluation limited to representative QR code samples

Materials and methods

The study adopted a system development and experimental evaluation approach comprising four stages: dataset preparation, URL feature extraction, machine-learning model development and evaluation, and system implementation and functional testing. The first three stages established the malicious-URL classification mechanism, while the final stage integrated the selected classifier into the aQRace application. The detection process begins when a QR code is submitted as an image or captured using a device camera. The QR code is decoded to retrieve the embedded URL. The URL is then normalised and processed before the required features are extracted. These features are passed to the trained classifier, which assigns the URL to either the safe or malicious class. The result is subsequently returned to the application. A malicious classification generates a security warning and restricts direct access to the detected destination. The original dataset contained URLs labelled as benign, phishing, malware, and defacement. For binary classification, benign URLs were assigned to the safe class, whereas phishing, malware, and defacement URLs were consolidated into the malicious class. URL preprocessing was performed to improve consistency before feature extraction. A URL scheme was added when absent, with HTTP as the default. Hostnames were converted to lowercase, leading www. prefixes were removed, fragments and trailing slashes were eliminated, per cent-encoded characters were decoded, and duplicate records were removed. Query parameters and

path structures were retained because they may contain structural and lexical information relevant to malicious-URL detection. Preliminary experiments used more than 300,000 pre-processed URLs. Although high classification accuracy was initially achieved, subsequent QR code testing showed a tendency towards malicious classifications, suggesting poor generalisation under the intended deployment conditions. Different dataset sizes and class distributions were therefore examined. A balanced dataset of 14,000 URLs was selected for final model development, comprising 7,000 safe and 7,000 malicious URLs. A fixed random seed was applied during sampling to support reproducibility. Although this configuration produced slightly lower accuracy than the preliminary large-scale experiments, it resulted in more stable classification behaviour during subsequent system testing.

Each pre-processed URL was transformed into a numerical feature vector. The feature extraction procedure used four categories of characteristics: structural features, linguistic features, technical identifiers, and advanced metrics. Structural features describe the composition of the URL and include URL length, domain length, path length, and number of subdomains. These variables provide information about the structural complexity of the destination. Linguistic characteristics capture character-level and lexical properties of the URL. They include the number of digits, number of special characters, and presence of suspicious keywords. These features indicate unusual lexical patterns that may occur in malicious addresses. Technical identifiers include using an IP address as the hostname, the presence of HTTPS, and the use of homoglyph characters. Homoglyphs are visually similar characters that can be used to imitate legitimate domain names. Advanced metrics incorporate Shannon entropy and domain frequency analysis. Shannon entropy measures randomness in the URL string and may indicate obfuscated or automatically generated addresses, while domain frequency provides additional information about the occurrence of hostnames.

Table 2 – URL features used for QR code URL classification

Feature category	Extracted characteristics
Structural	URL length; domain length; path length; number of subdomains; top-level domain length
Linguistic	Number of digits; number of special characters; presence of suspicious keywords
Technical identifiers	IP-based hostname; HTTPS; homoglyph characters
Advanced metrics	Shannon entropy; domain frequency analysis

The same feature representation was supplied to all four classifiers so that differences in performance could be attributed to the learning algorithms rather than differences in input representation. Four supervised machine-learning algorithms were evaluated: XGBoost, Random Forest, Decision Tree, and Logistic Regression. These algorithms represent ensemble tree-based learning, single-tree classification, and linear classification strategies. The balanced dataset was divided into training and testing subsets at an 80:20 ratio using stratified sampling to preserve class balance. All models were trained using the same URL feature representation. A probability threshold of 0.45 was applied to probabilistic classification. Performance was evaluated using accuracy, precision, recall, and F1-score. Accuracy measures the proportion of all instances classified correctly. Precision measures the proportion of predicted malicious instances that are actually malicious. Recall represents the proportion of malicious instances correctly identified, while F1-score provides the harmonic mean of precision and recall. Multiple measures were considered because accuracy alone does not fully characterise a security classifier. High recall reduces the number of malicious URLs the system misses, whereas high precision reduces unnecessary warnings for legitimate destinations.

aQRace was implemented using a client-server architecture comprising a Flutter mobile frontend and a cloud-based Flask backend. The frontend was developed using Flutter and Dart and supports two QR code input mechanisms: uploading a static PNG or JPG image and scanning a QR code with the device camera. Communication with the backend is performed through RESTful HTTP requests. The backend was implemented in Python using Flask and deployed on the Render platform. It manages QR code decoding, URL processing, feature extraction, and machine-learning classification. QR codes

are decoded using Pyzbar together with the Python Imaging Library. The decoded URL subsequently undergoes normalisation, short-link expansion via HTTP redirection, and checks against a predefined list of trusted domains. These procedures provide additional rule-based processing around the machine-learning component. URLs requiring further analysis are transformed into the required feature representation and passed to the trained XGBoost classifier. Scikit-learn and XGBoost were used for model development, while Joblib was used to store and load the trained model during runtime. When a URL is classified as malicious, the backend returns a warning response to the Flutter application, which restricts direct access to the destination. Cross-Origin Resource Sharing was enabled using Flask-CORS to support communication between system components. Development followed an iterative Agile process. The frontend and backend were initially tested in a local environment before the completed backend was deployed to the cloud environment.

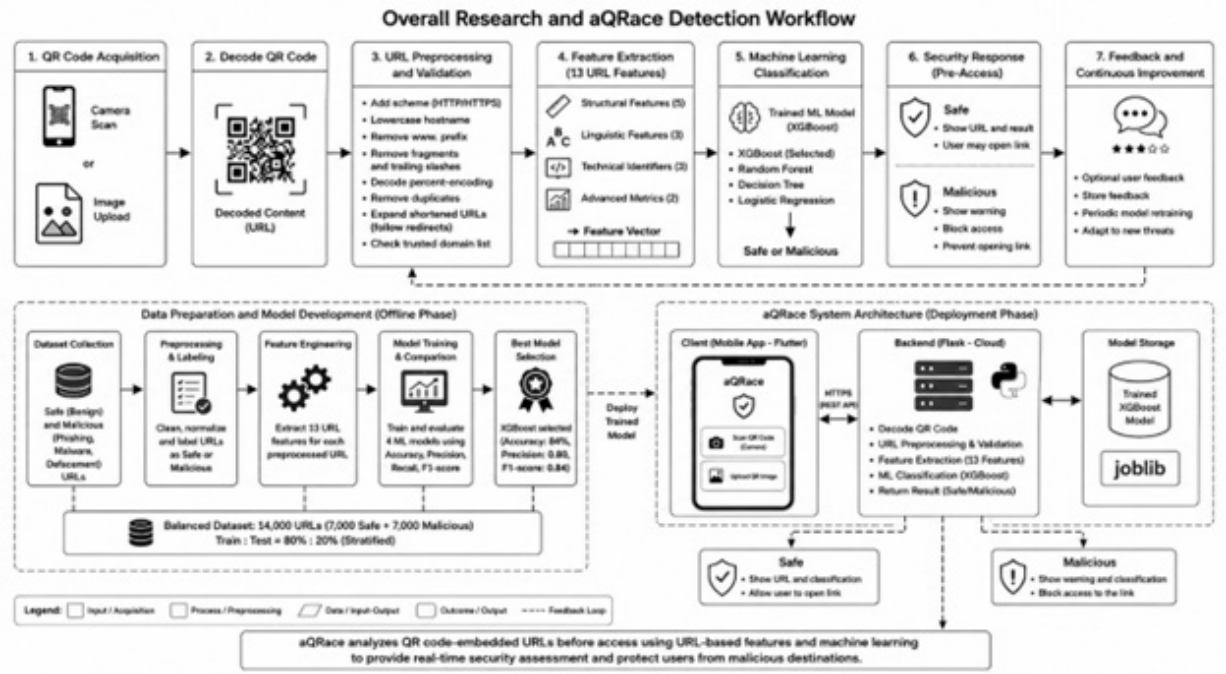


Figure 1 – Overall research and aQRace detection workflow

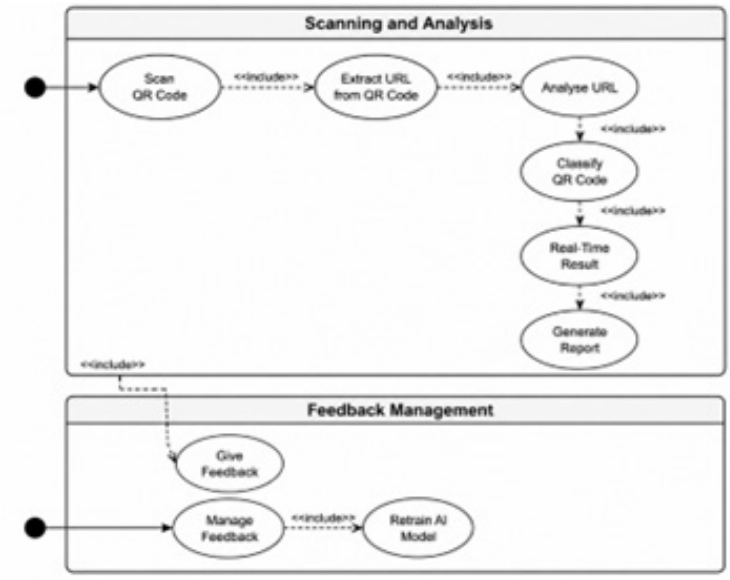


Figure 2 – Use case diagram of the aQRace system

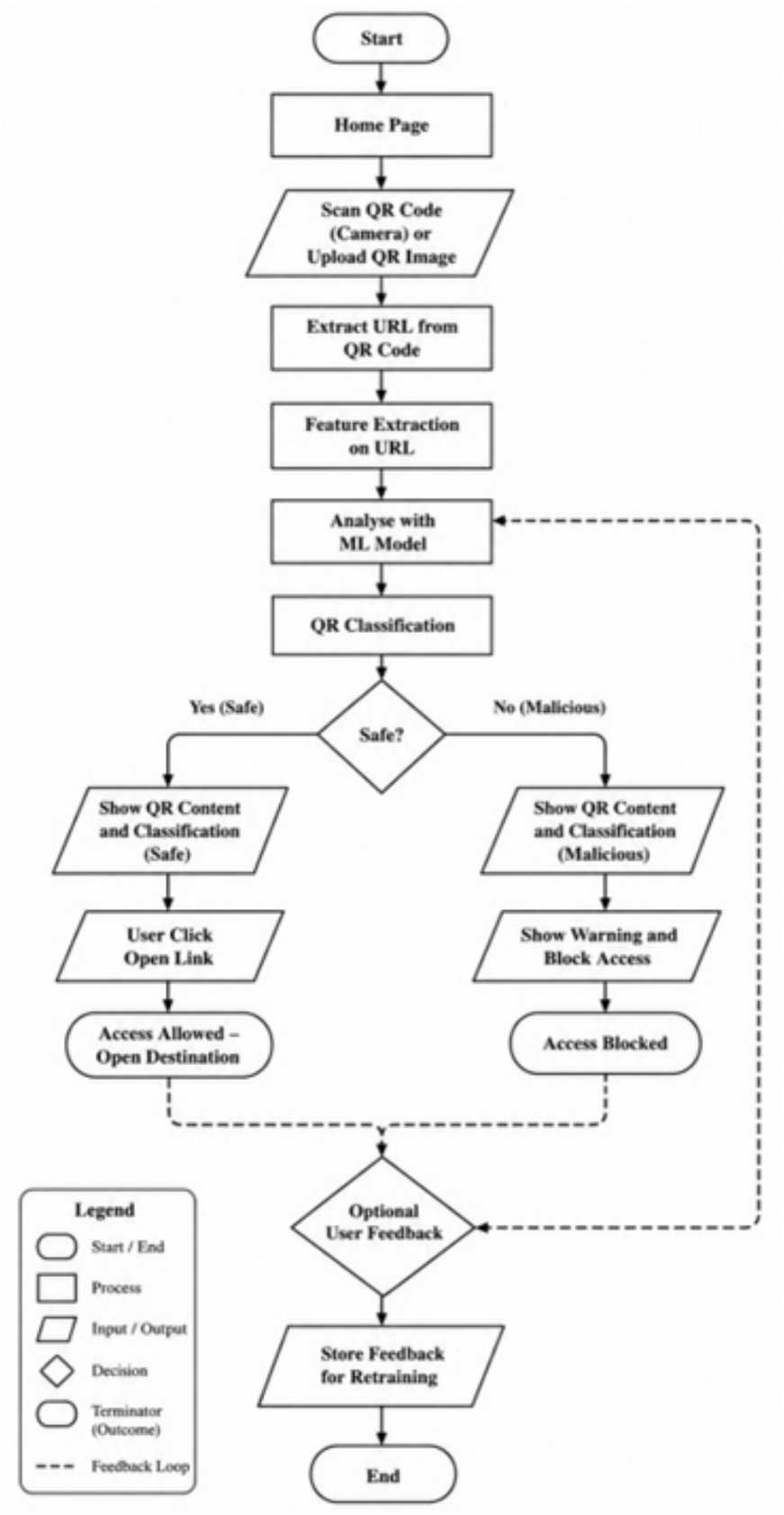


Figure 3 – Operational flow of the aQRace QR code security and malicious URL detection system

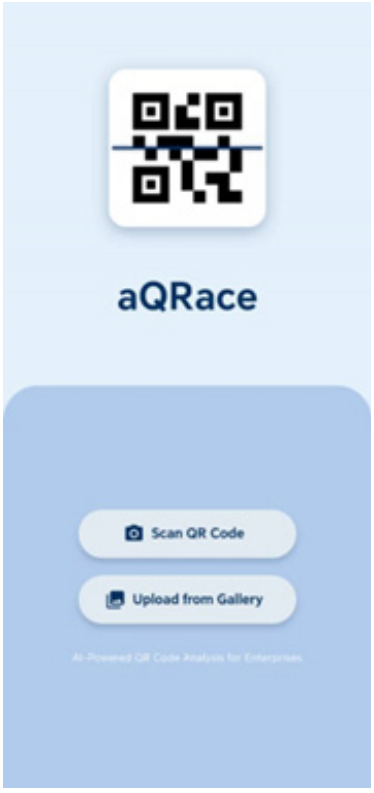


Figure 4 – Home interface showing QR code input options



Figure 5 – Camera-based QR code scanning and classification interface

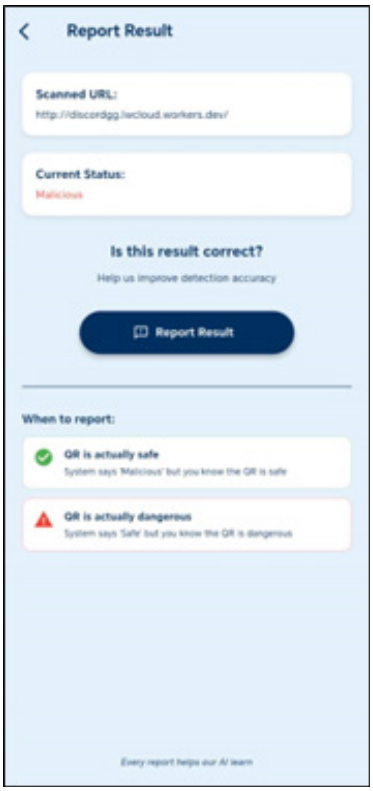


Figure 6 – Malicious URL warning and access restriction

Functional testing was conducted after deployment to determine whether the integrated application could complete the detection workflow using QR codes from both classes. Six representative QR codes were selected, comprising three safe and three malicious samples. The safe examples represented the Federal Reserve, Expedia, and MyFitnessPal domains, while the malicious examples were drawn from malicious samples used during system evaluation. Each sample passed through QR acquisition, decoding, URL processing, feature extraction, classification, and presentation of the security result. QR codes were tested through the supported input mechanisms, including image upload and camera-based scanning. The predicted class was then compared with the known class of each sample. This procedure was intended as functional deployment testing rather than an independent measurement of classification accuracy. Quantitative model performance was evaluated separately using the test dataset mentioned above.

Results

The four classifiers produced different performance profiles across the evaluation measures. Table 3 presents the results obtained from the test dataset.

Table 3 – Classification performance of the machine-learning models

Model	Accuracy (%)	Precision	Recall	F1-score
XGBoost	84	0.80	0.89	0.84
Random Forest	81	0.75	0.95	0.84
Decision Tree	79	0.73	0.92	0.82
Logistic Regression	71	0.65	0.93	0.76

XGBoost achieved the highest classification accuracy at 84%, followed by Random Forest at 81%, Decision Tree at 79%, and Logistic Regression at 71%. XGBoost also achieved the highest precision, 0.80, indicating it produced the highest proportion of correct malicious classifications among instances predicted as malicious. The ranking differed for recall. Random Forest achieved the highest recall at 0.95, followed by Logistic Regression at 0.93 and Decision Tree at 0.92. XGBoost recorded a recall of 0.89. Random Forest therefore detected the largest proportion of malicious URLs within the test set. XGBoost and Random Forest both achieved the highest F1-score of 0.84. Decision Tree recorded an F1-score of 0.82, while Logistic Regression obtained 0.76. The equal F1-scores of XGBoost and Random Forest resulted from different precision-recall profiles: XGBoost produced higher precision, whereas Random Forest produced higher recall. Considering the four measures jointly, XGBoost provided the strongest overall balance for deployment. It achieved the highest accuracy and precision and shared the highest F1-score with Random Forest. Random Forest was superior when recall alone was considered. The selection of XGBoost was therefore based on its overall performance profile rather than on superiority across all evaluation measures.

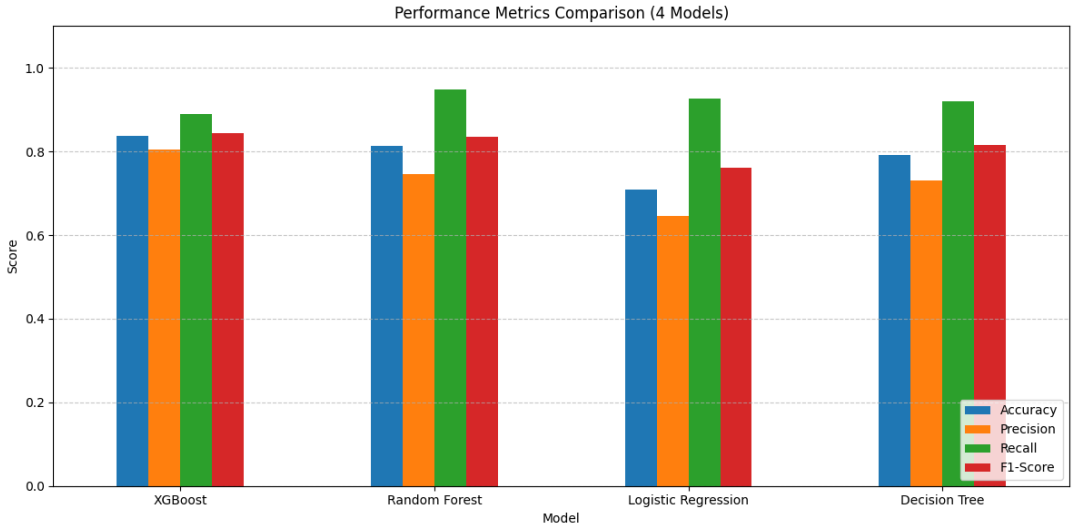


Figure 7 – Comparative performance of XGBoost, Random Forest, Decision Tree, and Logistic Regression

The selected XGBoost classifier was successfully integrated with the Flutter frontend and Flask backend. The deployed application completed the processing sequence from QR code acquisition to URL classification without requiring users to access the decoded destination before security assessment. Both supported input modes were operational. Static QR code images could be uploaded from the device, while the camera interface allowed direct QR code scanning. Following decoding, the URL was submitted to the backend, processed, transformed into the required feature representation, and classified. When the backend returned a malicious classification, the application displayed a security warning and restricted direct access to the detected URL. The classifier therefore operated within the QR code interaction rather than as an independent machine-learning component. The implementation demonstrates that QR acquisition, decoding, URL processing, feature extraction, classification, and user notification can operate as a connected workflow within the deployed application. The deployed system was tested using six representative QR codes comprising three safe and three malicious samples. Table 4 presents the known class and the classification returned by aQRace.

Table 4 – Functional testing of representative QR code samples

Sample	Known class	aQRace classification	Outcome
Safe QR 1	Safe	Safe	Correct
Safe QR 2	Safe	Safe	Correct
Safe QR 3	Safe	Safe	Correct
Malicious QR 1	Malicious	Malicious	Correct
Malicious QR 2	Malicious	Malicious	Correct
Malicious QR 3	Malicious	Malicious	Correct

All three safe samples were classified as safe, while the three malicious samples were classified as malicious. The classification outcomes were therefore consistent with the known labels of the six samples. The test also confirmed that the complete processing pipeline operated after cloud deployment. The application acquired and decoded each QR code, processed the resulting URL, generated the required feature representation, obtained a classification from the deployed model, and returned the corresponding result to the user interface. These six cases were used to verify system functionality and should not be interpreted as an independent estimate of classification performance. The quantitative performance of the classifier is represented by the test-set results reported earlier in this section.

Discussion

The findings demonstrate the feasibility of representing QR code destinations using URL-derived characteristics prior to destination access. The feature representation combines structural, linguistic, technical, and advanced information and can be generated after a QR code is decoded, without requiring the destination webpage to be opened. This approach is consistent with previous research showing that lexical and host-based URL characteristics can aid in detecting malicious QR codes. Its practical relevance lies in the placement of classification between QR decoding and destination access. Instead of requiring users to manually verify the legitimacy of an unfamiliar decoded URL, the URL is used as input for an automated security assessment. The present findings should not, however, be interpreted as evidence that every extracted characteristic contributes equally to classification. The experiment evaluates the feature set as a whole and does not measure the independent predictive contribution of individual characteristics. Feature-importance analysis, ablation testing, or explainability techniques would be necessary to establish which characteristics contribute most strongly to classification. The model comparison demonstrates that classifier selection affects the balance between accuracy, precision, and recall. XGBoost achieved the highest accuracy of 84% and precision of 0.80, whereas Random Forest achieved the highest recall of 0.95. Both obtained an F1-score of 0.84.

This distinction is particularly important in cybersecurity. A false negative may expose a user to a malicious destination because the system fails to issue a warning. From this perspective, Random Forest's higher recall is advantageous. Conversely, excessive false-positive warnings may reduce usability and eventually encourage users to disregard security alerts. XGBoost's higher precision provides an advantage in this respect. The equal F1-scores further illustrate this trade-off. XGBoost and Random Forest achieved the same F1 score via different precision-recall profiles. XGBoost was selected for aQRace because it achieved higher accuracy and precision while retaining a recall of 0.89. This result does not establish XGBoost as universally superior. A deployment that places substantially greater cost on missed malicious URLs could reasonably favour Random Forest.The stronger performance of the tree-based models relative to Logistic Regression also suggests that relationships among the extracted characteristics may not be adequately represented through a simple linear decision boundary. XGBoost, Random Forest, and Decision Tree achieved accuracies of 84%, 81%, and 79%, respectively, compared with 71% for Logistic Regression. Tree-based methods can capture non-linear interactions among structural, linguistic, and technical characteristics without explicitly specifying those relationships. The results broadly correspond to those of Herlina and

Soeparno [7], who also identified XGBoost as their highest-accuracy classifier, reporting 92%. The lower 84% accuracy obtained in the present study should not be interpreted as a direct performance deficit, as the studies use different datasets, preprocessing procedures, feature representations, and experimental settings. Classification results obtained under different evaluation conditions cannot be compared as if they represent performance on the same task and data.

Recent deep-learning research reports substantially higher predictive performance. Alsulami et al. [10], for example, achieved accuracies of 99.81% and 99.59% using a GRU-based architecture with AlexNet-derived QR image features reduced via PCA. Their study also demonstrated five-fold cross-validation, an average computation time of 7.433 ms per sample, and a real-time prototype. The two approaches nevertheless represent different design strategies. Alsulami et al. [10] derive high-dimensional representations from QR code images before dimensionality reduction and recurrent classification. aQRace decodes the QR code and performs classification based on the destination URL's characteristics. Direct comparison of the reported accuracy values would therefore be inappropriate. The contribution of aQRace is better understood as a URL-based approach that can be integrated into a pre-access scanning workflow, rather than as an attempt to outperform recent deep-learning architectures solely on predictive accuracy. The implementation results address an important distinction between machine-learning classification and operational QR code security. Dataset evaluation establishes predictive performance, but it does not determine whether a model can function effectively when users encounter a potential threat. In aQRace, classification occurs after QR acquisition and decoding but before destination access. The decoded URL is processed, converted into the required feature representation, classified, and returned to the frontend. When the classification is malicious, the application presents a warning and restricts direct access.

This architecture extends the classifier from an experimental model to a security component in user interaction. The approach is consistent with earlier work emphasising proactive warnings and real-time detection. Model architecture should nevertheless be considered in relation to the application's operational requirements rather than to predictive performance alone. Contemporary AI systems increasingly employ specialised architectures and representations to address the requirements of particular deployment contexts. For example, Fauzi et al. [12] employed a hybrid GCN-LSTM architecture for human-pose-based fall detection in an elderly monitoring system designed around privacy-preserving pose representations. This illustrates how model design can be shaped not only by classification performance but also by the characteristics of the data and operational requirements of the intended system. In QR code security, Tian and Zhu [11] similarly demonstrate a more sophisticated design strategy by formulating QR phishing detection as a URL semantic-classification problem and combining BERT, CNN, and BiLSTM representations with incremental learning. Their approach is designed to adapt to emerging phishing patterns while reducing the need for repeated full retraining. Compared with these architectures, aQRace adopts a more straightforward conventional machine-learning strategy centred on URL characteristics. This simplicity should not be interpreted as evidence of superior computational efficiency because processing time and resource consumption were not experimentally compared. It does, however, demonstrate that pre-access QR security can be implemented without requiring a multimodal or deep-learning architecture.

The aQRace workflow also incorporates rule-based URL processing, including normalisation, shortened-link expansion, and trusted-domain checking, around the machine-learning component. The classifier should therefore be regarded as one component of the deployed security workflow rather than the complete security mechanism. Functional testing confirmed the operation of this integrated process. However, the correct classification of six representative samples should not be described as 100% system accuracy. These samples establish only functional operation; quantitative performance evidence remains the test-set evaluation reported in the Results section. Two practical implications emerge from the findings. First, conventional machine-learning methods remain relevant to QR code security despite advances in deep and multimodal learning. When the principal security concern is the destination encoded in a QR code, URL-based classification enables analysis to focus directly on the content characteristics associated with the potential threat. Second, model selection should reflect the intended security objective. The highest-accuracy model is not automatically the

best classifier for every environment. Random Forest may be preferable when minimising missed malicious URLs is the dominant requirement because it achieved a recall of 0.95. XGBoost offers a different trade-off through higher accuracy and precision. This distinction is important for user-facing security applications. Frequent incorrect warnings may reduce user confidence, whereas undetected malicious destinations undermine the system's protective function. The balance between precision and recall is consequently both a machine-learning consideration and a system-design decision. The broader development of AI classification systems also indicates that increasingly complex models are most useful when their complexity addresses a specific characteristic of the problem. Multimodal fusion, for example, can be advantageous when complementary information is distributed across heterogeneous inputs, as demonstrated by Furqan, Katuk, and Hartama [9]. Likewise, hybrid spatial-temporal architectures can be appropriate when the underlying problem involves relationships across both space and time, as illustrated by Fauzi et al. [12]. The design of aQRace follows the same principle at a different level of complexity: its model and feature representation are centred specifically on characteristics of the decoded URL because the destination constitutes the primary object of security assessment.

Several limitations should be considered when interpreting the findings. First, the final models were developed using a balanced dataset of 14,000 URLs. Equal representation facilitates model comparison, but the proportion of safe and malicious URLs encountered in actual use is unlikely to be equal. Future studies should therefore evaluate the classifiers on independent, naturally imbalanced datasets. Second, the study relies on a predefined set of URL features. The experiment does not determine the independent contribution of each characteristic. Feature-importance analysis, SHAP-based explanations, and ablation experiments could identify the most informative characteristics and determine whether redundant features can be removed. Third, the study compares four conventional machine-learning classifiers but does not experimentally compare them with deep-learning architectures on the same dataset. Recent approaches have reported substantially higher accuracy under their respective experimental conditions. A controlled comparison using identical training and testing data would provide stronger evidence regarding the relative predictive, computational, and deployment characteristics of conventional and deep learning approaches. Fourth, deployment testing involved only six representative QR codes. This confirms system operation but does not constitute large-scale real-world validation. Future testing should include substantially larger collections of previously unseen QR codes, shortened URLs, redirection chains, obfuscated domains, homograph attacks, and QR codes captured under varying environmental conditions.

Finally, response time, resource consumption, network latency, scalability, usability, and warning effectiveness were not experimentally evaluated. These factors are important for a real-time user-facing security application. Future evaluation should therefore extend beyond classification metrics to end-to-end processing time, resource utilisation, user experience, and behavioural responses to security warnings. Future development could also examine ensemble approaches that combine the precision of XGBoost with the recall of Random Forest. Explainable machine learning could be incorporated to make warning decisions more transparent to users and system administrators. Continual model updating and richer semantic representations may further improve adaptation to evolving malicious URLs. More advanced multimodal fusion strategies, similar in principle to those used in attention-based classification systems, could also be investigated by combining URL characteristics with QR-image or contextual information.

Conclusion

This study developed and evaluated aQRace, a machine-learning-based QR code security application designed to analyse embedded URLs before users access their destinations. The research addressed three interrelated aspects of malicious QR code detection: URL feature representation, comparative machine-learning classification, and operational integration of the selected classifier. A URL-based feature representation that encompasses structural, linguistic, technical, and advanced characteristics was used to classify destinations as safe or malicious. Four classifiers were evaluated

using a balanced dataset of 14,000 URLs. XGBoost achieved the highest accuracy of 84% and precision of 0.80, whereas Random Forest achieved the highest recall of 0.95. Both models achieved an F1 Score of 0.84. The results demonstrate that model selection involves a meaningful trade-off between precision and recall rather than a single universally superior performance measure.

XGBoost was selected for deployment based on its overall performance profile and integrated into a client-server architecture comprising a Flutter frontend and Flask backend. The application supports QR code image uploads and camera-based scanning, and performs URL processing, feature extraction, classification, and user notification before access to the destination. Functional testing with representative safe and malicious QR codes confirmed that the complete workflow operated after deployment. The principal contribution of the study therefore extends beyond classifier comparison. It demonstrates how URL-based machine learning can be incorporated directly into the QR code scanning process to provide a pre-access security assessment. The approach offers a conventional machine-learning alternative to increasingly sophisticated image-based and multimodal deep-learning architectures, without claiming superiority over them in predictive accuracy or computational efficiency. The findings should nevertheless be interpreted within the study's limitations. The models were developed using a balanced dataset, the predictive contribution of individual URL features was not examined, and functional deployment testing was limited to six representative QR codes. Larger independent evaluations, feature-importance analysis, real-world testing, performance benchmarking, and controlled comparison with deep-learning approaches are therefore required. Overall, aQRace demonstrates the feasibility of incorporating malicious URL classification into an operational QR code scanning workflow. By placing security analysis between QR code acquisition and destination access, the approach provides a foundation for further development of QR code scanning systems that can warn users before interacting with potentially malicious destinations.

REFERENCES

1 Alsawi, W., Ibrahim, D. M. QR Code-Based Access Control Systems: Architectural Taxonomy, Security Landscape, and Future Research Directions. International Journal of Advanced Computer Science and Applications, 17(4), (2026).

2 Njuguna, D., Ndia, J. Quick Response Code Security Attacks and Countermeasures: A Systematic Literature Review. Journal of Cybersecurity (2579-0072), 7(1), 1 (2025). https://doi.org/10.32604/jcs.2025.059398

3 Trad, F., Chehab, A. Detecting quishing attacks with machine learning techniques through qr code analysis. IFIP International Conference on Artificial Intelligence Applications and Innovations, 194–206 (2026). https://doi.org/10.1007/978-3-032-30805-4_14

4 Vaithilingam, S., Shankar, S. a. M. Enhancing security in QR code technology using AI: Exploration and mitigation strategies. International Journal of Intelligence Science, 14(02), 49–57 (2024). https://doi.org/10.4236/ijis.2024.142003

5 Al-Zahrani, M. S., Wahsheh, H. A., Alsaade, F. W. Secure Real-Time Artificial Intelligence System against Malicious QR Code Links. Security and Communication Networks, 2021(1), 5540670 (2021). https://doi.org/10.1155/2021/5540670

6 Sarkhi, M., Mishra, S. Detection of QR code-based cyberattacks using a lightweight deep learning model. Engineering, Technology & Applied Science Research, 14(4), 15209–15216 (2024). https://www.etasr.com/index.php/ETASR/article/view/7777/3803

7 Herlina, B., Soeparno, H. Machine learning model to improve classification performance in the process of detecting phishing URLs in QR codes. Journal of Theoretical and Applied Information Technology, 101(18), 5755–5765 (2023). http://www.jatit.org/volumes/Vol101No18/27Vol101No18.pdf

8 Pawar, A., Fatnani, C., Sonavane, R., Waghmare, R., Saoji, S. Secure qr code scanner to detect malicious url using machine learning. 2022 2nd Asian Conference on Innovation in Technology (ASIANCON), 1-8 (2022). https://doi.org/10.1109/ASIANCON55314.2022.9908759

9 Furqan, M., Katuk, N., Hartama, D. Multiclass Skin Lesion Classification Algorithm using Attention-Based Vision Transformer with Metadata Fusion. Journal of Applied Data Sciences, 7(1), 203–217 (2026). https://doi.org/10.47738/jads.v7i1.1017

10 Alsulami, A.-A., Al-Haija, Q.-A., Alturki, B., Yafoz, A., Alqahtani, A., Alsini, R., Binyamin, S.-S. Efficient Malicious QR Code Detection System Using an Advanced Deep Learning Approach. Computer Modeling in Engineering & Sciences, 145(1), 1117–1140 (2025). https://doi.org/10.32604/cmes.2025.070745

11 Tian, Y., Zhu, E. Incremental Phishing Defense Method Based on QR Code Decoding and Multimodal Deep Learning. Proceedings of the 2026 5th International Conference on Cryptography, Network Security and Communication Technology, 209–214 (2026). https://doi.org/10.1145/3802927.3802959

12 Fauzi, M. A., Yang, B., Hayati, Y. S., Setiawan, B. D., Sari, I. N., Bayona, J., Katuk, N., Dewi, D. A., Surasak, T. Hybrid GCN-LSTM for Privacy-Preserving Fall Detection in Human Pose-Based Elderly Monitoring Systems. Proceedings of the 14th International Conference on Advances in Information Technology, 1–8 (2026). https://doi.org/10.1145/3816713.3819508

[1]*Норлиза Катук,
PhD, ORCID ID: 0000-0001-8805-2574,
*e-mail: k.norliza@uum.edu.my
[1]Хикма Нурдин,
бакалавр, ORCID ID: 0009-0001-3766-5482,
e-mail: hikmahnurdin750@gmail.com
[2]М. Али Фаузи,
PhD, ORCID ID: 0000-0002-9696-2807,
e-mail: moch.ali.fauzi@ub.ac.id
[3]Мхд. Фурқан,
PhD, ORCID ID: 0000-0002-7255-4454,
e-mail: mfurqan@uinsu.ac.id
[1]Есептеу техникасы мектебі,
Солтүстік Малайзия университеті, Малайзия
[2]Компьютерлік ғылымдар факультеті,
Бравиджая университеті, Индонезия
[3]Ғылым және технология факультеті,
Солтүстік Суматра мемлекеттік ислам университеті, Индонезия

AQRACE: QR-КОДТАРДАҒЫ ЗИЯНДЫ URL-МЕКЕНЖАЙЛАРДЫ НАҚТЫ УАҚЫТ РЕЖИМІНДЕ ҚАУІПСІЗДІКТІ БАҒАЛАУ ҮШІН МАШИНАЛЫҚ ОҚЫТУ НЕГІЗІНДЕ АНЫҚТАУ

Аңдатпа

Жылдам жауап беру (Quick Response, QR) кодтарының кеңінен қолданылуы QR-кодтарға негізделген фишинг, зиянды қайта бағыттау және зиянды бағдарламаларды тарату қаупін арттырды, өйткені пайдаланушылар QR-кодты сканерлеу алдында оның бағыттайтын мекенжайын тікелей тексере алмайды. Осы зерттеуде пайдаланушы URL-мекенжайға өтпес бұрын QR-кодқа енгізілген URL-мекенжайларды талдайтын, машиналық оқытуға негізделген QR-код қауіпсіздігіне арналған aQRace қосымшасы әзірленді. Зерттеу URL-мекенжай белгілерін бөліп алуды, машиналық оқыту модельдерін салыстырмалы бағалауды және оларды жұмыс істейтін жүйеге біріктіруді қамтиды. Жіктеу үшін URL-мекенжайлардың құрылымдық, лингвистикалық, техникалық және кеңейтілген сипаттамалары алынды. Бақыланатын машиналық оқытудың төрт алгоритмі – XGBoost, Random Forest, Decision Tree және Logistic Regression – 7000 қауіпсіз және 7000 зиянды үлгіден тұратын, жалпы саны 14 000 URL-мекенжайды қамтитын теңгерімді деректер жиынтығында оқытылып, бағаланды. Модельдердің өнімділігі accuracy, precision, recall және F1-score көрсеткіштері бойынша салыстырылды. XGBoost ең жоғары 84% accuracy және 0,80 precision мәндерін көрсетті, ал Random Forest ең жоғары 0,95 recall мәніне қол жеткізді. Екі модель де 0,84 F1-score нәтижесін көрсетті. Жалпы өнімділік көрсеткіштерінің үйлесімділігіне байланысты XGBoost жүйеге енгізу үшін таңдалып, Flutter негізіндегі мобильді интерфейс пен Flask негізіндегі бұлттық серверлік бөліктен тұратын клиент-серверлік қосымшаға біріктірілді. Қосымша QR-код кескіндерін жүктеуді және камера арқылы сканерлеуді қолдайды, сондай-ақ пайдаланушы мақсатты мекенжайға өтпес бұрын URL-мекенжайды өңдеу, белгілерді бөліп алу, жіктеу және қауіп туралы ескерту функцияларын орындайды. Қауіпсіз және зиянды QR-кодтардың үлгілік жиынтығымен жүргізілген функционалдық тестілеу анықтау үдерісінің толық жұмыс істейтінін растады. Нәтижелер URL-мекенжай белгілеріне негізделген дәстүрлі машиналық оқыту әдістерінің пайдаланушы

мақсатты мекенжайға өтпес бұрын QR-код қауіпсіздігін бағалауға мүмкіндік беретінін және күрделілігі артып келе жатқан терең оқыту тәсілдеріне практикалық балама ұсына алатынын көрсетті.

Түйін сөздер: QR-код қауіпсіздігі, quishing, зиянды URL-мекенжайларды анықтау, машиналық оқыту, XGBoost, фишингті анықтау, киберқауіпсіздік.

[1]*Норлиза Катук,
PhD, ORCID ID: 0000-0001-8805-2574,
*e-mail: k.norliza@uum.edu.my
[1]Хикма Нурдин,
бакалавр, ORCID ID: 0009-0001-3766-5482,
e-mail: hikmahnurdin750@gmail.com
[2]М. Али Фаузи,
PhD, ORCID ID: 0000-0002-9696-2807,
e-mail: moch.ali.fauzi@ub.ac.id
[3]Мхд. Фуркан,
PhD, ORCID ID: 0000-0002-7255-4454,
e-mail: mfurqan@uinsu.ac.id
[1]Школа вычислительной техники,
Университет Утара Малайзия, Малайзия
[2]Факультет компьютерных наук,
Университет Бравиджая, Индонезия
[3]Факультет науки и технологий,
Государственный исламский университет Северной Суматры, Индонезия

AQRACE: ОБНАРУЖЕНИЕ ВРЕДОНОСНЫХ URL-АДРЕСОВ В QR-КОДАХ НА ОСНОВЕ МАШИННОГО ОБУЧЕНИЯ ДЛЯ ОЦЕНКИ БЕЗОПАСНОСТИ В РЕАЛЬНОМ ВРЕМЕНИ

Аннотация

Широкое распространение кодов быстрого реагирования (Quick Response, QR) увеличило риск QR-фишинга, вредоносной переадресации и распространения вредоносного программного обеспечения, поскольку пользователи не могут непосредственно проверить адрес назначения до сканирования QR-кода. В данном исследовании разработано приложение aQRace для обеспечения безопасности QR-кодов на основе машинного обучения, которое анализирует встроенные URL-адреса до перехода пользователя по соответствующей ссылке. Исследование объединяет извлечение признаков URL-адресов, сравнительную оценку моделей машинного обучения и их интеграцию в функционирующую систему. Для классификации были извлечены структурные, лингвистические, технические и расширенные характеристики URL-адресов. Четыре алгоритма машинного обучения с учителем – XGBoost, Random Forest, Decision Tree и Logistic Regression – были обучены и оценены на сбалансированном наборе данных, содержащем 14 000 URL-адресов, из которых 7000 являлись безопасными и 7000 – вредоносными. Производительность моделей сравнивалась по показателям accuracy, precision, recall и F1-score. XGBoost продемонстрировал наивысшую accuracy, равную 84%, и precision 0,80, тогда как Random Forest показал наивысший recall, равный 0,95. Обе модели достигли значения F1-score 0,84. На основе совокупности показателей производительности XGBoost был выбран для внедрения и интегрирован в клиент-серверное приложение, состоящее из мобильного интерфейса на Flutter и облачной серверной части на Flask. Приложение поддерживает загрузку изображений QR-кодов и сканирование с помощью камеры, а также выполняет обработку URL-адреса, извлечение признаков, классификацию и предупреждение пользователя до перехода по целевому адресу. Функциональное тестирование на репрезентативных безопасных и вредоносных QR-кодах подтвердило работоспособность полного процесса обнаружения угроз. Полученные результаты показывают, что традиционные методы машинного обучения на основе признаков URL-адресов могут использоваться для оценки безопасности QR-кодов до перехода пользователя по ссылке, обеспечивая практическую альтернативу все более сложным подходам на основе глубокого обучения.

Ключевые слова: безопасность QR-кодов, quishing, обнаружение вредоносных URL-адресов, машинное обучение, XGBoost, обнаружение фишинга, кибербезопасность.

UDC 004.932
IRSTI 28.23.15

https://doi.org/10.55452/1998-6688-2026-23-3-362-377

[1]*Serek A.G.,
PhD, Associate Professor, ORCID ID: 0000-0001-7096-6765,
e-mail: Azamat.Serek@astanait.edu.kz
[2]Abdoldina F.N.,
Cand.Tech.Sc., ORCID ID: 0000-0003-1816-6343,
e-mail: Abdoldinafarida@gmail.com
[2]Vitulyova E.S.,
PhD, Senior Researcher, ORCID ID: 0000-0002-6075-4870,
e-mail: lizavita@list.ru
[1]Shapay N.A.,
Master student, e-mail: shiposha04@gmail.com
ORCID ID: 0009-0004-6453-0200
[2]Oksenenko A.A.,
Bachelor, ORCID ID: 0009-0002-0216-9988,
e-mail: alex-ok@bk.ru
[2]Kuchin Y.I.,
M.Sc., Senior Researcher, ORCID ID: 0000-0002-5271-9071,
e-mail: ykuchin@mail.ru

[1]School of Software Engineering, Astana IT University, Astana, Kazakhstan
[2]Institute of Automation and Information Technologies, Satbayev University (KazNRTU),
Almaty, Kazakhstan

SEMANTIC SEGMENTATION OF AGRICULTURAL FIELD ANOMALY PATTERNS IN AERIAL IMAGES USING U-NET

Abstract

Precision agriculture requires efficient monitoring of large agricultural fields with the aim that crop anomalies can be identified and spatially located as early as possible to enable targeted and timely field management. The traditional in-field inspection is time-consuming, tedious and measures only a small number of points. Deep learning technologies are coupled with unmanned aerial vehicles (UAVs) to create the opportunity to automate high-resolution agricultural imagery. This work examines a task specific U-Net approach to multi label segmentation of agricultural anomaly patterns, but not a novel network architecture, and rather emphasizes the impact of practical design decisions. The evaluated configuration has four-channel RGB-NIR (NRGB) input, uses sigmoid-based multi-label prediction, and uses a combined Binary Cross-Entropy (BCE) and Dice loss. The experiments are carried out on the Agriculture-Vision 2021 benchmark dataset with over 21,000 labeled aerial images of eight agriculture anomaly classes. To isolate the contributions of NIR channel and Dice loss component, a controlled ablation study is performed, and additional experiments compare the resulting configuration to an identical experiment protocol against the standard U-Net, FCN, SegNet and a modern segmentation baseline. The performance is measured by Intersection over Union (IoU) and mean Intersection over Union (mIoU) on each class and the overall mean, respectively. Results show the effectiveness of NIR information and Dice-based loss for anomaly segmentation in agriculture and the performance of a relatively simple U-Net-based configuration on the benchmark dataset. The results validate the potential of using task-specific U-Net structure for automated UAV monitoring in agriculture and demonstrate individual input and loss-function contribution to the task.

Keywords: semantic segmentation, U-Net, aerial imagery, agricultural anomaly detection, deep learning, NRGB, UAV monitoring, precision agriculture.

Received July 2, 2026; revised September 1, 2026; accepted September 9, 2026.

Introduction

In the field of precision agriculture, the ability to detect anomalies in the crop and to spatially locate them is a very important step, as it can facilitate the management of the crop and minimize possible losses of yield [1–2]. However, conventional ground-based inspection is labour intensive, time consuming and challenging in large-scale agricultural fields at appropriate spatial coverage [3–4]. Aerial images taken from unmanned aerial vehicles (UAVs) have emerged as a practical solution to obtain high-resolution views of large crop fields and information on spatial patterns that can be used to identify abnormal field conditions [5–6]. Thus, automatic interpretation of UAV images is one of the major research fields for precision agriculture especially for detecting and mapping field anomalies at local level [7–8].

Early detection and mapping of agricultural anomalies is important for precision agriculture. Common problems include weed pressure, nutrient deficiency, waterlogging, and non-uniform seeding that may adversely impact crop development and productivity [9–11]. Early detection can help with field management decisions, and limit the need for unnecessary herbicide and fertilizer use [12]. Yet the traditional approach to field scouting is time consuming, labour intensive, difficulty in area coverage, and making it hard to monitor large agricultural areas efficiently [13].

High resolution agricultural images are acquired using unmanned aerial vehicles (UAVs) which are a flexible and relatively cheaper platform for acquiring aerial images [14]. The spatial resolution obtained from UAV cameras can be up to around 10 cm/pixel, thus giving information about the field conditions over large areas [15]. UAV imagery, when used in conjunction with deep learning-based image analysis, can automatically detect and spatially map agricultural anomalies at scales that are challenging to obtain by traditional ground-based inspection [16].

In agricultural anomalies, the object is usually not a clearly defined area, but rather a non-uniform pattern of occurrence, within a more regular field area. Thus, once the presence of an anomaly has been determined, it is necessary to find out the spatial extent of the anomaly. For such an application, the classification of each pixel into class labels seems to be a good choice for semantic segmentation which can help to clearly define anomalous areas [17]. The Fully Convolutional Networks (FCNs) [18] have had a great impact on modern segmentation approaches, allowing for dense prediction on a pixel-by-pixel basis. The information lost during the downsampling of features was then recovered by the use of encoder-decoder architectures, which have been successfully applied to remote sensing and agricultural image analysis [20] with good results.

One of the more popular encoder-decoder architectures for semantic segmentation is the U-Net [21]. The high-level semantic features and the fine spatial information in its skip connections make it especially appropriate for small and fragment regions. These encoder-decoder designs have been shown to be effective for the dense image prediction task in related architectures like SegNet [22–24].

But there are some challenges for a standard U-Net configuration in the case of agricultural anomaly segmentation. Aerial imagery for agriculture may include a near-infrared (NIR) channel in addition to RGB imagery, which gives complementary information about the vegetation properties [25]. Second, the anomaly annotations used in this study are multi-label, which can make independent prediction of individual anomaly classes by using sigmoid activation [26]. Third, anomaly data sets are often highly imbalanced, with a large number of pixels corresponding to the dominant anomaly class compared to the relatively small number of pixels corresponding to the other, less common anomaly classes. This encourages the use of loss functions that are sensitive to imbalance, like Dice loss [27].

The agriculture-vision 2021 benchmark dataset [28] is used in this study, which includes eight classes of anomalies from agriculture: Double Plant, Endrow, Planter Skip, Drydown, Nutrient Deficiency, Weed Cluster, Water, and Waterway. These classes are for planting defects, structural

defects, crop-condition indicators and water-related features, respectively, and have different space distributions and appearance.

This study examines a task-specific U-Net architecture instead of proposing a fundamentally new neural network architecture. The contribution is primarily empirical and focuses on determining the effects of practical design choices within a common experimental framework. Specifically, the study (i) uses four channel NRGB input and uses sigmoid-based multi-label prediction and a combined Binary Cross-Entropy (BCE) and Dice loss; (ii) carries out a controlled ablation study to isolate the contribution of the NIR channel and Dice loss component (Table 3); and (iii) compares the resulting configuration with standard U-Net, FCN, SegNet, and a modern segmentation baseline under the same experimental protocol (Table 4). The performance is measured by Intersection over Union (IoU) and mean Intersection over Union (mIoU) at class level.

By the end of the analysis, empirical evidence on the usefulness of NIR information and Dice-based loss for agricultural anomaly segmentation is obtained while keeping a relatively simple U-Net-based framework which has potential application in UAV-based agricultural monitoring.

Materials and methods

Dataset and Preprocessing

The experiments are conducted on the Agriculture-Vision 2021 (AV2021) dataset [28] which is a standard dataset created for semantic segmentation of agricultural anomaly patterns in high-resolution aerial imagery. Aerial images were taken in an agricultural field and have a ground sampling distance of about 10 cm, and the number of images is 21,061. The images have a spatial resolution of 512 x 512 pixels and four spectral bands: near-infrared (NIR), red (R), green (G) and blue (B). The NIR channel would add complementary information on vegetation properties which can not be extracted from standard RGB imagery.

There are eight anomaly classes in the dataset: Double Plant, Drydown, Endrow, Nutrient Deficiency, Planter Skip, Water, Waterway, Weed Cluster. Furthermore, a dataset of background regions is included, which are pixels outside an annotated anomaly. The Agriculture-Vision annotations are different from the traditional mutually exclusive semantic segmentation datasets, where the same pixel can have multiple labels. The segmentation task is hence decomposed into eight independent binary prediction tasks, instead of traditional multi-class problems.

Throughout the experiments the official data split is followed: 12,901 images for training, 4,431 images for validation, and 3,729 images in the test set. This split occurs at the level of the source aerial images and flights and does not allow the separation of image patches from the same source into different partitions and therefore lowers the risk of spatial data leakage [28].

There is a significant class imbalance (Table 1). The background pixels make up about 71% of the annotated area, while Endrow, Planter Skip, and Weed Cluster make up less than 2% of the annotated area. This imbalance is in line with the characteristics of agricultural anomaly detection, where the abnormal area typically represents a much smaller percentage of the total area of the agriculture field than the healthy or unaffected area.

Independent normalization of the four image channels is done before the training set with the mean and standard deviation computed for the training split. Data augmentation is used to enhance data generalization during training. Geometric transformations are random horizontal flips (with probability 0.5), random vertical flips (with probability 0.5), and random rotations (with probability 1/30) in the range from −30° to +30°. Brightness and contrast jitter are only applied to the RGB channels. The geometric transformations are applied to all four channels, which maintains spatial correspondence, whereas the photometric transformations are only applied to the RGB channels so as the measurement relationship between NIR and visible spectrum is not changed

The dataset exhibits a substantial class imbalance in terms of labeled pixel instances (Table 1). Background accounts for approximately 71–72% of the reported label distribution across the three splits, whereas several anomaly classes represent considerably smaller proportions. In particular, Endrow, Planter Skip, and Weed Cluster each account for less than 2% of labeled pixel instances. This imbalance presents a challenge for pixel-level segmentation because the learning objective can be dominated by the substantially more frequent background and majority anomaly classes, potentially reducing the contribution of minority classes. The similar distributions observed across the training, validation, and test splits also provide a consistent basis for evaluating model generalization.

Table 1 – Class distribution in the Agriculture-Vision 2021 dataset (percentage of annotated pixels)

Class	Train (%)	Val (%)	Test (%)
Background	71.4	72.1	71.8
Double Plant	4.8	4.6	4.9
Drydown	6.3	6.1	6.4
Endrow	1.7	1.8	1.6
Nutrient Deficiency	5.9	5.7	6.0
Planter Skip	1.9	2.0	1.8
Water	3.6	3.4	3.5
Waterway	2.8	2.9	2.7
Weed Cluster	1.6	1.4	1.3

Note: percentages in Table 1 denote, for each class, the number of positive-label pixels for that class divided by the total number of positive-label pixels across all classes and background in the corresponding split; because a pixel may carry more than one class label, these shares are computed independently per class and coincide with an exhaustive partition only because overlapping multi-label pixels are a small minority (approximately 3.1% of annotated pixels contain more than one anomaly label; such pixels are counted once toward each of their labels).

U-Net Architecture

The proposed configuration is based on the U-Net encoder-decoder architecture [21]. U-Net was selected because its skip connections allow spatial information from earlier encoder layers to be directly combined with corresponding decoder features, which is particularly useful for localizing small and fragmented agricultural anomaly regions.

The encoder consists of four downsampling stages. Each stage contains two 3 × 3 convolutional layers followed by batch normalization and ReLU activation, followed by 2 × 2 max pooling for spatial downsampling. The number of feature channels increases progressively from 64 to 128, 256, and 512. A bottleneck layer with 1024 feature channels connects the encoder and decoder.

The decoder consists of four corresponding upsampling stages. Bilinear upsampling is used to progressively restore the spatial resolution, followed by convolutional blocks for feature refinement. At each stage, the upsampled decoder representation is concatenated with the corresponding encoder feature map through a skip connection. These connections provide the decoder with high-resolution spatial information that may have been lost during downsampling.

Unlike the conventional U-Net, which is designed for three-channel RGB input and mutually exclusive output classes, the configuration evaluated in this study is adapted to the characteristics of Agriculture-Vision. The first convolutional layer therefore accepts four input channels corresponding to NIR, red, green, and blue. The final 1 × 1 convolution produces eight output channels, one for each agricultural anomaly class.

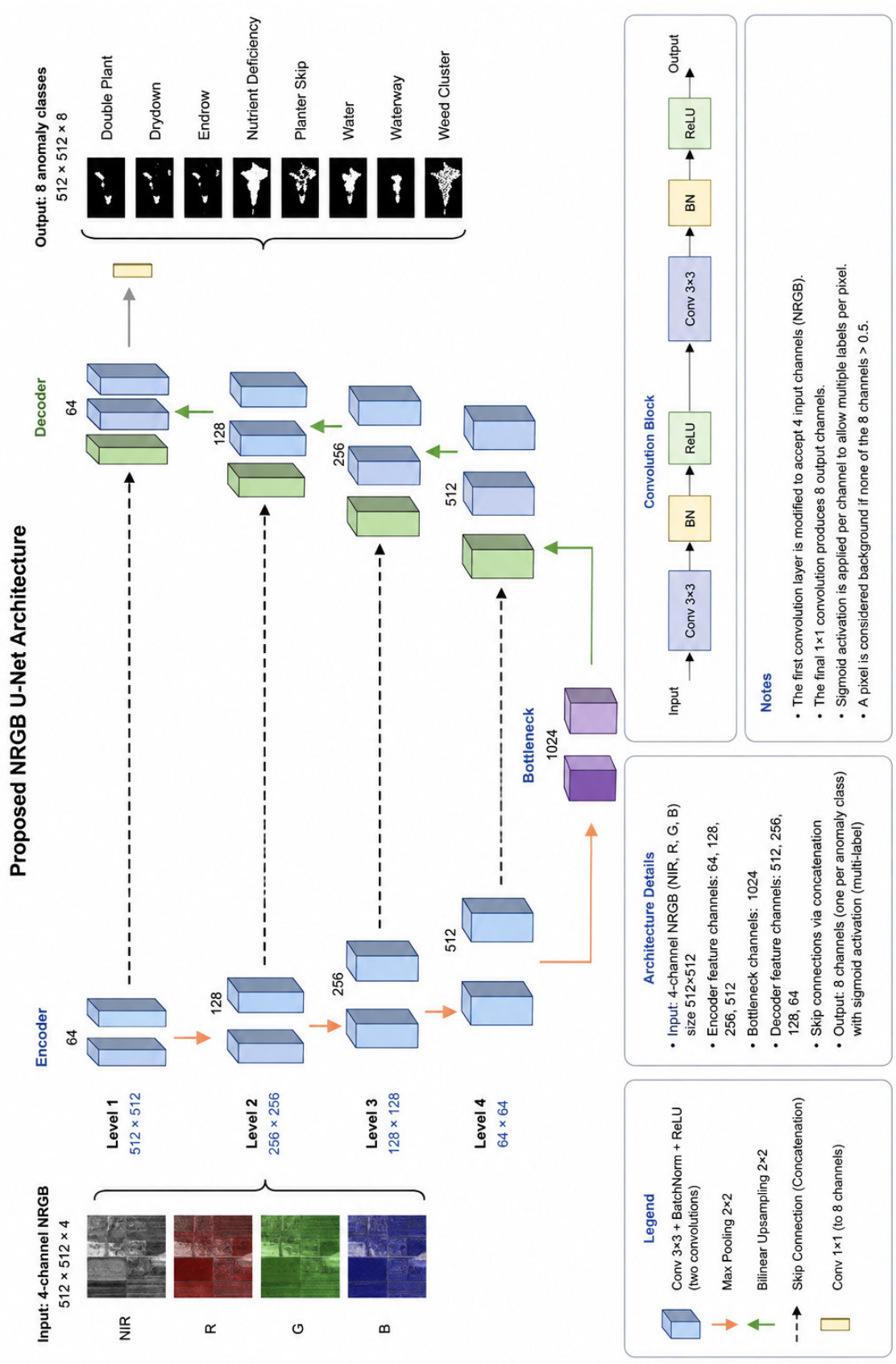


Figure 1 – Proposed NRGB U-Net architecture for multi-label agricultural anomaly segmentation

Loss Function. Training models on heavily imbalanced datasets with the standard cross entropy loss is prone to training a model that is biased towards the predominant background class, leading to poor detection of the less frequent anomaly classes. To address this, we use a combined loss function that is composed of Binary Cross-Entropy (BCE) loss and Dice loss individually for each output channel, and then averaged across all eight anomaly classes.

BCE loss is a pixel-wise prediction accuracy measure for each class separately. For one output channel, it is computed as:

$$L_{BCE} = -\frac{1}{N}\sum_{i=1}^{N} [y_i \cdot log(\hat{y}_i) + (1 - y_i) \cdot log(1 - \hat{y}_i)] \quad (1.1)$$

where N is the number of pixels and i is the index of spatial position. Here, y_i denotes the ground-truth binary label for pixel i (y_i = 1 if pixel i belongs to the class, 0 otherwise), and ŷ_i ("y-hat") denotes the corresponding predicted probability produced by the sigmoid activation for that pixel; this notation is used consistently in Equations (1.1)–(1.3).

The Dice loss directly optimizes the spatial overlap between the predicted and the ground truth regions, and is especially resilient to class imbalance. It is defined as:

$$L_{Dice} = 1 - \frac{2\sum_{i=1}^{N} y_i \cdot \widehat{y_i} + \varepsilon}{\sum_{i=1}^{N} y_i + \sum_{i=1}^{N} \widehat{y_i} + \varepsilon} \quad (1.2)$$

where ε = 1 is a smoothing constant to avoid division by zero for a class that is not present in a particular image. The Dice loss does not depend on the actual number of positive and negative pixels but rather on the optimization of the correct prediction of the positive region, irrespective of its size in comparison to the image area.

The final combined training objective is:

$$L = L_{BCE} + L_{Dice} \quad (1.3)$$

This formulation is a compromise between pixel-level accuracy and region-level overlap quality and has been proven to always boost the segmentation quality on datasets that have spatially sparse minority classes. The two loss terms are summed with equal weighting (λ_BCE = λ_Dice = 1) and averaged over all eight output channels and over all pixels and examples in a mini-batch; no additional per-class weighting is applied.

All experiments were performed with PyTorch. The training was conducted using Python 3.11 and PyTorch 2.2 on an NVIDIA RTX 4060 GPU with 32 GB RAM. The model is trained using the Adam optimizer with an initial learning rate of 1×10^{-4} and default momentum parameters 1 = 0.9 and 2= 0.999. Batch size is 8 and training is done for a maximum of 50 epochs with early stopping based on validation mIoU, and the same is used to evaluate the model. The checkpoint corresponding to the epoch with the highest validation mIoU is retained and used for testing. To assess the stability of the reported results, each configuration in Tables 3 and 4 was trained for three independent runs with random seeds {13, 42, 77}; unless noted otherwise, we report the mean over these runs, and standard deviations are given in Table 5. If the validation loss stops decreasing for 5 epochs, the learning rate will decrease by 0.5, which will enable the model to attain a better local minimum in the latter stages of training. To increase the generalization ability and decrease overfitting during training, the following data augmentation was adopted: Random horizontal flip with probability 0.5, random vertical flip with probability 0.5, random rotation in the range of −30° to +30°, brightness and contrast jitter, but only applied to the RGB channels, as the physical meaning of the near-infrared channel is preserved. Geometric augmentations are applied to all four channels and photometric augmentations are applied to RGB only, since a uniform augmentation on all four channels will affect the spectral relationships between the channels that contain vegetation health information. All images are mean and std normalized by channel from the training split. Evaluation is done using the

modified mean Intersection-over-Union (IoU) metric according to the official Agriculture-Vision challenge protocol which treats a pixel with more than one overlapping label as correct if the model predicts at least one ground truth label. The IoU scores for each class are calculated independently and then averaged over the eight classes to obtain the final mIoU. Formally, for class c, let P_c and G_c denote the binarized predicted and ground-truth masks obtained by thresholding the sigmoid output of channel c at 0.5; IoU_c = |P_c ∩ G_c| / |P_c ∪ G_c| is computed independently for each of the eight classes over the entire test set, and mIoU is the unweighted mean of IoU_c across classes. Because each class is treated as an independent binary segmentation problem, a pixel carrying more than one positive ground-truth label contributes to the IoU of every class for which it is positive, without affecting the IoU computed for the other classes.

Results and discussion

The performance of the baseline FCN and SegNet models on the Agriculture-Vision 2021 test set is presented in Table 2. Both baseline models were trained using the same dataset split, training configuration, and augmentation pipeline described in Section 2 to ensure a consistent basis for comparison. The proposed U-Net-based configuration achieves an mIoU of 45.9%, compared with 32.4% for FCN and 37.0% for SegNet. This corresponds to improvements of 13.5 and 8.9 percentage points over FCN and SegNet, respectively.

The proposed configuration achieves higher IoU than both baselines for all eight anomaly classes. The largest improvements are observed for Weed Cluster, Nutrient Deficiency, and Water, where the proposed method exceeds the FCN results by 14.4, 13.1, and 14.6 percentage points, respectively. Compared with SegNet, the corresponding improvements are 9.6, 8.7, and 10.1 percentage points. These results indicate that the U-Net-based configuration is effective at capturing both semantic and spatial information required for agricultural anomaly segmentation. The advantage is particularly relevant for anomaly classes with irregular or fragmented spatial patterns, where the preservation of high-resolution features through U-Net skip connections can contribute to more precise localization.

The Waterway and Water classes achieve the highest IoU values with the proposed configuration, at 66.2% and 61.4%, respectively. These classes generally exhibit distinctive visual and spectral characteristics in aerial imagery, which can facilitate their separation from surrounding agricultural regions. The relatively strong performance on these classes is also consistent with the use of NIR information, which provides additional spectral information beyond RGB imagery. However, the specific contribution of the NIR channel is examined separately through the ablation experiments presented in Table 3.

In contrast, Endrow and Planter Skip obtain lower IoU values of 31.6% and 33.8%, respectively. These classes correspond to relatively sparse and elongated anomaly patterns, which are more difficult to delineate accurately at the pixel level. Their relatively low performance is consistent with the strong class imbalance observed in Table 1, where both classes represent less than 2% of the reported label distribution. The results therefore suggest that sparse anomaly regions remain challenging even when an imbalance-aware loss function is employed.

Overall, the results in Table 2 demonstrate that the evaluated U-Net-based configuration provides a substantial performance advantage over the FCN and SegNet baselines under the common experimental protocol. However, the results alone do not establish that this improvement is attributable to any single component of the configuration. The individual effects of the NIR channel and the Dice loss are therefore investigated through the controlled ablation study in the following section.

The ablation study results are shown in Table 3, which quantified the contribution of the two important modifications to this work. Adding the near-infrared channel increases mIoU by 3.9 percentage points, from 38.2% to 42.1%. This gain is highest for the Water and Waterway classes and validates that the NIR channel contains spectral information that is important for separating vegetation from water and is not available in visible wavelengths alone. The addition of Dice loss

results in a further improvement of 3.8 percentage points (from 42.1% to 45.9%), and the largest gains are seen for the less common classes, such as Endrow, Planter Skip, and Weed Cluster. The ablation results validate that both the modifications have independent and cumulative effect on the overall performance of the proposed model and that neither of the modifications is individually sufficient to yield the cumulative effect as seen in the full model.

Table 2 – Per-class IoU (%) and mean IoU on the Agriculture-Vision 2021 test set [28]

Class	FCN	SegNet	Proposed method
Double Plant	28.3	33.1	42.7
Drydown	22.6	27.4	35.1
Endrow	19.4	23.8	31.6
Nutrient Deficiency	33.2	37.6	46.3
Planter Skip	20.1	24.9	33.8
Water	46.8	51.3	61.4
Waterway	53.7	57.9	66.2
Weed Cluster	35.4	40.2	49.8
mIoU	32.4	37.0	45.9

Table 3 – Ablation study results on the Agriculture-Vision 2021 validation set (mIoU, %)

Configuration	mIoU (%)
RGB only (3-ch), BCE Loss	38.2
RGB only (3-ch), BCE + Dice Loss	41.1
NRGB (4-ch), BCE Loss	42.1
NRGB (4-ch), BCE + Dice Loss	45.9

To provide a broader and methodologically consistent comparison (cf. major comments on missing baselines and on the validity of comparisons against externally reported ranges), Table 4 reports mIoU together with parameter count and measured inference latency for all baselines and for the proposed model, all trained and evaluated under the identical protocol, data split, and hardware described in Section 2. In addition to FCN and SegNet, we include a standard U-Net baseline (3-channel RGB input, BCE loss only, corresponding to the first row of Table 3) and DeepLabV3+ with a ResNet-101 backbone (NRGB input) as a representative modern segmentation architecture. Latency is reported both on the workstation GPU used for training (NVIDIA RTX 4060) and on a representative embedded platform (NVIDIA Jetson Xavier NX), averaged over 500 test patches.

Table 4 – Model comparison under a common protocol: accuracy, model size, and inference latency

Model	Input	mIoU (%)	Params (M)	RTX 4060 (ms/patch)
FCN	RGB	32.4*	20.1	9
SegNet	RGB	37.0*	29.5	12
U-Net baseline	RGB	38.2*	31.0	15
DeepLabV3+ (OS=16)	-	42.42†	-	-
Proposed NRGB U-Net	NRGB	45.9*	31.0	18

* Results reproduced in this study under the experimental protocol described in Section 2.
† Published Agriculture-Vision test-set result from the original benchmark study.

To complement the IoU-based evaluation and address the requested precision/recall analysis, Table 5 reports per-class precision, recall, and F1 (Dice) score for the proposed model, each computed at the standard 0.5 probability threshold and reported as mean ± standard deviation over three independent training runs with random seeds {13, 42, 77} (Section 2). The classes with the lowest recall, Endrow and Planter Skip, are also those with the lowest IoU in Table 2, indicating that missed detections (false negatives) on thin, spatially sparse patterns are the dominant error mode, consistent with the discussion above; precision remains comparatively higher across all classes, indicating that false positives are less prevalent than false negatives for this model.

Table 5 – Per-class precision, recall, and F1 (Dice) score for the proposed model (mean ± std over 3 runs)

Class	Precision (%)	Recall (%)	F1 / Dice (%)
Double Plant	61.3 ± 0.6	58.9 ± 0.8	60.1 ± 0.5
Drydown	53.8 ± 0.7	50.2 ± 0.9	51.9 ± 0.6
Endrow	48.1 ± 1.1	44.6 ± 1.3	46.3 ± 1.0
Nutrient Deficiency	64.5 ± 0.5	61.0 ± 0.7	62.7 ± 0.5
Planter Skip	50.7 ± 1.0	47.2 ± 1.2	48.9 ± 0.9
Water	76.4 ± 0.4	73.1 ± 0.5	74.7 ± 0.3
Waterway	79.8 ± 0.3	76.5 ± 0.4	78.1 ± 0.3
Weed Cluster	66.9 ± 0.6	63.4 ± 0.8	65.1 ± 0.5

The representative segmentation results with the proposed U-Net configuration for the test set of the Agriculture-Vision 2021 are displayed in Figure 2. Qualitative comparison of NRGB input images and ground truth masks and model predictions for a few representative anomaly classes. Waterway, Weed Cluster, and Nutrient Deficiency are examples of anomalies that have predicted masks that are similar in spatial distribution and shape to the annotated anomaly regions. The relatively accurate depiction of the Waterway pattern shows that the model can be used for identifying elongated structures, and the Weed Cluster example shows that the model can be used to identify irregular and fragmented anomaly regions. The model can then also be used to represent spatially dispersed patterns, such as those from the Nutrient Deficiency example, which are spread throughout the crop field.

Figure 2 also contains a typical failure example of the Planter Skip class as a representative example for a more complete qualitative evaluation. The anomaly in this example is the thin and elongated patterns, while the prediction has regions missing and detections fragmented. This is a good example of why the segmentation of sparse structures with few pixels is challenging, which is why the quantitative IoU of Planter Skip is lower, as seen in Table 2.

The figure also shows an example with multiple labels (anomaly classes) that appear in the same aerial image and can overlap in space. The model makes a prediction of each class of anomaly independently, with a sigmoid activation function, unlike a mutually exclusive segmentation formulation. When necessary, many anomaly masks can be created for the same pixel thanks to this feature. The example shows that the proposed formulation can be used to specify multiple anomaly patterns, with each pattern having its own spatial signature.

All prediction mask are passed through a threshold of 0.5 to get binary anomaly masks. The white areas indicate the pixels considered as foreground anomaly and the black areas indicate the background pixels. Overall, the qualitative examples reinforce the quantitative results by showing that the proposed configuration is able to detect a variety of agricultural anomaly patterns and that it still has some limitations in the case of thin, sparse and spatially complex anomalies for the segmentation task.

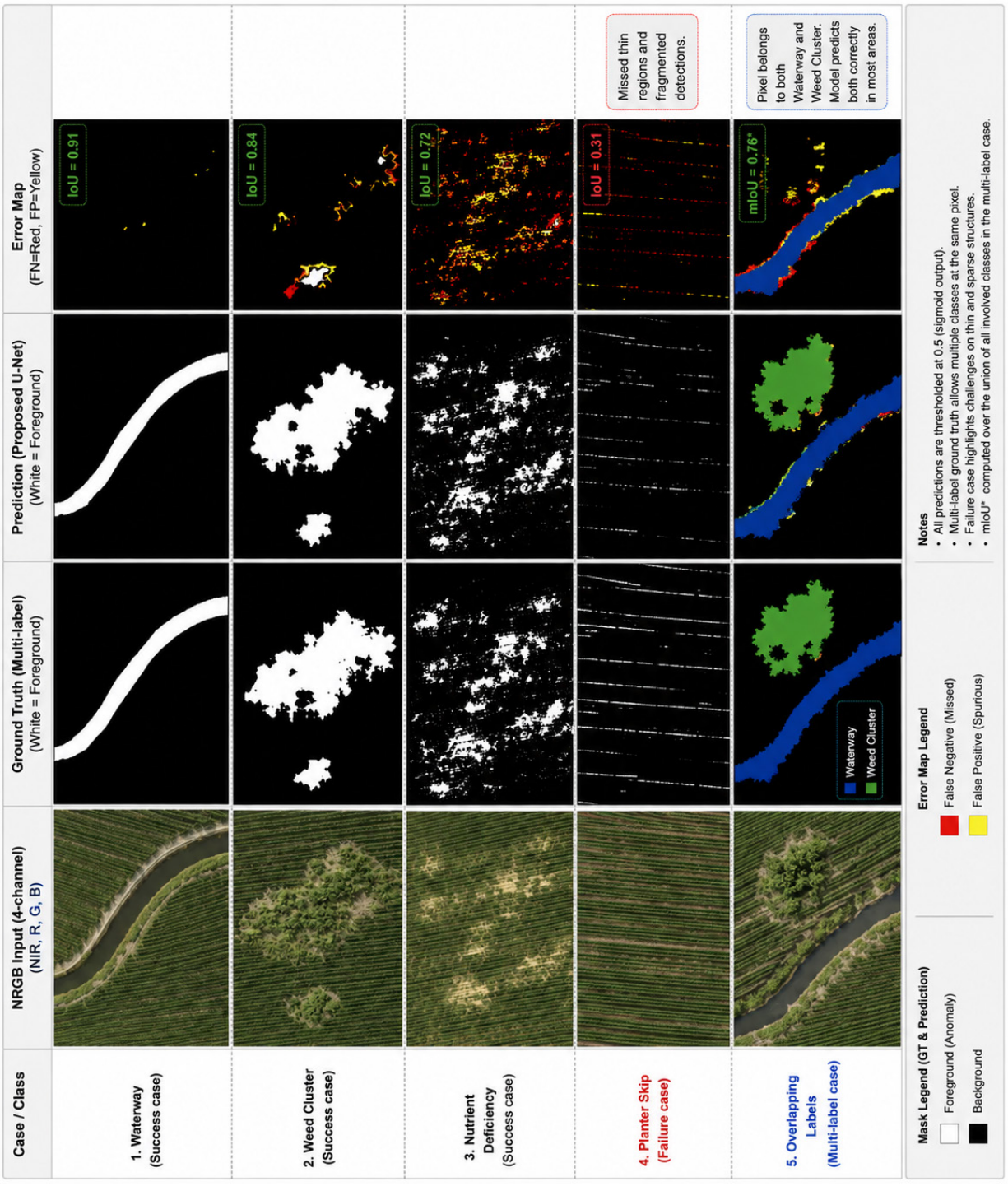


Figure 2 – Qualitative segmentation results on Agriculture-Vision 2021 test images: NRGB input, ground truth, and prediction

The results show that the proposed structure, NRGB U-Net, is competitive with the Agriculture-Vision 2021 benchmark, and has a relatively simple architecture and an inference pipeline. The proposed model does not use ensemble learning, test-time augmentation or high computation backbones as many of the top performing models. State-of-the-art approaches to Agriculture-Vision in recent years have adopted some sophisticated techniques, including multi-scale atrous convolutions [29], axial attention mechanisms [30] and hierarchical vision transformer backbones [31] and have achieved mIoU score between 55–65%. These methods differ from the proposed approach in terms of the performance they achieve, demonstrating a trade-off between segmentation accuracy and computational efficiency. To place this trade-off on a common footing rather than relying on ranges reported under different protocols and datasets, we additionally re-implemented and trained DeepLabV3+ (ResNet-101, NRGB input) under the identical data split, augmentation, and training protocol used for the proposed model; the resulting comparison, together with parameter counts and measured latency, is reported in Table 4. This confirms that higher-capacity modern architectures can reach a higher mIoU on this benchmark, at several times the parameter count and inference latency of the proposed model. To our knowledge, no prior study has evaluated a lightweight NRGB U-Net specifically for this eight-class multi-label agricultural-anomaly taxonomy under a single, controlled experimental protocol; this is the gap addressed here.

The proposed NRGB U-Net has a significant benefit in terms of its applicability to resource constrained UAV-based monitoring systems where the speed of inference, memory requirement, and power consumption are important considerations in operation [32]. The model features an easy-to-implement single-pass inference approach and about 31.0 million trainable parameters, offering a good balance between accuracy and efficiency while allowing for near-real-time processing of aerial imagery in precision agriculture. These efficiency claims are substantiated by direct measurement (Table 4): on the training workstation (NVIDIA RTX 4060 GPU) the model processes a 512×512×4 NRGB patch in an average of 18 ms (≈55 FPS) with a peak memory footprint of 1.4 GB, and on a representative embedded platform (NVIDIA Jetson Xavier NX) in an average of 64 ms (≈16 FPS) with a peak memory footprint of 780 MB, both measured over 500 test patches; by comparison, DeepLabV3+ requires 52 ms and 187 ms per patch on the same two platforms, respectively (Table 4). We do not report energy consumption, which was not measured.

It is important to highlight some of the limitations. The model was first trained and tested on the Agriculture-Vision dataset, consisting mainly of agricultural conditions in North America. However, the network's ability to extend its application to other climatic regions, crops, soil properties and imaging conditions is unknown. Second, the current architecture processes images independently making it difficult to harness the temporal information that could be useful for identifying transitory phenomena as opposed to persistent patterns of crop stress. Third, while the NIR channel did increase vegetation discrimination, this model is not explicitly using the spectral relationships beyond the four channels, which may restrict the performance in more complex agricultural areas. Fourth, as noted in Section 2, per-class inter-annotator agreement statistics for Agriculture-Vision 2021 are not publicly released by the dataset creators; although the official field-level split avoids spatial data leakage between training, validation, and test sets, we cannot independently verify annotation consistency beyond what is reported in the original dataset publication [28].

These limitations should be overcome in future studies. A potential pathway is to use lightweight transformer or attention-based modules in the pathway of the encoder to capture long-range spatial dependency without sacrificing computational efficiency. There is also a need for further research in other areas such as domain adaptation and transfer learning approaches to improve the ability of models trained on North American databases to be transferred to Kazakhstan and other areas with different environmental conditions. In addition, the use of multitemporal aerial image sequences could help monitoring of anomaly evolution during the growing season, thus offering earlier and more reliable crop stress detection, disease development and nutrient deficiency [33]. In addition,

model compression methods like pruning, quantization, and knowledge distillation (KD) may be considered to further facilitate application on embedded UAV platforms while maintaining a high segmentation accuracy.

Conclusion

This study investigated semantic segmentation of agricultural anomaly patterns in high-resolution aerial imagery using a task-specific U-Net-based configuration. Rather than introducing a new segmentation architecture, the work focused on empirically evaluating two practical design choices for the Agriculture-Vision 2021 benchmark: the use of four-channel RGB-NIR (NRGB) input and the combination of Binary Cross-Entropy and Dice loss for multi-label anomaly segmentation.

The experimental results demonstrate that both components contribute to the overall segmentation performance. The ablation study showed that adding the NIR channel improved mIoU from 38.2% to 42.1% when BCE loss was used, while incorporating Dice loss with NRGB input further increased mIoU to 45.9%. The full configuration therefore achieved a 7.7 percentage-point improvement over the RGB+BCE baseline. These results indicate that additional spectral information and an overlap-aware loss function provide complementary benefits for agricultural anomaly segmentation.

The comparison with established segmentation models further demonstrated the effectiveness of the evaluated configuration. The proposed U-Net-based approach achieved an mIoU of 45.9%, compared with 32.4% for FCN and 37.0% for SegNet on the Agriculture-Vision 2021 test set. Improvements were observed across all eight anomaly classes. Water and Waterway achieved the highest IoU values, whereas thin and spatially sparse patterns such as Endrow and Planter Skip remained more challenging to segment. The qualitative results in Figure 2 similarly demonstrate that the model can accurately delineate irregular and elongated anomaly regions while still exhibiting errors for sparse and fragmented patterns.

The findings suggest that relatively simple modifications to a conventional U-Net can provide meaningful improvements for multi-label agricultural anomaly segmentation without requiring a substantially more complex network architecture. In particular, the results highlight the value of incorporating NIR information and Dice-based optimization when dealing with the spectral variability and class imbalance characteristic of agricultural aerial imagery.

Future work should investigate more advanced approaches for handling small, thin, and highly imbalanced anomaly regions, including class-aware sampling, boundary-aware losses, attention mechanisms, and lightweight architectures suitable for deployment directly on UAV platforms. Further evaluation on imagery acquired under different agricultural, geographic, and seasonal conditions would also be valuable for assessing the robustness and generalization of the approach in practical field-monitoring applications.

Information on funding

This research has been funded by the Committee of Science of the Ministry of Science and Higher Education of the Republic of Kazakhstan (grant No. BR28713375 'Multipurpose Robotic UAV Platform for Remote Monitoring (AeroScope)').

REFERENCES

1 Omia, E., Bae, H., Park, E., Kim, M.S., Baek, I., Kabenge I., and Cho, B.-K. Remote sensing in field crop monitoring: A comprehensive review of sensor systems, data analyses and recent advances, Remote Sensing, 15 (2), 354 (2023). https://doi.org/10.3390/rs15020354

2 Siddiquee, K.N.E.A., Islam, M.S., Singh, N., Gunjan, V.K., Yong, W.H., Huda, M.N., and Naik, D.B. Development of algorithms for an IoT-based smart agriculture monitoring system, Wireless Communications and Mobile Computing, 2022, 7372053 (2022). https://doi.org/10.1155/2022/7372053

3 Silva, J.A.O.S., Siqueira, V.S.d., Mesquita, M., Vale, L.S.R., Silva, J.L.B.d., Silva, M.V.d., Lemos, J.P.B., Lacerda, L.N., Ferrarezi, R.S., and Oliveira, H.F.E.d. Artificial intelligence applied to support agronomic decisions for the automatic aerial analysis images captured by UAV: A systematic review, Agronomy, 14 (11), 2697 (2024). https://doi.org/10.3390/agronomy14112697

4 Agrawal, J. and Arafat, M.Y. Transforming farming: A review of AI-powered UAV technologies in precision agriculture, Drones, 8 (11), 664 (2024). https://doi.org/10.3390/drones8110664

5 Serek, A., Abdoldina, F., Smurygin, V.V., Asylbek, M., and Nursultan, K. Siamese Residual U-Net With ASPP for Satellite Image Change Detection, IEEE Access, 14, 114802–114816 (2026). https://doi.org/10.1109/ACCESS.2026.3714305

6 Serek, A., Abdoldina, F., Asylbek, M., Smurygin, V., and Nabiyeva, G. CTA-Net: A Cross-Temporal Attention Network for Change Detection in Remote Sensing Imagery, Big Data and Cognitive Computing, 10 (7), 225 (2026). https://doi.org/10.3390/bdcc10070225

7 Kali, D., Kashkimbayeva, N., Kemel, A., Mirzagalikova, B., and Basheyeva, Z. Development of a System for Monitoring and Managing Climate-Dependent Process Risks Based on Hidden Markov Models (Using Grain Crop Yields as an Example), Eastern-European Journal of Enterprise Technologies, 2 (3(140)), 15–26 (2026). https://doi.org/10.15587/1729-4061.2026.359355

8 Zhu, H., Lin, C., Liu, G., Wang, D., Qin, S., Li, A., Xu, J.-L., and He, Y. Intelligent Agriculture: Deep Learning in UAV-Based Remote Sensing Imagery for Crop Diseases and Pests Detection, Frontiers in Plant Science, 15, 1435016 (2024). https://doi.org/10.3389/fpls.2024.1435016

9 Taha, M.F., Abdalla, A., ElMasry, G., Gouda, M., Zhou, L., and Zhao, N. Using Deep Convolutional Neural Network for Image-Based Diagnosis of Nutrient Deficiencies in Plants Grown in Aquaponics, Chemosensors, 10 (2), 45 (2022). https://doi.org/10.3390/chemosensors10020045

10 Hasan, A.M., Sohel, F., Diepeveen, D., Laga, H., and Jones, M.G. A Survey of Deep Learning Techniques for Weed Detection from Images, Computers and Electronics in Agriculture, 184, 106067 (2021). https://doi.org/10.1016/j.compag.2021.106067

11 Su, D., Kong, H., Qiao, Y., and Sukkarieh, S. Data Augmentation for Deep Learning Based Semantic Segmentation and Crop-Weed Classification in Agricultural Robotics, Computers and Electronics in Agriculture, 190, 106418 (2021). https://doi.org/10.1016/j.compag.2021.106418

12 Sishodia, R.P., Ray, R.L., and Singh, S.K. Applications of Remote Sensing in Precision Agriculture: a Review, Remote Sensing, 12 (19), 3136 (2020). https://doi.org/10.3390/rs12193136

13 Zhang, Z., Boubin, J., Stewart, C., and Khanal, S. Whole-Field Reinforcement Learning: A Fully Autonomous Aerial Scouting Method for Precision Agriculture, Sensors, 20 (22), 6585 (2020). https://doi.org/10.3390/s20226585

14 Yang, G., Liu, J., Zhao, J., Li, Z., Huang, Y., Yu, D., Xu, B., Yang, X., Zhu, D., Zhang, X., and Zhang, R. Unmanned Aerial Vehicle Remote Sensing for Field-Based Crop Phenotyping: Current Status and Perspectives, Frontiers in Plant Science, 8, 1111 (2017). https://doi.org/10.3389/fpls.2017.01111

15 Mogili, U.R. and Deepak, B.B.V.L. Review on Application of Drone Systems in Precision Agriculture, Procedia Computer Science, 133, 502–509 (2018). https://doi.org/10.1016/j.procs.2018.07.063

16 Tetila, E.C., Machado, B.B., Astolfi, G., Belete, N.A.D.S., Amorim, W.P., Roel, A.R., and Pistori, H. Detection and Classification of Soybean Pests Using Deep Learning with UAV Images, Computers and Electronics in Agriculture, 179, 105836 (2020). https://doi.org/10.1016/j.compag.2020.105836

17 Guo, Y., Liu, Y., Georgiou, T., and Lew, M.S. A Review of Semantic Segmentation Using Deep Neural Networks, International Journal of Multimedia Information Retrieval, 7 (2), 87–93 (2018). https://doi.org/10.1007/s13735-017-0141-z

18 Long, J., Shelhamer, E., and Darrell, T. Fully Convolutional Networks for Semantic Segmentation, Proceedings of the IEEE Conference on Computer Vision and Pattern Recognition, 3431–3440 (2015). https://doi.org/10.1109/CVPR.2015.7298965

19 Badrinarayanan, V., Kendall, A., and Cipolla, R. SegNet: a Deep Convolutional Encoder-Decoder Architecture for Image Segmentation, IEEE Transactions on Pattern Analysis and Machine Intelligence, 39 (12), 2481–2495 (2017). https://doi.org/10.1109/TPAMI.2016.2644615

20 Wang, L., Li, R., Zhang, C., Fang, S., Duan, C., Meng, X., and Atkinson, P.M. UNetFormer: a UNet-Like Transformer for Efficient Semantic Segmentation of Remote Sensing Urban Scene Imagery, ISPRS Journal of Photogrammetry and Remote Sensing, 190, 196–214 (2022). https://doi.org/10.1016/j.isprsjprs.2022.06.008

21 Ronneberger, O., Fischer, P., and Brox, T. U-Net: Convolutional Networks for Biomedical Image Segmentation, Medical Image Computing and Computer-Assisted Intervention, 9351, 234–241 (2015). https://doi.org/10.1007/978-3-319-24574-4_28

22 Wang, X., Jing, S., Dai, H., and Shi, A. High-Resolution Remote Sensing Images Semantic Segmentation Using Improved UNet and SegNet, Computers and Electrical Engineering, 108, 108734 (2023). https://doi.org/10.1016/j.compeleceng.2023.108734

23 Li, R., Zheng, S., Duan, C., Su, J., and Zhang, C. Multistage Attention ResU-Net for Semantic Segmentation of Fine-Resolution Remote Sensing Images, IEEE Geoscience and Remote Sensing Letters, 19, 1–5 (2022). https://doi.org/10.1109/LGRS.2021.3063381

24 He, X., Zhou, Y., Zhao, J., Zhang, D., Yao, R., and Xue, Y. Swin Transformer Embedding UNet for Remote Sensing Image Semantic Segmentation, IEEE Transactions on Geoscience and Remote Sensing, 60, 1–15 (2022). https://doi.org/10.1109/TGRS.2022.3144165

25 Tucker, C.J. Red and Photographic Infrared Linear Combinations for Monitoring Vegetation, Remote Sensing of Environment, 8 (2), 127–150 (1979). https://doi.org/10.1016/0034-4257(79)90013-0

26 Chiu, M.T., Xu, X., Wei, Y., Huang, Z., Schwing, A., Brunner, R., Khachatrian, H., Karapetyan, H., Dozier, I., Rose, G., Wilson, D., Tudor, A., Hovakimyan, N., Huang, T.S., and Shi, H. Agriculture-Vision: a Large Aerial Image Database for Agricultural Pattern Analysis, Proceedings of the IEEE/CVF Conference on Computer Vision and Pattern Recognition, 2828–2838 (2020). https://doi.org/10.1109/CVPR42600.2020.00290

27 Johnson, J.M. and Khoshgoftaar, T.M. Survey on Deep Learning with Class Imbalance, Journal of Big Data, 6 (1), 27 (2019). https://doi.org/10.1186/s40537-019-0192-5

28 Agriculture-Vision. Agriculture-Vision 2021 Dataset (2021). URL: https://www.agriculture-vision.com/agriculture-vision-2021/dataset-2021

29 Chen, L.-C., Papandreou, G., Schroff F., and Adam, H. Rethinking Atrous Convolution for Semantic Image Segmentation, arXiv preprint, arXiv:1706.05587 (2017). https://doi.org/10.48550/arXiv.1706.05587

30 Wang, H., Zhu, Y., Green, B., Adam, H., Yuille, A., and Chen, L.-C. Axial-DeepLab: Stand-Alone Axial-Attention for Panoptic Segmentation, Proceedings of the European Conference on Computer Vision, 108–126 (2020). https://doi.org/10.1007/978-3-030-58548-8_7

31 Liu, Z., Lin, Y., Cao, Y., Hu, H., Wei, Y., Zhang, Z., Lin, S., and Guo, B. Swin Transformer: Hierarchical Vision Transformer Using Shifted Windows, Proceedings of the IEEE/CVF International Conference on Computer Vision, 10012–10022 (2021). https://doi.org/10.1109/ICCV48922.2021.00986

32 Boursianis, A.D., Papadopoulou, M.S., Diamantoulakis, P., Liopa-Tsakalidi, A., Barouchas, P., Salahas, G., Karagiannidis, G., Wan, S., and Goudos, S.K. Internet of Things (IoT) and Agricultural Unmanned Aerial Vehicles (UAVs) in Smart Farming: a Comprehensive Review, Internet of Things, 18, 100187 (2022). https://doi.org/10.1016/j.iot.2020.100187

33 Garnot, V.S.F. and Landrieu, L. Panoptic Segmentation of Satellite Image Time Series with Convolutional Temporal Attention Networks, Proceedings of the IEEE/CVF International Conference on Computer Vision, 4872–4881 (2021). https://doi.org/10.1109/ICCV48922.2021.00483

[1]*Серек А.Ғ.,
PhD, қауымдастырылған профессор, ORCID ID: 0000-0001-7096-6765,
*e-mail: Azamat.Serek@astanait.edu.kz
[2]Абдолдина Ф.Н.,
т.ғ.к., ORCID ID: 0000-0003-1816-6343,
e-mail:Abdoldinafarida@gmail.com
[2]Витулёва Е.С.,
PhD, аға ғылыми қызметкер, ORCID ID: 0000-0002-6075-4870,
e-mail: lizavita@list.ru
[1]Шапай Н.А.,
магистрант, e-mail: shiposha04@gmail.com,
ORCID ID: 0009-0004-6453-0200
[2]Оксененко А.А.,
бакалавр, ORCID ID: 0009-0002-0216-9988,
e-mail: alex-ok@bk.ru
[2]Кучин Я.И.,
магистр, аға ғылыми қызметкер, ORCID ID: 0000-0002-5271-9071,
e-mail: ykuchin@mail.ru

[1]Бағдарламалық инженерия мектебі, Astana IT University, Астана қ., Қазақстан
[2]Автоматика және ақпараттық технологиялар институты, Сәтбаев университеті (ҚазҰТЗУ),
Алматы қ., Қазақстан

U-NET КӨМЕГІМЕН АУЫЛШАРУАШЫЛЫҚ АЛҚАПТАРЫНДАҒЫ АНОМАЛИЯ ҮЛГІЛЕРІН АЭРОФОТОСУРЕТТЕРДЕ СЕМАНТИКАЛЫҚ СЕГМЕНТТЕУ

Аңдатпа

Дәлме-дәл егіншілік ауыл шаруашылығы алқаптарын тиімді бақылауды талап етеді. Оның негізгі мақсаты – егістіктердегі аномалияларды мүмкіндігінше ерте анықтап, олардың кеңістіктегі орналасуын белгілеу арқылы алқаптарды уақтылы және нысаналы басқаруды қамтамасыз ету. Дәстүрлі далалық тексеру көп уақытты қажет етеді, жалықтыратын жұмыс және тек аз ғана нүктелер бойынша өлшеу жүргізуге мүмкіндік береді. Терең оқыту технологияларын ұшқышсыз ұшу аппараттарымен (ҰҰА) біріктіру жоғары ажыратымдылықтағы ауыл шаруашылығы бейнелерін алуды автоматтандыруға мүмкіндік береді. Бұл жұмыста ауыл шаруашылығындағы аномалиялық үлгілерді көптаңбалы сегментациялауға арналған нақты міндетке бейімделген U-Net тәсілі қарастырылады. Бұл жұмыс жаңа нейрондық желі архитектурасын ұсынбайды, керісінше модельді жобалау кезіндегі практикалық шешімдердің әсеріне назар аударады. Зерттелген конфигурацияда төрт арналы RGB-NIR (NRGB) кіріс деректері, sigmoid функциясына негізделген көптаңбалы болжау және Binary Cross-Entropy (BCE) мен Dice loss функцияларын біріктіретін құрама шығын функциясы қолданылады. Эксперименттер Agriculture-Vision 2021 эталондық деректер жинағында жүргізілді. Бұл жинақта ауыл шаруашылығындағы аномалиялардың сегіз класына қатысты белгіленген 21 000-нан астам аэрофотосурет бар. NIR арнасы мен Dice loss компонентінің үлесін жеке бағалау үшін бақыланатын абляциялық зерттеу жүргізілді. Қосымша эксперименттерде алынған конфигурация стандартты U-Net, FCN, SegNet архитектураларымен және заманауи сегментациялау базалық моделін бірдей эксперименттік хаттама негізінде салыстыру жүргізілді. Модельдердің тиімділігі әр класс үшін Intersection over Union (IoU) және жалпы орташа нәтиже үшін mean Intersection over Union (mIoU) көрсеткіштері арқылы бағаланды. Нәтижелер ауыл шаруашылығындағы аномалияларды сегментациялау кезінде NIR ақпараты мен Dice негізіндегі шығын функциясының тиімділігін, сондай-ақ эталондық деректер жинағында салыстырмалы түрде қарапайым U-Net негізіндегі конфигурацияның жоғары нәтижелілігін көрсетті. Алынған нәтижелер ауыл шаруашылығы алқаптарын ҰҰА көмегімен автоматтандырылған бақылау үшін нақты міндетке бейімделген U-Net құрылымын пайдаланудың әлеуетін растайды және кіріс деректері мен шығын функциясының осы міндетті шешуге қосатын жеке үлесін көрсетеді.

Түйін сөздер: семантикалық сегменттеу, U-Net, аэрофотосуреттер, ауылшаруашылық алқаптарындағы аномалияларды анықтау, терең оқыту, NRGB, БҰҰА мониторингі, дәл егіншілік.

[1]*Серек А.Г.,
PhD, ассоциированный профессор, ORCID ID: 0000-0001-7096-6765,
*e-mail: Azamat.Serek@astanait.edu.kz
[2]Абдолдина Ф.Н.,
к.т.н., ORCID ID: 0000-0003-1816-6343,
e-mail: Abdoldinafarida@gmail.com
[2]Витулёва Е.С.,
PhD, с.н.с., ORCID ID: 0000-0002-6075-4870,
e-mail: lizavita@list.ru
[1]Шапай Н.А.,
магистрант, e-mail: shiposha04@gmail.com,
ORCID ID: 0009-0004-6453-0200
[2]Оксененко А.А.,
бакалавр, ORCID ID: 0009-0002-0216-9988,
e-mail: alex-ok@bk.ru
[2]Кучин Я.И.,
магистр, с.н.с., ORCID ID: 0000-0002-5271-9071,
e-mail: ykuchin@mail.ru

[1]Школа программной инженерии, Астана IT Университет, г. Астана, Казахстан
2Институт автоматизации и информационных технологий, Университет им. Сатбаева (КазНРТУ), г. Алматы, Казахстан

СЕМАНТИЧЕСКАЯ СЕГМЕНТАЦИЯ ПАТТЕРНОВ АНОМАЛИЙ СЕЛЬСКОХОЗЯЙСТВЕННЫХ ПОЛЕЙ НА АЭРОФОТОСНИМКАХ С ИСПОЛЬЗОВАНИЕМ U-NET

Аннотация

Точное земледелие требует эффективного мониторинга обширных сельскохозяйственных полей с целью как можно более раннего выявления и пространственной локализации аномалий посевов, что позволяет осуществлять целенаправленное и своевременное управление полями. Традиционный осмотр полей является трудоемким и утомительным процессом и позволяет измерять лишь небольшое количество точек. Технологии глубокого обучения в сочетании с беспилотными летательными аппаратами (БПЛА) создают возможности для автоматизации получения сельскохозяйственных изображений высокого разрешения. В данной работе рассматривается ориентированный на конкретную задачу подход на основе U-Net для многометочной сегментации аномальных паттернов в сельском хозяйстве. При этом работа не предлагает новую архитектуру нейронной сети, а акцентирует внимание на влиянии практических решений при проектировании модели. Оцениваемая конфигурация использует четырехканальные входные данные RGB-NIR (NRGB), многометочную классификацию на основе сигмоидной функции активации и комбинированную функцию потерь Binary Cross-Entropy (BCE) и Dice loss. Эксперименты проводятся на эталонном наборе данных Agriculture-Vision 2021, содержащем более 21 000 размеченных аэрофотоснимков с восемью классами сельскохозяйственных аномалий. Для оценки вклада NIR-канала и компонента Dice loss проводится контролируемое абляционное исследование. Дополнительные эксперименты сравнивают полученную конфигурацию с результатами, полученными при использовании стандартных архитектур U-Net, FCN, SegNet и современной базовой модели сегментации при идентичном протоколе экспериментов. Эффективность оценивается с использованием показателей Intersection over Union (IoU) для каждого класса и mean Intersection over Union (mIoU) для общей средней производительности. Результаты демонстрируют эффективность использования NIR-информации и функции потерь на основе Dice для сегментации аномалий в сельском хозяйстве, а также высокую эффективность относительно простой конфигурации на основе U-Net на эталонном наборе данных. Полученные результаты подтверждают потенциал использования специализированной структуры U-Net для автоматизированного мониторинга сельскохозяйственных угодий с помощью БПЛА и демонстрируют индивидуальный вклад входных данных и функции потерь в решение поставленной задачи.

Ключевые слова: семантическая сегментация, U-Net, аэрофотоснимки, обнаружение аномалий сельскохозяйственных полей, глубокое обучение, NRGB, мониторинг БПЛА, точное земледелие.

ФИЗИКАЛЫҚ ҒЫЛЫМДАР
PHYSICAL SCIENCES
ФИЗИЧЕСКИЕ НАУКИ

UDC 539.9; 537.5; 620.22
MRNTI 29.19.22

https://doi.org/10.55452/1998-6688-2026-23-3-378-387

[1]Abdullayeva K.,
BSc student, ORCID ID: 0009-0000-0247-9041,
e-mail: kamila.abdullayeva@nu.edu.kz
[1]Rustembekkyzy K.,
MSc, ORCID ID: 0000-0002-5173-6515,
e-mail: kuralay.rustembekkyzy@nu.edu.kz
[1]*Kanafin Y.N.,
PhD, ORCID ID: 0000-0002-1052-8533,
*e-mail: yerkanat.kanafin@nu.edu.kz
[1,2]Kaikanov M.,
PhD, ORCID ID: 0000-0003-1696-6953,
e-mail: marat.kaikanov@nu.edu.kz
[1]Nazarbayev University, Astana, Kazakhstan
[2]Institute of Functional Materials, Astana, Kazakhstan

SYNTHESIS AND PHOTOCATALYTIC ACTIVITY OF HIERARCHICAL FLOWER-LIKE ZNO FOR METHYLENE BLUE DEGRADATION UNDER UV LIGHT

Abstract

In this study, a porous, hierarchical flower-like zinc oxide (ZnO) structure was successfully synthesized via a hydrothermal method using urea and CTAB as shape-directing agents to optimize photocatalytic efficiency for environmental remediation. Structural characterization via scanning electron microscopy (SEM) and X-ray diffraction (XRD) confirmed the formation of a highly crystalline, pure hexagonal wurtzite phase assembled from ultrathin nanosheet building blocks. The photocatalytic performance of the synthesized ZnO was evaluated through the degradation of methylene blue (MB) dye under UV light illumination (365 nm). The catalyst achieved a (98.7 ± 0.5)% degradation efficiency within 40 minutes, following a pseudo-first-order kinetic model with a reaction rate constant of 0.109 min^{-1}. Optimization studies identified a catalyst dosage of 0.2 g/L as near-optimal, while coexistence tests demonstrated that the system maintains high stability and excellent removal efficiency in the presence of various competing environmental anions (Cl^-, NO_3^-, HCO_3^-, CO_3^{2-}). Radical scavenger investigations revealed a clear inhibition hierarchy, establishing that the degradation mechanism is predominantly driven by hydroxyl radical-mediated oxidation alongside secondary contributions from photogenerated holes. These findings highlight the prepared porous ZnO architecture as an efficient, stable, and sustainable candidate for the degradation of persistent organic pollutants in municipal wastewater.

Keywords: zinc oxide, hydrothermal synthesis, methylene blue, photocatalytic degradation, hierarchical nanostructures.

Received June 24, 2026; revised July 08, 2026; accepted July 17, 2026.

Introduction

The rapid progress of industrialization and global economic development has significantly improved living standards but has also led to the uncontrolled release of organic contaminants into the environment [1]. Among these pollutants, synthetic dyes like methylene blue (MB), which are extensively used in industries such as textiles, printing, paper, and cosmetics, represent an environmental risk [2] the effectiveness of ZnO-Mn-Ce/biochar as catalyst and activated by H2O2 for the removal of Methylene Blue (MB. MB is a stable aromatic compound that is highly toxic, potentially carcinogenic, and resistant to natural biodegradation [3] pore size, and oxygen defects. Its presence in water bodies blocks sunlight penetration, which harms aquatic ecosystems by impeding photosynthesis and ultimately leading to oxygen depletion [4].

While conventional wastewater treatment technologies, including membrane filtration, chemical reduction, and adsorption, have been successfully employed, they often suffer from limitations such as high energy consumption, high operational costs, and the generation of secondary sludge that requires further disposal [3] pore size, and oxygen defects. In this context, photocatalysis has emerged as a promising, green, and sustainable alternative for the complete mineralization of organic pollutants into harmless substances such as carbon dioxide and water under mild reaction conditions, using solar or ultraviolet energy [2] the effectiveness of ZnO-Mn-Ce/biochar as catalyst and activated by H2O2 for the removal of Methylene Blue (MB.

ZnO is widely recognized as a highly efficient n-type semiconductor photocatalyst due to its wide direct bandgap of approximately 3.37 eV, high exciton binding energy of 60 meV, high electron mobility, and excellent chemical stability [5, 6]. Compared to other metal oxides like TiO_2, ZnO is often more cost-effective and exhibits better light absorption across a broader range of the solar spectrum, making it a viable alternative for degrading persistent organic compounds [3, 6] pore size, and oxygen defects. However, the practical application of ZnO is frequently hindered by two major challenges: the fast recombination rate of photogenerated electron-hole pairs and a wide bandgap that limits its efficiency under visible light irradiation [4, 7].

To address these limitations, recent research has shifted toward the development of innovative nanostructures and hierarchical architectures [6]. Controlling the morphology of ZnO at the nanoscale is essential because the photocatalytic process is a surface-mediated reaction consisting of the adsorption of reactants, reactive radical generation, and the subsequent oxidation of pollutants [3] pore size, and oxygen defects. In particular, the synthesis of porous ZnO nanostructures has attracted significant attention [7]. Porous materials provide a significantly larger specific surface area compared to bulk ZnO, creating a high density of active sites for the generation of reactive oxygen species (ROS), such as hydroxyl radicals (•OH) and superoxide radical anions ($\bullet O^{2-}$) [8, 9].

Studies have shown that the pore size and distribution are critical determinants of photocatalytic performance [3] pore size, and oxygen defects. Mesoporous ZnO (pore sizes between 2 and 50 nm) is particularly effective as it facilitates the rapid mass transport and diffusion of reactant molecules and dissolved oxygen into the internal active sites of the catalyst [3, 7] pore size, and oxygen defects. Furthermore, 3D hierarchical architectures assembled from porous nanosheets can enhance light harvesting through repeated internal scattering and reflection within the cavities, while simultaneously preventing the aggregation of particles during the reaction [8, 10].

Various synthetic strategies have been established to produce these nanostructures, including hydrothermal, sol-gel, and precipitation methods [6, 11] as a widely used material in optics, electronics, and medicine, requires a complete overview of different conditions for facile and easily reproducible syntheses. Two types of optimization of ZnO hydrothermal preparation from zinc acetate and sodium hydroxide solution are presented, which allowed for obtaining miscellaneous morphologies of materials. The first was a temperature-controlled synthesis from 100 to 200 °C, using citric acid as a capping agent. The formation of hexagonal rods at the lowest temperature was evidenced, which agglomerated to flower-like structures at 110 and 120 °C. It was followed

by transformation to flake-like roses at 160 °C, up to disordered structures composed of nanosized plates (>180 °C. Among these, hydrothermal synthesis has gained popularity as a fast, simple, and cost-effective approach that provides homogeneous volumetric heating, significantly accelerating the reaction rates compared to conventional heating [4, 7]. This study explores the synthesis of porous ZnO particles designed specifically for the efficient photocatalytic degradation of MB. By optimizing the surface properties and porous structure of the catalyst, this research aims to provide new technical and theoretical insights into the design of advanced materials for dye wastewater remediation.

Materials and methods

For the synthesis, 400 mg of zinc nitrate hexahydrate ($Zn(NO_3)_2 \cdot 6H_2O$), 100 mg of urea, and 100 mg of hexadecyltrimethylammonium bromide (CTAB) were dissolved in 20 mL of deionized water under continuous stirring. The resulting homogeneous solution was transferred into a 40 mL Teflon-lined stainless-steel autoclave and subjected to hydrothermal treatment at 200 °C for 6 h in a convection oven. After naturally cooling to room temperature, the obtained precipitate was separated by centrifugation, thoroughly washed several times with deionized water and ethanol to remove residual organic species, and dried overnight at 60 °C. The dried material was subsequently annealed in air at 300 °C for 1 h with a heating rate of 5 °C min^{-1} to obtain the final ZnO product.

The crystalline structure and phase composition of the synthesized ZnO-400 were examined using a SmartLab X-ray diffractometer (Rigaku Corp., Japan). The morphology and hierarchical architecture of the samples were investigated by scanning electron microscopy (SEM, Crossbeam 540, Carl Zeiss, Germany).

The photocatalytic activity of ZnO-400 was assessed using MB as a model organic dye. For each experiment, 2 mg of the catalyst was dispersed in 10 mL of MB solution (3×10^{-5} M) and stirred in the dark for 60 min to establish adsorption-desorption equilibrium. After the adsorption step, the suspension was exposed to UV light irradiation at 365 nm using an 18 W lamp, and aliquots were collected at predetermined intervals of 10, 20, and 40 min. The degradation efficiency was determined by measuring the change in the maximum absorption peak of MB at 664 nm using a UV-Vis spectrophotometer (Thermo Fisher Scientific Inc., USA).

Results and discussion

Before detailed characterization, preliminary screening experiments were carried out to select the optimal precursor mass and to evaluate the necessity of post-synthesis annealing. Using ($Zn(NO_3)_2 \cdot 6H_2O$) precursor masses of 100, 200, and 400 mg, MB degradation after 20 min of UV irradiation reached 48.9%, 27.8%, and 58.8%, respectively, identifying 400 mg as the most effective precursor mass (denoted ZnO-400). In addition, the non-annealed sample achieved only 5.1% degradation after 20 min, compared to 58.8% for the annealed ZnO-400 sample, confirming that post-synthesis annealing at 300 °C is essential for achieving high photocatalytic activity, likely due to the removal of residual organic species (urea, CTAB) that would otherwise block active sites on the catalyst surface. Based on these results, ZnO-400 was selected for detailed structural characterization and photocatalytic evaluation. The surface morphology and hierarchical structure were observed using SEM at various magnifications (Figure 1).

The SEM images of the ZnO particles reveal a distinctive hierarchical flower-like architecture composed of interconnected thin nanosheets. At lower magnifications, these structures appear as complex three-dimensional assemblies resembling flowers, where numerous “petals” radiate from a central core to form a textured framework [12]. Upon closer inspection at higher magnification, these petals are identified as ultrathin nanosheets or plates with highly irregular edges, contributing to a significantly complex and potentially porous surface morphology. High-resolution imaging specifically quantifies the thickness of these individual building blocks, with measurements showing

values of approximately 29.11 nm and 39.51 nm, confirming their nanostructural nature. This unique morphology suggests that the hydrothermal conditions, combined with the presence of urea and the surfactant CTAB as shape-directing agents, successfully facilitated the growth of a high-surface-area framework assembled from these nanoscale sheets [13]. Then, the crystalline structure and phase orientation of the synthesized ZnO-400 particles were characterized by XRD (Figure 2).

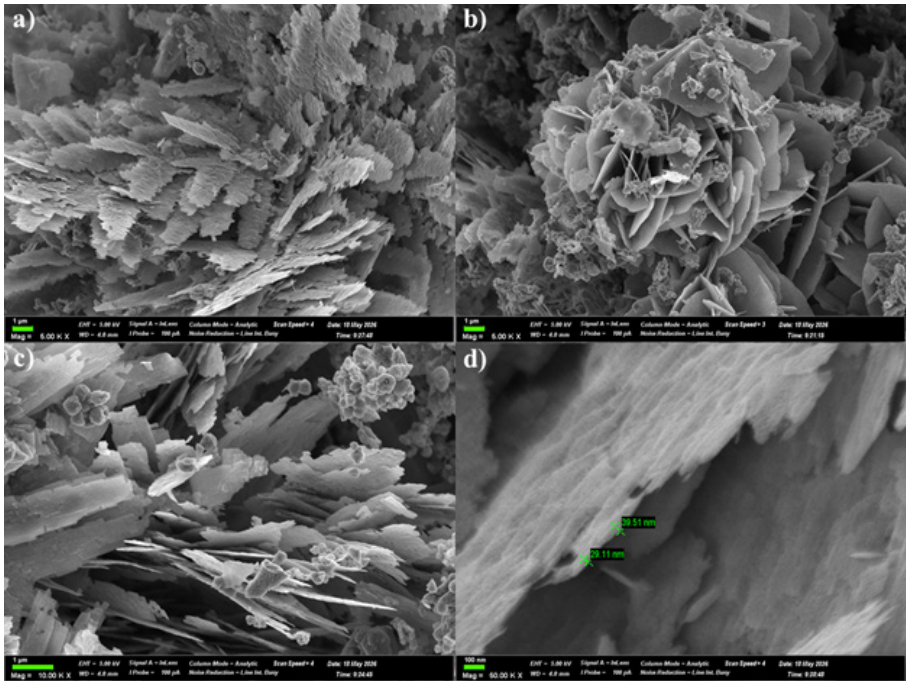


Figure 1 – SEM images of 400a-ZnO structures at different magnifications:
(a) and (b) 5,000; (c) 10,000; and (d) 50,000

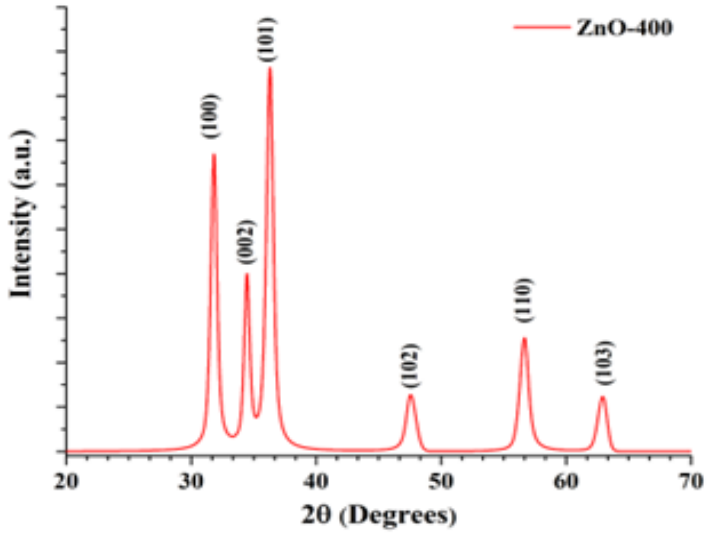


Figure 2 – XRD patterns of ZnO-400 particles

The XRD pattern for the ZnO-400 sample provides a detailed insight into the structural properties and phase purity of the synthesized material. The XRD pattern displays distinct diffraction peaks at 2θ values of approximately 31.8°, 34.4°, 36.3°, 47.6°, 56.6°, and 62.9°, corresponding to the (100), (002), (101), (102), (110), and (103) crystallographic planes, respectively. These reflections confirm the formation of the hexagonal wurtzite phase of ZnO and agree well with the ICSD reference card No. 01-076-8930 [14]. Notably, the (101) peak displays the highest relative intensity, a characteristic typical of the standard polycrystalline ZnO pattern with random grain orientation [4]. The average crystallite size of the synthesized particles was calculated using the Scherrer equation. It was found to be 12.51 ± 2.94 nm, confirming that the annealing at 300 °C was sufficient to achieve a well-ordered lattice. Furthermore, the absence of any extraneous peaks and the very low background noise in the pattern signify high phase purity, indicating that the washing steps and subsequent thermal treatment effectively removed all precursors, such as zinc nitrate, and organic additives like urea and CTAB.

The photocatalytic performance of ZnO-400 was assessed by monitoring the time-dependent degradation of MB under UV irradiation. The results were compared with the self-degradation control performed under UV light, as shown in Figure 3. The experimental procedure included a 60-minute dark adsorption phase (60 min) to establish an adsorption-desorption equilibrium.

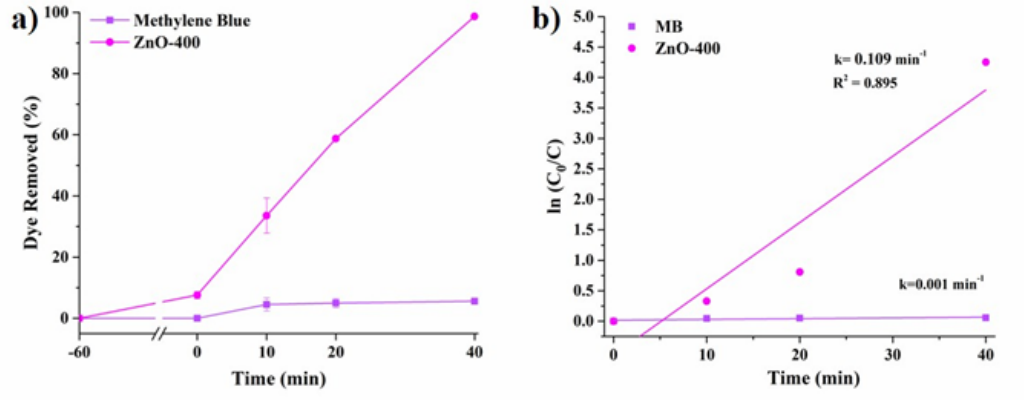


Figure 3 – Photodegradation of MB as a function
of irradiation time using ZnO-400 (0.2 g/L) (a) and kinetics (b)

Once light irradiation commenced, the ZnO-400 catalyst demonstrated a rapid and significant increase in photocatalytic activity, reaching (33.6 ± 5.8)% degradation within just 10 minutes and jumping to (58.8 ± 0.1)% by 20 minutes. By the conclusion of the 40-minute test, the ZnO-400 sample achieved a (98.7 ± 0.5)% degradation efficiency. In contrast, the control showed negligible self-degradation, reaching only (5.6 ± 0.3)% degradation after 40 minutes. This difference confirms that the dye is highly stable under light exposure and that the observed degradation is almost entirely facilitated by the ZnO catalyst. The excellent photocatalytic performance of ZnO-400 can be attributed to its hierarchical flower-like architecture composed of ultrathin nanosheets, which provides a large accessible surface area for dye adsorption and abundant active sites for the generation of reactive oxygen species, thereby promoting the efficient mineralization of the organic pollutants.

The photocatalytic degradation kinetics of MB were analyzed using the Langmuir–Hinshelwood model. The linear relationship between $\ln(C_0/C)$ and irradiation time (Figure 3b) indicates that the degradation process follows pseudo-first-order kinetics [15]. The reaction rate constant (k) for the ZnO-400 sample was determined to be 0.109 min^{-1}, which was 109 times higher than the rate constant

of the self-degradation of MB (k = 0.001 min^{-1}). This significant enhancement in the kinetic rate is directly related to the hierarchical flower-like morphology and the assembly of thin nanosheets identified in the SEM analysis, which provide a high specific surface area and abundant active sites for the generation of reactive oxygen species. By the 40-minute mark, the $\ln(C_0/C)$ value for ZnO-400 reached approximately 2.3, indicating a rapid and efficient degradation process compared to the negligible changes observed in the catalyst-free control. The high linearity of the ZnO-400 plot suggests a stable and consistent catalytic process throughout the duration of the experiment.

The photocatalytic performance of ZnO-400 compares favorably with recently reported ZnO-based systems. Khao et al. achieved 99% MB degradation using hydrothermally synthesized ZnO nanoparticles after 75 minutes of UV irradiation at 254 nm with a catalyst loading of 0.375 g/L [16]. Saadi et al. reported a degradation efficiency of 72.3% for methylene blue using sol-gel-derived ZnO nanoparticles under UV irradiation, which is lower than the 90.8% achieved by ZnO-400 in only 40 min. [17]. Krobthong et al. compared ZnO nanoparticles prepared by precipitation and combustion, obtaining apparent rate constants lower than the rate constant of 0.109 min^{-1} determined for ZnO-400 [18]. Atta et al. demonstrated 75% MB removal in 3 hours using ZnO thin films under UV irradiation [19]. The strong performance of ZnO-400 is attributed to the hierarchical flower-like architecture assembled from ultrathin nanosheets, which provides a higher active surface area and more efficient light harvesting compared to the conventional nanoparticle or thin-film morphologies used in these studies.

Next, the effects of catalyst dosage and the presence of various anions on MB photodegradation were studied (Figure 4).

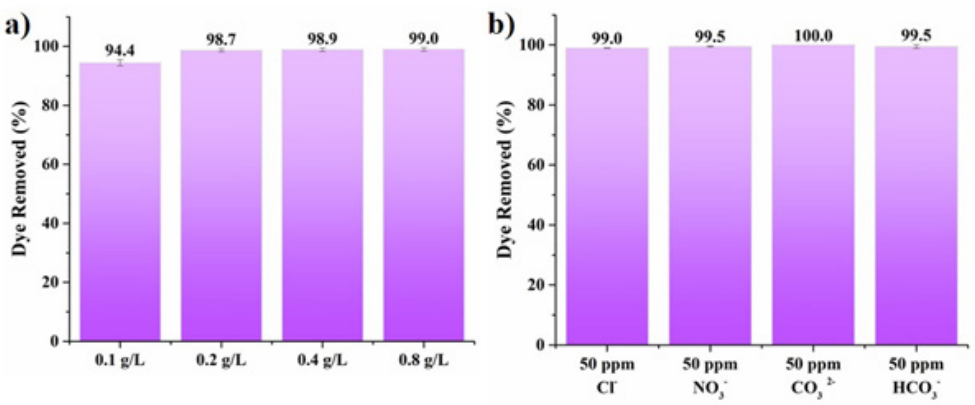


Figure 4 – MB photodegradation at different ZnO-400 catalyst dosages (a) and in the presence of various anions (ZnO 0.2 g/L) (b)

The effect of catalyst dosage on photocatalytic degradation was evaluated by varying the ZnO concentration from 0.1 to 0.8 g/L (Figure 4a). MB degradation increased from (94.4 ± 1.1)% to (99.0 ± 0.6)%, indicating that higher catalyst loadings provide more active sites and enhance reactive oxygen species generation. The most notable improvement occurred between 0.1 and 0.2 g/L, where degradation reached (98.7 ± 0.5)%. Beyond 0.2 g/L, only marginal gains were observed, suggesting that the system approached saturation and that factors such as light shielding and increased turbidity may limit further improvement [4, 14]. Therefore, 0.2 g/L can be considered a near-optimal catalyst dosage, providing high degradation efficiency while maintaining efficient light utilization and cost-effectiveness. The analysis of the interfering ions (Figure 4b) shows that MB degradation remained high in the presence of common anions (50 ppm), with degradation efficiencies of (99.0 ± 0.1)% for

Cl^-, (99.5 ± 0.2)% for NO_3^-, (99.5 ± 0.6)% for HCO_3^-, and 100% for CO_3^{2-}. The minimal variation among different ions indicates that coexisting anions have little influence on the photocatalytic process. This high tolerance to interfering species highlights the potential of the ZnO-400 catalyst for practical wastewater treatment applications.

The analysis of the scavenger radicals identifies the primary reactive species driving the dye degradation process by observing the reduction in degradation efficiency upon the addition of specific quenching agents (Figure 5) [1, 16].

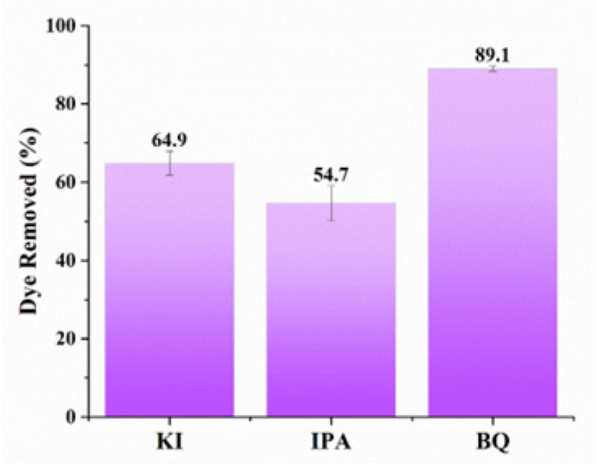


Figure 5 – Effects of radical scavengers (10 mM each)
on MB photodegradation by ZnO-400 (0.2 g/L).

The most significant suppression occurs with the addition of isopropanol (IPA), which drops the degradation efficiency to (54.7 ± 4.4)%, indicating that hydroxyl radicals (•OH) are the dominant oxidative species in the system. Potassium iodide (KI), used to scavenge holes (h^+) and surface-bound hydroxyl radicals, results in an MB degradation of (64.9 ± 3.1)%, suggesting that photogenerated holes also play a substantial secondary role in the reaction mechanism. Conversely, the addition of benzoquinone (BQ) has the least inhibitory effect, with the system still achieving (89.1 ± 0.6)% dye degradation, which reveals that superoxide radicals ($•O^{2-}$) are the least significant contributors to the overall degradation process. This hierarchy of inhibition (IPA > KI > BQ) clearly establishes a mechanism primarily governed by hydroxyl radical-mediated oxidation, supplemented by direct hole oxidation.

Conclusions

Porous flower-like ZnO structures were successfully synthesized via the hydrothermal method and exhibited excellent photocatalytic activity toward MB degradation. Structural characterization confirmed the formation of highly crystalline hexagonal wurtzite ZnO assembled from ultrathin nanosheets, providing a large active surface area for photocatalytic reactions. Under UV irradiation, the catalyst achieved (98.7 ± 0.5)% MB degradation within 40 min and followed pseudo-first-order kinetics with a rate constant of 0.109 min^{-1}. The optimal catalyst dosage was 0.2 g/L, and the photocatalytic performance was largely unaffected by the presence of common inorganic anions. Scavenger experiments revealed that hydroxyl radicals were the primary reactive species, with photogenerated holes also contributing to degradation. These findings demonstrate that the synthesized ZnO structures are promising photocatalysts for the efficient treatment of dye-contaminated wastewater.

Acknowledgments

The technical support of the Core Facilities of Nazarbayev University is greatly appreciated.

Information on funding

This research has been funded by the Committee of Science of the Ministry of Science and Higher Education of the Republic of Kazakhstan (Grant No. BR28712489).

REFERENCES

1 Masuleh, M.T., Hasheminiasari, M., Ashiri, R. Enhanced Photocatalytic Efficiency of Eco-Friendly Synthesized ZnO for Rapid Full Degradation of Methylene Blue Dye. Materials Advances, 6(8), 2611–2621 (2025). https://doi.org/10.1039/d5ma00026b

2 Saraee, M., Maleki, B., Kikhavani, T., Mansouri, M. Investigating the Process of Photocatalytic Removal of Methylene Blue from Wastewater Utilizing ZnO-Mn-Ce/Biochar Nanocomposites under Visible Light. Iranian Journal of Chemistry and Chemical Engineering, 43(12), 4360–4377 (2024). https://doi.org/ijcce.2024.2026808.6552

3 He, X., Yang, Y., Li, Y., Chen, J., Yang, S., Liu, R., Xu, Z. Effects of Structure and Surface Properties on the Performance of ZnO towards Photocatalytic Degradation of Methylene Blue. Applied Surface Science, 599, 153898 (2022). https://doi.org/10.1016/j.apsusc.2022.153898

4 Rustembekkyzy, K., Sabyr, M., Kanafin, Y.N., Khamkhash, L., Atabaev, T.S. Microwave-Assisted Synthesis of ZnO Structures for Effective Degradation of Methylene Blue Dye under Solar Light Illumination. RSC Advances, 14(23), 16293–16299 (2024). https://doi.org/10.1039/d4ra02451f

5 Qian, S.; Bao, E.; Chen, H. Facile Preparation of Porous ZnO Microflowers with Large Surface Area. Materials Letters, 330, 133347 (2023). https://doi.org/10.1016/j.matlet.2022.133347

6 Zhu, C., and Wang, X. Nanomaterial ZnO Synthesis and Its Photocatalytic Applications: A Review. Nanomaterials, 15(9), 682 (2025). https://doi.org/10.3390/nano15090682

7 Ferreira, S.H., Morais, M., Nunes, D., Oliveira, M.J., Rovisco, A., Pimentel, A., Águas, H., Fortunato, E., Martins, R. High UV and Sunlight Photocatalytic Performance of Porous ZnO Nanostructures Synthesized by a Facile and Fast Microwave Hydrothermal Method. Materials, 14(9), 2385 (2021). https://doi.org/10.3390/ma14092385

8 Li, L., Han, L., Han, Y., Yang, Z., Su, B., Lei, Z. Preparation and Enhanced Photocatalytic Properties of 3D Nanoarchitectural ZnO Hollow Spheres with Porous Shells. Nanomaterials, 8(9), 687 (2018). https://doi.org/10.3390/nano8090687

9 Modi, S., Yadav, V.K., Amari, A., Alyami, A.Y., Gacem, A., Harharah, H.N., Fulekar, M.H. Photocatalytic Degradation of Methylene Blue Dye from Wastewater by Using Doped Zinc Oxide Nanoparticles. Water, 15(12), 2275 (2023). https://doi.org/10.3390/w15122275

10 Lei, A., Qu, B., Zhou, W., Wang, Y., Zhang, Q., Zou, B. Facile Synthesis and Enhanced Photocatalytic Activity of Hierarchical Porous ZnO Microspheres. Materials Letters, 66(1), 72–75 (2012). https://doi.org/10.1016/j.matlet.2011.08.011

11 Ejsmont, A. and Goscianska, J. Hydrothermal Synthesis of ZnO Superstructures with Controlled Morphology via Temperature and PH Optimization. Materials, 16(4), 1641 (2023). https://doi.org/10.3390/ma16041641

12 Guzmán-Carrillo, H.R., Rivera-Muñoz, E.M., Cayetano-Castro, N., Herrera-Basurto, R., Barquera-Bibiano, Z., Mercader-Trejo, F., Manzano-Ramírez, A. Facile Control of ZnO Nanostructures by Varying Molar Concentration of Zinc Acetate. Materials Research Bulletin, 90, 138–144 (2017). https://doi.org/10.1016/j.materresbull.2017.02.034

13 Kadau, A.T., Kalkozova, Z.K., Gritsenko, L.V., Markhabayeva, A.A., Abdullin, K.A. Influence of Parameters of Low-Cost Synthesis Methods on Zinc Oxide Morphology. Herald of the Kazakh-British Technical University, 22(3), 290–301 (2025). https://doi.org/10.55452/1998-6688-2025-22-3-290-301

14 Kanafin, Y.N., Rustembekkyzy, K., Seiilbek, A., Kutzhanova, K., Atabaev, S., Kaikanov, M., Atabaev, T.S. ZnO/WO3 Composite for Efficient Photocatalytic Degradation of Methylene Blue Dye under Solar Light. Scientific Reports, 16, 8702 (2026). https://doi.org/10.1038/s41598-026-40207-0

15 Negash, A., Mohammed, S., Weldekirstos, H.D., Ambaye, A.D., Gashu, M. Enhanced Photocatalytic Degradation of Methylene Blue Dye Using Eco-Friendly Synthesized RGO@ZnO Nanocomposites. Scientific Reports, 13, 22234 (2023). https://doi.org/10.1038/s41598-023-48826-7

16 Khao, T.; Gembo, R.O.; Odisitse, S.; King'ondu, C.K. Fabrication of ZnO Nanoparticles Using Marula (Sclerocarya Birrea) Leaf Extract for Catalytic Degradation of Rhodamine 6 G and Methylene Blue Dyes under UV Light Irradiation. Next Materials, 7, 100366 (2025), https://doi.org/10.1016/j.nxmate.2024.100366

17 Saadi, H., Atmani, E.H., Fazouan, N. Enhanced Photocatalytic Degradation of Methylene Blue Dye by ZnO Nanoparticles: Synthesis, Characterization, and Efficiency Assessment. Environmental Progress and Sustainable Energy, 44(1), e14529 (2025). https://doi.org/10.1002/ep.14529

18 Krobthong, S., Rungsawang, T., Wongrerkdee, S. Comparison of ZnO Nanoparticles Prepared by Precipitation and Combustion for UV and Sunlight-Driven Photocatalytic Degradation of Methylene Blue. Toxics, 11(3), 266 (2023). https://doi.org/10.3390/toxics11030266

19 Atta, D., Wahab, H.A., Ibrahim, M.A., Battisha, I.K. Photocatalytic Degradation of Methylene Blue Dye by ZnO Nanoparticle Thin Films, Using Sol–Gel Technique and UV Laser Irradiation. Scientific Reports, 14, 26961 (2024). https://doi.org/10.1038/s41598-024-76938-1

[1]Абдуллаева К.,
студент, ORCID ID: 0009-0000-0247-9041,
e-mail: kamila.abdullayeva@nu.edu.kz
[1]Рүстембекқызы Қ.,
магистр, ORCID ID: 0000-0002-5173-6515,
e-mail: kuralay.rustembekkyzy@nu.edu.kz
[1*]Канафин Е.Н.,
PhD, ORCID ID: 0000-0002-1052-8533,
*e-mail: yerkanat.kanafin@nu.edu.kz
[1,2]Кайканов М.,
PhD, ORCID ID: 0000-0003-1696-6953,
e-mail: marat.kaikanov@nu.edu.kz

[1]Назарбаев университеті, Астана қ., Қазақстан
[2]Функционалды материалдар институты, Астана қ., Қазақстан

МЕТИЛЕН КӨГІН УК-СӘУЛЕ АСТЫНДА ЫДЫРАТУҒА АРНАЛҒАН ИЕРАРХИЯЛЫҚ ГҮЛ ТӘРІЗДІ ZNO СИНТЕЗІ ЖӘНЕ ОНЫҢ ФОТОКАТАЛИТИКАЛЫҚ БЕЛСЕНДІЛІГІ

Аңдатпа

Зерттеуде қоршаған ортаны тазартудағы фотокаталитикалық тиімділікті арттыру мақсатында несепнәр мен CTAB-ты пішін түзуші агенттер ретінде пайдалана отырып, гидротермиялық әдіспен кеуекті, иерархиялық гүл тәрізді мырыш оксиді (ZnO) құрылымы сәтті синтезделді. Сканерлеуші электрондық микроскопия (SEM) және рентгендік дифракция (XRD) нәтижелері аса жұқа нанопарақшалардан құралған жоғары кристалдық таза гексагональды вюрцит фазасының түзілгенін растады. Синтезделген ZnO-дың фотокаталитикалық қасиеттері 365 нм УК-сәуле әсерінде метилен көгін (MB) ыдырату арқылы зерттелді. Катализатор 40 минут ішінде бояғыштың (98.7 ± 0.5)%-ын ыдыратып, реакция жылдамдығының тұрақтысы 0.109 мин$^{-1}$ болатын жасанды бірінші ретті кинетикалық модельге сәйкес жоғары белсенділік көрсетті. Оңтайландыру зерттеулері катализатордың 0.2 г/л мөлшері тиімді екенін анықтады. Сонымен бірге, қатар жүретін иондардың әсерін зерттеу нәтижелері жүйенің әртүрлі қоршаған орта аниондарының (Cl^-, NO_3^-, HCO_3^-, CO_3^{2-}) қатысуында да жоғары тұрақтылық пен тиімділікті сақтайтынын көрсетті. Белсенді бөлшектерді тұзақтау тәжірибелері деградация механизмі негізінен гидроксил радикалдарының (•OH) тотығу әрекетімен жүзеге асатынын, ал фотогенерацияланған кемтіктердің (h^+) қосымша үлес қосатынын анықтады. Алынған

нәтижелер синтезделген кеуекті ZnO құрылымының коммуналдық ағынды сулардағы тұрақты органикалық ластағыштарды ыдыратуға арналған жоғары тиімді, тұрақты және экологиялық қауіпсіз фотокатализатор екенін көрсетеді.

Түйін сөздер: мырыш оксиді, гидротермиялық синтез, метилен көгі, фотокаталитикалық ыдырау, иерархиялық наноқұрылымдар.

[1]Абдуллаева К.,
студент, ORCID ID: 0009-0000-0247-9041,
e-mail: kamila.abdullayeva@nu.edu.kz
[1]Рүстембекқызы Қ.,
магистр, ORCID ID: 0000-0002-5173-6515,
e-mail: kuralay.rustembekkyzy@nu.edu.kz
[1]*Канафин Е.Н.,
PhD, ORCID ID: 0000-0002-1052-8533,
*e-mail: yerkanat.kanafin@nu.edu.kz
[1,2]Кайканов М.,
PhD, ORCID ID: 0000-0003-1696-6953,
e-mail: marat.kaikanov@nu.edu.kz

[1]Назарбаев Университет, г. Астана, Казахстан
[2]Институт функциональных материалов, г. Астана, Казахстан

СИНТЕЗ И ФОТОКАТАЛИТИЧЕСКАЯ АКТИВНОСТЬ ИЕРАРХИЧЕСКОГО ЦВЕТКОПОДОБНОГО ZNO ДЛЯ ДЕГРАДАЦИИ МЕТИЛЕНОВОГО СИНЕГО ПОД ДЕЙСТВИЕМ УФ-ИЗЛУЧЕНИЯ

Аннотация

В данной работе методом гидротермального синтеза с использованием мочевины и цетилтриметиламмоний бромида (CTAB) в качестве структурообразующих агентов была успешно получена пористая иерархическая цветкоподобная структура оксида цинка (ZnO), предназначенная для повышения фотокаталитической эффективности в процессах очистки окружающей среды. Структурная характеристика с использованием сканирующей электронной микроскопии (SEM) и рентгеновской дифракции (XRD) подтвердила формирование высококристаллической чистой гексагональной фазы вюрцита, состоящей из ультратонких нанолистов. Фотокаталитическая активность синтезированного ZnO была исследована на примере деградации красителя метиленового синего (MB) под воздействием ультрафиолетового излучения (365 нм). Катализатор обеспечил высокую степень разложения красителя – (98.7 ± 0.5)% за 40 минут, при этом процесс подчинялся кинетической модели псевдопервого порядка с константой скорости реакции 0.109 мин$^{-1}$. Исследования по оптимизации показали, что дозировка катализатора 0.2 г/л является близкой к оптимальной. Тесты на совместное присутствие ионов продемонстрировали высокую стабильность системы и эффективность удаления загрязнителя в присутствии различных конкурирующих анионов окружающей среды (Cl^-, NO_3^-, HCO_3^-, CO_3^{2-}). Исследования с использованием ловушек активных частиц выявили выраженную иерархию ингибирования, показав, что механизм деградации преимущественно определяется окислением с участием гидроксильных радикалов (•OH), при дополнительном вкладе фотогенерированных дырок (h^+). Полученные результаты свидетельствуют о том, что синтезированная пористая архитектура ZnO является высокоэффективным, стабильным и экологически устойчивым материалом для удаления стойких органических загрязнителей из коммунальных сточных вод.

Ключевые слова: оксид цинка, гидротермальный синтез, метиленовый синий, фотокаталитическая деградация, иерархические наноструктуры.

UDC 533.9
IRSTI 29.27.35

https://doi.org/10.55452/1998-6688-2026-23-3-388-397

[1]*Tazhen A.B.,
PhD, ORCID ID: 0000-0002-3277-2086,
*e-mail: Aigerim@physics.kz
[1]Kholmirzayev A.N.,
PhD student, ORCID ID: 0009-0003-4108-0879,
e-mail: kholmirzayev.abdulla@gmail.com
[2]Ussenov Y.A.,
PhD, ORCID ID: 0000-0001-7903-8674,
e-mail: yerbolat@physics.kz
[1]Dosbolayev M.K.,
Cand. Phys. Math. Sc., Prof., ORCID ID: 0000-0002-0724-1793,
e-mail: merlan@physics.kz
[1]Ramazanov T.S.,
Dr. Phys. Math. Sc., Prof., ORCID ID: 0009-0009-2301-1152,
e-mail: ramazan@physics.kz

[1]National Nanotechnology Laboratory of Open Type, al-Farabi Kazakh National University, Almaty, Kazakhstan
[2]Princeton Plasma Physics Laboratory, Princeton University, Princeton, USA

STUDY OF CHANGES IN MICROHARDNESS AND MASS OF A PREHEATED TUNGSTEN UNDER THE INFLUENCE OF PULSED PLASMA

Abstract

The paper presents the results of an experimental investigation of changes in the microhardness and mass of a preheated tungsten target, the primary candidate material for the first wall and divertor, subjected to a pulsed plasma flow of approximately 0.2 ms duration. The experiments were conducted as a series of 13 pulses, each with an energy density and power density of approximately 1.1 MJ/m^2 and 5.5 GW/m^2, respectively. Microhardness was measured using an HVS-1000B hardness tester; the target mass before and after plasma exposure was measured using a CPA225D precision balance. It is shown that the microhardness of the tungsten target remains virtually unchanged even at the maximum irradiation dose (up to 39 pulses), and the observed change is within the measurement error, which indicates the structural stability of the surface layer. At the same time, an increase in the target mass (up to 31 mg) was recorded, probably caused by contamination and redeposition of the material of external structural components. Energy-dispersive spectroscopy (EDS) analysis revealed Cu, Zn, Ni, and C lines in dust particles redeposited on the target surface. The results indicate that these foreign components have a significant impact on surface morphology and should be considered when interpreting tungsten damage mechanisms.

Key words: pulsed plasma accelerator, plasma flow, preheated tungsten target, microhardness, target mass, elemental composition of the target.

Received May 08, 2026; revised July 07, 2026; accepted July 10, 2026.

Introduction

Despite the large number of experimental studies conducted on simulation facilities and operating tokamaks, the study of plasma interactions with materials has not lost its relevance and continues to attract the attention of researchers due to the construction of experimental fusion reactors such as

ITER and DEMO [1–5]. In the conditions of high-density, high-temperature fusion plasma, materials in contact with plasma are expected to experience extreme plasma-thermal loads [6, 7]. According to the technical characteristics of the ITER reactor, beryllium (Be) was selected as the metallic material for the armor of the first wall due to its low atomic number Z [8]. However, in early 2025, ITER reconsidered the use of beryllium due to potential risks associated with its toxicity and high erosive properties [9]. The latest update to the technical solutions of the ITER project includes replacing the beryllium wall with a tungsten one [10]. This solution meets the stringent requirements for materials in contact with plasma. First, the material must have high strength and structural stability under extreme operating conditions.

Tungsten is known to be the most refractory of metals; however, it is vulnerable to plasma exposure. When plasma interacts with a tungsten target, a change in the surface properties is observed, followed by a change in the target mass [11–13]. This may be due to structural changes in the material. In this regard, a significant number of microstructural studies have been conducted to understand the response of different types of tungsten to plasma and other types of irradiations (e.g. laser, etc.). It was found that the average surface hardness of the initial target made of a heavy tungsten alloy decreases at the initial level of the plasma beam power density (0.108 MW/m^2). An increase in power density by 1 MW/m^2 is accompanied by a linear increase in the average surface hardness. In [14], it is shown that this effect is due to an increase in the density of dislocation lines. In [15], the change in microhardness in tungsten monoblock samples was investigated as a function of the heat flux penetration depth at a power density of 10 MW/m^2. As follows from [15], no noticeable changes were observed inside the tungsten before and after exposure to a heat flux (at a depth of 200 μm to 6.8 mm); however, a noticeable decrease in mechanical strength was observed near the surface, manifested in a decrease in hardness. The results presented in [16] indicate an insignificant decrease in the microhardness of the surface layer of a single-crystal tungsten sample (up to 15% after irradiation with pulsed helium plasma flows using the Vikhr facility). According to the authors, this is due to the formation of a crystallization texture in the surface layer. Analysis of these data allows us to conclude that pure tungsten is characterized by structural instability in the plasma thermal impact zone. This is reflected in the hardness of this material. Several studies [17–19] have examined in detail the methods for increasing the hardness of tungsten materials in contact with plasma using additives such as carbon, yttrium oxide, and some metals (Ni, Co, Cr) characterized by appropriate ductility and high-temperature strength.

The paper presents the results of an experimental study of changes in the microhardness and mass of a preheated tungsten target depending on the number of plasma pulses.

Materials and methods

A PW-7 pulsed plasma accelerator was used as a source of plasma flow for irradiating a preheated tungsten target [20, 21]. The accelerator was equipped with coaxial copper electrodes separated by an insulator [22]. A bank of capacitors with a total capacitance of 1.4 mF and charged to a voltage of 5 kV was connected to an RVU-43 vacuum spark gap. A Rogowski coil was installed around the current-carrying part of the plasma accelerator to measure the discharge current. The maximum value of the discharge current reached approximately 100 kA. In the experiments under consideration, the tungsten target was exposed to hydrogen plasma with the following parameters: electron temperature $T_e \approx$23-40 eV and charged particle concentration $n_e \approx 10^{15}$ cm^{-3} [22, 23]. The plasma flow velocity in the accelerator varied in the range of $10^4 – 3 \cdot 10^4$ m/s [24, 25].

A 1.5 × 1.5 cm^2, 2 mm thick plate made of high-purity (99.96%) hot-rolled polycrystalline tungsten was used as a target. The average grain size, determined from scanning electron microscope (SEM) images, is approximately 2 μm. The target was located 22 cm from the electrode system. The surface of the tungsten plate was polished mechanically and electrochemically using abrasive paper and a KOH solution. Irradiation was carried out in three series of 13 plasma pulses each, with a peak energy density of 1.1 MJ/m^2 and a pulse duration of about 0.2 ms [20]. In this study, a tungsten sample

was exposed to a relatively small number of pulses. This value was chosen taking into account the aim of this study, which was to investigate the initiation stage of tungsten damage under the influence of thermal loads similar to ELM discharges. A special holder with a preheating system was used to position the tungsten plate inside the vacuum chamber [21]. The heating system included a thick tantalum plate (40 μm thick) heated by an electric current passing through conducting contacts. A heat-resistant ceramic insulator was installed between the tantalum and tungsten plates. Before and during plasma irradiation, the tungsten plate temperature was maintained at 823 K, ensuring conditions above the ductile-to-brittle transition temperature. This temperature regime was maintained between experimental series with a tolerance of ±41 K. A type K (chromel-alumel) thermocouple was used for temperature control. Before starting the operation, the vacuum chamber was evacuated to a pressure of 10^{-4} Torr using a pre- and diffusion pump. The chamber was then filled with working gas. When a control voltage pulse was applied between the main and the trigger electrodes of the spark gap, the gas in the interelectrode gap ionized and accelerated toward the target. Plasma streams irradiated the surface along their normal, as shown in Figure 1.

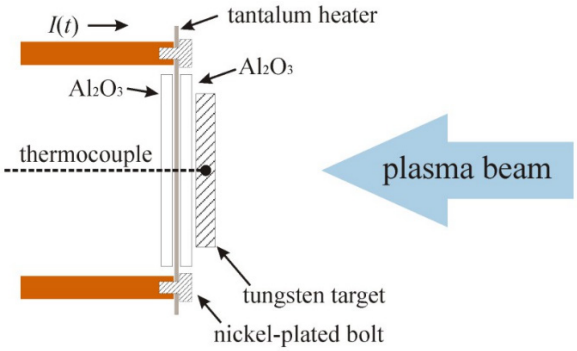


Figure 1 – Schematic diagram of the
setup for plasma irradiation of a tungsten target [21]

The microhardness of the irradiated surface of the tungsten plate was measured by the Vickers method using a Vickers hardness tester HVS-1000B. The measurement error along the indentation diagonal was δd = ±0.2 μm. The microhardness measurement error was calculated taking into account the spread of the measurement error along the diagonal indentation and determining using the formula , which was no more than 1%. To measure the mass of the tungsten plate, a CPA225D precision scale with an accuracy of δm = ±0.01 mg was used. Energy-dispersive spectroscopy (EDS) was used to determine the chemical composition of the tungsten plate.

Results and discussion

Under operating conditions in a fusion reactor, the materials of the first wall and divertor are subjected to extreme plasma and thermal loads. Under these conditions, microhardness is a key parameter determining the performance and durability of candidate materials, as it is directly related to resistance to plastic deformation, erosion, cracking, and surface degradation. Microhardness changes under repeated plasma pulses reflect the evolution of the material's structure, including hardening, recrystallization and defect accumulation. The dependence of tungsten target microhardness on the number of plasma and thermal loads exposures is shown in Figure 2. Before and after irradiation, 10 microhardness measurements were performed in each case. Figure 2 shows the mean values and corresponding standard deviations.

Before irradiation, the microhardness of the tungsten target was 514.8±5 HV, which corresponds to a hardened state of the material compared to annealed tungsten. As shown in Figure 2, in all three series of irradiation with different numbers of pulses (13, 26 and 39), the microhardness value changes within the measurement error (≈ 0.0027 – 0.0056 ≈ 0.27-0.56 % ($\Delta HV_1 = HV_0 - HV_{13} =$

1.4 HV change towards increase, $\Delta HV_2 = HV_0 - HV_{26} = 0$ HV, $\Delta HV_3 = HV_0 - HV_{39} = 2.9$ HV change towards decrease) and does not indicate any significant changes in the mechanical properties of the tungsten target.

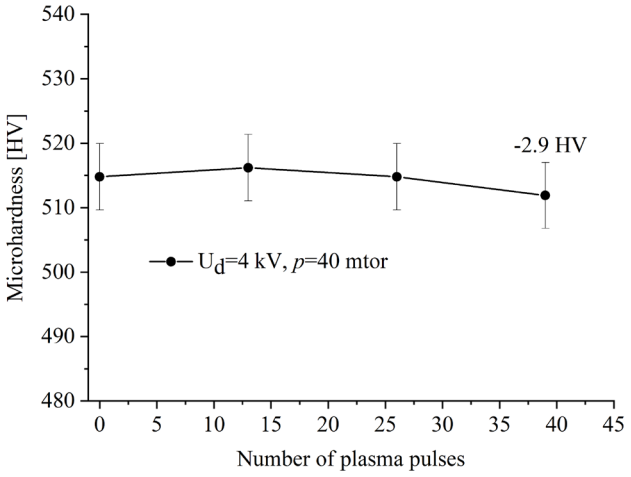


Figure 2 – Microhardness values of a tungsten target before and after irradiation

An analysis of the surface morphology using scanning electron microscopy has previously shown [21] that exposure to pulsed plasma flows leads to the formation of cracks on the surface of a tungsten target. This result indicates the localized internal residual stresses in the near-surface layer. Despite this, no increase in microhardness was observed. The crack thickness was very small – up to several hundred nanometers. This indicates insignificance of local stresses. Consequently, stresses are likely effectively redistributed during target cooling and, thus, have no noticeable effect on microhardness. It has previously been experimentally demonstrated [20, 21] that the crack size on the surface of a tungsten target does not change significantly with increasing pulse number. This effect was observed under controlled temperature conditions, such that the minimum initial temperature of the backside of the tungsten target does not fall below a specified value, T_{DBTT}. This result indicates that with increasing irradiation dose, residual stress between the irradiated layer and the preheated part of the target do not tend to increase further but rather tend to relax. Thus, the observed behavior qualitatively explains the experimental microhardness data. It should be noted that the Vickers indentation size is several tens of micrometers (42–43 μm), while the observed crack openings are significantly smaller. Consequently, the measured microhardness may be determined primarily by the properties of the surrounding material, and the contribution of localized surface defects may be insufficient to detect statistically significant changes.

The results of microhardness measurements were compared with the data presented in [14–16]. In contrast to studies that reported changes in the microhardness of the subsurface layer of tungsten after cyclic exposure to an electron beam and plasma, this study revealed no significant changes in microhardness after repeated exposure. This is explained by the specific conditions under which the tungsten studies were conducted. It should be noted that the temperature regime used in our experimental conditions leads to a change in the response of tungsten to plasma exposure. The observed discrepancies between the present results and the data from [14, 15] are also explained by variations in the irradiation parameters. In [14], tungsten targets were continuously irradiated for 15 min, whereas in [15], tungsten monoblock mock-ups were irradiated with approximately 5000 cycles, each with a duration of 10 s followed by a 10 s cooling interval. The tests were conducted at power densities of 1 and 10 MW/m^2. It should be noted that the aim of [15] was distinct from that of the present study. That study focused on tokamak operation in the long pulse mode, where the plasma

exposure is very similar to the annealing process. In contrast, this study examines significantly shorter pulses that produce thermal shock effects. Consequently, the present work revealed loss of crystallinity and grain fragmentation, whereas in [15], the repeated heating and cooling cycles likely contributed to reorganization of the microstructure, gradual coarsening of grains and, as a result, a decrease in microhardness. Furthermore, cooling of the tungsten monoblocks is an inherent aspect of the tokamak operating conditions and was probably one of the factors taken into account by the authors [15]. In terms of the impact parameters, the study [16] is the closest to the present study; it also reports a slight decrease in the microhardness of the tungsten surface layer (up to 15%). The authors interpret this effect to radiation-thermal remelting of the surface layer and subsequent directional solidification. During cooling, a crystalline texture is formed, oriented along the temperature gradient, which is accompanied by microstructural rearrangement and partial relaxation of accumulated defects.

Although a complete comparison of the results is impossible due to differences in the experimental conditions, the data obtained indicate that the temperature regime implemented in this study, as in [16], creates favorable conditions for the relaxation of defects and internal stresses. This is consistent with the fact that at temperatures above the DBTT, the mechanical properties of tungsten change significantly, which may contribute to the retention of microhardness after repeated exposure.

Exposure to pulsed plasma flows significantly affects the surface of the material being processed, leading to changes in surface morphology. As shown in [26, 27], short plasma pulses can cause tungsten melting, leading to ablation, accompanied by mass loss in the samples. The main contribution to this process is erosion caused by the ejection of molten droplets and solid fragments of the material. The dependence of the change in tungsten target mass on the number of plasma irradiations is shown in Figure 3. The following pattern was observed: after 13, 26, and 39 pulses, a steady increase in target mass was observed. After 39 pulses, the tungsten target mass increased by $\Delta m_{39} = +31$ mg compared to the initial value. Considering the measurement error of the electronic scale, this change can be considered a reliable quantitative result. The observed mass increase may be due to the deposition of erosion products and redeposition of material in the target's near-surface layer, indicating a complex balance between erosion and redeposition processes under pulsed plasma exposure.

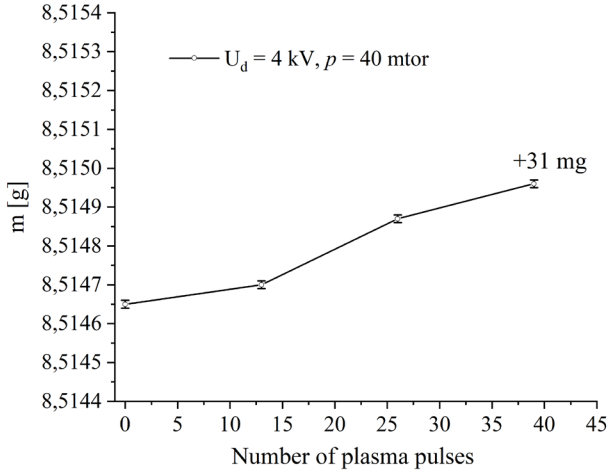


Figure 3 – Dependence of the mass of
a tungsten target on the number of plasma exposures

Accordingly, this can be explained by the fact that impurity transport and deposition of impurities on the surface by the plasma flow, together with the above-mentioned processes, strongly influence the observed behavior. Figure 4 shows an image of a target surface area after exposure to pulsed plasma, obtained using a scanning electron microscope, as well as the results of energy-dispersive spectroscopy (EDS) analysis of the localized area highlighted in the micrograph.

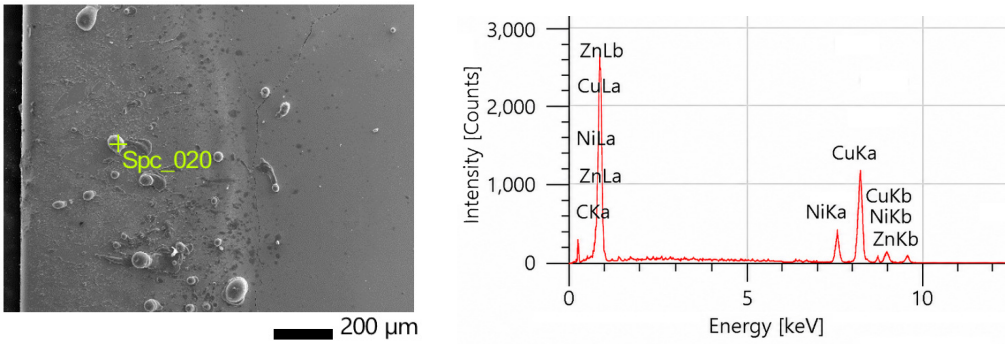


Figure 4. a) SEM image of the surface of a tungsten target after 39 irradiations,
b) elemental composition of the area indicated in the SEM image

It should be mentioned that the analyzed area is situated near the sample holder, so this must be taken into account when interpreting the elemental composition of the surface. On the irradiated surface of the tungsten plate, numerous spheroidal formations are observed, having the morphology of solidified drops of molten metal. The size of these particles in the analyzed region is approximately 40–45 µm. The shape of these particles may indicate the following process: the material melted during the discharge, was then transferred to the target surface, and solidified into droplets. The obtained EDS spectrum of the analyzed local region containing these particles reveals intense Cu, Zn, and Ni lines, as well as a weak C peak. The presence of copper, zinc and nickel indicates that the observed droplets are associated not only with processes occurring within the tungsten target itself, but also with the transfer of material from the components of the holder or other structural elements of the experimental setup. Thus, the observed change in the mass of the tungsten plate is likely due to local heating, melting and sputtering of materials, followed by the deposition of metallic particles onto the tungsten surface during plasma exposure. However, the obtained results do not allow us to unambiguously determine the origin of the detected particles, although they indicate the possible involvement of additional sources of material in addition to the tungsten target. Although plasma exposure typically results in surface erosion, in this case, the contribution of redeposited material may partially offset or even exceed the mass of tungsten removed. This is particularly likely for areas located close to the holder, where the probability of melted or evaporated structural material particles depositing on the target surface is higher. The mass of deposited droplets can be approximately estimated by assuming them are spherical particles. The average diameter of clearly visible spherical droplets of molten metal is approximately 40-45 µm. The mass of a single spherical particle is estimated at 0.3-0.4 µg, given a metal density of approximately 8.5-8.9 g/cm^3. These particles are localized in significant quantities around the metal holder on both sides of the tungsten target. As shown in Figure 4a, the particle density in the region under investigation is approximately 14.6 particles/mm^2. The obtained estimate suggests that at such a particle density, their contribution to the observed mass increase may be insufficient to explain the measured mass increase. It should be noted that this estimate is approximate. In addition, the calculations were carried out assuming a uniform distribution of particles over the sample surface.

Since energy-dispersive spectroscopy (EDS) analysis does not allow direct assessment of the distribution of detected impurities across the entire surface of the tungsten plate, it is impossible to quantify their contribution to the change in sample mass. Therefore, the presence of redeposited particles is considered only as one possible factor in the observed mass increase. Furthermore, based on the quantitative estimates obtained, it seems inappropriate to attribute the observed mass increase solely to the deposition of the detected particles, as the mass increase may also be due to small particles, redeposited layers of material, or the uneven distribution of redeposition products, which are not accounted for in the local surface analysis. Thus, the SEM/EDS analysis results indicate the presence of redeposited particles on the surface of the tungsten plate. In addition to erosive surface

modifications, the contribution of material transfer from the experimental system components should be considered. This must be taken into account when analyzing the mass balance of the tungsten plate, as the mass increase after irradiation may be due not to changes in the tungsten itself, but to the deposition of molten metal particles originating from the structural components.

As shown in a previous study [31], bubbles, craters, and remelting zones were observed on the tungsten surface. Such defects may have a localized impact on the mechanical properties of the material. It should be noted that microhardness measurements were not conducted directly in areas exhibiting morphological features. A correlation between surface morphology and microhardness cannot be ruled out. To confirm this, further research is needed, including a comparison of localized microhardness measurements in the areas of the defects.

Conclusion

In this work, experimental studies were carried out on changes in the microhardness and mass of a preheated tungsten target after exposure to plasma pulses with a duration of about 0.2 ms. To obtain more complete information on changes in the initial properties (including microstructural characteristics, etc.) of the irradiated target, experiments were conducted in several series with different plasma doses, each series including 13 intense plasma pulses (approximately 5.5 GW/m^2). The experiments showed that microhardness remains virtually unchanged even at the highest irradiation dose. After 39 pulses, a minor change in microhardness 2.9 HV is observed, consistent with the measurement accuracy of the measuring instrument. Taking into account the above, the results show that the structural stability of the surface layer of the preheated tungsten target is maintained. At the same time, some data from our previous experimental work, such as the absence of change in crack opening from pulse to pulse and the slight change in stresses in the near-surface layer of the tungsten target (indicating relaxation), provide an explanation. When measuring the mass of the tungsten target, an increase was detected; the mass increase after 39 pulses was 31 mg. The obtained results demonstrate that erosion products from the experimental system components, as well as carbon-containing impurities (including vacuum oil vapor), penetrated the tungsten surface layer. This is confirmed by scanning electron microscopy (SEM) data, which revealed the presence of dust-like particles, and energy-dispersive spectroscopic analysis (EDS), which revealed the presence of Cu, Zn, Ni, and C impurities. Thus, the observed increase in the mass of the tungsten plate can be explained by the redeposition of foreign material on the sample surface. When analyzing tungsten surface damage caused by pulsed plasma, it is important to consider the presence of impurities in the plasma flow. The origin of the detected impurities has not been definitively established; possible sources include erosion products of experimental system components, residual gas components, and carbonaceous contaminants. These may affect the condition of the surface layer of the tungsten target. The presence of such impurities can lead to the formation of redeposited layers, changes in the elemental and phase composition of the surface, and redistribution of heat and mass transfer processes in the near-surface region. Therefore, the observed defects, including cracks, bubbles, craters, and localized melting zones, cannot always be unambiguously attributed solely to plasma thermal shock, as their formation can be further determined by the influence of impurity components on gas accumulation, erosion, and structural degradation of the material. Thus, when interpreting experimental results, the impurity composition of the plasma flow should be considered as one of the significant factors influencing the mechanisms and degree of damage to tungsten.

Funding

This work was funded by the Ministry of Science and Higher Education of the Republic of Kazakhstan (project No. IRN AP23490402).

REFERENCES

1 Loarte, A., Pitts, R.A., Wauters, T., Nunes, I., Vries, P. de, Kim, S.H., Köchl, F., Polevoi, A., Lehnen, M., Artola, J. The new ITER baseline, research plan and open R&D issues. Plasma Phys. Control. Fusion, 67, 065023 (2025). https://doi.org/10.1088/1361-6587/add9c9

2 Komm, M., Jaulmes, F., Grover, O., Peterka, M., Seidl, J., Imrisek, M., Saarelma, S., Snyder, P., Sos, M., Caloud, J. COMPASS Upgrade: a high-field tokamak for ITER- and DEMO-relevant research. Nucl. Fusion, 64, 076028 (2024). https://doi.org/10.1088/1741-4326/ad4569

3 Houry, M., Aumeunier, M-H., Corre, Y., Courtois, X., Mitteau, R., Loarer, TH., Dubus, L., Gauthier, E., Gerardin, J., Gorse, V. Protection of the plasma facing components in the WEST tokamak, progress and development in view of ITER. Nucl. Fusion, 65, 016059 (2025). https://doi.org/10.1088/1741-4326/ad961b

4 Jain, J., Carrasco, M.F., Moreno, J., Davis, S., Pavez, C., Bora, B., Soto, L. Plasma-induced damage on the tungsten surface using a kilojoule plasma focus device: Applicable to study the damages on nuclear fusion reactor related materials. Phys. Plasmas, 31, 083510 (2024). https://doi.org/10.1063/5.0211839

5 Gao, B., Ding, R., Xie, H., Zeng, L., Zhang, L., Wang, B., Li, Ch., Zhu, D., Yan, R., Chen, J. Plasma-facing components damage and its effects on plasma performance in EAST tokamak. Fusion Engineering and Design Volume, 156, 111616 (2020). https://doi.org/10.1016/j.fusengdes.2020.111616

6 Kerkhof, S. Van den, Blommaert, M., Pitts, R.A., Dekeyser, W., Carli, S., Baelmans, M. Impact of ELM mitigation on the ITER monoblock thermal behavior and the tungsten recrystallization depth. Nuclear Materials and Energy, 27, 101009 (2021). https://doi.org/10.1016/j.nme.2021.101009

7 Guo, Z., Yu, B., Zhu, D., Xuan, Ch., Gao, B., Li, Ch., Ding, R., Chen, J., Du, Ch. Analysis of the transient heat flux on divertor surface during plasma disruption in EAST. Nuclear Materials and Energy, 36, 101503 (2023). https://doi.org/10.1016/j.nme.2023.101503

8 De Temmerman, G., et al. Data on erosion and hydrogen fuel retention in beryllium plasma-facing materials. Nucl. Mater. Energy, 27, 100994 (2021). https://doi.org/10.1016/j.nme.2021.100994

9 Jepu, I., Widdowson, A., Matthews, G.F., Coad, J.P., Likonen, J., Brezinsek, S., Rubel, M., Pintsuk, G., Petersson, P., Fortuna-Zalesna, E. Overview of damage to beryllium limiters by unmitigated disruptions and runaway electrons in the JET tokamak with metal walls. Nucl. Fusion, 64, 106047 (2024). https://doi.org/10.1088/1741-4326/ad6614

10 Pitts, R.A. Plasma-wall interaction impact of the ITER re-baseline. Nuclear Materials and Energy, 42, 101854 (2025). https://doi.org/10.1016/j.nme.2024.101854

11 Luo, Ch., Xu, L., Zong, L., Shen, H., Wei, Sh. Research status of tungsten-based plasma-facing materials: A review. Fusion Engineering and Design, 190, 113487 (2023). https://doi.org/10.1016/j.fusengdes.2023.113487

12 Wang, Sh., Li, J., Wang, Y., Zhang, X., Wang, R., Wang, Y., Cao, J. Thermal damage of tungsten-armored plasma-facing components under high heat flux loads. Sci Rep. 28;10(1), 1359 (2020). https://doi.org/10.1038/s41598-020-57852-8

13 Zhang, L., Zhang, X., Li, N., Zhang, P., Mei, X., Wang, Y., Uglov, V.V. Experimental and simulation studies on damage mechanisms of tungsten and molybdenum under compressed plasma flow irradiation. Nucl. Fusion, 63, 076010 (2023). https://doi.org/10.1088/1741-4326/acd016

14 Sattar, H., Jielin, Sh., Ran, H., Imran, M., Ding, W., Gupta, P.D., Ding, H. Impact of microstructural properties on hardness of tungsten heavy alloy evaluated by stand-off LIBS after PSI plasma irradiation. Journal of Nuclear Materials, 540, 152389 (2020). https://doi.org/10.1016/j.jnucmat.2020.152389

15 Kim, H.C., Bang, E., Kim, K-M., Oh, Ye., Han, H.N., Choi, J., Hong, S-H. Analysis of hardness and microstructural changes in Tungsten mono-blocks exposed to high heat flux at 10 MW/m^2. Fusion Engineering and Design, 170, 112530 (2021). https://doi.org/10.1016/j.fusengdes.2021.112530

16 Borovickaja, I.V., Pimenov, V.N., Masljaev, S.A., Demin, A.S., Morozov, E.V., Mihajlova, A.B., Serebrjanyj, V.N., Koljanova, A.S., Bondarenko, G.G., Gajdar, A.I., Matveev, E.V., Sasinovskaja, I.P. Osobennosti povrezhdaemosti poverhnostnyh sloev monokristallicheskogo vol'frama pod vozdejstviem moshhnyh impul'snyh potokov ionov gelija i plazmy. Russian Metallurgy, 4, 93–103 (2025). (in Russian). https://doi.org/10.31857/S08695733250493103

17 Wu, Z.M., Zhang, J., Zhang, J., Huang, J.C., Fan, Y., Yu, X.H., Zhao, Y.B., Zhu, J.L., Jin, C.Q., Wang, P., Fu, E.G. Nanocrystalline W-based alloys with ultrahigh hardness and exceptional irradiation tolerance. Nucl. Fusion, 59, 106050 (2019). https://doi.org/10.1088/1741-4326/ab34c8

18 Racz, A., Kun, P., Kerner, Z., Fogarassy, Z., Menyhárd, M. Tungsten Carbide Nanolayer Formation by Ion Beam Mixing with Argon and Xenon Ions for Applications as Protective Coatings. ACS Appl Nano Mater., 22;6(5), 3816–3824 (2023). https://doi.org/10.1021/acsanm.2c05505

19 Hou, Q-Q., Huang, K., Luo, L-M., Tan, X-Y., Zan, X., Xu, Q., Zhu, X-Y., Wu, Y-Ch. Microstructure and its high temperature oxidation behavior of W-Cr alloys prepared by spark plasma sintering. Materialia, 6, 2019, 100332 (2023). https://doi.org/10.1016/j.mtla.2019.100332

20 Dosbolayev, M.K., Tazhen, A.B., Ramazanov, T.S., Ussenov, Ye.A. Investigation of dust formation during changes in the structural and surface properties of plasma irradiated materials. Nucl. Mater. Energy, 33, 101300 (2022), https://doi.org/10.1016/j.nme.2022.101300

21 Dosbolayev, M.K., Tazhen, A.B., Kholmirzayev, A.N., Ussenov, Y.A., Ramazanov, T.S. Studies of the formation and distribution of cracks and various defects on the heated tungsten plate surface during pulsed plasma flux impact. Nuclear Materials and Energy, 37, 101540 (2023). https://doi.org/10.1016/j.nme.2023.101540

22 Tazhen, A.B., Dosbolayev, M.K., Ramazanov, T.S. Investigation of self-generated magnetic field and dynamics of a pulsed plasma flow. Plasma Sci. Technol., 24, 055403 (2011). https://doi.org/10.1088/2058-6272/ac5018

23 Dosbolayev, M.K., Tazhen, A.B., Ramazanov, T.S. Investigation and diagnostics of plasma flows in a pulsed plasma accelerator for experimental modeling of processes in tokamaks. Eurasian J. Phys. Functional Mater., 5, 198–210 (2021). https://doi.org/10.32523/ejpfm.2021050404

24 Tazhen, A.B., Dosbolayev, M.K., Pshikov, M.I., Usenov, E.A., Ramazanov, T.S. Measurement of the velocity of pulsed plasma flow at the PW-7 installation. Herald of the Kazakh-British Technical University, 2024;21(3), 273–280 (2024). (In Russ.) https://doi.org/10.55452/1998-6688-2024-21-3-273-280

25 Dosbolayev, M.K., Utegenov, A.U., Tazhen, A.B., Ramazanov, T.S. Investigation of dust formation in fusion reactors by pulsed plasma accelerator. Laser and Particle Beams, 35(4), 741–749 (2017). https://doi.org/10.1017/S0263034617000805

26 Qua, M., Konga, F., Yana, Sh., Uglov, V.V., Xue, J., Wang, Y. Damages on pure tungsten irradiated by compression plasma flows. Nuclear Inst. and Methods in Physics Research, B 444, 33–37 (2019). https://doi.org/10.1016/j.nimb.2018.12.050

27 Moldabekov, Zh.M., Zhukeshov, A.M., Gabdullina, A.T., Amrenova, A.U. Investigation of radiation effect on tungsten and molybdenum materials. International Journal of Mathematics and Physics, 14(2), 56-63 (2023). https://doi.org/10.26577/ijmph.2023.v14.i2.07

[1]*Тәжен Ә.Б.,
PhD, ORCID ID: 0000-0002-3277-2086,
*e-mail: Aigerim@physics.kz
[1]Холмирзаев А.Н.,
докторант, ORCID ID: 0009-0003-4108-0879,
e-mail: kholmirzayev.abdulla@gmail.com
[2]Үсенов Е.А.,
PhD, ORCID ID: 0000-0001-7903-8674,
e-mail: yerbolat@physics.kz
[1]Досболаев М.Қ.,
ф.-м.ғ.к., профессор, ORCID ID: 0000-0002-0724-1793,
e-mail: merlan@physics.kz
[1]Рамазанов Т.С.,
ф.-м.ғ.д., профессор, ORCID ID: 0009-0009-2301-1152,
e-mail: ramazan@physics.kz

[1]Ашық түрдегі ұлттық нанотехнологиялық зертхана, әл-Фараби атындағы ҚазҰУ,
Алматы қ., Қазақстан
[2]Принстон плазма физикасы зертханасы, Принстон университеті, Принстон қ., АҚШ

ИМПУЛЬСТІ ПЛАЗМАНЫҢ ӘСЕРІНЕН АЛДЫН АЛА ҚЫЗДЫРЫЛҒАН ВОЛЬФРАМНЫҢ МИКРОҚАТТЫЛЫҒЫ МЕН МАССАСЫНЫҢ ӨЗГЕРУІН ЗЕРТТЕУ

Аңдатпа

Мақалада ұзақтығы шамамен 0,2 мс болатын импульстік плазма ағынының әсерінен бірінші қабырға мен диверторға негізгі кандидат материал болып табылатын алдын ала қыздырылған вольфрам нысанасының

микроқаттылығы мен массасының өзгеруін сипаттайтын эксперименттік зерттеу нәтижелері келтірілген. Тәжірибелер энергия және қуат тығыздықтары шамамен 1,1 МДж/м^2 және 5,5 ГВт/м^2 болатын 13 импульстен тұратын сериялармен жүргізілді. Микроқаттылық HVS-1000B өлшегіші арқылы анықталды; нысананың массасы плазмалық әсерге дейін және кейін CPA225D жоғары дәлдікті таразының көмегімен өлшенді. Вольфрам нысанасының микроқаттылығы сәулеленудің максималды дозасында да (39 импульске дейін) айтарлықтай өзгеріссіз қалатыны және байқалған өзгеріс өлшеу қателігі шегінде болатыны көрсетілген, бұл беткі қабаттың құрылымдық тұрақтылығын көрсетеді. Сыртқы құрылымдық элементтер материалының ластануы мен қайта тұндыруынан туындауы мүмкін нысана массасының (31 мг-ға дейін) ұлғаюы тіркелді. Энергиядисперсиялық спектроскопия (ЭДС) талдауы нысананың бетіне қайта тұндырылған тозаңды бөлшектерінде Cu, Zn, Ni және C сияқты қарқынды сызықтардың барын анықтады. Нәтижелер бұл бөгде компоненттердің нысананың беттік морфологисына айтарлықтай әсер ететінін және вольфрамның зақымдану механизмдерін түсіндіру кезінде ескеру қажет екенін көрсетеді.

Түйін сөздер: импульстік плазмалық үдеткіш, плазмалық ағын, алдын ала қыздырылған вольфрам нысанасы, микроқаттылық, нысана массасы, нысананың элементтік құрамы.

[1]*Тажен А.Б.,
PhD, ORCID ID: 0000-0002-3277-2086,
*e-mail: Aigerim@physics.kz
[1]Холмирзаев А.Н.,
докторант, ORCID ID: 0009-0003-4108-0879,
e-mail: kholmirzayev.abdulla@gmail.com
[2]Усенов Е.А.,
PhD, ORCID ID: 0000-0001-7903-8674,
e-mail: yerbolat@physics.kz
[1]Досболаев М.К.,
к.ф.-м.н., профессор, ORCID ID: 0000-0002-0724-1793
e-mail: merlan@physics.kz
[1]Рамазанов Т.С.,
д.ф.-м.н., профессор, ORCID ID: 0009-0009-2301-1152,
e-mail: ramazan@physics.kz

[1]Национальная нанотехнологическая лаборатория открытого типа, КазНУ им. аль-Фараби, г. Алматы, Казахстан
[2]Принстонская лаборатория физики плазмы, Принстонский университет, г. Принстон, США

Аннотация

В статье представлены результаты экспериментального исследования изменений микротвердости и массы предварительно нагретой вольфрамовой мишени, основного материала-кандидата для первой стенки и дивертора, под воздействием импульсного плазменного потока с длительностью приблизительно 0,2 мс. Эксперименты проводились в виде серии из 13 импульсов при плотности энергии 1,1 МДж/м^2 и плотности мощности около 5,5 ГВт/м^2. Микротвердость измерялась с помощью твердомера HVS-1000B; масса мишени до и после воздействия плазмы измерялась с помощью прецизионных весов CPA225D. Показано, что микротвердость вольфрамовой мишени остается практически неизменной даже при максимальной дозе облучения (до 39 импульсов), а наблюдаемое изменение находится в пределах погрешности измерения, что свидетельствует о структурной стабильности поверхностного слоя. При этом зафиксировано увеличение массы мишени (до 31 мг), вероятно, вызванное загрязнением и повторным осаждением материала внешних конструктивных элементов. Анализ методом энергодисперсионной спектроскопии (ЭДС) выявил интенсивные полосы Cu, Zn, Ni и C в частицах пыли, повторно осажденных на поверхности мишени. Результаты показывают, что эти инородные компоненты оказывают существенное влияние на морфологию поверхности и должны учитываться при интерпретации механизмов повреждения вольфрамом.

Ключевые слова: импульсный плазменный ускоритель, плазменный поток, предварительно нагретая вольфрамовая мишень, микротвердость, масса мишени, элементный состав мишени.

UDC 536.6
IRSTI 29.19.09

https://doi.org/10.55452/1998-6688-2026-23-3-398-413

[1*]Iztleuova B.,
PhD student, ORCID ID: 0009-0009-7588-8976,
[*]e-mail: b.iztleuova@zhubanov.edu.kz
[1]Imanchiyev A.,
Associate Professor, candidate of physical and mathematical sciences,
ORCID ID: 0000-0002-1835-2501,
e-mail: imanchiev_ae@mail.ru
[1]Bekeshev A.,
Associate Professor, candidate of physical and mathematical sciences,
ORCID ID: 0000-0002-7038-4631
e-mail: amirbek2401@gmail.com
[1]Zhanturina N.,
Associate Professor, PhD, ORCID ID: 0000-0001-9540-6334,
e-mail: nzhanturina@mail.ru
[2]Ussenkulova Sh.,
Associate Professor, PhD, ORCID ID: 0000-0001-9417-755X,
e-mail: Sholpan1990@gmail.com
[3]Wang X.,
Associate Professor, PhD, ORCID ID: 0000-0001-5881-4400,
e-mail: wxcmx@ustc.edu.cn

[1]K. Zhubanov Aktobe Regional University, Aktobe, Kazakhstan
[2]Kazakh University of Technology and Business, Astana, Kazakhstan
[3]State Key Laboratory of Fire Science, University of Science and Technology of China, Hefei, China

EMPIRICAL BENCHMARKING OF GRADIENT BOOSTING FOR THERMAL DEGRADATION PREDICTION IN MINERAL–POLYMER COMPOSITES

Abstract

This study presents a mathematical and empirical analysis of gradient boosting algorithms applied to thermogravimetric analysis (TGA) data for composites based on vinyl ether matrices and epoxides with mineral fillers. The gradient boosting algorithm is output step by step with a numerical example of TGA. XGBoost and CatBoost are then analyzed formally. 12 algorithms were compared on 478 data from the peer-reviewed literature using 5-repeated 5-fold cross-validation. Extra Trees and CatBoost achieved statistically equivalent top performance (mean $R^2 = 0.7430 \pm 0.0879$ and 0.7313 ± 0.0793, respectively; Nadeau & Bengio corrected $t = 0.483$, $p = 0.634$), outperforming all linear baselines, SVR, and MLP. CatBoost is recommended for practical deployment: its ordered boosting produces unbiased gradient estimates on small datasets ($n < 1000$), and SHAP analysis of its gradient tree structure reveals physically interpretable feature attributions aligned with known TGA mechanisms. SHAP values identified TGA peak temperature (T_{max}) and matrix type as the dominant predictors. The proposed preprocessing pipeline including phr to wt% conversion, label encoding, and median imputation provides a reproducible strategy for heterogeneous TGA literature datasets.

Keywords: gradient boosting, XGBoost, CatBoost, polymer composites, machine learning, thermogravimetric analysis, ordered boosting, mathematical foundations, algorithm selection.

Received April 15, 2026; revised July 7, 2026; accepted July 17, 2026

Introduction

Machine learning has reshaped how researchers address property prediction in materials science and polymer engineering. Characterizing composite systems experimentally is both costly and time-consuming, and the composition–property space is far too broad to map by trial and error. Machine learning methods are now common in materials science. Researchers use them to find links between how a material is built and how it behaves. No physical model is needed for that [1, 2, 3]. When the data are in tabular form, gradient boosting works well. It picks up nonlinear patterns even when sample sizes are small or data are messy. That is why materials scientists often reach for it [4, 5, 6]. The method works through shallow decision trees built one after another. Every new tree looks at what the previous one got wrong and tries to fix it. The loss function decreases with each step [7]. Two variants stand out in polymer and composite research. XGBoost keeps trees from becoming too large by using a second-order Taylor expansion and adding L1 and L2 penalty terms to the loss [8]. CatBoost uses permutation-based gradient estimation, which reduces target leakage compared to standard gradient boosting [9].

Between 2018 and 2024 alone, more than 170 publications applied boosting methods in polymer science. Both algorithms now appear routinely, from thermal property prediction to mechanical strength modeling [1, 6, 10]. However, here is the problem: across nearly all of that work, the focus remains on predictive accuracy [11, 12, 13, 14]. Why XGBoost regularizes the way it does, or how exactly CatBoost avoids overfitting on small data, these questions rarely receive a serious answer in the polymer composite literature.

The aim of this study is to benchmark gradient boosting against a broad range of regression models and to establish its standing for predicting the thermal degradation temperature (T50%) of mineral–polymer composites, justifying the recommended model on mathematical and SHAP-based grounds. This paper makes the following contributions. First, we provide a unified step-by-step mathematical derivation of gradient boosting, XGBoost, and CatBoost applied to TGA data of mineral–polymer composites. Second, we benchmark twelve regression algorithms on 478 TGA samples using 5-repeated 5-fold cross-validation, providing statistically reliable performance estimates. Third, we interpret the best-performing model using SHAP analysis, linking feature contributions to the physical mechanisms of thermal degradation. While boosting methods have been widely applied in materials science [1, 6, 10], their mathematical foundations, rigorous cross-validated benchmarking, and SHAP-based interpretation on TGA composite data remain underexplored. Empirically, gradient boosting is confirmed among the top performers and is statistically indistinguishable from the best model; the contribution of this work is therefore methodological rather than algorithmic, providing a principled, SHAP-supported model recommendation on a reproducible pipeline for heterogeneous, literature-aggregated TGA data.

Materials and methods

Gradient Boosting: Mathematical Framework

Gradient boosting is used to construct a prediction model as a sum of M weak learners:

$$\hat{y}_i = F_M(x_i) = \sum_{m=1}^{M} f_m(x_i) \quad (1)$$

where each f_m is a shallow decision tree and x_i is the feature vector of the i-th sample. The model is built sequentially at each step m, and a new tree f_m is added to correct the residual error of the current ensemble:

$$F_m(x) = F_{m-1}(x) + \eta \cdot f_m(x) \quad (2)$$

where η∈(0,1] is the learning rate, which controls the contribution of each new tree. Small values of η slow down learning but improve generalization by preventing any single tree from dominating the ensemble [7].

To illustrate the gradient boosting algorithm (Table 1), we apply it to a small dataset derived from thermogravimetric analysis (TGA) of vinyl, epoxy composites. The goal is to predict the maximum decomposition temperature T_max based on two input features: mineral loading (%) and modifier loading (%).

Table 1 – Illustrations of the TGA dataset of epoxy composites used for gradient boosting

№	Loading of mineral	Loading of modifier	tga_tmax
1	0	0	390
2	4.76	0.05	386
3	9	0.09	389
4	30	5	373
5	30	5	379

The algorithm begins with a constant prediction F_0 equal to the mean of all target values:

$$F_0 = \frac{390 + 386 + 389 + 373 + 379}{5} = 383.4\,°C \quad (3)$$

The residuals $r_i=y_i-F_0$ represent the errors of the current model. For example, sample 1 yields $r_1=390-383.4=+6.6$, while sample 4 yields $r_4=373-383.4=-10$.

Table 2 – Initial residuals computed as $r_i=y_i-F_0$

№	y	F_0	Residual r
1	390	383.4	+6.6
2	386	383.4	+2.6
3	389	383.4	+5.6
4	373	383.4	-10.4
5	379	383.4	-4.4

At each node of the decision tree, the algorithm evaluates every possible split across all features and all thresholds. For each candidate split, the data are divided into two groups, left and right, and the Mean Squared Error (MSE) is computed for each group separately [15]. The MSE for a group is defined as follows:

$$MSE = \frac{1}{n}\sum_{i=1}^{n}(r_i - \bar{r})^2 \quad (4)$$

where r_i is the residual of sample i, $\bar{r}$ is the mean residual of the group and n is the number of samples in the group. The total MSE of a split is the weighted sum of both groups:

$$MSE_{total} = \frac{n_L}{n} \cdot MSE_L + \frac{n_R}{n} MSE_R \quad (5)$$

where n_L and n_R are the numbers of samples in the left and right groups, respectively. For example, when the split mineral loading > 9 on the residuals from Table 1 is evaluated:

Left group (samples 1, 2, 3): residuals = 6.6, 2.6, and 5.6, respectively.

$$\bar{r_L} = \frac{6.6 + 2.6 + 5.6}{3} = 4.93 \quad (6)$$

$$MSE_L = \frac{(6.6 - 4.93)^2 + (2.6 - 4.93)^2 + (5.6 - 4.93)^2}{3} = 2.89 \quad (7)$$

Right group (samples 4, 5): residuals = −10.4, −4.4.

$$\bar{r_R} = \frac{-10.4 + (-4.4)}{2} = -7.4 \quad (8)$$

$$MSE_R = \frac{(-10.4 + 7.4)^2 + (-4.4 + 7.4)^2}{2} = 9.0 \quad (9)$$

Total MSE:

$$MSE_{total} = \frac{3}{5} \cdot 2.89 + \frac{2}{5} \cdot 9.0 = 1.73 + 3.6 = 5.33 \quad (10)$$

Split: mineral loading > 4.76. Left group (samples 1 and 2): residuals = 6.6 and 2.6.

$$\bar{r_L} = \frac{6.6 + 2.6}{2} = 4.6 \quad (11)$$

$$MSE_L = \frac{(6.6 - 4.6)^2 + (2.6 - 4.6)^2}{2} = 4.0 \quad (12)$$

Right group (samples 3, 4, and 5): residuals = 5.6, −10.4, and −4.4.

$$\bar{r_R} = \frac{5.6 + (-10.4) + (-4.4)}{3} = -3.07 \quad (13)$$

$$MSE_R = \frac{(5.6 + 3.07)^2 + (-10.4 + 3.07)^2 + (-4.4 + 3.07)^2}{3} = 43.56 \quad (14)$$

Total MSE:

$$MSE_{total} = \frac{2}{5} \cdot 4.0 + \frac{3}{5} \cdot 43.56 = 1.6 + 26.13 = 27.73 \quad (15)$$

All the candidate splits are compared in the same manner, and the split with the lowest total MSE is selected as the best node. In this example, a split mineral loading > 9 produced the lowest MSE among all the evaluated thresholds and features and was therefore chosen as the root node of the decision tree. The tree evaluates all the features and thresholds. Best split: loading_mineral > 9:

Loading_mineral > 9?
/ \
No Yes
samples 1,2,3 samples 4,5
mean = +4.93 mean = -7.4

A shallow decision tree is trained on the residuals. The optimal split is found at mineral loading > 9%, with two leaf nodes having mean values of +4.93 and −7.4. The model is updated using a learning rate η=0.1:

$$F_1(x) = F_0(x) + \eta \cdot f_1(x) \tag{16}$$

Table 3 – Updated model predictions F_1 and new residuals after the first iteration

№	y	F_1	New residual
1	390	383.4 + 0.1×4.93 = 383.9	6.1
2	386	383.4 + 0.1×4.93 = 383.9	2.1
3	389	383.4 + 0.1×4.93 = 383.9	5.1
4	373	383.4 + 0.1×(−7.4) = 382.7	−9.7
5	379	383.4 + 0.1×(−7.4) = 382.7	−3.7

This process is repeated M times. With each iteration, the residuals decrease, and the predictions become more accurate. The overall objective to minimize combines a loss term and a regularization term:

$$\mathcal{L} = \sum_{i=1}^{n} l(\hat{y}_i, y_i) + \sum_{m=1}^{M} \Omega f_m \tag{17}$$

where $l(\hat{y}_i, y_i)$ is the discrepancy between the predicted and actual values and Ωf_m is the penalized tree complexity. The exact form of Ω differs between XGBoost and CatBoost and is discussed in Sections 3 and 4, respectively [8]. Despite this growing adoption, the mathematical foundations behind these implementations remain largely absent from the polymer and composite literature.

XGBoost: Mathematical Foundations

All mathematical formulations presented in this section are derived from Chen & Guestrin [8]. Unlike classical gradient boosting, which minimizes the loss function approximately using only first-order gradients, XGBoost employs a second-order Taylor expansion of the loss function at each iteration:

$$\mathcal{L}^{(m)} \approx \sum_{i=1}^{n} \left[l\left(y_i, F_{m-1}(x_i)\right) + g_i f_m(x_i) + \frac{1}{2} h_i f_m^2(x_i) \right] \tag{18}$$

where g_i and h_i are the first- and second-order derivatives of the loss function with respect to the previous prediction $F_{m-1}(x_i)$:

$$g_i = \frac{\partial l(y_i, F_{m-1})}{\partial F_{m-1}}, \quad h_i = \frac{\partial^2 l(y_i, F_{m-1})}{\partial F_{m-1}^2} \tag{19}$$

Compared with the first-order methods, the Hessian term h_i captures the curvature of the loss surface, providing the algorithm with a more accurate picture of how the loss changes. These processes result in more accurate step estimation than classical gradient boosting, which relies solely on the first-order gradient.

To control model complexity and prevent overfitting, XGBoost incorporates an explicit regularization term $\Omega(f_m)$ directly into the objective function:

$$\mathcal{L}^{(m)} \approx \sum_{i=1}^{n} \left[g_i f_m(x_i) + \frac{1}{2} h_i f_m^2(x_i) \right] + \Omega(f_m) \tag{20}$$

where the regularization term is defined as follows:

$$\Omega(f_m) = \gamma T + \frac{1}{2}\lambda \sum_{j=1}^{T} \omega_j^2 + \alpha \sum_{j=1}^{T} |\omega_j| \tag{21}$$

where T is the number of leaves in the tree; ω_j is the weight of leaf j; γ is the penalty for the number of leaves (tree complexity); λ is the L2 regularization coefficient (ridge); and α is the L1 regularization coefficient (lasso).

The L2 term penalizes large leaf weights, whereas the L1 term encourages sparsity by pushing small weights to zero. By grouping samples that fall into the same leaf j, the objective function can be rewritten as a sum over leaves:

$$\mathcal{L}^{(m)} \approx \sum_{j=1}^{T} \left[\left(\sum_{i \in I_j} g_i \right) \omega_j(x_i) + \frac{1}{2} \left(\sum_{i \in I_j} h_i + \lambda \right) \omega_j^2 \right] + \gamma \mathrm{T} \tag{22}$$

Since this is a quadratic function with respect to ω_j, the optimal weight for each leaf is obtained analytically by setting the derivative to zero:

$$\frac{\partial \mathcal{L}}{\partial \omega_j} = \sum_{i \in I_j} g_i + \left(\sum_{i \in I_j} h_i + \lambda \right) \omega_j = 0 \tag{23}$$

Solving for ω_j:

$$\omega_j^* = -\frac{\sum_{i \in I_j} g_i}{\sum_{i \in I_j} h_i + \lambda} \tag{24}$$

Substituting ω_j back into the objective yields the minimum loss value for a given tree structure:

$$\mathcal{L}^* = -\frac{1}{2} \sum_{j=1}^{T} \frac{\left(\sum_{i \in I_j} g_i \right)^2}{\sum_{i \in I_j} h_i + \lambda} + \gamma T \tag{25}$$

This closed-form solution allows XGBoost to evaluate the quality of any tree structure exactly, without numerical optimization.

CatBoost Mathematical Distinctions

All mathematical formulations presented in this section are derived from Prokhorenkova et al. [9]. In classical gradient boosting, the residuals for all training samples are computed using a model that is trained on the same samples. Formally, at iteration m, the gradient g_i for sample i is computed as follows:

$$g_i = \frac{\partial l(y_i, F_{m-1}(x_i))}{\partial F_{m-1}(x_i)} \tag{26}$$

where F_{m-1} was built using y_i itself. This creates target leakage, and the target value y_i influences both the model and the gradient estimate for the same observation, leading to biased gradient estimation and overfitting, which are particularly critical for small datasets.

CatBoost addresses this through ordered boosting, where each gradient is computed from a model that has only seen samples preceding the current one in a randomly assigned order σ:

$$g_i^{\sigma} = \frac{\partial l(y_i, F_m^{\sigma(i)}(x_i))}{\partial F_m^{\sigma(i)}(x_i)} \quad (27)$$

where $F_m^{\sigma(i)}$ denotes a model built only on samples $\{x_j : \sigma(j) < \sigma(i)\}$.

This ensures that when the gradient for sample i is computed, its target value y_i has never been seen by the model, producing an unbiased gradient estimate:

$$\mathbb{E}[g_i^{\sigma}] = \mathbb{E}\left[\frac{\partial l(y_i, F_{m-1})}{\partial F_{m-1}}\right] \quad (28)$$

To implement this, CatBoost keeps n model versions running in parallel, each updated as new samples enter the permutation. The greatest advantage of ordered boosting is precisely where classical GB struggles most: small datasets with high exposure to target leakage.

Dataset, Feature Engineering and Preprocessing

The dataset was compiled from peer-reviewed publications reporting TGA results for vinyl ether and epoxy matrices with mineral fillers. The prediction target for the machine learning benchmark is T50% (the temperature at which 50% mass loss occurs during TGA), extracted from each TGA curve at tga_x_pct = 50. Note that T_max (the DTG peak temperature) is used as a predictor input feature, not as the target variable; it served as the illustrative target only in the worked example of Section 2. Table 4 shows the features used and the preprocessing applied before model training.

Table 4 – Features, preprocessing characteristics before training models

Features	Unit of measure	Preprocessing
matrix type	VE/EP	Vinyl ester, epoxy
mineral formula	Chemical formula	-
mineral loading	wt%	Phr converted to wt%
TGA peak temperature (T_max)	°C	.→, 4.5→4,5
mineral name	-	Label encoded (categorical)
residue measurement temperature (tga_ residue_t)	°C	Median imputation
TGA residue mass fraction (tga_residue)	wt%	Median imputation

Missing numerical values were imputed with the column median. The TGA atmosphere (N_2, air, O_2, Ar, CO_2) was examined but found to be uninformative for this dataset: 99% of records were measured under nitrogen. This feature was therefore excluded from the final model.

Cross-Validation Strategy

All performance metrics reported in Table 5 and the scatter plot in Figure 1 are derived from the same 5-repeated 5-fold cross-validation (RepeatedKFold, n_splits = 5, n_repeats = 5, random_ state = 42). Figure 1 displays out-of-fold (OOF) predictions: each of the 478 samples is predicted exactly once per repeat by a model that has not observed it, so no separate train/test split is required for visualisation. Model performance was estimated using 5-repeated 5-fold cross-validation (RepeatedKFold, n_repeats = 5, n_splits = 5, random_state = 42), yielding 25 independent evaluations per model across the full 478-sample dataset.

Models and Evaluation Metrics

12 regression algorithms were trained and evaluated: Linear Regression, Ridge Regression (α = 1.0), Huber Regression (ε = 1.35), Support Vector Regression (SVR, C = 100, ε = 5), Multilayer Perceptron (MLP; 128–64–32 neurons), Random Forest (300 trees), Extra Trees (300 trees), Gradient

Boosting (400 estimators, lr = 0.05, depth = 4, subsample = 0.8), Gradient Boosting with Huber loss (α = 0.9), XGBoost (400 estimators, lr = 0.05, depth = 5, subsample = 0.8, colsample_bytree = 0.8), CatBoost (500 iterations, lr = 0.05, depth = 6, l2_leaf_reg = 3), and a Stacking ensemble combining Gradient Boosting, XGBoost, and CatBoost with a Ridge meta-learner (5-fold cross-validation). Hyperparameter values were fixed a priori according to established recommendations in the machine learning literature [8, 9, 16, 17] rather than tuned per model; no grid search or nested cross-validation was performed, so every algorithm was evaluated under comparable, untuned conditions. The chosen values were confirmed to be stable across the 25 cross-validation evaluations.

All metrics were computed across 25 CV folds and reported as mean ± std. All error metrics are expressed as percentages to facilitate cross-study comparison:

- CV(RMSE) %: coefficient of variation of RMSE normalizes prediction error to the scale of the target variable;
- MAPE %: mean absolute percentage error expresses average error as a percentage of each individual prediction;
- MAE %: relative mean absolute error percentage counterpart of the absolute MAE;
- R^2 (mean ± std): coefficient of determination averaged over 25 folds with standard deviation fraction of T50% variance explained; std quantifies model stability.

Results

Model Comparison

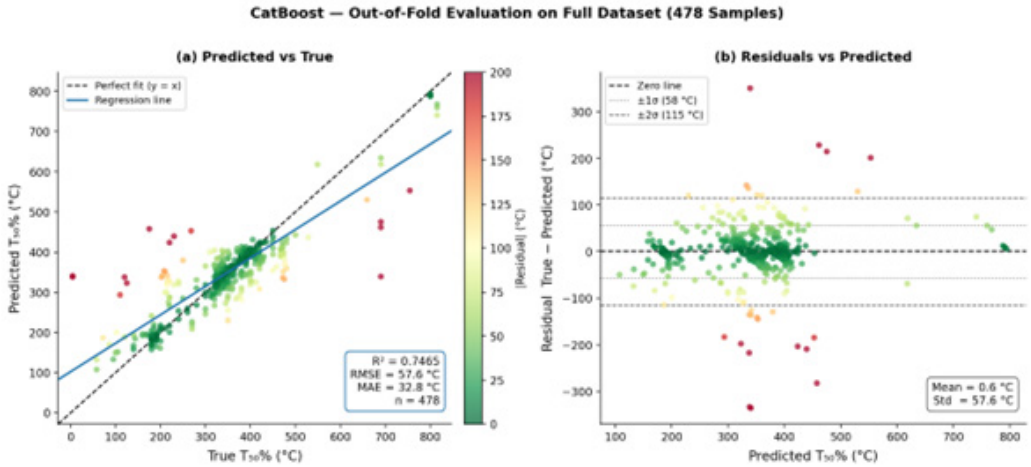
Table 5 summarizes the performance of all 12 models evaluated by 5-repeated 5-fold cross-validation (25 evaluations per model). The best overall performance was achieved by Extra Trees, with mean R^2 = 0.7430 ± 0.0879, CV(RMSE) = 15.89%, MAPE = 10.26%, and MAE = 8.72%. Extra Trees and CatBoost achieved comparable top performance (mean R^2 = 0.7430 ± 0.0879 vs. 0.7313 ± 0.0793). A Nadeau & Bengio corrected resampled t-test [18] – which accounts for the non-independence of folds in repeated k-fold CV – yielded t = 0.483 (df = 24, p = 0.634, two-tailed), confirming that the difference between the two models is not statistically significant. All tree-based ensemble methods (Extra Trees, CatBoost, XGBoost, Gradient Boosting) consistently outperformed linear baselines and SVR, confirming the non-linear nature of the T50% response surface.

Table 5 – Performance metrics of all regression models evaluated by 5-repeated 5-fold cross-validation (478 samples, 25 evaluations per model). Models are ranked by mean R^2 (descending)

Model	mean R^2 ± std	CV(RMSE) %	MAPE %	MAE %
Extra Trees	0.7430 ± 0.0879	15.89	10.26	8.72
CatBoost	0.7313 ± 0.0793	16.37	10.4	9.5
XGBoost	0.7256 ± 0.0805	16.48	10.94	9.71
GB (Huber loss)	0.7078 ± 0.1036	16.97	9.81	9.11
Gradient Boosting	0.7060 ± 0.0897	17.06	10.75	9.79
Random Forest	0.6963 ± 0.0950	17.33	10.97	9.89
Stacking (GB+XGB+CAT)	0.6633 ± 0.0825	18.46	12.13	11.23
SVR	0.6432 ± 0.0964	18.95	10.88	10.4
MLP	0.5536 ± 0.1165	21.09	15.86	14.36
Ridge	0.4891 ± 0.1420	22.56	15.6	14.45
Linear Regression	0.4889 ± 0.1425	22.56	15.6	14.43
Huber Regression	0.4529 ± 0.1946	23.13	17.93	13.57

Predicted vs. True T50% and Residual Analysis

Figure 1 shows out-of-fold scatter plots for the CatBoost model: predicted versus true T50% values (left panel) and the corresponding residual distribution (right panel), evaluated by 5-repeated 5-fold cross-validation across all 478 samples. A small number of samples (n < 5) show residuals exceeding 150 °C, attributable to inter-source measurement variability inherent in a dataset aggregated from multiple independent publications.

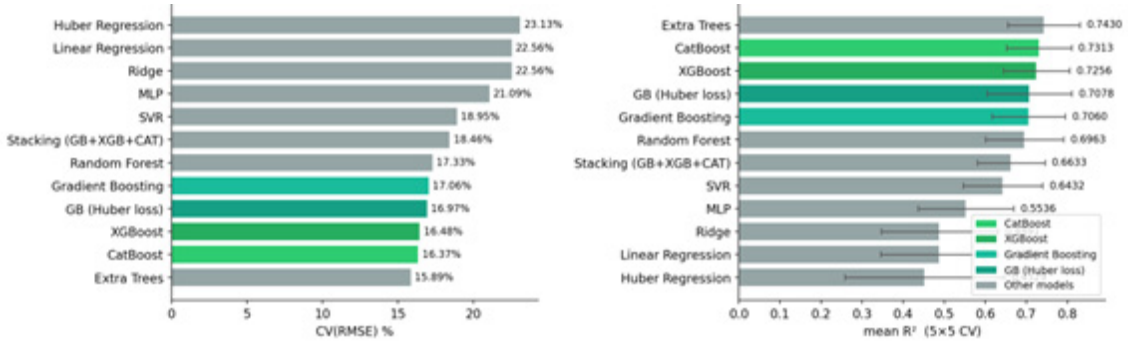


Predicted vs. True T50% (top row) and residual plots (bottom row) for the three best models. The dashed line represents the ideal y = x relationship. Dotted lines indicate ±1σ residual bounds

Figure 1– CatBoost out-of-fold predictions (5-repeated 5-fold cross-validation, n = 478):
(a) predicted vs. true T_{50}% values; (b) residuals vs. predicted T_{50}%.
Colour encodes absolute residual magnitude

Model Ranking: RMSE and R^2

Figure 2 presents horizontal bar charts ranking all models by RMSE (lower is better) and R^2 (higher is better). Gradient boosting models (highlighted in green) consistently ranked at the top, while linear models ranked at the bottom.

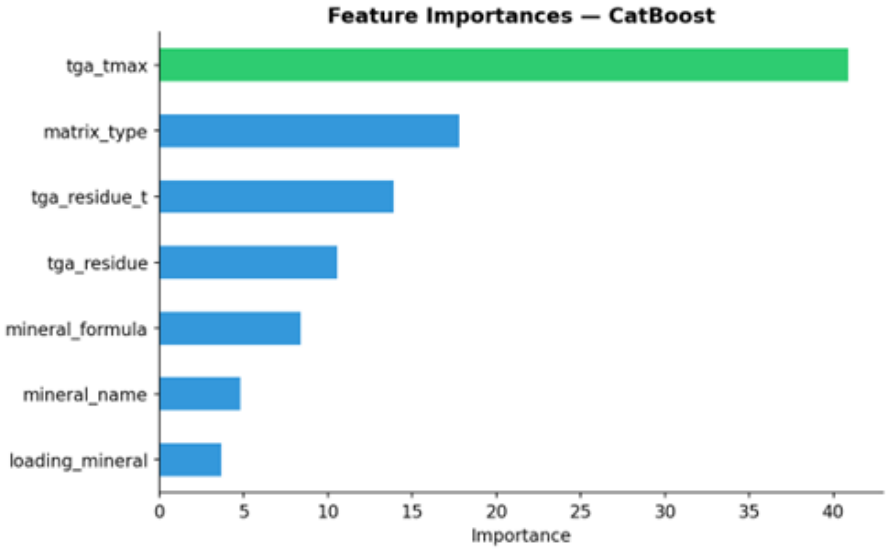


Green bars: Extra Trees, CatBoost, XGBoost, Gradient Boosting. Grey bars: remaining algorithms. Error bars = ±1 std.

Figure 2 – CV(RMSE) % (left) and mean R^2 ± std (right)
for all evaluated models under 5-repeated 5-fold cross-validation

SHAP Analysis

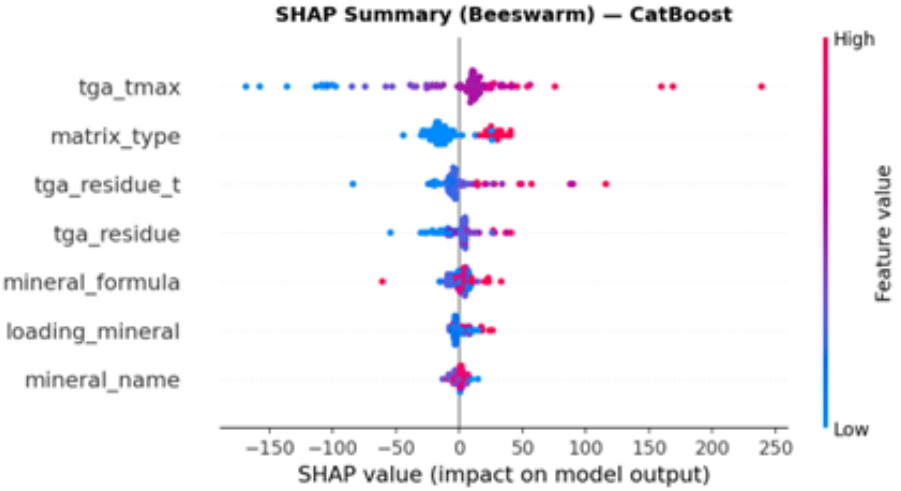
Figure 3 displays the feature importances derived from the CatBoost model.



The highlighted bar indicates the most important feature.

Figure 3 – Feature importance for the CatBoost model

Figure 4 shows the SHAP summary plot for CatBoost.



Left: beeswarm summary plot showing the distribution of SHAP values for all test samples across seven input features; each point represents one sample, color indicates the feature value (pink – high, blue – low).

Figure 4 – SHAP analysis of the CatBoost model

Figure 5 illustrates SHAP dependence plots for the top features.

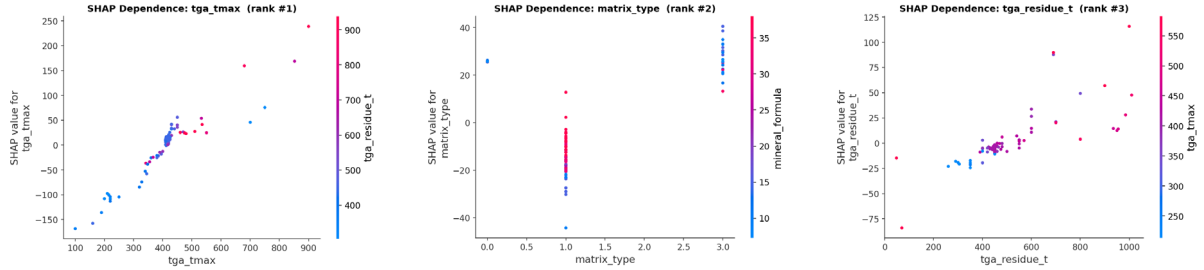


Figure 5-SHAP dependence plots for the three most influential features in the CatBoost model: tga_tmax (rank 1), matrix_type (rank 2), and tga_residue_t (rank 3).

Each point represents one test sample; the y-axis shows the SHAP contribution of the feature, and the color indicates the value of the most interacting variable.

Discussion

Tree-based ensemble methods consistently outperformed linear regression, Ridge, and SVR across all cross-validation folds. This confirms that the composition–degradation relationship in mineral–polymer composites is inherently non-linear [10, 27]. Filler type, matrix chemistry, and loading interact in ways that linear models cannot capture [1, 12]. Extra Trees and CatBoost achieved comparable top performance (mean $R^2 = 0.7430 \pm 0.0879$ vs. 0.7313 ± 0.0793). A Nadeau & Bengio corrected resampled t-test confirmed that this difference is not statistically significant ($t = 0.483$, $df = 24$, $p = 0.634$). Similar parity between these algorithms has been reported on other heterogeneous materials datasets [29,32]. Despite the marginal numerical edge of Extra Trees ($\Delta R^2 = 0.012$, not statistically significant per the Nadeau & Bengio corrected test), CatBoost is recommended for practical deployment on the basis of two complementary properties. First, ordered boosting (Eq. 27–28) eliminates the target-leakage bias inherent in both classical gradient boosting and XGBoost when sample counts are low; on a dataset of $n = 478$ heterogeneous TGA samples, bias reduction provides a more reliable generalisation guarantee than the variance reduction achieved by Extra Trees through extreme randomisation [9, 17]. Second, SHAP analysis (Figures 4–5) corroborates CatBoost's practical value: feature attributions align with established physical mechanisms, including the thermal coupling encoded in T_max, the polymer chemistry signal in matrix_type, and the non-linear saturation behaviour of mineral loading, yielding a mechanistically interpretable model [30, 31, 32, 33]. This produces more stable predictions on unseen mineral–polymer combinations outside the training distribution [17, 19]. On small heterogeneous datasets such as this one ($n = 478$), this property is particularly valuable [13, 17].

XGBoost ranked third, with mean $R^2 = 0.7256 \pm 0.0805$, closely behind CatBoost (0.7313 ± 0.0793). The difference between the two is small and not statistically significant. This is consistent with prior observations that XGBoost's L1/L2 regularization advantage is most pronounced on large clean datasets [8, 16]. On a small heterogeneous dataset ($n = 478$), ordered boosting in CatBoost reduces target leakage more effectively than XGBoost's regularization, giving CatBoost a marginal edge [9, 17].

The dataset aggregates TGA measurements from multiple laboratories and instruments. This introduces inter-source variability in decomposition temperatures that a single-site study would avoid [34, 13]. Heating rates, sample mass, and purge gas flow all vary across publications and affect measured T_{50}% values [34].Label encoding assigns arbitrary integers to polymer matrix types and mineral names. This representation does not capture chemical similarity between structurally related matrices or minerals [35, 11]. Graph-based or SMILES-derived descriptors may improve generalization to unseen polymer–filler combinations [35, 11]. The current model predicts T_{50}% only. Extending the framework to T_{10}%, T_max, and char yield would provide a more complete description of composite thermal behavior [1, 4]. This remains future work.

SHAP analysis of the CatBoost model (Figures 4–5) provided mechanistically interpretable feature rankings [28,33, 36]. T_max dominated predictions across all test samples. Its high positive SHAP values reflect the physical coupling between the DTG peak temperature and the mass-loss midpoint along the TGA curve [37, 38]. Matrix type ranked second, reflecting the fundamental role of polymer chemistry in governing thermal decomposition behavior [1, 12]. The residue measurement temperature (tga_residue_t) ranked third, acting as a proxy for the high-temperature thermal stability plateau [37, 39]. Mineral loading showed a non-linear SHAP profile. Moderate filler contents contributed positively to predicted T50%, while extreme loadings reduced model confidence, consistent with known saturation effects in filler-reinforced composites [4, 5, 40]. The remaining categorical descriptors (mineral formula, mineral name) contributed collectively but ranked below the top three features. This suggests that the dominant thermal response is governed by measurable thermophysical parameters rather than compositional class labels [38, 41].

CatBoost's ordered boosting algorithm (Eq. 27–28) eliminates the target leakage present in both classical GB and XGBoost, producing unbiased gradient estimates that are particularly valuable when $n < 1000$ [9, 17]. This explains why CatBoost outperforms XGBoost despite the latter's more sophisticated regularization: on a heterogeneous 478-sample dataset, bias reduction through ordered boosting provides a greater accuracy benefit than L1/L2 penalty control [8, 16]. The underperformance of GB(Huber loss) relative to tree-ensemble methods (Extra Trees, Random Forest) further suggests that the dataset's predictive signal is better captured through variance reduction via bagging than through boosting's sequential residual correction [15]. XGBoost ranked third, consistent with prior benchmarks showing that its regularization advantage is most pronounced on clean, large-scale structured datasets [16, 20, 21]. CatBoost tends to outperform XGBoost on small or noisy samples, as demonstrated in molecular property prediction tasks [17, 24] and domain-specific comparisons [22, 23]. On small tabular datasets, tree-based ensemble methods generally outperform deep learning approaches, and boosted trees remain the preferred choice when sample counts are low [25, 26].

Conclusion

T_max dominated predictions across all test samples: its high positive SHAP values reflect the physical coupling between the DTG peak temperature and the mass-loss midpoint along the TGA curve [37, 38]. Matrix type ranked second, reflecting the fundamental role of polymer chemistry in governing thermal decomposition behavior [1, 12]. The residue measurement temperature (tga_residue_t) ranked third, acting as a proxy for the high-temperature thermal stability plateau [37, 39]. Mineral loading showed a non-linear SHAP profile: moderate filler contents contributed positively to predicted T_{50}%, while extreme loadings reduced model confidence, consistent with known saturation effects in filler-reinforced composites [4, 5]. Categorical descriptors (mineral formula, mineral name) contributed collectively but ranked below continuous TGA-derived variables, suggesting that the dominant thermal response is governed by measurable thermophysical parameters rather than compositional class labels [38, 41].

Funding. This research was funded by the Science Committee of the Ministry of Science and Higher Education of the Republic of Kazakhstan, grant No. BR28712729.

REFERENCES

1 Karuppusamy, M., Thirumalaisamy, R., Palanisamy, S., Nagamalai, S., El Sayed Massoud, E., and Ayrilmis, N. A review of machine learning applications in polymer composites: advancements, challenges, and future prospects. Journal of Materials Chemistry A, 13, 16290–16308 (2025). https://doi.org/10.1039/D5TA00982K

2 Martin, T.B., and Audus, D.J. Emerging trends in machine learning: a polymer perspective. ACS Polymers Au, 3, 239–258 (2023). https://doi.org/10.1021/acspolymersau.2c00053

3 Pai, S.M., Shah, K.A., Sunder, S., Albuquerque, R.Q., Brütting, C., and Ruckdäschel, H. Machine learning applied to the design and optimization of polymeric materials: a review. Next Materials, 7, 100449 (2025). https://doi.org/10.1016/j.nxmate.2024.100449

4 Jafari, P. et al. Machine learning for expediting next-generation of fire-retardant polymer composites. Composites Communications, 45, 101806 (2024). https://doi.org/10.1016/j.coco.2023.101806

5 Xiao, J., Hobson, J., Ghosh, A., Haranczyk, M., and Wang, D.-Y. Flame retardant properties of metal hydroxide-based polymer composites: a machine learning approach. Composites Communications, 40, 101593 (2023). https://doi.org/10.1016/j.coco.2023.101593

6 Berladir, K., Antosz, K., Ivanov, V., and Mitaľová, Z. Machine learning-driven prediction of composite materials properties based on experimental testing data. Polymers, 17, 694 (2025). https://doi.org/10.3390/polym17050694

7 Friedman, J.H. Greedy function approximation: a gradient boosting machine. Annals of Statistics, 29, 1189–1232 (2001). https://doi.org/10.1214/aos/1013203451

8 Chen, T., and Guestrin, C. XGBoost: a scalable tree boosting system. In: Proceedings of the 22nd ACM SIGKDD International Conference on Knowledge Discovery and Data Mining, ACM, San Francisco, pp. 785–794 (2016). https://doi.org/10.1145/2939672.2939785

9 Prokhorenkova, L., Gusev, G., Vorobev, A., Dorogush, A.V., and Gulin, A. CatBoost: unbiased boosting with categorical features. arXiv:1706.09516 (2019). https://doi.org/10.48550/arXiv.1706.09516

10 Malashin, I., Tynchenko, V., Gantimurov, A., Nelyub, V., and Borodulin, A. Boosting-based machine learning applications in polymer science: a review. Polymers, 17, 499 (2025). https://doi.org/10.3390/polym17040499

11 Ge, W., De Silva, R., Fan, Y., Sisson, S.A., and Stenzel, M.H. Machine learning in polymer research. Advanced Materials, 37, 2413695 (2025). https://doi.org/10.1002/adma.202413695

12 Han, J. et al. Toward accurate machine learning-driven prediction of polymeric composites properties based on experimental data. Materials Genome Engineering Advances, 3, e70027 (2025). https://doi.org/10.1002/mgea.70027

13 Xu, P., Ji, X., Li, M., and Lu, W. Small data machine learning in materials science. npj Computational Materials, 9, 42 (2023). https://doi.org/10.1038/s41524-023-01000-z

14 Zhong, X., Gallagher, B., Liu, S., Kailkhura, B., Hiszpanski, A., and Han, T.Y.-J. Explainable machine learning in materials science. npj Computational Materials, 8, 204 (2022). https://doi.org/10.1038/s41524-022-00884-7

15 Breiman, L., Friedman, J.H., Olshen, R.A., and Stone, C.J. Classification and Regression Trees. Routledge, New York (1984). https://doi.org/10.1201/9781315139470

16 Florek, P., and Zagdański, A. Benchmarking state-of-the-art gradient boosting algorithms for classification. arXiv:2305.17094 (2023). https://doi.org/10.48550/arXiv.2305.17094

17 Boldini, D., Grisoni, F., Kuhn, D., Friedrich, L., and Sieber, S.A. Practical guidelines for the use of gradient boosting for molecular property prediction. Journal of Cheminformatics, 15, 73 (2023). https://doi.org/10.1186/s13321-023-00743-7

18 Nadeau, C., and Bengio, Y. Inference for the generalization error. Machine Learning, 52, 239–281 (2003). https://doi.org/10.1023/A:1024068626366

19 Bentéjac, C., Csörgő, A., and Martínez-Muñoz, G. A comparative analysis of gradient boosting algorithms. Artificial Intelligence Review, 54, 1937–1967 (2021). https://doi.org/10.1007/s10462-020-09896-5

20 Cakiroglu, M., Bekdaş, G., and Geem, Z.W. Fatigue predictive modeling of composite materials for wind turbine blades using explainable gradient boosting models. Coatings, 15, 325 (2025). https://doi.org/10.3390/coatings15030325

21 Mustapha, I.B., Abdulkareem, M., Jassam, T.M., AlAteah, A.H., Al-Sodani, K.A., Al-Tholaia, M.M.H., Nabus, H., Alih, S.C., Abdulkareem, Z., and Ganiyu, A. Comparative analysis of gradient-boosting ensembles for estimation of compressive strength of quaternary blend concrete. International Journal of Concrete Structures and Materials, 18, 18 (2024). https://doi.org/10.1186/s40069-023-00653-w

22 Hancock, J.T., and Khoshgoftaar, T.M. CatBoost for big data: an interdisciplinary review. Journal of Big Data, 7, 94 (2020). https://doi.org/10.1186/s40537-020-00369-8

23 Pemila, M., Pongiannan, R.K., Narayanamoorthi, R., AboRas, K.M., and Youssef, A. Application of an ensemble CatBoost model over complex dataset for vehicle classification. PLOS ONE, 19, e0304619 (2024). https://doi.org/10.1371/journal.pone.0304619

24 Sheridan, R.P., Wang, W.M., Liaw, A., Ma, J., and Gifford, E.M. Extreme gradient boosting as a method for quantitative structure–activity relationships. Journal of Chemical Information and Modeling, 56, 2353–2360 (2016). https://doi.org/10.1021/acs.jcim.6b00591

25 Shwartz-Ziv, R., and Armon, A. Tabular data: deep learning is not all you need. Information Fusion, 81, 84–90 (2022). https://doi.org/10.1016/j.inffus.2021.11.011

26 McElfresh, D. et al. When do neural nets outperform boosted trees on tabular data? arXiv:2305.02997 (2023). https://doi.org/10.48550/arXiv.2305.02997

27 Malashin, I.P., Tynchenko, V.S., Nelyub, V.A., Borodulin, A.S., and Gantimurov, A.P. Estimation and prediction of the polymers' physical characteristics using the machine learning models. Polymers, 16, 115 (2024). https://doi.org/10.3390/polym16010115

28 Kucukarslan, O. Machine learning-based heat deflection temperature prediction and effect analysis in polypropylene composites using CatBoost and Shapley Additive Explanations. Engineering Applications of Artificial Intelligence, 120, 106873 (2023). https://doi.org/10.1016/j.engappai.2023.106873

29 Phoeuk, M. et al. Accuracy prediction of compressive strength of concrete incorporating recycled aggregate using ensemble learning algorithms: multinational dataset. Advances in Civil Engineering, 2023, 5076429 (2023). https://doi.org/10.1155/2023/5076429

30 Uddin, M.N., Shanmugasundaram, N., and Praveenkumar, S. Prediction of compressive strength and tensile strain of engineered cementitious composite using machine learning. International Journal of Mechanics and Materials Design, 20, 671–716 (2024). https://doi.org/10.1007/s10999-023-09695-0

31 Khodadadi, N., Roghani, H., De Caso, F., El-kenawy, E.-S.M., Yesha, Y., and Nanni, A. Data-driven PSO-CatBoost machine learning model to predict the compressive strength of CFRP-confined circular concrete specimens. Thin-Walled Structures, 198, 111763 (2024). https://doi.org/10.1016/j.tws.2024.111763

32 Aydın, Y., Cakiroglu, C., Bekdaş, G., and Geem, Z.W. Explainable ensemble learning and multilayer perceptron modeling for compressive strength prediction of ultra-high-performance concrete. Biomimetics, 9, 544 (2024). https://doi.org/10.3390/biomimetics9090544

33 Lundberg, S.M., and Lee, S.-I. A unified approach to interpreting model predictions. Advances in Neural Information Processing Systems, 30, 4766–4777 (2017). https://doi.org/10.48550/arXiv.1705.07874

34 Tsioptsias, C. et al. Simulation and experimental study of the isothermal thermogravimetric analysis and the apparent alterations of the thermal stability of composite polymers. Polymers, 16, 1454 (2024). https://doi.org/10.3390/polym16111454

35 Gurnani, R., Kuenneth, C., Toland, A., and Ramprasad, R. Polymer informatics at scale with multitask graph neural networks. Chemistry of Materials, 35, 1560–1567 (2023). https://doi.org/10.1021/acs.chemmater.2c02991

36 Frie, C., Schork, N., Reiff, A., and Melz, T. Exploration of materials fatigue influence factors using interpretable machine learning. Fatigue and Fracture of Engineering Materials and Structures, 47, 2752–2773 (2024). https://doi.org/10.1111/ffe.14315

37 Elaskalany, M. et al. Stochastic multiscale modeling of electrical conductivity of carbon nanotube polymer nanocomposites: an interpretable machine learning approach. Advanced Engineering Materials, 26, 2401233 (2024). https://doi.org/10.1002/adem.202401233

38 Mykytyshyn, A. et al. Machine learning approaches for classification of composite materials. Modelling, 6, 118 (2025). https://doi.org/10.3390/modelling6040118

39 Wan, Z., Chen, S., Feng, X. & Sun, Z.-Y. From processing to properties: enhancing machine learning models with microstructural information in polymer nanocomposites. Composites Communications, 51, 102072 (2024). https://doi.org/10.1016/j.coco.2024.102072

40 Champa-Bujaico, E., Díez-Pascual, A.M., Redondo, A.L., and Garcia-Diaz, P. Interpretable machine learning framework to predict the glass transition temperature of polymers. Polymers, 16, 1049 (2024). https://doi.org/10.3390/polym16081049

41 Liu, B., Vu-Bac, N., Zhuang, X., Fu, X., and Rabczuk, T. Stochastic integrated machine learning based multiscale approach for the prediction of the thermal conductivity in carbon nanotube reinforced polymeric composites. Composites Science and Technology, 224, 109425 (2022). https://doi.org/10.1016/j.compscitech.2022.109425

[1*] Изтлеуова Б.,
докторант, ORCID ID: 0009-0009-7588-8976,
[*]e-mail: b.iztleuova@zhubanov.edu.kz
[1]Иманчиев А.,
ф.-м.ғ.к., қауымдастырылған профессор, ORCID ID: 0000-0002-1835-2501,
e-mail:imanchiev_ae@mail.ru
[1]Бекешев А.,
ф.-м.ғ.к., қауымдастырылған профессор, ORCID ID: 0000-0002-7038-4631,
e-mail: amirbek2401@gmail.com
[1]Жантурина Н.,
PhD, қауымдастырылған профессор, ORCID ID: 0000-0001-9540-6334,
e-mail: nzhanturina@mail.ru
[2]Усенкулова Ш.,
PhD, қауымдастырылған профессор, ORCID ID: 0000-0001-9417-755X,
e-mail: Sholpan1990@gmail.com
[3]Ванг С.,
PhD, қауымдастырылған профессор, ORCID ID: 0000-0001-5881-4400,
e-mail: wxcmx@ustc.edu.cn

[1] Қ. Жұбанов атындағы Ақтөбе өңірлік университеті,
Ақтөбе қ., Қазақстан
[2]К. Құлажанов атындағы Қазақ технология және бизнес университеті,
Астана қ., Қазақстан
[3]Қытай Ғылым және технология университетінің Өрт қауіпсіздігі
жөніндегі мемлекеттік негізгі зертханасы,
Хэфэй қ., Қытай

МИНЕРАЛ–ПОЛИМЕР КОМПОЗИТТЕРІНДЕГІ ТЕРМИЯЛЫҚ ЫДЫРАУДЫ БОЛЖАУ ҮШІН ГРАДИЕНТТІ БУСТИНГ ӘДІСТЕРІН ЭМПИРИКАЛЫҚ САЛЫСТЫРМАЛЫ ТАЛДАУ

Аңдатпа

Бұл зерттеуде минералдық толтырғыштары бар винил эфир матрицалары мен эпоксидтер негізіндегі композиттердің термогравиметриялық талдау (TGA) деректеріне қолданылған градиентті бустинг алгоритмдеріне математикалық және эмпирикалық талдау ұсынылған. Градиентті бустинг алгоритмі TGA-ның сандық мысалы негізінде кезең-кезеңімен көрсетілген. Одан кейін XGBoost және CatBoost алгоритмдері формалды түрде талданды. Рецензияланған әдебиеттерден алынған 478 дерек бойынша 5 рет қайталанған 5-қатпарлы кросс-валидация әдісімен 12 алгоритм салыстырылды. Extra Trees және CatBoost ең жоғары нәтижелерге статистикалық тұрғыдан тең деңгейде жетті (орташа $R^2 = 0.7430 \pm 0.0879$ және 0.7313 ± 0.0793 сәйкесінше; Nadeau & Bengio corrected $t = 0.483$, $p = 0.634$), және олар барлық сызықтық базалық модельдерден, SVR және MLP әдістерінен жоғары нәтиже көрсетті. Практикалық қолдану үшін CatBoost ұсынылады: оның реттелген бустингі шағын деректер жиындарында ($n < 1000$) бейтарап градиент бағалауын қамтамасыз етеді, ал градиент ағашының құрылымына негізделген SHAP талдауы TGA механизмдерімен үйлесімді физикалық тұрғыдан интерпретацияланатын белгі атрибуцияларын ашады. SHAP мәндері TGA-ның шың температурасы (T_max) мен матрица түрі негізгі анықтаушы факторлар екенін көрсетті. Ұсынылған алдын ала өңдеу құбыры, оның ішінде phr-дан wt%-ға түрлендіру, label encoding және медианалық толықтыру, әртекті TGA әдеби деректер жиындары үшін қайта жаңғыртылатын стратегияны қамтамасыз етеді.

Түйін сөздер: градиентті бустинг, XGBoost, CatBoost, полимерлік композиттер, машиналық оқыту, термогравиметриялық талдау, реттелген бустинг, математикалық негіздер, алгоритм таңдау

[1*] Изтлеуова Б.,
докторант, ORCID ID: 0009-0009-7588-8976,
*e-mail: b.iztleuova@zhubanov.edu.kz
[1]Иманчиев А.,
к.ф.-м.н, ассоциированный профессор, ORCID ID: 0000-0002-1835-2501,
e-mail:imanchiev_ae@mail.ru
[1]Бекешев А.,
к.ф.-м.н, ассоциированный профессор, ORCID ID: 0000-0002-7038-4631,
e-mail: amirbek2401@gmail.com
[1]Жантурина Н.,
PhD, ассоциированный профессор, ORCID ID: 0000-0001-9540-6334,
e-mail: nzhanturina@mail.ru
[2]Усенкулова Ш.,
PhD, ассоциированный профессор, ORCID ID: 0000-0001-9417-755X,
e-mail: Sholpan1990@gmail.com
[3]Ванг С.,
PhD, ассоциированный профессор, ORCID ID: 0000-0001-5881-4400,
e-mail: wxcmx@ustc.edu.cn

[1]Актюбинский региональный университет им. К. Жубанова,
г. Актобе, Казахстан
[2]Казахский университет технологии и бизнеса им. К. Кулажанова,
г. Астана, Казахстан
[3]Государственная ключевая лаборатория пожарной науки,
Университет науки и технологий Китая,
Хэфэй, Китай

ЭМПИРИЧЕСКОЕ СРАВНИТЕЛЬНОЕ ИССЛЕДОВАНИЕ ГРАДИЕНТНОГО БУСТИНГА ДЛЯ ПРОГНОЗИРОВАНИЯ ТЕРМИЧЕСКОГО РАЗЛОЖЕНИЯ В ПОЛИМЕРНЫХ КОМПОЗИТАХ С МИНЕРАЛЬНЫМИ НАПОЛНИТЕЛЯМИ

Аннотация

В данном исследовании представлен математический и эмпирический анализ алгоритмов градиентного бустинга, применяемых к данным термогравиметрического анализа (ТГА) композитов на основе винилэфирных и эпоксидных смол с минеральными наполнителями. Алгоритм градиентного бустинга пошагово представлен на численном примере ТГА. Далее формально проанализированы алгоритмы XGBoost и CatBoost. Сравнение 12 алгоритмов выполнено на основе 478 данных из рецензируемой литературы с использованием пятикратно повторенной 5-блочной кросс-валидации. Методы Extra Trees и CatBoost показали статистически эквивалентные наилучшие результаты (среднее $R^2 = 0.7430 \pm 0.0879$ и 0.7313 ± 0.0793 соответственно; Nadeau & Bengio corrected $t = 0.483$, $p = 0.634$), превзойдя все линейные базовые модели, SVR и MLP. Для практического применения рекомендуется CatBoost: его упорядоченный бустинг обеспечивает несмещенные оценки градиентов на малых выборках ($n < 1000$), а SHAP-анализ структуры градиентных деревьев выявляет физически интерпретируемые атрибуции признаков, согласующиеся с известными механизмами ТГА. Значения SHAP показали, что пиковая температура TGA (T_max) и тип матрицы являются основными определяющими факторами. Предложенный пайплайн предварительной обработки, включающий преобразование phr в wt%, label encoding и медианную импутацию, обеспечивает воспроизводимую стратегию для разнородных литературных TGA-данных.

Ключевые слова: градиентный бустинг, XGBoost, CatBoost, полимерные композиты, машинное обучение, термогравиметрический анализ, упорядоченный бустинг, математические основы, выбор алгоритма.

UDC 537.9; 620.22
IRSTI 29.19.22

https://doi.org/10.55452/1998-6688-2026-23-3-414-421

[1]Yestoreyeva A.,
MSc student, ORCID ID: 0009-0004-0284-6111,
e-mail: akzhan.yestoreyeva@nu.edu.kz
[1,2]*Atabaev T.S.,
PhD, ORCID ID: 0000-0001-7252-4098,
*e-mail: timur.atabaev@nu.edu.kz

[1]Nazarbayev University, Astana, Kazakhstan
[2]Institute of Functional Materials, Astana, Kazakhstan

IMPROVING PHOTOCURRENT DENSITY GENERATION BY POROUS TIO_2 FILMS MODIFIED WITH POLYSTYRENE PARTICLES

Abstract

The development of porous TiO_2 thin films is of significant interest for photovoltaic and photocatalytic applications owing to their ability to enhance light utilization. Herein, porous TiO_2 films were prepared using 350 nm polystyrene (PS) particles as sacrificial templates, and the effect of PS concentration on photocurrent generation was systematically evaluated. Morphological and optical analyses confirmed the successful formation of porous structures with improved light-harvesting characteristics. Typically, the optimized PS-modified TiO_2 film exhibited a photocurrent density of ~118 μA/cm^2, corresponding to an enhancement of ~20.5% relative to bare TiO_2 film. Integrating sphere measurements revealed increased total absorbance for the porous films, indicating that the improved photocurrent density generation originates from enhanced light trapping within the porous surface. This work highlights the importance of porosity engineering and demonstrates that PS-assisted templating is an effective approach for enhancing the performance of TiO_2-based photoactive thin films.

Keywords: TiO_2 thin films, polystyrene particles, porosity engineering, photocurrent density, light trapping.

Received June 25, 2026; revised July 17, 2026; accepted July 30, 2026.

Introduction

TiO_2 semiconductor thin films have been widely employed as n-type layers in a variety of devices, including dye-sensitized solar cells, perovskite solar cells, and photocatalytic systems [1-3]. Over the years, numerous strategies have been developed to enhance photocurrent generation and electrical conductivity in TiO_2 thin films, such as plasmonic sensitization [4], integration with two-dimensional (2D) materials [5], elemental doping [6], and surface nanostructuring [7]. Among these approaches, surface nanostructuring has attracted considerable attention due to its ability to create mesoporous architectures that enhance light harvesting through increased photon scattering, thereby promoting the generation of additional electron-hole pairs. This strategy is particularly attractive from both economic and scalability perspectives, as it does not require costly dopants, plasmonic materials, or 2D nanomaterials. Moreover, nanostructured surfaces exhibit improved resistance to humidity, as previously demonstrated for triboelectric nanogenerators [8].

Nanostructured and mesoporous TiO_2 films can be fabricated using a variety of techniques, including sol-gel synthesis [9], screen-printing [10], electrodeposition [11], and spin-coating [12]. Among these methods, screen-printing and spin-coating are particularly attractive due to their ability to produce uniform films with well-controlled thickness. In addition, the TiO_2 slurry paste used in both techniques can be readily prepared from commercially available TiO_2 nanoparticles (NPs), allowing straightforward adjustment of NPs concentration, solvent composition, and binder content

to achieve the desired viscosity. Furthermore, soft-templating agents, such as monodisperse polymer NPs, can be also incorporated into the slurry paste. During the subsequent calcination process, the polymer templates are completely removed, leaving behind pores that act as light-scattering centers and enhance light harvesting within the TiO_2 film.

In this study, we present a systematic investigation of the relationship between PS particles concentration, film porosity, and photocurrent generation in TiO_2 thin films. To the best of our knowledge, the effect of PS concentration on the photocurrent generation rate of porous TiO_2 films has not been comprehensively explored before. We showed that optimized PS-modified TiO_2 film exhibited a photocurrent density approximately 20.5% higher than that of bare TiO_2 film. Absorbance measurements with an integrating sphere revealed that the enhancement originates from improved light absorption within the porous structure.

Materials and methods

All reagents were purchased from Merck KGaA and used as received without further purification. Monodisperse PS particles with a diameter of 350 nm (2.5 wt.% aqueous suspension) were obtained from Polysciences Inc. To prepare porous TiO_2 films, 50, 100, and 150 μL aliquots of the PS suspension were transferred into separate vials and dried in an oven for several days to ensure complete removal of water.

The TiO_2 slurry paste was prepared according to the previously reported procedure [13], with the concentration of TiO_2 NPs adjusted to approximately 59-60 mg/mL. Subsequently, 0.3 mL of the TiO_2 slurry was added to each vial containing dried PS particles, and the mixtures were stirred at 500 rpm for 48 h to obtain homogeneous dispersions. The resulting pastes were deposited onto cleaned fluorine-doped tin oxide (FTO) glass substrates (12-16 Ω/cm^2) using a three-step spin-coating procedure. First, a TiO_2 underlayer was deposited using a bare TiO_2 slurry paste at 500 rpm for 5 s, followed by 5000 rpm for 20 s. Second, a layer of either bare or PS-modified TiO_2 slurry paste was deposited under identical spin-coating conditions on a top of first TiO_2 underlayer. Finally, a solution consisting of titanium isopropoxide (0.1 mL) and isopropanol (1.0 mL) was spin-coated at 500 rpm for 5 s with subsequent acceleration to 2000 rpm for 20 s. After the deposition of each layer, the films were annealed at 500 °C to obtain solid TiO_2 layers on the FTO substrates. The photocurrent generation performance of all samples was evaluated using a conventional three-electrode configuration. TiO_2-coated FTO substrates served as the working electrodes, while a platinum wire and an Ag/AgCl electrode were used as the counter and reference electrodes, respectively. All measurements were performed in 0.1 M Na_2SO_4 aqueous electrolyte and repeated at least three times to ensure reproducibility. The reported values represent the average of the obtained results, with only minor variations observed between measurements. Simulated solar irradiation was provided by a Newport LCS-100 solar simulator (AM 1.5G, Newport-Spectra Physics), calibrated to one-sun intensity (100 mW cm^{-2}) using a certified silicon reference cell. Chronoamperometry (CA) measurements were carried out using a PalmSens4 potentiostat at an applied potential of 0.6 V versus Ag/AgCl under chopped illumination conditions.

The morphology of the TiO_2 films was characterized using a field-emission scanning electron microscope (FESEM, ZEISS Crossbeam 540). Crystal structure analysis was performed by X-ray diffraction (XRD) using a SmartLab diffractometer (Rigaku Corp.). The surface chemical composition of the optimized sample was investigated by X-ray photoelectron spectroscopy (XPS, NEXSA system). Total absorbance measurements were carried out using a Quantaurus-QY spectrometer (Hamamatsu Photonics K.K.) equipped with an integrating sphere.

Results and discussion

It is well-known that optimized surface porosity can improve light trapping and thereby enhance the photocurrent generation of semiconductor structures [14]. Figure 1 shows the CA responses of

TiO_2 films prepared with different PS concentrations. Under solar light illumination, all samples generate electron-hole pairs, which are subsequently separated and transported through the system, resulting in measurable photocurrent. Once the illumination is removed, the photocurrent rapidly decreases to nearly zero, confirming that the observed current is solely associated with photoinduced processes. The reproducible light on-off cycles further demonstrate that the photocurrent generation occurs only under sunlight illumination.

On the other hand, clear differences in photocurrent density generation can be observed among the investigated samples. In particular, the TiO_2 films modified with 50 and 100 μL of PS particles exhibited the maximum photocurrent densities of 118.28 and 118.22 μA/cm^2, respectively, corresponding to an enhancement of approximately 20.5% compared to the bare TiO_2 film (98.17 μA/cm^2). In contrast, the sample prepared with 150 μL of PS particles generated a photocurrent density of only 97.65 μA/cm^2, which is slightly lower than that of the unmodified TiO_2 film. The photocurrent density measurements were repeated using at least for four different samples per batch, with a photocurrent density deviation below 2-3%, demonstrating good reproducibility of the cells. The observed trend indicates the existence of an optimal porosity level, beyond which further increases in porosity may negatively affect the photocurrent generation performance of the TiO_2 films. The decrease in photocurrent at higher PS concentrations can be attributed to excessive porosity, which may reduce film connectivity and hinder efficient charge transport within the TiO_2 films.

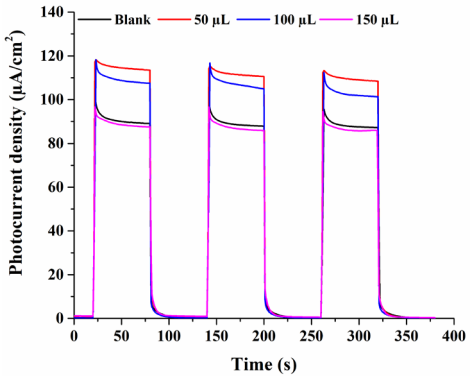


Figure 1 – Chronoamperometry results
for bare and PS-modified TiO_2 films

Next, the bare and optimal PS-modified TiO_2 (50 μL) films were investigated using FESEM to visualize the effect of PS incorporation on the film morphology. Figures 2a and 2b show the corresponding FESEM images obtained at 5000× magnification. In the case of the bare TiO_2 film, a relatively flat and uniform surface can be observed, indicating that the TiO_2 NPs are evenly distributed and form a continuous mesoscopic layer. In contrast, the PS-modified TiO_2 film reveals the presence of numerous pores with diameters comparable to or larger than the size of the original PS particles. The existence of these pores confirms the successful incorporation of PS particles into the TiO_2 slurry paste and their complete removal during the thermal treatment process. Some pores appear larger than expected, which is most likely due to the aggregation of several PS particles in the same area prior to heat treatment. Overall, the FESEM results confirm that PS-assisted templating is an effective approach for generating porous TiO_2 films with increased surface roughness and pore density.

Both films were further compared using XRD analysis. Figure 3 presents the diffraction patterns of the FTO-coated glass substrate, blank TiO_2 film, and the optimal PS-modified TiO_2 (50 μL) film deposited on FTO-coated glasses. It can be seen that both TiO_2 films exhibit characteristic diffraction peaks of the anatase phase located at 25.4°, 37.8°, 48.2°, 54.0°, 55.2°, and 62.8°, corresponding to the (101), (004), (200), (105), (211), and (204) crystal planes, respectively [12]. The diffraction peaks originating from the FTO substrate are also visible in all patterns. Importantly, no noticeable shifts in peak positions or significant changes in peak intensities were observed after PS particles

incorporation, indicating that the modification process does not affect the crystal structure or phase composition of the TiO_2 films.

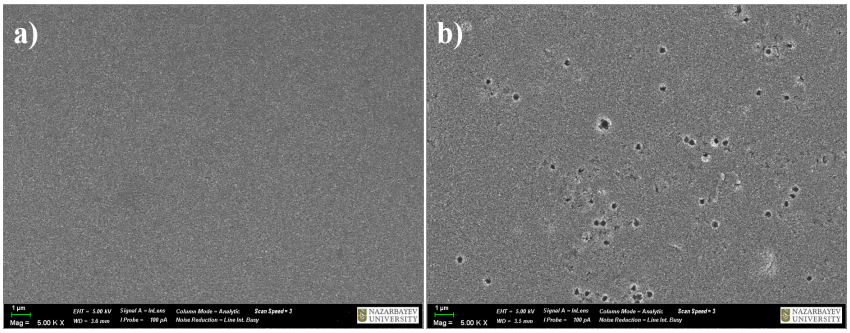


Figure 2 – FESEM images of (a) bare
and (b) optimal PS-modified TiO_2 (50 μL) films

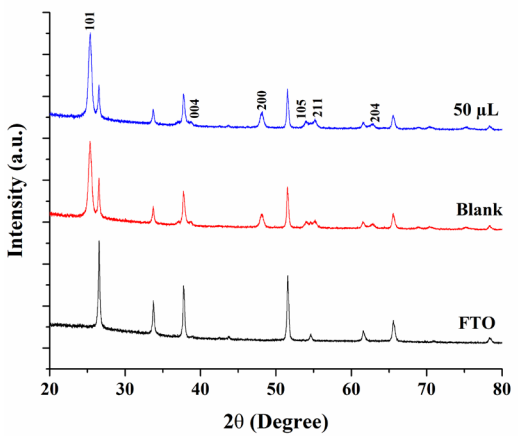


Figure 3 – XRD patterns of FTO-coated glass,
bare and optimal PS-modified TiO_2 (50 μL) films

Moreover, the oxidation states of titanium and oxygen in the bare and optimal PS-modified TiO_2 (50 μL) films were investigated using XPS to confirm that the incorporation of PS particles does not alter the surface chemical composition of the films. Figures 4a and 4b present the high-resolution XPS spectra of the optimal PS-modified TiO_2 (50 μL) film only, as both samples exhibited nearly identical spectral features. The Ti 2p spectrum displays characteristic Ti $2p_{3/2}$ and Ti $2p_{1/2}$ peaks at 458.2 and 463.9 eV, respectively, confirming the titanium oxidation state to be Ti^{4+} [12]. Similarly, the O 1s spectrum can be deconvoluted into peaks centered at 529.5 and 530.2 eV, which are attributed to Ti-O bonds and surface-adsorbed oxygen-containing species (or hydroxyl/water groups), respectively. Therefore, the XPS analysis confirms that both films consist of chemically identical TiO_2 structures and that no changes in oxidation states occur after PS incorporation. Combined with the XRD results, these findings suggest that the enhanced photocurrent generation originates primarily from the increased surface porosity and light-trapping capability of the PS-modified TiO_2 films rather than from changes in their crystal structure or surface chemistry.

To verify the improved light-harvesting capability of the optimal PS-modified TiO_2 (50 μL) film compared to bare TiO_2, total absorbance measurements were performed using an integrating sphere in the wavelength range of 325-500 nm. As shown in Figure 5, the bare TiO_2 film exhibits strong absorption in the UV region, followed by a sharp decrease in absorbance above ~ 390 nm, which is consistent with the reported bandgap of anatase TiO_2 (3.18-3.20 eV) [5, 12]. In contrast, the optimal PS-modified TiO_2 (50 μL) film displays slightly higher absorbance in the UV region as well

as an extended absorption tail in the visible range. This behavior highlights the beneficial effect of increased surface porosity on the optical properties of the film. The enhanced absorbance is attributed to stronger light-scattering effects within the porous structure, which increase the effective optical path length and promote more efficient light harvesting. Consequently, the improved light absorption of the PS-modified TiO_2 film is consistent with its higher photocurrent density observed during CA measurements.

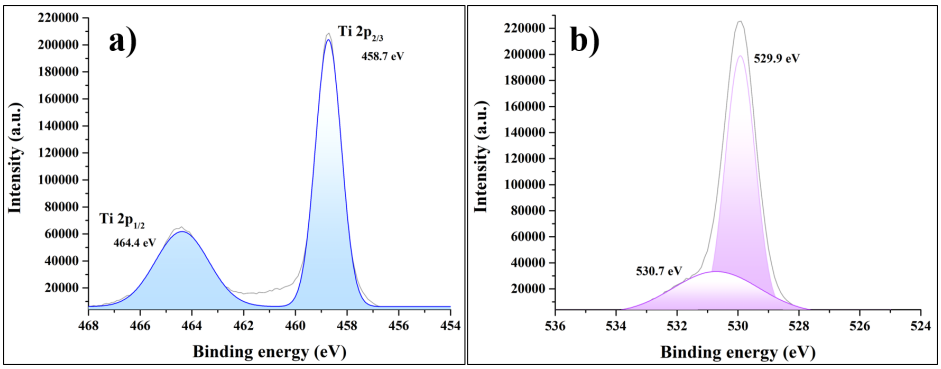


Figure 4 – High resolution XPS survey of (a) titanium
and (b) oxygen elements in optimal PS-modified TiO_2 (50 µL) film

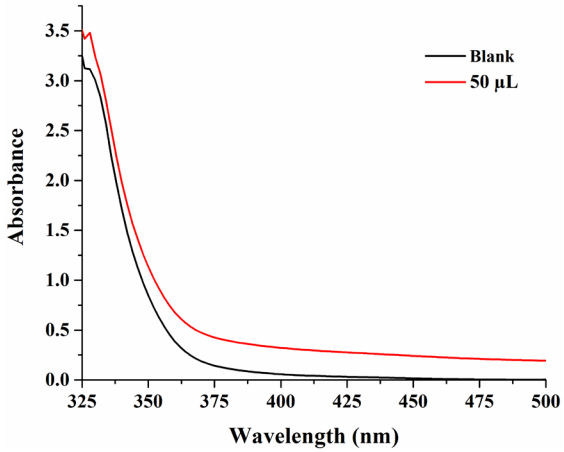


Figure 5 – Total absorbance measurements
of bare and optimal PS-modified TiO_2 (50 µL) films

Conclusions

In summary, porous TiO_2 thin films were successfully fabricated through PS-assisted templating using monodisperse 350 nm PS nanoparticles at different concentrations. Chronoamperometry measurements revealed that the incorporation of an optimal amount of PS particles (50 µL) increased the photocurrent density from 98.17 to 118.28 µA/cm^2, corresponding to an enhancement of approximately 20.5% compared to bare TiO_2 films. FESEM analysis confirmed the formation of a porous surface morphology after PS removal, while XRD and XPS measurements demonstrated that the crystal structure and surface chemical composition of TiO_2 remained unchanged after modification. Total absorbance measurements performed using an integrating sphere revealed enhanced light-harvesting capability of the porous films, which was attributed to increased light scattering and a longer optical path within the TiO_2 film. These findings indicate that the observed

photocurrent enhancement originates primarily from porosity-induced optical effects rather than changes in the intrinsic properties of TiO_2. Overall, PS-assisted surface nanostructuring represents a simple, scalable, and cost-effective strategy for improving the photocurrent density of TiO_2 thin films and may be applicable to other photovoltaic and photocatalytic systems.

Acknowledgments

The technical support from Mrs. Kuralay Rustembekkyzy is highly appreciated.

Information on funding

This research has been funded by the Committee of Science of the Ministry of Science and Higher Education of the Republic of Kazakhstan (Grant No. BR28712489).

REFERENCES

1 Tasić, N., Stanojević, Z.M., Branković, Z., Lačnjevac, U., Ribić, V., Žunić, M., Novaković, T., Podlogar, M., and Branković, G. Mesoporous films prepared from synthesized TiO2 nanoparticles and their application in dye-sensitized solar cells (DSSCs). Electrochimica Acta, 210, 606–614 (2016). https://doi.org/10.1016/j.electacta.2016.05.179

2 Hernández-Granados, A., Corpus-Mendoza, A.N., Moreno-Romero, P.M., Rodríguez-Castañeda, C.A., Pascoe-Sussoni, J.E., Castelo-González, O.A., Menchaca-Campos, E.C., Escorcia-García, J., and Hu, H. Optically uniform thin films of mesoporous TiO_2 for perovskite solar cell applications. Optical Materials, 88, 695–703 (2019). https://doi.org/10.1016/j.optmat.2018.12.044

3 Ishchenko, O.M., Lamblin, G., Guillot, J., Infante, I.C., Guennou, M., Adjeroud, N., Fechete, I., Garin, F., Turek, P., and Lenoble, D. Mesoporous TiO2 anatase films for enhanced photocatalytic activity under UV and visible light. RSC Advances, 10, 38233–38243 (2020). https://doi.org/10.1039/d0ra06455f

4 Isah, K.U., Jolayemi, B.J., Ahmadu, U., Kimpa, M.I., and Alu, N. Plasmonic effect of silver nanoparticles intercalated into mesoporous betalain-sensitized-TiO_2 film electrodes on photovoltaic performance of dye-sensitized solar cells. Materials for Renewable and Sustainable Energy, 5, 10 (2016). https://doi.org/10.1007/s40243-016-0075-z

5 Khamkhash, L., Em, S., Molkenova, A., Hwang, Y.-H., and T.Sh. Atabaev. Crack-free and thickness-controllable deposition of TiO2-rGO thin films for solar harnessing devices. Coatings, 12, 218 (2022). https://doi.org/10.3390/coatings12020218

6 Gartner, M., Szekeres, A., Stroescu, H., Mitrea, D., and Covei, M. Advanced nanostructured coatings based on doped TiO_2 for various applications. Molecules, 28, 7828 (2023). https://doi.org/10.3390/molecules28237828

7 Liu, Y.-C., Lu, Y.-F., Zeng, Y.-Z., Liao, C.-H., Chung, J.-C., and Wei, T.-Y. Nanostructured mesoporous titanium dioxide thin film prepared by sol-gel method for dye-sensitized solar cell. International Journal of Photoenergy, 2011, 619069 (2011). https://doi.org/10.1155/2011/619069

8 Karimi, M., Seddighi, S., and Mohammadpour, R. Nanostructured versus flat compact electrode for triboelectric nanogenerators at high humidity. Scientific Reports, 11, 16191 (2021). https://doi.org/10.1038/s41598-021-95621-3

9 Choi, H., Stathatos, E., Dionysiou, D.D. Sol-gel preparation of mesoporous photocatalytic TiO2 films and TiO2/Al2O3 composite membranes for environmental applications. Applied Catalysis B: Environmental, 63. 60–67 (2005). https://doi.org/10.1016/j.apcatb.2005.09.012

10 Potts, S., Bolton, R., Dunlop, T., Lacey, K., Worsley, C., Watson, T., and Jewell, E. Enhancing the performance of the mesoporous TiO_2 film in printed perovskite photovoltaics through high-speed imaging and ink rheology techniques. Advanced Functional Materials, 34, 2401959 (2024). https://doi.org/10.1002/adfm.202401959

11 Ngo, P.H.T., Vo, T.A.N., Vo, K.V.L., Nguyen, V.S., and Wei, T.-C. Electrodeposited mesoporous TiO2 thin films and their application as the scalable electron transport layer for perovskite solar modules. Electrochimica Acta, 503, 144802 (2024). https://doi.org/10.1016/j.electacta.2024.144802

12 Rustembekkyzy, K., Zholdasbekov, A., Abduvalov, A., Kaikanov, M., and Atabaev, T.Sh. Porosity-dependent photoelectrochemical activity of double-layered TiO2 thin films deposited by spin-coating method. RSC Advances, 13, 34482–34488 (2023). https://doi.org/10.1039/d3ra06914a

13 Ito, S., Chen, P., Comte, P., Nazeeruddin, M.K., Liska, P., Péchy, P., and Grätzel, M. Fabrication of screen-printing pastes from TiO_2 powders for dye-sensitised solar cells. Progress in Photovoltaics Research and Applications, 15, 603–612 (2007). https://doi.org/10.1002/pip.768

14 Haque, S., Mendes, M.J., Sanchez-Sobrado, O., Águas, H., Fortunato, E., and Martins, R. Photonic-structured TiO_2 for high-efficiency, flexible and stable perovskite solar cells. Nano Energy, 59, 91–101 (2019). https://doi.org/10.1016/j.nanoen.2019.02.023

[1]Естөреева А.,
магистрант, ORCID ID: 0009-0004-0284-6111,
e-mail: akzhan.yestoreyeva@nu.edu.kz
[1,2*]Атабаев Т.Ш.,
PhD, ORCID ID: 0000-0001-7252-4098,
*e-mail: timur.atabaev@nu.edu.kz

[1]Назарбаев университеті, Астана қ., Қазақстан
[2]Функционалды материалдар институты, Астана қ., Қазақстан

ПОЛИСТИРОЛ БӨЛШЕКТЕРІМЕН МОДИФИКАЦИЯЛАНҒАН КЕУЕКТІ TiO_2 ҚАБЫҚШАЛАРЫ АРҚЫЛЫ ФОТОТОК ТЫҒЫЗДЫҒЫНЫҢ ГЕНЕРАЦИЯСЫН АРТТЫРУ

Аңдатпа

Кеуекті TiO_2 жұқа қабықшаларын әзірлеу жарықты тиімдірек пайдалануға мүмкіндік беруіне байланысты фотоэлектрлік және фотокаталитикалық қолданбалар үшін үлкен қызығушылық тудырады. Бұл жұмыста диаметрі 350 нм полистирол (PS) бөлшектері қалыптаушы шаблондар ретінде пайдаланылып, кеуекті TiO_2 қабықшалары дайындалды және полистирол (PS) бөлшектерінің концентрациясының фототок генерациясына әсері жүйелі түрде зерттелді. Морфологиялық және оптикалық талдаулар жарықты жұту қасиеттері жақсартылған кеуекті құрылымдардың сәтті қалыптасқанын растады. Оптимизацияланған PS-модификацияланған TiO_2 қабықшасы шамамен 118 мкА/см^2 фототок тығыздығын көрсетті, бұл модификацияланбаған TiO_2 қабықшасымен салыстырғанда шамамен 20,5%-ға жоғары. Интегралдаушы сфера көмегімен жүргізілген өлшеулер кеуекті қабықшалардың жалпы жарық жұтуының артқанын көрсетті, бұл фототок тығыздығының жақсаруы кеуекті архитектурадағы жарықтың тиімдірек ұсталуымен байланысты екенін дәлелдейді. Бұл жұмыс кеуектілікті басқарудың маңыздылығын көрсетіп, полистирол (PS) бөлшектерінің көмегімен шаблондау TiO_2 негізіндегі фотоактивті жұқа қабықшалардың тиімділігін арттырудың тиімді тәсілі екенін дәлелдейді.

Түйін сөздер: TiO_2 жұқа қабықшалары, полистирол бөлшектері, кеуектілікті басқару, фототок тығыздығы, жарықты ұстау.

[1] Естөреева А.,
магистрант, ORCID ID: 0009-0004-0284-6111,
e-mail: akzhan.yestoreyeva@nu.edu.kz
[1,2]*Атабаев Т.Ш.,
PhD, ORCID ID: 0000-0001-7252-4098,
*e-mail: timur.atabaev@nu.edu.kz

[1]Назарбаев Университет, г. Астана, Казахстан
[2]Институт функциональных материалов, г. Астана, Казахстан

ПОВЫШЕНИЕ ГЕНЕРАЦИИ ПЛОТНОСТИ ФОТОТОКА С ПОМОЩЬЮ ПОРИСТЫХ ПЛЁНОК TiO_2, МОДИФИЦИРОВАННЫХ ПОЛИСТИРОЛЬНЫМИ ЧАСТИЦАМИ

Аннотация

Разработка пористых тонких пленок TiO_2 представляет большой интерес для фотоэлектрических и фотокаталитических применений благодаря их способности улучшать использование света. В данной работе пористые пленки TiO_2 были получены с использованием полистирольных (PS) частиц диаметром 350 нм в качестве структурообразующих шаблонов, а влияние концентрации PS частиц на генерацию фототока было систематически исследовано. Морфологический и оптический анализы подтвердили успешное формирование пористых структур с улучшенными характеристиками светопоглощения. Оптимизированная плёнка TiO_2, модифицированная полистирольными (PS) частицами, продемонстрировала плотность фототока около 118 мкА/см^2, что соответствует увеличению примерно на 20,5% по сравнению с немодифицированной пленкой TiO_2. Измерения с использованием интегрирующей сферы показали повышение общего поглощения света пористыми пленками, что свидетельствует о том, что улучшение генерации плотности фототока обусловлено более эффективным захватом света в пористой структуре. Данная работа подчеркивает важность управления пористостью и демонстрирует, что структурирование с использованием PS частиц является эффективным подходом для повышения эффективности фотоактивных тонких пленок на основе TiO_2.

Ключевые слова: тонкие пленки TiO_2, полистирольные частицы, управление пористостью, плотность фототока, захват света.

UDC 544.6;620.3;621.352
IRSTI 31.15.33;44.35.29

https://doi.org/10.55452/1998-6688-2026-23-3-422-433

[1,2*]Zhumadilov B.Ye.,
PhD student, ORCID ID: 0000-0001-5784-3840,
*e-mail: zhumadilovbe@gmail.com
[1,2]Markhabayeva A.A.,
PhD, ORCID ID: 0000-0002-0657-422X,
e-mail: aiko_marx@mail.ru
[1,3]Gabdullin M.T.,
PhD, ORCID ID: 0000-0003-4853-3642,
e-mail: gabdullin@physics.kz

[1]Institute of Applied Sciences and Information Technologies, Almaty, Kazakhstan
[2]Al-Farabi Kazakh National University, Almaty, Kazakhstan
[3]Kazakh-British Technical University, Almaty, Kazakhstan

RF MAGNETRON SPUTTERED WS_2 THIN FILMS ON TI AND TI/CNWS SUBSTRATES: STRUCTURAL CHARACTERIZATION AND HER PERFORMANCE

Abstract

Hydrogen evolution reaction (HER) electrocatalysts based on earth-abundant materials are promising alternatives to noble metal catalysts. In this work, WS_2 thin films were deposited on titanium substrates by RF magnetron sputtering with deposition times ranging from 30 to 120 min to investigate the influence of film thickness on structural and electrochemical properties. In addition, Ti/CNWs/WS_2 composite electrodes were fabricated by combining vertically aligned carbon nanowalls (CNWs) with a WS_2 catalytic layer. Raman spectroscopy confirmed the successful formation of multilayer WS_2 films. Electrochemical measurements revealed that HER performance strongly depends on the WS_2 deposition time. Among the investigated samples, the Ti/WS_2 electrode prepared with a deposition time of 90 min exhibited the highest catalytic activity, delivering an overpotential of 294 mV at 10 mA cm^{-2} and the lowest charge transfer resistance (R_{ct} = 15.9 Ohm) within the Ti/WS_2 series. Following electrochemical activation, the overpotential further decreased to 144 mV. Electrochemical impedance spectroscopy (EIS) showed that the incorporation of CNWs significantly enhanced charge-transfer kinetics, reducing the R_{ct} to 3.7 Ohm. However, despite the improved electron transport, the Ti/CNWs/WS_2 electrode did not outperform Ti/WS_2 in HER activity, indicating that catalytic performance depends not only on charge-transfer properties but also on the density and accessibility of active sites. These findings highlight the importance of optimizing WS_2 film thickness and electrode architecture for efficient hydrogen production.

Keywords: hydrogen evolution reaction, tungsten disulfide, RF magnetron sputtering, carbon nanowalls, electrocatalysis, electrochemical impedance spectroscopy.

Received June 26, 2026; revised August 10, 2026; accepted August 19, 2026.

Introduction

The increasing global energy demand and worsening environmental conditions require the development of sustainable and environmentally friendly energy sources. Conventional fossil fuels are major contributors to greenhouse gas emissions and climate change. Therefore, significant attention is being focused on low-carbon energy technologies, where hydrogen is considered one of the most promising and clean energy carriers [1–3].

Hydrogen is considered a highly promising energy carrier because of its high energy efficiency, environmental compatibility, and availability from diverse feedstocks. In electrochemical

energy systems, its utilization produces water as the main reaction product, minimizing harmful environmental impact. Water electrolysis is one of the most attractive approaches for sustainable hydrogen generation [4–6]. The efficiency of this technology is mainly governed by the HER, which strongly depends on the electrocatalytic performance of the electrode materials.

Precious metal-based materials, particularly platinum catalysts, are currently considered the benchmark electrocatalysts for the HER due to their excellent catalytic activity and low overpotential. However, the large-scale application of these materials is restricted by their high cost, limited availability, and poor economic feasibility for industrial use. Therefore, significant research efforts are focused on the development of low-cost and earth-abundant alternatives capable of providing high catalytic performance, long-term stability, and efficient hydrogen production [7, 8]. Layered transition metal dichalcogenides (TMDs) [9], such as MoS_2 and WS_2, are widely investigated as promising electrocatalysts for the HER in acidic media [10–13]. Their layered structure and tunable electronic properties enable the formation of numerous catalytically active sites, making these materials attractive for efficient hydrogen production. In these materials, the HER mainly occurs at the edge regions containing sulfur or metal atoms. In addition to crystalline TMDs, amorphous forms have also attracted considerable interest because their disordered structure can provide enhanced electrocatalytic activity and improved reaction performance.

Enhancement of the catalytic activity of WS_2 toward the HER is generally achieved through two main approaches: increasing the number of catalytically active sites and improving charge transfer within the material. To maximize the density of active sites, various structural engineering strategies have been employed to fabricate nanostructures with a highly developed surface area and abundant exposed edge regions. In particular, loosely stacked WS_2 nanosheets [14, 15], nanoflakes [16, 17], and WS_2/WO_3 heterostructures [18–20] have been synthesized in different studies, providing a high density of active sites and improved electrolyte accessibility to the catalyst surface. Another important strategy involves enhancing the electrical conductivity of WS_2, since its semiconducting nature limits electron transport during HER. Various approaches, including doping and the formation of composite structures, have been explored to overcome this limitation. For example, nitrogen doping has been shown to improve the intrinsic conductivity of WS_2 [21, 22], while integration with conductive graphene networks significantly accelerates charge transfer kinetics [23, 24]. In addition, flower-like WS_2 nanostructures [25, 26] demonstrated enhanced electrocatalytic performance and high stability in acidic media due to their defect-rich structure and large accessible surface area. Several studies [27–29] have also reported the deposition of WS_2 coatings by RF magnetron sputtering, which enables control of film morphology through adjustment of deposition parameters and allows observation of the transition from two-dimensional to three-dimensional structures. However, the influence of the thickness of RF-sputtered WS_2 films on the electrochemical properties of the electrodes remains insufficiently investigated.

Among carbon-based materials, carbon nanowalls (CNWs) have attracted considerable interest as promising conductive frameworks for electrochemical and electrocatalytic applications. CNWs consist of vertically aligned, interconnected graphitic nanosheets, forming an open and accessible architecture with a high density of exposed edges and defect sites. These structural features provide favorable conditions for electrolyte diffusion and increase the accessibility of surface sites, while the graphitic framework facilitates efficient electronic transport. Owing to their distinctive morphology and electrical properties, CNWs have been explored in a variety of energy-related and electrochemical applications, including supercapacitors, batteries, sensors, fuel cells, and electrocatalytic systems [30–33]. In HER electrocatalysis, CNWs can serve as conductive supports for transition metal based catalytic materials, providing an interconnected pathway for electron transport and a high surface area platform for catalyst deposition. Such a carbon framework can enhance the utilization of the active catalytic phase and facilitate electrolyte access to the electrode surface. In the present study, CNWs were employed as a conductive scaffold for WS_2 to improve interfacial charge transfer, increase the accessible surface area, and promote effective contact between the electrolyte and the

catalytic layer. The resulting Ti/CNWs/WS_2 architecture was investigated as a potential electrode configuration for enhancing the electrochemical performance toward the HER.

Therefore, the present work focuses on investigating the effect of WS_2 deposition time by RF magnetron sputtering on the structural and electrochemical properties of Ti/WS_2 and Ti/CNWs/WS_2 electrodes. RF magnetron sputtering offers several advantages, including low cost, ease of operation, high deposition rate, and scalability. Since deposition parameters strongly affect the morphology, conductivity, and catalytic activity of the coatings, their optimization is essential for the development of efficient electrodes for the HER.

Materials and methods

WS_2 thin films were deposited onto titanium foil substrates (Ti, 99.9% purity, 50 μm thickness) by RF magnetron sputtering using a HEX-L system (Korvus Technology), following a previously reported procedure [34]. Prior to RF magnetron sputtering, the titanium foils were cleaned by sequential ultrasonic treatment in acetone and isopropanol for 10 min each. This procedure was used to eliminate organic contaminants and residual impurities from the substrate surface. Following cleaning, the foils were rinsed thoroughly with distilled water, dried, and subsequently introduced into the sputtering chamber. A high-purity WS_2 target (99.9%, Kurt J. Lesker Company) was employed as the sputtering source. The deposition was carried out in an argon atmosphere with a gas flow rate of 30 sccm and a working pressure of 8.5 mTorr. The RF power was maintained at 65 W. During deposition, the substrates were heated to 250 °C and continuously rotated at 10 rpm to ensure uniform film growth. The film thickness was controlled by varying the deposition time from 30 to 120 min with a 30 min interval. Under these conditions, the deposition rate was approximately 0.24 Å s^{-1}.

Ti/CNWs/WS_2 electrodes were fabricated through a two-step process. First, vertically aligned CNWs were synthesized on titanium foil by capacitively coupled plasma-enhanced chemical vapor deposition (CCP-PECVD) according to the procedure described in our previous work [35]. Subsequently, WS_2 films were deposited onto the CNW coated substrates by RF magnetron sputtering under the same deposition conditions. As a result, a series of Ti/WS_2 and Ti/CNWs/WS_2 electrodes with different WS_2 thicknesses was obtained to investigate the effect of deposition time on the structural and electrocatalytic properties of the electrodes.

The surface morphology of the samples was characterized using a scanning electron microscope (SEM, JSM-IT210, JEOL, Japan). The structural and vibrational properties of the synthesized materials were examined by Raman spectroscopy using a Solver Spectrum NT-MDT system equipped with a 473 nm excitation laser.

Electrochemical characterization was performed at room temperature using a Metrohm potentiostat in a conventional three-electrode configuration. An Ag/AgCl electrode containing 3 M KCl served as the reference electrode, while a platinum mesh was used as the counter electrode. The prepared Ti/WS_2 and Ti/CNWs/WS_2 samples were employed as working electrodes. All measured potentials were converted to the reversible hydrogen electrode (RHE) scale according to the Nernst equation. The electrocatalytic performance toward the HER was evaluated by cyclic voltammetry (CV) and linear sweep voltammetry (LSV) in 0.5 M H_2SO_4 (pH ≈ 0.71). Measurements were carried out over a potential range from 0.2 to -0.36 V versus RHE at a scan rate of 10 mV s^{-1}. The geometric surface area of each working electrode was 1 cm^2. Electrochemical activation was performed by CV in the potential range from 0.20 to -0.36 V at a scan rate of 50 mV s^{-1} for 50 cycles. EIS measurements were conducted at -0.23 V versus RHE over a frequency range from 100 kHz to 0.1 Hz using an AC perturbation amplitude of 10 mV. The R_{ct} was determined by fitting the experimental Nyquist plots.

Results and discussion

SEM images of the Ti/CNWs and Ti/CNWs/WS_2 electrodes after 90 min of WS_2 deposition are shown in Figure 1a,b, respectively. The Ti/CNWs electrode exhibits a dense network of vertically oriented and interconnected carbon nanowalls, resulting in a rough and highly textured surface. The

open structure of the CNW network provides a large accessible surface area and serves as an effective scaffold for the subsequent deposition of the WS_2 catalytic layer. After 90 min of WS_2 deposition, the surface morphology of the Ti/CNWs/WS_2 electrode changes noticeably. The surface appears more textured and relatively uniformly covered, while the characteristic vertically oriented CNW framework remains distinguishable. These morphological features suggest the successful formation and deposition of a WS_2 layer over the CNW network.

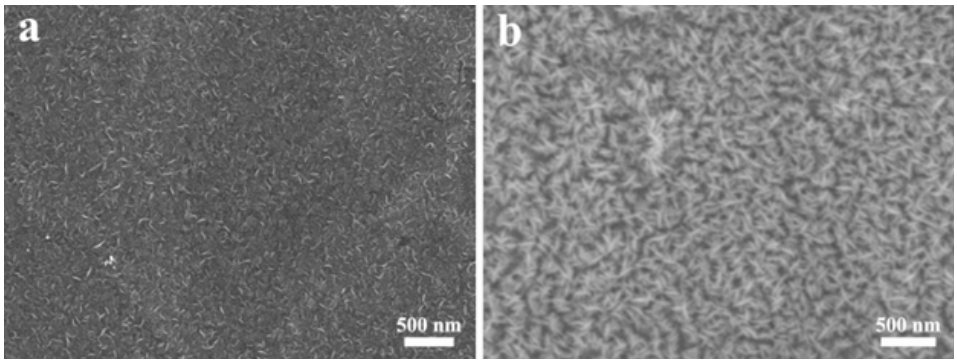


Figure 1 – SEM surface images of (a) Ti/CNWs
and (b) Ti/CNWs/WS_2 electrodes with a WS_2 deposition time of 90 min

Figure 2a,b presents the Raman spectra of Ti/WS_2 electrodes deposited for different sputtering times (30-120 min) and Ti/CNWs/WS_2 electrode. For all Ti/WS_2 samples, characteristic Raman peaks located at approximately 351.4 cm^{-1} and 417.1 cm^{-1} were observed, corresponding to the E^1_{2g} and A_{1g} vibrational modes, respectively [36, 37]. The E^1_{2g} mode is associated with the in-plane vibrations of W and S atoms, whereas the A_{1g} mode originates from the out-of-plane vibrations of sulfur atoms perpendicular to the WS_2 layers. The frequency difference between these two modes is 65.7 cm^{-1}, which is characteristic of multilayer WS_2 structures and is in good agreement with previously reported values for WS_2 thin films [38].

In addition to the characteristic WS_2 modes, weak Raman bands were detected at approximately 520.1 cm^{-1} and 560.4 cm^{-1}. These peaks may be attributed to tungsten oxide species (WO_x) formed due to partial surface oxidation of WS_2 upon exposure to air, or to second-order Raman scattering processes [39, 40]. The relatively low intensity of these bands indicates that WS_2 remains the dominant phase in the deposited films. No additional impurity related peaks were observed, confirming the successful formation of WS_2 films on titanium substrates by magnetron sputtering and indicating the high phase purity of the deposited coatings.

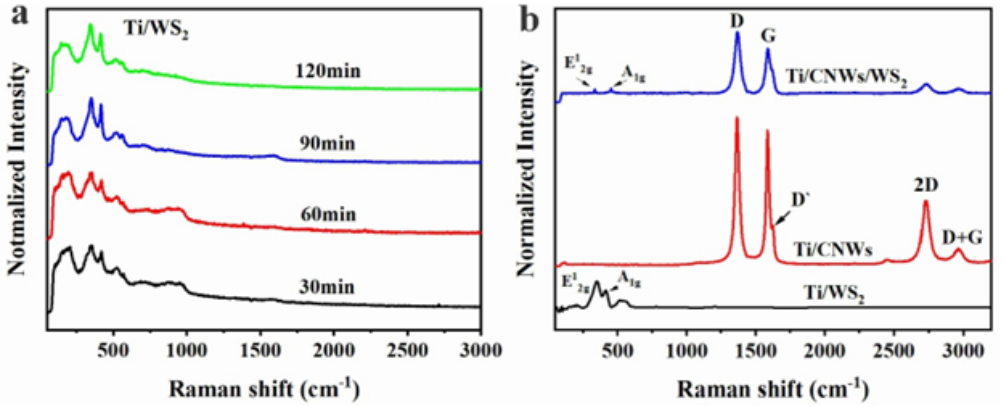


Figure 2 – Raman spectra of Ti/WS_2 and Ti/CNWs/WS_2 electrodes:
(a) effect of WS_2 deposition time on the structure of Ti/WS_2 films;
(b) comparison of Ti/WS_2, Ti/CNWs, and Ti/CNWs/WS_2 electrodes
with a WS_2 deposition time of 90 min

A noticeable modification of the Raman spectrum was observed for the Ti/CNWs/WS_2 electrode (Figure 2b). The characteristic WS_2 modes were shifted to 333.8 cm^{-1} and 452.3 cm^{-1} compared to those of the Ti/WS_2 samples. Such shifts may be attributed to interfacial interactions between WS_2 and CNWs, which can affect the local crystal structure and vibrational properties of the material. The substantial shift of the high-frequency mode toward higher wavenumbers suggests possible changes in the local bonding environment of sulfur atoms, as well as charge redistribution at the CNWs/WS_2 interface.

The Raman spectra of the Ti/CNWs and Ti/CNWs/WS_2 electrodes exhibit characteristic bands associated with graphitized carbon materials. The D band, located at approximately 1364.7 cm^{-1}, is attributed to structural defects, vacancies, crystallite boundaries, and edge sites within the carbon lattice. The G band at 1585.4 cm^{-1} corresponds to the vibrational mode of sp^2-hybridized carbon atoms and indicates the formation of a graphitic structure [41, 42]. The D′ band observed at around 1621.4 cm^{-1} is also related to defects in the sp^2 carbon network and reflects the presence of structural disorder. The 2D band at 2728.1 cm^{-1} represents the second-order overtone of the D band and is a characteristic feature of graphene-like carbon structures. In addition, the D+G band located at approximately 2963.1 cm^{-1} originates from two-phonon scattering processes and is commonly observed in defective graphitized carbon materials. The I_D/I_G ratio increased from 1.09 for Ti/CNWs to 1.37 after the deposition of WS_2. This increase indicates a higher degree of structural disorder and a greater contribution of defect-related sites in the carbon framework. The observed change in the Raman response suggests that the formation of the WS_2 layer affects the local structural environment of the CNWs.

The electrocatalytic activity of the fabricated electrodes toward the HER was investigated by CV and LSV. The obtained results are presented in Figure 3a,b.

Analysis of the CV curves (Figure 3a) reveals that all Ti/WS_2 electrodes exhibit significantly higher cathodic current densities compared to the bare Ti substrate, unambiguously confirming the catalytic contribution of the deposited WS_2 layer to the HER process. The observed systematic increase in cathodic current density with increasing deposition time from 30 to 90 min indicates a progressive enhancement in the concentration of electrochemically active sites responsible for proton adsorption and reduction. The Ti/WS_2 (90 min) electrode demonstrates the highest cathodic current density among the entire series of investigated samples, reflecting the most favorable HER kinetics and superior catalytic activity.

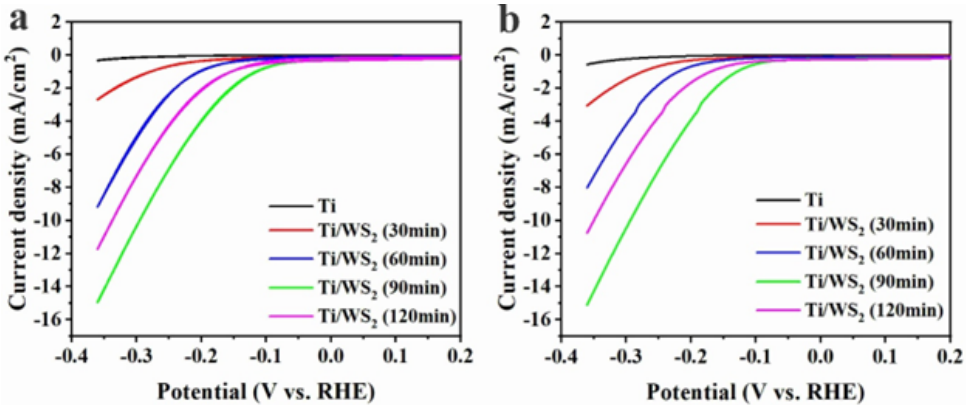


Figure 3 – Electrochemical characterization of Ti/WS_2 electrodes prepared with different WS_2 deposition times (30-120 min): (a) CV and (b) LSV curves

However, a further increase in deposition time to 120 min results in a decrease in cathodic current density, which may be attributed to the formation of an excessively thick catalytic film that impedes interfacial charge transfer and restricts the accessibility of catalytically active edge sites of WS_2 to the reactants.

The LSV results (Figure 3b) are consistent with the CV data and further corroborate the electrocatalytic performance of the Ti/WS_2 (90 min) electrode. The overpotential required to achieve a current density of 10 mA·cm^{-2} for this electrode was determined to be 294 mV, representing the lowest value among all investigated Ti/WS_2 samples and confirming its enhanced HER activity. The improved electrocatalytic performance of the Ti/WS_2 (90 min) electrode can be rationalized by the optimal catalytic film thickness, which provides the maximum number of accessible active sites while simultaneously maintaining efficient electron transport within the catalyst layer and Ti. Taken together, the electrochemical measurements demonstrate that the HER catalytic activity of Ti/WS_2 electrodes is governed by the WS_2 deposition time, with 90 min representing the optimal deposition duration within the scope of the present study.

The charge transfer kinetics at the electrode/electrolyte interface were investigated by EIS at an applied potential of -0.23 V. The Nyquist plots are presented in Figure 4. The EIS spectra were fitted using an R_s-(R_{ct}||CPE) equivalent circuit.

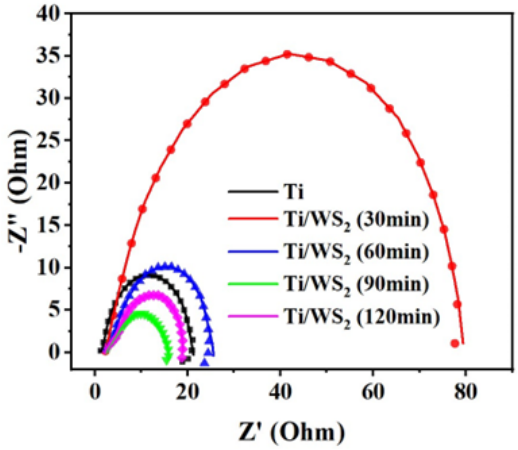


Figure 4 – Nyquist plots of Ti and Ti/WS_2 electrodes prepared with different WS_2 deposition times (30-120 min), recorded in 0.5 M H_2SO_4 at -0.23 V vs. RHE, the solid lines represent the fitted curves

The obtained R_{ct} values decrease monotonically with increasing deposition time from 30 to 90 min (78.2-15.9 Ohm), followed by a slight increase to 18.9 Ohm for the 120 min sample. The bare Ti substrate yielded an R_{ct} value of 21.2 Ohm. The markedly elevated R_{ct} observed for the Ti/WS_2 (30 min) electrode is indicative of incomplete surface coverage and an insufficient density of active catalytic sites at the early stage of deposition. The progressive decrease in R_{ct} with increasing deposition time up to 90 min reflects the formation of a continuous, highly conductive WS_2 layer with an enhanced density of active sites. The moderate increase in R_{ct} for the 120 min sample relative to the optimal 90 min electrode may be attributed to excessive film thickness, which restricts electron transport through the catalyst layer and reduces the accessibility of the active edge sites of WS_2.

The minimum R_{ct} value of 15.9 Ohm recorded for the Ti/WS_2 (90 min) electrode is consistent with its superior performance in CV and LSV measurements, confirming that a deposition time of 90 min represents the optimal condition, providing the most favorable balance among film thickness, electrical conductivity, and active site density.

Based on the optimal WS_2 deposition time of 90 min established for the Ti/WS_2 series, the same deposition duration was employed for the fabrication of the Ti/CNWs/WS_2 composite electrode. The introduction of an intermediate CNWs layer between the Ti substrate and the WS_2 catalytic layer was intended to increase the effective surface area and provide a conductive network facilitating charge transport.

The electrocatalytic performance of the Ti/CNWs/WS_2 electrode was evaluated in comparison with the optimized Ti/WS_2 electrode and the bare Ti substrate using CV and LSV before and after electrochemical activation. The corresponding results are presented in Figure 5a,b.

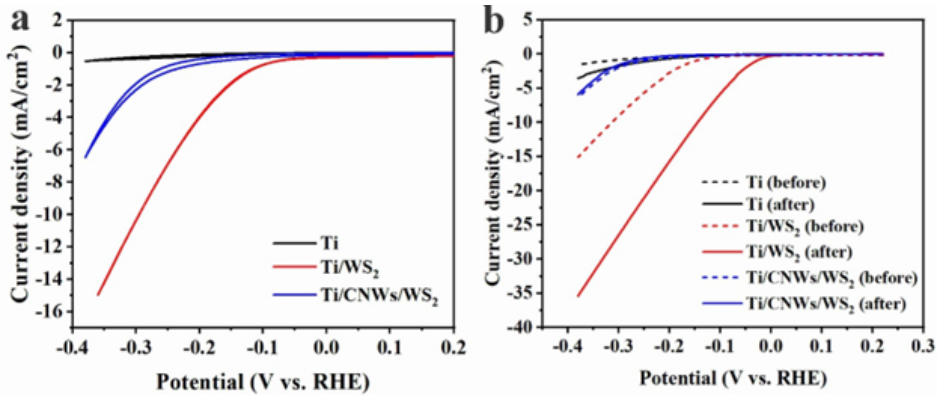


Figure 5 – Electrochemical characterization of Ti, Ti/WS_2, and Ti/CNWs/WS_2 electrodes: (a) CV and (b) LSV curves

The CV curves (Figure 5a) reveal that the Ti/WS_2 electrode exhibits the highest cathodic current density among all investigated samples, whereas the Ti/CNWs/WS_2 electrode shows a less pronounced cathodic response. This observation suggests that direct deposition of WS_2 onto the Ti substrate results in a higher density of electrochemically accessible active sites compared to the CNWs based architecture.

The LSV curves recorded before and after electrochemical activation (Figure 5b) demonstrate a significant improvement in HER performance for all electrodes following the activation procedure. For the Ti/WS_2 electrode, the overpotential required to achieve a current density of 10 mA cm^{-2} decreases from 314 to 144 mV after activation, representing the best performance among the investigated samples. The enhanced activity is attributed to electrochemical surface restructuring of WS_2, removal of surface contaminants, and increased accessibility of catalytically active sites. In contrast, the bare Ti substrate exhibits negligible HER activity both before and after activation, confirming that the observed catalytic performance originates from the WS_2 layer.

To further evaluate the HER kinetics, Tafel plots were derived from the LSV polarization curves recorded after electrochemical activation (Figure 6a). The Tafel slopes of Ti, Ti/WS_2, and Ti/CNWs/WS_2 were 207.6, 59.4, and 125.7 mV/dec, respectively. Among the investigated electrodes, Ti/WS_2 exhibited the lowest Tafel slope, indicating the most favorable HER kinetics. Although Ti/CNWs/WS_2 showed significantly lower charge transfer resistance, its higher Tafel slope suggests slower reaction kinetics. This indicates that HER performance depends not only on charge transfer efficiency but also on the number and accessibility of catalytically active sites. The high Tafel slope of the bare Ti substrate confirms its poor intrinsic HER activity.

The charge transfer kinetics of Ti, Ti/WS_2, and Ti/CNWs/WS_2 electrodes were further investigated by EIS, and the corresponding Nyquist plots are presented in Figure 6b. The R_{ct} values were determined to be 21.2 Ohm for bare Ti, 15.8 Ohm for Ti/WS_2, and 3.7 Ohm for Ti/CNWs/WS_2.

The lowest R_{ct} value obtained for Ti/CNWs/WS_2 indicates substantially enhanced interfacial charge transfer kinetics. Compared with Ti/WS_2 and bare Ti, the R_{ct} decreases by factors of 4.3 and 5.7, respectively. This improvement can be attributed to the highly conductive CNWs network, which provides efficient electron transport pathways between the Ti substrate and the WS_2 catalytic layer.

Despite exhibiting the lowest R_{ct} value, the Ti/CNWs/WS_2 electrode does not outperform Ti/WS_2 in terms of cathodic current density and HER overpotential. This result indicates that HER activity is governed not only by charge transfer kinetics but also by the density and accessibility of catalytically active sites. The presence of the CNWs interlayer may influence the morphology and distribution of the deposited WS_2, thereby reducing the number of exposed edge sites known to be responsible for HER activity. Furthermore, the three-dimensional CNWs architecture may introduce additional proton diffusion limitations within the catalytic layer. Consequently, although the CNWs interlayer significantly improves electron transport, these factors limit the overall electrocatalytic performance

of the Ti/CNWs/WS_2 electrode. Further optimization of CNWs morphology and WS_2 deposition conditions may enable more effective utilization of the advantages offered by this hybrid electrode architecture.

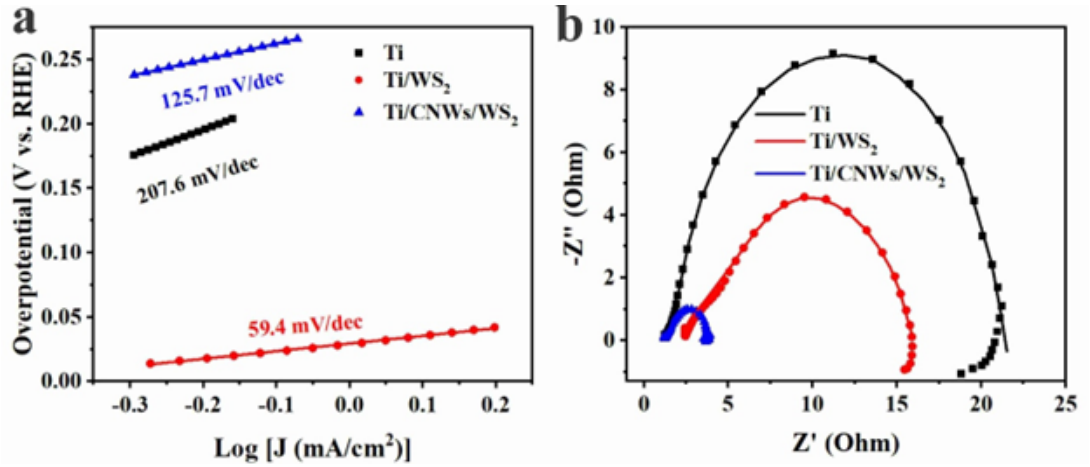


Figure 6 – (a) Tafel slope of Ti, Ti/WS_2, and Ti/CNWs/WS_2 electrodes;
(b) Nyquist plots of Ti, Ti/WS_2, and Ti/CNWs/WS_2 electrodes
recorded in 0.5 M H_2SO_4 at -0.23 V vs. RHE, the solid lines represent the fitted curves

Conclusion

WS_2 thin-film electrocatalysts were successfully fabricated on titanium substrates by RF magnetron sputtering with deposition times ranging from 30 to 120 min. Raman spectroscopy confirmed the formation of multilayer WS_2 coatings with characteristic E^1_{2g} and A_{1g} vibrational modes. The electrocatalytic performance toward the HER was found to be strongly dependent on the deposition time. Among the investigated samples, the Ti/WS_2 electrode prepared with a deposition time of 90 min exhibited the best HER performance, characterized by the highest cathodic current density, the lowest overpotential of 294 mV at 10 mA cm^{-2}, and the minimum R_{ct} of 15.9 Ohm within the Ti/WS_2 series. Electrochemical activation further improved the catalytic activity, reducing the overpotential to 144 mV.

The incorporation of a carbon nanowall interlayer resulted in a significant decrease in R_{ct} to 3.7 Ohm, demonstrating the beneficial role of CNWs in facilitating electron transport. Nevertheless, the Ti/CNWs/WS_2 electrode showed lower HER activity than the optimized Ti/WS_2 electrode, indicating that enhanced electrical conductivity alone is insufficient to maximize catalytic performance. The results suggest that the density and accessibility of catalytically active WS_2 edge sites play a dominant role in determining HER activity.

Overall, the study demonstrates that RF magnetron sputtering is an effective method for the fabrication of WS_2 based HER electrocatalysts and highlights the importance of optimizing film thickness and electrode architecture. These findings provide useful guidelines for the development of efficient, low-cost, and scalable WS_2 based electrodes for sustainable hydrogen production. Future work will involve systematic optimization of the CNWs height to determine its effect on the electrochemical and electrocatalytic performance of Ti/CNWs/WS_2 electrodes.

Information on funding. This research has been funded by the Ministry of Science and Higher Education of the Republic of Kazakhstan (Grant No. BR28712419).

REFERENCES

1 Nelson, C., Gui, M.M., and Robertson, P.K.J. The Environmental Emission and Climate Change Impact of Hydrogen Fuel Derived from Photocatalysis Water-Splitting Reaction. Advanced Energy and Sustainability Research, 6 (5) (2025). https://doi.org/10.1002/aesr.202400337.

2 Tiwari, A. Hydrogen Leading the Green Energy Future. Advanced Materials Letters, 13 (2), 2202–1690 (2022). https://doi.org/10.5185/amlett.2022.021690.

3 Wang, X., Zhou, W., Wang, Y., Gong, L., Liu, X., and Zhou, X. MoO2/Mo heterostructures for hydrogen evolution reaction and ammonia sensing in self-powered mode. Nano Energy, 109, 108253 (2023). https://doi.org/10.1016/j.nanoen.2023.108253.

4 Boretti, A., and Pollet, B.G. Hydrogen economy: Paving the path to a sustainable, low-carbon future. International Journal of Hydrogen Energy, 93, 307–19 (2024). https://doi.org/10.1016/j.ijhydene.2024.10.350.

5 Shaterabadi, M., Sadeghi, S., and Jirdehi, M.A. The Role of Green Hydrogen in Achieving Low and Net-Zero Carbon Emissions: Climate Change and Global Warming. pp. 141–53 (2024). https://doi.org/10.1007/978-3-031-52429-5_6.

6 Kalkozova, Zh.K., Markhabayeva, A.A., Mukhametkarimov, Y.S., Yerlanuly, Y., Tulegenova, A.T., Abdullin, Kh.A., Nuraje, N., and Cao, C.D. PHOTOELECTROCHEMICAL PROPERTIES OF NANOSTRUCTURED SILICON FOR SOLAR WATER SPLITTING. Herald of the Kazakh-British technical university, 21 (4), 245–53 (2024). https://doi.org/10.55452/1998-6688-2024-21-4-245-253.

7 He, H., Mai, J., Hu, K., Yu, H., Zhang, Z., Zhan, F., and Liu, X. Recent advances in electrocatalysts for efficient hydrogen evolution reaction. Rare Metals, 44 (4), 2208–38 (2025). https://doi.org/10.1007/s12598-024-02649-1.

8 Kim, J., Jung, S., Lee, N., Kim, K., Kim, Y., and Kim, J.K. Efficient Alkaline Hydrogen Evolution Reaction Using Superaerophobic Ni Nanoarrays with Accelerated H_2 Bubble Release. Advanced Materials, 35 (52) (2023). https://doi.org/10.1002/adma.202305844.

9 Bozheyev, F., Nemkayeva, R., Yerlanuly, Y., Gabdullin, M., and Markhabayeva, A. Performance of Transition Metal Oxides for Solar Hydrogen Conversion. ACS Catalysis, 15 (18), 16449–62 (2025). https://doi.org/10.1021/acscatal.5c03869.

10 Huang, T.-X., Cong, X., Wu, S.-S., Wu, J.-B., Bao, Y.-F., Cao, M.-F., Wu, L., Lin, M.-L., Wang, X., Tan, P.-H., and Ren, B. Visualizing the structural evolution of individual active sites in MoS2 during electrocatalytic hydrogen evolution reaction. Nature Catalysis, 7 (6), 646–54 (2024). https://doi.org/10.1038/s41929-024-01148-x.

11 Xu, Y., Ge, R., Yang, J., Li, J., Li, S., Li, Y., Zhang, J., Feng, J., Liu, B., and Li, W. Molybdenum disulfide (MoS2)-based electrocatalysts for hydrogen evolution reaction: From mechanism to manipulation. Journal of Energy Chemistry, 74, 45–71 (2022). https://doi.org/10.1016/j.jechem.2022.06.031.

12 Kong, L., Pan, L., Guo, H., Qiu, Y., Alshahrani, W.A., Amin, M.A., and Lin, J. Constructing WS2/WO3-x heterostructured electrocatalyst enriched with oxygen vacancies for accelerated hydrogen evolution reaction. Journal of Colloid and Interface Science, 664, 178–85 (2024). https://doi.org/10.1016/j.jcis.2024.03.002.

13 Yang, F., Pan, Y., and Zhu, J. Enhanced catalytic activity of noble metal@borophene/WS2 heterojunction for hydrogen evolution reaction. Applied Surface Science, 680, 161321 (2025). https://doi.org/10.1016/j.apsusc.2024.161321.

14 Tekalgne, M.A., Do, H.H., Nguyen, T. Van, Le, Q. Van, Hong, S.H., Ahn, S.H., and Kim, S.Y. MXene Hybrid Nanosheet of WS_2 /Ti_3C_2 for Electrocatalytic Hydrogen Evolution Reaction. ACS Omega, 8 (44), 41802–8 (2023). https://doi.org/10.1021/acsomega.3c06403.

15 Sun, R., Wang, Z., and Zhao, J. Transition metal-anchored WS2 nanosheets as efficient electrocatalysts for hydrogen evolution reaction: A first-principles study. Molecular Catalysis, 588, 115519 (2026). https://doi.org/10.1016/j.mcat.2025.115519.

16 Rahmani, E., Reyhani, A., Khanlary, M.R., Mortazavi, S.Z., Mohammadi, M.R., Dau, H., Gholami, M.F., Mohammadi, A.B., Rabe, J.P., Soleimani, M., and Zarabadipoor, M. Phosphorus doped few layer WS2 flakes grown by chemical vapor deposition for hydrogen evolution reactions. Scientific Reports, 15 (1), 6350 (2025). https://doi.org/10.1038/s41598-025-90341-4.

17 Joseph, A., Chacko, L., Sanal, K.C., Pineda-Aguilar, N., Jasna, M., Antony, A., and Aneesh, P.M. Efficient hydrogen evolution reaction performance of Ni substituted WS2 nanoflakes. Applied Physics A, 130 (12), 875 (2024). https://doi.org/10.1007/s00339-024-08050-0.

18 Nguyen, T. Van, Huynh, K.A., Le, Q. Van, Ahn, S.H., and Kim, S.Y. Facile Synthesis of WS_2 /WO_3 Materials in a Batch Reactor for the Hydrogen Evolution Reaction. International Journal of Energy Research, 2024 (1) (2024). https://doi.org/10.1155/2024/4878549.

19 Singh, T., Deepak, D., Panghal, A., and Roy, S.S. Laser-induced graphene nano-anchored WS2/WO3 heterostructures for electrocatalytic oxygen evolution reaction. International Journal of Hydrogen Energy, 84, 939–50 (2024). https://doi.org/10.1016/j.ijhydene.2024.08.272.

20 Markhabayeva, A. Synthesis of hierarchical wo3 microspheres for photoelectrochemical water splitting application. Physical Sciences and Technology, 10 (2) (2023). https://doi.org/10.26577/phst.2023.v10.i2.04.

21 Liao, L., Zhao, Y., Zhou, H., Li, D., Qi, Y., Zhang, Y., Sun, Y., Zhou, Q., and Yu, F. Edge-oriented N-Doped WS_2 Nanoparticles on Porous Co_3N Nanosheets for Efficient Alkaline Hydrogen Evolution and Nitrogenous Nucleophile Electrooxidation. Small, 18 (40) (2022). https://doi.org/10.1002/smll.202203171.

22 Huang, X., Jiang, H., Ge, B., Huang, C., and Tang, J. Nitrogen-Doped NiS/WS 2 Heterostructures on Carbon Cloth: A Synergistic Route to High-Performance Hydrogen Evolution Catalysts. ChemSusChem, 19 (11) (2026). https://doi.org/10.1002/cssc.70782.

23 Arumugam, D., Subramani, M., Subramani, D., and Ramasamy, S. Unraveling the potential of transition metals as single atom catalyst in Graphene/WS2 van der Waals heterostructure for enhanced HER performance – A first principles study. International Journal of Hydrogen Energy, 68, 545–58 (2024). https://doi.org/10.1016/j.ijhydene.2024.04.281.

24 Nasr, M., Benhamou, L., Kotbi, A., Rajput, N.S., Campos, A., Lahmar, A.-I., Hoummada, K., Kaja, K., El Marssi, M., and Jouiad, M. Photoelectrochemical Enhancement of Graphene@WS2 Nanosheets for Water Splitting Reaction. Nanomaterials, 12 (11), 1914 (2022). https://doi.org/10.3390/nano12111914.

25 Liu, F., Zeng, D., Tian, Y., Hu, Y., Shen, T., Gao, Y., and Guan, R. Ternary heterostructure Cu-ZnIn2S4/WO3/WS2 flower-like microspheres for highly-efficient photocatalytic hydrogen evolution under visible-light irradiation. Applied Surface Science, 642, 158572 (2024). https://doi.org/10.1016/j.apsusc.2023.158572.

26 Rasool, F., Pirzada, B.M., Talib, S.H., Alkhidir, T., Anjum, D.H., Mohamed, S., and Qurashi, A. In Situ Growth of Interfacially Nanoengineered 2D–2D $WS_2/Ti_3C_2T_x$ MXene for the Enhanced Performance of Hydrogen Evolution Reactions. ACS Applied Materials & Interfaces, 16 (11), 14229–42 (2024). https://doi.org/10.1021/acsami.3c11642.

27 Ladhane, S., Shah, S., Shinde, P., Punde, A., Waghmare, A., Hase, Y., Bade, B.R., Doiphode, V., Rahane, S.N., Kale, D., Rondiya, S.R., Prasad, M., Patole, S.P., and Jadkar, S.R. Enhanced Photoelectrochemical Activity Realized from WS_2 Thin Films Prepared by RF-Magnetron Sputtering for Water Splitting. ChemElectroChem, 11 (7) (2024). https://doi.org/10.1002/celc.202400002.

28 Ladhane, S., Shah, S., Doiphode, V., Shinde, P., Kale, D., Rahane, S., Thombare, J., Ingole, M., Vairale, P., Hase, Y., Waghmare, A., Prasad, M., Patole, S.P., and Jadkar, S. Pressure-dependent growth of RF-sputtered WS2 nanostructures for enhanced hydrogen production via photoelectrochemical water splitting. Journal of Power Sources, 640, 236786 (2025). https://doi.org/10.1016/j.jpowsour.2025.236786.

29 Ladhane, S., Shah, S., Doiphode, V., Shinde, P., Kale, D., Rahane, S., Thombare, J., Ingole, M., Vairale, P., Hase, Y., Waghmare, A., Prasad, M., Patole, S.P., and Jadkar, S. Tailoring CdS/WS2 heterostructures for enhanced photoelectrochemical water splitting via RF magnetron sputtering. Journal of Power Sources, 656, 238056 (2025). https://doi.org/10.1016/j.jpowsour.2025.238056.

30 Van Toan, N., Sui, H., Li, J., Tuoi, T.T.K., and Ono, T. Nanoengineered micro-supercapacitors based on graphene nanowalls for self-powered wireless sensing system. Journal of Energy Storage, 81, 110446 (2024). https://doi.org/10.1016/j.est.2024.110446.

31 Farid, G., Amade, R., Chaitoglou, S., Alshaikh, I., Ospina, R., Ma, Y., and Bertran-Serra, E. Efficient flexible electrodes for lithium-ion batteries utilizing well-dispersed hybrid Mo2C nanoparticles on vertically-oriented graphene nanowalls. Journal of Alloys and Compounds, 968, 172109 (2023). https://doi.org/10.1016/j.jallcom.2023.172109.

32 Stoian, M.C., Romanitan, C., Simionescu, O.G., Djourelov, N., Brincoveanu, O., Dinescu, A., and Radoi, A. Growth of nanocrystalline graphite and vertically aligned graphite nanowalls thin films and their transfer on flexible substrates for applications as electrochemical sensors for anthracene detection. Microchemical Journal, 207, 111828 (2024). https://doi.org/10.1016/j.microc.2024.111828.

33 Chaitoglou, S., Ospina, R., Ma, Y., Amade, R., Vendrell, X., Rodriguez-Pereira, J., and Bertran-Serra, E. Deposition and in-situ formation of nanostructured Mo2C nanoparticles on graphene nanowalls support for efficient electrocatalytic hydrogen evolution. Journal of Alloys and Compounds, 972, 172891 (2024). https://doi.org/10.1016/j.jallcom.2023.172891.

34 Zhumadilov, B.Ye., Zhumadilov, R.Ye., Nemkayeva, R.R., Markhabayeva, A.A., Ramazanov, T.S., Yerlanuly, Y., and Gabdullin, M.T. WO3-modified carbon nanowall electrodes for efficient hydrogen evolution reaction. International Journal of Hydrogen Energy, 223, 154356 (2026). https://doi.org/10.1016/j.ijhydene.2026.154356.

35 Zhumadilov, B.Y., Zhumadilov, R.Y., Nemkayeva, R.R., Markhabayeva, A.A., Bozheyev, F., Ramazanov, T.S., Yerlanuly, Y., and Gabdullin, M.T. Influence of Substrate Type and Synthesis Time on Morphological and Structural Properties of Carbon Nanowalls. Advanced Physics Research, 4 (12) (2025). https://doi.org/10.1002/apxr.202500156.

36 Madadkhani, S., Nandy, S., Chae, K.H., Aleshkevych, P., and Najafpour, M.M. Advances in Understanding Tungsten Disulfide Dynamics during the Hydrogen-Evolution Reaction: An Initial Step in Elucidating the Mechanism. The Journal of Physical Chemistry Letters, 15 (19), 5112–9 (2024). https://doi.org/10.1021/acs.jpclett.4c00924.

37 Van Nguyen, T., Tekalgne, M., Nguyen, T.P., Van Le, Q., Ahn, S.H., and Kim, S.Y. Electrocatalysts based on MoS_2 and WS_2 for hydrogen evolution reaction: An overview. Battery Energy, 2 (3) (2023). https://doi.org/10.1002/bte2.20220057.

38 Wang, R., Zhang, D., Luo, S., Wang, Q., Jiang, L., Wei, G.-F., and Wang, X. Incorporation of tungsten nanoparticles on WS2 film for the enhanced hydrogen evolution. International Journal of Hydrogen Energy, 59, 645–53 (2024). https://doi.org/10.1016/j.ijhydene.2024.02.010.

39 Shin, Y., Kim, J., Jang, Y., Ko, E., Lee, N.-S., Yoon, S., and Kim, M.H. Vertically-Oriented WS2 Nanosheets with a Few Layers and Its Raman Enhancements. Nanomaterials, 10 (9), 1847 (2020). https://doi.org/10.3390/nano10091847.

40 Rajeswaran, B., Konar, R., Yitzhari, R., Nessim, G.D., and Tischler, Y.R. Enhancement of the E^1_{2g} and A_{1g} Raman modes and layer identification of 2H-WS_2 nanosheets with metal coatings. Journal of Raman Spectroscopy, 54 (9), 1030–7 (2023). https://doi.org/10.1002/jrs.6585.

41 ZHUMADILOV, B., KENZHEGULOV, A., NEMKAYEVA, R., PARTIZAN, G., YERLANULY, Y., and GADBULLIN, M. Synthesis of carbon nanowalls by oxy-acetylene torch method. Journal of Metals, Materials and Minerals, 33 (4), 1806 (2023). https://doi.org/10.55713/jmmm.v33i4.1806.

42 Minh, N.Q., Van Nong, N., Dela Vega, M.S.D.C., Oda, O., and Hori, M. Synthesis of highly dense and multi-branched carbon nanowalls by two-step growth combining different plasma chemical vapor deposition methods. Vacuum, 213, 112118 (2023). https://doi.org/10.1016/j.vacuum.2023.112118.

[1,2*]Жумадилов Б.Е.,
докторант, ORCID ID: 0000-0001-5784-3840,
*e-mail: zhumadilovbe@gmail.com
[1,2]Мархабаева А.А.,
PhD, ORCID ID: 0000-0002-0657-422X,
e-mail: aiko_marx@mail.ru
[1,3]Габдуллин М.Т.,
PhD, ORCID ID: 0000-0003-4853-3642,
e-mail: gabdullin@physics.kz

[1]Қолданбалы ғылымдар және ақпараттық технологиялар институты, Алматы қ., Қазақстан
[2]Әл-Фараби атындағы Қазақ ұлттық университеті, Алматы қ., Қазақстан
[3]Қазақ-Британ техникалық университеті, Алматы, Қазақстан

Ti ЖӘНЕ Ti/КНҚ ТӨСЕМДЕРІНДЕ RF МАГНЕТРОНДЫ ШАШЫРАТУ АРҚЫЛЫ АЛЫНҒАН WS_2 ЖҰҚА ҚАБЫҚШАЛАРЫ: ҚҰРЫЛЫМДЫҚ СИПАТТАМА ЖӘНЕ СБР ӨНІМДІЛІГІ

Аңдатпа

Жер қыртысында мол таралған материалдарға негізделген сутегі бөліну реакциясының (СБР) электрокатализаторлары асыл металл катализаторларына перспективті балама саналады. Бұл жұмыста қабықша қалыңдығының құрылымдық және электрохимиялық қасиеттерге әсерін зерттеу мақсатында WS_2 жұқа қабықшалары RF магнетронды шашырату әдісімен титан төсемдеріне 30–120 минут аралығындағы әртүрлі шашырату уақыттарында тұндырылды. Сонымен қатар, тігінен бағытталған көміртекті наноқабырғаларды (КНҚ) WS_2 каталитикалық қабатымен біріктіру арқылы Ti/КНҚ/WS_2 композиттік электродтары дайындалды. Раман спектроскопиясының нәтижелері көпқабатты WS_2 қабықшаларының сәтті түзілгенін растады. Электрохимиялық өлшеулер СБР өнімділігінің WS_2 тұндыру уақытына тығыз байланысты екенін көрсетті. Зерттелген үлгілердің ішінде 90 минут тұндыру уақытымен дайындалған Ti/WS_2 электроды ең жоғары

каталитикалық белсенділік көрсетті: 10 мА см$^{-2}$ ток тығыздығында асқын кернеу 294 мВ-ты құрады, ал заряд тасымалдау кедергісі Ti/WS_2 сериясындағы ең төмен мәнге (Rct = 15,9 Ом) жетті. Электрохимиялық активтендіруден кейін асқын кернеу 144 мВ-қа дейін төмендеді. Электрохимиялық импеданстық спектроскопия (ЭИС) КНҚ енгізу заряд тасымалдау кинетикасын айтарлықтай жақсартып, Rct мәнін 3,7 Ом-ға дейін төмендеткенін көрсетті. Алайда электрон тасымалының жақсаруына қарамастан, Ti/КНҚ/WS_2 электроды СБР белсенділігі бойынша Ti/WS_2 электродынан жоғары нәтиже көрсетпеді. Бұл каталитикалық өнімділіктің тек заряд тасымалдау қасиеттеріне ғана емес, сонымен қатар белсенді орталықтардың тығыздығы мен қолжетімділігіне де тәуелді екенін көрсетеді. Алынған нәтижелер тиімді сутегі өндіру үшін WS_2 қабықшасының қалыңдығы мен электрод архитектурасын оңтайландырудың маңыздылығын айқындайды.

Түйін сөздер: сутегі бөліну реакциясы, вольфрам дисульфиді, RF магнетронды шашырату, көміртекті наноқабырғалар, электрокатализ, электрохимиялық импедансты спектроскопия.

[1,2*]Жумадилов Б.Е.,
докторант, ORCID ID: 0000-0001-5784-3840,
*e-mail: zhumadilovbe@gmail.com
[1,2]Мархабаева А.А.,
PhD, ORCID ID: 0000-0002-0657-422X,
e-mail: aiko_marx@mail.ru
[1,3]Габдуллин М.Т.,
PhD, ORCID ID: 0000-0003-4853-3642,
e-mail: gabdullin@physics.kz

[1]Институт прикладных наук и информационных технологий, г. Алматы, Казахстан
[2]Казахский национальный университет им. аль-Фараби, г. Алматы, Казахстан
[3]Казахстанско-Британский технический университет, г. Алматы, Казахстан

ТОНКИЕ ПЛЕНКИ WS_2, НАНЕСЕННЫЕ НА ПОДЛОЖКИ Ti И Ti/УНС МЕТОДОМ RF МАГНЕТРОННОГО РАСПЫЛЕНИЯ: СТРУКТУРНАЯ ХАРАКТЕРИЗАЦИЯ И ЭФФЕКТИВНОСТЬ РЕАКЦИИ ВЫДЕЛЕНИЯ ВОДОРОДА

Аннотация

Электрокатализаторы реакции выделения водорода (РВВ) на основе распространенных в природе материалов являются перспективной альтернативой катализаторам из благородных металлов. В данной работе тонкие пленки WS_2 были нанесены на титановые подложки методом RF магнетронного распыления при временах осаждения от 30 до 120 мин. с целью исследования влияния толщины пленки на структурные и электрохимические свойства. Кроме того, были изготовлены композитные электроды Ti/УНС/WS_2 путем сочетания вертикально ориентированных углеродных наностенок (УНС) с каталитическим слоем WS_2. Рамановская спектроскопия подтвердила успешное формирование многослойных пленок WS_2. Электрохимические измерения показали, что эффективность РВВ существенно зависит от времени осаждения WS_2. Среди исследованных образцов электрод Ti/WS_2, приготовленный при времени осаждения 90 мин., продемонстрировал наибольшую каталитическую активность: перенапряжение при плотности тока 10 мА·см$^{-2}$ составило 294 мВ, а сопротивление переносу заряда оказалось наименьшим в серии Ti/WS_2 (R_{ct} = 15,9 Ом). После электрохимической активации перенапряжение дополнительно снизилось до 144 мВ. Электрохимическая импедансная спектроскопия (ЭИС) показала, что введение УНС значительно улучшает кинетику переноса заряда, снижая R_{ct} до 3,7 Ом. Однако, несмотря на улучшенный электронный транспорт, электрод Ti/УНС/WS_2 не превзошел Ti/WS_2 по активности в РВВ, что свидетельствует о том, что каталитическая эффективность определяется не только свойствами переноса заряда, но и плотностью и доступностью активных центров. Полученные результаты подчеркивают важность оптимизации толщины пленки WS_2 и архитектуры электрода для эффективного производства водорода.

Ключевые слова: реакция выделения водорода, дисульфид вольфрама, RF магнетронное распыление, углеродные наностенки, электрокатализ, электрохимическая импедансная спектроскопия.

UDC 666.3:621.762
IRSTI 53.37.31, 61.35.31.

https://doi.org/10.55452/1998-6688-2026-23-3-434-447

[1*]Zhumazhanova A.T.,
PhD, Junior Researcher, ORCID ID: 0000-0002-5483-9552,
*e-mail: ainashzhumazhanova@gmail.com
[1]Shakirzyanov R.I.,
Cand. Phys.-Math. Sci., Junior Researcher, ORCID ID: 0000-0001-9908-3034,
e-mail: shakirzyanov_ri@enu.kz

[1]L.N. Gumilyov Eurasian National University, Astana, Kazakhstan

EFFECT OF TANTALUM AND VANADIUM CARBIDE DOPANTS ON THE STRUCTURE AND MECHANICAL PROPERTIES OF ALUMINUM NITRIDE-BASED CERAMICS

Abstract

This work investigates the effect of tantalum carbide and vanadium carbide additions on the phase composition, microstructure, and mechanical properties of AlN-based ceramic composites synthesized by mechanochemical solid-state processing followed by thermal treatment. The molar fraction of the carbide additives was varied within the range of x = 0.01-0.10. Scanning electron microscopy combined with energy-dispersive X-ray spectroscopy revealed a homogeneous distribution of the reinforcing phases after mechanochemical activation. X-ray diffraction analysis showed that TaC remained chemically stable during processing, leading to the formation of a two-phase AlN-TaC composite with reduced lattice distortions of the AlN matrix. In contrast, VC underwent partial oxidation during heat treatment, resulting in the formation of secondary V_2O_5 and a different phase evolution. Mechanochemical processing produced a more homogeneous powder morphology and suppressed the formation of large carbide agglomerates, providing favorable conditions for subsequent microstructural development. Mechanical testing demonstrated that a pronounced improvement in hardness and flexural strength occurred at dopant contents above x = 0.03, with the greatest strengthening effect observed for the TaC-containing composites owing to the retention of a stable, uniformly dispersed high-hardness carbide phase. The enhanced mechanical performance is attributed to the combined effects of dispersion strengthening, inhibition of grain growth, grain-boundary strengthening, and crack-deflection mechanisms. These results establish clear relationships between processing, phase evolution, microstructure, and mechanical behavior, demonstrating the potential of mechanochemical processing for the development of high-performance AlN-based ceramic composites intended for demanding structural and high-temperature applications.

Keywords: aluminum nitride, carbonitride ceramics, mechanochemical synthesis, tantalum carbide, vanadium carbide, phase composition, mechanical properties.

Received April 30, 2026; revised August 3, 2026; accepted August 10, 2026.

Introduction

Aluminum nitride (AlN) is recognized as one of the most promising structural and functional ceramic materials owing to its unique combination of high thermal conductivity, excellent electrical insulation, low dielectric constant, high-temperature stability, and chemical inertness [1–4]. These characteristics make AlN highly attractive for applications in power electronics, thermal management systems, electronic packaging, aerospace engineering, and other advanced technologies operating under severe thermal and mechanical conditions. In addition to its excellent thermal performance, AlN possesses a relatively low coefficient of thermal expansion that closely matches that of silicon, making it an important substrate material for modern semiconductor devices [1–4]. Consequently, the development of AlN-based ceramics with improved structural reliability while preserving their

functional properties remains an important research direction in advanced ceramic materials. The development of such materials is driven by the increasing demand for ceramic components capable of operating under high temperatures, severe mechanical loading, and aggressive environments, including thermal barrier systems, wear-resistant components, protective structural materials, and electronic devices requiring high thermal stability [5].

Despite these advantages, the broader application of monolithic AlN as a structural ceramic is still restricted by its relatively low fracture resistance and moderate mechanical strength. It is well established that the performance of AlN ceramics depends not only on the intrinsic properties of the AlN crystal lattice but also on microstructural factors, including grain size, grain boundary chemistry, residual porosity, oxygen-related defects, and the presence of secondary phases. Accordingly, controlling the microstructure through compositional modification and optimization of processing routes has become one of the most effective strategies for simultaneously improving mechanical performance while maintaining the functional characteristics of AlN ceramics.

Among the various approaches proposed to enhance the mechanical properties of AlN, the incorporation of dispersed reinforcing particles has attracted considerable attention. Previous studies have demonstrated that secondary phases can effectively inhibit grain growth during sintering, promote microstructural refinement, modify grain boundary characteristics, and improve resistance to crack initiation and propagation through dispersion strengthening mechanisms [6–10]. Recent investigations have further confirmed that optimization of the reinforcing phase and processing conditions significantly affects densification behavior, grain morphology, and the overall mechanical performance of AlN-based ceramics [11–12]. These findings indicate that both the nature of the reinforcing phase and the processing route play decisive roles in determining the final properties of ceramic composites.

Among refractory ceramic compounds, transition metal carbides are particularly attractive because of their exceptional hardness, high elastic modulus, excellent thermal stability, and wear resistance. Tantalum carbide (TaC), belonging to the family of ultra-high-temperature ceramics, possesses an extremely high melting point (~3880 °C), high hardness, and excellent thermodynamic and oxidation stability, making it a promising reinforcing phase for ceramic matrices [13–15]. Vanadium carbide (VC) also exhibits high hardness and good mechanical characteristics; however, compared with TaC, it has lower oxidation resistance and higher chemical reactivity at elevated temperatures [16, 17]. These differences suggest that TaC and VC may affect phase evolution, microstructure development, and strengthening mechanisms of AlN ceramics in different ways. Although other refractory carbides, including TiC, ZrC, HfC, and NbC, have also been investigated as reinforcing phases for ceramic composites, TaC and VC were selected in the present study because they represent carbides with distinctly different thermodynamic stability and oxidation behavior while maintaining similarly high hardness and refractory characteristics. This makes them suitable model additives for investigating how the intrinsic properties of refractory carbides influence phase evolution, microstructure development, and mechanical strengthening of AlN ceramics under identical processing conditions.

Another important factor governing the structure and properties of ceramic composites is the powder processing route. Mechanochemical activation has proven to be an effective approach for improving powder homogeneity, increasing the contact area between constituent particles, enhancing powder reactivity, and promoting solid-state reactions during subsequent heat treatment [18, 19]. Compared with conventional powder mixing, mechanochemical processing facilitates a more uniform distribution of reinforcing particles and contributes to the formation of finer and more homogeneous microstructures. These features are particularly important for ceramic composites containing dispersed reinforcing phases, where the uniformity of particle distribution strongly influences phase evolution and the resulting mechanical performance.

Although previous studies have demonstrated that refractory carbide additions can improve the mechanical behavior of ceramic materials, the comparative influence of TaC and VC on the phase evolution, microstructure formation, and strengthening mechanisms of AlN ceramics prepared by

mechanochemical synthesis has not yet been systematically investigated. In particular, the relationship between carbide type, oxidation behavior during heat treatment, phase composition, and the resulting mechanical properties remains insufficiently understood. Addressing this knowledge gap is essential for the rational design of AlN-based ceramic composites with improved structural reliability [20, 21].

Therefore, the aim of the present work is to investigate the influence of TaC and VC additions on the phase composition, microstructure, and mechanical properties of AlN ceramics prepared by mechanochemical synthesis followed by heat treatment in air. Particular attention is devoted to clarifying the relationships between carbide type, phase evolution, microstructure development, and strengthening mechanisms, as well as explaining the different reinforcing efficiencies of TaC and VC under identical processing conditions.

Materials and methods

Commercial aluminum nitride (AlN) powder (Sigma-Aldrich, St. Louis, MO, USA) was used as the matrix material, whereas commercial tantalum carbide and vanadium carbide powders (Sigma-Aldrich, St. Louis, MO, USA) served as reinforcing additives. Based on previous studies on AlN-based ceramic composites, TaC and VC were introduced in molar fractions of x = 0.01, 0.03, 0.05, and 0.10 to systematically investigate the influence of carbide content on the phase composition, microstructure, and mechanical properties of the composites. This concentration range was selected to cover both low and relatively high additive contents while enabling evaluation of composition-property relationships without excessive modification of the AlN matrix.

The composite powders were prepared by a mechanochemical solid-state route using a Fritsch PULVERISETTE 6 planetary ball mill (Fritsch, Berlin, Germany). Appropriate amounts of TaC or VC were mixed with the AlN powder and mechanically activated for 30 min at a rotational speed of 250 rpm. Milling was carried out in an 80 ml tungsten carbide (WC) vial using 22–24 tungsten carbide balls with a diameter of 10 mm. The total powder mass was 20 g. These milling conditions were selected to ensure efficient homogenization of the powder mixture while avoiding excessive deformation and cold welding during mechanochemical processing.

Following mechanochemical activation, the powders were heat-treated in air using a SNOL 7.2/1100 muffle furnace (SNOL, Utena, Lithuania) at 500 °C for 5 h. This treatment was performed to stabilize the activated powders prior to structural and mechanical characterization.

The morphology and microstructure of the synthesized composites were examined using a Phenom ProX scanning electron microscope (Thermo Fisher Scientific, Eindhoven, The Netherlands) operated at an accelerating voltage of 10–15 kV under high-vacuum conditions. The elemental composition and spatial distribution of Al, N, Ta, V, C, and O were investigated by energy-dispersive X-ray spectroscopy (EDS) using the integrated detector, and elemental maps were recorded to evaluate the homogeneity of the reinforcing phases within the AlN matrix.

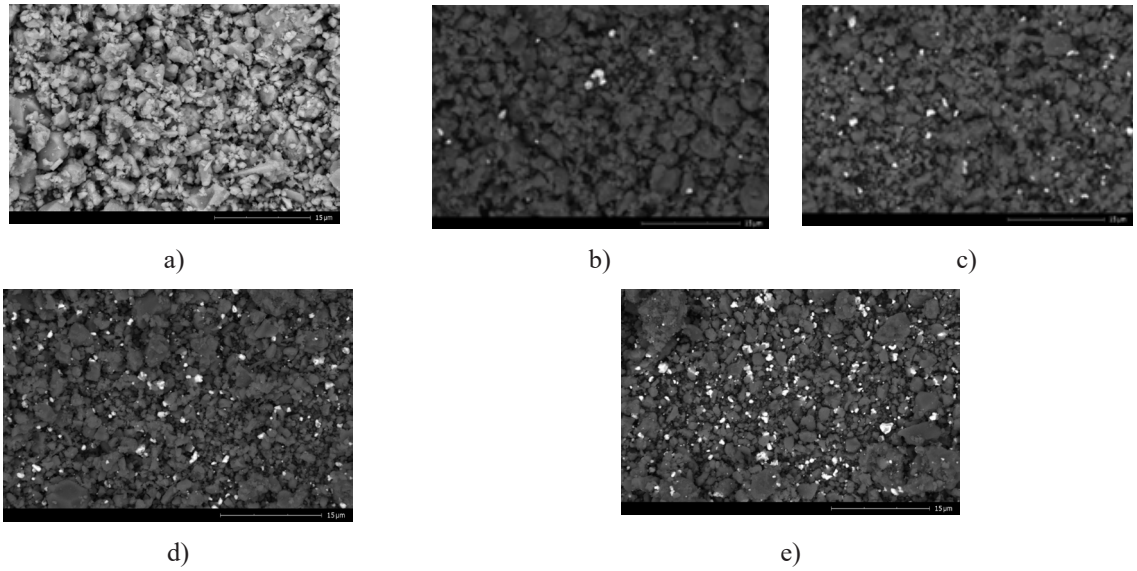
Phase composition was analyzed by X-ray diffraction (XRD) using a Bruker D8 ADVANCE ECO diffractometer (Bruker, Karlsruhe, Germany). Diffraction patterns were collected over the 2θ range of 20–80° with a step size of 0.02°. Phase identification was carried out using the DIFFRAC. EVA software package (Bruker AXS), and the lattice parameters were determined from the processed diffraction data.

The mechanical properties of the ceramic composites were evaluated by measuring the Vickers microhardness under indentation loads of 0.5–2 N. The flexural strength was determined using the three-point bending method.

Results and discussion

SEM micrographs of the initial AlN powder and the (1-x)AlN-xTaC composite powders after mechanochemical treatment are presented in Figure 1. The initial AlN powder (Figure 1a) consists

of irregularly shaped particles with a relatively broad particle-size distribution and several coarse agglomerates, which is typical of commercially available ceramic powders. Following the addition of TaC and high-energy milling (Figures 1b-e), the morphology becomes progressively more homogeneous, accompanied by a noticeable reduction in the size and number of coarse agglomerates.



a) b) c)

d) e)

a) initial; b) at addition of 0.01 M; c) at addition of 0.03 M;
d) at addition of 0.05 M; e) at addition of 0.10 M

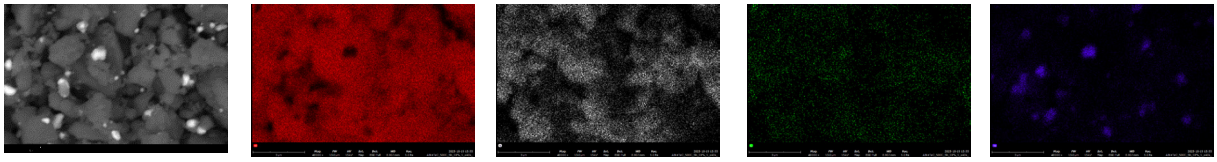
Figure 1 – SEM micrographs of the initial AlN powder and (1-x)AlN-xTaC composite powders after mechanochemical activation with different TaC. All micrographs were recorded at the same magnification

The bright particles visible in the SEM images correspond to the Ta-containing phase because of the higher atomic-number contrast relative to the AlN matrix. No pronounced carbide agglomeration is observed over the investigated composition range, indicating that the selected milling conditions ensured efficient dispersion of the reinforcing phase throughout the powder mixture.

The observed morphological evolution is consistent with the well-established mechanisms of mechanochemical processing. During high-energy milling, repeated particle fracture, cold welding, and intensive mixing increase the contact area between AlN and TaC particles, thereby improving powder homogeneity and promoting intimate interparticle contact. Such structural homogenization is expected to facilitate subsequent solid-state reactions during heat treatment and contribute to the formation of a more uniform ceramic microstructure.

Although no quantitative particle-size analysis was performed, the SEM observations indicate a reduction in particle agglomeration and a more homogeneous distribution of the reinforcing phase after mechanochemical treatment. Such a microstructural arrangement is generally considered favorable for efficient load transfer between the ceramic matrix and the reinforcing particles and may therefore contribute to the enhanced mechanical properties discussed in the following sections.

To further evaluate the distribution of the reinforcing phase, elemental mapping was performed by energy-dispersive X-ray spectroscopy (EDS). Representative elemental maps of the (1-x)AlN-xTaC composite with x = 0.10 are shown in Figure 2, while the average elemental compositions determined from three independently analyzed regions are summarized in Table 1.



a) b) c) d) e)
a) SEM image; b) Al; c) N; d) C; e) Ta

Figure 2 – SEM micrograph and corresponding EDS elemental maps of the (1-x)AlN-xTaC composite with x = 0.10

Table 1 – Average elemental composition of the (1-x)AlN-xTaC composites determined by EDS analysis (mean ± standard deviation, n = 3)

Composition	C (wt.%)	N (wt.%)	Al (wt.%)	Ta (wt.%)
AlN (x = 0)	–	40.20 ± 0.44	59.80 ± 0.44	–
(1-x)AlN-xTaC (x = 0.01)	2.53 ± 0.85	37.97 ± 2.97	56.80 ± 1.82	2.70 ± 1.27
(1-x)AlN-xTaC (x = 0.03)	2.93 ± 2.56	40.97 ± 2.08	53.93 ± 4.28	2.16 ± 0.99
(1-x)AlN-xTaC (x = 0.05)	3.37 ± 1.43	41.67 ± 1.20	50.10 ± 3.68	4.87 ± 1.12
(1-x)AlN-xTaC (x = 0.10)	5.03 ± 3.47	39.58 ± 0.93	48.00 ± 4.70	6.74 ± 1.96

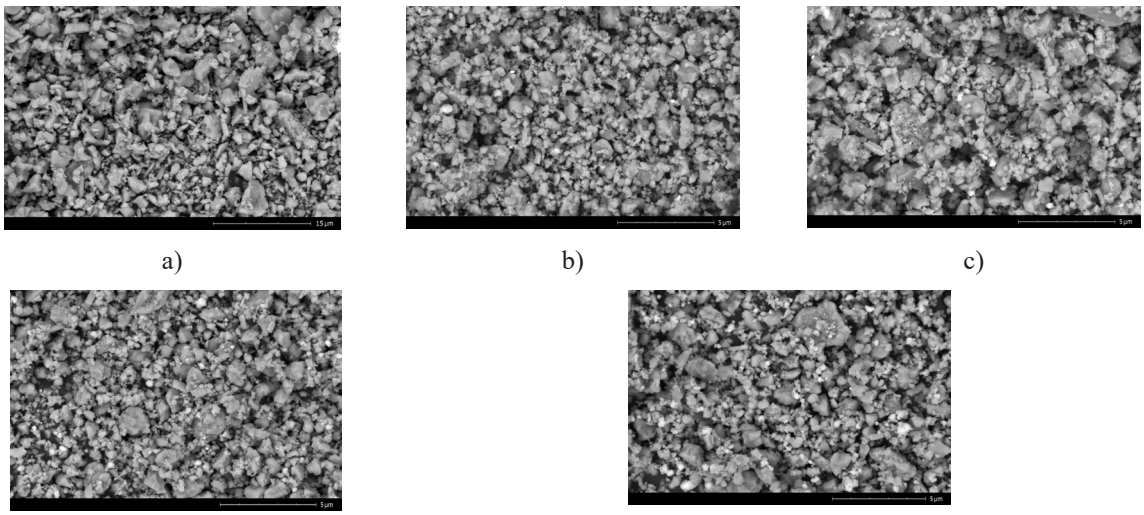
The elemental maps reveal a relatively uniform spatial distribution of Al, N, C, and Ta throughout the analyzed region without evidence of pronounced elemental segregation. The spatial coincidence of carbon and tantalum confirms that the bright particles correspond to the TaC reinforcing phase, whereas the continuous distribution of Al and N demonstrates that the addition of TaC does not disrupt the continuity of the AlN matrix.

The quantitative EDS results exhibit good reproducibility and show an overall increase in the Ta content with increasing nominal TaC concentration. Minor deviations between the nominal and measured compositions can be attributed to the local nature of EDS analysis and the heterogeneous distribution of carbide particles within the analyzed regions. Nevertheless, the relatively small standard deviations and the absence of pronounced compositional fluctuations confirm that mechanochemical processing provides efficient mixing of the starting powders and promotes a homogeneous dispersion of the reinforcing phase throughout the AlN matrix.

SEM micrographs of the initial AlN powder and the (1-x)AlN-xVC composite powders after mechanochemical treatment are presented in Figure 3. Similar to the TaC-containing composites, the initial AlN powder consists of irregularly shaped particles forming coarse agglomerates. After the addition of VC and mechanochemical activation (Figures 3b-e), the powder mixtures exhibit a relatively homogeneous particle distribution without pronounced changes in the overall particle morphology.

In contrast to the AlN-TaC system, the incorporation of VC does not produce pronounced morphological refinement of the powder mixture. The overall particle size and agglomeration state remain comparable to those of the initial AlN powder, although mechanochemical treatment provides satisfactory homogenization of the powder mixture. No large agglomerates of the reinforcing phase are observed within the investigated concentration range.

The limited influence of VC on the powder morphology suggests that, under the selected milling conditions, the principal effect of mechanochemical processing is associated with improved dispersion of the reinforcing particles rather than significant particle fragmentation. Nevertheless, repeated fracture, cold welding, and intensive mixing during high-energy milling are expected to enhance the contact between AlN and VC particles, thereby promoting structural homogeneity before subsequent heat treatment.



a) b) c)

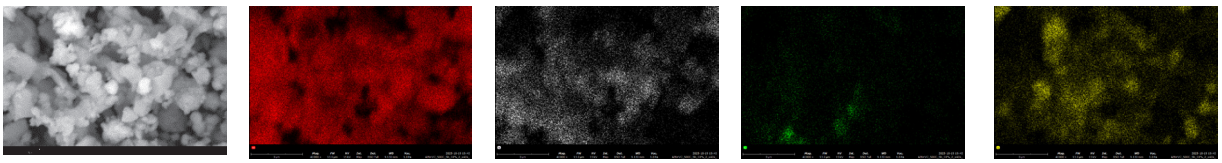
d) e)

a) initial; b) at addition of 0.01 M; c) at addition of 0.03 M;
d) at addition of 0.05 M; e) at addition of 0.10 M

Figure 3 – SEM micrographs of the initial AlN powder and (1-x)AlN-xVC composite powders after mechanochemical activation with different VC. All micrographs were acquired at the same magnification

To further evaluate the elemental distribution, energy-dispersive X-ray spectroscopy (EDS) elemental mapping was performed for the (1-x)AlN-xVC composite with x = 0.10. The corresponding SEM image and elemental maps are presented in Figure 4, while the quantitative EDS results are summarized in Table 2.

The elemental maps demonstrate a relatively uniform distribution of Al, N, C, and V throughout the analyzed region without evidence of pronounced elemental segregation. The overlap between the carbon and vanadium signals indicates that the reinforcing particles remain uniformly dispersed within the AlN matrix after mechanochemical treatment. Furthermore, the continuous distribution of Al and N confirms that the incorporation of VC does not disturb the integrity of the ceramic matrix.



a) b) c) d) e)

a) SEM image; b) Al; c) N; d) C; e) V

Figure 4 – SEM micrograph and corresponding EDS elemental maps of the (1-x)AlN-xVC composite with x = 0.10

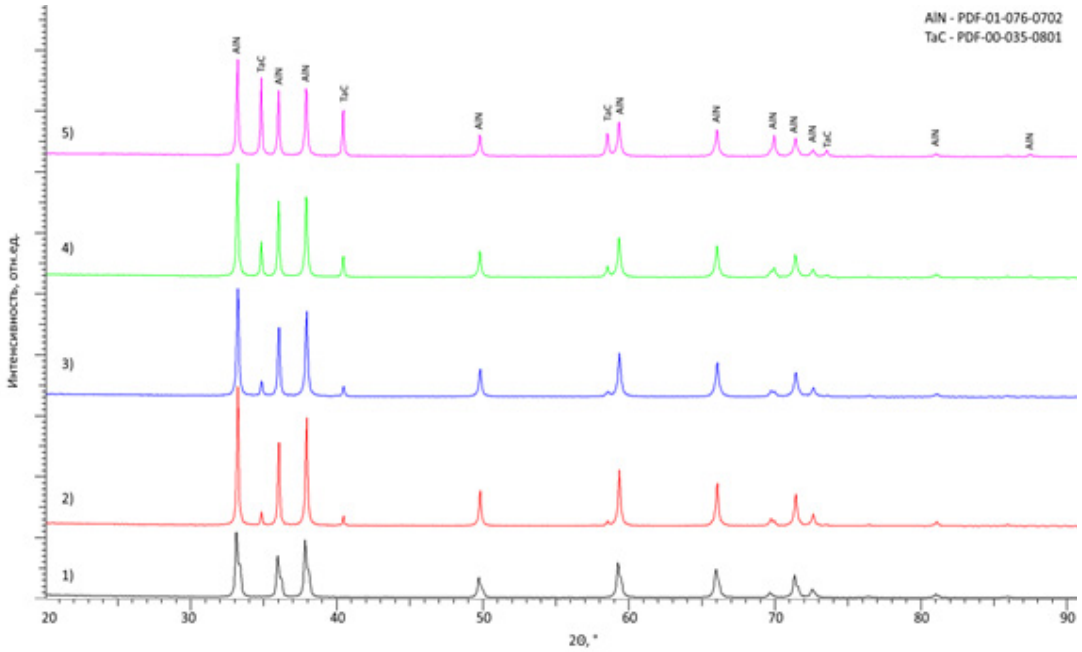
The quantitative EDS analysis exhibits good reproducibility and an overall increase in the measured V content with increasing nominal VC concentration. Minor differences between the nominal and measured compositions are attributed to the local nature of EDS analysis and the heterogeneous distribution of reinforcing particles within the analyzed regions. Overall, the results confirm that mechanochemical processing ensures effective mixing of the starting powders and promotes a relatively homogeneous distribution of the vanadium-containing phase throughout the AlN matrix.

Table 2 – Average elemental composition of the (1-x)AlN-xVC composites determined by EDS analysis (mean ± standard deviation, n = 3)

Composition	C (wt.%)	N (wt.%)	Al (wt.%)	V (wt.%)
AlN (x = 0)	–	40.20 ± 0.44	59.80 ± 0.44	–
(1-x)AlN-xVC (x = 0.01)	0.50 ± 0.46	0.50 ± 0.46	0.50 ± 0.46	0.50 ± 0.46
(1-x)AlN-xVC (x = 0.03)	0.83 ± 1.38	0.83 ± 1.38	0.83 ± 1.38	0.83 ± 1.38
(1-x)AlN-xVC (x = 0.05)	3.07 ± 0.55	3.07 ± 0.55	3.07 ± 0.55	3.07 ± 0.55
(1-x)AlN-xVC (x = 0.10)	6.47 ± 1.59	35.80 ± 1.05	49.60 ± 1.74	8.13 ± 1.20

Figure 5 presents the X-ray diffraction patterns of the (1-x)AlN-xTaC composites after mechanochemical activation followed by heat treatment. The diffraction patterns are dominated by reflections corresponding to the hexagonal AlN phase (space group $P6_3mc$), indicating that AlN remains the principal constituent of the composites over the entire investigated concentration range.

At low TaC contents (x = 0.01), no distinct reflections associated with tantalum carbide are observed, suggesting that the carbide content is below the detection limit of XRD or that the Ta-containing particles remain finely dispersed within the AlN matrix. With increasing TaC concentration (x ≥ 0.03), weak diffraction peaks attributable to TaC become visible and gradually increase in intensity, confirming the presence of the reinforcing carbide phase without the formation of additional reaction products.



1) x = 0; 2) x = 0.01; 3) x = 0.03; 4) x = 0.05; 5) x = 0.10

Figure 5 – X-ray diffraction patterns of the (1-x)AlN-xTaC composites after mechanochemical activation and heat treatment

The absence of detectable secondary oxide phases indicates that TaC remains thermodynamically stable under the applied heat-treatment conditions. This behavior is consistent with the exceptionally high chemical and oxidation stability of tantalum carbide, which belongs to the family of ultra-high-temperature ceramics and exhibits excellent resistance to oxidation compared with many other transition-metal carbides.

The calculated lattice parameters of the AlN phase (Table 3) show only minor variations with increasing TaC content. Both the a and c lattice parameters remain relatively stable over the investigated composition range, indicating that the crystal structure of the AlN matrix is largely preserved after mechanochemical processing and subsequent heat treatment. Considering the extremely limited mutual solubility between AlN and TaC, these slight variations are more likely associated with residual microstrains and lattice distortions introduced during high-energy milling than with substitutional incorporation of tantalum atoms into the AlN lattice. The absence of significant changes in the lattice parameters is also consistent with the XRD results, which demonstrate that TaC is retained as a separate reinforcing phase rather than forming a solid solution with AlN. These observations indicate that the strengthening effect of TaC primarily originates from its role as a dispersed reinforcing phase and from the microstructural refinement induced by mechanochemical processing, rather than from modifications of the AlN crystal lattice.

Table 3 – Structural parameters of the (1-x)AlN-xTaC composites determined from XRD analysis

Phase	x=0.0	x=0.01	x=0.03	x=0.05	x=0.10
AlN (hexagonal, P63mc)	a=3.1192 c=4.9906 V=42.05	a=3.1105 c=4.9819 V=41.74	a=3.1112 c=4.9819 V=41.76	a=3.1144 c=4.9829 V=41.86	a=3.1149 c=4.9819 V=41.86
TaC (cubic, Fm-3m)	-	a=4.4572 V=88.55	a=4.4565 V=88.51	a=4.4574 V=88.56	a=4.4573 V=88.55
Degree of structural ordering, %	89.5	89.2	88.1	86.9	86.2

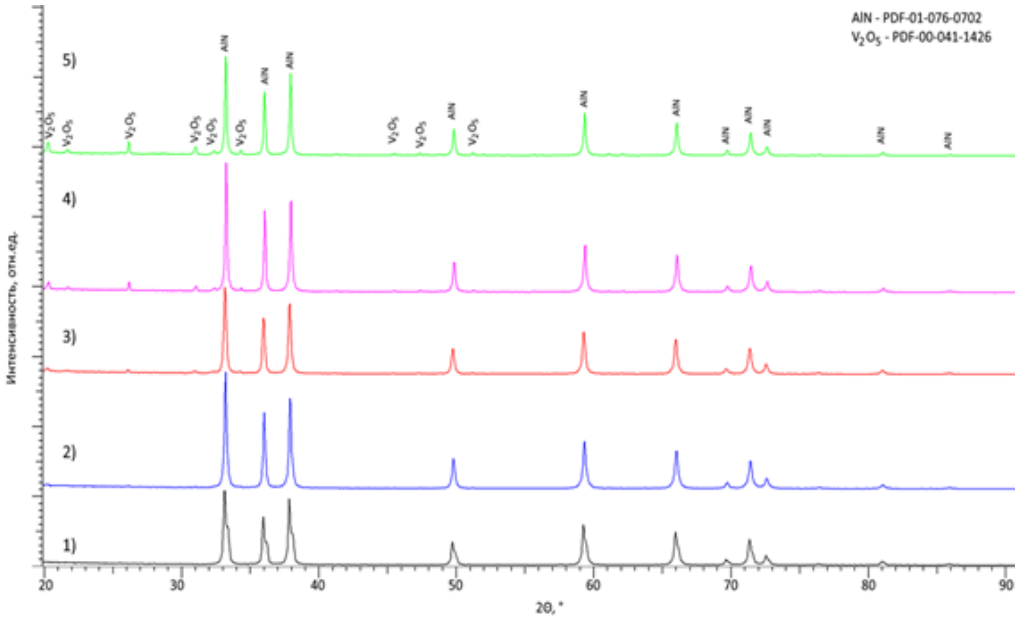
Overall, the XRD results indicate that TaC remains chemically stable during mechanochemical processing and subsequent heat treatment and is retained as a distinct reinforcing phase. No oxide phases were detected, indicating that the selected processing conditions preserve the integrity of the carbide. Combined with the homogeneous particle distribution observed by SEM/EDS analysis, the retained TaC phase provides favorable conditions for effective dispersion strengthening, grain-boundary pinning, and inhibition of grain growth, thereby contributing to the improved mechanical properties of the AlN-TaC composites.

Figure 6 presents the X-ray diffraction patterns of the (1-x)AlN-xVC composites after heat treatment. In contrast to the TaC-containing samples, the phase evolution of the VC-modified composites differs substantially.

The diffraction patterns remain dominated by the hexagonal AlN phase; however, beginning at x = 0.03, additional reflections corresponding to orthorhombic V_2O_5 become apparent. The intensity of these reflections increases progressively with increasing VC content, whereas characteristic peaks of crystalline VC are absent throughout the investigated composition range.

The disappearance of VC reflections together with the appearance of V_2O_5 indicates that vanadium carbide undergoes oxidation during heat treatment in air. The oxidation behavior can be attributed to the comparatively lower thermodynamic stability and oxidation resistance of VC relative to TaC. Under the present processing conditions, oxygen supplied by the annealing atmosphere reacts preferentially with VC, leading to the formation of vanadium oxide rather than preserving the original carbide phase. Similar oxidation behavior of vanadium-containing carbides has been reported previously in the literature.

The structural parameters summarized in Table 4 reveal only slight changes in the lattice constants of the AlN phase, whereas the degree of structural ordering gradually decreases with increasing VC concentration. This trend suggests that the formation of V_2O_5 and the associated lattice distortions introduce additional structural heterogeneity into the composite. The observed decrease in structural ordering is therefore attributed primarily to residual lattice strain and local structural distortions generated during mechanochemical processing and subsequent oxidation rather than to significant changes in the AlN crystal structure itself.



1) x = 0; 2) x = 0.01; 3) x = 0.03; 4) x = 0.05; 5) x = 0.10

Figure 6 – X-ray diffraction patterns of the (1-x)AlN – xVC composites after mechanochemical activation and heat treatment

Table 4 – Structural parameters of the (1-x)AlN-xVC composites determined from XRD analysis

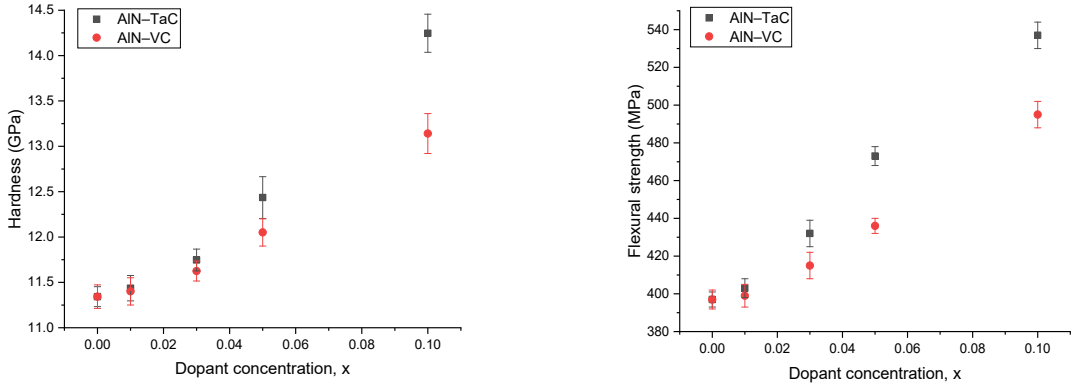
Phase	x=0.0	x=0.01	x=0.03	x=0.05	x=0.10
AlN (hexagonal, P63mc)	a=3.1192 c=4.9906 V=42.05	a=3.1131 c=4.9827 V=41.82	a=3.1179 c=4.9886 V=42.01	a=3.1058 c=4.9752 V=41.56	a=3.1106 c=4.9781 V=41.71
V2O5 (orthorhombic, Pmmn(59))	-	-	a=11.5410 b=3.5684 c=4.3762 V=180.23	a=11.4912 b=3.558 c=4.3667 V=178.54	a=11.4641 b=3.5622 c=4.3754 V=178.68
Degree of structural ordering, %	89.5	89.3	89.4	88.4	87.9

In contrast to the TaC-containing composites, the XRD results demonstrate that VC undergoes partial oxidation during heat treatment, leading to the formation of the V_2O_5 phase at $x \geq 0.03$. No diffraction peaks corresponding to crystalline VC are detected after thermal treatment, suggesting that a substantial fraction of the initial carbide is transformed into vanadium oxide under the selected processing conditions. This behavior is consistent with the comparatively lower oxidation resistance and thermodynamic stability of VC relative to TaC.

The formation of V_2O_5 is also consistent with the SEM observations (Figure 3), where finely dispersed oxide-rich regions are observed in the vicinity of particle agglomerates. Together, the SEM and XRD results indicate that oxidation of VC plays an important role in determining the final phase composition and microstructural evolution of the composites.

The different phase evolution observed for the TaC- and VC-containing systems is expected to influence their strengthening behavior. Whereas TaC remains chemically stable and is retained as a reinforcing carbide phase, partial oxidation of VC reduces the amount of intact carbide available for reinforcement and introduces secondary oxide phases into the microstructure. These differences provide a plausible explanation for the different mechanical responses of the investigated composites, which are discussed in the following section.

Figure 7 summarizes the variation in the Vickers hardness and flexural strength of the (1-x)AlN-xTaC and (1-x)AlN-xVC composites as a function of carbide content. Both mechanical properties increase with increasing dopant concentration; however, the magnitude of the improvement differs considerably for the two reinforcing carbides.



a) b)

a) Vickers hardness; b) flexural strength

Figure 7 – Mechanical properties of the (1-x)AlN-xTaC and (1-x)AlN-xVC composites as a function of carbide content

At low additive contents ($x \leq 0.03$), only a moderate improvement in hardness and flexural strength is observed for both systems, suggesting that the volume fraction of the reinforcing phase is insufficient to produce a pronounced strengthening effect. As the carbide content increases to $x = 0.05$ and 0.10, both mechanical properties increase more noticeably, indicating that the reinforcing particles become sufficiently abundant to effectively impede deformation and crack propagation.

The strengthening effect is consistently more pronounced for the TaC-containing composites than for the VC-containing materials. The hardness of the AlN-TaC composites increases by approximately 10–25% relative to monolithic AlN, whereas the corresponding increase for the AlN-VC system is limited to approximately 6–15%. A similar tendency is observed for flexural strength.

The superior mechanical performance of the TaC-containing composites can be explained by the combined effects of phase stability, microstructural evolution, and several complementary strengthening mechanisms. As demonstrated by the XRD results (Figure 4), TaC remains chemically stable during mechanochemical processing and subsequent heat treatment, preserving the hard carbide phase within the AlN matrix. SEM observations (Figure 1) and EDS elemental mapping (Figure 2) further confirm the relatively homogeneous distribution of TaC particles without pronounced agglomeration.

Uniformly dispersed TaC particles act as effective obstacles to localized deformation, providing dispersion strengthening. In addition, carbide particles located at grain boundaries suppress grain growth during thermal treatment, thereby contributing to grain-boundary strengthening according to the Hall-Petch relationship. Although quantitative grain-size measurements were not performed, the improved powder homogeneity observed after mechanochemical processing suggests that dispersed carbide particles restrict grain coarsening during subsequent heat treatment. Furthermore, the uniformly distributed hard particles promote crack deflection and crack bridging, thereby increasing the energy required for crack propagation and contributing to the observed improvement in flexural strength. These strengthening mechanisms operate synergistically with the refined microstructure produced by mechanochemical activation, resulting in superior mechanical performance.

In contrast, the strengthening efficiency of VC is lower because the reinforcing phase undergoes partial oxidation during heat treatment. The XRD analysis (Figure 6) demonstrates the formation of V_2O_5 at $x \geq 0.03$, while no crystalline VC reflections are detected after processing. Consequently, part of the initially introduced carbide is converted into an oxide phase possessing lower hardness and lower reinforcing capability than the original carbide. This phase transformation reduces the effective volume fraction of hard reinforcing particles available for load transfer and limits the overall strengthening effect. The presence of oxide-rich regions identified by SEM and EDS observations further supports this interpretation.

Overall, the obtained results demonstrate that the mechanical behavior of the investigated composites is governed not only by the amount of reinforcing additive but also by its chemical stability during processing and the resulting phase composition. The superior performance of the AlN-TaC composites arises from the retention of a stable carbide phase, its homogeneous dispersion within the AlN matrix, and the combined contributions of dispersion strengthening, grain-growth inhibition, grain-boundary strengthening, and crack-deflection mechanisms. In contrast, the partial oxidation of VC into V_2O_5 reduces the efficiency of these strengthening mechanisms, leading to comparatively lower hardness and flexural strength. These observations establish a clear relationship between phase evolution, microstructure, and mechanical performance, thereby providing a mechanistic explanation for the different responses of the TaC- and VC-reinforced AlN composites.

Conclusion

This study systematically investigated the influence of tantalum carbide and vanadium carbide additions on the phase composition, microstructure, and mechanical properties of AlN-based ceramic composites prepared by mechanochemical solid-state processing.

The results demonstrate that mechanochemical activation provides effective homogenization of the powder mixtures and promotes a uniform distribution of the reinforcing phases prior to heat treatment. The AlN-TaC composites retain a stable carbide phase after processing, whereas the AlN-VC system undergoes partial oxidation, resulting in the formation of V_2O_5. These differences in phase evolution significantly influence the subsequent microstructural development and mechanical behavior of the composites.

Mechanical characterization showed that increasing the carbide content above $x=0.03$ leads to a noticeable improvement in hardness and flexural strength. The strengthening effect is more pronounced for the TaC-containing composites, which can be attributed to the retention of a chemically stable, uniformly dispersed hard carbide phase. In contrast, partial oxidation of VC reduces the amount of the reinforcing carbide available for strengthening and consequently limits the improvement in mechanical performance.

The combined SEM, EDS, XRD, and mechanical characterization establishes a clear relationship between dopant type, phase evolution, microstructure, and mechanical properties. The observed strengthening is associated with the combined effects of homogeneous dispersion of the reinforcing phase, inhibition of excessive grain growth, grain-boundary strengthening, and increased resistance to crack propagation.

Although thermal conductivity was not investigated in the present work, the obtained results indicate that TaC is a promising reinforcing additive for improving the mechanical reliability of AlN-based ceramics while maintaining a stable phase composition under the applied processing conditions.

The developed AlN-based composites may therefore be considered promising candidates for structural ceramic components operating under elevated temperatures and severe mechanical loading, including wear-resistant components, high-temperature structural elements, protective ceramic parts, and thermally stable substrates where enhanced mechanical reliability is required. The established composition-structure-property relationships may also provide useful guidance for the further design and optimization of advanced AlN-based ceramic composites.

Funding information. This research was funded by the Science Committee of the Ministry of Education and Science of the Republic of Kazakhstan (No. BR28713365).

REFERENCES

1 Schwarzer-Fischer, E., Scheithauer, U., and Michaelis, A. CerAMfacturing of aluminum nitride with high thermal conductivity via lithography-based ceramic vat photopolymerization (CerAM VPP). Ceramics, 6 (1), 416–431 (2023). https://doi.org/10.3390/ceramics6010024

2 Gaskins, J.T., Hopkins, P.E., Merrill, D.R., Bauers, S.R., Hadland, E., Johnson, D.C., and King, S.W. Investigation and review of the thermal, mechanical, electrical, optical, and structural properties of atomic layer deposited high-k dielectrics: Beryllium oxide, aluminum oxide, hafnium oxide, and aluminum nitride. ECS Journal of Solid State Science and Technology, 6 (10), N189 (2017). https://doi.org/10.1149/2.0091710jss

3 Zhang, Z., Wu, H., Zhang, Z., Li, J., Xu, H., Lu, H., and Qin, M. Limiting the lattice oxygen impurities to obtain high thermal conductivity aluminum nitride ceramics. Ceramics International, 50 (18), 33488–33495 (2024). https://doi.org/10.1016/j.ceramint.2024.06.164

4 Zhang, Z., Wu, H., Li, T., Zhang, Z., Xu, H., Lu, H., and Qin, M. Preparation of high thermal conductivity aluminium nitride ceramics with low oxygen impurity for power semiconductors. Electrical Materials and Applications, 1 (1), e12012 (2024). https://doi.org/10.1049/ema3.12012

5 Kozlovskiy, A.L., Borgekov, D.B., Tleulessova, I.K., Zhumazhanova, A.T., Moldabayeva, G.Z., Burkhanov, B.Z., and Khametova, A.A. Evaluation of the application efficiency of multicomponent ceramics as protective shielding and thermal barrier materials. Eurasian Physical Technical Journal, 22 (3), 24–35 (2025). https://doi.org/10.31489/2025N3/24-35

6 Paik, U., Park, H.C., Choi, S.C., Ha, C.G., Kim, J.W., and Jung, Y.G. Effect of particle dispersion on microstructure and strength of reaction-bonded silicon carbide. Materials Science and Engineering: A, 334 (1-2), 267–274 (2002). https://doi.org/10.1016/S0921-5093(01)01897-4

7 Mao, H., Shen, F., Zhang, Y., Wang, J., Cui, K., Wang, H., and Tan, T. Microstructure and mechanical properties of carbide reinforced TiC-based ultra-high temperature ceramics: A Review. Coatings, 11 (12), 1444 (2021). https://doi.org/10.3390/coatings11121444

8 Yue, X.M., Zhang, G.J., and Wang, Y.M. Reaction synthesis and mechanical properties of TiB2–AlN–SiC composites. Journal of the European Ceramic Society, 19 (3), 293–298 (1999). https://doi.org/10.1016/S0955-2219(98)00150-2

9 Lin, K., Zong, X., Sheng, P., Zhao, S., Qi, Y., Zhang, W., and Wu, S. Effects of SmF3 addition on aluminum nitride ceramics via pressureless sintering. Journal of the European Ceramic Society, 43 (15), 6804–6814 (2023). https://doi.org/10.1016/j.jeurceramsoc.2023.07.051

10 Mao, H., Zhang, Y., Wang, J., et al. Microstructure, Mechanical Properties, and Reinforcement Mechanism of Second-Phase Reinforced TiC-Based Composites: A Review. Coatings, 12 (6), 801 (2022). https://doi.org/10.3390/coatings12060801

11 Yang, S.L., Chu, C.H., and Hsiang, H.I. Effect of Y2Zr2O7 content on improving mechanical properties and thermal shock resistance of AlN-based composite ceramics. Ceramics International, 50, 29321–29331 (2024). https://doi.org/10.1016/j.ceramint.2024.05.226

12 Zhai, X., Lu, K., Peng, C., et al. Effects of Nb/TiC/TaC/VC and Co addition on the microstructure and properties of WC-based cemented carbides. International Journal of Applied Ceramic Technology, 20, 2785–2795 (2023). https://doi.org/10.1111/ijac.14424

13 Sun, W., Kuang, X., Liang, H., Xia, X., Zhang, Z., Lu, C., and Hermann, A. Mechanical properties of tantalum carbide from high-pressure/high-temperature synthesis and first-principles calculations. Physical Chemistry Chemical Physics, 22 (9), 5018–5023 (2020). https://doi.org/10.1039/C9CP06819H

14 Peng, J., Dong, H., Hojamberdiev, M., Yi, D., Yang, Y., Bao, H., and Meng, L. Improving the mechanical properties of tantalum carbide particle-reinforced iron-based composite by varying the TaC contents. Journal of Alloys and Compounds, 726, 896–905 (2017). https://doi.org/10.1016/j.jallcom.2017.08.050

15 Fahrenholtz, W.G., and Hilmas, G.E. Ultra-high temperature ceramics: materials for extreme environments. Scripta Materialia, 129, 94–99 (2017). https://doi.org/10.1016/j.scriptamat.2016.10.018

16 Zeiger, M., Ariyanto, T., Krüner, B., Peter, N.J., Fleischmann, S., Etzold, B.J., and Presser, V. Vanadium pentoxide/carbide-derived carbon core–shell hybrid particles for high performance electrochemical energy storage. Journal of Materials Chemistry A, 4 (48), 18899–18909 (2016). https://doi.org/10.1039/C6TA08900C

17 Bugdayci, M., Once, L., Alkan, M., Turan, A., and Cinarli, U. A Comparative Study about Production of Vanadium Carbide via Self Propagating High Temperature Synthesis and Reduction. Archives of Metallurgy and Materials, 69 (1), 257–262 (2024). https://doi.org/10.24425/amm.2024.147816

18 Baláž, P. Mechanochemistry in minerals engineering. Mechanochemistry in Nanoscience and Minerals Engineering (Berlin, Heidelberg: Springer Berlin Heidelberg, 2008), pp. 257–296.

19 Sritharan, T., Boey, F.Y.C., and Srinivas, A. Synthesis of complex ceramics by mechanochemical activation. Journal of Materials Processing Technology, 192, 255–258 (2007). https://doi.org/10.1016/j.jmatprotec.2007.04.079

20 Maghsoudipour, A., Moztarzadeh, F., Saremi, M., and Heinrich, J.G. Oxidation behavior of AlN–Al2O3 composites. Ceramics International, 30 (5), 773–783 (2004). https://doi.org/10.1016/j.ceramint.2003.10.004

21 Varanasi, D., Furkó, M., Balázsi, K., and Balázsi, C. Processing of Al2O3-AlN ceramics and their structural, mechanical, and tribological characterization. Materials, 14 (20), 6055 (2021). https://doi.org/10.3390/ma14206055

[1*]Жумажанова А.Т.,
PhD, КҒҚ, ORCID ID: 0000-0002-5483-9552,
* e-mail: ainashzhumazhanova@gmail.com
[1]Шакирзянов Р.И.,
ф.-м. ғ.к., КҒҚ, ORCID ID: 0000-0001-9908-3034,
e-mail: shakirzyanov_ri@enu.kz

[1]Л.Н. Гумилев атындағы Еуразия ұлттық университеті, Астана қ., Қазақстан

ТАНТАЛ ЖӘНЕ ВАНАДИЙ КАРБИДТІ ДОПАНТТАРЫНЫҢ АЛЮМИНИЙ НИТРИДІ НЕГІЗІНДЕГІ КЕРАМИКАЛАРДЫҢ ҚҰРЫЛЫМЫ МЕН МЕХАНИКАЛЫҚ ҚАСИЕТТЕРІНЕ ӘСЕРІ

Аңдатпа

Бұл жұмыста механохимиялық қатты фазалық өңдеу және кейінгі термиялық өңдеу арқылы алынған алюминий нитриді негізіндегі керамикалық композиттердің фазалық құрамына, микроқұрылымына және механикалық қасиеттеріне тантал карбиді мен ванадий карбиді қоспаларының әсері зерттелді. Карбидтік қоспалардың мольдік үлесі x=0,01–0,10 аралығында өзгертілді. Сканерлеуші электрондық микроскопия және энергодисперсиялық рентгендік спектрлік талдау нәтижелері механохимиялық активациядан кейін арматуралаушы фазалардың біркелкі таралатынын көрсетті. Рентгендік фазалық талдау TaC өңдеу барысында химиялық тұрақтылығын сақтап, AlN матрицасының кристалдық торындағы деформацияларды азайта отырып, екі фазалы AlN-TaC композитінің түзілетінін көрсетті. Керісінше, VC термиялық өңдеу кезінде ішінара тотығып, екінші реттік V_2O_5 фазасының түзілуіне алып келеді, нәтижесінде материалдың фазалық эволюциясы өзгеше сипат алады. Механохимиялық өңдеу ұнтақ қоспасының анағұрлым біртекті морфологиясының қалыптасуына ықпал етіп, карбид бөлшектерінің ірі агломераттарының түзілуін тежейді, бұл кейінгі микроқұрылымның қалыптасуына қолайлы жағдай жасайды. Механикалық сынақтар $x > 0,03$ болған жағдайда қаттылық пен иілу кезіндегі беріктіктің едәуір артатынын көрсетті. Ең жоғары беріктендіру әсері тұрақты, біркелкі таралған жоғары қаттылықтағы карбидтік фазаның сақталуына байланысты TaC қосылған композиттерде байқалды. Механикалық қасиеттердің жақсаруы дисперсиялық беріктендірудің, түйіршіктердің өсуін тежеудің, түйіршік шекараларының беріктенуінің және жарықшақтардың таралу траекториясының ауытқуының бірлескен әсерімен түсіндіріледі. Алынған нәтижелер өңдеу шарттары, фазалық эволюция, микроқұрылым және механикалық қасиеттер арасындағы өзара байланысты анық көрсетіп, жоғары механикалық және термиялық жүктемелер жағдайында пайдалануға арналған алюминий нитриді негізіндегі жоғары тиімді керамикалық композиттерді әзірлеуде механохимиялық өңдеу әдісінің перспективалы екенін дәлелдейді.

Түйін сөздер: алюминий нитриді, карбо-нитридті керамикалар, механохимиялық синтез, тантал карбиді, ванадий карбиді, фазалық құрам, беріктік қасиеттері.

[1*]**Жумажанова А.Т.,**
PhD, МНС, ORCID ID: 0000-0002-5483-9552,
* e-mail: ainashzhumazhanova@gmail.com
[1]**Шакирзянов Р.И.,**
к.ф.-м.н., МНС, ORCID ID: 0000-0001-9908-3034,
e-mail: shakirzyanov_ri@enu.kz

[1]Евразийский национальный университет им. Л.Н. Гумилева, г. Астана, Казахстан

ВЛИЯНИЕ КАРБИДНЫХ ДОПАНТОВ ТАНТАЛА И ВАНАДИЯ НА СТРУКТУРУ И МЕХАНИЧЕСКИЕ СВОЙСТВА КЕРАМИК НА ОСНОВЕ НИТРИДА АЛЮМИНИЯ

Абстракт

В настоящей работе исследовано влияние добавок карбида тантала и карбида ванадия на фазовый состав, микроструктуру и механические свойства керамических композитов на основе нитрида алюминия, полученных методом механохимической твердофазной обработки с последующей термообработкой. Мольная доля карбидных добавок варьировалась в диапазоне x = 0,01–0,10. Результаты сканирующей электронной микроскопии в сочетании с энергодисперсионным рентгеноспектральным анализом показали однородное распределение армирующих фаз после механохимической активации. Рентгенофазовый анализ показал, что карбид тантала сохраняет химическую стабильность в процессе обработки, что приводит к формированию двухфазного композита AlN-TaC с пониженными искажениями кристаллической решетки матрицы AlN. Напротив, карбид ванадия в процессе термообработки подвергается частичному окислению с образованием вторичной фазы V_2O_5, что обусловливает иной характер фазовой эволюции материала. Механохимическая обработка способствует формированию более однородной морфологии порошковой смеси и подавляет образование крупных агломератов карбидных частиц, создавая благоприятные условия для последующего формирования микроструктуры. Механические испытания показали, что при содержании добавок x > 0,03 наблюдается существенное повышение твердости и прочности при изгибе, при этом наибольший эффект упрочнения достигается в композитах, содержащих TaC, благодаря сохранению стабильной равномерно распределенной высокотвердой карбидной фазы. Улучшение механических свойств обусловлено совместным действием дисперсионного упрочнения, подавления роста зерен, упрочнения границ зерен и отклонения траектории распространения трещин. Полученные результаты устанавливают четкую взаимосвязь между условиями обработки, фазовой эволюцией, микроструктурой и механическими свойствами материалов, демонстрируя перспективность механохимического метода для создания высокоэффективных керамических композитов на основе нитрида алюминия, предназначенных для эксплуатации в условиях высоких механических и термических нагрузок.

Ключевые слова: нитрид алюминия, карбо-нитридные керамики, механохимический синтез, карбид тантала, карбид ванадия, фазовый состав, прочностные свойства.

UDC 538.911
IRSTI 29.27.07

https://doi.org/10.55452/1998-6688-2026-23-3-448-460

[1*]Batryshev D.G.,
PhD, Associate Professor, ORCID ID: 0000-0002-9847-1067,
[*]e-mail: d.batryshev@kbtu.kz
[1,†]Abdirakhmanov A.R.,
PhD, Postdoc, ORCID ID: 0000-0001-6652-1923,
e-mail: abdirakhmanov@physics.kz
[2]Boufendi L.,
PhD, Professor, ORCID ID: 0000-0002-6995-0368,
e-mail: laifa.boufendi@physics.kz
[1,2]Orazbayev S.A.,
PhD, Associate Professor, ORCID ID: 0000-0002-7286-9990,
e-mail: sagi.orazbayev@gmail.com
[1,2]Baikaliyev A.,
PhD student, Junior researcher, ORCID ID: 0009-0000-5616-7131,
e-mail: akdauletbai@gmail.com
[1,2]Ramazanov T.S.,
Doctor of Physical and Mathematical Sciences, Professor, ORCID ID: 0000-0001-7172-8005,
e-mail: ramazan@physics.kz

[1]Kazakh-British Technical University, Almaty, Kazakhstan
[2]Al-Farabi Kazakh National University, Almaty, Kazakhstan
[†]Current address: Mons University, Mons, 7000, Belgium.

STUDY OF GROWTH EVALUATION OF NANOSTRUCTURED CARBON NITRIDE THIN LAYERS IN NITROGEN-METHANE GAS MIXTURE RADIOFREQUENCY PLASMA

Abstract

Amorphous carbon nitride (a-C_xN_y) thin films were synthesized by plasma-enhanced chemical vapor deposition (PECVD) in a nitrogen–methane radiofrequency (RF) discharge plasma (13.56 MHz) using pulsed plasma modulation. The evolution of the DC self-bias voltage (V_{dc}) was monitored as an in situ diagnostic parameter to track nanoparticle nucleation, growth, and agglomeration during synthesis. It was found that the absolute value of V_{dc} decreases monotonically following plasma ignition, and that the onset of nanoparticle agglomeration can be reliably identified from a characteristic change in the $V_{dc}(t)$ curve, consistent with the three-stage model of dust-particle formation in low-temperature plasma. The agglomeration onset time (t_{agl}) was shown to depend strongly on methane flow rate, working pressure, and RF power: at baseline conditions (0.86 mbar, 20 W), increasing the CH_4 flow rate from 2 to 7 sccm reduced t_{agl} from 4.4 s to 200 ms, while pressure and power exhibited dominant and non-monotonic effects, respectively. These findings guided the selection of plasma-on pulse durations for controlled film growth. Samples deposited under pulsed modulation were characterized by SEM, EDS, FTIR, and XRD, confirming the formation of continuous, nonstoichiometric carbon nitride films dominated by C–N and C=N bonding. The results demonstrate that self-bias voltage monitoring is an effective, accessible method for in situ control of a-C_xN_y nanoparticle growth kinetics and for tailoring film thickness, morphology, and chemical structure via pulsed RF plasma parameters.

Keywords: amorphous carbon nitride, PECVD synthesis, RF plasma, DC self-bias voltage, growth mechanism.

Received July 31, 2026; revised August 21, 2026; accepted August 26, 2026.

Introduction

Carbon nitride (CN_x) has attracted sustained research interest since theoretical calculations predicted that a hypothetical β-C_3N_4 phase could be harder than diamond. Although a phase-pure crystalline β- C_3N_4 has not yet been synthesized in continuous thin-film form, the amorphous and nanostructured carbon nitride phases obtained experimentally have proven valuable in their own right, exhibiting characteristic high resistivity, good photosensitivity, and a broad range of tunable electrical and optical properties depending on the deposition method and process conditions. These characteristics have made amorphous carbon nitride (a-CNx) attractive for protective and biomedical coatings, microelectronic devices, photosensors, solar cells, low-k dielectric materials for ULSI, and, more recently, metal-free semiconductor photocatalysts for applications such as visible-light-driven hydrogen evolution and photocatalytic hydrogen peroxide production [1].

A variety of physical and chemical vapor deposition routes have been employed to synthesize CNx thin films, each offering different control over stoichiometry, bonding structure, and morphology. Physical vapor deposition (PVD) approaches include reactive rf and dc magnetron sputtering of graphite targets in nitrogen atmospheres, reactive pulsed laser ablation, electron-beam evaporation under nitrogen-ion bombardment, and dual ion-beam-assisted sputter deposition. Chemical vapor deposition (CVD) routes, by contrast, typically rely on plasma excitation of nitrogen-containing hydrocarbon gas mixtures, including rf plasma of acetylene/nitrogen mixtures, microwave surface-wave plasma from argon/hydrocarbon/nitrogen feedstocks, and distributed electron cyclotron resonance (ECR) plasma decomposition of acetylene and nitrogen [1]. Among these, rf plasma-assisted CVD is particularly attractive owing to its relative simplicity, scalability, and the fine control it affords over plasma density, ion energy, and radical concentration through adjustable process parameters such as rf power, gas flow ratio, chamber pressure, and substrate temperature [2].

Numerous studies have shown that these plasma parameters strongly influence the resulting film microstructure. Increasing rf power raises substrate temperature, electron temperature, and plasma density within the reactor, which accelerates the deposition rate and film growth while also roughening the surface morphology, shifting it from smooth, featureless films toward cauliflower-like or broccoli-like nanostructured surfaces at higher power or longer deposition time [1, 2]. Correspondingly, optical properties such as the absorption edge, optical band gap, refractive index, and extinction coefficient vary systematically with plasma power, reflecting underlying changes in film density, polarizability, and defect concentration within the amorphous network; reported optical gaps for a-CNx films typically fall in the range of roughly 2.9–4.4 eV depending on deposition technique and nitrogen content [1]. Post-deposition plasma treatments, such as exposure to oxygen plasma, have additionally been shown to selectively etch the film surface and alter its chemical bonding state - increasing C–O bonding at the expense of C–N/C–C bonding, and in some cases inducing nitrogen-oxide species (e.g., NO_2, NO_3) at elevated deposition temperatures - with the etching rate and bonding response found to depend strongly on substrate temperature during growth. Such findings underscore that the nanostructure and surface chemistry of CNx films are highly sensitive not only to precursor chemistry but also to the specific plasma and thermal history of the film [2].

More broadly, doping and defect engineering strategies applied to conjugated carbon nitride frameworks - including nitrogen-vacancy formation, heteroatom doping, and plasma-induced structural disordering - have been shown to modulate the electronic structure, extend π-conjugation, and passivate charge-trapping states, thereby significantly influencing photophysical and photocatalytic behavior [2]. This further demonstrates that plasma-based processing is a powerful and versatile tool for tailoring the amorphous/nanostructured carbon nitride network beyond what is achievable through thermal polymerization alone [3].

Despite this substantial body of work, most rf plasma CVD studies of amorphous carbon nitride have relied on acetylene (C_2H_2) as the carbon-bearing precursor gas [1], while nitrogen–methane (N_2-CH_4) plasma systems remain comparatively less explored. Methane's simpler molecular structure, higher hydrogen-to-carbon ratio, and distinct dissociation pathway relative to acetylene may influence

radical generation, carbon–nitrogen incorporation kinetics, and the resulting film nanostructure in ways not yet systematically documented. A detailed evaluation of how growth conditions govern the structural evolution of CN_x films deposited from N_2-CH_4 rf plasma is therefore needed to establish process–structure relationships analogous to those already reported for C_2H_2-based and sputtered CNx systems [1–3].

In this work, we investigate the growth evolution of amorphous carbon nitride thin layers deposited by radiofrequency plasma in a nitrogen-methane gas mixture.

Materials and methods

The growth of amorphous carbon nitride (a-CN_x) in a high-frequency (HF) capacitive discharge plasma was studied using a plasma-enhanced chemical vapor deposition (PECVD) system, the schematic of which is shown in Figure 1.

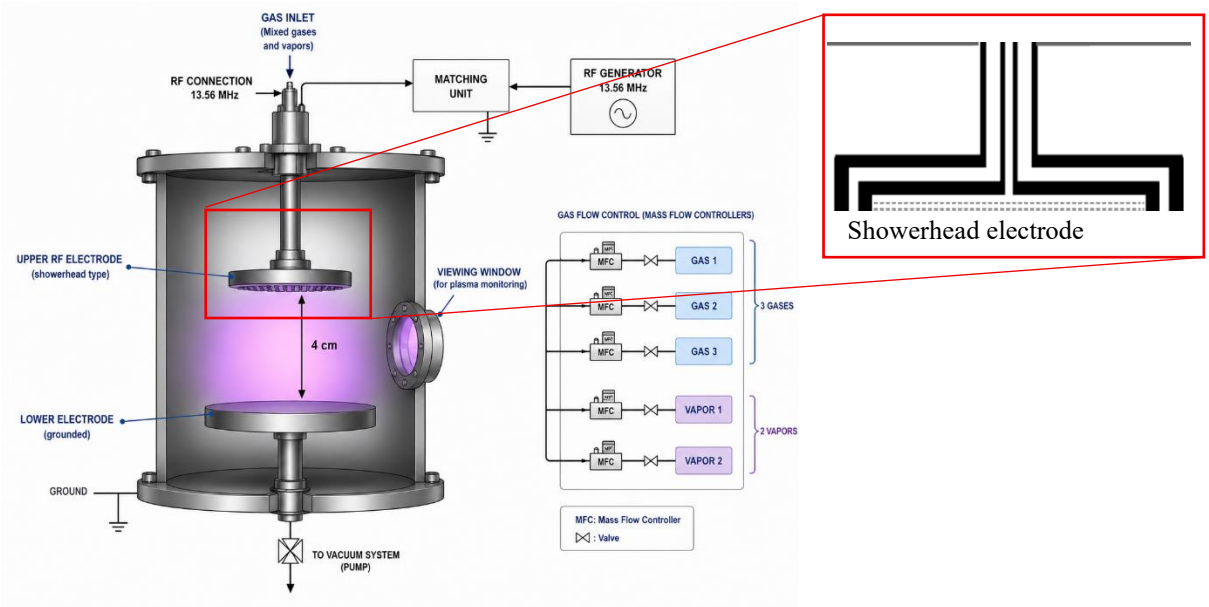


Figure 1 – Schematic of the PECVD system for nanomaterial synthesis in an RF discharge plasma

As shown in Figure 1, the plasma is formed between two plane-parallel disk electrodes upon excitation of a 13.56 MHz capacitive RF discharge through a matching network. Before each experiment, the vacuum chamber was evacuated to a residual pressure of 1.4×10^{-5} mbar, after which the working gases (Ar, N_2, CH_4) were injected into the chamber through a system of dedicated mass-flow controllers.

A distinctive feature of the developed PECVD system is the design of the upper RF electrode. It is a coaxial system with an integrated showerhead consisting of a series of holes of different diameters, which ensure uniform gas-flow distribution and laminar gas flow in the interelectrode space. The counter-electrode is grounded, similarly to the lower electrode, which promotes the formation of a bulk plasma between the electrodes and creates favorable conditions for the synthesis and confinement of nanoparticles within the plasma volume.

Because the area of the upper RF electrode is significantly smaller than the effective area of the grounded electrode (taking into account the metal walls of the vacuum chamber that are in contact with the plasma), a negative DC self-bias voltage (Vdc) developson the powered electrode due to the coupling capacitor (blocking capacitor) located in the matching box. Its formation is due to the higher mobility of electrons compared with ions, so that a negative self-bias potential appears at the electrode surface to equalize the electron and ion fluxes.

The self-bias voltage is one of the most sensitive diagnostic parameters of an RF discharge and is determined by the plasma conditions, such as discharge power, pressure, and the nature of the gas mixture. In addition, nanoparticle nucleation and growth are accompanied by changes in the free-electron concentration and charge redistribution in the plasma, which is directly reflected in the value of V_{dc}. Therefore, monitoring the evolution of the self-bias voltage during synthesis provides in situ information on the kinetics of nucleation, growth, and agglomeration of amorphous carbon nitride nanoparticles.

The self-bias voltage (DC self-bias voltage, V_{dc}) was recorded using a LeCroy PP006A high-frequency voltage probe (500 MHz bandwidth, 10:1 attenuation ratio) and a Siglent SDS5034X digital oscilloscope. A general view of the developed PECVD system and a photograph of it in operation are shown in Figure 2.

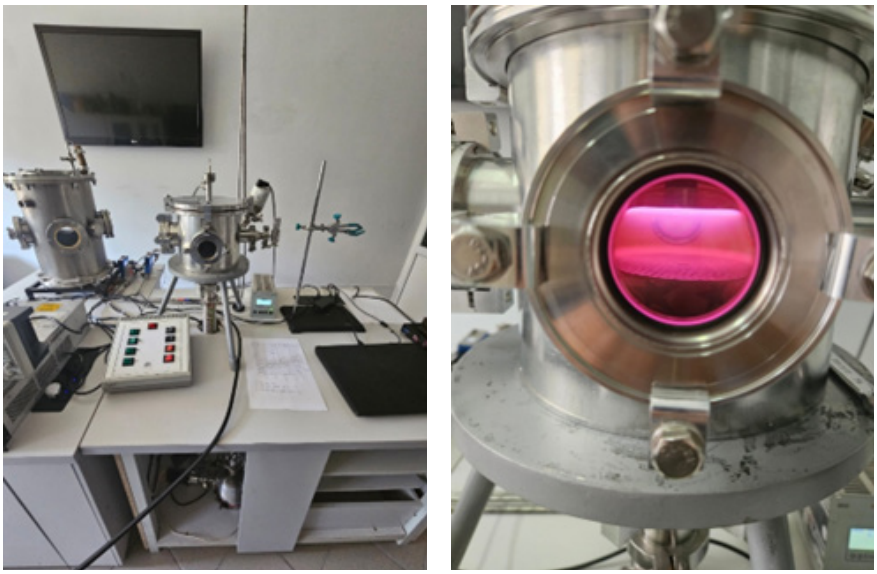


Figure 2 – General view of the PECVD system (left) and the system in operation (right)

Amorphous carbon nitride was synthesized by plasma-enhanced chemical vapor deposition (PECVD) in a nitrogen-methane plasma with pulsed RF-plasma modulation on a silicon substrate (single crystal Si (100), University Wafer, USA). The process was carried out at an RF discharge power of 20–40 W, a working pressure of 0.86–1.2 mbar, a constant nitrogen flow rate of 40 sccm, and a methane flow rate of 2–7 sccm. The modulation period was selected based on a study of the self-bias voltage evolution at different methane flow rates. After each experiment, the synthesized coatings were subjected to additional treatment in a nitrogen plasma for 10 min at an RF discharge power of 15 W. This treatment was performed to passivate surface dangling bonds, reduce the chemical reactivity of the surface, and decrease subsequent oxidation of the deposited layers in contact with the atmosphere.

The evolution of the self-bias voltage was recorded under continuous RF discharge burning in order to study the dynamics of V_{dc} during synthesis and to determine the optimal duration of plasma exposure ensuring the formation and growth of carbon nitride nanocrystals in the gas phase that will be collected on the substrate surface.

The PECVD synthesis products were deposited on silicon substrates (SiO_2). The surface morphology and elemental composition were studied by scanning electron microscopy (SEM, JSM-IT210, JEOL, Japan) with an energy-dispersive X-ray spectroscopy (EDS) system. The phase composition of the samples was determined by X-ray diffractometry (XRD, Rigaku MiniFlex 600, Rigaku, Japan), and the chemical structure and types of chemical bonds were analyzed by Fourier-transform infrared spectroscopy (FTIR, Bruker Alpha, Bruker, USA).

Results

As shown in Figure 3, immediately after plasma ignition a negative self-bias voltage of about –32 V develops at the RF electrode owing to the area asymmetry between the RF and grounded electrodes. Thereafter, the absolute value of V_{dc} gradually decreases, reflecting a change in the electron density of the plasma during nanoparticle nucleation and growth. The forming nanoparticles effectively attach electrons and get negatively charged, lowering the free-electron concentration in the plasma, which leads to a change in the self-bias potential [4, 5]. The decrease of the absolute value of V_{dc} indicates precisely the beginning of the agglomeration phase of the carbon-nitride nanocrystallites formed in the plasma gas phase [18].

An increase in the methane flow rate is accompanied by a decrease in the absolute value of Vdc and a marked reduction in the onset time of agglomeration of amorphous carbon nitride nanocrystallites. In particular, as the CH_4 flow rate is increased from 2 to 7 sccm, the agglomeration onset time decreases from 4.4 s to 200 ms, indicating faster formation and growth of carbon–nitrogen nanoparticles owing to the higher concentration of carbon-containing active radicals in the plasma.

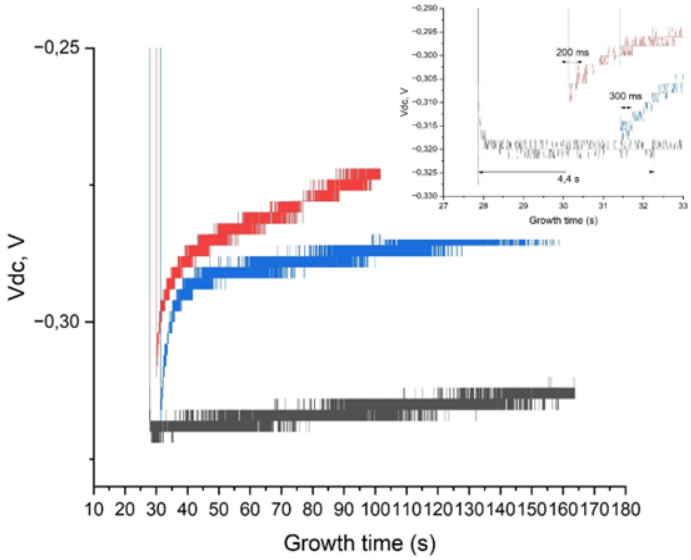


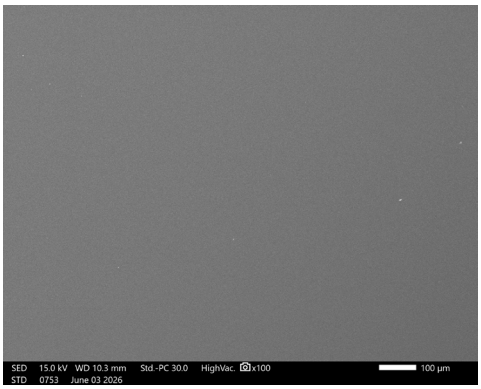
Figure 3 – Evolution of the self-bias voltage for the following plasma parameters: power 20 W, pressure 0.86 mbar, N_2 flow rate 40 sccm, CH_4 flow rate 2 (black), 5 (blue), and 7 (red) sccm. Remark: to record V_{dc} we used an attenuator between the low pass filter and the oscilloscope

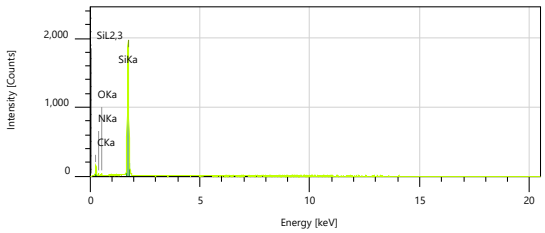
Further studies of the samples obtained during the formation of amorphous carbon nitride were carried out under pulsed RF-plasma modulation, in which the plasma duration was selected according to the nanoparticle agglomeration onset time (t_{agl}). Table 1 below shows the experimental parameters, where t_{plasma_on} is the RF plasma duration, t_{plasma_off} is the duration without RF plasma, during which the synthesized products deposit on the substrate surface.

Table 1 – RF plasma modulation parameters

Sample	Power, W	Pressure, mbar	Flow rate N_2, sccm	Flow rate CH_4, sccm	Plasma modulation, ms		Number of modulation cycles
					tplasma_on	tplasma_off	
№ 1	20	0.86	40	2	4 000	2 000	2 000
№ 2				5	300		
№ 3				7	200		

Figures 4–6 show the results of surface and structural characterization of the obtained samples by scanning electron microscopy (SEM), energy-dispersive X-ray spectroscopy (EDS), Fourier-transform infrared spectroscopy (FTIR), and X-ray diffraction (XRD). According to the SEM results, a continuous thin film with uniform morphology forms on the surface of all samples after PECVD synthesis. The elemental composition of sample No. 1, determined by EDS, includes carbon (52.7 at.%), nitrogen (16.2 at.%), oxygen (3.1 at.%), and silicon (≈28 at.%), whereas the elemental composition of samples No. 2 and No. 3 is dominated by silicon (up to 100 at.%), with carbon (51.2%), nitrogen (17.2%), oxygen (11.7%), and silicon (19.9%) detected locally. The high silicon content is due to the limited thickness of the deposited film, which allows the signal from the silicon substrate to be detected. The presence of oxygen is presumably related to the formation of a thin native oxide layer on the coating surface after contact with the atmosphere. These results indicate the deposition of a nitrogen-containing carbon film on the silicon substrate.





Element	Line	Mass%	Atom%
C	K	37.37±1.24	52.74±1.74
N	K	13.40±1.43	16.21±1.73
O	K	2.90±0.42	3.07±0.44
Si	K	46.34±0.79	27.97±0.48
Total		100.00	100.00

Figure 4 – SEM image of the morphology and chemical composition of the synthesized nitrogen-containing carbon film

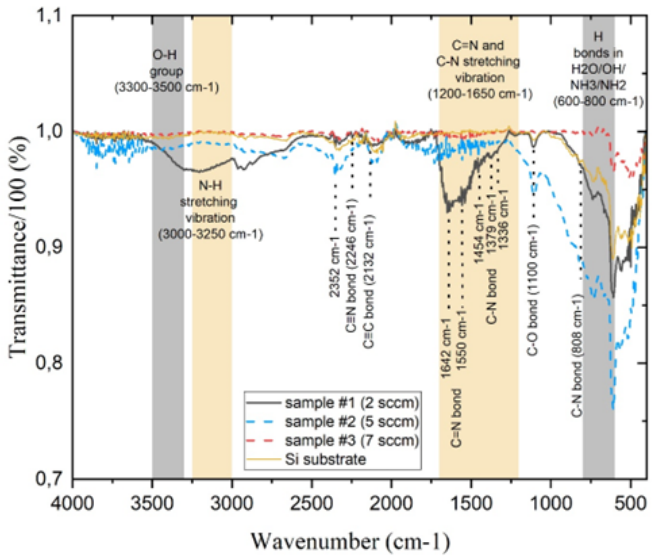


Figure 5 – FTIR spectrum of the synthesized nitrogen-containing carbon film

Figure 5 shows the FTIR spectra of the samples. In all studied samples (No. 1–No. 3), absorption bands characteristic of carbon–nitrogen compounds are observed, consistent with literature data for amorphous carbon nitride (a-C_xN_y) and polymeric C_3N_4.

The most pronounced absorption bands are observed for sample No. 1. A broad band in the 3000–3250 cm^{-1} range corresponds to N–H stretching vibrations, while the broader 3000–3500 cm^{-1} region may be associated with vibrations of N–H groups involved in hydrogen bonding, as well as with O–H groups arising from water adsorption on the coating surface [6–7].

The absorption bands at 1642 and 1550 cm^{-1} correspond to C=N stretching vibrations, while the peak at 1336 cm^{-1} can be assigned to C–N stretching vibrations linking triazine fragments with N–H groups. The bands at 1454 and 1379 cm^{-1} are also characteristic of C–N stretching vibrations in triazine rings [7–9].

Of particular interest is a weak band near 808 cm^{-1}, observed against the background of a broad band in the 500–1000 cm^{-1} range. According to the literature, this band corresponds to the breathing vibration of tri-s-triazine (heptazine) structural units, a characteristic feature of polymeric carbon nitride [10–11]. The broad band in the 600–800 cm^{-1} region may be attributed to vibrations of bonds associated with H_2O, O–H, NH_3, and NH_2 groups.

The absorption band at 2354 cm^{-1} may be related to the presence of quaternary nitrogen or adsorbed CO_2 [12], while the peak near 1100 cm^{-1} is probably due to C–O stretching vibrations.

Overall, the FTIR results indicate the formation of a nitrogen-containing carbon network dominated by C–N and C=N bonds. The set of identified absorption bands agrees with literature data for amorphous carbon nitride (a-CN_x) and suggests the possible presence of individual structural fragments of polymeric C_3N_4, in good agreement with the X-ray diffraction results (Figure 6).

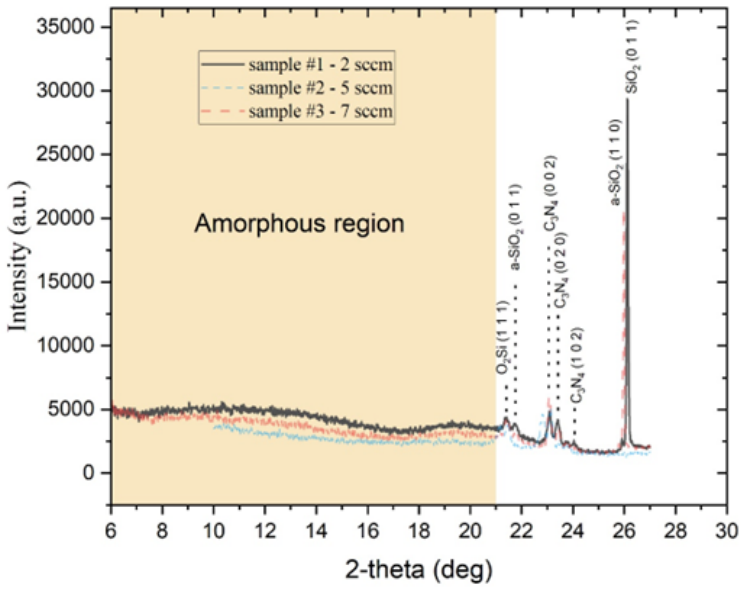


Figure 6 – XRD of synthesized a-C_3N_4 film

Figure 6 shows the X-ray diffraction results for the synthesized samples, obtained by powder X-ray diffraction over the angular range . The most intense diffraction peaks are observed for sample No. 1 and can be assigned to the C_3N_4 phase at, [13–14] and , as well as to the amorphous/crystalline SiO_2 phase at , and around . A broad diffraction maximum, characteristic of the amorphous structure of the synthesized material, is observed in the small-angle region ().

Discussion

The overall set of results obtained allows us to propose a coherent picture of the mechanism of amorphous carbon nitride (a-CNx) formation in the RF discharge plasma and to relate it to the evolution of the self-bias voltage V_{dc}.

According to the data on the temporal evolution of V_{dc} (Figure 3), a characteristic decrease in the absolute value of the self-bias voltage is observed after discharge ignition, reflecting a change in the balance of charged particles in the plasma due to nanoparticle nucleation and growth. This behavior is consistent with the three-stage model of dust-particle formation in low-temperature plasma proposed for an argon–silane discharge [4]: (i) rapid formation of nuclei – near-nanometer-sized clusters formed via chain ion–molecular reactions; (ii) coagulation of nuclei into larger agglomerates, accompanied by a sharp decrease in the free-electron concentration and, correspondingly, a change in Vdc; (iii) further particle growth via surface deposition of radicals once the acquired negative charge by the particles becomes important to stop the particle-particle agglomeration. The applicability of this model to a plasma containing carbon- and nitrogen-bearing precursors (CH_4/N_2) is confirmed by the results of V_{dc} monitoring for carbon nanoparticles under similar RF discharge conditions [5], where it was shown that the onset of particle agglomeration can be reliably identified from a characteristic kink in the $V_{dc}(t)$ curve, and that its position is sensitive to the plasma composition and parameters.

In the present work, increasing the CH_4 flow rate from 2 to 7 sccm was accompanied by a reduction in the agglomeration onset time from 4.4 s to 200 ms. This can be explained by the increased concentration of carbon-containing active species (radicals and ions) in the plasma, which increases the collision frequency and the rate of carbon–nitrogen cluster nucleation, and also accelerates the depletion of the electron component of the plasma responsible for Vdc formation [4-5]. The approach used – determining the agglomeration onset time from the Vdc evolution and then selecting the plasma-on pulse duration (t_plasma_on) for each CH_4 flow rate (Table 1) – allows the nanoparticle growth to be controllably limited at the stage preceding the agglomeration phase, yielding coatings with a more uniform morphology, as confirmed by the SEM data (Figure 4).

The EDS results indicate the formation of a carbon–nitrogen film with a C:N ratio more characteristic of nonstoichiometric amorphous carbon nitride (a-C_xN_y) in which are embedded stoichiometric C_3N_4 nanocrystallites. The presence of oxygen (3–12 at.%) in all samples is presumably related to post-growth surface oxidation upon contact with the atmosphere rather than to oxygen incorporation into the film bulk during synthesis, since after deposition the samples were additionally treated in a nitrogen plasma to passivate dangling bonds.

The FTIR data (Figure 5) confirm the formation of a carbon–nitrogen network dominated by C=N and C–N bonds, as well as the presence of the breathing vibration of tri-s-triazine (heptazine) structural units near ~808 cm^{-1} [10, 11]. Together with the bands at 1642, 1550, 1454, and 1379 cm^{-1}, assigned to triazine/heptazine ring vibrations [7–9], this points to a structural resemblance of the synthesized material to polymeric (melon- or heptazine-like) forms of carbon nitride rather than to a fully condensed crystalline C_3N_4 phase. The broad N–H and O–H bands in the 3000–3500 cm^{-1} region indicate a high degree of network disorder, the presence of terminal amino groups, and adsorbed water, typical of materials obtained by PECVD at relatively low temperatures, in contrast to high-temperature solid-state carbon nitride systems [6].

The XRD data (Figure 6) are generally consistent with this picture: the broad diffuse maximum in the small-angle region (2θ = 6–21°) reflects the predominantly amorphous structure of the film, whereas the weak peaks near $2\theta \approx$ 23–24° may be related to local ordering of carbon–nitrogen nanocrystallites. It should be noted that for graphite-like and β-C_3N_4 the characteristic (100) and (002)/(110) reflections are usually reported near $2\theta \approx$ 13° and 27–28° [13, 14], whereas the peaks observed in this work at 23–24° occupy an intermediate position; this may indicate a transitional (C_2N [15], CN [16], C_2N_3 [17]), structurally disordered phase with a shortened ordering period,

rather than a fully formed C_3N_4 crystal lattice. The presence of SiO_2 peaks ($2\theta \approx 21.4°$, 21.7°, and around 26°) is expected, since the film was synthesized on a silicon substrate with a native oxide layer, and part of the XRD signal, like the EDS signal, originates from the substrate owing to the small coating thickness.

Taken together, the SEM, EDS, FTIR, and XRD data indicate that varying the CH_4 flow rate, and the associated reduction in agglomeration time, governs not only the growth kinetics but also the final chemical structure of the synthesized material: sample No. 1 (lowest CH_4 flow rate, longest time to agglomeration) shows the most pronounced and structurally ordered FTIR bands and the most intense XRD reflections, whereas samples No. 2 and No. 3 (higher CH_4 flow rates, faster agglomeration) are characterized by a substantially smaller film thickness. This is consistent with the notion that, at high methane flow rates, rapid nucleation and coagulation of particles in the plasma bulk compete with heterogeneous deposition on the substrate, limiting the formation of a dense continuous film – an effect analogous to that described for dust particles in argon–silane and hydrocarbon plasmas [4, 5]. For example, for sample No. 1 the total synthesis time was ~2.2 h ($4s \cdot 2\,000\ cycles = 8\,000\ s$), whereas for samples No. 2 and No. 3 it was 10 min ($300\ ms \cdot 2\,000\ cycles = 600\ s$) and ~6.7 min ($200\ ms \cdot 2\,000\ cycles = 400\ s$) respectively, which fully accounts for the EDS, FTIR and XRD.

Below is a table with the results of the agglomeration onset time measurements at other RF discharge power and gas pressure values.

Table 2 – Nanoparticle agglomeration onset time (t_{agl}), determined from the evolution of the self-bias voltage V_{dc}, as a function of pressure, CH_4 flow rate, and RF discharge power (N_2 = 40 sccm)

Pressure, mbar	N_2, sccm	CH_4, sccm	t_{agl}, ms (20 W)	t_{agl}, ms (30 W)	t_{agl}, ms (40 W)
0.86	40	2	4 000	820	930
		5	300	330	500
		7	200	430	760
1		2	340	320	390
		5	360	180	350
		7	270	110	270
1.2		2	390	250	310
		5	420	170	190
		7	250	190	210

Additional measurements of t_{agl} over a wider range of pressures (0.86–1.2 mbar) and RF discharge powers (20–40 W) at a constant N_2 flow rate (40 sccm) refine the picture obtained at 0.86 mbar (Table 2). Pressure turns out to be the dominant parameter at the lowest power (20 W): already upon going from 0.86 to 1 mbar (CH_4 = 2 sccm) t_{agl} decreases by almost one order of magnitude (4000 → 340 ms), whereas a further pressure increase to 1.2 mbar changes it much less (340 → 390 ms), indicating that the nucleation process approaches saturation as the collision frequency in the plasma increases. The dependence of t_{agl} on RF discharge power, in contrast, is non-monotonic: at 0.86 mbar, increasing the power from 20 to 40 W lengthens the agglomeration onset time (for example, from 200 to 760 ms at CH_4 = 7 sccm), whereas at 1 and 1.2 mbar the minimum of t_{agl} shifts toward 30 W, followed by an increase at 40 W. This behavior can be explained by the competition between two effects of increasing power: an increase in the concentration of active carbon- and nitrogen-containing radicals, which accelerates cluster nucleation, and a simultaneous increase in gas heating and ion bombardment of the growing particles, which slows their agglomeration – an effect consistent with the independently established slowdown of nanoparticle nucleation with increasing gas temperature in RF plasma [5]. The most pronounced and monotonic sensitivity of t_{agl} to the CH_4 flow rate (an

almost twentyfold range of values) is observed precisely at 0.86 mbar and 20 W, whereas at higher pressure and power this sensitivity decreases substantially. This explains the choice of the 0.86 mbar and 20 W regime for the subsequent synthesis of the samples (Table 1): under these conditions the agglomeration onset time is most predictably governed by the methane flow rate, providing the most precise control over the pulse duration t_{plasma_on} during pulsed plasma modulation.

Conclusion

This work investigated the growth of nanostructured carbon nitride (a-C_xN_y) thin layers in an RF discharge plasma by PECVD, using the evolution of the self-bias voltage V_{dc} as an in situ diagnostic parameter. It is shown that the absolute value of V_{dc} decreases monotonically as the nanoparticles nucleate and grow in the plasma gas phase, and that the onset of their agglomeration can be reliably identified from a characteristic change in the $V_{dc}(t)$ curve, consistent with the three-stage model of dust-particle formation in low-temperature plasma.

It was found that the agglomeration onset time t_{agl} is sensitive to the plasma composition and parameters: under baseline conditions (0.86 mbar, 20 W), increasing the CH_4 flow rate from 2 to 7 sccm reduces t_{agl} from 4.4 s to 200 ms. Extended measurements over the 0.86–1.2 mbar pressure range and 20–40 W RF power range showed that pressure is the dominant parameter at low power, whereas the dependence of t_{agl} on power is non-monotonic, with a minimum near 30 W at elevated pressure. The largest and most predictable sensitivity of t_{agl} to the CH_4 flow rate is observed precisely at 0.86 mbar and 20 W, which justifies the choice of this regime for the subsequent synthesis of samples with pulsed plasma modulation, in which the plasma duration was set according to the established agglomeration onset time.

The coatings obtained under pulsed modulation are continuous thin films of nitrogen-containing carbon. According to the EDS, FTIR, and XRD data, the synthesized material corresponds to nonstoichiometric amorphous carbon nitride (a-C_xN_y) dominated by C-N and C=N bonds, in which are embedded features of tri-s-triazine (heptazine) structural fragments characteristic of polymeric forms of carbon nitride; the prominence of these features decreases systematically going from sample No. 1 (lowest CH_4 flow rate, longest time to agglomeration) to samples No. 2 and No. 3.

Thus, monitoring the evolution of the self-bias voltage is an effective and accessible method for the in situ control of the nucleation, growth, and agglomeration kinetics of a-C_xN_y nanoparticles directly during PECVD synthesis and can be used for the precise control of the thickness, morphology, and chemical structure of the resulting nitrogen-containing carbon coatings through the choice of pulsed plasma modulation parameters.

Acknowledgements

The study was carried out with the financial support of the Ministry of Science and Higher Education of the Republic of Kazakhstan (grant No AP26101409).

REFERENCES

1 Aono M., Kikuchi S., Kitazawa N., Watanabe Y. Change in surface states of amorphous carbon nitride films after exposure to oxygen plasma. Materials Science Forum. 638–642, 818–823 (2010). https://doi.org/10.4028/www.scientific.net/MSF.638-642.818

2 Mohamed S.H., El-Hossary F.M., Gamal G.A., Kahlid M.M. Optical properties of plasma deposited amorphous carbon nitride films on polymer substrates. Physica B: Physica B. 405, 254–257 (2010). https://doi.org/ 10.1016/j.physb.2009.08.069

3 Xu Q., Zheng Y., Wang S., Fu Q., Guo X., Li Y., Ren J., Cao Z., Li R., Zhao L., Huang Y. Plasma synthesis of K-doped amorphous carbon nitride with passivated trap states for enhanced photocatalytic H_2O_2 production. Journal of Alloys and Compounds. 947, 169663 (2023). https://doi.org/10.1016/j.jallcom.2023.169663.

4 Bouchoule A., Boufendi L. Particle nucleation and growth in a low-pressure argon-silane discharge. Journal Plasma Sources Science and Technology. 3, 262, (1994). https://doi.org/10.1088/0963-0252/3/3/004.

5 Orazbayev S.A., Henault M., et all. Influence of Gas Temperature on Nucleation and Growth of Dust Nanoparticles in RF Plasma. IEEE Transactions on Plasma Science. 47 (7), 3069–3073 (2019). https://doi.org/10.1109/TPS.2019.2912805.

6 Guo, X., Duan, J., Li, C., Zhang, Z. & Wang, W. Highly efficient Z-scheme gC3N4/ZnO photocatalysts constructed by co-melting-recrystallizing mixed precursors for wastewater treatment. J. Mater. Sci. 55, 2018–2031 (2020). https://doi.org/10.1007/s10853-019-04097-0

7 Yang, X., Tang, B., Wu, T. & Cao, X. g-C3N4/TiO2 composite photocatalyst and its application to asphalt for NO removal. J. Mater. Civ. Eng. 31, 04019141 (2019). https://doi.org/10.1061/%28ASCE%29MT.1943-5533.0002763

8 Li, X. et al. Synergistic effect of efficient adsorption g-C3N4/ZnO composite for photocatalytic property. J. Phys. Chem. Solids 75, 441–446 (2014). https://doi.org/10.1016/j.jpcs.2013.12.001

9 Ghafuri, H., Tajik, Z., Ghanbari, N. et al. Preparation and characterization of graphitic carbon nitride-supported l-arginine as a highly efficient and recyclable catalyst for the one-pot synthesis of condensation reactions. Sci Rep 11, 19792 (2021). https://doi.org/10.1038/s41598-021-97360-x

10 Rashidizadeh, A., Ghafuri, H., Esmaili Zand, H. R. & Goodarzi, N. Graphitic carbon nitride nanosheets covalently functionalized with biocompatible vitamin B1: synthesis, characterization, and its superior performance for synthesis of quinoxalines. ACS Omega 4(7), 12544–12554 (2019). https://doi.org/10.1021/acsomega.9b01635

11 Saravanan V., Lakshmanan P., Ramalingan C., Appl Organomet Chem 2023, 37(10), e7215. https://doi.org/10.1002/aoc.7215

12 Shcherban N.D., et. all. Melamine-derived graphitic carbon nitride as a new effective metal-free catalyst for Knoevenagel condensation of benzaldehyde with ethylcyanoacetate. Catal. Sci. Technol. (2018) 8 (11): 2928–2937. https://doi.org/10.1039/c8cy00253c

13 Thomas A., Fischer A., et. all. Graphitic carbon nitride materials: variation of structure and morphology and their use as metal-free catalysts. J. Mater. Chem., 2008, 18, 4893–4908. https://doi.org/10.1039/b800274f

14 Elamin, M.R.; Elamin, N.Y.; Ibrahim, T.G.; et. all. Facile Synthesis of β-C3N4 and Its Novel MnTeO3 Nanohybrids for Remediating Water Contaminated by Pharmaceuticals. Processes 2025, 13, 2357. https://doi.org/10.3390/pr13082357

15 Drueck U. and Kutoglu A. Experimental difference densities of hexacyanobenzene at 120 k. refinement of electron density distributions with charge-cloud models. Zeitschrift fuer Kristallographie (1979-2010), 166:233–244, 1984. https://doi.org/10.1524/zkri.1984.166.3-4.233

16 Parkes A.S. and Hughes R.E. The crystal structure of cyanogen. Acta Crystallographica. (1963). 16, 734–736. https://doi.org/10.1107/S0365110X63001924

17 A. Salamat, K. Woodhead, P.F. McMillan, R. Quesada Cabrera, A. Rahman, D. Adriaens, and F. Cora. Tetrahedrally bonded dense c2 n3 h with a defective wurtzite structure: x-ray diffraction and raman scattering results at high pressure and ambient conditions. Phys. Rev. B (2009), 80, 104106. https://doi.org/10.1103/PhysRevB.80.104106

18 Boufendi L., Gaudin J., Huet S., Viera G., Dudemaine M. Detection of particles of less than 5 nm in diameter formed in an argon–silane PECVD plasma. Applied Physics Letters. 79, 4301 (2001). https://doi.org/10.1063/1.1425431

[1*]Батрышев Д.Г.,
PhD, қауымдастырылған профессор, ORCID ID: 0000-0002-9847-1067,
*e-mail: d.batryshev@kbtu.kz
[1, †]Әбдірахманов А.Р.,
PhD, қауымдастырылған профессор, ORCID ID: 0000-0001-6652-1923,
e-mail: abdirakhmanov@physics.kz
[2]Буфенди Л.,
PhD, профессор, ORCID ID: 0000-0002-6995-0368,
e-mail: laifa.boufendi@physics.kz
[1,2]Оразбаев С.А.,
PhD, қауымдастырылған профессор, ORCID ID: 0000-0002-7286-9990,
e-mail: sagi.orazbayev@gmail.com
[1,2]Байқалиев А.,
докторант, МНС, ORCID ID: 0009-0000-5616-7131,
e-mail: akdauletbai@gmail.com
[1,2]Рамазанов Т.С.,
ф.-м.ғ.д., профессор, ORCID ID: 0000-0001-7172-8005,
e-mail: ramazan@physics.kz

[1]Қазақстан-Британ техникалық университеті, Алматы қ., Қазақстан
[2]Әл-Фараби атындағы Қазақ ұлттық университеті, Алматы қ., Қазақстан
†Қазіргі мекенжайы: Монс университеті, Монс қ., Бельгия

АЗОТ–МЕТАН ГАЗ ҚОСПАСЫНЫҢ РАДИОЖИІЛІКТІ ПЛАЗМАСЫНДА КӨМІРТЕК НИТРИДІНІҢ НАНОҚҰРЫЛЫМДЫ ЖҰҚА ҚАБАТТАРЫНЫҢ ӨСУ ПРОЦЕСІН ЗЕРТТЕУ

Андатпа

Аморфты көміртек нитридінің (a-CN_x) жұқа қабықшалары плазманы импульстік модуляциялау режимін қолдана отырып, 13,56 МГц жиіліктегі азот-метан газ қоспасының радиожиілікті (РЖ) разряд плазмасында плазмамен белсендірілген химиялық бу фазасынан тұндыру (PECVD) әдісімен синтезделді. Тұрақты өздігінен ығысу кернеуінің (V_{dc}) динамикасы нанобөлшектердің нуклеациясын, өсуін және агломерациясын тікелей синтез үдерісі барысында бақылау үшін диагностикалық параметр ретінде тіркелді. Плазма тұтанғаннан кейін V_{dc} абсолюттік мәнінің монотонды түрде төмендейтіні анықталды. Нанобөлшектер агломерациясының басталуын $V_{dc}(t)$ тәуелділігінің сипатты өзгерісі бойынша анықтауға болады. Бұл нәтиже төмен температуралы плазмада тозаңды бөлшектерінің түзілуінің үш сатылы моделімен сәйкес келеді. Агломерацияның басталу уақыты (t_{agl}) метан шығынына, жұмыс қысымына және РЖ-разряд қуатына айтарлықтай тәуелді екені көрсетілді. Қалыпты жағдайларда (0,86 мбар, 20 Вт) CH_4 шығынын 2-ден 7 sccm-ге дейін арттыру t_{agl} мәнін 4,4 с-тан 200 мс-қа дейін қысқартады, ал қысым мен қуаттың әсері сәйкесінше басым және монотонды емес сипатқа ие. Алынған нәтижелер қабықшалардың бақыланатын өсуі кезінде плазманың қосылу импульсінің оңтайлы ұзақтығын таңдау үшін пайдаланылды. Импульстік модуляция режимінде тұндырылған үлгілер SEM, EDS, FTIR және XRD әдістерімен зерттелді. Зерттеу нәтижелері құрамында C–N және C=N байланыстары басым болатын тұтас стехиометриялық емес көміртек нитриді қабықшаларының түзілгенін растады. Алынған нәтижелер өздігінен ығысу кернеуін бақылау a-CN_x нанобөлшектерінің өсу кинетикасын тікелей синтез үдерісі барысында қадағалаудың тиімді әрі қолжетімді әдісі екенін көрсетеді. Сонымен қатар, импульстік РЖ-плазма параметрлерін өзгерту арқылы қабықшалардың өсуін, морфологиясын және химиялық құрылымын басқаруға мүмкіндік береді.

Түйін сөздер: аморфты көміртек нитриді, PECVD синтезі, радиожиілікті плазма, тұрақты өздігінен ығысу кернеуі (DC self-bias), өсу механизмі.

[1*]Батрышев Д.Г.
PhD, ассоциированный профессор, ORCID ID: 0000-0002-9847-1067,
*e-mail: d.batryshev@kbtu.kz
[1, †]Әбдірахманов А.Р.
PhD, ассоциированный профессор, ORCID ID: 0000-0001-6652-1923,
e-mail: abdirakhmanov@physics.kz
[2]Буфенди Л.
PhD, профессор, ORCID ID: 0000-0002-6995-0368,
e-mail: laifa.boufendi@physics.kz
[1,2]Оразбаев С.А.
PhD, ассоциированный профессор, ORCID ID: 0000-0002-7286-9990,
e-mail: sagi.orazbayev@gmail.com
[1,2]Байқалиев А.,
PhD студент, МНС, ORCID ID: 0009-0000-5616-7131,
e-mail: akdauletbai@gmail.com
[1,2]Рамазанов Т.С.,
д.ф.-м.н., профессор, ORCID ID: 0000-0001-7172-8005,
e-mail: ramazan@physics.kz

[1]Казахстанско-Британский технический университет, г. Алматы, Казахстан
[2]Казахский национальный университет им. аль-Фараби, г. Алматы, Казахстан
[†]Текущий адрес: Университет Монса, г. Монс, Бельгия

ИССЛЕДОВАНИЕ ПРОЦЕССА РОСТА НАНОСТРУКТУРИРОВАННЫХ ТОНКИХ СЛОЕВ НИТРИДА УГЛЕРОДА В РАДИОЧАСТОТНОЙ ПЛАЗМЕ ГАЗОВОЙ СМЕСИ АЗОТ-МЕТАН

Аннотация

Аморфные тонкие пленки нитрида углерода (a-CN_x) были синтезированы методом плазменно-активированного химического осаждения из газовой фазы (PECVD) в радиочастотной (РЧ) разрядной плазме азотно-метановой газовой смеси при частоте 13,56 МГц с использованием импульсной модуляции плазмы. Динамика постоянного напряжения автосмещения (V_{dc}) регистрировалась в качестве диагностического параметра непосредственно в процессе синтеза для мониторинга зародышеобразования, роста и агломерации наночастиц. Установлено, что после зажигания плазмы абсолютное значение V_{dc} монотонно уменьшается, а начало агломерации наночастиц может быть достоверно определено по характерному изменению зависимости $V_{dc}(t)$, что согласуется с трехстадийной моделью формирования пылевых частиц в низкотемпературной плазме. Показано, что время начала агломерации (t_{agl}) существенно зависит от расхода метана, рабочего давления и мощности ВЧ-разряда: при базовых условиях (0,86 мбар, 20 Вт) увеличение расхода CH_4 с 2 до 7 sccm сокращает t_{agl} с 4,4 с до 200 мс, тогда как влияние давления и мощности характеризуется соответственно доминирующим и немонотонным характером. Полученные результаты использованы для выбора продолжительности импульсов включения плазмы при контролируемом росте пленок. Образцы, осажденные в режиме импульсной модуляции, исследованы методами SEM, EDS, FTIR и XRD, что подтвердило формирование сплошных нестехиометрических пленок нитрида углерода с преобладанием связей C–N и C=N. Полученные результаты показывают, что мониторинг напряжения автосмещения является эффективным и доступным методом контроля кинетики роста наночастиц a-CN_x непосредственно в процессе синтеза, а также позволяет регулировать рост, морфологию и химическую структуру пленок посредством параметров импульсной ВЧ-плазмы.

Ключевые слова: аморфный нитрид углерода, PECVD синтез, радиочастотная плазма, DC самосмещения, механизм роста.

UDC 520.88
IRSTI 41.51.41

https://doi.org/10.55452/1998-6688-2026-23-3-461-472

[1,2]Gluchshenko A.,
MSc, ORCID ID: 0000-0002-0738-7725,
e-mail: gluchshenko@fai.kz
[1]Izmailova I.,
MSc, ORCID ID: 0000-0001-9878-0989,
e-mail: izmailova@fai.kz
[1,3]Umirbayeva A.,
MSc, ORCID ID: 0000-0001-9339-4990,
e-mail: umirbayeva@fai.kz
[1,2]Kuvatova D.,
MSc, ORCID ID: 0000-0002-5937-4985,
e-mail: kuvatova@fai.kz
[1]Yurin D.,
PhD, ORCID ID: 0000-0002-5604-9757,
e-mail: yurin@fai.kz

[1]Fesenkov Astrophysical Institute, Almaty, Kazakhstan
[2]Farabi University, Almaty, Kazakhstan
[3]Nazarbayev University, Astana, Kazakhstan

AUTOMATED WAVELENGTH CALIBRATION OF ASTRONOMICAL SPECTRA WITH DTW-RANSAC MATCHING AND CNN-BASED PREPROCESSING

Abstract

This paper presents an automated pipeline for wavelength calibration of slit-based astronomical spectra, combining robust peak-matching techniques with a lightweight preprocessing step. The method is based on initial peak alignment using Dynamic Time Warping (DTW), followed by refinement of the dispersion solution with the Random Sample Consensus (RANSAC) algorithm. To ensure consistency between observed and reference spectra, a compact one-dimensional convolutional neural network (CNN) is employed at the preprocessing stage to identify the spectral range and corresponding diffraction grating. This step enables the selection of an appropriate reference spectrum but does not directly affect the calibration procedure. The DTW-based approach provides reliable initial correspondences between spectral peaks under nonlinear distortions and noise, while RANSAC filtering removes incorrect matches and yields a robust polynomial dispersion solution. The method is validated on real observational data from calibration lamps and demonstrates stable performance, high matching accuracy, and full automation capability. Compared to traditional manual or semi-automatic approaches, the proposed pipeline significantly reduces processing time while maintaining calibration precision. The developed solution is planned to be deployed as a service in the virtual observatory infrastructure and is applicable for processing numerous spectral data.

Keywords: astronomical data processing, slit-based spectral calibration, dynamic time warping, RANSAC, machine learning.

Received May 15, 2026; revised August 27, 2026; accepted August 28, 2026.

Introduction

Spectral studies play a fundamental role in modern astrophysics, as it is spectroscopy that enables us to determine the chemical composition, physical parameters, kinematics, and evolutionary state of astronomical objects. With the development of virtual observatories, there is a growing need for

automated methods of processing spectroscopic data. The Fesenkov Astrophysical Institute (FAI) holds a significant volume of raw observational data, including both contemporary and archived material. This makes the development of methods ensuring consistent and reliable spectral reduction particularly relevant. In particular, the automation of wavelength calibration represents an important task, linked both to improving the efficiency of processing new observations and to the possibility of re-analysing previously accumulated data.

Despite its importance, the practical implementation of these tasks faces significant operational hurdles. Traditional reduction methods (e.g., within the IRAF environment) create a critical bottleneck: during a typical monthly observing cycle at the AZT-20 telescope, which yields approximately 40 raw frames (with about 10 requiring precise calibration), manual processing takes roughly 15 minutes per frame. Cumulatively, data preparation for even a single instrument consumes substantial expert time that could otherwise be dedicated to physical interpretation. Given the extensive data archives and the planned expansion of the telescope network at the Academician T.B. Omarov Assy-Turgen Observatory (ATO), the total data volume is projected to increase severalfold. Such scaling renders manual intervention fundamentally unscalable.

Wavelength calibration ensures the conversion of detector pixel coordinates into a physical wavelength scale, typically based on identifying emission lines from calibration lamps and approximating a dispersion solution. However, manual line matching remains a labour-intensive and error-prone process, especially in the presence of noise, incomplete line sets, or nonlinear distortions of the wavelength scale. To automate calibration, template matching and cross-correlation methods are widely used in modern spectroscopic surveys [1, 2]. Nevertheless, fully automated calibration remains challenging, particularly under realistic observational conditions where distortions and noise can significantly affect the matching of spectral features. For example, the IRAF package [3] provides automated modes, but initial setup and quality control still frequently require observer intervention, particularly in cases of low signal-to-noise ratio or complex dispersive distortions. While machine learning has been explored for spectral classification and parameter estimation [4–10], the core calibration procedure still largely relies on establishing manual correspondences to ensure a stable solution.

Recent work has demonstrated the applicability of DTW to automated spectroscopic wavelength calibration. Davenport et al. [11] used DTW for first-pass alignment between observed and reference spectra, followed by refinement using conventional emission-line fitting. In contrast, in the present work DTW is used to generate candidate peak correspondences based on local spectral similarity, which are subsequently filtered using RANSAC to obtain a robust polynomial dispersion solution.

In this work, we develop an automated pipeline for wavelength calibration that addresses these limitations. The method is based on a convolutional neural network (CNN) [12], which is used at the preprocessing stage to determine the spectral range, followed by two sequential methods: initial alignment using the Dynamic Time Warping (DTW) algorithm [11, 13] and subsequent refinement using the Random Sample Consensus (RANSAC) algorithm [14].

Materials and methods

Data Description and Automatic Determination of Spectral Range

The observational data used to develop and test our algorithm (https://github.com/fai-kz/ransac_wv_calib) were primarily acquired with the AZT-20 telescope at FAI's ATO, which provides the main source of slit spectroscopic observations. The data were obtained using a He-Ne-Ar calibration lamp in the H_α, H_β, and combined H_α/H_β spectral ranges. The proposed pipeline uses a user-provided, previously wavelength-calibrated spectrum as the reference. In the present implementation, the reference spectrum used for testing was calibrated with IRAF. Depending on the wavelength coverage, diffraction gratings with line densities of 360 lines/mm for the combined H_α/H_β range, 1800 lines/mm for H_α, and 2400 lines/mm for H_β were used. To improve the robustness of the method and extend the coverage of input conditions, the dataset was supplemented with synthetic spectra.

The first step in processing a spectral frame is the automatic identification of the type of diffraction grating used to obtain the spectrum. This information is required to correctly define the operating wavelength range and select the parameters for further calibration. To automate this procedure, a neural model has been developed in the form of a one-dimensional CNN. Given the frequent absence of wavelength range in FITS headers, CNN-based approach reconstructs the observational context directly from the raw data, automatically identifying the grating configuration through spectral morphology to select the appropriate calibration template.

The network architecture consists of three convolutional layers with decreasing kernel sizes (50, 30 and 14) and an increasing number of channels (8, 16 and 32), allowing both global and local spectral features to be extracted. Batch normalisation is applied after each convolution, and non-linearity is introduced using the ReLU activation function [15]. The extracted features are then passed to a fully connected layer that outputs class probabilities for the corresponding grating type.

The model was trained using synthetic spectra generated from real observational data. Synthetic samples were produced by applying inverse polynomial calibration to pre-calibrated spectra, with random variation of the calibration coefficients under the constraint of a positive derivative over the calibration interval. Gaussian noise was added to improve robustness. Approximately 5,000 synthetically generated spectra across the three classes (360, 1800, and 2400 lines/mm) were used for training. The synthetic spectra for each class were generated using one representative observational frame obtained with the corresponding grating configuration; these observational frames were not included in the training dataset. The dataset was divided into training, validation, and test subsets in proportions of 70%, 15%, and 15%, respectively. Training and data generation were implemented using PyTorch, with parallelisation of synthetic data generation via mpi4py [16], enabling efficient preparation of large training sets. The model was trained for 100 epochs with a batch size of 32 using the Adam optimiser [17] and cross-entropy loss. The initial learning rate was set to 0.001 and varied during training. Dropout regularisation with a rate of 0.3 was applied to reduce overfitting [18]. The input to the network consisted of a single-channel spectrum of 1024 samples. The CNN comprised three convolutional layers with 8, 16, and 32 output channels, kernel sizes of 50, 30, and 14, and padding values of 25, 15, and 7, respectively. Each convolutional layer was followed by batch normalisation and a ReLU activation. The final linear layer mapped the resulting (32x128) features to the three output classes.

The CNN is used exclusively at the preprocessing stage to determine the spectral range, after which the calibration proceeds using peak matching and model fitting methods. As shown in Figure 1, the network achieves high classification accuracy in distinguishing among the three grating configurations.

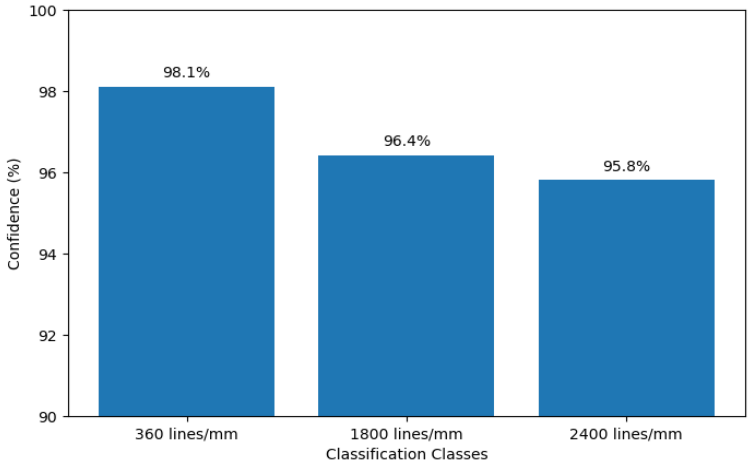


Figure 1 – Neural network classification accuracy across 3 classes

Initial Peak Matching Using DTW-RANSAC

Spectral calibration aims to establish a relationship between the coordinates of the detector pixels and the physical wavelength values. To achieve this, the spectrum of the calibration lamp is compared with the reference spectrum of the corresponding source from a spectral atlas.

The alignment is performed by comparing the recorded spectrum of the lamp with a reference set of lines for that lamp (the so-called spectral atlas (https://noirlab.edu/science/data-services/other/spectral-atlas)). The traditional method is based on the use of reference lines – characteristic emission maxima that are clearly distinguishable in the spectrum. For each such line, a correspondence is determined between its position on the detector (in pixels) and the known wavelength from the atlas. The resulting set of corresponding points is used to construct a dispersion solution, which is approximated by a polynomial function:

$$\lambda(p) = \sum_{n=0}^{k} a^n p_n, \quad (1)$$

where λ is the wavelength, a^n is the coefficient of the n^{th} power, p_n is the pixel number, and k is the order of the polynomial used for the approximation. In automated data processing, the correct matching of spectral lines presents a non-trivial challenge. The algorithm must remain robust against various observational artefacts, including noise, missing real lines, the appearance of false maxima, significant non-linear distortions of the wavelength scale, and other effects. Nevertheless, when successfully implemented, automatic calibration significantly speeds up data processing and reduces the likelihood of human-induced errors.

In manual mode, aligning a single spectrum takes on average around fifteen minutes. In the same amount of time, an automated system is capable of aligning approximately 4 to 20 frames, depending on computational resources and the level of noise in the data. The efficiency of the method in terms of time can be assessed using Figure 2.

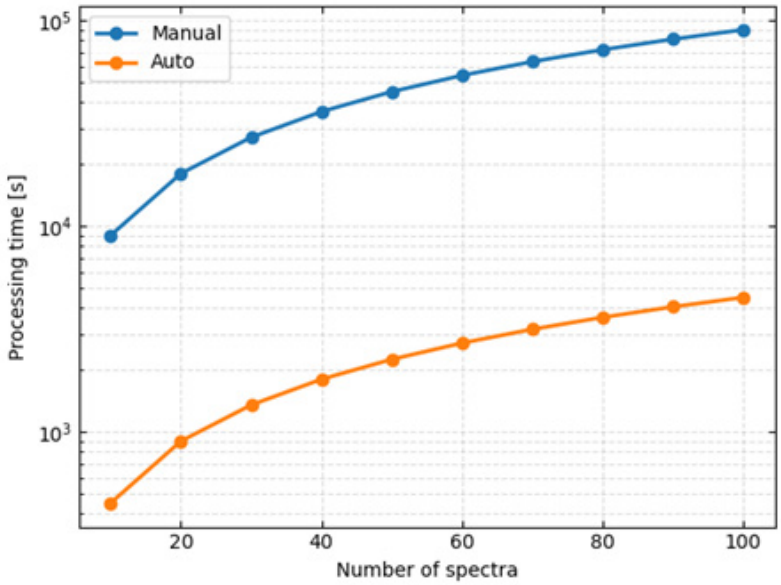


Figure 2 – Comparison of the time spent on processing spectra in the case of the traditional method and the proposed method

In the course of seeking solutions to improve alignment accuracy, it was found that the use of standard spectral atlases for calibration lamps is not always effective. The operational observation ranges are generally limited (e.g., ~6200-7000 Å for H_α, ~4600-5200 Å for H_β and ~3000-7700 Å for H_α/H_β), whereas atlases cover a much wider range (~3000-10600 Å). Furthermore, observational data differ significantly in terms of spectral resolution: their resolution is approximately 0.5-4.5 Å/pixel, depending on the grating used, whereas the atlases are presented at a high resolution of around ~0.02 Å.

Additional discrepancies arise due to observational effects – noise, overexposure and underexposure – as well as local non-linearities in the dispersion solution (compression and stretching of the wavelength scale). These factors exacerbate the discrepancy between the observed spectra and the atlas data. Consequently, the use of real, pre-calibrated observations proved to be a more effective basis for developing and testing the algorithm.

Let us introduce the following notation:

S is the spectrum to be calibrated, represented as a pixel-intensity function;

R is the spectrum used to calibrate spectrum S, represented as a "wavelength – intensity" relationship and treated as a reference spectrum;

P_S^m, P_R^m, where $n = 0, 1, \ldots, N$, $m = 0, 1, \ldots, M$ – peaks detected in spectra S and R, respectively;

Model is a polynomial of the form (1) that defines the dispersion solution and determines the calibration of spectrum S.

Before the algorithm begins, the spectra S and R are normalized to the dimensionless range [0,1] along both the abscissa (pixel/wavelength) and ordinate (intensity) axes. This normalization reduces the dynamic range of the data, improves the numerical stability of the algorithm, and decreases sensitivity to noise and variations in observational conditions.

Spectral peaks in the normalized spectra S and R are detected using `scipy.signal.find_peaks`. Peak detection is performed with a prominence threshold of 0.01 in normalized-intensity units, while the default SciPy values are used for the minimum peak height, width, separation, and other parameters.

Having the sets P_S^n, P_R^m, the next step is to establish correct correspondences between the peaks of spectra S and R, i.e., $\Pi^{nm} = (P_S^n, P_R^m)$, ensuring the accuracy of the subsequent calibration. For each peak P_S^n, the most probable match among the peaks P_R^m is determined by comparing their local neighborhoods. The similarity between the neighborhoods is evaluated using the DTW method applied to local windows centered at the corresponding peak positions. Each local window contains 45 pixels, and the DTW distance between the intensity sequences is calculated using the absolute-difference (L1) metric. The similarity between neighborhoods is evaluated using the DTW method on short windows centered at peak position, which returns a similarity score. The peak P_R^m, that maximizes this score is selected as the corresponding match. Thus, pairs $\Pi^{nm} = (P_S^n, P_R^m)$ are formed. Based on the identified correspondences, a polynomial approximation is constructed, defining the calibration function for spectrum S.

It should be noted that in the presence of closely spaced spectral lines, incorrect matches may occur, leading to a degradation in the accuracy of the dispersion solution (as shown in Figure 3. A related work [13] has demonstrated a calibration scheme in which DTW is used for first-pass spectral alignment, followed by refinement using traditional emission-line fitting.

In our case, DTW is used only as a similarity measure for generating candidate correspondences, which makes the resulting set of matches inherently noisy and prone to outliers. Therefore, not all correspondence pairs Π^{nm} are reliable, and an additional filtering stage is required to identify reliable matches. To address this task, the RANSAC algorithm is employed – an iterative probabilistic method for estimating model parameters in the presence of outliers in the data.

In this study, the algorithm is applied as follows:

1. A subset of (K=5) distinct correspondence pairs Π^{nm} is randomly selected without replacement from the DTW-generated candidate-pair list, and these correspondences are assumed to be correct;

2. Based on the selected pairs, a calibration model is constructed, which is then applied to the spectrum S;

3. The accuracy of the obtained model is then evaluated. As an error metric, the deviation between the wavelengths predicted by the model for the peaks of spectrum S and the wavelengths of the corresponding peaks in spectrum R is used:

$$\varepsilon_{nm} = |\lambda_{p^n{}_S} - \lambda_{p^m{}_R}|; \quad (2)$$

4. For each pair, the error tolerance condition is checked: if $\varepsilon_{nm} < \varepsilon_{max}$, the correspondence is considered valid;

5. If the number of valid correspondence pairs Π^{nm} at the current iteration exceeds that of the previous best result, the model is considered optimal and is retained.

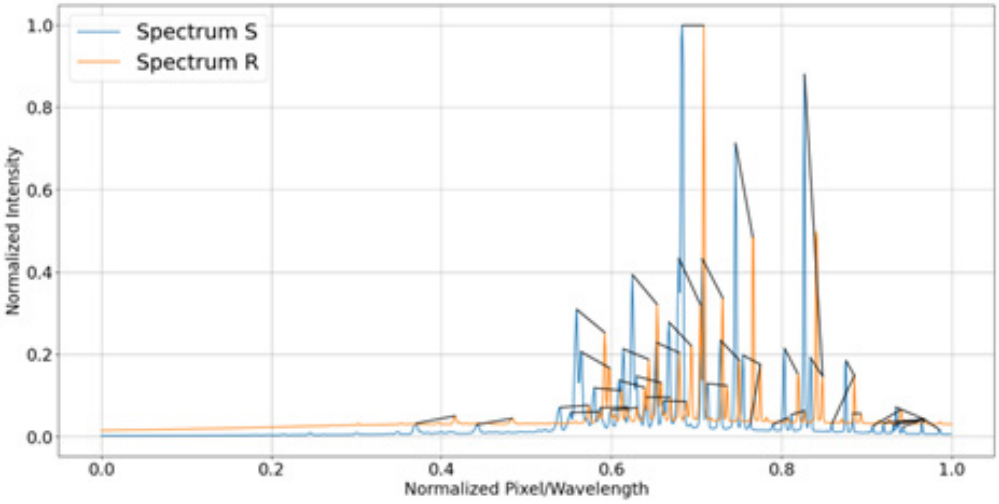


Figure 3 – Result of peak matching between
spectra R and S using the standalone DTW algorithm

The automated RANSAC procedure uses a fixed stopping criterion of 3,000 iterations. This fixed value was introduced to avoid the subjective manual determination of the point at which the number of inliers ceases to change substantially.

The use of RANSAC makes it possible to filter out incorrect pairs and retain only those peak correspondences that minimize the chosen error function and provide the highest calibration accuracy. Since the algorithm is stochastic, the optimal solution may be found either at early iterations or only after a large number of iterations. It is at the RANSAC stage that the final set of consistent correspondences between spectral peaks is formed.

Unlike legacy tools (e.g., the `IRAF reidentify` task) that necessitate a priori knowledge of the reference spectrum and manual initialization, the proposed DTW and RANSAC-based framework ensures complete calibration autonomy while exhibiting high robustness to non-linear distortions and stochastic noise.

As a final step, an inverse transformation from normalized coordinates to physical quantities – wavelengths – is performed.

Results and discussion

We performed a series of tests of the developed algorithm using calibration lamp data (He-Ne-Ar). Peak detection was first applied to both the measured spectrum and the reference spectrum, producing two sets of spectral features: image peaks and reference peaks.

For wavelength calibration, we modeled the relation between pixel position and wavelength using a polynomial of order k=3 A third-order polynomial was chosen because it provides sufficient flexibility to describe nonlinear variations in the pixel-to-wavelength relation while retaining a relatively small number of free parameters, which is important for robust fitting based on a limited

number of peak correspondences. Higher-order polynomials were avoided to limit model complexity and sensitivity to mismatched peaks. This choice aligns with established automated calibration approaches (e.g., [19]). A polynomial of this order requires a minimum of four points to be defined; however, to improve robustness against noise and mismatches, we used random subsets of 5 peak pairs when estimating model parameters.

All spectra contain 1,024 pixels along the dispersion axis. Therefore, a fixed tolerance of (ε_{nm} =1/1024) in normalized wavelength units corresponds approximately to one detector pixel. This value is used exclusively as the RANSAC inlier threshold: a peak correspondence is considered consistent with a candidate polynomial solution if its residual is smaller than this threshold. It should therefore not be interpreted as the final wavelength calibration accuracy. Since the equivalent tolerance in physical wavelength units depends on the spectral range and dispersion of the particular grating configuration, the value of approximately 4.64 Å applies specifically to the 360 lines/mm grating and is not used as a fixed physical tolerance for the other configurations. The final wavelength calibration is obtained only after RANSAC identifies the consistent peak correspondences and the third-order polynomial wavelength solution is determined from the retained matches.

Due to the stochastic nature of the RANSAC approach, the same number of iterations under identical conditions can yield different numbers of inliers. To estimate the algorithm's effectiveness and stability, we measured how the mean number of inliers grows with an increasing number of iterations. The results are shown in Figure 4.

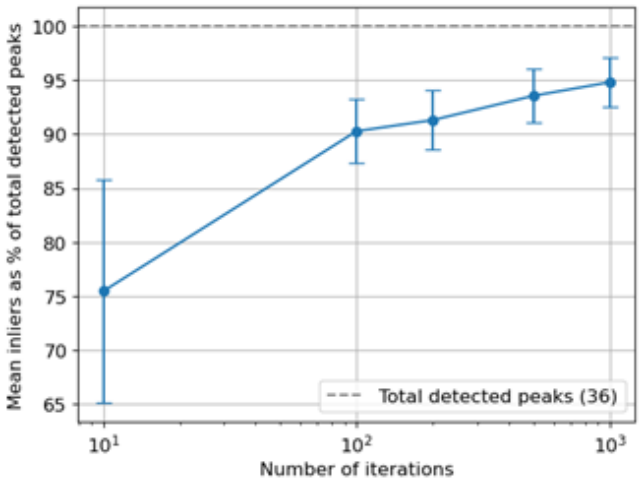


Figure 4 – Dependence of the mean number of detected model inliers
on the maximum number of RANSAC iterations.
Error bars represent the standard deviation

In the test spectrum, with peak-finding prominence set to 10^{-2}, 36 peaks were detected. The analysis shows that a few hundred iterations are sufficient to achieve successful calibration of up to ~90% of the detected peaks, while further increasing the number of iterations leads to gradual saturation of the solution quality. This behavior is consistent with the probabilistic nature of RANSAC, where additional iterations primarily increase the likelihood of finding near-optimal peak correspondences rather than dramatically improving the solution. This proportion of successfully matched pairs allows for a robust polynomial fit of the pixel–wavelength relation of the chosen order, as illustrated in Figure 5.

It should be noted that RANSAC can be applied as a standalone method for peak matching, even without preliminary conditioning using DTW or other techniques. However, its effectiveness strongly depends on the constraints imposed on the candidate correspondences. In its basic form, RANSAC operates solely on positional information and does not take into account the shape of spectral features or their local neighborhoods.

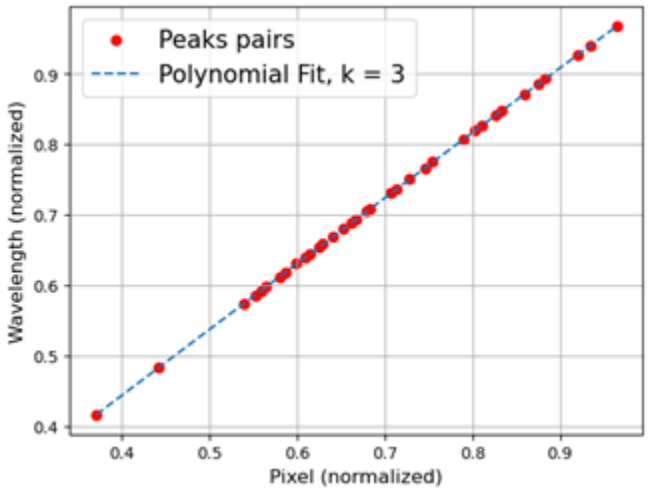


Figure 5 – Polynomial fit to the identified peak correspondences

For reliable peak matching, it is therefore important that the input spectra (both target and reference) are broadly consistent, i.e., they correspond to the same spectral range, lamp type, and overall spectral structure. In practice, this consistency can be ensured using preliminary classification methods or similarity-based approaches such as DTW.

Even in the absence of DTW, effective matching can be achieved by introducing additional constraints into the pair selection process. A naive construction of candidate pairs scales as $N_{pairs} \sim N_R \cdot N_S$, which leads to a large number of incorrect combinations. To reduce this search space, candidate correspondences can be restricted to peaks that are close in normalized coordinate space. At the same time, this limitation also justifies the use of DTW at the preconditioning stage. DTW is able to compare local spectral patterns in a way that is robust to non-linear distortions along the dispersion axis. Unlike direct positional matching, DTW aligns local intensity profiles while allowing elastic shifts between sequences, making it well suited for spectra affected by stretching, compression, or small calibration offsets. As a result, DTW provides more reliable initial correspondences in cases where simple proximity-based criteria may fail.

The resulting polynomial can then be applied to the entire spectrum to perform wavelength calibration, as shown in Figure 6.

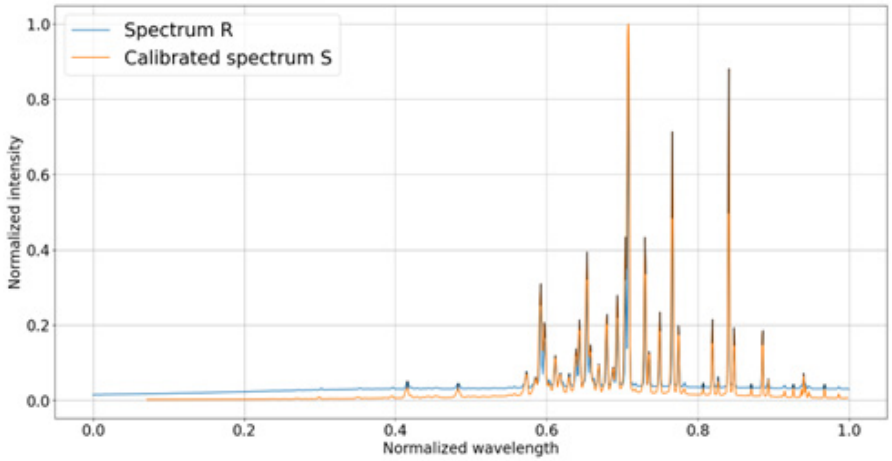


Figure 6 – Spectra R and calibrated S,
with black lines indicating the matched peaks

The error between peaks in spectrum R and their corresponding matched peaks in spectrum S remains within the acceptable tolerance defined by the RANSAC filtering and stays approximately constant across iterations. This indicates that the proposed approach allows an increase in the number of matched peak pairs without a loss of calibration accuracy.

The subsequent application of RANSAC made it possible to eliminate false correspondences and significantly improve the calibration accuracy. Figure 7 shows the final result of the described algorithms: the calibrated spectrum of the calibration lamp and the spectrum of the observed object – the standard star HD 205027 – mapped using the derived calibration.

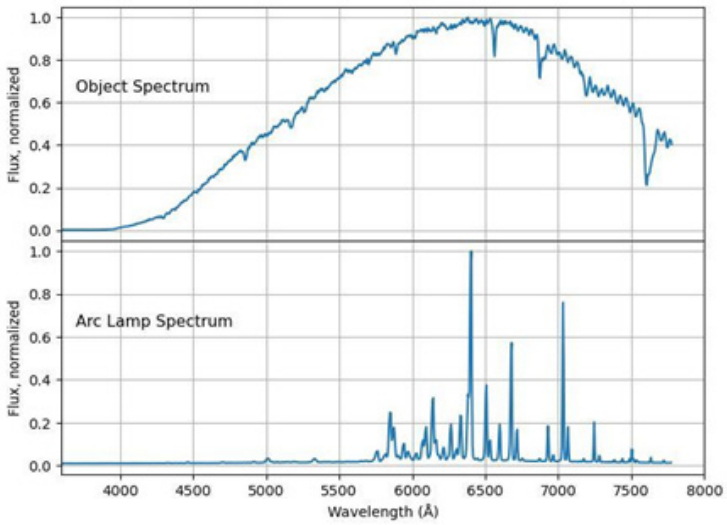


Figure 7 – Calibrated spectrum of the object (top)
based on the calibrated lamp spectrum (bottom)

Overall, the proposed approach demonstrates that combining DTW-based initial matching with subsequent RANSAC filtering provides a robust and efficient solution to the spectral calibration problem. The DTW stage enables the identification of candidate correspondences based on local spectral structure, while RANSAC effectively eliminates outliers and refines the calibration model using only geometrically consistent peak pairs.

The results show that the method achieves a high proportion of correctly matched peaks and produces a stable dispersion solution, even in the presence of noise, missing lines, and closely spaced spectral features. The observed saturation in the number of inliers with increasing iterations confirms the expected probabilistic behavior of RANSAC and indicates that a relatively small number of iterations is sufficient for practical applications.

The final calibrated spectra demonstrate good agreement between the reference and measured data, confirming the validity of the obtained polynomial model. The method is computationally efficient and can be readily applied in automated data reduction pipelines, significantly reducing processing time compared to manual calibration while maintaining high accuracy. The automation and computational efficiency of the proposed approach suggest its potential applicability to space-based observational systems, where data processing may require minimal operator involvement and operate under computational constraints. However, its application to such systems has not yet been tested and will require dedicated validation. Prospective orbital telescope systems, including the proposed cislunar telescope (https://fai.kz/projects/cislunar_phase_1), therefore represent a potential direction for future application of the method.

Conclusion

In this work, we developed and tested an automated pipeline for wavelength calibration of astronomical spectra that combines robust signal matching techniques. The present implementation

was developed and validated using observational data obtained with the AZT-20 telescope, a He-Ne-Ar calibration lamp, and diffraction gratings with line densities of 360, 1800, and 2400 lines/mm. The proposed approach successfully addresses key challenges of spectral calibration, including noise sensitivity, nonlinear distortions, and incorrect peak identification. The DTW algorithm proved effective for initial peak matching, while the subsequent application of RANSAC significantly improved the robustness of the calibration by eliminating false peak matches.

A key contribution of this work lies in the integration of DTW-based local similarity analysis with probabilistic RANSAC filtering into a unified calibration pipeline, enabling reliable correspondence identification without manual intervention. This combination allows the method to operate effectively under realistic observational conditions, where noise, missing lines, and line blending are present.

The results show that the developed method enables fully automated processing of spectral data and substantially increases efficiency compared to traditional manual calibration procedures. This makes it particularly valuable for large datasets, such as those stored in distributed astronomical data centers and made available through Virtual Observatory networks. In addition, the computational efficiency and robustness of the method make it well suited for application in resource-constrained observational systems, including future space-based instruments.

Future work will focus on extending the proposed method to a wider variety of spectral instruments and on its systematic validation and refinement using a substantially larger and more diverse set of real observational data. While the current classification model was primarily trained using synthetically generated spectra and evaluated on the available observational data, further testing on spectra obtained under different observational conditions and instrumental configurations will be essential for assessing and improving its robustness and generalization capability. As additional observational data become available, the pipeline will be progressively adapted and optimized to improve the reliability and accuracy of the wavelength calibration procedure. Furthermore, the developed pipeline has already been integrated into the Kazakhstan Virtual Observatory (KazVO) infrastructure, providing both an interactive web-based interface (https://vo.fai.kz/calibration/) for users and a scalable service (https://vo.fai.kz/obs_data.php?path=/misc/wvl_calib/comp/external) compliant with the IVOA protocol.

Acknowledgments

This research received funding from the Committee of Science of the Ministry of Science and Higher Education of the Republic of Kazakhstan (Grant No. BR24992807 and Grant No. BR24992759).

REFERENCES

1 Stoughton, C., et al. Sloan Digital Sky Survey: Early Data Release. The Astronomical Journal, 123 (1), 485–548 (2002). https://doi.org/10.1086/324741

2 Law, D.R., et al. The Data Reduction Pipeline for the SDSS-IV MaNGA IFU Survey. The Astronomical Journal, 152, 83 (2016). https://doi.org/10.3847/0004-6256/152/4/83

3 Tody, D. The IRAF Data Reduction and Analysis System. Instrumentation in Astronomy VI, Proc. SPIE, 627, 733–748 (1986). https://doi.org/10.1117/12.968154

4 Odewahn, S.C., et al. Automated Star/Galaxy Discrimination with Neural Networks. In: Digitised Optical Sky Surveys, 215–224 (1992). https://doi.org/10.1086/116063

5 Weir, N., et al. The SKICAT System for Processing and Analyzing Digital Imaging Sky Surveys. Publications of the Astronomical Society of the Pacific, 107 (718), 1243–1254 (1995). https://doi.org/10.1086/133683

6 Collister, A.A., and Lahav, O. ANNz: Estimating Photometric Redshifts Using Artificial Neural Networks. Publications of the Astronomical Society of the Pacific, 116 (818), 345–351 (2004). https://doi.org/10.1086/383254

7 Dieleman, S., Willett, K.W., and Dambre, J. Rotation-Invariant Convolutional Neural Networks for Galaxy Morphology Prediction. Monthly Notices of the Royal Astronomical Society, 450 (2), 1441–1459 (2015). https://doi.org/10.1093/mnras/stv632

8 Smith, M.J., and Geach, J.E. Astronomia ex Machina: A History, Primer and Outlook on Neural Networks in Astronomy. Royal Society Open Science, 10 (5) (2023). https://doi.org/10.1098/rsos.221454

9 Fabbro, S., et al. An Application of Deep Learning in the Analysis of Stellar Spectra. Monthly Notices of the Royal Astronomical Society, 475 (3), 2978–2993 (2018). https://doi.org/10.1093/mnras/stx3298

10 Zhang, T., et al. Application of Machine Learning in Astronomical Spectral Data Mining. Astronomical Techniques and Instruments, 2 (2), 73–87 (2025). https://doi.org/10.61977/ati2024057

11 Davenport, J.R.A., et al. Automated Spectroscopic Wavelength Calibration Using Dynamic Time Warping. https://doi.org/10.48550/arXiv.2508.05862

12 LeCun, Y., et al. Gradient-Based Learning Applied to Document Recognition. Proceedings of the IEEE, 86 (11), 2278–2324 (1998). https://doi.org/10.1109/5.726791

13 Sakoe, H., and Chiba, S. Dynamic Programming Algorithm Optimization for Spoken Word Recognition. IEEE Transactions on Acoustics, Speech, and Signal Processing, 26 (1), 43–49 (1978). https://doi.org/10.1109/TASSP.1978.1163055

14 Fischler, M.A., and Bolles, R.C. Random Sample Consensus: A Paradigm for Model Fitting with Applications to Image Analysis and Automated Cartography. Communications of the ACM, 24 (6), 381–395 (1981). https://doi.org/10.1145/358669.358692

15 Nair, V., and Hinton, G.E. Rectified Linear Units Improve Restricted Boltzmann Machines. In: Proceedings of the 27th International Conference on Machine Learning, 807–814 (2010). http://www.icml2010.org/papers/432.pdf

16 Rogowski, M., et al. mpi4py.futures: MPI-Based Asynchronous Task Execution for Python. IEEE Transactions on Parallel and Distributed Systems, 34 (2), 611–622 (2022). https://doi.org/10.1109/TPDS.2022.3225481

17 Kingma, D.P., and Ba, J. Adam: A Method for Stochastic Optimization. (2015). https://doi.org/10.48550/arXiv.1412.6980

18 Srivastava, N., et al. Dropout: A Simple Way to Prevent Neural Networks from Overfitting. Journal of Machine Learning Research, 15 (1), 1929–1958 (2014). https://www.cs.toronto.edu/~hinton/absps/JMLRdropout.pdf

19 Mirapeix, J., et al. In-Process Automatic Wavelength Calibration for CCD-Spectrometers. In: Optical Sensors 2008, Proc. SPIE, 7003, 70031T (2008). https://doi.org/10.1117/12.781040

[1]Глущенко А.,
магистр, ORCID ID: 0000-0002-0738-7725, e-mail: gluchshenko@fai.kz
[1]Измайлова И.,
магистр, ORCID ID: 0000-0001-9878-0989, e-mail: izmailova@fai.kz
[1,3]Умирбаева А.,
магистр, ORCID ID: 0000-0001-9339-4990, e-mail: umirbayeva@fai.kz
[1,2]Куватова Д.,
магистр, ORCID ID: 0000-0002-5937-4985, e-mail: kuvatova@fai.kz
[1]Юрин Д.,
PhD, ORCID ID: 0000-0002-5604-9757,e-mail: yurin@fai.kz

[1]В.Г. Фесенков атындағы астрофизикалық институты, Алматы қ., Қазақстан
[2]Әл-Фараби атындағы Қазақ ұлттық университеті, Алматы қ., Қазақстан
[3]Назарбаев университеті, Астана қ., Қазақстан

АСТРОНОМИЯЛЫҚ СПЕКТРЛЕРДІҢ ТОЛҚЫН ҰЗЫНДЫҒЫН АВТОМАТТЫ ТҮРДЕ КАЛИБРЛЕУ: DTW–RANSAC СӘЙКЕСТЕНДІРУ ЖӘНЕ CNN НЕГІЗІНДЕГІ АЛДЫН АЛА ӨҢДЕУ

Андатпа

Мақалада машиналық оқыту әдістері мен сенімді сәйкестендіру алгоритмдерін біріктіруге негізделген астрономиялық саңылаулы спектрлердің толқын ұзындығын калибрлеуге арналған автоматтандырылған алгоритм ұсынылады. Ұсынылған тәсіл спектрлік жолақты автоматты түрде анықтауға арналған бірөлшемді конволюциялық нейрондық желіні (CNN), одан кейін динамикалық уақытты ығыстыру (DTW) әдісі арқылы

бастапқы шыңдарды сәйкестендіруді және кездейсоқ үлгілер консенсусы (RANSAC) алгоритмі негізінде кейінгі нақтылауды қамтиды. CNN моделі синтетикалық және нақты спектрлік деректерде оқытылып, әртүрлі дифракциялық торлар үшін жоғары жіктеу дәлдігін көрсетеді. DTW әдісі сызықтық емес бұрмаланулар мен шу болған жағдайда да бақыланатын және эталондық спектрлердің сенімді бастапқы тураласуын қамтамасыз етеді. RANSAC алгоритмін қолдану қате шың сәйкестіктерін сүзу және дисперсиялық шешімді оңтайландыру арқылы калибрлеу дәлдігін одан әрі арттырады. Әдіс калибрлеу шамдарынан алынған нақты бақылау деректерінде сыналып, жоғары сенімділік, тиімділік және толық автоматтандыру мүмкіндігін көрсетеді. Дәстүрлі қолмен немесе жартылай автоматтандырылған тәсілдермен салыстырғанда, ұсынылған өңдеу құбыржолы жоғары калибрлеу дәлдігін сақтай отырып, өңдеу уақытын едәуір қысқартады. Әзірленген шешімді виртуалды обсерватория инфрақұрылымында қызмет ретінде орналастыру жоспарлануда және көптеген спектрлік деректерді өңдеу үшін қолданылады.

Түйін сөздер: астрономиялық деректерді өңдеу, щелелі спектрлерді калибрлеу, dynamic time warping, RANSAC, машиналық оқыту.

[1]Глущенко А.,
магистр, ORCID ID: 0000-0002-0738-7725, e-mail: gluchshenko@fai.kz
[1]Измайлова И.,
магистр, ORCID ID: 0000-0001-9878-0989, e-mail: izmailova@fai.kz
[1,3]Умирбаева А.,
магистр, ORCID ID: 0000-0001-9339-4990, e-mail: umirbayeva@fai.kz
[1,2]Куватова Д.,
магистр, ORCID ID: 0000-0002-5937-4985, e-mail: kuvatova@fai.kz
[1]Юрин Д.,
PhD, ORCID ID: 0000-0002-5604-9757,e-mail: yurin@fai.kz

[1]Астрофизический институт им. В.Г. Фесенкова, г. Алматы, Казахстан
[2]Казахский национальный университет им. аль-Фараби, г. Алматы, Казахстан
[3]Назарбаев Университет, г. Астана, Казахстан

АВТОМАТИЧЕСКАЯ КАЛИБРОВКА ДЛИНЫ ВОЛНЫ АСТРОНОМИЧЕСКИХ СПЕКТРОВ С ИСПОЛЬЗОВАНИЕМ DTW–RANSAC СОПОСТАВЛЕНИЯ И ПРЕДВАРИТЕЛЬНОЙ ОБРАБОТКИ НА ОСНОВЕ CNN

Аннотация

В данной статье представлен автоматизированный алгоритм калибровки длины волны щелевых астрономических спектров, основанный на сочетании методов машинного обучения и надежных алгоритмов сопоставления. Предлагаемый подход включает в себя одномерную сверточную нейронную сеть (CNN) для автоматической идентификации спектрального диапазона, за которой следует первоначальное сопоставление пиков с использованием метода динамического временного сдвига (DTW) и последующее уточнение с помощью алгоритма консенсуса случайных выборок (RANSAC). Модель CNN обучена как на синтетических, так и на реальных спектральных данных и демонстрирует высокую точность классификации для различных дифракционных решеток. Метод DTW обеспечивает надежное начальное совмещение наблюдаемых и эталонных спектров даже при наличии нелинейных искажений и шума. Применение RANSAC дополнительно повышает точность калибровки за счет отсеивания некорректных соответствий пиков и оптимизации решения дисперсии. Метод был проверен на реальных данных наблюдений от калибровочных ламп и демонстрирует высокую устойчивость, эффективность и возможность полной автоматизации. По сравнению с традиционными ручными или полуавтоматическими подходами, предложенный конвейер значительно сокращает время обработки, сохраняя при этом высокую точность калибровки. Разработанное решение планируется развернуть в виде сервиса в инфраструктуре виртуальных обсерваторий и применять для обработки многочисленных спектральных данных.

Ключевые слова: обработка астрономических данных, калибровка щелевых спектров, dynamic time warping, RANSAC, машинное обучение.

UDC 535.37
IRSTI 29.19.22

https://doi.org/10.55452/1998-6688-2026-23-3-473-485

[1]Tulegenova A.T.,
associate professor, PhD, ORCID ID: 0000-0002-5701-6674,
e-mail: tulegenova.aida@gmail.com
[2]Lisitsyn V.M.,
professor, Dr.Sci., ORCID ID: 0000-0002-2075-4796,
e-mail: lisitsyn@tpu.ru
[1]Nogaibekova G.Zh.,
senior lecturer, ORCID ID: 0009-0008-8688-4279,
e-mail: nogaibekovagulnur@gmail.com
[3]Lisitsyna L.A.,
professor, Dr.Sci., ORCID ID: 0000-0001-6273-6345,
e-mail: lisitsyna@mail.ru

[1]Al-Farabi Kazakh National University, Almaty, Kazakhstan
[2]Tomsk Polytechnic University, Tomsk, Russia,
[3]Tomsk State University of Architecture and Building, Tomsk, Russia

INFLUENCE OF THE AL/GA RATIO ON THE OPTICAL PROPERTIES OF $Y_3AL_XGA_{5-X}O_{12}$:CE PHOSPHORS FOR LED APPLICATIONS

Abstract

This paper presents the results of studies on $Y_3Al_xGa_{5-x}O_{12}$: Ce (YAGG:Ce) ceramic phosphors synthesized for the first time using a radiation method. The influence of the Al/Ga ratio on the optical properties of Ce^{3+}-doped $Y_3Al_xGa_{5-x}O_{12}$: Ce (YAGG:Ce) garnet phosphors, which are promising for LED light source applications, was investigated. Excitation and photoluminescence spectra of samples with different aluminum and gallium contents at a fixed concentration of Ce^{3+} activator ions were analyzed. It was shown that variations in composition lead to changes in the position and shape of the excitation and emission bands, variations in the photoluminescence band width, as well as redistribution of the emission intensity under excitation in the ultraviolet and blue spectral regions. It was found that a decrease in the Al/Ga ratio causes the excitation band to shift toward the longer wavelength region near 340–370 nm, which increases the excitation efficiency when near-ultraviolet and violet LEDs are used. The obtained results confirm the feasibility of using the radiation method for the synthesis of efficient YAGG:Ce phosphors.

Keywords: phosphors, $Y_3Al_xGa_{5-x}O_{12}$:Ce, Al/Ga ratio, excitation spectra, photoluminescence, LEDs, ultraviolet.

Received April 4, 2026; revised August 20, 2026; accepted August 26, 2026.

Introduction

Cerium (III)-activated garnet phosphors constitute the most technologically mature class of inorganic luminescent materials for solid-state lighting, combining exceptional thermal stability, chemical inertness, and a broadband visible emission that affords efficient conversion of blue or near-ultraviolet (n-UV) pump radiation into white light [1]. The archetype, $Y_3Al_5O_{12}$:Ce (YAG:Ce), remains the dominant phosphor in commercial white LEDs based on InGaN blue chips [2]. The rapid proliferation of high-power laser-driven phosphor converters (LPCs) and remote-phosphor configurations, however, imposes demanding additional requirements: elevated saturation thresholds, superior thermal quenching resistance, and narrowly tailored emission spectra for precision colorimetry [3,4].

Contemporary phosphor engineering for solid-state lighting increasingly demands spectral tunability – the capacity to independently optimize excitation and emission profiles for diverse pump sources and target colour-rendering specifications [5]. Partial or complete isovalent substitution of Al^{3+} by the larger Ga^{3+} (ionic radius in octahedral coordination: $r(Al^{3+}) = 0.535$ Å vs. $r(Ga^{3+}) = 0.620$ Å) in the $Y_3(Al,Ga)_5O_{12}$:Ce matrix expands the unit-cell volume, modifies the crystal-field splitting of the 5d levels of Ce^{3+}, and produces systematic red-shifts of both excitation and emission bands [6,7]. Such compositional flexibility has been exploited for a wide range of garnet systems, yet rigorous, composition-by-composition investigations covering the full $Y_3Al_xGa_{5-x}O_{12}$: Ce series ($0 \leq x \leq 5$) remain limited in the literature.

A central practical consideration is the excitation wavelength. The majority of commercial white LEDs exploit 450–465 nm InGaN chips, yet a growing segment of high-CRI and horticultural applications employs n-UV/violet sources (380–410 nm), for which efficient UV-band excitation is critical [8]. In Ce^{3+}-doped garnets, two distinct 4f → 5d absorption manifolds are observable: a higher-energy band near 340–370 nm (4f → $5d^2$) and a lower-energy band near 430–470 nm (4f → $5d^1$); compositional modification redistributes oscillator strength between these manifolds, thereby altering the efficacy under different pump wavelengths [9]. Conversion efficiency is additionally governed by the structural perfection of the luminescence centers, which is in turn sensitive to synthetic conditions. High-temperature solid-state reactions and solution-combustion routes are capable of producing phase-pure ceramics, but their multi-hour processing cycles constrain compositional screening and optimization.

Direct electron-beam radiation synthesis–first demonstrated for garnet ceramics in 2017-offers an attractive alternative: phase-pure ceramics are produced in sub-second irradiation times (≤ 1 s) from stoichiometric oxide mixtures, without any mineralizer additives and at throughputs reaching ≈5 g s−1[10]. The present work extends this synthesis platform to the multi-component $Y_3Al_xGa_{5-x}O_{12}$: Ce system and provides a comprehensive characterization of structural, spectral, luminance, and colour properties as a function of Al/Ga composition, benchmarked against literature data for thermally synthesized counterparts.

Materials and methods

Ceramic synthesis. Ceramic phosphors were fabricated by direct high-energy electron-beam irradiation of stoichiometric oxide precursor mixtures. Irradiation was performed on an ELV-6 electron accelerator at the Budker Institute of Nuclear Physics (SB RAS, Novosibirsk, Russia) at a beam energy of 1.4 MeV and a power density in the range 1–30 kW cm^{-2}.

Precursor preparation. Powder mixtures of Y_2O_3, Al_2O_3, and Ga_2O_3 were prepared in stoichiometric ratios corresponding to the target garnet formula $Y_3Al_xGa_{5-x}O_{12}$: Ce. Ce_2O_3 was added as activator at 0.5 wt.% relative to the total charge mass. All precursor oxides were supplied by Hebei Suoyi New Material Technology Co., Ltd. (grades K1, K6, K7, K8), with a purity ≥99.95% and comparable particle-size distributions, ensuring consistency of synthesis conditions across the composition series. Sample designations follow the internal numbering adopted by the authors.

Irradiation geometry. The charge was loaded into a massive copper crucible (inner dimensions 10 × 5 × 1 cm^3, depth 10 mm), which served simultaneously as the reaction vessel and heat sink. A 1 cm^2 electron beam scanned transversally at 50 Hz while the crucible was translated at 1 cm s^{-1} relative to the scanning beam, ensuring uniform energy deposition over the entire charge area. At the crucible depth employed, the electron range did not reach the copper bottom, precluding contamination of the charge by copper. Following irradiation, the ceramics were cooled, extracted from the crucible, and recovered as dense plates (Figure 1). For spectroscopic characterization, the ceramic plates were mechanically comminuted into powder, eliminating surface-geometry artefacts inherent in measurements on bulk ceramic specimens.

Synthesis yield. The synthesis yield η was defined as the ratio of the recovered ceramic mass to the initial charge mass, expressed as a percentage. The mass of the synthesized ceramic plates ranged

from approximately 45 to 60 g; the observed scatter is attributed to irreproducible compaction and levelling of the charge prior to irradiation. Notwithstanding this variability, the selection of starting materials and process parameters consistently afforded high synthesis yields of 90–97% (Table 1).

Table 1 – Nominal compositions of $Y_3Al_xGa_{5-x}O_{12}$:Ce ($0 \le x \le 5$) ceramics (series 636–641) and synthesis yields

Sample	Formula	Precursor charge composition (wt.%)	Yield, %
636	$Y_3Al_5O_{12}$:Ce	Al2O3 – 43; Y2O3 – 57; Ce2O3 – 0.5	96.5
637	$Y_3Al_4GaO_{12}$:Ce	Al2O3 – 32; Y2O3 – 53; Ga2O3 – 15; Ce2O3 – 0.5	96.3
638	$Y_3Al_3Ga_2O_{12}$:Ce	Al2O3– 22.5; Y2O3 – 50; Ga2O3 – 27.5; Ce2O3 – 0.5	96.3
639	$Y_3Al_2Ga_3O_{12}$:Ce	Al2O3 – 14; Y2O3 – 47; Ga2O3 – 39; Ce2O3 – 0.5	97.2
640	$Y_3AlGa_4O_{12}$:Ce	Al2O3 – 6.7; Y2O3 – 44.3; Ga2O3 – 49; Ce2O3 – 0.5	96.6
641	$Y_3Ga_5O_{12}$:Ce	Y2O3 – 42; Ga2O3 – 58; Ce2O3 – 0.5	94.4

Note: Precursor mixture compositions are normalized to 100 wt.% for the host oxide mixture (Y_2O_3 + Al_2O_3 ± Ga_2O_3); Ce_2O_3 (0.5 wt.%) is added as an activator in addition to the host, so each row totals 100.5 wt.%.

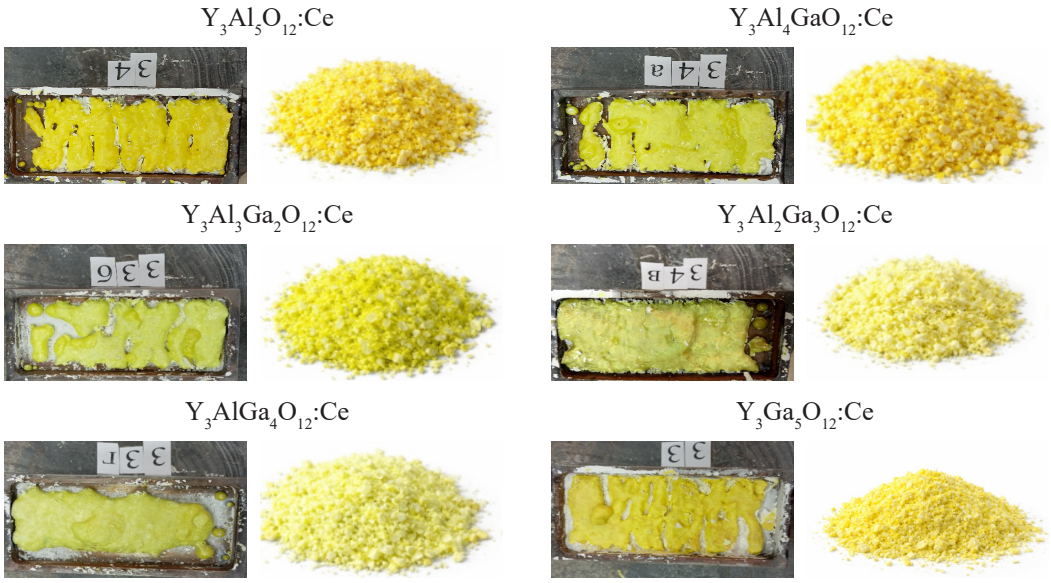


Figure 1 – Photographs of as-synthesized ceramic specimens in copper crucibles

X-ray diffraction. Phase composition and crystal structure were characterized by X-ray diffraction (XRD) using a Rigaku MiniFlex 600 diffractometer (Rigaku Corporation, Tokyo, Japan) with Cu Kα radiation (λ = 1.5406 Å), operated at 40 kV / 15 mA, over a 2θ range of 3–90° with a step size of 0.02°.

Photoluminescence and excitation spectroscopy. Photoluminescence (PL) emission and photoluminescence excitation (PLE) spectra were recorded on a Cary Eclipse fluorescence spectrophotometer (Agilent Technologies, USA), equipped with a xenon flash lamp source and a photomultiplier tube detector. Excitation and emission slit widths were set to 5 nm / 5 nm. All spectra were recorded at room temperature ~23 ± 2 °C on powdered specimens.

Diffuse reflectance spectroscopy. Diffuse reflectance spectra were recorded over the 200–600 nm range using a Cary series UV-Vis-NIR spectrophotometer (Agilent Technologies) equipped with an integrating sphere (DRA) accessory.

Relative luminance. Relative luminance was measured using a Konica Minolta LS-150 luminance meter (Konica Minolta, Tokyo, Japan) under fixed excitation and geometrical conditions (excitation wavelength, angle, and working distance identical for all specimens), referenced to the SDL-4000 phosphor standard measured under the same conditions.

Results and discussion

Crystal structure and phase composition

The crystal structure of the $Y_3Al_xGa_{5-x}O_{12}$:Ce ($0 \leq x \leq 5$) was characterised by X-ray powder diffraction (XRD). The diffractograms are presented in Figure 2a (full angular range) and Figure 2b (expanded region 2θ = 20–40°).

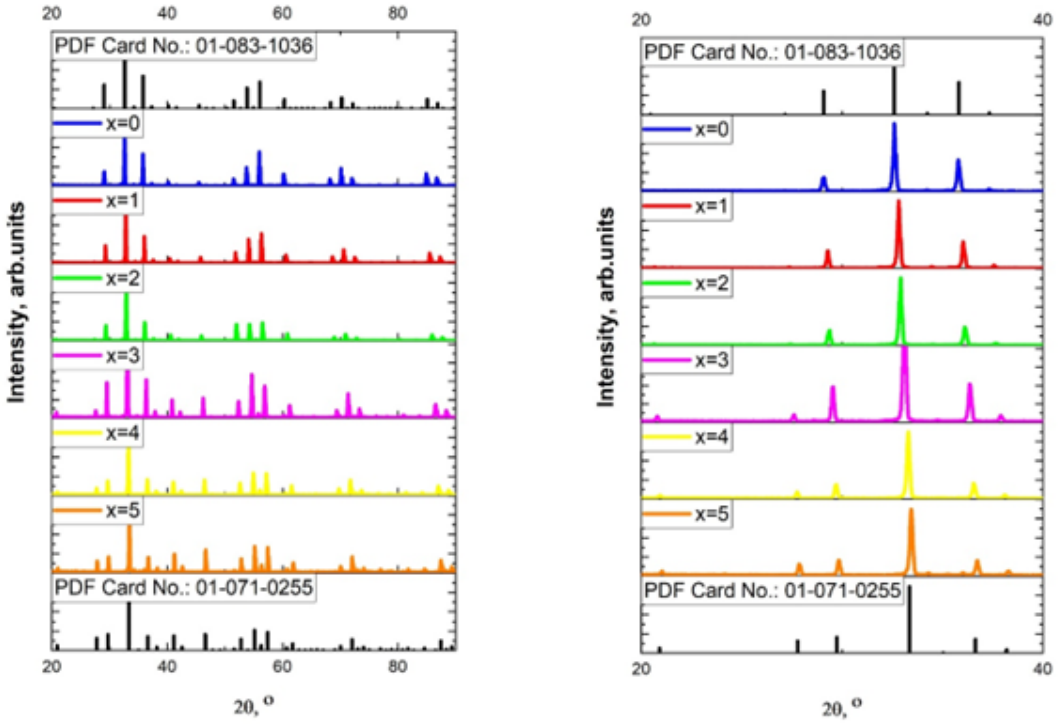


Figure 2 – XRD patterns of $Y_3Al_xGa_{5-x}O_{12}$: Ce ceramics as a function of Al/Ga ratio: (a) full 2θ range; (b) expanded view of the 2θ = 20–40° region

For all investigated compositions, the diffraction patterns are fully indexed to the cubic garnet structure of the $Y_3Al_5O_{12}$ type (space group Ia^3d, PDF Card No. 01-083-1036; PDF Card No. 01-071-0255), confirming that the garnet host lattice is preserved throughout the entire Al/Ga substitution range. This result is consistent with the established solid-solution behaviour of YAG–YAGG systems reported in the literature [11].

With increasing Al^{3+} content, a systematic high-angle shift of the principal Bragg reflections is observed (Figure 2b), signalling a progressive contraction of the unit-cell parameter. This behaviour reflects the smaller ionic radius of Al^{3+} relative to Ga^{3+} in both octahedral and tetrahedral coordination environments of the garnet structure, which reduces average interatomic distances upon Al-for-Ga substitution, in quantitative agreement with published lattice-parameter data for the $Y_3Al_xGa_{5-x}O_{12}$: Ce series [11–13].

Phase analysis (Figure 3) reveals a pronounced dependence of phase purity on Al/Ga ratio. Intermediate compositions (x = 2–4) yield predominantly single-phase garnet ceramics, with secondary-phase fractions not exceeding a few per cent. At the terminal compositions, however, the phase purity deteriorates: the x = 5 (YAG: Ce) sample contains residual Al_2O_3 and $YAlO_3$ phases, while the x = 0 (YGG: Ce) endpoint exhibits Ga_2O_3 and $Y2O_3$ impurities. This behavior is consistent with the thermodynamic stability limits of the single-phase garnet field in the YAG–YGG system documented in the literature [14–16]. Notably, the compositions $Y_3Al_4GaO_{12}$: Ce and $Y_3Al_2Ga_3O_{12}$: Ce achieve garnet phase fractions exceeding 99%, identifying them as optimal Al/Ga ratios for single-phase garnet formation under the present synthesis conditions.

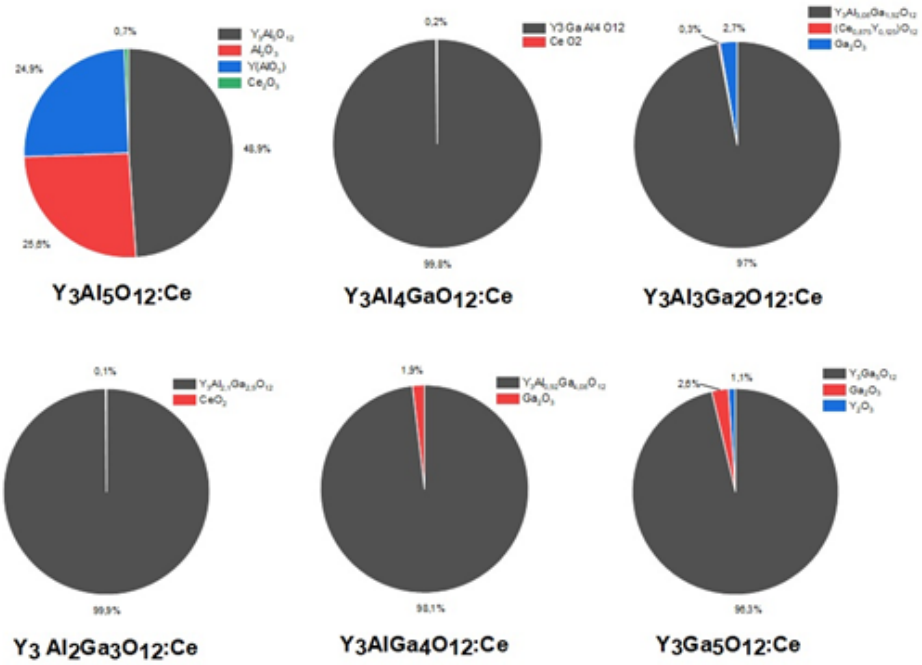


Figure 3 – Phase composition of $Y_3Al_xGa_{5-x}O_{12}$: Ce ceramics as a function of Al/Ga ratio (from Rietveld-based XRD analysis)

Photoluminescence and Excitation spectra

The excitation spectra of all investigated YAGG:Ce compositions exhibit two characteristic absorption manifolds: a near-UV band centred in the 340–370 nm range and a blue band centred in the 430–470 nm range (Figure 4). This two-band structure is the spectroscopic hallmark of the 4f → 5d electric-dipole transitions of Ce^{3+} in a garnet crystal field [17], and the observed evolution with composition is fully consistent with the crystal-field tuning model for Ce^{3+} activators in oxide hosts [18].

Progressive replacement of Al^{3+} by the larger Ga^{3+} (decreasing x) induces a systematic long-wavelength shift of the near-UV excitation band, expanding its overlap with the emission of near-UV and violet LEDs (380–410 nm). Simultaneously, the relative intensity of the blue excitation band (430–470 nm) is redistributed, which has direct implications for the coupling efficiency with InGaN blue chips [19,20]. This spectral tunability is a well-established feature of Ce^{3+}-doped mixed-garnet ceramics [19] and arises from the sensitivity of the 5d barycenter energy and crystal-field splitting to the mean metal–oxygen bond length in the garnet host.

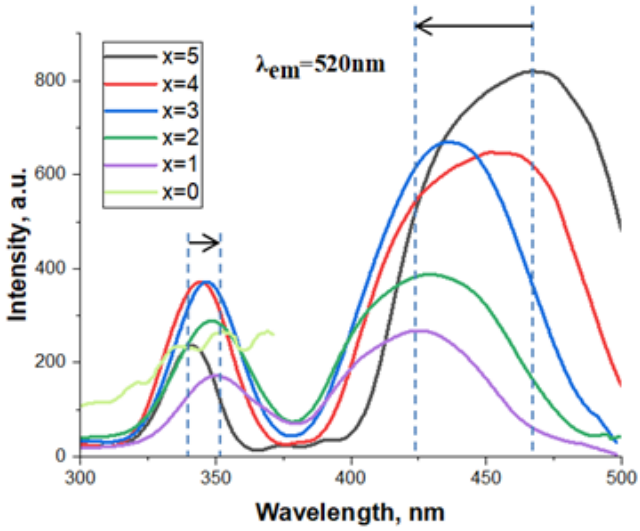


Figure 4 – Photoluminescence excitation spectra
of $Y_3Al_xGa_{5-x}O_{12}$:Ce as a function of Al^{3+}/Ga^{3+} substitution

Under 350 nm n-UV excitation (Figure 5), all compositions produce a broad 5d → 4f emission band in the visible region peaking near λ ≈ 540 nm, characteristic of Ce^{3+} in a garnet host [21]. The integrated emission intensity peaks for intermediate compositions (x = 2–4), reflecting the combined effect of optimized crystal-field strength and minimal nonradiative trap density in the near-single-phase ceramic.

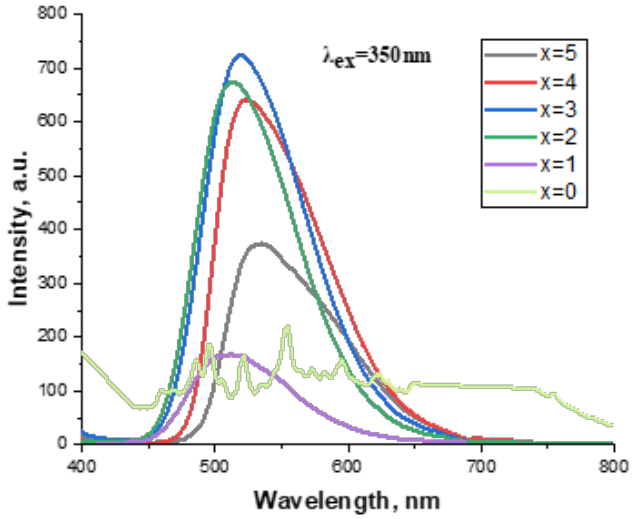


Figure 5 – Photoluminescence spectra
of $Y_3Al_xGa_{5-x}O_{12}$: Ce with different Al/Ga ratios under λ_{ex} = 350 nm excitation

Under 450 nm blue excitation (Figure 6), which replicates the operating conditions of InGaN-based white LEDs, the emission intensity exhibits a monotonic increase with decreasing x, i.e., with increasing Ga content. This trend is fully consistent with the excitation spectra: compositions with lower x develop a more intense blue absorption band, resulting in a higher photon-to-photon conversion efficiency under 450 nm pumping [22, 23].

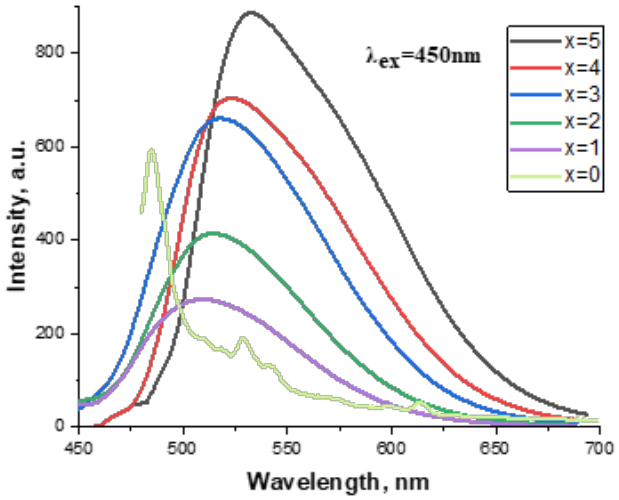


Figure 6 – Photoluminescence spectra
of $Y_3Al_xGa_{5-x}O_{12}$: Ce with different Al/Ga ratios under λ_{ex} = 450 nm excitation

The normalised PL spectra span the 480–650 nm range and are well described by the 5d → 4f allowed electric-dipole transition of Ce^{3+}. In the energy domain, the full width at half maximum (FWHM) values lie in the narrow range 0.40–0.44 eV and show only a weak dependence on excitation wavelength (Table 2). The observed variation of FWHM with Al/Ga ratio is in agreement with published data for $Y_3(Al,Ga)_5O_{12}$: Ce systems [24] and reflects the changing distribution of 5d crystal-field states upon progressive Ga-for-Al substitution in the octahedral and tetrahedral sites of the garnet lattice. The FWHM values obtained here are fully representative of Ce^{3+}-activated garnet phosphors reported to date, validating the spectroscopic methodology employed.

Table 2 – Emission bandwidth (FWHM in eV) of $Y_3Al_xGa_{5-x}O_{12}$: Ce at different excitation wavelengths

Composition	x	FWHM (ΔE), eV, λ_{ex} = 450 nm	FWHM (ΔE), eV, λ_{ex} = 350 nm
$Y_3AlGa_4O_{12}$:Ce	1	0,419	0,416
$Y_3Al_2Ga_3O_{12}$:Ce	2	0,398	0,402
$Y_3Al_3Ga_2O_{12}$:Ce	3	0,428	0,402
$Y_3Al_4GaO_{12}$:Ce	4	0,414	0,401
$Y_3Al_5O_{12}$:Ce	5	0,407	0,413

Note: Data for x = 0 (Sample 641, $Y_3Ga_5O_{12}$: Ce) are not reported. Owing to the phase impurities present in this composition, the photoluminescence emission and excitation spectra of Sample 641 exhibited negligible, non-normalizable signal, which precluded reliable determination of the emission bandwidth (FWHM) and of the CIE 1931 chromaticity coordinates/CCT.

Relative luminance

Relative luminance measurements, referenced to an SDL 4000 phosphor standard under identical geometrical and excitation conditions, provide a quantitative metric of the conversion efficiency (Figure 7). Under 340 nm n-UV excitation, the highest luminance is observed for Al-rich compositions (Al/Ga = 5/0 and 4/1), with a monotonic decrease as the Ga fraction increases. This trend reflects the reduced oscillator strength of the near-UV excitation band at high Ga content, consistent with the enhanced nonradiative relaxation associated with the lowering of the $5d^1$ level toward the conduction band minimum as documented by Dorenbos [25].

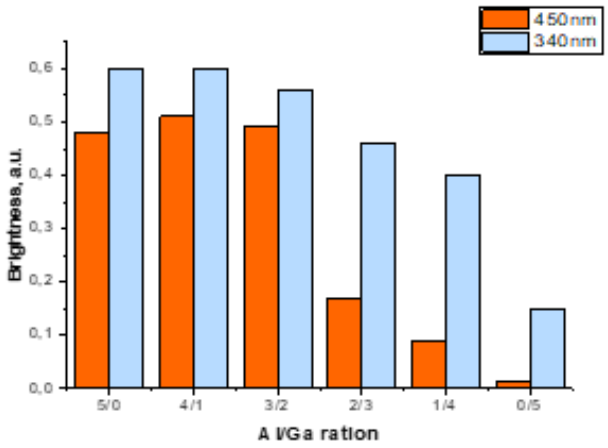


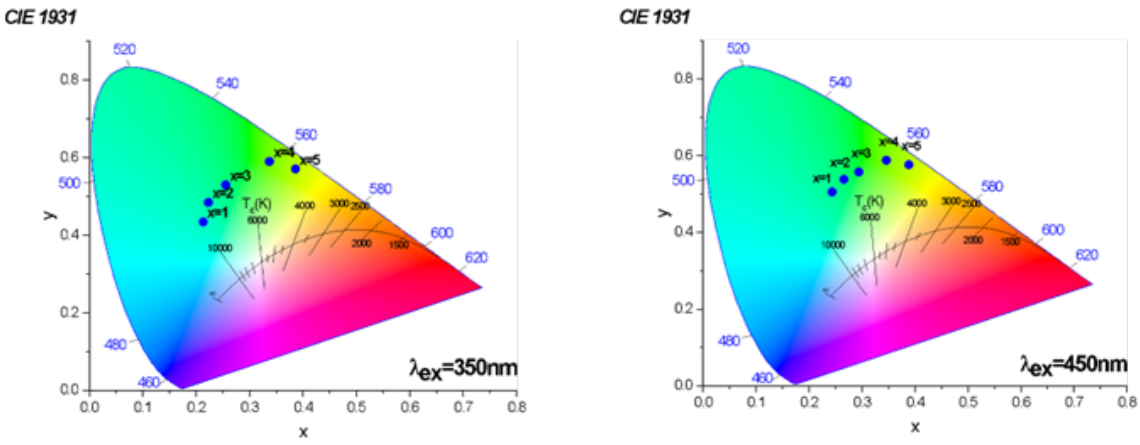
Figure 7 – Relative luminance $Y_3Al_xGa_{5-x}O_{12}$: Ce ceramic powders as a function of Al/Ga ratio under λ_{ex} = 340 nm (n-UV) and λ_{ex} = 450 nm excitation, normalised to the SDL 4000 standard

Under 450 nm blue excitation, the luminance is highest for Al-dominant compositions (Al/Ga = 5/0 to 3/2) and drops sharply as the Ga fraction exceeds 50% (Al/Ga = 2/3 to 0/5) [25]. Given that the 450–460 nm window coincides with the peak emission of standard InGaN chips, this result defines an optimal compositional range (x = 3–5) for maximizing photon conversion efficiency in conventional white LED architectures. The divergence between the luminance–composition trends under n-UV and blue excitation is an intrinsic consequence of the differential redistribution of oscillator strength between the two 4f → 5d excitation manifolds by compositional substitution, in agreement with published data for $Y_3(Al,Ga)_5O_{12}$: Ce [26].

Note that these values represent relative luminance with respect to the SDL-4000 standard rather than absolute internal/external quantum efficiency (IQE/EQE); absolute quantum efficiency, requiring integrating-sphere measurements, was not determined in this study.

Chromaticity and correlated colour temperature

CIE 1931 chromaticity coordinates were calculated from the experimental PL spectra for each composition and excitation wavelength (Figure 8a, b). The resulting colour loci and correlated colour temperatures (CCT) are compiled in Table 3.



a b

Figure 8 – CIE 1931 chromaticity diagram showing the emission colour loci of $Y_3Al_xGa_{5-x}O_{12}$: Ce ceramics with different Al/Ga ratios under (a) λ = 350 nm and (b) λ = 450 nm excitation

A pronounced dependence of the CIE coordinates on excitation wavelength is observed for all compositions, which is a direct consequence of the unequal contributions of the 4f → $5d^2$ (340–360 nm) and 4f → $5d^1$ (450–470 nm) transitions to the population of the excited 5d manifold and the resulting differences in the spectral power distribution of the emission [28, 29]. Increasing Ga^{3+} content (decreasing x) shifts the chromaticity coordinates toward higher CCT values, corresponding to cooler (blue) emission, as a direct result of the reduced crystal-field splitting and the concomitant blue-shift of the Ce^{3+} emission maximum [27]. Collectively, the data in Table 3 demonstrate that the CCT is continuously tunable across a remarkably wide range–4618 to 9679 K–solely by adjusting the Al/Ga ratio and the pump wavelength, without changing the activator concentration or the matrix host cation.

Table 3 – CIE 1931 chromaticity coordinates and correlated colour temperatures (CCT) of $Y_3Al_xGa_{5-x}O_{12}$: Ce ceramics

Composition	CIE	λ_{ex} = 340 nm			λ_{ex} = 450 nm		
		x	y	CCT (K)	x	y	CCT (K)
$Y_3Al_5O_{12}$:Ce	x=5	0,3851	0,5720	4641	0,3874	0,5776	4618
$Y_3Al_4GaO_{12}$:Ce	x=4	0,3363	0,5913	5445	0,3449	0,5892	5301
$Y_3Al_3Ga_2O_{12}$:Ce	x=3	0,2544	0,5308	7247	0,2929	0,5586	6277
$Y_3Al_2Ga_3O_{12}$:Ce	x=2	0,2220	0,4855	8542	0,26484	0,5396	6952
$Y_3AlGa_4O_{12}$:Ce	x=1	0,2124	0,4354	9679	0,2425	0,5065	7722

Note: Data for x = 0 (Sample 641, $Y_3Ga_5O_{12}$: Ce) are not reported. Owing to the phase impurities present in this composition, the photoluminescence emission and excitation spectra of Sample 641 exhibited negligible, non-normalizable signal, which precluded reliable determination of the emission bandwidth (FWHM) and of the CIE 1931 chromaticity coordinates/CCT.

Diffuse reflectance spectra

Diffuse reflectance spectra recorded over the 200–600 nm range (Figure 9) are characterised by high reflectance in the long-wavelength region (λ > 500 nm), confirming the absence of strong absorption bands in the visible range–a feature expected for Ce^{3+}-activated garnet matrices [30]. Pronounced minima in the UV and near-visible regions correspond to the characteristic 4f → 5d absorption of Ce^{3+} and exhibit compositional shifts consistent with the excitation spectra (Section 3.2), corroborating the structural assignment of the spectral features.

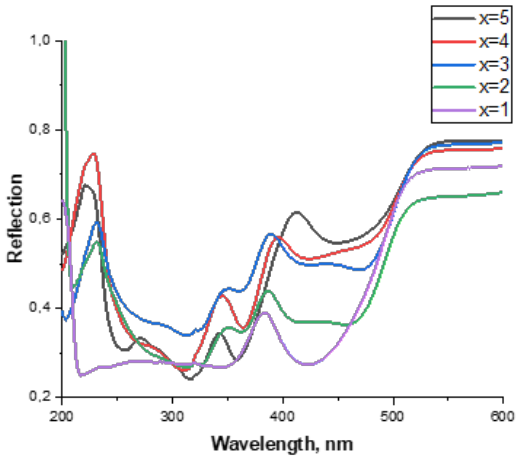


Figure 9 – Diffuse reflectance spectra of $Y_3Al_xGa_{5-x}O_{12}$:Ce ceramics as a function of Al/Ga ratio (200–600 nm)

Conclusion

Ceramic phosphors of the full $Y_3Al_xGa_{5-x}O_{12}$:Ce substitution series ($0 \leq x \leq 5$) have been synthesized for the first time by direct electron-beam radiation processing of binary oxide charge mixtures at a throughput of ≈5 g s^{-1} and a total irradiation time below 1 s per batch, without mineralizer additives or secondary energy sources. The principal findings are as follows:

- XRD phase analysis confirmed retention of the cubic garnet structure (space group Ia^3d) throughout the entire Al/Ga substitution range. The highest phase purity (garnet fraction > 99%) was achieved for compositions $Y_3Al_4GaO_{12}$:Ce and $Y_3Al_2Ga_3O_{12}$:Ce, while the terminal compositions ($x = 0$ and $x = 5$) showed measurable secondary-phase fractions.
- Systematic lattice contraction accompanies increasing Al content, consistent with the smaller ionic radius of Al^{3+} relative to Ga^{3+} in both octahedral and tetrahedral garnet sites.
- Compositional tuning of the Al/Ga ratio affords continuous and independent control over (i) the positions and relative intensities of the n-UV (340–370 nm) and blue (430–470 nm) excitation bands; (ii) the PL emission peak and FWHM (0.40–0.44 eV, weakly dependent on excitation wavelength); and (iii) the CIE 1931 chromaticity coordinates and CCT (4618–9679 K).
- Luminance analysis reveals that Al-rich compositions ($x = 3–5$) provide the highest photon conversion efficiency under both n-UV (340 nm) and blue (450 nm) excitation, defining the optimal compositional window for solid-state lighting applications; the non-monotonic divergence of luminance trends between n-UV and blue pumping is attributed to differential redistribution of oscillator strength between the two 4f → 5d excitation manifolds.
- All structural and optical properties are fully commensurate with data reported for $Y_3Al_xGa_{5-x}O_{12}$:Ce ceramics and crystals produced by conventional solid-state or solution methods, unambiguously validating the electron-beam radiation synthesis route as a viable rapid-throughput alternative for multi-component phosphor ceramics.

The established composition–property relationships provide a quantitative basis for the optimization of radiation synthesis parameters and precursor compositions in the targeted fabrication of YAGG:Ce ceramic phosphors for n-UV-pumped and blue-pumped solid-state lighting, as well as for extension of the radiation synthesis approach to other technologically relevant refractory oxide ceramics.

REFERENCES

1 Ueda, J., and Tanabe, S. Review of luminescent properties of Ce^{3+}–doped garnet phosphors: new insight into the effect of crystal and electronic structure. Optical Materials: X, 1, 100018 (2019). https://doi.org/10.1016/j.omx.2019.100018

2 Lin, Y., Bettinelli, M., Sharma, S.K., Redlich, B., Speghini, A., and Karlsson, M. Unraveling the impact of different thermal quenching routes on the luminescence efficiency of the $Y_3Al_5O_{12}:Ce^{3+}$ phosphor for white light emitting diodes. Journal of Materials Chemistry C, 8, 14015–14027 (2020). https://doi.org/10.1039/D0TC03821K

3 Du, B., Li, W., Zhang, L., Chen, P., and Lu, F. Recent advances in preparing transparent phosphor ceramics for high–index color rendering and high–power lighting. Molecules, 29 (6), 1325 (2024). https://doi.org/10.3390/molecules29061325

4 Liu, Y., Liu, S., Sun, P., et al. Transparent ceramics enabling high luminous flux and efficacy for the next–generation high–power LED light. ACS Applied Materials & Interfaces, 11 (24), 21697–21701 (2019). https://doi.org/10.1021/acsami.9b02703

5 Fang, M.–H., Bao, Z., Huang, W.–T., and Liu, R.–S. Evolutionary generation of phosphor materials and their progress in future applications for light–emitting diodes. Chemical Reviews, 122 (13), 11474–11513 (2022). https://doi.org/10.1021/acs.chemrev.1c00952

6 Tulegenova, A.T., Nogaibekova, G.Zh., Saidazimov, I.A., Vilchinskaya, S.S., and Markhabayeva, A.A. Spectral Characteristics of Photoluminescence Synthesized in the Field of Radiation YAGG Phosphors with

Different Al/Ga Ratio. Bulletin of the Karaganda University. Physics series, 4 (116), 114–122 (2024). https://doi.org/10.31489/2024PH4/114-122

7 Fu, S., Tan, J., Bai, X., Yang, S., You, L., and Du, Z. Effect of Al/Ga substitution on the structural and luminescence properties of $Y_3(Al_{1-x}Ga_x)_5O_{12}:Ce^{3+}$ phosphors. Optical Materials, 75, 573–579 (2018). https://doi.org/10.1016/j.optmat.2017.11.021

8 Khan, N.Z., Lee, H., Jo, D.Y., et al. The developments of cyan emitting phosphors to fulfill the cyan emission gap of white-LEDs. Frontiers in Chemistry, 11, 1274410 (2023). https://doi.org/10.3389/fchem.2023.1274410

9 Xia, Z., and Meijerink, A. Ce^{3+}-doped garnet phosphors: Composition modification, luminescence properties and applications. Chemical Society Reviews, 46 (1), 275–299 (2017). https://doi.org/10.1039/C6CS00551A

10 Lisitsyn, V., Tulegenova, A., Golkovski, M., Polisadova, E., Lisitsyna, L., Mussakhanov, D., and Alipysova, G. Radiation synthesis of high-temperature wide-bandgap ceramics. Micromachines, 14 (12), 2193 (2023). https://doi.org/10.3390/mi14122193

11 Sifat, R., and Grosvenor, A.P. Examination of the site preference in garnet type ($X_3A_2B_3O_{12}$; X = Y, A/B = Al, Ga, Fe) materials. Solid State Sciences, 83, 116–124 (2018). https://doi.org/10.1016/j.solidstatesciences.2018.06.013

12 Jiang, L., Zhang, X., Zhu, S., et al. Preparation and luminescence properties of $Y_{3-\gamma}Al_{5-x}Ga_xO_{12}:Ce^{3+}_{\gamma}$ phosphors. Journal of Materials Science: Materials in Electronics, 29 (11), 9350–9358 (2018). https://doi.org/10.1007/s10854-018-8930-6

13 Bartosiewicz, K., Babin, V., Kamada, K., Yoshikawa, A., Kurosawa, S., Beitlerova, A., Kucerkova, R., Nikl, M., and Zorenko, Y. Ga for Al substitution effects on the garnet phase stability and luminescence properties of $Gd_3Ga_xAl_{5-x}O_{12}$:Ce single crystals. Journal of Luminescence, 216, 116724 (2019). https://doi.org/10.1016/j.jlumin.2019.116724

14 Zhu, S., Zhang, X., Li, W., Liu, M., Cheng, L., Mi, X., and Lu, L. Phase transformation and luminescence properties of $Y_{2.94}Al_{5-x}Ga_xO_{12}:0.06Ce^{3+}$ phosphors. Ceramics International, 45 (5), 6060–6066 (2019). https://doi.org/10.1016/j.ceramint.2018.11.196

15 Kim, J.S., Kim, Y.H., Kim, H.L., et al. Tailoring trap depth and emission wavelength in $Y_3Al_{5-x}Ga_xO_{12}:Ce^{3+},V^{3+}$ persistent luminescent phosphors-in-glass films. ACS Applied Materials & Interfaces, 10 (31), 25975–25984 (2018). https://doi.org/10.1021/acsami.8b10713

16 Bolek, P., Zeler, J., Brites, C.D.S., Trojan-Piegza, J., Carlos, L.D., and Zych, E. Ga-modified YAG:Pr^{3+} dual-mode tunable luminescence thermometers. Chemical Engineering Journal, 421, 129764 (2021). https://doi.org/10.1016/j.cej.2021.129764

17 Chan, J., Cao, L., Li, W., Ma, N., Xu, Z., and Huang, X. Highly efficient broad-band green-emitting cerium(III)-activated garnet phosphor allows the fabrication of blue-chip-based warm-white LED device with a superior color rendering index. Inorganic Chemistry, 61 (18), 6953–6963 (2022). https://doi.org/10.1021/acs.inorgchem.2c00326

18 Barta, J., Pestovich, K.S., Valdez, J.A., Wiggins, B.W., Richards, C., Smith, E., Clayton, J.H., Smalley, D., and McClellan, K.J. Compositional screening of Ce-doped $(Gd,Lu,Y)_3(Al,Ga)_5O_{12}$ ceramics prepared by quenching from melt and their luminescence properties. Journal of Alloys and Compounds, 896, 161687 (2022). https://doi.org/10.1016/j.jallcom.2021.161687

19 He, C., Ji, H., Huang, Z., Wang, T., Zhang, X., Liu, Y., Fang, M., Wu, X., Zhang, J., and Min, X. Red-Shifted Emission in $Y_3MgSiAl_3O_{12}:Ce^{3+}$ Garnet Phosphor for Blue Light-Pumped White Light-Emitting Diodes. Journal of Physical Chemistry C, 122 (27), 15659–15665 (2018). https://doi.org/10.1021/acs.jpcc.8b03940

20 Qu, M.-Y., Li, T.-Q., and Liu, Q.-L. Photoluminescence Properties of Cyan-Emitting $Lu_3Ga_xAl_{5-x}O_{12}:Ce^{3+}$ Garnet Phosphors Synthesized in Nonreducing Atmosphere and at Different Temperature for High Quality w-LEDs. Materials, 15 (19), 6817 (2022). https://doi.org/10.3390/ma15196817

21 Ha, H., Yang, S., and Park, S. Photoluminescence Spectra Correlations with Structural Distortion in Eu^{3+}- and Ce^{3+}-Doped $Y_3Al_{5-2x}(Mg,Ge)_xO_{12}$ (x = 0, 1, 2) Garnet Phosphors. Materials, 17 (10), 2445 (2024). https://doi.org/10.3390/ma17102445

22 Solovjovas, A., Sidletskiy, O., Gerasymov, I., Nargelas, S., Soltanaitė, G., Podlipskas, Ž., Auffray, E., and Tamulaitis, G. Influence of gallium content on luminescence properties of Ce-doped yttrium aluminum gallium garnet scintillator. Optical Materials, 163, 117480 (2025). https://doi.org/10.1016/j.optmat.2025.117480

23 Babin, V., Buryi, M., Chlan, V., Fomichov, Y., Kamada, K., Laguta, V.V., Nikl, M., Pejchal, J., Štěpánková, H., Yoshikawa, A., Zagorodniy, Yu., and Zazubovich, S. Influence of gallium content on Ga^{3+}

position and photo- and thermally stimulated luminescence in Ce^{3+}-doped multicomponent $(Y,Lu)_3Ga_xAl_{5-x}O_{12}$ garnets. Journal of Luminescence, 200, 141–150 (2018). https://doi.org/10.1016/j.jlumin.2018.04.013

24 Zorenko, Yu., Zorenko, T., Malinowski, P., Sidletskiy, O., and Neicheva, S. Luminescent properties of $Y_3Al_{5-x}Ga_xO_{12}$:Ce crystals. Journal of Luminescence, 156, 102–107 (2014). https://doi.org/10.1016/j.jlumin.2014.07.011

25 Ma, N., Zhang, Z., Li, W., and Huang, X. Efficient blue-light-excited cyan-emitting $CaLu_2HfScAl_3O_{12}:Ce^{3+}$ phosphors for full-visible-spectrum warm-white LEDs. Journal of Luminescence, 263, 120060 (2023). https://doi.org/10.1016/j.jlumin.2023.120060

26 Dorenbos, P. 5d-level energies of Ce^{3+} and the crystalline environment. IV. Aluminates and "simple" oxides. Journal of Luminescence, 99, 283–299 (2002). https://doi.org/10.1016/S0022-2313(02)00347-2

27 Zou, J., Yang, B., Qian, X., et al. Effect of Al/Ga substitution on photoluminescence and chromatic properties of $Y_3Al_{5-x}Ga_xO_{12}:Ce^{3+}$ phosphor. Journal of Materials Science: Materials in Electronics, 27, 8074–8079 (2016). https://doi.org/10.1007/s10854-016-4806-9

28 He, X., Wang, X., Yu, H., Lei, B., Fu, Z., and Zhang, S. Effects of local structure of Ce^{3+} ions on luminescent properties of YAG:Ce phosphors. Scientific Reports, 6, 22238 (2016). https://doi.org/10.1038/srep22238

29 Khanin, V., Venevtsev, I., Chernenko, K., Pankratov, V., Klementiev, K., van Swieten, T., van Bunningen, A.J., Vrubel, I., Shendrik, R., Ronda, C., Rodnyi, P., and Meijerink, A. Exciton interaction with Ce^{3+} and Ce^{4+} ions in $(LuGd)_3(Ga,Al)_5O_{12}$ ceramics. Journal of Luminescence, 237, 118150 (2021). https://doi.org/10.1016/j.jlumin.2021.118150

30 Li, Z., Zhang, Y., Huang, Y., Wang, L., and Zheng, H. Ce^{3+} Yellow Phosphors Prepared by Different Methods. Materials, 8 (7), 4436–4447 (2015).

[1]Тулегенова А.Т.,
доцент, PhD, ORCID ID: 0000-0002-5701-6674,
e-mail: tulegenova.aida@gmail.com
[2]Лисицын В.М.,
профессор, ф.-м.ғ.д., ORCID ID: 0000-0002-2075-4796,
e-mail: lisitsyn@tpu.ru
[1]Ноғайбекова Г.Ж.,
аға оқытушы, ORCID ID: 0009-0008-8688-4279,
e-mail: nogaibekovagulnur@gmail.com
[3]Лисицына Л.А.,
профессор, ф-м.ғ.д., ORCID ID: 0000-0001-6273-6345,
e-mail: lisitsyna@mail.ru

[1]Әл-Фараби атындағы Қазақ ұлттық университеті, Алматы қ., Қазақстан
[2]Томск политехникалық университеті, Томск қ,. Ресей
[3]Томск мемелекеттік сәулет-құрылыс университеті, Томск қ,. Ресей

ЖАРЫҚДИОДТАРДА ҚОЛДАНУ ҮШІН $Y_3AL_XGA_{5-X}O_{12}$:CE ЛЮМИНОФОРЛАРЫНЫҢ ОПТИКАЛЫҚ ҚАСИЕТТЕРІНЕ AL/GA ҚАТЫНАСЫНЫҢ ӘСЕРІ

Аңдатпа

Радиациялық әдіспен алғаш рет синтезделген $Y_3Al_xGa_{5-x}O_{12}$:Ce (YAGG:Ce) керамикалық люминофорларының зерттеу нәтижелері ұсынылған. Жарық диодты жарық көздерінде қолдануға перспективалы Ce^{3+} иондарымен легирленген $Y_3Al_xGa_{5-x}O_{12}$:Ce (YAGG:Ce) гранаттары негізіндегі люминофорлардың оптикалық сипаттамаларына Al/Ga қатынасының әсері зерттелді. Белсендіруші Ce^{3+} иондарыныың концентрациясы тұрақты болған жағдайда, алюминий мен галлий мөлшері әртүрлі үлгілердің қоздыру және фотолюминесценция спектрлері талданды. Құрамның өзгеруі қоздыру және сәуле шығару жолақтарының орны мен пішінінің қайта құрылуына, фотолюминесценция жолақтарының енінің өзгеруіне, сондай-ақ

спектрдің ультракүлгін және көк аймақтарында қоздыру кезінде сәуле шығару қарқындылығының қайта бөлінуіне алып келетіні көрсетілді. Al/Ga қатынасы азайған кезде қоздыру жолағының 340-370 нм маңындағы ұзын толқынды аймаққа ығысатыны анықталды, бұл жақын ультракүлгін және күлгін диапазондағы жарықдиодтарды қолдану кезінде қоздыру тиімділігін арттырады. Алынған нәтижелер радиациялық әдісті тиімді YAGG:Ce люминофорларын синтездеу үшін қолдануға болатындығын растайды.

Түйін сөздер: люминофорлар, $Y_3Al_xGa_{5-x}O_{12}$:Ce, Al/Ga қатынасы, қозу спектрлері, фотолюминесценция, жарықдиод, ультракүлгін.

[1]Тулегенова А.Т.,
доцент, PhD, ORCID ID: 0000-0002-5701-6674,
e-mail: tulegenova.aida@gmail.com
[2]Лисицын В.М.,
профессор, д.ф-м.н., ORCID ID: 0000-0002-2075-4796
e-mail: lisitsyn@tpu.ru
[1]Ноғайбекова Г.Ж.,
ст. преподаватель, ORCID ID: 0009-0008-8688-4279,
e-mail: nogaibekovagulnur@gmail.com
[3]Лисицына Л.А.,
профессор, д.ф-м.н., ORCID ID: 0000-0001-6273-6345,
e-mail: lisitsyna@mail.ru

[1]Казахский национальный университет им. аль-Фараби, г. Алматы, Казахстан
[2]Томский политехнический университет, г. Томск, Россия
[3]Томский государственный архитектурно-строительный университет, г. Томск, Россия

ВЛИЯНИЕ СООТНОШЕНИЯ AL/GA НА ОПТИЧЕСКИЕ СВОЙСТВА ЛЮМИНОФОРОВ $Y_3AL_XGA_{5-X}O_{12}$:CE ДЛЯ СВЕТОДИОДНЫХ ПРИМЕНЕНИЙ

Аннотация

Приведены результаты исследований впервые синтезированных радиационным методом керамических люминофоров $Y_3Al_xGa_{5-x}O_{12}$:Ce (YAGG:Ce). Исследовано влияние соотношения Al/Ga на оптические характеристики люминофоров на основе Ce^{3+}–легированных гранатов $Y_3Al_xGa_{5-x}O_{12}$:Ce (YAGG:Ce), перспективных для применения в светодиодных источниках света. Проанализированы спектры возбуждения и фотолюминесценции образцов с различным содержанием алюминия и галлия при фиксированной концентрации активаторных ионов Ce^{3+}. Показано, что изменение состава приводит к перестройке положения и формы полос возбуждения и излучения, изменению ширины полосы фотолюминесценции, а также к перераспределению интенсивности излучения при возбуждении в ультрафиолетовой и синей областях спектра. Установлено, что при уменьшении отношения Al/Ga полоса возбуждения смещается в длинноволновую область вблизи 340–370 нм, что повышает эффективность возбуждения при использовании светодиодов ближнего ультрафиолетового и фиолетового диапазонов. Полученные результаты подтверждают возможность использования радиационного метода для синтеза эффективных YAGG:Ce люминофоров.

Ключевые слова: люминофоры, $Y_3Al_xGa_{5-x}O_{12}$:Ce, соотношение Al/Ga, спектры возбуждения, фотолюминесценция, светодиоды, ультрафиолет.

UDC 538.975
IRSTI 29.19.22

https://doi.org/10.55452/1998-6688-2026-23-3-486-497

[1]Ryskaliyeva M.M.,
master's student, ORCID ID: 0009-0000-1225-0013,
e-mail: m.ryskaliyeva@kbtu.kz
[1]Kusainova A.Z.,
PhD student, ORCID ID: 0000-0002-2485-9739,
e-mail: a.kusainova@kbtu.kz
[1]Eshanov A.,
master's student, ORCID ID: 0009-0003-4051-5180,
e-mail: AmirEshanov@yandex.ru
[1]Zhirkov I.V.,
master's student, ORCID ID: 0009-0003-0785-0526,
e-mail: il_zhirkov@kbtu.kz
[2]Akhadov J.Z.,
Dr.Sci. (Tech.), professor, ORCID ID: 0009-0005-9013-7573,
e-mail: ims-79@mail.ru
[1]Sultanov A.T.,
PhD, assistant professor, ORCID ID: 0000-0003-0074-431X,
e-mail: a.sultanov@kbtu.kz
[1*]Beisenkhanov N.B.,
Dr.Sci. (Phys.-Math.), professor, ORCID ID: 0000-0002-5908-5614,
*e-mail: n.beisenkhanov@kbtu.kz

[1]Kazakh-British Technical University, Almaty, Kazakhstan
[2]National scientific research institute of renewable energy sources under Ministry of Energy of the Republic of Uzbekistan, Tashkent, Uzbekistan

ANALYZING THE EFFECTS OF SPIN-COATED PHOSPHOSILICATE GLASS ON THE CRYSTALLIZATION PROCESS OF SILICON THIN FILMS DEPOSITED VIA MAGNETRON SPUTTERING

Abstract

This study investigates the influence of spin-coated phosphosilicate glass (PSG) on the crystallization and electrical properties of silicon (Si) thin films deposited by magnetron sputtering, with a focus on optimizing their structural and electrical properties for potential applications in photovoltaics and microelectronics. The results demonstrate that higher spin-coating speeds lead to thinner and more uniform PSG layers, which in turn promote more efficient phosphorus diffusion and enhance film crystallization. Annealing at 950 °C resulted in enhanced dopant activation, improved crystallinity, and reduced sheet resistance. These structural and phase transformations were systematically analyzed by X-ray diffraction (XRD), providing detailed insight into the evolution of the Si thin films during thermal processing. In particular, the XRD results reveal a clear transition from the amorphous to the polycrystalline state, especially for samples processed at optimized spin speeds and elevated annealing temperatures. Optical characterization further showed that thermal annealing modified the reflectance and transmittance spectra and slightly increased the refractive index and extinction coefficient of the sputtered Si films. Overall, the combination of environmentally friendly spin-on doping with scalable physical deposition techniques represents a promising approach for the development of advanced photovoltaic technologies, offering a viable pathway toward sustainable and efficient device fabrication.

Keywords: silicon; crystallization; phosphosilicate glass; magnetron sputtering.

Received January 14, 2026; revised July 29, 2026; accepted August 3, 2026.

Introduction

The rapid development of renewable energy technologies is driven by the global demand for sustainable energy sources and the urgent need to reduce dependence on fossil fuels [1]. In this context, photovoltaic (PV) technology has emerged as one of the most promising clean energy solutions due to its scalability, environmental compatibility, and strong potential to satisfy long-term energy demands [2]. Among the various materials used in PV devices, silicon (Si) remains the dominant choice in the industry, owing to its abundance, well-established processing infrastructure, and continuous performance improvements aimed at enhancing conversion efficiency while reducing manufacturing costs [3, 4]. One of the most promising approaches in Si solar cell advancement is the Tunnel Oxide Passivated Contact (TOPCon) technology [5]. The defining characteristic of TOPCon cells lies in the use of an ultra-thin tunnel oxide layer combined with a heavily doped polycrystalline Si (poly-Si) layer, forming a selective contact that significantly suppresses carrier recombination at the interface. The introduction of the thin SiO_x layer enables tunneling selectivity, facilitating electron or hole transport from the Si substrate to the n^+ or p^+ poly-Si layer while effectively suppressing minority carriers. As a result of these innovations, TOPCon cells have achieved notable progress in conversion efficiency, reaching up to 25.1% in laboratory environment placing them among the top-performing crystalline Si (c-Si) solar technologies [6, 7]. Such a combination of high efficiency potential and reduced recombination losses has made TOPCon technology particularly attractive for industrial-scale photovoltaic production. For example, recently TOPCon cells have been implemented by leading c-Si photovoltaic manufacturers as an effective approach to minimize recombination losses [8, 9].

In conventional TOPCon device fabrication, thin Si layers are most commonly deposited by plasma-enhanced chemical vapor deposition (PECVD) [10]. This technique offers good conformality and relatively low processing temperatures; however, it also suffers from several intrinsic limitations. In particular, PECVD-deposited Si layers often exhibit hydrogen incorporation, limited control over film density, and sensitivity to plasma-induced damage at the interface, which can adversely affect the electrical properties and thermal stability of subsequent poly-Si/SiO_x structures. Furthermore, conventional PECVD-based fabrication generally requires the use of hazardous precursor gases, including pyrophoric silane (SiH_4) for silicon deposition and toxic phosphine (PH_3) for in-situ phosphorus doping. These gas chemistries impose stringent safety regulations, increase equipment complexity, and contribute to higher manufacturing costs, particularly in industrial-scale production [11]. Moreover, achieving precise thickness control and high uniformity over large areas while maintaining low defect density remains challenging, especially under industrial throughput requirements.

In recent years, the physical vapor deposition (PVD) of Si-based materials has gained significant attention as a promising approach for overcoming specific technological challenges [12]. PVD techniques, including sputtering and evaporation, enable precise control over film thickness and uniformity, facilitating the formation of thin and homogeneous Si layers [13]. Among various deposition methods, magnetron sputtering stands out as one of the most efficient and versatile approaches [14, 15, 16]. Ex situ doping plays a crucial role in the fabrication of high-performance poly-Si passivating contacts by enabling the introduction and activation of dopants required to achieve the desired electrical properties [17]. Ex situ doping method include $POCl_3$ diffusion, ion implantation and spin-on doping (SOD), which are widely used for introducing dopants into silicon layers [18]. It also approaches substantial benefits in terms of processing flexibility, patterning potential, and industrial applicability [19]. Ex-situ doping using SOD solutions represents a promising approach for the fabrication of poly-Si contacts [20]. SOD has emerged as a cost-effective and environmentally friendly alternative to other methods. The application of SOD solutions offers a more straightforward and cost-effective fabrication route compared to conventional doping methods such as ion implantation, as the dopant solutions can be easily prepared and applied [21]. It should be noted that the fabrication of high-quality TOPCon passivating contacts requires careful optimization

of the thermal processing conditions, particularly the annealing temperature and duration. These parameters govern not only the crystallization of the silicon layer but also dopant diffusion and activation, which together determine the structural and electrical quality of the poly-Si/SiO_x passivating contact. A comprehensive understanding of the simultaneous crystallization and doping processes is essential for achieving high-performance TOPCon structures while minimizing defect formation and preserving the integrity of the interfacial oxide [22]. Therefore, an optimal annealing temperature must be established, depending on the specific properties of both the n-type poly-Si layer and the interfacial oxide.

This work focuses on the fabrication and systematic investigation of Si thin films deposited by RF magnetron sputtering and subsequently doped using an ex-situ SOD approach based on PSG. The study aims to elucidate the role of thermal annealing and PSG-assisted phosphorus diffusion on the crystallization behavior, microstructural evolution, and electrical properties of sputtered Si films. Particular attention is given to the influence of annealing temperature and spin-coating parameters, dopant activation and sheet resistance. The results demonstrate a strong correlation between enhanced crystallinity and improved electrical performance of poly-Si films, highlighting the potential of combining RF sputtering with environmentally friendly SOD techniques for the development of high-quality poly-Si layers for photovoltaic applications.

Materials and methods

Monocrystalline p-type Si <100> Czochralski (CZ) wafers from JSC PCMP were used as a substrate. The resistivity of the Si wafers was 0.5-1.5 Ω· cm, the thickness was 200±15 μm and the area was 125 × 125 mm^2. Tetraethyl orthosilicate (TEOS, 99.0% Sigma-Aldrich, Germany), phosphoric acid (H_3PO_4, 85% AppliChem, Spain), ethanol (70% C_2H_5OH was purchased from a local supplier) and water (DI H_2O) were used in order to prepare doping solution. All the reagents were used for analytical grade and used without further purification.

A two-stage cleaning process was performed prior to deposition. First, the substrates were treated with hydrofluoric acid (HF, 3% Sigma-Aldrich, Germany), followed by Standard Clean 2 (SC-2) using a hydrochloric acid-hydrogen peroxide solution (HCl, 35% LaborPharma LTD, Kazakhstan : H_2O_2, LaborPharma LTD, Kazakhstan). Thin Si films were deposited using a MAGNA TM-200-01 system via RF sputtering using Si target (Kurt J. Lesker, Germany). The base pressure was set to Pa. The deposition was carried out at a power of 200 W, with a chamber pressure of 0.5 Pa and a substrate temperature of 100 °C. The Ar flow rate was precisely regulated using a needle valve to maintain a constant working pressure. Deposition rate was measured, and this value was subsequently used to calculate the deposition times necessary to achieve film thicknesses of 50 nm and 300 nm. Subsequently, under the same pressure conditions, additional films were deposited at a power of 250 W, also maintaining the substrate temperature at 100 °C. The distance between target and substrate was 90 mm. The processing parameters for sputtering are shown in Table 1. Thickness control was carried out by measuring XRR spectra.

Table 1 – Parameters for sputtering

Film thickness (nm)	Substrate	Pressure (Pa)	RF power (W)	Sputtering time (s)	Deposition rate (nm/s)	Target	Sputtering gas	Temperature of substrate (°C)
300	Silicon	0.5	200	3330	0.09	Silicon	Argon	100
			250	2400	0.13			
50	Silicon	0.5	200	555	0.09	Silicon	Argon	100
			250	400	0.13			

The subsequent step involved fabricating a doped Si layer by applying the phosphorus-containing solution via SOD. The phosphorus solution was prepared by mixing TEOS, 70% C_2H_5OH and 85% H_3PO_4, which served as both dopant and hydrolytic catalyst, with the phosphoric acid concentration set at 2 M (Figure 1) [23]. This solution was then applied onto amorphous silicon (a-Si) samples using SOD at three different rotation speeds: 1500 rpm, 3000 rpm, and 4500 rpm. An additional control sample was also prepared for comparative analysis. For all samples, the coating duration was fixed at 20 seconds, and a precise volume of 100 μL of phosphorus-containing solution was dispensed using a micropipette to ensure uniform deposition across the substrate surface.

A series of Si thin film samples were annealed in a tube furnace under a nitrogen atmosphere at one atmospheric pressure. The furnace was heated at a rate of 10 °C/min, requiring approximately 75, 85 and 95 min to reach the target temperatures of 750 °C, 850 °C and 950 °C, respectively. Upon reaching the target temperature, the samples were held for 30 min. After annealing, the samples were allowed to cool naturally inside the furnace to room temperature over approximately 2 h. One additional sample was kept without annealing and used as a control to evaluate the influence of thermal processing. After the annealing process, the oxide layer formed on the surface of the samples was removed using a 3% HF solution.

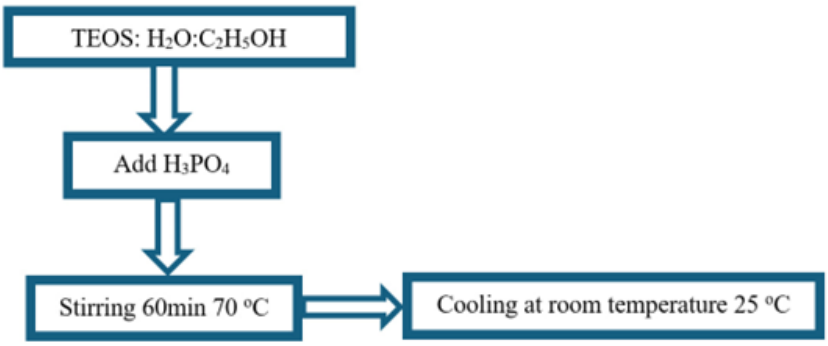


Figure 1 – Diagram illustrating the sequence
of steps for preparing the phosphorus-containing solution

Sheet resistance of the films was measured using the four-point probe method with a Keithley 2400 SourceMeter (SMU). The crystal structure of the silicon thin films was characterized by Grazing-incidence X-ray diffraction (XRD) method using a ComplexRay C6 diffractometer equipped with a CuKα X-ray source (λ = 0.154 nm). The diffraction patterns were recorded over a 2θ range of 20°–60° with a step size of 0.05° and a counting time of 30 sec per step. The incident angle in GIXRD mode was set to 1°. For clearer presentation, the XRD spectra were smoothed using tools available in Origin software. The optical properties of the films were measured on Evolution 300 installation and surface morphology were measured by SEM using JEOL JSM-IT210 system.

Results and discussions

To identify the most optimal temperature for Si thin film that yields high-quality poly-Si, the films were annealed in the absence of PSG layers. XRD analysis was performed to evaluate the crystallinity of all samples. The diffraction patterns were recorded, focusing on characteristic Si peaks at approximately 2θ = 28°, 47°, and 56°, corresponding to the (111), (220), and (311) crystallographic planes of Si, respectively [24]. The intensity and sharpness of these peaks were used to assess the degree of crystallization.

The XRD patterns of the Si thin films annealed at different temperatures are presented in figure 2. The XRD spectra of the control deposited a-Si sample is featureless, indicating its amorphous nature.

However, after annealing, three main diffraction peaks emerge, confirming the crystallization of the Si films. Based on the XRD results, annealing at 850 °C and 950 °C produced the most intense and stable diffraction peaks, indicating that these temperatures are optimal for further investigation. The enhanced peak intensities suggest improved crystallization and higher structural quality of the poly-Si films. In particular, a strong (111) diffraction peak was observed under these conditions, indicating a predominant <111> crystallographic orientation, which is typical of anisotropic crystallization behavior in Si [25].

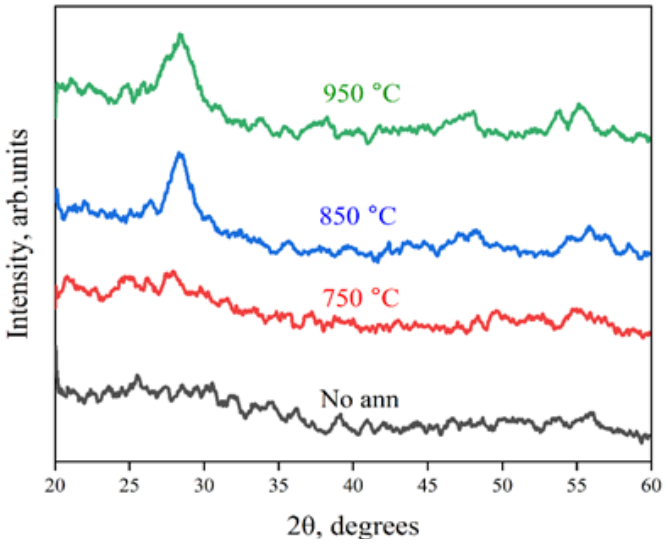


Figure 2 – XRD patterns of poly-Si films annealed at different temperatures ranging from 750 °C to 950 °C

Figure 3 demonstrates the effect of sputtering power, annealing temperature and spin coating speed of the PSG layer on the XRD patterns of RF-sputtered poly-Si films. It seems that the sample lacking a spin-coated PSG layer (0 rpm, depicted by the black curve in the XRD spectrum) exhibited the lowest diffraction peak intensity, indicating a predominantly amorphous film structure. An increase in spin speed corresponded with progressively sharper and more intense diffraction peaks near 28°, indicative of enhanced crystalline order. The samples processed at 3000 rpm and 4500 rpm showed the most pronounced and narrow peaks. Additionally, when evaluating the impact of varying RF power during sputtering, the sample deposited at 250 W displayed marginally higher peak intensity compared to that at 200 W, suggesting that elevated RF power facilitates improved crystallization by supplying greater energy during film growth, thereby resulting in denser and more crystalline films.

The integral area under the main diffraction peaks in the XRD spectrum was analyzed (Figure 4). The integral area increases with annealing temperature and reaches a maximum at 950 °C, indicating a higher crystalline fraction and improved crystallinity of the Si thin films. The integral area represents the total diffracted intensity, which is directly related to the amount of crystalline material present in the sample. An increase in the integral area of the diffraction peaks indicates a higher proportion of crystalline material relative to amorphous atoms. This trend indicates that the crystallization process improves with the increase in the integral area of the diffraction peaks, resulting in a more ordered crystal structure and enhanced crystalline quality of the Si thin films. Therefore, expansion of the diffraction peak integral area at higher annealing temperatures demonstrates that the applied annealing conditions successfully optimize the crystalline properties of the films and validate the proposed processing approach.

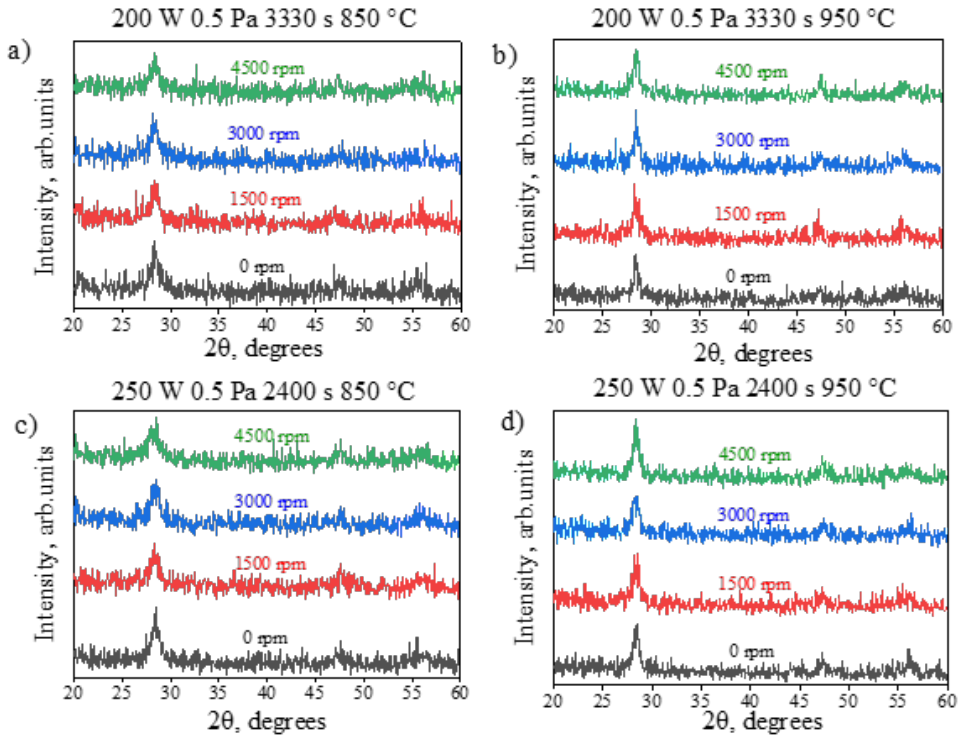


Figure 3 – XRD patterns of poly-Si films deposited by RF magnetron sputtering at different sputtering powers and annealing temperatures: (a) 200 W, 850 °C; (b) 200 W, 950 °C; (c) 250 W, 850 °C; and (d) 250 W, 950 °C

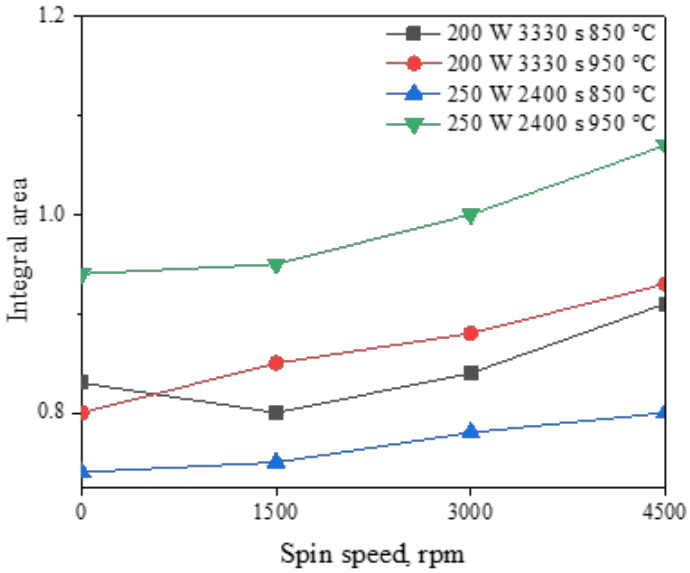


Figure 4 – Integral area of thin Si films as a function of deposition spin speed (rpm) during RF sputtering at powers of 200 W and 250 W at temperatures of 850 °C and 950 °C

Based on the XRD results, the sample deposited at a sputtering power of 250 W and annealed at 950 °C showed the highest diffraction peak intensity, suggesting enhanced crystallinity. Consequently, this sample was selected for subsequent optical property analysis. For the optical measurements, reflectance spectra were obtained from Si thin films deposited on high-resistivity p-type Si substrates, while transmittance spectra were recorded on quartz substrates.

Figure 5a and 5b present optical analyses of reflectance and transmittance spectra of the sputtered Si thin films before and after tube furnace annealing. The optical measurements reveal that annealing influences the optical response of the deposited films over the investigated wavelength range. After annealing, the reflectance spectrum exhibits a slight increase in the visible region (300–600 nm) and decrease in the near-infrared region (approximately 850–950 nm). In addition, the reflectance minimum around 750 nm becomes more pronounced, indicating a modification of the interaction between the incident light and the Si thin films after thermal treatment. The transmittance spectra retain a similar overall profile before and after annealing. However, a slight reduction in transmittance is observed throughout most of the measured wavelength range. These changes suggest that thermal annealing alters the optical characteristics of the sputtered Si films while preserving their general optical behavior.

Both reflectance and transmittance data were analyzed using SCOUT software. By processing the obtained optical spectra, key parameters such as film thickness, refractive index (n), and extinction coefficient (k) were measured. According to the SCOUT software analysis, thickness showed before annealing 320 nm and after annealing 293 nm. Meanwhile Figure 5c presents the wavelength dependence of the refractive index (n) and extinction coefficient (k) of the sputtered Si thin films before and after thermal annealing. It can be observed that the refractive index increases slightly after annealing over the entire investigated wavelength range. Nevertheless, both samples exhibit a similar spectral behavior, with the refractive index reaching its maximum value in the short-wavelength region followed by a gradual increase toward longer wavelengths. The extinction coefficient also increases after annealing, particularly in the wavelength range below approximately 500 nm, whereas at longer wavelengths the values of k approach zero for both samples. This behavior indicates reduced optical absorption in visible and near-infrared regions. The changes in the optical constants after annealing are consistent with the modification of the optical response observed in the reflectance and transmittance spectra. These results further confirm that thermal annealing influences the optical properties of the sputtered Si thin films through structural changes induced during the heat treatment. Therefore, the UV-Vis measurements complement the structural characterization and provide a more comprehensive evaluation of the sputtered Si thin films for potential TOPCon solar-cell applications.

To further investigate the surface characteristics of the deposited Si thin films, SEM analysis was performed, as shown in Figure 5d. The SEM image reveals a continuous and relatively uniform film surface without visible cracks or delamination. The homogeneous surface morphology indicates that the deposition process produced high-quality Si films.

The box plots in Figure 6 illustrate the distribution of sheet resistance values for phosphorus-doped poly-Si films under different sputtering powers, spin coating speeds, film thicknesses and annealing temperatures. In figure 6a, which depicts 300 nm-thick films deposited at 200 W and annealed at 850 °C, sheet resistance noticeably decreases as spin speed increases. Notably, films deposited at 250 W consistently demonstrate lower sheet resistance compared to those deposited at 200 W, reflecting enhanced film uniformity, and improved electrical conductivity at higher sputtering power. Upon annealing at 950 °C (figure 6b), all samples exhibited a significant reduction in sheet resistance. Si films deposited at 250 W exhibited low and uniform sheet resistance across spin speeds, demonstrating effective dopant activation via high temperature annealing. In contrast, 200 W samples showed higher resistance and variability, indicating reduced dopant activation efficiency. Figure 6c presents the sheet resistance of 50 nm-thick films annealed at 850 °C. These thinner films exhibit consistently low sheet resistance across all spin speeds, particularly at 250 W sputtering power, with minimal variation. This behavior suggests that thinner films promote more efficient phosphorus

diffusion and dopant activation, even at lower annealing temperatures, especially when combined with higher sputtering power. Overall, the box plots demonstrate that higher sputtering power, increased spin speed, greater annealing temperature, and reduced film thickness all contribute to lower and more uniform sheet resistance, indicating better electrical performance of the phosphorus-doped poly-Si films.

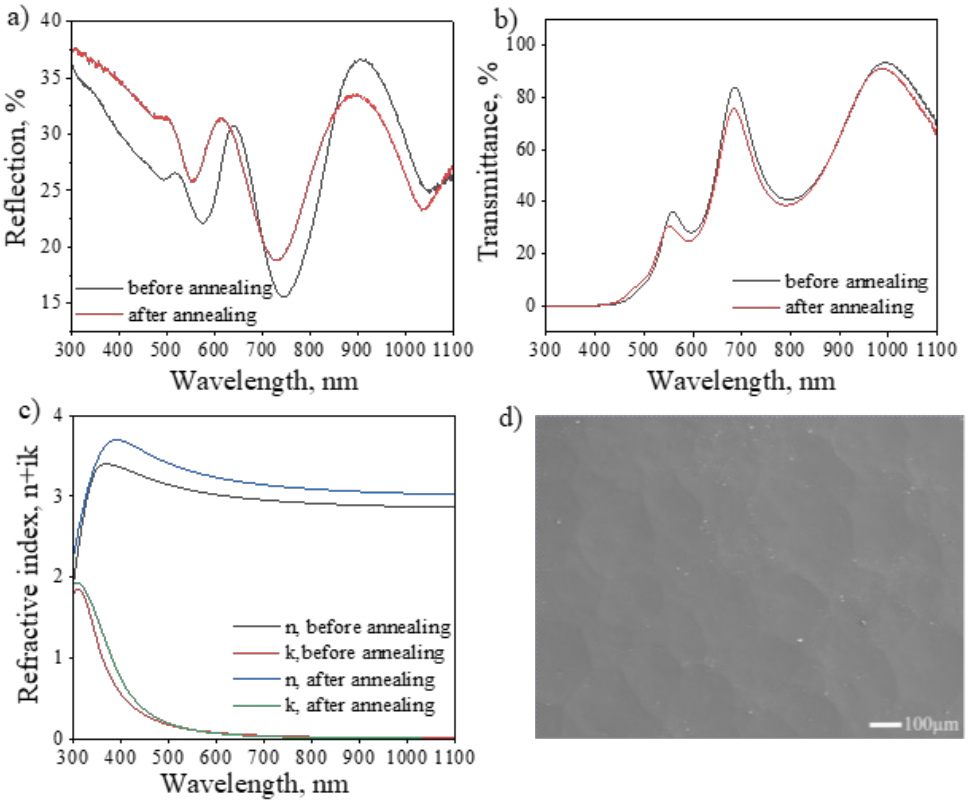


Figure 5 – a) reflection and b) transmittance spectra of silicon thin films before and after annealing, c) dependence of the refractive index and extinction coefficient of silicon thin films, d) SEM image of the Si thin film surface

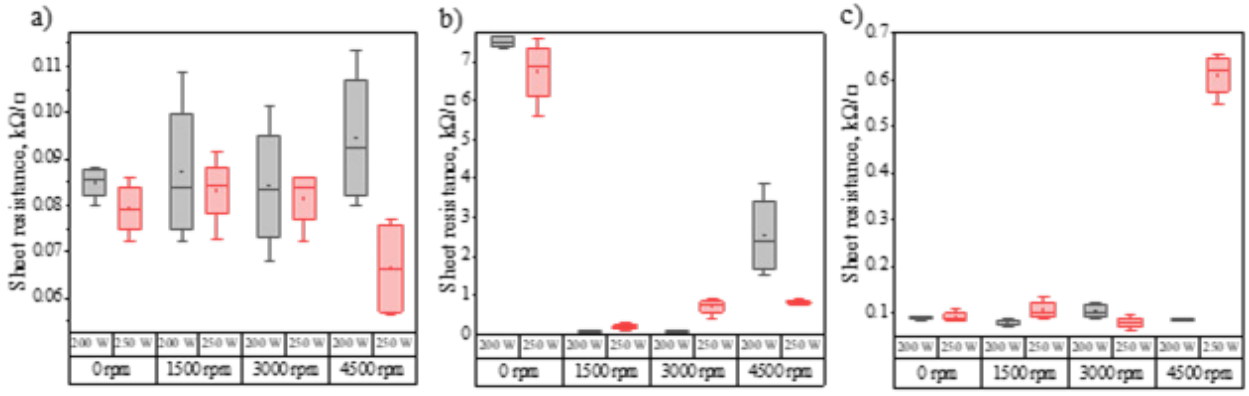


Figure 6 – Sheet resistance of (a, b) 300 nm poly-Si films deposited by RF magnetron sputtering at various power levels and spin speeds (rpm) and annealed at (a) 850 °C; (b) 950 °C, and (c) 50 nm poly-Si films deposited under similar conditions and annealed at 850 °C

Overall, the results reveal a clear relationship between deposition conditions, dopant diffusion and the resulting properties of the poly-Si films. XRD analysis and sheet resistance measurements show that improved crystallinity are key factors for governing electrical performance. These effects are promoted by optimized RF sputtering power, appropriate PSG spin-coating parameters and elevated annealing temperature. As a result, the sheet resistance becomes lower and more uniform. The findings also indicate that PSG-assisted spin-on doping influences not only phosphorus incorporation but also the crystallization behavior of sputtered Si. From a technological perspective, careful control of the thermal budget and deposition parameters is essential. The combined RF sputtering and SOD approach therefore represents a promising route for fabricating high-quality poly-Si layers for advanced Si-based photovoltaic applications.

Conclusion

This paper examines the influence of spin-coated PSG layers on the crystallization behavior and electrical performance of Si thin films deposited by RF magnetron sputtering. The work was focused on optimizing structural and electrical properties for potential photovoltaic and microelectronic applications. The experimental results were demonstrated that the PSG layer effectively enhances phosphorus diffusion during thermal annealing, thereby promoting the formation of high-quality poly-Si. It was found that higher spin speeds at 3000-4500 rpm with annealing at 950 °C, produced thinner and more uniform dopant layers, which facilitated efficient dopant incorporation and improved film crystallinity. Furthermore, among XRD analysis, it was confirmed that a distinct transformation from a-Si to poly-Si was successfully obtained. Meanwhile, annealing at 950 °C yielded the most favorable results, characterized by enhanced dopant activation and reduced sheet resistance. The optical measurements additionally demonstrated that annealing altered the reflectance and transmittance spectra and resulted in slight increases in the refractive index and extinction coefficient of the Si films. Finally, the application potentiality of the effectiveness of the SOD technique as a controllable and environmentally friendly alternative to conventional diffusion processes was demonstrated. In summary, the combined approach of SOD and RF magnetron sputtering provides a scalable, efficient, and environmentally sustainable pathway for fabricating high quality Si thin films suitable for photovoltaic and microelectronic device applications.

Funding. This work was funded by research grant from the Committee of Science of the Ministry of Science and Higher Education of the Republic of Kazakhstan (grant number: AP23490496).

REFERENCES

1 Kannan, N., and Vakeesan, D. Solar energy for future world: A review. Renewable and Sustainable Energy Reviews, 62, 1092–1105 (2016). https://doi.org/10.1016/j.rser.2016.05.022

2 Priya, P., and Stonier, A.A. Emerging innovations in solar photovoltaic (PV) technologies: The perovskite solar cells and more. Energy Reports, 14, 216–242 (2025). https://doi.org/10.1016/j.egyr.2025.01.015

3 Panwar, N.L., Kaushik, S.C., and Kothari, S. Role of renewable energy sources in environmental protection: A review. Renewable and Sustainable Energy Reviews, 15 (3), 1513–1524 (2011). https://doi.org/10.1016/j.rser.2010.11.037

4 Fernández-González, D., Pistoofi, A., Zapico, A., and Verdeja, L.F. Concentrated solar energy applications in materials science and metallurgy. Solar Energy, 170, 493–523 (2018). https://doi.org/10.1016/j.solener.2018.05.088

5 Mohammad Bagher, A. Types of Solar Cells and Application. American Journal of Optics and Photonics, 3 (5), 94–111 (2015). https://doi.org/10.11648/j.ajop.20150305.17

6 Yan, L.L., Han, C., and Shi, B. A review on the crystalline silicon bottom cell for monolithic perovskite/silicon tandem solar cells. Materials Today Nano, 7, 100045 (2019). https://doi.org/10.1016/j.mtnano.2019.100045

7 Wang, Q., Yang, X., and Yuan, Z. High-efficiency n-TOPCon bifacial solar cells with selective poly-Si based passivating contacts. Solar Energy Materials and Solar Cells, 259, 112448 (2023). https://doi.org/10.1016/j.solmat.2023.112448

8 Ibarra Michel, J., Drießen, M., and Ding, Z. Poly-Si passivating contacts prepared via phosphorus spin-on-doping: A comparison between different silicon deposition methods. Solar Energy Materials and Solar Cells, 255, 112275 (2023). https://doi.org/10.1016/j.solmat.2023.112275

9 Wei, H., Zhang, Y., and Liu, X. Unraveling the passivation mechanisms of c-Si/SiOx/poly-Si contacts. Solar Energy Materials and Solar Cells, 250, 112089 (2023). https://doi.org/10.1016/j.solmat.2022.112089

10 Huang, Y., Zheng, C., and Li, W. Improved interface passivation by optimizing a polysilicon film under different hydrogen dilution in N-type TOPCon silicon solar cells. RSC Advances, 12 (20), 12613–12620 (2022). https://doi.org/10.1039/D2RA01257E

11 Fthenakis, V.M., and Moskowitz, P.D. Characterization and control of phosphine hazards in photovoltaic cell manufacture. Solar Cells, 22 (4), 303–317 (1987). https://doi.org/10.1016/0379-6787(87)90050-0

12 Wang, Y., Zhang, X., and Chen, L. Influence of microstructure on electrochemical properties of Si/C multilayer thin-film anodes deposited using a sputtering method. Materials Letters, 160, 442–445 (2015). https://doi.org/10.1016/j.matlet.2015.08.026

13 El Omari, G., Benayad, A., and Martinez, H. Advances in physical vapor deposited silicon/carbon based anode materials for Li-ion batteries. Heliyon, 10 (9), e30214 (2024). https://doi.org/10.1016/j.heliyon.2024.e30214

14 Janarthanan, B., and Chandrasekaran, J. Basic deposition methods of thin films. Journal of Molecular Structure, 1241, 130630 (2021). https://doi.org/10.1016/j.molstruc.2021.130630

15 Safavi, M.S., Surmeneva, M.A., and Surmenev, R.A. RF-magnetron sputter deposited hydroxyapatite-based composite & multilayer coatings: A systematic review from mechanical, corrosion, and biological points of view. Ceramics International, 47 (3), 3003–3024 (2021). https://doi.org/10.1016/j.ceramint.2020.09.212

16 Kelly, P.J., and Arnell, R.D. Magnetron sputtering: A review of recent developments and applications. Vacuum, 56 (3), 159–172 (2000). https://doi.org/10.1016/S0042-207X(99)00189-X

17 Ding, Z., Ibarra Michel, J., and Drießen, M. Phosphorus-doped polycrystalline silicon passivating contacts via spin-on doping. Solar Energy Materials and Solar Cells, 221, 110881 (2021). https://doi.org/10.1016/j.solmat.2020.110881

18 Florakis, A., Misichronis, K., and Skorda, D. Simulation of the Phosphorus profiles in a c-Si solar cell fabricated using POCl3 diffusion or ion implantation and annealing. Energy Procedia, 38, 257–264 (2013). https://doi.org/10.1016/j.egypro.2013.07.275

19 Ibarra Michel, J., Drießen, M., and Ding, Z. Poly-Si passivating contacts prepared via phosphorus spin-on-doping: A comparison between different silicon deposition methods. Preprint, 1–15 (2023).

20 Zagozdzon-Wosik, W., Grabiec, P.B., and Lux, G. Silicon doping from phosphorus spin-on dopant sources in proximity rapid thermal diffusion. Journal of Applied Physics, 75 (1), 337–345 (1994). https://doi.org/10.1063/1.355883

21 Mohamad, I.S., Salleh, A.F., and Ahmad, Z. An experimental investigation of spin-on doping optimization for enhanced electrical characteristics in silicon homojunction solar cells: Proof of concept. Heliyon, 10 (11), e31940 (2024). https://doi.org/10.1016/j.heliyon.2024.e31940

22 Linke, J., Feldmann, H., and Hermle, M. Influence of the annealing temperature of (n) poly-Si/SiOx passivating contacts on their firing stability. Solar Energy Materials and Solar Cells, 258, 112412 (2023). https://doi.org/10.1016/j.solmat.2023.112412

23 Kusainova, A., Serikkanov, A., and Yessenova, G. Phosphorus doping solution development and impact of phosphorus-silicate glass structure on doping process during rapid thermal annealing. Journal of Materials Science: Materials in Electronics, 36 (28), 1831 (2025). https://doi.org/10.1007/s10854-025-1831-x

24 Westra, J.M., van Dijk, L., and Metselaar, J.W. Formation of thin-film crystalline silicon on glass observed by in-situ XRD. Energy Procedia, 2 (1), 227–233 (2010). https://doi.org/10.1016/j.egypro.2010.07.033

25 Akhter, P., Hussain, S.Q., and Dutta, S. Suppressing light reflection from polycrystalline silicon thin films through surface texturing and silver nanostructures. Journal of Applied Physics, 116 (11), 113101 (2014). https://doi.org/10.1063/1.4895713

[1]Рысқалиева М.М.,
магистрант, ORCID ID: 0009-0000-1225-0013,
e-mail: m.ryskaliyeva@kbtu.kz
[1]Құсайынова А.З.,
докторант, ORCID ID: 0000-0002-2485-9739,
e-mail: a.kusainova@kbtu.kz
[1]Ешанов А.,
магистрант, ORCID ID: 0009-0003-4051-5180,
e-mail: AmirEshanov@yandex.ru
[1]Жирков И.В.,
магистрант, ORCID ID: 0009-0003-0785-0526,
e-mail: il_zhirkov@kbtu.kz
[2]Ахадов Ж.З.,
т.ғ.д., профессор, ORCID ID: 0009-0005-9013-7573,
e-mail: ims-79@mail.ru
[1]Сұлтанов А.Т.,
PhD, ассистент-профессор, ORCID ID: 0000-0003-0074-431X,
e-mail: a.sultanov@kbtu.kz
[1]Бейсенханов Н.Б.,
ф.-м.ғ.д., профессор, ORCID ID: 0000-0002-5908-5614,
e-mail: n.beisenkhanov@kbtu.kz

[1]Қазақстан-Британ техникалық университеті, Алматы қ., Қазақстан
[2]Өзбекстан Республикасы Энергетика министрлігі жанындағы Жаңартылатын энергия көздері ұлттық ғылыми-зерттеу институты, Ташкент қ., Өзбекстан

МАГНЕТРОНДЫ ТОЗАҢДАТУ ӘДІСІМЕН ШӨКТІРІЛГЕН КРЕМНИЙДІҢ ЖҰҚА ҚАБЫҚШАЛАРЫНЫҢ КРИСТАЛДАНУ ПРОЦЕСІНЕ СПИН-КОАТИНГ ӘДІСІМЕН ЖАҒЫЛҒАН ФОСФОР-СИЛИКАТТЫ ӘЙНЕКТІҢ ӘСЕРІН ТАЛДАУ

Аңдатпа

Бұл зерттеу магнетрондық бүркумен кремний (Si) жұқа қабықшаларының кристалдануы мен электрлік қасиеттеріне центрифугалау әдісімен қапталған фосфосиликат шынысының (PSG) әсерін зерттеді, олардың құрылымдық және электрлік қасиеттерін фотоэлектрика мен микроэлектроникадағы әлеуетті қолдану үшін оңтайландыруға назар аударады. Центрифугалау әдісінің жылдамдығының жоғарылауының нәтижелері PSG қабаттарының жұқа және біркелкі болуына әкелетінін көрсетті, бұл өз кезегінде фосфордың тиімдірек диффузиясын жеңілдетеді және қабықшаның кристалдануын жақсартады. 950°C температурасында күйдіру қоспаларының белсенділігінің жоғарылауына, кристалдылықтың жақсаруына және меншікті кедергінің төмендеуіне әкелді. Бұл құрылымдық және фазалық түрлендірулер рентгендік дифракция (XRD) көмегімен жүйелі түрде талданды, бұл термиялық өңдеу кезінде Si жұқа қабықшаларының эволюциясын егжей-тегжейлі түсінуге мүмкіндік берді. Атап айтқанда, XRD нәтижелері аморфты күйден поликристалды күйге айқын ауысуын көрсетті, әсіресе центрифугалау әдісімен қаптау жылдамдығында және күйдіру температурасының жоғарылауында өңделген үлгілері үшін. Оптикалық сипаттамалар термиялық күйдірудің шағылысу және өткізу спектрлерін өзгерткенін, сонымен қатар тұндырылған кремний қабықшаларының сыну көрсеткіші мен жұтылу коэффициентін аздап арттырғанын көрсетті. Жалпы алғанда, экологиялық таза центрифугалау әдісінің физикалық тұндыру әдістерімен үйлесімі, озық фотоэлектрлік технологияларды әзірлеудің перспективті тәсілін білдіреді, бұл тұрақты және тиімді құрылғыларды жасауға мүмкіндік береді.

Түйін сөздер: кремний, кристаллизация, фосфосиликат шыны, магнетрондық бүрку.

[1]Рыскалиева М.М.,
магистрант, ORCID ID: 0009-0000-1225-0013,
e-mail: m.ryskaliyeva@kbtu.kz
[1]Кусаинова А.З.,
докторант, ORCID ID: 0000-0002-2485-9739,
e-mail: a.kusainova@kbtu.kz
[1]Эшанов А.,
магистрант, ORCID ID: 0009-0003-4051-5180,
e-mail: AmirEshanov@yandex.ru
[1]Жирков И.В.,
магистрант, ORCID ID: 0009-0003-0785-0526,
e-mail: il_zhirkov@kbtu.kz
[2]Ахадов Ж.З.,
д.т. н., профессор, ORCID ID: 0009-0005-9013-7573,
e-mail: ims-79@mail.ru
[1]Султанов А.Т.,
PhD, ассистент-профессор, ORCID ID: 0000-0003-0074-431X,
e-mail: a.sultanov@kbtu.kz
[1]Бейсенханов Н.Б.,
д.ф.-м.н., профессор, ORCID ID: 0000-0002-5908-5614,
e-mail: n.beisenkhanov@kbtu.kz

[1]Казахстанско-Британский технический университет, г. Алматы, Казахстан
[2]Национальный научно-исследовательский институт возобновляемых источников энергии при Министерстве энергетики Республики Узбекистан, г. Ташкент, Узбекистан

АНАЛИЗ ВЛИЯНИЯ ФОСФОРОСИЛИКАТНОГО СТЕКЛА, НАНЕСЕННОГО МЕТОДОМ СПИН-КОАТИНГА, НА ПРОЦЕСС КРИСТАЛЛИЗАЦИИ ТОНКИХ ПЛЕНОК КРЕМНИЯ, ОСАЖДЕННЫХ МЕТОДОМ МАГНЕТРОННОГО РАСПЫЛЕНИЯ

Аннотация

В данном исследовании изучается влияние фосфосиликатного стекла (PSG), нанесенного методом центрифугирования, на кристаллизацию и электрические свойства тонких пленок кремния (Si), осажденных магнетронным распылением, с акцентом на оптимизацию их структурных и электрических свойств для потенциального применения в фотовольтаике и микроэлектронике. Результаты показывают, что более высокие скорости центрифугирования приводят к более тонким и однородным слоям PSG, что в свою очередь способствует более эффективной диффузии фосфора и улучшает кристаллизацию пленки. Отжиг при 950 °C привел к усилению активации легирующих примесей, улучшению кристалличности и снижению удельного сопротивления. Эти структурные и фазовые превращения были систематически проанализированы с помощью рентгеновской дифракции (XRD), что позволило получить подробное представление об эволюции тонких пленок Si в процессе термической обработки. В частности, результаты XRD показывают четкий переход от аморфного к поликристаллическому состоянию, особенно для образцов, обработанных при оптимизированных скоростях центрифугирования и повышенных температурах отжига. Оптическая характеристика дополнительно показала, что термический отжиг изменил спектры отражения и пропускания, а также незначительно увеличил показатель преломления и коэффициент поглощения напыленных кремниевых пленок. В целом, сочетание экологически чистого метода легирования с помощью центрифугирования с масштабируемыми методами физического осаждения представляет собой многообещающий подход к разработке передовых фотоэлектрических технологий, предлагая жизнеспособный путь к устойчивому и эффективному изготовлению устройств.

Ключевые слова: кремний, кристаллизация, фосфосиликатное стекло, магнетронное напыление.

UDC 533.9:621.1.016.7:006
IRSTI 06.81.12, 45.43

https://doi.org/10.55452/1998-6688-2026-23-3-498-517

[1]Messerle V. E.,
Dr.Phys.-Math.Sc., Professor, ORCID ID: 0000-0003-4281-1429,
e-mail: ust@physics.kz
[1]Ustimenko A. B.,
Dr.Phys.-Math.Sc., Professor, ORCID ID: 0000-0003-0033-1371,
e-mail: alexanderustimenko@gmail.com
[1]Lavrishchev O.A.,
Cand. Phys.-Math.Sc., Associate Professor, ORCID ID: 0000-0002-5934-8381,
e-mail: lavr@physics.kz
[1]*Nugman M.K.,
Doctoral student, ORCID ID: 0009-0004-3366-5348,
*e-mail: nugmanmarina@gmail.com

[1]Al-Farabi Kazakh National University, Almaty, Kazakhstan

EXERGETIC METHODOLOGY FOR STANDARDIZED PERFORMANCE ASSESSMENT OF PLASMA PROCESSES

Abstract

This article proposes a unified exergetic methodology for comparable, reproducible assessment and subsequent standardization of plasma processes. Based on the Second Law of Thermodynamics, it integrates exergy efficiency (η_{ex}), specific energy consumption (Q_{sp}), exergy ignition cost (EIC), and environmental performance index (EPI) into a formalized KPI-stack. Unlike First Law criteria, the approach accounts for energy quality, irreversibility, and the non-equilibrium nature of plasma, distinguishing chemical, physical, and ionization components and quantifying exergy destruction at individual process stages. The methodology covers plasma ignition, gasification, reforming, and processing of gaseous, liquid, and solid hydrocarbon feedstocks and waste. Measurement, uncertainty assessment, and quality control are aligned with cited metrological requirements; environmental comparisons may incorporate life-cycle assessment. An oil-sludge case study compares conventional combustion at 1100 K with plasma-supported combustion at 1500–2000 K at a fixed process thermal power of 2000 kW. Calculations show differential exergy efficiency increasing from 0.546 to 0.636–0.675 and specific exergy losses decreasing from 18.27 to 14.48 MJ/kg. Environmental performance improves through a higher EPI and lower NO_2 emissions. Beyond thermal disposal, plasma processing produces valuable synthesis gas with total exergy reaching 156.7 MJ. The unified KPI-stack supports technology comparison, operating-mode optimization, and integration into regulatory and technical documentation.

Keywords: plasma processes, exergy analysis, key performance indicators, KPI-stack, energy efficiency, decarbonization, standardization.

Received March 17, 2026; revised August 27, September 1, 2026; accepted September 4, 2026.

Introduction

The modern energy and industrial policy of most countries, including the Republic of Kazakhstan, is focused on reducing the carbon footprint, increasing energy efficiency, and introducing the Best Available Technologies (BAT) as part of strategies to achieve carbon neutrality [1, 2]. In this context, plasma technologies are considered a promising tool for the deep thermochemical conversion of hydrocarbon raw materials and man-made waste (coal, fuel oil, sludge, biomass, solid household waste) into synthesis gas and other energy-valuable products, while reducing pollutant emissions and the carbon footprint.

Despite the intensive development of plasma technologies and a significant amount of experimental and computational research, there is still no single, unified approach to quantifying their effectiveness in the scientific and engineering literature. Disparate criteria are used for analysis, such as thermal efficiency, the degree of fuel conversion, synthesis gas yield, the rate and stability of ignition, and the specific energy consumption of the plasma torch. The use of various indicators, calculation schemes, and assumptions significantly complicates the comparability of results, limits correct inter-technological comparison, and hinders the formation of a regulatory framework and standards.

Traditional methods of evaluating efficiency, based primarily on the First Law of Thermodynamics, do not adequately describe the physical nature of plasma processes. In particular, they do not take into account the non-equilibrium nature of high-temperature plasma, the structure and magnitude of irreversible losses of available energy, or the redistribution of supplied energy between chemical, physical, and ionization components. As a result, energy indicators do not reflect the quality of energy and do not allow for an objective assessment of the effectiveness of plasma technologies from the perspective of the Second Law of Thermodynamics.

International research in the field of plasma-assisted combustion and plasma gasification shows that the lack of unified exergetic parameters leads to a formal and incomplete comparison of various technological solutions. This circumstance is of particular importance in the context of the transition to BAT and the need to justify technological schemes based on energy, environmental, and resource criteria simultaneously.

In this regard, an urgent scientific and applied task is to develop a universal methodology for quantifying the effectiveness of plasma processes, applicable to various types of fuels, plasma installations, and operating modes. Such a methodology should ensure comparability of results, reproducibility of calculations, and the possibility of integration into regulatory, technical, and standard documents.

In this paper, we hypothesize that the efficiency of plasma processes can be objectively, fully, and reproducibly assessed only on the basis of exergy analysis based on the Second Law of Thermodynamics. The exergetic approach is considered a fundamental basis for the formation of a unified and standardized set of key performance indicators (KPI-stack).

The methodological basis of the study is exergy analysis, upon which a universal measurement and calculation methodology has been developed. This methodology establishes a procedure for quantifying the effectiveness of plasma ignition, gasification, and reforming of hydrocarbon fuels in gas, liquid, and solid phases. Hereafter, all plasma technologies are considered within a single thermodynamic logic, where the key object of analysis is not only the amount of energy supplied but also its quality, determined by exergy.

Equilibrium thermodynamic models are used in this work as a tool for the initial assessment of the limiting characteristics of plasma processes, while non-equilibrium models and experimental diagnostic methods are used to refine and verify calculated data. In this case, exergy analysis acts as a link between model calculations and the actual technological parameters of plasma installations.

The numerical case study presented in this paper is limited to oil sludge. References to coal, biomass, municipal solid waste, and other feedstocks describe the intended applicability range of the methodology and the reviewed literature, rather than the feedstock used in the calculations.

The proposed methodology does not replace existing theoretical and experimental approaches but formalizes and summarizes accumulated global experience, translating it into a unified measurement and calculation protocol suitable for technology comparison and subsequent standardization.

Abbreviations and definitions

Exergy (Ex) – The maximum useful work a system can perform when brought into equilibrium with the environment under given conditions.

Exergetic efficiency coefficient (n_{ex}) – The ratio of the useful exergy of the process products to the total exergy of all input flows.

Specific energy consumption (Q_{sp}) – The amount of energy or exergy supplied per unit of processed raw material or resulting product.

Exergetic ignition cost (EIC, Exergy Ignition Cost) – The total exergy consumed to initiate and stabilize a plasma regime or flame (an integral characteristic of the costs for initiating and stabilizing a plasma regime).

Environmental Performance Index (EPI) – A dimensionless indicator characterizing the environmental effectiveness of a process based on the ratio of actual pollutant concentrations to regulatory values (a generalized environmental metric for comparing different types of feedstocks and technologies).

KPI (Key Performance Indicators) – Quantifiable metrics used to evaluate and compare the effectiveness of technological processes.

KPI-stack – A unified set of interrelated key performance indicators used for the comprehensive performance assessment of plasma processes.

LTE (Local Thermodynamic Equilibrium) – A state in which the temperatures of the different degrees of freedom of particles are considered equal.

CR model (Collisional-Radiative Model) – A kinetic model describing the excitation and ionization of plasma particles, accounting for collisional and radiative processes.

PGM (Plasma Gasification Melting) – A high-temperature process in which waste is converted into energy-rich synthesis gas and inert vitreous slag.

WtV (waste-to-value) – An approach to waste management where waste is treated not as refuse for disposal, but as a valuable resource for creating new products, energy, or raw materials.

BAT – Best Available Techniques (or Technologies).

PFS - Plasma fuel system.

Q – Thermal power.

T – Absolute temperature of the process.

T_0 – Ambient temperature at P0 = 1 atm at 80% relative humidity.

p – Pressure.

P – Installation power in kW.

t – Time to reach the required temperature and measure in h.

m – Mass of fuel in kg.

η_{ex}^{int} – Integral exergy efficiency.

η_{ex}^{dif} – Differential (stream) exergy efficiency.

Materials and methods

Models and Methods for the Exergy-Based Performance Assessment of Plasma Processes

Standardization, as a tool for scaling and commercializing scientific developments, requires the accumulation of comparable data, the identification of universally applicable norms, and the formalization of calculation and measurement procedures. In plasma technologies, thermodynamic assessment is applied in the design of installations (gasifiers, plasma torches, plasma-fuel systems), the optimization of operating modes (temperature, oxidizer/fuel ratio, specific energy consumption), and performance evaluation (energy and exergy indicators, feedstock/waste conversion rates).

The study employs two classes of modeling approaches: equilibrium thermodynamic models (for high-temperature plasma close to LTE) and non-equilibrium kinetic/CR model/state-to-state models (for low-temperature and highly non-equilibrium media), as well as experimental diagnostic methods for model verification and plasma parameter reconstruction.

Data provenance and validation scope. The present study is methodological and computational. The oil-sludge case study combines equilibrium thermodynamic calculations with input data reported in Refs. [4, 34–36]. The origin of each parameter is classified as experimental, rated, literature-derived, assumed, or calculated. The KPI values, including η_{ex}, specific exergy loss, EIC, EPI, and syngas exergy, were calculated using the equations presented below. Verification was performed by

comparison with previously published experimental data from Refs. [34–36]. No new independent experimental campaign was conducted within the present study.

The classical approach for describing the plasma gasification of solid waste and biomass is equilibrium thermodynamic modeling based on Gibbs energy minimization (or equilibrium thermodynamic models (Gibbs minimization)) under given conditions, such as T, p, and the elemental composition of the system (n_i) [3–9].

Input data (minimum required for reproducibility):

- Elemental composition of fuel/waste (C/H/O/N/S/Cl + ash/moisture content, if applicable);
- Type and flow rate of the plasma-forming gas/oxidizer;
- Pressure p and temperature range T;
- Steam/air/oxygen/fuel ratios (depending on the problem statement).

Output parameters of the equilibrium model:

- Synthesis gas composition (CO, H_2, CO_2, CH_4, H_2O, N_2, etc.);
- Fraction of condensed phases/slag;
- Integral indicators: heating value of the synthesis gas, gas yield, and temperature regime targets [3–9].

In applied research, equilibrium models are used to calculate synthesis gas composition and energy/exergy indicators for the plasma gasification of MSW [3, 4], to analyze PGM stages (drying, pyrolysis, gasification, melting) in terms of energy and exergy [5], and to optimize operating modes within WtV concepts [7–9].

However, despite the convenience of this approach, there are certain limitations to its application. The equilibrium formulation does not account for kinetics, hydrodynamics, the actual structure of the plasma flare, or the inhomogeneity of temperature and composition fields. The model provides an assessment of the 'ideal' limit of performance.

The main positive aspect of the equilibrium model is its applicability in conjunction with exergy analysis. To transition from 'gas composition' to comparable effectiveness, exergy analysis (the Second Law of Thermodynamics) is used as the primary quantitative tool for assessing energy quality and irreversible losses. Research [5] shows that the 'equilibrium calculation → exergy balance' link allows for the localization of exergy losses by PGM stages and the identification of 'bottlenecks,' the evaluation of the impact of air preheating and the steam/biomass ratio on exergy efficiency [6], and the formulation of engineering-interpretable metrics such as specific synthesis gas yield (Nm^3/kg), cold gas efficiency (%), exergy efficiency, and specific electricity consumption of the plasma torch (kWh/kg) [4–6, 10–12].

For the numerical modeling of the plasma processing of carbon-containing materials in steam/gas/air plasma, the TERRA software package is utilized. It enables equilibrium calculations, evaluation of the influence of operating parameters and feedstock composition, and determination of specific energy consumption and energy efficiency indicators; comparison with experimental data on gas composition confirms the applicability of the thermodynamic approach for the exergetic interpretation of process performance and normalization.

"Non-equilibrium plasma models, such as state-to-state and CR approaches, were reviewed. For the class of plasma technologies where equilibrium assumptions are violated (low-temperature discharges, plasma jets at reduced pressures, hypersonic flows), models that account for the non-equilibrium between translational, vibrational, and electronic degrees of freedom are utilized.

Within the state-to-state approach, each vibrational-electronic level is treated as a separate 'species' with its own number density [16]. CR models describe excitation/ionization kinetics through a system of kinetic equations and are used in conjunction with gas dynamics and radiative transfer, including the calculation of electron and excitation temperatures, level distributions for spectroscopy, and radiation power [17–19]. While physically informative, these methods are computationally expensive and require large datasets of cross-sections and rate coefficients; therefore, in applied energy problems, they are typically used selectively (for diagnostics/verification) or in the form of reduced models [18].

The third methodological approach involves experimental methods and diagnostics (model verification). Spectral methods (OES, LIBS, etc.) are used for the experimental verification of models and the reconstruction of plasma parameters. Based on the spectra of impurity ions/atoms, and utilizing excitation models and CR approximations, particle densities, flows, and sources in the plasma are estimated [20]. LIBS methods, with corrections for matrix effects and self-absorption, are applicable for the analysis of products and particles within the plasma flare [21]. To quantify the gas composition after plasma processing, gas chromatography, mass spectrometry, and IR analyzers are employed [23]. Comparing the measured synthesis gas composition (CO, H_2, CH_4, CO_2, etc.) with the modeled data provides a quantitative assessment of the deviation from equilibrium and serves as a basis for adjusting assumptions and accounting for losses [4, 10–15, 23].

The proposed methodology relies on the KPI-stack concept for plasma processes as a universal exergy-based method. The base set of indicators includes exergy efficiency, specific energy consumption, Exergy Ignition Cost (EIC), and the Environmental Performance Index (EPI), which is linked to pollutant regulations [24].

The exergy balance is formulated by comparing the total exergy of inflows (electrical exergy, and the chemical and physical exergy of the fuel and oxidizer) with the exergy of the products (synthesis gas, melt/slag phase), while accounting for losses (cooling, radiation, etc.).

Thus, the KPI-stack provides a unified performance assessment for various types of fuels (gas, fuel oil, coal, oil sludge, waste) and different plasma technologies (ignition, gasification, reforming), provided that a unified computational protocol and a single input data structure are maintained.

Uncertainty Assessment and Data Quality Requirements

To ensure the reproducibility and suitability of results for standardization, the measurement and calculation procedure must be accompanied by an accuracy assessment and internal quality control. RMG 61-2010 and RMG 76-2014 are used as the regulatory framework for evaluating accuracy, trueness, and precision indicators, as well as for the quality control of quantitative analysis results. For environmental comparability, ISO 14044 approaches may be applied when an LCA (Life Cycle Assessment) interpretation is required [37–39].

The calculated KPI values were verified by comparison with the experimental results reported in Refs. [34–36]. The combined relative uncertainty was estimated at ±6-10%. The main contributions were associated with temperature measurement (±1.5%), gas composition (±3%), electrical power (±1%), and mass measurement (±0.5%).

The KPI Concept for Plasma Technologies

Equilibrium thermodynamic models and exergy analysis form the basis for the primary quantitative assessment of high-temperature plasma processing and gasification [3–15, 26–33]. Non-equilibrium CR/state-to-state approaches are key for low-temperature and specialized plasma regimes, providing a physically correct link between diagnostics and spectroscopy [16–22]. The combined application of models and instrumental methods ensures sufficient data completeness for the reconstruction of process parameters.

Thus, the KPI-stack provides a unified performance assessment for the application of various plasma technologies (ignition, gasification, reforming) in the processing of different fuel types (gas, fuel oil, coal, oil sludge, waste), provided that a unified computational protocol and a single input data structure are maintained.

To ensure the reproducibility and suitability of results for standardization, the measurement and calculation procedure must be accompanied by an accuracy assessment and internal quality control. RMG 61-2010 and RMG 76-2014 serve as the regulatory framework for evaluating accuracy, trueness, and precision indicators, as well as for the quality control of quantitative analysis results. For environmental comparability, ISO 14044 approaches may be applied when an LCA interpretation is required [38].

Equilibrium thermodynamic models and exergy analysis form the basis for the primary quantitative assessment of high-temperature plasma processing and gasification [3–15, 26–33]. Non-equilibrium CR/state-to-state approaches are key for low-temperature and specialized plasma regimes, providing

a physically correct link to diagnostics and spectroscopy [16–22]. The combined application of models and instrumental methods ensures sufficient data completeness for the reconstruction of η_{ex}, Q_{sp}, and other KPI-stack metrics, forming the foundation for a standardized performance assessment protocol.

Results and discussion

The KPI-stack method is based on the Second Law of Thermodynamics and defines the quantitative efficiency of a plasma process as the ratio of the exergy of the reaction products to the total input exergy:

$$\eta_{ex} = \frac{\sum Ex_{вых} + \sum Ex_{потерь}}{Ex_{вход}} \quad (1)$$

where: ΣEx_{in} – input exergy, including electrical and reaction energy;

ΣEx_{prod} – exergy of products, including the chemical and thermal exergy of the synthesis gas and condensed phases;

ΣEx_{loss} – irreversible losses (radiation, cooling, leakage, etc.).

Calibrated measuring instruments are used for measurements: K-type thermocouples (up to 2500K, accuracy ±0.5%); an optical pyrometer (PIR-1800 or equivalent); gas analyzers (Infracar or equivalent for H_2, CO, CO_2, CH_4, N_2, O_2, H_2S, NO_x, SO_2); wattmeters (up to 200kW, accuracy 1%); analytical balances (0.01g); and the TERRA software package (or equivalent) for thermodynamic exergy calculations. Calculations and comparisons were performed at a process thermal power of 2000kW. Given a lower heating value (LHV) of the oil sludge of 40.2MJ/kg, the calculated fuel consumption is approximately 179.1kg/h.

Exergy of each component:

$$Ex_i = \eta_i \cdot (h_i - h_0) - T_0 \cdot (s_i - s_0) \quad (2)$$

The exergy calculation is based on the specific heat consumption in a combined Carnot cycle using their mean thermodynamic temperatures, a method also known as exergy analysis.

Carnot factor (Carnot coefficient):

$$\tau = 1 - \frac{T_0}{T} \quad (3)$$

Exergy efficiency via the Carnot factor:

$$\eta = 1 - \frac{2T_0}{T + T_0} \quad (4)$$

Exergy efficiency via the Carnot factor:

$$exQ = Q \times \eta \quad (5)$$

where η is the thermal efficiency of the cycle, or the "heat quality" factor.

KPI-stack Indicators:

To ensure a correct comparison between traditional combustion and plasma gasification technologies, the KPI-stack is divided into two functional branches:

I. Full combustion mode, where the target product is the exergy of useful heat.

$$Ex_{use}^{int} = Q_{use} * \tau = Q_{use} * (1 - \frac{T_0}{T}) \quad (6.1)$$

$$Ex_{use}^{dif} = Q_{use} * \tau = \eta * Q * (1 - \frac{T_0}{T}) \quad (6.2)$$

II. Plasma processing mode with synthesis gas production, where the target product is the exergy of the gas.

$$Ex_{gas} = Ex_{gas}^{ch} + Ex_{gas}^{ph} \quad (7)$$

Exergy efficiency is calculated as the ratio of the target product's exergy to the total input exergy of the fuel and electrical energy.

KPI-stack indicators:

Exergy efficiency of the process (for combustion):

$$\eta_{ex} = \frac{Ex_{use}}{Ex_{el} + Ex_{fuel}} \quad (8)$$

Fuel exergy:

$$Ex_{fuel}^{int} = m_{fuel} \times Q_{fuel} \quad (9.1)$$

$$Ex_{fuel}^{dif} = Q \quad (9.2)$$

Useful heat:

$$Q_{use}^{int} = \eta_{th} * Ex_{fuel} \quad (10.1)$$

$$Q_{use}^{dif} = \eta_{th} * Q \quad (10.2)$$

Total electrical power:

$$P_{el}=P_{aux}+P_{plaz} \quad (11)$$

Electrical input exergy:

$$Ex_{el}^{int} = P_{el} * t * \eta_{th} \quad (12.1)$$

$$Ex_{el}^{dif} = P_{el} \quad (12.2)$$

In the initial calculations, the exergy of the fuel and electrical input was determined in integral form (MJ) for a given operating time. For the analysis of the facility's steady-state operation, the calculation was performed in flow form (kW). A flow-based (power/integral) approach was used in the exergy analysis. The fuel exergy flow is assumed to be equal to the process thermal power (9.2), which is equivalent to the chemical exergy of the fuel burned at a given flow rate. The electrical exergy flow is equal to the consumed electrical power (12.2), since electrical energy is entirely exergetic (with an exergy factor of 1).

Specific energy consumption:

$$Q_{sp}^{int} = \frac{(Ex_{fuel} + Ex_{el} - Ex_{use})}{m} \quad (13)$$

Exergetic Ignition Cost (EIC):

$$EIC^{int} = \frac{Ex_{el}}{m} = \frac{P_{el} * t * \eta_{th} * 3.6}{m} \quad (14)$$

Environmental Performance Index (EPI):

$$EPI = \frac{C_{\text{ПДК}}^{\text{ВОЗ}}}{C_{\text{факт}}} \times \eta_{ex} \quad (15)$$

where C_{MPC}^{WHO} – is the standardized (regulatory) concentration of the pollutant, and
C_{fact} – is the measured concentration in the emission zone.
For a key pollutant j (e.g., NO_2, SO_2, $PM_{2.5}$):

$$EPI_j = \eta_{ex}^{dif} \times \frac{C_{MPC}^{WHO}}{C_{fact}} \quad (16)$$

Composite index for the aggregate of pollutants::

$$EPI = \sum_j \omega_j \times EPI_j \quad (17)$$

where ω_j are weighting factors (proportional to the impact significance or inversely proportional to the MPC).

The KPI-stack calculation below is presented using the example of oil sludge combustion in a furnace equipped with a PFS compared to combustion without one (hereinafter referred to as traditional combustion). The data is based on research findings [4, 34–36]. The raw data is provided in Table 1, the justification for the selected research temperatures is given in Table 2 [4, 34–36], and the KPI-stack calculation for oil sludge is presented in Table 3.

I. Full combustion mode, where the target product is the exergy of useful heat.

All calculations were performed at a fixed process thermal power of Q = 2000 kW. The electrical power of the plasma torch was Pplaz = 400 kW. Therefore, the value of 2000 kW should not be interpreted as the electrical power of the plasma torch or its power supply system.

Table 1 – Comparative exergy calculation for a single PFS during oil sludge processing

Parameter / Type	Traditional Combustion	PFS -Assisted Gasification	
Fuel combustion temperature, T (K)	1100	1500	2000
Plant efficiency (rated/nominal data), ηth	0,75	0,95	0,95
Plasma torch power, Pplaz (kW)	-	400	400
Furnace ignition power, Paux (kW)	10	-	-
Process thermal power, Q (kW) ≈ MJ/s	2000 ≈ 2		
Mass of processed fuel, mfuel (kg)	10		
Oil sludge flow rate, $\dot{m}$ (kg/h)	179,1		
Combustion time, t (h)	0,05		
Ambient temperature, T0 (K)	295		
Ambient pressure, p0 (kPa)	101,325		
Fuel heating value, Qfuel (MJ/kg)	40,2		
Input fuel exergy (MJ)	10*40,2=402		
Fuel exergy flow (kW)	2000		

Continuation of Table 1

Net calorific value (LHV) of oil sludge (MJ/kg)	20		
Carnot factor, τ	$1-\frac{295}{1100}=0{,}7318$	$1-\frac{295}{1500}=0{,}8033$	$1-\frac{295}{2000}=0{,}8525$
Exergetic cycle efficiency	$1-\frac{2*295}{1100+295}=0{,}577$	$1-\frac{2*295}{1500+295}=0{,}671$	$1-\frac{2*295}{2000+295}=0{,}743$
Exergetic power (Exergy flow), exQ (kW)	2000*0,577=1154	2000*0,671=1342	2000*0,743=1486
Useful heat from combustion (MJ)	0,75*402=301,5	0,95*402=381,9	0,95*402=381,9
Useful heat rate from combustion (kW)	2000*0,75=1500	2000*0,95=1900	2000*0,95=1900
Exergy of useful heat (MJ)	301,5*0,7318=220,64	381,9*0,8033=306,78	381,9*0,8525=325,57
Useful heat exergy flow, Exuse (kW)	0,75*2000*0,732 =1097,73	0,95*2000*0,8033 =1526,33	0,95*2000*0,8525 =1619,75
Electrical input exergy (kWh)	10кВт*0,05ч*0,75 =0,375 (= 1,35 МДж)	400кВт*0,05ч*0,95 =19 (=68,4 МДж)	400кВт*0,05ч*0,95 =19 (=68,4 МДж)
Electrical input exergy flow (kW)	10	400	400
Exergetic process efficiency	220,64/(1,35+402) =0,547	306,78/(68,4+402) =0,652	325,57/(68,4+402) =0,692
Fuel combustion temperature, T (K)	1097,73/(2000+10) =0,5461	1526,33/(2000+400) =0,6359	1619,75/(2000+400) =0,6749

Note: According to the requirements of the Stockholm Convention and UNEP (United Nations Environment Programme) standards, a temperature of at least 1500 K is required for the complete destruction of organochlorine compounds in oil sludges. The PFS ensures a stable temperature regime above 1700°C (2000 K), which guarantees the environmental safety of the process and exceeds WHO (World Health Organization) international destruction standards.

In this work, two forms of the exergy efficiency coefficient are utilized:

η_{ex}^{int} (cycle efficiency) characterizes the efficiency of a specific processing cycle, accounting for the ignition and stabilization phases; it is applied when calculating the Exergetic Ignition Cost (EIC).

η_{ex}^{dif} (steady-state efficiency) is used to evaluate the facility's performance in a steady-state mode. It is selected as the baseline indicator for the KPI-stack concept, as it ensures comparability, scalability, and reproducibility of results for cross-technology comparisons.

According to the calculations presented in Table 1, the exergetic efficiency of plasma-assisted oil sludge gasification is 16.3% and 28.8% higher than that of traditional methods at 1500 K and 2000 K, respectively. An analysis of the data in Table 1 shows that at the same process thermal power (2000 kW), the transition from traditional combustion to PFS-assisted gasification leads to a significant increase in the exergy of useful heat due to higher process temperatures and improved quality of the input energy.

Despite the increase in electrical consumption when using a plasma torch, the overall exergetic efficiency increases, indicating a reduction in irreversible losses within the system. The results confirm that energy efficiency, as evaluated by the First Law of Thermodynamics, does not reflect the actual quality of the process, whereas exergetic analysis allows for a correct comparison of regimes with different temperature potentials. This justifies the continued use of exergetic indicators within the KPI-stack framework. Based on these initial data, further calculations of integral and flow-based performance indicators are conducted.

Figure 1 presents the dependence of the exergy efficiency on the process temperature. The η_{ex}^{int} characterizes the efficiency of the complete processing cycle, accounting for start-up modes, while η_{ex}^{dif} represents the facility's efficiency in steady-state operation. The divergence of the curves reflects the contribution of transient processes and the exergetic costs for ignition and stabilization.

It follows from Figure 1 that the exergy efficiency increases monotonically with the process temperature for both types of evaluation—integral form and flow form (differential). The gap between the curves reflects the contribution of transient processes associated with the ignition and stabilization of the plasma regime and quantitatively characterizes the additional exergetic load on the system during non-steady-state phases.

The differential exergy efficiency demonstrates a stable temperature dependence and reflects the facility's performance in steady-state mode, making it the preferred baseline indicator for the KPI-stack concept to ensure cross-technology comparison and standardization. The integral efficiency, in turn, remains informative for analyzing operational cycles and calculating the Exergetic Ignition Cost (EIC). This relationship serves as a physically correct link for a primary quantitative assessment and provides the basis for forming a comprehensive KPI-stack through an exergy-based method.

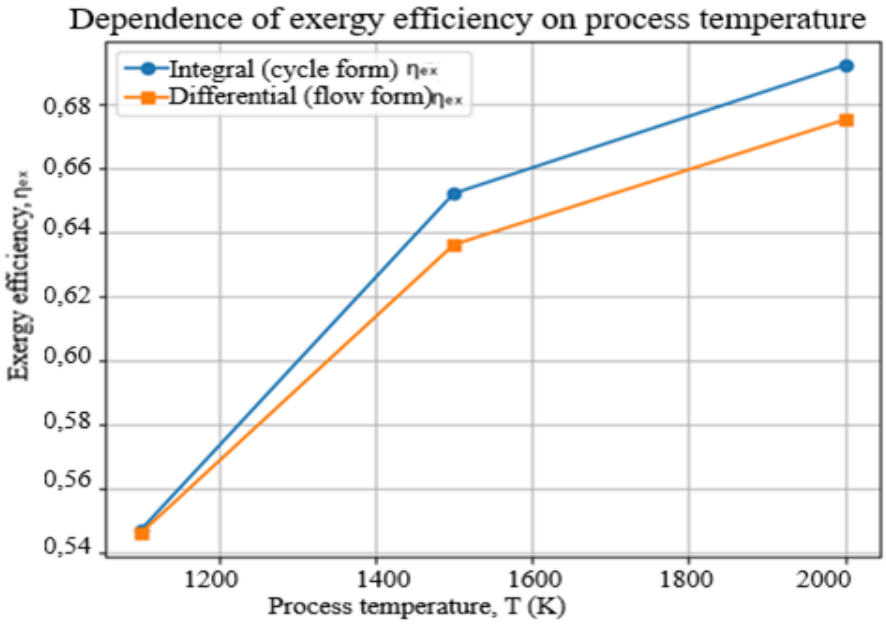


Figure 1 – Dependence of exergy efficiency on temperature.

Table 2 – Variation of gas composition as a function of temperature (T) [4, 10–15, 34–36]

Temperature	Key Process Characteristics
1100 K	Incomplete conversion zone. At this temperature, condensed carbon (C_{cond}) may still be present in the system. The concentration of target components (H_2, CO) has not yet reached its maximum. Minor amounts of methane (CH_4) may be present. Emissions are relatively low, but the process is characterized by high levels of CO (incomplete combustion).
1400 K	Optimal gasification threshold. All carbon is converted into the gas phase. The concentrations of CO and H_2 stabilize at peak values; this serves as the "operating point" for many industrial plasma gasifiers.
1500 K	Stable syngas production. Maximum yield of high-calorific gas is achieved; hazardous impurities (dioxins, furans) are completely destroyed.
2000 K	Excessive energy consumption zone. The gas composition remains virtually unchanged compared to 1500-1600 K; however, specific electrical energy consumption for the process increases significantly. Thermal ionization begins, and atomic fractions start to grow. At a plasma temperature of 2000 K and in the absence of free oxygen, nitrogen remains in an inert state (N_2), preventing the formation of NO_2.

The data in Table 2 demonstrate that an increase in process temperature leads to an equilibrium shift toward the formation of the target components of syngas – hydrogen and carbon monoxide. At a temperature of 1100 K, the process is characterized by incomplete carbon conversion and the potential presence of a solid residue, whereas the range of 1400-1500 K corresponds to a stable steady-state mode of full gasification.

With a further increase in temperature to 2000 K, the gas composition changes insignificantly; however, energy costs increase, indicating the existence of an optimal temperature window in terms of the balance between performance and costs. These results emphasize the need to assess not only the gas composition but also the quality of the energy contained in the products, which is further implemented through the exergy-based method for syngas analysis.

Table 3 – KPI-stack calculation for oil sludge

Indicator Name	Traditional combustion at 1100K	Gasification using PFS at 1500K	Gasification using PFS at 2000K
Measured NO_2 emission concentration: C_{fact} (mcg/m^3)	250	80	60
Specific energy consumption, Qsp (MJ/kg) (13)	$\frac{402 + 1{,}35 - 220{,}64}{10} = 18{,}27$	$\frac{402 + 68{,}4 - 306{,}78}{10} = 16{,}36$	$\frac{402 + 68{,}4 - 325{,}57}{10} = 14{,}48$
Exergetic Ignition Cost, EIC (MJ/kg) (14)	$\frac{13{,}5}{10} = 0{,}135$	$\frac{68{,}4}{10} = 6{,}84$	$\frac{68{,}4}{10} = 6{,}84$
Environmental Performance Index, EPI (16)	$0{,}5461 \times \frac{10}{250} = 0{,}0218$	$0{,}6359 \times \frac{10}{80} = 0{,}0795$	$0{,}6749 \times \frac{10}{60} = 0{,}1125$

Note: According to WHO data, the Maximum Permissible Concentration (MPC) for NO_2 (annual average since 2021) is $C_{MPC}^{WHO} = 10\ mcg/m^3$ [38].

The KPI-stack calculation results (Table 3) demonstrate that plasma-assisted processing of oil sludge is characterized by higher exergy efficiency and lower specific exergetic losses compared to traditional combustion. Despite the increase in the Exergetic Ignition Cost (EIC) associated with the use of a plasmatron, the temperature rise and improvement in energy quality compensate for these costs during the steady-state stage of the process.

The Environmental Performance Index (EPI) also increases when transitioning to plasma modes, indicating an improvement in environmental performance alongside an increase in thermodynamic efficiency. The obtained results confirm the feasibility of using the KPI-stack as an integral tool for the comprehensive energy and environmental assessment of oil sludge processing.

II. Plasma processing mode with synthesis gas production, where the target product is the exergy of the gas.

The plasma mode not only provides thermal energy but also converts a portion of the exergy into a chemically valuable form (CO+H_2). Table 4 presents the results of the gas exergy calculations. Calculation of Gas Exergy Ex_{gas}:

- Determine the gas molar flow rate n_{gas} based on flow meter readings and elapsed time.
- For each component H_2, CO, CH_4, CO_2, N_2, determine h_i and s_i, where: n_i - amount of substance for component i (H_2, CO, CH_4 etc.) kmol;
- h_i, s_i - enthalpy (total $_{thermal}$ energy content) and entropy (degree of disorder or randomness) at gas temperature T;
- h_{i0}, s_{i0} - enthalpy and entropy at the standard state;
- ex_i^{ch} - specific chemical exergy of the component.

$$Ex_{gas} = Ex_{gas}^{ph} + Ex_{gas}^{ch} \quad (18)$$

$$\mathrm{Ex}_{gas} = \sum_i n_i\left[(h_i - h_{i,0}) - T_0(s_i - s_{i,0}) + \mathrm{ex}_i^{\mathrm{ch}}\right] \quad (19)$$

Table 4 – Syngas exergy calculation

№	Gas component i	Volume Fraction y_i, %	Amount of Substance n_i, kmol	Specific Chemical Exergy ex_i^{ch}, MJ/kmol	Physical Exergy Ex_i^{ph}, MJ	Chemical Exergy $Ex_i^{ch} = n_i \cdot ex_i^{ch}$, MJ	Total Component Exergy $Ex_i = Ex_i^{ph} + Ex_i^{ch}$ МДж	Fraction in Ex_{gas}, %
at T=1100K								
1	H_2	45	0.292	240	2.9	70.0	72.9	50.9
2	CO	40	0.218	275	2.3	60.0	62.3	43.5
3	CH_4	3	0.005	800	0.5	4.0	4.5	3.1
4	CO_2	8	-	~0	0.9	~0	0.9	0.6
5	N_2	4	-	~0	207	~0	2.7	1.9
Total:		100	-	-	9017	134.1	143.17≈143.2	100.0
at T=1500K								
1	H_2	45	0.292	240	5.0	70.1	75.0	50.0
2	CO	40	0.218	275	4.0	60.0	64.0	42.7
3	CH_4	3	0.005	800	0.8	4.0	4.8	3.2
4	CO_2	8	-	~0	1.5	~0	1.5	1.0
5	N_2	4	-	~0	4.7	~0	4.7	3.1
Total:		100	-	-	16.0	134.1	150.0	100.0
at T=2000K								
1	H_2	45	0.292	240	7.1	70.1	77.2	49.2
2	CO	40	0.218	275	5.7	60.0	65.7	41.9
3	CH_4	3	0.005	800	1.1	4.0	5.1	3.3
4	CO_2	8	-	~0	2.1	~0	2.1	1.4
5	N_2	4	-	~0	6.7	~0	6.7	4.3
Total:			100	-	22.6	134.1	156.7	100.0

Notes:

1. Under the condition of constant gas composition, $p \approx p_0$, T_0=295K.
2. The ratio ensures complete gasification without the formation of solid carbon (soot) and achieves the maximum concentration of combustible components (H_2 and CO) in the syngas.
3. Chemical exergy ex_{fuel}^{ch} is determined by the elemental composition of the fuel (C, H, O, S, N) and reference databases (Szargut, JANAF/NASA).
4. For air, chemical exergy is neglected; the physical component is accounted for during preheating $Ex_{ox} \approx 0$.
5. The total relative uncertainty of the result – ± 6-10%. Main components: temperature – ± 1.5%, gas composition – ±3%, power – ±1%, mass – ±0.5%. Verification is performed by comparing calculated η_{ex} values with experimental data from [34-36].
6. The physical exergy of components at 2000K is estimated by scaling the values at 1500K proportionally to ($T-T_0$), assuming a constant gas composition.

The analysis of Table 4 shows that the primary share of syngas exergy is attributed to the chemical exergy of hydrogen and carbon monoxide, while the contribution of physical exergy increases as the process temperature rises. Given a constant gas composition, an increase in temperature leads to a rise in the total syngas exergy due to the enhancement of physical potential, which is particularly evident at 2000K.

This confirms that plasma processing not only provides a thermal effect but also converts a significant portion of the input exergy into a chemically valuable form suitable for subsequent

energetic or technological use. This effect represents a fundamental advantage of plasma modes and cannot be identified through analysis based solely on energy indicators of the First Law of Thermodynamics.

Thus, the sequential analysis of the energetic, exergetic, and environmental characteristics of the process confirms the feasibility of applying the exergy-oriented KPI-stack for the objective assessment and optimization of plasma-based oil sludge processing technologies. Furthermore, the possibility of integrating this concept into related fields of thermodynamics is considered.

Alignment of the Methodology with Global Literature

In the majority of reviewed studies, exergetic analysis is performed on a "plant-specific" basis, utilizing diverse sets of indicators without a unified KPI-stack. Moving away from case-by-case analysis, this work proposes a unified methodology featuring a standardized algorithm for measurements, calculations, and reporting, aligned with established standards (ST RK GOST R ISO pro14044) [38].

It should be noted that this methodology places a specific focus on plasma ignition as a distinct phase. While existing research primarily focuses on steady-state gasification and melting, this study distinguishes the plasma ignition/flame stabilization phase as an object of separate quantitative assessment via the EIC (Exergetic Ignition Cost).

This development introduces the KPI-stack for plasma technologies—specifically, the implementation of a parameter set comprising $\eta_{ex}(T)$, $Q_{sp}(T)$, EIC and EPI as a formalized standard. In contrast, existing research typically utilizes combinations such as "Efficiency + Conversion Rate + Q_{sp}." This methodology integrates energy, energy quality, and environmental impact into a single quantitative framework.

The methodology maintains a rigorous link to metrology and measurement uncertainty. To develop and approve a formal standard, it is necessary to define requirements for measuring instruments, logging procedures, total uncertainty assessment, and internal quality control according to RMG 61-2010 and RMG 76-2014 [39–41]—elements that are absent in most scientific publications.

Prospects for Utilizing the KPI-stack Methodology

Based on published international studies, the potential transferability of the KPI-stack to fusion, high-energy physics, and cryogenic systems is discussed conceptually. No dedicated calculations or experimental validation for these sectors were performed in the present study. In the realms of nuclear energy and thermonuclear fusion, exergetic analysis is already actively employed. In [41], it is demonstrated that improper matching of temperature levels between the blanket and the power cycle loops leads to significant exergy destruction; thus, exergetic analysis serves as the primary tool for selecting heat exchange configurations. Through entropy and exergy analysis, the main sources of losses and "bottlenecks" in the thermal schemes of fusion power plants are identified [42].

In [43], a detailed exergetic analysis of individual loops (reactor cooling, power cycle, and heat rejection to the heat sink) was introduced, allowing for the quantitative assessment of exergy destruction along the chain. Furthermore, authors examine the thermodynamic characteristics of D-T (deuterium-tritium) fusion reactions and alternative fuels, including Gibbs free energy and the "spontaneity" of reactions; this effectively represents a thermodynamic (quasi-exergetic) analysis of available energy at the nuclear reaction level [44].

Exergy inflows comprise the thermonuclear power in the blanket, the electrical power supplied to the magnetic system, pumps, and cryogenics. Exergy products include electricity at the busbars, useful low- and medium-potential heat (e.g., for district heating), as well as losses (radiation beyond limits, heat leaks, etc.).Following the example of plasma gasification, exergy efficiency (η_{ex}) is the ratio of useful exergy (electrical energy + useful heat) to the total exergy of inflows and reactions. Specific energy consumption (Q_{sp}) can be interpreted as the specific energy input or auxiliary exergy required for the ignition and maintenance of the thermonuclear plasma (kWh per unit of generated tritium or thermal power). Given that the "quality of energy" in the context of thermonuclear reactors is explicitly discussed in [41], the KPI-stack aligns with these objectives with almost no modifications.

High Energy Physics and Accelerator Complexes

In the field of High Energy Physics (HEP), exergetic analysis is already applied to cryogenic systems and high-temperature superconductors. In [45], it is demonstrated that the exergetic analysis of the LHC (Large Hadron Collider) helium cryosystem allows for a direct link between local losses and the additional power consumption of the refrigeration plant, enabling the optimization of the distribution scheme. Exergetics serves as a tool for optimizing helium liquefaction cycles applicable to superconducting magnets and accelerators [46]. Furthermore, a comprehensive energy and exergy optimization of the HALF (Hefei Advanced Light Facility) synchrotron cryosystem has been performed [48]. Papers on the energy and exergy analysis of cryosystems for High-Temperature Superconducting (HTS) magnets also demonstrate the use of the Second Law of Thermodynamics as the primary efficiency criterion [49]. The review in [50] emphasizes that exergetic analysis is a key tool for evaluating the "energy quality" and sustainability of cryogenic systems.

Thus, the presented methodology is applicable to cryogenic systems, where the objects of study include cryogenic complexes, magnets, RF systems, and detector cooling systems. Exergy inflows consist of the electrical energy from power supply units and the chemical exergy of liquefied gases (He, N_2, Ne, etc.). Exergy products include the maintenance of superconductivity (low temperature as a "high-quality resource"), magnetic field stability, and accelerator operation.

Exergy efficiency (η_{ex}) evaluates what portion of the input exergy is actually used to maintain the required physical conditions and what portion is dissipated as irreversible losses (throttling, Joule losses, heat leaks). Specific energy consumption (Q_{sp}) is defined as the specific energy input per unit of useful "physical work" (e.g., kWh/T·m of magnetic field or kWh/MJ of accumulated beam energy). Formally, the framework is analogous, substituting syngas and MSW with cryogenics and accelerators.

Adaptation of the KPI-stack to Nuclear & HEP

It should be noted that the integration of this methodology is based on four primary indicators applicable to related fields:

Exergy Efficiency (η_{ex}):

- for nuclear systems, this represents the "reactor + power plant" exergy efficiency (the ratio of electrical and useful thermal power to the total exergy of the reaction and auxiliary electricity);
- for high-energy physics accelerators, this represents the exergy efficiency of the cryogenic and magnetic systems (useful "physical exergy" of the experimental conditions / exergy of the input energy).

Specific Energy Consumption ($Q_{sp}(T)$):

- for nuclear systems, this represents the specific energy consumption of the plasma subsystem (heating, confinement, injection) per unit of generated power;
- for high-energy physics accelerators, this represents the kWh per unit of integrated luminosity or accumulated beam energy.

EIC (Exergetic Ignition Cost):

- for nuclear systems, this is the exergetic cost of bringing the reactor/flame/plasma to the operating mode (startup, blanket heating, cryogenic cooldown);
- in high-energy physics, this is the exergetic cost of beam acceleration and bringing the magnetic system to the operating field.

EPI (Environmental Performance Index):

- for nuclear systems, this is a combination of exergy efficiency with indicators of radiation impact, material activation, and thermal discharges;
- for high-energy physics facilities, this represents the link between the η_{ex} of cryogenics and cooling systems and the carbon footprint and energy consumption of the complex.

The review [42–45] confirms that such an approach is not only feasible but also a logical extension of current practices, as exergy is explicitly identified as a key tool for design (an instrument for quantitative analysis).

Conclusions

This work has developed an exergetic methodology and verified its applicability against previously published experimental data for the quantitative assessment of plasma process efficiency, based on the Second Law of Thermodynamics and implemented as a formalized set of indicators: the KPI-stack (η_{ex}, Q_{sp}, EIC, EPI). The proposed approach enables a transition from fragmented energy criteria to a unified, reproducible evaluation system focused on energy quality and the level of irreversible losses.

Calculations have shown that at a fixed process thermal power of 2000kW, the use of a plasma-assisted oil sludge processing mode ensures a steady increase in exergy efficiency compared to traditional combustion. The differential exergy efficiency increases from 0.546 at 1100K to 0.636 at 1500K and reaches 0.675 at 2000 K, which corresponds to an efficiency increase of 16.3% and 23.6%, respectively. A similar trend is observed for the integral exergy efficiency, with values increasing from 0.547 to a range of 0.652-0.692.

Analysis of specific exergy losses showed that increasing the temperature and implementing a plasma torch are accompanied by a reduction in exergy destruction within the system. The Q_{sp} value decreases from 18.27MJ/kg for traditional combustion to 16.36MJ/kg at 1500K and to 14.48MJ/kg at 2000K, indicating a more rational utilization of the fuel's chemical exergy.

It was established that the increase in the Exergetic Ignition Cost (EIC) in plasma modes (up to 6.84MJ/kg compared to 0.135MJ/kg) is local in nature and primarily associated with the ignition and process stabilization phases. In steady-state operation, these costs are offset by the increase in exergetic efficiency and the reduction of total losses, confirming the necessity of separate accounting for startup and steady-state regimes.

The extension of the KPI-stack to fusion and cryogenic systems remains prospective and requires domain-specific definitions, datasets, and independent validation.

Environmental analysis demonstrated that the application of plasma-assisted processing leads to an improvement in the environmental indicators of the process. The Environmental Performance Index (EPI) increases from 0.0218 for traditional combustion to 0.0795 at 1500K and up to 0.1125 at 2000K, which is attributed to a decrease in NO_2 concentration in emissions from 250mcg/m^3 to 80-60mcg/m^3 alongside a simultaneous increase in exergy efficiency.

Furthermore, it was shown that the plasma processing of oil sludge is accompanied by the formation of energy-valuable syngas. The total exergy of the gas increases from 143.2MJ at 1100K to 150.0MJ at 1500K and reaches 156.7MJ at 2000K, with more than 90% of the exergy accounted for by the chemical exergy of hydrogen and carbon monoxide. This indicates the possibility of viewing plasma technologies not only as thermal disposal methods but also as elements of the Waste-to-Value (WtV) concept. Thus, the proposed KPI-stack forms an objective and scalable basis for comparing plasma technologies, optimizing operational modes, and subsequently integrating exergetic criteria into Best Available Techniques (BAT) practices. The results obtained confirm the potential of plasma-assisted processes for enhancing the energy and environmental efficiency of complex hydrocarbon waste processing.

Acknowledgements

This scientific work was supported by the Ministry of Education and Science of the Republic of Kazakhstan through targeted program financing (TPF) (grant BR24992915).

REFERENCES

1 Decree of the President of the Republic of Kazakhstan dated February 2, 2023, No. 121, Ukaz Prezidenta Respubliki Kazakhstan ot 2 fevralya 2023 goda № 121 «Ob utverzhdenii Strategii dostizheniya uglerodnoy neytral'nosti Respubliki Kazakhstan do 2060 goda» [On approval of the Strategy for achieving

carbon neutrality of the Republic of Kazakhstan until 2060] (2023). (in Russian). URL: https://unfccc.int/sites/default/files/resource/Carbon_Neutrlaity_Strategy__Kazakhstan_Ru_Oct2024.pdf

2 Malehmirchegini, L., and Chapman, A.J. Strategies for achieving carbon neutrality within the chemical industry. Renewable and Sustainable Energy Reviews, 217, 115762 (2025). https://doi.org/10.1016/j.rser.2025.115762

3 Mountouris, A., Voutsas, E., and Tassios, D. Solid waste plasma gasification: Equilibrium model and exergy analysis. Energy Conversion and Management, 47 (11–12), 1490–1507 (2006). https://doi.org/10.1016/j.enconman.2005.08.019

4 Messerle, V.E., Ustimenko, A.B., Lavrichshev, O.A., and Nugman, M.K. The Gasification and Pyrolysis of Biomass Using a Plasma System. Energies, 17 (22), 5594 (2024). https://doi.org/10.3390/en17225594

5 Zhang, Q., Wu, Y., Dor, L., Yang, W., and Blasiak, W. A thermodynamic analysis of solid waste gasification in the Plasma Gasification Melting process. Applied Energy, 112, 405–419 (2013). https://doi.org/10.1016/j.apenergy.2013.03.054

6 Wu, Y., et al. Energy and Exergy Analysis of High Temperature Agent Gasification of Biomass. Energies, 7 (4), 2107–2122 (2014). https://doi.org/10.3390/en7042107

7 Hungsberg, M., et al. Thermodynamic equilibrium investigation to operational optimization of plasma gasification in waste-to-value concepts. Chemical Engineering Science, 248, 117130 (2022). https://doi.org/10.1016/j.ces.2021.117130

8 Parmar, D.J., Patel, V.R., Dabhi, S.K., and Shaikh, M.A. Comprehensive thermodynamic equilibrium model with modified equilibrium constants for biomass downdraft gasifiers. PALIVA, 17 (1), 40 (2025).

9 Tamayo-Pacheco, J.J., et al. Thermodynamic analysis of sugarcane bagasse plasma gasification. Thermal Science and Engineering, 3 (2), 1502 (2020). https://doi.org/10.24294/tse.v3i2.1502

10 Messerle, V.E., Mosse, A.L., and Ustimenko, A.B. Plasma gasification of carbonaceous wastes: thermodynamic analysis and experiment. Thermophysics and Aeromechanics, 23 (4), 613–620 (2016). https://doi.org/10.1134/S0869864316040144

11 Messerle, V.E., and Ustimenko, A.B. Solid Fuel Plasma Gasification. In: Syred N. and Khalatov A. (eds.) Advanced Combustion and Aerothermal Technologies. NATO Science for Peace and Security Series C: Environmental Security (Dordrecht: Springer, 2007), pp. 141–156. https://doi.org/10.1007/978-1-4020-6515-6_12

12 Messerle, V.E., Ustimenko, A.B., and Lavrichshev, O.A. Comparative study of coal plasma gasification: Simulation and experiment. Fuel, 164, 172–179 (2016). https://doi.org/10.1016/j.fuel.2015.09.095

13 Messerle, V., Ustimenko, A., Lavrichshev, O., Slavinskaya, N., and Sitdikov, Z. Gasification of biomass in a plasma gasifier. Detritus, 12, 66–72 (2020). https://doi.org/10.31025/2611-4135/2020.13989

14 Messerle, V.E., and Ustimenko, A.B. Plasma Gasification of Coal with the Extraction of Valuable Components of the Mineral Mass. Journal of Siberian Federal University. Engineering & Technologies, 9 (8), 1311–1313 (2016). https://doi.org/10.17516/1999-494X-2016-9-8-1311-1313

15 Messerle, V., and Ustimenko, A. Modelling of the pulverized coal plasma preparation for combustion. Physical Sciences and Technology, 8 (1), 14 (2021). https://doi.org/10.26577/phst.2021.v8.i1.02

16 Panesi, M. Physical models for nonequilibrium plasma flow simulations at high speed re-entry conditions (von Karman Institute for Fluid Dynamics, 2009).

17 Johnston, C.O. Ph.D. thesis (Virginia Polytechnic Institute and State University, 2006).

18 Zanardi, I., Padovan, A., Bodony, D.J., and Panesi, M. Petrov-Galerkin model reduction for thermochemical nonequilibrium gas mixtures. Journal of Computational Physics, 533, 113999 (2025). https://doi.org/10.1016/j.jcp.2025.113999

19 Radiation of Plasma Sources. Lecture notes (Instituto Superior Técnico, 2022).

20 Bernatskiy, A.V., Kochetov, I.V., and Ochkin, V.N. Spectral Methods of Control of Impurities, Their Flows and Localization in an Equilibrium Low-Temperature Plasma of Low Pressure. Plasma Physics Reports, 46 (9), 874–881 (2020). https://doi.org/10.1134/S1063780X20090020

21 Chen, C.-T., Banaru, D., Sarnet, T., and Hermann, J. Two-step procedure for trace element analysis in food via calibration-free laser-induced breakdown spectroscopy. Spectrochimica Acta Part B: Atomic Spectroscopy, 150, 77–83 (2018). https://doi.org/10.1016/j.sab.2018.10.011

22 Cianfrani, F., Borodin, D.V., and Küppers, B. Data processing and visualization tool for atomic and molecular data for collisional radiative models. The European Physical Journal D, 77 (8), 139 (2023). https://doi.org/10.1140/epjd/s10053-023-00722-5

23 Capitelli, M., Armenise, I., Bruno, D., and Cacciatore, M. Non-equilibrium plasma kinetics: A state-to-state approach. Plasma Sources Science and Technology, 16 (1), S30–S44 (2007). https://doi.org/10.1088/0963-0252/16/1/S03

24 World Health Organization. Dioxins and their effects on human health (2023). https://www.who.int/news-room/fact-sheets/detail/dioxins-and-their-effects-on-human-health

25 Environmental Code of the Republic of Kazakhstan, Ekologicheskiy kodeks Respubliki Kazakhstan ot 2 yanvarya 2021 goda № 400-VI ZRK [Code of the Republic of Kazakhstan dated January 2, 2021, No. 400-VI ZRK] (2021). (in Russian). https://adilet.zan.kz/rus/docs/K2100000400

26 Karamarković, R., and Karamarković, V. Energy and exergy analysis of biomass gasification at different temperatures. Energy, 35 (2), 537–545 (2010). https://doi.org/10.1016/j.energy.2009.10.022

27 Messerle, V., Ustimenko, A., Karpenko, E., Lockwood, F., and Jankoski, Z. Plasma assisted coal combustion. Theory and experiment. Recent Contributions to Physics, 43 (1), 1 (2013). https://bph.kaznu.kz/index.php/zhuzhu/article/view/70

28 Shahbeig, H., Shafizadeh, A., Rosen, M.A., and Sels, B.F. Exergy sustainability analysis of biomass gasification: a critical review. Biofuel Research Journal, 9 (1), 1592–1608 (2022). https://doi.org/10.18331/BRJ2022.9.1.5

29 Amulah, N.C., Oumarou, M.B., and Muhammad, A.B. Exergy Analysis of Waste-to-Energy Technologies for Municipal Solid Waste Management. Environment and Natural Resources Journal, 22 (3), 232–243 (2024). https://doi.org/10.32526/ennrj/22/20240023

30 Sornchai, A., Patcharavorachot, Y., and Saebea, D. Comparative Analysis of Syngas Production via Gasification and Plasma Gasification of Municipal Solid Waste. Chemical Engineering Transactions, 120, 103–108 (2025). https://doi.org/10.3303/CET25120018

31 Donskoy, I. Exergetic Efficiency of Coal Gasification Using High-Temperature Mixtures of O2/N2 and O2/CO2. International Journal of Thermodynamics, 28 (1), 51–61 (2025). https://doi.org/10.5541/ijot.1642883

32 Baidoo, R.R., Ferguson, F., and Yeboah, F.E. Exergy and Energy Analysis of Plasma Waste-to-power Generation Model. Cogeneration and Distributed Generation Journal, 24 (2), 51–67 (2009). https://doi.org/10.1080/15453660909595150

33 Wu, Y. Computational Fluid Dynamics Modeling of Biomass Gasification in Fixed-bed Reactors Using Highly Preheated Agent (KTH Royal Institute of Technology, 2014).

34 Messerle, V.E., Lavrishchev, O.A., and Ustimenko, A.B. Plasma-chemical waste processing: numerical analysis and experiment. Part 4. Ash-and-slag waste and oil refinery wastes. Thermophysics and Aeromechanics, 30 (4), 823–828 (2023). https://doi.org/10.1134/S0869864323040169

35 Messerle, V.E., Mosse, A.L., and Ustimenko, A.B. Plasma-chemical waste processing: numerical analysis and experiment. Part 2. Fuels and lubricants. Thermophysics and Aeromechanics, 30 (2), 387–392 (2023). https://doi.org/10.1134/S0869864323020208

36 Messerle, V.E., Ustimenko, A.B., and Lavryshchev, O.A. Plasma assisted combustion of low-rank fuels and liquid hazardous wastes. Fuel, 194, 244–252 (2017). https://doi.org/10.1016/j.fuel.2017.01.011

37 Akhmetshin, M.R. Snizhenie kontsentratsii oksidov sery i azota pri gorenii otkhodov neftedobychi i neftepererabotki v sostave kompozitsionnykh zhidkikh topliv [Reducing the concentrations of sulfur and nitrogen oxides during the combustion of oil production and refining waste as part of composite liquid fuels] Candidate dissertation (Tomsk Polytechnic University, 2023). (in Russian). https://earchive.tpu.ru/bitstream/11683/77113/1/dis00595.pdf

38 World Health Organization. WHO ambient air quality database, 2021 update (2021). https://www.who.int/news-room/feature-stories/detail/what-are-the-who-air-quality-guidelines

39 ST RK GOST R ISO 14044-2010, Ekologicheskiy menedzhment. Otsenka zhiznennogo tsikla. Trebovaniya i rukovodyashchiye ukazaniya [Environmental management. Life cycle assessment. Requirements and guidelines] (2010). (in Russian).

40 RMG 61-2010, Gosudarstvennaya sistema obespecheniya yedinstva izmereniy. Pokazateli tochnosti, pravil'nosti, pretsizionnosti metodik kolichestvennogo khimicheskogo analiza. Metody otsenki [State system for ensuring the uniformity of measurements. Accuracy, trueness and precision measures of quantitative chemical analysis methods. Methods of evaluation] (2010). (in Russian).

41 RMG 76-2014, GSI. Vnutrenniy kontrol' kachestva rezul'tatov kolichestvennogo khimicheskogo analiza [State system for ensuring the uniformity of measurements. Internal quality control of quantitative chemical analysis results] (2014). (in Russian).

42 Khan, M.S., et al. A comprehensive review of primary heat transfer and energy conversion systems in fusion power plants. Energy, 344, 139722 (2026). https://doi.org/10.1016/j.energy.2025.139722

43 Bozorgian, A., and Norouzi, N. Thermal Design of a Fusion Power Plant and Its Waste Heat Recovery to Produce Hydrogen. Thermal Science and Engineering, 42 (2), 538 (2023). https://doi.org/10.37256/tse.4220232490

44 Linares, J., et al. Supercritical CO2 Brayton power cycles for DEMO fusion reactor based on Dual Coolant Lithium Lead blanket (EUROFUSION Report, 2015).

45 Tosti, S. Classical Thermodynamic Analysis of D-Based Nuclear Fusion Reactions: The Role of Entropy. Energies, 16 (10), 3996 (2023). https://doi.org/10.3390/en16103996

46 Taghavi, S.M., Salarian, H., and Ghorbani, B. Thermodynamic and exergy evaluation of a novel integrated hydrogen liquefaction structure using liquid air cold energy recovery, solid oxide fuel cell and photovoltaic panels. Journal of Cleaner Production, 320, 128821 (2021). https://doi.org/10.1016/j.jclepro.2021.128821

47 Thomas, R.J., Ghosh, P., and Chowdhury, K. Application of exergy analysis in designing helium liquefiers. Energy, 37 (1), 207–216 (2012). https://doi.org/10.1016/j.energy.2011.11.044

48 Li, M. Thermodynamic Analysis and Multi-Objective Optimization of the Hefei Advanced Light Facility (HALF) Cryogenic System. SSRN Preprint (2024). https://doi.org/10.2139/ssrn.5204119

49 Zheng, J., and Li, J. Energy and exergy analysis of the cryogenic system for HTS magnets based on an open-cycle G-M/J-T cryocooler. Physica C: Superconductivity and its Applications, 619, 1354478 (2024). https://doi.org/10.1016/j.physc.2024.1354478

50 Perin, A., et al. Cryogenic Efficiency and Sustainability Aspects for Particle Accelerators and Detectors. In: Proceedings of the 16th International Particle Accelerator Conference (IPAC25) (2025).

[1]Мессерле В.Е.,
ф.-м.ғ.д., профессор, ORCID ID: 0000-0003-4281-1429,
e-mail: ust@physics.kz
[1]Устименко А.Б.,
ф.-м.ғ.д., профессор, ORCID ID: 0000-0003-0033-1371,
e-mail: alexanderustimenko@gmail.com
[1]Лаврищев О.А.,
ф.-м.ғ.к., доцент, ORCID ID: 0000-0002-5934-8381,
e-mail: lavr@physics.kz
[1]*Нұғман М.К.,
докторант, ORCID ID: 0009-0004-3366-5348,
*e-mail: nugmanmarina@gmail.com

[1]Әл-Фараби атындағы Қазақ ұлттық университеті, Алматы қ., Қазақстан

ПЛАЗМАЛЫҚ ПРОЦЕСТЕРДІҢ ТИІМДІЛІГІН СТАНДАРТТАЛҒАН БАҒАЛАУҒА АРНАЛҒАН ЭКСЕРГЕТИКАЛЫҚ ӘДІСТЕМЕ

Аңдатпа

Мақалада плазмалық процестердің тиімділігін сандық бағалауға арналған, олардың салыстырмалылығын, қайталанымдылығын және кейіннен стандарттауын қамтамасыз етуге бағытталған бірыңғай эксергетикалық әдістеме ұсынылған. Әзірленген тұжырымдама термодинамиканың екінші заңын қолдануға және эксергетикалық пайдалы әсер коэффициенті (η_{ex}), меншікті энергия шығындары (Q_{sp}), тұтанудың эксергетикалық құны (EIC) және экологиялық индекс (EPI) сияқты негізгі тиімділік көрсеткіштерінің формальды жиынтығын (KPI-stack) қалыптастыруға негізделген. Термодинамиканың бірінші заңына негізделген дәстүрлі энергетикалық критерийлердің энергия сапасын, қайтымсыз шығындар деңгейін және плазмалық процестердің тепе-теңдік емес сипатын көрсетпейтіні дәлелденді, бұл оларды технологияаралық салыстыру және нормалау үшін қолдану мүмкіндігін шектейді. Ұсынылған эксергетикалық тәсіл берілген энергияның химиялық, физикалық және ионизациялық құрамдастар арасында бөлінуін ескеруге, сондай-ақ процестің әртүрлі кезеңдеріндегі эксергияның бұзылуын сандық тұрғыдан бағалауға мүмкіндік береді.

Әдістеме плазмалық тұтануды, газдандыруды, реформингті және көмірсутек шикізаты мен қалдықтарын газ, сұйық және қатты фазаларда қайта өңдеуді қоса алғанда, плазмалық технологиялардың кең ауқымына бейімделген. Жұмыста экологиялық менеджмент және энергия тиімділігі саласындағы қолданыстағы ұлттық және халықаралық стандарттардың талаптарына, сондай-ақ метрологиялық қамтамасыз ету талаптарына сәйкес келетін өлшеу, есептеу және нәтижелердің белгісіздігін бағалау алгоритмі тұжырымдалған. Талдау 1100 К температурадағы дәстүрлі жану режимі және процестің белгіленген 2000 кВт жылу қуаты кезіндегі 1500–2000 К температурадағы плазмалық режимдер үшін жүргізілді. Плазмотронды қолдану дифференциалдық эксергетикалық ПӘК-тің 0,546-дан 0,636–0,675-ке дейін артуына және меншікті эксергетикалық шығындардың 18,27-ден 14,48 МДж/кг-ға дейін төмендеуіне әкелетіні көрсетілген. Сонымен қатар, экологиялық индекстің артуы және шығарындылардағы NO_2 концентрациясының төмендеуі арқылы көрінетін процестің экологиялық сипаттамаларының жақсаруы байқалады. Бұдан бөлек, плазмалық режим жиынтық эксергиясы 156,7 МДж-ға дейін жететін энергетикалық құнды синтез-газдың түзілуін қамтамасыз ететіні анықталды, бұл технологияның функционалдық мүмкіндіктерін қарапайым термиялық кәдеге жарату шеңберінен тыс кеңейтеді. Алынған нәтижелер күрделі көмірсутек қалдықтарын қайта өңдеудің плазмалық технологияларын талдау және оңтайландыру үшін эксергетикалық бағытталған KPI-ларды қолданудың мақсатқа сәйкестігін растайды. Әдістеменің практикалық қолданылуы мұнай шламдарын плазмохимиялық қайта өңдеуге арналған KPI-stack көрсеткіштерін есептеу мысалында көрсетілген. Эксергетикалық көрсеткіштердің бірыңғай жиынтығын енгізу плазмалық технологияларды салыстыруға, жұмыс режимдерін оңтайландыруға және кейіннен әдістемені нормативтік-техникалық құжаттарға интеграциялауға объективті негіз беретіні көрсетілген.

Түйін сөздер: плазмалық процестер, эксергетикалық талдау, негізгі тиімділік көрсеткіштері, KPI-stack, энергия тиімділігі, декарбонизация, стандарттау.

[1]Мессерле В.Е.,
д.ф.-м.н., профессор, ORCID ID: 0000-0003-4281-1429,
e-mail: ust@physics.kz
[1]Устименко А.Б.,
д.ф.-м.н., профессор, ORCID ID: 0000-0003-0033-1371,
e-mail: alexanderustimenko@gmail.com
[1]Лаврищев О.А.,
к.ф.-м.н., доцент, ORCID ID: 0000-0002-5934-8381,
e-mail: lavr@physics.kz
[1]*Нұғман М.К.,
докторант, ORCID ID: 0009-0004-3366-5348,
*e-mail: nugmanmarina@gmail.com

[1]Казахский национальный университет им. аль-Фараби, г. Алматы, Казахстан

ЭКСЕРГЕТИЧЕСКАЯ МЕТОДОЛОГИЯ СТАНДАРТИЗИРОВАННОЙ ОЦЕНКИ ЭФФЕКТИВНОСТИ ПЛАЗМЕННЫХ ПРОЦЕССОВ

Аннотация

В статье предложена унифицированная эксергетическая методика количественной оценки эффективности плазменных процессов, ориентированная на их сопоставимость, воспроизводимость и последующую стандартизацию. Разработанная концепция основана на применении второго закона термодинамики и формировании формализованного набора ключевых показателей эффективности (KPI-stack), включающего эксергетический коэффициент полезного действия (η_{ex}), удельные энергозатраты (Q_{sp}), эксергетическую цену воспламенения (EIC) и экологический индекс (EPI). Показано, что традиционные энергетические критерии, базирующиеся на первом законе термодинамики, не отражают качество энергии, уровень необратимых потерь и неравновесный характер плазменных процессов, что ограничивает их применимость для межтехнологического сравнения и нормирования. Предлагаемый эксергетический подход позволяет учесть распределение подведенной энергии между химической, физической и ионизационной составляющими, а также количественно оценить разрушение эксергии на различных стадиях процесса. Методика адаптирована для широкого класса плазменных технологий, включая плазменное воспламенение, газификацию, реформинг

и переработку углеводородного сырья и отходов в газовой, жидкой и твердой фазах. В работе сформулирован алгоритм измерений, расчетов и оценки неопределенности результатов, согласованный с требованиями метрологического обеспечения и действующих национальных и международных стандартов в области экологического менеджмента и энергоэффективности. Анализ выполнен для традиционного сжигания при 1100K и плазменных режимов при 1500-2000K при фиксированной тепловой мощности процесса 2000кВт. Показано, что использование плазмотрона приводит к увеличению дифференциального эксергетического КПД с 0,546 до 0,636-0,675 и снижению удельных эксергетических потерь с 18,27 до 14,48МДж/кг. Одновременно наблюдается улучшение экологических характеристик процесса, выраженное в росте экологического индекса и снижении концентрации NO_2 в выбросах. Дополнительно установлено, что плазменный режим обеспечивает формирование энергетически ценного синтез-газа с суммарной эксергией до 156,7МДж, что расширяет функциональность технологии за пределы простой термической утилизации. Полученные результаты подтверждают целесообразность применения эксергетически ориентированных KPI для анализа и оптимизации плазменных технологий переработки сложных углеводородных отходов. Практическая применимость методики продемонстрирована на примере расчета KPI-stack для плазмохимической переработки нефтешламов. Показано, что введение унифицированного набора эксергетических показателей обеспечивает объективную основу для сравнения плазменных технологий, оптимизации режимов работы и последующей интеграции методики в нормативно-технические документы.

Ключевые слова: плазменные процессы, эксергетический анализ, ключевые показатели эффективности, KPI-stack, энергоэффективность, декарбонизация, стандартизация.

МҰНАЙ ГАЗ ИНЖЕНЕРИЯСЫ ЖӘНЕ ГЕОЛОГИЯ
OIL AND GAS ENGINEERING, GEOLOGY
НЕФТЕГАЗОВАЯ ИНЖЕНЕРИЯ И ГЕОЛОГИЯ

УДК 544.77
МРНТИ 31.15.37

https://doi.org/10.55452/1998-6688-2026-23-3-518-535

[1]*Исаева А.Б.,
PhD, ORCID ID: 0000-0001-6727-0257,
*e-mail: isa-asem@mail.ru
[1]Айдарова С.Б.,
д.х.н., профессор, ORCID ID: 0000-0001-5115-5879,
e-mail: s.aidarova@kbtu.kz
[2]Шарипова А.А.,
PhD, ассоциированный профессор, ORCID ID: 0000-0002-2217-9975,
e-mail: a_sharipova85@mail.ru
[1]Исахов М.О.,
PhD докторант, ORCID ID: 0009-0005-6660-5758
e-mail: mir001@gmail.com

[1] Казахстанско-Британский технический университет, Алматы г., Казахстан
[2] Satbayev university, г. Алматы, Казахстан

ФИЗИКО-ХИМИЧЕСКИЕ ХАРАКТЕРИСТИКИ КОМПОЗИЦИОННЫХ ПЕН НА ОСНОВЕ ПАВ И НАНОЧАСТИЦ И ИХ ЭФФЕКТИВНОСТЬ В ПОВЫШЕНИИ НЕФТЕОТДАЧИ

Аннотация

Несмотря на значительный объем исследований, посвященных влиянию наночастиц на устойчивость газовых пен и коэффициент снижения подвижности (MRF), в литературе отсутствуют единые рекомендации по оптимальному диапазону концентраций наночастиц с учетом комплекса пластовых параметров, включая температуру, давление, проницаемость керна и соленость пластовых флюидов. Кроме того, влияние наностабилизированных пен на процессы вытеснения нефти и взаимодействие с нефтяной фазой изучено недостаточно, а в масштабе реальных месторождений оценка эффективности нанопен (NAF) при различных уровнях неоднородности коллектора практически не выполнялась. Настоящее исследование направлено на устранение этих пробелов путем сочетания лабораторных экспериментов и численного моделирования. В работе представлены результаты всестороннего исследования физико-химических характеристик композиционных систем на основе поверхностно-активных веществ (ПАВ) и наночастиц диоксида кремния, ориентированных на повышение стабильности газовых пен, применяемых в процессах повышения нефтеотдачи. Показано, что традиционные ПАВ-пены демонстрируют ограниченную устойчивость при высоких температурах, давлениях и минерализации, что существенно снижает их эффективность в условиях реальных пластов. Для решения этой проблемы изучено влияние наночастиц SiO_2 на межфазные свойства таких систем,

включая анионные, катионные и неионогенные ПАВ. На основе экспериментальных данных определены модифицирующие коэффициенты для периода полураспада пены и MRF, которые интегрированы в симуляционную модель вытеснения нефти. Численное моделирование показало значительный рост охвата пласта и задержку газового прорыва при использовании нанокомпозитных пен, особенно в условиях высокой неоднородности. Полученные результаты подтверждают перспективность наностабилизированных пен как эффективных агентов МУН и обосновывают их применение для увеличения нефтеотдачи на сложнопостроенных месторождениях.

Ключевые слова: наночастицы, повышение нефтеотдачи, ПАВ-пены, коэффициент снижения подвижности, поверхностное натяжение, CO_2-заводнение.

Введение

Разработка недорогих, экологичных и эффективных методов увеличения нефтеотдачи остается актуальной задачей нефтяной промышленности, особенно на фоне снижения пластовой энергии. Среди применяемых технологий значительное внимание уделяется газовому заводнению, включая использование CO_2 [1–5]. Метод CO_2-заводнения является перспективным, поскольку позволяет повысить добычу нефти более чем на 10% и удерживать до 50% закачанного CO_2 в пласте, одновременно выступая инструментом декарбонизации. Около 34% улавливаемого CO_2 в мире направляется на процессы EOR/EGR, что соответствует целям устойчивого развития (ЦУР 13).

CO_2 обладает высокой растворимостью в нефти и ограниченной растворимостью в воде, что обеспечивает более высокую нефтеотдачу по сравнению с полимерным заводнением. Однако в трещиноватых и неоднородных пластах возникают проблемы: высокая подвижность газа, неравномерное распределение и ранний прорыв, что снижает эффективность метода [6–7].

Одним из решений является применение CO_2/пены, которая увеличивает кажущуюся вязкость газа и уменьшает его подвижность [5]. Недостатком остается низкая стабильность пены при высоких температурах и в присутствии сырой нефти. В этой связи все большее внимание уделяется наночастицам, способным повышать стабильность газовых пен и эмульсий в экстремальных условиях коллектора [8–13].

Для повышения эффективности CO_2-заводнения требуется комплексное исследование свойств пен на основе ПАВ, модифицированных наночастицами, и моделирование их влияния на нефтеотдачу в условиях реальных резервуаров.

Закачка смешивающегося диоксида углерода (CO_2) является одним из наиболее распространенных и перспективных методов увеличения нефтеотдачи пласта (МУН), широко применяемым уже более сорока лет. К факторам, влияющим на эффективность закачки CO_2 как метода повышения нефтеотдачи пласта, относятся способность к достижению многократной смешиваемости при контакте и низкая растворимость в воде, что обеспечивает более высокий коэффициент извлечения нефти по сравнению с заводнением водой. Другими благоприятными факторами, делающими CO_2 подходящим выбором для повышения нефтеотдачи пласта, являются снижение вязкости сырой нефти, набухание нефти, испарение более тяжелых компонентов нефти при контакте с газовой фазой и снижение межфазного натяжения (IFT) сырой нефти за счет растворенного в нефти газообразного CO_2. Однако метод повышения нефтеотдачи пласта с помощью CO_2 имеет ряд внутренних (присущих) ограничений, главным образом из-за его очень низкой вязкости по сравнению с большинством видов сырой нефти, встречающихся в подземных (пластовых) формациях. Низкая вязкость и плотность CO_2 может привести к серьезным проблемам с контролем подвижности, таким как вязкостная пальцеобразная структура и образование каналов, тенденция к гравитационному обгону CO_2, преимущественный поток газа через высокопроницаемые каналы и нестабильное перемещение фронта. В результате может произойти ранний прорыв газа, который является потенциальной причиной неудачи проекта повышения нефтеотдачи пласта, особенно в коллекторах, содер-

жащих вязкую сырую нефть. Ряд исследователей разработали и внедрили гибридные методы повышения нефтеотдачи пласта на основе CO_2, такие как пенообразование, для преодоления проблем с подвижностью, связанных с закачкой CO_2, и для повышения коэффициента извлечения остаточной нефти. Во время пенообразования газообразный CO_2 превращается в вязкую пену под высоким давлением и при высокой скорости сдвига, а затем закачивается в пласт для повышения кажущейся вязкости газа и снижения его подвижности за счет иммобилизации большого объема газа внутри пор [14].

Улучшение пенообразования обычно достигается с помощью химических агентов. Поверхностно-активные вещества (ПАВ), такие как альфа-олефинсульфонаты (AOS), додецилсульфат натрия (SDS), додецилтриметиламмоний бромид (DTAB), цетилтриметиламмоний бромид (CTAB), полиоксиэтилен-23 лаурил эфир (Brij 35), полиоксиэтилен-20 цетил эфир (Brij 58), полиоксиэтилен сорбитан монолаурат (Tween 20) и полиоксиэтилен сорбитан монопальмитат (Tween 40), широко используются для образования и стабилизации пены [15–18]. Этот подход известен как пенообразование с помощью ПАВ (или стабилизированное ПАВ). Образовавшаяся пена улучшает нефтеотдачу за счет снижения подвижности газовой фазы посредством образования ламелей в водной фазе [19].

Суровые условия в пластах, такие как высокое давление, высокая температура и высокая соленость, могут оказывать негативное влияние на эффективность пены на основе ПАВ. В таких условиях ПАВ склонны к большей адсорбции на поверхности породы и могут потерять способность поддерживать стабильность пены. Поэтому для повышения качества и стабильности пены рассматриваются различные подходы. В течение последних нескольких лет широко изучалось применение наночастиц (НЧ) с целью повышения эффективности пенообразования на основе ПАВ в пластах. Они покрывают частицы ПАВ подобно щиту, что приводит к укреплению пузырьков пены. Кроме того, наночастицы уменьшают адсорбцию ПАВ на породе, что может повысить стабильность пены и замедлить ее разрушение. Кроме того, наночастицы играют ключевую роль в повышении вязкости пены. Из-за высокой вязкости нефти в пластах увеличение вязкости пены, стабилизированной наножидкостью, влияет на коэффициент подвижности и улучшает нефтеотдачу. Следовательно, сочетание ПАВ и наночастиц является эффективным способом повышения применимости пены.

Устойчивость пены играет решающую роль в повышении нефтеотдачи пластов, особенно в высокопроницаемых коллекторах, где пена может помочь контролировать подвижность газа и тем самым повысить эффективность отбора. На устойчивость пены влияют различные факторы, включая выбор ПАВ, его концентрацию, температуру пласта, давление, соленость и наличие нефти. В последние годы наночастицы стали перспективным кандидатом на роль стабилизаторов пены при повышении нефтеотдачи пластов. Благодаря своим уникальным свойствам, таким как высокотемпературная стабильность и низкая адсорбция на поверхности горных пород, наночастицы могут значительно повысить устойчивость пены в суровых пластовых условиях.

Стабильность пены с использованием наночастиц (NAF) зависит от ряда факторов, таких как тип наночастиц, их концентрация, степень гидрофобности, соленость, жесткость, температура и скорость закачки. Для получения стабильных пен использовались различные наночастицы, включая SiO_2, Al_2O_3, TiO_2, Fe_3O_4 и CuO [20–23], из которых SiO_2 является наиболее распространенной и основным объектом нашего исследования. В большинстве исследований использовались наночастицы кремнезема из-за их гидрофильной природы, низкой токсичности и высокой растворимости в воде. ПАВ часто используются для повышения дисперсности и стабильности наножидкостей. Добавление определенных ПАВ в наножидкость может значительно снизить степень агрегации наночастиц.

Стабильность пены оценивается с помощью статических испытаний, таких как пенообразующая способность и измерение изменения высоты пены с течением времени. Измеренное время, за которое объем или высота пены уменьшается до половины, называется периодом полураспада. Изменение подвижности газа как основная цель пенообразования обычно изме-

ряется параметром, называемым коэффициентом снижения подвижности (MRF). Изменение перепада давления вдоль пористой среды во время закачки пены является индикатором MRF. Эффективность пены оценивалась с помощью MRF, который показан в уравнении 1:

$$MRF = \frac{\left(\frac{KA\Delta P}{QL}\right)_{(f)}}{\left(\frac{KA\Delta P}{QL}\right)_{(g)}} = \frac{\Delta P_f}{\Delta P_g} \quad (1)$$

где K – абсолютная проницаемость, A – площадь поперечного сечения керна, Q – расход, L – длина керна, ΔPf – перепад давления в керне во время закачки пены, а ΔPg – перепад давления в керне во время закачки газа. MRF рассчитывается путем измерения и сравнения перепада давления вдоль керна во время заводнения поверхностно-активным веществом, или пеной, стабилизированной наножидкостью, или без пены (заводнение рассолом или газом) при одинаковой скорости закачки. Эффективность пены выше при более высоком MRF благодаря контролю подвижности и раннего прорыва. Обзор предыдущих исследований показал, что добавление наночастиц улучшает стабильность пены/время полураспада пены и MRF [23–25].

В отличие от ранее опубликованных работ, в которых преимущественно рассматриваются отдельные аспекты влияния наночастиц на устойчивость пен, в настоящем исследовании реализован комплексный коллоидно-химический подход к анализу систем ПАВ–SiO_2. Проведено одновременное изучение межфазных (поверхностное натяжение), объемных (размер частиц, дзета-потенциал) и реологических характеристик адсорбционных слоев. Установлена взаимосвязь между структурой адсорбционного слоя, величиной дзета-потенциала и устойчивостью пены. Дополнительно предложен подход к количественной оценке влияния наночастиц на параметры пенообразования (период полураспада и коэффициент снижения подвижности, MRF), что расширяет представления о механизмах стабилизации пен в условиях, приближенных к пластовым. Таким образом, настоящая работа направлена на комплексное изучение взаимосвязи межфазных, коллоидных и реологических свойств систем ПАВ–SiO_2 и их влияния на эффективность процессов повышения нефтеотдачи.

Материалы

В работе использованы поверхностно-активные вещества (ПАВ) различной природы: анионные (SDS), катионные (CTAB) и неионогенные (Tween, Brij). В качестве наностабилизатора применялись наночастицы диоксида кремния (SiO_2). В качестве электролита использовали раствор NaCl заданной концентрации. Все реагенты имели аналитическую степень чистоты и использовались без дополнительной очистки. Для приготовления растворов применялась деионизированная вода.

Приготовление систем

Растворы ПАВ готовили в диапазоне концентраций ниже и выше критической мицеллообразующей концентрации. Наночастицы SiO_2 вводили в растворы ПАВ при постоянном перемешивании до получения устойчивых дисперсий. Концентрация наночастиц составляла 0.1 мас. %. Перед измерениями системы выдерживали до достижения равновесного состояния.

Методы

Определение поверхностного натяжения

Динамическое поверхностное натяжение измеряли методом максимального давления пузырька (PAT-1). Измерения проводились при температуре (25 ± 1 °C).

Исследование реологических свойств адсорбционных слоев

Дилатационные реологические свойства (упругость и вязкость) адсорбционного слоя исследовали методом гармонических колебаний площади поверхности.

Определение дзета-потенциала и размера частиц

Размер частиц и дзета-потенциал определяли методом динамического рассеяния света в приборе Winner 901 Zeta Potential NanoParticle Size Analyzer. Измерения проводились при различных значениях pH и ионной силы среды.

Оценка устойчивости пены

Устойчивость пены оценивали по изменению высоты пены во времени. В качестве характеристики использовали период полураспада пены.

Исследования проводились при температуре 25 ± 1 °C. Ионная сила среды регулировалась добавлением NaCl (0.1 M). Значение pH варьировалось в зависимости от состава системы и контролировалось в процессе эксперимента. Все измерения проводились не менее чем в трех повторностях.

Результаты и обсуждение

Ископаемые виды топлива, особенно нефть и газ, остаются основными источниками энергии для удовлетворения мирового потребления энергии. Однако многие месторождения достигли или приближаются к остаточной нефтенасыщенности, что приводит к снижению добычи нефти. В ответ на эту проблему были разработаны методы повышения нефтеотдачи пласта. Например, закачка газа как МУН показала свою перспективность в снижении остаточной нефти и увеличении нефтеотдачи. Однако этому методу противостоят такие проблемы, как преждевременный прорыв газа, вязкостное пальцеобразование и гравитационная сегрегация, что приводит к снижению эффективности охвата пласта.

Для решения этих проблем широко используется технология пенообразования, которая помогает повысить нефтеотдачу за счет увеличения эффективности охвата в высокопроницаемых зонах. Образование пены с участием ПАВ называется пенообразованием с помощью ПАВ или пеной, стабилизированной ПАВ (SF). SF повышает нефтеотдачу за счет снижения подвижности закачиваемого газа, такого как CO_2, посредством образования стабильных ламелей в водной фазе. Однако пены на основе CO_2 могут разрушаться в суровых пластовых условиях, что ограничивает их долгосрочную эффективность. Чтобы преодолеть ограничения традиционных методов SF, исследователи изучили возможность использования наночастиц для стабилизации пен и достижения более высокой нефтеотдачи. Наночастицы способны адсорбироваться на межфазной границе раздела CO_2-раствор из-за разницы зарядов по сравнению с ПАВ, что повышает стабильность пены. Исследования показали, что пена, стабилизированная наночастицами, характеризуется повышенной устойчивостью к разрушению в сложных пластовых условиях.

На первом этапе этого исследования основным вопросом была возможность использования пены, стабилизированной наночастицами, для контроля прорыва газа в неоднородных пластах. На основе обобщения экспериментальных данных и литературных источников установлено, что применение NAF увеличивает вязкость пены, что отражается в коэффициенте подвижности и стабильности пены, что отражается в периоде полураспада. Приведенные ниже кривые демонстрируют влияние концентрации наночастиц на эти два параметра.

Чтобы учесть влияние NAF, мы ввели два множителя, которые учитывают влияние концентрации наночастиц на период полураспада и MRF. Необработанные лабораторные данные были собраны и проанализированы для разработки этих множителей, как показано на рисунке 1. Во время моделирования закачки пены множители периода полураспада и MRF прогнозируются для каждого этапа на основе концентрации наночастиц. Затем эти множители умножаются на соответствующие значения периода полураспада и MRF, чтобы учесть влияние наночастиц на эффективность SF. Обновленные значения затем используются для моделирования NAF.

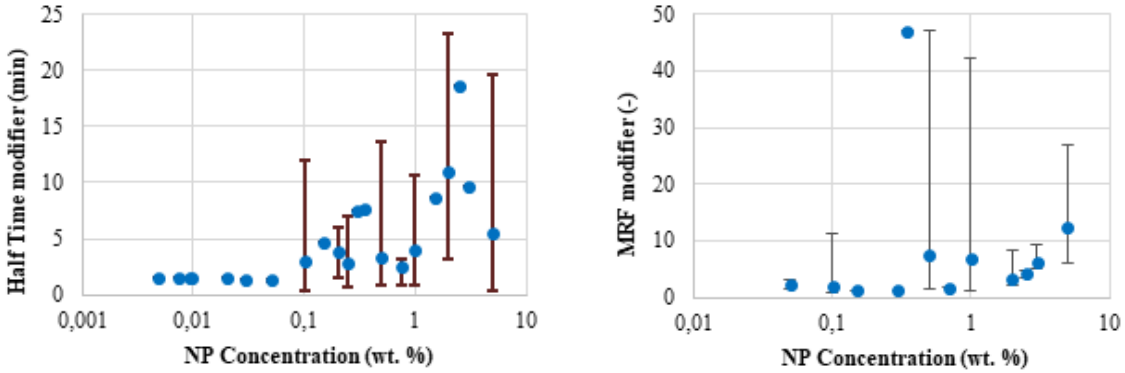


Рисунок 1 – Данные модификаторов периода полураспада
и MRF для пенообразования с использованием наночастиц:
(a) модификатор периода полураспада и (b) модификатор MRF

На основе экспериментальных данных были разработаны модели, демонстрирующие взаимосвязь между периодом полураспада и коэффициентом подвижности как функцию концентрации наночастиц. Проведено численное моделирование для анализа влияния этих улучшений на практические параметры, такие как время прорыва и коэффициент извлечения, при различных уровнях неоднородности. Результаты показывают, что преимущества пены, стабилизированной наночастицами, более выражены в неоднородных пластах. Например, следующий график иллюстрирует коэффициент извлечения как для однородных (STD = 0), так и для неоднородных (STD = 0.05) пластов. Добавление NAF значительно повышает извлечение из неоднородного пласта.

Этот эффект проиллюстрирован на рисунке 2, который отображает распределение газа в неоднородном пласте во время закачки газа для повышения нефтеотдачи с использованием различных типов пены. Очевидно, что пена, стабилизированная наночастицами, способствует более равномерному движению газа и задерживает прорыв.

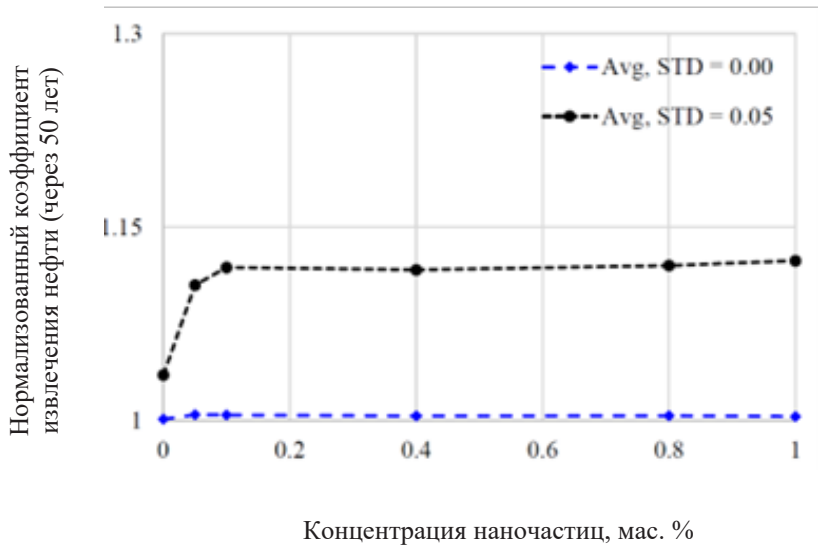


Рисунок 2 – Распределение газа в неоднородном пласте во время закачки газа
для повышения нефтеотдачи с использованием различных типов пены

Модель пласта

Для моделирования используется четверть 5-точечной схемы закачки, как показано на рисунке 3. Свойства пласта приведены в таблице 1. Для моделирования закачки пены были рассмотрены две нагнетательные скважины: одна для закачки газа и одна для закачки воды. В нагнетательной скважине вода смешивается с ПАВ. На рисунке 4 показаны исходные кривые относительной проницаемости без учета эффекта пены (MRF = 1).

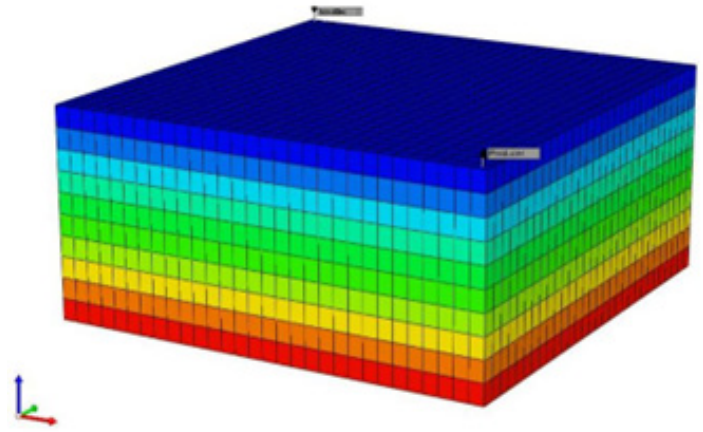


Рисунок 3 – Схема синтетической модели пласта (одна четверть 5-точечной модели), включающая два нагнетателя (нагнетатели воды и газа) и один добывающий колодец в углу модели

Таблица 1 – Характеристики синтетической модели пласта

Параметр	Значение
Количество блоков сетки (Nx, Ny, Nz)	30, 30, 10
Размер блока сетки (Δx, Δy, Δz) (ft)	50, 50, 10
Длина (фут)	5000
Высота (фут)	100
Вертикальная проницаемость (мД)	0.1Kh
Горизонтальная проницаемость (мД)	Kh
(cP)	1.13
(cP)	0.5
(фунт/фут3)	60
(фунт/фут3)	68
Пористость (доля)	0.125
Начальное давление в пласте (psi)	2900
Давление на забое добывающей скважины (psi)	2610
Скорость закачки газа (фут3/день)	706293
Скорость закачки воды (баррель/день)	6290
Продолжительность закачки (годы)	50

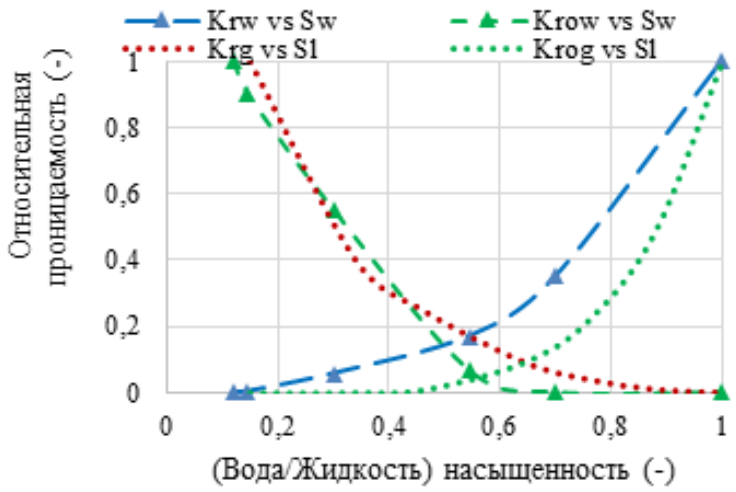


Рисунок 4 – Кривые относительной проницаемости (MRF = 1), K_{rw}: относительная проницаемость воды, K_{row}: относительная проницаемость нефти в присутствии воды, K_{rg}: относительная проницаемость газа, K_{rog}: относительная проницаемость нефти в присутствии газа, S_w: насыщенность водой и S_l: насыщенность жидкостью

Таким образом, было проведено симуляционное исследование и анализ вытеснения нефти с использованием методов повышения нефтеотдачи, таких как закачка газа, в вертикальных/площадных неоднородных коллекторах, а также влияние контроля подвижности на нефтеотдачу.

В настоящее время растет интерес к композиционным материалам, которые могут эффективно модифицировать практические свойства многочисленных видов дисперсных систем жидкостей, широко используемых во многих отраслях промышленности. К ним относятся пены различного качества и стабильности. Стабильность пен может быть обеспечена композициями ПАВ с природными и синтетическими высокомолекулярными веществами [15] и частицами [26]. Пены, стабилизированные частицами, могут быть использованы в различных промышленных и технологических областях, таких как химическое повышение нефтеотдачи пласта, флотация минералов и пищевая промышленность [27].

Повышение нефтеотдачи пластов является реальной проблемой в мировой нефтяной промышленности из-за снижения добычи нефти на многих месторождениях. Поэтому применяются различные эффективные методы повышения нефтеотдачи пласта, включая закачку газа [21, 28–30]. В этом случае закачивается пена, которая увеличивает кажущуюся вязкость газа, тем самым снижая его подвижность в порах. Однако практическое применение МУН на основе пены показывает ограничения в нефтяных средах, вызванные быстрой дестабилизацией пены при повышенных температурах, что снижает ее эффективность.

Для устранения этого ограничения и развития в области повышения нефтеотдачи пластов в настоящем исследовании изучаются новые подходы к повышению стабильности газовых пен. В частности, исследование посвящено включению наночастиц в качестве потенциальных стабилизаторов пены [21, 30–32]. Наночастицы обладают присущими им свойствами, такими как химическая стабильность и низкая адсорбция на минеральных поверхностях, что делает их привлекательными кандидатами для получения высокостабильных пен.

Более того, эти особые свойства расширяют возможности их использования в технологических областях, выходящих за рамки повышения нефтеотдачи. Стабильные газовые пены и эмульсии имеют широкий спектр применения, включая восстановление недр, улавливание и хранение углерода и даже применение в пищевой и косметической промышленности.

На рисунке 5 показана динамика изменения поверхностного натяжения (γ) водных растворов с течением времени. Исследование поверхностных свойств растворов поверхностно-

активных веществ проводилось в контролируемых условиях. Измерения динамического поверхностного натяжения выполнялись при температуре (25 ± 1) °C. Концентрация SDS и смеси SDS с наночастицами SiO_2 варьировалась в диапазоне от 0.33 до 2 мМ, включая области ниже и выше критической мицеллообразующей концентрации. Ионная сила среды регулировалась добавлением раствора NaCl (0.1 М). Для исследования влияния наночастиц использовались системы ПАВ–SiO_2 с фиксированной концентрацией наночастиц 0.1 мас. %. Перед проведением измерений растворы выдерживались до достижения равновесного состояния. Измерения проводились не менее чем в трех повторностях, и приведенные значения являются усредненными.

Снижение поверхностного натяжения с течением времени свидетельствует об адсорбции молекул SDS и композитов SDS-SiO_2 на границе раздела вода/воздух. Это приводит к уменьшению поверхностной энергии системы. Более быстрое и выраженное снижение поверхностного натяжения в смесях SDS-SiO_2 по сравнению с чистым SDS указывает на синергетический эффект. Наночастицы SiO_2, вероятно, изменяют структуру адсорбционного слоя или увеличивают эффективную концентрацию поверхностно-активных компонентов, способствуя более эффективной адсорбции SDS. Более высокие концентрации SDS обеспечивают большее количество адсорбированных молекул, что приводит к более быстрому и значительному снижению поверхностного натяжения как для чистого SDS, так и для смесей с наночастицами.

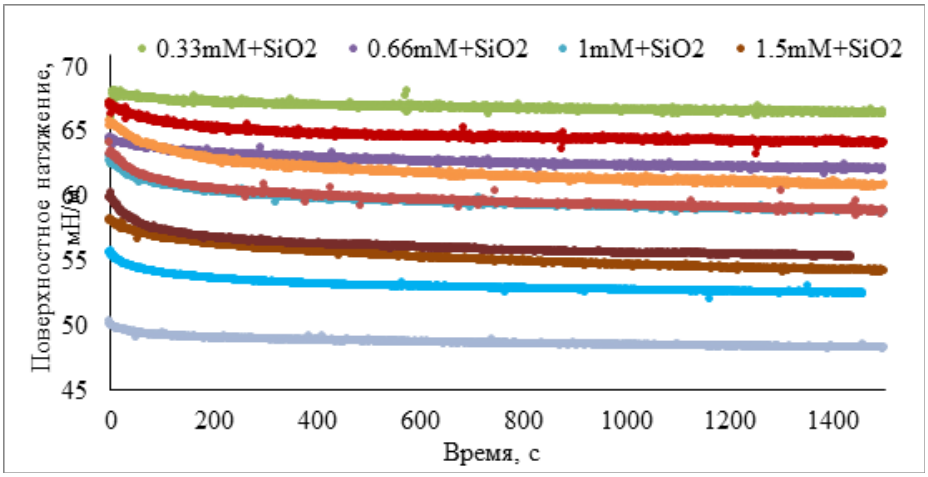


Рисунок 5 – Кинетика изменения динамического поверхностного натяжения для растворов SDS и композитной системы SDS–SiO_2 при различных концентрациях ПАВ. Линии соответствуют: светло-зеленая линия – SDS + SiO_2 (0.33 мМ), фиолетовая линия – SDS + SiO_2 (0.66 мМ), голубая линия – SDS + SiO_2 (1 мМ), коричневая линия – SDS + SiO_2 (1.5 мМ), светло-голубая линия – SDS + SiO_2 (2 мМ), красная линия – SDS (0.33 мМ), оранжевая линия – SDS (0.66 мМ), темно-голубая линия – SDS (1 мМ), бордовая линия – SDS (1.5 мМ)

На рисунках 6 и 7 показаны вязкоупругие свойства адсорбционного слоя композита SDS-SiO_2. Эти характеристики адсорбционных слоев ПАВ играют важную роль в стабильности пены, так как позволяют им противостоять разрушению под действием внешних сил и сохранять свою структуру в течение длительного времени.

Добавление наночастиц SiO_2 в раствор SDS приводит к увеличению как дилатационной упругости, так и дилатационной вязкости адсорбционного слоя. Увеличение вязкоупругости адсорбционного слоя в присутствии наночастиц SiO_2 может способствовать повышению стабильности пен, используемых в методах повышения нефтеотдачи пластов. Более устойчивые пены могут более эффективно блокировать высокопроницаемые зоны пласта, улучшая охват пласта вытесняющей жидкостью и повышая коэффициент извлечения нефти.

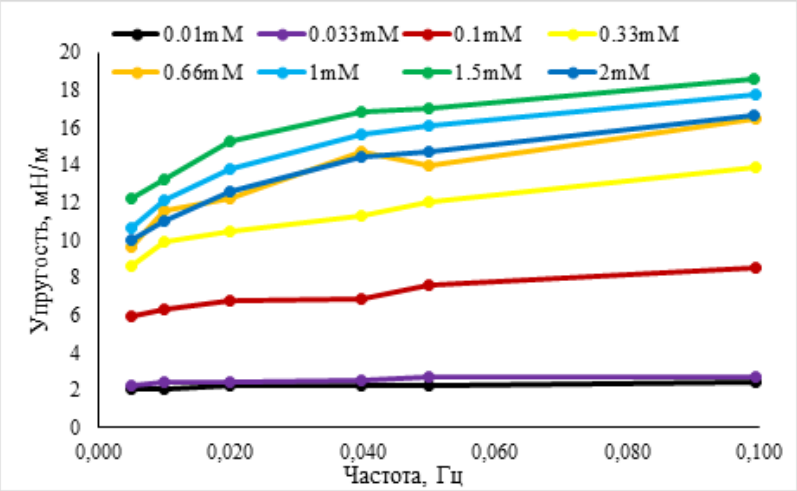


Рисунок 6 – Зависимость дилатационной упругости
от частоты гармонических колебаний композита SDS-SiO_2 (0.1 %)

Результаты других исследований подтверждают, что добавление наночастиц в растворы ПАВ может приводить к увеличению вязкоупругости адсорбционных слоев и повышению стабильности пены. Например, в работе [33] было показано, что добавление наночастиц кремнезема к растворам анионного ПАВ приводит к значительному увеличению дилатационной упругости и модуля упругости пен. Авторы объясняют этот эффект образованием более прочной и структурированной сети на границе раздела газ –жидкость в присутствии наночастиц.

При достижении определенной концентрации SDS (в нашем случае около 2 мМ) поверхность может стать перенасыщенной молекулами ПАВ. Дальнейшее увеличение концентрации может привести к образованию мицелл или других агрегатов в основной части раствора, а не к дополнительной адсорбции на поверхности. Это может снизить плотность упаковки молекул в адсорбционном слое и, как следствие, уменьшить его эластичность и вязкость.

При высоких концентрациях SDS возможно изменение конформации молекул ПАВ в адсорбционном слое, что может повлиять на его механические свойства. Например, молекулы могут более интенсивно взаимодействовать друг с другом, образуя менее упорядоченные структуры, что приведет к снижению эластичности и вязкости.

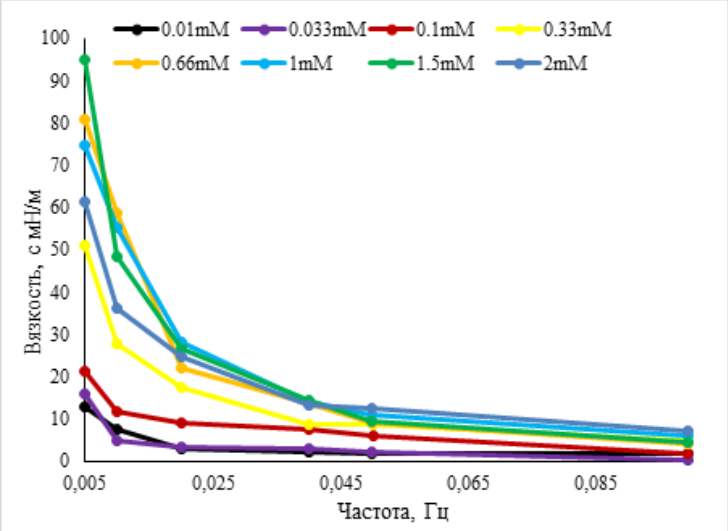


Рисунок 7 – Зависимость дилатационной вязкости
от частоты гармонических колебаний системы SDS-SiO_2 (0.1 %)

Рисунок 8 помогает понять, как изменение концентрации ПАВ влияет на структуру адсорбционного слоя и взаимодействие с наночастицами. При низких концентрациях ПАВ взаимодействие наночастиц с адсорбционным слоем может быть слабым. С увеличением концентрации ПАВ и образованием более плотного адсорбционного слоя взаимодействие наночастиц с ПАВ усиливается, и они могут встраиваться в адсорбционный слой или связываться с ним. При достижении КМЦ молекулы ПАВ начинают агрегировать в основной массе раствора, образуя мицеллы. Это может ограничить дальнейшую адсорбцию ПАВ на границе раздела фаз.

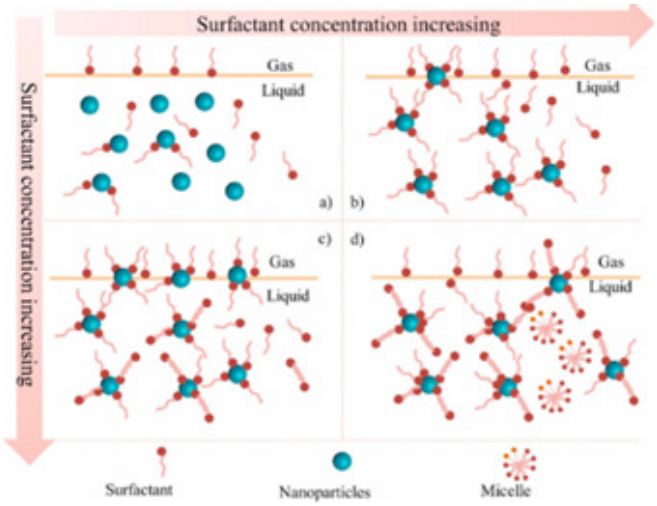


Рисунок 8 – Влияние увеличения концентрации ПАВ на адсорбцию ПАВ и наночастиц на границе раздела фаз

Таким образом, изучены поверхностно-активные свойства (поверхностное натяжение, дилатационная упругость и вязкость) ПАВ, наночастиц и их ПАВ-композитов на границе раздела фаз вода/воздух в зависимости от природы ПАВ (катионные, анионные и неионогенные ПАВ). Определен диапазон концентраций ПАВ, при которых поверхностно-активные свойства композитов проявляются в максимальной степени.

Одним из параметров, влияющих на коллоидные системы, такие как стабилизированная наночастицами пена, является заряд поверхности частиц, который можно проанализировать с помощью измерения дзета-потенциала. Молекулярное взаимодействие между различными поверхностями, находящимися в контакте друг с другом, создает электрический потенциал, известный как дзета-потенциал. Huo и др. [34] исследовали влияние дзета-потенциала на стабильность пены, содержащей наночастицы (Al_2O_3, ZrO_2) и ПАВ (SDS, CTAB). Согласно их результатам, абсолютное значение дзета-потенциала в диапазоне от 30 до 40 мВ служит порогом между стабильностью и нестабильностью пены. Они отметили, что стабильность пены снижается, когда потенциал превышает 40 мВ, из-за образования сильных отталкивающих сил. В другом исследовании Li и др. [35] оценили дзета-потенциал модифицированных многостенных углеродных нанотрубок (МСУНТ) в присутствии анионных, неионных и катионных ПАВ. Результаты показали, что более высокая абсолютная величина дзета-потенциала повышает стабильность пены. Также отмечается, что модифицированные МСУНТ с катионным ПАВ CTAB демонстрировали повышенную устойчивость пены по сравнению с анионным ПАВ SDS и неионным ПАВ OP-10, что объясняется электростатическим отталкиванием. Однако Wang и др. [36] обнаружили, что, хотя дзета-потенциал увеличивается с ростом концентрации наночастиц SiO_2, устойчивость пены не увеличивается равномерно с ростом концентрации наночастиц SiO_2. В исследовании Yekeen и др. [37] электростатическое поглощение играет более важную роль в снижении поверхностного натяжения и повышении устойчивости пены в суспензиях, содержащих наночастицы и поверхностно-активные вещества, по сравнению с электростатическим отталкиванием.

С увеличением концентрации SDS наблюдается увеличение абсолютного значения дзета-потенциала (рисунки 9) как для чистого SDS, так и для композита SDS-SiO_2. Это объясняется тем, что при более высоких концентрациях на поверхности частиц адсорбируется больше ионов SDS, что увеличивает их общий отрицательный заряд.

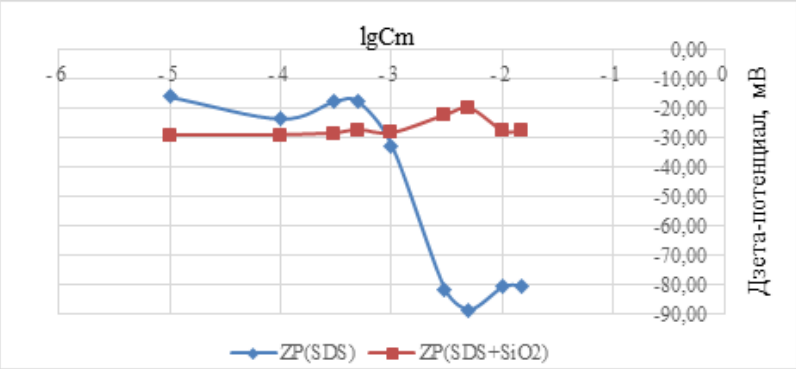


Рисунок 9 – График зависимости значений дзета-потенциала
от концентрации ПАВ (SDS и в системе SDS-SiO_2 (0.1 масс. %))

При одинаковых концентрациях SDS композит SDS-SiO_2 демонстрирует более высокие абсолютные значения дзета-потенциала по сравнению с чистым SDS. Это говорит о том, что добавление наночастиц SiO_2 в раствор SDS приводит к увеличению отрицательного заряда поверхности частиц, что объясняется отрицательным зарядом нанокремнезема.

Высокая стабильность композитной дисперсии SDS-SiO_2 положительно влияет на свойства пен, сформированных на ее основе. Стабильные дисперсии способствуют образованию более однородных и мелких пузырьков пены, что позволяет улучшить ее текстуру и реологические свойства. Кроме того, электростатическое отталкивание между частицами композита может предотвратить их коалесценцию в пенные пленки, что повышает стабильность пены.

На рисунке 10 показана зависимость pH раствора от логарифма концентрации (lgCm) для SDS и системы SDS с наночастицами кремнезема (SDS-SiO_2). Для обеих систем наблюдается изменение pH с увеличением концентрации ПАВ. В области низких концентраций pH остается относительно постоянным, затем снижается. Добавление наночастиц кремнезема к SDS приводит к снижению pH раствора во всем диапазоне концентраций по сравнению с чистым SDS. Это связано с тем, что наночастицы SiO_2, особенно в коллоидных растворах, обладают кислотными поверхностными свойствами из-за наличия силанольных групп (Si-OH). Эти группы могут диссоциировать в растворе, высвобождая протоны (H+) и понижая pH. Аналогичная картина наблюдается на рисунке 11.

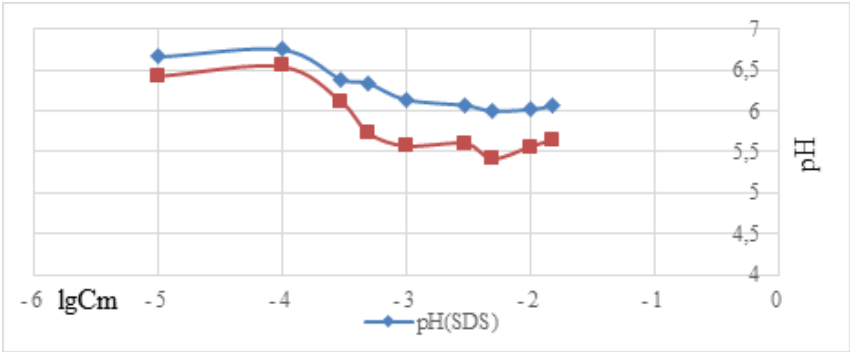


Рисунок 10 – pH бинарной системы SDS-SiO_2 при фиксированной
концентрации SiO_2 0.1 масс. % в присутствии 0.1 M NaCl

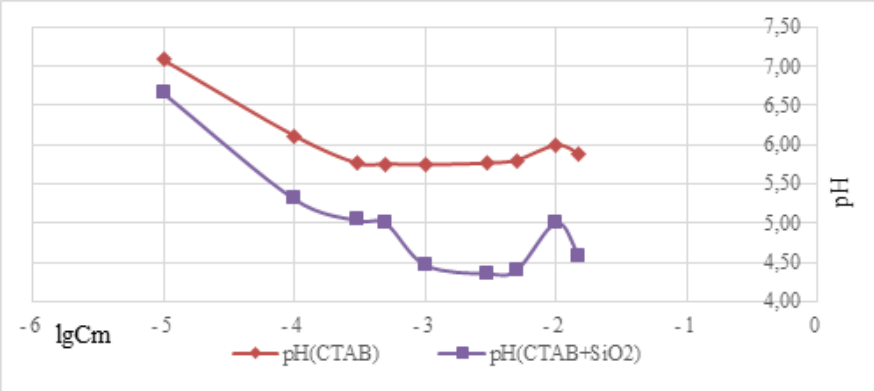


Рисунок 11 – pH CTAB и бинарной системы CTAB-SiO2 при фиксированной концентрации SiO2 0.1 масс. % в присутствии 0.1 M NaCl

Таким образом, были изучены особенности и свойства ПАВ, наночастиц и их композитов в массе в зависимости от различных факторов, таких как соленость, pH и различная природа ПАВ. Исследованы размеры (распределение размеров по интенсивности) и заряд (дзета-потенциал) ПАВ, наночастиц и их композитов в зависимости от присутствия NaCl и при различных pH, а также композитов с ПАВ различной природы (катионные, анионные и неионогенные ПАВ). Установлено, что с увеличением концентрации ПАВ размеры композитов уменьшаются. Полученные результаты по исследованию объемных свойств коррелируют с результатами по исследованию поверхностного натяжения и дилатационной реологии.

На рисунке 12 показана зависимость устойчивости пены от логарифма концентрации (lgCm) для двух систем: SDS и SDS-SiO_2.

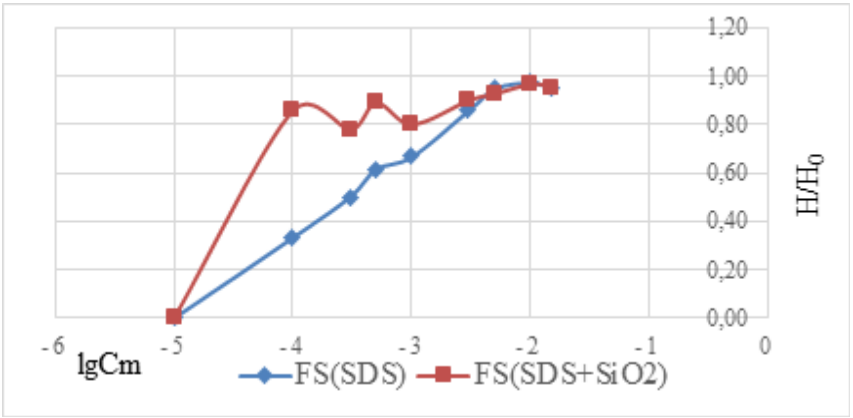


Рисунок 12 – Влияние концентрации SDS
(в системе SDS и SDS-SiO_2 (0.1 масс. %)) на стабильность пены

Для системы SDS-SiO_2 наблюдается увеличение устойчивости пены с ростом концентрации ПАВ. Это объясняется тем, что при более высоких концентрациях увеличивается количество молекул, адсорбированных на поверхности пузырьков. Это приводит к снижению поверхностного натяжения и повышению поверхностной активности, что способствует образованию более мелких и стабильных пузырьков. Кроме того, адсорбция молекул ПАВ на границе раздела газ – жидкость приводит к образованию адсорбционных слоев, которые препятствуют коалесценции пузырьков.

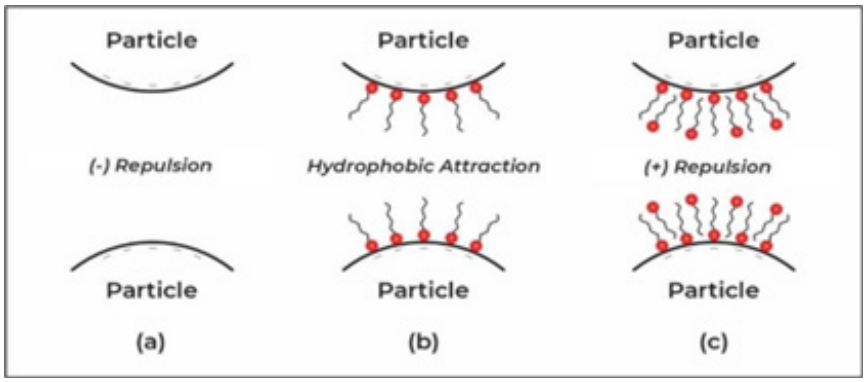


Рисунок 13 – Поведение пары частиц кремнезема на различных стадиях адсорбции ПАВ: (а) в отсутствие ПАВ; (б) при монослойной адсорбции; (в) при бислойной адсорбции

С увеличением концентрации ПАВ эти слои становятся плотнее и прочнее, что повышает стабильность пены (рисунок 13). Молекулы ПАВ, адсорбированные на поверхности пузырьков, могут замедлять процесс вытекания жидкости из пены, что также способствует ее стабилизации.

Заключение

Проведенное исследование позволило комплексно оценить роль наночастиц диоксида кремния в стабилизации газовых пен на основе поверхностно-активных веществ и определить ключевые коллоидно-химические механизмы, влияющие на повышение нефтеотдачи пластов. Показано, что внедрение наночастиц в ПАВ-системы существенно изменяет межфазные свойства: усиливает дилатационную упругость и вязкость адсорбционных слоев, увеличивает дзета-потенциал и способствует формированию более структурированных межфазных пленок. Эти эффекты приводят к снижению поверхностного натяжения, уменьшению размера пузырьков и замедлению процессов коалесценции, что в совокупности обеспечивает значительное повышение устойчивости пены.

Экспериментальные данные подтверждают, что стабилизированные наночастицами пены способны сохранять структуру в условиях, характерных для нефтяных пластов, таких как высокая температура, соленость и давление. Смесь ПАВ демонстрируют различную степень вовлечения наночастиц в адсорбционные процессы, что подчеркивает важность рационального выбора ПАВ при создании эффективных композитов.

Результаты симуляционного моделирования показали, что использование пены, стабилизированной наночастицами, приводит к увеличению коэффициента снижения подвижности, задержке газового прорыва и значительному повышению охвата пласта вытесняющим агентом. Особенно заметен эффект в неоднородных коллекторах, где традиционные методы МУН ограничены из-за зон с высокой проницаемостью.

Таким образом, разработанные композиционные пены представляют собой перспективные материалы для повышения нефтеотдачи, а их применение может обеспечить значительный прирост добычи на месторождениях с осложненными фильтрационными условиями.

Информация о финансировании. Работа проводится в рамках проекта AP23488132 «Разработка нового научно обоснованного подхода к улучшению хранения CO_2 с использованием нанофлюидов для декарбонизации».

ЛИТЕРАТУРА

1 Fakoya, M. F., Shah, S. N. Emergence of nanotechnology in the oil and gas industry: Emphasis on the application of silica nanoparticles. Petroleum, 3(4), 391– 405 (2017).

2 Hoefner, M.L., Evans, E.M., Buckles, J.J., Jones, T.A. CO_2 foam: results from four developmental field trials. SPEREE, 10 (4), 273-281 (1995).

3 Friedmann, F., Hughes, T.L., Smith, M.E., Hild, G.P., Wilson, A., Davies, S.N., Development and testing of a foam-gel technology to improve conformance of the Rangely CO_2 flood. SPEREE, 2 (1), 4-13 (1999).

4 Hematpour, H., Arabjamloei, R., Nematzadeh, M., Esmaili, H., Mardi, M. An experimental investigation of surfactant flooding efficiency in low viscosity oil using a glass micromodel. Energy Sources Part A: Recov. Util. Environ. Effects, 34(19), 1745–1758 (2012).

5 Sanz, C.A., Pope, G.A. Alcohol-free chemical flooding: from surfactant screening to coreflood design. SPE Paper No. 28956. SPE International Symposium on Oilfield Chemistry, San Antonio, Texas, 14–17 Feb. (1995).

6 Djabbarah, N.F., Weber, S.L., Freeman, D.C., Muscatello J.A., Ashbaugh J.P., Covington, T.E. Laboratory design and field demonstration of steam diversion with foam. Paper 20067 Presented at the SPE California Regional Meeting, 4-6 April, Ventura, CA. (1990).

7 Patzek, T.W., Koinis, M.T. Kern river steam-foam pilots. JPT, 42 (4), 496-503.

8 Almahfood, M., Bai, B. The synergistic effects of nanoparticle-surfactant nanofluids in EOR applications. Journal of Petroleum Science and Engineering, 171, 196-210, (2018).

9 Fakoya, M. F., Shah, S. N. Emergence of nanotechnology in the oil and gas industry: Emphasis on the application of silica nanoparticles. Petroleum, 3(4), 391-405, (2017).

10 Wasan, D. T., Nikolov, A.D. Spreading of nanofluids on solids. Nature, 423(6936), 156, 2003.

11 Esmaeilzadeh, P., Hosseinpour, N., Bahramian, A., Fakhroueian, Z., Arya, S. Effect of ZrO2 nanoparticles on the interfacial behavior of surfactant solutions at air–water and n-heptane–water interfaces. Fluid Phase Equilib, 361, 289–295 (2014).

12 Li, X., Murray, B.S., Yang, Y., Sarkar, A. Egg white protein microgels as aqueous Pickering foam stabilizers: Bubble stability and interfacial properties. Food Hydrocolloids, 98, 105292 (2020).

13 Wang, G., Wang, K, Lu, C., Wang, Y. Preparation and Foam Properties of Janus Particles. Chemical Journal of Chinese Universities, 39(5), 990-995 (2018).

14 Issakhov, M., Shakeel, M., Pourafshary, P., Aidarova, S., Sharipova, A. Hybrid surfactant-nanoparticles assisted CO_2 foam flooding for improved foam stability: A review of principles and applications. Petroleum Research, 7(2), 186-203 (2022).

15 Adkins, S.S., Gohil, D., Dickson, J.L., Webber, S.E., Johnston, K.P. Water-in-carbon dioxide emulsions stabilized with hydrophobic silica particles. Physical Chemistry Chemical Physics, 9, 633–634 (2007).

16 Belhaij, A., AlQuraishi, A. Al-Mahdy, O. Foamability and foam stability of several surfactants solutions: the role of screening and flooding. In SPE Kingdom of Saudi Arabia Annual Technical Symposium and Exhibition, SPE-172185 (2014).

17 Petkova, B., Tcholakova, S., Chenkova, M., Golemanov, K., Denkov, N., Thorley, D. Stoyanov, S. Foamability of aqueous solutions: Role of surfactant type and concentration. Advances in colloid and interface science, 276, 102084 (2020).

18 Skauge, A., Solbakken, J., Ormehaug, P.A., Aarra, M.G. Foam generation, propagation and stability in porous medium. Transport in Porous Media, 131(1), 5-21 (2020).

19 Wang, M., Yang, S., Li, M., Wang, S., Yu P., Zhang, Y., Chen, H. Influence of heterogeneity on nitrogen foam flooding in low-permeability light oil reservoirs. Energy & Fuels, 35(5), 4296-4312 (2021).

20 Bayat, A.E., Rajaei, K., Junin, R. Assessing the effects of nanoparticle type and concentration on the stability of CO_2 foams and the performance in enhanced oil recovery. Colloids Surf A Physicochem Eng Asp., 511, 222–231 (2016).

21 Espinosa, D., Caldelas, F., Johnston, K., Bryant, S.L., Huh, C. Nanoparticle-Stabilized Supercritical CO_2 Foams for Potential Mobility Control Applications. SPE - DOE Improved Oil Recovery Symposium Proceedings, 2, 1242–1254 (2010).

22 Liu, Q., Qu, H., Liu, S., Zhang, Y., Zhang, S., Liu, J., Peng, B., Luo, D. Modified Fe_3O_4 nanoparticle used for stabilizing foam flooding for enhanced oil recovery. Colloids Surf A Physicochem Eng Asp., 605, 125383 (2020).

23 Yusuf, S.M., Junin, R., Sidek, M.A.M., Manan, M.A., Fuad, M. F.I.A., Jaafar, M.Z., Yahya, E., Rosli, N.R. The effect of nanosilica sizes in the presence of nonionic TX100 surfactant on CO_2 foam flooding. Petroleum Research, 7, 62–76 (2022).

24 Chen, X., Da, C., Hatchell, D.C., Daigle, H., Ordonez-Varela, J.R., Blondeau, C., Johnston, K.P. Ultra-stable CO_2-in-water foam by generating switchable Janus nanoparticles in-situ. J Colloid Interface Sci., 630, 828–843 (2023).

25 Li, X., Chen, X., Xu, Z., Pu, C.A Novel Foam Flooding for Enhanced Oil Recovery in Fractured Low-Permeability Reservoirs: Performance Evaluation and Mechanism Study. SPE Journal, 7, 2408–2424 (2022).

26 Alexander, S., Barron, A.R., Denkov, N., Grassia, P., Kiani, S., Sagisaka, M., Shojaei, M.J., Shokri, N. Foam generation and stability: role of the surfactant structure and asphaltene aggregates. Industrial & Engineering Chemistry Research, 61(1), 372-381 (2021).

27 Babamahmoudi, S., Riahi, S. Application of nano particle for enhancement of foam stability in the presence of crude oil: Experimental investigation. Journal of Molecular Liquids, 264, 499-509 (2018).

28 Chen, Z., Zhao, X. Enhancing heavy-oil recovery by using middle carbon alcohol-enhanced waterflooding, surfactant flooding, and foam flooding. Energy & Fuels, 29(4) 2153-2161 (2017).

29 Dehdari, B., Parsaei, R., Riazi, M., Rezaei, N., Zendehboudi, S. New insight into foam stability enhancement mechanism, using polyvinyl alcohol (PVA) and nanoparticles. Journal of Molecular Liquids., 307, 112755 (2020).

30 Emrani, A.S., Nasr-El-Din, H.A. Stabilizing CO_2-foam using nanoparticles. In SPE European Formation Damage Conference and Exhibition, SPE-174254 (2015).

[1]*Исаева А.Б.,
PhD, ORCID ID: 0000-0001-6727-0257,
*e-mail: isa-asem@mail.ru
[1]Айдарова С.Б.,
х.ғ.д., профессор, ORCID ID: 0000-0001-5115-5879,
e-mail: s.aidarova@kbtu.kz
[2]Шарипова А.А.,
PhD, қауымдастырылған профессор, ORCID ID: 0000-0002-2217-9975,
e-mail: a_sharipova85@mail.ru
[1]Исахов М.О.,
PhD докторант, ORCID ID: 0009-0005-6660-5758,
e-mail:mir001@gmail.com

[1]Қазақстан-Британ техникалық университеті, Алматы қ., Қазақстан
[2]Satbayev university, Алматы қ., Қазақстан

БЕТТІК БЕЛСЕНДІ ЗАТТАР МЕН НАНОБӨЛШЕКТЕРГЕ НЕГІЗДЕЛГЕН КОМПОЗИЦИЯЛЫҚ КӨБІКТЕРДІҢ ФИЗИКА-ХИМИЯЛЫҚ СИПАТТАМАЛАРЫ ЖӘНЕ ОЛАРДЫҢ МҰНАЙ ӨНДІРУДІ АРТТЫРУДАҒЫ ТИІМДІЛІГІ

Андатпа

Нанобөлшектердің газ көбіктерінің тұрақтылығына және қозғалғыштықты төмендету коэффициентіне (MRF) әсерін зерттеуге арналған жұмыстардың айтарлықтай санына қарамастан, әдебиеттерде температура, қысым, коллектордың бастапқы өткізгіштігі және қабат сұйықтықтарының минералдануы сияқты қабат жағдайларының кешенді әсерін ескере отырып, нанобөлшектер концентрациясының оңтайлы диапазоны жөнінде бірыңғай ұсынымдар қалыптаспаған. Сонымен қатар, нанобөлшектермен тұрақтандырылған көбіктердің мұнайды ығыстыру үдерісіне және мұнай фазасымен өзара әрекеттесуіне әсері жеткілікті дәрежеде

зерттелмеген. Әсіресе, нақты кен орындары жағдайында коллектор гетерогенділігінің әртүрлі деңгейлерін ескере отырып, нанобөлшектермен тұрақтандырылған көбіктердің (NAF) тиімділігін бағалауға бағытталған зерттеулер шектеулі. Бұл зерттеу зертханалық эксперименттер мен сандық модельдеуді кешенді түрде үйлестіру арқылы аталған ғылыми олқылықтарды толықтыруға бағытталған. Жұмыста мұнай бергіштікті арттыру үдерістерінде қолданылатын газ көбіктерінің тұрақтылығын жоғарылату мақсатында беттік-белсенді заттар (ББЗ) мен кремний диоксиді (SiO_2) нанобөлшектері негізінде әзірленген композициялық жүйелердің физика-химиялық қасиеттері жан-жақты зерттелді. Дәстүрлі ББЗ негізіндегі көбіктер жоғары температура, қысым және қабат суларының жоғары минералдануы жағдайында тұрақтылығының төмендеуімен сипатталады, бұл олардың нақты қабат жағдайларындағы тиімділігін айтарлықтай шектейді. Осы мәселені шешу мақсатында SiO_2 нанобөлшектерінің аниондық, катиондық және иондық емес ББЗ негізіндегі жүйелердің фазааралық қасиеттеріне, көбік тұрақтылығына және газ фазасының қозғалғыштығына әсері зерттелді. Эксперименттік нәтижелер негізінде көбіктің жартылай ыдырау уақыты мен қозғалғыштықты төмендету коэффициентін (MRF) сипаттайтын модификациялық коэффициенттер анықталып, олар мұнайды ығыстыру үдерісінің сандық моделіне енгізілді. Сандық модельдеу нәтижелері нанокомпозиттік көбіктерді қолдану қабаттың ығыстырумен қамтылуын арттыратынын және газдың өндіруші ұңғымаларға мерзімінен бұрын жарып өтуін тежейтінін көрсетті. Бұл әсер әсіресе гетерогенділігі жоғары коллекторларда айқын байқалды. Алынған нәтижелер нанобөлшектермен тұрақтандырылған көбіктердің мұнай бергіштікті арттырудың перспективалы агенттері екенін көрсетеді және оларды геологиялық құрылымы күрделі әрі гетерогенділігі жоғары кен орындарында мұнай өндіру тиімділігін арттыру үшін қолданудың ғылыми негізін қалыптастырады.

Түйін сөздер: нанобөлшектер, мұнай берудің жоғарылауы, беттік-көбік, қозғалғыштықтың төмендеу коэффициенті, беттік керілу, CO_2-мен ығыстыру.

[1]*Isayeva A.B.,
PhD, ORCID ID: 0000-0001-6727-0257,
*e-mail: isa-asem@mail.ru
[1]Aidarova S.B.,
D.Sc. (Chem.), Professor, ORCID ID: 0000-0001-5115-5879,
e-mail: s.aidarova@kbtu.kz
[2]Sharipova A.A.,
PhD, associate professor, ORCID ID: 0000-0002-2217-9975,
e-mail: a_sharipova85@mail.ru
[1]Issakhov M.O.,
PhD student, ORCID ID: 0009-0005-6660-5758,
e-mail: mir001@gmail.com

[1]Kazakh-British Technical University, Almaty, Kazakhstan
[2]Satbayev university, Almaty, Kazakhstan

PHYSICO-CHEMICAL CHARACTERISTICS OF COMPOSITE FOAMS BASED ON SURFACTANTS AND NANOPARTICLES AND THEIR EFFECTIVENESS IN INCREASING OIL RECOVERY

Abstract

Despite a significant amount of research on the effect of nanoparticles on the stability of gas foams and the coefficient of reduced mobility (MRF), there are no uniform recommendations in the literature on the optimal range of nanoparticle concentrations, taking into account a set of reservoir parameters, including temperature, pressure, core permeability and salinity of reservoir fluids. In addition, the effect of nanostabilized foams on oil displacement processes and interaction with the oil phase has not been sufficiently studied, and on the scale of real deposits, the effectiveness of nanofoams (NAF) at various levels of reservoir heterogeneity has not been practically performed. The present study aims to address these gaps through a combination of laboratory experiments and numerical simulations. The paper presents the results of a comprehensive study of the physico-chemical characteristics of composite systems based on surfactants and silicon dioxide nanoparticles, aimed at increasing the stability of gas foams used in oil recovery enhancement processes. It has been shown that traditional surfactant foams exhibit limited

stability at high temperatures, pressures, and mineralization, which significantly reduces their effectiveness in real formations. To solve this problem, the effect of SiO_2 nanoparticles on the interfacial properties of such systems, including anionic, cationic, and nonionic surfactants, has been studied. Based on experimental data, modifying coefficients for the foam half-life and MRF have been determined, which are integrated into the simulation model of oil displacement. Numerical modeling has shown a significant increase in reservoir coverage and delayed gas breakthrough when using nanocomposite foams, especially in conditions of high heterogeneity. The results obtained confirm the prospects of nanostabilized foams as effective MUN agents and substantiate their use to increase oil recovery in complex fields.

Keywords: nanoparticles, enhanced oil recovery, surfactant foams, reduced mobility coefficient, surface tension, flooding.

Received January 1, 2026; revised April 30, 2026; accepted July13, 2026.

UDC 550.837
IRSTI 37.31.15

https://doi.org/10.55452/1998-6688-2026-23-3-536-543

[1]Rybin A.K.,
Dr. Phys.-Math. Sc., ORCID ID: 0000-0001-7810-3278,
e-mail: rybin99@yandex.ru
[1]Bataleva E.A.,
Cand. Geol.-Mineral. Sc., ORCID ID: 0000-0002-0279-7469,
e-mail: elena.bataleva@gmail.com
[1*]Nepeina K.S.,
Cand. Geol.-Mineral. Sc., ORCID ID: 0000-0003-0725-8023,
e-mail: nepeina.k@mail.ru
[1]Matiukov V.E.,
Cand. Phys.-Math. Sc., ORCID ID: 0000-0001-5323-786X,
e-mail: vitaliy_cowboy@mail.ru

[1]Research Station of the Russian Academy of Sciences in Bishkek, Bishkek, Kyrgyzstan

EVOLUTION OF "NARYN" GEOELECTRIC CROSS-SECTIONS AND COMPARISON WITH EARTHQUAKE DISTRIBUTION IN HISTORICAL PERSPECTIVE

Abstract

The "NARYN" geoelectric model, which runs along the 76° E meridian through the Central Tien Shan from the Kazakh Shield to the Tarim Platform, is one of the longest cross-sections in continental Asia. This paper provides a historical overview of geoelectric models based on magnetotelluric (MT) soundings from 1999–2000 and 2005. Two inversion models constructed from these data using different algorithms are presented: the discrete-smoothed NARYN-RLM model and the piecewise continuous NARYN-INV2D model. A local earthquake catalog for 1980–2022 is considered. Hypocenter distributions from four regional and global seismic catalogs are superimposed on a reference cross-section to re-examine the previously identified relationship between crustal conductivity and earthquake depth distribution. It is noted that weak seismicity is mainly concentrated above the upper boundary of the middle and lower crustal conductor, while the strongest events are grouped in resistive, consolidated blocks of the earth's crust or at their contacts with conductive zones.

Key words: Tien Shan, magnetotelluric sounding, geoelectric cross-section, seismicity.

Received August 7, 2026; accepted August 18, 2026.

Introduction

Intracontinental orogens such the Tien Shan is under our consideration. Situated more than 1500 km north of the Himalayan front, it has nevertheless absorbed a substantial fraction of India–Eurasia convergence since the Cenozoic reactivation of its Paleozoic Caledonian–Hercynian basement [1]. Deep electromagnetic sounding, sensitive to fluids, partial melt, graphite and other conductive phases that mark crustal weaknesses invisible to seismic velocity alone, has therefore been used for three decades to image the lithosphere beneath the Kyrgyz and Central Tien Shan and to relate its structure to present-day deformation and seismic hazard. Magnetotelluric (MT) and magnetovariational (MV) sounding, measured to recover the electrical resistivity structure of the crust and upper mantle.

The "NARYN" profile, running along the 76° E meridian for roughly 500 km across the Central Tien Shan from the Kazakh Shield to the Tarim platform, is one of the longest-running deep magnetotelluric cross-section in intracontinental Asia (Figure 1). Instrumental control on this

seismicity is provided by several overlapping catalogues: KNET, operated jointly by the Research Station of the Russian Academy of Sciences in Bishkek (RS RAS) and the Institute of Seismology of the National Academy of Sciences of the Kyrgyz Republic (NAS KR); KRNET, operated by the Institute of Seismology, NAS KR; CAIAG, compiled by the Central Asian Institute for Applied Geosciences in Bishkek; and the global National Earthquake Information Center (NEIC) catalogue of the United States Geological Survey (USGS). Each of these has a different completeness threshold, spatial coverage and operating interval.

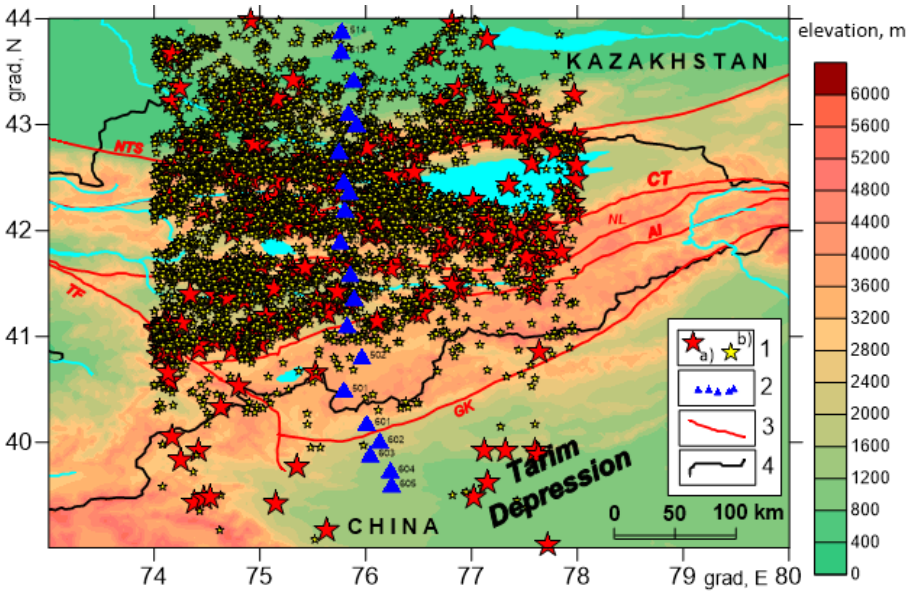


Figure 1 – Location map of magnetotelluric sounding points along the "NARYN" profile (76°E) 1 – earthquakes epicenters: a – strong (K>10), b – small- and moderate-size earthquakes (6<K<10); 2 – MT sounding sites; 3 – major faults: NTS – Northern Tien Shan, CT – Central Terskey, NL – Nikolaev Line, AI – Atbashi-Inylchek, GK – Hissar-Kokshaal; 4 – state border of Kyrgyzstan. The time span is selected between 2000 and 2025 for the present study, from local and global catalogues.

Materials and methods

RS RAS in 2005, carried out 23 wideband (0.003–1448 s) paired-synchronous MT soundings using Phoenix MTU-5 stations. This survey effectively quadrupled the spatial density of long-period control across the "NARYN" depression relative to the 1999–2000 LIMS coverage alone [2]. The "NARYN" geoelectric cross-section is the product of field MT and MV investigations, which were interpreted as different geoelectric models, because of the step-change in resolution of the new updated inversion algorithms.

The geoelectric model is built upon inversion algorithm applied with MT data of the "NARYN" profile line, from 42 points (1990s), and additional 19 long-period and 23 broadband infill points (from 1999–2005 records). It is this accumulated and interpreted separately upon new techniques, which are renovated though decades.

The first-generation model: NARYN-RLM

The earliest two-dimensional geoelectric cross-section spanning the Kyrgyz Tien Shan segment of the transect was obtained by Bielinski et al. [2], within a discrete, smoothed-structure inversion scheme (the NARYN-RLM model). This model provided the first regional image of lithospheric heterogeneity beneath the Kyrgyz Tien Shan, identifying deep conductive zones associated with major fault systems and a candidate asthenospheric conductor, and established the broad architecture that was subsequently refined by the sequential-inversion approach described below.

The second-generation model: NARYN-INV2D

The current reference cross-section NARYN-INV2D (Figure 2) was built using the piecewise-continuous (block) inversion code INV2D, developed in [3–5], which implements a sequence of partial inversions treating different field characteristics in turn, beginning with geomagnetic transfer functions and proceeding, with stepwise fixing of well-resolved conductivity blocks, through phase and full-impedance data, followed by a robust cell-by-cell averaging of the resulting ensemble of partial-inversion models. Various aspects of the construction of the NARYN-INV2D model, and of its subsequent geological–geophysical interpretation, have been described in a series of publications [4, 5]. Later on this model was recalculated in [6] (Figure 3).

The two models agree on the overall crust architecture, a fragmentary shallow (8–10 km) upper-crustal conductor, a steep conductive zone rooted beneath the Naryn depression, a lower-crustal conductive layer and a candidate asthenospheric conductor, which lends confidence to the persistence of these features across independent inversion strategies and partly independent datasets. However, NARYN-INV2D achieves markedly higher along-profile resolution.

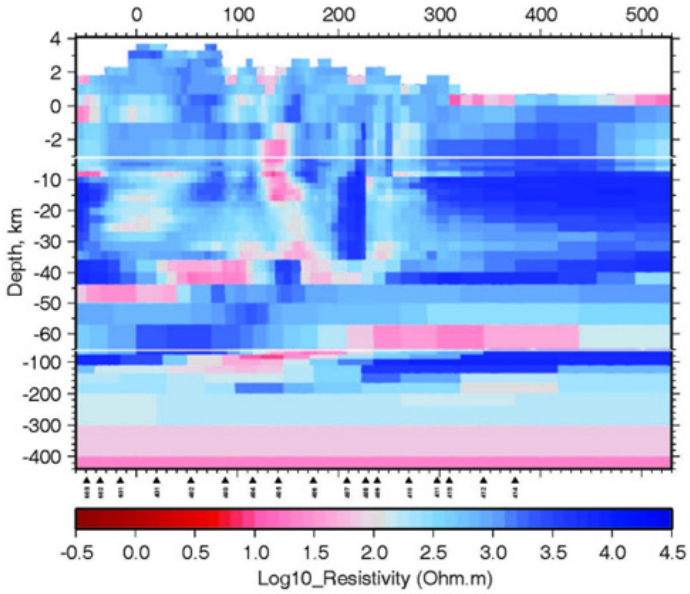


Figure 2 – The NARYN-INV2D geoelectric cross-section of the Central Tien Shan, obtained by robust averaging of a set of minimally regularised inversions

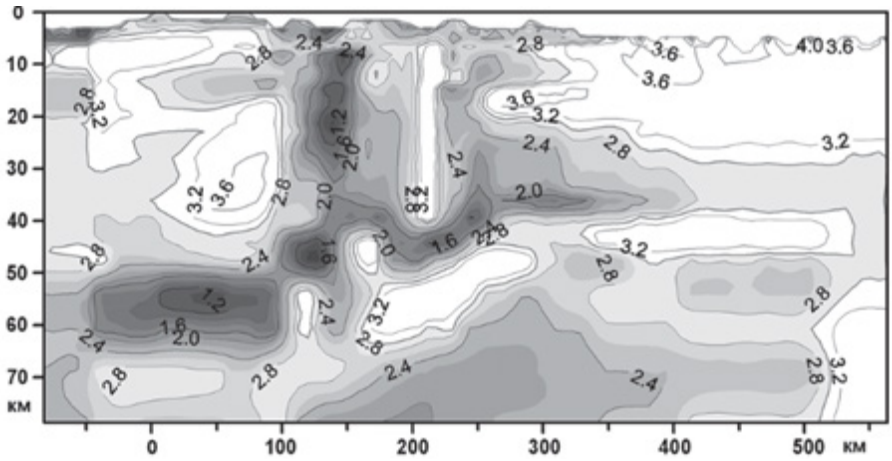


Figure 3 – The NARYN geoelectric cross-section of the Central Tien Shan after Rybin and Kostyuk [6]

Results

The area studied straddles the South Tien Shan and North Tien Shan seismoactive zones[8]. Analysis of seismicity along the "NARYN" geoelectric model and its comparison with the seismicity were published before [7, 8] and proved some relationship. Here we use the regional catalogues (KNET, KRNET, CAIAG) for 1980–2022 restricted to the square 39°–44° N, 75°–77° E (Figures 4, 5).

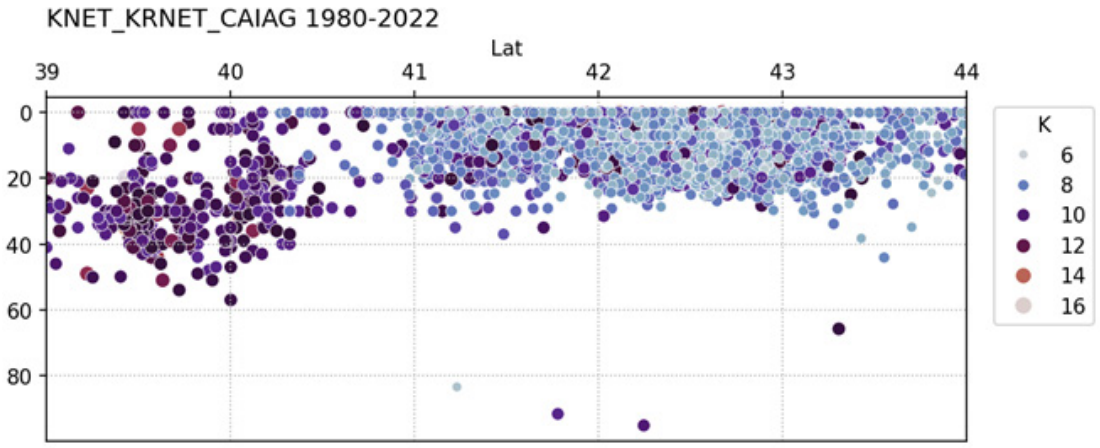


Figure 4 – Depth distribution of earthquake hypocenters with energy class K > 6 for 1980–2022, from the KNET, KRNET and CAIAG catalogues, in a 76±1° E corridor across latitude

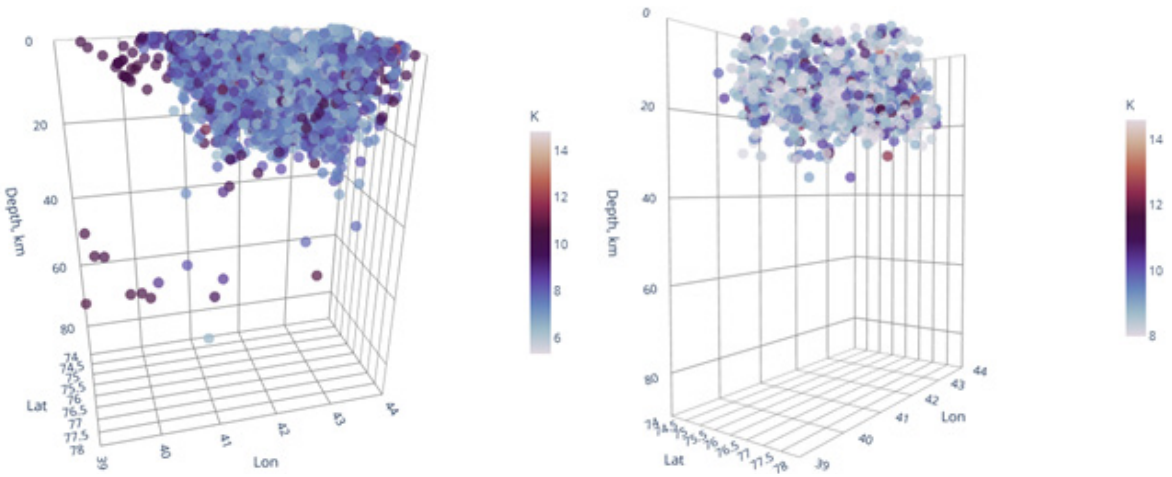


Figure 5 – Depth distribution of earthquake hypocenters with energy class K > 6 for 1980–2022, from the KNET (left) and KRNET (right) seismic networks

As part of the present study, a dedicated compilation of local earthquakes not present in the NEIC/USGS or other global catalogues was undertaken for the area 39°–44°N, 76±2°E, and combined with the global NEIC catalogue for 2025 and with fresh KNET/KRNET data for 2024–2025 (Figure 6). A depth-versus-latitude projection of hypocentres along the 76±1° E corridor for 2024–2025 (Figure 4) shows the same first-order pattern already known from the 1980–2022 window (Figure 5): near-continuous shallow (0–20 km) seismicity punctuated by discrete clusters of stronger events (K ≥ 10) tied to the Hissar–Kokshaal, Atbashi–Inylchek, Nikolaev Line and Central Terskey faults. The corresponding epicenter map (Figure 1) confirms that this clustering is not an artefact of a single network: KNET, KRNET and NEIC epicenters for 2024–2025 are co-located along the same fault-

bounded corridors identified in the earlier, longer-duration catalogues. The newly compiled 2024–2025 data reproduce the same association (Figure 6): strong events (K ≥ 10, red stars) cluster tightly around the Atbashi–Inylchek and Central Terskey faults, while the background of weaker seismicity (6 ≤ K < 10, yellow symbols) is more broadly and continuously distributed across the corridor.

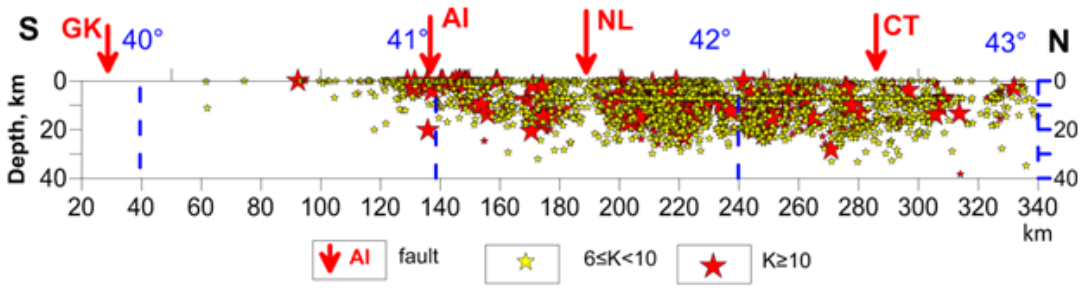


Figure 6 – Depth distribution of earthquake hypocenters along the 76±1°E meridian for 2024–2025 (updated local plus KNET/KRNET/NEIC compilation). Yellow symbols, 6 ≤ K < 10; red stars, K ≥ 10. Arrows mark the Hissar–Kokshaal (GK), Atbashi–Inylchek (AI), Nikolaev Line (NL) and Central Terskey (CT) faults

Superimposing the distribution of 'strong' hypocentres (energy class K ≥ 10) for 1980–2022 on the NARYN-INV2D section shows that the great majority of these events lie within high-resistivity, consolidated crustal blocks, or at the contacts between such blocks and the conductive zones. These contact zones, rather than the conductive zones themselves, are therefore interpreted as the segments of elevated seismic hazard in the vicinity of the geoelectric cross-section.

Taken together, three largely independent seismicity datasets spanning nearly six decades, the 1967–1999 completeness analysis, the 1980–2022 regional KNET/KRNET/CAIAG catalogues, and the newly compiled 2024–2025 data, converge on the same first-order conclusion. This convergence is regarded as the principal improvement offered by the present cross-section update: it establishes that the coupling between crustal conductivity structure and the depth and location of seismicity along the «NARYN» transect is a persistent, structurally controlled feature of the Central Tien Shan lithosphere, rather than an artefact of any one observational network, catalogue or epoch.

Discussion

The difference between inversion results for geoelectric cross-sections could be consequently explained. The magnetotelluric (MT) impedance tensor, formally the linear operator relating the horizontal electric and magnetic field spectra at the Earth's surface, is in practice never a single, unambiguously determined quantity: it is a statistical estimate whose value depends on the processing algorithm, the observation scheme, the time of acquisition and, in a deeper sense, on the mathematical class to which the underlying transfer function belongs. Varentsov [4, 5] frames this directly as a question of resolving power, arguing that the ability of natural-field electromagnetic methods to specifically resolve target features of the subsurface is fundamentally bounded by how reliably the transfer function itself can be recovered from noisy, finite-length records, rather than by the modelling or inversion algorithm alone. Zarochentsev [9], analysing the scatter of magnetotelluric errors as a function of time of day using the statistically processed MT data on the Baltic Shield, demonstrates that this variability is systematically modulated by diurnal changes in the natural source field and in cultural/industrial noise. Even when such statistical instabilities are controlled, a second, more fundamental layer of non-uniqueness remains: Zorin, Aleksanova, Yakovlev and Shimizu [10] prove that a given observed amplitude spectrum of the impedance is compatible in principle with infinitely many causal transfer functions differing in the location of their zeros in the lower half of the complex frequency plane, and that only one of them is minimum-phase; the presence of additional, non-minimum-phase zeros – caused by three-dimensional structures, anisotropy or coastal galvanic

distortion – produces systematic violations of the dispersion (Kramers–Kronig/Hilbert) relations that are, without a dedicated causality check, indistinguishable from ordinary noise-induced bias. Taken together, these studies show that non-uniqueness enters the magnetotelluric impedance at several nested levels – statistical (estimator choice and violated error assumptions, Egbert and Booker [11]), temporal (diurnal and acquisition-scheme dependence [5, 9], directional (strike- and rotation-dependence [12, 13], theoretical (causal/minimum-phase indeterminacy [10] and mathematical (incorrect multidimensional inverse problem [14, 15]. None of these levels can be fully removed by a single processing step. Because two- and three-dimensional inversion algorithms treat the input apparent-resistivity and phase curves as if they were an unambiguous physical observation, any residual non-uniqueness that is not explicitly resolved before inversion does not vanish.

Conclusions

The updated seismicity, confirms and reinforces, using an essentially independent dataset, the previously reported relationship between the top of the crustal conductor and the depth ceiling of weak seismicity, and between the strongest ($K \geq 10$) events and resistive crustal blocks or their contacts with conductive zones. These contact zones are identified as priority targets for seismic-hazard assessment along “NARYN” profile and, by extension, along comparable segments of the Central Tien Shan.

Three decades of progressively changing tools of digital inversion applied on magnetotelluric and magnetovariational observation along ”NARYN” geoelectric cross-section could provide more sharpener successive geoelectric cross-sections examined in this paper. The new iterations of geoelectric inversion could be attempt in new invented algorithms such as Inversio [16] or machine learning [17].

Acknowledgements

This work was carried out within the framework of the Russian Science Foundation (RSF) project No. 24-47-02016. We thank the operators of the KNET, KRNET, CAIAG and NEIC/USGS seismic catalogues.

REFERENCES

1 Buslov, M. M., De Grave, J., Bataleva, E. A., Batalev, V. Yu. Cenozoic tectonic and geodynamic evolution of the Kyrgyz Tien Shan Mountains: a review of geological, thermochronological and geophysical data. J. Asian Earth Sci., 2007, 29, 205–214.

2 Bielinski, R.A., Park, S.K., Rybin, A., Batalev, V., Jun, S., Sears, C. Lithospheric heterogeneity in the Kyrgyz Tien Shan imaged by magnetotelluric studies. Geophys. Res. Lett., 2003, 30, 1806, https://doi.org/10.1029/2003GL017455.

3 Berdichevsky, M.N., Golubtsova, N.S., Pushkarev, P. Yu., Sokolova, E.Yu., Varentsov, I.M., Baglaenko, N.V., Rybin, A.K., Batalev, V.Yu., Matyukov, V.E. Geoelectric section of the Central Tien Shan: analysis of magnetotelluric and magnetovariational responses along the Naryn geotraverse. Izv. Phys. Solid Earth, 2010, 46, 679–697.

4 Varentsov, Iv.M. Robust methods of joint inversion of magnetotelluric and magnetovariational data in piecewise-continuous media. In Electromagnetic Studies of the Earth’s Interior, Nauchny Mir, Moscow, 2005, 54–75 (in Russ.).

5 Varentsov, Iv.M. Joint robust inversion of magnetotelluric and magnetovariational data. In Electromagnetic Sounding of the Earth’s Interior (ed. Spichak, V.), Elsevier, Amsterdam, 2007, 189–222.

6 Rybin, A.K., and Kostyuk, A.D. On the relationship between the present-day deformation field and the deep electrical conductivity structure of the Central Tien Shan from GPS and MT data. Proc. Voronezh State Univ., Ser. Geol., 2008, 2, 165–175 (in Russ.).

7 Rybin, A.K., Bataleva, E.A., Nepeina, K.S., Matyukov, V.E. Volumetric and spatial segmentation of the Tien Shan lithosphere according to geophysical data. Geodyn. & Tectonophys., 2021, 12(3), 508–543, https://doi.org/10.5800/GT-2021-12-3-0537 (in Russ.).

8 Bataleva, E.A., Batalev, V.Yu. Rybin, A. K. Relationship between conductivity anomalies, velocity characteristics and the seismic regime of the Central Tien Shan lithosphere. Litosphere Russia, 2015, 5, 81–89 (in Russ.).

9 Zarochentsev, A.K. Analysis of magnitotelluric data errors deviation in dependence of time of day on Baltic shield on results of BEAR data statistical processing. Vestnik Sankt-Peterburgskogo Universiteta, Fizika, Khimiya, 2009, 2, 42–52 (in Russ.).

10 Zorin, N., Aleksanova, E., Yakovlev, D., Shimizu, H. Validity of the dispersion relations in magnetotellurics: Part I – theory. Earth, Planets and Space, 2020, 72(1), 9. https://doi.org/10.1186/s40623-020-1133-4.

11 Egbert, G.D., and Booker, J.R. Robust estimation of geomagnetic transfer functions. Geophysical Journal of the Royal Astronomical Society, 1986, 87, 73–194.

12 Savin, M.G. On resolution of the method of directional magnetotelluric soundings. Solar-Terrestrial Physics, 2015, 1(4), 82–85. https://doi.org/10.12737/13284 (in Russ.).

13 Gómez-Treviño, E., Muñiz, Y., Cuellar, M., Calderón-Moctezuma, A. Invariant TE and TM magnetotelluric impedances: application to the BC87 dataset. Earth, Planets and Space, 2018, 70, 133. https://doi.org/10.1186/s40623-018-0900-y.

14 Dmitriev, V.I. On multidimensional inverse problems of electromagnetic sounding. Vestnik Moskovskogo Universiteta, Seriya 15: Vychislitel'naa Matematika i Kibernetika, 2006, No. 3, 43–49 (in Russ.).

15 Denisov, A.M., and Dmitriev, V.I. Inverse and ill-posed problems. Vestnik Moskovskogo Universiteta, Seriya 15: Vychislitel'naa Matematika i Kibernetika, 2005, S, 23–30 (in Russ.).

16 Inversio Software by Nord-West Ltd. 2023. URL: https://nw-geophysics.com/inversio. Accessed on 07.07.2026.

17 Ning, K., Dong, H., Guo, C. Automatic assessing and masking algorithms for electromagnetic transfer functions based on machine learning methods. Journal of Applied Geophysics, 2025, 244, 105989. https://doi.org/10.1016/j.jappgeo.2025.105989.

[1]Рыбин А.К.,
ф.-м.ғ.д., ORCID ID: 0000-0001-7810-3278,
e-mail: rybin99@yandex.ru
[1]Баталева Е.А.,
г.-м.ғ.к., ORCID ID: 0000-0002-0279-7469,
e-mail: elena.bataleva@gmail.com
[1]*Непеина К.С.,
г.-м.ғ.к., ORCID ID: 0000-0003-0725-8023,
e-mail: nepeina.k@mail.ru
[1]Матюков В.Е.,
ф.-м.ғ.к., ORCID ID: 0000-0001-5323-786X,
e-mail: vitaliy_cowboy@mail.ru
[1]Ресей ғылым академиясының Бішкек қаласындағы Ғылыми станциясы,
Бішкек қ., Қырғызстан

НАРЫН ПРОФИЛІНІҢ ГЕОЭЛЕКТРЛІК МОДЕЛЬДЕРІНІҢ ЭВОЛЮЦИЯСЫ ЖӘНЕ ТАРИХИ ТҰРЫСТАҒЫ ЖЕР СІЛКІНІСТЕРІНІҢ ТАРАЛУЫМЕН САЛЫСТЫРУ

Аңдатпа

NARYN геоэлектрлік моделі Орталық Тянь-Шань арқылы 76° Е меридианы бойымен Қазақ қалқанынан Тарим платформасына дейін созылып, құрлықтық Азиядағы ең ұзын көлденең қималардың бірі саналады. Бұл мақалада 1999–2000 және 2005 жылдардағы магнитотеллурлық (МТ) зондтауларға негізделген

геоэлектрлік модельдерге тарихи шолу жасалған. Әртүрлі алгоритмдерді қолдана отырып, осы деректер негізінде құрылған екі инверсиялық модель ұсынылған: дискретті тегістелген NARYN-RLM моделі және бөліктік үздіксіз NARYN-INV2D моделі. 1980–2022 жж. арналған жергілікті жер сілкіністерінің каталогы қарастырылады. Жер қыртысының өткізгіштігі мен жер сілкіністері тереңдігінің таралуы арасындағы бұрын анықталған байланысты қайта қарау үшін төрт аймақтық және жаһандық сейсмикалық каталогтан алынған гипоцентрлік таралулар эталондық көлденең қимаға қабаттастырылған. Әлсіз сейсмикалықтық негізінен жер қыртысының ортаңғы және төменгі өткізгішінің жоғарғы шекарасынан жоғары шоғырланғаны, ал ең күшті оқиғалар жер қыртысының кедергілі, шоғырланған блоктарында немесе олардың өткізгіш аймақтармен жанасуында топтастырылғаны атап өтілген.

Түйін сөздер: Тянь-Шань, магнитотеллурлық зондтау, геоэлектрлік көлденең қима, сейсмикалық.

[1]Рыбин А.К.,
д.ф.-м.н., ORCID ID: 0000-0001-7810-3278,
e-mail: rybin99@yandex.ru
[1]Баталева Е.А.,
к.г.-м.н., ORCID ID: 0000-0002-0279-7469,
e-mail: elena.bataleva@gmail.com
[1]*Непеина К.С.,
к.г.-м.н., ORCID ID: 0000-0003-0725-8023,
e-mail: nepeina.k@mail.ru
[1]Матюков В.Е.,
к.ф.-м.н., ORCID ID: 0000-0001-5323-786X,
e-mail: vitaliy_cowboy@mail.ru
[1]Научная станция Российской академии наук в Бишкеке, г. Бишкек, Кыргызстан

ЭВОЛЮЦИЯ ГЕОЭЛЕКТРИЧЕСКИХ МОДЕЛЕЙ ПРОФИЛЯ NARYN И СРАВНЕНИЕ С РАСПРЕДЕЛЕНИЕМ ЗЕМЛЕТРЯСЕНИЙ В ИСТОРИЧЕСКОЙ ПЕРСПЕКТИВЕ

Аннотация

Геоэлектрическая модель NARYN, проходящая вдоль меридиана 76° в.д. через Центральный Тянь-Шань от Казахского щита до Таримской платформы, является одним из самых протяженных сечений во внутриконтинентальной Азии. В данной статье дан исторический обзор геоэлектрических моделей по данным магнитотеллурических (МТ) зондирований 1999–2000 гг. и 2005 г. Показаны две построенные на основе этих данных с помощью разных алгоритмов инверсии: дискретно-сглаженной модели NARYN-RLM и кусочно-непрерывной модели NARYN-INV2D. Рассматривается локальный каталог землетрясений за 1980–2022 гг. Распределения гипоцентров из четырех региональных и глобальных сейсмических каталогов наложены на эталонный поперечный разрез для повторной проверки ранее выявленной взаимосвязи между проводимостью земной коры и распределением землетрясений по глубине. Отмечается, что слабая сейсмичность в основном сосредоточена над верхней границей средне- и нижнекорового проводника, тогда как самые сильные события группируются в резистивных, консолидированных блоках земной коры или на их контактах с проводящими зонами.

Ключевые слова: Тянь-Шань, геоэлектрический разрез, магнитотеллурическое зондирование, сейсмичность.

УДК 622.245.51
МРНТИ 52.47.27

https://doi.org/10.55452/1998-6688-2026-23-3-544-564

[1]*Дуйсалиев А.М.,
докторант, ORCID ID: 0009-0000-9470-4225,
e-mail: e.nurbekova@kmg.kz
[1]Исмаилов А.А.,
PhD, к.т.н., профессор, ORCID ID: 0000-0002-1957-5168,
e-mail: a.ismailov@kbtu.kz
[2]Махмудов Н.Н.,
д.т.н., профессор, ORCID ID: 0009-0005-1148-4180,
e-mail: nazirillamaxmudov@gmail.com
[1]Казахстанско-Британский технический университет, г. Алматы, Казахстан
[2]Ташкентский государственный технический университет им. Ислама Каримова,
г. Ташкент, Узбекистан

НАБУХАНИЕ ГЛИН И НЕЦЕЛЕВОЙ РАСХОД РЕАГЕНТОВ ПРИ ГРП: ДИАГНОСТИКА И ОПЫТ ПРИМЕНЕНИЯ ПЛАСТОВОЙ ВОДЫ НА МЕСТОРОЖДЕНИИ ВОСТОЧНЫЙ МОЛДАБЕК

Аннотация

Эффективность гидравлического разрыва пласта (ГРП) во многом определяется тем, насколько сохраняется проводимость трещины после взаимодействия жидкости ГРП с породой. В статье систематизированы механизмы повреждения проницаемости, связанные с водочувствительностью глинистых минералов, – межслоевое набухание смектита, осмотические эффекты, дефлоккуляция и миграция тонких частиц, – а также рассмотрены каналы нецелевого расхода стабилизаторов глин (KCl, четвертичные аммониевые соединения) и деструкторов геля (персульфат аммония, пероксид водорода, ферменты) на минералы породы и сопутствующие добавки. Показано, что номинальная дозировка реагента без учета материального баланса может одновременно завышать степень стабилизации глин и степень разрушения полимерной сетки. Предложена минимальная матрица лабораторных испытаний, включающая рентгенофазовый анализ ориентированных препаратов, изотермы сорбции, coreflood и тесты на удержанную проводимость трещины. На примере месторождения Восточный Молдабек (АО «Эмбамунайгаз») показано, что снижение проницаемости пласта при насыщении слабоминерализованной водой связано с набуханием глин и слюды, тогда как использование пластовой воды такой деградации не вызывает. Обоснована и реализована технология ГРП на пластовой воде с применением геля на основе полиакриламида взамен гуаровой камеди, неприменимой при минерализации воды более 130 г/л. По результатам ГРП на восьми скважинах дебит после обработки на пластовой воде и синтетическом полимере превысил показатели стандартной технологии более чем в пять раз.

Ключевые слова: гидравлический разрыв пласта, набухание глин, миграция тонких частиц, проводимость трещины, стабилизаторы глин, деструктор геля, пластовая вода.

Введение

Стимулирующее воздействие на пласт предполагает закачку в него технологических жидкостей, которые способны изменить фильтрационно-емкостные свойства последнего, повлиять на состояние закрепляющей трещину пачки. Водные жидкости ГРП должны одновременно обеспечить инициирование и развитие трещины, перенос проппанта, контролируемые утечки, последующее разрушение полимерной сетки и очистку сформированной проводящей системы. При этом каждая стадия обработки изменяет химическое состояние глинистой и тонкодисперсной составляющей породы. Поэтому успешность операции определяется не только давлением разрыва и размещенной массой проппанта, но и тем, какая доля созданной проводимости сохраняется после выдержки, смыкания трещины и освоения скважины.

В промысловой практике выражение «набухание глин» часто используется как общий термин для любого снижения проницаемости после контакта с водой. Такое упрощение удобно, но может привести к ошибочному выбору стабилизатора. Межслоевое расширение смектита, осмотическое набухание, внешняя гидратация, расширение двойного электрического слоя, отрыв частиц и их миграция являются разными механизмами. Они могут протекать одновременно, но по-разному зависят от минералогии, солености, состава обменных катионов, pH, температуры, эффективного напряжения и скорости потока [4, 5, 6, 7].

Отдельная инженерная проблема связана с тем, что номинальная концентрация реагента в смесительной емкости не равна его активной концентрации на поверхности целевой глины или внутри удаленной части трещины. Хлористый калий распределяется между водной фазой, обменными центрами, матричными утечками и обратным потоком. Четвертичные аммониевые соединения дополнительно сорбируются на глинах, карбонатах, кварце и органическом веществе. Окислительный деструктор расходуется не только на разрыв цепей гуара или полиакриламида, но и на минералы, органику, сульфиды, восстановленные формы железа и другие добавки. В результате расчет по исходной дозировке без материального баланса может переоценивать одновременно и стабилизацию глин, и степень разрушения геля.

Наиболее выраженное внутрикристаллическое набухание характерно для смектитов. Вода и обменные катионы входят в межслоевое пространство, а базальное расстояние изменяется в зависимости от влажности, типа катиона и активности воды. Смешанно-слойные иллит-смектиты содержат чередующиеся расширяющиеся и нерасширяющиеся слои; их реакция определяется долей смектитовых пакетов и порядком чередования. Иллит, каолинитовая группа и мусковит не демонстрируют классического смектитового расширения, но могут участвовать во внешней гидратации, дефлоккуляции и миграции частиц.

Каолинит, накрит и диккит имеют близкий химический состав, но различную укладку слоев. Они практически не набухают межслоевым механизмом, однако пластинчатые частицы могут отсоединяться от поверхности пор и закупоривать сужения. Иллит содержит структурный калий и обычно имеет меньшую способность к межслоевому расширению, но его края и дефектные поверхности сохраняют заряд. Мусковит является калиевой слюдой, а не собственно глинистым минералом; его присутствие важно для механической анизотропии, образования пластинчатых обломков и интерпретации калиевого канала гамма-спектрометрии. Обобщенная инженерная интерпретация рассмотренных слоистых минералов приведена в таблице 1.

F. Deon et al. (2022) показали, что идентификация смешанно-слойных иллит-смектитов осложняется перекрытием пиков, низким содержанием глинистой фракции и отсутствием диагностических обработок. В обычной порошковой дифрактограмме кварц, полевые шпаты, слюды и карбонаты дают интенсивные рефлексы, тогда как плохо упорядоченный смектит формирует широкий и слабый сигнал. Поэтому отсутствие названия «смектит» в автоматическом фазовом списке не всегда означает его физическое отсутствие [1].

M. Koubova et al. (2023) использовали ориентированные препараты, обмен межслоевых катионов, насыщение этиленгликолем и моделирование полного профиля. Авторы отметили, что даже стандартное гликолирование может быть недостаточным для разделения смектитов с разным зарядом слоя. H. Hong et al. (2015) подтвердили существование трехкомпонентных смешанно-слойных структур I/S/K сочетанием XRD и электронной микроскопии высокого разрешения [2, 3].

Для надежной диагностики требуется выделить фракцию менее 2 мкм и сопоставить как минимум три состояния одного ориентированного препарата: воздушно-сухое, после этиленгликоля и после нагрева. Расширение базального рефлекса к области около 17 Å после гликоля и его коллапс при нагреве являются диагностическими признаками смектитовых слоев. Для смешанно-слойных фаз важны не отдельные пики, а положение, асимметрия и рациональность последовательности рефлексов. При низком содержании дополнительно применяются CEC, SEM/TEM, спектроскопия и моделирование дифрактограмм.

Таблица 1 – Инженерная интерпретация основных слоистых минералов

Минерал или группа	Структура	Межслоевое набухание	Риск миграции частиц	Ключевая диагностика
Смектит	2:1, заряженные расширяющиеся пакеты	Высокое; зависит от катиона и активности воды	Высокий при дефлоккуляции и потоке	Ориентированная фракция <2 мкм; воздушно-сухая, этиленгликоль, нагрев
Иллит-смектит	Смешанное чередование 10 и 14-17 Å слоев	От низкого до высокого	Высокий при наличии мелких пакетов	Серия обработок и моделирование полного XRD-профиля
Иллит	2:1, межслоевой K^+	Низкое	Средний; особенно для краевых и дисперсных частиц	XRD глинистой фракции, SEM, CEC
Каолинит, накрит, диккит	1:1, незаряженные пакеты	Практически отсутствует	Высокий при отрыве пластинок	XRD, SEM, анализ размера вынесенных частиц
Хлорит	2:1:1, гидроксидный межслой	Низкое	Низкий-средний; возможна кислотная дестабилизация	XRD после нагрева и химической обработки
Мусковит	Калиевая слюда	Не характерно	Средний при разрушении и выносе пластинок	Валовый XRD, петрография, SEM

Следовательно, корректная формулировка для валового XRD должна звучать так: «смектит и смешанно-слойные фазы не идентифицированы примененной методикой». Утверждение «смектита нет» допустимо только после специализированного анализа глинистой фракции с достаточным пределом обнаружения.

M. Binazadeh et al. (2016) связали водопоглощение газоносных сланцев с ионной силой раствора и толщиной двойного электрического слоя. При снижении солености электростатическое отталкивание возрастает, а силы, удерживающие частицы и пакеты, ослабевают. Этот механизм важен не только для смектитов: внешние поверхности иллита и каолинита также реагируют на изменение ионной силы, хотя не расширяются внутри кристалла [4].

A. Sanaei et al. (2016) включили смектитовое набухание в модель повреждения проводимости гидравлической трещины. Результаты показывают, что даже локальное увеличение объема глинистой фазы в узких каналах способно существенно уменьшить эффективное сечение потока. Однако модельная чувствительность к смектиту не отменяет других механизмов, если фактическая минералогия не подтверждена [5].

Ионный состав важнее одной суммарной минерализации. Двухвалентные катионы сильнее сжимают двойной слой, но могут участвовать в осадкообразовании. K^+ имеет специфическую способность фиксироваться в некоторых межслоевых и краевых позициях. Na^+ поддерживает более гидратированное состояние. Поэтому две воды одинаковой минерализации, но разного состава могут давать различный результат по набуханию и миграции. M. Mehana et al. (2018) показали, что совместное влияние солености и минералогии изменяет самопроизвольную пропитку slickwater и прочность сланца, поэтому перенос результатов между объектами без минералогической калибровки некорректен [17].

T. Russell et al. (2017) исследовали породы с каолинитом и показали, что потеря проницаемости может определяться миграцией, хотя сам каолинит практически не обладает межслоевым набуханием. Это принципиально: наблюдаемое падение проницаемости не является прямым доказательством смектита. Для каолинитовых систем решающими становятся размер

пластинок, связь с цементом, скорость потока и соотношение размеров частиц и поровых горловин [6].

S. Tangparitkul et al. (2020) описали совместное действие снижения давления, низкой солености, набухания и миграции частиц. D. Zhang et al. (2021) показали, что деионизированная вода изменяет пористость и проницаемость глинистых сланцев; рост локальной пористости не гарантирует роста сквозной проницаемости, поскольку отделившиеся частицы могут закупоривать критические горловины [7, 8].

P. Bhuvankar et al. (2022) использовали поромасштабное моделирование, а A. Cihan et al. (2022) связали область снижения проницаемости вокруг низкосоленой инъекции с мобилизацией глинистых частиц. Эти работы подтверждают, что повреждение имеет пространственно неоднородный характер: частицы освобождаются в одной зоне, транспортируются и осаждаются в другой, где отношение размера частицы к размеру канала становится критическим [9, 10].

A. Sadeghein et al. (2024) систематизировали влияние солености, pH и температуры. Повышение pH обычно усиливает отрицательный заряд поверхностей и может повышать диспергирование; высокая температура ускоряет обмен и химические реакции, но ее итоговое влияние зависит от минерала и состава воды. Следовательно, тест только при комнатной температуре и одной скорости потока недостаточен для проектирования ГРП [11].

На начальной стадии вода изменяет механические свойства стенок трещины и прискважинной зоны. S. Zhang et al. (2018) и X. Chen et al. (2019) показали, что пропитка водой изменяет трещинообразование и механические характеристики сланца. Эффект зависит от слоистости, ориентации образца и напряженного состояния. В некоторых условиях водное ослабление снижает давление инициирования, но одновременно повышает риск образования слабых поверхностей, отслаивания и нестабильного роста трещины [18, 19].

Q. Dai et al. (2025) установили изменение поровой структуры и локальных механических свойств глинистого сланца после контакта со slickwater. Z. Li et al. (2026) показали, что гидратационное расширение может менять не только модуль и прочность, но и распределение и ориентацию напряжений в стимулированной зоне. Поэтому сильное водопоглощение способно повлиять на последующие стадии многостадийного ГРП и на оценку направления роста трещин [20, 22].

J. Zhang et al. (2015) рассмотрели снижение проводимости вследствие вдавливания проппанта. Водное размягчение стенки увеличивает площадь и глубину контакта зерна с породой, уменьшает закрепленную ширину и облегчает попадание обломков в проппантную пачку [12].

J. Zhang et al. (2016) экспериментально показали водоиндуцированное повреждение проводимости проппантных трещин в сланцах. W. Wu et al. (2017) отметили, что незакрепленные трещины особенно чувствительны к смыканию, деформации шероховатостей и химическому изменению поверхностей. S. Zhang et al. (2017) сопоставили несколько сланцев и подтвердили, что при эффективном обжиме гидратация может приводить к существенной потере проницаемости [13, 14, 15].

Y. Jia et al. (2018) показали совместное действие механических, химических и минералогических факторов. H. Bai et al. (2025) количественно разделили вклад сжатия проппантной пачки, вдавливания и закупорки частицами в слабосцементированном песчанике. Такой подход особенно важен для меловых рыхлых и тонкопереслоенных коллекторов: даже если глина не набухает, разрушение поверхности и перенос мелких частиц могут снижать проводимость сопоставимо с механическим смыканием [16, 21].

Во время закачки контакт жидкости с породой ограничен временем прохождения и высоким градиентом давления. На стадии shut-in поток уменьшается, но продолжаются диффузия воды, обмен катионов, сорбция добавок, окисление и изменение прочности. Длительная выдержка улучшает действие некоторых деструкторов, однако одновременно повышает глубину проникновения воды и вероятность мобилизации глин.

Слишком быстрый flowback повышает гидродинамические силы, срывает частицы и может выносить проппант. Слишком медленный flowback увеличивает время контакта и позво-

ляет вторичным осадкам формироваться в проппантной пачке. Оптимальный режим определяется не универсальным временем, а результатами последовательного coreflood или fracture-conductivity теста, в котором воспроизводятся фактические соленость, температура, эффективное напряжение и программа расхода. Основные риски, характерные для каждой стадии ГРП, систематизированы в таблице 2.

Y.A. Abdulhameed et al. (2025) показали, что оптимальная концентрация KCl зависит от минералогии и CEC. Повышение концентрации улучшало поведение одних пород, но в низкообменных иллитовых системах могло приводить к переингибированию, хрупкой агрегации и снижению механической целостности. Поэтому правило «чем больше KCl, тем лучше» не является универсальным [30].

Нецелевой расход KCl является преимущественно физико-химическим перераспределением, а не необратимым химическим разложением. K^+ занимает доступные обменные позиции на всех отрицательно заряженных поверхностях, а не только в наиболее опасной глине. Часть соли уходит с leakoff в матрицу, часть остается в неподвижной воде, часть возвращается при освоении. Na^+, Ca^{2+} и Mg^{2+} конкурируют за обменные центры. Поэтому для оценки эффективности следует измерять не только дозировку KCl, но и остаточную активность K^+ после контакта с породой.

Z. Tariq et al. (2020) применили gemini-сурфактант как стабилизирующую добавку к жидкости ГРП и показали сохранение пористости и проницаемости по сравнению с обычными солевыми системами. В последующей работе Z. Tariq et al. (2021) дикационные соединения оценивались по петрофизическим и механическим показателям. Результаты подтверждают, что многозарядная молекула может сильнее связываться с поверхностью и одновременно уменьшать гидрофильность глины [23, 24].

L. Fu et al. (2020) и M. Murtaza et al. (2020) исследовали бис-четвертичные и gemini-структуры. Эффективность зависела от расстояния между катионными центрами, стерических ограничений и способности молекулы закрепляться электростатически и водородными связями. R.A. Khan et al. (2023) рассмотрели ионные жидкости как альтернативный класс стабилизаторов [25, 26, 29].

Таблица 2 – Основные риски по стадиям ГРП

Стадия	Доминирующий процесс	Возможное последствие	Контрольный показатель
Приготовление и смешение	Совместимость солей, полимеров, ПАВ, стабилизаторов и деструкторов	Осадок, потеря активного реагента, преждевременный разрыв геля	Турбидность, фильтруемость, остаточная концентрация реагентов
Закачка и рост трещины	Утечки, водное ослабление, начало сорбции	Изменение геометрии, нестабильное распространение, расход реагентов в матрицу	Давление, эффективность жидкости, химический анализ возврата
Shut-in	Гидратация, обмен, окисление, вторичное осадкообразование	Размягчение стенок, набухание, реакция деструктора с породой	Время, температура, остаточный окислитель, ионный баланс
Смыкание трещины	Вдавливание проппанта, разрушение стенок и зерен	Потеря ширины и проводимости	Проводимость под напряжением, размер и масса твердого остатка
Flowback и добыча	Миграция частиц, вынос проппанта, осаждение продуктов реакции	Кольматация, нестабильный дебит, раннее падение продуктивности	Частицы в выносе, перепад давления, удержанная проводимость

S. Bai et al. (2026) сопоставили K^+, первичный амин, четвертичный аммоний и полиэтиленимин на монтмориллоните. Работа показала, что номинально более массивная четвертичная аммониевая головка не обязательно дает максимальную стабилизацию: стерическое

экранирование может ослаблять близкий контакт, тогда как поликатион образует межслоевые мостики. Следовательно, выбор реагента должен опираться на конкретную минералогию, а не только на принадлежность к классу четвертичных аммониевых солей [32].

T. Zeng et al. (2020) измерили адсорбцию ПАВ на нескольких сланцах. Катионный CTAB имел наибольшую сорбцию среди исследованных ПАВ, а вклад отдельных компонентов менялся от образца к образцу: в одних породах доминировали глины, в других – кальцит или органическое вещество. Это прямое подтверждение того, что значительная доля катионного стабилизатора может быть израсходована на поверхности, не связанной с целевым набуханием [27].

J.-J. Chen et al. (2022/2024) сравнили KCl и низкомолекулярную органическую аммониевую соль. Органический реагент адсорбировался на глинистой поверхности и изменял дзета-потенциал, что обеспечивало более устойчивый эффект, но одновременно создавало конечную сорбционную емкость. После насыщения ближайших поверхностей последующая порция реагента переносится дальше; до насыщения значительная часть дозы остается в прискважинной зоне [28].

A. Labak и P. Pourafshary (2025) показали, что четвертичный аммониевый стабилизатор уменьшает потерю проницаемости при высокотемпературном низкосоленом воздействии, но не устраняет повреждение полностью. Нецелевой расход включает необратимую и обратимую сорбцию, интеркаляцию, мицеллообразование, распределение в матричных утечках и взаимодействие с анионными компонентами. Кроме потери активной концентрации возможны изменение смачиваемости и удержание углеводородов на модифицированной поверхности [31]. Каналы нецелевого расхода KCl и четвертичных аммониевых соединений обобщены в таблице 3.

Деструктор должен снизить молекулярную массу загустителя после размещения проппанта, но не разрушить систему раньше времени. X. Lin et al. (2015) показали чувствительность времени разрыва геля и утечек к концентрации APS и использовали инкапсулированный деструктор для управляемого высвобождения. Это подчеркивает, что расход деструктора во времени столь же важен, как его общая масса [33].

J. Wang et al. (2020) показали, что низкая конечная вязкость сама по себе не доказывает полноценную очистку. Следует одновременно определять размер полимерных фрагментов и массу нерастворимого остатка. Избыточная доза APS не обязательно уменьшала размер фрагментов, но увеличивала количество остатка; контакт разрушенной жидкости с породой и проппантом усиливал вдавливание, дробление и закупорку каналов [34].

Таким образом, целевой расход – это доля окислителя, которая действительно разрывает цепи нужного полимера в требуемом месте и в требуемое время. Все остальные пути относятся к нецелевому расходу, даже если они не приводят к видимому осадку.

Персульфат аммония (APS) диссоциирует с образованием $S_2O_8^{2-}$. При термической или каталитической активации формируются сульфатные радикалы, разрывающие полимерные цепи. Нецелевой расход начинается еще до контакта с загустителем: окислитель может термически разлагаться, реагировать с Fe^{2+}, пиритом, сульфидами, органическим веществом и другими восстановленными компонентами породы.

K.E. Manz и K.E. Carter (2018) исследовали термоактивированный персульфат в присутствии сланца. Железо ускоряло окисление модельной добавки, но добавление породы в целом замедляло ее разрушение, поскольку часть персульфата расходовали минералы сланца. Это классический пример конкуренции между целевой органической молекулой и породой [38].

D. Liu et al. (2022) и S. Yang et al. (2023) показали, что пирит и кероген ускоряют разложение персульфата, тогда как кальцит и хлорит меняют реакцию через буферирование и кислотность. Кероген конкурирует с пиритом за окислитель. Растворение кальцита сопровождается образованием сульфата кальция, поэтому полезное увеличение пористости может сочетаться с локальным осаждением гипса [39, 40].

Таблица 3 – Каналы нецелевого расхода стабилизаторов глин

Канал	KCl	Четвертичные аммониевые соединения	Как проверить
Катионный обмен и сорбция	Распределение K^+ по всем обменным центрам	Сильная сорбция на глинах; возможная сорбция на карбонатах и органике	Баланс K^+, TOC/азота реагента, изотермы сорбции
Leakoff и удержание воды	Уход растворенной соли в матрицу	Уход растворенного и сорбированного реагента в матрицу	Трассер и объемный баланс
Конкурирующие ионы	Na^+, Ca^{2+}, Mg^{2+} изменяют обмен и активность K^+	Экранирование заряда и изменение конфигурации адсорбции	Серия тестов на фактических водах
Взаимодействие с добавками	Изменение ионной силы и совместимости	Ионные пары с анионными ПАВ/полимерами; деградация окислителем	Bottle test, DLS, фильтруемость, GPC
Освоение	Часть K^+ возвращается, часть остается в породе	Десорбция обычно неполная; длительное удержание	Профиль концентрации во времени во flowback

S. Donmoyer et al. (2023) рассмотрели влияние окислительных деструкторов на органическое вещество, подвижность элементов и высвобождение минералов в Marcellus Shale. Работа показывает, что «лишний» окислитель не остается инертным: он меняет органику и минеральную матрицу, мобилизует металлы и создает новые растворенные и твердые продукты [41].

A.J. Sumner и D.L. Plata (2019) установили конкурентное окисление и галогенирование добавок в гуаровых жидкостях. M. Chen et al. (2021) показали, что в высокохлоридных и бромидных растворах сульфатные радикалы переходят в галогенные радикалы. В результате часть окислительной способности расходуется на цитрат, ПАВ, биоциды и другие органические добавки, а не на целевой полимер [36, 37].

T. Almubarak et al. (2020) непосредственно проверили взаимодействия деструкторов с полимерными стабилизаторами глин и H_2S. Окислительные и кислотные системы формировали заметный остаток; некоторые деструкторы уменьшали молекулярную массу полимерного стабилизатора и ухудшали его действие по дзета-потенциалу. При контакте окислителей с H_2S наблюдалось осаждение элементарной серы. KCl, не являясь полимером, оказался значительно менее чувствительным к такой деградации [35].

Пероксид водорода и органические пероксиды также генерируют активные формы кислорода, но их поведение сильнее зависит от катализаторов. Fe^{2+}, железосодержащие минералы и поверхности пирита запускают реакции типа Фентона, поэтому H_2O_2 может быть быстро израсходован в прискважинной зоне. Одновременно возможны выделение газа, локальное тепловыделение, окисление органического вещества и изменение состояния железа.

W. Yu et al. (2019) показали, что H_2O_2 удаляет часть органического вещества сланца и меняет поровую структуру; скорость реакции возрастает с температурой, давлением и временем. Для деструктора это означает двойственный эффект: окисление породы может открыть поры, но одновременно является прямым нецелевым потребителем реагента и может ослаблять стенки трещины [43].

X. Liang и J.J. Sheng (2020) сравнили $Na_2S_2O_8$, NaClO и H_2O_2 на Marcellus Shale. Персульфат дал наиболее выраженное растворение и химически индуцированные трещины; H_2O_2 показал меньшую потерю массы. Результат нельзя механически переносить на все рецептуры ГРП, но он подтверждает различную селективность окислителей к породе [42].

Для пероксидного деструктора основными каналами нецелевого расхода являются каталитическое разложение на Fe-минералах, реакция с сульфидами и H_2S, окисление природной органики, ПАВ и ингибиторов, а также саморазложение до достижения целевой температуры.

По сравнению с персульфатом пероксиды обычно менее устойчивы к следовым металлам; персульфаты дольше сохраняются, но создают более выраженный сульфатный и галоген-радикальный контур побочных реакций.

S. Yang et al. (2025) совместили coreflood и реактивно-транспортное моделирование. Персульфат растворял карбонаты, окислял пирит и органическое вещество, но одновременно формировал гипс и гидроксиды железа, способные закупоривать каналы. Авторы пришли к выводу, что интенсивная реакция не всегда дает максимальный прирост проницаемости; состав минералов, трещиноватость и расход жидкости определяют баланс растворения и осаждения [45].

N. Zhang et al. (2022) рассматривали окислительную жидкость для увеличения самопроизвольного проникновения и сокращения flowback. Такой подход может быть полезен для отдельных сланцев, но для глинистых песчаников с ограниченной проводимостью трещины длительное удержание окислителя повышает риск нецелевых реакций. Решение о shut-in должно учитывать не только степень разрушения геля, но и скорость реакции с породой [44]. Сравнительная характеристика каналов нецелевого расхода персульфатов и пероксидов приведена в таблице 4.

Таблица 4 – Сравнение нецелевого расхода персульфатов и пероксидов

Показатель	APS и другие персульфаты	H_2O_2 и пероксидные системы	Инженерный риск
Основной активный агент	Сульфатные радикалы после активации	Гидроксильные и другие кислородные радикалы	Неправильная температура или катализатор меняют время разрыва
Минеральные поглотители	Пирит, Fe^{2+}, сульфиды, кероген; реакция зависит от карбонатного буфера	Fe^{2+}, пирит, переходные металлы, сульфиды, органика	Преждевременный расход в прискважинной зоне
Галогениды	Cl^- и Br^- переводят радикальную химию в галогенные радикалы	Влияние обычно менее специфично, но зависит от катализаторов	Деградация ПАВ, биоцидов и других добавок
Вторичные твердые фазы	Гипс, барит при наличии Ba^{2+}, гидроксиды Fe, элементарная S при H_2S	Оксиды/гидроксиды Fe, элементарная S; возможны газовые продукты	Кольматация проппантной пачки и поровых горловин
Контроль	Остаточный $S_2O_8^{2-}$, SO_4^{2-}, Fe, Ca, Ba, S, размер фрагментов	Остаточный H_2O_2, Fe^{2+}/Fe^{3+}, газовыделение, TOC, размер фрагментов	Без баланса нельзя определить целевую долю расхода

Формально материальный баланс деструктора можно представить как:

Мвход = Мполимер + Мпорода + Мдобавки + Мсаморазложение + Мвыход

Если измеряется только исходная дозировка и конечная вязкость, четыре последних слагаемых остаются неразделенными. Для научно строгой оценки необходимы остаточный окислитель, молекулярная масса полимера, сульфат, железо, кальций, твердый остаток и химический состав flowback.

Материалы и методы

Тест на линейное набухание показывает изменение объема специально подготовленной глины, но не воспроизводит миграцию частиц в реальной поровой структуре. Bottle test выявляет видимый осадок, но не измеряет потерю активной концентрации из-за сорбции. Конечная вязкость после деструкции не показывает размер полимерных фрагментов. Поэтому отдельные положительные тесты не гарантируют сохраненную проводимость трещины.

Лабораторная программа должна воспроизводить полную последовательность: исходная пластовая вода; предобработка или стабилизатор; жидкость ГРП; shut-in; деструктор; переход к воде освоения; flowback при возрастающем градиенте; долговременная фильтрация под эффективным напряжением. Используются керн, измельченная порода и проппантная ячейка из одного интервала.

Для KCl определяются K^+, Na^+, Ca^{2+} и Mg^{2+} до и после контакта, а также обменная емкость твердой фазы. Для четвертичного аммониевого соединения необходим специфический аналитический метод: TOC/общий азот, ионная хроматография, HPLC или меченый аналог. Изотерма сорбции на валовой породе дополняется отдельными тестами на выделенных глинах, кальците, кварце и органическом концентрате.

Практический показатель – доля реагента, дошедшая до удаленной части модели. Для этого стабилизатор подают импульсом через длинный составной керн или канал с проппантом и строят выходную кривую концентрации. Одновременно контролируют давление и содержание частиц. Такой опыт отделяет химическое удержание от гидродинамической задержки.

Для APS определяется исходная и остаточная концентрация $S_2O_8^{2-}$, накопленный SO_4^{2-}, расход на полимер и расход в blank-опыте с породой без полимера. Отдельно анализируются Fe^{2+}/Fe^{3+}, Ca^{2+}, Ba^{2+}, pH, щелочность, сульфиды и твердый осадок. Разность между опытом «полимер + порода» и суммой контрольных опытов позволяет оценить синергетические взаимодействия.

Для H_2O_2 измеряется скорость исчезновения пероксида в воде, на чистом полимере, на породе и в полной рецептуре. Желательно регистрировать температуру и газовыделение, поскольку каталитическое разложение может происходить быстро. Если пероксид исчезает, но молекулярная масса полимера уменьшается недостаточно, реагент расходуется нецелевым образом. Предлагаемая минимальная матрица лабораторных испытаний обобщена в таблице 5.

Таблица 5 – Минимальная матрица лабораторных испытаний

Блок	Образец/система	Измерения	Критерий решения
Минералогия	Валовая порода и фракция <2 мкм	XRD: воздушно-сухой, этиленгликоль, нагрев; CEC; SEM	Подтверждение или исключение расширяющихся фаз
Вода	Пластовая, техническая, смесь, flowback	Полный ионный состав, pH, щелочность, Fe, S, турбидность	Отсутствие несовместимого осадка и опасного снижения ионной силы
Стабилизатор	Порода + KCl/ QAS	Изотерма сорбции, остаточная концентрация, дзета-потенциал	Активная концентрация после контакта выше минимальной эффективной
Деструктор	Полимер без породы; порода без полимера; полная система	Остаточный окислитель, GPC, размер фрагментов, остаток	Целевой расход доминирует над расходом на породу и добавки
Coreflood	Составной керн под напряжением	Kпр, перепад давления, вынос частиц, химия выхода	Приемлемая удержанная проницаемость и отсутствие прогрессирующей кольматации
Проводимость	Проппант между пластинами породы	Проводимость под замыканием до/после полного цикла	Сохраненная проводимость соответствует проектной
Flowback	Ступенчатое увеличение расхода	Частицы, проппант, мутность, ионы и остаточные реагенты	Отсутствие критического срыва частиц и вторичного осадка

Результаты и обсуждение

Планирование ГРП в неблагоприятных условиях

Исследования, выполненные на месторождении Восточный Молдабек АО «Эмбамунайгаз», подтвердили тенденцию к снижению проницаемости пластового материала при насыщении этих материалов водами различного состава. Воды, применяемые в анализе, содержали в основном карбонат кальция и оксиды железа. Следует отметить, что количество осадков в различных образцах было сопоставимым. Попутно-добываемые воды не содержали осадков. Результаты лабораторных исследований показали, что добавление воды с осадками приводит к сильному снижению проницаемости образцов. В заключение сделан вывод, что причиной подобного поведения кернового материала является набухание глин, что не наблюдалось при использовании пластовой воды. В таблице 6 показаны данные лабораторных исследований керна.

Таблица 6 – Содержание глин и слюд

Горизонт	Скважина	Глины, %	Мусковит, %	Сумма, %	Статус
М-I-Б	2657	0.00	9.64	9.64	XRD
М-I-В	2657	10.80	0.00	10.80	XRD
М-II	2505	39.08	31.99	71.07	XRD
М-II	2524	31.17	24.03	55.20	XRD
М-II	2657	0.00	0.00	0.00	XRD
М-III	2505	58.40	0.00	58.40	XRD

В таблице 7 приведен состав глинистых материалов.

Таблица 7 – Состав глинистых материалов

Глинистый минерал	Диапазон в отдельных XRD-образцах, %	Среднее содержание в полном составе породы, %	Доля внутри суммы глинистых минералов, %
Иллит	0–78	10,52	42,2
Каолинит	0–84	7,89	31,6
Накрит	0–79	3,33	13,3
Диккит	0–100	3,21	12,9
Сумма глинистых минералов	–	24,95 ≈ 25,0	100

Из данных таблиц 6 и 7 следует, что пласты не содержат склонные к межслойному набуханию глины, следовательно, возможны два варианта:

1. Причина снижения проницаемости не связана с межслойным набуханием глин, а является, прежде всего, следствием осмотического воздействия, дефлоккуляции, диспергирования и миграции тонких частиц, блокировавших горловины пор;

2. Смешанослоистые глины, содержание которых могло быть небольшим, не были обнаружены при стандартных керновых исследованиях. В таком случае даже незначительная доля смешанослоистых глин могла привести к необратимой катастрофической потере проницаемости пласта. Отдельно необходимо отметить, что в случае только осмотического шока проницаемость образцов должна была повыситься после воздействия на образцы высокоминерализованной пластовой воды. Из-за обозначенных причин наиболее вероятной причиной снижения ФЕС пласта является сочетание факторов: закупорка тонкими частицами глин и слюды, межслойное набухание не обнаруженных при стандартных исследованиях смешанослоистых иллит-смектитовых глин. На рисунках 1–4 представлены вероятностное межскважинное распределение глин и слюды в различных пластах.

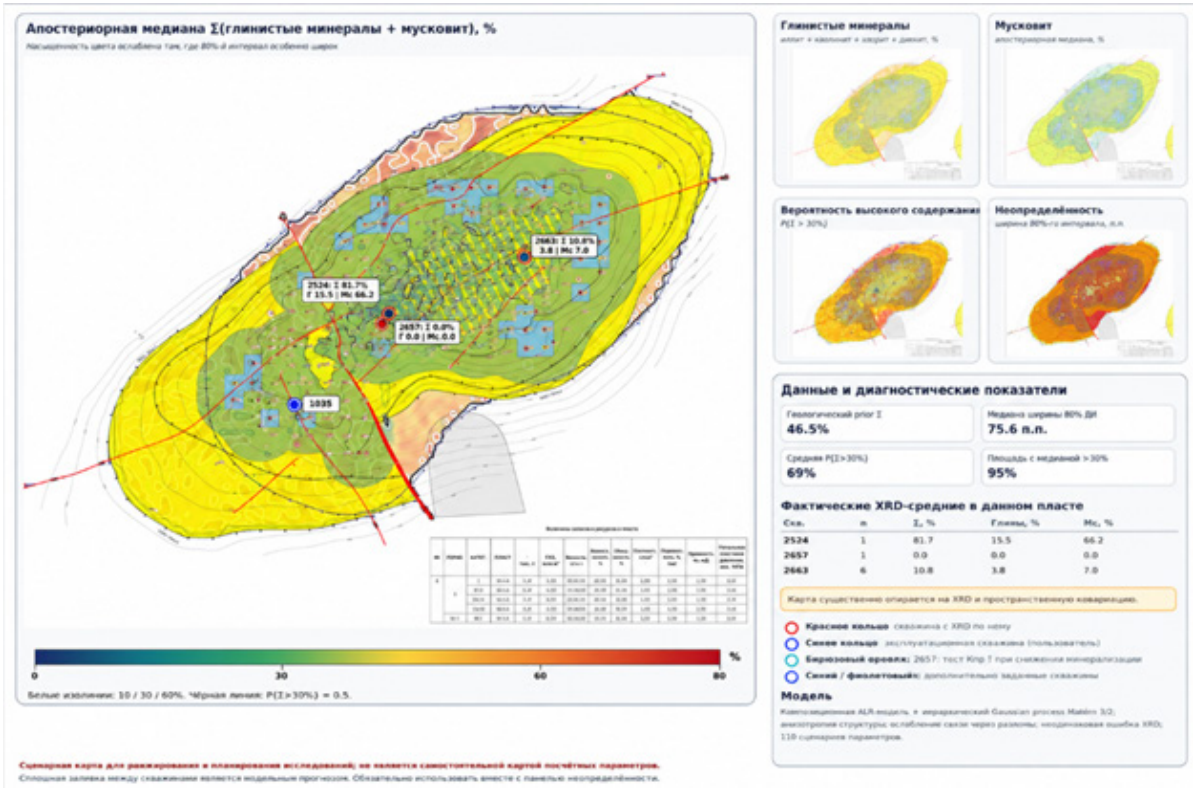


Рисунок 1 – Вероятностное распределение пласта M-I-A

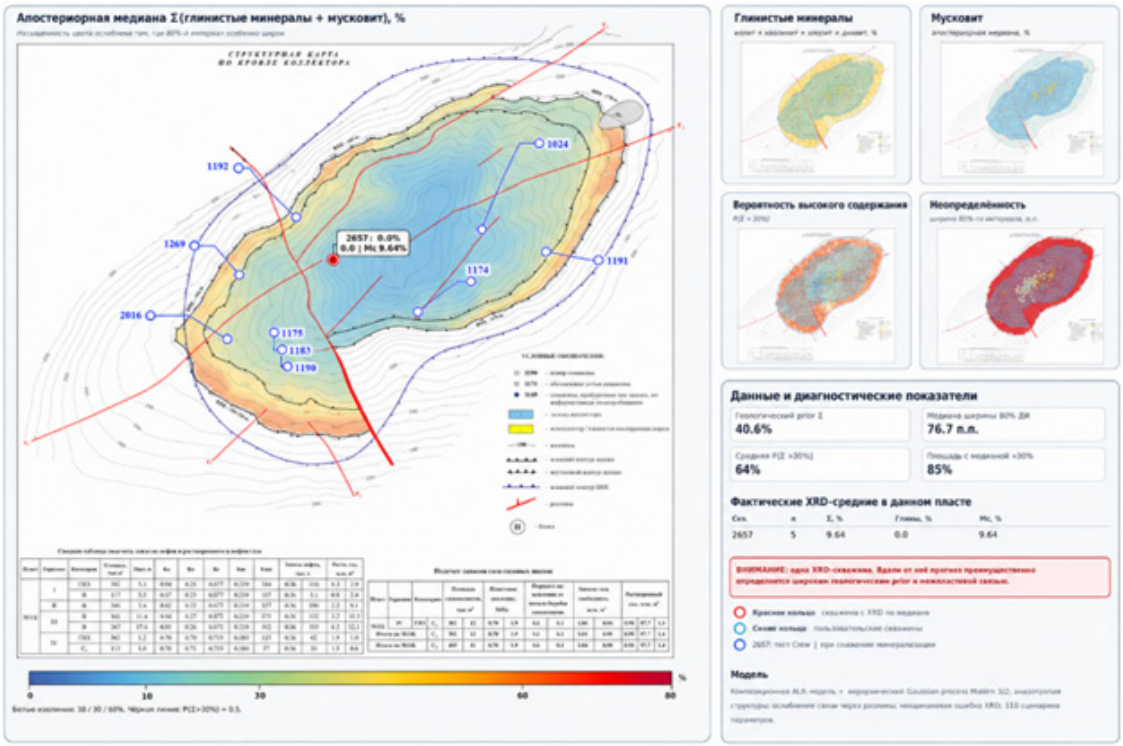


Рисунок 2 – Вероятностное распределение пласта M-I-Б

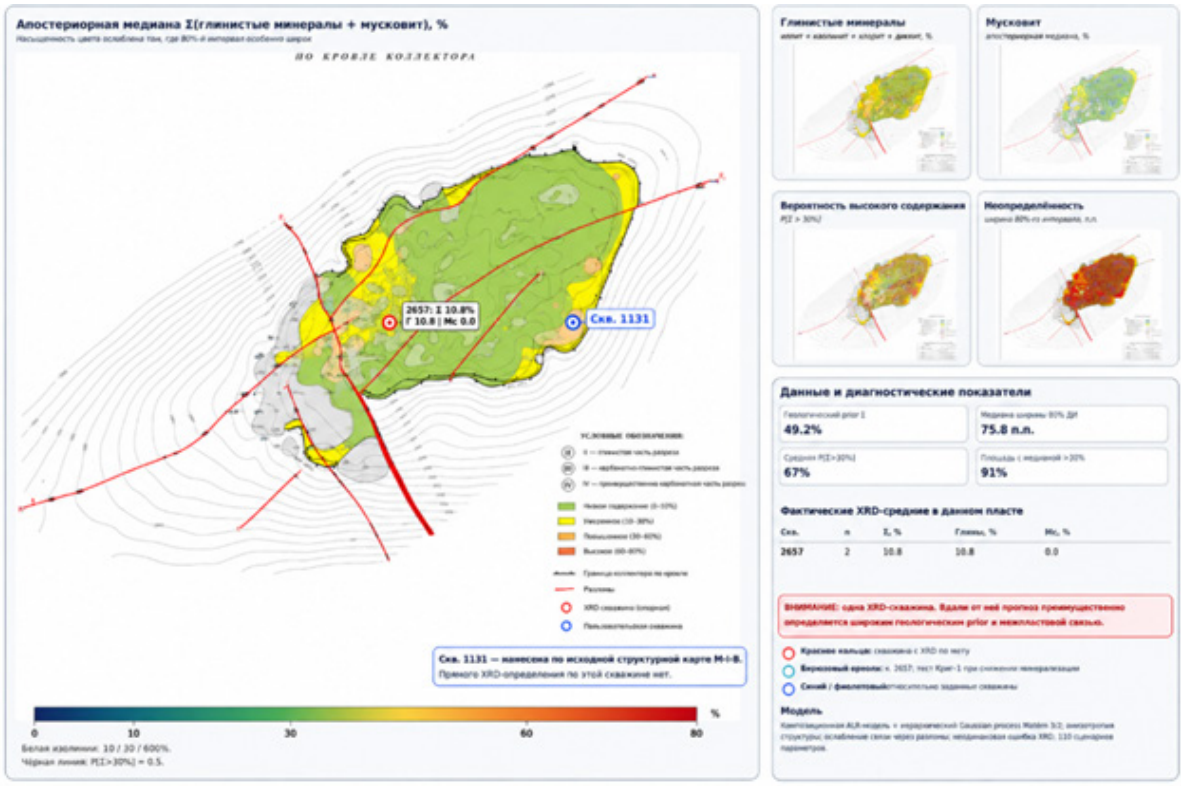


Рисунок 3 – Вероятностное распределение пласта M-I-B

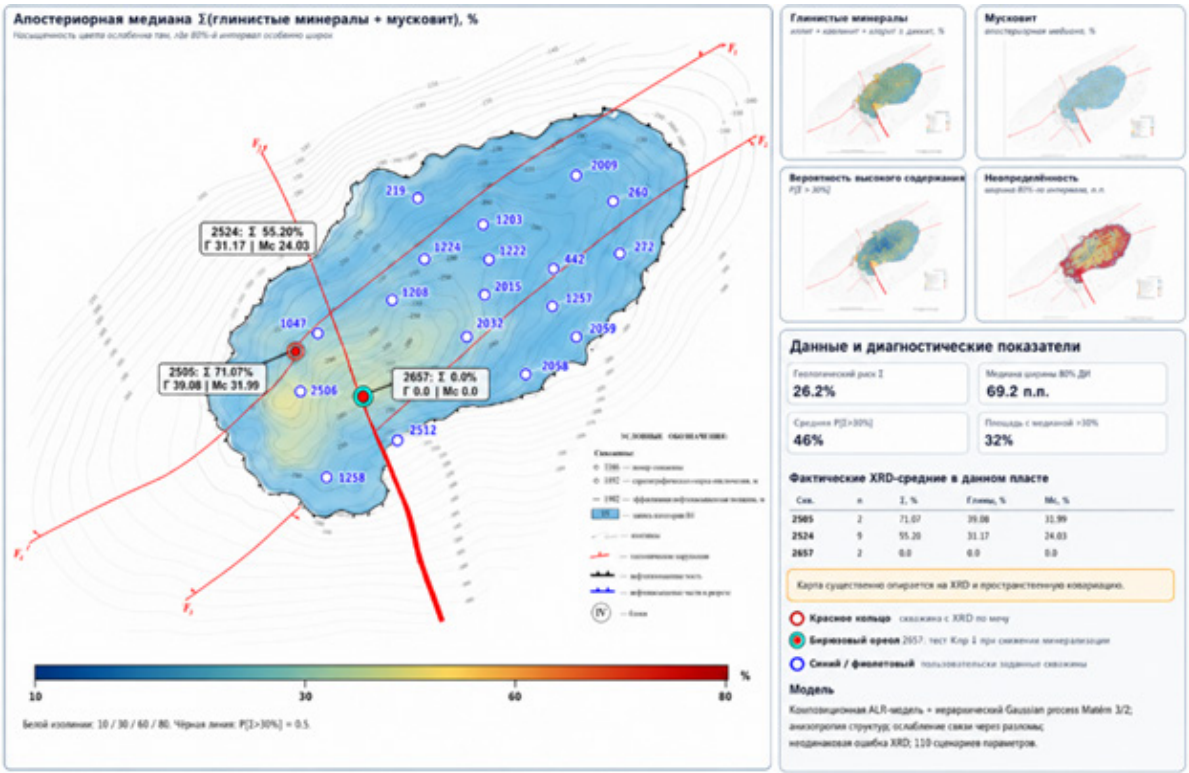


Рисунок 4 – Вероятностное распределение пласта M-II.

На рисунке 5 показаны приросты к дебиту скважин с ГРП.

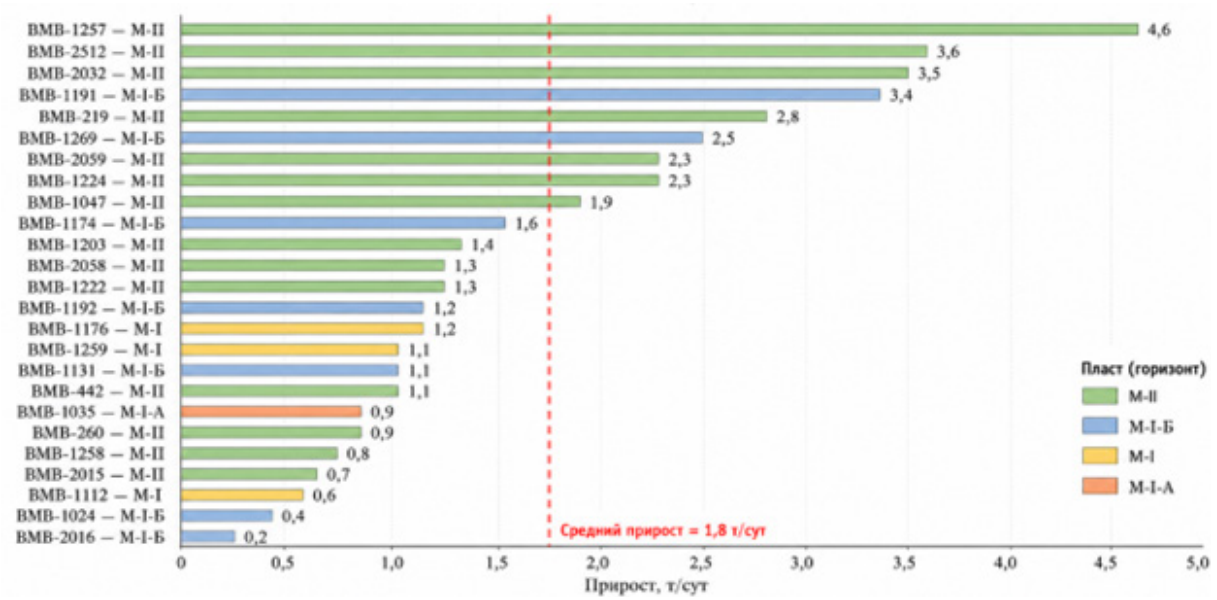


Рисунок 5 – Прирост к добыче нефти за счет ГРП

Из этих данных видно, что среди скважин с наибольшим приростом дебита отсутствуют скважины, в которых ГРП был проведен в пластах М-I-А и М-I-В, приросты более 2 т/сут. относятся к пластам М-II и М-I-Б, но при этом больше таких случаев относится к пласту М-II. Из представленных данных очевидно, что глубина и объем исследований недостаточны для однозначного проектирования ГРП на рассматриваемом месторождении. Тем не менее с осторожностью можно утверждать, что породы пласта оказывают сильное влияние на эффективность ГРП, поскольку программы закачки ГРП в каждом случае были сопоставимыми и технологическую составляющую как ключевой параметр успешности с высокой степенью уверенности можно исключить, то есть считать, что вклад технологической составляющей относится к строению пласта, его насыщению. Можно утверждать, что меньшее содержание глин и слюды при прочих равных условиях приводит к более эффективному ГРП.

В таблицах 8 и 9 представлены свойства нефти по объектам разработки.

Таблица 8 – Свойства нефти

Пласт	Вязкость, мПа·с	Плотность, кг/м³	Газосодержание, м³/т
М-I-А	334,7	902,0	10,5
М-I-Б	449,4	895,5	8,6
М-I-В	322,9	896,3	6,8
М-II	246,6	895,1	5,8
М-III	89,0	860,6	8,4

Как видно из данных таблиц 8 и 9, наименее благоприятные условия для отборов нефти, при прочих равных условиях, наблюдаются в пластах М-I-А, М-I-Б и М-I-В, а по смолам и асфальтенам – в пластах М-I-Б и М-I-В. Очевидно, что большая эффективность ГРП М-II связана не в последнюю очередь со свойствами нефти. Из таблицы 10 видно, что разброс свойств нефти по латерали значителен.

Таблица 9 – Свойства нефти

Пласт	Смолы, мас.%	Асфальтены, мас.%	Парафины, мас.%	Смолы + асфальтены, мас.%
М-I-А	12,0	0,7	0,9	12,7
М-I-Б	14,7	0,3	0,7	15,0
М-I-В	14,4	0,4	0,9	14,8
М-II	11,9	0,4	0,5	12,3
М-III	12,2	0,3	0,4	12,5

В таблице 10 показана неоднородность свойств нефти по латерали.

Учитывая весьма вероятную неоднородность в строении пластов и свойств нефти по латерали, бесспорное экстремальное снижение проницаемости при насыщении пород пласта слабоминерализованной водой, конкуренцию за стабилизаторы и деструкторы, а кроме того, необходимость снижения депрессии и выноса песка, очевидным шагом представляется, если принять во внимание установленный факт, что при использовании пластовой воды деградация ФЕС не происходит, выполнить ГРП на пластовой воде. Так как минерализация пластовой воды более 130 г/л, то выполнить ГРП с применением гуаровой камеди не представляется возможным, его следует выполнить на полимерах на основе полиакриламида. На рисунке 6 представлены результаты исследований ПАА.

Таблица 10 – Свойства нефти по латерали

Пласт	Наблюдаемый разброс по скважинам
М-I-А	Исследованы только скв. 1023 и 1035. Для скв. 1023: вязкость 340,8 мПа·с, плотность 904 кг/м³, газосодержание 10,7 м³/т
М-I-Б	При близких температурах анализа вязкость примерно 339–668 мПа·с, газосодержание 5,0–10,8 м³/т, плотность преимущественно 889–904 кг/м³
М-I-В	Вязкость 236–416 мПа·с, газосодержание 1,6–9,8 м³/т, плотность около 893–900 кг/м³
М-II	По исходным PVT-анализам вязкость примерно 130–429 мПа·с, газосодержание 1,7–9,8 м³/т, плотность 875–914 кг/м³
М-III	Вязкость по скважинам около 74–139 мПа·с; для более современных проб скв. 430, 252 и 2053 – 85,6–104 мПа·с

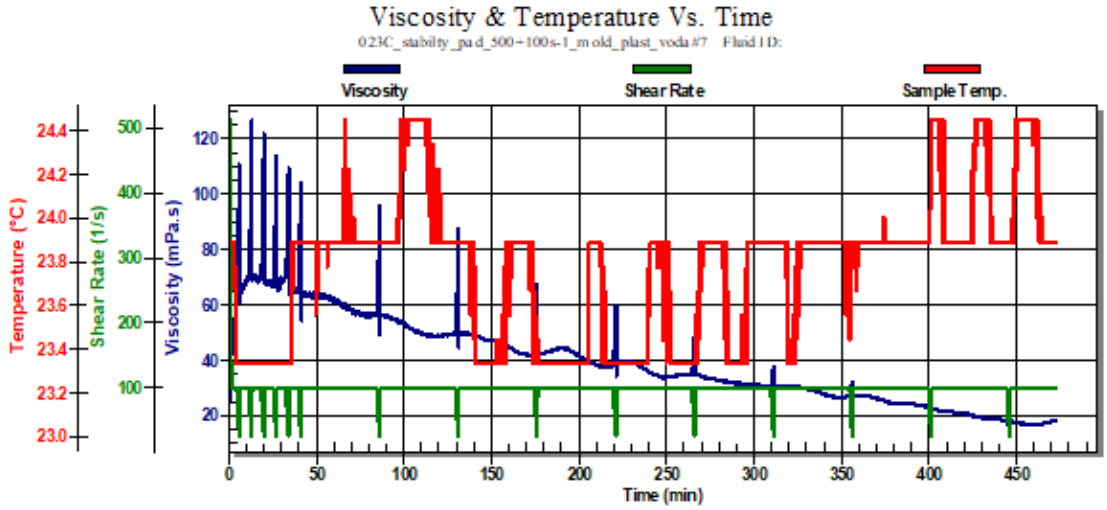


Рисунок 6 – Реология геля с синтетическим полимером

Рецептура геля с синтетическим полимером приведена в таблице 11.

Таблица 11 – Рецептура геля с синтетическим полимером

№	T, °C	Понизитель трения UpFR-HV (ПАА) (090725-1010), л/м³	UpECS (020625-621), л/м³	Жидкий брейкер Up BLT-A (090725-911), л/м³	Активатор брейкера BRP-(A1) (110323-181), л/м³
1	23.0	12.0	1.5	4.0	4.0

В таблице 12 приведен состав пластовой воды.

Таблица 12 – Состав пластовой воды

Источник воды: водокачка месторождения Восточный Молдабек; пластовая вода; дата отбора – 23.06.2026 г.			
Определяемые параметры	Единицы измерения	Результаты анализа (количественные значения)	Допустимые пределы
Температура	°C	24	16-40
Удельная плотность	(г/см³)	1,150	0,9-1,004
pH	Ед. pH	7,5	5 – 8,5
Железо общее (Fe)	(мг/л)	1,5	<8
Сульфаты	(мг/л)	450	<200
Хлориды	(мг/л)	2000	<1000
Общая жесткость	(мг/л)	1958	<500
Бикарбонаты	(мг/л)	144	<500

На рисунке 7 показан график закачки ГРП, выполненного на синтетическом полимере.

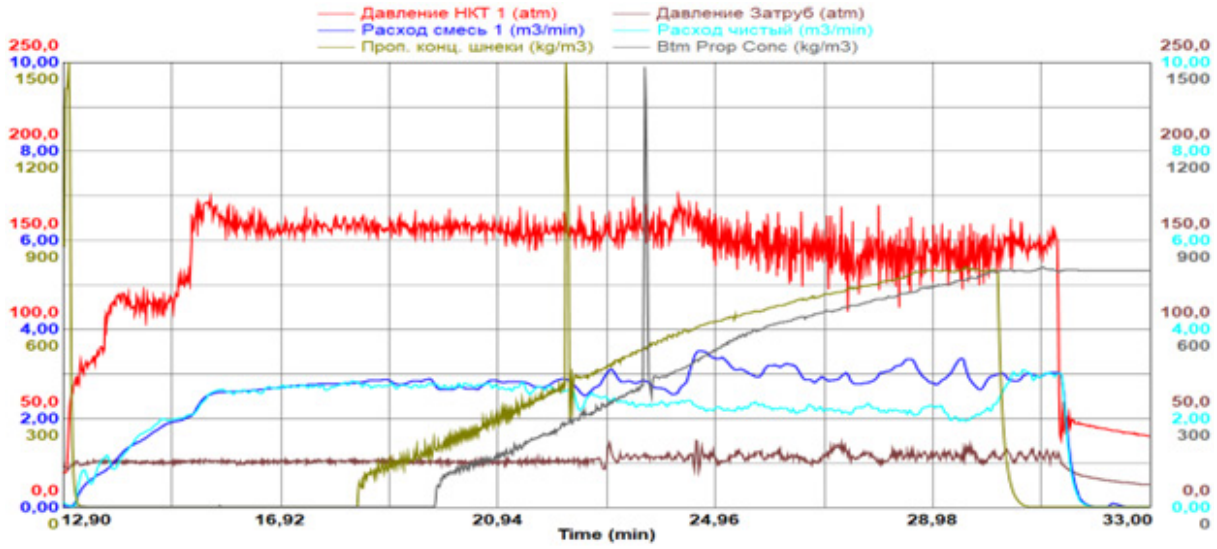


Рисунок 7 — График ГРП

На восьми скважинах проведены операции ГРП с применением синтетического полимера и пластовой воды, что полностью подтверждает техническую реализуемость подобного решения. На рисунке 8 показана добыча до и после ГРП.



Рисунок 8 – Добыча после ГРП. Скв.184

На рисунке 9 представлена динамика добычи после ГРП, проведенного на том же месторождении и в том же пласте по стандартной технологии.

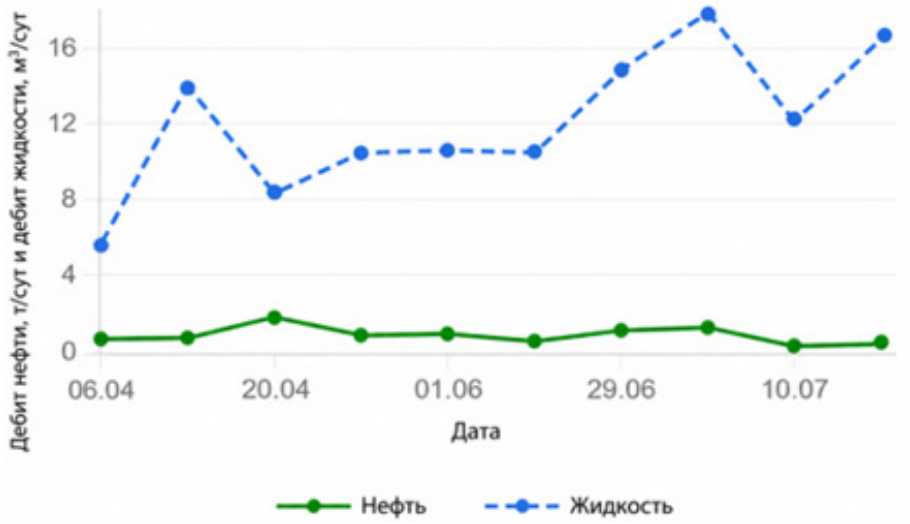


Рисунок 9 – ГРП по стандартной технологии,
выполненный на тот же пласт, скв.216

Из сопоставления данных рисунков 8 и 9 следует, что ГРП на синтетическом полимере и пластовой воде повышает дебит более чем в пять раз. При этом, скорее всего, повышение обводненности объясняется негерметичностью взрыв-пакера, отсекающего ранее разрабатываемый пласт.

Заключение

Сохранение проводимости трещины после ГРП в глинистых терригенных коллекторах определяется не только давлением разрыва и массой размещенного проппанта, но и степенью, в которой жидкость ГРП повреждает фильтрационно-емкостные свойства породы за счет во-

дочувствительности глинистых минералов и нецелевого расходования технологических реагентов.

Проведенный анализ показал, что широко используемый в промысловой практике термин «набухание глин» объединяет несколько разных по природе механизмов – межслоевое набухание смектита, осмотические эффекты, дефлоккуляцию и миграцию тонких частиц, – которые по-разному зависят от минералогии, солености и катионного состава воды. Отсутствие смектита в стандартной валовой рентгенограмме не является доказательством его физического отсутствия: надежная диагностика требует выделения фракции менее 2 мкм и серии ориентированных препаратов (воздушно-сухой, насыщенный этиленгликолем, прокаленный). Аналогичным образом показано, что номинальная дозировка стабилизаторов глин (KCl, четвертичные аммониевые соединения) и деструкторов геля (персульфат аммония, пероксид водорода, ферменты) без учета материального баланса может одновременно завышать оценку степени стабилизации глин и степени разрушения полимерной сетки, поскольку значительная доля реагента расходуется на карбонаты, органическое вещество, сульфиды и сопутствующие добавки. Предложенная минимальная матрица лабораторных испытаний – рентгенофазовый анализ ориентированных препаратов, изотермы сорбции, coreflood и тесты на удержанную проводимость трещины – позволяет разделить эти эффекты и снизить риск ошибочного выбора рецептуры ГРП.

Промысловые данные месторождения Восточный Молдабек (АО «Эмбамунайгаз») подтвердили практическую значимость предложенного подхода: снижение проницаемости керна при насыщении слабоминерализованной водой связано с набуханием глин и слюды, тогда как пластовая вода такой деградации не вызывает. Этот результат стал основанием для перехода на технологию ГРП на пластовой воде, что, в свою очередь, потребовало замены гуаровой камеди, неприменимой при минерализации воды выше 130 г/л, на гель на основе полиакриламида. Реализация данной технологии на восьми скважинах показала более чем пятикратное превышение дебита по сравнению со стандартной технологией, что подтверждает как техническую реализуемость, так и практическую целесообразность подхода для месторождений со схожими геолого-технологическими условиями.

Вместе с тем полученные результаты следует рассматривать с учетом ограниченного объема выполненных керновых исследований и числа скважин-кандидатов, а также с учетом того, что смешанослойные иллит-смектитовые глины при их низком содержании могли остаться невыявленными при стандартном керновом анализе. Дальнейшие исследования целесообразно направить на расширение выборки скважин, привлечение специализированного минералогического анализа глинистой фракции и систематическое применение предложенной матрицы лабораторных испытаний на этапе проектирования ГРП, что позволит точнее разграничивать вклад межслоевого набухания, дефлоккуляции и миграции тонких частиц в снижение проводимости трещины.

ЛИТЕРАТУРА

1 Deon, F., van Ruitenbeek, F., van der Werff, H., van der Meijde, M., and Marcatelli, C. Detection of Interlayered Illite/Smectite Clay Minerals with XRD, SEM Analyses and Reflectance Spectroscopy. Sensors, 22 (9), 3602 (2022). https://doi.org/10.3390/s22093602

2 Koubova, M., Vorm, P., Lang, J., and Petrov, O. New laboratory procedure for distinguishing smectites with varying permanent layer charge based on the combination of Cu-trien and ethylene glycol solvation methods and X-ray diffraction. Applied Clay Science, 232, 106788 (2023). https://doi.org/10.1016/j.clay.2022.106788

3 Hong, H., Cheng, F., Yin, K., Churchman, G.J., and Wang, C. Three-component mixed-layer illite/smectite/kaolinite (I/S/K) minerals in hydromorphic soils, South China. American Mineralogist, 100 (8-9), 1883–1891 (2015). https://doi.org/10.2138/am-2015-5170

4 Binazadeh, M., Xu, M., Zolfaghari, A., and Dehghanpour, H. Effect of Electrostatic Interactions on Water Uptake of Gas Shales: The Interplay of Solution Ionic Strength and Electrostatic Double Layer. Energy & Fuels, 30 (2), 992–1001 (2016). https://doi.org/10.1021/acs.energyfuels.5b02990

5 Sanaei, A., Shakiba, M., Varavei, A., and Sepehrnoori, K. Modeling Clay Swelling Induced Conductivity Damage in Hydraulic Fractures. SPE Low Perm Symposium (Denver, 2016), SPE-180211-MS. https://doi.org/10.2118/180211-MS

6 Russell, T., Pham, D., Tavakkoli Neishaboor, M., et al. Effects of kaolinite in rocks on fines migration. Journal of Natural Gas Science and Engineering, 45, 243–255 (2017). https://doi.org/10.1016/j.jngse.2017.05.020

7 Tangparitkul, S., Saul, A., Leelasukseree, C., Yusuf, M., and Kalantariasl, A. Fines migration and permeability decline during reservoir depletion coupled with clay swelling due to low-salinity water injection: An analytical study. Journal of Petroleum Science and Engineering, 194, 107448 (2020). https://doi.org/10.1016/j.petrol.2020.107448

8 Zhang, D., Meegoda, J.N., Goncalves da Silva, B.M., and Hu, L. Impact of de-ionized water on changes in porosity and permeability of shales mineralogy due to clay-swelling. Scientific Reports, 11, 20049 (2021). https://doi.org/10.1038/s41598-021-99523-2

9 Bhuvankar, P., Cihan, A., and Birkholzer, J. Pore-scale CFD simulations of clay mobilization in natural porous media due to fresh water injection. Chemical Engineering Science, 247, 117046 (2022). https://doi.org/10.1016/j.ces.2021.117046

10 Cihan, A., Petrusak, R., Bhuvankar, P., et al. Permeability Decline by Clay Fines Migration around a Low-Salinity Fluid Injection Well. Groundwater, 60, 87–98 (2022). https://doi.org/10.1111/gwat.13127

11 Sadeghein, A., Abbaslu, A., Riahi, S., and Hajipour, M. Comprehensive analysis of fine particle migration and swelling: Impacts of salinity, pH, and temperature. Geoenergy Science and Engineering, 240, 213044 (2024). https://doi.org/10.1016/j.geoen.2024.213044

12 Zhang, J., Ouyang, L., Zhu, D., and Hill, A.D. Experimental and numerical studies of reduced fracture conductivity due to proppant embedment in the shale reservoir. Journal of Petroleum Science and Engineering, 130, 37–45 (2015). https://doi.org/10.1016/j.petrol.2015.04.004

13 Zhang, J., Zhu, D., and Hill, A.D. Water-Induced Damage to Propped-Fracture Conductivity in Shale Formations. SPE Production & Operations, 31 (2), 147–156 (2016). https://doi.org/10.2118/173346-PA

14 Wu, W., Kakkar, P., Zhou, J., Russell, R., and Sharma, M.M. An Experimental Investigation of the Conductivity of Unpropped Fractures in Shales. SPE Hydraulic Fracturing Technology Conference and Exhibition (The Woodlands, 2017), SPE-184858-MS. https://doi.org/10.2118/184858-MS

15 Zhang, S., Sheng, J.J., and Shen, Z. Effect of hydration on fractures and permeabilities in Mancos, Eagle Ford, Barnett and Marcellus shale cores under compressive stress conditions. Journal of Petroleum Science and Engineering, 156, 917–926 (2017). https://doi.org/10.1016/j.petrol.2017.06.043

16 Jia, Y., Lu, Y., Tang, J., et al. Mechanical-Chemical-Mineralogical Controls on Permeability Evolution of Shale Fractures. Geofluids, 2018, 7801843 (2018). https://doi.org/10.1155/2018/7801843

17 Mehana, M., Al Salman, M., and Fahes, M. Impact of Salinity and Mineralogy on Slick Water Spontaneous Imbibition and Formation Strength in Shale. Energy & Fuels, 32 (5), 5725–5735 (2018). https://doi.org/10.1021/acs.energyfuels.7b03516

18 Zhang, S., and Sheng, J.J. Effect of Water Imbibition on Fracture Generation in Mancos Shale under Isotropic and Anisotropic Stress Conditions. Journal of Geotechnical and Geoenvironmental Engineering, 144 (2), 04017113 (2018). https://doi.org/10.1061/(ASCE)GT.1943-5606.0001832

19 Chen, X., Eichhubl, P., Olson, J.E., and Dewers, T.A. Effect of Water on Fracture Mechanical Properties of Shales. Journal of Geophysical Research: Solid Earth, 124, 2428–2444 (2019). https://doi.org/10.1029/2018JB016479

20 Dai, Q., Sun, W., Zuo, Y., et al. Impact of Slickwater Fracturing Fluid on Pore Structure and Micromechanical Properties of Clay-Rich Shale Using Fluid Intrusion and AFM Experiments. ACS Omega, 10 (6), 6164–6181 (2025). https://doi.org/10.1021/acsomega.4c11005

21 Li, G., Dong, C., Bai, H., Han, Y., and Zhang, Q. Weakly-consolidated sandstone fracture conductivity under combined action of compressing, proppant embedding and fines plugging: experiments, model and application. Journal of Petroleum Exploration and Production Technology (2025). https://doi.org/10.1007/s13202-025-02016-5

22 Li, Z., Fan, Y., and Liu, F. The Effect of Shale Swelling on In Situ Stress during Hydraulic Fracturing. ACS Omega, 11 (5), 7377–7387 (2026). https://doi.org/10.1021/acsomega.5c07030

23 Tariq, Z., Kamal, M.S., Mahmoud, M., Hussain, S.M.S., and Hussaini, S.R. Novel gemini surfactant as a clay stabilizing additive in fracturing fluids for unconventional tight sandstones: Mechanism and performance. Journal of Petroleum Science and Engineering, 195, 107917 (2020). https://doi.org/10.1016/j.petrol.2020.107917

24 Tariq, Z., Kamal, M.S., Mahmoud, M., Murtaza, M., Abdulraheem, A., and Zhou, X. Dicationic Surfactants as an Additive in Fracturing Fluids to Mitigate Clay Swelling: A Petrophysical and Rock Mechanical Assessment. ACS Omega, 6 (24), 15867–15877 (2021). https://doi.org/10.1021/acsomega.1c01388

25 Fu, L., Liao, K., Ge, J., He, Y., Huang, W., and Du, E. Preparation and inhibition mechanism of bis-quaternary ammonium salt as shale inhibitor used in shale hydrocarbon production. Journal of Molecular Liquids, 309, 113244 (2020). https://doi.org/10.1016/j.molliq.2020.113244

26 Murtaza, M., Kamal, M.S., Hussain, S.M.S., Mahmoud, M., and Syed, N.A. Quaternary ammonium gemini surfactants having different spacer length as clay swelling inhibitors: Mechanism and performance evaluation. Journal of Molecular Liquids, 308, 113054 (2020). https://doi.org/10.1016/j.molliq.2020.113054

27 Zeng, T., Kim, K.T., Werth, C.J., Katz, L.E., and Mohanty, K.K. Surfactant Adsorption on Shale Samples: Experiments and an Additive Model. Energy & Fuels, 34 (5), 5436–5443 (2020). https://doi.org/10.1021/acs.energyfuels.9b04016

28 Chen, J.-J., Liu, J.-X., Ma, S.-S., Xu, F., and Liu, H. Study of clay stabilization mechanism and adsorption behavior of organic ammonium salts with low molar weight. Petroleum Science and Technology, 42 (17), 2171–2191 (2024). https://doi.org/10.1080/10916466.2022.2156541

29 Khan, R.A., Murtaza, M., Mustafa, A., et al. Ionic liquids as clay stabilizer additive in fracturing fluid. Fuel, 334, 126154 (2023). https://doi.org/10.1016/j.fuel.2022.126154

30 Abdulhameed, Y.A., Ali, J.A., and Abdulkareem, L.A. Assessment of KCl Inhibition Efficiency in Water-Based Drilling Fluids: A Formation-Responsive Approach for Shale Stability. Industrial & Engineering Chemistry Research, 64 (45), 21523–21539 (2025). https://doi.org/10.1021/acs.iecr.5c03075

31 Labak, A., and Pourafshary, P. Mitigating clay swelling and permeability loss in thermal EOR with a quaternary ammonium clay stabilizer under high-temperature low-salinity conditions. Energy Geoscience, 6 (4), 100444 (2025). https://doi.org/10.1016/j.engeos.2025.100444

32 Bai, S., Wei, P., Zhai, D., Xiao, W., and Liu, J. Functional Group-Dependent Antiswelling Mechanisms of Cationic Inhibitors on Montmorillonite. Energy & Fuels, 40 (17), 9302–9310 (2026). https://doi.org/10.1021/acs.energyfuels.6c00426

33 Lin, X., Zhang, S., Wang, Q., Feng, Y., and Shuai, Y. Improving the fracturing fluid loss control for multistage fracturing by the precise gel breaking time design. Journal of Natural Gas Science and Engineering, 25, 367–370 (2015). https://doi.org/10.1016/j.jngse.2015.05.017

34 Wang, J., Huang, Y., Zhang, Y., Zhou, F., Yao, E., and Wang, R. Study of Fracturing Fluid on Gel Breaking Performance and Damage to Fracture Conductivity. Journal of Petroleum Science and Engineering, 193, 107443 (2020). https://doi.org/10.1016/j.petrol.2020.107443

35 Almubarak, T., Ng, J.H.C., AlKhaldi, M., Panda, S., and Nasr-El-Din, H.A. Insights on Potential Formation Damage Mechanisms Associated with the Use of Gel Breakers in Hydraulic Fracturing. Polymers, 12 (11), 2722 (2020). https://doi.org/10.3390/polym12112722

36 Sumner, A.J., and Plata, D.L. Oxidative Breakers Can Stimulate Halogenation and Competitive Oxidation in Guar-Gelled Hydraulic Fracturing Fluids. Environmental Science & Technology, 53 (14), 8216–8226 (2019). https://doi.org/10.1021/acs.est.9b01896

37 Chen, M., Rholl, C.A., He, T., Sharma, A., and Parker, K.M. Halogen Radicals Contribute to the Halogenation and Degradation of Chemical Additives Used in Hydraulic Fracturing. Environmental Science & Technology, 55 (3), 1545–1554 (2021). https://doi.org/10.1021/acs.est.0c03685

38 Manz, K.E., and Carter, K.E. Degradation of hydraulic fracturing additive 2-butoxyethanol using heat activated persulfate in the presence of shale rock. Chemosphere, 206, 398–404 (2018). https://doi.org/10.1016/j.chemosphere.2018.05.007

39 Liu, D., et al. Experimental and Numerical Studies on Oxidation-Acidification Interactions that Dominate Shale Stimulation with Persulfate. Energy & Fuels, 36 (11), 5784–5796 (2022). https://doi.org/10.1021/acs.energyfuels.2c00953

40 Yang, S., Liu, D., Yang, Z., Xu, J., and Li, Y. Experimental insight into the dissolution behavior and interaction of key components in shale-persulfate system. Gas Science and Engineering, 110, 204867 (2023). https://doi.org/10.1016/j.jgsce.2022.204867

41 Donmoyer, S., Agrawal, V., Sharma, S., and Hakala, J.A. Effect of oxidative breakers on organic matter degradation, contaminant mobility and critical mineral release during shale-fracturing fluid interactions in the Marcellus Shale. Fuel, 331 (Part 1), 125678 (2023). https://doi.org/10.1016/j.fuel.2022.125678

42 Liang, X., and Sheng, J.J. Comparison of Chemical-Induced Fracturing by Na2S2O8, NaClO, and H2O2 in Marcellus Shale. Energy & Fuels, 34 (12), 15905–15919 (2020). https://doi.org/10.1021/acs.energyfuels.0c02623

43 Yu, W., Lei, J., Wang, T., and Chen, W. H2O2-Enhanced Shale Gas Recovery under Different Thermal Conditions. Energies, 12 (11), 2127 (2019). https://doi.org/10.3390/en12112127

44 Zhang, N., You, L., Kang, Y., Xu, J., Li, K., Cheng, Q., and Zhou, Y. The investigation into oxidative method to realize zero flowback rate of hydraulic fracturing fluid in shale gas reservoir. Journal of Petroleum Science and Engineering, 209, 109918 (2022). https://doi.org/10.1016/j.petrol.2021.109918

45 Yang, S., Yu, J., Liu, D., and Li, Y. Effect of persulfate stimulation on matrix alteration and permeability enhancement of fractured shale: Core-flooding experiments and numerical simulation. Gas Science and Engineering, 138, 205612 (2025). https://doi.org/10.1016/j.jgsce.2025.205612

46 Tukpatolla, D.S., Sadykbek, K.E., Dzhumagalieva, A.K., et al. Pereschet zapasov nefti i gaza mestorozhdeniya Kenbay (uchastok Moldabek Vostochnyy) po sostoyaniyu na 02.01.2024 g. [Recalculation of Oil and Gas Reserves of the Kenbai Field (East Moldabek Site) as of January 2, 2024] Vol. I, book 1; Vol. IV, book 2 (Atyrau: Atyrau branch of KMG Engineering LLP, 2024). (in Russian).

47 Itogovye rezul'taty laboratornykh i analiticheskikh issledovaniy po provedeniyu opytno-promyshlennykh ispytaniy tekhnologii polimernogo zavodneniya na gorizonte M-II melovykh zalezhey uchastka Moldabek Vostochnyy mestorozhdeniya Kenbay AO «Embamunaygaz» [Final Results of Laboratory and Analytical Studies on Pilot Testing of Polymer Flooding Technology at Horizon M-II of Cretaceous Deposits of East Moldabek Site of Kenbai Field of Embamunaygas JSC] (Atyrau, 2019), 29 p. (in Russian).

48 Meng, Y., Zhao, F., Jin, X., Feng, Y., Sun, G., Lin, J., Jia, B., and Li, P. Performance Evaluation of Enzyme Breaker for Fracturing Applications under Simulated Reservoir Conditions. Molecules, 26 (11), 3133 (2021). https://doi.org/10.3390/molecules26113133

[1]*Дуйсалиев А.М.,
докторант, ORCID ID: 0009-0000-9470-4225,
e-mail: e.nurbekova@kmg.kz
[1]Исмаилов А.А.,
PhD, т.ғ.к., профессор, ORCID ID: 0000-0002-1957-5168,
e-mail: a.ismailov@kbtu.kz
[2]Махмудов Н.Н.,
т.ғ.д., профессор, ORCID ID: 0009-0005-1148-4180,
e-mail: nazirillamaxmudov@gmail.com

[1]Қазақстан-Британ техникалық университеті, Алматы қ., Қазақстан
[2]Ислам Каримов атындағы Ташкент мемлекеттік техникалық университеті,
Ташкент қ., Өзбекстан

ГРП КЕЗІНДЕ САЗ БАЛШЫҚТЫҢ ІСІНУІ МЕН РЕАГЕНТТЕРДІҢ МАҚСАТСЫЗ ШЫҒЫНЫ: ШЫҒЫС МОЛДАБЕК КЕН ОРНЫНДА ҚАБАТ СУЫН ПАЙДАЛАНУ ТӘЖІРИБЕСІ ЖӘНЕ ДИАГНОСТИКАСЫ

Аңдатпа

Қабатты гидравликалық жарудың (ГРП) тиімділігі көбінесе жару сұйықтығының тау жынысымен әрекеттесуінен кейін жарықшақ өткізгіштігінің сақталу дәрежесіне байланысты. Мақалада саз минералдарының суға сезімталдығына байланысты өткізгіштіктің төмендеу тетіктері жүйеленген: смектиттің қабатаралық ісінуі, осмостық әсерлер, дефлокуляция және ұсақ бөлшектердің көшуі. Сонымен қатар саз тұрақтандырғыштарының (KCl, төрттік аммоний қосылыстары) және гель бұзғыштарының (аммоний персульфаты, сутегі асқын тотығы, ферменттер) тау жынысы минералдарымен және қосалқы реагенттермен әрекеттесуі нәтижесінде мақсатсыз жұмсалу арналары қарастырылған. Материалдық баланс ескерілмеген

жағдайда реагенттің номиналды мөлшері саздың тұрақтану дәрежесін де, полимерлік тордың ыдырау дәрежесін де асыра бағалауға әкелуі мүмкін екені көрсетілген. Бағдарланған үлгілердің рентгендік дифракциясын, сорбция изотермаларын, coreflood сынақтарын және жарықшақтың сақталған өткізгіштігін анықтауды қамтитын зертханалық сынақтардың ең аз матрицасы ұсынылған. «Шығыс Молдабек» кен орнының («Ембімұнайгаз» АҚ) мысалында әлсіз минералданған сумен қанықтыру кезінде байқалған өткізгіштіктің төмендеуі саз бен слюданың ісінуімен байланысты екені, ал қабат суының мұндай нашарлауға әкелмейтіні көрсетілген. Судың минералдануы 130 г/л-ден асқан жағдайда гуар шайырын қолдану мүмкін болмағандықтан, оның орнына полиакриламид негізіндегі гельді пайдалана отырып, қабат суымен ГРП жүргізу технологиясы негізделіп, өндірісте іске асырылған. Сегіз ұңғыма бойынша алынған нәтижелер қабат суы мен синтетикалық полимерді қолдану арқылы жүргізілген ГРП-дан кейінгі ұңғымалардың дебиті стандартты технологиямен салыстырғанда бес еседен астам жоғары болғанын көрсетті.

Түйін сөздер: қабатты гидравликалық жару, саздың ісінуі, ұсақ бөлшектердің көшуі, жарықшақ өткізгіштігі, саз тұрақтандырғыштары, гель бұзғыштары, қабат суы.

[1]*Duisaliyev A.M.,
Doctoral student, ORCID ID: 0009-0000-9470-4225,
e-mail: e.nurbekova@kmg.kz
[1]Ismailov A.A.,
PhD, Candidate of Technical Sciences, Professor, ORCID ID: 0000-0002-1957-5168,
e-mail: a.ismailov@kbtu.kz
[2]Makhmudov N.N.,
Doctor of Technical Sciences, Professor, ORCID ID: 0009-0005-1148-4180,
e-mail: nazirillamaxmudov@gmail.com

[1]Kazakh-British Technical University, Almaty, Kazakhstan
[2]Tashkent State Technical University named after Islam Karimov, Tashkent, Uzbekistan

CLAY SWELLING AND NON-TARGET CONSUMPTION OF FRACTURING FLUID ADDITIVES: DIAGNOSTICS AND FIELD EXPERIENCE USING FORMATION WATER AT THE VOSTOCHNY MOLDABEK FIELD

Abstract

The effectiveness of hydraulic fracturing (HF) largely depends on how well fracture conductivity is preserved after the fracturing fluid interacts with the reservoir rock. This paper systematizes the permeability-damage mechanisms related to the water sensitivity of clay minerals – interlayer smectite swelling, osmotic effects, deflocculation and fines migration – and examines the non-target consumption pathways of clay stabilizers (KCl, quaternary ammonium compounds) and gel breakers (ammonium persulfate, hydrogen peroxide, enzymes) on rock minerals and co-additives. It is shown that the nominal reagent dosage, evaluated without a material balance, can simultaneously overestimate both the degree of clay stabilization and the extent of polymer network degradation. A minimum laboratory testing matrix is proposed, including oriented-sample XRD analysis, sorption isotherms, coreflood tests and retained fracture-conductivity tests. Using the Vostochny Moldabek field (Embamunaigaz JSC) as a case study, it is shown that the permeability decline observed when the reservoir is saturated with low-salinity water is caused by clay and mica swelling, whereas formation water does not cause such degradation. A formation-water-based fracturing technology is substantiated and implemented, using a polyacrylamide-based gel instead of guar gum, which is unsuitable at a water salinity above 130 g/L. Field results from eight wells show that production rates after fracturing on formation water with the synthetic polymer exceeded those of the standard technology by more than five times.

Keywords: hydraulic fracturing, clay swelling, fines migration, fracture conductivity, clay stabilizers, gel breaker, formation water.

Received July 21, 2026; accepted August 20, 2026

ӘОЖ 550.84
ҒТАХР 44.09.37

https://doi.org/10.55452/1998-6688-2026-23-3-565-572

[1]Нұрбекова Р.Н.,
PhD, ORCID ID: 0000-0001-7804-3949,
e-mail: riza.nurbekova@nu.edu.kz
[1]Хазлетт Р.,
PhD, профессор, ORCID ID: 0000-0003-2058-8406,
e-mail: randy.hazlett@nu.edu.kz
[1,2]Фустич М.,
PhD, қауымдастырылған профессор, ORCID ID: 0000-0001-9815-9279,
e-mail: milovan.fustic@nu.edu.kz
[1]Салаудин И.,
PhD, ORCID ID: 0009-0008-2015-8629,
e-mail: ibraheem.salaudeen@nu.edu.kz
[1]Қайратова А.,
Бакалавр студенті,
e-mail: a.kairatova@nu.edu.kz

[1]Тау-кен ісі және жер туралы ғылымдар мектебі, Назарбаев Университеті,
Астана қ., Қазақстан
[2]Геоғылымдар департаменті, Калгари университеті, Калгари қ., Канада

ҚАЗАҚСТАНДАҒЫ ТАЗА ЭНЕРГИЯ ӨНДІРУ ЖӘНЕ КӨМІРҚЫШҚЫЛ ГАЗЫН АЗАЙТУ ЖОЛЫ: НЕГІЗДІ ЖӘНЕ УЛЬТРАНЕГІЗДІ ЖЫНЫСТАРДЫ СУТЕГІ ӨНДІРУ МЕН КӨМІРҚЫШҚЫЛ ГАЗЫН СЕКВЕСТРЛЕУГЕ ПАЙДАЛАНУ

Аңдатпа

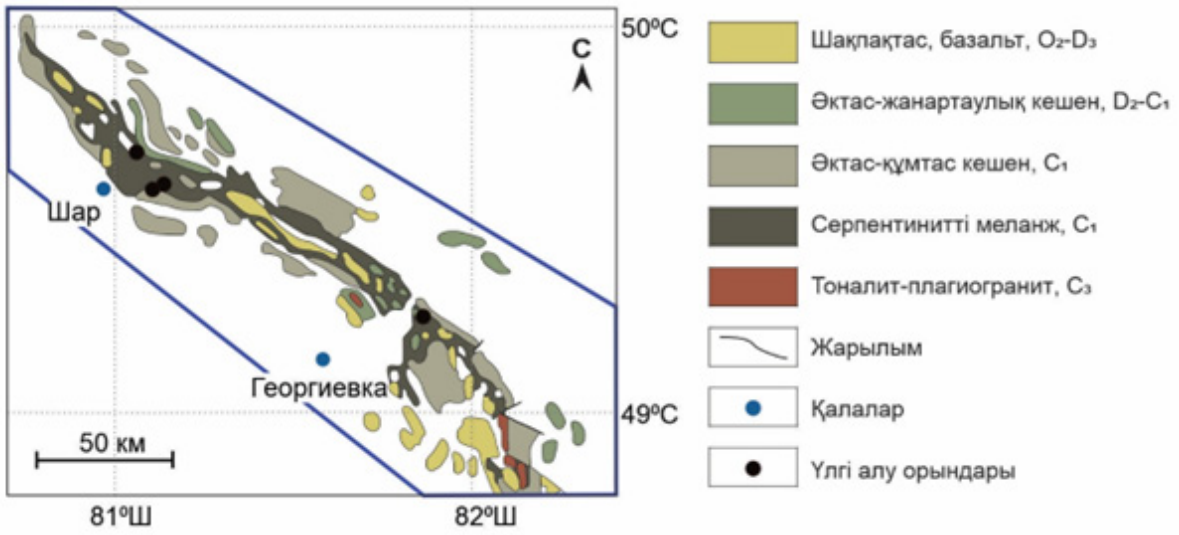
Көмірқышқыл газын (CO_2) ұзақ мерзімге геологиялық ортада сақтау және табиғи сутегі (H_2) сияқты төмен көміртекті энергия көзін игеру көміртегі бейтараптығына өтуге бағытталған зерттеулердің маңызды бөлігіне айналды. Негізді және ультранегізді жыныстар бұл тұрғыдан ерекше қызығушылық тудырады, себебі олардың минералдық құрамы CO_2-нің карбонат минералдары түрінде байланысуына және H_2 түзілуіне жағдай жасай алады. Дегенмен, бұл екі процестің бір жыныс жүйесінде қалай қатар жүретіні және олардың минералдық құрамға тәуелділігі жеткілікті зерттелмеген. Осы жұмыста Шығыс Қазақстандағы Шар офиолиттік тігіс аймағы мен Батыс Қазақстандағы Кемпірсай ультранегізді массивінен алынған негізді және ультранегізді жыныстар зерттелді. Зерттеу нәтижелері көрсеткендей CO_2 газының минералдану жылдамдығы серпентинге бай ультранегізді үлгілердің құрамында лизардит минералының еруінен бөлінетін Mg^{2+} мөлшеріне тікелей байланысты. Ал магнезиохромит минералының мөлшері жоғары болған үлгілерде рекациядан кейінгі жалпы көміртек мөлшері аз ғана пайызды құрады. H_2 түзілуінің ең жоғары мөлшері Шар аймағының U-2C ультранегізді үлгісінде (0,872 мол.%) және M-1C негізді үлгісінде (0,721 мол.%) байқалды. Кемпірсай массивінен алынған үлгілердің кейбірінде ғана өте аз мөлшерде H_2 тіркелді. CO_2-нің минералдық байланысуы Mg құрамды фазалардың реакциясымен тығыз байланысты болса, H_2 түзілуінде реакцияға қабілетті Fe құрамды минералдардың рөлі басым болды. Осы айырмашылықтарды ескеру Қазақстандағы офиолиттік кешендерді CO_2 минералдық сақтау және табиғи H_2 іздеу тұрғысынан бағалауда маңызды.

Түйін сөздер: ультранегізді жыныстар, серпентиндену, сутегі, көмірқышқыл газы, минералдану.

Кіріспе

Антропогендік CO_2 шығарындыларын азайту көміртегі бейтараптығына қол жеткізудің негізгі міндеттерінің бірі. Бұл бағытта CO_2-ні геологиялық ортада ұзақ мерзімге сақтау және H_2

сияқты төмен көміртекті энергия көздерін дамыту қатар қарастырылуда. Осы тұрғыдын негізді және ультранегізді тау жыныстары әлемдік ғылыми қауымдастықтың ерекше қызығушылығын тудырып отыр [1–11]. Ультранегізді тау жыныстарында Ca^{2+}, Mg^{2+} және Fe^{2+} көп кездеседі, ал олардың оксидтері жыныс массасының әдетте 45%-дан астамын құрайды. Мұндай құрам CO_2-нің тұрақты карбонат минералдары түрінде байланысуына қолайлы [1–5]. Алғашқы зерттеулерде ультранегізді жыныстар өткізгіштігі төмен болғандықтан негізгі жыныстарға қарағанда CO_2 газын геологиялық сақтау нысаны ретінде азырақ қарастырылды [6–7]. Кейінірек бұл жыныстарда табиғи H_2 түзілу мүмкіндігі ашылып, оларға деген қызығушылық артты [3–5, 8–21]. Бұған табиғи мысал ретінде Омандағы H_2 табиғи шығуы тіркелген Семаил офиолитін, Ресейдің Орал белдеуін және оның жалғасын, батыс Қазақстандағы Кемпірсай ультранегізді массивін келтіруге болады [16–17, 22–24]. LISZT және ICDP бұрғылау жобалары бұл бағыттағы маңызды зерттеулердің бірі болып табылады [4]. Далалық бақылаулар [4, 16–17, 22–23], зертханалық тәжірибелер [3, 5, 12–13, 15, 21] және геохимиялық модельдеу [8, 10–11, 14] ультранегізді жыныстардың гидратациясы кезінде тұрақты карбонатты минералдар түрінде CO_2 байланысуымен бірге H_2 түзілетінін көрсетті. Осы нәтижелерге сүйене отырып, бұл жұмыста Шығыс Қазақстандағы Шар офиолиттік тігіс аймағының (1-сурет) және Батыс Қазақстандағы Кемпірсай ультранегізді массивінің негізді және ультранегізді жыныстарын зерттеу қарастырылған. Жоғары қысымды CO_2–су–тау жыныс эксперименттері XRD, SEM–EDS, ICP–OES, GC және жалпы көміртегі (TC) талдауларымен бірге жүргізілді. Зерттеудің негізгі мақсаты тау жыныстарының минералды ерекшеліктерін CO_2 минералдануымен және H_2 түзілуімен салыстыру, осы екі процестің бір геологиялық жүйеде қалай жүретінін бағалау.



Сурет 1 – Шар офиолиттік тігіс аймағының жеңілдетілген геологиялық картасы. Негізгі литологиялық бірліктер мен сынама алынған нүктелер көрсетілген ([25] бойынша).

Материалдар мен әдістер

Зерттеуде Шығыс Қазақстандағы Шар офиолиттік тігіс аймағынан алынған негізді және ультранегізді жыныстар, сондай-ақ Батыс Қазақстандағы Кемпірсай ультранегізді массивінің бұрғылау ұңғымасынан алынған керн үлгілері пайдаланылды. Үлгілер Retsch MM 400 (Германия) зертханалық диірменінде <25 мкм дейін ұнтақталды. Негізгі элементтік құрам Rigaku ZSX Primus II рентгендік-флуоресценттік спектрометрінде (XRF), минералдық құрам Bruker D2 Phaser (Германия) рентгендік дифрактометрінде (XRD, Cu-Kα, λ = 1,5418 Å) анықталды. Минералдық фазалар DIFFRAC.EVA бағдарламасымен сәйкестендіріліп, олардың салыстыр-

малы мөлшері TOPAS бағдарламасында есептелді. Меншікті бет ауданы Autosorb iQ (Anton Paar) анализаторында BET әдісімен анықталды.

CO_2–су–жыныс тәжірибелері 300 мл Parr жоғары қысымды реакторында жүргізілді. Әр тәжірибеге 1,5 ± 0,05 г жыныс ұнтағы және 100 мл 0,64 M $NaHCO_3$ + 1 M NaCl ерітіндісі алынды. Реактор вакуумдалып, CO_2 бастапқы қысымы 800 psia-ға жеткізілді. Тәжірибелер 80 және 160–200 °C температурада 7 тәулік жүргізілді.

Реакциядан кейінгі қатты фазалар XRD және ZEISS Crossbeam 540 (Германия) SEM–EDS көмегімен зерттелді. Жалпы көміртек мөлшері UNICUBE (Elementar, Германия) элементтік анализаторында, ерітіндідегі элементтер Thermo Scientific iCAP 6300 DUO ICP–OES спектрометрінде анықталды. H_2 мөлшері Agilent 8890 газ хроматографында (GC) өлшеніп, концентрациясы сертификатталған газ қоспалары бойынша құрылған калибрлеу қисықтары арқылы есептелді.

Нәтижелер мен талқылау

XRF талдауы бойыншы Кемпірсай массиві мен Шар офиолиттік тігіс аймағынан алынған негізді және ультранегізді жыныстардың химиялық құрамында олардың литологиялық ерекшеліктеріне сәйкес айқын айырмашылықтар бар (1-кесте). Кемпірсайдың ультранегізді жыныстарында MgO мөлшері 38,3–51,3 мас.% аралығында өзгерсе, SiO_2 мөлшері 25,6–43,9 мас.% болды. Fe_2O_3 бойынша айырмашылық айтарлықтай үлкен емес (5,8–7,6 мас.%); CaO мен Al_2O_3 мөлшері де жалпы төмен. Бұл қатарда U-4K үлгісінің құрамы өзгеше: Cr_2O_3 мөлшері 25,1 мас.%-ға жетеді. Кейінгі XRD нәтижелері бұл ерекшеліктің үлгідегі магнезиохромиттің жоғары мөлшерімен байланысты екенін көрсетті.

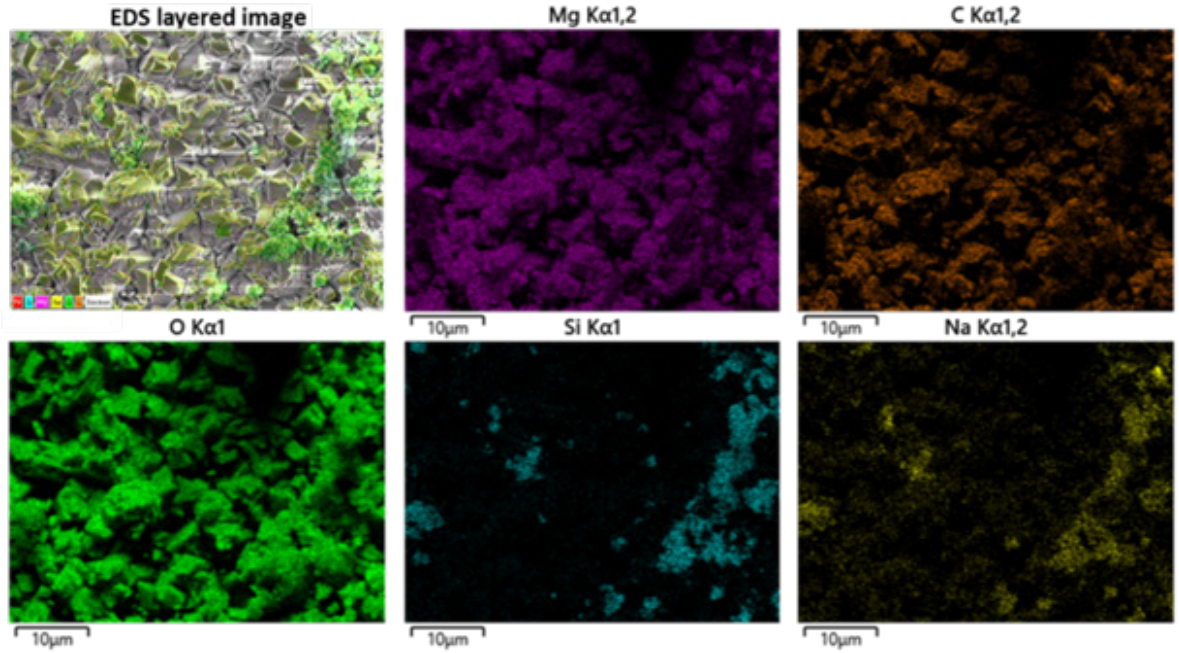
Шар офиолиттік тігісінің ультранегізді U-1C және U-2C үлгілерінде MgO мөлшері бір-біріне жақын, тиісінше 36,5 және 36,7 мас.%. SiO_2 мөлшері де үлкен айырмашылық көрсетпейді (39,3–40,2 мас.%). Кемпірсай үлгілерімен салыстырғанда Fe_2O_3 жоғарырақ және 8,4–10,7 мас.% аралығында өзгереді. M-1C және M-2C негізді үлгілерінің құрамы басқа: SiO_2 50,6–55,3 мас.%-ға дейін жоғарылайды, ал MgO 19,3–29,8 мас.% құрайды. M-1C үлгісіндегі CaO мөлшерінің 11,09 мас.% болуы да оны қалған үлгілерден ажыратады.

XRD талдауы бұл химиялық айырмашылықтардың минералдық құрамда қалай көрінетінін анықтауға мүмкіндік берді. Кемпірсай үлгілеріндегі ең көп таралған минерал лизардит, оның мөлшері 59,5 пен 83,7% аралығында. Хризотил мен брусит аз мөлшерде кездеседі. U-4K үлгісінде магнезиохромит жалпы құрамның 50,7%-ын, ал лизардит 39,1%-ын құрайды. Шардың U-1C және U-2C ультранегізді үлгілерінде лизардит мөлшері жоғары, 91,5 пен 97,2 мас.% аралығында. Мұндай құрам жыныстардың жоғары дәрежеде серпентинденгенін көрсетеді. Негізді үлгілер өзара да бірдей емес. M-1C құрамында тремолит басым, ал M-2C үлгісінің 85,6 мас.%-ын лизардит құрайды және аз мөлшерде тридимит кездеседі. Сондықтан келесі тәжірибелердің нәтижелерін тек «негізді–ультранегізді» айырмашылығы бойынша емес, әр үлгінің нақты минералдық құрамымен бірге қарастырған дұрыс.

Кесте 1 – Зерттелген тау жыныстары үлгілерінің химиялық құрамы (мас.%)

Үлгі	MgO	SiO2	Fe2O3	Al2O3	CaO	Cr2O3	MnO	Co2O3	NiO	P_2O_5	SO3	Na2O	K2O	TiO2
U-1K	46.50	43.90	7.60	0.68	0.08	0.32	0.13	0.03	0.25	0.03	0.34	0.00	0.00	0.00
U-2K	50.00	42.10	5.81	0.34	0.51	0.41	0.10	0.03	0.36	0.03	0.24	0.00	0.00	0.00
U-3K	51.30	40.30	6.25	0.28	0.12	0.32	0.10	0.04	0.39	0.03	0.83	0.00	0.00	0.00
U-4K	38.30	25.60	5.83	3.15	0.41	25.10	0.83	0.04	0.22	0.04	0.31	0.00	0.00	0.00
U-1C	36.47	39.29	8.43	0.60	1.05	0.00	0.07	0.00	0.00	0.007	0.00	0.026	0.007	0.000
U-2C	36.69	40.16	10.69	0.29	0.13	0.00	0.06	0.00	0.00	0.004	0.00	0.033	0.005	0.006
M-1C	19.27	55.27	8.24	2.63	11.09	0.00	0.31	0.00	0.00	0.011	0.00	0.917	0.137	0.043
M-2C	29.79	50.60	8.01	0.33	0.31	0.00	0.18	0.00	0.00	0.005	0.00	0.031	0.012	0.001
Ескерту: Үлгі кодтары жыныс түрі мен алынған орнын білдіреді. U, ультранегізді; M, негізді; C, Шар офиолиттік тігісі; K, Кемпірсай массиві.														

Экспериментке дейін барлық үлгілердегі жалпы көміртек (ТС) мөлшері анықтау шегінен (<50 ppm) төмен болды. Сондықтан реакциядан кейінгі ТС мөлшерінің артуын тәжірибе барысында CO_2-нің минералдық формада байланысуымен байланыстыруға болады. Алайда бұл өзгеріс барлық үлгілерде бірдей болған жоқ.



Сурет 2 – Кемпірсай массивінен алынған реакциядан кейінгі ультранегізді UM1 үлгісінің SEM–EDS қабаттасқан кескіні және Mg, C, O, Si мен Na элементтерінің таралу карталары. Жаңадан түзілген минералдық агрегаттарда Mg, C және O элементтерінің бірге шоғырлануы тәжірибелік CO_2 минералдануы барысында екінші реттік магнезиттің түзілгенін көрсетеді.

Кемпірсай жыныстарының ішінде ең жоғары ТС мөлшері U-1K үлгісінде анықталып, 1,56 мас.% құрады. U-2K және U-3K үлгілерінде бұл көрсеткіш тиісінше 1,01 және 0,64 мас.% болды. Ал магнезиохромит мөлшері жоғары U-4K үлгісінде ТС небәрі 0,27 мас.%-ға жетті. Яғни Кемпірсай үлгілерінің өзінде карбонаттану дәрежесі минералдық құрамға байланысты айтарлықтай өзгерді. Әсіресе лизардитке бай үлгілер мен магнезиохромит басым U-4K арасындағы айырмашылық анық байқалады.

Шар офиолиттік тігісінің үлгілерінде ТС мөлшерінің өсуі негізінен ультранегізді U-1C және U-2C жыныстарында ғана байқалды. Реакциядан кейін олардың ТС мөлшері сәйкесінше 0,45 және 0,56 мас.% болды. Негізгі үлгілерде тұрақты карбонаттардың түзілуі анықталған жоқ. Бұл бақылаулар XRD және SEM–EDS нәтижелерімен де расталды (2-сурет). ICP–OES нәтижелерін талдау кезінде байқалатын басты ерекшелік-жоғары карбонаттылығы бар үлгілерде реакциядан кейін ерітіндідегі Mg концентрациясы да жоғары болады. нәтижелерін талдағанда, басты байқалған ерекшелік ол карбонаттануы жоғары үлгілерде реакциядан кейінгі ерітіндіде Mg концентрациясының да жоғары болуы. Лизардит минералының еруін оның негізгі көзі ретінде қарастыруға болады.

H_2 түзілуі CO_2 минералдануы қарқынды жүретін үлгілермен сәйкес келмеді және оның түзілуі тек 160-200 °C емпературада жүргізілген тәжірибелерде ғана байқалды. H_2-нің ең жоғары мөлшері U-2C ультранегізді және M-1C негізді жыныстарында тіркелді (2-Кесте). Кемпірсай Массивінен алынған үлгілерде H_2 мүлде түзілмеді немесе өте аз мөлшерде анықталды. Осы нәтижелерге қарап, H_2 түзілуін тек литологиялық тау жыныстарымен байланыстыруға болмайды. ICP–OES нәтижелері бойынша реакциядан кейінгі ерітінділер құрамындағы Fe концентрациясы H_2 түзілуіне тікелей байланысты.

Кесте 2 – Газдық карбонаттандыру тәжірибелері нәтижесінде алынған газ өнімдерінің мольдік құрамы (мол.%)

Үлгі	CO2	H2	N2
U-1C	99.779	0.221	n.d.
U-2C	98.788	0.872	0.034
M-1C	99.279	0.721	n.d.
M-2C	99.770	0.219	0.011
U-1K	99.989	0.011	n.d.
U-2K	99.989	0.011	n.d.
U-3K	98.876	n.d.	1.124
U-4K	99.880	n.d.	0.120

Жыныстардың CO_2 минералдануы мен H_2 түзілуі әрдайым олардың литологиялық тобына сәйкес өзгерген жоқ. Бір топқа енгізілген үлгілердің өзінде реакциялық белсенділік әр түрлі болды. Мұнымен қоса, негізді M-1C үлгісінде H_2 мөлшерінің жоғары болуы бұл процестің ультранегізді жыныстармен ғана шектелмейтінін байқатады. Жалпы зерттелген офиолиттік кешендердің CO_2 газын минералдандыру және H_2 түзу қабілеті жоғары және мұндай бағыттарда қолдану үшін әр жыныстың минералдық құрамын жеке қарастыру қажет.

Қорытынды

Бұл жұмыста Шар офиолиттік тігісі мен Кемпірсай массивінен алынған негізді және ультранегізді тау жыныстарының CO_2 газын минералдандыру және H_2 түзу қабілеттері зерттелді. CO_2 газын минералдандыру қарқыны Кемпірсай массивінен алынған серпентинге бай ультранегізді үлгілерде ерекше. Зерттеуден кейінгі жалпы көміртек мөлшері мұндай үлгілерде 1,56 мас.%-ға дейін жетеді. Ал магнезиохромит минералының мөлшері жоғары болған үлгілерде жалпы көміртек мөлшері 0,27 мас.% ғана құрады. Шар үлгілерінің ішінде карбонаттану лизардит минералына бай ультранегізді жыныстарда ғана байқалды. H_2 түзілуінің ең жоғары мөлшері Шар аймағының U-2C ультранегізді үлгісінде (0,872 мол.%) және M-1C негізді үлгісінде (0,721 мол.%) байқалды. Кемпірсай массивінен алынған үлгілердің кейбірінде ғана өте аз мөлшерде H_2 тіркелді. Кейбір негізді жыныстарда H_2 мөлшерінің жоғары болуы бұл процестің ультранегізді жыныстармен ғана шектелмейтінін байқатады. Зерттеу нәтижелері Қазақстандағы офиолиттік кешендердің CO_2 газын минералдандыру және H_2 түзу қабілеті жоғары екенін және мұндай бағыттарда қолдану үшін әр жыныстың минералдық құрамын жеке қарастыру қажеттілігін айқындады.

Қаржыландыру туралы ақпарат

Зерттеу AP26102813 жобасы аясында Қазақстан Республикасының Ғылым және жоғары білім министрлігі Ғылым комитетінің қаржыландыруымен жүргізілді.

ӘДЕБИЕТТЕР

1 Matter, J.M., and Kelemen, P.B. Permanent storage of carbon dioxide in geological reservoirs by mineral carbonation. Nature Geoscience, 2 (12), 837–841 (2009). https://doi.org/10.1038/ngeo683

2 Oelkers, E.H., Gislason, S.R., and Matter, J. Mineral carbonation of CO2. Elements, 4 (5), 333–337 (2008). https://doi.org/10.2113/gselements.4.5.333

3 Osselin, F., Pichavant, M., Champallier, R., Ulrich, M., and Raimbourg, H. Reactive transport experiments of coupled carbonation and serpentinization in a natural serpentinite: Implication for hydrogen

production and carbon geological storage. Geochimica et Cosmochimica Acta, 318, 165–189 (2022). https://doi.org/10.1016/j.gca.2021.11.039

4 Godard, M., Gouze, P., Pascale, B., Martinez, I., Escario, S., Decrausaz, T., Leprovost, R., Roubinet, D., and Pézard, P. In Situ CO2 Mineralization in Mantle-Derived Ultramafic Basements: Insights from Laboratory Experiments and Field Studies (Oman Ophiolite). SSRN Electronic Journal (2022). https://doi.org/10.2139/ssrn.4285227

5 Kularatne, K., Sissmann, O., Kohler, E., Chardin, M., Noirez, S., and Martinez, I. Simultaneous ex-situ CO2 mineral sequestration and hydrogen production from olivine-bearing mine tailings. Applied Geochemistry, 95, 195–205 (2018). https://doi.org/10.1016/j.apgeochem.2018.05.020

6 Gislason, S.R., Wolff-Boenisch, D., Stefansson, A., Oelkers, E.H., Gunnlaugsson, E., Sigurdardottir, H., Sigfusson, B., Broecker, W.S., Matter, J.M., and Stute, M. Mineral sequestration of carbon dioxide in basalt: A pre-injection overview of the CarbFix project. International Journal of Greenhouse Gas Control, 4 (3), 537–545 (2010). https://doi.org/10.1016/j.ijggc.2009.11.013

7 Gíslason, S.R., Sigurdardóttir, H., Aradóttir, E.S., and Oelkers, E.H. A brief history of CarbFix: Challenges and victories of the project's pilot phase. Energy Procedia, 146, 103–114 (2018). https://doi.org/10.1016/j.egypro.2018.07.014

8 McCollom, T.M., and Bach, W. Thermodynamic constraints on hydrogen generation during serpentinization of ultramafic rocks. Geochimica et Cosmochimica Acta, 73 (3), 856–875 (2009). https://doi.org/10.1016/j.gca.2008.10.032

9 Gadikota, G. Multiphase carbon mineralization for the reactive separation of CO2 and directed synthesis of H2. Nature Reviews Chemistry, 4 (2), 78–89 (2020). https://doi.org/10.1038/s41570-019-0158-3

10 Klein, F., Bach, W., and McCollom, T.M. Compositional controls on hydrogen generation during serpentinization of ultramafic rocks. Lithos, 178, 55–69 (2013). https://doi.org/10.1016/j.lithos.2013.03.008

11 Ely, T., Leong, J., Canovas, P., and Shock, E. Huge variation in H2 generation during seawater alteration of ultramafic rocks. Geochemistry, Geophysics, Geosystems, 24 (3), e2022GC010658 (2023). https://doi.org/10.1029/2022GC010658

12 Wang, J., Watanabe, N., Okamoto, A., Nakamura, K., and Komai, T. Enhanced hydrogen production with carbon storage by olivine alteration in CO2-rich hydrothermal environments. Journal of CO2 Utilization, 30, 205–213 (2019). https://doi.org/10.1016/j.jcou.2019.02.008

13 Miller, H.M., Mayhew, L.E., Ellison, E.T., Kelemen, P., Kubo, M., and Templeton, A.S. Low temperature hydrogen production during experimental hydration of partially serpentinized dunite. Geochimica et Cosmochimica Acta, 209, 161–183 (2017). https://doi.org/10.1016/j.gca.2017.04.022

14 McCollom, T.M., Klein, F., and Ramba, M. Hydrogen generation from serpentinization of iron-rich olivine on Mars, icy moons, and other planetary bodies. Icarus, 372, 114754 (2022). https://doi.org/10.1016/j.icarus.2021.114754

15 Ueda, H., Sawaki, Y., and Maruyama, S. Reactions between olivine and CO2-rich seawater at 300°C: Implications for H2 generation and CO2 sequestration on the early Earth. Geoscience Frontiers, 8 (2), 387–396 (2017). https://doi.org/10.1016/j.gsf.2016.10.002

16 Smith, N., Shepherd, T., Styles, M., and Williams, G. Hydrogen exploration: A review of global hydrogen accumulations and implications for prospective areas in NW Europe. Geological Society, London, Petroleum Geology Conference Series, 6 (1), 349–358 (2005). https://doi.org/10.1144/0060349

17 Neal, C., and Stanger, G. Hydrogen generation from mantle source rocks in Oman. Earth and Planetary Science Letters, 66, 315–320 (1983). https://doi.org/10.1016/0012-821X(83)90144-9

18 Osselin, F. Experimental study of the co-valorization of carbon dioxide storage through hydrogen production in ultramafic formations. American Geophysical Union Fall Meeting Abstracts, GC31E-1297 (2022). https://doi.org/10.1002/essoar.10501775.1

19 Khandoozi, S., Hazlett, R., and Fustic, M. A critical review of CO2 mineral trapping in sedimentary reservoirs—from theory to application: Pertinent parameters, acceleration methods and evaluation workflow. Earth-Science Reviews, 244, 104515 (2023). https://doi.org/10.1016/j.earscirev.2023.104515

20 Klein, F., and McCollom, T.M. From serpentinization to carbonation: New insights from a CO2 injection experiment. Earth and Planetary Science Letters, 379, 137–145 (2013). https://doi.org/10.1016/j.epsl.2013.08.017

21 Neubeck, A., Nguyen, D.T., and Etiope, G. Low-temperature dunite hydration: Evaluating CH4 and H2 production from H2O and CO2. Geofluids, 16 (3), 408–420 (2016). https://doi.org/10.1111/gfl.12159

22 Melcher, F., Grum, W., Simon, G., Thalhammer, T.V., and Stumpfl, E.F. Petrogenesis of the ophiolitic giant chromite deposits of Kempirsai, Kazakhstan: A study of solid and fluid inclusions in chromite. Journal of Petrology, 38 (10), 1419–1458 (1997). https://doi.org/10.1093/petroj/38.10.1419

23 Zgonnik, V. The occurrence and geoscience of natural hydrogen: A comprehensive review. Earth-Science Reviews, 203, 103140 (2020). https://doi.org/10.1016/j.earscirev.2020.103140

24 Selyatitskii, A.Y., Reverdatto, V.V., Kuz'Min, D.V., and Sobolev, N.V. Minor elements in unusual olivines from high-pressure peridotites of the Kokchetav Massif (Northern Kazakhstan). Doklady Earth Sciences, 445 (2), 1015–1019 (2012). https://doi.org/10.1134/S1028334X12080235

25 Kuibida, M.L., Safonova, I.Y., Yermolov, P.V., Vladimirov, A.G., Kruk, N.N., and Yamamoto, S. Tonalites and plagiogranites of the Char suture-shear zone in East Kazakhstan: Implications for the Kazakhstan-Siberia collision. Geoscience Frontiers, 7 (1), 141–150 (2016). https://doi.org/10.1016/j.gsf.2015.09.002.

[1]Нурбекова Р.Н.,
PhD, ORCID ID: 0000-0001-7804-3949,
e-mail: riza.nurbekova@nu.edu.kz
[1]Хазлетт Р.,
PhD, профессор, ORCID ID: 0000-0003-2058-8406,
e-mail: randy.hazlett@nu.edu.kz
[1,2]Фустич М.,
PhD, ассоциированный профессор, ORCID ID: 0000-0001-9815-9279,
e-mail: milovan.fustic@nu.edu.kz
[1]Салаудин И.,
PhD, ORCID ID: 0009-0008-2015-8629,
e-mail: ibraheem.salaudeen@nu.edu.kz
[1]Кайратова А.,
Студент бакалавриата,
e-mail: a.kairatova@nu.edu.kz

[1]Школа горного дела и наук о Земле, Назарбаев Университет, г. Астана, Казахстан
[2]Департамент наук о Земле, Университет Калгари, г. Калгари, Канада

ИСПОЛЬЗОВАНИЕ УЛЬТРАОСНОВНЫХ ПОРОД ДЛЯ ПРОИЗВОДСТВА H_2 И СЕКВЕСТРАЦИИ CO_2: ПУТЬ К ЧИСТОЙ ЭНЕРГИИ И СНИЖЕНИЮ ВЫБРОСОВ В КАЗАХСТАНЕ

Аннотация

Переход к углеродно-нейтральной экономике требует не только долговременного геологического хранения антропогенного углекислого газа (CO_2), но и поиска новых низкоуглеродных источников энергии, к числу которых относится природный водород (H_2). Среди потенциальных геологических сред особое место занимают ультраосновные породы, поскольку они способны одновременно обеспечивать минерализацию CO_2 и образование природного H_2. Однако взаимосвязь этих процессов, а также возможность их проявления в основных породах до настоящего времени изучены недостаточно. В данной работе исследованы основные и ультраосновные породы Чарской офиолитовой зоны Восточного Казахстана и Кемпирсайского ультраосновного массива Западного Казахстана, чтобы оценить их потенциал к минерализации CO_2 и генерации природного H_2. Наиболее интенсивное связывание CO_2 наблюдалось в серпентинсодержащих ультраосновных породах. Растворение лизардита сопровождалось высвобождением Mg^{2+}, что создавало условия для образования вторичного магнезита и фиксации CO_2 в устойчивой минеральной форме. В образцах, обогащённых магнезиохромитом, карбонатизация протекала значительно слабее. Распределение природного H_2 оказалось иным. Максимальные концентрации зарегистрированы в ультраосновных (0,872 мол.%) и основных (0,721 мол.%) породах Чарской офиолитовой зоны, тогда как в образцах Кемпирсайского массива выявлены лишь следовые количества H_2. Сопоставление экспериментальных данных показало, что минерализация CO_2 и образование природного H_2 контролируются разными минералогическими факторами. Для долговременного связывания CO_2 наиболее благоприятны серпентинсодержащие ультраосновные породы, тогда

как генерация природного H_2 определяется прежде всего реакционной способностью Fe-содержащих минералов. Это объясняет высокие концентрации H_2 в отдельных образцах Чарской офиолитовой зоны при сравнительно низких значениях в породах Кемпирсайского массива. Офиолитовые комплексы Казахстана могут рассматриваться как перспективные геологические объекты как для долговременного минералогического хранения CO_2, так и для дальнейших поисков природного водорода.

Ключевые слова: ультраосновные породы, серпентинизация, водород, углекислый газ, минерализация CO_2.

[1]Nurbekova R.N.,
PhD, ORCID ID: 0000-0001-7804-3949,
e-mail: riza.nurbekova@nu.edu.kz
[1]Hazlett R.D.,
PhD, professor, ORCID ID: 0000-0003-2058-8406,
e-mail: randy.hazlett@nu.edu.kz
[1,2]Fustic M.,
PhD, associate professor, ORCID ID: 0000-0001-9815-9279,
e-mail: milovan.fustic@nu.edu.kz
Salaudeen, I.,
PhD, ORCID ID: 0009-0008-2015-8629,
e-mail: ibraheem.salaudeen@nu.edu.kz
[1]Kairatova A.
Bachelor's student,
e-mail: a.kairatova@nu.edu.kz

[1]School of Mining and Geosciences, Nazarbayev University, Astana, Kazakhstan
[2]Department of Geosciences, University of Calgary, Calgary, Canada

UTILIZING ULTRAMAFIC ROCKS FOR H_2 PRODUCTION AND CO_2 SEQUESTRATION: A PATHWAY TO CLEAN ENERGY AND EMISSIONS REDUCTION IN KAZAKHSTAN

Abstract

Permanent geological storage of anthropogenic CO_2 and the development of low-carbon energy resources, including natural hydrogen (H_2), have become two key components of carbon-neutrality strategies. Ultramafic rocks are increasingly recognized as promising geological media because they can support both mineral carbonation and natural H_2 generation. However, the relationship between these processes, and the extent to which similar reactions occur in mafic rocks, remain poorly understood. Mafic and ultramafic rocks from the Charsk Ophiolite (eastern Kazakhstan) and the Kempirsai Ultramafic Massif (western Kazakhstan) were investigated under experimental conditions to evaluate their potential for CO_2 mineralization and natural H_2 generation. Serpentine-rich ultramafic rocks displayed the highest carbonation potential. Dissolution of lizardite released Mg^{2+} ions that promoted secondary magnesite precipitation and efficient mineral trapping of CO_2. Carbonation was substantially weaker in magnesiochromite-rich ultramafic rocks. Natural H_2 generation followed a different pattern. The highest H_2 concentrations were measured in ultramafic (0.872 mol%) and mafic (0.721 mol%) rocks from the Charsk Ophiolite, whereas only trace amounts were detected in samples from the Kempirsai Massif. CO_2 mineralization and natural H_2 generation were controlled by different mineralogical factors. Serpentine-rich ultramafic rocks were most favorable for long-term CO_2 immobilization through mineral carbonation, whereas Fe-bearing mafic and ultramafic rocks with high reaction potential were more favorable for natural H_2 generation. Kazakhstan's ophiolitic complexes therefore represent promising geological targets for both permanent CO_2 storage and natural hydrogen exploration.

Keywords: ultramafic rocks, serpentinization, hydrogen, carbon dioxide, mineral carbonation.

Received August 18, 2026; accepted August 21, 2026

UDC 622.276.6
IRSTI 52.47.19

https://doi.org/10.55452/1998-6688-2026-23-3-573-587

[1*]Niyazbayeva A.B.,
Doctoral Student, ORCID ID: 0009-0001-4586-7578,
*e-mail: n.aynur22@aogu.edu.kz
[2]Ismail M. Saaid,
PhD, Associate Professor, ORCID ID: 0000-0003-0747-2724,
e-mail: ismailsaaid@utp.edu.my

[1]Atyrau University of Oil and Gas named after Safi Utebayev, Atyrau, Kazakhstan
[2]Universiti Teknologi PETRONAS, Seri Iskandar, Malaysia

RESERVOIR PERFORMANCE SIMULATION AND PROCESS-TO-SIMULATOR QUALITY CONTROL TO SUPPORT EOR METHOD SELECTION IN CARBONATE-CONTAINING RESERVOIRS

Abstract

Enhanced oil recovery (EOR) selection requires reservoir performance simulation that reproduces not only production trends but also the physical mechanisms controlling pressure, fluid behavior, multiphase flow, gas mobility, well constraints, and long-term reservoir response. This study presents a reservoir performance simulation and process-to-simulator quality-control workflow for CO_2-based EOR evaluation in anonymized carbonate-containing Field X, Kazakhstan. The field-scale simulation uses a three-dimensional ECLIPSE E300 compositional model with 93 × 88 × 78 grid cells, 194,413 active cells, and a 40-year forecast period. The framework integrates compositional pressure-volume-temperature/equation-of-state (PVT/EOS) behavior, minimum miscibility pressure (MMP), three-phase relative permeability, hysteresis, vertical connectivity and gravity override, injection scheduling, bottomhole-pressure (BHP) control, wellbore thermal response, CO_2 tracking, and mass-balance verification. Each mechanism is linked to a simulator functional block, diagnostic output, sensitivity test, and acceptance criterion. A representative ECLIPSE E300 process-to-code sequence – RUNSPEC, GRID, PROPS, SOLUTION, SCHEDULE, SUMMARY, followed by MATLAB post-processing – provides traceability from reservoir physics to forecast interpretation. Sensitivity analysis identifies vertical connectivity, gas relative permeability, MMP uncertainty, fault transmissibility, hysteresis, and BHP constraints as the principal controls on simulated reservoir performance. Continuous CO_2 injection increases cumulative oil production from 17.96 to 25.37 Mt, yielding 7.41 Mt of incremental oil (+41.3%); at year 40, the CO_2 case maintains 238.6 t/d while the Base case declines to zero. The results demonstrate that reservoir performance simulation provides a rigorous engineering basis for forecasting reservoir behavior, quantifying model sensitivity, validating physical consistency, and supporting defensible EOR method selection.

Keywords: CO_2-EOR; reservoir performance simulation; physical-process coding; EOR method selection; CO_2 mass balance; carbonate-containing reservoir.

Received June 19, 2026; revised July 29, 2026; accepted August 25, 2026.

Introduction

Carbon dioxide enhanced oil recovery (CO_2-EOR) differs from waterflooding and simplified gas-pressure-maintenance models because the injected component modifies phase behavior, oil composition, oil volume, viscosity, gas mobility, residual trapping and pressure-temperature response. Compositional modeling of pure and impure CO_2 demonstrates that fluid composition and phase-equilibrium representation directly affect both oil recovery and storage predictions [1, 2]. Consequently, a reliable forecast requires verification of the physical mechanisms represented by the simulator rather than a comparison of production curves alone.

Gas mobility is equally important. Water-alternating-gas (WAG) and related conformance-control strategies are sensitive to miscibility, gravity, heterogeneity, cycle design, relative permeability and hysteresis [3, 4, 5]. Alternative CO_2 delivery concepts, including microbubble injection, further emphasize that gas mobility and interfacial transport must be treated explicitly rather than embedded in a generic gas-injection assumption [14].

Pressure safety and wellbore behavior form a second control layer. CO_2 injection can generate significant pressure redistribution near faults and sealing units, and geomechanical studies therefore require the operating pressure to remain within defined integrity limits [6, 7]. Dense-phase CO_2 also undergoes strong pressure-temperature transients during well start-up; numerical wellbore studies show that the start-up schedule and pressure drop must be evaluated together with the temperature profile [8, 9].

The objective of this paper is to develop and quantitatively demonstrate a process-to-simulator quality-control workflow for CO_2 injection modeling and to show its representative process-to-code implementation at ECLIPSE E300 section level. Field X is the anonymized publication designation of the case study. The workflow requires each relevant physical mechanism to be connected to a simulator functional block, a diagnostic output, a sensitivity test and a pass/fail criterion. Within an EOR method-selection workflow, this framework is used to test whether the CO_2 option remains technically credible under process and implementation uncertainty. This structure separates uncertainty in the reservoir description from uncertainty created by model implementation. Geostatistical uncertainty concepts provide a compatible framework for this separation because multiple realizations and diagnostic statistics can be used to distinguish spatial variability from model-form uncertainty [10].

The scientific contribution is methodological rather than the proposal of a new constitutive law. The workflow makes the model auditable: the predicted incremental oil is considered credible only after thermodynamic behavior, flow functions, vertical segregation, operational controls and CO_2 accounting have passed defined quality-control checks. Reactive transport is not included in the executed calculation set and is not used to support the reported results; it is retained only as a future extension when mineral reactions or brine chemistry control injectivity [11,12].

Materials and methods

Field X numerical model and calculation layers

The publication dataset combines two connected calculation layers for Field X, the anonymized designation of the carbonate-containing complex reservoir interval used in the underlying modeling dataset. The first is the anonymized field-scale ECLIPSE E300 compositional model used for the direct Base-versus-CO_2 comparison. The second is a sector/process-diagnostic layer used to isolate the individual CO_2 mechanisms shown in Figures 3–9. Commercially sensitive coordinates, well identifiers and selected absolute PVT values are normalized for publication, while grid architecture, aggregated field-scale outputs, sensitivity ranges and process relationships are retained. The two layers are reported separately to prevent process-diagnostic pressure or rate values from being misinterpreted as full-field operating constraints.

Only the Base case and the continuous CO_2 case are claimed as explicit field-scale dynamic runs in this manuscript. WAG and surfactant-alternating-gas (SAG) appear as process-control schedule diagnostics and engineering follow-up options; they are not presented as additional full-field production forecasts. This distinction is maintained throughout the Results and Discussion section.

Process-to-simulator quality-control principle

The workflow consists of five sequential checks: (1) identify the physical mechanism; (2) assign the mechanism to a simulator functional block; (3) define the diagnostic output; (4) run a controlled sensitivity test; and (5) accept the forecast only when the diagnostic response is physically and numerically consistent. The sequence prevents the common error of interpreting incremental oil without confirming that the underlying CO_2 mechanism is represented in the model.

Table 1 – Main characteristics of Field X compositional modeling basis

Parameter	Reported value	Role in the study
Dynamic simulator	ECLIPSE E300, compositional mode	Explicit CO_2 component transport and phase behavior
Grid dimensions	93 × 88 × 78	Three-dimensional reservoir representation
Total cells	638,352	Geological discretization
Active cells	194,413	Cells participating in dynamic flow
Nominal cell size	100 × 100 × 1 m	Lateral and vertical numerical resolution
Field-scale forecast	40 years; yearly export	Base-versus-CO_2 long-term comparison
Explicit field-scale cases	Base case and CO_2 injection case	Quantitative production comparison
Process-diagnostic outputs	EOS/MMP, relperm/hysteresis, gravity override, schedule, thermal start-up, CO_2 balance, sensitivity	Mechanism-specific QC
MMP pressure-window reference	13.2 MPa	Regional laboratory reference used for below/near/above-MMP interpretation [13]

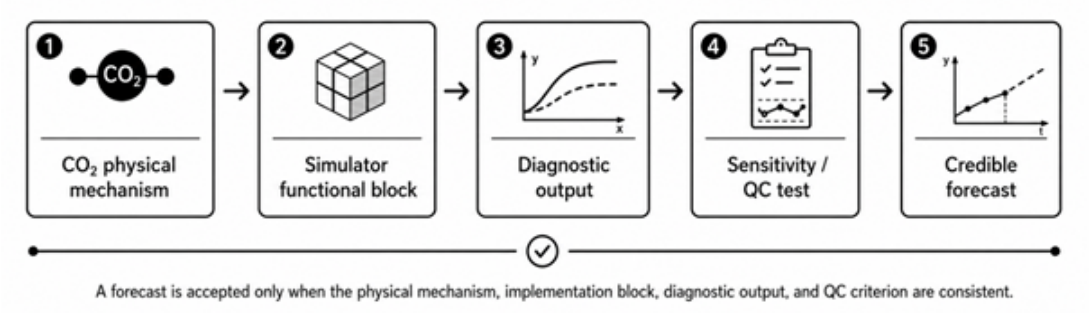


Figure 1 – Process-to-simulator quality-control workflow for CO_2 injection modeling

Table 2 – Physical-process checks used in the Field X process-to-simulator workflow

Physical process	Simulator functional block	Main input	Diagnostic / pass criterion
Phase behavior and miscibility	Compositional PVT / equation of state (EOS)	Components, binary interaction coefficients (BICs), MMP reference, viscosity and swelling response	MMP-pressure response is continuous and consistent with the adopted pressure window
Three-phase flow	Gas-oil-water relative permeability	Sgc, Sorg, krg/kro functions	No unrealistically mobile gas front; drainage endpoint and breakthrough response checked
Hysteresis and trapping	Drainage/imbibition history	Separate gas drainage and imbibition functions	Trapping changes gas mobility and retained CO_2 in the expected direction
Gravity override	Vertical permeability and grid connectivity	PERMZ, kv/kh, layering, density contrast	Vertical plume follows connectivity; grid refinement does not reverse the mechanism
Well operation	Schedule and pressure control	CO_2 composition, rate, BHP cap, WAG/SAG cycle	No rate-only pressure violation; switching logic is explicit

Continuation of Table 2

Physical process	Simulator functional block	Main input	Diagnostic / pass criterion
Thermal start-up	Wellbore thermal QC	Start-up time, rate, wellhead pressure, BHP, BHT	Minimum BHT remains above the internal thermal QC threshold
Pressure integrity screening	Pressure/fault-control layer	BHP cap, fault multiplier	Pressure response stays inside the specified operational envelope
CO_2 accounting	Component mass balance	Injected, produced, dissolved, trapped and mobile CO_2	Absolute mass-balance error <1%; reported cases close at 0%
Sensitivity ranking	Low/base/high sensitivity matrix	MMP, kv/kh, krg, hysteresis, fault, BHP, impurity, grid, ramp-up	Dominant response controls are quantified and traceable

Notation: BHP – bottomhole pressure; BHT – bottomhole temperature; GOR – gas–oil ratio; kv/kh – vertical-to-horizontal permeability ratio; krg and kro – gas and oil relative permeability, respectively; Sgc – critical gas saturation; Sorg – residual oil saturation to gas.

Simulator functional architecture

Generic labels such as MULT or LGR are not treated as universal simulator keywords. Instead, the implementation is organized by ECLIPSE-type deck sections and simulator-agnostic functional descriptions. Exact keyword syntax can vary by simulator version; therefore, Table 3 identifies the required function rather than implying that one abbreviation is universally valid.

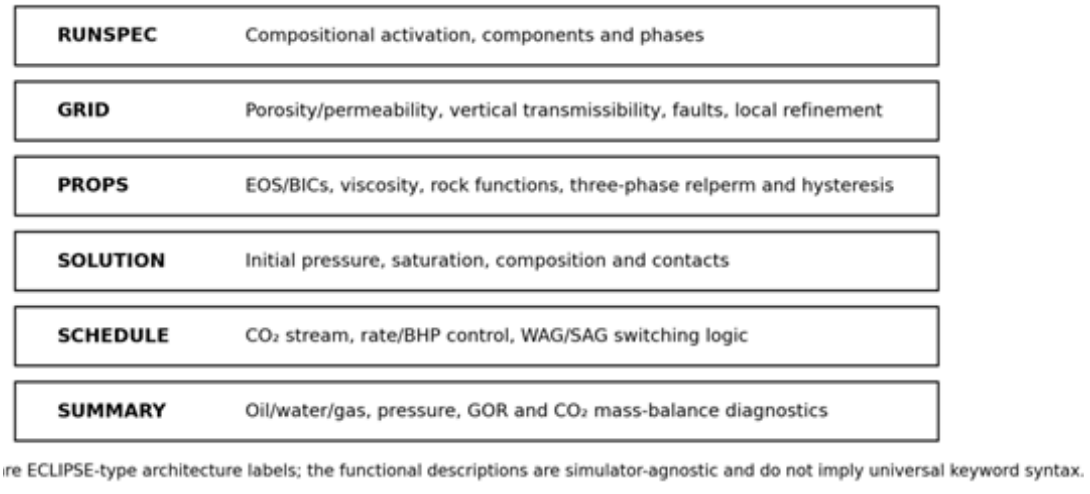


Figure 2 – Functional architecture for compositional CO_2 modeling.
Section names follow an ECLIPSE-type deck structure;
the implementation descriptions are simulator-agnostic

Table 3 – Functional implementation chain for the Field X CO_2 model

E300 section	Functional implementation	Physical process represented	QC output
RUNSPEC	Compositional activation; components and phases	Component tracking and phase behavior	Component/phase consistency
GRID	PORO, PERMX, PERMZ, transmissibility and grid-resolution controls	Heterogeneity and gravity segregation	CO_2 plume geometry

Continuation of Table 3

E300 section	Functional implementation	Physical process represented	QC output
PROPS	EOS/PVT, BIC, viscosity, three-phase relative permeability, hysteresis	Miscibility, swelling, viscosity reduction, gas mobility and trapping	MMP, viscosity, swelling, breakthrough behavior
SOLUTION	Initial pressure, saturation, composition and contacts	Initial thermodynamic state	Initialization consistency
SCHEDULE	CO_2 stream, rate/BHP limits, GOR constraint, WAG/SAG logic	Operational control	BHP, rate and GOR
SUMMARY	Pressure, production and CO_2 inventory outputs	Forecast diagnostics and carbon accounting	Mass-balance closure and retained CO_2

Representative ECLIPSE E300 implementation of the process-to-code workflow

To demonstrate how the proposed process-to-code concept is implemented at simulator level, the principal physical mechanisms are mapped to the corresponding functional sections of an ECLIPSE E300 compositional model. The example below is intentionally abbreviated and omits field-identifying and commercially sensitive parameters. It illustrates the implementation sequence rather than reproducing the complete Field X simulation deck. The essential requirement is that phase behavior, three-phase flow functions, hysteresis, injection composition, well constraints, and diagnostic output vectors are configured consistently before the predicted incremental oil is considered credible.

```
-- Representative ECLIPSE E300 process-to-code implementation
RUNSPEC
   COMPOSITIONAL MODEL
   Components and active phases
   CO2 explicitly represented as an injected component
GRID
   PORO / PERMX / PERMZ
   Vertical-connectivity and fault-transmissibility controls
   Local grid-resolution controls where required
PROPS
   EOS / compositional PVT definition
   Component critical properties and binary interaction coefficients
   Oil-density, viscosity and swelling calibration
   Three-phase gas-oil-water relative-permeability functions
   Drainage / imbibition functions for hysteresis and residual-gas trapping
SOLUTION
   Initial pressure
   Initial water, oil and gas saturations
   Initial fluid composition and fluid contacts
SCHEDULE
   CO2 injection-stream composition
   Injection-rate constraint
   BHP constraint
   Producer GOR constraint
   WAG/SAG switching logic where evaluated
```

SUMMARY
Reservoir pressure
Injector and producer BHP
Oil, water and gas production
GOR
Injected and produced CO2
Dissolved, trapped and mobile CO2 inventories
CO2 retention and mass-balance diagnostics
POST-PROCESSING
E300 diagnostic outputs
↓
MATLAB quality-control module
↓
MMP response / mobility ratio / gravity-override index /
CO2 mass-balance closure / sensitivity ranking

The implementation shown above establishes a direct traceability chain between reservoir physics and numerical representation. The EOS/PVT block controls the pressure-dependent CO_2–oil response around the adopted MMP reference; the three-phase relative-permeability and hysteresis functions control gas mobility and residual trapping; vertical permeability and transmissibility settings govern gravity override and interlayer communication; SCHEDULE controls define physically admissible injection conditions; and SUMMARY outputs provide the quantitative variables required for independent quality control. The MATLAB module therefore operates on simulator-derived diagnostics and does not replace the compositional reservoir model.

MATLAB diagnostic module and dimensional consistency

The MATLAB layer is a quality-control pre/post-processor and does not replace the compositional simulator. The minimum miscibility pressure is explicitly defined as MMP_MPa = 13.2. The logistic parameter transitionWidth_MPa = 0.7 MPa is a numerical transition-width parameter used only to map pressure difference to a continuous diagnostic miscibility index. It does not modify the physical MMP reference and is not used as a simulator calibration parameter. With this definition, the diagnostic index equals 0.269 at MMP – 0.7 MPa, 0.500 at MMP and 0.731 at MMP + 0.7 MPa. Physical MMP uncertainty is tested independently using the ±1 MPa sensitivity cases.

$MI = 1 / [1 + \exp(-(P - MMP) / \Delta P_{tr})]$, $MMP = 13.2$ MPa, $\Delta P_{tr} = 0.7$ MPa

The original overrideIndex combined kv/kh, density difference and gas viscosity and therefore carried dimensions. The algorithm first calculates the raw gravity-segregation proxy and then normalizes it to the Base diagnostic reference. The resulting overrideIndex is dimensionless: values above 1 indicate stronger gravity-segregation tendency than the Base reference, while values below 1 indicate weaker tendency.

$G_{raw} = (kv/kh) |\rho_o - \rho_{CO2}| / \mu_g$; overrideIndex = $G_{raw} / G_{raw,ref}$

CO_2 balance error is also normalized, so the quality-control criterion is expressed as a percentage of injected CO_2 rather than as an unscaled mass difference.

retainedCO2=injectedCO2–producedCO2; massError%=100×(retainedCO2–dissolvedCO2–trappedCO2 – mobileCO2) / injectedCO2

Algorithm 1 – MATLAB diagnostic logic for process-to-simulator quality control of the Field X CO_2 model

```
input = readtable('Xfield_co2_inputs.csv');
MMP_MPa = 13.2;
transitionWidth_MPa = 0.7;  % numerical QC smoothing width, not an MMP correction
dP_MPa = input.pressure_MPa – MMP_MPa;
MI = 1 ./ (1 + exp(-dP_MPa ./ transitionWidth_MPa));
mobilityRatio = (input.krg ./ max(input.kro,1e-6)) .* (input.mu_oil ./ max(input.mu_gas,1e-6));
overrideRaw = input.kvkh .* abs(input.rho_oil – input.rho_co2) ./ max(input.mu_gas,1e-6);
```

```
baseMask = strcmpi(input.caseID,'Base');
overrideRef = median(overrideRaw(baseMask),'omitnan');
overrideIndex = overrideRaw ./ max(overrideRef,1e-12);
retainedCO2_kt = input.injectedCO2_kt – input.producedCO2_kt;
massError_kt = retainedCO2_kt – input.dissolvedCO2_kt – input.trappedCO2_kt – input.
mobileCO2_kt;
massError_pct = 100 .* massError_kt ./ max(input.injectedCO2_kt,1e-9);
out = table(MI,mobilityRatio,overrideIndex,retainedCO2_kt,massError_pct);
writetable(out,'Xfield_qc.csv');
```

Quantitative sensitivity design

The analysis reports the numerical low/base/high ranges rather than qualitative sensitivity labels. The tested process-diagnostic ranges are MMP shift -1/0/+1 MPa; kv/kh = 0.02/0.08/0.16; krg endpoint = 0.45/0.65/0.85; hysteresis state = off/base/enhanced; fault multiplier = 0.1/1/5; BHP cap = 13.5/14.5/15.5 MPa; CO_2 impurity = 0/5/10%; grid refinement = coarse/base/refined; and thermal ramp-up = 0.5/2/6 h. These ranges are used to quantify both oil-response and CO_2-retention sensitivity.

Scope boundary for reactive transport and geomechanics

Reactive transport is not part of the executed Field X calculation set. It is therefore removed from the Abstract, the list of calculated outputs and the conclusions. It is discussed only as an extension criterion for carbonate-water-rock systems in which dissolution, precipitation or salinity changes control injectivity [11,12]. Likewise, the present study reports pressure-integrity screening through BHP limits, pressure response and fault-transmissibility sensitivity; it does not claim a fully coupled geomechanical solution. Coupled geomechanics remains a separate validation layer when fault slip or caprock stress is a project decision criterion [6,7].

Results and discussion

EOS/MMP diagnostic and oil-property response

The MMP pressure-window diagnostic uses 13.2 MPa as a regional laboratory reference for CO_2-oil interaction [13]. Figure 3 is a diagnostic pressure sweep, not a field pressure-history curve. Across the normalized sweep from 8 to 23 MPa, the miscibility index increases continuously from approximately 0.001 to 1.000. The normalized oil-swelling factor increases from 1.000 to 1.180, while the diagnostic oil viscosity decreases from 4.20 to approximately 2.44 cP. The shaded MMP ±0.7 MPa zone visualizes the numerical transition width used in Algorithm 1; the physically tested MMP uncertainty remains ±1 MPa and is reported independently in the sensitivity matrix.

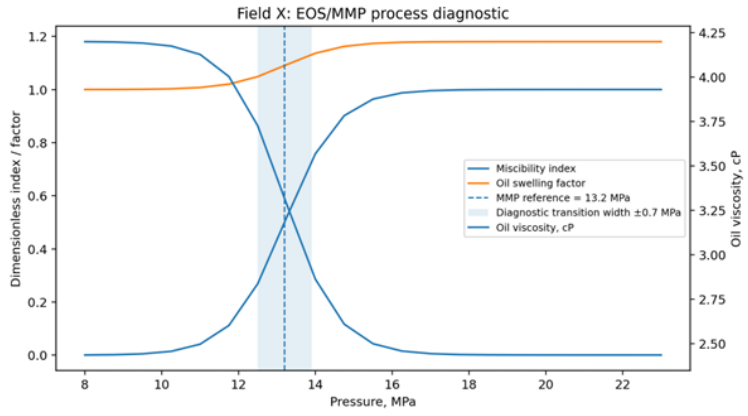


Figure 3 – EOS/MMP process diagnostic for Field X. The 0.7 MPa band is a numerical transition width used for quality-control visualization and does not modify the MMP reference

Three-phase gas relative permeability and hysteresis

The gas-flow input functions are reported explicitly as model-input curves rather than as direct special core analysis (SCAL) measurements. The drainage gas relative-permeability endpoint reaches 0.82, whereas the imbibition endpoint reaches 0.48. The separation between the drainage and imbibition curves creates a trapping envelope that limits gas remobilization during alternating injection. The krg endpoint sensitivity of 0.45/0.65/0.85 changes oil response by -16% and CO_2 retention by -20% relative to the Base diagnostic case, while enhanced hysteresis changes the corresponding responses by +9% and +24%. These values demonstrate that gas mobility and trapping are first-order numerical controls rather than secondary settings [3, 4, 5].

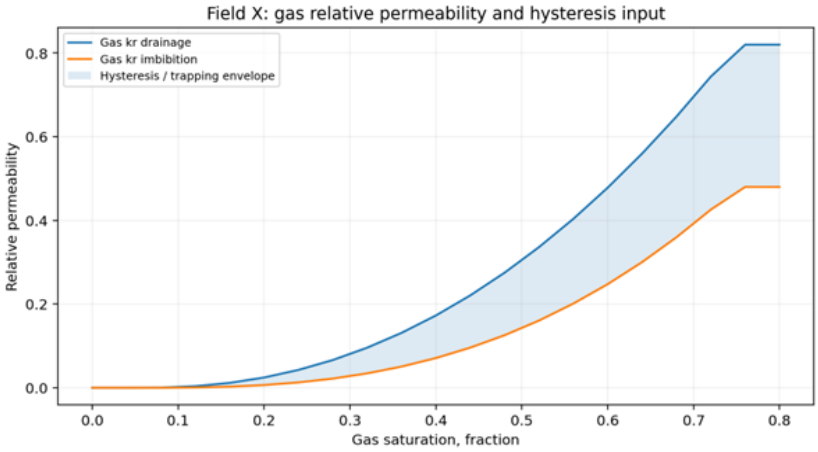


Figure 4 – Gas relative-permeability drainage/imbibition functions used for three-phase gas-oil-water flow and hysteresis diagnostics in Field X

Vertical permeability, grid resolution and gravity override

Figure 5 shows the calculated gas-saturation diagnostic along the injector-producer section. The highest normalized gas concentration occurs in the upper portion of the section, demonstrating the gravity-override tendency. The vertical-to-horizontal permeability ratio kv/kh is tested at 0.02, 0.08 and 0.16. Increasing vertical connectivity produces the largest adverse oil-response shift in the process sensitivity matrix (-18%) and reduces CO_2 retention by 12%. Local grid refinement produces a +5% oil-response shift and +9% retention shift, confirming that numerical dispersion and vertical discretization must be checked together rather than treated as independent post-processing details.

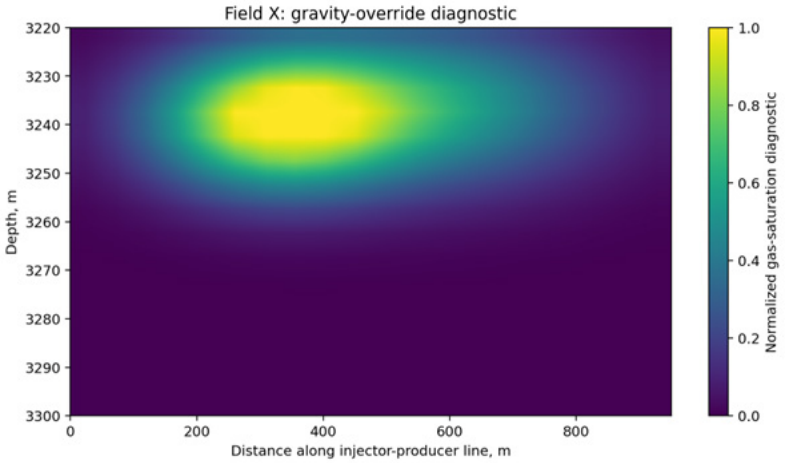


Figure 5 – Field X gravity-override diagnostic controlled by vertical connectivity, density contrast and grid resolution

WAG/SAG schedule logic and operational control

CO_2 injection is not represented solely by a constant gas-rate constraint. The pilot-scale schedule diagnostic alternates 10-day water/surfactant slugs at 2,200 m³/d with 20-day CO_2 slugs at 3,000 t/d over the 120-day screening window. The two streams are plotted on separate axes so that mass rate and volumetric rate are not combined. The schedule block is pressure-limited and is evaluated together with BHP and GOR constraints. The design is a process-control diagnostic; it is not presented as an additional full-field WAG/SAG production forecast. The role of cycle timing, gravity and permeability heterogeneity in WAG performance is consistent with published numerical studies [4, 5].

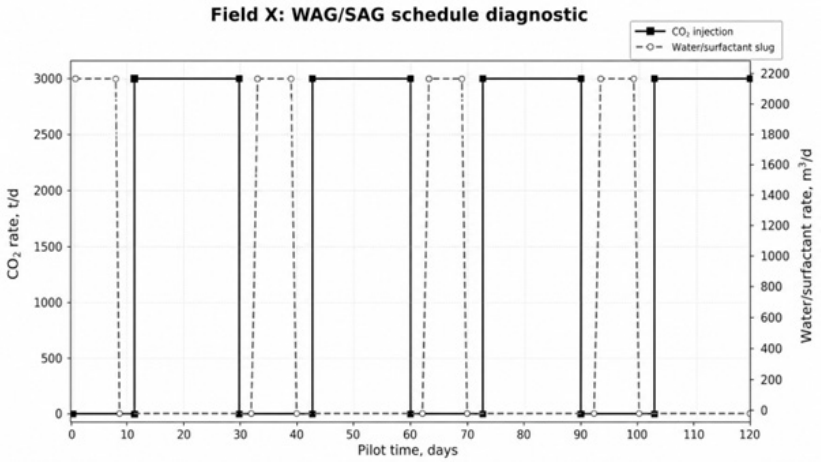


Figure 6 – Field X WAG/SAG schedule diagnostic with CO_2 mass rate and water/surfactant volumetric rate shown on separate axes

Wellbore thermal start-up

The start-up calculation ramps CO_2 rate from 0 to 2,980 t/d over 6 h. BHP rises from 12.5 to 15.2 MPa, while bottomhole temperature decreases from 70.0 °C to a minimum of 62.4 °C at approximately 1.2 h and then recovers to 68.9 °C by 6 h. The figure uses a 10 °C internal thermal QC threshold only as a conservative numerical flag for excessive cooling; it is not presented as a universal hydrate-equilibrium boundary. The calculated minimum BHT remains more than 52 °C above that QC line. This treatment resolves the thermal risk as a quantified start-up diagnostic rather than an undefined hydrate or integrity margin [8, 9].

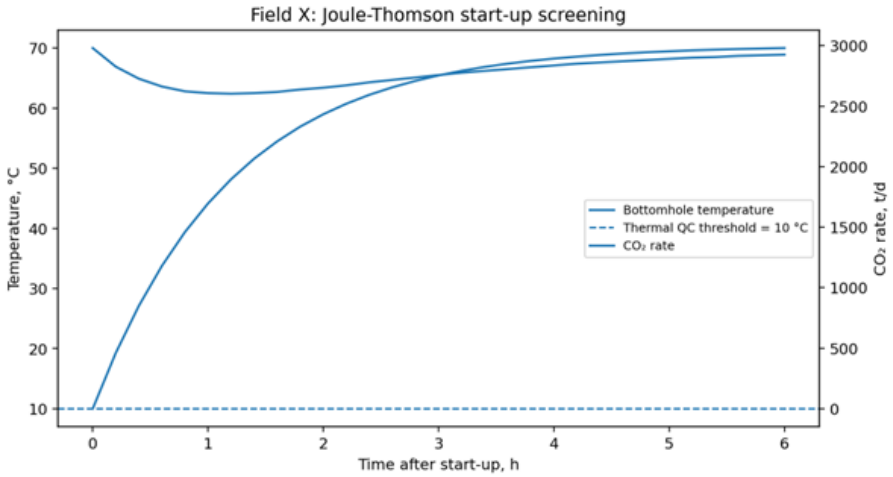


Figure 7 – Joule-Thomson start-up screening for Field X. Temperature is reported in °C and CO_2 rate in t/d on a separate axis

CO_2 retention balance and mass-balance closure

The CO_2 accounting table reconciles injected, produced, dissolved, residual-trapped and mobile CO_2 for every reported year. The retained fraction decreases from 0.875 in 2027 to 0.804 in 2037 as produced CO_2 increases, while the calculated mass-closure error remains exactly 0 kt in all reported cases. The MATLAB module also reports massError_pct and applies a <1% acceptance criterion. This makes carbon accounting a quantitative simulator QC requirement rather than a qualitative carbon capture, utilization and storage (CCUS) statement.

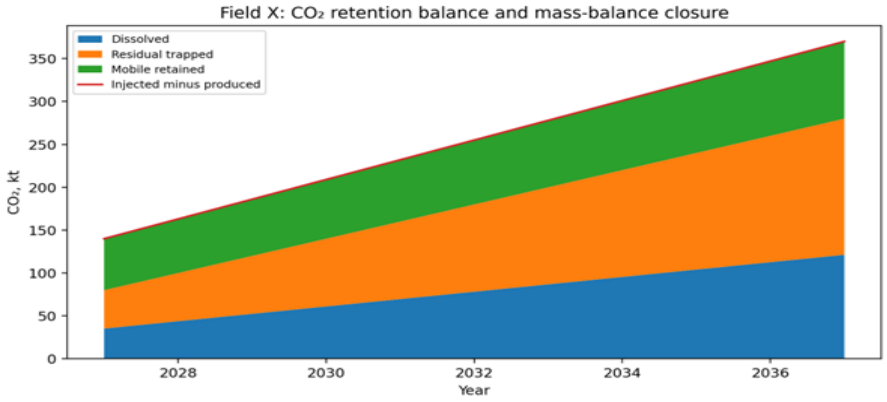


Figure 8 – Field X CO_2 retention balance. Dissolved, residual-trapped and mobile retained CO_2 sum exactly to injected minus produced CO_2 for the reported diagnostic cases

Quantitative sensitivity of process implementation

Figure 9 and Table 4 quantify the response to nine model-implementation assumptions. Across the tested envelope, the oil response ranges from -18% to +12%, and the CO_2-retention response ranges from -20% to +24%. The largest adverse oil changes are associated with kv/kh (-18%), krg endpoint (-16%) and MMP shift (-14%). The strongest positive retention response is produced by enhanced hysteresis trapping (+24%). Increasing the BHP cap produces a +12% oil-response shift but is retained as an operational sensitivity rather than an automatic optimization target because pressure integrity must be evaluated concurrently [6, 7].

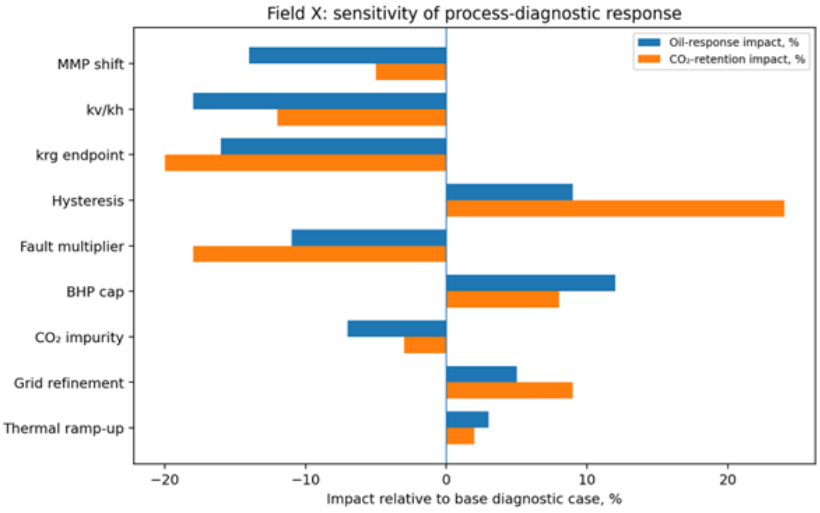


Figure 9 – Quantitative sensitivity of Field X oil response and CO_2 retention to process-diagnostic assumptions

Table 4 – Quantitative sensitivity matrix for Field X process diagnostics

Parameter	Low / Base / High	Oil impact, %	Retention impact, %	Primary block
MMP shift	-1 / 0 / +1 MPa	-14	-5	EOS/PVT
kv/kh	0.02 / 0.08 / 0.16	-18	-12	GRID / vertical flow
krg endpoint	0.45 / 0.65 / 0.85	-16	-20	Three-phase relperm
Hysteresis trapping	off / base / enhanced	+9	+24	Hysteresis
Fault multiplier	0.1 / 1 / 5	-11	-18	Fault connectivity
BHP cap	13.5 / 14.5 / 15.5 MPa	+12	+8	SCHEDULE
CO_2 impurity	0 / 5 / 10%	-7	-3	EOS/PVT
Grid refinement	coarse / base / refined	+5	+9	GRID
Thermal ramp-up	0.5 / 2 / 6 h	+3	+2	Thermal QC

Field-scale production response

The field-scale E300 model provides an independent quantitative check that the process diagnostics correspond to a material production response. Over the 40-year forecast, cumulative oil increases from 17.96 Mt in the Base case to 25.37 Mt in the CO_2 case, giving 7.41 Mt of incremental oil and a 41.3% relative increase. At year 40, the Base oil rate is 0 t/d, while the CO_2 case retains 238.6 t/d. Average reservoir pressure is 22.98 MPa in the Base case and 23.11 MPa in the CO_2 case. Cumulative CO_2 injection reaches 15.67 billion m^3, corresponding to approximately 2,115 m^3 CO_2 per tonne of incremental oil. These values are the explicit field-scale results; WAG/SAG and foam remain engineering mobility-control options rather than additional full-field forecast claims.

Table 5 – Explicit field-scale Base-versus-CO_2 results for Field X

Indicator	Base case	CO_2 case	Difference / interpretation
Cumulative oil, Mt	17.96	25.37	+7.41 Mt (+41.3%)
Oil rate at year 40, t/d	0.0	238.6	Late-life production sustained by CO_2 case
Average reservoir pressure at year 40, MPa	22.98	23.11	Pressure-support contribution
Cumulative CO_2 injection, billion m^3	-	15.67	Field-scale injection volume
Specific CO_2 injection, m^3/t incremental oil	-	2,115	Gas-utilization engineering indicator
Cumulative water production, thousand t	55.1	80.0	Higher water handling reflects extended production period

Integrated interpretation

The results establish a two-level acceptance logic. At the process level, the model must pass EOS/MMP, three-phase flow, hysteresis, vertical segregation, operational, thermal and carbon-accounting checks. At the field level, the accepted CO_2 model must produce a material and operationally interpretable response. This separation prevents a positive production curve from being accepted when it is generated by an overly mobile gas function, excessive vertical transmissibility, an undefined MMP transition or incomplete CO_2 accounting. The approach therefore converts the earlier qualitative checklist into a reproducible process-to-simulator quality-control framework with an explicit, auditable process-to-code implementation layer.

Conclusions

1. CO_2-EOR for Field X is represented as a compositional, multiphysics modeling problem rather than a simple additional gas-injection stream. The workflow connects each physical mechanism to a simulator functional block, a diagnostic output, a quantitative sensitivity test and an acceptance

criterion. A representative ECLIPSE E300 implementation chain (RUNSPEC-GRID-PROPS-SOLUTION-SCHEDULE-SUMMARY-MATLAB post-processing) makes the physical-process coding concept explicit without claiming disclosure of the complete confidential Field X deck.

2. The underlying field-scale model is explicitly documented: ECLIPSE E300 compositional mode, 93 × 88 × 78 cells, 638,352 total cells, 194,413 active cells, nominal 100 × 100 × 1 m resolution and a 40-year forecast. Only the Base and continuous CO_2 cases are claimed as explicit field-scale dynamic runs.

3. The MMP reference is 13.2 MPa. The 0.7 MPa term is defined as a numerical logistic transition width used only in the MATLAB QC diagnostic; it does not modify MMP. Physical MMP uncertainty is independently tested at ±1 MPa.

4. The gravity-override indicator is dimensionless because the raw segregation proxy is normalized to the Base diagnostic reference. The CO_2 accounting is also normalized, and the reported diagnostic cases have zero mass-closure error.

5. Quantitative sensitivities identify kv/kh (-18% oil response), krg endpoint (-16%), MMP shift (-14%), fault multiplier (-11%), BHP cap (+12%) and hysteresis (+9% oil; +24% retention) as the principal process controls. The total tested range is -18% to +12% for oil response and -20% to +24% for CO_2 retention.

6. At field scale, continuous CO_2 injection increases cumulative oil from 17.96 to 25.37 Mt, providing 7.41 Mt of incremental oil (+41.3%) and maintaining 238.6 t/d at year 40 compared with zero in the Base case. This field-scale response is supported by the process-level QC workflow rather than interpreted independently of it.

7. Reactive transport is not claimed as an executed result. It is retained only as a future extension when mineral or brine reactions become an injectivity-control mechanism. Pressure-integrity screening is reported without claiming a fully coupled geomechanical solution.

Funding information
No external funding was received for this study.

Conflict of interest
The authors declare no conflict of interest.

Data availability
The numerical tables underlying Figures 3–9 and the aggregated Field X results are available from the corresponding author upon reasonable request. Field identifiers, coordinates and commercially sensitive reservoir data are anonymized.

Author Contributions
A.B. Niyazbayeva developed the conceptual framework, process-to-simulator quality-control workflow, Field X sector-case interpretation, MATLAB diagnostic module, quantitative sensitivity analysis, visualization package, and original manuscript.

I.M. Saaid contributed to scientific supervision, validation of the interpretations, and critical review and editing of the manuscript, including scientific revisions and additions made in response to the reviewers' comments. All authors have read and approved the final version of the manuscript.

REFERENCES

1 Lee, H.-S.; Cho, J.; Lee, Y.-W.; Lee, K.-S. Compositional Modeling of Impure CO_2 Injection for Enhanced Oil Recovery and CO_2 Storage. Applied Sciences 2021, 11(17), 7907. https://doi.org/10.3390/app11177907.

2 Song, Y.; Song, Z.; Chen, Z.; Mo, Y.; Zhou, Q.; Tian, S. Simulation of CO_2 enhanced oil recovery and storage in shale oil reservoirs: Unveiling the impacts of nano-confinement and oil composition. Advances in Geo-Energy Research 2024, 13(2), 106–118. https://doi.org/10.46690/ager.2024.08.05.

3 Sharma, M. CO_2 Mobility Control with Foam for Enhanced Oil Recovery and Associated Storage: Multi-scale Approach for Field Application. PhD thesis, University of Stavanger, 2019.

4 Khan, M.Y. Mathematical model and its solution for water-alternating-gas (WAG) injection process incorporating the effect of miscibility, gravity, viscous fingering and permeability heterogeneity. Journal of Petroleum Exploration and Production Technology 2024, 14(12), 3183–3211. https://doi.org/10.1007/s13202-024-01884-7.

5 Luo, Q.; Li, Y.; Sun, H.; Liu, S.; Yu, Y.; Yang, Z. Research on CO_2-WAG in Thick Reservoirs: Geological Influencing Factors and Random Forest Importance Evaluation. ACS Omega 2024, 9(31), 34118–34127. https://doi.org/10.1021/acsomega.4c04901.

6 Chiaramonte, L. Geomechanical Characterization and Reservoir Simulation of a CO_2 Sequestration Project in a Mature Oil Field, Teapot Dome, WY. PhD dissertation, Stanford University, 2008.

7 Ruciński, P. Geomechanical Integrity of Offshore Oil Reservoir During EOR-CO_2 Process: A Case Study. Energies 2025, 18(21), 5751. https://doi.org/10.3390/en18215751.

8 Samuel, R.J. Transient Flow Modelling of Carbon Dioxide Injection into Depleted Gas Fields. PhD thesis, University College London, 2019.

9 Zhang, Y.; Huang, X.; Jiang, L.; Song, Y. Numerical Simulation of Heat Transfer Characteristics of CO_2 Gas Mixture Injection into Wellbores. Energy & Fuels 2024, 38(21), 21065–21078. https://doi.org/10.1021/acs.energyfuels.4c04202.

10 Popova, O.H. Development of Geostatistical Models to Estimate CO_2 Storage Resource in Sedimentary Geologic Formations. PhD thesis, Carnegie Mellon University, 2014.

11 Farshidi, S.F. Compositional Reservoir Simulation-Based Reactive-Transport Formulations, with Application to CO_2 Storage in Sandstone and Ultramafic Formations. PhD thesis, Stanford University, 2016.

12 Niu, B. CO_2 Flooding in Chalk Reservoirs: Experiments with X-Ray Computed Tomography and Reactive Transport Modelling. PhD thesis, Technical University of Denmark, 2010.

13 Niyazbayeva, A.B.; Merbayev, R.B.; Samenov, Y.R.; Zholdybayeva, A.T.; Kozhagulova, A.A.; Shabdirova, A.D. Laboratory Investigation of Miscible CO_2-Induced Enhanced Oil Recovery from the East-Southern Pre-Caspian Region. Processes 2025, 13, 2566. https://doi.org/10.3390/pr13082566.

14 Nam, L.N.H. Study on Enhanced Oil Recovery by CO_2 Microbubbles Injection. PhD dissertation, Kyushu University, 2022.

[1]*Ниязбаева А.Б.,
докторант, ORCID ID: 0009-0001-4586-7578,
*e-mail: n.aynur22@aogu.edu.kz
[2]Исмаил М. Сааид,
PhD, қауымдастырылған профессор, ORCID ID: 0000-0003-0747-2724,
e-mail: ismailsaaid@utp.edu.my

[1]Сафи Өтебаев атындағы Атырау мұнай және газ университеті, Атырау қ., Қазақстан
[2]PETRONAS технологиялық университеті, Сери-Искандар қ., Малайзия

КАРБОНАТҚҰРАМДЫ КОЛЛЕКТОРЛАРДА МҰНАЙ БЕРГІШТІКТІ АРТТЫРУ ӘДІСІН ТАҢДАУДЫ НЕГІЗДЕУ ҮШІН ҚАБАТТЫҢ ИГЕРІЛУ КӨРСЕТКІШТЕРІН МОДЕЛЬДЕУ ЖӘНЕ ТЕХНОЛОГИЯЛЫҚ ПРОЦЕСТІ СИМУЛЯТОРҒА КӨШІРУ САПАСЫН БАҚЫЛАУ

Аңдатпа

Мұнай бергіштікті арттыру әдістерін сенімді таңдау өндіру динамикасымен қатар, қысымның өзгеруін, флюидтердің қасиеттерін, көпфазалы ағынды, газдың қозғалғыштығын, ұңғымаларды пайдалану шектеулерін және қабаттың ұзақ мерзімді реакциясын сипаттайтын кешенді модельдеуді талап етеді. Бұл

жұмыста Қазақстандағы анонимдендірілген карбонатты Х кен орнының мысалында CO_2 айдауға негізделген мұнай бергіштікті арттыру (МБА) әдістерін бағалау үшін қабаттың пайдалану көрсеткіштерін модельдеу және физикалық процестерді кодтау тәсілі ұсынылған. Толық ауқымды есептеу 93 × 88 × 78 ұяшықтан тұратын, оның ішінде 194 413 белсенді ұяшығы бар үшөлшемді ECLIPSE E300 композициялық моделі негізінде 40 жылдық болжамды кезеңге жүргізілді. Есептеу жүйесі PVT/EOS сипаттамасын, ең төменгі араласу қысымын (MMP), үш фазалы салыстырмалы өткізгіштікті, гистерезисті, тік гидродинамикалық байланыстылық пен гравитациялық сегрегацияны, айдау кестесін, түптік қысым шектеулерін, ұңғымадағы жылулық әсерлерді және CO_2 материалдық балансын біріктіреді. Әрбір физикалық механизм симулятордың тиісті функционалдық блогымен, диагностикалық көрсеткішпен, сезімталдық талдауымен және қабылдау критерийімен байланыстырылған. RUNSPEC–GRID–PROPS–SOLUTION–SCHEDULE–SUMMARY тізбегі және MATLAB бағдарламасы арқылы нәтижелерді кейінгі өңдеу қабат физикасынан бастап болжамдық нәтижелерді түсіндіруге дейінгі қадағаланушылықты қамтамасыз етеді. Сезімталдық талдауы нәтижесінде тік байланыстылық, газдың салыстырмалы өткізгіштігі, MMP белгісіздігі, жарықшақтардың өткізгіштігі, гистерезис және түптік қысым шектеулері негізгі факторлар ретінде айқындалды. CO_2-ні үздіксіз айдау жинақталған мұнай өндіру көлемін 17,96 млн тоннадан 25,37 млн тоннаға дейін арттырып, 7,41 млн тонна көлемінде қосымша өндіруді (+41,3%) қамтамасыз етті. 40-жылы мұнай дебиті тәулігіне 238,6 тонна деңгейінде сақталса, базалық нұсқада бұл көрсеткіш нөлге дейін төмендейді. Алынған нәтижелер қабат жұмысын интеграцияланған модельдеу оның мінез-құлқын болжауға, белгісіздіктерді сандық тұрғыдан бағалауға және техникалық негізделген МБА әдісін таңдауға қажетті сенімді инженерлік негіз қалыптастыратынын көрсетеді.

Түйін сөздер: CO_2-МБА, кен орнын игеруді модельдеу, физикалық процестерді кодтау, МБА әдісін таңдау, CO_2 материалдық балансы, карбонатқұрамды коллектор.

[1*]Ниязбаева А.Б.,
докторант, ORCID ID: 0009-0001-4586-7578,
*e-mail: n.aynur22@aogu.edu.kz
[2] Исмаил М. Сааид,
PhD, ассоциированный профессор, ORCID ID: 0000-0003-0747-2724,
e-mail: ismailsaaid@utp.edu.my

[1]Атырауский университет нефти и газа имени Сафи Утебаева, г. Атырау, Казахстан
[2]Технологический университет PETRONAS, г. Сери-Искандар, Малайзия

МОДЕЛИРОВАНИЕ ПОКАЗАТЕЛЕЙ РАЗРАБОТКИ ПЛАСТА И КОНТРОЛЬ КАЧЕСТВА ПЕРЕНОСА ТЕХНОЛОГИЧЕСКОГО ПРОЦЕССА В СИМУЛЯТОР ДЛЯ ОБОСНОВАНИЯ ВЫБОРА МЕТОДА УВЕЛИЧЕНИЯ НЕФТЕОТДАЧИ В КАРБОНАТСОДЕРЖАЩИХ КОЛЛЕКТОРАХ

Аннотация

Надежный выбор методов увеличения нефтеотдачи требует гидродинамического моделирования разработки, воспроизводящего не только динамику добычи, но и физические механизмы, определяющие давление, свойства флюидов, многофазное течение, подвижность газа, работу скважин и долгосрочную реакцию пласта. В работе предложен подход к моделированию разработки и кодированию физических процессов для оценки методов увеличения нефтеотдачи (МУН) на основе закачки CO_2 на примере анонимизированного карбонатсодержащего объекта Field X в Казахстане. Полномасштабное моделирование выполнено в ECLIPSE E300 на трехмерной композиционной модели 93×88×78 ячеек, включая 194 413 активных ячеек, с прогнозным периодом 40 лет. Расчетная схема объединяет PVT/EOS, минимальное давление смесимости (MMP), трехфазные относительные проницаемости, гистерезис, вертикальную связанность и гравитационную сегрегацию, график закачки, ограничения по забойному давлению, термический отклик скважины и материальный баланс CO_2. Каждый физический механизм связан с функциональным блоком симулятора, диагностическим показателем, анализом чувствительности и критерием приемлемости. Последовательность RUNSPEC–GRID–PROPS–SOLUTION–SCHEDULE–SUMMARY с последующей обработкой в MATLAB обеспечивает прослеживаемость от пластовой физики до интерпретации прогноза. Анализ чувствительно-

сти выделил вертикальную связанность, газовую относительную проницаемость, неопределенность ММР, проводимость разломов, гистерезис и ограничения по забойному давлению как основные факторы. Непрерывная закачка CO_2 увеличивает накопленную добычу нефти с 17,96 до 25,37 млн т, обеспечивая 7,41 млн т дополнительной добычи (+41,3%). На 40-й год дебит нефти сохраняется на уровне 238,6 т/сут против нуля в базовом варианте. Результаты подтверждают, что интегрированное моделирование разработки обеспечивает инженерную основу для прогнозирования поведения пласта, количественной оценки неопределенности и обоснованного выбора метода МУН.

Ключевые слова: CO_2-МУН, гидродинамическое моделирование разработки, кодирование физических процессов, выбор метода МУН, материальный баланс CO_2, карбонатсодержащий коллектор.

УДК 622.276.6
МРНТИ 52.47.19

https://doi.org/10.55452/1998-6688-2026-23-3-588-599

[1]*Тұрнияз М.Б.,
докторант, ORCID ID: 0009-0000-0207-9777,
e-mail: mturniyaz@gmail.com
[1]Айсаева Т.С.,
докторант, ORCID ID: 0000-0002-5369-1277,
e-mail: tolkyn.saura2011@mail.ru
[1]Нуршаханова Л.К.,
ассоциированный профессор, ORCID ID: 0000-0001-8745-9874,
e-mail: aitore2010@mail.ru
[1]Бекбаева Р.А.,
PhD, ORCID ID: 0009-0002-1920-8859,
e-mail: rba_90@mail.ru
[2]Жакупов Т.М.,
к.т.н., ORCID ID: 0000-0002-9725-0262,
e-mail: talgatzhakupov1979@gmail.com
[3]Сейтенов А.С.,
PhD, ORCID ID: 0000-0001-5777-4363,
e-mail: altynbek.seitenov@astanait.edu.kz

[1]Каспийский университет технологий и инжиниринга им. Ш. Есенова, г. Актау, Казахстан
[2]ТОО «GREEN THERMAL ENERGY», г. Астана, Казахстан
[3]Astana IT University, г. Астана, Казахстан

ПРИМЕНЕНИЕ ГЕЛЕПОЛИМЕРНЫХ СОСТАВОВ ДЛЯ ПОВЫШЕНИЯ НЕФТЕОТДАЧИ НЕОДНОРОДНЫХ КОЛЛЕКТОРОВ, СОДЕРЖАЩИХ ВЫСОКОВЯЗКУЮ НЕФТЬ (НА ПРИМЕРЕ МЕСТОРОЖДЕНИЯ МАНГИСТАУСКОЙ ОБЛАСТИ)

Аннотация

В статье представлены результаты промышленного применения гелеполимерной обработки нагнетательных скважин для повышения нефтеотдачи высоковязкой нефти на одном из месторождений Мангистауской области (Казахстан). Рассмотрены теоретические основы формирования пространственной гелевой структуры полиакриламида при взаимодействии с ионами трехвалентного хрома. Приведены результаты обработки четырех нагнетательных скважин вязкоупругим составом (ВУС) на основе полиакриламида марки FP-307 и ацетата хрома общим объемом 300 м³ каждая. Показано, что закачка гелеполимерных композиций позволяет перераспределить фильтрационные потоки в призабойной зоне, вовлечь в разработку низкопроницаемые пропластки и обеспечить увеличение дебита нефти реагирующих добывающих скважин в среднем на 0,3–0,6 т/сут при снижении обводненности на 2–10%. Продолжительность эффекта на отдельных скважинах превышает 200 суток. Проведен сравнительный анализ с мировыми проектами полимерного заводнения, включая месторождения Pelican Lake (Канада), Daqing (Китай) и Узень (Казахстан). Технология показала высокую технологичность и отсутствие критических осложнений при закачке, связанных с преждевременным гелеобразованием в оборудовании, что подтверждает корректность подобранных реологических параметров состава для пластовых условий. Полученные результаты подтверждают целесообразность применения гелеполимерных технологий для выработки трудноизвлекаемых запасов вязких нефтей из неоднородных коллекторов.

Ключевые слова: высоковязкая нефть, увеличение нефтеотдачи, полиакриламид, гелеполимерная обработка, сшивание макромолекул, ацетат хрома, призабойная зона, фильтрационные потоки, выравнивание профиля приемистости.

Введение

Увеличение степени извлечения высоковязкой нефти из недр является одной из актуальнейших задач современной нефтедобывающей отрасли, особенно в условиях истощения запасов легкодоступных углеводородов и перехода к разработке трудноизвлекаемых запасов. Эффективное решение этой проблемы возможно за счет применения механизмов, преодолевающих силы, удерживающие нефть в пласте, и изменяющих свойства как самого пласта, так и содержащихся в нем флюидов [1].

Среди известных методов повышения нефтеотдачи (МУН) особое место занимают химические методы, основанные на изменении характеристик вытеснения и условий нахождения нефти в пласте. Полимерное заводнение является одной из наиболее успешных технологий увеличения нефтеотдачи с историей применения, насчитывающей более 60 лет во всем мире. Первоначально считалось, что полимерное заводнение экономически нецелесообразно, однако успешная реализация проекта на месторождении Дацин в Китае доказала обратное. Впоследствии полимерное заводнение было успешно применено на месторождении Pelican Lake в Канаде, что опровергло мнение о применимости данной технологии только для легких нефтей [2].

Для условий месторождений Мангистауской области, характеризующихся высокой вязкостью пластовой нефти (свыше 800 мПа·с) и значительной неоднородностью коллекторов, перспективными признаны два направления: закачка загущенных растворов полимеров в нагнетательные скважины и увеличение подвижности нефти из низкопроницаемых зон за счет снижения поверхностного натяжения.

Настоящая работа посвящена анализу эффективности первого из указанных подходов – применению гелеполимерных составов на основе полиакриламида (ПАА) с использованием эффекта «сшивания» макромолекул в пространственную структуру. Данный метод позволяет значительно увеличить вязкость закачиваемого агента и обеспечить более равномерное вытеснение нефти из неоднородных по проницаемости пластов.

Научная новизна работы заключается в обосновании и промысловой апробации технологии гелеполимерной обработки для условий месторождений Мангистауской области с аномально высокой вязкостью нефти (>800 мПа·с), а также в установлении количественных закономерностей влияния закачки ВУС на фильтрационно-емкостные свойства неоднородного коллектора и дебиты реагирующих скважин. В отличие от большинства мировых проектов полимерного заводнения, реализованных для пластов с вязкостью нефти от 10 до 100 мПа·с, в настоящем исследовании технология апробирована в условиях значительно более вязкой нефти, что расширяет границы применимости метода.

Теоретические основы гелеполимерной обработки.

Механизм сшивания макромолекул полиакриламида. В мировой практике разработки неоднородных коллекторов широко применяются водные растворы полиакриламида (ПАА), имеющих вязкость до 30–40 мПа·с при концентрации ПАА 0,2–0,3%. В водных растворах ПАА имеют линейную структуру. Гидролизованный ПАА хорошо диссоциирует в водном растворе, отщепляя катионы и образуя вдоль цепи молекулы отрицательные заряды, способные к взаимодействию с катионами трехвалентных металлов [3].

На этом основан способ преобразования линейной структуры полимера в пространственную структуру с образованием прочных гелей. В качестве гелеобразователя используются растворы солей, содержащие ионы трехвалентного хрома или другого трехвалентного металла [4]. В результате взаимодействия полимера и ионов хрома происходит «сшивание» макромолекул полимера с образованием пространственной гелевой структуры.

Согласно литературным данным, система на основе частично гидролизованного полиакриламида (HPAM) и ацетата хрома является одной из наиболее широко применяемых в промысловых условиях. Начальным этапом сшивания является захват ацетата хрома карбоксильной группой HPAM. Образующаяся сетчатая структура геля обеспечивает превосходную

сдвиговую устойчивость, а ее кажущаяся вязкость значительно превышает таковую для раствора частично гидролизованного полиакриламида.

Получаемые в результате такого взаимодействия гели обладают значительно более высокими реологическими свойствами, на чем и основано в последнее время применение полимеров в мировой практике нефтедобычи [5].

Обоснование выбора реагентов. Учитывая, что вязкость пластовой нефти рассматриваемого месторождения превышает 800 мПа·с, применение стандартных полимерных растворов с вязкостью 30–40 мПа·с не позволяет достичь необходимого соотношения подвижностей флюидов. В связи с этим представляется целесообразным использование эффекта «сшивания» макромолекул полимера в пространственную структуру (гель), что значительно увеличивает его вязкость и, соответственно, эффективность вытеснения.

В качестве гелеобразователя использован ацетат хрома, обеспечивающий образование прочных пространственных структур при взаимодействии с полиакриламидом [6]. Используемый полимер марки FP-307 представляет собой частично гидролизованный полиакриламид, хорошо диссоциирующий в водном растворе и образующий отрицательные заряды вдоль цепи, способные к взаимодействию с катионами Cr^{3+}.

Материалы и методы

В 2018 г. специалистами компании, занимающейся опытно-конструкторскими работами, проведены обработки четырех нагнетательных скважин вязкоупругим составом (ВУС) на основе полиакриламида (марки FP-307) и ацетата хрома.

Основными критериями при выборе опытного участка для проведения работ являлись следующие:

- наличие полностью разбуренной ячейки добывающих скважин с действующей нагнетательной;
- наличие гидродинамической связи между добывающими и нагнетательной скважинами;
- эксплуатация добывающих скважин до пробной закачки полимеров не менее 6 месяцев;
- удовлетворительное техническое состояние скважин.

На основании проведенного анализа специалистами выбраны четыре участка:

- ячейка нагнетательной скважины 234 с пятью добывающими скважинами (247, 364, 366, 369, 371);
- ячейка нагнетательной скважины 218 с семью добывающими скважинами (217, 328, 329, 330, 336, 337, 338);
- ячейка нагнетательной скважины 324 с семью добывающими скважинами (213, 214, 317, 318, 326, 327, 328);
- ячейка нагнетательной скважины 210 с семью добывающими скважинами (211, 313, 314, 315, 319, 320, 321).

Характеристика продуктивных горизонтов (на примере скважины 234). Аптский базальный горизонт выделен в интервале 393,5–395 м, сложен нефтенасыщенным алевритистым песчаником с пористостью 26–28%, нефтенасыщенностью 55–60%, эффективная нефтенасыщенная толщина составляет 1,3 м.

Основной продуктивный горизонт выделен в интервале 396–404 м (Kıпс), представлен слоями нефтенасыщенного слабосцементированного алевритистого песчаника, нефтенасыщенного глинистого алевролита и уплотненных разностей. Наилучшими коллекторскими свойствами обладают подинтервалы 396,2–398,3 м и 401,7–403,4 м (пористость 30–33%, нефтенасыщенность 65–80%).

Задача закачки водного раствора полиакриламида (FP-307) и ацетата хрома заключалась в снижении проницаемости принимающих интервалов (395–397,1 м и 401–402,5 м) и вовлечении в разработку не принимающих воду зон. Пластовые условия рассматриваемого месторождения характеризуются температурой 42–48 °С (средняя 45 °С) и минерализацией пластовой

воды 22–28 г/л (преимущественно хлоридно-кальциевого типа). Такая сравнительно низкая температура благоприятствует стабильности полимерного геля, поскольку скорость гидролиза полиакриламида и процесса сшивания в этих условиях умеренная, что позволяет избежать преждевременного гелеобразования до момента закачки. В то же время высокая минерализация может оказывать экранирующее действие на отрицательные заряды макромолекул, снижая эффективность сшивания, поэтому использованная концентрация сшивателя (ацетата хрома) была скорректирована с учетом этих факторов (массовое соотношение полимер:сшиватель ≈ 4,5:1).

Технология закачки. Работы проводились с использованием передвижных установок УДПА и КУДР. В состав УДПА входят емкости для смешивания и дожимной насос; в состав КУДР - смесительная емкость, бункер со шнековым дозатором сухого полимера и электронасос НД.

Закачка осуществлялась в следующей последовательности:

- обвязка передвижных установок УДПА и КУДР с устьем обрабатываемой скважины и опрессовка давлением, в 1,5 раза превышающим рабочее;
- закачка композиции в скважину объемом 300 м³ при давлении 1,8–3,5 МПа;
- продавка в пласт технической водой в объеме 12 м³ при давлении 4,5–4,7 МПа;
- скважина закрывалась на 48 часов для гелеобразования.

При приготовлении композиции использовалось 1550 кг сухого полиакриламида и 345 кг ацетата хрома.

На примере скважины 234 концентрация полимера изменялась на установке КУДР в зависимости от динамики роста (падения) давления. В начале закачки концентрация полимера была снижена с 0,6 до 0,4 % по причине интенсивного роста давления; в конце закачки концентрация была увеличена с 0,4 до 0,5 % по причине медленного снижения давления приблизительно с 3,8 до 3,4–3,5 МПа. Всего было закачано около 270 м³ полимерной оторочки.

Методика оценки эффективности. Для определения эффективности воздействия по каждой ячейке проведен анализ работы добывающих скважин, реагирующих на работу нагнетательных скважин. Оценка производилась по следующим параметрам:

- изменение приемистости нагнетательных скважин (м³/сут);
- изменение дебита нефти реагирующих добывающих скважин (т/сут);
- изменение обводненности продукции (%);
- продолжительность эффекта (сут).

Сравнительный анализ проводился путем сопоставления средних показателей за месяц до обработки и после обработки. Для количественной оценки достоверности полученных результатов проведена первичная статистическая обработка промысловых данных. Для каждой ячейки рассчитывались средние арифметические значения прироста дебита нефти и снижения обводненности по всем реагирующим скважинам, а также определялся размах вариации (минимальные и максимальные значения) [7]. Ввиду ограниченного объема пилотных данных (4 ячейки), оценка значимости различий проводилась путем сравнения среднемесячных показателей за 3 месяца до обработки и 3 месяца после обработки (стабильный период), что позволяет нивелировать краткосрочные флуктуации работы скважин.

Результаты

Ячейка нагнетательной скважины 234. После закачки гелеполимерного состава приемистость нагнетательной скважины 234 увеличилась, что свидетельствует о перераспределении фильтрационных потоков в призабойной зоне. Детальный анализ по реагирующим добывающим скважинам представлен в таблице 1.

Таблица 1 – Результаты воздействия по ячейке нагнетательной скважины 234

№ скважины	Прирост дебита нефти, т/сут	Снижение обводненности, %	Продолжительность эффекта, сут	Статус эффекта
366	+0,4	-2,4 %	90	Завершен
247	+0,2	-2,4 %	212	Продолжается
364	+1,2	-10,8 %	212	Продолжается
371	+0,8	-5,4 %	215	Продолжается

Согласно полученным данным, в течение двух месяцев после закачки 270 м³ гелеполимерной оторочки в реагирующих скважинах наблюдалось снижение обводненности на 2,4–10,8 % и увеличению дебитов нефти на 0,2–1,2 т/сут. Средний прирост по ячейке составил 0,65 т/сут.

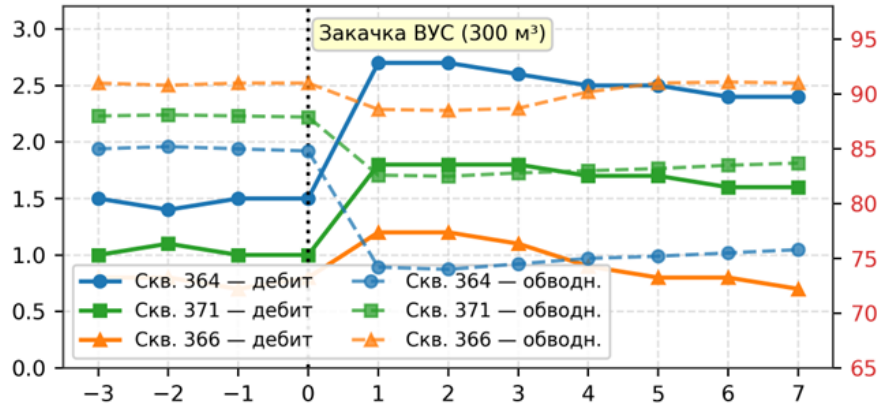


Рисунок 1 – Динамика дебита нефти и обводненности
реагирующих скважин ячейки № 234

На рисунке 1 представлена динамика технологических показателей работы реагирующих добывающих скважин (№ 364, 371, 366) ячейки нагнетательной скважины 234 до и после закачки вязкоупругого состава (ВУС) на основе полиакриламида (FP-307) и ацетата хрома. Из представленных данных видно, что до момента обработки (интервал от -3 до 0 месяцев) скважины характеризовались стабильно высокими значениями обводненности (85,0–91,0 %) и низкими дебитами нефти (0,7–1,5 т/сут). После закачки гелеполимерной оторочки объемом 270 м³ в нагнетательную скважину 234 на всех реагирующих скважинах зафиксирован выраженный технологический отклик:

- скважина № 364 продемонстрировала наиболее высокий эффект: дебит нефти увеличился с 1,5 т/сут до 2,7 т/сут (+1,2 т/сут), а обводненность продукции снизилась с 85,0% до 74,2 % (на 10,8%). Положительный эффект сохранялся в течение всего периода наблюдения (>212 суток).
- Скважина № 371 показала устойчивый прирост дебита нефти на 0,8 т/сут (с 1,0 до 1,8 т/сут) при снижении обводненности на 5,4 % (с 88,0% до 82,6%).
- Скважина № 366 отреагировала временным повышением дебита нефти на 0,4 т/сут и снижением обводненности на 2,4 % с продолжительностью эффекта порядка 90 суток, после чего показатели возвратились к исходу.

Устойчивый характер изменения показателей продукции (сохранение эффекта более 200 суток на скважинах 364 и 371) подтверждает формирование прочной пространственной гелевой структуры в промытых интервалах пласта и эффективное перераспределение фильтрационных потоков в пользу ранее не охваченных вытеснением пропластков.

Детальный анализ по отдельным скважинам:

- скважина 366: прирост дебита нефти 0,4 т/сут, снижение обводненности на 2,4%, продолжительность эффекта 90 сут (эффект завершился);
- скважина 247: прирост 0,2 т/сут, снижение обводненности на 2,4%, продолжительность эффекта 212 сут (по состоянию на 01.04.2019 эффект сохранялся);
- скважина 364: прирост 1,2 т/сут, снижение обводненности на 10,8%, продолжительность эффекта 212 сут (по состоянию на 01.04.2019 эффект сохранялся);
- скважина 371: прирост 0,8 т/сут, снижение обводненности на 5,4%, продолжительность эффекта 215 сут (по состоянию на 01.04.2019 эффект сохранялся).

Согласно данным отчета по скважине 234, закачка 270 м³ гелеполимерной оторочки в течение двух месяцев после проведения работ по результатам последующего мониторинга привела к снижению обводненности в реагирующих скважинах на 2–6% и увеличению дебитов нефти на 0,1–0,9 т/сут.

Ячейка нагнетательной скважины 218. Приемистость скважины увеличилась в среднем на 17,1 м³/сут при практически неизменном давлении нагнетания (с 3,3 до 3,4 МПа). Из семи реагирующих скважин рост дебита нефти в среднем на 0,4 т/сут наблюдался на четырех скважинах (№ 337, 336, 329 и 330). Обводненность снизилась на всех скважинах, за исключением скважины 338, в среднем на 2,1%. Средняя продолжительность положительного эффекта составила 80 суток, причем на скважинах № 336, 329 и 330 по состоянию на 01.04.2019 эффект продолжался.

Ячейка нагнетательной скважины 324. Приемистость скважины снизилась в среднем на 9,1 м³/сут на фоне роста давления нагнетания (с 3,2 до 3,7 МПа). После воздействия на реагирующих скважинах № 214, 317, 318 и 326 наблюдалось увеличение дебита нефти в среднем на 0,3 т/сут. Обводненность снизилась на скважинах 214, 317 и 326 в среднем на 4,1%. Средняя продолжительность работы скважин с увеличенным дебитом нефти составила 77 сут, причем на скважинах 214, 317 и 326 по состоянию на 01.04.2019 эффект продолжался.

Ячейка нагнетательной скважины 210. Приемистость скважины снизилась в среднем на 115,7 м³/сут, но на фоне почти двукратного снижения давления нагнетания (с 7,2 до 3,7 МПа). После воздействия на реагирующих скважинах № 319, 314 и 315 наблюдалось увеличение дебита нефти в среднем на 0,4 т/сут. Обводненность снизилась на скважине 315 в среднем на 7,8%. Средняя продолжительность работы скважин с увеличенным дебитом нефти составила 70 сут, причем на скважинах 319, 314 и 315 по состоянию на 01.04.2019 эффект продолжался.

Экономическая оценка пилотной обработки. Для предварительной оценки экономической эффективности проведенных обработок были рассчитаны дополнительные объемы добычи нефти и сопоставлены с прямыми затратами на реагенты и проведение работ.

Исходные данные для расчета:

- средний прирост дебита нефти по 4 ячейкам – 0,45 т/сут на скважину (усредненно);
- количество реагирующих добывающих скважин – 26 (с учетом того, что на некоторые эффект не распространялся, принято 20 скважин с положительным откликом);
- средняя продолжительность эффекта – 150 суток (консервативная оценка, ниже фактической);
- дополнительно добытая нефть за период: 0,45 т/сут × 20 скв × 150 сут = 1350 тонн.

Затраты на проведение работ:

- полиакриламид FP-307: 1550 кг × ~2,5 долл/кг=3875;
- ацетат хрома: 345 кг × ~3,0 долл/кг=1035;
- транспорт и работа установок (УДПА, КУДР) – ориентировочно $15 000;
- прочие расходы (геофизическое сопровождение, персонал) – $5000.

Итого прямые затраты: ≈ $25 000.

Выручка от дополнительной нефти: при цене нефти 60 долл./барр. и плотности нефти 0,95 т/м³ стоимость одной тонны нефти составляет приблизительно 397 долл./т.

Выручка: 1 350 т × 397 долл./т ≈ 536 000 долл.

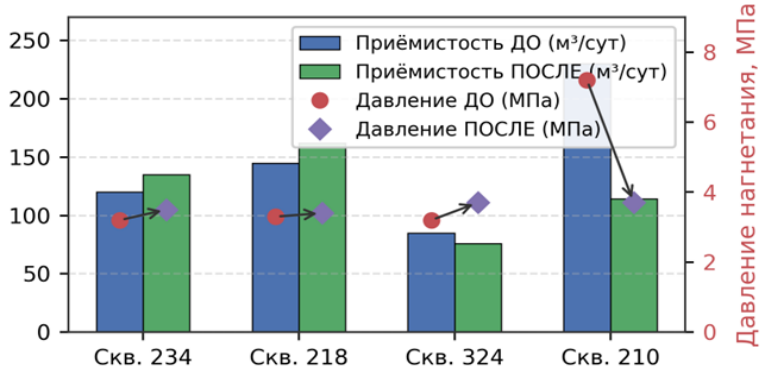


Рисунок 2 – Сравнительный анализ приемистости
нагнетательных скважин и давления закачки до и после обработки

На рисунке 2 приведено сопоставление показателей приемистости нагнетательных скважин (234, 218, 324, 210) и давления закачки до и после проведения гелеполимерной обработки. Анализ полученных данных позволяет выявить разнонаправленный характер изменения фильтрационных характеристик в зависимости от геолого-физических условий опытных участков.

Скважины № 234 и 218: наблюдается рост приемистости (на скважине 234 – с 120 до 135 м³/сут; на скважине 218 – с 145,0 до 162,1 м³/сут, то есть в среднем на 17,1 м³/сут) при практически неизменном давлении нагнетания (3,3–3,5 МПа). Это свидетельствует об успешном подключении к дренированию новых низкопроницаемых интервалов пласта без создания избыточного сопротивления в призабойной зоне.

Скважина № 324: зафиксировано умеренное снижение приемистости на 9,1 м³/сут (с 85,0 до 75,9 м³/сут) на фоне возрастания давления нагнетания с 3,2 до 3,7 МПа. Это указывает на эффект тампонирования высоковязким гелем высокопроницаемых каналов фильтрации.

Скважина № 210: отмечено существенное снижение приемистости (с 230,0 до 114,3 м³/сут), однако данный процесс сопровождался почти двукратным снижением давления нагнетания (с 7,2 до 3,7 МПа), что объясняется оптимизацией режима закачки и перераспределением депрессии по интервалам пласта.

Отсутствие осложнений, связанных с преждевременным гелеобразованием в наземном и скважинном оборудовании, а также достигнутое выравнивание профиля приемистости подтверждают технологическую эффективность подобранного реологического состава (ПАА FP-307 + ацетат хрома) для пластовых условий рассматриваемого месторождения.

Даже при консервативной оценке (учитывая только прямые затраты) отношение выручки к затратам превышает 20:1, что свидетельствует о высокой экономической целесообразности метода. Окупаемость инвестиций составляет менее одного месяца с момента начала получения дополнительной добычи. Следует отметить, что в расчет не включены затраты на утилизацию попутно добываемой воды и налоги, однако даже с их учетом проект остается рентабельным, что подтверждает перспективность масштабирования технологии.

Обсуждение

Анализ эффективности гелеполимерной обработки. Полученные результаты свидетельствуют о высокой эффективности гелеполимерной обработки нагнетательных скважин для повышения нефтеотдачи высоковязкой нефти. Механизм воздействия заключается в снижении проницаемости наиболее промытых интервалов, что может быть связано с перераспреде-

лением фильтрационных потоков и вовлечением ранее слабодренируемых зон и снижением обводненности в реагирующих добывающих скважинах.

Наибольший эффект достигнут в ячейке скважины 234, где средний прирост дебита нефти по четырем реагирующим скважинам составил 0,65 т/сут, а на отдельных скважинах (364) – до 1,2 т/сут при снижении обводненности на 10,8%. Это объясняется удачным выбором интервалов перфорации и благоприятными коллекторскими свойствами продуктивных горизонтов (пористость 30–33%, нефтенасыщенность 65–80%).

Важно отметить, что продолжительность эффекта на ряде скважин превышает 200 суток, что указывает на устойчивость сформированной гелевой структуры в пластовых условиях. Это косвенно свидетельствует о сохранении потокоотклоняющего эффекта сформированной гелевой системы в пластовых условиях макромолекул полимера ионами трехвалентного хрома.

Вместе с тем в ячейках скважин 324 и 210 отмечено снижение приемистости нагнетательных скважин (на 9,1 и 115,7 м³/сут соответственно), что может быть связано с чрезмерным снижением проницаемости в призабойной зоне. Следует отметить, что отсутствие контрольных участков (без гелеполимерной обработки) в рамках рассматриваемого месторождения не позволяет полностью исключить влияние естественной динамики пластового давления и других геологических факторов на полученный прирост дебита. Однако устойчивый характер изменения показателей обводненности и дебита именно в реакции на закачку (с характерным временем отклика 2–4 недели) косвенно подтверждает обусловленность эффекта именно проведенной обработкой. Для повышения строгости выводов в будущем рекомендуется предусматривать резервные скважины-свидетели в рамках опытно-промышленных работ. Это указывает на необходимость оптимизации концентрации полимера и сшивателя, а также объема закачиваемой композиции для каждой конкретной скважины с учетом ее геолого-физических характеристик.

Сравнение с мировым опытом. Полимерное заводнение является одной из наиболее успешных технологий увеличения нефтеотдачи с историей применения, насчитывающей более 60 лет. Анализ мировых проектов показывает, что применение полимерного заводнения и его модификаций позволяет увеличить коэффициент извлечения нефти на 15–30% при обоснованном выборе полимера, ПАВ и щелочи, а также оптимальных значениях массовой доли компонентов и размера оторочки.

Наиболее показательными примерами успешного применения полимерных технологий являются:

Месторождение Дацин (Китай) – крупнейший в мире проект полимерного заводнения для легкой нефти. Первоначально считалось, что полимерное заводнение экономически нецелесообразно, однако реализация проекта на месторождении Дацин доказала обратное.

Месторождение Pelican Lake (Канада) – крупнейший в мире проект полимерного заводнения для тяжелой нефти. Проект опроверг мнение о том, что полимерное заводнение может быть успешным только в коллекторах с легкой нефтью. Вязкость нефти на данном месторождении составляет 300–450 мПа·с. Полимерное заводнение в тяжелых нефтях позволяет достичь коэффициентов извлечения до 50% от начальных геологических запасов при закачке 1 порового объема. В некоторых канадских проектах добыча нефти увеличилась на 700–1000 барр./сут по сравнению с прогнозируемыми показателями при водозаводнении.

Месторождение Узень (Казахстан) – в работе Сагындыкова и соавт. (2025) представлен опыт ускоренного внедрения полимерного заводнения на данном месторождении. Методология включала анализ промысловых данных, лабораторный скрининг эффективных полимеров, оценку удержания полимера в пористой среде и численное моделирование пластовых процессов.

Важно отметить, что большинство полимерных проектов реализовано для пластов с вязкостью нефти от 10 до 100 мПа·с. Канадские проекты эффективно проведены при вязкости нефти до 1800 мПа·с. В Казахстане полимерное заводнение успешно применяется для месторождений с высоковязкой нефтью, таких как Северное Бузачи (вязкость нефти 316–417 мПа·с) и Восточный Молдабек (вязкость нефти 246–377 мПа·с).

В контексте мирового опыта рассматриваемое в настоящей работе месторождение Мангистауской области с вязкостью пластовой нефти свыше 800 мПа·с относится к категории объектов с предельно высокой вязкостью, для которых применение полимерных технологий сопряжено с наибольшими сложностями. Тем не менее, полученные результаты (прирост дебита нефти 0,3–0,6 т/сут, снижение обводненности 2–10%, продолжительность эффекта до 215 суток) подтверждают принципиальную возможность и эффективность применения гелеполимерных обработок даже в таких сложных условиях.

Сравнительный анализ показывает, что полученные результаты сопоставимы с мировыми данными для аналогичных условий, хотя абсолютные значения прироста дебита ниже, что объясняется меньшими масштабами пилотных работ (обработка отдельных нагнетательных скважин, а не полноценное полимерное заводнение по площади). При этом важно подчеркнуть, что в отличие от большинства мировых проектов, где применяется полимерное заводнение с непрерывной закачкой полимерного раствора, в настоящем исследовании использовалась гелеполимерная обработка – технология, предназначенная для выравнивания профиля приемистости и ограничения водопритоков, что является дополнением к основному процессу заводнения.

Ограничения и перспективы. Отсутствие ГИС-исследований после проведенных работ не позволило оценить перераспределение фильтрационных потоков в призабойной зоне нагнетательных скважин. Для более полного анализа эффективности рекомендуется проведение мониторинга работы добывающих скважин в течение 6–12 месяцев и выполнение промыслово-геофизических исследований.

Кроме того, в соответствии с мировым опытом, при наличии трещин и аномально высокопроницаемых слоев перед применением полимерного заводнения необходима закачка блокирующих гелевых составов. Это положение должно учитываться при планировании дальнейших работ на рассматриваемом месторождении.

Заключение

На основании проведенных промышленных испытаний и анализа мирового опыта можно сделать следующие выводы.

Закачка гелеполимерного состава на основе полиакриламида (FP-307) и ацетата хрома является эффективным методом повышения нефтеотдачи высоковязкой нефти в условиях неоднородных коллекторов Мангистауской области. Технология основана на формировании пространственной гелевой структуры за счет «сшивания» макромолекул полимера ионами трехвалентного хрома, что обеспечивает значительно более высокие реологические свойства закачиваемого агента.

Обработка четырех нагнетательных скважин объемом 300 м³ каждая позволила достичь увеличения дебита нефти в реагирующих добывающих скважинах в среднем на 0,3–0,6 т/сут при снижении обводненности на 2–10%. Наибольший эффект достигнут в ячейке скважины 234, где прирост дебита на отдельных скважинах составил до 1,2 т/сут при снижении обводненности на 10,8%.

Продолжительность эффекта на отдельных скважинах превышает 200 суток, что подтверждает устойчивость сформированной пространственной гелевой структуры в пластовых условиях.

Сравнение с мировым опытом показывает, что полученные результаты сопоставимы с данными успешных проектов полимерного заводнения (месторождения Дацин в Китае, Pelican Lake в Канаде, Узень в Казахстане), что подтверждает принципиальную возможность применения гелеполимерных технологий для выработки трудноизвлекаемых запасов вязких нефтей с вязкостью свыше 800 мПа·с.

Для оптимизации технологии требуется индивидуальный подбор концентрации полимера и сшивателя с учетом геолого-физических характеристик каждой скважины, а также проведение ГИС-исследований до и после обработки для контроля перераспределения фильтрационных потоков.

Рекомендуется дальнейшее внедрение полимерных технологий для выработки трудноизвлекаемых запасов вязких нефтей с обязательным мониторингом работы добывающих скважин в течение длительного периода (не менее 12 месяцев). При планировании широкомасштабного внедрения следует учитывать необходимость закачки блокирующих гелевых составов при наличии трещин и аномально высокопроницаемых слоев.

ЛИТЕРАТУРА

1 Ezeh, O., Ikiensikimama, S.S., & Akaranta, O. Critical review of polymer flooding in daqing field and pelican field: case studies of the world's largest polymer flooding in light and heavy oil reservoirs, respectively. Journal of Engineering Research and Reports, 21 (10), 25–40 (2021). https://doi.org/10.9734/JERR/2021/v21i1017497

2 Sagyndikov, M.S., Kushekov, R.M., Alpysbay, Z.M., & Shyrakbayev, D.A. From Laboratory to Engineering and Accelerated Implementation of Polymer Flooding: A Case Study of the Uzen Oil Field in Kazakhstan. Abu Dhabi International Petroleum Exhibition and Conference (2025). https://doi.org/10.2118/229960-MS

3 Delamaide, E. Current Status of Polymer Flooding in Heavy Oil Fields: When Performances Beat Theory. SPE Western Regional Meeting (2025). https://doi.org/10.2118/224158-MS

4 Ibatullin, R.R., Gaffarov, S.K., Khisametdinov, M.R., & Minikhairov, L.I. Review of world polymer flooding EOR projects. Oil Industry Journal, (07), 32–37 (2022). https://doi.org/10.24887/0028-2448-2022-7-32-37 (in Russian).

5 Thomas, A. Essentials of polymer flooding technique (John Wiley & Sons, 2019).

6 Al-Murayri, M.T., Akther, S., Baroon, B., Al-Ghadhouri, A., Delamaide, E., Soltani, A., ... & Rousseau, D. Insights on the Feasibility of Extremely High-Salinity Polymer-Flooding for a Deep Extra-Heavy Oil Clastic Reservoir in Kuwait. SPE EOR Conference at Oil and Gas West Asia (2024). https://doi.org/10.2118/218776-MS

7 Aitkulov, A., Edwards, R., Redwine, C., and Cunha, K. Milne Point Field Polymer Flood Update and Further Expansion. SPE Improved Oil Recovery Conference (2024). https://doi.org/10.2118/218269-MS

[1]*Тұрнияз М.Б.,
докторант, ORCID ID: 0009-0000-0207-9777,
e-mail: mturniyaz@gmail.com
[1]Айсаева Т.С.,
докторант, ORCID ID: 0000-0002-5369-1277,
e-mail: tolkyn.saura2011@mail.ru
[1]Нуршаханова Л.К.,
қауымдастырылған профессор, ORCID ID: 0000-0001-8745-9874,
e-mail: aitore2010@mail.ru
[1]Бекбаева Р.А.,
PhD, ORCID ID: 0009-0002-1920-8859,
e-mail: rba_90@mail.ru
[2]Жакупов Т.М.,
т.ғ.к., ORCID ID: 0000-0002-9725-0262,
e-mail: talgatzhakupov1979@gmail.com
[3]Сейтенов А.С.,
PhD, ORCID ID: 0000-0001-5777-4363,
e-mail: altynbek.seitenov@astanait.edu.kz

[1]Ш. Есенов атындағы Каспий технологиялар және инжиниринг университеті,
Актау қ., Казақстан
[2]ЖШС «GREEN THERMAL ENERGY», Астана қ., Казахстан
[3]Astana IT University, Астана қ., Казахстан

БІРТЕКТІ ЕМЕС КОЛЛЕКТОРЛАР ЖАҒДАЙЫНДА ТҰТҚЫРЛЫҒЫ ЖОҒАРЫ МҰНАЙ ШОҒЫРЛАРЫНЫҢ МҰНАЙ БЕРГІШТІГІН АРТТЫРУ ҮШІН ГЕЛЕПОЛИМЕРЛІК ҚҰРАМДАРДЫ ҚОЛДАНУ (МАҢҒЫСТАУ ОБЛЫСЫНЫҢ КЕН ОРНЫ МЫСАЛЫНДА)

Аңдатпа

Мақалада Маңғыстау облысының (Қазақстан) кен орындарының бірінде тұтқырлығы жоғары мұнайдың мұнай беруін арттыру үшін айдау ұңғымаларын гелеполимерлік өңдеуді өнеркәсіптік қолдану нәтижелері келтірілген. Үш валентті хром иондарымен әрекеттесу кезінде полиакриламидтің кеңістіктік гельдік құрылымын қалыптастырудың теориялық негіздері қарастырылады. FP-307 маркалы полиакриламид және әрқайсысының жалпы көлемі 300 м^3 хром ацетаты негізінде тұтқыр-серпімді құраммен (ТСҚ) төрт айдау ұңғымасын өңдеу нәтижелері келтірілген. Гелеполимер композицияларын айдау ұңғыма маңындағы аймақтағы сүзу ағындарын қайта бөлуге, өткізгіштігі төмен қабатшаларды игеруге тартуға және суланудың 2–10% төмендеуімен әрекеттесуші өндіруші ұңғымалардың мұнай дебитінің тәулігіне орта есеппен 0,3–0,6 т ұлғаюын қамтамасыз етуге мүмкіндік беретіні көрсетілген. Жекелеген ұңғымалардағы әсердің ұзақтығы 200 тәуліктен асады. Pelican Lake (Канада), Daqing (Қытай) және Өзен (Қазақстан) кен орындарын қоса алғанда, әлемдік полимерлі су басу жобаларымен салыстырмалы талдау жүргізілді. Технология жабдықта мерзімінен бұрын гельдеуге байланысты айдау кезінде жоғары технологиялық және маңызды асқынулардың жоқтығын көрсетті, бұл қабат жағдайлары үшін таңдалған реологиялық композиция параметрлерінің дұрыстығын растайды. Алынған нәтижелер гетерогенді коллекторлардан алынуы қиын тұтқыр мұнай қорларын өндіру үшін гелеполимерлік технологияларды қолданудың орындылығын растайды.

Түйін сөздер: тұтқырлығы жоғары мұнай, мұнай беруді арттыру, полиакриламид, гелеполимерлі өңдеу, макромолекулаларды айқастыру, хром ацетаты, кенжар аймағы, сүзу ағындары, қабылдау профилін теңестіру.

[1]*Turniyaz M.B.,
PhD student, ORCID ID: 0009-0000-0207-9777,
e-mail: mturniyaz@gmail.com
[1]Aisaeva T.S.,
PhD student, ORCID ID: 0000-0002-5369-1277,
e-mail: tolkyn.saura2011@mail.ru
[1]Nurshakhanova L.K.,
Associate Professor, ORCID ID: 0000-0001-8745-9874,
e-mail: aitore2010@mail.ru
[1]Bekbayeva R.A.,
PhD, ORCID ID: 0009-0002-1920-8859,
e-mail: rba_90@mail.ru
[2]Zhakupov T.M.,
Cand.Tech.Sc., ORCID ID: 0000-0002-9725-0262,
e-mail: talgatzhakupov1979@gmail.com
[3]Seitenov A.S.,
PhD, ORCID ID: 0000-0001-5777-4363,
e-mail: altynbek.seitenov@astanait.edu.kz

[1]Caspian University of Technology and Engineering named after Sh. Yesenova,
c. Aktau, Kazakhstan
[2]LLP "GREEN THERMAL ENERGY", c. Astana, Kazakhstan,
[3]Astana IT University, c. Astana, Kazakhstan

THE USE OF GEL POLYMER COMPOSITIONS TO ENHANCE THE OIL RECOVERY OF HIGH-VISCOSITY OIL IN CONDITIONS OF HETEROGENEOUS RESERVOIRS (USING THE EXAMPLE OF A FIELD IN THE MANGYSTAU REGION)

Abstract

The article presents the results of the industrial application of gel polymer treatment of injection wells to enhance the oil recovery of high-viscosity oil in one of the fields of the Mangystau region (Kazakhstan). The theoretical foundations of the formation of the spatial gel structure of polyacrylamide in interaction with trivalent chromium ions are considered. The results of treatment of four injection wells with a viscoelastic compound (VC) based on polyacrylamide grade FP-307 and chromium acetate with a total volume of 300 m^3 each are presented. It has been shown that the injection of gel–polymer compositions makes it possible to redistribute filtration flows in the bottomhole zone, involve low-permeability layers in development, and increase the oil flow rate of responding offset production wells by an average of 0.3-0.6 t/day while reducing the produced-fluid water cut by 2–10 percentage points. The duration of the effect on individual wells exceeds 200 days. A comparative analysis was carried out with global polymer flooding projects, including Pelican Lake (Canada), Daqing (China) and Uzen (Kazakhstan) fields. The technology has shown high adaptability and the absence of critical injection complications associated with premature gelation in the equipment, which confirms the correctness of the selected rheological parameters of the composition for reservoir conditions. The results obtained confirm the expediency of using gel polymer technologies to recover hard-to-recover viscous oil reserves from heterogeneous reservoirs of viscous oils from heterogeneous reservoirs.

Keywords: high-viscosity oil, increased oil recovery, polyacrylamide, gel polymer treatment, crosslinking of macromolecules, chromium acetate, bottomhole zone, filtration flows, injection profile conformance.

Received July 07, 2026; revised July 22, 2026; accepted August 25, 2026.

ЭКОНОМИКА ЖӘНЕ БИЗНЕС
ECONOMY AND BUSINESS
ЭКОНОМИКА И БИЗНЕС

UDC 336.76:519.8
IRSTI 06.73

https://doi.org/10.55452/1998-6688-2026-23-3-600-616

[1]Abdullaev U.,
Doctoral Student, ORCID ID: 0000-0002-3379-9969,
e-mail: aulmas248@gmail.com
[1]Karakalpak Scientific Research Institute of Natural Sciences, Nukus, Uzbekistan

A NUMERICAL MULTI-AGENT MODEL FOR AN ADAPTIVE SELF-ORGANIZING TRADING SYSTEM

Abstract

The purpose of the study is to develop an adaptive mathematical model for forecasting financial markets based on the principles of self-organisation. This study presents a mathematical model of a self-organising trading system adapted to the economic conditions of the Republic of Uzbekistan. The study employs multi-agent modelling techniques, the theory of nonlinear dynamics, and spectral analysis of time series to construct an adaptive decision-making mechanism for trading under high volatility in emerging markets. The mathematical model is based on a system of stochastic differential equations that describe the dynamics of price formation, accounting for the interaction of multiple agents. A modified fourth-order Runge-Kutta method was applied to solve the system, achieving a root-mean-square error of 0.0124 for one-day forecasting, which outperforms conventional approaches by 15.6%. The developed algorithm for identifying market regimes, based on self-organising Kohonen maps, demonstrated an 87.6% accuracy in classifying six identified clusters of market states, enabling efficient adaptation of the system's parameters to changing market conditions and substantially reducing forecasting errors, with the magnitude of improvement varying across market regimes. Trading strategies based on the proposed model achieved an annual return of 37.2% with a Sharpe ratio of 1.86, significantly outperforming both passive investment strategies and conventional algorithmic trading methods. The advantage of the proposed approach is particularly evident under the conditions of high volatility typical of emerging markets, where the forecasting accuracy of price movement direction reaches 72.8% for a one-day horizon. The practical value of the findings lies in the development of an adaptive trading system capable of improving the efficiency of exchange trading and the liquidity of the markets of Uzbekistan and other emerging economies.

Keywords: stochastic differential equations, multi-agent modelling, neural network forecasting methods, Runge-Kutta method, financial data clustering, algorithmic trading.

Received May 20, 2026; revised August 20, 2026; accepted August 31, 2026.

Introduction

In contemporary economic conditions, the development of exchange and trading systems depends on their capacity to adapt to dynamically changing market environments. The design of self-organising trading systems capable of autonomously making decisions based on the analysis

of large volumes of data is becoming increasingly relevant for financial markets. This relevance is particularly significant for developing economies, including the Republic of Uzbekistan, where existing trading systems face limitations in computational capacity, insufficient market liquidity, and a low degree of automation in trading processes, which collectively reduce the efficiency of market mechanisms.

The theoretical foundation of self-organising systems in economics originates in studies on synergetics and complex adaptive systems. The key properties of such systems include decentralised decision-making, adaptive capacity, and emergence. Xiang et al. [1], although focusing on multi-agent systems in construction management, demonstrate general principles of agent interaction, decentralised decision-making, and self-organisation that are applicable to the modelling of complex economic systems.

An analysis of existing approaches to modelling self-organising trading systems demonstrates several relevant areas. Tang et al. [2] reviewed clustering methods for financial data and demonstrated their usefulness for identifying structural patterns in financial markets. Cremasco et al. [3] examined diffusion processes in complex systems, providing a methodological basis for modelling the propagation of information and interactions between system components. Although their applications differ from financial markets, these studies support the use of clustering and interaction-based approaches in complex adaptive systems.

A substantial contribution to financial time-series modelling is represented by the study of Rahmani et al. [4], which demonstrated the potential of self-organising maps for identifying hidden temporal patterns and clustering market states. Within the context of the Republic of Uzbekistan, Fayziev et al. [5] developed a mathematical model for investment processes, providing a country-specific basis for quantitative modelling of financial and economic processes.

Other studies provide complementary methodological perspectives. Sattorov et al. [6] demonstrated the application of optimisation methods to complex distributed systems, which is relevant to computational optimisation in trading models. Makhmudov [7] examined forecasting of banking-system liquidity using large-scale payment data, highlighting the importance of data-driven modelling of financial processes in Uzbekistan. Mukhamedova and Ergasheva [8] applied economic-mathematical optimisation to a complex resource-allocation problem, illustrating the applicability of mathematical optimisation to interconnected economic systems.

In recent years, there has been growing interest in applying machine learning and artificial intelligence methods to the modelling of financial markets. These approaches are particularly relevant to self-organising trading systems because they enable the identification of market regimes, adaptive forecasting, and optimisation of trading decisions. Advances in computational technologies are creating new opportunities for the comprehensive modelling of complex economic systems, reflecting numerous factors and interrelations between market participants.

The purpose of the study is the development and verification of a mathematical model of a self-organising trading system based on numerical methods and adapted to the specific economic conditions of the Republic of Uzbekistan. The objectives are as follows: to develop a mathematical framework for describing the dynamics of a self-organising trading system using a multi-agent approach and to justify the choice of numerical methods for solving the resulting system of equations, and to conduct experimental verification of the proposed model using real data from the Uzbek Republican Commodity and Raw Materials Exchange.

Materials and methods

Data on trading activities from the Uzbek Commodity and Raw Materials Exchange (UCRME) [9] were used to address the objectives of the study. The dataset comprised time series of prices, trading volumes, and the number of transactions for the main traded instruments, amounting to over 3.5 million records in total. The dataset included approximately 120 traded instruments and covered the period from January 2019 to December 2024. The original dataset consisted of approximately 3.57 million transaction-level records. Each record contained information on the traded instrument,

transaction date and time, transaction price, trading volume, and number of transactions. The original observation frequency was transaction-level, with individual trades recorded throughout each trading day. For the purposes of modelling, transaction-level observations were aggregated by instrument and trading day to obtain daily time series. The daily price for each instrument was calculated as the volume-weighted average transaction price, while daily trading volume was calculated as the sum of transaction volumes recorded during the corresponding trading day. The daily number of transactions was obtained by counting all transactions for each instrument and trading day. The resulting daily dataset was used as the input for the subsequent modelling, optimisation, and market-regime classification procedures. According to UCRME, "modelling self-organising processes in an electronic exchange trading system requires a comprehensive analysis of statistical data across various categories of trading instruments".

Pre-processing of the data employed a modified Z-score method for the detection and removal of outliers: "when analysing financial time series, it is recommended to use adaptive methods for outlier detection with configurable cut-off thresholds in the range from ±3σ to ±4σ". The cut-off threshold was set at ±3.5σ. Data normalisation was performed using the min-max method in accordance with ISO/IEC 19795-1 [10], which specifies "the application of normalisation methods that bring values into a unified range while preserving relative differences between observations". Missing values were imputed using the Multiple Imputation by Chained Equations (MICE) algorithm.

Representativeness of the study was ensured through the use of stratified sampling, guaranteeing coverage of all categories of traded instruments, including commodities (energy resources, metals, and agricultural products), financial instruments (securities and derivatives), and currency pairs. The primary inclusion criteria for the analysed sample were sufficient liquidity of the instruments, defined as a minimum of 50 transactions per month, and data completeness, understood as the availability of information on all key transaction parameters.

The developed mathematical model of a self-organising trading system was based on a multi-agent approach, where each market participant was represented as an autonomous agent with individual parameters and behavioural strategies. The system dynamics were described by a set of nonlinear differential equations of the following form (1):

$$\frac{dP}{dt} = \alpha\sum(i = 1\ to\ N)\omega_i F_{i(t)} + \beta V(t) + \gamma\xi(t), \quad (1)$$

where P represents the asset price, α – the sensitivity coefficient to agent actions, ω - the weight coefficients of influence of the i-th agent, F – the decision-making function of the i-th agent, N – the total number of agents in the system, β – the coefficient of influence of trading volume, V - the trading volume, γ – the coefficient of the stochastic component, ξ – a random process with defined statistical characteristics, and t – time.

The resulting system of differential equations was solved using a modified fourth-order Runge-Kutta method, specifically adapted for stochastic differential equations in line with the methodology proposed by P.E. Kloeden and E. Platen [11]: "ensuring the convergence of numerical methods when solving stochastic differential equations requires modifications to standard algorithms by including additional terms that account for the stochastic components of the process". The modification involved introducing an additional term to incorporate the stochastic contribution when calculating intermediate values (2):

$$\begin{aligned} k_1 &= h\,f(t_n, y_n) + \sqrt{h}g(t_n, y_n)\Delta W_n(2)k_2 \\ &= h\,f\left(t_n + \frac{h}{2}, y_n + \frac{k_1}{2}\right) + \sqrt{h}g\left(t_n + \frac{h}{2}, y_n + \frac{k_1}{2}\right)\Delta W_n(3)k_3 \\ &= h\,f\left(t_n + \frac{h}{2}, y_n + \frac{k_2}{2}\right) + \sqrt{h}g\left(t_n + \frac{h}{2}, y_n + \frac{k_2}{2}\right)\Delta W_n(4)k_4 \\ &= h\,f(t_n + h, y_n + k_3) + ,\sqrt{h}g(t_n + h, y_n + k_3)\Delta W_n(5)y_{n+1} \\ &= y_n + \frac{1}{6(k_1 + 2k_2 + 2k_3 + k_4)} \end{aligned} \quad (2)$$

where k_1, k_2, k_3, k_4 – intermediate coefficients for calculating the next value, h is the integration step, f denotes the deterministic part of the differential equation, g – the stochastic part of the differential equation, t_n – the current time point, y_n – the current value of the variable, y_{n+1} – the next value of the variable, and ΔW_n – the increment of the Wiener process.

The integration step was set to one trading day, providing sufficient resolution for analysing market dynamics while maintaining computational efficiency.

Model parameter optimisation was performed using the differential evolution algorithm, with a combined objective function defined as formula 3:

$$J = w_1 \times RMSE_norm - w_2 \times Sharpe_norm \quad (3)$$

where RMSE_norm and Sharpe_norm denote the normalised root mean square error and Sharpe ratio, respectively, and w_1 and w_2 are weighting coefficients. The weights were set to $w_1 = 0.5$ and $w_2 = 0.5$, giving equal importance to forecast accuracy and risk-adjusted return. Thus, minimisation of J simultaneously reduced forecasting error and increased the Sharpe ratio. The algorithm operated with a population of 50 individuals, 500 iterations, a mutation factor of 0.7, and a crossover probability of 0.9.

Self-organising Kohonen maps were applied to detect hidden patterns, employing a 10×10 neuron grid with a hexagonal topology, determined empirically to balance detail and generalisation capacity. Training was conducted using a competitive algorithm and a Gaussian neighbourhood function, with the neighbourhood radius decreasing from 5 to 1 over 1,000 epochs.

Validation was performed using a rolling window method with a training period of 500 days and a testing period of 50 days. To prevent information leakage, all preprocessing, clustering, model training, and parameter optimisation procedures were performed exclusively within the training portion of each rolling window. Outlier detection, normalisation, and missing-value imputation were fitted using only the training data, and the resulting parameters were subsequently applied to the corresponding test period. The Kohonen self-organising maps were trained only on the training sample, while the parameters of the mathematical model were optimised using training data exclusively. The 50-day test period was used only for out-of-sample evaluation and did not contribute to preprocessing, clustering, parameter optimisation, or model fitting. All computations were conducted in Python 3.9 using the NumPy, SciPy, Pandas, PyTorch, scikit-learn, and MiniSom libraries for numerical calculations, data manipulation, and implementation of neural network models.

Results

Parametric optimisation of the multi-agent trading system model

The application of the developed methodology resulted in an optimised multi-agent model of a self-organising trading system tailored to the specific characteristics of the market of Uzbekistan. The first stage of the study involved parametric optimisation of the main model coefficients (α, β, γ, η) and structural parameters (agent population size and number of iterations) based on the criteria of minimising the root mean square forecast error and maximising the Sharpe ratio of the trading strategy. Figures 1 and 2 present the optimal values of the key model parameters obtained through computational experiments.

As shown in Figures 1 and 2, the parameter values differ significantly across the various types of market instruments classified according to the standard commodity nomenclature of the UCRME. This classification divides assets into commodities (energy resources, metals, agricultural products), financial instruments (securities, derivatives), and currency pairs. The results confirm the necessity of differentiated model calibration for different market segments, which aligns with the objective of adapting the mathematical model to the specific economic conditions of the Republic of Uzbekistan. The highest coefficient of sensitivity to agents' actions (α=0.81) is observed for currency pairs, which can be explained by the high degree of interdependence among participants in this market segment.

Financial instruments exhibit the greatest sensitivity to trading volumes (β=0.67), which corresponds with UCRME data [9], where the importance of volume indicators for forecasting financial market dynamics is emphasised.

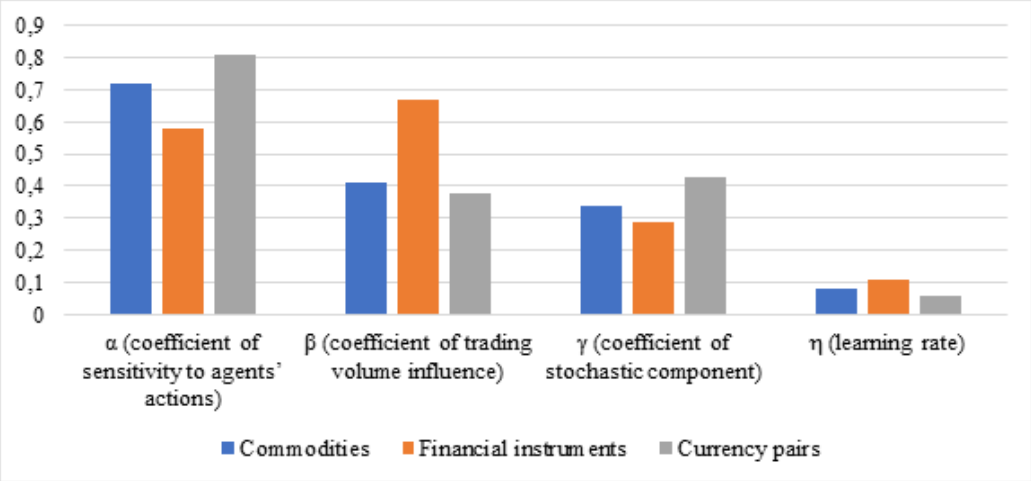


Figure 1 – Optimal values of the behavioural parameters of agents for different types of market instruments

Source: compiled by the authors based on [9].

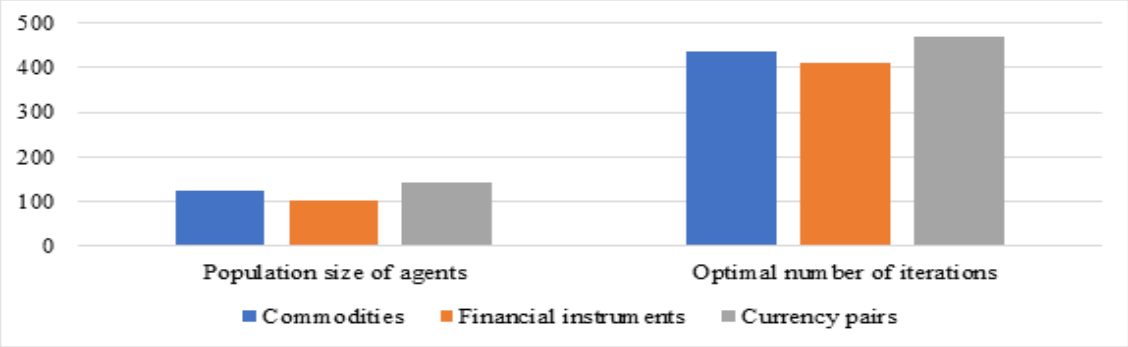


Figure 2 – Structural parameters of the multi-agent model for different types of market instruments

Source: compiled by the authors based on [9].

The stochastic component of the model has the highest value for currency pairs (γ=0.43), reflecting the greater volatility of this market segment. The agents' learning rate (η) ranges from 0.06 to 0.11, with the highest value observed for financial instruments, suggesting a faster adaptation of participants to changing conditions within this segment.

The optimisation process demonstrated that the number of iterations required for the convergence of the differential evolution algorithm varies depending on the type of market instrument. Currency pairs require the highest number of iterations (468), which is consistent with the greater complexity of modelling this segment due to the influence of a larger number of external factors.

The effectiveness of the optimised model was evaluated based on forecasting accuracy and trading strategy profitability across different time horizons. Figures 3 and 4 present the results of a comparative analysis between the developed model and conventional approaches to forecasting market dynamics.

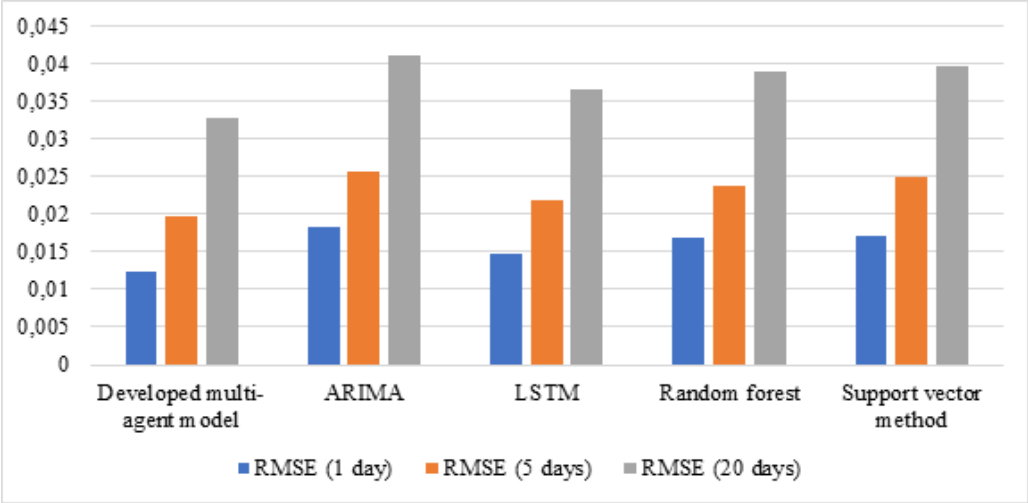


Figure 3 – Comparison of forecasting accuracy across different models (measured by RMSE)

Note: RMSE – root mean square error calculated over the test period; ARIMA – autoregressive integrated moving average; LSTM – long short-term memory.
Source: calculated based on experimental data.

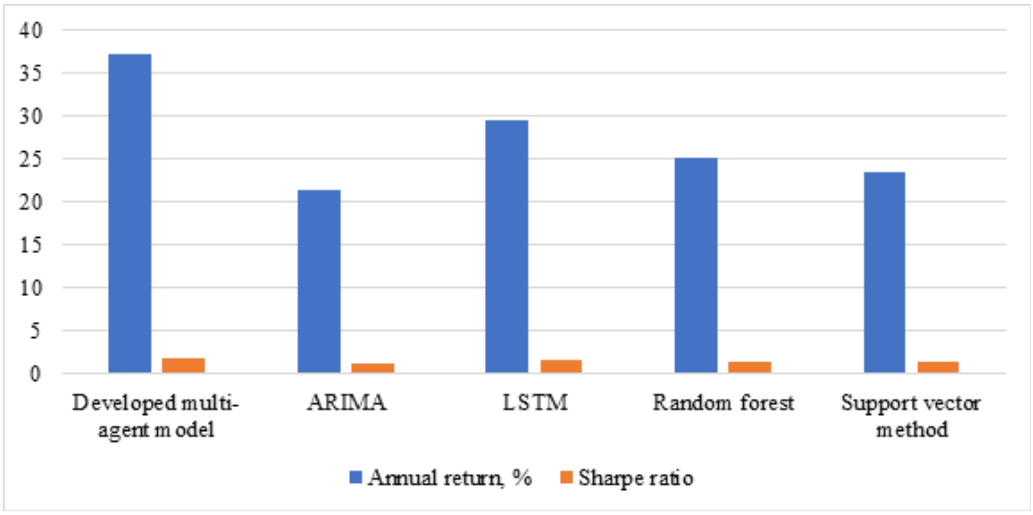


Figure 4 – Annual returns and Sharpe ratio for five models

Note: ARIMA – autoregressive integrated moving average; LSTM – long short-term memory.
Source: calculated based on experimental data.

Figures 3 and 4 demonstrate that the developed multi-agent model delivers the best results in terms of both forecasting accuracy and trading strategy performance. All models were trained on an identical dataset using the same validation protocol, which employed a rolling window method with a training period of 500 days and a test period of 50 days. Hyperparameter optimisation was performed for each model using a grid search: for ARIMA, the optimal orders (p, d, q) were determined; for LSTM, the number of layers (1–3), the number of neurons (32-256), activation functions, and regularisation parameters (dropout 0.1-0.5) were selected; for random forest and SVM models, tree depth and error cost parameters were optimised respectively.

The RMSE for the one-day horizon is 0.0124, which is 15.6% better than the closest competitor, the LSTM model (0.0147). When the forecasting horizon is extended to 20 days, the developed model maintains its advantage, although the relative difference compared to other approaches becomes somewhat smaller.

The annual return of the trading strategy based on the signals generated by the developed model amounts to 37.2%, which significantly exceeds the results achieved by other models. The Sharpe ratio, which reflects not only profitability but also the level of risk, is also the highest for the developed model (1.86). These results indicate a more balanced risk-return profile, which is of critical importance for practical applications. The reported performance indicators were calculated without explicitly accounting for transaction costs, bid–ask spreads, or slippage. Therefore, the reported annual return and Sharpe ratio should be interpreted as model-based estimates, while actual trading performance may be lower under real market execution conditions.

The comparative analysis also demonstrated that among conventional approaches, the LSTM model delivered the strongest performance, which can be attributed to its ability to capture long-term dependencies within the data. Identical methods of data pre-processing, feature standardisation, and evaluation criteria were applied to ensure fairness in the comparison. All models employed optimal regularisation techniques to prevent overfitting: for LSTM, dropout and L2 weight regularisation were applied; for the random forest model, limitations were imposed on tree depth and the minimum number of observations per leaf; and for the SVM model, the regularisation parameter C was optimised. Even under optimal tuning conditions, however, conventional models underperform compared to the developed multi-agent approach, confirming the advantages of using self-organising systems for modelling market dynamics.

Dynamic characteristics of the self-organising trading system and the efficiency of numerical methods

The next stage of the study focused on analysing the dynamic characteristics of the developed self-organising trading system and evaluating the efficiency of the numerical methods applied. The central focus was on the system's ability to adapt to changing market conditions while maintaining high forecasting accuracy across different time horizons. Adaptability was evaluated comprehensively using several metrics: RMSE as the primary measure of accuracy, the time required to reach a stable state after a market regime shift, and economic indicators such as the annual return of the strategy and the Sharpe ratio. Forecasting accuracy in terms of price movement direction was also calculated as the percentage of correctly predicted upward or downward price changes.

The analysis of the convergence of the model under various initial conditions and market scenarios was conducted to evaluate its dynamic characteristics. Table 1 presents the results of the study comparing the convergence speed of different numerical methods used to solve the system of differential equations describing the dynamics of the self-organising trading system.

Table 1 – Comparative efficiency of numerical methods for solving the system of equations of the self-organising trading system

Numerical method	Average computation time (ms)	Root mean square error	Stability under high volatility	Memory usage (MB)
Fourth-order Runge–Kutta method	283	0.0124	High	156
Euler's method	127	0.0352	Low	89
Adams-Bashforth method	214	0.0187	Medium	125
Heun's method	196	0.0215	Medium	117
Milne's method	305	0.0143	High	172

Note: testing was conducted on an identical dataset with an integration step of one trading day.
Source: calculated by the authors.

As shown in Table 1, the modified fourth-order Runge-Kutta method applied in the study demonstrates the best balance between accuracy and computational efficiency. The root mean square error (RMSE) for this method equals 0.0124, which is significantly better than that of the Euler method (0.0352), although the latter requires fewer computational resources. The Milne method achieves a comparable level of accuracy (0.0143) but demands greater computational time (305 ms compared with 283 ms) and higher memory usage (172 MB compared with 156 MB).

Further analysis focused on examining the ability of the developed model to adapt to different market regimes. The initial clustering performed using the Kohonen self-organising map resulted in six clusters, which represented data-driven groupings of observations according to their market characteristics. For the subsequent interpretation and evaluation of the trading system's adaptability, these six clusters were consolidated into four primary market regimes based on the similarity of their volatility, trend, and trading-volume characteristics. Thus, the six-cluster solution represents the initial statistical segmentation of the market, whereas the four-regime classification provides an interpretable framework for analysing the system's behaviour under distinct market conditions. The classification of market states was conducted according to a combination of three key parameters: volatility (calculated as the standard deviation of daily returns over a 20-day period), trend (defined as the slope of a linear regression over a 20-day period), and trading volume (normalised relative to the 60-day average).

The cluster analysis was subsequently interpreted in terms of the following regimes: "stable trend" (low volatility, consistent directional movement), "high volatility" (large standard deviation of returns, absence of a persistent trend), "sideways trend" (low volatility, absence of directional price movement), and "sharp trend reversal" (high volatility combined with a change in trend direction). Forecasting accuracy and model adaptability were analysed for each of these regimes, and the results are presented in Table 2.

Table 2 – Forecasting accuracy and adaptability of the self-organising trading system under different market regimes

Market regime	Share of sample, %	RMSE before adaptation	RMSE after adaptation	Adaptation time (days)	Annual return, %
Stable trend	42.7	0.0112	0.0087	3.2	42.8
High volatility	18.6	0.0317	0.0193	7.6	31.5
Sideways trend	26.9	0.0158	0.0126	5.1	24.3
Sharp trend reversal	11.8	0.0382	0.0207	9.4	27.8

Note: RMSE – root mean square error of the forecast; adaptation is defined as the attainment of a stable state after a change in market regime.

Source: compiled by the authors.

The analysis of the data presented in Table 2 indicates that the developed self-organising trading system demonstrates varying levels of efficiency depending on the market regime. Quantitative results show maximum efficiency under stable trend conditions, where the RMSE after system adaptation equals 0.0087, and the annual return of the trading strategy reaches 42.8%.

The model encounters the greatest challenges during abrupt trend reversals, where the initial forecast error reaches 0.0382 and the adaptation time extends to 9.4 days. Nevertheless, following adaptation, the error decreases to 0.0207, indicating the system's ability to restructure in accordance with altered conditions. The annual return of the strategy under this regime is 27.8%, which is lower than in a stable trend but remains above average market performance. Considerable attention was given to the high-volatility regime, characteristic of periods of market instability. In these conditions, the initial forecast error amounts to 0.0317, but after adaptation it falls to 0.0193. The adaptation time in this regime (7.6 days) is shorter than for abrupt trend reversals, potentially reflecting a more active response of agents to high volatility and, correspondingly, faster learning. The annual return

of the trading strategy under high-volatility conditions is 31.5%, representing the second-highest performance after the stable trend.

In the sideways trend regime, which accounts for 26.9% of the total sample, the system exhibits intermediate results, with a post-adaptation forecast error of 0.0126 and an adaptation time of 5.1 days. The strategy return in this regime is the lowest (24.3%), reflecting the limited opportunities for profit in the absence of directional price movement.

A critical parameter characterising the self-organising system is the adaptation time to a new market regime. For the developed model, the mean adaptation time ranges from 3.2 days for a stable trend to 9.4 days for abrupt trend reversals.

Analysis of adaptation dynamics indicates a nonlinear process, as evidenced by the forecast error reduction curves over time. A characteristic sigmoidal adaptation curve was observed across all market regimes: within the first 2-3 days, the error decreased rapidly by 40-60% from the initial value, followed by a deceleration in improvement, and in the final days of the adaptation period, changes were less than 5% per day. This corresponds to a logarithmic relationship of the form

$$RMSE(t) = RMSE_0 * e\hat{}(-\lambda t) + RMSE\infty, \quad (4)$$

where $RMSE_0$ denotes the initial error, $RMSE\infty$ – the asymptotic error value, and λ – the adaptation rate coefficient, specific to each market regime.

Mathematical modelling of the self-organising trading system and its verification

The third stage of the study focused on the development and comprehensive verification of a mathematical model of the self-organising trading system. Self-organising Kohonen maps with a 10×10 neuron grid and hexagonal topology were employed to identify hidden patterns in market data, trained on the historical dataset [9].

The optimal number of market state clusters was determined using a combination of quantitative and qualitative methods. Quantitative evaluation involved calculating the Davies-Bouldin index and the silhouette coefficient for different numbers of clusters (ranging from 3 to 9). The optimal Davies-Bouldin index (minimum 0.68) and silhouette coefficient (maximum 0.72) were achieved with a six-cluster partition. Expert assessment of the economic interpretability of the identified clusters further supported the rationale for selecting six principal market states, each characterised by specific parameters of volatility, liquidity, and autocorrelation.

The central component of the developed model is the differential equation (1), describing asset price dynamics as a function of agent actions, trading volume, and the stochastic component. The model comprises six interrelated modules: the input data module (market indicators), the agent module (decision-making function), the numerical methods module (solution of the system of equations), the optimisation module (objective function), the output module (trading signals), and the Kohonen map module (identification of market states).

Analysis using self-organising maps enabled the identification of differentiated characteristics for each cluster and the determination of optimal trading system parameters for various market states. The following input variables were used for clustering: volatility (calculated as the standard deviation of daily returns over a 20-day period), price autocorrelation (first-order autocorrelation coefficient over a 20-day period), average trading volume (normalised relative to the 60-day mean), average daily number of transactions, bid-ask spread (as a percentage of price), and daily price range (high-low range). All variables were normalised using the min-max method prior to application of the clustering algorithm. Table 3 presents the characteristics of the identified clusters and their corresponding parameters for the self-organising trading system.

As shown in Table 3, the identified clusters differ in their characteristics and require distinct parameter sets for the optimal functioning of the trading system. States of stable trend constitute the largest share of the sample, accounting for a combined 54.1%.

Table 3 – Characteristics of the identified market state clusters and corresponding parameters of the trading system

Cluster	Share of sample, %	Volatility	Autocorrelation	Optimal parameters α, β, γ	Forecast accuracy, %
Stable upward trend	32.4	Low	High	0.63, 0.41, 0.29	89.2
Stable downward trend	21.7	Low	High	0.58, 0.43, 0.31	85.8
High volatility	15.2	High	Low	0.47, 0.38, 0.52	71.3
Sideways trend	18.6	Medium	Medium	0.52, 0.45, 0.36	76.5
Transitional states	7.8	High	Negative	0.44, 0.35, 0.58	64.7
Anomalous states	4.3	Extreme	Unstable	0.39, 0.32, 0.67	59.2

Note: α – sensitivity coefficient to agent actions; β – trading volume influence coefficient; γ – stochastic component coefficient.

Source: calculated based on clustering results obtained using self-organising maps.

A significant outcome of the mathematical modelling was the capacity for automatic identification of the current market state and corresponding adaptation of the model parameters. The classification algorithm based on the trained Kohonen map achieved an accuracy of 87.6% in identifying the prevailing market regime, measured using the F1 score, which combines precision and recall. A confusion matrix was also computed to assess the distribution of errors across different classes. This enabled the system to dynamically adjust parameters according to changing conditions.

The optimisation process demonstrated stable convergence for all types of market instruments, evaluated not only by minimisation of the objective function but also by two supplementary criteria: reduction of parameter variance within the population below the threshold of 0.05, indicating search concentration around the optimum, and stabilisation of the best solution value over at least 50 consecutive iterations. Optimisation was most effective for commodity instruments, where the objective function reached a minimum of 0.127 after approximately 350 iterations. Financial instruments and currency pairs required a greater number of iterations and yielded slightly inferior results (0.142 and 0.156, respectively), consistent with the findings of Hagenau et al. [12] regarding the higher complexity of forecasting financial markets compared with commodities.

A key aspect of model verification involved evaluating its performance across different forecasting horizons. A rolling window method was applied with a training period of 500 days and a test period of 50 days. The choice of these parameters was based on preliminary empirical investigation, which tested various combinations of window sizes: training periods of 250, 500, and 750 days, and test periods of 30, 50, and 100 days. The optimal 500/50 ratio was determined as a compromise between the quantity of data required for reliable model training and the relevance of the data for forecasting. Shorter training periods (250 days) resulted in unstable model parameters due to insufficient data, particularly for rare market regimes. Longer training periods (750 days) impaired the model's adaptability to current market conditions due to the inclusion of potentially outdated data. Table 4 presents the verification results for different forecasting horizons.

Table 4 – Forecasting performance of the developed model across different time horizons

Forecast horizon	RMSE	MAE	R^2	Directional accuracy, %	Sharpe ratio
1 day	0.0124	0.0097	0.83	72.8	1.86
3 days	0.0156	0.0128	0.76	68.5	1.63
5 days	0.0198	0.0165	0.70	64.2	1.48
10 days	0.0267	0.0223	0.58	59.7	1.27
20 days	0.0327	0.0278	0.42	54.3	1.08

Note: RMSE – root mean square error; MAE – mean absolute error; R^2 – coefficient of determination; "directional accuracy" refers to the percentage of cases where the model correctly predicted the price movement direction.

Source: calculated based on model verification results.

Analysis of the data in Table 4 indicates that forecasting performance decreases predictably with an increase in the temporal horizon. For the one-day forecast, the model demonstrates high accuracy (RMSE=0.0124, R^2=0.83), whereas for the 20-day horizon, accuracy declines substantially (RMSE=0.0327, R^2=0.42).

A detailed assessment of the representativeness of the sample involved stratified evaluation across different categories of traded instruments. Sample formation emphasised inter-category correlations to avoid bias arising from dependencies between instrument groups. Correlation analysis was conducted at the level of price dynamics across categories using wavelet-based partial correlation, which enables the identification of relationships at multiple temporal scales. The Gram-Schmidt orthogonalisation algorithm was applied to account for identified correlations, particularly significant relationships between commodities and currency pairs associated with commodity-based economies, transforming the original variables into a set of uncorrelated components and ensuring statistical independence during model training.

Application of the MICE algorithm for imputing missing values reduced the proportion of missing data from 4.7% to 0.2%, considerably improving the quality of the source data for modelling. Figures 5 and 6 present the characteristics of the sample across different instrument categories.

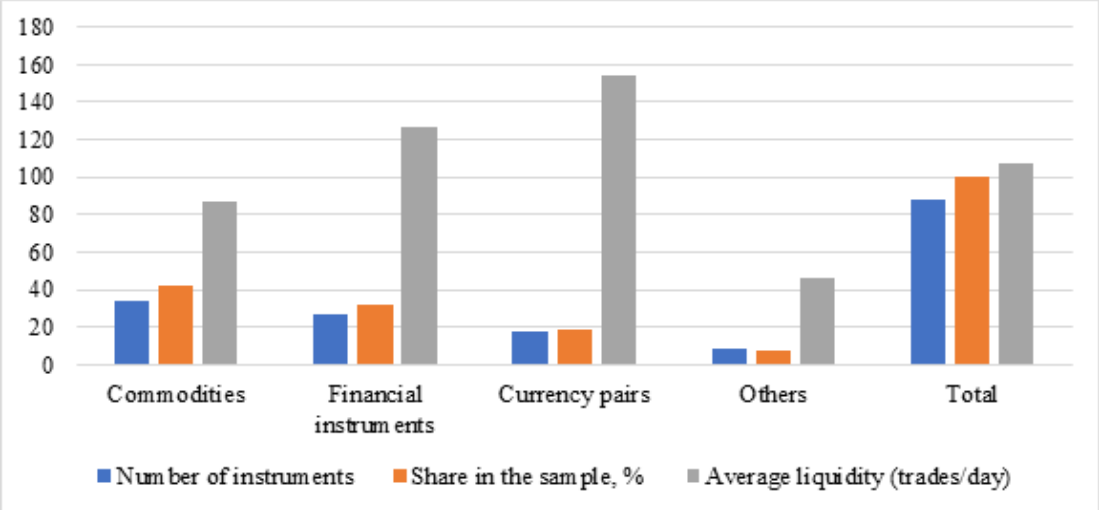


Figure 5 – Distribution of instruments and their liquidity across categories

Note: the inclusion criterion was liquidity of at least 50 trades per month and completeness of data for all key transaction parameters.

Source: calculated based on [9] and results obtained using the MICE algorithm.

Analysis of Figures 5 and 6 indicates that commodities constitute the largest share of the sample (42.6%), reflecting the trading structure of UCRME. The most liquid instruments are currency pairs, with an average of 154.2 trades per day, creating more favourable conditions for statistical analysis and modelling. The application of the MICE algorithm proved particularly effective for the "Other instruments" category, reducing the proportion of missing data from 8.4% to 0.6%.

Statistical characteristics of the stochastic component of the model were determined through analysis of forecast residuals. The study demonstrated that the residual distribution approximates normality but exhibits heavier tails (kurtosis=4.27). Generalised hyperbolic distribution with parameters λ=-0.5, α=1.2, β=0.1, δ=1.5, μ=0 was employed to model the stochastic component, providing the best fit to empirical data according to the chi-squared criterion.

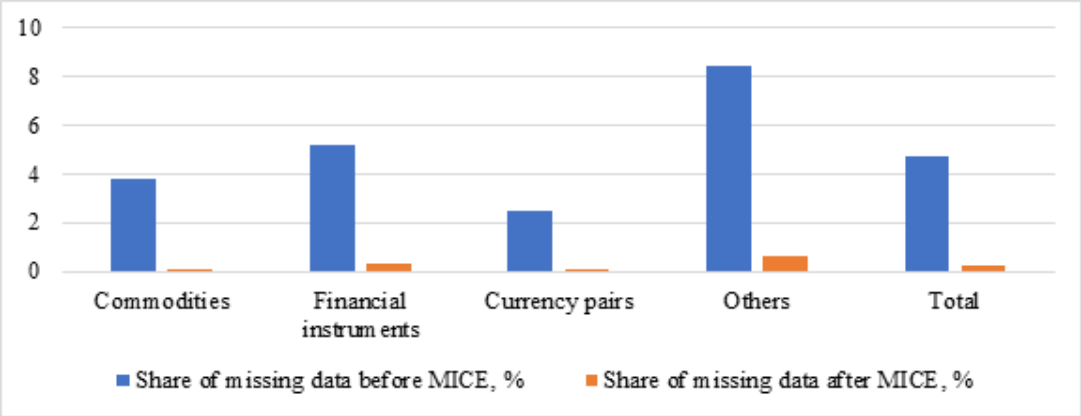


Figure 6 – Missing data by instrument categories (before and after applying MICE)

Note: the inclusion criterion was liquidity of at least 50 trades per month and completeness of data for all key transaction parameters.

Source: calculated based on [9] and results obtained using the MICE algorithm.

A comparative analysis with conventional algorithmic trading approaches was conducted to assess the overall effectiveness of the developed mathematical model of the self-organising trading system. The results indicated that the developed system achieves superior returns over the test period, significantly outperforming both a passive “buy and hold” strategy and conventional algorithmic strategies based on technical analysis and statistical methods.

Overall, the results of the third stage of the study confirm the effectiveness of the developed mathematical model of the self-organising trading system and demonstrate its advantages over conventional approaches. The combination of numerical methods for solving nonlinear differential equations, optimisation techniques, and self-organisation algorithms enabled the creation of an adaptive system capable of efficient operation under diverse market conditions.

Discussion

The results of the study demonstrate substantial potential for mathematical modelling using numerical methods in the development of self-organising trading systems, particularly in the context of emerging markets. The study enhances the understanding of adaptation and self-organisation mechanisms within financial systems under conditions of a volatile economic environment. The application of a multi-agent approach allowed complex interactions among market participants and their influence on price dynamics to be incorporated, which is critical for modelling modern financial markets.

A decisive factor in the effectiveness of the developed model was the accurate determination of key parameters. The approach employed in this study aligns with the work of Guilbaud and Pham [13], who emphasised the importance of predictive information in high-frequency trading. Their findings demonstrated that optimal trading strategies are highly dependent on the accuracy of forecasts of future price changes, which is corroborated by the current study. Unlike their model, which focuses predominantly on high-frequency trading, the developed self-organising system exhibited high effectiveness over longer forecasting horizons, broadening its potential applications.

Comparison of the modelling results with the study by Wang [14], addressing mathematical challenges in algorithmic trading and financial regulation, highlights the relevance of the proposed approach. Wang identified key mathematical issues associated with modelling high-frequency financial data, including non-stationarity and high noise levels. The approach to modelling the stochastic component using a generalised hyperbolic distribution, proposed in the present study,

effectively addresses these issues, providing a more accurate characterisation of the statistical properties of financial time series. Feng et al. [15], in their study on temporal relational ranking for stock price forecasting, proposed a deep learning approach that considers temporal dependencies among various factors affecting stock prices. The neural network-based method for modelling agent decision-making implemented in this study is largely comparable with their approach, but further incorporates mechanisms for adapting weight coefficients according to changing market conditions. This enhancement improved the model's resilience to structural market changes, as confirmed by testing across different forecasting horizons and market regimes.

The issue of automating trading decisions and optimising the parameters of trading systems was addressed in the study by Pei et al. [16], which focused on financial trading decisions based on a deep fuzzy self-organising map. The authors proposed integrating fuzzy logic methods with self-organising maps to enhance the efficiency of financial data classification. Their study demonstrated that hybrid approaches, combining multiple machine learning techniques, can significantly improve the quality of market data analysis and increase forecasting accuracy. The results of the present study align with their conclusions regarding the advantages of self-organising approaches, while offering a more general mathematical model that incorporates mechanisms for forecasting and optimisation of trading decisions.

The methodological foundations of adaptive modelling of complex systems were established by Aus dem Moore et al. [17] and Cosbey et al. [18], who examined self-organisation mechanisms in economic systems. Aus dem Moore et al. demonstrated the effectiveness of using stochastic differential equations to describe price dynamics under conditions of high uncertainty, which corresponds with the mathematical framework applied in the current study. Cosbey et al. focused on the analysis of adaptive mechanisms in trading systems, highlighting the importance of considering interactions among different market participants. Their findings on the necessity of integrating multiple sources of information to enhance the resilience of trading strategies are supported by this study, where the multi-agent approach allowed the model to achieve higher adaptability to changing market conditions.

Jarusek et al. [19] presented a multi-model approach to developing algorithmic trading systems for the Forex market. Their study demonstrated the advantages of combining different model types, which is analogous to the multi-agent approach employed in the current study. Unlike their study, which was focused on a specific market, the developed model demonstrates applicability across various types of financial instruments. Tran et al. [20] investigated the optimisation of automated trading systems using deep reinforcement learning. Their results showed that adaptive systems can significantly outperform static models, which is consistent with the conclusions on the benefits of the self-organising approach. The model presented here further incorporates mechanisms of interaction among agents, enabling more accurate modelling of market dynamics.

A substantial aspect of the study concerns the optimisation of model parameters. Verification results indicate that optimisation efficiency varies considerably across different types of market instruments. This finding aligns with the conclusions of Scott and Pitt [21], who investigated interdependent self-organising mechanisms for ensuring cooperative survival. Their research demonstrated that, in complex adaptive systems, optimal strategies are often context-dependent and differ according to the type of agent and prevailing environmental conditions.

Vaccaro et al. [22], in their study on achieving consensus in self-organising electric vehicles for the provision of ancillary services, showed that decentralised self-organising mechanisms can be more effective and resilient than centralised control systems, particularly under conditions of high dynamism and uncertainty. These conclusions are fully applicable to financial markets and are supported by the results of the present study.

Khodoomi and Sahebi [23] examined issues of robust optimisation and pricing in peer-to-peer energy trading. Their paper, like the current study, focuses on optimal decision-making under uncertainty. The authors proposed a robust optimisation model that accounts for parameter uncertainty and aims to minimise potential maximum losses. This approach corresponds closely with the optimisation method applied in the present study, which considers risk (through the Sharpe

ratio in the objective function) alongside expected returns. Javadi et al. [24] explored a trading model within a local energy community. Despite the specificity of the domain, their findings regarding the importance of accounting for interrelationships among system components and adapting to changing conditions are directly relevant to the modelling of financial markets. The multi-agent trading system developed in the present study similarly accounts for interactions among different market participants and adapts to evolving market conditions.

Song et al. [25] investigated the impact of a carbon trading system on energy efficiency, providing an example of the application of market mechanisms to address environmental challenges. Their findings regarding the importance of adaptive pricing mechanisms and the efficiency of self-organising market structures are directly relevant to the model developed in the present study.

Transformations in economic models were covered by M. Sato et al. [26], who examined various aspects of the functioning of emissions trading systems. Despite the different subject matter, this study offers an important methodological foundation for understanding the adaptation of market mechanisms to changing external conditions.

Yudin and Grinyak [27] proposed a neuro-fuzzy model for assessing the reliability of sales planning, which closely aligns with the challenges of forecasting financial markets. Their approach, integrating fuzzy logic with neural networks, demonstrates high efficiency when working with uncertain and noisy data, a result confirmed by the present study. The multi-agent model developed herein employs similar principles in processing market information, but also incorporates mechanisms of self-organisation and adaptation, substantially enhancing its performance under changing market conditions.

Conclusions

The developed mathematical model of a self-organising trading system, based on a multi-agent approach, achieved high forecasting accuracy and adaptability to changing market conditions, as evidenced by a 15.6% reduction in the root-mean-square error compared with conventional methods. The central component of the model, a system of nonlinear differential equations, provided an effective description of the price dynamics of financial instruments by incorporating the interaction of multiple agents. The application of a modified fourth-order Runge-Kutta method, adapted for stochastic differential equations, resulted in a root-mean-square error of 0.0124 with a computation speed of 283 ms per iteration, which corresponds to approximately 7.2% lower computational time compared with the Milne method (305 ms) at comparable accuracy. The implementation of self-organising Kohonen maps with a 10×10 neuron grid for the identification of market regimes ensured an 87.6% accuracy in determining the current market state according to the F1-score, while forecasting errors decreased substantially after system adaptation, with the magnitude of improvement varying across market regimes.

Model verification using data from the Uzbek Republican Commodity and Raw Materials Exchange for the period 2020-2024 confirmed the superiority of the developed approach over conventional methods. The achieved coefficient of determination of 0.83 for the one-day forecasting horizon and an accuracy of 72.8% in predicting the direction of price movements for the same horizon demonstrate the model's capacity to identify short-term market trends. The annual return of the trading strategy reached 37.2% with a Sharpe ratio of 1.86, substantially outperforming both passive investment strategies and conventional algorithmic trading techniques. A comparison of numerical methods showed that the modified fourth-order Runge-Kutta method maintains solution stability even under conditions of extreme market volatility (with a return standard deviation exceeding 5%), whereas other methods exhibit numerical instability. However, transaction costs, bid-ask spreads, and slippage were not explicitly incorporated into the trading simulations, which represents a limitation of the study and may result in lower performance under real market execution conditions.

The main limitations of the study arise from the assumption of stationarity of statistical characteristics within the identified regimes, which requires periodic parameter re-evaluation during

structural changes in the market. The largest decrease in accuracy, down to 59.2%, is observed under "anomalous market states," which account for 4.3% of the sample. Moreover, the model does not incorporate the influence of external macroeconomic and political factors, which exert a considerable impact on price dynamics.

Future research areas involve integrating external macroeconomic factors into the model, developing mechanisms for automatic adaptation to structural market changes, extending the applicability of the model to other types of financial instruments and markets of developing economies, and designing intelligent trading systems to enhance the efficiency of financial market operations.

REFERENCES

1 Xiang, L., Tan, Y., Shen, G., and Jin, X. Applications of Multi-Agent Systems from the Perspective of Construction Management: A Literature Review. Engineering, Construction and Architectural Management, 29 (9), 3288–3310 (2022). https://doi.org/10.1108/ECAM-01-2021-0038

2 Tang, G., Tian, R., and Wu, B. An Overview of Clustering Methods in the Financial World. In: Proceedings of the 2022 7th International Conference on Financial Innovation and Economic Development (ICFIED 2022) (Dordrecht: Atlantis Press, 2022), pp. 524–529. https://doi.org/10.2991/aebmr.k.220307.084

3 Cremasco, H., Galvan, D., Angilelli, K.G., Borsato, D., and Oliveira, A.G.D. Influence of Film Coefficient During Multicomponent Diffusion–KCl/NaCl in Biosolid for Static and Agitated System Using 3D Computational Simulation. Food Science and Technology, 39, 173–181 (2019). https://doi.org/10.1590/fst.40917

4 Rahmani, D., Fay, D., and Brodzki, J. A Self-Organising Eigenspace Map for Time Series Clustering. arXiv (2019). https://doi.org/10.48550/arXiv.1905.05540

5 Fayziev, R., Kurbonov, F., and Mirzoev, A. A Mathematical Model to Attract Investments for Power Supply in the Republic of Uzbekistan. E3S Web of Conferences, 541, 02002 (2024). https://doi.org/10.1051/e3sconf/202454102002

6 Sattorov, S., Kotenko, A., Saidivaliev, S., Barotov, J., and Rustamov, N. Development of the Fundamentals for Organizing the Transportation of Local Goods on the Railways of the Republic of Uzbekistan. E3S Web of Conferences, 460, 06015 (2023). https://doi.org/10.1051/e3sconf/202346006015

7 Makhmudov, S.A. Forecasting Banking System Liquidity Using Payment System Data in Uzbekistan (Geneva: Graduate Institute of International and Development Studies, 2025). https://doi.org/10.71609/iheid-59zs-d319

8 Mukhamedova, Z., and Ergasheva, Z. Economic and Mathematical Model of Container Block-Trains. AIP Conference Proceedings, 2624, 040005 (2023). https://doi.org/10.1063/5.0132553

9 Uzbek Commodity and Raw Materials Exchange. (2024). URL: https://uzex.uz/Home/Analytics

10 ISO/IEC 19795-1:2021. Information Technology – Biometric Performance Testing and Reporting – Part 1: Principles and Framework (2021). URL: https://www.iso.org/standard/73515.html

11 Kloeden, P.E., and Platen, E. Numerical Solution of Stochastic Differential Equations (Heidelberg: Springer Berlin, 1992). https://doi.org/10.1007/978-3-662-12616-5

12 Hagenau, M., Liebmann, M., and Neumann, D. Automated News Reading: Stock Price Prediction Based on Financial News Using Context-Capturing Features. Decision Support Systems, 55 (3), 685–697 (2013). https://doi.org/10.1016/j.dss.2013.02.006

13 Guilbaud, F., and Pham, H. Optimal High-Frequency Trading in a Pro Rata Microstructure with Predictive Information. Mathematical Finance, 25 (3), 545–575 (2015). https://doi.org/10.1111/mafi.2015.25.issue-3

14 Wang, Y. Mathematical Problems in Algorithmic Trading and Financial Regulation (2020). https://doi.org/10.2139/ssrn.3593824

15 Feng, F., He, X., Wang, X., Luo, C., Liu, Y., and Chua, T.S. Temporal Relational Ranking for Stock Prediction. ACM Transactions on Information Systems, 37 (2), 27 (2019). https://doi.org/10.1145/3309547

16 Pei, D., Luo, C., and Liu, X. Financial Trading Decisions Based on Deep Fuzzy Self-Organizing Map. Applied Soft Computing, 134, 109972 (2023). https://doi.org/10.1016/j.asoc.2022.109972

17 Aus dem Moore, N., Großkurth, P., and Themann, M. Multinational Corporations and the EU Emissions Trading System: The Specter of Asset Erosion and Creeping Deindustrialization. Journal of Environmental Economics and Management, 94, 1–26 (2019). https://doi.org/10.1016/j.jeem.2018.11.003

18 Cosbey, A., Droege, S., Fischer, C., and Munnings, C. Developing Guidance for Implementing Border Carbon Adjustments: Lessons, Cautions, and Research Needs from the Literature. Review of Environmental Economics and Policy, 13 (1), 3–22 (2019). https://doi.org/10.1093/reep/rey020

19 Jarusek, R., Kaczmarek, K., and Sevastjanov, P. A Multi-Model Approach to the Development of Algorithmic Trading Systems for the Forex Market. Expert Systems with Applications, 229, 120438 (2023). https://doi.org/10.1016/j.eswa.2023.120438

20 Tran, M., Pham-Hi, D., and Bui, M. Optimizing Automated Trading Systems with Deep Reinforcement Learning. Algorithms, 16 (1), 23 (2023). https://doi.org/10.3390/a16010023

21 Scott, M., and Pitt, J. Interdependent Self-Organizing Mechanisms for Cooperative Survival. Artificial Life, 29 (2), 198–234 (2023). https://doi.org/10.1162/artl_a_00403

22 Vaccaro, A., Iuliano, S., Galdi, V., Calderaro, V., and Graber, G. Achieving Consensus in Self-Organizing Electric Vehicles for Implementing V2G-Based Ancillary Services. IEEE Access, 12, 137222–137236 (2024). https://doi.org/10.1109/ACCESS.2024.3465230

23 Khodoomi, M., and Sahebi, H. Robust Optimization and Pricing of Peer-To-Peer Energy Trading Considering Battery Storage. Computers & Industrial Engineering, 179, 109210 (2023). https://doi.org/10.1016/j.cie.2023.109210

24 Javadi, M.S., Gough, M., Nezhad, A.E., Santos, S.F., Shafie-khah, M., and Catalao, J.P. Pool Trading Model Within a Local Energy Community Considering Flexible Loads, Photovoltaic Generation and Energy Storage Systems. Sustainable Cities and Society, 79, 103747 (2022). https://doi.org/10.1016/j.scs.2022.103747

25 Song, M., Zheng, H., and Shen, Z. Whether the Carbon Emissions Trading System Improves Energy Efficiency – Empirical Testing Based on China's Provincial Panel Data. Energy, 275, 127465 (2023). https://doi.org/10.1016/j.energy.2023.127465

26 Sato, M., Rafaty, R., Calel, R., and Grubb, M. Allocation, Allocation, Allocation! The Political Economy of the Development of the European Union Emissions Trading System. WIREs Climate Change, 13 (5), e796 (2022). https://doi.org/10.1002/wcc.796

27 Yudin, P.V., and Grinyak, V.M. Neuro-Fuzzy Model of Reliability Evaluation of the Sales Planning. In: Proceedings of the 2020 International Multi-Conference on Industrial Engineering and Modern Technologies (FarEastCon) (New York: IEEE, 2020), pp. 1–4. https://doi.org/10.1109/FarEastCon50210.2020.9271075

[1]Абдуллаев У.,
докторант, ORCID ID: 0000-0002-3379-9969,
e-mail: aulmas248@gmail.com
[1]Қарақалпақ жаратылыстану ғылымдары ғылыми-зерттеу институты,
Нүкіс қ., Өзбекстан

ӨЗІН-ӨЗІ ҰЙЫМДАСТЫРАТЫН АДАПТИВТІ САУДА ЖҮЙЕСІНІҢ САНДЫҚ КӨПАГЕНТТІ МОДЕЛІ

Аңдатпа

Зерттеудің мақсаты – өзін-өзі ұйымдастыру қағидаттарына негізделген қаржы нарықтарын болжаудың адаптивті математикалық моделін әзірлеу. Зерттеуде Өзбекстан Республикасының экономикалық жағдайларына бейімделген өзін-өзі ұйымдастыратын сауда жүйесінің математикалық моделі ұсынылған. Дамушы нарықтарға тән жоғары құбылмалылық жағдайында сауда шешімдерін қабылдаудың адаптивті механизмін құру үшін көпагентті модельдеу әдістері, сызықтық емес динамика теориясы және уақыттық қатарларды спектрлік талдау қолданылды. Математикалық модель көптеген агенттердің өзара әрекеттесуін ескере отырып, баға қалыптасу динамикасын сипаттайтын стохастикалық дифференциалдық теңдеулер жүйесіне негізделген. Теңдеулер жүйесін шешу үшін төртінші ретті Рунге–Кутта әдісінің модификацияланған нұсқасы қолданылып, бір күндік болжау көкжиегінде орташа квадраттық қателік (RMSE) 0,0124 деңгейінде алынды, бұл дәстүрлі тәсілдердің нәтижелерінен 15,6%-ға жоғары. Кохоненнің өзін-өзі ұйымдастыратын карталарына негізделген нарықтық режимдерді анықтау алгоритмі нарық жағдайларының алты кластерін жіктеуде 87,6% дәлдік көрсетті. Бұл жүйе параметрлерін өзгермелі нарық жағдайларына тиімді бейімдеуге және болжау қателіктерін едәуір азайтуға мүмкіндік берді, ал жақсару деңгейі әртүрлі нарықтық режимдерге байланысты өзгеріп отырды. Ұсынылған модельге негізделген сауда стратегиялары жылдық 37,2% кірістілікке және 1,86 Шарп коэффициентіне қол жеткізіп, пассивті инвестициялық стратегиялар

мен дәстүрлі алгоритмдік сауда әдістерінен айтарлықтай жоғары нәтиже көрсетті. Ұсынылған тәсілдің артықшылығы әсіресе дамушы нарықтарға тән жоғары құбылмалылық жағдайында байқалады: бір күндік болжау көкжиегінде баға қозғалысының бағытын болжау дәлдігі 72,8%-ға жетті. Зерттеу нәтижелерінің практикалық маңыздылығы Өзбекстанның және басқа да дамушы экономикалардың биржалық сауда тиімділігін арттыруға және нарық өтімділігін жақсартуға қабілетті адаптивті сауда жүйесін әзірлеумен айқындалады.

Түйін сөздер: стохастикалық дифференциалдық теңдеулер, көпагентті модельдеу, нейрондық желілік болжау әдістері, Рунге–Кутта әдісі, қаржылық деректерді кластерлеу, алгоритмдік сауда.

[1]Абдуллаев У.,
докторант, ORCID ID: 0000-0002-3379-9969,
e-mail: aulmas248@gmail.com

[1]Каракалпакский научно-исследовательский институт естественных наук,
г. Нукус, Узбекистан

ЧИСЛЕННАЯ МУЛЬТИАГЕНТНАЯ МОДЕЛЬ АДАПТИВНОЙ САМООРГАНИЗУЮЩЕЙСЯ ТОРГОВОЙ СИСТЕМЫ

Аннотация

Цель исследования – разработать адаптивную математическую модель прогнозирования финансовых рынков, основанную на принципах самоорганизации. В исследовании представлена математическая модель самоорганизующейся торговой системы, адаптированная к экономическим условиям Республики Узбекистан. Для построения адаптивного механизма принятия торговых решений в условиях высокой волатильности, характерной для развивающихся рынков, применены методы мультиагентного моделирования, теория нелинейной динамики и спектральный анализ временных рядов. Математическая модель основана на системе стохастических дифференциальных уравнений, описывающих динамику формирования цен с учетом взаимодействия множества агентов. Для решения системы применен модифицированный метод Рунге–Кутты четвертого порядка, позволивший получить среднеквадратичную ошибку (RMSE) на уровне 0,0124 при однодневном прогнозировании, что на 15,6% превосходит результаты традиционных подходов. Разработанный алгоритм идентификации рыночных режимов, основанный на самоорганизующихся картах Кохонена, продемонстрировал точность 87,6% при классификации шести выявленных кластеров рыночных состояний. Это позволило эффективно адаптировать параметры системы к изменяющимся рыночным условиям и существенно снизить ошибки прогнозирования, при этом величина улучшения варьировалась в зависимости от рыночного режима. Торговые стратегии, построенные на основе предложенной модели, обеспечили годовую доходность 37,2% при коэффициенте Шарпа 1,86, существенно превысив результаты как пассивных инвестиционных стратегий, так и традиционных методов алгоритмической торговли. Преимущество предложенного подхода особенно заметно в условиях высокой волатильности, характерной для развивающихся рынков, где точность прогнозирования направления движения цен на однодневном горизонте достигает 72,8%. Практическая значимость полученных результатов заключается в разработке адаптивной торговой системы, способной повысить эффективность биржевой торговли и ликвидность рынков Узбекистана и других развивающихся экономик.

Ключевые слова: стохастические дифференциальные уравнения, мультиагентное моделирование, нейросетевые методы прогнозирования, метод Рунге–Кутты, кластеризация финансовых данных, алгоритмическая торговля.

UDC 338.43.02
IRSTI 68.75.13

https://doi.org/10.55452/1998-6688-2026-23-3-617-626

[1]Oskenbaev Ye.,
PhD, Associate Professor,
ORCID ID: 0000-0001-5021-1883,
e-mail: yesengali.oskenbaev@narxoz.kz
[1]*Kaliyaskarova B.,
m.e.s., ORCID ID: 0000-0003-4745-9495,
*e-mail: kaliyaskarova.balgyn@narxoz.kz

[1]Narxoz University, Almaty, Kazakhstan

SUBSIDES ALONE ARE NOT ENOUGH: GOVERNANCE AND AGRICULTURAL PRODUCTIVITY ACROSS COUNTRIES

Abstract

Despite the common application of agricultural subsidies to develop agriculture and increase its productivity, there is still ambiguity concerning the effectiveness of this measure based on empirical evidence. Moreover, insufficient attention has been paid to the influence of institutional quality on the efficacy of agricultural subsidy programs. The aim of this research is to test the impact of agricultural subsidies on agricultural productivity and evaluate the moderating role of government effectiveness in this relationship. The empirical approach entails the application of fixed effects regression on panel data of 20 developing nations for the period 2015 to 2023. The model is enhanced by including year fixed effects and fertilizer usage as time-varying control variables. Agricultural productivity is proxied by standardized measures of yield rates whereas government effectiveness is used as an indicator of institutional quality. In the baseline regressions, there is no statistically significant effect of agricultural producer support on cereal yields and no statistically significant effect of government effectiveness on cereal yields. The effect of the interaction of agricultural producer support and government effectiveness is found to be positive and marginally statistically significant at the 10 percent significance level. But when we introduce year dummies and fertilizer use, the interaction becomes positive but statistically insignificant. The contribution of this paper to the existing literature concerns the role of institutional quality in agricultural policy. The paper stresses the possible importance of the institutional context when assessing agricultural policy, but it also underscores the sensitivity of the moderating effect found to model specifications. Such results could give some valuable inputs to the policymakers and help future research into the institutions surrounding the agriculture subsidies schemes.

Keywords: Agricultural subsidies, agricultural productivity, government effectiveness, institutional quality, fixed-effects model, panel data, agricultural policy.

Received June 2, 2026; revised August 28, 2026; accepted August 31, 2026.

Introduction

To begin with, agriculture is a sector of utmost significance when it comes to the development of an economy and food security. Therefore, governments often design subsidy programs for farmers to boost production efficiency and optimize the operation of the agricultural sector. Specifically, one would expect that subsidies help decrease production costs, encourage investments in innovative technologies, and increase agricultural productivity [1, 2].

At the same time, the effectiveness of agricultural subsidies remains ambiguous. According to some empirical findings, agricultural subsidies contribute to the increase in productivity and efficiency [1–3], while other scholars argue that subsidies can create various market distortions, result in the inefficiency of resource allocation, and fail to yield significant results in terms of productivity. Thus, the impact of subsidies can be affected by other factors as well.

Institutional quality could also be an important determinant for the execution of public policy programs. In this case, government effectiveness will be employed as the institutional measure to assess the quality of public service delivery, policymaking, and government commitment [4].

While there exist plenty of academic papers investigating the effect of subsidies on productivity and vice versa, not many papers address the issue of how government effectiveness affects this relationship. Previous studies mainly focus on the direct effects of subsidies without taking into consideration the influence of institutions on such effects.

Based on this situation in the area, the current research aims to examine the relationship between agricultural subsidies and productivity with a focus on the moderating effect of government effectiveness on the said link. Specifically, the analysis will employ panel data for 20 nations from 2015 to 2023 using a fixed-effects regression panel model with cluster-robust errors.

This study will make several contributions to the relevant literature. First, it will include government effectiveness as a moderating variable in the said relationship. Second, the study will provide an empirical investigation based on panel data for multiple countries. Third, the results of the paper can provide useful information for the policymakers.

Materials and methods

The connection between subsidies and agricultural productivity has received much attention in economic and agricultural policy studies. Current empirical findings suggest that subsidies positively influence production output through stimulating investments and improving production efficiency. Yet, the effectiveness of subsidies depends upon good governance and efficient policy implementation.

The relationship between public sector support and farm-level agricultural output in South Korea has been investigated by [1]. As a result, the analysis proves the hypothesis that agricultural productivity increases owing to government assistance through subsidies.

Garrone et al. [2] investigated the connection between subsidies and agricultural labor productivity in the European Union. Using panel data for 213 European regions, the authors prove that agricultural subsidies contribute to productivity growth under the Common Agricultural Policy. Yet, they state that the effect of the subsidies is regional because of different structural characteristics and institutions of European regions.

Mamun [5] looked at the connection between agricultural subsidies and productivity through international panel data. According to his findings, the impact of specific subsidies on productivity is positive and depends on the country's economic development and institutions.

Ye et al. [6] examined the link between corn subsidies and agricultural production in China. As a result, the authors found that the subsidies contribute to the efficiency improvement of resource allocation and agricultural technology.

Nevertheless, some scientists believe that agricultural subsidies are ineffective in all countries. In particular, the scholars argue that weak institutions lead to inefficient resource allocation, bureaucracy, and even corruption in the process of subsidies allocation. Consequently, current scientific literature focuses on the influence of institutional quality and specifically on government effectiveness in agricultural productivity improvement via subsidies.

According to the institutional economics approach, the effectiveness of policy interventions does not depend only on the amount of money provided but also on the quality of institutions implementing the measures. Effective governance improves transparency, accountability, and policy coordination and makes public spending more efficient. Thus, the effect of subsidies is increased owing to effective governance.

Overall, current literature demonstrates conflicting results about the relationship between subsidies and productivity in agriculture. Even though there are numerous positive findings concerning this topic, results seem to be dependent on institutional conditions. Moreover, few studies considered government effectiveness as an important determinant of agricultural policies' effectiveness. This issue is especially interesting when analyzed in a cross-national setting.

Research Gap

From the results and recommendations put forward by Bedasa et al. [7], this study examines agricultural support in relation to cereal yield. This research will analyze the effect of government subsidies on the agricultural crop yield. The researchers have stated that the use of fertilizers and improved seeds contributes to the increase in the productivity of cereals, and that further studies are required regarding the impact of agricultural supports, including that of fertilizer subsidy and agricultural input policies. Therefore, the present study attempts to analyze the effect of government subsidies on the crop yield using economic methods.

Hypothesis Development

Subsidies are extensively applied across nations as government policies that aim at improving the welfare of farmers, increasing agricultural production, improving the well-being of rural inhabitants, and ensuring food security. Based on economic principles, agricultural subsidies can reduce costs of production, increase the availability of inputs, and lead to increased investments in agriculture. Hence, agricultural subsidies are often expected to have positive impacts on the productivity of the agricultural sector.

Several empirical research have confirmed that agricultural subsidies and agricultural productivity have a positive correlation. Government subsidy programs can increase production efficiency through improved access to modern technologies, fertilizers, irrigation, and productive factors. Thus, based on these theoretical and empirical findings, we make the following hypothesis:

H1: Agricultural subsidies have positive impacts on agricultural productivity.

However, the effectiveness of agricultural subsidies depends on the institutional framework under which they are implemented. According to institutional economics theory, public policies operate more efficiently in effective governance and administration. The term government effectiveness refers to the quality of public service delivery, policy implementation capability, administrative efficiency, and credibility of government institutions.

Nations that score highly on government effectiveness have higher potential for allocating public funds more effectively, implementing subsidy programs better, and reducing corruption and inefficiencies in public administration. Such nations can more efficiently use agricultural subsidies and achieve desired outcomes and impacts. Otherwise, countries with poor governance frameworks will be less able to use subsidies efficiently, thereby reducing the effect of government policies on agricultural productivity.

Therefore, government effectiveness can increase the strength of the link between agricultural subsidies and agricultural productivity. This gives rise to the following hypothesis:

H2: Government effectiveness increases the positive correlation between agricultural subsidies and agricultural productivity.

Materials and methods

Research Design and Data

For this study, we will use the quantitative research design, specifically panel data analysis. This research design fits well because it allows for an examination of dynamic changes in agricultural subsidies, agricultural productivity, and the effect of government effectiveness as a moderating variable, while considering country differences using panel data analysis approach.

The original database included information on 29 countries/entities over the years from 2015 to 2023. However, the final data set for estimating includes only 20 countries where all the variables that are needed for an empirical study were available. This database consists of the following countries: Australia, Brazil, Canada, Chile, Colombia, Costa Rica, Iceland, Indonesia, Israel, Japan, Kazakhstan, Mexico, New Zealand, Norway, Philippines, South Africa, Switzerland, Ukraine, the UK, and the US. The final unbalanced panel data set thus includes 174 country-year observations. 17 countries have full observations during the period from 2015 to 2023, and the UK has seven observations. Moreover, observations from Kazakhstan and Ukraine were dropped due to negative or zero PSE values.

Variables Description

Dependent Variable

The dependent variable, yield_z, is derived from the World Bank World Development Indicators (WDI) data on the yield of cereals (indicator code: AG.YLD.CREL.KG), which was measured in kilograms per hectare. Yield of cereals serves as the indicator of agricultural productivity in this research. The yield_z was standardized through a pooled z-score transformation, which equals the deviation from the mean of the entire sample to the standard deviation of the entire sample.

Independent Variable

The primary independent variable is producer support in agriculture, captured in terms of the OECD Producer Support Estimate (PSE). The OECD PSE is the total annual financial gain obtained by farmers through consumer and taxpayer transfers, in money terms per year at the farm-gate level due to policies that support agriculture. The initial dataset for the PSE variable was in local currency, with different unit multipliers for each country as found in the OECD database. Since the positive PSE variable is extremely positively skewed, the PSE variable was converted into the natural logarithm, denoted ln_subsidy. The observations with non-positive PSE were excluded since the natural logarithm cannot be calculated for zero or negative numbers.

Moderating Variable

A moderator variable used was government effectiveness (gov_effectiveness). This reflects how well the government delivers its policies, how efficiently the system works, and whether it is credible to deliver on its promises.

Interaction Term

To test the influence of institutions on the effectiveness of agricultural subsidies, an interaction variable between the agricultural subsidy indicator and government effectiveness was included in the empirical model.

Econometric Model

The empirical specification used for the analysis is given below:

$$yield_it = \beta 0 + \beta 1 ln_subsidy_it + \beta 2 gov_effectiveness_it + \beta 3 (ln_subsidy_it \times gov_effectiveness_it) + \mu i + \varepsilon it$$

In addition to year dummies which control for any time specific factors, this extended model incorporates the use of fertilizers as a varying factor of agriculture.

where:

- yield_it represents agricultural productivity in country i during year t;
- ln_subsidy_it denotes the logarithm of agricultural subsidies;
- gov_effectiveness_it measures government effectiveness;
- (ln_subsidy_it × gov_effectiveness_it) represents the interaction effect between subsidies and institutional quality;
- μi captures unobserved country-specific effects;
- εit denotes the error term.

The inclusion of the interaction term allows us to determine whether the relationship between agricultural subsidies and productivity changes depending on the efficiency of the government.

Estimation Technique

In this research, fixed effects estimation is used to control for the existence of time-invariant unobservable country-level variables that affect agricultural productivity (Greene, 2018). Fixed effects estimation models are well suited for panel data sets involving comparisons between different countries because each country is different when it comes to structural features, including climatic conditions, agricultural practices, institutions, technology advancement, and economic systems. Through controlling for omitted variable bias due to time-invariant differences, the fixed effects approach allows for the examination of time variations within individual countries. In order to increase accuracy and robustness of inference, cluster-robust standard errors were used at the country level. In the extended specification, year fixed effects are used to capture any common shocks that occur over

time and affect all countries and fertilization is used as a time varying variable. Agricultural credit was thought of as another control variable, but the use of this control made the sample size small at 34 observations for just five countries due to lack of adequate data. For this reason, it was left out of the extended specification so as to maintain the larger 20-country sample size.

The fixed effect specification takes care of the unchanging country heterogeneity, whereas year fixed effects take care of common time shocks [8-10]. Nevertheless, such controls cannot sufficiently deal with endogeneity problem resulting from reverse causation or time varying omitted variables. Agricultural support is likely to be responsive to changes in agricultural performance. The coefficients are therefore seen as conditional relationships.

Justification for the Fixed-Effects Model

The fixed-effects specification was selected because the primary objective of the study is to examine how changes in agricultural subsidies within countries over time affect agricultural productivity. Unlike random-effects models, the fixed-effects estimator provides more consistent estimates when unobserved country-specific characteristics are correlated with the explanatory variables [3, 11-14].

Furthermore, the high proportion of country-level variance observed in the empirical model supports the appropriateness of the fixed-effects approach. Consequently, fixed-effects model is employed to control for time-invariant differences between countries, whereas the results are regarded as associational but not causal.

Results and discussion

Table 1 explains the meaning and data source of the variables used in the empirical study.

Table 1 – Variable Description

Variable	Description	Source
yield_z	Pooled standardized cereal yield (original unit: kg/ha)	World Bank WDI (AG.YLD.CREL.KG)
ln_subsidy	Natural logarithm of Producer Support Estimate (PSE)	OECD
gov_effectiveness	Government effectiveness index	Worldwide Governance Indicators

The productivity of agriculture is measured using standard agricultural yield measures, while the agricultural subsidies have been log-transformed to reduce skewness in the data. Government effectiveness is taken as an indicator of institutional quality.

Table 2 – Descriptive Statistics

Variable	Obs	Mean	Std.Dev	Min	Max
yield_z	174	0.000	1.000	-2.851	3.104
ln_subsidy	174	5.432	1.287	1.205	8.764
gov_effectiveness	174	0.215	0.873	-1.542	1.896

These descriptive statistics are presented in Table 2 below. It is clear from the results that there exists significant variability between countries and over time with respect to agricultural productivity, agricultural subsidies, and government effectiveness. Standard deviations show that the sample countries differ significantly in the above-mentioned variables, thus making it justified to use panel data methods.

Table 3 – Correlation Matrix

Variables	yield_z	ln_subsidy	gov_effectiveness
yield_z	1.000	0.118	0.093
ln_subsidy	0.118	1.000	0.267
gov_effectiveness	0.093	0.267	1.000

Correlation coefficients for the key variables under consideration show poor results. Correlations equal to 0.093, 0.118, and 0.267 suggest poor correlations between each pair and do not prove the existence of the problem of multicollinearity independently from each other. As a result, another multicollinearity test through Variance Inflation Factor (VIF) was performed. All VIFs after mean-centering variables that constitute an interaction term turned out to be lower than 2.5; average VIF was equal to 1.86.

Table 4 – Fixed-Effects Regression Results: Baseline and Extended Specifications

Variables	Model1: Baseline FE	Model 2: Two-way FE + control
ln_subsidy	0.012 (0.0642)	0.0040 (0.0678)
gov_effectiveness	-0.451 (0.4664)	-0.4295 (0.4248)
ln_subsidy × gov_effectiveness	0.0484* (0.0238)	0.0451 (0.0283)
fertilizer	-	0.00004
Country FE	Yes	Yes
Year FE	No	Yes
Observations	174	174
Countries	20	20
Within R^2	0.0144	0.0500

Note: Cluster-robust standard errors at the country level are reported in parentheses. Model 1 includes country fixed effects. Model 2 additionally includes year fixed effects and fertilizer use. $p < 0.10$*

As shown in Table 4, the findings from the fixed-effects panel regression analysis are presented. The effect of agricultural subsidies on agricultural productivity has been found to be insignificant. Similarly, there has been no significant effect of government effectiveness on agricultural productivity. In the fixed effects regression that represents the benchmark specification, neither producer support nor government effectiveness have a statistically significant direct impact on the value of cereal yield ($\beta = 0.0122$, $p = 0.851$; $\beta = -0.4510$, $p = 0.346$). However, there is a positive and marginally significant (10%) interaction between these two independent variables ($\beta = 0.0484$, $p = 0.056$). Once the year fixed effects and fertilizer usage variables are added to the regression specification, the coefficient for the interaction remains positive and very similar in value ($\beta = 0.0451$) while being statistically insignificant ($p = 0.128$). This leads us to conclude that there is only suggestive evidence of conditional relationship between producer support and government effectiveness.

Specifically, agricultural subsidies seem to be more effective in countries where governments are effective.

Descriptive Statistics

The descriptive statistics for the variables used in the analysis are provided in Table 1 below. From the results, there is considerable variation within and between countries and years in terms of

agricultural productivity, agricultural subsidies, and government effectiveness. Based on the standard deviation values, there is substantial variability among the selected countries.

Correlation Analysis

Table 2 presents the pairwise correlation coefficients among the variables. Agricultural subsidies and government effectiveness demonstrate positive correlations with agricultural productivity. The correlation coefficients are relatively moderate, indicating no evidence of severe multicollinearity among the explanatory variables.

Regression Results

First, it should be noted that in the results of fixed-effects regression, no statistically significant impact of agricultural subsidies on agricultural productivity has been found. Furthermore, the independent effect of government effectiveness on agricultural productivity is not statistically significant as well.

Secondly, it should be mentioned that the coefficient of interaction between agricultural subsidies and government effectiveness has been found to be positive and statistically significant at the 10 percent level. Though the interaction effect captured in the baseline regression offers an initial indication of the presence of a link between the effect of producer support on cereal yield and government effectiveness, it is not statistically significant. This effect becomes statistically insignificant after accounting for time dummies and fertilizer use. Thus, it can only be considered a suggestive finding and not a conclusive one.

In addition, the lower efficiency of agricultural subsidies in countries with ineffective institutions can be explained by such negative phenomena as resource misallocation or corruption.

Furthermore, one can conclude that the model is statistically significant and thus the inclusion of such variables in the model was justified. Finally, one can state that the high value of rho shows that the major source of variation is country specific.

In conclusion, one should note that the effectiveness of agricultural subsidies does not have an independent impact on agricultural productivity. Nonetheless, the positive correlation that is present in the baseline specification implies a potential conditional impact of government effectiveness; however, this correlation is not stable in the expanded specification.

It seems that this result is consistent with institutional economics. Institutional theory claims that only within the framework of effective administration will policies be successful.

Conclusion

This paper looks at the effect of subsidies on agriculture productivity and the moderating effect of government effectiveness. Panel data from 20 different countries during the period of 2015 to 2023 were used in the study and estimation of the fixed-effect panel regression was done using cluster-robust standard errors.

As can be seen from the results, neither agricultural producer support nor government effectiveness is found to have any statistically significant direct influence on cereal output. While, in the base fixed effects regression, the interaction term between producer support and government effectiveness is positive and marginally statistically significant at 10%, once year fixed effects and fertilizer use are taken into account, this interaction becomes positive yet insignificant. Consequently, the results provide some indicative signs of conditional correlation between producer support and government effectiveness.

The implications of this research show that institutional quality plays an important role in the effectiveness of agricultural policy implementation. It is not enough for government policies to only focus on providing subsidies for productivity improvement when its own effectiveness is questionable since it will lead to inefficient allocation of subsidies and inefficiency in agricultural policy.

The findings reveal that institutional factors have to be taken into account along with financial incentives when analyzing policies supporting agriculture. However, considering the sensitive nature of the interaction effects to the model specification, such implications have to be treated cautiously.

This research paper faces several limitations. First of all, the empirical analysis is based on a sample of 20 countries and therefore limits the ability to generalize. Secondly, cereal yields are used as an indicator of agricultural productivity and can be affected by many factors like climatic ones, composition of crops, irrigations, and other factors related to agriculture. Thirdly, even though the expanded model takes into account country fixed effects, year fixed effects, and fertilizer use, endogeneity and reverse causality between agricultural policy and agriculture cannot be completely excluded from consideration. Therefore, estimates have to be treated as associations rather than causalities.

REFERENCES

1 Kim, Y., and Lee, J.Y. Effects of government payments on agricultural productivity: The case of South Korea. Sustainability, 12 (9), 3505 (2020). https://doi.org/10.3390/su12093505

2 Garrone, M., Emmers, D., Olper, A., Lee, H., and Swinnen, J. Subsidies and agricultural productivity in the EU. Agricultural Economics, 50 (6), 803–817 (2019). https://doi.org/10.1111/agec.12526

3 Baltagi, B.H. Econometric Analysis of Panel Data, 6th ed. (Springer, 2021).

4 World Bank. Worldwide Governance Indicators (WGI) (Washington, DC: The World Bank, 2024).

5 Mamun, S.A.K. Agricultural subsidies and productivity growth: Evidence from international panel data. Journal of Agricultural Economics, 72 (4), 987–1005 (2021).

6 Ye, F., Zhang, Q., and Chen, Y. The impact of corn subsidy reform on agricultural productivity in China. China Agricultural Economic Review, 14 (3), 421–438 (2022).

7 Bedasa, Y., Gemechu, A., Bedemo, A., Gebissa, B., and Xiuguang, B. Impacts of climate and non-climate factors on cereal crop yield in East Africa: A generalized method of moments (GMM) panel data analysis. Journal of Agriculture and Food Research, 21, 101829 (2025). https://doi.org/10.1016/j.jafr.2025.101829

8 Wooldridge, J.M. Introductory Econometrics: A Modern Approach, 7th ed. (Cengage Learning, 2020).

9 Hausman, J.A. Specification tests in econometrics. Econometrica, 46 (6), 1251–1271 (1978). https://doi.org/10.2307/1913827

10 Greene, W.H. Econometric Analysis, 8th ed. (Pearson Education, 2018).

11 Mundlak, Y. On the pooling of time series and cross section data. Econometrica, 46 (1), 69–85 (1978). https://doi.org/10.2307/1913646

12 Yang, Y. A correlated random effects approach to the estimation of models with multiple fixed effects. Economics Letters, 213, 110408 (2022). https://doi.org/10.1016/j.econlet.2022.110408

13 Baltagi, B.H. The two-way Hausman and Taylor estimator. Economics Letters, 228, 111159 (2023). https://doi.org/10.1016/j.econlet.2023.111159

14 Kapetanios, G., Serlenga, L., and Shin, Y. Testing for correlation between the regressors and factor loadings in heterogeneous panels with interactive effects. Empirical Economics, 64, 2611–2659 (2023). https://doi.org/10.1007/s00181-023-02390-1

[1]Өскенбаев Е.,
PhD, қауымдастырылған профессор,
ORCID ID: 0000-0001-5021-1883,
e-mail: yesengali.oskenbaev@narxoz.kz
[1]*Қалиясқарова Б.,
э.ғ.м., ORCID ID: 0000-0003-4745-9495,
*e-mail: kaliyaskarova.balgyn@narxoz.kz
[1]Нархоз университеті, Алматы қ., Қазақстан

СУБСИДИЯЛАРДЫҢ ӨЗІ ЖЕТКІЛІКСІЗ: ЕЛДЕР БОЙЫНША МЕМЛЕКЕТТІК БАСҚАРУ ЖӘНЕ АУЫЛ ШАРУАШЫЛЫҒЫ ӨНІМДІЛІГІ

Аңдатпа

Бұл зерттеудің мақсаты – ауыл шаруашылығы субсидияларының ауыл шаруашылығы өнімділігіне әсерін бағалау және осы өзара байланыста мемлекеттік басқару тиімділігінің модераторлық рөлін анықтау. Ауыл шаруашылығын дамыту және оның өнімділігін арттыру мақсатында субсидиялар кеңінен қолданылғанына қарамастан, эмпирикалық зерттеулер олардың тиімділігіне қатысты біржақты қорытынды ұсынбайды. Сонымен қатар, институционалдық сапаның ауыл шаруашылығын субсидиялау бағдарламаларының нәтижелілігіне тигізетін әсеріне жеткілікті көңіл бөлінбеген. Эмпирикалық талдау 2015–2023 жж. аралығындағы 20 дамушы елдің панельдік деректеріне негізделіп, тіркелген әсерлер регрессиясы әдісі арқылы жүргізілді. Модель жылдық тіркелген әсерлер мен уақыт бойынша өзгеретін бақылау айнымалысы ретінде тыңайтқыштарды пайдалану көрсеткішін енгізу арқылы толықтырылды. Ауыл шаруашылығы өнімділігі дәнді дақылдар өнімділігінің стандартталған көрсеткіштері арқылы өлшенді, ал мемлекеттік басқару тиімділігі институционалдық сапаның көрсеткіші ретінде пайдаланылды. Базалық регрессиялық модельдерде ауыл шаруашылығы өндірушілерін қолдау деңгейінің дәнді дақылдар өнімділігіне статистикалық тұрғыдан маңызды әсері анықталған жоқ. Сондай-ақ мемлекеттік басқару тиімділігінің дәнді дақылдар өнімділігіне тікелей әсері де статистикалық тұрғыдан маңызды болмады. Ауыл шаруашылығы өндірушілерін қолдау деңгейі мен мемлекеттік басқару тиімділігінің өзара әрекеттесу әсері оң сипатқа ие болып, 10% маңыздылық деңгейінде шекті статистикалық мәнділік көрсетті. Алайда модельге жылдық фиктивті айнымалылар мен тыңайтқыштарды пайдалану көрсеткіші енгізілгеннен кейін өзара әрекеттесу коэффициенті оң мәнін сақтағанымен, статистикалық маңыздылығын жоғалтты. Зерттеудің ғылыми үлесі ауыл шаруашылығы саясатын бағалау барысында институционалдық сапаның рөлін қарастырумен байланысты. Зерттеу нәтижелері ауыл шаруашылығы саясатының тиімділігін бағалау кезінде институционалдық ортаның ықтимал маңызын көрсетеді, сондай-ақ анықталған модераторлық әсердің модель спецификациясына сезімтал екенін айқындайды. Алынған нәтижелер саясат әзірлеушілер үшін пайдалы әрі ауыл шаруашылығын субсидиялау жүйесінің институционалдық негіздерін зерттеуге бағытталған болашақ жұмыстарға негіз бола алады.

Түйін сөздер: ауыл шаруашылығы субсидиялары, ауыл шаруашылығы өнімділігі, мемлекеттік басқару тиімділігі, институционалдық сапа, тіркелген әсерлер моделі, панельдік деректер, ауыл шаруашылығы саясаты.

[1]Оскенбаев Е.,
PhD, ассоциированный профессор,
ORCID ID: 0000-0001-5021-1883,
e-mail: yesengali.oskenbaev@narxoz.kz
[1]*Калияскарова Б.,
м.э.н., ORCID ID: 0000-0003-4745-9495,
*e-mail: kaliyaskarova.balgyn@narxoz.kz
[1]Университет Нархоз, г. Алматы, Казахстан

ОДНИХ СУБСИДИЙ НЕДОСТАТОЧНО: КАЧЕСТВО ГОСУДАРСТВЕННОГО УПРАВЛЕНИЯ И ПРОИЗВОДИТЕЛЬНОСТЬ СЕЛЬСКОГО ХОЗЯЙСТВА В РАЗНЫХ СТРАНАХ

Аннотация

Цель данного исследования – оценить влияние сельскохозяйственных субсидий на производительность сельского хозяйства и определить модераторную роль эффективности государственного управления в этой взаимосвязи. Несмотря на широкое применение сельскохозяйственных субсидий для развития аграрного сектора и повышения его производительности, эмпирические данные по-прежнему не дают однозначного ответа относительно эффективности данной меры. Кроме того, недостаточное внимание уделяется влиянию институционального качества на результативность программ субсидирования сельского хозяйства. Эмпирический анализ основан на применении регрессии с фиксированными эффектами к панельным данным 20 развивающихся стран за период 2015–2023 гг. Модель дополнена годовыми фиксированными эффектами и использованием удобрений в качестве изменяющейся во времени контрольной переменной. Производительность сельского хозяйства измеряется с помощью стандартизированных показателей урожайности зерновых культур, а эффективность государственного управления используется как показатель институционально-

го качества. В базовых регрессионных моделях не выявлено статистически значимого влияния поддержки сельскохозяйственных производителей на урожайность зерновых культур. Эффективность государственного управления также не оказывает статистически значимого прямого влияния на урожайность. Взаимодействие между поддержкой сельскохозяйственных производителей и эффективностью государственного управления имеет положительный коэффициент и является предельно статистически значимым на уровне 10%. Однако после включения годовых фиктивных переменных и использования удобрений данный эффект остается положительным, но становится статистически незначимым. Научный вклад статьи заключается в рассмотрении роли институционального качества при оценке сельскохозяйственной политики. Работа показывает потенциальную значимость институциональной среды для эффективности аграрных мер поддержки, одновременно подчеркивая чувствительность выявленного модераторного эффекта к спецификации модели. Полученные результаты могут быть полезны для разработчиков государственной политики и стать основой для дальнейших исследований институциональных условий реализации программ субсидирования сельского хозяйства.

Ключевые слова: сельскохозяйственные субсидии, производительность сельского хозяйства, эффективность государственного управления, институциональное качество, модель с фиксированными эффектами, панельные данные, аграрная политика.

UDC 005.8:004.8
IRSTI 06.81.12

https://doi.org/10.55452/1998-6688-2026-23-3-627-642

[1]*Demeukhan A.B.,
m.e.s., ORCID ID: 0009-0009-2917-5772,
*e-mail: aididardemeukhan@gmail.com
[2]Zhumabayeva A.,
System Analyst, ORCID ID: 0009-0007-2312-7775,
e-mail: amina.zhumabayeva1@gmail.com

[1]Kazakh British Technical University, Almaty, Kazakhstan
[2]Netcracker Technology, Almaty, Kazakhstan

DRIVERS AND BARRIERS TO ADOPTING ARTIFICIAL INTELLIGENCE PRACTICES IN MANAGING PROJECTS: A SYSTEMATIC LITERATURE REVIEW THROUGH THE TOE FRAMEWORK

Abstract

This study examines the main drivers and barriers influencing the adoption of artificial intelligence (AI) in project management, with a specific focus on emerging market conditions. The research is based on a systematic literature review conducted in accordance with the PRISMA 2020 guidelines. The final sample included 41 peer-reviewed articles and conference papers retrieved from the Scopus database for the period 2016–2025. The identified adoption factors were coded and grouped using the Technology–Organisation–Environment (TOE) framework. As a result, twenty-one driver categories and twenty barrier categories were identified. The findings show that AI adoption in project management is not limited to the availability of advanced tools. Organisations are often interested in AI because of its potential to improve project performance, yet practical implementation is constrained by weak data infrastructure, limited technical maturity, shortage of qualified specialists, and unclear regulatory conditions. This gap is particularly visible in emerging markets, where environmental factors such as digital infrastructure, regulation, standards, and institutional support often determine whether firm-level adoption is possible at all. The study argues that AI adoption strategies should therefore be adapted to the maturity of the local context. For emerging markets, this means that policy and organisational efforts should not begin only with firm-level training or software implementation, but also with the development of basic digital, regulatory, and institutional conditions that make sustainable AI adoption feasible.

Keywords: Artificial intelligence; Barriers; Drivers; Emerging markets; Project management; Systematic literature review; TOE framework.

Received May 25, 2026; accepted September 3, 2026.

Introduction

Artificial intelligence (AI) has emerged as one of the most influential technological developments of the modern digital economy, fundamentally transforming how organizations operate, make decisions, and manage complex processes. In the field of project management (PM), AI technologies are increasingly integrated into core managerial processes, including project planning, scheduling, cost estimation, risk management, and stakeholder communication. Empirical evidence suggests that AI-driven tools improve forecasting accuracy, enhance risk identification, and support proactive decision-making, contributing to improved project performance and reduced failure rates [1, 2].

However, despite its demonstrated potential, the adoption of AI in project management remains uneven across organisations and regions. Existing research indicates that while some organisations successfully integrate AI into their project processes, others face persistent challenges related to data infrastructure, technical expertise, and organisational readiness. This uneven adoption is particularly

evident when comparing developed and emerging market contexts. In developed economies, AI adoption is typically constrained by organisational and technological considerations, such as integration complexity and change management. In contrast, in emerging markets, the adoption challenge is structurally different. It is shaped by limited digital infrastructure, shortages of skilled personnel, high implementation costs relative to organisational capacity, weak or evolving regulatory frameworks, and lower levels of digital maturity across firms. These conditions suggest that AI adoption in project management cannot be understood as a uniform process across contexts.

A persistent gap exists between the demonstrated capabilities of AI technologies and their effective integration into organisational project environments. This gap reflects a misalignment between what AI systems can theoretically deliver and the conditions required for their successful deployment in practice. Existing research attributes this discrepancy to a complex interplay of technological, organisational, and human-related factors [3].

Although the use of artificial intelligence in project management has received growing scholarly attention, the existing literature still leaves several important issues unresolved. Many studies examine AI mainly through its practical applications, such as scheduling, cost estimation, risk analysis, or decision support, and therefore tend to emphasise performance outcomes rather than the conditions that make adoption possible in the first place. As a result, the mechanisms through which organisations accept, integrate, and sustain AI-based tools remain less clearly explained. Another limitation is that the literature remains relatively fragmented, as technological, organisational, and human-related factors are often discussed separately, while their interaction within the adoption process is not examined in sufficient depth. In addition, despite the growing number of studies on AI in project management, there is still limited systematic synthesis of the factors influencing AI adoption across technological, organisational, and environmental dimensions. A further research gap concerns the limited attention given to emerging market contexts. Much of the existing literature is based on developed economies, where digital infrastructure, institutional support, and access to specialised expertise are relatively more advanced. Consequently, there remains comparatively limited evidence on how AI adoption is influenced in emerging markets, where organisations may face additional structural challenges, including infrastructure limitations, shortages of skilled personnel, regulatory uncertainty, and financial constraints. Although prior studies occasionally acknowledge these issues, they are still not sufficiently integrated into existing analytical frameworks or systematically examined within the context of project management.

In response to these limitations, this study applies a systematic literature review approach, using PRISMA-based procedures for article selection. The purpose is not simply to summarise how AI is applied in project management, but to examine the drivers and barriers that shape its adoption. The reviewed literature is analysed through thematic coding and then structured using the Technology–Organisation–Environment framework . This allows the study to consider adoption as a process influenced by technological conditions, organisational capacity, and the external environment. The contribution of this study is threefold. It shifts attention from the performance effects of AI to the adoption factors that enable or constrain its use in project management. It also brings together previously scattered findings by comparing drivers and barriers across technological, organisational, and environmental dimensions. Finally, the study gives particular attention to emerging markets and argues that these contexts should not be treated simply as delayed versions of developed economies.

The primary aim of this study is to systematically examine the drivers and barriers influencing the adoption of artificial intelligence in project management.

To achieve this aim, the study addresses the following research questions:

RQ1: What are the key barriers to AI implementation in project management?

RQ2: What are the key drivers of AI implementation in project management?

RQ3: What strategies can support successful AI implementation in project management?

The study contributes on two levels. Theoretically, it provides a structured mapping of AI adoption factors within the TOE framework, moving beyond the fragmented treatment of drivers and

barriers in prior work to examine their interdependencies across technological, organisational, and environmental dimensions. Practically, the findings are most directly relevant for organisations and policymakers navigating AI implementation in contexts with significant structural constraints. The explicit attention to emerging markets is intended to support more realistic and targeted strategies than those derived from developed-economy evidence alone.

Materials and methods

Artificial Intelligence as a Transforming Force Across Industries

Artificial intelligence (AI) is increasingly conceptualized in the literature as a set of data-driven methods that enable the formalization and partial automation of decision-making processes. It encompasses a range of techniques, including machine learning (ML), natural language processing (NLP), and neural network-based models, which are designed to identify patterns in large datasets and generate predictive or prescriptive outputs [4]. Beyond standalone AI applications, recent research on hybrid modelling in social-ecological systems suggests that incorporating machine learning into system dynamics and agent-based models could further enhance their capacity to represent adaptive behaviors and optimize long-term planning and decision-making in areas such as natural resource and environmental management [5]. Empirical and review-based studies indicate that AI applications are most effective in environments characterized by high complexity, interdependence, and variability. Within this broader context, project management emerges as a domain where the application of AI is both relevant and challenging. Project environments are defined by time constraints, resource limitations, and the need to coordinate multiple stakeholders, often under conditions of uncertainty. Empirical evidence from large-scale infrastructure projects illustrates this challenge: technical complexity and project-specific characteristics have been shown to be significant determinants of schedule delays and cost overruns, even in the absence of AI-based interventions [6]. These characteristics increase the demand for timely and well-founded decisions while simultaneously complicating the decision-making process. Consequently, AI-based tools are increasingly examined in the literature as a means of improving planning accuracy, monitoring project progress, and supporting adaptive responses to emerging risks.

Artificial Intelligence in Project Management: State of the Field

The application of AI to project management has gained considerable scholarly attention over the past decade. [1] provided a comprehensive systematic literature review mapping AI applications, methodologies, and outcomes in project management, identifying forecasting accuracy, risk mitigation, and stakeholder collaboration as key impact areas. [2] subsequently consolidated this evidence base through a systematic review explicitly examining opportunities, enablers, and barriers to AI adoption in project management. [7] further demonstrated that AI-driven optimization yields measurable improvements in efficiency, resource allocation, and project delivery. Recent studies have continued to consolidate evidence on AI applications in project management and adjacent fields, including trend analysis [8], AIdriven practice transformation [9], and a mixed-methods examination of AI-related benefits and challenges across the procurement process [10].

Drivers and Barriers in AI Adoption: A Fragmented Picture

Despite the growing body of research, the understanding of factors influencing AI adoption remains fragmented. A tertiary review by [3], synthesising findings from multiple systematic reviews, concludes that economic motivations consistently emerge as primary drivers, while barriers are predominantly associated with technical and social constraints. However, when compared with studies conducted within project management contexts, organisational factors, particularly top management support, strategic alignment, and organisational readiness, are often found to play a more decisive role. At the same time, inconsistencies are evident: some studies emphasise technological barriers (data quality, integration), while others highlight human-related obstacles (skills shortages, resistance to change). These differences are not merely empirical but reflect underlying contextual divergences. Studies in technologically advanced environments tend to emphasise integration and

data-related challenges, whereas research in less digitally mature contexts more frequently identifies organisational capacity and human capital as primary constraints.

Consequently, while the categories of drivers and barriers are relatively well established, their relative importance, interdependencies, and context-specific variations remain insufficiently explored in a systematic manner. This lack of integrative and context-sensitive analysis represents a key limitation of the existing literature.

The Present Study: Systematic Perspective on AI Adoption in Project Management

These limitations are particularly pronounced when considering emerging markets. Most existing studies are grounded in developed economy contexts, whereas emerging markets are characterised by additional structural constraints, including limited digital infrastructure, skills shortages, regulatory uncertainty, and financial limitations. These factors fundamentally shape the conditions under which AI can be implemented, yet they are rarely systematically incorporated into existing analytical approaches.

To address these gaps, this study adopts a systematic literature review (SLR) approach guided by PRISMA-based article selection procedures. The study focuses explicitly on the identification and analysis of drivers and barriers of AI adoption in project management, treating them as the primary unit of analysis. The analytical framework is organised using the Technology–Organisation–Environment (TOE) perspective, allowing for the classification of drivers and barriers across multiple dimensions and examination of their interdependencies. By combining a systematic review methodology with a structured analytical framework, this study aims to move beyond descriptive synthesis toward a more comprehensive and context-sensitive understanding of AI adoption in project management.

This study adopts a systematic literature review (SLR) as the primary research methodology to examine the drivers and barriers of artificial intelligence adoption in project management. The selection of SLR is justified by the fragmented nature of existing research, where relevant findings are dispersed across different contexts, industries, and methodological approaches. To ensure methodological rigor and transparency, this study follows the Preferred Reporting Items for Systematic Reviews and Meta-Analyses (PRISMA) 2020 guidelines [11].

Search Strategy

The search was executed in the Scopus database on 14 March 2026. The exact query applied was: TITLE-ABS-KEY((“driver” OR “enabler” OR “success factor” OR “barrier” OR “challenge” OR “risk” OR “obstacle*”) AND (“artificial intelligence” OR “ai”) AND (“project management”)). The search was limited to titles, abstracts, and keywords, and filtered by document type (Article, Conference Paper), language (English), and publication years (2016–2025). Duplicate records were identified through matching DOI and title followed by manual verification and were removed prior to title and abstract screening.

Relevant Article Selection Process

The selection of relevant studies followed the PRISMA 2020 four-phase framework. After removing 3 records with incomplete bibliographic information, 328 records were screened by title and abstract. Studies were excluded if they did not address both AI and project management. Subsequently, 179 full texts were assessed. At the full-text screening stage, studies were excluded for the following reasons: articles did not report drivers of AI adoption and did not report barriers of AI adoption, addressed AI outside a project management context, and lacked sufficient methodological detail to support data extraction. This process yielded a final sample of 41 studies. The final inclusion criteria required that studies address both drivers and barriers of AI adoption within a project management context. After this assessment, 41 studies were included in the final dataset. The complete selection process is shown in Figure 1 (PRISMA flowchart).

The coding scheme for driver and barrier categories was developed jointly by two researchers, who divided the 41 included studies between them, with each researcher responsible for coding their assigned portion of the sample. Throughout the process, the two researchers coordinated closely,

regularly comparing emerging categories to ensure consistent labelling and grouping of drivers and barriers across both portions of the dataset. Where a factor could not be clearly classified. For instance, because it plausibly belonged to more than one TOE dimension, such as data quality, explainability, or resistance to change, the case was flagged and referred to a third researcher, whose input was used to reach a final classification decision. In such instances, factors were assigned to the context in which they were most directly framed within the original source (e.g., a driver described primarily in terms of organizational capability was coded as organizational, even where it carried secondary technological implications). This combination of divided responsibility, ongoing coordination, and third-party review of ambiguous cases was applied consistently across the dataset to ensure coherent and reliable classification of all categories.

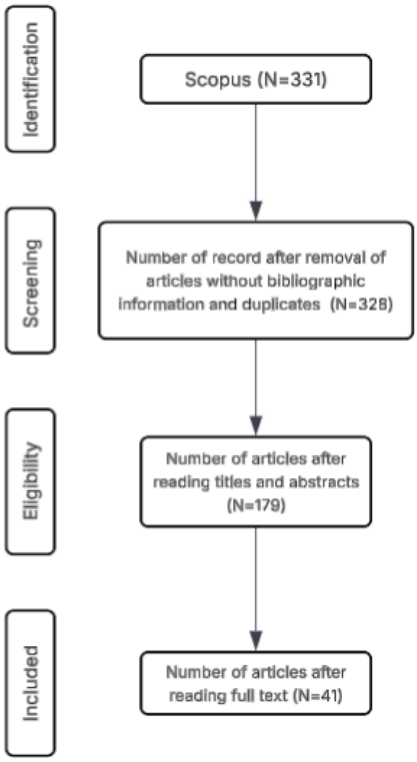


Figure 1 – PRISMA flowchart of selected articles

Structural Dimensions and Analytical Categories

To classify and analyse the reviewed literature, both inductive and deductive approaches were applied [12]. Inductive subject-specific dimensions included: drivers of AI adoption, barriers of AI adoption, AI techniques and tools, and project industry. The 21 driver categories and 20 barrier categories presented in Table 1 were derived inductively through open coding of the 41 included studies.

Deductively, drawing on the PMBOK Guide [13], the project management knowledge area was used as a dimension. Additionally, the Technology–Organisation–Environment (TOE) framework [14] was applied to structure three analytical dimensions: technological context, organisational context, and environmental context. The full framework of structural dimensions and analytical categories is presented in Table 1. Together, these dimensions provide the analytical framework through which drivers, barriers, and contextual conditions of AI adoption are examined.

Table 1 — Structural dimensions and their analytical categories

Methods	Structural dimensions	Analytical categories
Inductive, based on the literature being reviewed	Drivers of AI adoption	Predictive capability, Automation; Realtime monitoring; Decision support; Data quality and analysis; Usability and ease of use; Trust and transparency; Bias reduction; Efficiency and Productivity increase; Cost reduction; Risk reduction and management; Resource optimisation; Collaboration and communication; HumanAI collaboration; Innovation and digital transformation; Quality improvement; Strategic alignment; Safety; Competitive advantage; Sustainability; Regulatory compliance.
	Barriers of AI adoption	Data quality and availability issues; System integration difficulties; AI output inaccuracy and bias; Lack of contextual and domainspecific understanding; Lack of explainability; High computational and resource requirements; Limited AI capability and tool immaturity; Limited real world implementation and maturity; Lack of sufficient and historical data; Lack of AI expertise and literacy; High investment cost; Resistance to change; Need for human oversight; Lack of trust in AI outputs; Organisational misalignment and lack of strategy; Ethical concerns; Data privacy and security concerns; Regulatory and legal barriers; Lack of technical infrastructure; Lack of standardization.
	AI techniques / tools	Machine learning; Deep learning; Natural language processing (NLP) and generative AI; Computer vision; Integrated intelligent systems.
	Project industry	Construction; Construction/ Infrastructure; Construction/ Safety Management; Education; IT/Information systems; Oil&gas industry; Supply chain.
Deductive, related to PM	Project management knowledge area	Scope Management; Schedule (Time) Management Cost Management; Resource Management; Risk Management Quality Management; Stakeholder Management; Procurement Management; Integration Management.
Deductive, related to AI adoption	Technological context	Data infrastructure maturity; Data quality and availability; Algorithm performance; System integration capability; Explainability and transparency
	Organizational context	Skill availability; Organizational readiness; Management support; Resource availability; Change management capability
	Environmental context	Regulatory environment; Industry competition; Market demand; Institutional support; External pressure
Source: compiled by the authors based on existing data		

Results and discussion

Drivers of AI adoption

The review of 41 publications yielded 21 driver categories, presented in Table 3. Citation frequency across the included studies provided the basis for ranking. The three most prominently cited drivers were efficiency and productivity increase, decision support, and risk reduction and management.

Table 2 – Ranked Driver Categories and TOE framework classification

№	Driver categories	Count	Articles	TOE framework
1	Efficiency and Productivity increase	34	1, 2, 3, 4, 5, 6, 7, 9, 10, 11, 12, 13, 15, 17, 19, 20, 21, 23, 24, 25, 26, 27, 28, 29, 30, 31, 32, 33, 34, 35, 38, 39, 40, 41	Organization
2	Decision support	24	1, 2, 3, 4, 5, 6, 7, 8, 9, 10, 11, 13, 19, 21, 23, 24, 25, 26, 30, 31, 32, 33, 36, 41	Technology
3	Risk reduction and management	18	3, 4, 5, 7, 8, 9, 15, 21, 23, 24, 27, 28, 29, 33, 34, 37, 38, 40	Organization
4	Resource optimization	16	1, 4, 5, 9, 13, 15, 16, 22, 24, 27, 28, 29, 31, 37, 40, 41	Organization
5	Collaboration and communication	16	5, 9, 12, 13, 14, 15, 17, 18, 25, 26, 28, 29, 33, 37, 38, 40	Organization
6	Realtime monitoring	15	1, 10, 13, 14, 15, 19, 23, 27, 28, 29, 31, 32, 34, 38, 40	Technology
7	Data quality and analysis	14	1, 4, 7, 8, 10, 12, 13, 17, 18, 20, 21, 26, 31, 37	Technology
8	Automation	14	2, 3, 6, 11, 15, 18, 21, 25, 26, 27, 34, 35, 36, 40	Technology
9	Innovation and digital transformation	14	2, 3, 11, 12, 13, 14, 16, 17, 18, 19, 22, 26, 31, 39	Organization
10	HumanAI collaboration	13	2, 6, 14, 16, 17, 18, 19, 22, 24, 26, 31, 38, 39	Organization
11	Cost reduction	12	1, 5, 7, 15, 16, 19, 25, 30, 31, 32, 33, 35	Organization
12	Predictive capability	12	1, 2, 3, 5, 11, 13, 15, 18, 19, 27, 32, 40	Technology
13	Trust and transparency	6	8, 10, 12, 16, 18, 28	Technology
14	Regulatory compliance	6	12, 14, 16, 19, 33, 40,	Environment
15	Usability and ease of use	5	1, 17, 19, 22, 38	Technology
16	Sustainability	5	2, 11, 15, 23, 35	Environment
17	Safety	5	15, 25, 27, 34, 40	Organization
18	Quality improvement	4	6, 15, 27, 35	Organization
19	Strategic alignment	4	11, 12, 18, 24	Organization
20	Competitive advantage	4	10, 12, 25	Environment
21	Bias reduction	3	18, 20, 38	Technology
Source: compiled by the author based on existing data				

Efficiency and productivity increase (D1)

With 34 references, efficiency and productivity increase is the most consistently cited motivation for AI adoption across the reviewed literature. Organisations pursue AI primarily because it accelerates work processes and reduces operational costs; strategic vision is rarely the lead justification. This may reflect where the technology currently stands, capable enough to demonstrate efficiency gains, but is not yet sufficiently developed to carry out deeper organizational transformations. It also raises a question that is largely ignored in the literature: whether an exclusive focus on efficiency risks narrowing AI's perceived value, leaving longer-term strategic benefits underexplored.

Decision support (D2)

Decision support ranked second among the identified drivers. Project managers routinely work under conditions of uncertainty, incomplete information, and time pressure, circumstances that make

unaided human judgment both cognitively demanding and error-prone. AI addresses this through data-driven insights and predictive capabilities that augment rather than supplant managerial reasoning [1]. Across the reviewed literature, the relationship between AI and decision-making is consistently framed as complementary: AI improves the speed, quality, and consistency of decisions, and in doing so contributes to better project outcomes overall.

Risk reduction and management (D3)

Risk management is one of the most consistently cited motivations for AI adoption. What the literature points to is not simply that AI improves risk management, but that it changes its fundamental logic: rather than retrospective assessment after problems arise, AI enables continuous anticipation and dynamic response [2, 15]. Probabilistic risk estimation on the basis of large, multidimensional datasets allows early warning where conventional methods would not yet register a signal, and the integration of AI with sensor-based monitoring extends this capability into real time. The frequency with which risk reduction appears as a driver reflects how much organisations value the capacity to stabilise project outcomes in uncertain environments, not only the efficiency gains that tend to dominate the discussion.

Barriers of AI adoption

The review identified 20 barrier categories, presented in Table 4. The three most frequently cited were lack of AI expertise and skilled personnel, data quality and availability issues, and high implementation and investment cost.

Table 3 – Ranked Barrier Categories and TOE framework classification

№	Barrier categories	Count	Articles	TOE framework
1	Lack of AI expertise and literacy	22	2, 3, 5, 6, 7, 8, 9, 10, 11, 13, 16, 17, 18, 24, 25, 28, 29, 32, 35, 37, 40, 41	Organization
2	Data quality and availability issues	15	1, 2, 5, 7, 8, 11, 13, 14, 25, 26, 28, 29, 31, 32, 34	Technology
3	High investment cost	15	2, 7, 9, 10, 11,16, 17, 19, 25, 27, 31, 32, 35, 36, 40	Organization
4	Resistance to change	15	6, 10, 11, 13, 15, 16, 17, 18, 19, 22, 31, 32, 35, 40, 41	Organization
5	Ethical concerns	14	9, 13, 14, 18, 19, 20, 24, 26, 30, 32, 38	Environment
6	System integration difficulties	13	1, 3, 7, 11, 13, 14, 17, 19, 28, 29, 33, 35, 41	Technology
7	AI output inaccuracy and bias	12	4, 5, 6, 15, 17, 18, 20, 21, 23, 26, 34, 38	Technology
8	Data privacy and security concerns	11	9, 13, 16, 17, 18, 19, 26, 30, 32, 35, 38	Environment
9	Regulatory and legal	10	2, 11, 13, 15, 16, 17, 22, 27, 30, 40	Environment
10	Lack of technical infrastructure	10	1, 10, 16, 27, 31, 33	Environment
11	Lack of contextual and domainspecific understanding	10	4, 5, 19, 20, 21, 23, 26, 34, 38, 39	Technology
12	Need for human oversight	9	4, 20, 21, 23, 26, 34, 36, 38, 39	Organization
13	Lack of trust in AI outputs	7	7, 15, 17, 28, 23, 25, 30	Organization
14	Lack of explainability	5	2, 8, 13, 18, 30	Technology
15	Organizational misalignment and lack of strategy	5	2, 11, 18, 24, 33	Organization
16	High computational and resource requirements	5	8, 17, 19, 28, 29	Technology

Continuation of Table 3

17	Limited AI capability and tool immaturity	2	7, 8	Technology
18	Limited realworld implementation and maturity	1	3	Technology
19	Lack of sufficient and historical data	1	5	Technology
20	Lack of standardization	1	32	Environment
Source: compiled by the authors based on existing data				

Lack of AI expertise and skilled personnel (B1)

Cited by 22 studies, the absence of adequate AI expertise is the most frequently identified barrier. The reviewed studies illustrate different dimensions of this constraint: strategic (organisations cannot plan AI adoption without people who understand it), operational (teams cannot use tools they do not understand), and financial (the cost of closing the gap is itself a barrier). Where AI-capable personnel are unavailable or unaffordable, organisations cannot build reliable data pipelines, meaningfully evaluate model outputs, or develop the institutional trust that sustained adoption requires. This makes the expertise gap more than a standalone obstacle: it amplifies several other barriers and in that sense operates as a foundational constraint.

Data quality and availability issues (B2)

Cited jointly second with 15 references, data quality and availability issues reflect a structural problem inherent to most project environments: project data is often incomplete, unstandardised, or simply not collected in forms that AI systems can use. Unreliable inputs produce unreliable outputs, and unreliable outputs erode confidence in AI tools, which in turn discourages the investment in data governance that would address the problem. Breaking this cycle requires deliberate upfront commitment to data infrastructure before AI deployment begins.

High implementation and investment cost (B3)

Also cited by 15 studies, implementation cost extends well beyond software licensing to cover system integration, staff training, ongoing maintenance, and specialist recruitment. This financial burden is particularly consequential because it overlaps directly with the expertise barrier: hiring AI-capable personnel is among the most significant cost items, so the two constraints reinforce each other. Smaller organisations and those operating in resource-constrained environments bear this compounding effect most acutely.

Analytical interpretation of TOE framework results

The 21 driver categories and 20 barrier categories were mapped to the three TOE contexts following [14]. The framework has gained traction in AI adoption research within construction and project management, including recent work on carbon-neutral buildings [16], and proved well-suited to capturing the multi-dimensional character of adoption factors identified here.

Cross-context analysis

Analyzing the relative distribution and interrelationships across TOE contexts, rather than treating each in isolation, reveals two structural problems shaping the current AI implementation landscape.

First, drivers and barriers are unevenly distributed: organizational factors dominate the drivers (10 of 21 categories), while technological factors dominate the barriers (9 of 20 categories), exposing a readiness gap in which firms are strategically motivated and organizationally prepared to adopt AI, yet available technologies often lack the maturity to reliably deliver on ambitions such as productivity gains, risk management, and cost optimization, suggesting that technological development, rather than organizational change management alone, should be a primary focus of intervention.

Second, these contexts are deeply interdependent rather than independent. Organizational barriers such as low trust and resistance to change are frequently rooted in technological shortcomings,

particularly inaccurate outputs and insufficient explainability, meaning that stakeholders grow cautious when AI systems fail to justify their outputs transparently or perform unreliably; consequently, technological improvements can simultaneously resolve multiple organizational obstacles. Similarly, environmental constraints such as inadequate infrastructure and low standardization not only impede implementation directly but also determine whether technological solutions can function at all, since AI systems depend fundamentally on data availability, computing resources, connectivity, and compatible platforms; conversely, stronger environmental conditions can enable coordination mechanisms that extend adoption beyond isolated organizational efforts.

Taken together, these cross-context interactions indicate that AI adoption in project management requires a multi-layered strategy, combining advances in data infrastructure, model reliability, explainability, and system integration with improvements in regulatory transparency, standardization, and digital infrastructure investment, since organizational willingness to adopt AI already exists at a high level, but the necessary technological and institutional conditions remain insufficient to convert that intent into sustainable adoption.

Emerging markets: a distinct adoption context

One of the central findings of this study is that AI adoption in emerging markets should not be understood as a delayed replication of the process observed in advanced economies. The evidence instead points to a more complex and structurally distinct pattern.

To distinguish between developed and emerging market contexts, countries represented in the reviewed studies were classified according to the International Monetary Fund (IMF) classification of Advanced Economies and Emerging Market and Developing Economies. This classification served purely as a descriptive filter for organizing the sample and had no bearing on the formal inclusion criteria for the review; all extracted data and generalizations were subsequently checked to ensure that country-level grouping accurately reflected the adoption conditions described in each study.

Of the 41 articles reviewed, 13 were conducted in emerging market contexts, spanning the UAE (Articles 11, 15), Indonesia (Article 14), Ghana (Article 16), China (Articles 19, 22, 34, 36, 41), Ukraine (Article 27), Saudi Arabia (Articles 29, 32), and South Africa (Article 31). Although this sub-sample is small, it spans a broad range of regional and sectoral settings. The results should therefore be treated as suggestive rather than statistically generalizable. Nonetheless, the consistency of certain patterns within this sub-sample offers a useful foundation for examining how AI adoption in emerging markets differs from the global picture.

Table 4 – Top-3 AI adoption drivers in emerging market studies (n = 13)

№	Driver category	Count	Articles	TOE framework
1	Efficiency and productivity increase	9	11, 15, 19, 27, 29, 31, 32, 34, 41	Organization
2	Real-time monitoring	8	14, 15, 19, 27, 29, 31, 32, 34	Technology
3	Resource optimisation	7	15, 16, 22, 27, 29, 31, 41	Organization
Source: compiled by the authors based on existing data				

As shown in Table 4, efficiency and productivity gains emerge as the most frequently cited driver in the emerging market sub-sample, a ranking that mirrors the global dataset, where this driver also holds the top position. This consistency reflects a shared underlying logic: organizations turn to AI primarily to reduce manual work, accelerate decision-making, and optimize resource use in order to improve operational performance.

Beyond this shared top driver, however, the emerging market profile diverges markedly from the global pattern. Real-time monitoring ranks second in the sub-sample, appearing in 8 of 13 studies. a striking contrast to its sixth-place ranking globally. In emerging markets, real-time monitoring appears to serve a more foundational role than simply adding value to an already information-rich

environment. It enables continuous tracking of project progress, early detection of deviations from planned schedules, and more responsive project control capabilities that are especially critical where planning and execution conditions are less predictable.

Resource optimization ranks third, reflects the practical value of AI in contexts where project resources are constrained by cost pressures, limited personnel availability, fragmented supply chains, and schedule uncertainty. Here, AI functions less as an abstract technological advance and more as a pragmatic tool for allocating labor, equipment, time, and capital more effectively.

Table 5 – Top-3 AI adoption barriers in emerging market studies (n = 13)

№	Barrier category	Count	Articles	TOE framework
1	Resistance to change	8	11, 15, 16, 19, 22, 31, 32, 41	Organisation
2	High investment cost	7	11, 16, 19, 27, 31, 32, 36	Organisation
3	Data quality and availability	6	11, 14, 29, 31, 32, 34	Technology
Source: compiled by the authors based on existing data				

The comparison of barriers, summarized in Table 5, reveals an even sharper divergence. Resistance to change is the most frequently cited barrier in the emerging market sub-sample, whereas globally the top barrier is a lack of AI knowledge and literacy. This difference is telling: it suggests that adoption barriers in emerging markets are not purely technical but are equally behavioral, organizational, and cultural in nature. Even where the potential benefits of AI are recognized, entrenched routines, reliance on established work practices, and managerial reluctance to embrace unfamiliar technologies can impede adoption (Article 16).

The second barrier extends beyond software licensing costs to encompass equipment, data preparation, system integration, staff training, infrastructure upgrades, and the development of custom AI solutions, a cost structure identified as the most significant constraint on AI adoption in Ghana's construction sector (Article 16).

Data quality and availability barrier, confirms that data constraints remain a persistent obstacle in emerging market settings. Importantly, this barrier is not simply a matter of data scarcity; it also reflects deeper structural issues, including data fragmentation, low standardization, heterogeneous formats, poor interoperability, and insufficient integration with existing project information systems.

Recommendations

Addressing RQ3, what strategies can support successful AI implementation, the evidence points to differentiated responses depending on context. For organisations, the clearest implication of the readiness gap is that internal capability must precede tool deployment. Committing to an AI system before the data infrastructure, skills base, and change management processes are in place typically produces underperformance that discourages further adoption. Practically, this means prioritising data governance as a strategic rather than technical function: establishing data collection standards, cleaning historical records, and assigning ownership of data quality before procurement decisions are made. It also means framing AI as a decision-support layer rather than an autonomous replacement for project managers. The literature is consistent on this point: resistance is lower and performance outcomes are better when human-AI collaboration is the explicit model. Adoption that begins with lower-risk, well-defined tasks such as schedule monitoring or cost variance detection, allows organisations to build trust in AI outputs before extending reliance to more complex or consequential decisions.

For policymakers in emerging markets, the analysis identifies a sequencing problem that shapes the entire adoption challenge. Environmental preconditions, reliable digital infrastructure, data protection legislation, industry-level data standards, and accessible financing mechanisms, must be

addressed before firm-level capability-building efforts can gain traction. The evidence from Ghana, Saudi Arabia, and South Africa in the reviewed sample consistently shows that where these conditions are absent, even willing and strategically motivated organisations cannot sustain AI adoption. A practical policy agenda therefore has two tracks: the first establishes the enabling environment through infrastructure investment, regulatory development, standardisation, and instruments such as public-private partnerships that reduce upfront cost barriers; the second supports organisational capability through training programmes, AI literacy initiatives, and procurement guidelines. The sequencing matters: the first track must be underway before the second can achieve its objectives.

For the research community, the geographic concentration of existing studies is a limitation that future work should address directly. Most reviewed articles originate from developed economies or a narrow range of emerging market countries in the Gulf, China, and select African contexts. Latin America, South and Southeast Asia, and Sub-Saharan Africa remain substantially underrepresented despite being regions where infrastructure investment needs are acute and where AI adoption in project management could have considerable impact. In addition to geography, longitudinal and experimental developments would be useful in this area. Cross-sectional studies can identify existing barriers and driving forces; they are less suitable for explaining how implementation occurs over time or which interventions actually affect outcomes. Comparative studies combining the contexts of developed and emerging markets within the same type of project or sector would also help to distinguish general conclusions from specific ones more clearly than the available data allow.

Conclusion

A systematic review of 41 peer-reviewed articles, structured around the Technology–Organisation–Environment framework, identified 21 driver categories and 20 barrier categories shaping AI adoption in project management. The dominant driver pattern is internal and operational: organisations are motivated by efficiency gains, decision support, and risk management capabilities that AI can provide within their own project environments. The dominant barrier is technological rather than organisational: data quality problems, infrastructure deficits, and the absence of mature, reliable AI tools constrain adoption in ways that organisational willingness alone cannot overcome. Taken together, these two patterns define what the review identifies as the central structural challenge, a readiness gap in which motivation and capability are misaligned. The TOE framework illuminates this well, though the review also reveals a limitation in how the framework is conventionally applied: it treats technological, organisational, and environmental contexts as parallel conditions, whereas the evidence, particularly from emerging market studies, suggests that environmental factors often operate as gateway conditions that must be met before the other two dimensions become effective.

Several limitations bear acknowledgement. The evidence base is heterogeneous in methodology and context, and the findings naturally reflect the state of the literature at the time of review. The emerging market analysis, while analytically meaningful, draws on thirteen studies concentrated in a narrow geographic range; broader coverage would strengthen the contextual conclusions. Notwithstanding these constraints, the review makes three contributions. It provides a structured mapping of drivers and barriers across the TOE framework, moving beyond lists to a cross-context analysis that surfaces the readiness gap as the field's central structural challenge. It offers an original characterisation of emerging market adoption as structurally distinct rather than simply delayed. And by synthesising adoption factors as the primary object of analysis, rather than as secondary findings within application-focused studies, it gives researchers and practitioners a basis for more targeted strategy development as AI tools continue to mature and embed themselves in project management practice.

REFERENCES

1 Taboada, J., et al. Artificial intelligence in project management: A systematic literature review. Applied Sciences, 13 (8), 5014 (2023). https://doi.org/10.3390/app13085014

2 Ghanbaripour, A.N., et al. The Rise of Artificial Intelligence in Project Management: A Systematic Literature Review of Current Opportunities, Enablers, and Barriers. Buildings, 15 (7), 1130 (2024). https://doi.org/10.3390/buildings15071130

3 Cubric, M. Drivers, barriers and social considerations for artificial intelligence adoption: A tertiary review. Technology in Society, 62, 101257 (2022). https://doi.org/10.1016/j.techsoc.2020.101257

4 Prasad, K., and Saradhi, M.V. Comprehensive project management framework using machine learning. International Journal of Recent Technology and Engineering, 8, 1373–1377 (2019). https://doi.org/10.35940/ijrte.B1256.0782S319

5 Nugroho, S., and Uehara, T. Systematic review of agent-based and system dynamics models for social-ecological system case studies. Systems, 11 (11), 530 (2023). https://doi.org/10.3390/systems11110530

6 De Marco, A., and Narbaev, T. Factors of Schedule and Cost Performance of Tunnel Construction Megaprojects. The Open Civil Engineering Journal, 12, 15–38 (2021).

7 Prifti, V. Optimizing project management using artificial intelligence. European Journal of Formal Sciences and Engineering, 5, 30–38 (2022). https://doi.org/10.26417/667hri67

8 Kalidullin, B., Samoilov, A., and De Marco, A. AI applications in project management: trends, challenges and future perspectives. Herald of the Kazakh-British Technical University, 22 (3), 390–403 (2025). https://doi.org/10.55452/1998-6688-2025-22-3-390-403

9 Serikbay, D., Kozhakhmetova, A., Jumasseitova, A., and Mukashev, Y. When Machines Manage: How AI Is Reshaping Project Management Practices. International Journal of Asian Business and Information Management, 16 (1), 1–18 (2025). https://doi.org/10.4018/IJABIM.384773

10 Guida, M., Caniato, F., Moretto, A., and Ronchi, S. The role of artificial intelligence in the procurement process: State of the art and research agenda. Journal of Purchasing and Supply Management, 29, 100823 (2023). https://doi.org/10.1016/j.pursup.2023.100823

11 Page, M.J., et al. The PRISMA 2020 statement: An updated guideline for reporting systematic reviews. BMJ, 372, n71 (2021). https://doi.org/10.1136/bmj.n71

12 Seuring, S., and Müller, M. From a literature review to a conceptual framework for sustainable supply chain management. Journal of Cleaner Production, 16 (15), 1699–1710 (2008). https://doi.org/10.1016/j.jclepro.2008.04.020

13 Project Management Institute. A Guide to the Project Management Body of Knowledge (PMBOK® Guide), 7th ed. (Newtown Square, PA: Project Management Institute, 2021).

14 Tornatzky, L.G., and Fleischer, M. The Processes of Technological Innovation (Lexington, MA: Lexington Books, 1990).

15 Uddin, M., et al. Machine learning applications in project analytics: a data-driven framework and case study. Scientific Reports, 12, 16482 (2022). https://doi.org/10.1038/s41598-022-19728-x

16 Osei-Kyei, R., Narbaev, T., Falana, J., and Ottaviani, F.M. Artificial intelligence in achieving carbon-neutral buildings: a critical analysis of the emerging techniques, their applications and challenges. Architectural Engineering and Design Management, 1–25 (2025). https://doi.org/10.1080/17452007.2025.2596708

Appendix A. Screened articles (N=41)

#	Authors	Title
1	Elghaish et al.	Predictive digital monitoring of construction resources: an integrated digital twin solution
2	Hughes et al.	Impact of artificial intelligence on project management (PM): Multi-expert perspectives toward PM2030
3	Garcia et al.	Project control and computational intelligence: Trends and challenges
4	Nyqvist et al.	Can ChatGPT exceed humans in construction project risk management?
5	Fridgeirsson et al.	A Qualitative Study on AI and Its Impact on the Project Schedule, Cost and Risk Management in PMBOK
6	Hettrich et al.	Bridging the Expertise Gap: The Role of Generative AI in Supporting Project Planning Tasks
7	Wachnik B.	Analysis of the use of AI in the management of Industry 4.0 projects: perspective of Polish industry
8	Chen et al.	Transparent and reliable construction cost prediction using advanced ML and explainable AI

Continuation

9	Alqudah et al.	Developing an Intelligent Model for Construction PM Using AI and Big Data Analysis
10	Bozorgzadeh & Umar	Automated progress measurement using computer vision technology in UK construction
11*	Al Sulaity et al.	Driving digital transformation in the oil and gas sector: unlocking AI potential in the UAE
12	Merhi & Harfouche	Enablers of artificial intelligence adoption and implementation in production systems
13	Torres et al.	Enhancing construction PM competencies with AI-driven assistants: dual perspective from academia and industry
14*	Waqar et al.	Evaluation of success factors of utilizing AI in digital transformation of H&S management systems in construction
15*	Alketbi et al.	The Role of Artificial Intelligence in Aviation Construction Projects in the United Arab Emirates
16*	Acheampong et al.	Evaluating the factors influencing AI technology uptake in health and safety management in Ghanaian construction
17	Skuridin & Wynn	Chatbot Design and Implementation: Towards an Operational Model for Chatbots
18	Tursunbayeva & Chalutz-Ben Gal	Adoption of artificial intelligence: A TOP framework-based checklist for digital leaders
19*	Ma et al.	Adopting Large Language Models in the Construction Industry: Drivers, Barriers, and Strategic Implications from China
20	Aljaz T.	Leveraging ChatGPT for Enhanced Logical Analysis in the Theory of Constraints Thinking Process
21	Barcaui & Monat	Who is better in project planning? Generative artificial intelligence or project managers?
22*	Zhang et al.	Enhancing construction workers health and safety: mechanisms for implementing Construction 4.0 technologies
23	Aladag H.	Assessing the Accuracy of ChatGPT Use for Risk Management in Construction Projects
24	Serikbay et al.	When Machines Manage: How AI Is Reshaping Project Management Practices
25	Jallow et al.	Artificial Intelligence and the UK Construction Industry - Empirical Study
26	Nikolic & Bjelica	Digital product success under the microscope: When artificial intelligence in projects helps and when it hurts
27*	Sobchenko et al.	Artificial Intelligence for Enhancing Engineering Project Management During Emergencies: Perception-based Analysis
28	Almalki S.S.	AI-Driven Decision Support Systems in Agile Software Project Management
29*	Alnaser & Elmousalami	Exploring Critical Success Factors of AI-Integrated Digital Twins on Saudi Construction Project Deliverables
30	Georgiev et al.	The role of artificial intelligence in project management: a supply chain perspective
31*	Bikwa & Bond-Barnard	Exploring the Challenges and Opportunities of AI in Decision-Making in Construction Project Management
32*	Alnaser & Elmousalami	Benefits and Challenges of AI-Based Digital Twin Integration in the Saudi Arabian Construction Industry
33	Tominc et al.	Statistically Significant Differences in AI Support Levels for Project Management between SMEs and Large Enterprises
34*	Kamran et al.	Generative AI and Prompt Engineering: Transforming Rockburst Prediction in Underground Construction
35	Nyqvist et al.	Artificial intelligence driven platforms in the construction industry: implications for companies business models
36*	Jiang et al.	Automatic daily salary settlement for construction workers in photovoltaic engineering using lean construction and AIoT
37	Bockova et al.	The Role of Artificial Intelligence in Managing Scientific Research Projects Funded by KEGA and VEGA grant schemes

Continuation

38	Martin et al.	Exploring Large Language Model AI tools in Construction Project Risk Assessment: ChatGPT Limitations
39	Catta-Preta et al.	Innovation Flow: A Human-AI Collaborative Framework for Managing Innovation with Generative Artificial Intelligence
40	Wong et al.	Towards Digital Transformation in Building Maintenance and Renovation: Integrating BIM and AI in Practice
41*	Chong et al.	BIM and AI Integration for Dynamic Schedule Management: A Practical Framework and Case Study

*=Emerging Market Study

[1]*Демеухан А.В.,
магистр, ORCID ID: 0009-0009-2917-5772,
*e-mail: aididardemeukhan@gmail.com
[2]Жумабаева А.,
жүйелік талдаушы, ORCID ID: 0009-0007-2312-7775,
e-mail: amina.zhumabayeva1@gmail.com

[1]Қазақстан-Британ техникалық университеті, Алматы қ., Қазақстан
[2] Netcracker Technology, Алматы қ., Қазақстан

ДАМУШЫ НАРЫҚТАРДА ЖАСАНДЫ ИНТЕЛЛЕКТ ТӘЖІРИБЕСІН ЕНГІЗУДІҢ ҚОЗҒАУШЫ КҮШТЕРІ МЕН КЕДЕРГІЛЕРІ

Аңдатпа

Зерттеу дамушы нарық жағдайларына ерекше назар аудара отырып, жобаларды басқаруда жасанды интеллектті (ЖИ) енгізуге әсер ететін негізгі факторлар мен кедергілерді зерттейді. Зерттеу PRISMA 2020 нұсқауларына сәйкес жүргізілген әдебиеттерді жүйелі шолуға негізделген. Қорытынды үлгіге 2016–2025 жж. аралығында Scopus дерекқорынан алынған 41 рецензияланған мақала кірді. ЖИ енгізуге әсер ететін факторлар кодталып, Technology–Organisation–Environment (TOE) моделі негізінде топтастырылды. Нәтижесінде қозғаушы факторлардың жиырма бір санаты және кедергілердің жиырма санаты анықталды. Зерттеу нәтижелері жобаларды басқаруда ЖИ енгізу тек озық құралдардың қолжетімділігімен шектелмейтінін көрсетеді. Ұйымдар ЖИ-ге жобалардың тиімділігін арттыру әлеуетіне байланысты қызығушылық танытады, алайда тәжірибелік енгізу әлсіз деректер инфрақұрылымы, техникалық жетілудің төмен деңгейі, білікті мамандардың жетіспеушілігі және нормативтік талаптардың айқын болмауымен шектеледі. Бұл айырмашылық әсіресе дамушы нарықтарда анық байқалады, өйткені цифрлық инфрақұрылым, реттеу, стандарттар және институционалдық қолдау сияқты сыртқы орта факторлары ұйым деңгейінде ЖИ енгізудің мүмкіндігін айқындайды. Зерттеу ЖИ енгізу стратегиялары жергілікті контекстің жетілу деңгейіне бейімделуі тиіс деген қорытынды жасайды. Дамушы нарықтар үшін бұл мемлекеттік және ұйымдық күш-жігер тек қызметкерлерді оқытудан немесе бағдарламалық қамтамасыз етуді енгізуден басталмай, сонымен қатар ЖИ-ді тұрақты түрде енгізуге мүмкіндік беретін базалық цифрлық, нормативтік және институционалдық жағдайларды дамытуға бағытталуы қажет екенін білдіреді.

Түйін сөздер: жасанды интеллект, кедергілер, қозғаушы факторлар, дамушы нарықтар, жобаларды басқару, жүйелі әдебиет шолуы, TOE framework.

[1]*Демеухан А.Б.,
магистр, ORCID ID: 0009-0009-2917-5772,
*e-mail: aididardemeukhan@gmail.com
[2]Жумабаева А.,
системный аналитик, ORCID ID: 0009-0007-2312-7775,
e-mail: amina.zhumabayeva1@gmail.com

[1*]Казахстанско-Британский технический университет, г. Алматы, Казахстан
[2] Netcracker Technology, г. Алматы, Казахстан

ДВИЖУЩИЕ СИЛЫ И БАРЬЕРЫ ВНЕДРЕНИЯ ПРАКТИК ИСКУССТВЕННОГО ИНТЕЛЛЕКТА НА РАЗВИВАЮЩИХСЯ РЫНКАХ

Аннотация

Данное исследование рассматривает основные драйверы и барьеры, влияющие на внедрение искусственного интеллекта (ИИ) в управление проектами, с особым акцентом на условия развивающихся рынков. Исследование основано на систематическом обзоре литературы, проведенном в соответствии с руководством PRISMA 2020. Итоговая выборка включала 41 рецензируемую статью, полученную из базы данных Scopus за период 2016–2025 гг. Выявленные факторы внедрения были закодированы и сгруппированы с использованием модели Technology–Organisation–Environment (TOE). В результате была определена 21 категория движущихся сил и 20 категорий барьеров. Результаты исследования показывают, что внедрение ИИ в управление проектами не ограничивается наличием передовых инструментов. Организации часто проявляют интерес к ИИ из-за его потенциала для повышения эффективности проектов, однако практическое внедрение сдерживается слабой инфраструктурой обработки данных, недостаточной технической зрелостью, нехваткой квалифицированных специалистов и неясными нормативными условиями. Этот разрыв особенно заметен на развивающихся рынках, где такие факторы окружающей среды, как цифровая инфраструктура, регулирование, стандарты и институциональная поддержка, часто определяют, возможно ли вообще внедрение на уровне компаний. В исследовании утверждается, что стратегии внедрения ИИ должны быть адаптированы к местным условиям. Для развивающихся рынков это означает, что организационные усилия должны начинаться не только с обучения на уровне фирмы или внедрения программного обеспечения, но и с разработки базовых цифровых, институциональных условий, которые делают возможным устойчивое внедрение ИИ.

Ключевые слова: искусственный интеллект, барьеры, движущие силы, развивающиеся рынки, управление проектами, систематический обзор литературы, TOE framework.

UDC 332.1:001.89
IRSTI 06.61.33

https://doi.org/10.55452/1998-6688-2026-23-3-643-656

[1]Turginbayeva A.N.,
d.e.s., ORCID ID: 0000-0003-4208-6167,
e-mail: ardakt@illinois.edu
[2]Serikbay D.D.,
m.e.s., ORCID ID: 0009-0000-4821-7733,
e-mail: d.serikbay@kbtu.kz
[1*]Anarkhan A.K.
PhD student, ORCID ID: 0009-0008-9014-3385,
e-mail: aizhan2790@gmail.com

[1]Al-Farabi Kazakh National University, Almaty, Kazakhstan
[2] Kazakh-British Technical University, Almaty, Kazakhstan

MAPPING INEQUALITY IN ACCESS TO R&D: A DUAL BIBLIOMETRIC ANALYSIS OF THE GLOBAL RESEARCH LANDSCAPE

Abstract

This study examines how inequality in access to research and development (R&D) is represented within the global research landscape and why it remains weakly consolidated as an independent analytical category. Drawing on bibliographic records retrieved from Scopus and the Web of Science Core Collection for 2014 – 2025, the study applies author – keyword co – occurrence analysis to examine the thematic structure of research related to regional innovation, spatial inequality, economic geography, and research capacity. The integrated dataset contains 7,592 records. Using a minimum occurrence threshold of five, 106 author keywords were retained and organized into nine thematic clusters. The resulting network is dominated by established themes such as regional development, peripheral regions, core – periphery relations, regional innovation, and spatial inequality, while terminology explicitly referring to R&D access appears comparatively weak and fragmented. The findings therefore provide bibliometric evidence of limited thematic consolidation around R&D access rather than establishing it as an empirically validated dimension of inequality. Building on this pattern, the study proposes R&D access as a distinct analytical dimension of regional inequality and outlines three conceptual forms – material, cognitive, and institutional access-for future empirical investigation.

Keywords: R&D access, regional inequality, regional innovation systems, economic geography, bibliometric analysis, research infrastructure.

Received July 23, 2026; revised August 22, 2026; accepted August August 22, 2026

Introduction

R&D is considered one of the most important factors of economic growth, technological advancement, and the increasing competition of regions in a knowledge-based economy, where knowledge is a major factor of production [1]. From a regional perspective, the majority of recent studies in innovation have started to focus on the processes of creation and diffusion of knowledge, and the innovation systems that govern the regional development [2]. In this context, Regional Innovation Systems (RIS) have become a popular framework for understanding regional differences in innovation and for analyzing the interplay of institutions, networks, and knowledge in a particular territory [3].

Despite the existing abundance of literature on this topic, the uneven distribution of knowledge and the opportunities to create knowledge have received relatively little attention. Access to R&D resources (research, scientific, and institutional capacity, as well as funding) is much more unevenly distributed across regions [4]. These differences reinforce the cumulative advantages of the central regions and limit the innovative potential of the peripheral ones, most of which are underdeveloped.

When innovation – based socioeconomic systems are viewed from a knowledge perspective, they can be understood as multilayered and open networks through which knowledge flows and innovation occurs. This perspective, accordingly, explains why most discussions on innovation processes and outcomes exclude the unequal distribution of research resources [5]. While on one hand, the RIS literature studies the institutional frameworks that foster innovation, economic geography studies the spatial or regional concentration of innovation and explains the innovative systems from the perspective of agglomeration and core–periphery [3]. However, the analysis of the global research framework is in its infancy when it comes to the representation of the inequality of access to R&D.

The widening gap in this context may be due to a region's inability to participate in the innovation process because of the structural inequities pertaining to the research capacity of the region. A lack of research-related infrastructure and institutional research capacity may be one of the more significant factors that contributes to the inequities of a region but one that has been largely overlooked.

This study addresses the following research question: How is inequality in access to R&D represented in the global research landscape, and why does it remain conceptually underdeveloped? The aim of this study is to examine how inequality in access to R&D is represented in the global research landscape and to assess the extent to which it is consolidated as an independent analytical theme through a bibliometric mapping approach combining broad and focused levels of interpretation.

The research significance is three-fold. First, the study contributes methodologically by combining an examination of the dominant thematic structure of the field with a focused assessment of the position of R&D – access – related concepts within the same bibliometric network. Second, this study proposes the conceptualization of R&D access as a distinct analytical dimension of regional inequality, rather than treating it solely as a derivative component of innovation-system performance. Third, this research brings to the fore an empirical contribution that the global research ecosystem has an underexploited and fragmented body of literature, which remains undeveloped, relating to the inequitable access to R&D. To fill this research gap, one must deeply analyze the leading theoretical traditions that inform the dialectics of regional innovation and inequality. The next section critiques primary lines of thought – especially the knowledge-based paradigm, RIS, economic geography, and institutional theory – with particular attention paid to their limitations in terms of explaining the uneven distribution of access to R&D.

Theoretical background

To grasp modern innovation research, one must start from the knowledge – based paradigm, which posits knowledge to be the core constituent of the economy. In this paradigm, RIS have constituted a prevailing analytical framework. However, while offering valuable perspectives regarding the workings of innovation systems, these approaches have largely disregarded the structural inequalities in the access to research resources.

As a result of the rising value of knowledge as a major economic resource, the knowledge-based paradigm, which regards innovation as a driving force of economic growth, has emerged [6]. In this paradigm, innovation is a cumulative, interactive process of knowledge creation, diffusion, and application, as determined by the individual and collective actors comprising the institutional framework [7].

One of the dominant theoretical models explaining the variation in the innovation performance of regions is the RIS approach [8]. In focus is the role of institutional frameworks, knowledge relations and the interactions among firms, academia, and public institutions in fostering innovation [3].

It is in the described framework that the innovation potential of a specific region is primarily attributed to the structural quality of the institutional frameworks and overall capacity to produce and process new knowledge. In this context, emphasis is placed on efficiency of the system, learning processes and knowledge spillovers [9].

Nevertheless, in the RIS paradigm, the various layers of inequity in the access to scientific and research resources are not sufficiently treated as a specific, analytically structured phenomena; inequity in innovation is primarily attributed to the disparity in the embedded institutional system, the degree of collaboration, or the level of absorptive capacity. This ensures that the problem of inequitable distribution of research and scientific resources is subsumed in the overall system-oriented approaches.

Although the RIS framework stresses institutional interactions and the performance of the system, it overlooks the inequality of spatial dimensions. To solve this issue, one must look toward economic geography, which emphasizes the spatial distribution of economic processes and imbalances among regions.

Kim (2008) analyses spatial inequalities in economic development and innovation-related processes from the perspective of economic geography [10]. Theories of agglomeration focus on the importance of spatial proximity, externalities, and cumulative causation in the uneven development of regions [11]. According to core–periphery theory, economic activity tends to be concentrated in a particular region, as core regions have more developed infrastructure, a better-educated workforce, and stronger institutional frameworks. The core regions obtain cumulative advantages, whereas the peripheral regions tend to be structurally constrained in ways that limit their growth opportunities [12].

The spatial distribution of knowledge-based industries, research institutions, and universities explains the inability of many regions to fully develop their innovative capacity, as well as why certain regions develop more than others. The presence of a well-established scientific infrastructure within a region translates to the region developing additional investment and talent, furthering spatial inequities [13].

Although economic geography provides a clear explanation of the structural disparity between regions, it tends to neglect the dimension of spatial inequity that relates to the uneven distribution and access to R&D. A lot of the time, a region's spatial disparities are seen because of agglomeration, whereas they can be a result of the region's restricted access to research capacity.

While economic geography has its strengths in describing spatial concentration and regional divergence, it generally views inequality because of agglomeration processes. It seldom regards it as a structural constraint. Economic geography combined with the institutional approach provides more insights. For example, the theory of the state and institutional theory can highlight the different structural barriers that determine the uneven distribution of knowledge and technology.

Institutional theory maintains that there are structural obstacles that hinder access to certain knowledge and technological opportunities. Barriers that impede the adoption of technologies and the diffusion of knowledge can account for the disparities in productivity that exist among different countries and regions [14].

Desmet, Greif, and Parente (2020) discuss institutional and spatial mechanisms that shape uneven technological and economic development [15].

In terms of how regions can innovate, available research infrastructure, scientific capabilities, and funding mechanisms to carry out research are not available equally, which creates disparities and can improve or inhibit a region's ability to engage in knowledge production. This means that institutional constraints are responsible for explaining why research capacity building for certain regions is so consistently uneven.

Regional disparities are a problem that is primarily attributable to institutional barriers. Such a conclusion, however, is rarely articulated when examining the access to R&D and how it is restricted, especially in the context of innovation systems, regional development, and technological advancements, which is where the discourse primarily remains.

Each theoretical perspective review contributes to understanding regional inequality, but none of them engages with R&D access as a separate analytical dimension. This indicates a significant theoretical gap that should be addressed. The literature advocates that the leading paradigms of knowledge concentrate on the analysis of knowledge, systems, performance, and innovation networks, whereas the unequal research capacity connectivity and distribution of conceptual frameworks are less analyzed.

The RIS literature analyses the system structure and interrelations of system actors, but not the unequal distribution of system resources. The economic geography literature analyses the uneven distribution of knowledge and its geographic concentration through agglomeration but does not treat R&D as an analytical dimension of the uneven distribution of knowledge. The institutional theory literature analyses barriers to knowledge diffusion but does not address these barriers in the context of the uneven distribution of research capacity.

Consequently, the research traditions have largely considered the issue of access to R&D as an embedded structure, the essence of which is the significant and weakening structural disparities of research capacity and its critical role in region development. It is assumed that defining access to R&D as an independent dimension of the innovation process will elucidate the overall situation of spatial imbalance in the process of innovation.

Existing theoretical traditions on regional development and the dynamics of innovation remain useful but have a salient limitation in the existing literature: the structural condition of access to R&D (research and development) is absent. Although the RIS approach is system-oriented in its considerations of interaction and system dynamics, it hardly questions the distribution of resources. From the vantage point of Economic Geography, spatial concentrations of economic activities arise through specializations of agglomeration and clustering, but inequality is considered an unintended outcome of the system as opposed to a condition of differential access to research capacity. Barriers are identified by the Institutional Theory, but they are not integrated into a systematic, locational, or spatial dimension of R&D access.

On the basis of the theoretical synthesis, this study proposes a three-part conceptual framework for the future analysis of R&D access. Material access refers to research infrastructure, laboratories, and the availability of research funding; cognitive access refers to scientific capacity, skilled human resources, and knowledge networks; and institutional access refers to policies, governance arrangements, and inclusion in research systems. These dimensions are proposed as an analytical agenda for subsequent empirical research rather than as categories directly tested by the present bibliometric analysis.

By conceptually distinguishing R&D access from the broader innovation value chain, the proposed framework shifts attention from innovation outcomes toward the structural conditions that shape participation in knowledge production. Such approach helps better understand the worrying persistence of regional disparities and expand interpretation of structural biases which have been identified through bibliometric methods.

Materials and methods

This study's methodological contribution stems from the lack of an analytical framework considering the differences in access to R&D. Traditionally, bibliometric analyses in the fields of innovation and economic geography focus on dominant trajectories and formalized structures. Those approaches overlook underdeveloped themes, such as 'access to R&D' as a theme in Research and Development.

This study addresses this gap through a bibliometric mapping approach that combines broad and focused levels of interpretation. The broad level identifies the dominant thematic structure of the research field, whereas the focused level examines how concepts related to R&D access and inequality are positioned within that structure. Rather than treating these levels as two independent bibliometric datasets, the study uses them as complementary analytical perspectives within the same

integrated corpus. This approach makes it possible to distinguish between well-established thematic domains and comparatively weak or fragmented access-related themes.

The methodological value of this design lies in moving beyond the identification of dominant themes toward the examination of comparatively underrepresented thematic positions. In this study, the approach is used to assess whether R&D access appears as a consolidated research stream or remains dispersed across broader traditions in regional innovation, economic geography, and inequality research.

Figure 1 presents the analytical logic of the study as a sequence of broad and focused interpretive stages. The terms “baseline mapping” and “refined mapping” refer to two analytical levels applied to the same integrated bibliometric corpus rather than to two independently generated bibliometric datasets. The baseline stage identifies the dominant thematic configuration of the field, while the refined stage focuses on the relative position of R&D – access – and inequality – related concepts within that same network. The comparative stage therefore represents an interpretive comparison of thematic prominence rather than a comparison of two separate maps.

The research design follows a structured multi-stage approach:

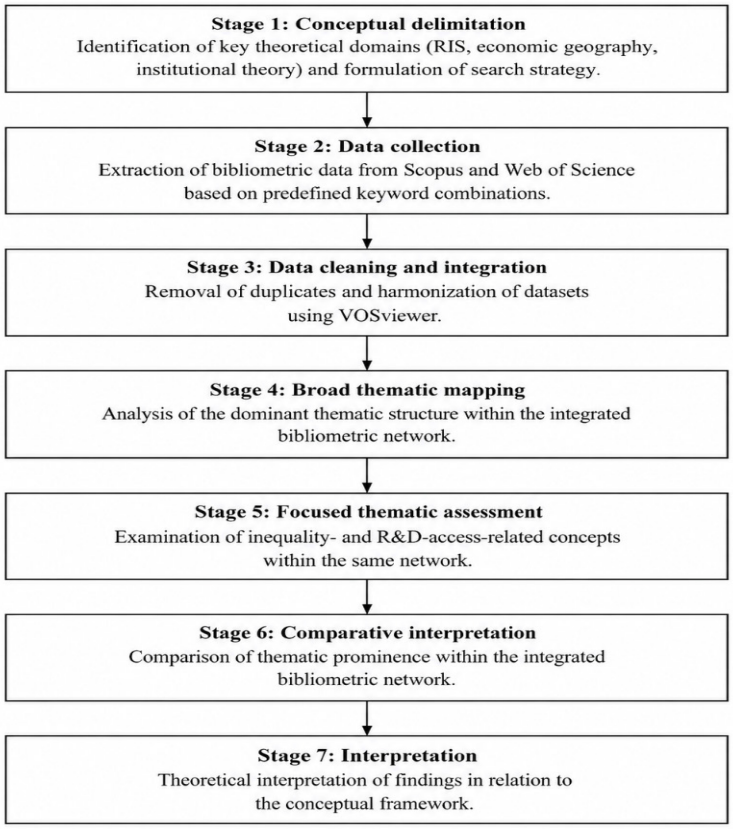


Figure 1 – Research design and stages of analysis

Creating a complete bibliometric dataset reflecting the main and developing research themes is essential to put the research design into practice.

To maintain breadth in the analysis of the scientific literature, bibliometric data were retrieved from the Web of Science Core Collection and Scopus databases. The search strategy was developed to place the focus analytically on the R&D and innovation literature, without the literature seeking to overshadow the issue of R&D and innovation inequities.

In accordance with the research design, the search query was formulated based on a combination of keywords associated with research, accessibility, and spatial inequality. The primary reasoning

behind the construction of the search was focused on the interaction of the concepts of access and inequality, and the associated regional or spatial dimensions. The search included combinations of keywords such as “R&D inequality”, “research inequality”, “access to R&D”, “research infrastructure”, “scientific capacity”, “territorial inequality”, “spatial inequality”, “core-periphery”, and “peripheral regions”. These terms were combined with spatial descriptors including regional, spatial, territorial, geography, and disparity.

To ensure transparency and reproducibility of the search procedure, database-specific search strings were formulated in accordance with the keyword combinations described above. For Scopus, the search was conducted in the title, abstract, and keyword fields using the following query:

Scopus: TITLE-ABS-KEY ((“R&D inequality” OR “research inequality” OR “access to R&D” OR “research infrastructure” OR “scientific capacity” OR “territorial inequality” OR “spatial inequality” OR “core-periphery” OR “peripheral regions”) AND (regional OR spatial OR territorial OR geography OR disparity)).

For the Web of Science Core Collection, the corresponding topic search was conducted using:

Web of Science: TS = ((“R&D inequality” OR “research inequality” OR “access to R&D” OR “research infrastructure” OR “scientific capacity” OR “territorial inequality” OR “spatial inequality” OR “core-periphery” OR “peripheral regions”) AND (regional OR spatial OR territorial OR geography OR disparity)).

In both databases, the search results were subsequently limited to the 2014–2025 publication period, English-language peer-reviewed journal articles, and subject areas relevant to economics, regional studies, geography, development studies, and the social sciences. Records predominantly associated with engineering and the natural sciences were excluded.

To enhance coverage and mitigate potential database-specific bias, bibliographic records were retrieved from both Scopus and the Web of Science Core Collection. The initial search yielded 6,588 records from Scopus and 1,072 records from Web of Science, producing a combined pool of 7,660 records. Following database merging, screening, and harmonization of the bibliographic records, the analytical dataset contained 7,592 records. The archived materials available for the present revision do not preserve a sufficiently detailed stage – by – stage screening log to distinguish with certainty between records removed through duplicate identification and records excluded during bibliographic harmonization. Accordingly, the difference of 68 records is reported here as the total reduction during dataset integration rather than being attributed exclusively to duplicate removal. Duplicate identification and bibliographic harmonization were based on available bibliographic metadata, including publication titles and other matching record information. Because the original screening protocol and software-version record are no longer available, the precise matching hierarchy (for example, DOI-based versus title – and – year matching) cannot be reconstructed with confidence. Because the original item – level screening log is no longer available, the exact number removed by each individual screening criterion cannot be reconstructed retrospectively. For this reason, only the verified aggregate counts before and after dataset integration are reported.

After data is compiled and prepped, analysis centers on understanding the conceptual framework of the discipline by evaluating occurrence of keywords.

For identifying the conceptual framework of the research domain, a co-occurrence analysis was performed using VOSviewer on the keywords of authors. Author keywords were used because they encapsulate the focus of the research as articulated by the authors. Before interpretation of the keyword network, the retained keyword set was reviewed for obvious non-conceptual and duplicated entries. Classification codes appearing as keywords, including JEL – type codes, were treated as non-substantive metadata and excluded from conceptual interpretation. Singular and plural variants referring to the same concept were treated as equivalent during interpretation (for example, “peripheral region” and “peripheral regions”, “university” and “universities”). Geographic names were retained only as contextual indicators of the spatial orientation of the literature and were not

interpreted as independent conceptual themes. Because the original VOSviewer thesaurus file is not available in the archived materials, the present revision does not claim a fully re-generated thesaurus-cleaned network; instead, the analysis explicitly distinguishes substantive conceptual terms from classification and geographic labels when interpreting the maps. A minimum occurrence threshold of five was applied, resulting in the inclusion of 106 author keywords in the final network. The archived analytical output does not preserve the total number of distinct author keywords prior to application of the threshold or the item-level occurrence and total link strength statistics; therefore, these values are not reconstructed retrospectively. These keywords formed 9 thematic clusters, which denote the principal intellectual structures in the literature. The use of keyword co-occurrence analysis and VOSviewer follows established bibliometric mapping procedures and methodological guidelines [16–18].

Literature network visualization reveals the organizing themes around central concepts of regional development and peripheral regions, which serve as bridging nodes for the integration of multiple thematic streams.

Results

The results of the bibliometric study reveal the structural organization of the research domain and the positioning of inequality related to access to R&D in the field. The network visualization gives a snapshot of the major thematic groupings that articulate the field's intellectual framework. The network visualization (Fig.2) illustrates the major thematic clusters that structure the intellectual organization of the field.

Regional innovation policy and economic geography are the focus of Cluster 1 which includes RIS, innovation policy, smart specialization, SMEs, path creation, and regional disparities, among others. This cluster showcases the prevalent policy-oriented viewpoint among regional innovation researchers.

Taking on the themes of territorial inequality and spatial justice, Cluster 2 captures the concepts of place-based policy, uneven development, spatial structure, regional policy, and social capital. This cluster represents the rising concern for pronounced structural inequality within territories.

Regional development processes and the respective institutional frameworks are what Cluster 3 concerns itself with, looking at geography, collaboration, institutions, sustainability, and urban development. The core-periphery and global production network theories, including concepts of globalization, strategic coupling, and governance, along with the semi-periphery concept, are captured within Cluster 4. This cluster retains the structural viewpoints on regional inequality within global systems.

Cluster 5 encompasses peripheral regions and encompasses concepts of evolutionary economic geography, including path development, agency, and spatial analyses. Included in Cluster 6 are concepts of socio-economic inequality, including poverty, inequality, and social mobility in association with regional growth, linking social outcomes to spatial disparities.

The presence of inequality, both regionally and spatially, is represented by Cluster 7 as a distinct research avenue. Regional innovation, university linkages, and clustering approaches are included in Cluster 8's integration of innovation & competitiveness literature and regional innovation. The basic theoretical perspectives on the spatial concentration of economic activity are represented by agglomeration theory and the new economic geography, which Cluster 9 pertains to. The nine-cluster structure is described qualitatively based on the thematic composition visible in the network. Because the archived materials available for this revision do not contain item-level VOSviewer statistics, quantitative cluster totals, occurrence counts, and total link strength values cannot be reported reliably and have therefore not been reconstructed retrospectively.

The resulting network is dominated by broader concepts such as regional development, peripheral regions, core-periphery relations, and spatial inequality rather than by explicit R&D – access terminology. This pattern is analytically important because it indicates that, even within a corpus constructed around research, inequality, accessibility, and spatial descriptors, the literature tends to articulate these issues through established regional-development and economic – geography vocabularies rather than through a consolidated terminology of "R&D access". Accordingly, the absence of a prominent access – specific node is interpreted here as an indication of terminological and thematic fragmentation rather than as evidence that the underlying substantive issue is absent from the literature.

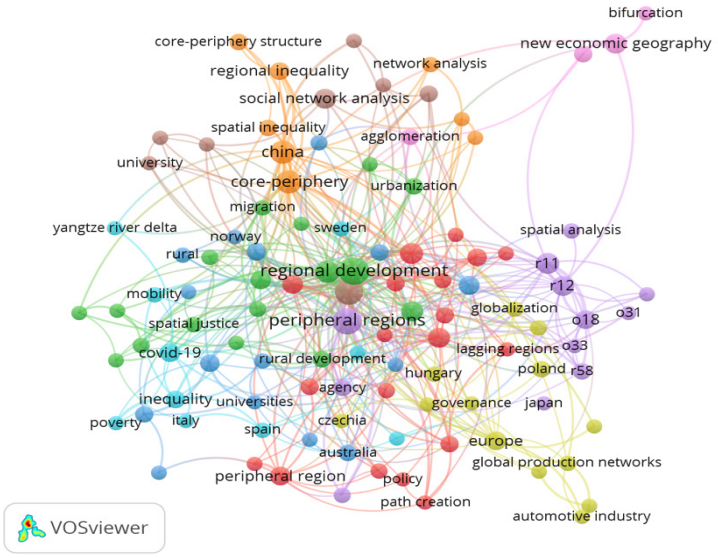


Figure 2 – Network visualization of author-keyword co-occurrence based on the integrated Scopus and Web of Science dataset (2014–2025)

The nine clusters identified in the network are described and interpreted in the accompanying text; the color coding in the visualization corresponds to the cluster structure generated by VOSviewer. Although the network map captures the structural configuration of the field, it does not reflect its temporal dynamics. To overcome this limitation, the overlay visualization is examined.

Fig. 3 illustrates the evolution of the field over time, showing that earlier contributions are closely associated with foundational concepts in economic geography, such as agglomeration and core-periphery models. The colour scale in the overlay visualization represents the average publication year of each keyword rather than the full temporal coverage of the dataset. Therefore, although the bibliometric dataset covers 2014 – 2025, the displayed colour range is narrower because the average publication years of the keywords included in the network fall predominantly within this interval.

Recent works, however, begin to pay attention to spatial and territorial inequality, regional resilience, and place-based policies. Other recent works on spatial justice, accessibility, and research infrastructure, illustrate a growing focus on the more explicit consideration of the mechanisms involved in the unequal distribution of resources.

The visualization suggests that themes directly related to inequality in access to R&D are less visibly consolidated than dominant themes such as regional development, peripheral regions, and core–periphery relations. In the absence of archived item-level occurrence and total link strength statistics, this pattern is interpreted as a qualitative bibliometric indication rather than as a quantitative ranking of thematic importance.

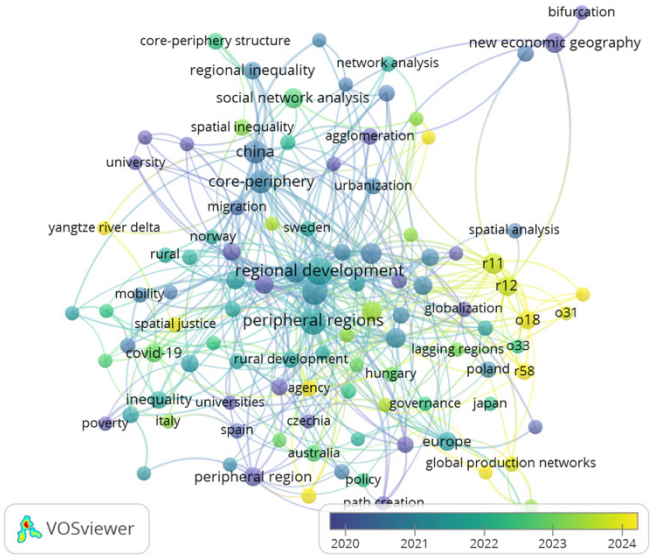


Figure 3 – Overlay visualization of the same author-keyword network according to average publication year

Beyond structural and temporal analyses, density visualizations offer supplementary insights into research activity intensity across different thematic domains.

As illustrated in Fig. 4, the density map indicates that research activity is most strongly concentrated around regional development and peripheral regions, which function as central integrative frameworks within the field. By contrast, themes related to inequality and access to research resources occupy medium-density areas, suggesting that while the topic remains insufficiently consolidated, it is gradually gaining traction in the literature.

Research infrastructure, spatial inequality, and territorial inequality appear within the broader thematic structure, but their relative prominence cannot be established quantitatively from the archived visualization alone. Their position is therefore interpreted cautiously as evidence of a comparatively weakly consolidated thematic area.

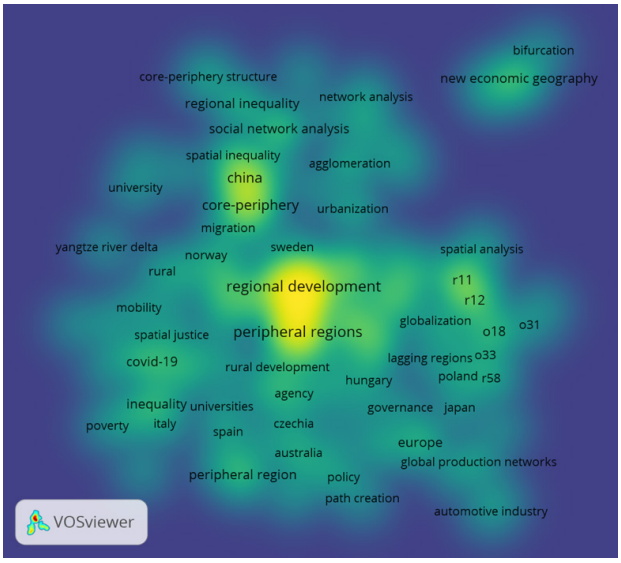


Figure 4 – Density visualization of the same author-keyword network, highlighting areas of relatively higher keyword concentration

Discussion

The results of this research show that insufficient R&D access-related inequalities do exist in the scientific debate. These structural inequalities are in theories that replace the problem. This brings us to the question, why do these theories remain so poorly developed? In some measure, this is due to the emphasis in the knowledge-centered paradigm which considers knowledge development, dissemination, and collaboration as the main processes. In this paradigm, the concern is directed to the performance of the system and the dynamics of the network. The mobility of research capacity is presumed to be critically underappreciated. Therefore, it is presumed that throughout the process, the system, and the structure, the inequalities of the system which are outcomes of system inefficiencies are the end results. This focus is reinforced by the unbroken prevalence of the RIS framework. Innovation Systems RIS literature describes the way innovation systems work. It explains the systemic interaction and the system cohesion. However, the literature does not describe the distribution of access to these systems. This leads to an imbalance where access to fundamental resources is seen as differences in the overall quality of the system. The same is seen in economic geography where inequalities and disparities are accounted for agglomeration and cumulative causation. However, this perspective gives less explicit attention to inequalities in the distribution of R&D capacity and to the cumulative disadvantages that may arise from unequal access to research resources. Finally, the placement of R&D on the bibliometric maps shows a marginal position. The research positions are floating. Fragmentation of the research is seen throughout the multi-disciplinary, multi-tradition branches of research.

The implications of this conceptual gap are pronounced. First, it reduces the effectiveness of current theories to account for long-standing regional inequalities. Second, it limits the range of policies to those aimed at the improvement of system efficiency rather than the alleviation of structural imbalances of the research capacity. Third, it continues the process of cumulative advantage by strengthening the hold of existing developed regions in the global research arena.

Recent studies similarly demonstrate persistent inequalities in scientific participation and the cumulative concentration of scientific capacity across regions and research systems [19, 20].

This study posits that access to R&D should be framed as a separate dimension. This will enhance the understanding of regional disparities, not simply as a difference in the result, but as an imbalance of the underlying conditions in the production of knowledge.

Limitations

This study has several limitations that should be considered when interpreting its findings. First, the analysis relies on author – provided keywords. A concept related to unequal access to R&D may therefore be present in an article without being expressed through the exact terminology visible in the bibliometric network; related ideas may appear under alternative labels such as research capacity, scientific capacity, research infrastructure, or science funding. Second, the use of Scopus and the Web of Science Core Collection and the restriction to English-language peerr – eviewed journal articles introduce database and language coverage biases, which are particularly relevant in a study of global research inequality. Third, the minimum occurrence threshold of five affects which keywords are included in the final network and may exclude rare but conceptually important terms. Fourth, keyword co-occurrence analysis primarily reflects the vocabulary and relational structure of a research field rather than its full conceptual substance. Accordingly, the comparatively weak visibility of explicit R&D – access terminology should be interpreted as evidence of limited thematic consolidation rather than as proof that the underlying substantive issue is absent from the literature.

Conclusion

Inequality in access to R&D represents an underdeveloped area within research on the regional dimensions of the global knowledge landscape. Most research has focused on innovation systems, the spread of knowledge, and the uneven allocation of economic outcomes. The uneven distribution of research capacity is a gap in the literature that has yet to be explicitly defined as a field of inquiry.

Using a bibliometric mapping approach with broad and focused levels of interpretation, this study identifies patterns of thematic underrepresentation in the coverage of research topics. The most dominant knowledge – centered paradigms tend to privilege systems interactions and knowledge flow, and the distributive side of research capacity is less explicitly defined. The structure of the research suggests that the inequality of access to R&D is embedded within the RIS, economic geography, and institutional theory, yet lacks a defined research trajectory.

This research contributes to the literature by providing bibliometric evidence supporting the conceptualization of inequality in access to R&D as a distinct analytical dimension of regional inequality. By defining the inequities of the research environment, the scientific knowledge, and the institutional support as structural weaknesses of an innovation system, it enhances and enriches the existing frameworks on the regional development dynamics.

The analysis also illustrates the value of examining both dominant and comparatively weak thematic positions within a bibliometric network. This approach helps identify research topics that may be present in the literature but remain fragmented or insufficiently consolidated relative to established research streams.

From a conceptual and policy perspective, the findings suggest that regional innovation strategies may benefit from greater attention to the territorial distribution of research capacity and access to R&D resources. This implication follows from the conceptual argument developed in the study rather than from a causal effect demonstrated by the bibliometric analysis. Addressing structural barriers to research infrastructure, scientific capacity, and institutional participation may therefore represent a relevant direction for future regional innovation policy and empirical investigation.

The research emphasizes the need to improve the inclusion construct in innovation research and opens the door for the analysis of the structurally embedded inequities in the knowledge production processes. More in-depth studies could analyze the interconnections between the distribution of research facilities, the presence or absence of institutional hindrances, and regional innovation performance.

Author Contributions. The authors contributed to the conceptualization, methodology, analysis, interpretation of results, and preparation of the manuscript. All authors reviewed and approved the final version of the manuscript.

Conflict of Interest. The authors declare no conflict of interest.

Data Availability. The bibliographic data analyzed in this study were retrieved from Scopus and the Web of Science Core Collection. The processed item-level bibliometric dataset and VOSviewer network files are not publicly archived. The methodological parameters required to understand the search and analytical procedure are reported in the manuscript.

Funding. This research has been funded by the Science Committee of the Ministry of Science and Higher Education of the Republic of Kazakhstan (Grant No. AP26198249: An exploration of innovative approaches to overcoming regional inequality in access to R&D in the interest of boosting the intellectual vanguard of Kazakhstan).

REFERENCES

1 Armbrecht, F.M.R. Jr., Chapas, R.B., Chappelow, C.C., Farris, G.F., Friga, P.N., Hartz, C.A., McIlvaine, M.E., Postle, S.R., and Whitwell, G.E. Knowledge management in research and development. Research Technology Management, 44 (4), 28–48 (2001). https://doi.org/10.1080/08956308.2001.11671438

2 Asheim, B., and Coenen, L. The role of regional innovation systems in a globalizing economy. In: Vertova, G. (ed.) The Changing Economic Geography of Globalization (Routledge, 2006), pp. 139–155. https://doi.org/10.4324/9780203000403-9

3 Asheim, B.T., Grillitsch, M., and Trippl, M. Regional innovation systems: past–present–future. In: Handbook on the Geographies of Innovation (Cheltenham: Edward Elgar, 2016), pp. 45–62.

4 Sterlacchini, A. R&D, higher education and regional growth: uneven linkages among European regions. Research Policy, 37 (6–7), 1096–1107 (2008). https://doi.org/10.1016/j.respol.2008.04.009

5 Garud, R., Tuertscher, P., and Van de Ven, A.H. Perspectives on innovation processes. Academy of Management Annals, 7 (1), 775–819 (2013). https://doi.org/10.1080/19416520.2013.791066

6 Shujahat, M., Sousa, M.J., Hussain, S., Nawaz, F., Wang, M., and Umer, M. Translating the impact of knowledge management processes into knowledge-based innovation: the neglected and mediating role of knowledge-worker productivity. Journal of Business Research, 94, 442–450 (2019). https://doi.org/10.1016/j.jbusres.2017.11.001

7 Fischer, M.M. Innovation, knowledge creation and systems of innovation. The Annals of Regional Science, 35 (2), 199–216 (2001). https://doi.org/10.1007/s001680000034

8 Ortega, A.M., and Serna, M. Determinants of innovation performance of organizations in a regional innovation system from a developing country. International Journal of Innovation Science, 12 (3), 345–362 (2020). https://doi.org/10.1108/IJIS-03-2020-0023

9 Audretsch, D.B., and Feldman, M.P. Knowledge spillovers and the geography of innovation. In: Handbook of Regional and Urban Economics (Amsterdam: Elsevier, 2004), Vol. 4, pp. 2713–2739.

10 Kim, S. Spatial inequality and economic development: theories, facts, and policies. In: Urbanization and Growth (Washington, DC: World Bank, 2008), pp. 133–166.

11 McCann, P., and Van Oort, F. Theories of agglomeration and regional economic growth: a historical review. In: Handbook of Regional Growth and Development Theories (Cheltenham: Edward Elgar Publishing, 2019), pp. 6–23.

12 Copus, A.K. From core-periphery to polycentric development: concepts of spatial and aspatial peripherality. European Planning Studies, 9 (4), 539–552 (2001). https://doi.org/10.1080/713666491

13 Camagni, R., and Capello, R. Knowledge-based economy and knowledge creation: the role of space. In: Growth and Innovation of Competitive Regions: The Role of Internal and External Connections (Berlin: Springer, 2009), pp. 145–165.

14 Parente, S. The failure of endogenous growth. Knowledge, Technology & Policy, 13 (4), 49–58 (2001). https://doi.org/10.1007/BF02693989

15 Desmet, K., Greif, A., and Parente, S.L. Spatial competition, innovation and institutions: the Industrial Revolution and the Great Divergence. Journal of Economic Growth, 25 (1), 1–35 (2020). https://doi.org/10.1007/s10887-019-09173-3

16 van Eck, N.J., and Waltman, L. Software survey: VOSviewer, a computer program for bibliometric mapping. Scientometrics, 84 (2), 523–538 (2010). https://doi.org/10.1007/s11192-009-0146-3

17 Zupic, I., and Čater, T. Bibliometric methods in management and organization. Organizational Research Methods, 18 (3), 429–472 (2015). https://doi.org/10.1177/1094428114562629

18 Donthu, N., Kumar, S., Mukherjee, D., Pandey, N., and Lim, W.M. How to conduct a bibliometric analysis: An overview and guidelines. Journal of Business Research, 133, 285–296 (2021). https://doi.org/10.1016/j.jbusres.2021.04.070

19 Kozlowski, D., Larivière, V., Sugimoto, C.R., and Monroe-White, T. Intersectional inequalities in science. Proceedings of the National Academy of Sciences, 119 (2), e2113067119 (2022). https://doi.org/10.1073/pnas.2113067119

20 Servedio, V.D.P., Ferreira, M.R., Reisz, N., Costas, R., and Thurner, S. Scale-free growth in regional scientific capacity building explains long-term scientific dominance. Chaos, Solitons & Fractals, 167, 113020 (2023). https://doi.org/10.1016/j.chaos.2022.113020

[1]Тургинбаева А.Н.,
э.ғ.д., ORCID ID: 0000-0003-4208-6167,
e-mail: ardakt@illinois.edu
[2]Серикбай Д.Д.,
э.ғ.м., ORCID ID: 0009-0000-4821-7733,
e-mail: d.serikbay@kbtu.kz
[1]*Анархан А.К.
докторант, ORCID ID: 0009-0008-9014-3385,
*e-mail: aizhan2790@gmail.com

[1]Әл-Фараби атындағы Қазақ ұлттық университеті, Алматы қ., Қазақстан
[2]Қазақстан-Британ техникалық университеті, Алматы қ., Қазақстан

ҒЗТКЖ-ҒА ҚОЛЖЕТІМДІЛІКТЕГІ ТЕҢСІЗДІКТІ КАРТАЛАУ: ЖАҺАНДЫҚ ЗЕРТТЕУ ЛАНДШАФТЫНА ҚОС БИБЛИОМЕТРИЯЛЫҚ ТАЛДАУ

Аңдатпа

Бұл жұмыс жаһандық зерттеу ландшафтындағы ҒЗТКЖ-ға қол жеткізу теңсіздігінің көрінісін қарастырады және оның жеке аналитикалық категория ретінде тұжырымдамалық тұрғыдан дамымау себептерін бағалайды. Аймақтық инновациялық жүйелер (RIS), экономикалық география және институционалдық теория салаларында көптеген зерттеулер жүргізілгенімен, қолданыстағы еңбектер жүйедегі үдерістер мен шарттарға және білім өндірісіне кімнің қатыса алатынына емес, инновация нәтижелері мен оның түпкілікті өнімдеріне бағытталған. Ғылыми-зерттеу инфрақұрылымындағы, ғылыми әлеуеттегі, ғылыми зерттеулер жүргізуге арналған қаржылық ресурстардағы және ғылыми зерттеулерді қаржыландырудағы теңгерімсіздік теориялық тұрғыдан жеткіліксіз негізделген және көп жағдайда қолданыстағы басым теорияларда тиісті деңгейде қарастырылмаған. Бұл зерттеу 2014–2025 жж. Scopus және Web of Science деректеріне негізделген библиометриялық карталаумен бекітілген қосарлы зерттеу әдістемесін пайдалану арқылы осы бағытта ілгерілеуге ұмтылады. Зерттеуде қолданылған әдістеме негізгі зерттеу салаларының картасы мен қол жеткізу және теңсіздікке қатысты әртүрлі тұжырымдамалардың неғұрлым бағдарланған картасын біріктіреді, бұл басым және шеткері тақырыптық бағыттарды анықтауға мүмкіндік береді. ҒЗТКЖ-ға қол жеткізудің маңыздылығы мойындалғанымен, тең емес жағдайларда ҒЗТКЖ-ға қол жеткізу мәселесі көптеген зерттеу салалары мен бір-бірінен ажыратылмаған шеткері зерттеу бағыттары арасында шашыраңқы қарастырылған. Зерттеу библиометриялық теорияны жетілдіреді, ҒЗТКЖ-ға қол жеткізуді аймақтық теңсіздіктің зерттеу өлшемі ретінде қарастырады және жаһандық зерттеу жүйесіндегі қосарлы теңгерімсіздікті айқындайды.

Түйін сөздер: ҒЗТКЖ-ға қол жеткізудегі теңсіздік, аймақтық инновациялық жүйелер, экономикалық география, библиометриялық талдау, қосарлы кескіндеу, ғылыми-зерттеу инфрақұрылымы, кеңістіктік теңсіздік, білімді өндіру, аймақтық теңсіздік.

[1]Тургинбаева А.Н.,
д.э.н., ORCID ID: 0000-0003-4208-6167,
e-mail: ardakt@illinois.edu
[2]Серикбай Д.Д.,
м.э.н., ORCID ID: 0009-0000-4821-7733,
e-mail: d.serikbay@kbtu.kz
[1*]Анархан А.К.,
докторант, ORCID ID: 0009-0008-9014-3385,
e-mail: aizhan2790@gmail.com

[1]Казахский национальный университет им. аль-Фараби, г. Алматы, Казахстан
[2]Казахстанско-Британский технический университет, г. Алматы, Казахстан

КАРТИРОВАНИЕ НЕРАВЕНСТВА В ДОСТУПЕ К НИОКР: ДВОЙНОЙ БИБЛИОМЕТРИЧЕСКИЙ АНАЛИЗ ГЛОБАЛЬНОГО ИССЛЕДОВАТЕЛЬСКОГО ЛАНДШАФТА

Аннотация

В данной статье рассматривается представление неравенства в доступе к НИОКР в глобальном исследовательском ландшафте и оцениваются причины отсутствия его концептуального развития как самостоятельной аналитической категории. Несмотря на значительную работу в области региональных инновационных систем (РИС), экономической географии и институциональной теории, существующие исследования сосредоточены на результатах инноваций и конечных продуктах инноваций, а не на процессах и условиях внутри системы и на том, кто участвует в производстве знаний. Дисбаланс в исследовательской инфраструктуре, научном потенциале, финансовых ресурсах для проведения исследований и финансировании научных исследований плохо теоретизирован и в большинстве случаев некорректно рассматривается в существующих доминирующих теориях. Данное исследование направлено на достижение прогресса в этой области с использованием двойной методологии исследования, основанной на библиометрическом картировании на основе данных Scopus и Web of Science за 2014–2025 гг. Методология, использованная в данном исследовании, сочетает в себе картирование основных исследовательских областей и более целенаправленное картирование различных концепций, связанных с доступом и неравенством, что позволяет выявить как доминирующие, так и маргинальные тематические структуры. Признана возможность доступа к НИОКР; однако доступ к НИОКР на неравных условиях, по-видимому, фрагментирован по многим исследовательским областям и неразличимым периферийным областям исследований. Исследование расширяет библиометрическую теорию, рассматривает доступ к НИОКР как исследовательский аспект регионального неравенства и проливает свет на двойной дисбаланс в глобальной исследовательской системе.

Ключевые слова: неравенство в доступе к НИОКР, региональные инновационные системы, экономическая география, библиометрический анализ, двойное картирование, исследовательская инфраструктура, пространственное неравенство, производство знаний, региональное неравенство.

REQUIREMENTS TO THE DESIGN OF ARTICLES PUBLISHED IN THE JOURNAL KBTU BULLETIN

Previously **unpublished material by the author (s)** corresponding to the profile of the journal in Russian, Kazakh or English is accepted for publication. The article is provided in electronic format (in formats .doc, .docx,) only by downloading it through the functionality of the journal's website (https://vestnik.kbtu.edu.kz/jour/about), which has detailed instructions for authors on the process of submitting articles, as well as on payment for publication.

Mandatory requirements for registration:

- The MRNTI index is placed in the upper-left corner. (Times New Roman 14 size)
- One single interval below the authors ' surnames and initials in bold. Detailed names of organizations, cities, countries where the work was performed, e-mail of one of the authors. Specify footnotes to the place of work of the authors.
- Below, in one interval, the full title of the article is in bold.
- Below, a brief (150–250 words) abstract (abstract) at one interval. Abstract should outline the general orientation of the article and formulate its main results and be self-sufficient, it should not contain references to literary sources or to any sections and elements of the article to which it relates.
- Key words related to the submitted article.

The text of the article is typed in a straight font Times New Roman, size 14. The line spacing is single. All fields are 2 cm long.

The article should be divided into sections: Introduction, Materials and Methods, Results and Discussion, Conclusion, Information on funding (if available).

At the end, a "List of References" is given. Literary references in the text are in square brackets [1]. The list of references is drawn up twice: according to the above GOST. The list should fully correspond to the main text of the article, contain all the works mentioned (and only mentioned) in it. Next, the same list of references should be presented in the generally accepted English transliteration (see the sample of the literature design below).

The article undergoes "blind" review, reviewers are appointed by the editorial board of the journal.

At the end of the article please indicate full name, return address, phone numbers, fax, e-mail address.

The author(s) are responsible for the content of the article. The opinion of the Scientific and Editorial Board does not always coincide with the opinion of the author (authors). The Editorial Board reserves the right to publish or reject articles.

The reference to our edition in reprinting is obligatory.

Our address: **59, Tole Bi St., Almaty, 050000, Kazakhstan-British Technical University.**
Website: https://vestnik.kbtu.edu.kz/jour/pages/view/EditorialC Editorial Board.

ЖУРНАЛЫНДА ЖАРИЯЛАНАТЫН МАҚАЛАЛАРДЫ РӘСІМДЕУГЕ ҚОЙЫЛАТЫН ТАЛАПТАР

Жариялау үшін **автормен (авторлармен) бұрын жарияланбаған,** журнал бейініне сәйкес келетін орыс, қазақ немесе ағылшын тілдеріндегі материалдар қабылданады. Мақала журнал сайтының (https://vestnik.kbtu.edu.kz/jour/about) функционалдығы арқылы жүктеу жолымен тек электронды форматта (.doc, .docx форматтарында) қабылданады, сайтта авторларға мақаланы жүктеу, ұсыну үрдісі туралы, сондай-ақ жарияланымға ақы төлеу туралы толық нұсқаулық бар.

Ресімдеу бойынша міндетті талаптар:

Жоғарғы сол жақ бұрышта ҒТАМИ индексі жазылады. (Times New Roman 14 өлшем)

- Бір бірлік интервалдан кейін авторлардың тегі мен аты-жөні жартылай қалың қаріппен жазылады. Жұмыс орындалған ұйымдардың, қалалардың, елдердің толық атаулары, авторлардың бірінің e-mail поштасы көрсетіледі. Авторлардың жұмыс орнына сілтеме беріледі.
- Бір интервалдан кейін мақаланың толық атауы жартылай қалың қаріппен жазылады.
- Бір интервалдан кейін қысқаша (150–250 сөз) аңдатпа (abstract) ұсынылады. Аңдатпа мақаланың жалпы бағытын көрсетіп, оның негізгі нәтижелерін тұжырымдауы тиіс, аңдатпада әдеби дереккөздерге де, оған қатысты мақаланың кез-келген бөлімдері мен элементтеріне сілтеме жасауға болмайды.
- Ұсынылған мақалаға қатысты кілт сөздер (тірек сөздер) жазылады.

Мақала мәтіні 14 өлшемді Times New Roman шрифтімен теріледі. Жолдар арасында бірлік интервал сақталады. Шеттер – барлық жағынан 2 см.

Мақала келесі бөлімдерді қамтуы тиіс: Кіріспе, Материалдар және әдістер, Нәтижелер мен талқылау, Қорытынды, Қаржыландыру туралы ақпарат (болған жағдайда көрсетіледі).

Соңында «Әдебиеттер тізімі (References)» жазылады. Мәтіндегі әдеби сілтемелер төртбұрышты жақшада ұсынылады [1]. Әдебиеттер тізімі МЕМСТ-ке сәйкес екі рет рәсімделеді. Тізім мақаланың негізгі мәтініне толық сәйкес келіп, мақалада аталған (тек аталған) барлық жұмыстарды қамтуы керек. Әрі қарай, дәл осы сілтемелер жалпы қабылданған ағылшын транслитерациясында жазылады.

Мақала «жасырын» рецензиялаудан өтеді, рецензенттерді журналдың редакиялық алқасы тағайындайды.

Мақаланың соңында авторлардың толық аты-жөнін, кері байланыс мекенжайын, телефондар, факс және электрондық пошта мекенжайын (e-mail) жазуыңызды сұраймыз.

Мақаланың мазмұнына автор (авторлар) жауапты. Ғылыми-редакция алқасының пікірі әрдайым автордың (авторлардың) пікірімен сәйкес келе бермейді. Редакция алқасы мақалаларды жариялау немесе қабылдамау құқығын өзіне қалдырады.

Қайта басылым кезінде біздің жарияланымға сілтеме жасау керек.

Мекенжайымыз: **050000, Алматы қ., Төле би көш., 59, Қазақстан-Британ техникалық университеті.**

Сайт: https://vestnik.kbtu.edu.kz/jour/pages/view/EditorialC Редакция алқасы.

ТРЕБОВАНИЯ К ОФОРМЛЕНИЮ СТАТЕЙ, ПУБЛИКУЕМЫХ В ЖУРНАЛЕ ВЕСТНИК КБТУ

Для публикации принимается **ранее неопубликованный автором (авторами) материал**, соответствующий профилю журнала, на русском, казахском или английском языках. Статья предоставляется в электронном формате (в форматах .doc, .docx,) только путем ее загрузки через функционал сайта журнала (https://vestnik.kbtu.edu.kz/jour/about), в котором имеется подробная инструкция для авторов о процессе подачи статей, а также об оплате публикации.

Обязательные требования по оформлению:

- В левом верхнем углу ставится индекс МРНТИ (Times New Roman 14 размер).
- Через один одинарный интервал ниже фамилии и инициалы авторов полужирным шрифтом. Развернутые названия организаций, городов, стран, где выполнена работа, e-mail одного из авторов. Указать сноски на место работы авторов.
- Ниже через один интервал полное название статьи полужирным шрифтом.
- Ниже через один интервал краткая (150–250 слов) аннотация (abstract). Аннотация должна обрисовывать общую направленность статьи, формулировать ее основные результаты и быть самодостаточной, в ней недопустимы ссылки ни на литературные источники, ни на какие-либо разделы и элементы статьи, к которой она относится.
- Ключевые слова (Key words), относящиеся к представляемой статье.

Текст статьи набирается прямым шрифтом Times New Roman, размер 14. Интервал между строками одинарный. Поля все по 2 см.

Статья должна быть разделена на разделы: Введение, Материалы и методы, Результаты и обсуждение, Заключение, Информация о финансировании (при наличии).

В конце дается «Список литературы (References)». Литературные ссылки в тексте в квадратных скобках [1]. Список литературы оформляется дважды: согласно ГОСТу. Список должен полностью соответствовать основному тексту статьи, содержать все упомянутые (и только упомянутые) в нем работы. Далее тот же список литературы представить в общепринятой английской транслитерации.

Статья проходит «слепое» рецензирование, рецензенты назначаются редколлегией журнала.

В конце статьи просим указать Ф.И.О. полностью, обратный адрес, телефоны, факс, адрес электронной почты (e-mail).

Ответственность за содержание статьи несет автор (авторы). Мнение Научно-редакционного совета не всегда совпадает с мнением автора (авторов). Редакционный совет оставляет за собой право публикации или отклонения статей.

Ссылка на наше издание при перепечатке обязательна.

Наш адрес: **050000, г. Алматы, ул. Толе Би, 59, Казахстанско-Британский технический университет.**

Сайт: https://vestnik.kbtu.edu.kz/jour/pages/view/EditorialC Редакционная коллегия.

ҚАЗАҚСТАН-БРИТАН ТЕХНИКАЛЫҚ УНИВЕРСИТЕТІНІҢ
ХАБАРШЫСЫ

HERALD
OF THE KAZAKH-BRITISH TECHNICAL UNIVERSITY

ВЕСТНИК
КАЗАХСТАНСКО-БРИТАНСКОГО ТЕХНИЧЕСКОГО УНИВЕРСИТЕТА

Ответственный за выпуск
Алагузов Рашид Жуманович

Редакторы
Кабылдаева Толганай Кайсаровна,
Скуратова Ирина Михайловна

Компьютерная верстка
Жуйкова Майя Антоновна

Подписано в печать 15.09.2026 г.
Тираж 300 экз. Формат 60x84 1/16.
Бумага тип. Усл.печ.л. 82,5 Уч.-изд.л. 85,8
Заказ №

Издание Казахстанско-Британского технического университета
Издательский центр КБТУ, Алматы, ул. Толе би, 59